14th International Conference on Clouds and Precipitation

Proceedings — Volume 1

Bologna, Italy

19-23 July 2004

Front cover: *Peace and charm of morning haze on the hills at sunrise*
Photograph (©) C. Doswell, all rights reserved. Used by permission.

Back cover: *Regularity and depth of a fair weather cumulus field reflecting in a pond*
Photograph (©) C. Doswell, all rights reserved. Used by permission.

Foreword

The 14th International Conference on Clouds and Precipitation continues the long tradition of this conference. The sites and dates of the previous 13 conferences show that this conference series is indeed international. Since the first conference was held in Zürich in 1954, this meeting represents the 50th anniversary. Today, our field of science is evolving and changing. We have just begun to understand many critical problems associated with clouds and precipitation. Although much progress has been made, we are envious of the younger generation of scientists who have so many interesting scientific challenges ahead of them.

The main work of the International Commission on Clouds and Precipitation revolves around organizing this conference every four years, as well as special meetings during the IAMAS and IUGG Conferences. All Commission members were involved in preparing the Program. We had 685 papers submitted and a total of 538 extended abstracts made it into these Proceedings. They are distributed over a large range of topics from Aerosol-Cloud Interactions to Microphysics of Clouds and Precipitation, from Modeling of Cloud-scale Processes to Cloud Dynamics and Structure, and Cloud Processes and the Mesoscale. A table elsewhere shows the individual topics and the numbers of papers on each subject.

The Commission made a firm choice not to have parallel sessions, which made it difficult to select papers for oral presentation. This selection process involved making decisions about regional and institutional representation, topic, encouragement of new scientists, etc, using very brief abstracts. As a consequence, much of the good science is given in the poster sessions. It will be difficult to digest all the new and interesting information in the papers being presented, so hopefully, participants will go home and examine the printed Proceedings and associated CD in greater depth and ask their colleagues for more information.

There is no permanent office which helps organize the conference and prepare the Proceedings. The process involves many people volunteering their time and working long hours. It has been a pleasure to work with these dedicated people and we are very appreciative of their efforts. Lists of the Program (all ICCP members) and Local Arrangements Committees are given on separate pages. However, we would like to especially thank Maria Teresa Tibaldi and Vincenzo Levizzani for the local organization and Monika Bailey for her work on the preparation of the Conference Program.

George Isaac
President, ICCP and
Chair, Program Committee

Sandro Fuzzi
Chair, Local Arrangements
Committee

14th International Conference on Clouds and Precipitation
Bologna, Italy
18-23 July 2004

Conference Organization

International Commission on Clouds and Precipitation (ICCP)

(All members were on the Program Committee)

G.A. Isaac, President	Canada	Z. Levin, Vice President	Israel
D. O'C. Starr, Secretary	USA		
M. Barth	USA	A. Blyth.	UK
A. Bott	Germany	N. Chaumerliac	France
A. Chernikov	Russia	T. Choularton	UK
P.C.S. Devara	India	Yasushi Fujiyoshi	Japan
S. Fuzzi	Italy	W.W. Grabowski	USA
J. Hallett	USA	J. Jensen	USA
A. Korolev	Canada	D. Lamb	USA
H. Larsen	New Zealand	Jinli Liu	China
U. Lohmann	Canada	S. P. Malinowksi	Poland
M. Nicolini	Argentina	K.J. Noone	Sweden
G. Raga	Mexico	J. Stith	USA
D. Terblanche	South Africa		

Honorary Members: Sir John Mason, UK and H. Pruppacher, Germany
Past Presidents: P. Jonas, UK and P. Hobbs, USA

Local Arrangements Committee

Sandro Fuzzi, Chair
Vincenzo Levizzani, Deputy chair
Franco Prodi, ISAC Director
Maria Teresa Tibaldi, Secretary
Giuseppe Bortolotti, Francescopiero Calzolari, Elsa Cattani, Fabrizia Cavalli, Stefano Decesari, Lorenza Emblico, Maria Cristina Facchini, Carlo Franceschi, Elisabetta Masetti, Mihaela Mircea, Francesca Pollini, Sara Poluzzi, Fabrizio Roccato, Francesca Torricella, Giuliano Trivellone

The International Commission on Clouds and Precipitation

dedicates

the 14th International Conference on Clouds and Precipitation

to

Prof. Dr. Hans R. Pruppacher

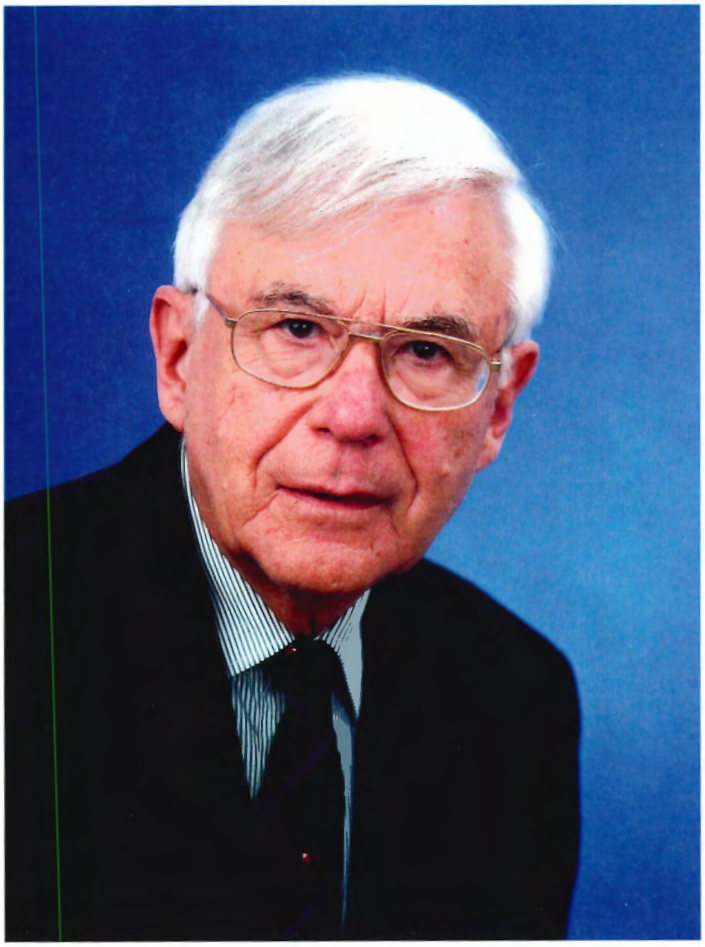

for his fundamental contribution to increase the level of understanding of clouds and precipitation and their physical and chemical mechanisms. Hans Pruppacher has dedicated a lifetime to explore the frontiers of cloud microphysics, steer interdisciplinary research, and teach a great number of students the fundamentals of science and life.

Thank you, Hans!

Paper	Table of Contents – Papers	Page

TOPIC 1: AEROSOL-CLOUD INTERACTIONS

1:1 ENTRAINMENT, DRIZZLE, AND STRATOCUMULUS CLOUD ALBEDO 1
Andrew Ackerman, Michael Kirkpatrick, David Stevens, Owen Toon

1:2 EVIDENCE FOR NATURAL VARIABILITY IN MARINE STRATOCUMULUS CLOUD PROPERTIES DUE TO CLOUD-AEROSOL INTERACTIONS 5
Bruce Albrecht, Tarah Sharon, Haf Jonsson, Patrick Minnis, J. Kirk Ayers, Mandana M. Khaiyer

1:3 RELATIONSHIP BETWEEN CIRRUS ANVIL ICE CRYSTAL PROPERTIES AND AEROSOL CONCENTRATION, AMBIENT RELATIVE HUMIDITY AND VERTICAL VELOCITY DURING CRYSTAL-FACE 9
Constantin Andronache, Vaughan Phillips

1:4 COMPARISONS OF MICROPHYSICAL MODEL AND BULK METHOD ESTIMATIONS OF SULFATE AEROSOL WET SCAVENGING RATES 13
Constantin Andronache

1:5 IN-SITU MASS SPECTROMETRIC MEASUREMENTS OF AIRCRAFT EXHAUST AEROSOL PARTICLES 17
Stephan Borrmann, S. Henseler, N. Hock, S. Weimer, B. Kärcher, A. Petzold, J. Schneider

1:6 MEASUREMENTS OF CLOUD–AEROSOL INTERACTIONS IN WARM CLOUDS AT THE JUNGFRAUJOCH MOUNTAIN TOP SITE IN SWITZERLAND 20
Keith Bower, M. R. Alfarra, M. J. Flynn, Martin Gallagher, Hugh Coe, Thomas Choularton, E. Weingartner, C. Corrigan, M. Gysel, U. Baltensperger

1:7 CHANGES IN SIZES AND CHEMICAL COMPOSITION OF CCN IN POLLUTED ENVIRONMENTS AND THE EFFECTS ON CLOUD AND PRECIPITATION DEVELOPMENT 24
Roelof T Bruintjes, Li Jia, Peter Busek, Vidal Salazar, Daniel Breed , T. Jensen, Kristy Ross, Stuart Piketh

1:8 TEMPORAL AND SPATIAL VARIABILITY OF MINERAL AEROSOLS FROM NORTH AFRICA 28
Leila Carvalho, Charles Jones, Natalie M. Mahowald, Chao Luo

1:9 SATELLITE OBSERVATION AND RADIATIVE MODELING OF THE INFLUENCE OF AEROSOL PARTICLES FROM BIOMASS BURNING ON CLOUD MICROPHYSICAL PROPERTIES 32
Elsa Cattani, Vincenzo Levizzani, Ana Maria Silva

1:10 A MODELING STUDY OF AEROSOL IMPACTS ON PRECIPITATION AND CLOUD-RADIATIVE PROPERTIES USING A WARM CLOUD PARAMETERIZATION 35
Chao-Tzuen Cheng, Wei-Chyung Wang, Jen-Ping Chen

1:11 THE INFLUENCE OF AEROSOL ON THE MICROPHYSICS AND PRECIPITATION FROM MIXED PHASE LAYER AND CONVECTIVE CLOUD. 39
Thomas Choularton, K. Bower, H. Coe, J. Allan, M. Cubison, M.W. Gallagher, G. McFiggans, D. Grosvenor , P. Clarke , P. Williams

1:12 SIMULATIONS OF ICE CRYSTAL NUCLEATION AND GROWTH: RESULTS FROM THE AIDA CLOUD EXPANSION CHAMBER 43
Paul Connolly, Paul Field, Ottmar Moehler, S. Büttner, H. Saathoff, A. J. Heymsfield, M. W. Gallagher, T. W. Choularton

1:13 SATELLITE DERIVED CLOUD PROPERTIES RELEVANT FOR CLOUD RADIATIVE FORCING: A CASE STUDY OF INTERACTION BETWEEN CLOUDS AND DUST AEROSOL PARTICLES 47
M. J. Costa, E. Cattani, A. M. Silva, V. Levizzani

1:14 CONSIDERATION OF CLOUD DYNAMICS EFFECTS ON THE PARAMETERIZATION OF CLOUD RADIATIVE PROPERTIES 51
Peter Daum, Yangang Liu

1:15 PRELIMINARY STUDY ON TROPOSPHERIC ION-INDUCED NUCLEATION 55
Raffaella D'Auria, Richard P. Turco

1:16 PHYSICAL AND CHEMICAL IMPACTS ON THE ICE NUCLEATING PROPERTIES OF ATMOSPHERIC PARTICLES 59
Paul Demott, Daniel Cziczo, Jose Jimenez, Sarah Brooks, Mathews Richardson, Edward Dunlea, Kirsten Koehler, Anthony Prenni, Sonia Kreidenweis, Randy Borys, Daniel Murphy

1:17 HAILSTONE SIZE DISTRIBUTION IN ATMOSPHERIC SAHARAN DUST OUTBREAKS 63
Jean Dessens, Jose Luis Sanchez, Claude Berthet, Roberto Fraile

1:18 ICE FORMATION IN A BIOMASS BURNING CLOUD: MODEL SIMULATIONS OF DROP FREEZING IN IMMERSION AND CONTACT MODES. 66
Karoline Diehl, Martin Simmel, Sabine Wurzler

1:19 SENSITIVITY OF CONTINENTAL LOW-CLOUDS MICROPHYSICAL PROPERTIES TO CHANGES IN AEROSOL NUMBER CONCENTRATION 70
Régis Dupuy, Paolo Laj

1:20 SMOKE INTERACTIONS WITH CLOUDS 74
Graham Feingold, H. Jiang, J. Y. Harrington

1:21 INVESTIGATION OF THE ICE NUCLEATION ABILITY OF TWO DESERT DUST AEROSOL SAMPLES AT -50C 78
Paul Field, Richard Cotton, Ottmar Mohler, M. Schnaiter, Martina Kramer, P. Connolly, A. J. Heymsfield

1:22 PRECIPITATION INFLUENCE ON PARTICULATE MATTER DISPERSION IN COSENZA (ITALY) 82
Monica Filice, Pierantonio De Luca, Alfonso Nastro

1:23 THE ROLE OF THE AEROSOL PARTICLE CHARACTERISTIC ON DRIZZLE FORMATION 86
Istvan Geresdi, Roy M. Rasmussen

1:24 SEPARATION BETWEEN CLOUD SEEDING AND AIR POLLUTION EFFECTS 90
Amir Givati, Daniel Rosenfeld

1:25 SIMULTANEOUS AIRCRAFT OBSERVATION OF AEROSOL AND CLOUD DROPLET CONCENTRATIONS 94
Toshio Harimaya, Akiko Homma, Akira Sasaki, Yutaka Ishizaka

1:26 PO VALLEY NUCLEATION EVENTS: A SIGNIFICANT SOURCE OF CCN 98
Laura Hiltunen, Jorma Joutsensaari, Maria Cristina Facchini, F. Cavalli, Ari Laaksonen

1:27 LONG-TERM, WINTERTIME CLOUD DROPLET, CONDENSATION NUCLEUS AND PRECIPITATION MEASUREMENTS IN THE NORTHERN COLORADO ROCKIES, USA 100
Edward Hindman, Randolph Borys, Douglas H. Lowenthal

1:28 REEXAMINATION OF THE INFLUENCES OF CARBONACEOUS CHEMICALS ON CLOUD DROP ACTIVATION 104
Wei-Chun Hsieh, Jen-Ping Chen

1:29 ON THE ROLE OF THE GIANT AND SUPER-GIANT PARTICLES IN THE FORMATION OF CONVECTIVE PRECIPITATION AND HAIL 108
B. A. Kamalov

1:30 ON THE PRECIPITATION FORMATION IN DESERT AND NEAR-DESERT REGIONS 111
B. A. Kamalov

1:31 THE CITY INFLUENCE ON PRECIPITATION IN CENTRAL ASIA 113
B. A. Kamalov

1:32 PARAMETRIZATION OF WATER-SOLUBLE VOLUME FRACTION OF ATMOSPHERIC AEROSOL 116
Konrad Kandler, Bernhard Busch, Lothar Schütz

1:33 AEROSOL IMPACTS ON PRECIPITATION FROM CONVECTIVE CLOUDS 119
Alexander Khain, Daniel Rosenfeld, A Pokrovsky

1:34 RESPONSE OF THE COUPLED CLIMATE SYSTEM TO INDIRECT AEROSOL FORCING 123
Jón Egill Kristjánsson, Trond Iversen, Alf Kirkevåg, Øyvind Seland

1:35 THE SEARCH FOR THE OPTIMAL SIZE OF HYGROSCOPIC SEEDING PARTICLES 127
Ronen Lahav, Daniel Rosenfeld

1:36 ADDING SALT TO MINERAL DUST PARTICLES AND THE INTERACTION WITH CLOUDS-A CASE STUDY FROM THE MEIDEX CAMPAIGN 131
Zev Levin, Amit Teller, Eliezer Ganor, Yan Yin

1:37 ANALYSIS OF THE EFFECTS OF ATMOSPHERIC ICE NUCLEI CONCENTRATIONS ON RADIANT PROPERTIES OF COLD CLOUD 135
Juan Li, Jietai Mao, Laiguang You, Zhijin Hu

1:38 REVIEW AND IMPLICATION OF WMO AND IUGG RECOMMENDATIONS CONCERNING THE EFFECT OF AEROSOL POLLUTION AND BIOMASS BURNING ON PRECIPITATION 139
Roland List

Paper	Table of Contents – Papers	Page

1:39 OVERVIEW OF AEROSOL-CLOUD INTERACTIONS IN THE CLIMATE SYSTEM 142
Ulrike Lohmann

1:40 CIRRUS CLOUD MICROPHYSICS AND ITS DEPENDENCY ON AEROSOL TYPE, TEMPERATURE AND COOLING RATE 146
Alexander Mangold, Martina Krämer, Ottmar Möhler, Robert Wagner, Harald Saathoff, H. Teichert, Volker Ebert

1:41 EFFECTS OF AEROSOLS AND THERMODYNAMICS ON THE GLOBAL DISTRIBUTION OF TRMM-DERIVED WARM CLOUD PROPERTIES 150
Toshihisa Matsui, Hirohiko Masunaga, Roger Pielke Sr. , Wei-Kuo Tao

1:43 VARIATIONS OF CLOUD CONDENSATION NUCLEI AND CLOUD DROPLET NUMBER CONCENTRATION DUE TO THE REPRESENTATION OF SIZE DEPENDENT CHEMICAL COMPOSITION OF AEROSOL: A MODELLING STUDY 153
Michaela Mircea, Maria Cristina Facchini, Stefano Decesari, Fabrizia Cavalli, Sandro Fuzzi

1:44 HTDMA MEASUREMENTS AND THERMODYNAMIC MODELLING OF AQUEOUS AEROSOLS CONTAINING ORGANICS: A STUDY OF THE LETOVICITE AND MALEIC ACID SYSTEM 157
Michaela Mircea, Maria Cristina Facchini, Stefano Decesari, Fabrizia Cavalli, Sandro Fuzzi, Jenny Rissler, Erik Swietlicki, Simon Clegg

1:45 FORMATION, GROWTH AND HABIT OF ICE CRYSTALS NUCLEATED ON MINERAL DUST AEROSOL 160
Ottmar Möhler, Robert Wagner, C. Linke, M. Schnaiter, H. Saathoff, Alexander Mangold, Martina Krämer, V. Ebert, L. Schütz, P.R. Field, P.J. Connolly, A.J. Heymsfield

1:46 MODELLING STUDIES OF CIRRUS CLOUDS OBSERVED DURING THE INCA CAMPAIGN, IMPLICATION FOR THE NUCLEATION MECHANISM. 164
Marie Monier, Wolfram Wobrock, Andrea Flossmann

1:47 IMPROVED METHODOLOGY FOR THE COMBINED SPECTROSCOPIC AND CHROMATOGRAPHIC INVESTIGATION OF WATER-SOLUBLE ORGANIC COMPOUNDS IN ATMOSPHERIC AEROSOLS AND FOG 168
Fabio Moretti, Emilio Tagliavini, Stefano Decesari

1:48 MICROPHYSICAL AND CHEMICAL CHARACTERISTICS OF CLOUD DROPLET RESIDUALS AND INTERSTITIAL PARTICLES IN CLEAN CONTINENTAL CLOUDS 171
Kevin Noone, Admir Targino, Gustavo Olivares, Lynn Russell, David Covert, John Ogren, Stephan Borrmann, Frank Drewnick , Johannnes Schneider, S. Henseler, N. Hock, S. Weimer

1:49 EFFECTS OF CLOUD SCAVENGING ON AEROSOL SINGLE-SCATTERING ALBEDO 175
John A Ogren, Elisabeth Andrews, David Covert, Kevin Noone

1:50 SAHARAN DUST AS ICE NUCLEI 177
Riza Gurcan Oraltay, Nejdet Fersiz, John Hallett

1:51 SAHARA DUST IMPACT ON PRECIPITATION IN SEVERE STORM EVENTS OVER WEST – CENTRAL MEDITERRANEAN AREA. 181
Massimiliano Pasqui, Bernardo Gozzini, Francesco Pasi

1:52 HIGH-RESOLUTION SENSITIVITY STUDY OF AEROSOL-CLOUD INTERACTIONS IN MARINE STRATUS CLOUDS 185
Irena Paunova, Henry Leighton

1:53 PREDICTION AND OBSERVATION OF AEROSOL PROCESSING BY A CUMULUS: EVIDENCE FOR PARTICLE REMOVAL AND NUCLEATION IN CLOUDS 189
Justin Peter, Steven T. Siems, Jørgen B. Jensen, John L. Gras, Yutaka Ishizaka, Jörg Hacker

1:54 AEROSOL AND POCKETS OF OPEN CELLS 193
Markus D. Petters, Jefferson R. Snider, Ian C. Faloona

1:55 PREDICTION OF CLOUD DROPLET NUMBER CONCENTRATION FROM CLOUD CONDENSATION NUCLEI DATA 197
Markus D. Petters, Jefferson R. Snider

1:56 PREDICTION OF CLOUD CONDENSATION NUCLEI FROM PARTICLE PHYSICOCHEMICAL DATA 201
Markus D. Petters, Jefferson R. Snider, Cynthia Twohy, James R. Anderson

1:57 MICROTOPS OBSERVATIONS OF COLUMNAR AEROSOL OPTICAL DEPTH, OZONE AND WATER VAPOR OVER GADANKI (13.5^{0}N, 79.2^{0}E) 205
Y. Jaya Rao, Panuganti Devara , Atul Kumar Srivastava, Y. Bhavani Kumar, D. Narayana Rao

Paper	Table of Contents – Papers	Page

1:58	AEROSOL IMPACTS ON PRECIPITATION FROM CONVECTIVE CLOUDS: IN SITU AND REMOTE SENSING OBSERVATIONS *Daniel Rosenfeld*	209
1:59	THE EFFECT OF AEROSOL CHEMICAL COMPOSITION ON CLOUD DROPLET NUMBER *Kristy Ross, Stuart Piketh, Roelof Bruintjes*	213
1:60	SPATIAL AND SEASONAL VARIATIONS OF CLOUD CONDENSATION NUCLEI AND AEROSOLS IN THE UNITED ARAB EMIRATES *Vidal Salazar, Roelof Bruintjes, Daniel Breed, Tara Jensen, Stuart Picketh, Abdulla Al Mandoos, Abdulla Al Mangoosh, K. Ross*	217
1:61	SIMULATION OF EFFECTS OF NATURAL AND SEEDING HYGROSCOPIC PARTICLES ON MICROPHYSICS OF ASCENDING CLOUD PARCELS *Yaron Segal, Alexander Khain, Mark Pinsky, Daniel Rosenfeld*	221
1:62	FINGERPRINTING CLOUD CONDENSATION NUCLEI *Glen Shaw*	225
1:63	INTEGRATING PHOTOCHEMICAL-AEROSOL-CLOUD PROCESSES INTO A ONE DIMENSIONAL ATMOSPHERIC BOUNDARY LAYER MODEL *Chein-Jung Shiu, Jen-Ping Chen, Shaw Chen Liu*	227
1:64	WARM MICROPHYSICS IN AN OROGRAPHIC CLOUD AND PROCESSING OF AEROSOL PARTICLES *Martin Simmel, Karoline Diehl, Sabine Wurzler*	231
1:65	EFFECTS OF THE AEROSOL ON THE OPTICAL PROPERTIES OF CLOUDS *Sabina Stefan, Gabriela Iorga*	235
1:66	STUDIES OF THE AEROSOL INDIRECT EFFECT IN NCAR CAM2.0 *Trude Storelvmo, Jón Egill Kristjánsson*	239
1:67	ANALYSIS OF CLIMATE CHANGE BY AEROSOL DIRECT AND INDIRECT EFFECTS WITH AEROSOL TRANSPORT-RADIATION MODEL *Toshihiko Takemura, Toru Nozawa*	243
1:68	THE IMPACT OF AEROSOLS ON CLOUD AND PRECIPITATION PROCESSES: CLOUD-RESOLVING MODEL SIMULATIONS *Wei-Kuo Tao, Xiaowen Li, Alexander Khain, Joanne Simpson, Danniel Johnson, L. Remer*	246
1:69	SCAVENGING OF CONDENSATION NUCLEI IN CLOUDS: DEPENDENCE OF SIGN OF ELECTROSCAVENGING EFFECT ON DROPLET AND CCN SIZES *Brian A. Tinsley*	248
1:70	*MODELLING THE HYGROSCOPIC PROPERTIES OF AEROSOLS* *David Topping, Gordon Mcfiggans, Hugh Coe, Michael Cubison*	251
1:71	THE IMPACTS OF SAHARAN DUST ON FLORIDA CONVECTION *Susan C. Van Den Heever, William R. Cotton*	253
1:72	THE LEIPZIG AEROSOL CLOUD INTERACTION SIMULATOR: DESCRIPTION AND FIRST RESULTS *Heike Wex, Frank Stratmann, Alexei Kiselev, Jost Heintzenberg*	257
	TOPIC 2: CLIMATE CHANGE AND PRECIPITATION	
2:1	CORRELATION BETWEEN NUMBER OF THUNDER-DAYS AND DURATION OF THUNDERSTORM ACTIVITY IN EASTERN GEORGIA *Avtandil Amiranashvili, Bakuri Beritashvili, Irina Mkurnalidze*	261
2:2	SPATIAL-TEMPORARY CHARACTERISTICS OF NUMBER OF DAYS WITH A HAILS IN THE WARM PERIOD OF YEAR IN GEORGIA *Avtandil Amiranashvili, Vazha Amiranashvili, Albert Nodia, Tamila Khurodze, A.F. Toronjadze, Tamar Bibilashvili*	265
2:3	INFLUENCE OF THE ANTHROPOGENIC POLLUTION OF THE ATMOSPHERE AND THUNDERSTORMS ON THE PRECIPITATIONS REGIME AND THEIR CHEMICAL COMPOSITION IN ALAZANI VALLEY CONDITIONS *Avtandil Amiranashvili, Vazha Amiranashvili, L.L. Bachiashvili, Tamar Bibilashvili, G.D. Supatashvili*	267

3:15 EVALUATION OF THE MULTI-SCALE MODELING FRAMEWORK USING DATA FROM THE ATMOSPHERIC RADIATION MEASUREMENT PROGRAM 404
Mikhail Ovtchinnikov, Thomas P. Ackerman, Roger T. Marchand, Marat Khairoutdinov

3:16 CONVECTIVE ORGANIZATION IN A RADIATIVE-CONVECTIVE EQUILIBRIUM CLOUD RESOLVING MODEL - RADIATIVE AND MOISTURE FEEDBACKS 408
Lyle Pakula, Graeme L. Stephens, Marat Khairoutdinov

3:17 RETRIEVAL OF MICROPHYSICS OF DRIZZLING WATER CLOUDS 412
Nick Schutgens

3:18 VARIOUS APPLICATIONS ON TROPICAL CONVECTIVE SYSTEMS USING A GODDARD CUMULUS ENSEMBLE (GCE) MODEL 413
Chung-Lin Shie, Wei-Kuo Tao, Joanne Simpson

3:19 CLOUDS AND THE EARTH'S CLIMATE: AN OBSERVATIONAL STUDY OF CLOUD FEEDBACKS AND THE REGULATION OF THE HYDROLOGICAL CYCLE OF THE TROPICAL ATMOSPHERE 417
Graeme L. Stephens, Tristan L'Ecuyer

3:20 THE ROLE OF SHALLOW CONVECTION IN THE WATER AND ENERGY CYCLES OF THE ATMOSPHERE 421
Knut von Salzen, Norman McFarlane, Michael Lazare

3:21 CLOUD OBJECT MODELING AND OBSERVATIONS FOR CLIMATE STUDIES 424
Kuan-Man Xu, Bruce Wielicki, Takmeng Wong, Lindsay Parker

TOPIC 4: INTERACTIONS BETWEEN CLOUDS AND ATMOSPHERIC CHEMISTRY

4:1 THE IMPORTANCE OF CLOUD DROP REPRESENTATION ON CLOUD PHOTOCHEMISTRY 428
Mary C. Barth, Roberto Cancel, Kristy Ross, Si-Wan Kim

4:2 TRANSFORMATION AND CLOUD INTERACTION OF ATMOSPHERIC AEROSOLS 432
Hugh Coe, M. Rami Alfarra, J. D. Allan, K. N. Bower, M. Cubison, P. I. Williams, G. Mcfiggans, D. Topping, H. Coe, J. T. Jayne, M. R. Canagaratna, D. R. Worsnop, J. L. Jimenez, S. Fuzzi, M.-C. Facchini, S. Decesari, A. Berner

4:3 THE SURFACE TENSION OF FOG WATER SAMPLES, CLOUD WATER, RAINWATER AND DELIQUESCED AEROSOLS, AND ITS LINKAGE TO THE ORGANIC CHEMICAL COMPOSITION 436
Stefano Decesari, Maria Cristina , Facchini, Mihaiela Mircea, Fabrizia Cavalli, Sandro Fuzzi

4:4 POLAR NIGHT INVESTIGATION OF CHEMICAL COMPONENTS IN FRESH SNOW PARTICLES AND AEROSOL/GAS IN THE ATMOSPHERE AT NY-AELESUND 440
Tatsuo Endoh, Tsuneya Takahashi, Izumi Noguchi, Seiji Koga, Naoyuki Kurita, Noriyuki Tanaka, Makoto Wada

4:5 EFFECT OF ARCTIC SULFURIC ACID AEROSOLS ON WINTERTIME LOW-LEVEL ICE CRYSTALS, HUMIDITY, AND TEMPERATURE OVER THE ARCTIC 444
Eric Girard, Alexandru Stefanof

4:6 CLOUD PROCESSING OF GASES AND AEROSOLS IN A REGIONAL AIR QUALITY MODEL (AURAMS) 448
Wanmin Gong, Ashu P. Dastoor, Véronique S. Bouchet, Sunling Gong, Paul A. Makar, Michael D. Moran, Balbir Pabla, Sylvain Ménard, Louis-Philippe Crevier, Sophie Cousineau, S. Venkatesh

4:7 LABORATORY STUDIES ON THE UPTAKE OF AMMONIA, BTEX AND ALKYLBENZENES BY ICE CRYSTALS 452
Ines Hoog, Subir K. Mitra, Elke Fries, Wolfgang Jaeschke, Stephan Borrmann

4:8 MICROPHYSICS OF PYROCUMULONIMBUS CLOUDS 455
Eric Jensen, Andrew S. Ackerman, Ann Fridlind

4:9 CHANGES IN ACIDITY OF OPENING RAINFALL AND THROUGHFALL IN RELATION TO CANOPY OPENNESS IN FORESTS 458
Katsuhiro Kikuchi, Yoshiaki Sasaki

4:10 DROPLET EVAPORATION: THEORETICAL IMPLICATIONS OF RECENT DATA FOR BINARY NITRIC ACID SOLUTIONS 462
Dennis Lamb, Alfred Moyle, Huiwen Xue

4:11 HOW EFFICIENT IS CLOUD DROPLET FORMATION OF ORGANIC AEROSOLS? 465
Ulrike Lohmann, Keith Broekhuizen, Richard Leaitch, Nicole Shantz, Jonathan Abbatt

4:12 AEROSOL RELATED EXTENDED KESSLER-TYPE PARAMETERIZATION FOR USE IN LARGER SCALE MODELS 469
Frank Müller, Frank Schimmel, Andreas Chlond

4:13 COMPARATIVE STUDY OF THE UPTAKE OF NITRIC ACID TO AEROSOL AND CLOUD PARTICLES IN THE MID AND UPPER TROPOSPHERE 473
Jason Shepherd, Hugh Coe, Gordon Mcfiggans

4:14 DROP-SCALE NUMERICAL MODELING OF CHEMICAL PARTITIONING DURING CLOUD HYDROMETEOR FREEZING 475
Amy L. Stuart, Mark Z. Jacobson

4:15 CHEMICAL EFFECTS ON DROP SPECTRAL BROADENING 479
Huiwen Xue, Graham Feingold

TOPIC 5: WARM CLOUD MICROPHYSICS

5:1 EQUILIBRIUM WET GROWTH/EVAPORATION OF PARTICLES CONTAINING SOLUBLE AND INSOLUBLE KERNELS 483
Vladimir Arkhipov, Mark Pinsky, Alexander Khain

5:2 AIRCRAFT MEASUREMENTS OF HIGH AVERAGE CHARGES ON CLOUD DROPS 487
Kenneth Beard, Harry T. Ochs, Cynthia H. Twohy

5:3 OBSERVATIONS OF REDUCED LIQUID WATER CONTENT IN THE CENTRE OF CUMULUS CLOUD UPDRAFTS 491
Alan M Blyth, Sonia G Lasher-Trapp, William A Cooper

5:4 RELATIONSHIPS BETWEEN WATER VAPOR PATH AND PRECIPITATION OVER THE TROPICAL OCEANS 495
Christopher S. Bretherton, Matthew E. Peters, Larissa Back

5:5 RELATIONSHIP BETWEEN THE HYDROMETEOR SIZE DISTRIBUTION AND CLOUD MICROPHYSICAL PROPERTIES USING DISDROMETRIC DATA 499
Clelia Caracciolo , Franco Prodi, Alessandro Battaglia

5:6 CONDENSATIONAL GROWTH OF DROPLETS IN WARM CUMULUS CLOUDS 503
Alison Coals, Alan Blyth, Jean-Louis Brenguier, Alan Gadian, Wojtek Grabowski

5:7 STUDY OF THE PRECIPITATION IN ATHENS (GREECE) WITH A 2D VIDEO DISTROMETER AND RAINGAUGES 507
Eric Defer, Kostas Lagouvardos, Vassiliki Kotroni, John Kalogiros

5:8 PRECIPITATION AND LIGHTNING ACTIVITY IN ATHENS (GREECE) 510
Eric Defer, Kostas Lagouvardos, Vassiliki Kotroni

5:9 THE EFFECT OF TURBULENT VELOCITY FLUCTUATIONS ON DROP SPECTRUM BROADENING IN STRATOCUMULUS CLOUDS 513
Carynelisa Erlick, Alexander Khain, Mark Pinsky, Yaron Segal

5:10 THE STUDY ON CONVECTIVE CLOUD IN QINGHAI AND SEEDING EXPERIMENT WITH 3D MODEL 517
Wen Fang , Guo Guang Zheng, Guan Fang He

5:11 CLOUD DROPLET COLLISION RATES IN EVOLVING TURBULENT FLOWS 520
Charmaine Franklin, Paul Vaillancourt, M.K. Yau, Peter Bartello

5:12 CLOUD WATER CONTENT AND CLOUD PARTICLE CHARACTERISTICS REVEALED BY DUAL WAVELENGTH CLOUD RADAR OBSERVATIONS 524
Nicolas Gaussiat, Robin Hogan, Anthony Illingworth

5:13 SUPERSATURATION MEASUREMENTS IN A STRATOCUMULUS 528
Hermann Gerber

5:14 PRECIPITATION DEVELOPMENT IN CLOUDS WITH MARITIME VERSUS CONTINENTAL CHARACTERISTICS 530
Sabine Goke, Harry Ochs, Robert Rauber, Neil F. Laird

5:15 RAINDROP SHAPE AND SIZE DISTRIBUTION: IMPACT ON RADAR PRECIPITATION RETRIEVALS 533
Eugenio Gorgucci, V. Chandrasekar , V. N. Bringi, Luca Baldini

5:16 NORMALIZED DROP SIZE DISTRIBUTIONS 537
Jan Handwerker, Winfried Straub, Klaus D. Beheng

5:17 EVALUATION OF QUANTITATIVE PRECIPITATION ESTIMATION (QPE) ALGORITHMS FROM WEATHER RADAR AND RAIN-GAUGE DATA 541
Yuxiang He, Hui Xiao, Shuyan Liu

5:18 THE COMPARISON OF MICROWAVE STATISTICAL ALGORITHMS FOR PRECIPITATION RETRIEVAL OVER LAND 544
Wenying He, Hongbing Chen, Jinli Liu

5:19 OBSERVATIONS OF FLORIDA CONVECTIVE STORMS USING DUAL WAVELENGTH AIRBORNE RADAR 547
Gerald Heymsfield, Andrew Heymsfield, L. Belcher

5:20 THE EFFECTS OF PARTICLE CLUSTERING ON IN-SITU AND REMOTE SENSING MEASUREMENTS OF MEANS AND VARIANCES 551
Art Jameson

5:21 RELATIONSHIP BETWEEN THE LOW-LEVEL CLOUD FIELDS FROM SATELLITES AND PRECIPITATION FROM GROUND OVER CHINA 554
Kazuaki Kawamoto, Tadahiro Hayasaka

5:22 LARGE WATER DROPS IN CONTINENTAL CUMULUS IN THEIR "FIRST-ECHO" STAGE 556
Charles Knight

5:23 ON THE ROLE OF LARGE-SCALE TURBULENCE IN CLOUD MICROSTRUCTURE FORMATION 560
Yefim Kogan

5:24 MODEL SIMULATIONS ON THE FORMATION OF UNACTIVATED FOGS 564
Harri Kokkola, Sami Romakkaniemi, Ari Laaksonen

5:25 DRIZZLE VARIABILITY IN MARINE STRATUS DURING EPIC 2001 566
Pavlos Kollias, Christopher Fairall, Bruce Albrecht

5:26 PARTICLE IMAGE VELOCIMETRY OF CLOUD DROPLETS IN THE PROCESS OF TURBULENT MIXING 570
Piotr Korczyk, Szymon P. Malinowski, Tomasz A. Kowalewski

5:27 RECONSIDERATION OF CERTAIN ASPECTS OF THE Z –R PROBLEM 573
Michael Larsen, Alexander B. Kostinski

5:28 THE SCALING OF DROP SIZE DISTRIBUTIONS AND THEIR NORMALIZATION 576
Gyu Won Lee, Isztar Zawadzki

5:29 TETHERED-BALLOON BORNE MEASUREMENTS IN BOUNDARY LAYER CLOUDS PART II: MICROPHYSICAL PROPERTIES 580
Katrin Lehmann , Sebastian Schmidt, Holger Siebert, Manfred Wendisch

5:30 SIMULATIONS OF STRATOCUMULI CLOUDS WITH A 3D CLOUD MODEL WITH WARM DETAILED MICROPHYSICS 584
Matthieu Leporini, Wolfram Wobrock, Andrea Flossmann

5:31 CLOUD CONDENSATION NUCLEI IN CLEAR AND POLLUTED ATMOSPHERIC CONDITIONS IN THE AMAZONIAN REGION 588
Jorge Martins, Fábio Gonçalves, J.C.P. Oliveira, A.A. Costa, J.B.V. Leal Júnior, M.A. Silva Dias

5:32 OBSERVATIONS OF VERTICAL VARIABILITY OF CLOUD HYDROMETEORS IN STRATIFORM REGIONS BEHIND BOW ECHOES: IMPLICATIONS FOR DOWNDRAFT FORMATION 592
Greg M. Mcfarquhar, Michael S. Timlin, Robert Rauber, Brian Jewett

5:33 ANALYSIS OF DIFFERENT CLOUD MODELS' OUTPUT OF THE SAME STORM FOR CLOUD RADIATION DATABASE GENERATION 596
C.M. Medaglia, Stefano Dietrich, Vassiliki Kotroni, Sabatino Di Michele, C. Adamo, R. Bechini, G.J. Tripoli, K. Lagouvardos

5:34 AN EXAMINATION OF THE IMPACT OF DRIZZLE DROPS ON SATELLITE-RETRIEVED EFFECTIVE PARTICLE SIZES 600
Patrick Minnis, Robert F. Arduini, David F. Young, J. Kirk Ayers, Bruce A. Albrecht, Tarah Sharon, Bjorn Stevens

5:35 MULTIPEAK RAINDROP SPECTRA OBSERVATIONS FROM CONVECTIVE SHOWERS IN MEXICO 604
G. Montero-Martínez, Fernando García-García

5:36 LABORATORY MEASUREMENTS OF THE EFFECT OF TEMPERATURE ON THE COALESCENCE EFFICIENCY OF SMALL PRECIPITATION DROPS 608
Harry T. Ochs, Jennifer Davison, Kenneth Beard, Jeffrey Van Dorn

5:37 CHARACTERISTICS OF DRIZZLING AND NON-DRIZZLING STRATOCUMULUS AS REVEALED BY VERTICAL POINTING CLOUD RADAR AND LIDAR 612
Ewan O'Connor, Robin Hogan, Anthony Illingworth, Jean–Louis Brenguier

5:38 STATISTICAL ANALYSIS OF MICRO RAIN RADAR SPECTRA 616
Igor Petenko, Gerhard Peters

5:39 PROFILES OF MICROPHYSICAL RAIN PARAMETERS AS OBSERVED WITH MICRO RAIN RADARS 620
Gerhard Peters, Bernd Fischer, Hans Münster

5:40 THE MICROPHYSICAL AND THERMODYNAMIC CHARACTERISTICS OF TROPICAL CONVECTIVE CLOUDS BY RESULTS OF MEASUREMENTS ON CUBA 624
Victor V. Petrov, Daniel Martinez, Carlos A. Perez

5:41 RAIN ENHANCEMENT BY SEEDING WITH CHARGED DROPLETS 628
Mark Pinsky, Alexander Khain, Vladimir Arkhipov, Yuri Feldman, Yaroslav Ryabov

5:42 TOWARD THE PARAMETERIZATION OF TURBULENT EFFECTS ON PARTICLE COLLISIONS IN TURBULENT CLOUDS 632
Mark Pinsky, Alexander Khain, B. Grits, Michael Shapiro

5:43 MEASUREMENTS OF PHORETIC VELOCITIES OF AEROSOL PARTICLES IN MICROGRAVITY CONDITIONS 636
Franco Prodi , Gianni Santachiara , Stefania Travaini , Andrei Vedernikov , Frank Dubois , Jean Claude Legros

5:44 EXPERIMENTAL STUDY OF DRIZZLE FORMATION - RESULTS FROM DYCOMS-II 640
Piotr Rasinski, Hanna Pawlowska

5:45 DROPLET GROWTH BY TURBULENT COAGULATION 643
Nicole Riemer, Anthony Wexler

5:46 THEORETICAL STUDY OF COLLISION INDUCED DROPLET BREAKUP PHENOMENA 647
Norbert Roth, Matthias Hase, Bernhard Weigand

5:47 PARTICLE–TURBULENCE INTERACTIONS IN CLOUDS: A MEASUREMENT PERSPECTIVE 651
Raymond Shaw

5:48 OBSERVATIONAL STUDY ON THE MICROPHYSICAL STRUCTURES OF RAINFALL-PRODUCING STRATI-FORM CLOUDS 654
Niu Shengjie, Sun Zhaobo, Fan Shuxian

5:49 CHARACTERISTICS OF RAINDROP SPECTRA OF STRATIFORM-CLOUD PRECIPITATION IN AUTUMN 2002 IN HENAN 657
Aili Shi, Guoguang Zheng, Gen Huang, Yuquan Zhou

5:50 CHARACTERISTICS OF WATER VAPOR CONDITIONS IN AUTUMN STRATIFORM CLOUDS AND THEIR POTENTIAL FOR RAINFALL ENHANCEMENT IN HENAN PROVINCE IN 2002 661
Aili Shi, Guoguang Zheng

5:51 THE BIAS IN MOMENT ESTIMATORS FOR PARAMETERS OF DROP-SIZE DISTRIBUTION FUNCTIONS: SAMPLING FROM EXPONENTIAL DISTRIBUTIONS 664
Paul Smith, Donna Kliche

5:52 THE EFFECT OF SURFACTANTS ON KÖHLER CURVES RECONSIDERED 668
Riikka Sorjamaa, Tomi Raatikainen, Ari Laaksonen

5:53 WHEN IS BETTER TO DETERMINE THE SUPER-SATURATION INTEGRAL FOR A TIME STEP OF THE SIMULATION ? 670
Cristina Stefanof, Alexandru Stefanof, Wanda Szyrmer, Jean-Pierre Blanchet

5:54 A COMPARISON OF THE MICROPHYSICAL AND KINEMATIC CHARACTERISTICS OF MIDLATITUDE AND TROPICAL CONVECTIVE UPDRAFTS 674
Jeffrey Stith, Julie Haggerty, Cedric Grainger, Andrew Detwiler

5:55 ANALYSES OF MICROPHYSICAL AND DYNAMICAL CHARACTERISTICS OF SUMMER CLOUDS IN THE UPPER REACHES OF THE YELLOW RIVER 678
Anping Sun, Lunge Li, Guoguang Zheng, Hengchi Lei, Guanghe Wang

5:56 STORM SYSTEMS AND PRECIPITATION PROCESSES IN EAST ASIAN MONSOON RAIN 682
Tsutomu Takahashi

5:57 EFFECT OF TURBULENCE ON COLLISION EFFICIENCY OF CLOUD DROPLETS 686
Lian-Ping Wang, Orlando Ayala, Scott E. Kasprzak, Wojciech W. Grabowski

5:58 EFFECTS OF STOCHASTIC COALESCENCE AND AIR TURBULENCE ON THE SIZE DISTRIBUTION OF CLOUD DROPLETS 690
Lian-Ping Wang, Yan Xue, Orlando Ayala, Wojciech W. Grabowski

5:59 CLOUD DROPLET SIZE SPECTRAL BROADNESS OF ADIABATIC CLOUDS 694
Seong Soo Yum, James G. Hudson

5:60 THE PHYSICAL CAUSES OF THE VARIABILITY OF DROP SIZE DISTRIBUTIONS 698
Isztar Zawadzki, Gyu Won Lee

TOPIC 6: COLD CLOUD MICROPHYSICS

6:1 A NEW HABIT DIAGRAM AND MASS PARAMETERS FOR ATMOSPHERIC ICE CRYSTALS FROM –20 °C TO – 70 °C 703
Matthew Bailey, John Hallett

6:2 MESOSCALE STRUCTURE OF FRONTAL WINTER CLOUD AND PRECIPITATION SYSTEMS OVER UKRAINE 707
Vladimir Bakhanov, Olexandra Manzhara, Boris Dorman

6:3 NUMERICAL SIMULATION OF CLOUD MICROSTRUCTURE EFFECT ON SATELLITE SIGNAL 711
Vladimir Bakhanov, Oleksiy Kryvobok, Boris Dorman

6:4 PROPERTIES OF SNOWFLAKES OF DIFFERENT RIMING DEGREE AND CRYSTAL TYPES 715
Eszter Barthazy, Raphael Schefold

6:5 HOW DO UPDRAFTS AND EMBEDDED CONVECTION INFLUENCE RIMING? 719
Björn Baschek, Raphael Schefold, Eszter Barthazy

6:6 MONTECARLO COMPUTATIONS OF SOLAR REFLECTANCE FROM ICE AND WATER CLOUDS AT NEAR IR FREQUENCIES 723
Alessandro Battaglia, Simone Mantovani , Franco Prodi, Federico Porcù

6:7 THE SHAPES OF VERY SMALL CIRRUS PARTICLES DERIVED FROM IN SITU MEASUREMENTS 727
Darrel Baumgardner, Helene Chepfer, Graciela B. Raga, Gregory.L. Kok

6:8 10-YEAR STATISTICS ON FREEZING PRECIPITATION ACROSS THE FORMER USSR FROM SURFACE WEATHER OBSERVATIONS 731
Natalia A. Bezrukova, Richard Jeck, Ludmila S. Minina, Marat F. Khalili, Evgeni A. Stulov

6:9 A SYSTEMATIC RETRIEVAL OF ICE CLOUD MICROPHYSICAL AND RADIATIVE PROPERTIES USING A SYNERGETIC RADAR/LIDAR ALGORITHM 735
Dominique Bouniol, Alain Protat, Martial Haeffelin

6:10 SIMULATIONS OF THE JULY 16 AND 21 CRYSTAL-FACE CIRRUS CASES USING A CLOUD-RESOLVING MODEL FORCED BY A ENSEMBLE OF MESOSCALE MODELS 739
Robert Carver, Jerry Harrington, Johannes Verlinde

6:11 A STUDY OF THE EFFECT OF CLOUD DROPLETS ON THE DIFFUSIONAL GROWTH RATE OF ICE PARTICLES 743
Nesvit E. Castellano, Eldo. E. Avila, Clive Saunders

6:12 OBSERVATIONS AND MODELLING OF CIRRUS OUTFLOW FROM HECTOR DURING THE EMERALD-II CAMPAIGN 747
Paul Connolly, T. W. Choularton, M. W. Gallagher, K. N. Bower, M. J. Flynn, J. W. Whiteway

6:13 PARCEL MODELLING OF ICE NUCLEATION IN THE AIDA AEROSOL CHAMBER 751
Richard Cotton, Paul Field, Ottmar Mohler, M. Schnaiter, Martina Kramer, P. Connolly, A. J. Heymsfield

6:14 A WINTER SEASON PHYSICAL EVALUATION OF THE EFFECTS OF CLOUD SEEDING IN THE COLORADO MOUNTAINS USING RAMS 755
William Cotton, Ray McAnelly, Gustavo Carrio

6:15 PRELIMINARY COMPARISON OF AMSR-E OBSERVATION AND NUMERICAL SIMULATION WITH CLOUD RESOLVING MODEL FOR SOLID PRECIPITATION IN WINTER DURING THE WAKASA 2003 759
Hisaki Eito, Kazumasa Aonashi, Guosheng Liu, Chiashi Muroi, Syugo Hayashi , Teruyuki Kato , Masanori Yoshizaki

6:16 HAILSTONE SIZE DISTRIBUTION AND DENT OVERLAP IN HAILPADS 763
Roberto Fraile, Laura López, Covadonga Palencia, Amaya Castro

6:17 THEORY OF HOMOGENEOUS FREEZING NUCLEATION BASED ON NEW SIZE DEPENDENT SURFACE FREE ENERGY AND MEASURED VAPOR PRESSURE OF SUPERCOOLED WATER 767
Norihiko Fukuta

6:18 ASSESSMENT AND TUNING OF THE BEHAVIOR OF A MICROPHYSICAL CHARACTERIZATION SCHEME BASED ON RADAR POLARIMETRIC VARIABLES 771
Michele Galletti, Pier Paolo Alberoni, Vincenzo Levizzani

6:19 MICROPHYSICAL ANALYSIS INSIDE A SUPERCELL 775
Eduardo García-Ortega, Laura López, J.L. Marcos, José Luis Sánchez

6:20 MICROPHYSICAL RELATIONSHIPS IN CRYSTAL-FACE ANVIL CIRRUS 779
Timothy Garrett, Hermann Gerber, Darrel Baumgardner, M. Poellot, Cynthia Twohy, Elliot Weinstock

6:21 CHARACTERIZATION OF MIXED PHASE CLOUD AND PRECIPITATION 782
John Hallet

6:22 MELT CHARACTERISTICS OF FALLING SNOW PARTICLES 786
John Hallet, Gurcan Oraltay

6:23 HOMOGENEOUS ICE NUCLEATION IN TROPICAL CONVECTION AND ITS INFLUENCE ON CIRRUS ANVIL MICROPHYSICS 788
Andrew Heymsfield, Larry Miloshevich, Carl Schmitt, Aaron Bansemer, Cynthia Twohy, Michael Poellot, Ann Fridlind

6:24 3-D NUMERICAL SIMULATION OF HAILSTORMS IN DIFFERENT REGIONS 792
Zhaoxia Hu, Yanchao Hong, Hongyu Li

6:25 EVALUATION OF GROUND-BASED RADAR AND IN-SITU AIRCRAFT DATA COMPARISON IN WINTER STORMS 796
David Hudak, Peter Rodriguez, Mengistu Wolde, Brian Currie, Stewart Cober, Isztar Zawadzki, George Isaac

6:26 USE OF MASS VERSUS VOLUME UNITS FOR CLOUD MICROPHYSICAL PARAMETERS 800
George Isaac, Ismail Gultepe, Stewart Cober

6:27 THE STRUCTURE OF HAIL STORM DEVELOPED AT HANSHIN AREA IN JAPAN 804
Hiroyuki Konishi, Yukari Shusse, Yoshimasa Takaya

6:28 OBSERVATION OF SUBLIMATING ICE PARTICLES IN CLOUDS 808
Alexei Korolev, George A. Isaac

6:29 SUPERSATURATION OF WATER VAPOR IN CLOUDS. 812
Alexei Korolev, Ilia P. Mazin

6:30 NUMERICAL STUDY IMPACT OF SOME BASIS CHARACTERISTICS OF FREEZING NUCLEI ON CLOUD MICROPHYSICS AND PRECIPITATION 816
Svetlana Krakovskaia, Anne Pirnach

6:31 ANALYSIS OF RADAR AND IN SITU MEASUREMENTS OF SNOWFALL IN EASTERN NORTH DAKOTA 820
Paul Kucera, Andrew Newman

6:32 OBSERVATIONS OF QUASI-STATIONARY, SHALLOW OROGRAPHIC SNOW CLOUD: SPATIAL DISTRIBUTIONS OF SUPER LIQUID WATER AND ICE HYDROMETEOR 823
Kenichi Kusunoki, Masataka Murakami, Narihiro Orikasa, Yoshinobu Tanaka, Mizuho Hoshimoto, Yoshinori Yamada, Hakaru Mizuno, Kyosuke Hamazu, Hideyuki Watanabe

6:33 TRANSITION OF LEESIDE PRECIPITATION PROPERTIES OBSERVED BY KA-BAND RADAR AND GROUND-BASED 2D-GREY PROBE 827
Kenichi Kusunoki, Masataka Murakami, Narihiro Orikasa, Yoshinobu Tanaka, Koyuru Iwanami, Masayuki Maki, Park Sanggoon, Ryohei Misumi, Kyosuke Hamazu, Hiroshi Kosuge

6:34 GIANT AND ULTRAGIANT AEROSOL PARTICLES: SOURCE OF LARGE SUPERCOOLED DROPS IN MIXED-PHASE CLOUDS? 831
Sonia Lasher-Trapp, Sarah Bereznicki, Justin Stachnik

6:35 A COMPARISON OF THE MICROPHYSICAL AND RADIATIVE PROPERTIES OF CIRRUS, WAVE AND ANVIL CLOUDS 835
Paul Lawson, Brad Baker, Bryan Pilson

6:36 THE 2D-S (STEREO) PROBE: PRELIMINARY TESTS OF A NEW HIGH-SPEED, HIGHRESOLUTION PARTICLE IMAGING PROBE 839
Paul Lawson, Darren O'Connor, Patrick Zmarzly, Kim Weaver

6:37 SIMULATION OF PRECIPITATION MECHANISM WITHIN TYPICAL COLD-FRONTAL CLOUD SYSTEM 843
Hongyu Li, Yanchao Hong

6:38 NUMERICAL SIMULATION AND SEEDING EXPERIMENTS OF TWO SEVERE CONVECTIVE EVENTS IN BEIJING AREA 846
Shuyan Li, Zhuang Xie

6:39 NUCLEATION IN SYNOPTICALLY FORCED CIRROSTRATUS 850
Ruei-Fong Lin, David Starr, Jens Reichardt, Paul J. Demott

6:40 A CRITICAL OVERVIEW OF AERODYNAMICS AND HEAT AND MASS TRANSFER OF ICE PARTICLES, GRAUPEL AND HAILSTONES 854
Roland List

6:41 THE 1954 INTERNATIONAL CONFERENCE ON EXPERIMENTAL METEOROLOGY IN ZURICH, SWITZERLAND (A HISTORICAL NOTE) 858
Roland List

6:42 CIRRUS CLOUD PROPERTIES DERIVED FROM THE MOMENTS OF MILLIMETER WAVELENGTH DOPPLER SPECTRUM 861
Gerald Mace, Min Deng

6:43 MORPHOLOGY OF ICE CRYSTALS AT LOW TEMPERATURES: LABORATORY MEASUREMENTS AND ATMOSPHERIC MODELING IMPLICATIONS 865
Nathan Magee, Dennis Lamb, Alfred M. Moyle

6:44 EFFECTS OF WIND SHEAR ON CIRRUS: AN LEM AND RADAR CASE-STUDYI 868
J.H. Marsham, S. Dobbie

6:45 CLOUD PHASE STRUCTURE (PARAMETERIZATION, EXPERIMENTAL PROBLEMS) 872
Ilya Mazin

6:45A RETRIEVAL OF CLOUD PHASE AND ICE CRYSTAL HABIT FROM SATELLITE DATA 876
Sally McFarlane, Roger Marchand, Thomas Ackerman

6:46 LABORATORY MEASUREMENTS OF HETEROGENEOUS ICE NUCLEATION: CONTACT NUCLEATION INSIDE-OUT 880
Youshi Mi, Adam Durant, Raymond Shaw

6:47 ON A NATURE OF FORMING OF THE GLORY IN CLOUDS 884
Anatoly N. Nevzorov

6:48 MICROPHYSICAL PROPERTIES OF ANVILS OBTAINED FROM AIRCRAFT MEASUREMENTS DURING X-BAIU-02 FIELD CAMPAIGN 888
Narihiro Orikasa, Masataka Murakami, Kazumasa Mori, Hiroshi Kuroiwa, Haruya Minda

6:49 THE IMPACT OF VARIOUS NUCLEATION PROCESSES ON ANVIL GLACIATION ON A CRYSTAL-FACE THUNDERSTORM 892
Vaughan Phillips, Steve Sherwood, C. Andronache, A. Bansemer, B. Conant, A. Heymsfield, G. Heymsfield, M. Poellot, T. Vanreken

6:50 A CASE STUDY OF TROPICAL CIRRUS ANVIL MICROPHYSICS FROM CRYSTAL-FACE 896
Michael Poellot, Paul Kucera, Andrew Heymsfield, Cynthia Twohy, Hermann Gerber

6:51 NUMERICAL SENSITIVITY STUDIES OF AXIS RATIO CHANGES OF COLLIDING ICE CRYSTALS 900
Rebekka Posselt, Sabine Wurzler, Karoline Diehl

6:52 CLASSIFICATION AND SCATTERING PROPERTIES OF WINTERLY PRECIPITATION PARTICLES 904
Walter Randeu, Franz Teschl, Norbert Witternigg, Michael Schönhuber

6:53 FREEZING DRIZZLE FORMATION OVER THE OREGON CASCADES DURING IMPROVE II 908
Roy Rasmussen, Kyoko Ikeda, Greg Thompson, Istvan Geresdi

6:54 FALL ATTITUDES OF PRISTINE DENDRITIC SNOW CRYSTALS ESTIMATED FROM RADAR DEPOLARIZATION MEASUREMENTS 912
Roger Reinking, Sergey Matrosov

6:55 SENSITIVITY OF CLOUD MICROPHYSICS AND SURFACE PRECIPITATION TO CCN AND GCCN CONCENTRATIONS IN A WINTER STRATIFORM EVENT 916
Stephen Saleeby, William Cotton

6:56 COMBINED MEASUREMENTS OF SNOWFLAKE CHARACTERISTICS IN THE MELTING LAYER 920
Raphael Schefold, Bjorn Baschek, Aaron Bransemer, Eszter Barthazy

6:57 EFFECTS OF COLLISIONAL BREAKUP ON MIXED-PHASE DEEP CONVECTION SIMULATED BY A SPECTRAL (BIN) CLOUD MODEL AND COMPARISON TO DROP SIZE SPECTRA MEASURED AT THE GROUND 924
Axel Seifert, Alexander Khain, Ulrich Blahak

6:58 STATISTICAL PROPERTIES OF VOLUMES SWEPT BY NON-SPHERICAL ICE PARTICLES IN A 3-D TURBULENT FLOW 928
Michael Shapiro, Hod Wirzberger, Mark Pinsky, Boris Grits, Alexander Khain

6:59 GROWTH OF SNOW CRYSTALS FROM FROZEN WATER DROPLETS 932
Chuji Takahashi

6:60 EXPERIMENTAL STUDIES ON THE SUBLIMATION OF A SNOW CRYSTAL 936
Tsuneya Takahashi, Tatsuo Endoh

6:61 COMPARING ICE-CLOUD MICROPHYSICAL PROPERTIES USING CLOUDNET AND ARM DATA 940
Gerd-Jan van Zadelhoff, David P. Donovan

6:62 ICE CRYSTAL BREAKUP ON IMPACT 944
German Vidaurre, John Hallett

6:63 LABORATORY STUDIES ON THE ICE NUCLEATING ABILITY OF POLLEN PARTICLES IN IMMERSION FREEZING AND CONTACT FREEZING MODES 946
Nadine von Blohn, Subir K. Mitra, Stephan Borrmann

6:64 DISCUSSION ON ARTIFICIAL PRECIPITATION ENHANCEMENT CONDITIONS IN CYCLONE 950
Yilin Wang

6:65 A SIMPLE MODEL OF SNOWFLAKE AGGREGATION 954
Chris Westbrook, Robin Ball, Paul Field, Andrew Heymsfield

6:66 THE MICROPHYSICAL AND ELECTRICAL STRUCTURE OF CONVECTIVE ANVILS 957
Paul Willis, J. E. Dye, S. Lewis, W.D. Hall

6:67 HORIZONTAL AND VERTICAL CLOUD STRUCTURE OBTAINED USING W-BAND AIRBORNE RADAR 961
M. Wolde, S. Haimov, D. Marcotte, W. Strapp, G. Vali, G. Isaac

6:68 THE MOLECULAR DIFFUSION OF ICE CRYSTALS OF VARIOUS SHAPES 965
Hyun Youk, Roland List, Theophilus Ola

6:69 SIMULATION AND OBSERVATION ON SUPERCOOLED LIQUID WATER AND ICE CRYSTALS OF PRECIPITATING STRATIFORM CLOUDS IN HENAN PROVINCE 969
Shi Yueqin, Liu Qijun, Liu Weiguo

6:70 THE STUDY OF HAIL IDENTIFICATION CRITERIA 973
Sun Yuwen, Ying Duan , Zhihui Wu, Hai Zhi

6:71 CLOUD MICROSTRUCTURE DETECTION AND ANALYSIS IN BEIJING AND ITS NEIGHBORING AREA 975
Qiang Zhang, Hongyu Li, Lei Zhang

6:72 WIND TUNNEL MEASUREMENTS OF DRAG COEFFICIENTS OF SPHERICAL AND SPHEROIDAL HAILSTONES 978
Guoguang Zheng, Roland List

TOPIC 7: CLOUD ELECTRICITY

7:1 SIMULATION OF THE DEVELOPMENT OF ELECTRIC FIELD IN A 3-DIMENSIONAL WINTER THUNDERCLOUDS FIELD USING THE RAMS MODEL 982
Orit Altaratz, Tamir Reisin, Zev Levin

7:2 LABORATORY INVESTIGATION OF POSITIVE DISCHARGES FROM ICE CRYSTALS: POSSIBLE RELEVANCE TO LIGHTNING INITIATION AND ICE MULTIPLICATION 986
Matthew Bailey, John Hallett, Danyal Petesen, William Beasley

7:3 AN EXPLICIT ELECTRICAL SCHEME FOR USE IN A CLOUD RESOLVING MODEL 990
Christelle Barthe, Jean-Pierre Pinty

7:4 PRECIPITATION AND LIGHTNING ACTIVITY OVER THE MEDITERRANEAN SEA 994
Eric Defer, Kostas Lagouvardos, D. Katsanos, Vassiliki Kotroni

7:5 DERIVATION OF THUNDERSTORM ICE HYDROMETEOR CHARACTERISTICS FROM LIGHTNING MEASUREMENTS 997
Wiebke Deierling, Walter A. Petersen, John Latham, Scott M. Ellis, Hugh J. Christian Jr.

7:6 AIRBORNE OBSERVATIONS OF MICROPHYSICS AND ELECTRIC FIELDS IN ANVILS OF FLORIDA THUNDERSTORMS 1001
James Dye, Sharon Lewis, William Hall, John Willett, Paul Willis, A. C. Grainger, D. Mach, M. Bateman, H. J. Christian

7:7 THE ELECTRICAL FIELD BENEATH THE THUNDERSTORMS AND ITS RELATIONSHIP WITH THE METEOROLOGICAL VARIABLES 1005
Valter Gennaro, Dario B. Giaiotti, Fulvio Stel

7:8 CHARACTERISTICS OF THE PRECIPITATING SYSTEMS DURING THE 2002 DRY-TO-WET FIELD CAMPAIGN IN THE AMAZON REGION 1008
Carlos Augusto Morales, Luiz Augusto Toledo Machado, Maria Assunção Faus Silva Dias, Wando Amorim, Maria Eugenia Baruzzi Frediani

7:9 LIGHTNING BY CAVITY QUANTUM ELECTRODYNAMICS? 1011
T.V. Prevenslik

7:10 CHARACTERISTICS OF WINTER THUNDERCLOUDS IDENTIFIED WITH DUAL POLARIZATION RADAR IN HOKURIKU, JAPAN 1015
Keiichiro Sakashita , Hiroshi Uyada, Takeshi Maesaka, Taro Shinoda, K. Kontani, K. Shinjo

7:11 C-G LIGHTNING ACTIVITIES AND RAINDROP ELECTRIC CHARGE DISTRIBUTIONS OBSERVED DURING BAIU MONSOON SEASON 1019
Kenji Suzuki, Tetsuya Kawano, Masanori Yoshizaki

7:12 THE IMPACT OF LIGHTNING ON A LIFE CYCLE OF CONVECTIVE CLOUDS: A NUMERICAL STUDY 1023
Zlatko Vukovic, Bosko Telenta

7:13 THE RESEARCH ON PRECIPITATION AND LIGHTNING MAP 1027
Xia Wan, Qiang Zhang, Xiaoyun Cai

TOPIC 8: INSTRUMENTATION

8:1 IMPROVED RETRIEVAL OF STRATUS CLOUD MICROPHYSICAL PROPERTIES USING MILLIMETER-WAVE RADAR AND VISIBLE OPTICAL DEPTH 1029
Richard T. Austin, Graeme L. Stephens

8:2 A NEW LOOK AT THE BRIGHT BAND 1033
Kristina Mann Baker, Johannes Verlinde

8:3 CUMULUS CLOUD PROCESSING OF AEROSOL PARTICLES IN THE MEXICAN EAST PACIFIC 1037
Darrel Baumgardner, Jose Carlos Jiménez, Graciela B. Raga

8:4 RAINFALL ESTIMATES OF CONVECTIVE CLOUDS USING METEOSAT-6 RAPID SCAN DATA IN CENTRAL EUROPE 1041
Franz H. Berger

8:5 THOR - CLOUD THICKNESS FROM OFFBEAM LIDAR RETURNS 1044
Robert F. Cahalan, Matthew Mcgill, John Kolasinski, Tamas Varnai, Kenneth Yetzer

8:6 ON THE SENSITIVITY OF MODIS VISIBLE/1.6 μM CHANNELS TO RADAR-MEASURED GROUND PRECIPITATION 1048
Davide Capacci , Alessandro Battaglia, Simone Mantovani , Federico Porcù , Bryan Conway, Franco Prodi

8:7 ANALYSIS OF PLUDIX DISDROMETER PERFORMANCE DURING THE BBC-2 CAMPAIGN 1052
Clelia Caracciolo , Franco Prodi, Remko Uijlenhoet, Stefano Natali

8:8 PHASE-DOPPLER INTERFEROMETRY FOR IMPROVED CLOUD MICROPHYSICAL MEASUREMENTS 1056
Patrick Chuang, William Bachalo

8:9 MEASUREMENTS OF THE DROPLET SPECTRA WITH THE FSSP-100:A STOCHASTIC MODEL OF PROBE FUNCTIONING 1059
Afranio Coelho, Jean-Louis Brenguier, Thierry Perrin

8:10 EVALUATING CLOUD LIQUID WATER IN NWP AND CLIMATE MODELS USING MEASUREMENTS FROM THE BALTEX CLOUD LIQUID WATER NETWORK: CLIWA-NET 1063
Susanne Crewell, Ulrich Löhnert, Erik Van Meijgaard

8:11 POLARIZATION-LIDAR PROBING OF CLEAR AND CLOUDY ATMOSPHERE OVER GADANKI, A REMOTE CONTINENTAL STATION IN INDIA 1066
Panuganti C.S. Devara, Y. Jaya Rao, Atul Kumar Srivastava, Y. Bhavani Kumar, D. Narayana Rao

8:12 IN SITU CLOUD SENSING WITH MULTIPLE SCATTERING LIDAR 1070
K. Franklin Evans, R. Paul Lawson, Pat Zmarzly, Darren O'Connor, Warren J. Wiscombe

8:13 A COMPARISON BETWEEN THE ROSEMOUNT ICING DETECTOR AND THE SMALL ICE DETECTOR 1074
Paul Field, Phil Brown, George Isaac, Walter Strapp, Alexei Korolev, Stewart Cober, Edwin Hirst, Richard Greenaway, Paul Kaye

8:14 A FIELD INTERCOMPARISON OF A PHASE DOPPLER PARTICLE ANALYSER AND FSSP AT THE SPHINX MOUNTAIN LABORATORY. 1078
Mike Flynn, Martin Gallagher, Keith Bower

8:15 AIRBORNE DIGITAL IN-LINE HOLOGRAPHIC DETECTOR FOR CLOUD PARTICLE STUDIES 1081
Jacob Fugal, Ewe Wei Saw, Alex V. Sergeyev, Raymond A. Shaw

8:16 ON THE MEASUREMENT OF RAINDROPS FALL SPEEDS AT THE GROUND USING OPTICAL ARRAY PROBES 1085
Fernando García-García, G. Montero-Martínez

8:17 ASSESSING CLOUD SPATIAL AND VERTICAL DISTRIBUTION WITH INFRARED CLOUD ANALYZER 1089
Iliana Genkova, Chuck Long, Thierry Besnard, Didier Gillotay

8:18 NEPHELOMETER MEASUREMENTS IN FLORIDA THUNDERSTORMS 1092
Hermann Gerber, Timothy Garrett, Andrew Heymsfield, Michael Poellot, Cynthia Twohy

8:19 FLOW FIELD AND PARTICLE TRAJECTORY SIMULATIONS OF A STRATOSPHERIC COUNTERFLOW VIRTUAL IMPACTOR 1095
Måns Håkansson, Kevin Noone, Johan Ström

8:20 MEASUREMENTS OF "LARGE" CCN 1099
James G. Hudson, Seong Soo Yum

8:21 AN AUTOMATED SYSTEM FOR IDENTIFYING TYPES OF SOLID PRECIPITATION BY IMAGE PROCESSING 1103
Masaaki Ishizaka, Toru Shiina, Ken Muramoto, Sento Nakai, Atsushi Sato

8:22 ANALYSIS OF MILLIMETER-WAVE MEASUREMENTS OF FROZEN HYDROMETEORS 1107
Min-Jeong Kim, James Weinman, D.-E. Chang, J.R. Wang, S. Tanelli, J. Roman, S. Sekelsky

8:23 THE COMPACT CLOUD SPECTROMETER AND IMPACTOR 1108
Gregory L. Kok, Cynthia Twohy, Darrel Baumgardner

8:24 SHATTERING DURING SAMPLING BY OAPS AND HVPS 1111
Alexei Korolev, George Isaac

8:25 WARM RAIN PROCESSES OVER THE TROPICAL OCEANS AND IMPLICATIONS FOR CLIMATE 1115
William K. M. Lau, Huey-Tzu Jenny Wu

8:26 AN IMPROVED ALGORITHM FOR IN SITU ICE WATER CONTENT MEASUREMENTS WITH APPLICATIONS TO CIRRUS AND OTHER ICE CLOUDS 1119
Paul Lawson, Brad Baker

Paper	Table of Contents – Papers	Page

8:27	RAINFALL MEASUREMENTS FROM SPACE: WHERE ARE WE? *Vincenzo Levizzani, Alberto Mugnai*	1123
8:28	ALL-SKY VISIBLE AND INFRARED IMAGES FOR CLOUD MACRO CHARACTERISTICS OBSERVATION *Daren Lu, Juan Huo, Wenxing Zhang*	1127
8:29	MICROPHYSICALLY-BASED RETRIEVAL OF RAINING CLOUDS BY GROUND-BASED MULTISPECTRAL MICROWAVE RADIOMETRY *Frank S. Marzano, Domenico Cimini, Randolph Ware*	1130
8:30	FIRST AIRBORNE CLOUD MEASUREMENTS WITH A COUNTERFLOW VIRTUAL IMPACTOR EQUIPPED WITH A PASSIVE WIND TUNNEL FOR OPERATION ON SLOWLY FLYING AIRCRAFT *Stephan Mertes, Alfons Schwarzenböck*	1134
8:31	LINK BETWEEN SIZE-RESOLVED HYGROSCOPIC GROWTH MEASUREMENTS OF AEROSOL PARTICLES ENTERING A HILL CLOUD AND NUMBER SIZE DISTRIBUTIONS OF INTERSTITIAL AND CLOUD DROP RESIDUAL PARTICLES MEASURED IN-CLOUD *Stephan Mertes, Katrin Lehmann, Diane Galgon, Andreas Nowak, Andreas Massling, W. Wieprecht*	1138
8:32	METEOROLOGICAL SURVEILLANCE TECHNIQUES BASED ON UNMANNED AERIAL VEHICLE SYSTEM *Slobodan Petkovic, Goran Memon*	1142
8:33	USE OF DIGITAL HOLOGRAPHY FOR SIZE ESTIMATION OF AEROSOL PARTICLES FROM THEIR BROWNIAN MOTION *Franco Prodi, Gianni Santachiara , Stefania Travaini , F. Belosi, Andrei Vedernikov , Frank Dubois , Jean Claude Legros*	1146
8:34	COMPUTATIONAL FLUID DYNAMICS STUDIES OF AN ICE NUCLEUS CHAMBER *David Rogers, Derek Straub, Paul J. Demott*	1150
8:35	OXYGEN A-BAND MEASUREMENTS FOR SOLAR PHOTON PATH LENGTH DISTRIBUTION STUDIES *Thomas Scholl, Klaus Pfeilsticker*	1154
8:36	THE STUDY OF CLOUD WATER RESOURCES BY DOPPLER RADAR *Lixin Shi , Duan Ying, Zhihui Wu, Dazhang Tang*	1158
8:37	AIRBORNE DATA ACQUISITION SYSTEMS *Sergey N. Skuratov, Victor V. Petrov, Victor P. Korneev, Vladimir A. Glushykhin, Vasily V. Volkov*	1160
8:38	ASSESSMENT OF SUPERSATURATION IN DIFFUSION CHAMBERS *Jefferson R. Snider, Markus D. Petters*	1163
8:39	DEVELOPMENT OF A LOW POWER AND HIGH SENSITIVITY CLOUD PROFILING FM-CW RADAR AT 95 GHZ *Toshiaki Takano, Hiroshi Kumagai, Tamio Takamura, Teruyuki Nakajima*	1167
8:40	APPLICATIONS OF PMW RAINFALL ALGORITHMS TO MEDITERRANEAN AREA EVENTS *F Torricella, V Levizzani, V Poli*	1171
8:41	USING ICE CRYSTAL ANALOGUES TO VALIDATE CLOUD ICE PARAMETER RETRIEVALS FROM THE CPI ICE SPECTROMETER DATA. *Z Ulanowski, Paul Connolly, Mike Flynn, Martin Gallagher, A.J.M. Clarke, E. Hesse*	1175
8:42	RADIATIVE TRANSFER IN SHALLOW CUMULUS CLOUD FIELDS: OBSERVATIONS AND FIRST ANALYSIS WITH THE DIRAM INSTRUMENT DURING THE BBC-2 FIELD CAMPAIGN IN MAY 2003 *Han Van Dop, Keith Wilson*	1179
8:43	FIRST MEASUREMENTS WITH AN EXPANSION TYPE CCN COUNTER *Stefan Van Ekeren, M. Fierz, U. Baltensperger, H. Burtscher, E. Weingartner*	1183
8:44	SATELLITE RAINFALL ESTIMATION OVER SOUTH AMERICA: THE HYDROESTIMATOR TECHNIQUE *Daniel Vila, Alexandra A. Lima*	1186
8:45	SMALL-SCALE RAIN NONUNIFORMITY AND ITS EFFECT ON CORRECTION OF NONUNIFORM BEAM FILLING IN SPACEBORNE RADAR RAIN MEASUREMENT *Ling Zhang, Daren Lu, Shu Duan, Jinli Liu*	1190
8:46	ONE MEASUREMENT OF CLOUD LIQUID CONTENT BY AN AIRBORNE UP-LOOKING MICROWAVE RADIOMETER *Xiaoqing Zhang, Hengchi Lei*	1194

TOPIC 9: APPLICATIONS OF CLOUD PHYSICS

9:1 PHYSICOSTATISTICAL MODEL FOR ROAD ICING FORECAST AND CONTROL 1196
Natalia A. Bezrukova, Evgeni A. Stulov, Marat F. Khalili

9:2 APPLICATION OF A SEMI-SPECTRAL CLOUD WATER PARAMETERIZATION TO COOLING TOWER PLUMES 1200
Emmanuel Bouzereau, Luc Musson-Genon, Bertrand Carissimo, Éric Dupont

9:3 OVERVIEW OF THE RECENT NATIONAL RESEARCH COUNCIL OF THE NATIONAL ACADEMY OF SCIENCES REPORT ON: CRITICAL ISSUES IN WEATHER MODIFICATION RESEARCH 1204
Roelof T Bruintjes, Michael Garstang

9:4 NUMERICAL SIMULATION OF AFFECTING RANGE FOR CLOUD SEEDING WITHIN SUPER-COOLED STRATIFORM CLOUD 1208
Jin Dai, Xing Yu, Peng Fan, Zhengqi Chen

9:5 OBSERVATION STUDY FOR PHYSICAL EFFECT OF LIQUID CARBON DIOXIDE ON CLOUD 1212
Peng Fan, Hong-Tian Chen, Heng-Chi Lei

9:6 FLYING CASE STUDY OF A PRECIPITATION SHEET CLOUDS ARTIFICIAL RAIN ENHANCEMENT MICRO DETECTION ON MAY 9TH, 1995, IN JILIN PROVINCE 1215
Shufang Gu, Jianchun Gao, Dezhen Jin, Jinghong Zhang, Qiang Wei, Zhongming Hu, Zhixin Chen, Zhanzhu Li, Xiaomei Wang, Junmei Guo

9:7 PRECIPITATION CHARACTERISTICS OF CLOUDS OVER THE UNITED ARAB EMIRATES 1218
Tara Jensen, Roelof Bruintjes, Daniel W. Breed, Vidal Salazar, Abdulla Al Mangoosh, Abdulla Al Mandoos

9:8 OBSERVATION EXPERIMENT OF AIRBORNE MICROWAVE RADIOMETER IN WEATHER MODIFICATION 1222
Dezhen Jin, Shufang Gu, Jinghong Zhang, Maolun Li, Xinzhi Chen, Hengchi Lei, Zhong Wei, Zhilai Shen

9:9 THE COMPREHENSIVE OBSERVATION ANALYSIS OF A LC SEEDING MAN-MADE STEERING ICE CRYSTAL EXPERIMENT 1225
Dezhen Jin, Hengchi Lei, Jiaoheng Zheng, Hui Xiao, Lian Cui, Yuxia Wu, Jian Liu

9:10 PRECIPITATION OVER THE SEA IN THE COASTAL AREA OF ISRAEL; A POSSIBLE NEW SOURCE OF WATER 1228
Zev Levin, Joseph Breitgand, David Shtivelman

9:11 DETECTION OF DIFFUSION ON MOUNTAINS OF BEIJING 1232
Ruijie Li

9:12 EFFECT EVALUATION OF SEEDING WITH ROCKETS IN BEIJING REGION 1234
Shuyan Li , Wei Li

9:13 VIL AS AN INDICATOR OF HAIL SIZE 1238
Laura López, Eduardo García-Ortega, Jean Dessens, José Luis Sánchez

9:14 AN ALGORITHM FOR CONTINUOUS EVALUATION OF CLOUD BASE HEIGHT, CLOUD BASE TEMPERATURE, AND CLOUD COVERAGE AT LOCAL SCALE 1242
Esmaiel Malek

9:15 THE MACROSCOPIC AND MULTIPLE PARAMETER MEASURING SYSTEM OF AIRCRAFT PRECIPITATION ENHANCEMENT 1246
Li Maolun, Jin Dezhen

9:16 DIAGNOSIS OF THERMODYNAMIC CONDITIONS REQUIRED FOR OCCURRENCE OF FREEZING RAIN 1249
Hiroki Matsushita, Fumihiko Nishio

9:17 A REAL-TIME SATELLITE-BASED ICING DETECTION SYSTEM 1253
Patrick Minnis, William Smith Jr, Louis Nguyen, Mandana M. Khaiyer, Douglas A. Spangenberg, Patrick W. Heck, Rabindra Palikonda, Ben C. Bernstein, Frank Mcdonough

9:18 COMPARATIVE STUDY OF NUCLEATION BY ALCOHOLIC SOLUTION OF BENZOIN, BENZOIN DUST, AND BENZIL DUST. 1257
Sahana Paul, Anupam Hazra, Utpal Kumar De, Sanjay Bhar, Kushalendu Goswami

9:19 THE SCREEN OF WEATHER MODIFICATION LN MEDIUM 1261
Ying Qi, Xuelin Wang, Jiaoheng Zhen, Feng He, Zhixin Chen, Xiaomei Wang, Junmei Guo, Xiangren Yu

9:20 A THREE-DIMENSIONAL MODELING STUDY OF HAILSTORM SEEDING 1264
Vlado Spiridonov, Lena Jovanovska

9:21 COMPUTATION OF ELECTROMAGNETIC CHARACTERISTICS OF FROZEN HYDROMETEORS AND COMPARISONS WITH MILLIMETER-WAVE MEASUREMENTS 1268
James Weinman, Min-Jeong Kim

9:22 THE DEVELOPMENT OF GROUND-BASE WEATHER MODIFICATION TOOLS IN CHINA 1272
Yuzhong Wu, Guangxue Chen

9:23 STATISTICAL EVALUATION FOR THE PRECIPITATION EFFECTIVENESS OF CLOUD SEEDING IN HENAN COUNTY OF CHINESE QINGHAI PROVINCE 1276
Zhanyu Yao, Chenhai Xu, Hui Xiao, Lijun Wang, Anping Sun, Jiangping Pu

9:24 COMPARISON BETWEEN SIMULATION OF TRANSPORT AND DIFFUSION OF SEEDING AGENT IN PRECIPITATION ENHANCEMENT BY AIRCRAFT WITH NOAA SATELLITE DATA 1278
Xing Yu, Jin Dai, Peng Fan, Zhengqi Chen

9:25 THE RESEARCH OF SEEDING AGENT DIFFUSION TRAIL 1282
Jinghong Zhang , Shufang Gu, Zhixin Chen, Xiaomei Wang

9:26 AN EXPERIMENTAL STUDY OF THE EFFECTS OF EXPLOSION ON A CONVECTIVE ECHO 1285
Hesheng Zhou, Qing Luo, Huanbin Xu, Jianxin Li, Can Xu, Gang Liu, Liyun Yin, Wei Wei, Libing Liu, Qing Wang, Shuguang Meng

TOPIC 10: CLOUD PARAMETERIZATION IN MODELS

10:1 THE EFFECTS OF ADDING SMALL CRYSTALS IN THE ICE PARTICLE SIZE DISTRIBUTION ON THE EVOLUTION OF MIXED-PHASE CLOUD 1289
Faisal Boudala, George Isaac

10:2 A LONG TERM COMPARISON OF CLOUD PROPERTIES OBSERVED BY VERTICALLY POINTING RADAR AND LIDAR WITH THEIR REPRESENTATION IN OPERATIONAL NWP MODELS 1293
Malcolm Brooks, Robin Hogan, Anthony Illingworth

10:3 PARAMETERIZATION OF THE STRATOCUMULUS CLOUD TOPPED BOUNDARY LAYER: EVALUATION OF THE ECHAM BOUNDARY LAYER SCHEME AGAINST LARGE-EDDY SIMULATIONS 1295
Andreas Chlond, Frank Mueller, Igor Sednev

10:4 PARAMETERIZATION OF MICROPHYSICAL PROCESSES IN A NON HYDROSTATIC PREDICTION MODEL 1297
Oxana Drofa, Piero Malguzzi

10:5 PARAMETRIZATION OF MICROPHYSICS FOR CONVECTIVE-SCALE NUMERICAL WEATHER PREDICTION 1301
Richard Forbes

10:6 TEST AND IMPROVEMENTS OF GCM CLOUD PARAMETERIZATION USING THE CCCMA SCM WITH SHEBA DATASET 1304
Qiang Fu, Jian Yuan, Norm Mcfarlane

10:7 MODEL DYNAMIC AND MICROPHYSICAL VERIFICATION OF THE 13-14 DECEMBER 2001 IMPROVE 2 CASE 1308
Matthew Garvert, Christopher Woods, Brian Colle, Cliff Mass, Peter V. Hobbs

10:8 RELATIONSHIP BETWEEN SOLAR RADIATIVE BIASES AND DEEP CONVECTION ANVIL DIMENSIONS 1312
Francesca Di Giuseppe, Adrian Tompkins

10:9 FORECASTING ICING CONDITIONS DURING ALLIANCE ICING RESEARCH STUDY II WITH THE CANADIAN METEOROLOGICAL CENTRE GLOBAL ENVIRONMENTAL MULTISCALE MODEL 1316
Anna Glazer, George Isaac

10:10 CLOUDS AND CLIMATE: PROGRESS AND PROSPECTS 1320
Wojciech Grabowski

10:11 QUANTITATIVE PRECIPITATION FORECASTING OF WINTERTIME STORMS IN THE SIERRA NEVADA: SENSITIVITY TO THE MICROPHYSICAL PARAMETERIZATION 1324
Vanda Grubisic, Ramesh Vellore, Arlen Huggins

10:12 MICROPHYSICAL PARAMETERIZATION AND VARIABILITY FOR MIXED PHASE CLOUDS USING IN-SITU OBSERVATIONS 1326
Ismail Gultepe, George Isaac

10:13 HIERARCHY OF MICROPHYSICAL PARAMETERIZATIONS SUITABLE FOR CLOUD AND MESOSCALE MODELS. 1330
William Hall, Roy M. Rasmussen

10:14 COMPARISON OF OBSERVED CLOUD PROPERTIES AT THREE GROUND BASED SITES WITH THEIR REPRESENTATION IN OPERATIONAL MODELS: THE EU CLOUDNET PROJECT 1334
Anthony Illingworth, Cloudnet Team

10:15 TROPICAL CIRRUS PARAMETERIZATION FOR TRIMODAL SIZE SPECTRA 1337
Dorothea Ivanova, David Mitchell, Greg Mcfarquhar

10:16 SUBGRID-SCALE ACTIVATION OF CCN 1340
Hongli Jiang, William R. Cotton

10:17 REPRESENTING STRATOCUMULUS CLOUDS IN NUMERICAL MODELS: SENSITIVITY TO MODEL PHYSICS AND VERTICAL RESOLUTION 1344
Colin Jones

10:18 USING REMOTE SENSING DATA TO EVALUATE THE LOKAL-MODELL PERFORMANCE 1348
Christian Keil

10:19 CLOUD-RESOLVING MODEL AS A PARAMETERIZATION OF CLOUDS IN A GENERAL CIRCULATION MODEL 1352
Marat Khairoutdinov, David Randall

10:20 ON CHARACTERIZATION OF SUB-GRID VARIABILITY IN STRATIFORM CLOUDS BASED ON MMCR DATA 1354
Zena Kogan, David B. Mechem, Yefim L. Kogan

10:21 DEVELOPMENT OF THE PARAMETERIZATIONS TO PREDICT THE INITIAL SIZE DISTRIBUTION OF CLOUD DROPLETS FOR THE CLOUD MICROPHYSICAL MODEL IN THE GLOBAL OR REGIONAL MODELS – NUMERICAL SIMULATION WITH A HYBRID CLOUD MICROPHYSICAL MODEL – 1358
Naomi Kuba

10:22 DERIVING PROGNOSTIC EQUATIONS FOR CLOUD FRACTION AND LIQUID WATER CONTENT 1362
Vincent Larson

10:23 NEW PARAMETERIZATIONS FOR THE AUTOCONVERSION PROCESS AND THE DISPERSION EFFECT 1366
Yangang Liu, Peter Daum, Robert Mcgraw

10:24 CLOUD PROPERTIES SIMULATED BY A SINGLE-COLUMN MODEL 1370
Yali Luo, Steven Krueger

10:25 SIMULATION OF A SQUALL LINE CONVECTIVE SYSTEM USING SPECTRAL (BIN) MICROPHYSICS AND BULK PARAMETERIZATIONS 1374
Barry H. Lynn, Axel Seifert, A. Khain

10:26 CONVECTIVE CLOUDY BOUNDARY LAYER PARAMETERIZATION USING A MASS FLUX APPROACH 1378
Anne Mathieu, Frederic Hourdin, Alain Lahelle, Martial Haeffelin, Philippe Drobinski, C. Rio

10:27 EXPLICIT PREDICTION OF HAIL USING A TRIPLE-MOMENT BULK MICROPHYSICS SCHEME 1382
Jason Milbrandt, M. K. Yau

10:28 NUMERICAL MODELLING OF RISING THERMAL: APPLICATION FOR CUMULUS CLOUDS PARAMETERIZATION 1386
Georgy Mostovoy, Pat Fitzpatrick

10:29 RESULTS FROM A NEW MAXIMUM SIMPLICATION MODEL OF CLOUD PROPERTIES BENEATH THE MARINE BOUNDARY LAYER 1389
Sungsu Park, Conway Leovy, Margaret Rozendaal

10:30 A STUDY OF DRIZZLE FORMATION FOR GENERAL CIRCULATION MODEL PARAMETERIZATIONS 1393
Hanna Pawlowska, Jean-Louis Brenguier

10:31 A QUASI 2-MOMENT MIXED-PHASE BULK MICROPHYSICAL SCHEME FOR USE IN A CLOUD RESOLVING MODEL 1397
Jean-Pierre Pinty

10:32 STOCHASTIC CONVECTIVE PARAMETERIZATION WITH MULTIPLE PLUMES 1401
Robert Plant, George Craig

10:33 SENSITIVITIES IN MODEL RESULTS DUE TO CHANGES IN THE PARAMETERIZATION OF CLOUD MICROPHYSICS 1404
Thorsten Reinhardt, Ulrike Wacker

10:34 MODELLING CIRRUS CLOUDS IN THE TROPICAL TROPOPAUSE LAYER 1408
Chuansen Ren, A. Robert Mackenzie

10:35 RETRIEVING INHOMOGENEOUS CLOUDS 1412
Ronald Scheirer, Sebastian Schmidt

10:36 A COMPARISON OF SPECTRAL BIN AND TWO-MOMENT BULK MIXED-PHASE MICROPHYSICS 1416
Axel Seifert, Alexander Khain, Andrei Pokrovsky, Klaus D. Beheng

10:37 NUMERICAL SIMULATION OF THE 16TH JULY CRYSTAL-FACE STORM AND COMPARISON WITH OBSERVATIONS 1420
Axel Seifert, Andrew J. Heymsfield, Aaron Bansemer

10:38 USING SUBGRID CLOUD VARIABILITY IN NON LINEAR PRECIPITATION PROCESSES 1424
Adrian Tompkins, Robert Pincus

10:39 A 3D SPECTRAL ICE HABIT PREDICTION SYSTEM FOR IMPROVING CLOUD RADIATION SIMULATIONS 1428
Gregory Tripoli, Tempeii Hashino, Giulia Panegrossi, Sabatino Di Michele, Stefano Dietrich, Alberto Mugnai

10:40 A STATISTICAL ACTIVATION SCHEME FOR TURBULENCE CLOSURE MODELS 1432
Shouping Wang, Jean-Christophe Golaz

10:41 COMPARISON OF MODEL AND RADAR DERIVED CLOUD VERTICAL STRUCTURE AND OVERLAP 1434
Ulrika Willén, S. Crewell

10:42 THE BEHAVIOUR OF DIFFERENT CLOUD PROCESS PARAMETRIZATIONS IN A LARGE-SCALE MODEL 1438
Damian R. Wilson, Amanda Kerr-Munslow, Andrew C. Bushell

10:43 MODELLING CLOUDS AND RADIATION IN THE ARCTIC 1442
Klaus Wyser, Colin Jones, Ulrika Willen

10:44 A QUASI-IMPLICIT CALCULATING SCHEME OF CLOUD MODEL 1446
Shi Yueqin, Hu Zhijin

10:45 A MICROPHYSICAL PARAMETERIZATION FOR CONVECTIVE CLOUDS IN THE ECHAM GCM DESCRIPTION AND FIRST RESULTS 1450
Junhua Zhang, Ulrike Lohmann

10:46 THE DEVELOPMENT OF A NEW EXPLICIT MICROPHYSICAL SCHEME USING IN MM5 1454
Zhen Zhao, Hengchi Lei, Yu-Xia Wu

TOPIC 11: MODELING OF CLOUD-SCALE PROCESSES

11:1 NUMERICAL MODELLING OF MOIST DECAYING TURBULENCE: CLOUD-CLEAR AIR MIXING AT RESOLUTION BETTER THAN 1CM. 1457
Miroslaw Andrejczuk, Wojciech W. Grabowski, Szymon P. Malinowski, Piotr K. Smolarkiewicz

11:2 ADVANCES IN CLOUD ASSIMILATION AT ECMWF USING ARM RADAR DATA 1461
Angela Benedetti, Marta Janisková

11:3 PAFOG - A NEW EFFICIENT FORECAST MODEL OF RADIATION FOG EVENTS 1465
Andreas Bott

11:4 THE SENSITIVITY OF LARGE-EDDY SIMULATIONS OF STRATOCUMULUS TO THE PARAMETRIZATION OF DRIZZLE. 1469
Philip Brown, Glen Richardson, Robert Wood

11:5 MODELLING STUDIES OF ICE CONCENTRATION IN FRONTAL CIRRUS CLOUDS 1473
John Cardwell, T. W. Choularton

11:6 AN ASSESSMENT OF THE MESO-NH CLOUD SCHEME USING SATELLITE OBSERVATIONS FROM THE VISIBLE TO THE MICROWAVES 1476
Jean-Pierre Chaboureau, P. Dubuisson, J. Pardo, C. Prigent, J.-P. Pinty, P. J. Mascart, E. Richard

11:7 MULTIMODEL ENSEMBLE FORECASTS OF PRECIPITATION OVER THE ALPINE REGION DURING THE MAP- SPECIAL OBSERVING PERIOD USING MESOSCALE MODELS. 1480
Federico Ceccarelli, T.N. Krishnamurti, B. Mackey, C.F. Ratto

11:8 IMPLEMENTATION OF A NEW ICE AGGREGATION AND SEDIMENTATION SCHEME IN A BULK-MICROPHYSICAL MODEL, DERIVED FROM AIRCRAFT OBSERVATIONS 1484
Richard Cotton, Paul Field

11:9 COMPARISON OF OBSERVED AND SIMULATED DEEP CONVECTIVE CLOUD OBJECTS 1488
Zachary Eitzen, Kuan-Man Xu

11:10 SENSITIVITY OF SIMULATED WARM RAIN FORMATION TO COLLISION AND COALESCENCE EFFICIENCIES, BREAKUP, AND TURBULENCE COMPARISON OF TWO BIN-RESOLVED NUMERICAL MODELS 1492
Ann Fridlind, Axel Seifert, Andrew Ackerman, Eric Jensen

11:11 NUMERICAL STUDY OF A SEVERE STORM IN BEIJING 1495
Danhong Fu, Xueliang Guo

11:12 UNDERSTANDING OF FOG STRUCTURE, DEVELOPMENT, AND FORECASTING, COST 722 1499
Alan Gadian, Andreas Bott

11:13 CONSTANT SLOPE OR CONSTANT INTERCEPT? THE IMPACT ON PRECIPITATION USING SINGLE-MOMENT MICROPHYSICS 1500
Matthew Gilmore, Susan C. Van Den Heever, Jerry M. Straka, Robert Wilhelmson, William R. Cotton, Erik N. Rasmussen

11:14 SUBGRID-SCALE CCN ACTIVATION 1504
Jean-Christophe Golaz, Shouping Wang, Vincent E. Larson

11:15 NUMERICAL MODELING OF MICROPHYSICAL VARIABLES USING RAMS AT AMAZONIAN REGION, BRAZIL 1508
Fábio Gonçalves, Jorge Martins, M.A. Silva Dias

11:16 RADIATIVE IMPACTS ON THE GROWTH OF DROPS WITHIN SIMULATED MARINE STRATOCUMULUS CLOUDS 1511
Jerry Harrington, Christopher Hartman

11:17 AN IMPROVEMENT FOR LIQUID-PHASE MICROPHYSICS IN JMA-NHM. 1515
Akihiro Hashimoto, Masataka Murakami, Syugo Hayashi, Chiashi Muroi, Teruyuki Kato, Masanori Yoshizaki

11:18 RAPPORT FROM THE WMO INTERNATIONAL CLOUD MODELING WORKSHOP 11-16 JULY 2004 1519
Daniela Jacob, Wojciech Grabowski, Andreas Chlond, Stefan Hagemann

11:19 THE MODELLING OF PROCESS OF RAINFALL FORMATION BY CLOUDS SEEDING 1520
Bakhtior Kadyrov

11:20 THE DERIVATION OF THE GAS DYNAMICS EQUATIONS BY CONSIDERING CHANGES OF THE VELOCITY DISTRIBUTION FUNCTION ON SCALES OF THE MOLECULE FREE PATH 1523
Alexander Kochin

11:21 EVALUATION OF MM5 HIGH-RESOLUTION SUMMERTIME PRECIPITATION FORECASTS OVER THE URBAN AREA OF ATHENS, GREECE 1525
Vassiliki Kotroni, Konstantinos Lagouvardos

11:22 CLOUD WATER AND RAINWATER NUMERICAL SIMULATION WITH LASG-REM MODEL 1529
Shuyan Li, Wenan Xiao, Hengchi Lei

11:23 MULTI-DIMENSIONAL LONGWAVE RADIATIVE FORCING OF PBL CLOUD SYSTEMS 1533
David Mechem, Mikhail Ovtchinnikov, Yefim Kogan, Frank Evans, Anthony Davis, Robert Cahalan, Ezra Takara, Robert Ellingson

11:24 PARAMETERISATION OF NON-INDUCTIVE CHARGING IN THUNDERSTORM REGIONS FREE OF CLOUD DROPLETS 1537
Rumjana Mitzeva, Clive Saunders, Boryana Tsenova

11:25 INNER STRUCTURE AND PRECIPITATION MECHANISM IN OROGRAPHIC SNOW CLOUDS OVER THE COMPLEX TERRAIN IN CENTRAL JAPAN 1541
Masataka Murakami, Narihiro Orikasa, Ken-Ichi Kusunoki, Kazumasa Mori, Akihiro Ikeda, Mitsunori Saitoh

11:26 NUMERICAL STUDY ON STRUCTURE AND MAINTENANCE MECHANISM OF TYPHOON SPIRAL BANDS USING THE CLOUD RESOLVING STORM SIMULATOR 1545
Mitsuharu Nomura, Kazuhisa Tsuboki

11:27 NUMERICAL SIMULATION OF THE WARM-SEASON FRONTAL CLOUD SYSTEMS WITH STRONG PRECIPITATION 1549
Anne Pirnach

11:28 CELL MERGER SIMULATIONS WITH THREE-DIMENSIONAL ENVIRONMENTAL DATA 1553
Diana R. Pozo, Israel Borrajero, Julio C. Marín, Graciela Raga, Daniel Martínez

11:29 MODELING TROPICAL ATMOSPHERIC CONVECTION IN THE CONTEXT OF THE WEAK TEMPERATURE GRADIENT APPROXIMATION 1557
David J. Raymond, Xiping Zeng

11:30 NUMERICAL STUDY ON SNOW CLOUD STREETS IN COLD AIR STREAM OVER THE SEA USING THE CLOUD RESOLVING STORM SIMULATOR 1561
Atsushi Sakakibara, Kazuhisa Tsuboki

11:31 RADIATIVE AND MICROPHYSICAL PROPERTIES OF MIXED-PHASE ALTOCUMULUS A MODEL EVALUATION OF SUPERCOOLING EFFECTS 1565
Kenneth Sassen, Vitaly I. Khvorostyanov

11:32 ON THE DEPENDENCY OF PRECIPITATION FROM MIXED-PHASE CONVECTIVE STORMS ON VERTICAL WIND SHEAR, BUOYANCY AND CLOUD CONDENSATION NUCLEI 1569
Axel Seifert, Klaus D. Beheng

11:33 CLOUD-ENSEMBLE SIMULATIONS OF TROPICAL CONVECTION UNDER DIFFERENT MICROPHYSICAL REGIMES 1573
Antônio Charles Silvério, Alexandre Araújo Costa, José Carlos Parente De Oliveira, Gerson Paiva De Almeida, Sergio Sousa Sombra

11:34 CIRRUS SIMULATIONS OF CRYSTAL-FACE 23 JULY 2002 CASE 1576
David Starr, Ruei-Fong Lin, Belay Demoz, Andrew Lare

11:35 MESOSCALE SIMULATIONS OF CRYSTAL-FACE 23 JULY 2002 CASE 1580
David Starr, Ruei-Fong Lin, Andrew Lare, Belay Demoz, Thomas Rickenbach, Donghai Wang, Lihua Li, G. Thomas Arnold, Yansen Wang

11:36 A COMPARISON OF CONSERVATION PROPERTIES OF MICROPHYSICAL PARAMETERIZATIONS: CONTINUOUS GAMMA DISTRIBUTION FUNCTION WITH FIXED SHAPE PARAMETER 1584
Jerry M. Straka, Mathew S. Gilmore, Erik N. Rasmussen, Katherine M. Kanak

11:37 A MICROPHYSICS PARAMETERIZATION SCHEME FOR RADAR DATA ASSIMILATION 1588
Wanda Szyrmer, Isztar Zawadzki, Stephane Laroche

11:38 FORMATION OF A FIRE-INDUCED CONVECTIVE CLOUD: A MODEL STUDY OF THE CHISHOLM FIRE, 28 MAY 2001 1592
Joerg Trentmann, Tanja Winterrath, G. Luderer, Christiane Textor, Michael D. Fromm, Rene Servranckx, Daniel Rosenfeld, Pao K. Wang, Peter V. Hobbs, Meinrat O. Andreae

11:39 EVALUATION OF CLOUDS AND PRECIPITATION FROM A GLOBAL NWP MODEL 1596
Paul A. Vaillancourt, Stéphane Bélair, Michel Roch, Anne-Marie Leduc

11:40 INCORPORATION OF A 1D ACOUSTIC-ELECTROSTATIC COALESCENCE MODEL INTO THE 3D CLOUD MODEL 1600
Zlatko Vukovic, Mladjen Curic

11:41 THE IMPACT OF EXTREME WATER VAPOR SUPPLY ON OROGRAPHIC-CONVECTIVE-STRATIFORM MIXED CLOUD 1604
Weijia Wang, Xialing Tao

11:42 THREE-DIMENSIONAL NUMERICAL SIMULATION OF TORRENTIAL RAINSTORMS IN WUHAN 1608
Hui Xiao, Xiaobo Wang, Feifei Zhou, Yanchao Hong

11:43 CHARACTERISTIC ANALYSES OF THE CONCENTRATIONS OF ATMOSPHERIC ICE FORMING NUCLEI IN THE SOURCE AREA OF YELLOW RIVER 1612
Hui Xiao, Yuxiang He, Bojie Chen, Zhanyu Yao

11:44 NUMERICAL SIMULATION OF THE INFLUENCE OF ATMOSPHERIC ICE NUCLEI DISTRIBUTION ON CONVECTIVE CLOUD SEEDING EFFECT 1616
Hui Xiao, Shuyan Liu, Zhaoxia Hu, Qiang Zhang

TOPIC 12: CLOUD DYNAMICS AND STRUCTURE

12:1 DETERMINING CLOUD SCALING ANISOTROPY EXPONENTS USING DIRECTIONAL STRUCTURE FUNCTIONS APPLIED TO MODIS SATELLITE IMAGES 1620
Jean-Bernard Addor

12:2 THE LIQUID WATER/ICE CONTENT IN MID-LATITUDE CONVECTIVE STORMS 1624
Ingo Bertram, Axel Seifert, Klaus D. Beheng

12:3 THE DIURNAL CYCLE OF SOUTHEAST PACIFIC STRATOCUMULUS DYNAMICS AND ENTRAINMENT OBSERVED IN EPIC 2001 1628
Christopher S. Bretherton, Peter Caldwell, Robert Wood

12:4 CAN THE FRACTAL DIMENSION OF CLOUDS BE MEASURED? 1632
Joseph Brewer, Larry Di Girolamo

12:5 CHARACTERIZATION OF MESOSCALE FEATURES IN SE PACIFIC STRATOCUMULUS 1636
Kimberly Comstock, Christopher Bretherton, Sandra Yuter, R. Wood

12:6 VELOCITY FIELDS IN CUMULUS DERIVED FROM AIRBORNE DUAL-DOPPLER MEASUREMENTS 1639
Rick Damiani, Samuel Haimov, Gabor Vali

12:7 FACTORS CONTROLLING THE FORMATION AND EVOLUTION OF CUMULONIMBUS ANVILS OVER SOUTHERN FLORIDA 1643
Ann Fridlind, Andrew Ackerman, Eric Jensen

12:8 CHARACTERISTICS OF PRECIPITATING CLOUDS OVER ASIA DURING SUMMER AS DERIVED FROM TRMM PR AND TMI 1646
Yunfei Fu, Rui Li, Guosheng Liu, Jinli Liu, Daren Lu

12:9 CLOUD HOLES 1650
Hermann Gerber, Glendon Frick, Simon Malinowski, Jean-Lui Brenguier, F. Burnet

12:10 CENTRIFUGAL PRECIPITATION TRANSPORT IN TORNADIC SUPERCELLS: AN ALGORITHM CONSISTENT FOR USE WITH BULK MICROPHYSICS SCHEMES 1654
Matthew Gilmore, Robert P. Davies-Jones, Jerry M. Straka, Erik N. Rasmussen, Robert B. Wilhelmson

12:11 SMALL SCALE MIXING PROCESSES AT THE TOP OF A MARINE STRATOCUMULUS - A CASE STUDY. 1657
Krzysztof E. Haman, Szymon P. Malinowski, Joanna Remiszewska, Marcin Kurowski, Hermann Gerber, Jean-Louis Brenguier

12:12 IMPACTS OF UNIFORM FLOW ON THE DIFFUSION OF THE ICE NUCLEI IN STRATUS 1661
Hui He, Wankui Chen

12:13 STRUCTURES OF CLOUDS AND PRECIPITATION PRODUCING MECHANISMS 1665
Peter Hobbs, Arthur Rangno

12:14 A 3D STOCHASTIC CLOUD MODEL FOR INVESTIGATING THE RADIATIVE PROPERTIES OF INHOMOGENEOUS CIRRUS CLOUDS 1669
Robin Hogan, Sarah Kew

12:15 A NUMERICAL STUDY OF THE SNOWFALL AROUND THE NIIGATA REGION 1673
Katsushi Iwamoto, Sento Nakai, Masaaki Ishizaka, Masujiro Shimizu, Atsushi Sato, Toshisuke Maruyama

12:16 INVESTIGATION OF THE EVOLUTION OF RELATIVE HUMIDITY DURING TURBULENT MIXING USING PDF METHODS 1675
Christopher A. Jeffery

12:17 STRUCTURE AND EVOLUTION OF LONG-LIVED SLOW-MOVING LINE-SYSTEM IN MOIST AND WARM ENVIRONMENT IN EAST ASIA. 1679
Sachie Kanada, Teruyuki Kato, Masanori Yoshizaki

12:18 OCEANIC DIURNAL PRECIPITATING SYSTEMS OVER THE TROPICAL WESTERN PACIFIC, NORTH OF NEW GUINEA ISLAND 1683
Masaki Katsumata, Kunio Yoneyama

12:19 THE LIFE CYCLE OF CONVECTIVELY GENERATED STRATIFORM CLOUDS 1687
Steven K. Krueger, Michael A. Zulauf, Yali Luo

12:20 STRUCTURE OF LWC AND TEMPERATURE FIELDS IN SMALL CUMULUS CLOUDS SEEN FROM STATIONARY (TETHERED BALLOON) AND MOVING (AIRCRAFT) PLATFORMS. 1691
Marcin Kurowski, Holger Siebert, Krzysztof E. Haman, Szymon P. Malinowski

12:21 HUMIDITY CHARACTERISTICS IN THE DETRAINMENT REGION OF SMALL CUMULUS 1695
Neil Laird, Robert M. Rauber, Harry T. Ochs

12:22 COMPARISON STUDY OF A TYPHOON PRECIPITATION OVER SOUTH CHINA SEA 1697
Jinli Liu, Gang Zhao, Jiantong Li, Daren Lu, Yong Zhang, Ling Zhang

12:23 NUMERICAL SIMULATION OF RETRIEVING THREE-DIMENSIONAL WIND FIELD FROM DUAL DOPPLER RADAR 1701
Shuyan Liu, Hui Xiao, Yuxiang He

12:24 SIMULATIONS OF MEIYU FRONT WITH A NEW MICROPHYSICS SCHEME 1704
Xiaofeng Lou, Zhijin Hu, Penyun Wang, Xiuji Zhou, Yueqing Shi, Jing Sun

12:25 MIXING OF CLOUD AND CLEAR AIR IN CENTIMETER SCALES OBSERVED IN LABORATORY BY MEANS OF PARTICLE IMAGE VELOCIMETRY 1707
Szymon P. Malinowski, Piotr Korczyk, Tomasz A. Kowalewski

12:26 EFFECTS OF MESOSCALE CONVERGENCE ON CONVECTIVE RAINFALL SIMULATED WITH AN AXISYMMETRIC CLOUD MODEL WITH DETAILED MICROPHYSICS 1711
Ryohei Misumi, Ken-Ichi Maruyama, Masayuki Maki, Koyuru Iwanami, Sang-Goon Park, Mihoko Suto

12:27 AN OBSERVATIONAL STUDY OF THE NIIGATA SNOWSTORM OF 4-6 JANUARY 2003 1715
Sento Nakai, Masaaki Ishizaka, Katsushi Iwamoto, Masujiro Shimizu, Atsushi Sato, Toshisuke Maruyama

12:28 INSIGHTS ON THE UPDRAUGHT EXTINCTION BY SATELLITE OBSERVATIONS AND CLOUD MICROPHYSICAL MODEL 1719
Alvise Papa, Federico Porcù, Alessandro Battaglia, Pao K Wang, Stefano Natali, Franco Prodi

12:29 ANVIL CIRRUS STRUCTURE 1723
Jacob Petre, Johannes Verlinde

12:30 THE INFLUENCE OF MELTING ON THE PRECIPITATION PRODUCTION IN A MARITIME STORM-CLOUD 1726
Vaughan Phillips, Alexander Khain

12:31 EVALUATION OF VERTICAL AIR VELOCITY AND ITS DISTRIBUTION IN FOUR OPERATIONAL FORECAST MODELS USING CONTINUOUS DOPPLER CLOUD RADAR MEASUREMENTS 1730
Alain Protat, Dominique Bouniol, Martial Haeffelin

12:32 STRUCTURE AND LENGTH SCALES OF A STRATOCUMULUS FIELD DEVELOPING UNDER CONTINENTAL INFLUENCE: THE BBC CASE 23.09.01 1734
Markus Quante, Jens Meywerk, Dagmar Nagel

12:33 MAINTENANCE MECHANISM OF CONVECTIVE CELLS WITHIN MESOSCALE CONVECTIVE SYSTEM IN HUMID SUBTROPICAL REGION 1738
Shingo Shimizu, Hiroshi Uyeda, T. Shinoda, K. Tsuboki, H. Yamada, B. Geng, T. Kato

12:34 THE BALTEX BRIDGE CAMPAIGNS – A QUEST FOR CONTINENTAL CLOUD STRUCTURES 1742
Clemens Simmer, V. Venema, M. Diederich, S. Crewell, Arnout Feijt, Jean-Louis Brenguier

12:35 CU OF NORTH-WEST OF RUSSIA (GENERALIZED CHARACTERISTICS) 1746
Andrey Sinkevich, Yulia Dovgaluk, Yury Ponomarev, Vladimir Stepanenko, Nikolay Veremey

12:36 VERTICAL MOTIONS AT CIRRUS ALTITUDES 1750
Johan Ström

12:37 CIRRUS CLOUD OCCURRENCE AS FUNCTION OF AMBIENT RELATIVE HUMIDITY: A COMPARISON OF OBSERVATIONS OBTAINED DURING THE INCA EXPERIMENT 1754
Johan Ström, Marco Seifert, Bernd Kärcher, Joelle Ovarlez, Andreas Minikin, Jean-Francois Gayet, Radovan Krejci, Andreas Petzold, Frederique Auriol, W. Haag, R. Busen, U. Schumann, H. C. Hansson

12:38 AIRBORNE RADAR OBSERVATIONS OF NON-DRIZZLING MARINE STRATOCUMULUS 1758
Gabor Vali

12:39 ITERATIVE AMPLITUDE ADAPTED FOURIER TRANSFORM SURROGATE CLOUD FIELDS 1761
Victor Venema, Steffen Meyer, Sebastián Gimeno García, Clemens Simmer, Susanne Crewell, Ulrich Löhnert, Thomas Trautmann

12:40 SIZE DISTRIBUTIONS OF SNOW AND AEROSOL PARTICLES IN A CONTINUOUS PRECIPITATION WITH A CHANGE OF SURFACE OZONE CONCENTRATION AT NY-ÅLESUND, ARCTIC 1765
Makoto Wada, Hiroyuki Konishi, Shinji Morimoto, Takashi Yamanouchi

12:41 PRECIPITATION TYPE CLASSIFICATION IN THE BALTIC AREA IN RADAR OBSERVATIONS AND IN REMO 1769
Andi Walther, Jürgen Fischer, Ralf Bennartz

12:42 OBSERVATION OF A MESOSCALE CONVECTIVE SYSTEM IN A BAIU-FRONTAL DEPRESSION GENERATED NEAR THE EAST COAST OF THE EURASIAN CONTINENT 1773
Hiroyuki Yamada, Biao Geng, K. Krishna Reddy, Hiroshi Uyeda

TOPIC 13: CLOUD PROCESSES AND THE MESOSCALE

13:1 THE ANALYSIS OF PRECIPITATION CHARACTERISTICS IN HEBEI PROVINCE 1777
Zhihui Wu, Duan Ying, Xiaobin Wang, Lixin Shi , Xinmin Zhang

13:2 MODELLING THE IMPACT OF URBAN AREAS ON PRECIPITATION INITIATION 1781
M.G.D. Carraça, C.G. Collier

13:3 TROPOSPHERIC DRYNESS AND CLOUDS OVER TROPICAL INDIAN OCEAN. 1785
Frédérique Cheruy, Gian-Luigi Liberti, Caterina Iori

13:4 CLOUDS SPACE AND TIME SCALE IN THE MEDITERRANEAN AREA: CLIMATE MODEL AND OBSERVATIONS. 1789
Frédérique Cheruy, Gian-Luigi Liberti

13:5 OBSERVATIONS OF CLOUDS AND PRECIPITATION OVER THE ARCTIC OCEAN BY USING THE RESEARCH VESSEL "MIRAI" 1793
Yasushi Fujiyoshi, Kazuho Yoshida, Hideyuki Kasuya, Osamau Tsukamoto, Hajime Okamoto, Hiroaki Horie

13:6 ENVIRONMENTAL VARIABLES AFFECTING THE HAILSTONE'S SIZE DISTRIBUTION 1796
Dario B. Giaiotti, Fulvio Stel

13:7 A STUDY ON PRECIPITATION FORMATION MECHANISM OF COLD FRONTAL CLOUD SYSTEM IN HENAN PROVINCE 1799
Yanchao Hong, Zhongxiu Liu

13:8 STRUCTURE AND DYNAMICS OF THE DEVELOPMENT AND CLASSIFICATION OF THE HAIL-STORM PROCESSES IN UZBEKISTAN 1803
Kh.A. Imamdzhanov

13:9 A CLIMATOLOGY OF CONVECTIVE PRECIPITATING PATTERNS IN AFRICA 1806
Arlene Laing, Richard Carbone, Vincenzo Levizzani

13:10 ANALYSIS CHARACTERISTIC OF SPRING PRECIPITATION CLOUD IN SHAAXI AND GANSU PROVINCE 1808
Heng-Chi Lei, Yu-Xia Wu, Peng Fan

13:11 STUDY OF A TYPICAL COLD FRONT RAIN BELT MICRO CHARACTERISTICS, PRECIPITATION MECHANISM AND ARTIFICIAL WEATHER MODIFICATION POTENTIAL 1811
Jian Liu, Yong Yu, Tong Jiang, Xinzhi Chen

13:12 CONVECTIVE SYSTEM AREA EXPANSION AND ITS RELATIONSHIP WITH PRECIPITATION INTENSITY 1815
Luiz Augusto T Machado, Henri Laurent

13:13 NUMERICAL SIMULATION OF A SUPERCELL STORM OVER CAMAGÜEY, CUBA. 1818
Daniel Martinez, Diana R. Pozo, Arnoldo Bezanilla, Sadiel Novo

13:14 IMPACT OF TOPOGRAPHY RESOLUTION AND UPPER AIR DATA ON REAL DATA THUNDERSTORM SIMULATION USING RAMS 1822
Parthasarathi Mukhopadhyay

13:15 MESOSCALE AND MICROSCALE STRUCTURES OF PRECIPITATION BANDS ASSOCIATED WITH BAIU FRONT□AIRCRAFT OBSERVATIONS AND NUMERICAL SIMULATIONS 1825
Masataka Murakami, Akihiro Hashimoto, Narihiro Orikasa, Kazumasa Mori, Hiroshi Kuraiwa, Akihide Kamei, Haruya Minda

13:16 THE RELATIONSHIP BETWEEN SOUTH AMERICAN LOW-LEVEL JET EVENTS WITH THE FORMATION AND MAINTENANCE OF MESOSCALE CONVECTIVE SYSTEMS 1829
Matilde Nicolini, Paola Salio, Juan Carlos Torres, Edward J Zipser

13:17 NUMERICAL INVESTIGATION OF THE INTER WAVE-ROTOR STRUCTURE OF FRONTAL CLOUDS AT DIFFERENT STAGES OF THEIR DEVELOPMENT 1833
Ludmila Palamarchuk, Anna Pirnach, Vitaliy Shpyg

13:18 THREE DIMENSIONAL KINEMATIC AND MICROPHYSICAL EVOLUTION OF MAP IOP3B OROGRAPHIC PRECIPITATION 1837
Olivier Pujol, Jean-François Georgis, Michel Chong, Frank Roux

13:19 FORMATION OF THE CONVECTIVE CELL IN SHEET CLOUD AND THE NUMERICAL EXPERIMENTS OF ITS INFLUENCE ON THE PRECIPITATION 1841
Yanbin Qi, Dezhen Jin, Yanli Qi

13:20 DIURNAL CYCLE OF MESOSCALE CONVECTIVE SYSTEMS OVER SOUTHEASTERN SOUTH AMERICA 1844
Paola Salio, Edward Zipser, Matilde Nicolini, Chuntao Liuct

13:21 UNIVERSAL LAWS FOR POSTFRONTAL SHOWER CLOUDS 1848
Michael Theusner, Thomas Hauf

13:22 WRF SIMULATIONS OF RAINFALL COHERENCE OVER THE CONTINENTAL UNITED STATES 1852
Stanley B. Trier, C. Davis, E. Carbone, S. Frederick

13:23 ON THE FORMATION OF LONGITUDINAL CLOUD MODE IN THE WINTER MONSOON OVER JAPAN 1855
Akira Watanabe

13:24 KEY PARAMETERS AND PROCESSES LEADING TO TORRENTIAL RAINFALL EVENTS IN THE SOUTH – EASTERN MASSIF CENTRAL, FRANCE 1859
Wolfram Wobrock, Andrea Flossmann, G. Delrieu, S. Anquetin

13:25 DRIZZLE AND CLOUD STRUCTURE IN SE PACIFIC STRATOCUMULUS 1863
Robert Wood, Kim Comstock, Peter Caldwell, Chris Bretherton, S.E. Yuter

13:26 ON HETEROGENEITY OF DRIZZLE IN A STRATOCUMULUS-TOPPED MARINE BOUNDARY LAYER 1867
Bai Yang, Yefim Kogan

13:27 OROGRAPHIC PRECIPITATIONS. PHYSICAL PROCESSES AND CONTRIBUTION TO THE RAINFALL REGIME OF THE CÉVENNES – VIVARAIS REGION. 1871
Eddy Yates, Sandrine Anquetin, Jean-Martial Cohard

13:28 A CASE STUDY ON THE COLD-FRONT AND CYCLONE CLOUDS WITH THEIR MULTI-SCALE STRUCTURES AND PRECIPITATING MECHANISMS IN CHINA 1875
Yuquan Zhou, Yanchao Hong, Aifang Su, Yimei Huang

TOPIC 14: CLOUD PROCESSES

14:1 PROMINENT FEATURES OF THE GRAVITY WAVES GENERATED BY TROPICAL CONVECTION DETECTED BY VHF DOPPLER RADAR: A CASE STUDY. 1879
S. Abhilash, K. Mohankumar

14:2 IMPACT OF HORIZONTAL MODEL RESOLUTION ON CLOUD PARAMETERS FORECASTED BY A NON-HYDROSTATIC MESOSCALE MODEL 1883
Felix Ament, Susanne Crewell, Clemens Simmer

14:3 RIMING AND OTHER CHARACTERISTICS OF COLUMNS AND ROSETTES OBSERVED IN WAVE CLOUDS 1887
Brad Baker, Paul Lawson

14:4 RADAR CHARACTERISTICS OF PRECIPITATING CLOUDS IN THE UNITED ARAB EMIRATES 1891
Daniel Breed, Roelof Bruintjes, Nancy Rehak, Abdulla Al Mangoosh, Abdulla Al Mandoos

14:5 LOCAL OROGRAPHY INFLUENCE ON VORTICITY INSIDE CB CLOUD 1895
Mladjen Curic, Dejan Janc, Vladan Vuckovic, Dragana Vujovic

14:6 MICROPHYSICS OF PRECIPITATION ASSOCIATED WITH CLOUDBURSTS FORCED BY OROGRAPHY AND LARGE-SCALE SYNOPTIC CONDITIONS IN DIFFERENT CONVECTIVE REGIMES 1899
Someshwar Das, Raghavendra Ashrit

14:7 A PRELIMINARY STUDY ON THE VARIABLE TENDENCY AND PHYSICAL CAUSE OF FORMATION OF THE NATURAL PRECIPITATION OVER HEBEI AREA 1903
Ying Duan, Baodong Yang, Jinping Guo, Zhihui Wu, Laiguang You, Yuegai An

14:8 THE CLOUD PHYSICAL CHARACTERISTICS AND PRECIPITATION OF CONVECTIVE CLOUD SYSTEMS MODIFIED BY URBANIZATION IN BEIJING REGION 1907
Xueliang Guo, Jing Wang, Danhong Fu

14:9 PARAMETERIZATION OF NON-INDUCTIVE CHARGE TRANSFER BASED ON DISCRIMINANT AND REGRESSION ANALYSES OF LABORATORY DATA 1911
Anastasia Kirilova, Rumjana Mitzeva, Boryana Tsenova

14:10 SIMULATION OF CONVECTIVE SYSTEMS USING MESOSCALE MODEL WITH SPECTRAL MICROPHYSICS 1915
Barry Lynn, Alexander Khain, Andrei Pokrovsky, Daniel Rosenfeld, Axel Seifert

14:11 THE INFLUENCE OF RAINDROP CLUSTERING ON NEW REPRESENTATIONS OF COLLISION-INDUCED BREAKUP: IMPLICATIONS FOR RAINDROP SIZE DISTRIBUTIONS 1919
Greg M. Mcfarquhar

14:12 SOME IMPORTANT MULTI-SCALE FEATURES OF VERTICAL MOISTURE TRANSPORT RELATED TO CLOUD STREETS 1923
Mikhail Mezrin, Evgeny Starokoltsev, Y. Fujiyoshi, M. Yoshizaki

14:13 A MODELLING STUDY OF MIXED-PHASE CONVECTIVE CLOUD SEEDING AND ITS EFFECT ON THUNDERSTORM CHARGING 1927
Rumjana Mitzeva, S. Petrova, John Latham

14:14 STRUCTURE AND DEVELOPMENT OF TWO MERGED RAINBANDS ALONG THE BAIU FRONT AND THE "WATER VAPOR FRONT" OVER THE EAST CHINA SEA DURING X-BAIU-99 1931
Qoosaku Moteki, Hiroshi Uyeda, Teruyuki Kato, Masanori Yoshizaki

14:15 FORMATION PROCESS OF AN OROGRAPHIC LINE-SHAPED RAINFALL SYSTEM FROM A VIEWPOINT OF CELLULAR ECHOES ON THE SOUTH OF THE BAIU FRONT IN WESTERN KYUSHU, JAPAN 1935
Ayako Nakamura, Hiroshi Uyeda, Masanori Yoshizaki, Yoshinobu Tanaka, Shuji Shimizu

14:16 SIMULATION OF DEVELOPMENT OF DEEP CONVECTION FROM SHALLOW CLOUDS. 1939
Tomoe Nasuno

14:17 OBSERVATIONAL STUDY OF THE SNOWFALL SYSTEM ASSOCIATED WITH A MESOSCALE LOW FORMED OVER THE SEA OF JAPAN 1943
Tadayasu Ohigashi, Kazuhisa Tsuboki

14:18 APPLICATION OF CLUSTER ANALYSIS TECHNIQUES TO THE VERIFICATION OF QUANTITATIVE PRECIPITATION FORECASTS 1947
Stefano Serafin, Alessio Bertò, Andrea Buzzi, Rossella Ferretti, Dino Zardi

14:19 PRECIPITATION CHARACTERISTICS OF CUMULONIMBUS CLOUDS IN THE SOUTHERN REGION OF THE MEIYU FRONT OVER CHINA CONTINENT 1951
Yukari Shusse, Kazuhisa Tsuboki

14:20 TETHERED-BALLOON BORNE MEASUREMENTS IN BOUNDARY LAYER CLOUDS. PART I:TURBULENCE AND DYNAMICS 1955
Holger Siebert, Katrin Lehmann , Manfred Wendisch, Szymon P. Malinowski

14:21 THE RESPONSE OF HEATING AND MOISTURE IN CONTINENTAL AND OCEANIC MESOSCALE CONVECTIVE SYSTEMS TO THERMODYNAMIC AND DYNAMICAL PROCESSES 1959
Chiharu Takahashi, Hiroshi Uyeda

14:22 EFFECTS OF MOISTURE PROFILE ON THE DYNAMICS AND ORGANIZATION OF SQUALL LINES 1963
Tetsuya Takemi

14:23 STRUCTURE OF HEAVY RAINFALL SYSTEMS ASSOCIATED WITH A MESOSCALE LOW ALONG THE BAIU FRONT 1967
Kazuhisa Tsuboki, Takeshi Maesaka, Miki Hattori, Mitsuharu Nomura, Taro Shinoda, Hiroshi Uyeda

14:24 ORGANIZATION AND RAINFALL CHARACTERISTICS OF MONSOONAL CONVECTION DURING THE SOUTH EAST ASIAN SUMMER MONSOON 1971
Jian-Jian Wang

14:25 OBSERVATION AND NUMERICAL SIMULATION OF CLOUD PHYSICAL PROCESSES ASSOCIATED WITH TORRENTIAL RAIN OF THE MEI-YU FRONT IN SOUTH CHINA 1975
Pengyun Wang, Jing Yang, Xiangqian Gu, Xiaofeng Lou, Jing Sun

Topic	Table of Contents – Topics	No of Papers	Volume	Page
1	Aerosol-Cloud Interactions	72	1	1
2	Climate Change and Precipitation	28	1	261
3	Cloud-Climate Interactions	21	1	354
4	Interactions between Clouds and Atmospheric Chemistry	15	1	428
5	Warm Cloud Microphysics	60	1	483
6	Cold Cloud Microphysics	72	2	703
7	Cloud Electricity	13	2	982
8	Instrumentation	46	2	1029
9	Applications of Cloud Physics	26	2	1196
10	Cloud Parameterization in Models	46	2	1289
11	Modeling of Cloud-Scale Processes	44	3	1457
12	Cloud Dynamics and Structure	42	3	1620
13	Cloud Processes and the Mesoscale	28	3	1777
14	Cloud Processes	25	3	1879

Author Index

Abbatt, J. 465
Abhilash, S. 1879
Ackerman, A.S. 1, 455 1492,1643
Ackerman, T.P. 397, 404 876
Adamo, C. 596
Addor, J.-B. 1620
Al Mandoos, A. 217, 1218 1891
Al Mangoosh, A. 217, 1218 1891
Alberoni, P.P. 771
Albrecht, B.A. 5, 566 600
Alfarra, M.R. 20, 432
Allan, J.D. 39, 432
Altaratz, O. 982
Ament, F. 1883
Amiranashvili, A.G. 261, 265 267, 354
Amiranashvili, V.A. 265, 267 354
Amorim, W. 1008
An, Y. 1903
Anderson, J.R. 201
Andreae, M.O. 1592
Andrejczuk, M. 1475
Andrews, E. 175
Andronache, C. 9, 13, 892
Anquetin, S. 1859,1871
Aonashi, K. 759
Araújo Costa, A. 1573
Arduini, R.F. 600
Arkhipov, V. 483, 628
Arnold, G.T. 1580
Artaxo, P. 321
Ashrit, R. 1899
Auriol, F. 1754
Austin, R.T. 1029
Avila, E.E. 743
Ayala, O. 686
Ayers, J.K. 5, 600

Bachalo, W.A. 1056
Bachiashvili, L.L. 267
Back, L.E. 495
Bailey, M. 703,986
Baker, B. 835, 1119 1887
Baker, K.M. 1033
Bakhanov, V.P. 707, 711
Baldi, M. 269
Baldini, L. 533
Ball, R.C. 954
Baltensperger, U. 20, 1183
Bansemer. A. 788, 892 920, 1420
Bartello, P. 520
Barth, M.C. 428
Barthazy, E. 715, 719 920
Barthe, C. 990
Baruzzi Frediani, M.E. 1008
Baschek, B. 719, 920
Bateman, M. 1001
Battaglia, A. 499, 723 1048, 1719
Baumgardner, D.G. 727, 779 1037, 1108
Beard, K.V. 487, 608
Bechini, R. 596
Beheng, K.D. 537, 1416 1569, 1624
Bélair, S. 1596
Belcher, L. 547
Belosi, F. 1146
Benedetti, A. 1461
Bennartz, R. 1769
Bereznicki, S. 831
Berger, F.H. 1041
Berges, J.C. 273
Beritashvili, B.Sh. 261
Berner, A. 432
Bernstein, B.C. 1253
Berthet, C. 63
Bertò, A. 1947
Bertram, I. 1624
Besnard, T. 1089
Bezanilla, A. 1818
Bezrukova, N.A. 731, 1196
Bhar, S. 1257
Bibilashvili, T. 265, 267
Blahak, U. 924
Blanchet, J.-P. 670
Blyth, A.M. 491, 503
Bonafè, U. 389
Borrajero, I. 553
Borrmann, S. 17, 171 452, 946
Bortoli, D. 389
Borys, R. D. 59, 100
Bott, A. 1465, 1499
Bouchet, V.S. 448
Boudala, F.S. 1289
Bouniol, D. 735, 1730
Bouzereau, E. 1200
Bower, K.N. 20, 39, 356 432, 747, 1078
Breed, D.W. 24, 217 1218, 1891
Breitgand, J. 1228
Brenguier, J.-L. 360, 371, 503 612, 1059, 1393 1650, 1657, 1742
Bretherton, C.S. 495, 1628 1636, 1863
Brewer, J. 1632
Bringi, V.N. 533
Broekhuizen, K. 465
Brooks, M.E. 1293
Brooks, S. 59
Brown, P.R.A. 1077, 1469
Bruintjes, R.T. 24, 213,217 1204, 1218 1891
Buelow, K. 292
Burnet, F. 360, 1650
Burtscher, H. 1183
Busch, B. 116
Busek, P. 24
Busen, R. 1754
Bushell, A.C. 1438
Büttner, S. 43, 304
Buzzi, A. 1947

Cahalan, R.F. 1044, 1533
Cai, X. 1027
Caldwell, P. 1628, 1863
Calzolari, P. 389
Canagaratna, M.R. 32
Cancel, R. 428
Capacci, D. 1048
Caracciolo, C. 499, 1052
Carbone, R.E. 1806, 1852
Cardwell, J. 1473
Carissimo, B. 1200
Carraça, M.G.D. 1781
Carrió G.G. 367, 755
Carvalho, L.M.V. 28
Carver, R.W. 739
Castellano, N.E. 743
Castro, A. 277, 763
Cattani, E. 32, 47
Cavalli, F. 98, 153 157, 436
Ceccarelli, F. 1480
Cesarone, F. 269
Chaboureau, J.-P. 1476
Chandrasekar, V. 533
Chang, D.-E. 1107
Chen, B. 1612
Chen, G. 1272
Chen, H. 544
Chen, H.-T. 1212
Chen, J.-P. 35, 104, 227
Chen, W. 1661
Chen, X. 1222, 1261 1811
Chen, Zhengqi 1208, 1278
Chen, Zhixin 1215, 1282
Cheng, C.-T. 35
Cheng, Y. 281
Chepfer, H. 727
Chéruy, F. 1785, 1789
Chlond, A. 469, 1295, 1519
Chong, M. 1837
Chopin, F. 273
Chosson, F. 371
Choularton, T.W. 20, 39, 43 356, 747 1473
Christian, H.J. 1001
Christian Jr, H.J. 997
Chuang, P.Y. 1056
Cimini, D. 1130
Clarke, A.J.M. 1175
Clarke, P. 39
Clegg, S. 157
Coals, A. 503
Cober, S.G. 400, 796 800, 1074
Coe, H. 20, 39, 251 432, 473
Coelho, A.A. 1059
Cohard, J.-M. 1871
Colle, B. 1308
Collier, C.G. 1781

Comstock, K. 1636, 1863
Conant, B. 92
Connolly, P.J. 43, 78, 160
364, 747
751, 1175
Conway, B. 1048
Cooper, W.A. 491
Corrigan, C. 20
Costa, M.J. 32, 47
Costa, A.A. 588
Cotton, R. J. 78, 751
1340, 1484
Cotton, W.R. 253, 367
755, 916
1500
Cousineau, S. 448
Covert, D.S. 171, 175
Craig, G.C. 1401
Crevier, L.-P. 448
Crewell, S. 1063, 1434
1742, 1761
1883
Cubison, M. 39, 251, 432
Cui, L. 1225
Ćurić, M. 1600, 1895
Currie, B. 796
Cziczo, D. 59

D'Auria, R. 55
Dai, J. 1208, 1278
Dalu, G.A. 269
Damiani, R. 1639
Das, S. 1899
Dastoor, A.P. 448
Daum, P.H. 1366
Davies-Jones, R.P. 1654
Davis, A.B. 1533
Davis, C.A. 1852
Davison, J. 608
De, U.K. 1257
De Luca, P. 82
Decesari, S. 153,157
168, 432
436
Defer, E. 507, 510,994
Deierling, W. 997
Delrieu, G. 1859
DeMott, P.J. 59, 850, 1150
Demoz, B. 1576, 1580
Deng, M. 861
Dessens, J. 63, 1238
Detwiler, A. 674
Devara, P.C.S. 205, 1066
Di Girolamo, L. 1632
Di Giuseppe, E. 285
Di Giuseppe, F. 1312
Di Michele, S. 596, 1428
Diallo, T.D. 309
Diederich, M. 1742
Diehl, K. 66, 231, 900
Dietrich. S. 596, 1428
Dobbie, S. 868
Donovan, D.P. 940
Dorman, B.A. 707, 711
Dovgaluk, Y.A. 1746
Drewnick, F. 171
Drobinski, P. 1378
Drofa, O.V. 1301
Duan, S 1190
Duan, Y. 973, 1158
1777, 1903
Dubois, F. 636, 1146
Dubuisson, P. 1476
Dunlea, E. 59
Dupont, E. 1200
Dupuy, R. 70
Durant, A.J. 880
Dye, J.E. 957, 1001

Ebert, V. 146, 160
Eito, H. 759
Eitzen, Z.A. 1488
Ellingson, R.E. 1533
Ellis, S.M. 997
Ellis, T.D. 375
Endoh, T. 440, 936
Epifani, C. 285, 288
Erlick, C. 513
Esposito, S. 285, 288
Evangelisti, F. 389
Evans, K.F. 1070, 1533
Facchini, M.C. 98, 153, 157
432, 436
Fairall, C.W. 566
Faloona, I.C. 193
Fan, P 1208, 1212
1278, 1808
Fan, S. 654
Fang, W. 517
Feijt, A. 1742
Feingold, G. 74, 479
Feldman, Y. 628
Ferretti, R. 1947
Fersiz, N. 177
Field, P.R. 43, 78, 160
364, 751, 954
1074, 1484
Fierz, M. 1183
Filice, M. 82
Fischer, B. 620
Fischer, J. 1769
Fitzpatrick, P.J. 1386
Flossmann , A.I. 164, 584
1859
Flynn, M.J. 20, 747
1078, 175
Fonseca, V.L. 277
Forbes, R.M. 1297
Fraile, R. 63, 277, 763
Franklin, C.N. 520
Frederick, S. 1852
Frick, G. 1650
Fridlind, A. 455, 788
1492, 1643
Fries, E. 452
Fromm, M.D. 1592
Fu, D. 1495, 1907
Fu, Q. 1304
Fu, Y. 1646
Fugal, J.P. 1081
Fujiyoshi, Y. 1793, 1923
Fukuta, N. 767
Fuzzi, S. 153, 157
432, 436
Gadian, A.M. 503, 1499
Galgon, D. 1138
Gallagher, M.W. 20, 39, 43
1078, 1175
Galletti, M. 771
Ganor, E. 131
Gao, J. 1215
García-García, F. 604, 1085
García-Ortega, E. 75, 1238
Garrett, T.J. 779, 1092
Garstang, M. 1204
Garvert, M.F. 1308
Gaussiat, N. 524
Gayet, J.-F. 1754
Geng, B. 1738, 1773
Genkova, I. 1089
Gennaro, V. 1005
Georgis, J.-F. 1837
Gerber, H. 528, 779, 896
1092, 1650, 1657
Geresdi, I. 86, 908
Giaiotti, D.B. 1005, 1796
Gillotay, D. 1089
Gilmore, M.S. 1500, 1584
1654
Gimeno García, S. 1761
Girard, E. 444
Givati, A. 90
Glazer, A. 1316
Glushykhin, V.A. 1160
Göke, S. 530
Golaz, J.-C. 1432, 1504
Gonçalves, F.L.T.588, 1508
Gong, S. 448
Gong, W. 448
Gorgucci, E. 533
Goswami, K. 1257
Gouvea, M. 321
Gozzini, B. 181
Grabowski, W.W. 335, 379
503, 686, 1320
1457, 1519
Grainger, A.C. 674, 1001
Gras, J.L. 189
Greenway, R.S. 1074
Grits, B. 632, 928
Grosvenor, D. 39
Grubišić, V. 313, 1324
Gu, S. 1215, 1222
1282
Gu, X. 1975
Gulev, S.K. 327, 347, 350
Gultepe, I. 800, 1326
Guo, Jinping 1903
Guo, Junmei 1215, 1261
Guo, Xueliang 1495, 1907
Gysel, M. 20

Haag, W. 1754
Habilomatis, G.P. 383
Hacker, J. 189
Haeffelin, M. 735, 1378
1730
Hagemann, S. 1519
Haggerty, J. 674
Haimov, S. 674, 961, 1639
Håkansson, M. 1095

Hall, W.D. 957, 1001 1330
Hallett, J. 177, 703 782, 786 944, 986
Haman, K.E. 1657, 1691
Hamazu, K. 823, 827
Handwerker, J. 537
Hansson, H.C. 1754
Harimaya, T. 94
Harrington, J.Y. 74, 739 1511
Hartman, C.M. 1511
Hase, M. 647
Hashimoto, A. 1515, 1825
Hashino, T. 1428
Hattori, M. 1967
Hatzianastassiou, N. 383
Hauf, T. 1848
Hayasaka, T. 387, 554
Hayashi, S. 759, 1515
Hayashi, T. 440
Hazra, A. 1257
He, F. 1261
He, G.-F. 517
He, H. 1661
He, W. 544
He, Y. 541, 1612 1701
Heck, P.W. 1253
Heintzenberg, J. 257
Hendricks, J. 393
Henseler, S. 17, 171
Hesse, E. 1157
Heymsfield, A.J. 43, 78, 160 547, 751, 788 892, 896, 954 1092, 1420
Heymsfield, G.M. 547, 892
Hiltunen, L. 98
Hindman, E.E. 100
Hirst, E. 1074
Hobbs, P.V. 1308, 1592 1665
Hock, N. 17, 171
Hogan, R.J. 524, 612 1293, 1669
Homma, A. 94
Hong ,Y. 792, 843 1608, 1799 1875
Hoog, I. 452
Horie, H. 1793
Hoshimoto, M. 823
Hourdin, F. 1378
Hsieh, W.-C. 104
Hu, Zaoxia 792, 1616
Hu, Zhijin 135, 1446 1704
Hu, Zhongming 1215
Huang, Gen 657
Huang, Yimei 1875
Hudak, D. 796
Hudson, J.G. 694, 1099
Huggins, A.W. 313, 1324
Huo, J. 1127
Ikeda, A. 1541
Ikeda, K. 908
Illingworth, A. 524, 612 1293, 1334
Imamdzhanov, Kh.A. 1803
Iorga, G. 235
Iori, C. 1785
Isaac, G.A. 796, 800 808, 961 1074, 1111 1289, 1316 1326
Ishizaka, M. 1103, 1673 1715
Ishizaka, Y. 94, 189
Ivanova, D.C. 1337
Iversen, T. 123
Iwamoto, K. 1673, 1715
Iwanami, K. 827, 1711
Jacob, D. 292, 1519
Jacobsonr, M.Z. 475
Jaeschke, W. 452
Jamali, J.B. 329
Jameson, A.R. 551
Janc, D. 1895
Janisková, M. 1461
Jayne, J.T. 432
Jeck, R.K. 731
Jeffery, C.A. 1675
Jensen, E. 455, 1492 1643
Jensen, J.B. 189
Jensen, L.T. 1218
Jensen, T. 24, 217
Jewett, B. 592
Jia, L. 24
Jiang, H. 74, 367 1340
Jiang, T. 1811
Jiménez, J.C. 1037
Jimenez, J.L. 59, 432
Jin, D. 1215, 1222 1841 1225 1246
Johnson, D. 246
Jones, C. 28, 294
Jones, C.G. 1344, 1442
Jonsson, H. 5
Joutsensaari, J. 98
Jovanovska, L. 1264
Kadyrov, B.Sh. 1520
Kalogiros, J. 507
Kamalov, B. A. 108, 111 113
Kamei, A. 1825
Kanada, S. 1679
Kanak, K.M. 1584
Kandler, K. 116
Kapala, A. 347, 350
Kärcher, B. 393, 1754
Kasprzak, S.E. 686
Kästner, M. 297
Kasuya, H. 1793
Kato, T. 339,759 1515, 1679 1738, 1931
Katsanos, D. 994
Katsumata, M. 1683
Kawamoto, K. 387, 554
Kawano, T. 1019
Kaye, P.H. 1074
Keil, C. 1348
Kelman, G. 301
Kerr-Munslow, A.M. 1438
Kew, S.F. 1669
Khain, A. 119, 221, 246 301, 483, 513 628, 632, 924 928, 1374, 1416 1726, 1915
Khairoutdinov, M.F. 379, 404 408, 1352
Khaiyer, M.M. 5, 1253
Khalili, M.F. 1196
Khurodze, T.V. 265
Khvorostyanov, V.I. 1565
Kikuchi, K. 458
Kim, M.-J. 1107, 1268
Kim, S.-W. 428
Kirilova, A. 1911
Kirkevåg, A. 123
Kirkpatrick, M 1
Kiselev, A. 257
Kliche, D.V. 664
Knight, C.A. 556
Kochin, A.V. 1523
Koehler, K. 59
Koga, S. 440
Kogan, Y.L. 560, 1354 1533, 1867
Kogan, Z.N. 1354
Kok, G.L. 727, 1108
Kokkola, H. 325, 564
Kolasinski, J. 1044
Kollias, P. 566
Konishi, H. 804, 1765
Kontani, K. 1015
Korczyk, P. 570, 1707
Korneev, V.P. 1160
Korolev, A.V. 808, 812 1074, 1111
Kostinski, A.B. 573
Kosuge, H. 827
Kotroni, V. 507, 510 596, 994, 1525
Kowalewski, T.A. 570, 1707
Krakovskaia, S.V. 816
Krämer, M. 78, 146 160, 751
Kreidenweis, S. 59
Krejci, R. 1754
Krishnamurti, T.N. 1480
Kristjánsson, J.E. 123, 239
Krueger, S.K. 1370, 1687
Kryvobok, O.A. 711
Kuba, N. 1358
Kucera, P.A. 820, 896
Kumagai, H. 1167
Kumar, B.Y. 205, 1066

Kurbatkin, V.P. 305
Kurihara, K. 339
Kurita, N. 440
Kuroiwa, H. 888, 1825
Kurowski, M. 1657, 1691
Kusunoki, K. 823, 827
1541

L'Ecuyer, T. 417
Laaksonen, A. 98, 325
564, 668
Labellec, A. 1378
Lagouvardos, K. 508, 510
596, 994, 1525
Lahav, R. 127
Laing, A.G. 1806
Laird, N.F. 530, 1695
Laj, P. 70
Lamb, D. 462, 865
Lanconelli, C. 389
Lara, L. 321
Lare, A. 1576,1580
Laroche. S. 1588
Larsen, M.L. 573
Larson, V.E. 1362,1504
Lasher-Trapp, S.G. 491, 831
Latham, J. 356, 997
1927
Lau, W.K.M. 1115
Laurent, H. 1815
Lawson, R.P. 835, 839
1070, 1119, 1887
Lazare, M. 421
Leaitch, R. 465
Leal Júnior, J.B.V. 588
Leduc, A.-M. 1596
Lee, G.W. 576, 698
Legros, J.C. 636, 1146
Lehmann, K. 580, 1138
1955
Lei, H. 678, 1194
1212, 1222
1225,1454
1529, 1808
Leighton. H.G. 185
Leovy, C.B. 1389
Leporini, M. 584
Lesins, G. 281
Levin, Z. 131, 982
1228
Levizzani, V. 32, 47
771, 1123
1171, 1806
Lewis, S. 957, 1001
Li, H. 792, 843, 975
Li, Jiantong 309, 1697
Li, Jianxin 1285
Li, Juan 135
Li, Lihua 1580
Li, Lunge 678
Li, M. 1222, 1246
Li, Rui 1646
Li, Ruijie 1232
Li, S. 846, 1529
Li, W. 1234
Li, X. 246
Li, Z. 1215

Liberti, G.L. 1785, 1789
Lima, A.A. 1186
Lin, R.-F. 850, 1576, 1580
Linke, C. 160, 364
List, R. 139, 854
858, 965, 978
Liu, Gang 1285
Liu, Guosheng 759, 1646
Liu, Jian 1225, 181
Liu, Jiinli 544, 1190
1646, 1697
Liu, L. 1285
Liu, Q. 969
Liu, S. 541, 1234
1616, 1701
Liu, S.C. 227
Liu, W. 969
Liu, X. 309
Liu, Y. 51, 1366
Liu, Zhongxiu 1799
Liu, Zuoting 281
Liuct, C. 1844
Lohmann, U. 142, 281
393, 465, 1450
Löhnert, U. 1063, 1761
Long, C. 1089
López, L. 763, 775, 1238
Lou, X. 1704, 1975
Lowenthal, D.H. 100
Lu, D. 1127, 1190
1646, 197
Luderer, G. 1592
Luo, C. 28
Luo, Q. 1285
Luo, Yali 1370, 1687
Luo, Yunfeng 281
Lupi, A. 389
Lynn, B. 1374, 1915

Mace, G.G. 861
Mach, D. 1001
Machado, L.A.T. 1008, 1815
Machey, B. 1480
MacKenzie, A.R. 1408
Maesaka, T. 1015, 1967
Magee, N. 865
Mahowald, N.M. 28
Makar, P.A. 448
Maki, M. 827, 1711
Malek, E. 1242
Malguzzi, P. 1301
Malinowski, S.P. 570, 1457
1650, 1657
691, 1707
1955
Mangold, A. 146, 160
Mantovani, S. 723, 1048
Manzhara, A.A. 707
Mao, J. 135, 309
Maracchi, G. 269
Marchand, R.T. 397, 404, 876
Marcos, J.L. 775
Marcotte, D. 961
Marín, J.C. 1553
Marsham, J.H. 868
Martínez, D. 624, 1553
818

Martins, J.A. 588, 1508
Maruyama, K.-I. 1711
Maruyama, T. 1673, 1715
Marzano, F.S. 1130
Mascart, P.J. 1476
Mass, C.F. 1308
Massling, A. 1138
Masunaga, H. 150
Mathieu, A. 1378
Matrosov, S.Y. 912
Matsui, T. 150
Matsushita, H. 1249
Mazin, I.P. 812, 872
McAnelly, R.L. 755
McDonough, F. 1253
McFarlane, N.A. 421, 1304
McFarlane, S.A. 876
McFarquhar, G.M 335, 400
592, 1337
1919
McFiggans, G. 39, 251
432, 473
McGill, M. 1044
McGraw, R. 1366
Mechem, D.B. 1354, 1533
Medaglia, C.M. 596
Memon, G. 1142
Ménard, S. 448
Meneguzzo, F. 269
Meng. S. 1285
Mertes, S. 1134, 1138
Meyer, S. 1761
Meywerk, J. 1734
Mezrin, M.Yu. 1923
Mi, Y. 880
Miekeley, N. 321
Miguélez, L. 277
Milbrandt, J.A. 1382
Miloshevich, L.M. 788
Minda, H. 888, 1825
Minikin, A. 1754
Minina, L.S. 731
Minnis, P. 5, 600, 1253
Mircea, M. 153, 157, 436
Misumi, R. 827, 1711
Mitchell, D.L. 313, 1337
Mitra, S.K. 452, 946
Mitzeva, R. 1537, 1911
1927
Mizuno, H. 823
Mkurnalidze, I.P. 261
Moehler, O. 78, 751
Mohankumar, K. 1879
Möhler, O. 43, 146
160, 364
Monier, M. 164
Montero-Martínez, G. 604, 1085
Morales, C.A. 1008
Moran, M.D. 448
Moretti, F. 168
Mori, K. 888, 1541
1825
Morimoto, S. 1765
Mostovoy, G.V. 1386
Moteki, Q. 1931
Moyle, A.M. 462, 865
Mugnai, A. 1123, 1428

Mukhopadhyay, P. 1822
Müller, F. 469, 1295
Münster, H. 620
Murakami, M. 823, 827
888, 1515
1541, 1825
Muramoto, K. 1103
Muroi, C. 339, 759, 1515
Murphy, D. 59
Musson-Genon, L. 1200

Nagel, D. 1734
Nakai, S. 1103, 1673
1715
Nakajima, T. 1167
Nakamura, A. 1935
Nardino, M. 389
Nastro, A. 82
Nasuno, T. 1939
Natali, S. 1052, 1719
Nevzorov, A.N. 884
Newman, A.J. 820
Nguyen, L. 1253
Nicolini, M. 1829, 1844
Nishio, N. 1249
Niu, S. 654
Nodia, A.G. 265
Noguchi, I. 440
Nomura, M. 1545, 1967
Noone, K.J. 171, 175
1095
Novo, S. 1818
Nowak, A. 1138
Nozawa, T. 243

O'Connor, D. 839, 1070
O'Connor, E.J. 612
Ochs III, H.T. 487, 530
608, 1695
Ogren, J.A. 171, 175
Ohigashi, T. 1943
Okamoto, H. 1793
Ola, T. 965
Olivares, G. 171
Oliveira, J.C.P. 588
Omidiora, O.F. 317
Oraltay, R.G. 177, 786
Orikasa, N. 823, 827
888, 1541
825
Ovarlez, J. 1754
Ovtchinnikov, M. 404, 1533

Pabla, B. 448
Paiva de Almeida, G. 1573
Pakula, L.A. 408
Palamarchuk, L.V. 1833
Palencia, C. 763
Palikonda, R. 1253
Panegrossi, G. 1428
Papa, A. 1719
Pardo, J. 1476
Parente de Oliveira, J.C. 1573
Park, S. 1389
Park, S.-G. 827, 1711
Parker, L. 42
Pasi, F. 181
Pasqui, M. 181
Paul, S. 1257
Pauliquevis, T. 321
Paunova, I.T. 185
Pawlowska, H. 640, 1393
Perez, C.A. 624
Perrin, T. 1059
Petenko, I.V. 616
Peter, J.R. 189
Peters, G. 616, 620
Peters, M.E. 495, 1163
Petersen, W.A. 997
Petkovic, S. 1142
Petre, J. M. 1723
Petrov, V.V. 624, 1160
Petrova, S. 1927
Petters, M.D. 193, 197
201
Petzold, A. 1754
Pfeilsticker, K. 1154
Phillips, V.T.J. 9, 892, 1726
Pielke Sr. R. 150
Piketh, S.J. 24, 213, 217
Pilson, B. 835
Pincus, R. 1424
Pinsky, M. 221, 483
513, 628
32, 928
Pinty, J.-P. 990, 1397
1476
Pirnach, A.M. 816, 1549
1833
Plant, R.S. 1401
Podgurskaya, V.N. 343, 345
Podzun, R. 292
Poellot, M.R. 779, 788
892, 896
1092
Pokrovsky, A. 119, 1416
1915
Poli, V. 1171
Ponomarev, Y. Ph. 1746
Porcù, F. 723, 1048
1719
Posselt, R. 900
Pozo, D.R. 1553, 1818
Prenni, A. 59
Prevenslik, T.V. 1011
Prigent, C. 1476
Prodi, F. 499, 636
723, 1048
1052, 1146
1719
Protat, A. 735, 1730
Pu, J. 1276
Pujol, O. 837

Qi, Yanbin 1841
Qi, Yanli 1841
Qi, Ying 1261
Quante, M. 1734
Raatikainen, T. 668
Raga, G.B. 727, 1037
1553
Ramesh, A. 329
Randall, D.A. 379, 1352
Randeu, W.L. 904
Rangno, A.L. 1665
Rao, D.N. 205, 1066
Rao, Y.J. 205, 1066
Rasinski, P. 640
Rasmussen, E.N. 1500, 1584
1654
Rasmussen, R.M. 86, 908
1330
Ratto, C.F. 1480
Rauber, R.M. 530, 592
1695
Raymond, D.J. 1557
Reddy, K.K. 1773
Rehak, N. 1891
Reichardt, J. 850
Reinhardt, T. 1404
Reinking, R.F. 912
Reisin, T. 982
Remer, L. 246
Remiszewska, J. 1657
Ren, C. 1408
Richard, E. 1476
Richardson, G. 1469
Richardson, M. 59
Rickenbach, T. 1580
Riemer, N. 643
Rio, C. 1378
Rissler, J. 157
Roch, M. 1596
Rodriguez, P. 796
Rogers, D.C. 1150
Romakkaniemi, S. 325, 564
Roman, J. 1107
Rosenfeld, D. 90, 119
127, 209
221, 301
1592, 1915
Ross, K.E. 24, 213
217, 428
Roth, N. 647
Roux, F. 1837
Rozendaal, M.A. 1389
Rudeva, I. 327
Russell, L.M. 171
Ryabov, Ya. 628

Saathoff, H. 43, 146, 160
Sahraei, J. 356
Saito, M. 1541
Sakakibara, A. 1561
Sakashita, K. 1015
Salazar, V. 24, 217, 1218
Saleeby, S.M. 916
Salio, P. 1829, 1844
Sánchez, J.L. 63, 775, 1238
Santachiara, G. 636, 1146
Sasaki, A. 94
Sasaki, H. 339
Sasaki, Y. 458
Sassen, K. 1565
Sato, A. 1103, 1673
1715
Sato, Y. 339
Saunders, C.P.R. 743, 1537
Saw, E.W. 1081
Schefold, R. 715, 719, 920
Scheirer, R. 1412

Schimmel, F. 469
Schmidt, S. 580, 1412
Schmitt, C. 788
Schnaiter, M. 78, 160
364, 751
Schneider, J. 171
Scholl, T. 1154
Schönhuber, M. 904
Schröder, M. 371
Schumann, U. 1754
Schutgens, N.A.J. 412
Schütz, L. 116, 160
Schwarzenböck, A. 1134
Sednev, I. 1295
Segal, Y. 221, 513
Seifert, A. 924, 1374
1416, 1420
1492, 1569
1624, 1754
1915
Sekelsky, S. 1107
Seland, Ø. 123
Serafin, S. 1947
Sergeyev, A.V. 1081
Servranckx, R. 1592
Shahabfar, A. 329
Shantz, N. 465
Shapiro, M. 632, 928
Sharon, T. 5, 600
Shaw, G.E. 225
Shaw, R.A. 651, 880
1081
Shen, Z. 1222
Shepherd, J. 473
Sherwood, S. 892
Shi, A. 657, 661
Shi, L. 1158, 1777
Shi, Y. 969, 1446, 1704
Shie, C.-L. 413
Shiina, T. 1103
Shimizu , M. 1673, 1715
Shimizu, S. 1738, 1935
Shinjo, K. 1015
Shinoda, T. 1015, 1738
1967
Shiu, C.-J. 227
Shpital, T.N. 343, 345
Shpyg, V.M. 1833
Shtivelman, D. 1228
Shusse, Y. 804, 1951
Siebert, H. 580, 1691
1955
Siems, S.T. 189
Silva, A.M. 32, 47
Silva Dias, M.A. 588, 1008
1508
Silvério, A.C. 1573
Simmel, M. 66, 231
Simmer, C. 347, 350
1742, 1761
1883
Simpson, J. 246, 413
Sinkevich, A.A. 1746
Skuratov, S.N. 1160
Smirnova, T.Y. 333
Smith, P.L. 664
Smith, Jr., W.L. 1253
Smolarkiewicz, P.K. 1457
Snider, J.R. 193, 197
201, 1163
Sorjamaa, R. 668
Sousa Sombra, S. 1573
Spangenberg, D.A. 1253
Spiridonov, V. 1264
Srivastava, A.K. 205, 1066
Stachnik, J. 831
Starokoltsev , E.V. 1923
Starr, D. 850, 1576
1580
Stefan, S. 235
Stefanof, A. 444, 670
Stefanof, C. 670
Steinwagner, J. 237
Stel, F. 1005, 1796
Stepanenko, V.D. 1746
Stephens, G.L. 375, 408
417, 1029
Stern, W. 294
Stevens, B. 600
Stevens, D. 1
Stith, J.L. 674
Storelvmo, T. 239
Straka, J.M. 1500, 1584
1654
Strapp. J.W. 961, 1074
Stratmann, F. 257
Straub, D. 1150
Straub, W. 537
Ström, J. 1095, 1750
1754
Stuart, A.L. 475
Stulov, E.A. 731, 1196
Su, A. 1875
Sun, A. 678, 1276
Sun, J. 1704, 1975
Sun, Y. 973
Sun, Z. 654
Supatashvili, G.D. 267
Suto, M. 1711
Suzuki, K. 1019
Swietlicki, E. 157
Szyrmer, W. 670, 1588
Tagliavini, E. 168
Takahashi, C. 932, 936
1959
Takahashi, T. 440, 682
Takamura, T. 1167
Takano, T. 1167
Takara, E.E. 1533
Takaya, Y. 804
Takemi, T. 1963
Takemura, T. 243
Tanaka, N. 440
Tanaka, Y. 823, 827
1935
Tanelli, S. 1107
Tang, D. 1158
Tao, W.-K. 150, 246, 413
Tao, X. 1604
Taoyue 1799
Targino, A. 171
Tavartkiladze, K.A. 354
Teichert, H. 146
Telenta, B.T. 1023
Teller, A. 131
Teschl, F. 904
Textor, C. 1592
Theusner, M. 1848
Thompson, D.W.J. 375
Thompson, G. 908
Timlin, M.S. 592
Tinsley, B.A. 248
Tolkacheva, G.A. 333
Tompkins, A.M. 1312, 1424
Toon, O. 1
Topping, D. 251, 432
Toronjadze, A.F. 265
Torres, J.C. 1829
Torricella, F. 1171
Trautmann, T. 1761
Travaini, S. 636, 1146
Trentmann, J. 1592
Trier, S.B. 1852
Tripoli, G.J. 596, 1428
Trivellone, G. 389
Tsenova, B. 1537, 1911
Tsuboki, K. 1545, 1561
1738, 1943
1951, 1967
Tsukamoto, O. 1793
Turco, R.P. 55
Twohy, C.H. 201, 487
779, 788
896, 1096
1108
Uijlenhoet, R. 1052
Ulanowski, Z. 1175
Uyeda, H. 1015, 1738
1773, 1931
1935, 1959
1967
Vaillancourt, P.A. 520, 1596
Vali, G. 961, 1639, 1758
van den Heever, S.C. 253, 1500
van Dop, H. 1179
Van Dorn, J. 608
van Ekeren, J.S. 1183
van Meijgaard, E. 1063
van Zadelhoff, G.-J. 940
Vanreken, T. 892
Várnai, T. 1044
Vedernikov, A. 636, 1146
Vellore, R.K. 1324
Venema, V. 1742, 1761
Venkatesh, S. 448
Vento, D. 285, 288
Veremey, N.E. 1746
Verlinde, J. 739, 1033, 1723
Vidaurre, G. 944
Vila, D.A. 1180
Vitale, V. 389
Volkov, V.V. 1160
von Blohn, N. 946
von Salzen, K. 42
Vučković, V. 1895
Vujović, D. 1895
Vukovic, Z.R. 1023, 1600
Wacker, U. 1404
Wada, M. 440, 1765
Wagner, R. 146, 160, 364
Waliser, D.E. 294

Walther, A. 1769
Wan, X. 1027
Wang, D. 1580
Wang, G. 678
Wang, H. 335
Wang, J. 1907
Wang, J.-J. 1971
Wang, J.R. 1107
Wang, L. 1276
Wang, L.-P. 686, 690
Wang, P. 1704, 1975
Wang, P.K. 1592, 1719
Wang, Q. 1285
Wang, S. 1432, 1504
Wang, W. 1604
Wang, W.-C. 35
Wang, Xia 1027
Wang, Xiaobin 1777
Wang, Xiaobo 1608
Wang, Xiaomei 1215, 1261
1282
Wang, Xuelin 1261
Wang, Yansen 1580
Wang, Yilin 1261
Ware, R. 1130
Watanabe, A. 1855
Watanabe, H. 823
Weaver, K. 839
Wei, Q. 1215
Wei, W. 1285
Wei, Z. 1222
Weigand, B. 647
Weimer, S. 171
Weingartner, E. 20, 1183
Weinman, J.A. 1107, 1268
Weinstock, E.M. 779
Wendisch, M. 580, 1955
Westbrook, C.D. 954
Wex, H. 257
Wexler, A.S. 643
Whiteway, J.W. 747
Wielicki, B.A. 424
Wieprecht, W. 1138
Wilhelmson, R.B. 1500, 1654
Willén, U. 1434, 1442
Willett, J.C. 1001
Williams, P.I. 39, 432
Willis, P.T. 957, 1001
Wilson, D.R. 1438
Wilson, K.M. 1179
Winterrath, T. 1592
Wirzberger, H. 928
Wiscombe, W.J. 1070
Witternigg, N. 904
Wobrock, W. 164, 584
1859
Wolde, M. 796, 961
Wong, T. 424
Wood, R. 1469, 1628
1636, 1863
Woods, C.P. 1308
Worsnop, D.R. 432
Wu, H.-T.J. 1115
Wu, Yuxia 1225, 1454
1808
Wu, Y. 1272
Wu, Z. 973, 1158
1777, 1903
Wurzler, S. 66, 231, 900
Wyser, K. 1442
Xiao, Huanbin 1285
Xiao, Hui 541, 1225
1276, 1608
1612, 1616
1701
Xiao, W. 1529
Xie, Z. 846
Xu, Can 1285
Xu, Chenhai 1276
Xu, H. 1285
Xu, J. 387
Xu, K.-M. 424, 1488
Xue, H. 462, 479
Xue, Y. 690
Yamada, H. 1738, 1773
Yamada, Y. 823
Yamanouchi, T. 1765
Yang, Bai 1867
Yang, Baodong 1903
Yang, J. 1975
Yao, Z. 1276, 1612
Yasunaga, K. 339
Yates, E. 1871
Yau, M.K. 520, 1382
Yetzer, K. 1044
Yin, L. 1285
Yin, Y. 131
Yoneyama, K. 1683
Yoshida, K. 1793
Yoshizaki, M. 759, 1019
1515, 1679
1923, 1931
1935
You, Laiguang 135, 1903
Youk, H. 965
Young, D.F. 600
Yu, Xiangren 1261
Yu, Xing 1208, 1278
Yu, Y. 1811
Yuan, J. 1304
Yum, S.S. 694, 1099
Yuter, S.E. 1636, 1863
Zabolotskaya, T.N. 343, 345
Zardi, D. 1 947
Zawadzki, I. 576, 698
796, 1588
Zeng, X. 1557
Zhang, Jinghong 1215, 1222
1282
Zhang, Junhua 281, 1450
Zhang, Lei 975
Zhang, Ling 1190, 1697
Zhang, Q. 975, 1027
1616
Zhang, W. 1127
Zhang, Xiaoqing 1194
Zhang, Xinmin 1777
Zhang, Y. 1697
Zhao, G. 1697
Zhao, Z. 1454
Zhen, J. 1222, 1225
1261
Zheng, G. 517, 657
661, 678
978, 1875
Zhi, H. 973
Zhou, F. 608
Zhou, H. 1285
Zhou, X. 1704
Zhou, Y. 657, 1875
Zipser, E.J. 1829, 1844
Zmarzly, P. 839, 1070
Zolina, O. 327, 347, 350
Zulauf, M.A. 1687

ENTRAINMENT, DRIZZLE, AND STRATOCUMULUS CLOUD ALBEDO

Andrew Ackerman[1], Michael Kirkpatrick[2], David Stevens[3], and Owen Toon,[4]

[1]NASA Ames Research Center, Moffett Field, CA, USA

[2]University of Tasmania, Hobart, TAS 7001, Australia

[3]Lawrence Livermore National Laboratory, Livermore, CA 94552, USA

[4]University of Colorado, Boulder, CO 80309, USA

1 Introduction

Increases in the concentrations of aerosols that serve as cloud condensation nuclei (CCN) are observed to enhance cloud droplet concentrations. The resulting increase of cloud reflectivity is expected to offset some of the global warming caused by the atmospheric accumulation of greenhouse gases, but the magnitude of the indirect aerosol effect is highly uncertain. For clouds with a fixed volume of condensed water, droplets become smaller as their numbers increase, thereby increasing cloud optical depth and albedo (Twomey 1974). Beyond this first indirect aerosol effect, smaller droplets are less efficient at producing precipitation, and decreased precipitation has been proposed to increase cloud water and cloud cover (Albrecht 1989; Pincus and Baker 1994), further increasing cloud reflectivity.

Here we focus on the response of cloud water to increasing droplet concentrations in marine stratiform clouds, Measurement of this response is extremely challenging because regional-scale variations in aerosols are invariably accompanied by co-varying changes in meteorological conditions (Schwartz et al. 2002). Ship tracks, which are plumes of enhanced albedo in clouds polluted by ship exhaust (Durkee et al. 2000), provide a natural laboratory for isolating the effects of aerosols on cloud properties. Results from simple theoretical models (Albrecht 1989; Pincus and Baker 1994) indicate that cloud water should consistently increase in ship tracks, an expectation that is not confirmed by observations.

The first airborne measurements of ship tracks do support the theoretical expectations, as cloud water was measured to nearly double as droplet concentrations (N) tripled from their background values of ~ 30 cm^{-3} (Radke et al. 1989). Subsequent observations, however, tend to show just the opposite relationship, if any, with cloud water generally *decreasing* as droplet concentrations increase. For example, in situ measurements of over 60 ship track interceptions during the Monterey Area Ship Track (MAST) experiment show that cloud water increases in some and decreases in others, with a slight decrease on average (Ackerman et al. 2000). High-resolution, airborne remote-sensing of three ship tracks during MAST also showed cloud water decreasing on average (Platnick et al. 2000). More recently, satellite observations of hundreds of ship tracks over the northeastern Pacific Ocean show a significant average decrease in cloud water (Coakley and Walsh 2002). We find through comparisons with detailed model simulations that omitting clear and partly cloudy pixels from the satellite data introduces a sampling bias that could lead to a real signal of cloud cover increasing with N being misinterpreted, or aliased, as an apparent decrease in cloud water (Ackerman et al. 2003). Overall, the observational evidence for cloud water consistently increasing with droplet concentrations in polluted clouds is ambiguous at best.

The simulations we used in the foregoing analysis were limited to a single meteorological setting, based on measurements of drizzling stratocumulus (Duynkerke et al. 1995) over the northeastern Atlantic obtained during ASTEX. For the present study we ran additional stratocumulus simulations based on measurements from two field campaigns off the coast of southern California. Contrary to the ASTEX case, in both the FIRE-I and DYCOMS-II cases cloud water decreases as droplet concentrations increase beyond a threshold value of N that depends on the meteorology.

2 Model Simulations

As in Ackerman et al. (2003) we run a sequence of large-eddy simulations (Stevens et al. 2002) with bin microphysics (Ackerman et al. 1995) and two-stream radiative transfer (Toon et al. 1989), here on a computational domain of $64 \times 64 \times 86$ cells, 3.2 km wide in each horizontal direction and 1.5 km vertically. Grid spacing is uniform horizontally and stretched vertically to give cells of height 6 m close to the bottom surface and in the vicinity of the inversion. Sub-grid scale fluxes are modeled using a dynamic scheme based on Germano et al. (1991).

As seen in Figure 1, only when the average precipitation rate at the surface exceeds ~ 0.1 mm d^{-1} does the average liquid water path (LWP) increase with droplet concentrations. An increase of LWP with droplet concentrations is seen for the simulations of

Corresponding author's address: Andrew Ackerman, NASA Ames Research Center, Mail Stop 245-4, Moffett Field, CA 94035; E-mail: andrew.ackerman@nasa.gov.

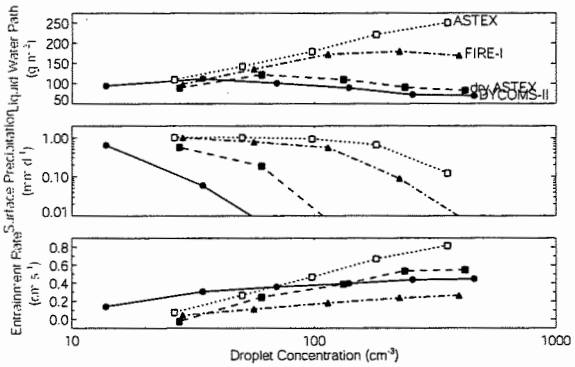

Figure 1: Domain-average liquid water path, surface precipitation, and entrainment rate as a function of cloud droplet number concentration (N), averaged over the last two hours of 8-h nocturnal simulations. The air overlying the boundary layer is warmer and dryer than in the ASTEX observations.

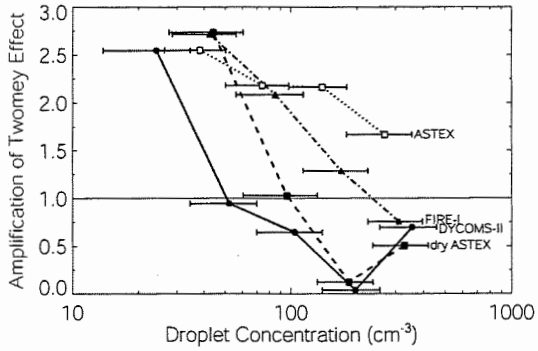

Figure 2: Ratio between differences in our simulation averages to Twomey's measuring the change of cloud albedo (A) with respect to relative changes in cloud droplet number concentration (N).

the ASTEX conditions over the entire range of CCN concentrations considered. For the DYCOMS-II and FIRE-I conditions LWP again increases with N, but only at droplet concentrations below $\sim$ 35 and 225 cm^{-3}, respectively.

These increases in LWP with N occur despite an increase in the rate at which the boundary layer entrains warmer, dryer air from above. The entrainment rate always increases with N in our simulations. Divergence of the precipitation flux dries out cloudy air near cloud top, which reduces the moisture available to evaporatively cool downdrafts (Stevens et al. 1998). Precipitation thus decreases the kinetic energy available for the work required by the boundary layer to entrain less dense air from above. A reduction of precipitation thereby accelerates entrainment by the boundary layer.

increased entrainment for larger N

The response of LWP to increasing droplet concentrations is determined by a competition between the tendency for LWP to increase from the *direct* effect of drizzle decreasing as N increases and the opposite tendency for LWP to decrease from the drying effect of increased entrainment, an *indirect* effect of drizzle decreasing as N increases. Only when drizzle is sufficiently strong does the direct effect dominate.

While the three meteorological settings differ in a number of ways, including boundary-layer depth, sea-surface temperature, wind strength, and subsidence rate, our results indicate that the relative humidity of air overlying the boundary layer is a primary factor determining the response of LWP to changes in droplet concentrations. LWP monotonically increases with droplet concentrations in out simulations only when the air above the boundary layer is moist. In the case of ASTEX the relative humidity above the boundary layer is $\sim$70%, and LWP monotonically increases with N. When that air is much dryer, as in the case of DYCOMS-II, with a relative humidity of $\sim$10%, LWP decreases as N increases, except at extremely low droplet concentrations, in which stratocumulus are replaced by cumulus clouds (Stevens et al. 1998). In the intermediate case of FIRE-I, with a relative humidity close to 40%, LWP is seen to increase with N only at low-to-moderate droplet concentrations, and reverses at higher droplet concentrations.

To isolate the effect of relative humidity above the boundary layer, we ran another sequence of simulations using the ASTEX meteorology, modified with warmer, dryer air above the boundary layer. The relative humidity above the boundary layer is $\sim$25% in this case, and LWP is seen in Figure 1 to decrease as droplet concentrations increase beyond 70 cm^{-3}. Thus, we find that the LWP response to the competing effects of decreasing drizzle depends on the relative humidity above the boundary layer.

3 Cloud Albedo Changes

We can use these nocturnal simulations to assess change changes in cloud albedo (A) by employing an analytic expression for A that assumes a diffuse source of incident sunlight. Twomey (1991) uses the same expression to derive the change in cloud albedo with respect to a change in droplet concentration under the assumption that LWP and the dispersion of the droplet size distributions are independent of droplet concentration.

Figure 2 shows the amplification of the Twomey effect, which we define as $\Delta A/\Delta \ln N$ from our model simulations divided by $A(1-A)/3$, which is Twomey's approximation to this rate of change. At low droplet concentrations, corresponding to clean conditions, the strong increase of LWP with N for all the cases is attributable to the effect of heavy drizzle on boundary-

radiative cooling by reflection of sunlight drives boundary layer convection

light drizzle important for modulating entrainment

layer dynamics. Not only does average LWP strongly depend on N in this regime (Ackerman et al. 1993), but the horizontal distribution of cloud water is also profoundly affected (Stevens et al. 1998; Ackerman et al. 2003), as seen in visible satellite imagery of some ship tracks (Scorer 1987). The strong increase with N of both cloud cover (see Ackerman et al (2003)) and average LWP more than doubles the Twomey effect at low N.

At greater droplet concentrations, cloud cover becomes more uniform and the effect of increasing droplet concentrations on cloud albedo is dominated by the response of average LWP. When moist air overlies the boundary layer as in ASTEX, the Twomey effect is seen to be amplified by the increase of LWP with N, while for cases with very dry air overlying the boundary layer we find that the Twomey effect is offset. For the DYCOMS-II and dry ASTEX cases the Twomey effect is almost entirely negated by the decrease in LWP with increasing N at moderate droplet concentrations. For the FIRE-I case, with moderate relative humidity above the boundary layer, the albedo changes are seen to bridge these extremes, with an amplification of the Twomey effect for $N < 225$ cm^{-3}, and a suppression of the Twomey effect at higher droplet concentrations.

Reflection of sunlight is the means by which low-lying clouds impact the planetary radiative heat budget. However, a small fraction of incident solar radiation is absorbed by clouds, and this solar heating offsets some of the radiative cooling that drives boundary-layer convection, thereby modulating the dynamics of the boundary layer and thus the reflectivity of clouds. As found in simulations of trade cumulus clouds (Stevens et al. 2001), by driving turbulent convection within an overlying stratocumulus layer, radiative cooling acts as a positive feedback that amplifies changes in the underlying dynamics. By reducing the net radiative cooling near the top of a cloud layer, solar heating reduces the positive feedback of the system, thus reducing the changes in LWP with droplet concentrations. Daytime simulations for the ASTEX cases confirm this expectation. For example, we find for the baseline ASTEX conditions that the amplification of the Twomey effect decreases from 2.2 for the nocturnal simulations to 2.0 for summer daytime simulations as CCN concentrations increase from 150 to 300 cm^{-3}. For the corresponding dry ASTEX simulations the Twomey amplification increases from 0.1 to 0.4. Thus, in both cases the albedo change in the daytime simulations is consistently closer to Twomey's approximation than seen in Figure 4 for nocturnal simulations.

4 Conclusions

Our analysis suggests that the very concept of "non-precipitating clouds" can be misleading. For cases in which little or no precipitation falls from a cloud layer, it is a mistake to assume that sedimentation of droplets within the cloud layer can be safely ignored. To the contrary, it is the change in light drizzle within such clouds that modulates the drying of the boundary layer by entrainment.

Our results also suggest a revised view of remote-sensing measurements that show cloud liquid water path to be depressed in polluted clouds. We find no reason to contest the argument that omitting partly-cloudy and clear pixels introduces a sampling bias that can lead to misleading conclusions (Ackerman et al. 2003), as this criticism still applies to satellite observations at 1-km resolution (Coakley and Walsh 2002), and this bias increases as the size of the pixel increases. Our simulations show, however, that even without such a sampling bias, cloud water can indeed decrease as droplet concentrations increase. The mechanism we have described may well explain the decrease in LWP observed in high-resolution imagery of ship tracks (Platnick et al. 2000), as measurements with 50-m horizontal resolution are far less vulnerable to a sampling bias than are relatively coarse satellite data.

need for higher satellite obsvt

Global estimates of the aerosol indirect effect from satellite observations (Nakajima et al. 2001) not only require estimates of regional changes in cloud droplet concentrations, but also co-varying climatologies of relative humidity above stratocumulus regions. We speculate that our results may help to explain why forward climate models, which consistently show an amplification of the Twomey effect (Haywood and Boucher 2000), tend to overestimate the indirect aerosol effect compared to inverse calculations from simpler models constrained by the historical temperature record (Knutti et al. 2002).

how does solar heating impact on radiative cooling and effect dynamics

References

Ackerman, A. S. et al. (2000). Effects of aerosols on cloud albedo: Evaluation of Twomey's parameterization of cloud susceptibility using measurements of ship tracks. *J. Atmos. Sci. 57*, 2684–2695.

Ackerman, A. S., O. B. Toon, and P. V. Hobbs (1993). Dissipation of marine stratiform clouds and collapse of the marine boundary layer due to the depletion of cloud condensation nuclei by clouds. *Science 262*, 226–229.

Ackerman, A. S., O. B. Toon, and P. V. Hobbs (1995). A model for particle microphysics, turbulent mixing, and radiative transfer in the stratocumulus-topped marine boundary layer and comparisons with measurements. *J. Atmos. Sci. 52*, 1204–1236.

Ackerman, A. S., O. B. Toon, D. E. Stevens, and J. A. Coakley (2003). Enhancement of cloud cover and suppression of noctural drizzle in stratocumulus polluted by haze. *Geophys. Res. Lett. 30(7)*, 1381. doi:10.1029/2002GL016634.

- how does RH change above the air for INDOEX simulations
- how does entrainment vary with reduction in precipitation
- does cloud cover become more uniform with increasing R

(effect of drying from semi-direct effect, see the reduced entrainment of pcpt^n in boundary layer

Albrecht, B. (1989). Aerosols, cloud microphysics, and fractional cloudiness. *Science 245*, 1227–1230.

Coakley, J. A. and C. D. Walsh (2002). Limits to the aerosol indirect radiative effect derived from observations of ship tracks. *J. Atmos. Sci. 59*, 668–680.

Durkee, P. A. et al. (2000). The impact of ship-produced aerosols on the microstructure and albedo of warm marine stratocumulus clouds: A test of MAST hypotheses 1i and 1ii. *J. Atmos. Sci. 57*, 2554–2569.

Duynkerke, P. G., H. Zhang, and P. J. Jonker (1995). Microphysical and turbulent structure of nocturnal stratocumulus as observed during ASTEX. *J. Atmos. Sci. 52*, 2763–2777.

Germano, M., U. Piomelli, P. Moin, and W. H. Cabot (1991). A dynamic subgrid-scale viscosity model. *Phys. Fluids A 3*, 1760–1765.

Haywood, J. and O. Boucher (2000). Estimates of the direct and indirect radiative forcing due to tropospheric aerosols: A review. *Rev. Geophys. 38*, 513–543.

Knutti, R., T. F. Stocker, F. Joos, and G.-K. Plattner (2002). Constraints on radiative forcing and future climate change from observations and climate model ensembles. *Nature 416*, 719–723.

Nakajima, T., A. Higurashi, K. Kawamoto, and J. E. Penner (2001). A possible correlation between satellite-derived cloud and aerosolmicophrophysical parameters. *Geophys. Res. Lett. 28*, 1171–1174.

Pincus, R. and M. B. Baker (1994). Effect of precipitation on the albedo susceptibility of clouds in the marine boundary layer. *Nature 312*, 250–242.

Platnick, S. et al. (2000). The role of background cloud microphysics in the radiative formation of ship tracks. *J. Atmos. Sci. 57*, 2607–2624.

Radke, L. F., J. A. Coakley, and M. D. King (1989). Direct and remote sensing observations of the effects of ships on clouds. *Science 246*, 1146–1149.

Schwartz, S. E., Harshvardhan, and C. M. Benkovitz (2002). Influence of anthropogenic aerosol on cloud optical depth and albedo shown by satellite measurements and chemical transport modeling. *Proc. Natl. Acad. Sci. 99*, 1784–1789.

Scorer, R. S. (1987). Ship trails. *Atmos. Environ. 21*, 1417–1425.

Stevens, B. et al. (2001). Trade-wind cumuli under a strong inversion. *J. Atmos. Sci. 58*, 1870–1891.

Stevens, B., W. R. Cotton, G. Feingold, and C.-H. Moeng (1998). Large-eddy simulations of strongly precipitating, shallow, stratocumulus-topped boundary layers. *J. Atmos. Sci. 55*, 3616–3638.

Stevens, D. E., A. S. Ackerman, and C. S. Bretherton (2002). Effect of domain size and numerical resolution on the simulation of shallow cumulus convection. *J. Atmos. Sci. 59*, 3285–3301.

Toon, O. B., C. P. McKay, T. P. Ackerman, and K. Santhaman (1989). Rapid calculation of radiative heating and photodissociation rates in inhomogeneous multiple scattering atmospheres. *J. Geophys. Res. 94*, 16287–16301.

Twomey, S. (1974). Pollution and the planetary albedo. *Atmos. Environ. 8*, 1251–1256.

Twomey, S. (1991). Aerosols, clouds, and radiation. *Atmos. Environ. 25*, 2435–2442.

Evidence for Natural Variability in Marine Stratocumulus Cloud Properties Due to Cloud-Aerosol Interactions

Bruce Albrecht[1], Tarah Sharon[1], Haf Jonsson[2], Patrick Minnis[3], J. Kirk Ayers[4], Mandana M. Khaiyer[5]

[1] MPO/RSMAS, University of Miami, Miami, Florida, 33149,USA
[2]Center for Interdisciplinary Remotely Piloted Aircraft Studies, Marina, California, 93933, USA
[3]Atmospheric Sciences Division, NASA Langley Research Center, Hampton, Virginia, 23666. USA
[4]SAIC, Hampton VA, 23666
[5]AS&M, Inc., Hampton, VA 23666

1. INTRODUCTION

Large rifts and gradients are observed frequently in the extensive stratocumulus decks that exist over the eastern areas of the Pacific and the Atlantic. These rifts--areas of low reflectivity and broken cloud conditions--are sometimes large enough to have a large impact on the albedo of the large-scale cloud fields, and indicate substantial natural variability in the properties of the cloud deck (Fig. 1). Consequently, these features present a natural setting to study the relationship between marine aerosol properties and cloud and drizzle characteristics.

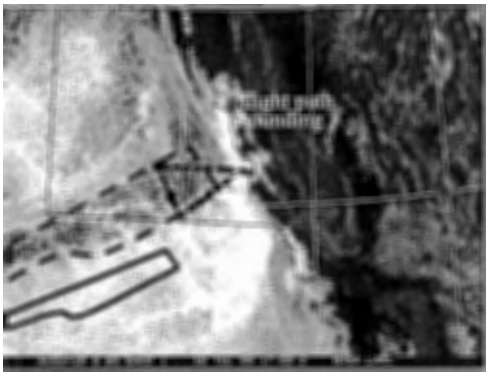

Fig.1 *GOES visible Satellite Image of stratus clouds and embedded rift observed off the coast of California, 16 July 1999 1700 UTC, with progression of rift shown by the dashed (1700 UTC) and solid thick line (2300 UTC). Flight path is also overlaid to identify location of soundings (circles) and the path of aircraft.*

Corresponding author's address: Bruce Albrecht, RSMAS/MPO, University of Miami, Miami, FL 33181;E-Mail: balbrecht@rsmas.miami.edu

Rifts may reflect aspects of the "indirect" aerosol effects where the radiative characteristics and the lifetime of clouds can be modulated by natural and anthropogenic changes in aerosols (e.g. Twomey, 1974 and 1979: Albrecht, 1989; Rotstayn, 1999). In rifts, it is hypothesized that CCN concentrations may be reduced relative to those in the surrounding cloud and these lower CCN concentrations may moderate cloud amount due to enhanced precipitation processes (Stevens et al., 2004).

Rifts may also be good indicators of feedbacks between drizzle and observed cloud structure. If CCN concentrations increase, clouds become optically thicker and the probability of precipitation decreases. This situation is consistent with areas of cloud enhancement along ship tracks (shown in Fig. 1) where a smaller mean droplet size is observed (Albrecht, 1989; Durkee et al.). Hence, once drizzle begins, although the mechanism for initiation is not fully known, CCN are removed and the CCN spectra modified by in-cloud collision and coalescence processes. This cleansing process may lead to an optically less reflective area in the satellite image, or an area in which cloud lifetime decreases due to enhanced drizzle (Albrecht, 1989). If this process is operating, then clean air conditions can support drizzle formation.

rifts are places for both direct and indirect effects

2. OBSERVATIONS

In this study, aircraft observations from the Interdisciplinary Remotely-Piloted Aircraft Studies (CIRPAS) Twin Otter are used to characterize the variability in drizzle, cloud, and aerosol properties associated with a cloud rift and the surrounding solid clouds observed off the coast of California. A flight made on 16 July 1999 provided measurements directly across an interface between solid and rift cloud conditions (Fig. 1). Aircraft instrumentation allowed for

measurements of aerosol, cloud droplet, and drizzle spectra. CCN concentrations were measured in addition to standard thermodynamic variables and the winds. A Forward Scatter Spectrometer Probe (FSSP) measured size distribution of cloud-sized droplets. A Cloud Imaging Probe (CIP) was used to measure distributions of drizzle-sized droplets. Aerosol distributions were obtained from a Cloud Aerosol Scatterprobe (CAS). The CAS probe measured aerosols, cloud droplets and drizzle-sized drops; for this study. The CAS probe was used to measure aerosols in the size range of 0.5 μm – 1 μm. Smaller aerosols were characterized using an Ultrafine Condensation Particle Counter (CPC) sensor. The CPC was used to measure particles with diameters greater than 0.003 μm. By subtracting different count concentrations measured with the CPC, this probe was capable of identifying ultrafine particles – those falling in the size range of 3 nm – 7 nm – that are believed to be associated with new particle production.

less pcpl in surrounds drizzle area

4. RESULTS

The aircraft observations indicate mesoscale patches of clouds and drizzle in the rift area compared with relatively small drizzle production in the solid cloud surrounding the rift. Aircraft soundings were obtained in the rift and the surrounding solid cloud. In addition, constant level legs (~20 minutes in duration) were flown at 700, 400, 200, and 100 m across the solid cloud/rift boundary. A relative time scale with a value of 0 at the boundary, positive values in the rift, and negative values in the solid cloud was developed for each of the legs.

Soundings in the rift and the solid cloud areas have very similar thermodynamic characteristics both in and above a strong inversion at about 750 m in both areas. Potential temperature increases about 10 K across the inversion with height and the mixing ratio decreased by about 2.5 g/kg over the depth of the inversion (~ 10 m).

The variability in the effective diameter (D_{eff}) in the solid and the rift cloud is shown in Fig. 2. Although larger droplets are observed beneath the solid cloud deck adjacent to the rift boundary, the concentrations of these larger droplets is small compared with concentrations observed from the cloud observed in the rift. At 200 meters the effective diameter of drizzle drops in the rift area is greater than that under the stratus deck. Effective diameters in the solid cloud deck (400 m level) are slightly less than 100 μm, whereas those associated with the rift peak at about 180 μm along the 200 m level. Although some drizzle is observed beneath the solid cloud near the cloud-rift boundary, the large-drop concentrations here are about 10 liter^{-1} compared with about 150 liter^{-1} in the rift cloud at the same level.

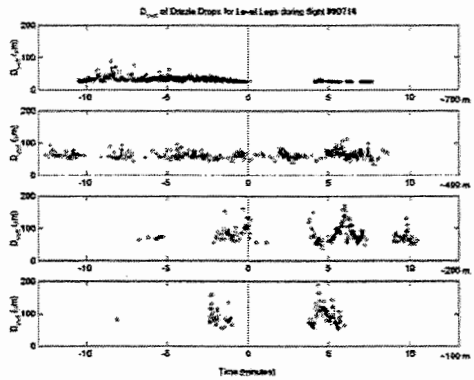

Fig. 2. Effective diameter for cloud drops along the four horizontal legs. The vertical gray line indicates the boundary between the solid stratus deck and rift region with the solid cloud to the left of this boundary. The x-axis is time of flight in minutes from the rift-cloud boundary

The variability in drizzle characteristics across the cloud/rift boundary is consistent with a substantial observed variation in CCN concentrations. CCN concentrations of ~30 cm^{-3} are observed in the rift compared with ~60 cm^{-3} in the solid cloud (Fig. 3). In addition to the CCN variations, substantial differences in the CN sampled on this flight were observed. Regions of new particle production, as indicated by large concentrations of particles in the 3-7 nm range, are observed near the top of the boundary layer in the clear area adjacent to the edge of the rift (Fig. 4). This area of small particles is also observed in the cloud free area sampled on the on the 700 m flight leg where no CCN were observed (see Fig. 3). This region occurs below the inversion and appears to exist in an area influenced by outflow from the solid cloud top and is not related to conditions above the inversion, since concentrations of aerosols in the 3-7 nm range are nearly identical over the rift and the solid cloud areas. Since new particle production can take place in very clean air, we interpret this area as being cleansed by processes in the nearby solid cloud deck.

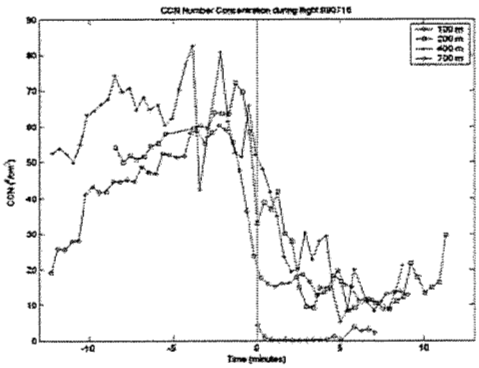

Fig. 3. CCN concentrations for the four level legs. The vertical gray line indicates the boundary between the solid stratus deck and rift region. In cloud measurements made in clouds have been omitted due to instrument limitations under cloud conditions.

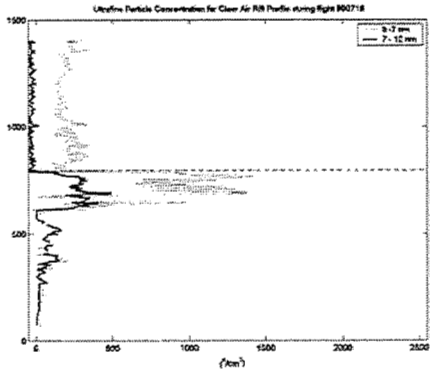

Fig.4. Ultrafine particle profiles obtained in clear area of the that is adjacent to the rift/solid cloud boundary.

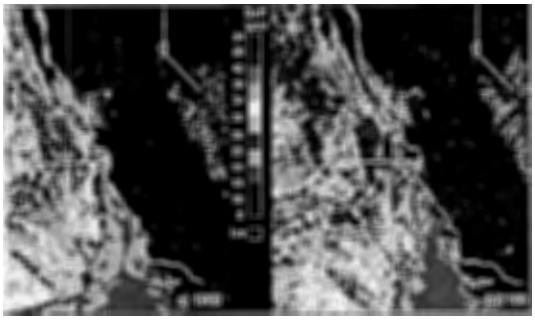

Fig. 5. Radiative effective cloud droplet diameter derived from GOES-10 data off the coast of California during 16 July 1999 at (a) 1900 UTC and (b) 2100 UTC.

Although the data are insufficient to document fully the dynamics associated with the stratus deck region and rift areas, microphysical conditions appear to dominate the differences in this area. A large-scale picture of the cloud droplet sizes is available in the satellite analyses. The radiative effective droplet diameter D_{eff} was derived from the GOES-10 data using the methods of Minnis et al. (1995, 1998) every half hour during the flights. The distribution of D_{eff} at both 1900 UTC (Fig. 5) and 2100 (UTC) clearly show the rift areas as regions with D_{eff} values greater than about 35 μm. The solid deck areas around the rifts typically have values of 26 to 35 μm, while those for the clouds farther south away from the rift areas range from 14 to 22 μm. Fig. 6 and similar images for other hours during the day indicate that much of the aircraft-sampled rift was gradually divided into smaller sections apparently as a result of the ship tracks that are evident as nearly linear features of reduced D_{eff} in Fig. 6 and seen in the visible image (Fig. 1). The introduction of additional aerosols from ships and from the continental air alters the microphysical structure of the rift clouds and may contribute to a reduction of drizzle and a brightening of clouds in rift areas.

4. DISCUSSION AND CONCLUSIONS

A review of observations from previous stratocumulus studies indicates that observations of drizzle in marine stratocumulus clouds have been generally associated with observations in rift areas. We revisited aircraft observations made during the FIRE stratocumulus experiment in 1986. These observations have been used to examine the microphysical structure for a case where the NCAR Electra made an extensive set of observations in a rift area where drizzle was observed (Austin et al., 1995). The UK C-130 aircraft sampled surrounding solid clouds where no drizzle was observed and cloud droplet concentrations of about 150 cm^{-3} compared with 50 cm^{-3} in the rift area were observed. The drizzle and cloud contrasts from these FIRE observations are consistent with our DECS results and provide further evidence for bi-stable cloud conditions where the rift areas are associated with mesoscale drizzle patches and low CCN concentrations compared with lower drizzle rates and higher CCN concentrations in the solid cloud area.

rift areas, low CCN
Conc^n s but no drizzle

The results in this study provide direct evidence of indirect aerosol effects associated with natural variability in the cloud characteristics. More specifically, these results provide evidence of the second indirect aerosol effect that relates increases in fractional cloudiness to decreases in drizzle associated with higher CCN concentrations. The opposite effect is seen in ship tracks observed within the rift during this study that tend to be more reflective in the gradient areas due to a susceptibility for indirect effects in these areas. Decreased albedos and more open cellular structures characterize the rift and gradient areas where drizzle processes work to diminish CCN concentrations. Evidence for air that has been cleansed of all CCN concentrations by cloud process is evident in the observations presented. The presence of natural long-lived variations in marine stratocumulus cloud associated with the naturally forming rift areas and man-induced ship tracks clearly supports a the theory of bi-stable CCN and cloud states (Baker and Charlson, 1989) and provides convincing evidence of the importance of the second aerosol indirect effect. Since cloud rifts can affect extensive areas of the Earth's extensive stratocumulus decks, it is important to understand the physical mechanisms that cause these areas to form initially, since these mechanisms may be closely tied to other components the climate system.

5. ACKNOWLEDGMENTS

This research was supported under NSF Grant ATM 9902416. The CCN observations presented were kindly provided by Tim VanReken.. The satellite analyses were supported by NOAA Agreement NA00AABRG0330 under the PACS Program.

6. REFERENCES

Albrecht, B. A., 1989: Aerosols, cloud microphysics, and fractional cloudiness, *Science*, **245**, 1227-1230.

Austin, P., Y. Wang, R. Pincus, and V. Kujala, 1995: Precipitation in stratocumulus clouds: Observational and modeling results, *J. Atmos. Sci.*, **52**, 2329-2352.

Baker M. B., and R. J. Charlson, 1989: Bistability in CCN concentrations and thermodynamics in the cloud-topped boundary layer. *Nature*, **345**, 142-144.

Durkee, P. A., K. J. Noone, and R. T. Bluth. The Monterey Area Ship Track Experiment, *J. Atmos. Sci.*, **57**, 2523-2541, 2000b.

Ferek, Ronald J. Timothy Garrett, et al., 2000: Drizzle suppression in ship tracks, *J. Atmos. Sci.*, **57**, 2707-2728.

Rotstayn, Leon D., 1999: Indirect forcing by anthropogenic aerosols: A global climate model calculation of the effective-radius and cloud-lifetime effects, *J. Geophys. Res.*, **104**, 9369-9380.

Twomey, S., 1977: The influence of pollution on the shortwave albedo of clouds, *J. Atmos. Sci.*, **34**, 1149-1154.

Twomey, S. (1974), Pollution and the planetary albedo, *Atmos. Environ.*, **8**, 1251-1256.

Minnis, P., D. P. Garber, D. F. Young, R. F. Arduini, and Y. Takano, 1998: Parameterization of reflectance and effective emittance for satellite remote sensing of cloud properties. *J. Atmos. Sci.*, **55**, 3313-3339.

Minnis, P., D. P. Kratz, J. A. Coakley, Jr., M. D. King, D. Garber, P. Heck, S. Mayor, D. F. Young, and R. Arduini (1995), Cloud Optical Property Retrieval (Subsystem 4.3). "Clouds and the Earth's Radiant Energy System (CERES) Algorithm Theoretical Basis Document, Volume III: Cloud Analyses and Radiance Inversions (Subsystem 4)", *NASA RP 1376 Vol. 3*, edited by CERES Science Team, pp. 135-176.

Stevens, B., G. Vali, K. Comstock, R. Wood, M. C. VanZanten, P. Austin, C. Bretherton, and D. H. Lenschow, 2004: Pockets of Open Cells (POCs) and Drizzle in Marine Stratocumulus, Bull. Amer. Met. Soc. (Submitted)

RELATIONSHIP BETWEEN CIRRUS ANVIL ICE CRYSTAL PROPERTIES AND AEROSOL CONCENTRATION, AMBIENT RELATIVE HUMIDITY AND VERTICAL VELOCITY DURING CRYSTAL-FACE

C. Andronache[1] and V. Phillips[2]

[1]Boston College, Chestnut Hill, MA 02467, USA
[2]Princeton University, GFDL, Princeton NJ 08452, USA

1. INTRODUCTION

Tropical cirrus clouds are high ice clouds that form at altitudes of ~ 9-18 km and one generating mechanism is the moist deep convection. This process pumps water vapor and ice crystals into the upper troposphere (UT) and interactions with the atmospheric flow leads to anvil formation. Cirrus anvils can spread over large areas, persist for several hours and play an important role in the atmospheric radiative budget. There is a need for development and validation of cloud processes parameterizations in GCM models (Kärcher and Lohmann, 2002). The Cirrus Regional Study of Tropical Anvils and Cirrus Layers - Florida Area Cirrus Experiment (CF) addresses scientific issues that can improve our understanding of ice clouds role in the climate system (Toon et al., 2003). Some important CF goals are: a) evaluate the sensitivity of cirrus anvils to their generating convective systems; b) improve understanding of cirrus anvil evolution processes and dependence on UT conditions. Within this framework, the goals of this study are: 1) analyze the dependence of ice crystals (IC) properties on small vertical motions in anvil, dependence of relative humidity and aerosol loading, and 2) use a cloud microphysical model to study the sensitivity of IC to updraft velocity in convective core and impact on anvil characteristics.

2. DATA

The CRYSTAL-FACE mission collected an extensive data set during July 2002 in the Florida region. Measurements were made from ground sites, aircraft, and satellites. For the purpose of this paper, we use data from the WB-57 aircraft which sampled in-situ cirrus anvils, aerosols, gas species concentrations, and radiative fluxes in the tropopause region. The Citation aircraft sampled the lower portions of the cirrus anvils including measurements closer to the convective source. The Twin Otter aircraft sampled aerosols and environmental conditions in the boundary layer region feeding into the convective systems. Data from Citation and Twin Otter are used for the microphysical model initialization.

To address the problem of IC dependence on aerosol, vertical velocity (w) and relative humidity with respect to ice (RH_i) we use aerosol and ice particle, water vapor, and meteorological data. The aerosol and ice particle data were measured using the Cloud, Aerosol and Precipitation Spectrometer (CAPS), which combines the capabilities of the Forward Scattering Spectrometer Probes (FSSP) models 100 and 300 (FSSP-300 and FSSP-100), 2D optical probe (2D-OAP), the Multiangle Aerosol Spectrometer Probe (MASP) and the hot-wire liquid water probe, in one system (Baumgardner et al., 2001). CAPS measures particles with diameters in the range: 0.35 μm-1.35 mm, in 25 channels (which define 25 diameter intervals, covering sizes from submicronic aerosol particles, to very large IC particles), and liquid water content (LWC) from 0.01 to 3 g m^{-3}. The water vapor on WB-57 used in this study was measured using the JPL Near-IR Water Spectrometer for in-situ measurements. The instrument is based upon a near-IR tunable diode laser source operating near 1.37 mm. The spectrometer features an open-path, multipass (Herriott) cell for true in situ monitoring of H_2O concentrations with precision levels exceeding those of Lyman-a and frost-point hygrometers. External sampling outside the aircraft boundary layer minimizes measurement uncertainties and enables high-speed in situ sampling along the

Corresponding author's address: Constantin Andronache, Boston College, Gasson Hall 012, 140 Commonwealth Ave., Chestnut Hill, MA, 02467, USA; E-Mail: andronac@bc.edu

aircraft flight track. Measurement precision is ± 0.05 ppmv in the stratosphere for a 2 s measurement integration period (May, 1998). The NASA Ames Meteorological Measurement System (MMS) provides high resolution in situ airborne state data (Chan et al., 1993).

3. RESULTS AND DISCUSSION

3.1 Results from data analysis

CAPS data allow to investigate the relationship between IC concentration (defined as IC particles larger than a selected threshold diameter, TD). Data was analyzed for WB-57 flights from the following 2002 July days: 7, 9, 11, 13, 16, 19, 21, 23, 27, and 28. An example of several variables of interest is shown in Figure 1.

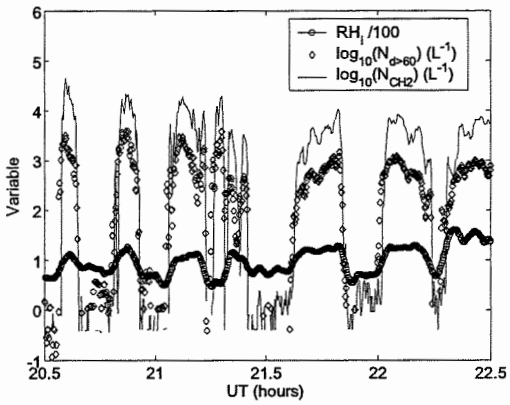

Figure 1. Time series from Flight WB-57 on July 16, 2002. Shown are: the normalized relative humidity with respect to ice, *RHi* /100, the ice concentration $N(d > 60\ \mu m)$ and $N(d$: 1- 3 μm) (or N_{CH2}). For figure clarity the RH_i values are smoothed.

Figure 1 shows that $N(d > 60\ \mu m)$ correlates quite well with $N(d$: 1- 3 μm) and with presence of supersaturated air with respect to ice. We found that $N(d$: 1- 3 μm) is also well correlated with $N(d$: 0.35 - 1 μm) which is a good indicator of total aerosol concentration. Because $N(d$: 0.35- 1 μm) is the first CAPS channel, to avoid possible instrumental sensitivity errors, we chose to use channel two in these plots. Analysis shows also that significant presence of $N(d > 60\ \mu m)$ is related to small updrafts in anvil, a feature found in most analyzed flights. WB-57 samples from the ten analyzed flights show that the small vertical velocity in anvil is normal distributed. This allows comparisons of IC properties for samples taken in updrafts and downdrafts as illustrated below.

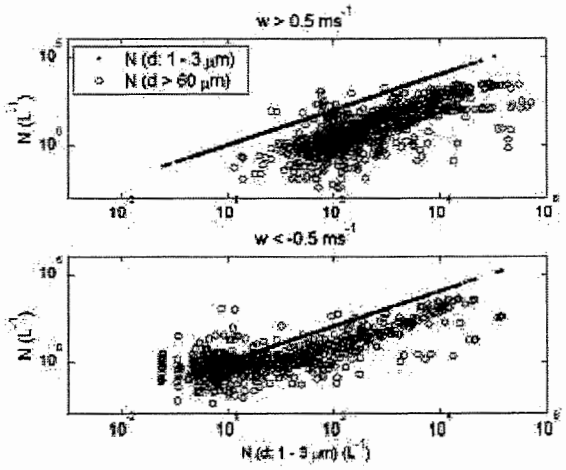

Figure 2. a) Scatter plot of IC particle concentrations larger 60 μm, $N(d > 60\ \mu m)$, versus particle concentration in the second channel $N(d$: 1 - 3 μm) for cases with vertical velocity $w > 0.5$ ms^{-1}; b) the same plots for cases with $w < -0.5$ ms^{-1}. Data used combines all ten analyzed flights WB-57 (days: 7, 9, 11, 13 16, 19, 21, 23, 26 and 28).

Figure 2 shows remarkable positive correlation between IC concentration (illustrated here as particles with $d > 60\ \mu m$) and particles in channel 2, for aerosol concentrations less than ~ E4 (L^{-1}) in updrafts. Above this limit, the correlation becomes weaker. Note the decrease of correlation in downdrafts where becomes evident that most samples are found at low concentrations (0.1 – 100 L^{-1}). This behavior can be summarized for all flights by plotting the probability of occurrence of N in updrafts and downdrafts.

Figure 3 focuses on small IC concentration dependence of vertical velocity ($N(d > 5\ \mu m)$ is dominated by small ice crystals). Concentration is higher in updrafts and can reach ~E5 L^{-1} with a maximum probability for concentrations of ~ E3 L^{-1}. In downdrafts, probability of large IC concentration decreases substantially, while probability increases to have small concentrations of $N(d > 5\ \mu m) \sim 1$ L^{-1}.

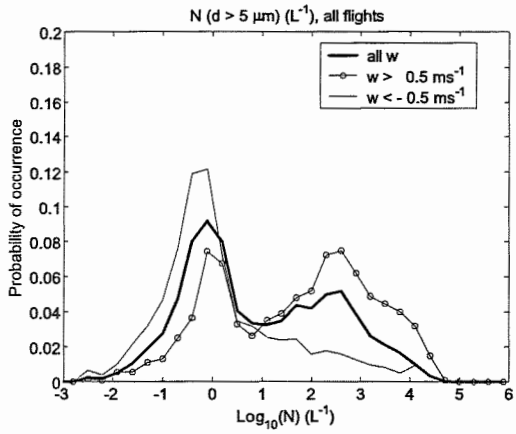

Figure 3. Probability of occurrence of IC concentrations with diameter $d > 5$ μm shown on x axis in Log_{10} scale. The solid line is for all analyzed cases (all w values), line with open circles is for cases with $w > 0.5$ ms^{-1}, and the dotted line is for cases with $w < -0.5$ ms^{-1}.

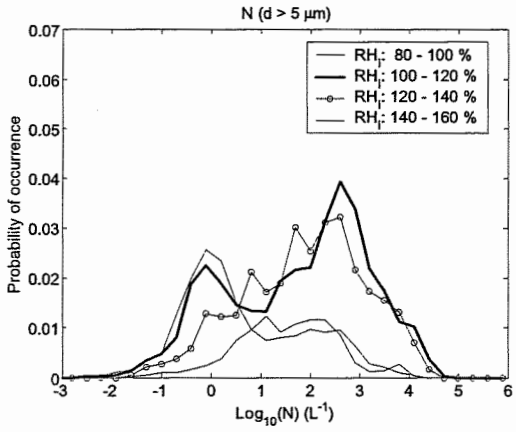

Figure 4. Probability of occurrence of IC concentrations with $d > 5$ μm shown on x axis in Log_{10} scale.

Probability of highest concentrations is found for RH_i between 100 and 140 % (possibly dominated by heterogeneous aerosol freezing formation) (Figure 4). Presence of cases for RH_i: 140 – 160 % suggests possible homogeneous aerosol freezing. Presence of IC for $RHi < 100$ % is due to samples in downdrafts and in mixed undersaturated air where IC persist for some time before sublimation.

Overall we found that: a) IC has a positive correlation with CAPS particle concentration in channel 2 $N(d$:1-3 μm), which is indicative of the total aerosol concentration. The correlation increases in updrafts and becomes weaker in downdrafts; b) the probability of occurrence of large IC concentration increases in updrafts; c) the largest probability of significant IC was found for $RH_i \sim 100$-140 %.

3.2 Microphysical model results

The explicit microphysical model (EMM) is an extension to the 1-D Multi-Thermal Model (MTM) of cumulus glaciation by Blyth and Latham (1997) and has fully interactive components for water vapor, cloud-water, ice and rain, as well as aggregation of ice, heterogeneous and homogeneous freezing, and melting (Phillips et al., 2003). Precipitation size-bins are advected in 2-D in the plane that passes through the updraft and downdraft, while cloud-water and vapor are advected in 1-D in the updraft and cloudy region (SCR). An evolving 2-D field of air velocity is prescribed with a simple analytical model, for the tracing of hydrometeors trajectories.

Ice particles are grouped into several basic species in the model, according to their mode of formation: (1) primary ice nucleated by condensation/deposition freezing between -5 and -30 deg C; (2) homogeneously frozen precipitation-particles; (3) H-M splinters emitted from particles in species (1) and (2); (4) frozen raindrops formed heterogeneously and from collisions with ice in species (1) – (3); and finally, subsequent generations of H-M splinters and raindrops frozen in collisions with these H-M splinters (Hallett and Mossop). Homogeneous freezing of droplets in a given size-bin is assumed to be instantaneous, occurring when the temperature falls below a size-dependent threshold.

A particle scheme within the EMM predicts the continuous evolution of the size, bulk density and axial ratio of the identical ice particles in every size-bin of the local size distribution for each basic species. In the particle scheme, empirical formulae (Phillips et al., 2003) are combined to predict the shape and density of each successive layer of ice from riming, aggregation and vapor deposition.

The dynamical framework of the cloud is prescribed in the manner described by Phillips et al. (2003). Values of the dynamical parameters are adjusted to match observed values from a CRYSTAL-FACE cumulonimbus case of 7th July 2002. There is a sequence of thermals in the

updraft ascending at about half the local value of the peak updraft speed which increases linearly with height. These thermals lift the cloud-top in stages to its maximum altitude, as in the original MTM. A downdraft is included that is 1 km deep and is adjacent to each thermal. Particles are swept into the downdraft from the tops of the thermals. Ice particles in the downdraft are evaporated at a rate that is such as to maintain exact ice saturation. Environmental air is entrained into the updraft from all levels at a rate such that the liquid water content matches the value observed by the Citation aircraft. The vapor mixing ratio of the environmental air is obtained from the sounding observations for this CRYSTAL-FACE case.

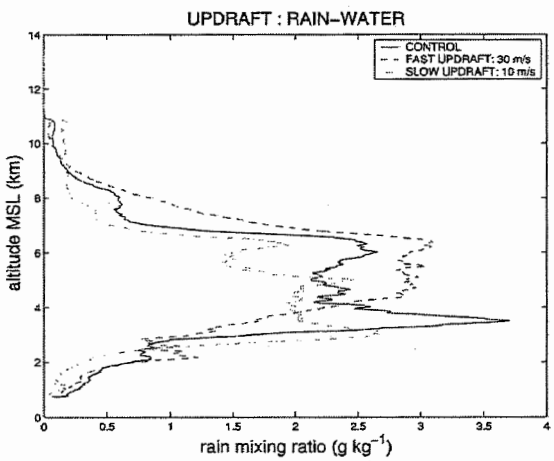

Figure 5. EMM simulation of rain mixing ratio vertical profile changes with vertical velocity. The control run corresponds to w=20 ms^{-1}.

Model results show that the increase of vertical velocity in updraft core leads to: a) increase of mixing ratio of cloud water, rain and total ice concentration. An example of changes induced by core vertical velocity is shown in Figure 5. The control run corresponds to w=20 ms^{-1}, and the two cases used for sensitivity calculations correspond to w =10 and 30 ms^{-1}. Note that for fast updraft, the rain mixing ratio maximum is lifted to higher altitude and this has consequences on the total IC concentration in the upper part of the convective core and in anvil region. b) Increase of total number concentration of IC in anvil region; c) there is an appreciable sensitivity of the super cooled cloud droplet concentration in the mixed phase region and this tends to affect anvil ice concentration.

how good is model of ice nucl° + how good are aerosol°

Acknowledgements

We thank D. Baumgardner, P. Bui, L. Pfister, R. Herman, B. Anderson, A. Heymsfield, C. Schmitt, J. C. Wilson, and all CRYSTAL-FACE team.

References

Baumgardner D., H. Jonsson, W. Dawson, D. O'Connor, and R. Newton, 2001: The cloud, aerosol and precipitation spectrometer: a new instrument for cloud investigations, Atmos. Res., 59-60, pp. 251-264.

Blyth, A.M. and Latham, J., 1997: A multi-thermal model of cumulus glaciation via the Hallett-Mossop process. Q. J. R. Meteorol. Soc., 123, 1185-1198.

Chan, K. R., L. Pfister, T.P. Bui, S. W. Bowen, J. Dean-Day, B.L. Gary, D.W. Fahey, K.K. Kelly, C.R. Webster, and R. D. May, 1993: A case study of the mountain lee wave event of January 6 1992, Geophys. Res. Lett., 20, 2551-2554.

Gaines, S. E., S. W. Bowen, R. S. Hipskind, T.P. Bui, and K. R. Chan, 1992: Comparisons of the NASA ER-2 meteorological measurement system with radar tracking and radiosonde data, J. Atmos. Ocean. Tech., 9, 210-225.

Kärcher, B. and U. Lohmann, 2002: A Parameterization of cirrus cloud formation: Homogeneous freezing of supercooled aerosols, J. Geophys. Res. 107 (D2), 4010, doi:10.1029/2001JD000470.

May, R. D.,1998: Open-path, Near-Infrared Tunable Diode Laser Spectrometer for Atmospheric Measurements of H_2O, J. Geophys. Res., Vol 103, No. D15, 19161-19172.

Phillips, V.T.J., Choularton, T.W., Illingworth, A.J., Hogan, R.J., and P.R. Field, 2003: Simulations of the glaciation of a frontal mixed-phase cloud with the Explicit Microphysics Model. Q. J. R. Meteorol. Soc., 129, 1351-1371.

Toon, O., Jensen, E., Starr, D., Anderson, D., 2003: An overview of the CRYSTAL-FACE mission, EAE03-A-13187, European Geophysical Society XXVIII General Assembly, Nice, France, April 6-11.

COMPARISONS OF MICROPHYSICAL MODEL AND BULK METHOD ESTIMATIONS OF SULFATE AEROSOL WET SCAVENGING RATES

Constantin Andronache

Boston College, Gasson Hall 012, Chestnut Hill, MA, 02467, USA

develop model for scavenging coefficient of gaseous species

1. INTRODUCTION

The wet removal of atmospheric particles (AP) by precipitation is an efficient atmospheric aerosol sink. It influences the tropospheric aerosols turnover time and their effects on environment. The detailed mechanism of the wet scavenging process involves microphysical interactions between AP and hydrometeors (Hales, 1995; Pruppacher and Klett, 1997; Jennings, 1998; Andronache 2003). In this study it is considered that an AP is removed from the atmosphere by rainfall when it becomes incorporated into a raindrop that falls to the Earth's surface. The APs wet removal is represented in current models by scavenging coefficients in aerosol mass continuity equations. The methods used to determine the aerosol wet scavenging coefficient, as reported in previous work, are: 1) microphysical model based on prescribed hydrometeor size distribution and collection efficiency (E) between raindrops and aerosols (Scott, 1982; Jylha, 1991; Pruppacher and Klett, 1997), and 2) bulk average estimations of the scavenging coefficient, L, based on the scavenging ratio determined from observations (Hales, 1995; Okita et al., 1996). Ultimately, a scavenging coefficient based on prescribed E and rainfall rate R is needed in mesoscale and large scale models of aerosol transport as well as for rapid assessments of aerosol fate in local pollution studies. The goals of this work are: 1) Calculate bulk average values of L based on mass balance of sulfate at several Atmospheric Integrated Research Monitoring Network (AIRMoN) sites in the Eastern United States; 2) Compare L bulk values with estimations based on a microphysical model of L for sulfate aerosol for hourly measured precipitation rates, R, at the same locations.

Corresponding author's address: Constantin Andronache, Boston College, Gasson Hall 012, 140 Commonwealth Ave., Chestnut Hill, MA, 02467, USA; E-Mail: andronac@bc.edu

2. METHOD

2.1 Bulk method

A bulk average value of L can be determined based on the mass balance of the aerosol of interest in an imaginary atmospheric box above a station of observation. The box covers a horizontal area A and extends from surface to a height h_2 (Hales, 1995; Okita et al., 1996). Thus, $L=FM^{-1}$ where F is the flux of aerosol at the Earth's surface and M is the mass of aerosol in the considered box. The flux, $F=C_wRA$, where C_w is the SO_4 concentration in precipitation water recorded at the Earth's surface, and R is the precipitation rate. The aerosol mass in the box is $M=\langle C_a(z)\rangle Ah$, where $\langle C_a(z)\rangle$ is the SO_4 vertical average concentration in the box, and h is the height of the cloud layer with precipitation (assumed mainly between the cloud base level and the freezing level). Thus,

$$L=\frac{F}{M}=\frac{C_wR}{\langle C_a(z)\rangle h} \quad (1)$$

where,

$$\langle C_a(z)\rangle=\frac{1}{(h_2-h_1)}\int_{h_1}^{h_2}C_a(0)\exp(-\frac{z}{H})dz \quad (2)$$

with the solution

$$\langle C_a(z)\rangle=\frac{C_a(0)H}{h}\exp(-\frac{h_1}{H})\left[1-\exp(-\frac{h}{H})\right] \quad (3)$$

where, $C_a(0)$ is the SO_4 concentration measured at surface, h_1 is the cloud base height, H is the scale height of SO_4 aerosol, h_2 is the height of the box, and $h=h_2-h_1$. We define a factor, f that depends on the characteristic heights h_1, h, and H

$$f=H\exp(-\frac{h_1}{H})\left[1-\exp(-\frac{h}{H})\right] \quad (4)$$

and L becomes

$$L = \frac{C_w R}{\langle C_a(0) \rangle f} \tag{5}$$

which is applied to measurements taken at stations from the networks described below (Table 1). The dependence of f on h for several values of the scale height of sulfate is discussed in detail in Andronache (2004). With this formulation, L can be calculated for observations made at a time scale of the order of one hour similar to the approach taken by Okita et al (1996).

2.2 Microphysical method

The microphysical method used to estimate L follows the concepts introduced by Scott (1982) and is illustrated here for removal of spherical APs by falling spherical raindrops inside clouds. By definition,

$$L(a) = \int_0^\infty \frac{\pi D^2}{4} V(D) E(a,D) N(D) dD \tag{6}$$

is the in-cloud scavenging (ICS) coefficient, and this is a good approximation for the wet scavenging coefficient (Scott, 1982; Andronache, 2004). $V(D)$ is the raindrop fall velocity; $E(a,D)$ is the collision efficiency of the raindrop of diameter D with an AP of diameter a, and $N(D)dD$ is the precipitation size distribution. Scott considered a typical AP diameter inside cloud of 10 μm (after the growth of AP) and selected a value E=0.65 which will be used for calculations in this work. Following Scott (1982), a is assumed 10 μm, and we drop the dependence of L on a. L is linked to the rainfall rate, R, defined as (in units mm h^{-1})

$$R = 3.6 \int_0^\infty X(D) V(D) N(D) dD \tag{7}$$

Defining the total water concentration M (g m^{-3})

$$M = \int_0^\infty X(D) N_0 \exp(-\lambda D) dD \tag{8}$$

where $X(D)$ is the mass of one raindrop, and assuming a Marshall and Palmer precipitation size distribution

$$N(D)dD = N_0 \exp(-\lambda D) dD \tag{9}$$

with N_0=1.E8 m^{-4} , $\lambda=2367M^{-0.25}$, $V(D)=130xD^{0.5}$ (m s^{-1}) and $M=0.074R^{0.89}$ (M in g m^{-3} and R in mm h^{-1}), it can be shown that

$$L = 1.26 \times R^{0.78} \tag{10}$$

where L (h^{-1}) and R (mm h^{-1}).

3. RESULTS AND CONCLUSIONS

Calculations of average bulk values of L are made for data from several networks. Thus, C_w and R are measured on a daily basis in the AIRMoN , which is part of the National Atmospheric Deposition Program/National Trends Network (NADP/NTN) (Hales et al., 1987). AIRMoN was formed for studying precipitation chemistry trends with greater temporal resolution. Precipitation samples are collected daily from a network of nine sites and analyzed for the same constituents as the NADP/NTN samples (for a detailed overview of the AIRMoN network see Hicks et al., 2001). Daily values of $C_a(0)$ are taken from the Interagency Monitoring of Protected Visibility Environments (IMPROVE) program. Hourly values of precipitation rate, R, are taken from the National Climatic Data Center (NCDC). The location of all stations form the AIRMoN network are shown in Figure 1.

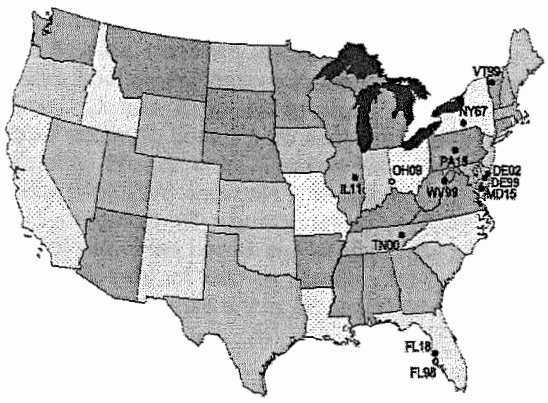

Figure 1. AIRMoN sites.

To calculate the average bulk L, the value of factor f in equation (4) must be determined. We consider a typical height scale of SO_4, H=2 km, and h_1 is taken as the top of the BL (1 km). For the base calculation we choose f=0.48 corresponding to H=2 km and h=1 km. h is the thickness of the cloud layer most active in wet scavenging and is taken 1 km for the calculations reported here, while variability in h is expected from case to case (details and sensitivity calculations are given in Andronache, 2004). With this reference value for h, the bulk estimates of L are shown in Table 1 for all nine stations. For all stations, there is significant positive correlation between L and rainfall rate R. Note that the fit compares well with the model described above by equation (10) and shown in Figure 2 where data from all 9 stations are combined.

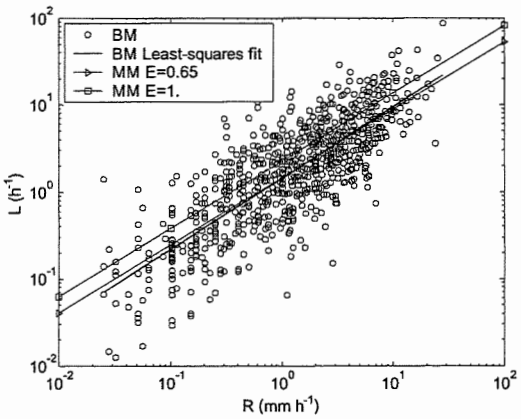

Figure 2. Wet scavenging coefficient of SO_4 aerosol, L for all data combined from the nine stations analyzed versus rainfall rate R. Shown are: Estimations from observations using the Bulk Method (BM) (open circles), Least-squares fit of the Bulk Method estimations (solid line), and Microphysical Model (MM) estimations corresponding to the collection efficiency E=0.65 between rain drops and aerosol particles (solid line with squares). The MM estimations for E=1 are shown by a solid line with triangles.

The microphysical model estimations for E=0.65 agree quite well with the bulk estimations. To get an idea on the upper limit of MM estimations, we plotted L for E=1. The average value of L and the standard deviation as well as the least-squares fit line parameters are given in Table 1 for each station. These estimations are consistent with other reported results obtained from other case studies (Okita et al., 1996; Jylha 1991).

Table 1. AIRMoN network stations used in this study and average, < >, and standard deviation, Std, of the wet scavenging coefficients for sulfate aerosol, L. The coefficients a and b of the least squares fit of the form $L=aR^b$ with L (h^{-1}) and precipitation rate R (mm h^{-1}) based on the bulk method are shown in the last two columns. The last row shows a and b corresponding to the microphysical model.

Station	<L> h^{-1}	Std(L) h^{-1}	a	b
DE02 Lewes	4.56	10.89	1.42	0.83
FL18 Tampa Bay	7.79	10.3	2.49	0.71
IL11 Bondville	2.08	2.65	1.26	0.93
MD15 Smith Island	2.17	2.45	1.06	0.74
NY67 Ithaca	2.17	2.47	1.18	0.81
PA15 Penn State	1.80	2.24	1.03	0.80
TN00 Walker Branch W.	4.13	5.39	1.69	0.72
VT99 Underhill	2.42	3.46	1.37	0.68
WV99 Caanan Valley	1.55	2.4	0.92	0.87
All stations	3.9	7.4	1.43	0.81
Model			1.26	0.78

The agreement between the two methods indicates that generally the network observations support the typical conditions employed by the microphysical model suitable for mesoscale modeling. Furthermore, the statistical analysis of the observations provide an independent and robust characterization of the wet scavenging. We found that L varies between 2 and 8 h^{-1}, with a standard deviation in the range [2-10] h^{-1} for the analyzed stations

We estimated the 0.5-folding time (t_{05}), defined as the time required to decrease the aerosol concentration to half of the initial concentration at the beginning of rain. We found that for R=1 mm h^{-1}, the 0.5-folding time of aerosol concentration is about 0.5 h. Even for large uncertainties in some parameters, t_{05} is of the order of hours for weak precipitation, and is of the order of minutes for

very intense rain (R~ 100 mm h^{-1}). The use of high resolution data reveal that t_{05} is a useful parameter to characterize the decay of aerosol after the beginning of rain, which can be valuable in pollution studies.

The study also suggests that a higher resolution data of aerosol concentrations, precipitation (such as hourly measurements), and simultaneous information on the vertical structure of precipitating clouds (that can be obtained from radars and regional weather modeling systems) can reduce the uncertainties in the bulk method and provide further insight for the microphysical modeling approach.

Acknowledgments

The author acknowledges the use of data from the National Climatic Data Center (NCDC), from the Interagency Monitoring of Protected Visibility Environments (IMPROVE) and from the Atmospheric Integrated Research Monitoring Network (AIRMoN).

References

Andronache, C., 2003: Estimated variability of below-cloud aerosol removal by rainfall for observed aerosol size distributions. Atmos. Chem. And Phys., 3, 131-143.

Andronache, C., 2004: Estimates of sulfate aerosol wet scavenging coefficient for locations in the Eastern United States, Atmos. Environ., 38, 795-804.

Hales, J. M., Hicks, B. B., and Miller, J. M., 1987: The role of research measurements networks as contributions to federal assessment of acid deposition. Bulletin of the American Met. Soc. 68, 216-225.

Hales, J. M., 1995: Acidic precipitation, Chapter 12 in volume Composition, chemistry and climate of the atmosphere, edited by H. B. Singh, Nostrand Reinhold, pp. 527.

Hicks, B. B., T. P. Meyers, R. P. Hosker Jr., R. S. Artz, 2001: Climatological features of regional surface air quality from the Atmospheric Integrated Research Monitoring Network (AIRMoN) in the USA, Atmos. Environ. 35, 1053-1068.

Jennings, S. G., 1998: Wet processes affecting atmospheric aerosols, Chapter 14 in Atmospheric Particles, edited by R. M. Harrison and R. Van Grieken, John Wiley & Sons Ltd, pages 476-507.

Jylha, K., 1991, Empirical scavenging coefficients of radioactive substances released from Chernobyl, Atmos. Environ. 25A, 263-270.

Malm, W.C., Gebhart, K.A., Molenar, J., Cahill, T.A., Eldred, R.E., and Huffman, D., 1994: Examining the Relationship Between Atmospheric Aerosols and Extinction at Mount Rainier National Park. Atmos. Environ. 28, No. 2, 347-360.

Okita, T., H. Hara, and N. Fukuzaki, 1996: Measurements of atmospheric SO_2 and SO_4, and determination of the wet scavenging of sulfate aerosol for the winter monsoon season over the sea of Japan, Atmos. Environ. 30, 3733-3739.

Pruppacher H. R., and Klett J. D., 1997: Microphysics of cloud and precipitation, Kluwer Academic Publishers, Dordrecht, Boston, London, pp. 954.

Scott, B. C., 1982: Theoretical estimates of the scavenging coefficient for soluble aerosol particles as a function of precipitation type, rate and altitude, Atmos. Environ. 16, 1753-1762.

IN-SITU MASS SPECTROMETRIC MEASUREMENTS OF AIRCRAFT EXHAUST AEROSOL PARTICLES

S. Borrmann[(1)], S. Henseler[(1)], N. Hock[(1)], S. Weimer[(1)], B. Kärcher[(2)], A. Petzold[(2)], and J. Schneider[(1)]

(1) Institute for Atmospheric Physics, Johannes-Gutenberg-University, D-55099 Mainz, Germany
Cloud Physics and Chemistry Department, Max-Planck-Institute for Chemistry, D-55128 Mainz, Germany
(2) Institute for Atmospheric Physics, Deutsches Zentrum für Luft und Raumfahrt (DLR), D-82230 Weßling , Germany

1. INTRODUCTION

Cirrus clouds in the upper troposphere may be influenced by aircraft exhaust particles at cruise altitudes. The upper troposphere is an altitude region where the aerosol background is very low. It is thought that the background aerosol is composed of sulfuric acid/water clusters, which form due to the high supersaturation in the UT/LS (upper troposphere/ lower stratosphere), as well as other components imported by vertical transport and originating in the boundary layer or the free troposphere. Aircraft exhaust particles are mainly composed of soot and sulfuric acid. Also, unburned hydrocarbons can condense on the soot or sulfuric acid particles (Schumann *et al.,* 2002). The concentration of the latter is dependent on the fuel sulfur content and also on the conversion efficiency of fuel sulfur to SO_3 and H_2SO_4, which was found to be 2.3% (Sorokin et al., 2004). If the soot particles are activated by sulfuric acid to take up water, internally mixed particles will form. These particles may trigger the formation of ice crystals and hence lead to the formation of cirrus clouds. For the better understanding of these processes, in-situ measurements of the chemical composition of aircraft exhaust particles are of considerable interest. In contrast to off-line methods (e.g. filter sampling), in-situ methods have the advantage to measure also volatile aerosol components.

2. MEASUREMENTS

For the first time, the Aerodyne Aerosol Mass Spectrometer (AMS) was employed on a jet aircraft - the research aircraft Falcon (operated by the German Aerospace Center (DLR)) – which is capable of reaching the upper troposphere and lower stratosphere. The measurements were part of the research project PAZI (Particles From Aircraft: Impact on Cirrus Clouds and Climate), which is funded by the German Hermann-von-Helmholtz Gemeinschaft Deutscher Forschungszentren (HGF) research organization.

Corresponding author's address: Stephan Borrmann, Institute for Atmospheric Physics, Johannes Gutenberg-University, Mainz, D-55099 Mainz, Germany and Max-Planck-Institute for Chemistry; E-Mail: borrmann@mpch-mainz.mpg.de

The measurements took place in May 2003 over Southern Germany at latitudes between 47 and 50°N and longitudes between 10 and 14°E. The measurement flights included sampling in aircraft exhaust at cruising altitude as well as background flights in regions with little air traffic.

The AMS detects particles in the size range between 50 and 1500 nm and measures quantitatively the mass concentrations and size distributions of major aerosol components like nitrate, sulfate, ammonium, as well as the sum of the non-refractory organics, which is equal to organic carbon. For a detailed description of the AMS see for example Jayne et al., (2000) or Bahreini et al. (2003). A schematic of the instrument inside the aircraft is depicted in Figure 1. After being transmitted through an isokinetic inlet from the ambient air into the aircraft (see Figure 2) the aerosol particles enter the vacuum chamber via an aerodynamic lens, which focuses the particles onto a narrow beam. This beam hits a hot surface (approx. 500 °C) after a flight distance of 0.39 m. By chopp ing the particle beam, the time of flight of the particle can be measured, and from this the so-called "vacuum aerodynamic diameter"

$$D_{va} = \frac{\rho_p}{\rho_0}\frac{1}{\chi}D_v$$

can be obtained. Here, D_v is the volume equivalent diameter, ρ_p is the particle density, ρ_0 the unit density, and χ is the dynamic shape factor.
Upon evaporation, the molecules are ionized by

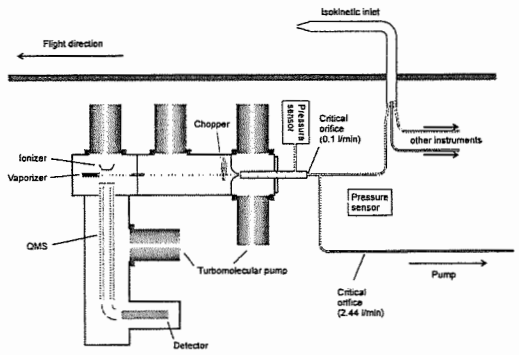

Fig. 1. Schematic of the AMS in the Falcon research aircraft.

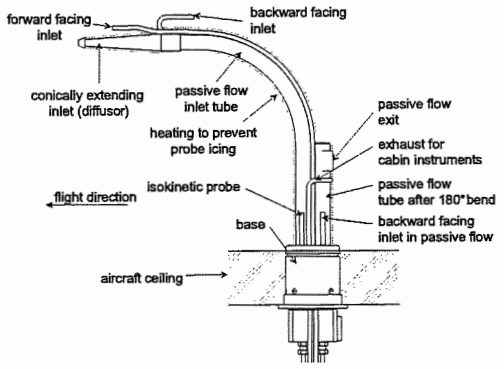

Fig. 2. Aerosol inlet of the Falcon aircraft. (Fiebig, 2001). The AMS was sampling through the isokinetic inlet probe.

electron impact and chemically analyzed by means of a quadrupole mass spectrometer. Based upon careful laboratory calibration with a monodisperse test aerosol (usually ammonium nitrate) the AMS is able to convert signal heights into mass concentrations.
Additionally, the aircraft was equipped with several condensation particle counters with different lower size limit cut-off diameters.
The aerosol inlet (Figure 2) was described by Fiebig (2001). It samples the air through an isokinetic probe with an upper cut-off diameter of more than 1500 nm for altitudes up to 12 km. The air flows towards the AMS at a flow rate of flow of 2.2 lpm, actively pumped and regulated by a critical orifice. The AMS samples the particles through a 100 µm pinhole at a nominal inlet flow rate of 1.4 cm^3s^{-1}.

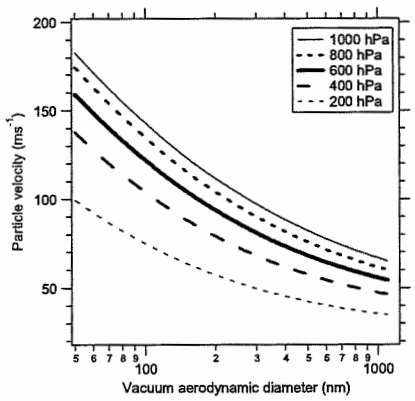

Fig. 3. Particle velocity inside the time-of-flight chamber as a function of sampling pressure.

The particle velocity inside the time-of-flight chamber of the AMS is dependent not only on the particles' "vacuum-aerodynamic" diameter, but also on the pressure up-stream of the critical 100 µm orifice.
Figure 3 depicts the relationship between the particle velocity and D_{va} for various pressures obtained from laboratory calibration prior to the aircraft campaign.

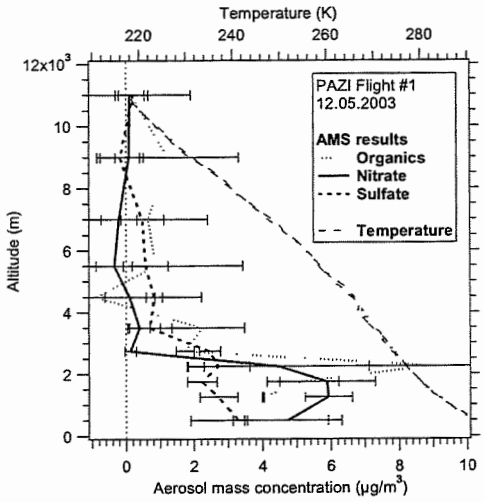

Fig. 4. Vertical profile of the major aeros components sulfate, nitrate, and organic carbc (termed "organics") during the Flight on May, 1: 2003.

3. RESULTS AND DISCUSSION

3.1 Background Aerosol

The measurements concentrated on the investigation of aircraft exhaust of commercial jet airliners at cruise altitude, i.e. between 10 and 12 km, but during ascent and descent, vertical profiles of the background aerosol were sampled. Figure 4 gives two vertical profiles of aerosol sulfate, nitrate and organic carbon during the ascent and descent of the measurement flight on May 12, 2003.
The upper edge of the boundary layer can clearly be recognized by the sharp decrease in the aerosol nitrate and organic content, but the aerosol sulfate mass concentration decreases markedly slower and maintains concentrations around 1 µg/m^3 in the mid-troposphere, where nitrate has already decreased below the AMS detection limit.

3.2 Aircraft Exhaust Aerosol

During the research flight on May 14, 2004, several distinct aircraft plume penetrations occurred, identified by the total particle concentration (D_p > 16 nm) measured with a condensation particle counter operated by DLR. The mass spectra recorded during these events were averaged and compared to background aerosol mass spectra recorded between the plume encounters (Fig. 5). The background mass spectrum is very clear with only few mass peaks (m/z 20, 23, 44, and 113) exceeding the noise level. m/z 44 is identified as CO_2^+, an ion that was frequently

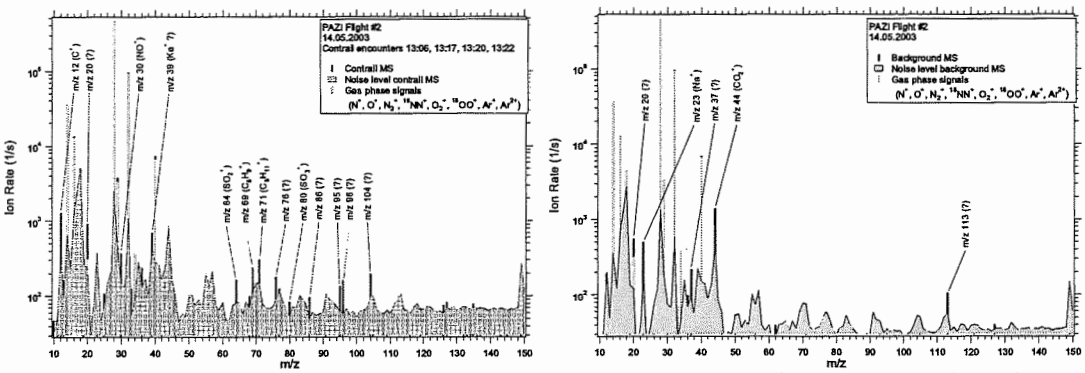

Fig. 5. Aerosol mass spectra recorded during contrail encounters (left) and background (right)

observed when sampling photochemically aged organic aerosol (e.g. Schneider et al., 2004), a possible candidate for m/z 23 would be Na^+, while the nature of the ion with m/z 113 remains speculative.

In the aircraft plume, ions with m/z = 64 (SO_2^+), 71 ($C_5H_{11}^+$), 80 (SO_3^+), 69 ($C_5H_9^+$), that are not present in the background aerosol, have been observed. Also, several unidentified ions (e.g. m/z = 68, 70, 76, 126, 127, 134) have been detected during the plume penetrations. We assume that these ions origin from low volatile organic species (from unburned fuel) that condensed on soot (or possibly also H_2SO_4) particles. The signals at m/z = 64 (SO_2^+) and 80 (SO_3^+) indicate that H_2SO_4 is present in the particles. However, more detailed data analysis will be necessary to clarify the nature of the yet unidentified ions.

ACKNOWLEDGMENTS

We thank R. Busen of DLR for the coordination of the PAZI aircraft campaign, and M. Fiebig (DLR) for the condensation particle counter data, the mechanical workshop of the Max Planck Institute, Th. Böttger, and W. Schneider for the preparation of the AMS for the aircraft missions. Funding was supplied by the Max-Planck-Institute for Chemistry, the University of Mainz, and the HGF.

REFERENCES

Jayne, J. T., D. C. Leard, X. Zhang, P. Davidovits, K. A. Smith, C. E. Kolb, and D. R. Worsnop, Development of an aerosol mass spectrometer for size and composition analysis of submicron particles, Aerosol. Sci. Technol., 33, 49-70, 2000.

Bahreini, R., J. L. Jimenez, J. Wang, J. T. Jayne, D. R. Worsnop, R. C. Flagan, and J. H. Seinfeld, Aircraft-based Aerosol Size and Composition Measurements during ACE-Asia using an Aerodyne Aerosol Mass Spectrometer, J. Geophys. Res., 108, 8645, doi:10.1029/2002JD003226, 2003.

Fiebig, M., The tropospheric aerosol at mid-latitudes – microphysics, optics, and climate forcing illustrated by the LACE 98 field study, Doctoral Thesis (in German), University of Munich, 2001

Schneider, J., S. Borrmann, A. G. Wollny, M. Bläsner, N. Mihalopoulos, K. Oikonomou, J. Sciare, A. Teller, Z. Levin, D. R. Worsnop, Online mass spectrometric aerosol measurements during the MINOS campaign (Crete, August 2001), Atmos. Chem. Phys., 4, 65-80, 2004.

Schumann, U, F. Arnold, R. Busen, J. Curtius, B. Kärcher, A. Kiendler, A. Petzold, H. Schlager, F. Schröder, and K.-H. Wohlfrom (2002). Influence of fuel sulfur on the composition of aircraft exhaust plumes: The experiments SULFUR 1–7, J. Geophys. Res., 107, 4247- 4274.

Sorokin, A., E. Katragkou, F. Arnold, R. Busen, and U. Schumann (2004). Gaseous SO3 and H2SO4 in the exhaust of an aircraft gas turbine engine: measurements by CIMS and implications for fuel sulfur conversion to sulfur (VI) and conversion of SO_3 to H_2SO_4, Atm. Env., 38, 449–456.

vertical profiles of aerosol conc^n in clean + polluted condition

MEASUREMENTS OF CLOUD–AEROSOL INTERACTIONS IN WARM CLOUDS AT THE JUNGFRAUJOCH MOUNTAIN TOP SITE IN SWITZERLAND

Keith N. Bower[1], M. R. Alfarra[1], M. J. Flynn[1], M. W. Gallagher[1], H. Coe[1], T. W. Choularton[1], E. Weingartner[2], C. Corrigan[2], M. Gysel[2]*, and U. Baltensperger[2]

[1]The Physics Department, UMIST, PO Box 88, Manchester, M60 1QD. United Kingdom
[2] Paul Sherrer Institute, Villigen, CH-XXXX, Switzerland (NB. *now at [1])

1. INTRODUCTION

Measurements investigating the relationship between warm clouds and the aerosol population upon which they form, were carried out during the CLACE-2 experiment in July 2002 at the Global Atmospheric Watch (GAW) research station in the Sphinx laboratory (3580m asl) at the Jungfraujoch (JFJ) mountain top site (located at 46.55 N, 7.98 E) in the Swiss Alps. This high altitude site on a mountain col is dominated by airflow from either the north-west or south-east, the directions being determined largely by the Alpine orography. Material in the airmass measured at the JFJ can thus have its origins several 100s of kilometres away in either the free troposphere or can be uplifted from the boundary layer in the surrounding valleys. As a result, aerosol concentrations and airmass ages observed at the site can be highly variable, as too can be the properties and formation mechanism of the clouds enveloping the ridge.

highly aged particles allow to examine indirect effect

2. AIMS

The main aim of CLACE-2 was to investigate the hygroscopic properties and chemical composition of the aerosol particles and their interaction with warm (non-glaciated) clouds. More specifically, to use measurement techniques and models of aerosol thermodynamics to make comprehensive predictions of the sub and super saturated water affinity of particles in a wide variety of conditions, and to test these using further detailed measurements. To achieve this, measurements were required of the chemical composition of particles in the boundary layer and free tropospheric air of varying ages at the JFJ Research Station using an Aerosol Mass Spectrometer to achieve high time and aerosol size resolution. Measurements were further required of the size dependent composition of total and interstitial aerosol particles during cloud events using twin inlets to infer the composition of particles activated during cloud events.

Corresponding author's address: Keith N. Bower, The Physics Department, UMIST, PO Box 88, Sackville Street, Manchester, M60 1QD. United Kingdom
E-Mail: k.bower@umist.ac.uk

3. INSTRUMENTATION

A suite of instrumentation was deployed to make measurements of the size distribution, composition and hygroscopicity of the aerosol, as well as the microphysics of the clouds. Use was made of a dual sampling inlet system (previously developed, installed and tested at the site by the Paul Scherrer Institute (PSI)) to enable sequential measurements to be made of both the total sub-micron aerosol population (comprising the dry cloud droplet residuals and interstitial particles) and of the separate interstitial particles (derived using a cyclone inlet with a 1μm 50% cutoff). Air from this system was brought into the lab and aerosol measurements performed at low humidities (RH<20%). An Aerodyne Aerosol Mass Spectrometer (AMS) was attached to this inlet to enable determination of the size segregated mass loadings of the non-refractory (ie. volatile and semi-volatile) chemical components (eg sulphate, nitrate, ammonium and organic components) of both the total inlet residuals and interstitial aerosol. Also attached were instruments measuring aerosol size distributions (eg by electrical mobility (SMPS) and optical techniques), and aerosol number, surface area and BC mass concentrations. A Hygroscopic Tandem Differential Mobility Analyser (HTDMA) was deployed to measure the hygroscopicity of the interstitial aerosol brought into the lab separately, and under ambient conditions (i.e. at external temperatures T<0degC). Ambient aerosol size distributions were also measured (by an externally housed SMPS).

Measurements of the activated aerosol fraction were also made externally. Cloud droplet size distributions (2-47μm) were measured by means of a means of a PMS Forward Scattering Spectrometer Probe (FSSP 100 - DMT modified) alongside an Airborne Droplet Analyser (ADA), a new phase doppler anemometry system (developed by Aerometrics and supplied by TSI) deployed and tested in the field for the first time. Both the FSSP and ADA were mounted on rotators to enable both to be directed into the prevailing winds. The FSSP was fitted with a fan (as is normally the case for its use by UMIST as a ground based instrument) nominally providing it with an aspiration velocity of 10m/s The local windspeed was measured using a heated sonic anemometer (made by Metek) enabling calculation of the local 3-D wind vector, and hence calculation of the

rotation angle for the two droplet sizing probes. Additionally this enabled calculation of the correction factor for the FSSP sample volume for wind ramming effects. A lidar was also deployed within a dome atop the Sphinx laboratory, to observe spatial and temporal evolution of the backscatter (at 355, 532 and 1064nm) enabling derivation of extinction coefficients for comparison with those derived from the local aerosol measurements.

4. RESULTS

4.1 AMS Data from the Total Inlet

Figures 1 (right) and 2 (below) show the average size distribution and time series loadings respectively of sulphate, nitrate and organics observed by the AMS sampling on the total inlet during CLACE-2. It can be seen that the organic loading is often comparable to that of sulphate during this summer experiment period

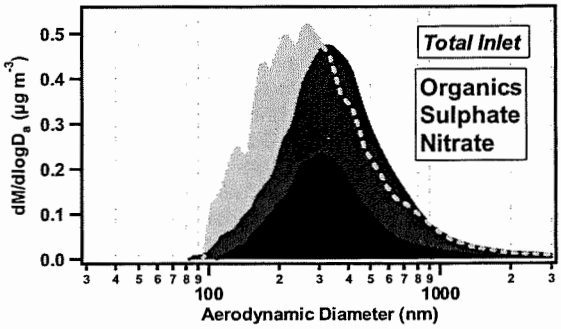

Figure 1: The average (vacuum aerodynamic) size distributions of the mass loadings of sulphate nitrate and organic species sampled by the AMS on the total inlet during CLACE-2

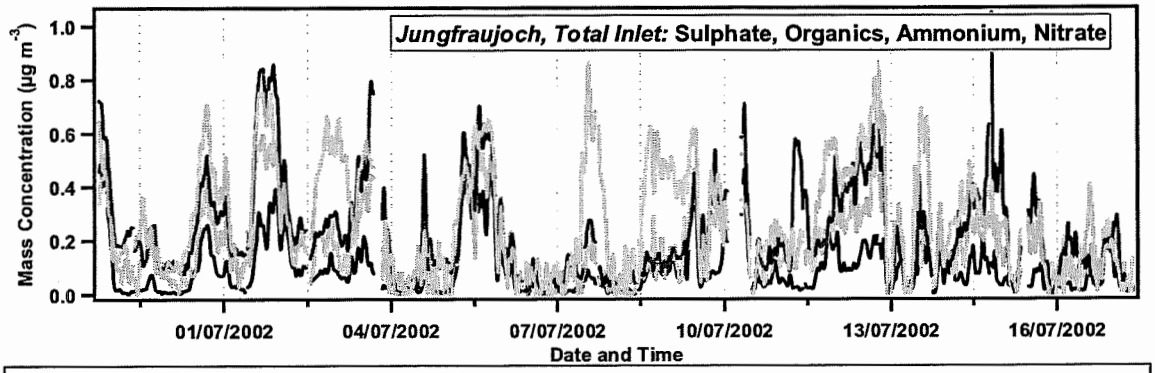

Figure 2: The time series of the loadings (in µg m^{-3}) of sulphate, nitrate and organics observed and sampled on the total inlet by the AMS during CLACE-2

Additionally, a clear diurnal cycle can be observed in the mass loadings (particularly for organics) during the first part of the experiment. This is presumably the result of katabatic winds advecting valley air up to the site during the afternoon periods, while at nighttime anabatic flow brings cleaner free tropospheric air to the site from aloft. These observations were confirmed by lidar measurements.

Further examination of the key mass fragments that contribute to the organic loading reveals that mass 44 (which is characteristic of decarboxylation of highly oxidised and hence more aged organic species on the vaporiser in the AMS) dominates, while mass fragment 57 (which is characteristic of aliphatic chains more typical of recently emitted species) contributes little. Taking a ratio of the loading of mass 44 to that of the total loading of organics for CLACE-2 gives a value of around 0.13 (see Figure 3 right). This compares with the extremes in ratios observed elsewhere, 0.15 for well-aged aerosol, and 0.04 for freshly emitted urban pollution. Additionally, a comparison of the average organic mass spectrum from JFJ reveals a high degree of correlation with the

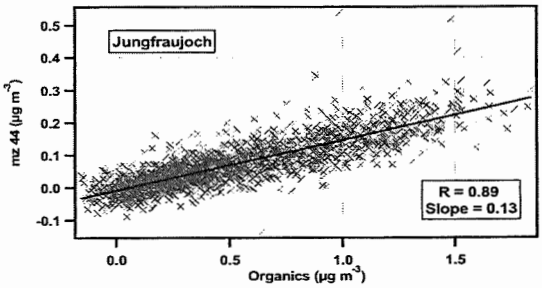

Figure 3: Scatter plot of the AMS mass fragment 44 loading to the total AMS organic loading for CLACE-2

Laboratory derived mass spectrum for fulvic acid. The latter has been found to be a good representative polycarboxylic acid for the highly oxidised, aged, processed soluble organics found in samples from many sites around the world (Decesari et al. 2000). This provides clear evidence that this type of compound is particularly significant in the JFJ aerosol.

4.2 AMS and Aerosol Hygroscopicity

Figure 4 shows the average hygroscopic growth factor observed for 100nm dry aerosol subjected to a relative humidity of 85%, as measured by the HTDMA deployed by PSI during CLACE-2 (diamonds). For comparison the growth factors measured in an urban environment in Milan (in summer 1998 (triangles)) and at JFJ in an earlier winter experiment (squares) are also shown. It can be seen that a single growth mode is observed with a growth factor (GF) of around 1.3 for the CLACE-2 case. This is smaller than that observed in the presumably more aged winter (free troposphere) case but larger and quite different to the bimodal distribution observed in the urban (freshly emitted pollution) case. A comparison of the time series of this GF with a time series of the ratio of inorganic to total non-refractory mass loading as derived by the AMS during CLACE-2 shows a high degree of positive correlation between the two time-series, revealing that increases in GF occur when the inorganic fraction of total non-refractory mass increases. A model was used to calculate the expected growth factor using the measured aerosol composition as a function of size derived by the AMS. Good agreement was observed between the calculated GF and that observed by the HTMA – particularly for aerosol of 250nm dry size.

4.3 Aerosol Cloud Interactions

Figure 5 illustrates the difference in nitrate loading observed between (interstitial and total) sample inlets during cloudy and non-cloudy periods. The upper time series shows the difference plot of these two loadings. This clearly correlates with the droplet number concentration of cloud particles (as measured by the FSSP) which is shown as the series of open circles. A similar result is seen for the other major species.

Cloud droplet spectral distributions showed considerable variation during CLACE-2. Simple mono-modal distributions and complex bi or multimodal droplet spectra were seen. Two such extreme cases will be presented. In the first case a large number of small droplets were observed in a monomodal spectrum. Examination of the size distribution of sulphate, nitrate and organic loadings from the total and interstitial inlets as measured by the AMS (Fig.6 where the solid shading is the total inlet loading, and the lighter shading the difference between total and interstitial inlets) reveals that most sulphate, organic and nitrate is activated above 150nm, and that little of each is activated below 150 nm. By contrast, in the second case study the droplet spectrum shows considerable bimodality. In this case, the AMS size distributions (Fig. 7) show much sulphate mass is activated between 600-1000 nm, but that there is little activation of sulphate below this size range. However, organics appear to be substantially activated at 400nm and below. Thus AMS results indicate significant differences in the composition of aerosol residuals between these different periods.

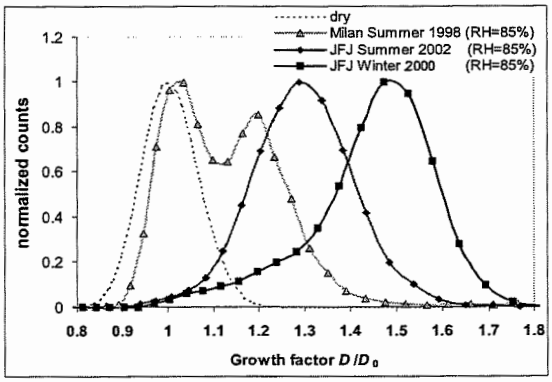

Figure 4: The average hygroscopic growth factor of dry 100nm aerosol subjected to an RH of 85% as measured by the PSI HTDMA during CLACE-2

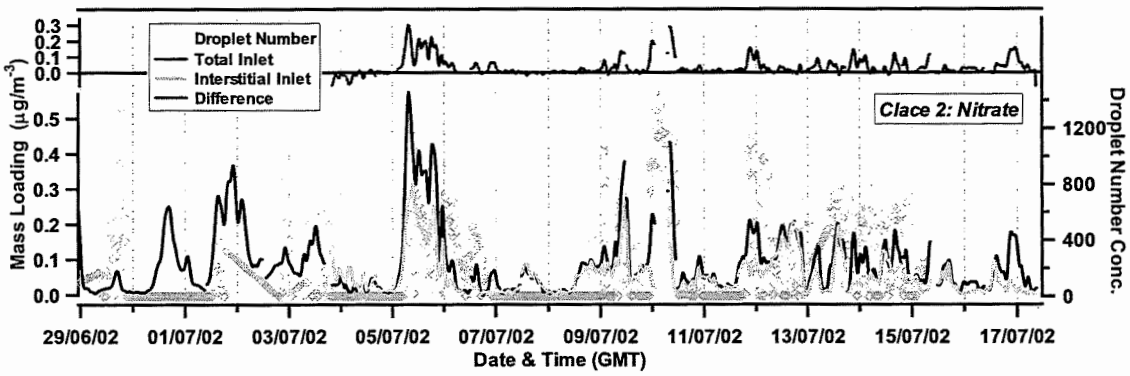

Figure 5: Time series loadings of nitrate from the total and interstitial inlets, the difference in these loadings (upper curve), together with the droplet number concentrations (open circles, number cm^{-3}) as measured by the FSSP during CLACE-2

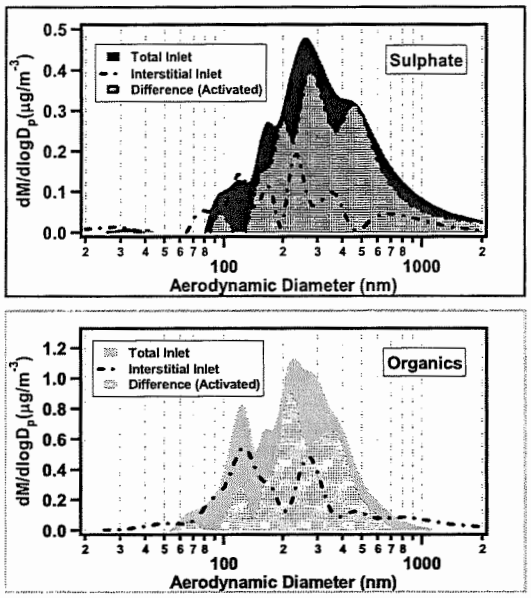

Figure 6: AMS total and interstitial inlet size distributions of sulphate (top) and organic (bottom) for the case study period in which the cloud droplet spectrum case study containing a large concentration of small cloud droplets was observed

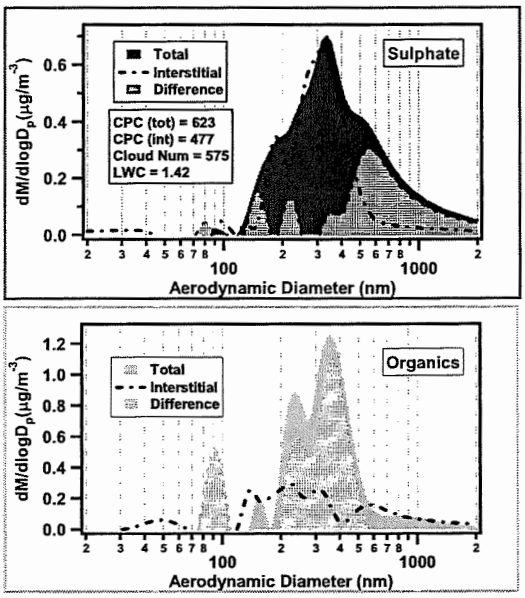

Figure 7: As Fig 6 but for period corresponding to the strong bimodal droplet spectrum case study

compos^n of aerosol particles depending on

5. CONCLUSIONS

Free tropospheric mass loadings and size distributions of a range of volatiles and semi volatiles (non-refractory materials) were successfully measured by the AMS at the JFJ site. Organic and sulphate mass loadings were similar and ranged from 0.1-to 0.6 ug m^{-3}.

Organic species present were typical of more aged/processed aerosol. A large fraction of the organic loading was made up of the mass 44 fragment. The average organic mass spectrum showed very good correlation with a Fulvic Acid type species (spectrum measured previously in the lab).

Both AMS and HTDMA results suggest the aerosol at JFJ in summer are mostly internally mixed, and display a single hygroscopic growth mode.

A diurnal cycle in observed aerosol composition in the early part of the experiment suggests that katabatic flow advects polluted air masses up from the polluted PBL during the summer days, while at night cleaner air is observed during anabatic conditions

Dry residual and interstitial particles were discriminated using the dual inlet system at the JFJ site.

Significant variations in cloud droplet spectra were observed during the CLACE-2 experiment, with mono modal cloud spectra generally having a higher number concentration of smaller drops (Dmode~10 um). These were probably orographically produced during upslope conditions. Bimodal droplet spectra were also observed. These indicate the presence of two activation processes, one associated with the synoptically formed cloud, the other from activation locally in stronger updraughts.

Activation of sulphate and nitrate was observed for particles > 100nm in size in the high droplet number cases. There was also evidence that activation of organic particles below 100nm occurs at certain times. However, the observed variation in cloud microphysical parameters is considered to be more likely caused by the mixing of clouds with different activation histories i.e. due to dynamical effects rather than due to differences arising as a result of the activation of a complex externally mixed aerosol population.

6. ACKNOWLEDGEMENTS

The UK portion of this work was supported by the UK Natural Environment Research Council (NERC).

2 diff activation modes depending on aerosol compos^n

CHANGES IN SIZES AND CHEMICAL COMPOSITION OF CCN IN POLLUTED ENVIRONMENTS AND THE EFFECTS ON CLOUD AND PRECIPITATION DEVELOPMENT

R. T Bruintjes[1], Li Jia[2], Peter Busek[2], V. Salazar[1], D. Breed[1], T Jensen[1], K. Ross[3] and S. Piketh[3]

[1]National Center for Atmospheric Research, P.O. Box 3000, Boulder, CO 80307, USA.
[2]Arizona State University, Tempe, Arizona
[3]University of Witwatersrand, Johannesburg, South Africa)

1. INTRODUCTION

Biomass burning and human activities are releasing large amounts of aerosols into the atmosphere. These particles enhance scattering and absorption of solar radiation. They also produce brighter clouds that are less efficient at releasing precipitation. These in turn lead to large reductions in the amount of solar irradiance reaching the Earth's surface, a corresponding increase in solar heating of the atmosphere, changes in atmospheric temperature structure, suppression of rainfall, and less efficient removal of pollutants. These aerosol effects can lead to a weaker hydrological cycle, which connects directly to the availability of fresh water that could result in a major environmental issue (Twomey, 1977; Albrecht, 1989, Ramanathan et al. 2001).

Aerosol effects on clouds and precipitation is obviously complex - a multi-order problem. Evidence of cloud and precipitation changes due to aerosols (changes in "natural" Cloud Condensation Nuclei (CCN)) is becoming widespread. There is ample evidence now that biomass burning and other anthropogenic sources of aerosols affect the radiative properties of clouds and precipitation processes in clouds leading also to changes in the dynamical processes in clouds (i.e. effects on cloud lifetimes). Increased CCN lead to higher droplet concentrations and narrower droplet spectrum (which manifests itself as a higher cloud albedo) leading to suppressed drizzle formation and longer lasting stratiform clouds (ship-track studies, Albrecht, 1989). Recent satellite studies of cloud microstructure downwind of biomass burning in Indonesia, Australia, and other areas have suggested similar effects (suppressed precipitation formation in the affected clouds, Rosenfeld, 2000). The intriguing evidence of increased positive lightning flashes in storms affected by the Mexican fires of 1998 is yet another example of the multi-order effects aerosols have on clouds, precipitation and the microphysics relevant to cloud electrification (Lyons, 1998).

The effects of aerosols on cloud microphysical and dynamical processes and precipitation were also highlighted by the results from experiments to enhance rainfall by hygroscopic seeding. Evidence exists that: 1) the particles produced by hygroscopic flares do indeed broaden the droplet spectrum and 2) seem to increase the lifetime of precipitating convective clouds possibly by changing the downdraft/updraft structures (WMO, 2000).

Both biomass burning particles and hygroscopic seeding particles are entrained into clouds and participate in the microphysical processes in clouds. Some intriguing similarities have recently been observed in biomass experiments that have direct impact on the hygroscopic seeding experiments.

2. RECENT BIOMASS SMOKE STUDIES

The initial droplet spectra in clouds are dependent on the chemistry, size and concentration of CCN. Recent results from biomass burning experiments have indicated that the chemistry of particles initially emitted from fires undergo chemical transformations in the atmosphere that affect both the chemical composition and the size of the particles (Li et al, 2003, Bruintjes et al., 2004). More KCl particles occur in young smoke (Fig. 1), whereas more K_2SO_4 and KNO_3 particles are present in aged smoke.

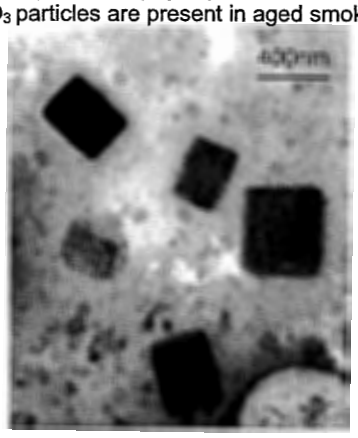

Figure 1: TEM images of the initial KCl particles emitted from savannah fires in Southern Africa.

This change indicates that KCl particles from the fires were converted to K_2SO_4 and KNO_3 through reactions with S- and N-bearing species from biomass burning as well as other sources (Fig. 2). These chemical reactions have been previously observed (Posfai et al., 1995) and seem to be similar to those observed in polluted marine environments as reported

Corresponding author's address: Roelof T. Bruintjes, National Center for Atmospheric Research, P.O. Box 3000, Boulder, CO 80307, USA; Email: roelof@ucar.edu

similarity b/n weather modification + climate studies

by McInnes et al. (1994). These reactions were also found in recent studies in the United Arab Emirates where large amounts of SO_2 are emitted into the atmosphere from the oil related industries (Fig. 3). Within a half hour the KCl particles were converted to K_2SO_4 and KNO_3.

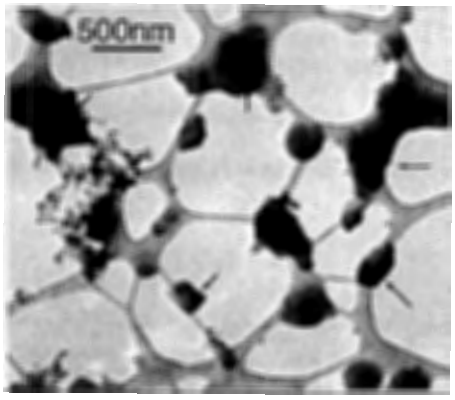

Figure 2: TEM images from reacted particles in smoke plumes that aged for more than 20 minutes from two different fires in southern Africa. Particles are soot, tar balls and KSO_4 and KNO_4 (arrowed) with possible organic coatings.

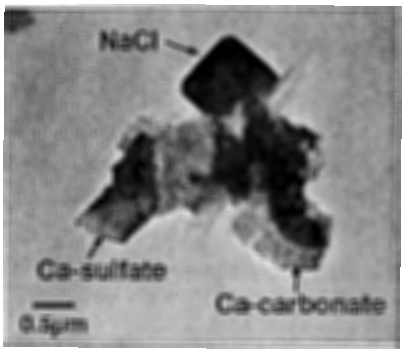

Figure 3: TEM image of sea-salt and partially reacted sea-salt particles over the UAE.

These data suggest that anthropogenic pollution and biomass burning aerosols experience chemical transformation processes as they age and interact with other atmospheric gases and particles that in turn will modify their efficiency as CCN particles and hence cloud characteristics (Bruintjes et al., 2004).

Less known is how the aerosol particle size distributions change during the chemical transformation processes. If changes do occur during these transformations it may have important implications for the CCN activity and the characteristics of the initial cloud droplet size distribution and precipitation development in clouds growing in these environments.

The concentrations of the initial KCl particles produced by the fires seem to be a function of the flaming temperature of the wildland fires (Ward and Hardy 1991). It is assumed that the potassium and chlorine salts are released from the biomass material and volatilized by the extreme temperatures in the flames before re-condensing into particles during the cooling stage. Ward and Hardy (1991) found that fires with higher intensity (longer flame lengths) produce proportionately larger particles than are found in low-intensity and smoldering combustion fires. However, they did not investigate the differences in chemistry between the particles. Larger and smaller particles, especially if they are inorganic salts or inorganic salts mixed with other substances will behave differently as CCN. In addition, chemical transformation processes may also be dependent on the size of the initial particles produced. These effects may have important effects on cloud processes.

The above-mentioned studies indicate that in order to increase our understanding of aerosol-cloud interactions and the precipitation development in clouds in natural and polluted environments, we need to integrate chemistry and cloud microphysical measurements. Very few studies in the past have integrated these measurements.

3. RECENT FLARE STUDIES.

In addition to their role as natural CCN from marine and biomass burning sources, KCl and NaCl are also used in hygroscopic flares for cloud seeding to enhance rainfall (WMO 2000). Modeling studies have indicated that a particle size of ~ 1 μm diameter should be optimal for cloud seeding to enhance rainfall (Cooper et al, 1997). Recent studies at NCAR indicated that the hotter the flare burns, the larger the salt particles produced by the flares. While it was initially thought that cooler burning flares would produce larger particles it should be noted that the flare burning temperature is comparable to the temperatures observed in wildland fires. There is circumstantial evidence that hotter wildland fires also produce larger particles (Ward and Hardy, 1991).

Based on the limitations of aircraft measurements of the particle spectra of the flares and the need for a systematic study on the particles generated by airborne hygroscopic cloud seeding flares, a test facility was designed and constructed at NCAR to simulate the burning of a flare on the wing of an aircraft. The test facility was designed to provide a reproducible environment for combustion of flares and measurement of the resultant particles. The facility was used to examine different commercially produced seeding flares as well as testing new formulations. Twenty different flare compositions were evaluated at the test facility. There were two important goals in the evaluation of the different compositions. The first was to determine, as a function of time of burning of the flare, the concentrations and chemical composition of the particles produced by the flares and, second, the

associated particle size spectra. Many of the different compositions including the cooler burning flares produced similar or worse (smaller particles) results than the spectra obtained from the original South African flare.

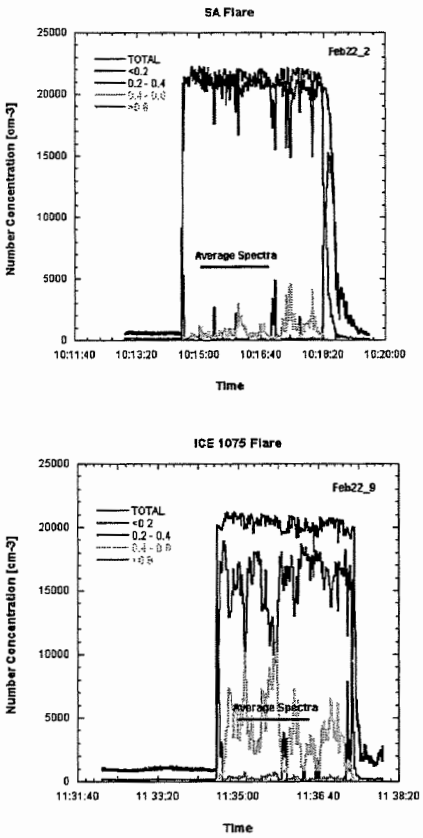

Figure 4: Time series of particle concentrations as a function of size for the SA (a) and ICE (b) flares (see text for description)

Figures 4a and b detail the time series during burning of particle sizes for the South African (SA) flare and a new formulation produced by Ice Crystal Engineering (ICE) of North Dakota. The data are shown as the number concentration of the particles versus time in the size ranges 0.2 μm and smaller, 0.2-0.4 μm, 0.4-0.8 μm, and greater than 0.8 μm diameter. These size ranges break out the important size regimes of particles for the effectiveness of the hygroscopic flares as highlighted by modeling studies. The ICE flare (Fig. 4b) has a similar composition than the South African (SA) flare but with calcium chloride instead of sodium chloride. This flare has 70% potassium perchlorate while the SA flare uses 65% potassium perchlorate as the oxidizer. Comparing the data from the SA and ICE (70%) flares, it is clear that the 70% ICE flare produced significantly larger concentrations of particles in the size range >0.4 diameter than the SA flare. The majority of the particles for the SA flare fall below 0.3 μm diameter. Although the differences could be attributed to the different compositions, disparities in the grades of chemicals used and manufacturing procedures can also give rise to the differences.

Figure 5 displays the number concentration as a function of diameter for particles measured by the PCASP aerosol probe. These spectra were averaged over the period represented by the horizontal bars in Fig. 4. It is clear from this figure that although the total concentrations were very similar, the ICE flare produced substantially larger concentrations of larger particles than the SA flare in the size range 0.5 to 3 μm diameter. A definite shift to larger sizes is evident in the ICE flare.

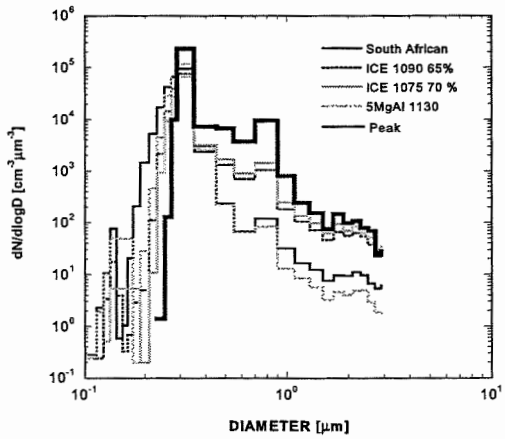

Figure 5: Size distribution for two SA flares, two ICE flares and in region of hotter burn for ICE flare (see text for description)

The volume distributions show similar shifts. In earlier studies of particle sizes produced by the SA flares, it appeared that a cooler burning flare would produce larger particles. The data gathered from these studies do not support that hypothesis. It is interesting to note that at the beginning and end of the flare burn, where the burn will be the coolest, small particles predominate. It is also important to note that for the ICE flare the variations of the concentrations in the size range 0.2 to 0.4 μm and 0.4 to 0.8 μm diameter are anti-correlated. As the particle concentrations in the size range 0.4 to 0.8 μm increase the concentrations in the size range 0.2 to 0.4 μm decrease (Fig. 4b).

In order to explain the variations in concentrations during the burning of the flare, especially in the above mentioned two size ranges, it was noticed from both airborne and ground-based visual observations that the tube does not burn consistently down with the flare. At times the burning will occur in the tube and when a section of the tube falls off, the burn will be in

the ambient air. This behavior is erratic and will change from flare to flare. However, when the burn occurs inside the tube, it can be assumed that the temperature is hotter than when the burning part is not inside the tube and thus more ventilated and cooler. This would explain the variations in particle size with larger particles produced when the burn occurs in the tube (temperature increases), and a sudden shift to smaller particles when the part of the tube is suddenly disposed and burning was more ventilated. This suggests that hotter burning flares consistently produce larger particles. This conclusion is somewhat supported by the observations in biomass burning mentioned in the previous section. The size of the re-condensed particles is possibly related to cooling rate. Because the hygroscopic particles are released at cloud base, they would be directly incorporated in cloud droplets before chemical reactions could take place as found in the biomass burning and polluted marine experiments.

4. CONCLUSIONS

Some general conclusions are summarized as follows:

- Biomass burning and industrial particles are mostly sub-micron with KCl dominant initially in flaming fires.
- Initial KCl particles through chemical processes transform to potassium sulfate and nitrate with the latter usually smaller.
- Flare and biomass burning temperatures both range between 1000 and 2000°C.
- Hot flaming fires and flares volatilize potassium and chloride and nucleate as KCL particles.
- The size of re-nucleated particles possibly depends on cooling rate. Experiments are ongoing to quantify these effects.
- Measurements in both forest fires and flare seeding indicate that several complex processes act simultaneously to produce and modify the CCN characteristics.
- Hotter burning flares seem to produce larger particles. This is different than originally anticipated.
- CCN activity is continuously changed in the atmosphere through chemical gas-to-particle and particle-to-gas processes.

These results have direct implications for the dispersing and targeting of hygroscopic seeding material, especially in polluted environments. Based on these experiments it may be possible to tailor the particle size distribution from the flares to specific situations and environments. The flare development technology also provides an excellent opportunity to include other materials such as desert dust and organic materials in the flares in the future to study the specific effects of these substances on water and ice nucleation and other microphysical processes in clouds.

5. ACKNOWLEDGEMENTS

This study was part of the Southern African Regional Science Initiative - SAFARI 2000. This research was sponsored by a grant (NAG5-7939) from NASA through the University of Virginia to NCAR, Ice Crystal Engineering, and the Department of Water Resources Studies (DWRS) in the United Arab Emirates. The National Center for Atmospheric Research is sponsored by the National Science Foundation.

6 REFERENCES

Albrecht, B.A., 1989: Aerosols, cloud microphysics, and fractional cloudiness. Science, **245**, 1227-1230.

Bruintjes, R.T., K.E. Ross, S.J. Piketh, R.P. Burger, R.J. Swap and T.L. Jensen, In-situ measurements of aerosols, CCN and cloud droplet spectra during SAFARI 2000 and impacts on cloud microphysics, *Journal of Geophysical Research*, Submitted for publication.

Cooper, W.A., R.T. Bruintjes, and G.K. Mather, Calculations pertaining to hygroscopic seeding with flares. *J. Appl. Meteor.*, **36**, 1449-1469, 1997.

Li, J., M. Posfay, P.V. Hobbs, and P.R. Buseck, 2003: Individual aerosol particles from biomass burning in southern Africa: 2. Compositions and aging of inorganic particles. J. of Geophys. Res., **108**, D13, 8484, SAF20.

Lyons, W. A., T. E. Nelson, E. R. Williams, J. A. Cramer, and T. R. Turner, Enhanced positive cloud-to-ground lightning in thunderstorms ingesting smoke from fires. *Science.* ***282***:77-80, 1998.

McInnes, L.M., D.S. Covert, P.K. Quinn, and M.S. Germani, Measurements of chloride depletion and sulfur enrichment in individual seasalt particles collected from the marine boundary layer, *J. Geophys. Res.*, **99**, 8257-8268, 1994.

Posfai, M., J.R. Anderson, P.R. Buseck, and H. Sievering, Compositional variations of sea-salt-mode aerosol particles from the North Atlantic, *J.Geophys. Res.*, **100**,23063-23074, 1995.

Ramanathan, V, P.J. Crutzen, J.T. Kiehl, and D. Rosenfeld, 2001. Aerosols, Climate, and the hydrological cycle. *Science* **294**, 2119-2124.

Rosenfeld, D. 2000: Suppression of rain and snow by urban and industrial pollution. *Science*, **287**, 1793-1796.

Twomey, S., 1977: The influence of pollution on the short-wave albedo of clouds. *J. Atmos. Sci.*, **34**, 1149-1152.

Ward, D.E., and C.C. Hardy, 1991: Smoke emissions from wildland fires. Environmental International, **17**, 117-134.

World Meteorological Organization (WMO), 2000: Report of the WMO workshop on hygroscopic seeding, *WMP Report No. 35, World Meteorological Organization*, WMO/TD No. 1006, Geneva, Switzerland, 68pp.

TEMPORAL AND SPATIAL VARIABILITY OF MINERAL AEROSOLS FROM NORTH AFRICA

Leila M. V. Carvalho[1], Charles Jones[2], Natalie M. Mahowald [2,3] and Chao Luo [2]

[1]Dept. Atmospheric Sciences, University of São Paulo, São Paulo, SP 05508-900, Brazil
[2]Institute for Computational Earth System Science, University of California Santa Barbara, CA-93106, USA
[3]National Center for Atmospheric Research, Boulder, CO, USA

1. INTRODUCTION

Dust from North Africa desert represents one of the largest sources of mineral aerosols to the atmosphere. Mineral aerosols are hypothesized to impact the Earth's climate through direct and indirect radiative forcing (e.g. Miller and Tegen 1998) and biogeochemical processes (e.g. Martin 1990). Their generation, transport and spatial extent are affected by variations in the precipitation and circulation over the tropics in a large range of time-scales (Mahowald et al. 2003, Jones et al. 2003). For instance, Jones et al (2003) have shown that easterly waves activity during the boreal summer affects the transport of dust over the Tropical Atlantic Ocean. In the current study we use 22 years (1979-2000) of model simulation of mineral aerosols during the boreal summer season (June to September – JJAS) and a tracking technique (Carvalho and Jones 2001) to determine trajectories and properties of daily anomalies of surface dust concentration that propagate from North Africa over the tropical Atlantic ocean.

2. DATASET AND DUST TRANSPORT MODEL

In this study, we use a 22-year simulation (1979-2000) of dust transport with the model described in Mahowald et al. (2003). The transport model is the Model of Atmospheric Transport and Chemistry (Rasch et al. 1997) driven by meteorological fields from the NCEP/NCAR reanalysis. Daily averaged surface dust concentrations generated by the model are interpolated to a 2.5° x 2.5° grid (0° to 30°N and 105°W to 20°E) during JJAS. The focus on JJAS is due to the enhanced activity of easterly waves during this season (Jones et al. 2003). Anomalies in the surface dust concentration (SDA) were obtained by removing the daily climatology.

3. THE TRACKING TECHNIQUE

The tracking of the SDA involved several steps. The standard deviation of the summer SDA (Fig. 1) indicates that variations above 10 ppb are observed over the tropics in a large area extending from Africa toward the Americas.

Corresponding author's address: Leila M. V. Carvalho, University of São Paulo, São Paulo, SP 05508-900, Brazil; E-Mail: leila@model.iag.usp.br.

Therefore, we consider in the tracking algorithm connected grid points with SDA ≥ 10ppb. Because we are interested in identifying large SDA regions, all SDA with spatial extent less than 4 grid points were eliminated. The Maximum Spatial Correlation Tracking Technique (MASCOTTE – Carvalho and Jones 2001) was then adapted to track the displacement and properties of the SDA.

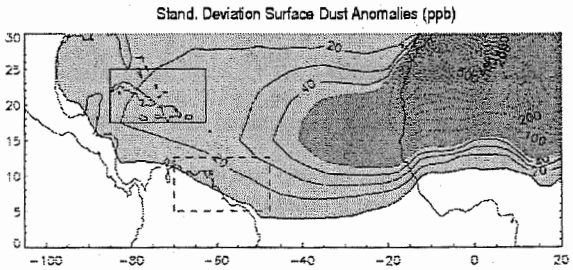

Fig.1. SDA standard deviation anomalies during JJAS. Spatial localization of the Caribbean Islands (full line box) and Northern South America (dashed line box) are also indicated. See text for details.

The underline principle of the MASCOTTE algorithm is to find consecutive locations of the SDA in time based on the maximum spatial correlation observed between a given SDA in the time t and all possible SDA (selected according to the criteria described above) in the entire domain of Fig.1 in the time t+Δt. This technique has been successfully applied with similar purposes in Jones et al. (2004). For the current study, the following SDA properties were computed as the method tracks its trajectory: a) the SDA geometric center (gc) and area; b) the maximum, minimum and mean concentration anomaly during the life cycle, c) the extent and geometric center of the maximum anomaly embedded in the SDA; d) the spatial variance; f) the intersection of the SDA with the Caribbean islands and Northern South America (see boxes in Fig.1).

During a SDA life cycle, a merge with other SDA may occur because of variations in the dynamical conditions of the atmosphere. In other situations, it is possible that a SDA splits and the regions with positive anomalies propagate in different directions, depending on the circulation features. The MASCOTTE algorithm tracks these events such that one can observe the entire life history of a SDA from its origin to its end. Figure 2 shows the climatology of the displacement of all SDA geometric centers during JJAS separated

according to the life cycle duration. Only the beginning (asterisk symbol) and the end of the trajectory are indicated in the figure for the sake of clarity. The number shown at the end of the displacement indicates the month when the SDA propagation started. Evidently, the actual trajectory of the SDA is not as linear as shown in Fig. 2 and all complexity of individual paths is omitted in this figure.

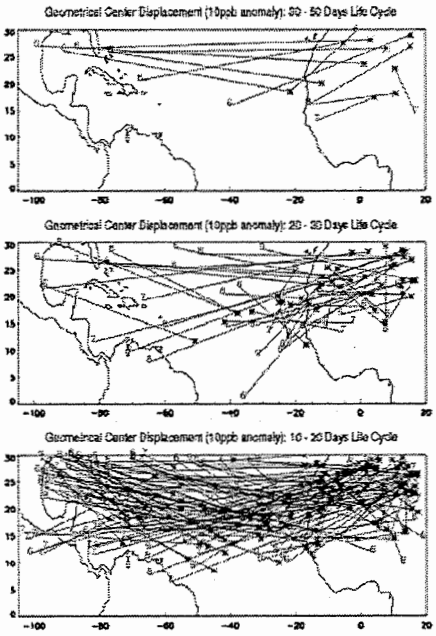

Fig. 2. Displacement of the SDA separated according to the life cycle : 30-50 days (top), 20-30 days (middle) and 10-20 days (bottom). Asterisk symbol indicate the origin and numbers at the end of the displacement shows the month when the event started.

Due to the assumptions of a minimum threshold for the intensity of the SDA as well as for its size, it was often observed situations when the SDA is intensified and increased in size far away from the source. These SDA trajectories can be short and may begin in any region of the Atlantic. One possible dynamical mechanism consistent with the enhancement of the SDA over the Atlantic west of 30W is related to the interaction of the SDA with easterly waves (Jones et al. 2003). The 'backward' displacement of some SDA geometric center from the Atlantic to Africa in some cases is indicative of the merge with another large SDA originating from Africa and the consequent shifting of the geometric center toward that continent.

Another important property of the SDA is the interannual and monthly variability. Figure 3 shows the interannual variability of all SDA with life cycle duration ≥ 5 days and ending westward of 20W. Dark bars (stripped bars) indicate years above (below) one standard deviation from the mean.

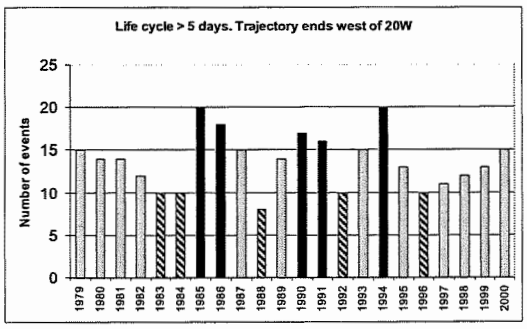

Fig. 3. Interannual variation of the SDA.

The large interannual variation is quite clear such that 1994 and 1985 show the most enhanced SDA activity whereas 1988 was the weakest. The interannual variability of DA that reached the Caribbean Islands box and the North of South American box are shown in Fig. 4.

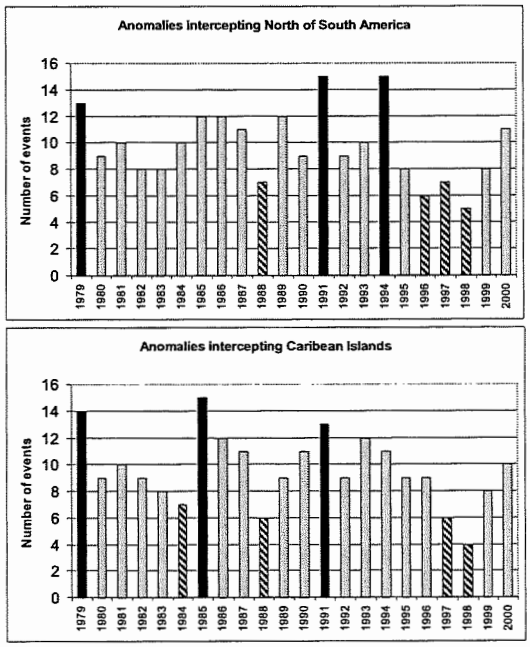

Fig.4 The same as Fig. 3 but for trajectories that intercepted the north of South America (top) and the Caribbean area (bottom). See Fig. 1 for reference on these regions.

Although some differences in the years of maximum and minimum activity may occur, the interannual variability for both set of trajectories (Fig. 4) follows similar patterns observed for the total variability. This is because about 82% of the total trajectories that intercepted the Northern South America box also intercepted the Caribbean box. Nonetheless, 7-10 years cycle seems more evident for the SDA that reached the Caribbean islands.

Monthly variations of the SDA are shown in Fig.5 and indicate a dependence on the life cycle duration.

For instance, if one considers the same set of trajectories of Fig. 3, June through August shows equivalent number of events, whereas September shows about 60% of the previous 3 months. However, as we consider longer trajectories, there is a significant decrease in July compared to June and August.

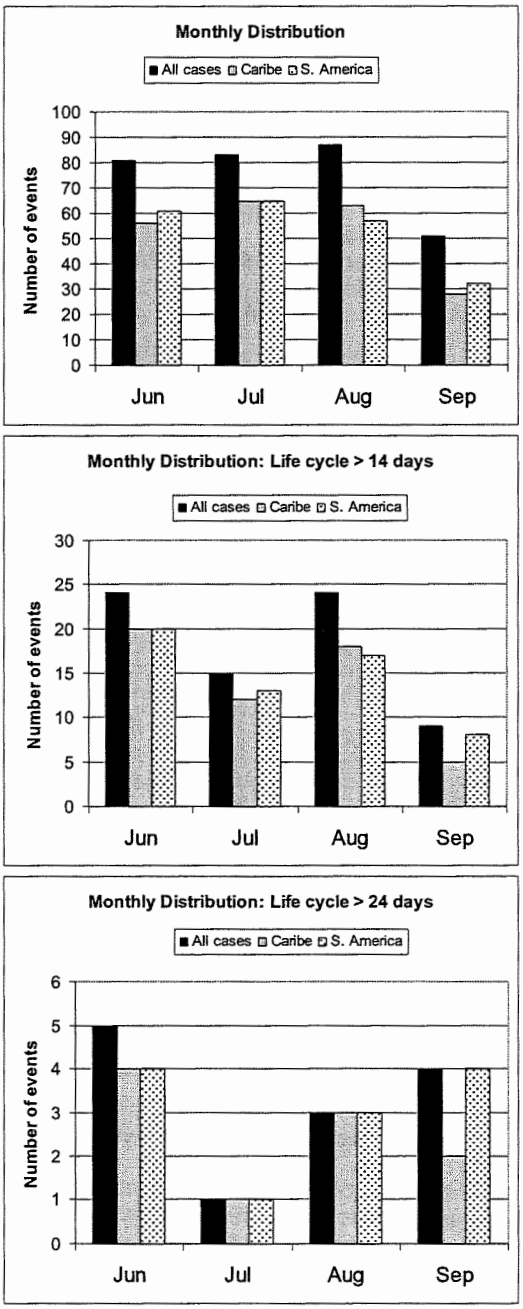

Fig.5 Monthly distribution of events: Life cycle > 4days (top); Life cycle >14 days (middle); Life cycle > 24 days (bottom).

The maximum anomaly during the SDA life cycle can be quite variable, especially for long life cycles. Short life cycles with trajectories closer to the source present the largest anomalies (not shown). Figure 6 shows the distribution of the average anomaly concentration over all life cycles ≥ 5 days ending west of 20W. In these cases, the number of events with average anomalies between 10ppb (the minimum threshold considered here) and 50ppb is almost one order of magnitude greater than the other classes of values.

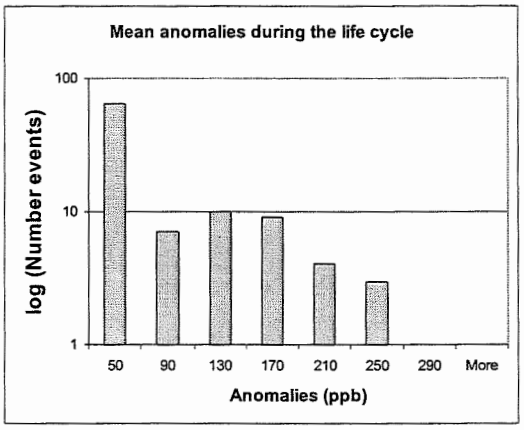

Fig. 6. Mean SDA anomaly distribution (number of events shown in $\log_{10}$ scale) from the time when it was first detected to the end of the trajectory (life cycle > 5 days)

Similarly, the maximum area observed for a given SDA can be quite variable along its life cycle. Figure 7 shows the distribution of the maximum equivalent radius (ie., $[\text{Maximum Area}/\pi]^{0.5}$) observed for trajectories with life cycle ≥ 5 days which ended west of 20W. We recall that the tracking method assumes a minimum SDA area or an equivalent radius of ~ 400km. The distribution seems unimodal with mode between 1000 and 1300km.

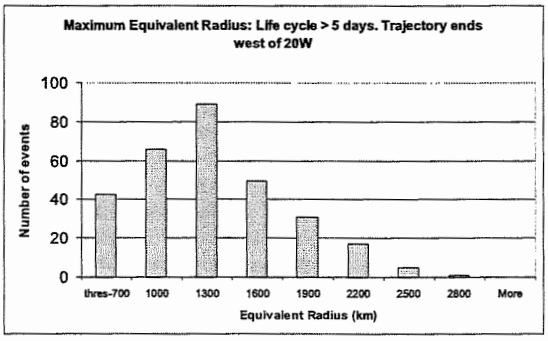

Fig. 7. Distribution of the maximum equivalent radius during the SDA life cycle (km). The SDA threshold is 10ppb and minimum equivalent radius ~ 400km.

4. CONCLUSIONS

The current study focuses on the description of trajectories and properties of dust anomalies originated from African deserts that propagate westward. Some of these anomalies eventually reach the Caribbean Islands and the eastern coast of the Americas. We showed the large range of possible trajectories, suggesting that anomalies may enhance in distinct places over the Atlantic. Although the origin of the dust considered in this paper is essentially from the African deserts, tracking the anomalies is potentially useful to identify dynamical mechanisms that may enhance dust anomalies and the regions where they are more susceptible to occur. Furthermore, properties such as the interannual and monthly variability of those anomalies are important to further understand the natural climate processes controlling the spatial and temporal distribution of SDA.

5. Acknowledgements

C. Jones, N. Mahowald and C. Luo thank the support from NASA – IDS program (NAG5-9671). The authors would like to specially thank the help of John Del Corral and Pete Peterson in parts of this work. L. M. V. Carvalho acknowledges FAPESP (01-13154-9) CNPq as well as the World Meteorological Organization (IAMAS) and the International Commission on Clouds and Precipitation (ICCP) for the financial travel support to participate in the 14th ICCP conference.

6. References

Carvalho, L. M. V., and C. Jones, 2001: A satellite method to identify structural properties of mesoscale convective systems based on maximum spatial correlation tracking technique (MASCOTTE). *J. Appl. Meteor,* **40,** 1683-1701

Jones, C. N. Mahowald, C. Luo, 2003: The role of easterly waves on African desert dust transport. *J. Climate*, **16**,3617-2638.

Jones, C., L. M. V. Carvalho, R.W. Higgins, D. E. Waliser, J.K.E. Schemm, 2004a: Climatology of tropical intraseasonal convective anomalies 1979-2002. *J. Climate*,**17**,523-539

Mahowald, N. M., C. Luo, J. del Corral, C. Zender, 2003: Interannual variability in atmospheric mineral aerosols from a 22-year model simulation and observational data. *J. Geophys. Res.* 10.1029/2002JD002821

Martin, J.H., 1990: Glacial-Interglacial CO_2 Change: The Iron Hypothesis, *Paleoceanography*, **5:1**, 1-13

Miller, R.L., and I. Tegen, 1998: Climate Response to Soil Dust Aerosols, *J. of Climate*, **11**, 3247-3267

Rasch, P.J., N.M. Mahowald, and B.E. Eaton, 1997: Representations of transport, convection and the hydrologic cycle in chemical transport models: Implications for the modeling of short-lived and soluble species, *J Geophys. Res.*, ***102*** (D23), 18127-28138

Trajectory analyses of dust aerosols

SATELLITE OBSERVATION AND RADIATIVE MODELING OF THE INFLUENCE OF AEROSOL PARTICLES FROM BIOMASS BURNING ON CLOUD MICROPHYSICAL PROPERTIES

E. Cattani[1], M. J. Costa[1, 2], V. Levizzani[1] and Ana Maria Silva[2]

[1]ISAC-CNR, Bologna, I-40129, Italy
[2]Dept. of Physics and Évora Geophysics Centre, University of Évora, Évora, P-7000, Portugal

1. INTRODUCTION

Various types of aerosols affect cloud microphysical properties and cloud lifetime through the so-called "indirect effect". The decrease of particles size when the cloud is polluted by small aerosol particles serving as additional cloud condensation nuclei and the reduction of the efficiency of the precipitation forming processes are phenomena described in numerous recent studies (Bréon et al. 2002; Rosenfeld 1999, 2000). Biomass burning aerosol is considered highly responsible of cloud property modifications, due to the high frequency of extended forest and cropland fires all over the planet.

In case of lack of wet scavenging biomass aerosol can reside in the atmosphere for time scales of days to weeks and may therefore be transported to considerable distances in an elevated (2-4 km) polluted layer (Keil and Haywood 2003). Cloudy scenarios are thus possible where the cloud layer is located below the aerosol layer and separated from it. The presence of the aerosol layer above the cloud deck can significantly affect the satellite retrieval of cloud properties (effective radius and optical thickness) and lead to an erroneous detection of the "indirect effect" (Haywood 2003).

Radiative transfer simulations in the VIS, NIR and IR for a scenario characterized by a stratocumulus cloud deck with and without an overlying biomass burning aerosol layer are carried out. The idea is to evaluate the variations of the radiance data within the satellite channels due to the aerosol presence, and understand the eventual effects on the retrieval of the cloud particle effective radius and optical thickness. The vertical structure of the atmosphere in terms of cloud and aerosol layer top and bottom heights and the optical properties of the aerosol and other parameters useful for the description of the simulated scenario are those of the Southern African Regional Science Initiative (SAFARI 2000) (Swap et al. 2003), a multi-national measurement campaign that took place in Southern Africa in August and September 2000 during the fire season.

2. THE RADIATIVE TRANSFER MODEL

The simulated radiances are computed by means of the RSTAR4b (Nakajima and Tanaka 1986, 1988; Stamnes et al. 1988) radiative transfer model (RTM). RSTAR4b is a 1D, plane-parallel model that is used in the present work to compute radiances at the VIS, NIR and IR wavelengths, in presence of water or ice clouds and aerosol. The RTM can simulate radiance data as measured by a satellite sensor using the response functions of the various channels, but monochromatic radiance simulations are allowed as well. The radiative transfer calculations are based on a combined discrete-ordinate / matrix-operator method, with the delta-M approach for the representation of the phase function and the corrections for the singly scattered radiation. The atmosphere is vertically divided in several homogeneous sublayers and limited at the ground by a Lambertian surface. The vertical profiles of temperature, pressure and gases are taken from the atmospheric models of the Air Force Geophysical Laboratory (AFGL) (Kneizys et al. 1988). The gas absorption is computed by means of a three term k-distribution. Finally, Mie theory is used to compute the scattering properties (extinction and absorption cross sections) and the phase function of aerosol and cloud particles.

3. RADIATIVE TRANSFER SIMULATIONS

The input parameters for RSTAR4b RTM are taken from the SAFARI experiment. Keil and Haywood (2003) describe the typical scenario observed off the Angolan and Namibian coasts during September 2000. According to this description the low-level stratiform clouds are confined between 400 and 700 m, whereas the majority of the biomass aerosol particles are located at variable altitudes between 1.8 and 3.7 km.

For the simulations clouds are considered as an homogeneous vertical layer, characterized by a unique size distribution, that is a monomodal log-normal distribution. Typical values for the cloud liquid water path (LWP) during the SAFARI field campaign range from about 70 to 10 g m^{-2}, with a cloud particle effective radius (R_e) of ~7 – 8 μm near the cloud top. Taking into account these values the radiative transfer computations are carried out for R_e values between 5 and 15 μm and cloud optical thickness at the reference 0.5 μm wavelength between 2 and 15.

The standard tropical atmospheric model is chosen for the simulations, where some modifications are brought in order to include the pronounced temperature inversion of ΔT =16 K (Keil and Haywood

Corresponding author's address: Elsa Cattani, Institute of Atmospheric Sciences and Climate (ISAC-CNR), Bologna, Italy; E-Mail:e.cattani@isac.cnr.it.

2003) that defines the top of the observed stratocumulus layer.

4. BIOMASS BURNING AEROSOL CHARACTERISTICS

A new aerosol type, more suitable to represent the radiative effects produced by the biomass burning aerosol observed during SAFARI 2000 was included among those already available with RSTAR4b. The built-in aerosol models of the RTM include the 'soot' aerosol (d'Almeida et al. 1991), but this latter aerosol type is representative only of more absorbing substances emitted into the atmosphere by combustion processes and results in scattering properties that don't match those reported by Haywood et al. (2003) as characteristic of this aerosol event. Thus the RSTAR4b data set of the Mie efficiency factors for the computation of the extinction and absorption cross sections and phase function was increased by including a new set of factors computed for proper refractive index values. The spectral aerosol refractive index values to be input into RSTAR4b are computed taking into account the Aerosol Robotic Network (AERONET; Holben et al. 1998) data and the refractive index spectral dependence shown by the RSTAR4b 'soot' aerosol. In particular, the refractive indexes relative to the AERONET Etosha-Pan site (Namibia) were chosen, concentrating on those retrieved on the 13th of September 2000 (see Tab. 1). They fairly agree with the refractive index value at 0.55 μm (1.54 – 0.018*i*), characteristic of the aged regional haze rich in biomass burning aerosol of the SAFARI 2000 campaign (Haywood et al. 2003).

A log-normal size distribution with two modes at 0.12 and 0.26 μm is used for the radiative transfer simulations.

The spectral single-scattering albedo computed by using this RSTAR4b set-up (Fig. 1) agrees quite well with the data reported by Haywood et al. (2003) and Dubovik et al. (2002).

Wavelength (μm)	0.441	0.673	0.873	1.02
Refractive index (real)	1.514	1.542	1.564	1.582
Refractive index (imaginary)	0.019	0.016	0.016	0.015

Table 1. AERONET refractive index values, 13 September, 2000, Etosha-Pan site.

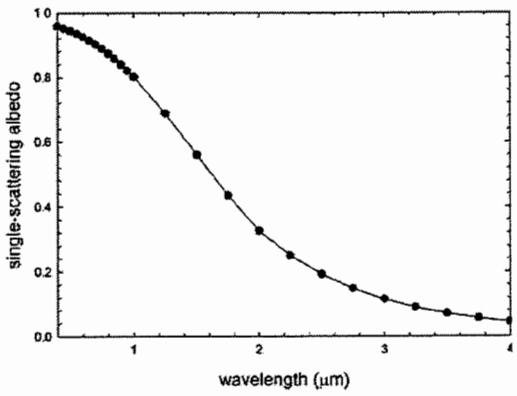

Fig. 1 Aerosol single-scattering albedo simulated with RSTAR4b.

5. CONCLUSIONS

To evaluate the radiative effect of the biomass burning aerosol on the retrieval of the cloud parameters it is necessary to reproduce correctly the spectral dependence of the aerosol scattering properties. This is especially true for the effective radius that can be retrieved using different wavelengths in the NIR portion of the electromagnetic spectrum (Rosenfeld et al., 2004). As demonstrated in Haywood et al. (2004) the R_e may be underestimated or overestimated, according to the wavelength used for the retrieval, i.e. 1.6 or 3.7 μm, respectively, due to the variations of the scattering properties of the aerosol in the NIR spectral interval. This effect should be accounted for when attempting to evaluate any potential aerosol "indirect effect". Nevertheless, it is very difficult to quantify it due to the limited availability of spectral aerosol scattering data.

The present work is in progress and many more cases are to examined to derive unambiguous results both on the effect of aerosol layers on the cloud property retrieval and on cloud-aerosol interactions. The reader is directed to first results by Cattani et al. (2003) and Costa et al. (2003).

6. ACKNOWLEDGEMENTS

The authors are grateful to the OpenCLASTR project for making available for use the RSTAR (system for transfer of atmospheric radiation) package. A special thank goes to the AERONET PI B. Holben for the effort in establishing and maintaining the Etosha-Pan site.

7. REFERENCES

d'Almeida, G. A., P. Koepke, and E. P. Shettle, 1991: Atmospheric aerosols. *Global climatology and radiative characteristics*. A. Deepak Publishing.

how biomass burning aerosols affect MODIS radiances

Bréon, F., D. Tanré, and S. Generoso, 2002: Aerosol effect on cloud droplet size monitored from satellite. *Science*, **295**, 834-838.

Cattani, E., M. J. Costa, F. Torricella, V. Levizzani, and A. M. Silva, 2003: Comparisons of cloud microphysical properties retrieved from different algorithms during aerosol transport events. *Proc. 2003 EUMETSAT Meteorological Satellite Conf.*, EUM P 39, 671-677.

Costa, M. J., E. Cattani, F. Torricella, A. M. Silva, and V. Levizzani, 2003: Cloud microphysical properties retrieval in the presence of strong aerosol events. *Proc. 2003 EUMETSAT Meteorological Satellite Conf.*, EUM P 39, 678-685.

Dubovik, O., B. Holben, T. F. Eck, A. Smirnov, Y. J. Kaufman, M. D. King, D. Tanré, and I. Slutsker, 2002: Variability of absorption and optical properties of key aerosol types observed in worldwide locations. *J. Atmos. Sci.*, **59**, 590-608.

Haywood, J. M., 2003: The physical properties and climate effects of biomass burning aerosol and dust aerosol. THE EGGES (available on-line at www.the-eggs.org), issue 4.

Haywood, J. M., S. R. Osborne, and S. J. Abel, 2004: The effect of overlaying absorbing aerosol layers on remote sensing retrievals of cloud effective radius and cloud optical depth. *Quart. J. Roy. Meteor. Soc.*, **130**, 779-800.

Haywood, J. M., S. R. Osborne, P. N. Francis, A. Keil, P. Formenti, M. O. Andreae, and P. H. Kaye, 2003: The mean physical and optical properties of regional haze dominated by biomass burning aerosol measured from the C-130 aircraft during SAFARI 2000. *J. Geophys. Res.*, **108** (D13), 8473, doi:10.1029/2002JD002226.

Holben, B. N., T. F. Eck, I. Slutsker, D. Tanré, J. P. Buis, A. Setzer, E. Vermote, J. A. Reagan, Y. J. Kaufman, T. Nakajima, F. Lavenu, I. Jankowiak, and A. Smirnov, 1998: AERONET- A federated instrument network and data archive for aerosol characterization. *Remote Sens. Environ.*, **66**, 1-16.

Keil, A., and J. M. Haywood, 2003: Solar radiative forcing by biomass burning aerosol particles during SAFARI 2000: A case study based on measured aerosol and cloud properties. *J. Geophys. Res.*, **108** (D13), 8467, doi:10.1029/2002JD002315.

Kneizys, F. X., E. P. Shettle, L. W. Abreu, J. H. Chetwynd, G. P. Anderson, W. O. Gallery, J. E. A. Selby, and S. A. Clough, 1988: *User guide to LOWTRAN7.* AFGL-TR-88-0177.

Nakajima, T., and M. Tanaka, 1986: Matrix formulation for the transfer of solar radiation in a plane-parallel scattering atmosphere. *J. Quant. Spectrosc. Radiat. Transfer*, **35**, 13-21.

Nakajima, T., and M. Tanaka, 1988: Algorithms for radiative intensity calculations in moderately thick atmospheres using a truncation approximation. *J. Quant. Spectrosc. Radiat. Transfer*, **40**, 51-69.

Rosenfeld, D., 1999: TRMM observed first direct evidence of smoke from forest fires inhibiting rainfall. *Geophys. Res. Lett.*, **26**, 3105-3108.

Rosenfeld, D., 2000: Suppression of rain and snow by urban and industrial air pollution. *Science*, **287**, 1793-1796.

Rosenfeld, D., E. Cattani, S. Melani, and V. Levizzani, 2004: Considerations on daylight operation of 1.6 μm vs 3.7 μm channel on NOAA and Metop satellites. *Bull. Amer. Meteor. Soc.*, **85**, in press.

Stamnes, K., S.-C. Tsay, W. Wiscombe, and K. Jayaweera, 1988: Numerically stable algorithm for discrete-ordinate-method radiative transfer in multiple scattering and emitting layered media. *Appl. Opt.*, **27**, 2502-2509.

Swap, R. J., H. J. Annegarn, J. T. Suttles, M. D. King, S. Platnick, J. L. Privette, and R. J. Scholes, 2003: Africa burning: A thematic analysis of the Southern African Regional Science Initiative (SAFARI 2000). *J. Geophys. Res.*, **108** (D13), 8465, doi:10.1029/2003JD003747.

A MODELING STUDY OF AEROSOL IMPACTS ON PRECIPITATION AND CLOUD-RADIATIVE PROPERTIES USING A WARM CLOUD PARAMETERIZATION

Chao-Tzuen Cheng[1], Wei-Chyung Wang[1], and Jen-Ping Chen[2]

[1]Atmospheric Sciences Research Center, State University of New York, Albany, NY 12203, USA
[2]Department of Atmospheric Sciences, National Taiwan University, Taipei, Taiwan, R.O.C.

1. INTRODUCTION

Aerosols affect cloud formation, spatial extent, lifetime, surface rainfall, and radiation. Its first and second indirect effects, respectively proposed by Towmey (1977) and Albrecht (1989), illustrate the aerosol effects on cloud-radiative properties and its role in climate change. In the mean time, cloud microphysical processes can alter the concentration of aerosol in the air through the processes of wet deposition. Cloud-aerosol interaction is important but cannot be well simulated by most numerical models mainly because in many models, their explicit moist schemes do not consider aerosol information and cloud drop number density.

However, Chen and Liu (2004) have recently developed a two moments warm cloud parameterization (hereafter, the C&L scheme), which is able to directly interact the aerosol size distribution with cloud microphysical processes. Due to its explicit link between aerosols and clouds, this scheme can be used to study the aerosol effects on cloud microphysics and the related radiative issues. Because C&L scheme is developed and validated based on simulations of a parcel model, it is favorable to implement the C&L scheme into a model with high spatial resolution. In this study, the Mesoscale Model of version 5.3 (MM5) of Pennsylvania State University-National Centre for Atmospheric Research is chosen to be the platform for such a study.

2. WARM CLOUD PARAMETERIZATION, AND AEROSOL TREATMENT

Corresponding author's address: Chao-Tzuen Cheng, Atmospheric Sciences Research Center, State University of New York at Albany, CESTM, 251 Fuller Rd., Albany, NY 12203, USA; E-Mail: ctcheng@climate.cestm.albany.edu

In the C& L scheme, two moments (number and mass) of water condensates are carried as prognostic variables and their bulk formulas were developed based on the resultant statistics (Lee, 1989) of a detail model (Chen et al. 1994; Chen and Lamb 1999). The initialization of cloud drop is determined by the activation of aerosol into cloud condensation nuclei (CCN) for further development of clouds. This explicit direct interaction between aerosol and condensate evolutions allows us to study the impacts of aerosol number on the water content, droplet number, and duration of condensates and the associated cloud-radiative properties.

With a known aerosol size distribution and relative humidity, the number of aerosols activated as CCN for initializing cloud formation can be estimated. In this study, to avoid the issues of dealing with complicated aerosol parameterization, several assumptions are made for incorporating this warm cloud scheme into MM5.

Following Chen and Liu (2004), aerosol is assumed as ammonium sulfate and with tri-modal lognormal size distribution; all aerosols with sizes larger than a critical size (decided by the Köhler theory) are activated as CCN. Once some aerosols are activated, the critical radius can indicate the part of aerosols that are not activated and therefore available for the next-time activation. Namely, the critical radius acts as a cutoff radius, which separates the original aerosol size distribution into two parts: the part available and the other part unavailable for activation. Thus, cutoff radius and aerosol size distribution before activation can provide enough information to estimate the amount of aerosols available for activation.

When advection of aerosol is taken into account in a 3-D model, cutoff radius must be rebuilt after aerosol being advected. Thus, *total aerosol number* of tri-modal lognormal distribution and *cutoff radius* are two unknown necessary to be solved and two known values are required to retrieve them. In this study, two

mail Hailong to look into Chen scheme

Chen's aerosol-cloud double moment scheme used to study interactions

no treatment of root radius allows to consider advection of aerosols

prognostic variables are added in MM5: the first one is the mass of aerosols in the air that are available for activation and the other one is the mass of aerosols contained in the water condensates. To maintain the aerosol size distribution of the former one, no mass removal through sedimentation and precipitation processes of the later one is considered. Therefore, the later one is called "pseudo aerosol", which is only needed for obtaining cutoff radius and aerosol size distribution and does not really represent the aerosols dissolved in water in the air.

Since only two new prognostic variables for aerosol are added, it is not possible to vary the modes and widths of the tri-modal lognormal distribution. Thus, only the total number (or mass) is varying with time and the shape of size distribution is fixed. Then, cutoff radius can be calculated iteratively by numerical method.

Four prognostic variables, the numbers of cloud drop and raindrop and the masses of aerosol and pseudo aerosol, are added into MM5. For these newly added prognostic variables, their spatial distributions at cloud boundary are highly discontinuous. Thus, a more precise and stable advection scheme is necessary. For this, a second order advection scheme, the total variance diminishing scheme (Hirsch, 1988; Allen, 1991; and Bott, 1992), is implemented to calculate the advection of cloud and aerosol substances.

Initial condition of aerosol concentration is assumed horizontally homogeneous along with a constant value in the lowest five σ levels and decreases exponentially in the vertical with a scale height of 2.8 km.

We used the C&L scheme in three experiments with different initial conditions of aerosol. The control run is initialized with clean continental background aerosol concentration (Whitby, 1978) and the other two multiplied the background concentration by a factor of 10 and 0.1, respectively. Analyses of results focus on the results of the fourth nested domain of MM5 with a horizontal resolution of 3 km. Experimental domain is set in East Asian area with the fourth nested domain located in north Taiwan (from 120.5°E to 122.5°E and 24.5°N to 25.5°N). The case of a cold front passing north Taiwan during May 16 and 17 is simulated.

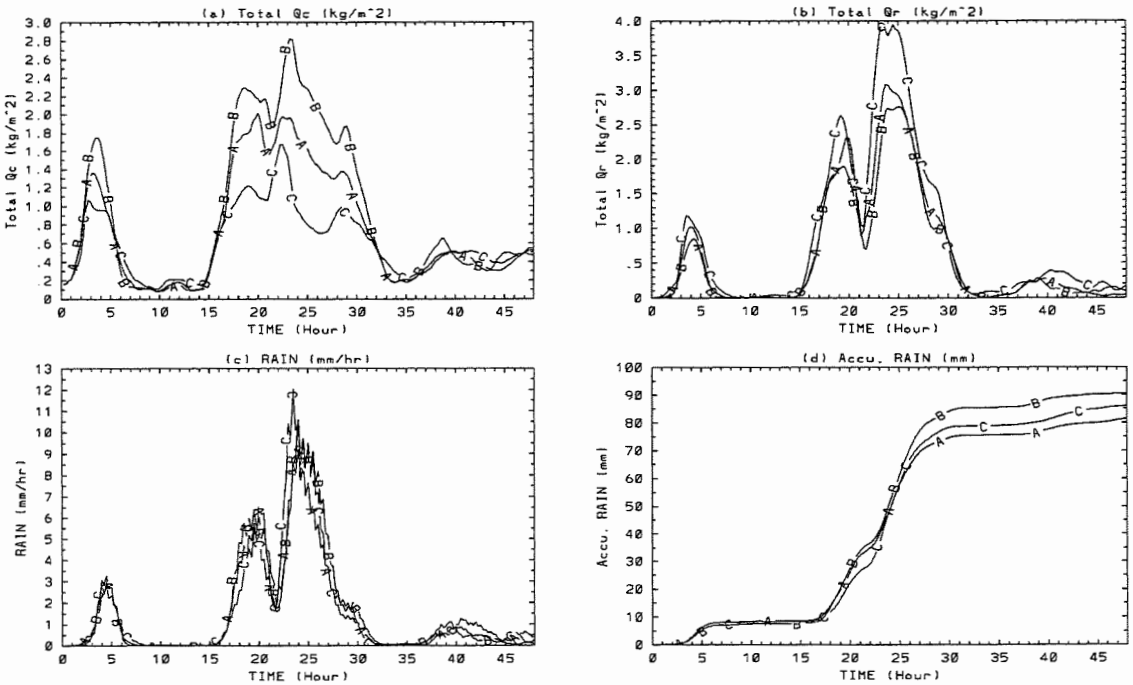

Figure 1. Time series of domain averaged (a) column integral cloud water (kg/m^2), (b) column integral rainwater (kg/m^2), (c) surface rainfall rate (mm/hr), and (d) accumulative surface rainfall (mm). Lines A, B, and C indicate the results of control run, C&Lx10, and C&Lx0.1, respectively.

3. RESULTS

3.1 Mass mixing ratios, drop numbers, and surface rainfall

The cloud drop number strongly depends on the aerosol concentration because the later decides the number of CCN. More aerosols provide more CCN, resulting in more cloud drops and cloud water (Fig. 1a). However, this relation is not valid for raindrop, rainwater, and surface rainfall rate. Simulations show (Fig. 1b) that more aerosols cause more cloud water and cloud drops, but less rainwater and raindrops.

The total water condensates in the air do not show much difference from simulation to simulation (Fig. 1c and d), nor does the surface rainfall rate. They are not sensitive to aerosol concentration. This result is very different from other explicit moist schemes and could be caused by the different parameterizations in microphysics and fall speeds of condensates.

In many explicit moisture schemes, rainwater is initialized by "auto conversion" process, which converts cloud water into rainwater and is a major source of rainwater. In addition to auto conversion, the fall speed is also primarily parameterized by rainwater amount since many moist schemes do not simulate raindrop number. Thus, in these scheme, more cloud water is usually associated with more rain water as well as the surface rainfall.

In the C&L scheme, auto conversion and fall speed depend on both condensate masses and numbers. More (less) cloud drops are associated with smaller (larger) droplet sizes, resulting in weaker (stronger) auto conversion, and less (more) raindrops and rainwater. For rains, less (more) raindrops with larger (smaller) raindrop sizes result in faster (slower) fall speeds. Faster (slower) fall speed contributes to smaller (larger) rainwater content. The droplet size in the C&L scheme depends on the droplet number, due to its larger variation, rather than on the changes of water contents. It is not easy to conclude how the surface rainfall, which is the product of rainwater and fall speed, changes (Fig. 1d) with the aerosol concentration, because rainwater and fall speed react oppositely to the aerosol concentration in the C&L scheme.

3.3 Cloud-radiative properties

According to the results of aerosol sensitivity experiments, both cloud water and cloud drop numbers increase as aerosol concentration increases, showing both the first and second indirect effects of aerosol. Although the total water condensate in the air is similar among experiments, the optical depth of the condensates can be very different. Because cloud drops are much smaller and more abundant than raindrops, the optical depth of water condensate is dominated by the one of cloud.

Figure. 2 shows the diagnostic cloud optical depth and the outgoing shortwave radiative flux differences (from the control run) at the top of the model. With considering the changes of effective radius, the relative change of cloud optical depth (Fig. 2a) is larger than that of cloud water (Fig. 1a). Due to the change of cloud optical depth, the reflected shortwave flux at the model top shows its sensitivity (Fig. 2c) to the aerosol concentration changes even though the simulated case is a case with deep convection (hour 15 to hour 32) where shortwave reflectivity is already very big. More (less) aerosols result in larger (smaller) cloud optical depth, causing stronger (weaker) cloud albedo effect. The changes in outgoing shortwave radiation at top of the model can be up to ±30~40 W/m^2

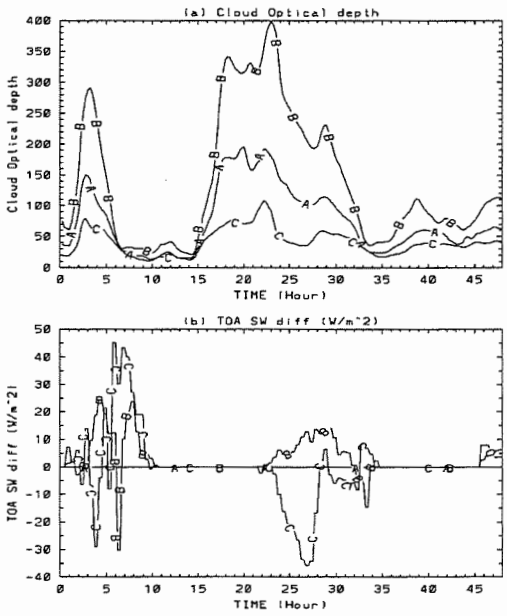

Figure 2. Time series of domain averaged (a) column cloud optical depth, and (b) differences of reflected shortwave fluxes at the model top from the control run (W/m^2). Lines A, B, and C indicate the results of the control run, C&Lx10, and C&Lx0.1, respectively.

4. CONCLUSION AND DISCUSSION

The warm cloud parameterization of Chen and Liu (2004), which allows aerosol cloud direct interaction, is incorporated into MM5 for the studies of aerosol impacts on precipitation and cloud radiative properties. Several assumptions are made for the simplified aerosol treatment to deal with the issue of aerosol distribution after advection. Experiments are conducted for testing the model sensitivity to the aerosol concentration. According to simulations, the water content, droplet number, and optical properties of condensates show their great dependences on the aerosol concentration.

With this new warm cloud parameterization, the model is able to simulate the following relation: more aerosols causes more cloud water and drops with smaller droplet sizes: on the other hand, it causes less rainwater and drops with larger droplet sizes. According to our experiments, surface precipitation does not show significant changes among experiments.

Due to the more cloud water and the more cloud drops in the conditions of high aerosol concentration, cloud optical depth increases significantly, resulting in larger cloud albedo. The enhancement of cloud albedo effect is expected to be larger in cases of no deep convection. To further understand the aerosol effects on cloud microphysics, more experiments with different meteorological conditions s will be tested in the near future.

ACKNOWLEDGEMENTS

The research is sponsored by the Climate Dynamics and Atmospheric Chemistry of the U.S. National Science Foundation and the Office of Biological and Environmental Sciences, U. S. Department of Energy.

REFERENCES

Albrecht, B. A., 1989: Aerosols, cloud microphysics, and fractional cloudiness, *Science*, **245**, 1227–1230.

Allen et al., 1991: Application of a monotonic upstream-biased transport scheme to three-dimensional constituent transport calculations. *Mon. Wea. Rev.*, **119**, 2456-2464.

Bott, 1992: Monotone flux limitation in the area-preserving flux-form advection algorithm. *Mon. Wea. Rev.*, **120**, 2592-2602.

Chen, J.-P., 1994: Predictions of saturation ratio for cloud microphysical methods., *J. Atmos. Sci.*, **51**, 1332–1338.

——, and Lamb, D., 1994: Simulation of cloud microphysical and chemical processes using a multicomponent framework. Part I: Description of the microphysical model. *J. Atmos. Sci.*, **51**, 2613–2630.

——, McFarquhar, G. M., Heymsfield, A. J. and Ramanathan, V., 1997: A modeling and observational study of the detailed microphysical structure of tropical cirrus anvils. *J. Geophys. Res.*, **102**, 6637–6653.

Hirsch, 1988: Numerical computation of internal and external flows. Wiley, v.1-v.2.

Twomey, S., 1977: The influence of pollution on the shortwave albedo of clouds, *J. Atmos. Sci.*, **34**, 1149–1152.

Whitby, K. T., 1978: The physical characteristics of sulfur aerosols. *Atmos. Environ.*,**12**, 135–159.

looks at effects of aerosol on cloud quantities using new scheme

THE INFLUENCE OF AEROSOL ON THE MICROPHYSICS AND PRECIPITATION FROM MIXED PHASE LAYER AND CONVECTIVE CLOUD.

T.W.Choularton, K. Bower, H. Coe, J. Allan, M. Cubison, M.W.Gallagher, G.McFiggans, D. Grosvenor P. Clarke and P. Williams

Physics Department, UMIST, Manchester, M60 1QD, UK

1. INTRODUCTION

The Aerosol Indirect Effects in mixed Phase cloud are clearly very important but have received comparatively little attention compared to warm clouds and cirrus. The paper will investigate the effects of changes in both Cloud Condensation Nuclei and Ice Nuclei on the evolution of the microphysics in convective clouds of varying depth and temperature and also frontal layer clouds often containing embedded convection.

In this paper evidence will be presented for the formation of Cloud Condensation nuclei in the urban environment. The use of an Aerodyne Aerosol Masss Spectromer (AMS) will enable us to examine the chemical composiiton of the particles forming in this environment. The results of detailed field experiments performed on an ageing aerosol plume from London will be shown . These results were obtained as part ofa detailed field project on plume photochemistry called TORCH conducted in Essex (downwind of London) in August 2003. Making use of the results from this experiment the chemical proceses resulting in the transformation of the aerosol in the plume are discussed. The paper will then discuss the implications of these results from the microphyscis of mixed phase clouds forming in the urban plume.

2. MEASUREMENTS

The main experiemntal site was in Writtle College about 50 km to the NE of London, this site was not dominated by local sources although evidence of particulate emitted from road traffic relatively close to the site was observed. Results are presented from two major sets of weather conditions. The first consisted of SW flow on the margins of an anticyclone which brought ageing pollution in the plume from London. The other major weather type occurred when the air stagnated over the site. This resulted in exceptionally high temperatures by day, up 38C, the highest ever recorded in the UK but at night the aged aerosol particles acted as cloud condensation nuclei for events of radiaton fog. The measurements of atmospheric aeroosl made consisted of :Aerosol number and size distribution; Total particle number; Aerosol Mass Spectrometry (AMS) for online quantification of component mass loading and size distribution (< 1um); impactors (NH4+, Na+, Cl-, SO42-), Water Soluble Organics, incl. functionality as a function of molecular weight (ISAO, Fuzzi); impactors for EC/OC and primary organic speciation (PAHs etc) (analyses conducted by Ulrich Poeschl); Hygroscopic properties of submicron aerosol; Concentration and Surface fluxes of NO2 and NH3.

measmts + models to look at effects on water and ice.

3. RESULTS FROM MEASUREMENTS OF CCN FROM THE URBAN ENVIRONMENT

Figure 1 shows the size resolved chemical composition of the Aerosol from the AMS in both periods of SW flow advecting the air from London, and in stagnant periods (day and night separately). At the smallest sizes in he London plume fig 1a the organic component consists of aliphatic hydrocarbons which are hydrophobic. These are recent emissions from internal combustion (probably motor vehicles). At larger sizes, and generally during the anticyclonic event, it is clear that in all cases the aerosol is heavily processes and the organic material is dominated by oxidised fulvic acid like structures and is predominantly hygroscopic. At night a large take-up of nitrate has occurred. Figure 2 shows measurements of the

hygroscopic growth between 10% and 90% relative humidity for the aerosol as a function of size. The example shown is for the daytime period of the stagnant anticyclonic episode. Results for for air advected from London and also for particles measured in central Manchester are similar except for the presence of ultra-fine hydrophobic particles. It can be seen that the aged particles are all quite hygroscopic with growth factors in the range 1.5 to 1.8. These particles are, therefore, capable of acting as CCN.

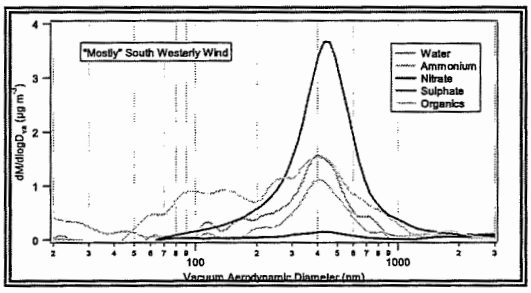

Fugure 1a Size resolved aerosol chemistry in the London Plume

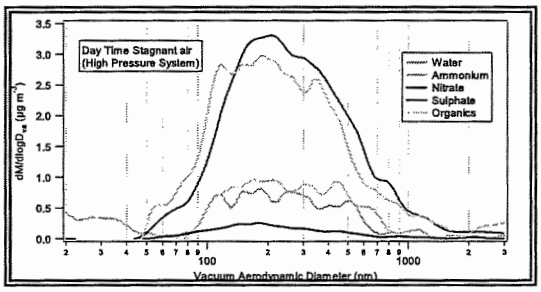

Figure 1b Size resolved aerosol chemistry in anticyclonic conditions by day

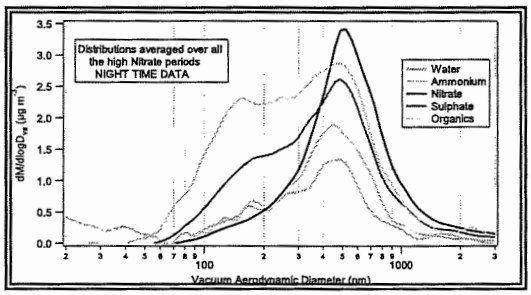

Figure 1C Size resolved aerosol composition in anticyclonic conditions by night

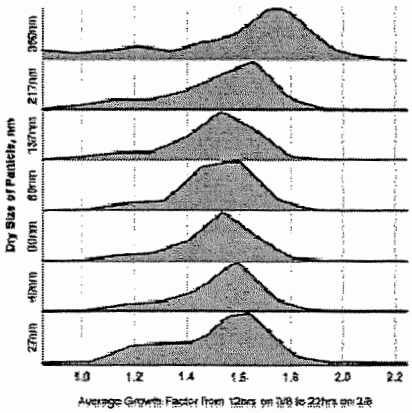

Figure 2 Example of hygroscopic growth facors for particles observed during the anticyclonic event by day

4. MODELLING

Modelling studies to link the aerosol measurements to the cloud formation on urban aerosol were performed at UMIST using the Met Office Cloud Resolving Model (CRM) and an explicit microphysics model. The dynamics predicted by the CRM, which has parameterised microphysics will be used to drive the UMIST explicit microphysics model. This approach has the

advantage that very detailed microphysics can be used and a number of simulations investigating the sensitivity of the cloud to changes in the treatment of the microphysics can be performed. However, changes in the pattern of latent heat release etc and its effect on the cloud dynamics cannot be treated in an approach of this kind.

4 .RESULTS FOR MIXED PHASE LAYER CLOUDS

For frontal clouds the results show a marked sensitivity to both CCN and IN concentrations. These have a marked effect on the distributed of ice and water in the cloud and in particular changes in the pattern of latent heat release can strongly affect the intensity of precipitation and hence the water budget of the cloud. The effects are a complex and strong function of IN. Layers of supercooled water can occur at cloud top with temperatures as low as –35C. Secondary ice particle production by the Hallett-Mossop process alters the number concentration of ice particles in clouds with liquid water at temperatures around –6C. These splinters do not play a major role on the formation of precipitation being lost through aggregation.

Table 1 21 November 2000 Cloud base 0C Cloud top –31C

Run	Max W ms-1	Max Z (dbZ)	Max ice No (l-1)
Observed	1.3	30	65
Control	1.3	32	47
No H-M	1.4	33	47
10 X IN	1.6	31	500
01. X IN	3.0	41	14

Tables 1 and 2 show the sensitivity of frontal layer clouds, modelled using the CRM, to changing the number of Ice Nuclei (IN)by factors of 10 and including the Hallett-Mossop process. In each case the control run includes a treatment of the Hallett-Mossop process (H-M) and ice nucleus concentration is given by the Meyers scheme. The main difference between the two examples is that in case 1 the cloud top is –31C and so primary nucleation is very important whereas it is much less important in the case shown in table 2 as the cloud top is at –16C

Table 2 30 March 1999 Cloud Base 2C Cloud top –16C

Run	Max W Ms-1	Max Z (dbZ)	Max ice No (l-1)
Observed	1.3	30	2500
Control	1.4	30	65
No-HM	1.1	31	3
10 X IN	1.2	38	60
0.1 x IN	1.7	41	150

It can be seen that for the deep cloud (table 1) the results are very insensitive to the Hallett-Mossop process. This is predominantly due to a lack of liquid water content around –6C where this process is most effective. The large snow flakes falling from above have removed this liquid water. It can be seen, however, that the ice crystal concentrations are sensitive to the number of ice nuclei. Further the maximum vertical wind is changed by changing the numbers of ice nuclei due to changes in the position of maximum latent heat release within the cloud.

The cloud with the warmer cloud top shown in table 2, however contains substantial liquid water around –6C .

The observed maximum ice crystal concentration is much higher in this case and the Hallett-Mossop process dominates the cloud. Indeed it can be seen that reducing the number of primary ice nuclei causes the total ice crystal concentration to increase by increasing the effectiveness of H-M

In order to achieve modelled ice crystal concentrations equal to the maximum umber observed it was necessary to use the explicit microphysics model.

5. RESULTS FOR CONVECTIVE CLOUDS

Convective clouds behave very differently. IN are unimportant relative to CCN. In the early stages of cloud formation increased CCN number concentrations and increased droplet numbers reduce the efficiency of the production of warm rain by collision coalescence before the ice phase is initiated. A secondary effect of this is that

reduced warm rain production means that more liquid water is carried high into the cloud. When this freezes latent heat release can, in the right conditions, increase the updraught sufficiently to significantly raise the cloud top height. Figure 3 shows the effect of changing the number of activated CCN on ice concentrations, ice fluxes and cloud top height for a case of deep tropical convection.

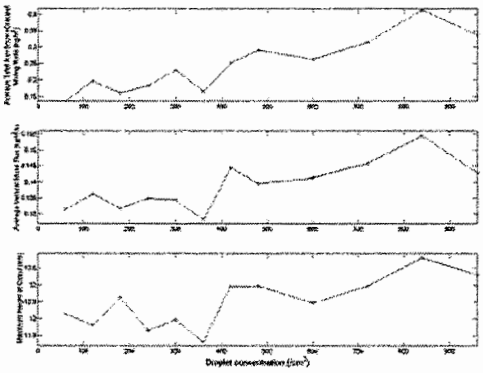

Figure 3. Ice mixing ratio, vertical ice flux and maximum cloud top height against number of droplets activated at cloud base

In clouds with tops warmer than –35C the Hallett-Mossop process is responsible for much of the precipitation forming ice. This process can be suppressed by increasing CCN concentrations and so the onset of precipitation can be both delayed and suppressed. In deeper clouds with colder tops homogeneous nucleation is dominant near cloud top. This ice is recycled and the cloud glaciates. The effect of this is to enhance precipitation production and reduce the sensitivity of precipitation production to CCN concentrations.

6. CONCLUSIONS

It is shown that urban areas are important sources of Cloud Condensation Nuclei. Oxidised organic compounds play an important role in contributing to the hygroscopic nature of these particles and hence their ability to pick up inorganic gases into aqueous solution.

These high numbers of CCN have important effects on the microphysics and dynamics of mixed phase cloud by suppressing autoconversion in warm regions of the cloud and suppressing secondary ice particle multiplication by the Hallett-Mossop process in others.

These processes can suppress precipitation formation unless Ice Nuclei are able to produce sufficient ice particles. The long lived layer clouds the outcome is very sensitive to the number of IN available. In shorter lived convective clouds the IN do not have enough time to be effective and it is only when the clouds become cold enough for homogeneous freezing to produce large numbers of ice particles that efficient precipitation production is restored.

7. ACKNOWLEDGEMENTS

This work was supported by the Natural Environment Research Council UK

make comment on impt of various processes for which data may not be available

SIMULATIONS OF ICE CRYSTAL NUCLEATION AND GROWTH: RESULTS FROM THE AIDA CLOUD EXPANSION CHAMBER

P. J. Connolly[1], P. R. Field[2], O. Moehler[3], S. Büttner[3], H. Saathoff[3], A. J. Heymsfield[4], M. W. Gallagher[1], T. W. Choularton[1].

1. UMIST Manchester UK, 2. Met Office Exeter UK, 3. Forchungzentrum Karlsruhe Germany, 4. NCAR Colorado USA

1. INTRODUCTION

A detailed understanding of ice crystal nucleation and subsequent growth under conditions that are relevant to the atmosphere is vital for improved predictions of climate change and interpretation of cloud processes. Understanding how ice crystal habits form and grow at low temperatures in clouds is important, as it is now understood that there is a large sensitivity of the microphysics of cirrus clouds to the earth's radiation budget.

In July 2002 and September 2003 experiments were performed at the AIDA cloud chamber facility in Germany to look at nucleation and growth of ice crystals on a variety of mineral dusts under simulated cirrus conditions.

Measurements of ambient temperature, pressure and water vapour were made in simulated updrafts with the AIDA facilities suite of instruments. In addition to the measurements made, the resulting ice crystal size and habit distributions were sampled at several points from the chamber by several cloud microphysical probes. They were, the Small Ice Detector (SID), the Video Ice Particle Sampler (VIPS), the Cloud Particle Imager (CPI), the Welas optical particle counter probe and a new miniature FSSP; the Cloud Droplet Probe (CDP).

In this contribution, measurements of ice particle habit and size as a function of vapour supersaturation for Arizona test dust aerosol at -20°C will be presented and the results will be interpreted with a simple model of ice crystal growth from the vapour.

2. EXPERIMENTS

Updrafts were simulated in the AIDA chamber by lowering the total pressure to simulate an adiabatic expansion. The aerosol particles were added to the chamber before the expansion at conditions that were at, or slightly below ice saturation. Usually, the expansion started with an ice coating on the walls of the chamber, and a total pressure of 1000 mbar. A lowering of the total pressure resulted in a decrease in temperature of the air/water vapour mixture within the chamber. Typical cooling rates obtained corresponded to adiabatic uplift in the atmosphere of 1-6 ms^{-1}. The decrease in temperature of the gas could not matched with the decrease in temperature of the walls as the aluminium vessel had a large heat capacity, hence there was a vapour and heat flux from the ice coated walls into the gas. Nevertheless, use of a fan to promote mixing ensured the temperature conditions of the gas within different regions of the chamber were within approximately 0.3°C. For more details on the technicalities of the AIDA chamber see Möhler *et al.*, 2003.

The microphysical instruments used in this study are the CPI and the CDP. They were positioned below the chamber and were aspirated to sample the airflow from the chamber. Typically, the controlled expansion lasted approximately 5 minutes, during which time the size of the particles sampled grew to a maximum and then sublimed. Key to understanding ice crystal growth is information on ice crystal habit, and this was supplied by the CPI. The automated classification scheme is based on geometrical properties of the imaged crystals and is optimised by several studies of aircraft data in cirrus. Seven classes of crystal habit are included in the scheme and are shown in Table 2-1.

Table 2-1. Showing a summary of the particle classification scheme used by the CPI.

Habit code	Habit description
"sph"	Spherical particles
"col"	Columnar crystals
"plt"	Plate crystals
"ros"	Rosettes
"bud"	Budding rosettes
"sir"	Small irregular particles <200μm in size
"bir"	Large irregular particles >200μm in size

3. RESULTS

The results from the CPI for three activations are shown in Figure 3-1. The experiments were performed using Arizona Test Dust (ATD) as the nucleating dust at a starting temperature of -20°C In all three expansions the initial ice formation was noted to occur when the ambient relative humidity (RH) was below water saturation and was in the range of 110-115% relative humidity with respect to ice (RHI). Concentrations sampled with the CPI for this mode were approximately 100 to 200 per litre (plates a, b) i, Figure 3-1). The time at which this threshold RHI was reached varied for the three expansions owing to the

Corresponding author's address: P. J. Connolly, UMIST, Sackville St, Manchester ENGLAND; Email: p.connolly@postgrad.umist.ac.uk

nucl^n and growth of ice crystals

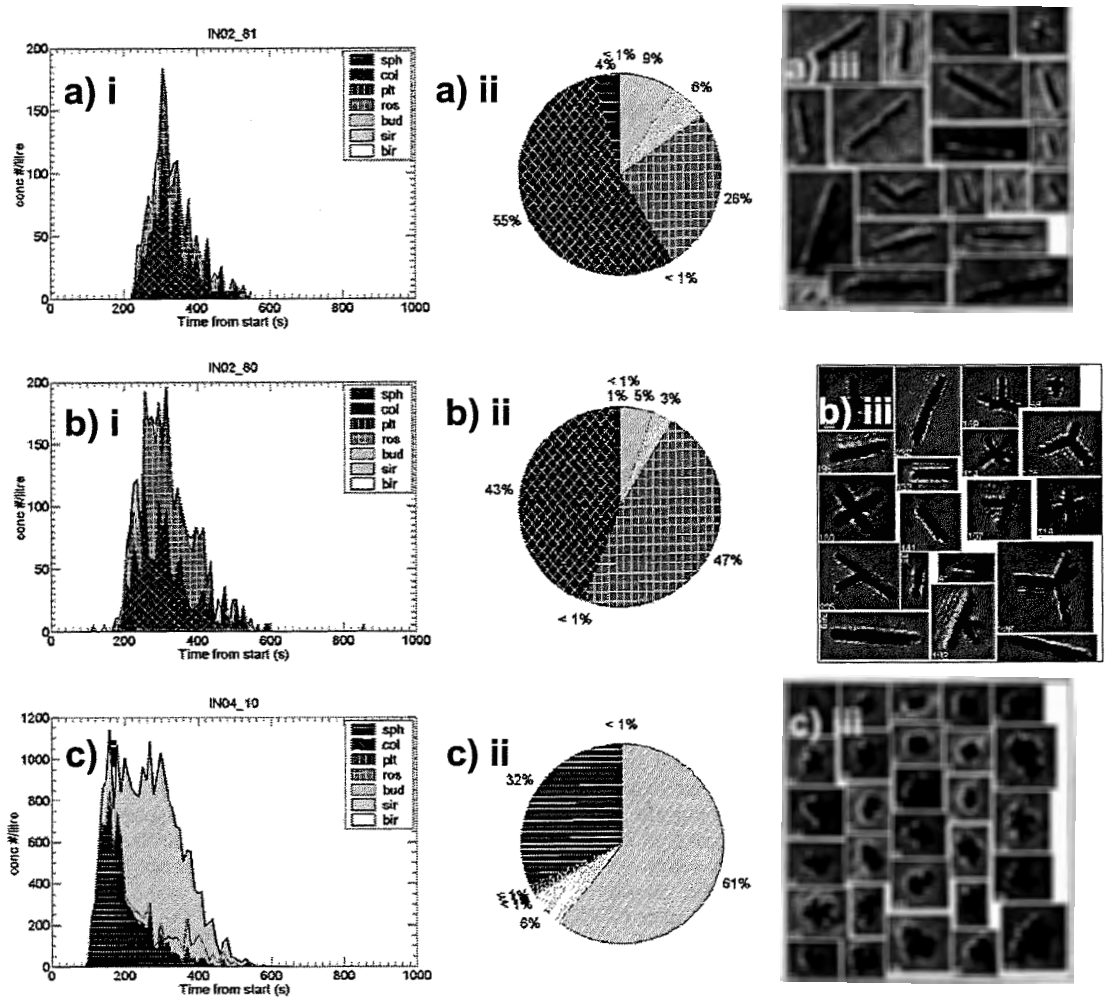

Figure 3-1. Showing a summary of the results from the CPI for experiments on Arizona Test Dust at -20°C. The area plots are plots of habit-segregated particle concentration vs. time, and the pie charts are a summary for the whole expansion. Horizontal hatching denotes spherical particles, diagonal hatching is for columns, vertical hatching is for plates, cross hatching is for rosettes, grey un-hatched is for budding rosettes, diagonal hatching is for small irregular crystals and white un-hatched is for large irregular crystals.

differences in initial water vapour concentration within the vessel.

For first two experiments (IN02_80, IN02_81), once nucleation had occurred, subsequent growth of the crystals depleted the vapour until ice saturation was met. At a later time the crystals sublimed. In these two expansions, pristine columns were observed to form very soon after nucleation, as noted by the high fraction of columns (plates a, b) i, Figure 3-1) at 250 seconds from the time pumping started.

The highest fraction of habits in both these experiments are columns and rosette types (plates a, b) ii Figure 3-1). Actually a close examination of the CPI images (plate b) iii Figure 3-1) reveals that the crystals falling into the rosette class may be side plane habits.

During the third activation in this study (IN04_10), more water vapour was initially present in the chamber in and therefore, growth of the crystals that nucleated via deposition from the vapour was not able to deplete the vapour sufficiently to inhibit the ambient RH from becoming water supersaturated very quickly. During this time, strong increases in forward scattering are correlated with a strong increase concentration from both the CDP and the CPI. We also note that the CPI initially shows a high fraction of spheroids followed by

more irregular habits (plate c) i Figure 3-1). We infer from these measurements that liquid activation followed by some immersion freezing process is taking place.

The high fraction of small spherical particles initially sampled by the CPI is likely an under estimate of the actual fraction of spherical particles, as preliminary tests have shown that the sample volume of the CPI decreases as the reciprocal of the third power of particle size for particles smaller than 90μm.

As the ice crystal grow, the habits then become more irregular as noted by the increase in the fraction of small irregular crystals (plate c) i, Figure 3-1). Few pristine plates were also observed, with the totals being less than 1 percent by concentration (plate c) ii, Figure 3-1). A close examination of the CPI images reveals that what are classed as small irregular particles are actually plate-like polycrystals (plate c) iii, Figure 3-1).

A summary of the results from the AIDA chamber for nucleation on ATD is given in Table 4-1.

4. ICE GROWTH MODEL

The model of ice crystal growth described by Chen and Lamb, 1994 was used in the interpretation of the data. In this model, either oblate or prolate spheroids (corresponding to plates or columnar habits) are grown depending on a user input for the ratio of the deposition coefficient on the a-axis to that on the c-axis. This term is given the name the inherent growth ratio, Γ. It describes the aspect ratio that an ice crystal will assume some time later and is usually taken to be a function of temperature. The results in section 3, however suggest that Γ is a strong function of nucleating mode.

More sophisticated models of ice growth exist (for example Wood *et al.*, 2001); however the model of Chen and Lamb, 1994 was deemed suitable for a simple study of growth rates in the AIDA chamber.

The model was constrained to the water vapour, temperature and pressure time series measurements

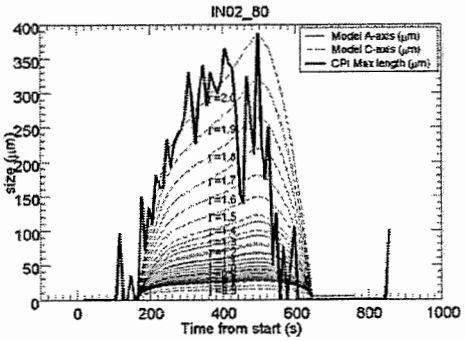

Figure 5-1. Comparison showing the simulated growth rates against that measured with the CPI for IN02_80.

for values of the inherent growth ratio, Γ in the range 0.5 to 2.0. The linear growth time trace inferred from the model was then matched with that sampled by the microphysical probes by minimising the chi-squared test for two series of data.

Figure 5-1 shows the results of the comparison between the model and the CPI for IN04_80 (see Figure 3-1). A value of Γ of 2.0 best matches the observations.

It should be noted that after 400 seconds from the initial pumping start time, the largest crystals in the chamber start to sediment out and therefore the observations begin to deviate from the model at this point (see Figure 5-1). This was deduced from measurements of the total water and water vapour, and noting that after 400 seconds the total water measurement showed a slight decrease.

Table 4-1 shows values of Γ inferred from the model for the three experiments described here. It is noted that a value of 1.0 for the inherent growth ratio fits the observations for the case where plate-like polycrystals were observed (i.e. the immersion freezing case). Choosing a value of 1.0 for the inherent growth ratio of polycrystals is an over simplification of the actual faceted growth that is occurring, but it is the best that can be achieved with the Chen and Lamb, 1994 framework.

Table 4-1. Showing a summary of the chi-squared fit to the values of the inherent growth ratio in the model for the three experiments.

Exp	T (°C)	RHI_{nuc}	RHI_{growth}	Γ
IN02_80	-19.0 to -26	1.15	1.05	2
IN02_81	-19.0 to -26	1.15	1.05	1.9
IN04_10	-18.5 to -27	ws	<ws	1.0

5. DISCUSSION

These results show that different modes of ice nucleation can result in different ice crystal habits. Nucleation and subsequent growth below water saturation at –20°C on ATD resulted in elongated columns, side-planes and what appear to be rosettes, whereas nucleation above water saturation implying immersion freezing resulted in many plate-like polycrystals.

The results of Bailey and Hallett, 2000: 2002: 2004 concluded that the dominant ice crystal habit from –20 though to –42°C were plate-like polycrystals and that columnar forms are extremely rare. In their experiments, nucleation was initiated on soda lime threads coated with some ice nucleating material by applying a brief adiabatic expansion. It is possible that this affected the nucleation mode with a preference for immersion freezing nucleation.

The results from Nelson and Knight, 1998 explain ice crystal habit variation by layer nucleation. They infer from laboratory measurements and theoretical arguments that if the freezing mode is such that the ice particles freeze with dislocations on there crystallographic c-axis and then growth occurs below a critical ice supersaturation required for layer nucleation then columnar habits will form. Nelson and Knight,

1998 observe an increasing likelihood of plate crystals at temperatures below -10°C, however it is possible that their nucleation method induced defects in the crystals, which then orientated the crystal growth in favour of plates

Wood *et al.*, 2001 applied the theory of Nelson and Knight, 1998 to a numerical model of ice growth that explicitly solves the Laplace equation around a hexagonal ice crystal. They inferred from modelling and field data that elongated columns will form at -20°C (an otherwise plate regime) under low RHI if the crystals freeze with dislocations only on their c-axis. As we have seen it is likely that deposition nucleation on ATD can orient the crystals in this manor.

It is not clear at this point whether it is the nucleation mode of the high RHI experienced during growth in the liquid activation experiments that is determining the ice crystal habits as we still have to analyse more case studies from the recent IN04 experiment.

The Arizona test dust used in these experiments was noted to have the most active deposition nucleation mode out of any of the three dusts used in IN02 and IN04.

6. CONCLUSIONS

Experiments were conducted at the AIDA facility to investigate ice nucleation and growth at different RHI on ATD.

It was found that deposition nucleation on ATD and subsequent growth at low RHI resulted in elongated columnar habits that were mainly pristine, in contrast to the results of Bailey and Hallett.

An experiment where liquid activation followed by immersion freezing was the strongest mode of ice nucleation resulted in a ten fold increase in concentration and habits that were mostly polycrystalline plates.

When compared to the results of Nelson and Knight, 1998: Wood *et al.*, 2001 this seems to suggest that the deposition mode results in crystals that freeze with dislocations on their c-axis and when grown under low RHI in the AIDA chamber result in elongated columns, and side planes.

It is likely that the immersion freezing mode results in ice crystals that freeze with dislocations on all faces and then the crystals grow in the normal plate regime. It is not clear at this time whether growth of the crystals that nucleated via the deposition mode at high RHI would have resulted in plate like polycrystals.

Application of a simple model of ice crystal growth to the data resulted in values of the inherent growth ratio that can be used in an explicit cloud model for growth habits resulting from nucleation via deposition or immersion freezing at -20°C.

7. ACKNOWLEDGMENTS

The author would like to thank Dr. J. Hallett and Dr. M. Bailey for their helpful discussions on nucleation and growth of ice crystals on Arizona Test Dust. Thanks are also given to SPEC inc. for providing the habit classification scheme used to process the CPI data. Acknowledgement is also given to NERC for funding the PhD work of Paul Connolly.

8. REFERENCES

Bailey, M. and J. Hallett, 2000: Nucleation, growth and habit distribution of cirrus type crystals under controlled laboratory conditions. 13th ICCP, Reno, 629-632.

——, 2002: Nucleation effects on the habit of vapour grown ice crystals from -18 to -42C. Q. J. R. Meteorol. Soc, 128, 1461-1483.

——, 2004: Growth Rates and Habits of Ice Crystals between -20C and -70C. J. Atmos. Sci., 61, 514-544.

Chen, J.-P. and D. Lamb, 1994: The Theoretical Basis for the Parameterisation of Ice Crystal Habits: Growth by Vapour Deposition. J. Atmos. Sci., 51, 1206-1221.

Möhler, O., O. Stetzer, S. Schaefers, C. Linke, M. Schnaiter, R. Tiede, H. Saathoff, M. Krämer, A. Mangold, P. Budz, P. Zink, J. Schreiner, K. Mauersberger, W. Haag, B. Kächer, and U. Schurath, 2003: Experimental investigation of homogeneous freezing of sulphuric acid particles in the aerosol chamber AIDA. Atmos. Chem. Phys., 3, 211-223.

Nelson, J. and C. Knight, 1998: Snow Crystal Habit Changes Explained by Layer Nucleation. J. Atmos. Sci., 55, 1452-1465.

Wood, S. E., M. B. Baker, and D. Calhoun, 2001: New model for the vapour growth of hexagonal ice crystals in the atmosphere. J. Geophy. Res., 106, 4845-4870.

SATELLITE DERIVED CLOUD PROPERTIES RELEVANT FOR CLOUD RADIATIVE FORCING: A CASE STUDY OF INTERACTION BETWEEN CLOUDS AND DUST AEROSOL PARTICLES

M. J. Costa [1, 2], E. Cattani [2], A. M. Silva [1], and V. Levizzani[2]

[1]Department of Physics and Évora Geophysics Centre, University of Évora, 7000 Évora, Portugal
[2]Institute of Atmospheric Sciences and Climate (ISAC-CNR), 40129 Bologna, Italy

1. INTRODUCTION

Clouds are the major factor regulating the Earth radiation budget. Special attention has been dedicated in the last few years to cloud interactions with aerosol particles through modeling studies, *in situ* measurements and remote sensing techniques (Bréon et al. 2002; Kawamoto and Nakajima 2003). Aerosols are considered responsible for significant modifications of cloud properties such as the decrease of the droplet size due to an increase in droplet concentration and respective enhancement of cloud reflectivity (Twomey 1974). In addition, changes in cloud lifetime and precipitation efficiency have also been suggested (Rosenfeld 1999, 2000). Particularly, aerosol particles mobilized in great quantities from desert areas, the "desert dust", represent one of the main natural sources of atmospheric aerosol. Dust aerosol layers are capable of traveling thousands of kilometers at high altitudes, depending on the meteorological conditions. Apart from the possible consequences of cloud-aerosol interactions, desert dust particles apparently have a strong ability to act as ice nuclei. This statement is supported by observations of the conversion of supercooled water clouds to ice clouds at temperatures about 20°C higher than those that are expected for homogeneous nucleation of cloud droplets in the middle and upper troposphere. This can lead to the formation of cirrus clouds at much higher temperatures than normally thought (Sassen 2002; DeMott et al. 2003).

The alterations suffered by clouds through their interaction with aerosols, specifically with desert dust, may have strong implications on the interaction with solar and terrestrial radiation, leading to different radiative forcing estimates with respect to clouds in "clean" atmospheric environments (continental or marine). The aim of the present work is to determine the cloud optical thickness (COT) and droplet effective radius (DER) (indicative properties of the possible cloud-aerosol interaction effect) of continental and marine cloud layers, which experience interaction with dust aerosol layers. These cloud properties are derived from the inversion of satellite spectral measurements in the visible (VIS) and near infrared (NIR) spectral regions (Nakajima and Nakajima 1995). The retrieved cloud properties are in turn used in combination with a suitable radiative transfer model to estimate the radiation fluxes and subsequently evaluate the cloud radiative forcing during selected episodes of strong desert dust transports. The methodology is applied to a summer 2002 case over southwestern Europe, during the VELETA 2002 (eValuation of the Effects of eLevation and aErosols on the ultravioleT rAdiation) intensive measurement campaign.

Corresponding author's address: Maria João Costa, Department of Physics, University of Évora, Portugal; E-Mail: mjcosta@uevora.pt

2. METHOD

Satellite measurements are those of the MODerate Resolution Imaging Spectroradiometer (MODIS) onboard Terra and Aqua satellites (1 x 1 km^2 spatial resolution) in three spectral channels: 0.62 - 0.67 μm; 3.66 - 3.84 μm; 10.78 - 11.28 μm.

The methodology used to derived the cloud properties (Costa et al. 2004) consists of a first cloud detection phase and a subsequent step of particle phase determination (liquid water or ice), assuming that clouds at one time are made of either liquid water or ice particles (no mixed phase clouds are considered). The procedure relies on a bi-spectral technique that uses satellite measurements in the VIS and infrared (IR) spectral regions centered at 0.65 μm and 11 μm, respectively. The satellite measurements are initially classified in terms of the underlying surface (land or water) using a land-sea mask. Subsequently, the histograms of the VIS radiances and IR brightness temperatures are analyzed to determine threshold values that define the limits between clear sky, water clouds and ice clouds. Such threshold classification is done at the pixel level and when the pixel is cloudy, four possible cases are distinguished: water clouds over the ocean, ice clouds over the ocean, water clouds over land, and ice clouds over land.

The VIS, NIR (centered at 3.75 μm) and IR radiance measurements corresponding to the pixels classified in the four categories are used to retrieve cloud optical thickness, effective radius and cloud top temperature using the algorithm proposed by Nakajima and Nakajima (1995) and Kawamoto et al. (2001). The four categories are treated separately because relevant differences in cloud and surface characterization must be taken into account. The algorithm relies on the comparison between the modeled cloud radiances in

the three spectral bands and the corresponding satellite radiance measurements. The latter are deprived of the undesirable components, such as the solar radiation reflected by the surface and the thermal radiation emitted from the cloud layer and the surface, in order to retain only the cloud signal. These corrections are based on the use of LookUp Tables (LUTs) calculated using the radiative transfer code RSTAR (Nakajima and Tanaka 1986, 1988). The LUTs contain the radiative quantities necessary for the cloud properties retrieval, namely the cloud reflected radiances and hemispherical albedo in the VIS and NIR, the transmission in the VIS, NIR and IR spectral bands and the reflection and atmospheric emitted radiation in the NIR and IR spectral bands. The LUTs are built for a grid of selected values of the COT, DER, cloud top temperature, equivalent water vapor above the cloud, equivalent water vapor of the cloud layer, solar zenith, satellite zenith and relative azimuth angles. The cloud is characterized by a lognormal hydrometeor size distribution. Mean values of surface temperature and reflectance, as well as a mid latitude summer atmospheric vertical profile (McClatchey et al. 1971), are used. Besides the cloud optical thickness, effective radius, and top temperature, the cloud top height and pressure are also retrieved from the top temperature values by linear interpolation of the selected atmospheric vertical profile.

3. RESULTS

The case study refers to the period 15 - 20 July 2002 during the VELETA 2002 intensive field campaign in the south of the Iberian Peninsula (Sierra Nevada area, Spain; see Fig. 1). Measurements from a set of radiometers and sun/sky photometers installed in several locations in the area, as well as LIDAR measurements (Alados-Arboledas et al. 2003) were available along with other data. The first days of the case study were characterized by extremely clear conditions in terms of the atmospheric aerosol load (background situation). In the last days of the campaign (18 - 20 July 2002) a dust plume coming from North Africa (Sahara) overpassed the area and was detected by the LIDAR at the same atmospheric level as the cloud systems.

3.1 Cloud Properties

The analysis was initially concentrated on the retrieved effective radius values to detect any cloud modification induced by the aerosol. The particle effective radius for each day was averaged in the area delimited by the dashed box 1 in Fig. 1.

In the first two days (15 and 16 July) there were very few clouds (mainly stratiform) forming over the Mediterranean Sea in the area of box 1. On 17 July, one day prior the start of the dust transport event over the area, most of the clouds were developing over land; the averaged effective radius and the respective

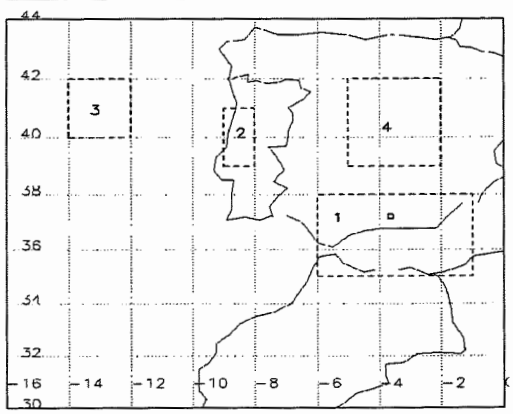

Figure 1. Map of the geographical area considered in the study. The dashed boxes indicate the areas selected for the analysis of the: 1) particle effective radius variation; 2) clouds in dust free atmosphere; 3) maritime clouds in dusty atmosphere; 4) continental clouds in dusty atmosphere. The square inside box 1 indicates the location where the VELETA field campaign took place. Boxes 2, 3, and 4 correspond to different days.

standard deviation are 7.9 ± 1.3 μm. In this case, the cloud top height was of about 1km. Two days later (19 July) the averaged effective radius and standard deviation are 6.2 ± 1.2 μm. Clearly there was a decrease of the mean particle effective radius in the area, which may be an indication that clouds were subject to the influence of dust aerosol particles. Additional information from the LIDAR measurements in the area of Granada (see square in box 1 of Fig. 1) indicate that the dust aerosol layer extended approximately from 2 to 4 km height. The cloud top height for the same day over the area is shown in the frequency histogram of Fig. 2. More than 60% of the cloudy pixels in the area are associated to cloud top height values between 2 and 4 km, which hints to the dust aerosol particles detected by the LIDAR system at the same level being incorporated by the clouds developing in the area. Moreover, this fact supports the hypothesis that the calculated effective radius

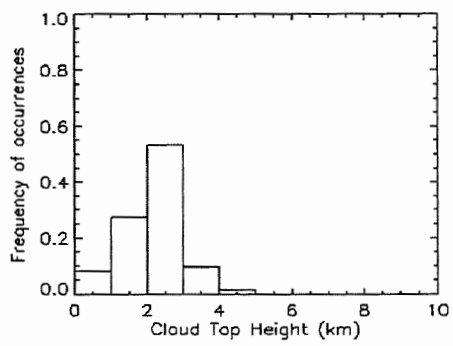

Figure 2. Frequency histogram of cloud top height derived for 19 July 2002, 1340 UTC, over the area delimited by the dashed box 1 in Fig. 1.

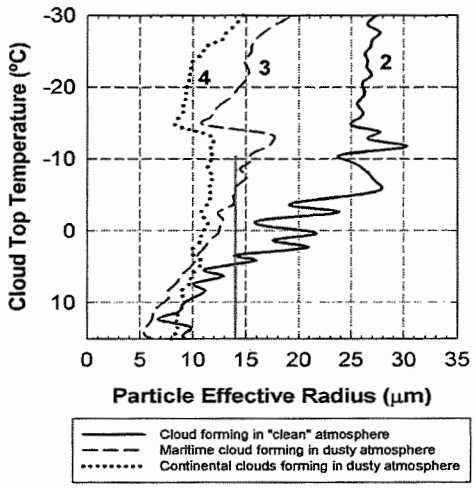

Figure 3. Cloud top temperature as a function of particle effective radius derived for three different situations. The numbers indicate the correspondence with the dashed boxes of Fig. 1. The vertical gray line indicates the 14 μm precipitation threshold (Rosenfeld and Gutman 1994).

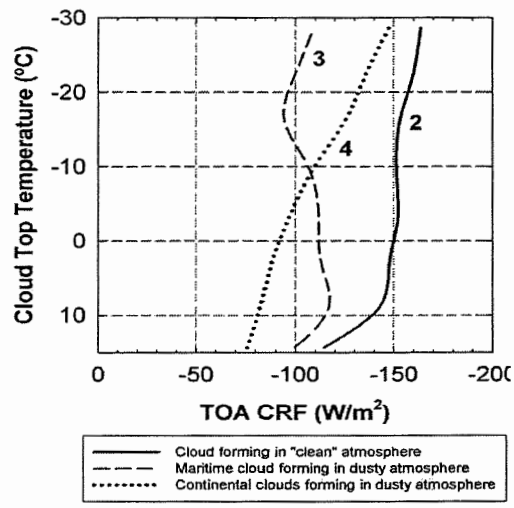

Figure 4. Cloud radiative forcing at the top of the atmosphere for the curves in Fig. 3.

decrease (7.9 μm on 17 to 6.2 μm on 19 July) is due to the interaction of clouds with dust aerosol particles.

The relation between the effective radius and the cloud top temperature for developing convective clouds can reveal information on the microphysical processes occurring in the cloud, and consequently on the precipitation formation process (Rosenfeld and Lensky 1998). The evolution of the particle effective radius as the cloud top temperature decreases is investigated in Fig. 3 for three selected situations: clouds forming in a dust-free atmosphere; clouds over a maritime environment forming in the presence of dust particles; clouds forming in a continental dusty atmosphere. Each curve represents the median effective radius value for each 1°C temperature interval, corresponding to the dashed boxes in Fig. 1. The vertical solid gray line in Fig. 3 represents the 14 μm precipitation threshold beyond which precipitation from convective clouds is likely to occur (Rosenfeld and Gutman 1994). Box 2 in Fig. 1 (curve 2 in Fig. 3) delimits an area where convective clouds were developing out of a clean maritime atmosphere. The evolution of the particle radius in this case allows for distinguishing the microphysical zones defined by Rosenfeld and Lensky (1998): in the lower atmosphere cloud droplet size increases probably by coalescence, followed by a rainout zone between 20 and 25 μm. As the cloud top temperature decreases, a mixed phase can be distinguished followed by the glaciated zone, which is reached at a temperature of about -15°C. Curve 3 in Fig. 3 (box 3 in Fig. 1) represents the effective radius evolution for maritime clouds growing in presence of dust particles. As for curve 4 (box 4 in Fig. 1), it represents the evolution of a continental cloud developing also in presence of dust. In both cases, the microphysical zones distinguished for curve 2 are not present and a zone extending down to below –10°C in the case of continental clouds (curve 4) shows up where cloud droplets grow apparently by diffusional growth (slower growth than by coalescence). Maritime dusty clouds (curve 3) reach the 14 μm precipitation threshold but it is not clear if the rainout process actually occurs. Both cases seem to present a mixed phase that extends from –15°C to lower temperature values.

3.2 Direct Cloud Radiative Forcing

The cloud radiative forcing (CRF) was calculated from the net shortwave (N_{SW}) and longwave (N_{LW}) fluxes at the top of the atmosphere (TOA) according to equation 1, being the net fluxes given by N_{SW} =*SW*↓-*SW*↑ and N_{LW}=*LW*↓-*LW*↑).

$$CRF = (N_{SW} + N_{LW})^{cloud} - (N_{SW} + N_{LW})^{clear} \qquad (1)$$

The fluxes are calculated with the RSTAR code (Nakajima and Tanaka 1986, 1988), using the derived cloud properties. The graph in Fig. 4 shows the cloud radiative forcing derived for the situations in Fig. 3. Note that the cloud developing in the dust-free atmosphere (curve 2) presents the most negative forcing, slightly increasing as the temperature decreases. As for the continental cloud growing in the presence of dust (curve 4), it presents the lowest (less negative) TOA CRF values at temperatures above –10°C, becoming increasingly higher towards the highest atmospheric layers, even higher than that

obtained for the maritime clouds contaminated with dust.

4. CONCLUSIONS

The case studied revealed a decrease of the cloud droplet effective radius when dust aerosol particles were present over the area and at the same atmospheric levels. The evolution of the cloud top temperature and the effective radius for convective clouds in the area indicates that clouds that come in contact with dust particles are in fact affected by them: particles grow less and this most probably affects precipitation, diminishing or even suppressing it. The corresponding TOA CRF was subsequently calculated and found that the "clean" clouds reflect more radiation to space than the dust contaminated ones.

5. ACKNOWLEDGEMENTS

MODIS data were acquired as part of the NASA's Earth Science Enterprise. The algorithms were developed by the MODIS Science Teams. The data were processed by the MODIS Adaptive Processing System (MODAPS) and Goddard Distributed Active Archive Center (DAAC), which also archives and distributes them. The authors are grateful to the OpenCLASTR project (http://www.ccsr.u-tokyo.ac.jp/~clastr/) for making available the RSTAR (system for transfer of atmospheric radiation) and CAPCOM (Comprehensive Analysis Program for Cloud Optical Measurement) packages for use in this research. This study was funded by EURAINSAT (http://www.isac.cnr.it/~eurainsat/), a shared-cost project (contract EVG1-2000-00030) co-funded by the Research Directorate General of the European Commission within the research and technological development activities of a generic nature of the Environment and Sustainable Development subprogram (5th Framework Programme). Funding was also provided by the Portuguese Foundation for Science & Technology under grant POCTI/CTA/42917/2001. We thank the MADOC, the Armilla Air Force Base, The Sierra Nevada National Park and the City Halls of Pitres and Motril, Granada, Spain, for their gracious support. The authors also thank José António Rodrigues for providing the LIDAR measurements.
One of the authors (MJC) was financially supported by the Subprograma Ciência e Tecnologia do 2º Quadro Comunitário de Apoio.

6. REFERENCES

Alados-Arboledas, L., J. Lorente J. A. Martínez, V. Cachorro, A. Labajo, B. De la Morena, J. P. Díaz, M. Pujadas, H. Horvath, A. M. Silva, G. Pavesse, and J. Rodrigues, 2003: VELETA 2002 field campaign. *Geophys. Res. Abstracts*, **5**, 12218.

Bréon, F.-M., D. Tanré, and S. Generoso, 2002: Aerosol effect on cloud droplet size monitored from satellite. *Science*, **295**, pp 834-838.

Costa, M. J., E. Cattani, V. Levizzani, and A. M. Silva, 2004: Cloud microphysical properties retrieval during intense biomass burning events over Africa and Portugal. In: *Measuring precipitation from space: EURAINSAT and the future*, V. Levizzani, P. Bauer, and F. J. Turk Eds., Kluwer Acad. Publ., Dordrecht (The Netherlands), *submitted*.

DeMott, P. J., K. Sassen, M. Poellot, D. Baumgardner, D. C. Rogers, S. Brooks, A. J. Prenni, and S. M. Kreidenweis, 2003: African dust aerosols as atmospheric ice nuclei. *Geophys. Res. Lett.*, **30**, No. 14, 1732, doi:10.1029/2003GL017410.

Kawamoto, K., T. Nakajima, and T. Y. Nakajima, 2001: A global determination of cloud microphysics with AVHRR remote sensing. *J. Climate*, **14**, 2054-2068.

Kawamoto, K., and T. Nakajima, 2003: Seasonal variation of cloud particle size from AVHRR remote sensing. *Geophys. Res. Lett.*, **30**, 1810-1813.

McClatchey, R. A., W. Fenn, J. E. A. Selby, F. E. Volz, and J. S. Garing, 1971: Optical properties of the Atmosphere. AFCRL-TR- 71-0279, *Envir. Research Papers*, **354**, Air Force Cambridge Research Laboratories, Hanscom AFB, Bedford, MA, 85 pp.

Nakajima, T. Y., and T. Nakajima, 1995: Wide-area determination of cloud microphysical properties from NOAA AVHRR measurements for FIRE and ASTEX regions. *J. Atmos. Sci.*, **52**, 4043-4059.

Nakajima, T., and M. Tanaka, 1986: Matrix formulation for the transfer of solar radiation in a plane-parallel scattering atmosphere. *J. Quant. Spectrosc. Radiat. Transfer*, **35**, 13-21.

Nakajima, T., and M. Tanaka, 1988: Algorithms for radiative intensity calculations in moderately thick atmospheres using a truncation approximation. *J. Quant. Spectrosc. Radiat. Transfer*, **40**, 51-69.

Rosenfeld, D., and G. Gutman, 1994: Retrieving microphysical properties near the tops of potential rain clouds by multispectral analysis of AVHRR data. *Atmos. Res.*, **34**, 259-283.

Rosenfeld, D., and I. Lensky, 1998: Satellite-based insights into precipitation formation processes in continental and maritime convective clouds. *Bull. Amer. Meteor. Soc.*, **79**, 2457-2476.

Rosenfeld, D., 1999: TRMM observed first direct evidence of smoke from forest fires inhibiting rainfall. *Geophys. Res. Lett.*, **26**, 3105-3108.

Rosenfeld, D., 2000: Suppression of rain and snow by urban and industrial air pollution. *Science*, **287**, 1793-1796.

Sassen, K., 2002: Indirect climate forcing over the western US from Asian dust storms. *Geophys. Res. Lett.*, doi:10.1029/2001GL014034.

Twomey, S., 1974: Pollution and the planetary albedo. *Atmos. Res.*, **8**, 1251-1256.

effects on cloud top temperature and effective radius as derived from desert dust aerosols

CONSIDERATION OF CLOUD DYNAMICS EFFECTS ON THE PARAMETERIZATION OF CLOUD RADIATIVE PROPERTIES

Peter H. Daum [1] and Yangang Liu

[1] Environmental Sciences Department, Brookhaven National Laboratory, Upton, NY 11973-5000

1. INTROCUTION

Effective radius r_e (defined as the ratio of the third to the second moment of a droplet size distribution) is one of the key variables that are used for calculation of the radiative properties of liquid water clouds (Hansen and Travis 1974). The inclusion and parameterization of r_e in climate models has proven to be critical for assessing global climate change (Slingo 1990; Dandin et al, 1997). It has been demonstrated empirically (Pontikis and Hicks, 1992; Bower and Choularton 1992; Bower et al. 1994; Martin et al. 1994; Liu and Hallett 1997; Reid et al. 1998; Liu and Daum 2000a), as well theoretically (Liu and Hallett 1997; Liu and Daum 2000b), that the effective radius can be expressed as a "1/3" power law of the ratio of the cloud liquid water content to the droplet concentration ,

$$r_e = \left(\frac{3}{4\pi\rho_w}\right)\beta\left(\frac{L}{N}\right)^{1/3} = \beta r_v , \qquad (1)$$

where r_e is the effective radius, L is the liquid water content, N is the droplet concentration, ρ_w is the water density, r_v is the volume-mean radius, and the effective radius ratio β is a dimensionless parameter that depends on the spectral shape of the cloud droplet size distribution. The only difference among different parameterizations lies in the specification of the effective radius ratio β as a function of the relative dispersion (defined as the ratio of the standard deviation to the mean radius of the droplet size distribution).

2. EXPRESSIONS FOR EFFECTIVE RADIUS RATIO

For clouds with a monodisperse droplet size distribution as described by a delta function $n(r)=N\delta(r-r_e)$, $\beta = 1$. This value of the effective radius ratio β was used by Bower and Choularton (1992), and Bower et al. (1994) to estimate the r_e of layer clouds and small cumuli. Martin et al. (1994) derived estimates of the effective radius ratio β of 1.08 for maritime, and 1.14 for continental stratocumulus clouds based upon analysis of in situ microphysical data. These expressions with fixed values of the effective radius ratio β totally ignore the dependence of β on the spectral shape. Pontikis and Hicks (1992) analytically derived an expression that relates the effective radius ratio β to the relative dispersion. Liu and Hallett (1997) derived another expression for the effective radius ratio β from the Weibull droplet size distribution which was itself obtained from the recently developed systems theory (e.g., Liu et al. 1995, Liu and Hallett 1998; Liu et al. 2002). Expressions can also be derived from the gamma and lognormal distributions that have been widely used to describe droplet size distributions. Liu and Daum (2000a, b) compared all the existing expressions to observations, and found that the expression corresponding to the Weibull or gamma distributions best describes the dependence of the effective radius ratio β on the relative dispersion, and the two expressions perform almost equally well. The expression corresponding to the gamma droplet size distribution is

$$\beta = \frac{(1+2\varepsilon^2)^{2/3}}{(1+\varepsilon^2)^{1/3}} , \qquad (2)$$

where ε is the relative dispersion. Thus, the key to further improving the parameterization of effective radius is to specify the relative dispersion. It would also be desirable to formulate the parameterization of the relative dispersion in terms of the liquid water

[1] Corresponding author: Peter H. Daum, Brookhaven National Laboratory, Bldg. 815E, Upton, NY 11973
phdaum@bnl.gov

content and/or the droplet concentration because these two variables are often predicted/diagnosed in state-of-the art climate models (Ghan et al. 1997a, b; Rotstayn 1997).

3. EFFECTS OF PRE-CLOUD AEROSOLS

Recently, we (Liu and Daum 2002) have shown that the addition of anthropogenic aerosols to a marine air mass enhances not only the droplet concentration, but also the relative dispersion. This phenomenon is illustrated in Fig. 1, which shows the dependence of the relative dispersion on the droplet concentration under the influence of anthropogenic aerosols. The points connected by lines represent cases identified by different investigators (see Liu and Daum 2002 for details) as evidence for the indirect aerosol effect. In each case, the points with lower droplet concentration were characterized as clean clouds and the higher points were characterized as similar clouds that were polluted by anthropogenic aerosols. The increased relative dispersion acts to offset the cooling of the first indirect aerosol effect by as much as 10 - 80 % (Liu and Daum 2002), depending on the relationship between the relative dispersion and the droplet concentration. More evidence for the effect of the enhanced dispersion on indirect aerosol forcing has been later reported (Peng and Lohmann 2003; Rotstayn and Liu 2003).

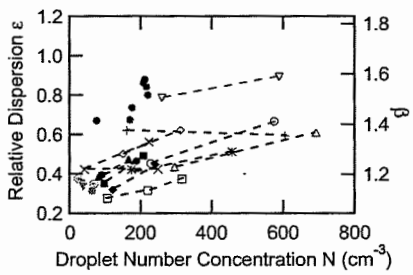

Figure 1. Relationship between the relative dispersion and the droplet concentration. See Liu and Daum (2002) for details about the data.

Although Fig. 1 clearly exhibits a substantial increase in the relative dispersion as the droplet concentration increases, the relationship is noisy. The "noise" likely arises from differences in cloud dynamics such as updraft velocity and turbulence.

4. EFFECT OF CLOUD UPDRAFT

It is desirable from Eq. (1) to parameterize the relative dispersion (or the effective radius ratio β) in terms of the ratio of the liquid water content to the droplet concentration (or the volume–mean radius). Physically, uniform/regular adiabatic growth tends to cause narrowing of the droplet size distribution as droplet grow, producing a decrease of the relative dispersion with increasing volume-mean radius (i.e., narrowing toward larger sizes). Furthermore, presenting data this way also relaxes the assumption of a constant liquid water content (updraft velocity) used in previous studies of the dispersion effect. In fact, Wood et al. (2000) found that there is a negative correlation between the effective radius ratio β and the volume-mean radius, and that this correlation is better than that between the effective radius ratio β and the droplet concentration alone, suggesting that specifying the relative dispersion as a function of the ratio of the liquid water content and the droplet concentration will improve the parameterization of the relative dispersion.

Figure 2 shows the relative dispersion as a function of the volume-mean radius calculated cloud droplet size distributions measured with a FSSP probe. The data come from several projects (NARE, ARM 1997 spring IOP, ARM 1997 Fall IOP, ARM 1998 Spring IOP, ARM 2000 IOP, and FIRE-RACE). Each point in this figure represents a flight average. The result from Wood et al. (2000) (tilted dash) is also shown as a comparison. It is evident from this figure that the relative dispersion generally decreases when the volume-mean radius increases as expected from the uniform adiabatic growth theory. The scatter is likely caused by differences in turbulent entrainment and mixing processes. It is interesting to note that data from Wood et al. (2000) lie near the lower boundary, suggesting that the data were probably taken from clouds with minimal entrainment and mixing.

5. EFFECT OF ENTRAINMENT AND MIXING

It has been observed that updraft cores of clouds tend to exhibit a smaller spectral dispersion but a larger droplet concentration compared to cloud edges and cloud tops as a result of turbulent entrainment and mixing processes (Politovich 1993; Telford 1996). These studies seem to suggest the notion that a stronger turbulence causes a larger relative dispersion and a larger volume-mean radius (broadening toward

larger sizes) contrary to that of adiabatic growth. The examples (solid curve) shown in Fig. 2 provide additional evidence for this argument. Each curve represents a single flight sorted according to the relative dispersion. It is noteworthy that although the effects of updraft and pre-cloud aerosols are expected to be minimized for a given cloud by grouping the data according to the relative dispersion, some of the effects still remain elusive.

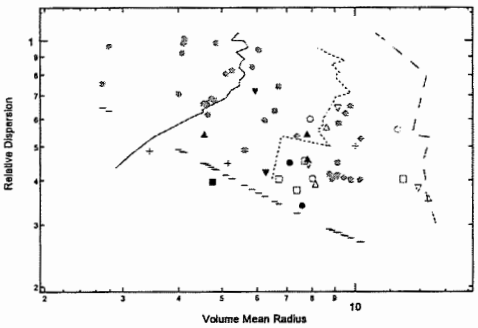

Figure 2. Relationship between the relative dispersion and the volume-mean radius. The data come from several projects (NARE, ARM 1997 spring IOP, ARM 1997 Fall IOP, ARM 1998 Spring IOP, ARM 2000 IOP, and FIRE-RACE). Each point in this figure represents a flight average used to reflect adiabatic growth (aerosol effect and updraft effect). Each curve represents data from a flight sorted according to the relative dispersion, being used to reflect the effect of turbulent entrainment and mixing.

6. NEW EXPRESSION FOR EFFECTIVE RADIUS

For the purpose of the parameterization of the effective radius, it is desirable to perform similar analysis for the relationship between the effective radius ratio β and the mean-volume radius. Figure 3 shows the results for the same data set as in Fig. 2.

Two points can be inferred from this figure. First, similar to the relative dispersion, the effective radius ratio generally decreases when the volume mean radius increases. Second, as a first order approximation, the dependence of the radius ratio on the volume-mean radius can be approximated by a power-law

putting representation of vertical vcty into effective radius.

$$\beta = a r_v^{-b}, \tag{3}$$

where the exponent b (slope) is a constant; but, the coefficient a (intercept) seems different and is likely determined by the process of turbulent entrainment and mixing. We have b = 0.20 and a = 1.9 on average.

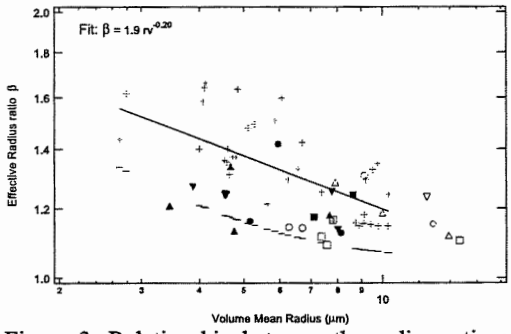

Figure 3. Relationship between the radius ratio and the volume-mean radius.

Substitution of Eq. (3) into Eq. (1) yields the improved expression for the effective radius

$$r_e = a r_v^{1-b} = \left(\frac{3}{4\pi\rho_w}\right) a \left(\frac{L}{N}\right)^{(1-b)/3} \tag{4}$$

Because b is positive, the exponent of the power-law is less than 1/3 as assumed by most studies so far. Furthermore, it has been long argued that the relative dispersion is a function of the turbulence intensity. For example, Cooper (1989) suggested that a simple mixing would lead to a linear relation between the relative dispersion and the relative dispersion of the vertical velocity fluctuation. Consequently, we speculate that the effective radius is described by

$$r_e = a r_v^{1-b} = a_w \varepsilon_w^{b_w} \left(\frac{L}{N}\right)^{(1-b)/3}, \tag{5}$$

where ε_w represents the relative dispersion of the vertical velocity fluctuation or its equivalent such as turbulent dissipation rate. Obviously, more work is needed to confirm Eq. (5) and to determine the coefficient a_w and exponent b_w.

7. CONCLUSIONS

The "1/3" power-law expression that has been widely used in the parameterization of the effective

radius is investigated. It is demonstrated that specification of the relative dispersion is the key to further improving the parameterization of the effective radius. It is argued from uniform adiabatic growth theory that the relative dispersion should be represented in terms of the ratio of the liquid water content to the droplet concentration instead of the droplet concentration alone. Microphysical measurements from several projects conducted over continental and maritime air masses are analyzed. The results show that not only the relative dispersion decreases when the volume-mean radius increases as expected from the uniform adiabatic theory, but also turbulent entrainment and mixing processes play an important role in the relationship of the relative dispersion to the volume-mean radius. Furthermore, it is empirically demonstrated that the dependence of the radius radio β on the volume-mean radius can be approximately described by a power law. The exponent b in the power-law remains roughly unchanged under different conditions of entrainment and mixing whereas the coefficient a depends strongly on turbulent entrainment and mixing processes. The overall result indicates that consideration of the effect of the relative dispersion leads to a power-law expression for the effective radius with an exponent other than the "1/3" as commonly used. It is also suggested that a simple power-law describe the effect of turbulent entrainment and mixing processes based on the results obtained in this study.

ACKNOWLEDGEMENTS

The data from FIRE-RACE and NARE are provided by Ms. Peng and Dr. Leaitch at Canada, respectively. This research was supported by the Environmental Sciences Division of the US Department of Energy, as part of the Atmospheric Radiation Measurement Program and was performed under contract DE-AC02-98CH10886.

REFERENCES (INCOMPLETE)

Bower, K. N. and T. W. Choularton, 1992: A parameterization of the effective radius of ice-free clouds for use in global climate models. Atmos. Res., **27**, 305 – 339.

Bower, K. N., T. W. Choularton, J. Latham, J. Nelson, M. B. Baker, and J. Jensen, 1994: A parameterization of warm clouds for use in atmospheric general circulation models. J. Atmos. Sci., 51, 2722-2732.

Cooper, W. A., 1989: Effects of variable droplet growth histories on droplet size distributions. Part I: Theory, J. Atmos. Sci., 46, 1301-1311.

Dandin, P., C. Pontikis, and E. Hicks, 1997: Sensitivity of a GCM to changes in the droplet effective radius parameterization. Geophys. Res. Lett., 24, 437-440.

Liu, Y., and P. H. Daum, 2000a: Spectral dispersion of cloud droplet size distributions and the parameterization of cloud droplet effective radius. Geophys. Res. Lett., 27, 1903-1906.

Liu, Y., and P. H. Daum, 2000b: Which size distribution function to use in parameterization of effective radius. Proc. 13th Int. Conf. On Clouds and Precipitation, 586-589, Reno, USA.

Liu, Y., and P. H. Daum, 2002: Indirect warming effect from dispersion forcing. Nature, 419, 580-581.

Liu, Y. and J. Hallett., 1997: The "1/3" Power-law between effective radius and liquid-water content. Q. J. R. Meteor. Soc. 123, 1789-1795.

Liu, Y. and J. Hallett., 1998: On size distributions of cloud droplets growing by condensation: A new conceptual model. J. Atmos. Sci., 55, 527-536.

Liu, Y. et al., 1995: On droplet size distributions. Atmos. Res., 35, 201-216.

Liu, Y. et al., 2002: A generalized systems theory for the effect if varying fluctuations on cloud droplet size distribution. J. Atmos. Sci., 59, 2279-2290.

Peng, Y., and U. Lohmann, 2003: Sensitivity study of the spectral dispersion of the cloud droplet size distribution on the indirect aerosol effect. Geophys. Res. Lett. 30(10), 1507.

Rotstayn, L. D., 1997: A physically based scheme for the treatment of stratiform clouds and precipitation in large-scale models. I: Description and evaluation of the microphysical processes. Q. J. R. Meteor. Soc., 123, 1227-1282.

PRELIMINARY STUDY ON TROPOSPHERIC ION-INDUCED NUCLEATION

Raffaella D'Auria and Richard P. Turco

Department of Atmospheric Sciences, University of California, Los Angeles,
Los Angeles, California, 90095-1565

1 INTRODUCTION

In situ formation of new atmospheric particles is a well documented phenomena [e.g., Weber et al. 1995; Weber et al., 1999; Clarke et al., 1998; Clarke et al., 1999]. However the mechanisms that lead to new aerosols (i.e., nucleation) are at present not fully understood as the classical nucleation theory fails in many experimental situations to explain the phenomena [e.g., Weber et al, 1995; Weber et al., 1999; Weber et al., 2001, Clarke et al., 1998]. Recently *in situ* measurements have shown that tropospheric ions can grow to relatively massive aggregates (up to 2500 amu) [Eichkorn et al., 2002; Heitmann and Arnold, 1983; Eisele, 1988; Tanner and Eisele, 1991]. These ion aggregates are composed of water, sulfuric acid and possibly acetone [Eichkorn et al., 2002] or ammonia, pyridine and other alkaline containing species [Tanner and Eisele, 1991]. Ionic aggregates have greater stability than their neutral counterparts owing to the electrostatic ion-neutral interactions that favor condensation while inhibiting evaporation. Given the right environmental conditions, ionic aggregates can form a substantial reservoir for atmospheric condensation nuclei (CN) that in turn can affect the cloud condensation nuclei (CCN) balance. Such tropospheric environment include areas characterized by low preexisting aerosol concentration and high precursor gases concentration. It is worthwhile noticing that the principal source of atmospheric ions is the galactic cosmic radiation which intensity is modulated by the solar activity. Thus the exploration of the ion-nucleation hypothesis could cast light on the possible connection between solar activity and particle formation. The atmospheric ion production rate varies with the latitude and height and reaches a maximum at about 13 km. In this framework we have developed a methodology to characterize the thermodynamical properties of ionic clusters from the molecular to the macroscopic scale. The thermodynamic of the cluster is than used to resolve in detail the kinetic of the clustering mechanism about the ion. To date the technique has been used to evaluate the stability regimes and growth of several atmospheric occurring clusters, including: the hydronium ion-water aggregates, the nitrate ion-nitric acid and the nitrate ion-water-nitric acid clusters. Here we present results from these cases and discuss the on going investigation of tropospheric ionic species that have been identified from the *in situ* measurements. In the following sections it is described what informations are needed in order to characterize the growth of the atmospheric ion clusters, section 2 and how this information can be gathered, section 3. Finally the atmospheric applications are reviewed, section 4 and a brief discussion follows, section 5.

Corresponding author's address: Raffaella D'Auria, Department of Atmospheric Sciences, University of California, Los Angeles, Los Angeles, California, 90095-1565, USA; e-mail: dauria@atmos.ucla.edu.

2 GROWTH OF THE ION CLUSTERS

The growth of ionic clusters can be studied as a series of steps that correspond to the condensation/evaporation of a ligand molecule on the preexisting ion. Such steps are best represented by chemical equilibria between two size consecutive clusters and the ligand molecule as shown in equation (1),

$$\underbrace{c_0 \cdot (l)_{n-1}}_{c_{n-1}} + l \underset{k_{r,n}}{\overset{k_{f,n-1}}{\rightleftharpoons}} \underbrace{c_0 \cdot (l)_n}_{c_n} \quad , \qquad (1)$$

where c_0 represents the core ion, l the clustering species, n an integer that indicates the number of ligands per cluster, and $k_{f,n-1}$ and $k_{r,n}$ represent the forward and reverse reaction rate for reaction (1) respectively. The knowledge of the forward and reverse rate coefficients for the pressure and temperature of interest permits us to establish the kinetic of the clustering mechanism. As n goes from 1 to some upper limit number of molecules

in-situ measurements of tropospheric ions

per cluster, N, the evolution of the clustering sequence can be described by the following system of differential equations relating the rate of change in the population of clusters of the different sizes

$$\begin{cases} \dot{c}_0 &= -k_{f,0}\cdot l\cdot c_0 + k_{r,1}\cdot c_1 - \epsilon_{rec}\cdot\bar{c}\cdot c_0 + Q_0 \\ \vdots & \\ \dot{c}_n &= k_{f,n-1}\cdot l\cdot c_{n-1} - k_{r,n}\cdot c_n + \\ & -k_{f,n}\cdot l\cdot c_n - \epsilon_{rec}\cdot\bar{c}\cdot c_n + k_{r,n+1}\cdot c_{n+1} \\ \vdots & \\ \dot{c}_N &= k_{f,N-1}\cdot l\cdot c_{N-1} - k_{r,N}\cdot c_N - \epsilon_{rec}\cdot\bar{c}\cdot c_N, \end{cases} \quad (2)$$

where ϵ_{rec} is the recombination rate that takes into account the sink of clusters as they recombine with opposite charged ions, $\bar{c}$ is the total concentration of ionic clusters of the opposite sign, and Q_0 is the production rate. When the total concentration of clusters of a certain sign, $\bar{c}$, together with the ligand concentration, l, are assumed to be constant the (2) is a linear system of first order differential equation that can be numerically integrated to find the relative concentrations of the different size clusters at different times. Typical values for the parameters in (2) are: $\epsilon_{rec} \approx 1 \times 10^{-6}$ cm$^3/s$ [Bates, 1982]; while, $Q_0 \approx 10$ ion-pairs/cm^3/s. With these ionization and recombination rates the steady state ion concentration (of each sign) is about 3×10^3 cm^{-3}, a value in agreement with observations [e.g. Cole and Pierce, 1965]. Note that the assumption of a constant value for the ligand concentration l implies that the presence of ions, for the typical concentration of 10^3 cm^{-3} and the chemistry that they imply, does not directly influence the abundance of the local vapors (for example water and nitric acid).

The problem of solving the thermodynamics of the clustering process is brought back to one of obtaining the forward and reverse rate coefficients of the class of reactions (1) for $n = 1, \ldots, N$ at the temperature and pressure of interest. If reaction (1) is elementary (i.e. occurs in the one step described) as the concentration reaches equilibrium, then the following equality is achieved,

$$K_{n-1,n} = \frac{k_{f,n-1}}{k_{r,n}} , \quad (3)$$

where $K_{n-1,n}$ is the constant of reaction (1). On the other hand the constant of reaction can be expressed as,

$$K_{n-1,n} = \exp\left(-\frac{\Delta G^0_{n-1,n}}{RT}\right) , \quad (4)$$

where $\Delta G^0_{n-1,n}$ is the Gibbs free energy change associated with reaction (1) at standard condition (i.e. for the ligand partial pressure of 1 atm), R is the gas constant, and T is the system temperature. Knowledge of $\Delta G^0_{n-1,n}$ determines $K_{n-1,n}$ through equation (4). When $k_{f,n-1}$ can be expressed with some analytical formula or its value can be reasonably assumed, $k_{r,n}$ follows from (3) and hence (2) may be integrated.

The forward rate coefficients, k_f, is determined by collisional parameters (molecular speed, impact cross section) as well as steric and surface factors, which may be summarized in the form of an accommodation coefficient. Typical values of k_f for ligand uptake onto small ions are of the order of 10^{-9} $cm^3 \cdot s^{-1}$ [Ferguson et al., 1974]. Complex ligands may have forward reaction rate coefficients that are up to an order of magnitude smaller [e.g., Gilligan and Castleman, 2001]. The forward reaction rates for several species of interest can often be found in the literature or otherwise calculated as the ion-neutral collisional rate [e.g., Su and Bowers, 1979].

3 ION CLUSTERS THERMOCHEMISTRY

The challenge in modeling the kinetic growth of ionic clusters consists in gathering the required thermochemical informations as illustrated above. In particular there are two distinct regimes to consider, the macroscopic class which clusters are massive enough to be regarded as small spherical droplets, and the microscopic one, in which class falls the properties of very small molecular aggregate for which the extrapolation of macroscopic parameters (i.e., density, surface tension, shape and dielectric constant) down to the molecular level does not held satisfying results.

3.1 Macroscopic regime

The thermochemistry of macroscopic ion clusters can be described via the liquid drop Thomson model [Thomson, 1906]. The Thomson model is a convenient way of dealing with charged drops for

which the effect of their own curvature and the presence of the charge affect the change in Gibbs free energy associated with the passage from a system made up of an homogeneous vapor phase to one composed of a liquid droplet of radius r and the surrounding vapor phase. The macroscopic assumption of capillarity is made and the droplet can be characterized from a macroscopic quantity such as surface tension, σ, corresponding bulk phase density, ρ (also, the droplet is assumed to be spherical). Given these approximations the Gibbs free energy change associated with the charged droplet formation is written as,

$$\Delta G_{0,n} = -nRT\ln S + 4\pi r^2\sigma N_A + \frac{N_A q^2}{8\pi\epsilon_0}\left(1-\frac{1}{\epsilon_r}\right)\left(\frac{1}{r}-\frac{1}{r_0}\right), \quad (5)$$

where S is the saturation ratio defined as the ratio of the ligand partial pressure on the saturation vapor pressure above a flat surface of the same condensed substance of which the droplet is made, ϵ_0 is the dielectric constant in vacuum, ϵ_r is the dielectric constant of the clustering condensed phase, r_0 is the radius of the core ion, and N_A is the Avogadro's number. The first term in (5) simply express the energy associated with the condensation/evaporation of n molecules from the vapor to the condensed phase, the second term accounts for the work that has to be done to build up a water liquid spherical interface of radius r, and, finally, the third term is the Born energy of solvation. From (5) $\Delta G^0_{n-1,n}$ can be computed, given that the partial pressure of the ligand is set equal to 1 atm (standard condition), as,

$$\Delta G^0_{n-1,n} = \Delta G^0_{0,n} - \Delta G^0_{0,n-1} \quad . \quad (6)$$

The Thomson equation not only contains all the capillarity approximations but is also non charge specific. Only the term containing the ionic radii accounts for difference between ions. Nevertheless the data available seem to approach the macroscopic model for number of ligands per cluster of the order of ten or less, as it will be shown later (see also, for example, Holland and Castleman, 1982).

3.2 Microscopic regime

For the microscopic clusters, i.e., those with less than about 10 ligands (D'Auria and Turco, 2001a; 2001b), thermochemistry information can be assumed from the literature when clustering experiments have been done for the species of interest or calculated via quantum mechanical simulations of the clusters structure and energetics. In such way we have studied several cluster families of atmospheric relevance in the framework of density functional theory (DFT) which provides an excellent compromise between results accuracy and computational resources. A detailed comparison of experimental data and DFT simulation results is addressed in D'Auria et al., 2004 for the hydronium ion-water series.

In Figure 1 a plot of the $\Delta G_{0,n}$ as a function of the number of ligand per cluster is shown for typical temperatures characterizing the lower polar winter stratosphere. Note the presence of the minimum before the maximum. The maximum, when present, represent the height of the energetic barrier to nucleation. The presence of the minimum, which individuates a region of stable pre-nucleating clusters, is a distinct signature of the ions and would disappear for neutral aggregates. These very feature bears consequences that will be addressed in the following section.

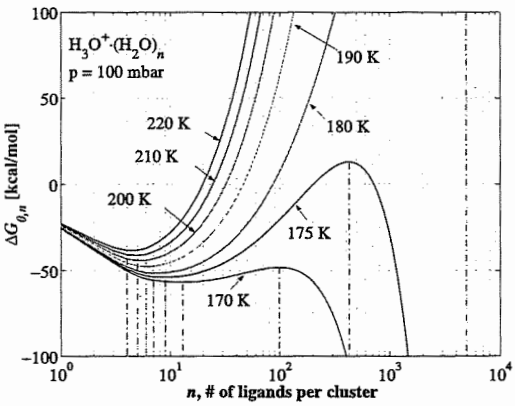

Figure 1: General behavior of the Gibbs free energy change associated with the formation of a ionic cluster (in the present case hydronium ion-water) composed of n (water) ligands. Note that for $1 \leq n \leq 10$ the curves are obtained from either real data or DFT simulations.

4 ATMOSPHERIC APPLICATIONS

When all of the necessary informations about a ion cluster system are known it is possible to precede to solve the system (2). In such a way the development of the ion family size distribution can be followed in time under a series of environmental conditions. To date we have analyzed the behavior of

hydronium ion-water clusters and nitrate ion-water-nitric acid aggregates. In this original study such clusters were characterized for the lower polar winter stratospheric environment in view of their possible role in the heterogeneous chemistry that occurs in such environment. Results from such study are discussed in two papers, i.e., D'Auria and Turco, 2001a and D'Auria and Turco, 2001b.

The code used to define the kinetic growth of the clusters can be used as a module to interact with a full microphysical scheme, as is the APM developed by this group [e.g., Yu, 1998]. In this way the ion nucleation of small clusters is integrated with other concurring/competing microphysical phenomena and an evaluation of its relative importance can be assessed.

4.1 The hydronium ion–water system

In this section we present a preliminary result that shows the most typical sizes of the hydronium ion-water aggregates in the atmosphere (considering all regimes from the troposphere to the summer polar mesosphere). In Figure 2 a plot of the number of ligands for which the $\Delta G_{0,n}$ has a minimum, n_{min}, is shown for different atmospheric regimes. Note that such number correspond to a maximum in the pre-nucleating ion cluster size distribution.

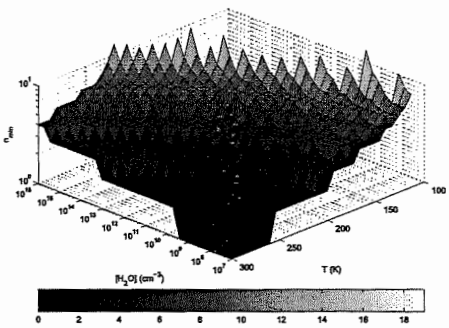

Figure 2: The plot shows n_min as a function of water absolute concentration and temperature which identify several atmospheric regimes (see text).

Most tropospheric regimes would fall in the $[H_2O] = 10^{16}$–10^{15} cm^{-3} and T = 300–220 K. It appears that such regimes correspond to distribution of pre-nucleating $H_3O^+ \cdot (H_2O)_n$ clusters characterized by n_{min} of the order of 10. Upon condensation on such clusters of other components (i.e., ammonia, sulfuric acid, etc.) it is likely that this cluster can get activate to grow to larger nuclei. Such hypothesis is currently under study.

5 CONCLUSIONS

In summary a methodology to study and characterize the atmospheric relevant ionic cluster families across the entire spectrum of sizes is presented here. Preliminary applications to some atmospheric ionic aggregates are briefly reviewed.

ACKNOWLEDGMENTS

This work has been funded by NASA under grant NAG1-1899.

REFERENCES

Bates, D. R.; 1982: Recombination of small ions in the troposphere and lower stratosphere, Planet. Space Sci., 30, 1275–1282.

Clarke, A. D.; Davis, D.; Kapustin, V. N.; et al.; 1998: Particle Nucleation in the Tropical Boundary Layer and Its Coupling to Marine Sulfur Sources, Sciences, 282, 89–92.

Cole, R. K.; Pierce, E. T.; 1965: Electrification in the Earth's atmosphere for altitudes between 0 and 100 kilometers, J. Geophys. Res., 70, 2735–2749.

Clarke, A. D.; Kapustin, V. N.; Eisele, F. L.; et al.; 1999: Particle Production near Marine Clouds: Sulfuric Acid and Predictions from Classical Binary Nucleation, Geophys. Res. Lett., 26, 2425–2428.

D'Auria, R.; Turco, R. P.; Houk, K. N.; 2004: Effects of Hydration on the Properties of Protonated-Water–Nitric Acid Clusters, J. Phys. Chem. A, *In press.*

D'Auria, R.; Turco, R. P.; 2001a: Ionic clusters in the polar winter stratosphere, Geophys. Res. Lett., 28, 3871–3874.

D'Auria, R.; Turco, R. P.; 2001b: A Thermodynamic–Kinetic Model for Ionic Cluster Formation, Growth and Nucleation, Proc. of the Workshop on Ion-Aerosol-Cloud Interactions, ed. J. Kirkby, CERN, Geneva, CERN 2001-007

Eichkorn, S.; Wilhelm, S.; Aumfmholf, H.; et al.; 2002: Cosmic ray-induced aerosol-formation: First observational evidence from aircraft-based ion mass spectrometer measurements in the upper troposphere, Geophys. Res. Lett., 29, 43-1–43-4.

Eisele, F. L.; 1988: First tandem mass spectrometric measurement of tropospheric ions, J. Geophys. Res., 93, 716–724.

Ferguson, E. E.; 1974: Laboratory measurements of ionospheric ion-molecule reaction rates, Rev. Geophys., 12, 703–713.

Gilligan, J. J.; Castleman, A. W.; 2001: Acid dissolution by aqueous surfaces and ice: Insights from a study of water cluster ions, J. Phys. Chem., 105, 5601–5605.

Heitmann, H.; Arnold, F.; 1983: Composition measurements of tropospheric ions, Nature, 306, 747–751.

Holland, P. M.; Castleman, Jr., A. W.; 1982: Thomson equation revisited in light of ion-clustering experiments, J. Phys. Chem., 86, 4181–4188.

Su, T.; Bowers, M. T.; 1979: in *Gas phase ion-chemistry, I*, 83–118, Edited by M. T. Bowers, Academic Press.

Tanner, D. J.; Eisele, F. L.; 1991: Ions in oceanic and continental air masses, J. Geophys. Res., 96, 1023–1031.

Thomson, J. J.; 1928: in *Conduction of electricity through Gases, I*, 325–326, Cambridge University press, Cambridge.

Weber, R. J.; McMurry, P. H.; Eisele, F. L.; Tanner, D. J; 1995: Measurement of Expected Nucleation Precursor Species and 3–500-nm Diameter Particles at Mauna Loa Observatory, Hawaii, J. Atmos. Sci., 52, 2242–2257.

Weber, R. J.; McMurry, P. H.; Mauldin, P. H., III; et al.; 1999: New particle formation in the remote troposphere: A comparison of observations at various sites, Geophys. Res. Lett., 26, 307–310.

Weber, R. J.; Moore, K.; Kapustin, V.; et al.; 2001: Nucleation in the equatorial Pacific during PEM-Tropics B: Enhanced boundary layer H_2SO_4 with no particle production, J. Geophys. Res., 106, 32,767–32,776.

Yu, F.; 1998: A study of the formation and evolution of aerosols and contrails in aircraft wakes: Development, validation and application of an advanced particle microphysics (apm) model, Ph.D. thesis, Univ. of Calif., Los Angeles.

PHYSICAL AND CHEMICAL IMPACTS ON THE ICE NUCLEATING PROPERTIES OF ATMOSPHERIC PARTICLES

Paul DeMott[1] Daniel Cziczo[2], Jose Jimenez[3], Sarah Brooks[1], Mathews Richardson[1], Edward Dunlea[3], Kirsten Koehler[1], Anthony Prenni[1], Sonia Kreidenweis[1], Randy Borys[4] and Daniel Murphy[2]

[1]Colorado State University, Department of Atmospheric Science, Fort Collins, CO, 80523, USA
[2]National Oceanic and Atmospheric Administration, Aeronomy Laboratory, Boulder, CO 80305, USA
[3]University of Colorado, Department of Chemistry and Biochemistry, Boulder, CO, 80309, USA
[4]Desert Research Institute, Storm Peak Laboratory, Steamboat Springs, CO, 80477, USA

1. INTRODUCTION

Nucleation of ice particles in the atmosphere occurs by homogeneous freezing of liquid particles and by heterogeneous nucleation due to the action of insoluble ice nuclei (IN). Homogeneous freezing herein refers to spontaneous ice embryo formation within either dilute droplets or concentrated solutions at temperatures below about -36°C. Heterogeneous nucleation can occur via multiple ice formation mechanisms at all temperatures below 0°C, given a sufficiently effective ice nucleus. These two fundamental ice nucleation processes interact directly in the cirrus cloud regime. This particular regime provides the focus for much of the work reported in this paper, but the methodologies applied are currently being extended to cover all mixed phase (ice present with liquid) clouds.

Understanding the range of temperature and relative humidity conditions that can support cirrus cloud formation in the presence of diverse types of aerosol particles present in the atmosphere is critical to an assessment of the effects of these cold clouds on climate (e.g., Kärcher and Lohmann 2003). While some atmospheric measurements have been made to infer the activation conditions for homogeneous freezing and the presence or absence of heterogeneous nuclei around cirrus clouds (Haag et al. 2003), few direct measurements of these nuclei as functions of temperature and ice supersaturation exist.

Measurements of the concentrations and compositions of total aerosol particles and those active in homogeneous and heterogeneous ice formation processes are being made to investigate natural and anthropogenic influences on ice nuclei populations throughout the range of conditions relevant for tropospheric clouds. These studies are conducted for particles in free tropospheric air, as sampled from a mountaintop location (Storm Peak Laboratory, 3220 m MSL) in the western United States. Focused laboratory studies are also underway. Results from ambient particle measurements during three weeks in autumn (November 2001) are reviewed in this paper. New measurements in April to May of 2004 will further explore apparent influences of organic species on ice formation processes and the important roles of aerosol size distribution and mineral dust concentrations in determining the concentrations and activation conditions of heterogeneous ice nuclei. Preliminary new results will be presented at conference time.

1. Corresponding author's address: Paul J. DeMott, Department of Atmospheric Science, Colorado State University, Fort Collins, CO, USA 80523; E-Mail: pdemott@lamar.colostate.edu

2. EXPERIMENTAL METHODS

The key experimental methods used in sampling natural aerosol particles effective in forming ice are shown in Figure 1 and are described further by Cziczo et al. (2003) and DeMott et al. (2003). Ice nuclei compositions are determined by processing submicron particles for selected cloud formation conditions in a continuous flow ice thermal diffusion chamber (CFDC), separating nucleated ice crystals from the flow using a laboratory counterflow virtual impactor (LCVI), and performing compositional analyses of individual evaporated residual nuclei by mass spectroscopy (PALMS instrument) and transmission electron microscopy (TEM).

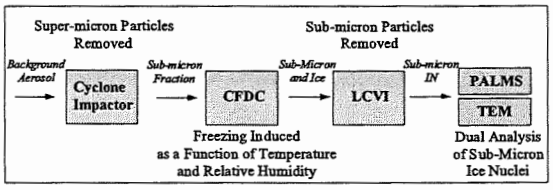

Figure 1 Experimental methods used during aerosol particle sampling in November 2001, as described in the text.

The CFDC instrument determines the concentration of aerosol particles that nucleate ice as functions of temperature and relative humidity. The Particle Analysis by Laser Mass Spectrometry (PALMS) instrument obtains complete positive or negative ion mass spectrum of the residual nuclei after laser ablation.

3. RESULTS

Key results from the first study have been reported by DeMott et al. (2003). Information was gained

role of organic species on ice crystal for[n] mechanism from Storm Peak observations

concerning the onset conditions for homogeneous freezing on background particles, the apparent influence of particle chemistry on this phase transition, the concentrations of heterogeneous IN present at low temperatures in free tropospheric air, and factors influencing heterogeneous IN concentrations.

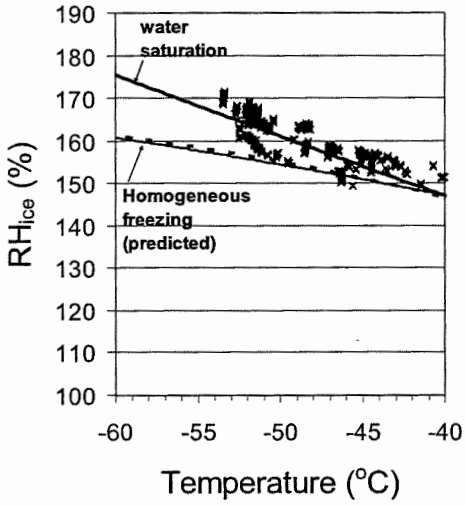

Figure 2 Approximate onset ice relative humidity (RH_{ice}) versus temperature conditions for apparent homogeneous freezing observed for natural aerosol particles in the CFDC. The data shown span a range of freezing conditions representing 0.05 to 1 % of all ambient particles above 100 nm freezing (ice particle concentrations from 0.125 to 5 cm^{-3} represented). The expected conditions for homogeneously freezing 1% of 100 nm pure ammonium sulfate particles based on Koop et al. (2000) and Chen et al. (2000) are shown as dashed and thin solid lines, respectively.

3.1 Homogeneous freezing by natural aerosol particles

Examples of time series of experimental data are given elsewhere (Cziczo et al. 2003; DeMott et al. (2003). These demonstrate the transition from relatively small numbers of particles nucleating as IN at lower relative humidity to homogeneous freezing of soluble and partially soluble particles as water saturation is approached and exceeded. These data were used to construct Figure 2, which shows the onset conditions (as defined in the figure caption) required for homogeneous freezing of ambient particles. The major findings are that the lowest onset ice relative humidity (RH_{ice}) versus temperature for activating homogeneous freezing is in good agreement with some laboratory studies of sulfate particle freezing. Nevertheless, as pointed out by DeMott et al. (2003), much higher RH_{ice} is sometimes required and this appears associated with the presence of organic species in aerosol particles.

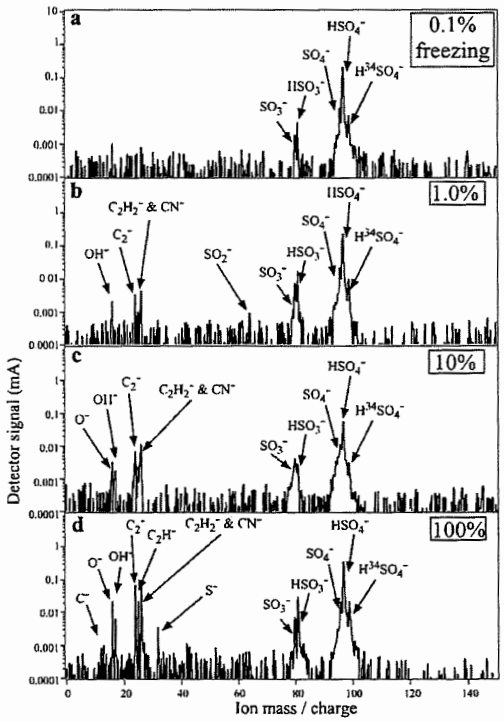

Figure 3 PALMS negative ion mass spectra showing the increasingly organic nature of particles as the fraction of particles (above 100nm, as a reference) freezing homogeneously increases from panels **a** to **d**. From Cziczo et al. 2004b).

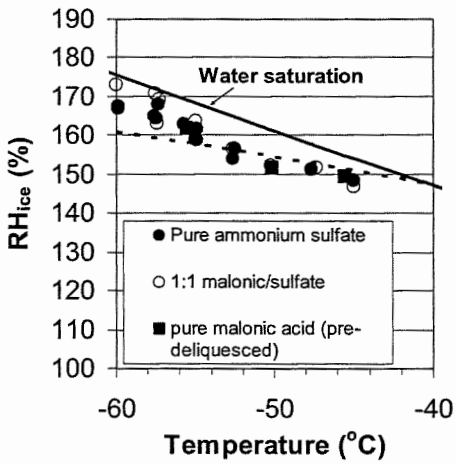

Figure 4 Laboratory measurements of the conditions for homogeneously freezing liquid particles formed on pure ammonium sulfate, pure malonic acid and 1:1 mixtures of these by mass. All particles are 100 nm at their dry size and freezing conditions represent 1% of particles nucleating in 12 s. The dashed line is the predicted homogeneous freezing condition.

This latter point is demonstrated in Figure 3. Particles freezing at the lowest RH_{ice} onset freezing conditions, as shown in Figure 2, are primarily sulfates. Particles include more and more organic fragments as the fraction of particles freezing (or nucleation rate) increases. This result does not occur simply because smaller particles, enriched in organics, freeze at higher nucleation rates (Cziczo et al. 2004b). Rather, these results demonstrate a clear fractionation of composition versus nucleation rate in the CFDC. This suggests a kinetic influence of certain organics on nucleation. We cannot state with certainty that these influences will occur on the time scale of cirrus cloud formation, but recent field measurements support that they do (Cziczo et al. 2004a).

Experiments have been done in the laboratory to explore organic effects on homogeneous freezing. Some recent results for mixtures of sulfates and dicarboxylic acid particles suggest no impact on the freezing conditions of particles of 100 nm initial (dry) size in the cirrus regime (Figure 4). Organic impacts must involve other soluble or surface active organic species.

3.2 Heterogeneous ice nucleation by natural aerosol particles

Concentrations of heterogeneous ice nuclei measured during the November 2001 campaign were modest, but significant as regards cirrus cloud forming in synoptic lifting or in the lower cooling rates thought to be present in subvisual cirrus (DeMott et al. 2003). Average concentrations as a function of ice supersaturation are summarized in Figure 4 for data within two different temperature regimes. At temperatures warmer than -35°C, ice formation is solely by heterogeneous nucleation in the CFDC. At below -38°C, heterogeneous ice nucleation is detectable up until the onset conditions for homogeneous freezing, where strong homogeneous nucleation masks the more selective process. These data suggest a difference in the way the heterogeneous nuclei population activates in the different temperature regimes, although the greatest differences occur in the ice saturation regime that includes water supersaturated conditions in the warmer regime. This may reflect differences between deposition and freezing nucleation mechanisms. IN concentrations during the 2001 study were much lower than those extrapolated on the basis of the IN parameterization of Meyers et al. (1992). This parameterization has been used extensively in cloud modeling, but is clearly inappropriate for the location of this study and the time of year. The solution to the inadequacies of this type of parameterization may be in explicitly recognizing the additional relation of IN concentrations to changes in the aerosol particle size distribution, particularly the apparent relation with the concentration of accumulation mode aerosol (DeMott et al. 2003). It will also be important to account quantitatively for IN sources and seasonal cycles.

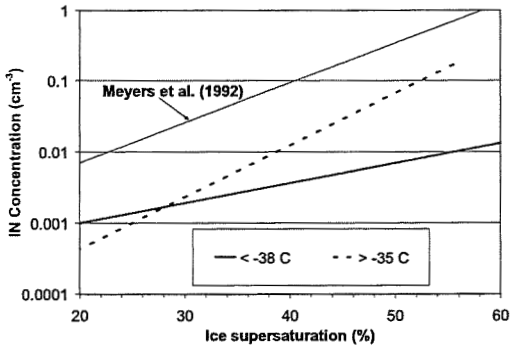

Figure 4 Average ice nuclei concentrations in the heterogeneous nucleation regime during the November 2001 study, distinguished for temperatures above -35°C and below -38°C. Also shown are IN concentrations predicted by extrapolating the IN versus ice supersaturation relation given by Meyers et al. (1992).

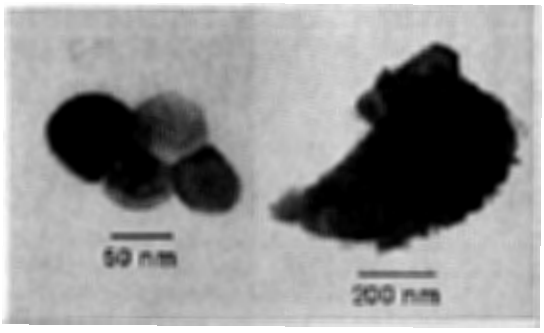

Figure 5 Images of two particles categorized as being of mineral or fly ash origin. The particle on the left is primarily composed of titanium and likely of anthropogenic origin from a high temperature process. The particle on the right that also includes Si, Na, Mg, Fe and S is more typical of a natural mineral dust particle and represented 80% of particles categorized as mineral dust/fly ash.

The compositions of heterogeneous IN measured in this study suggest important global sources. Ion mass spectra of IN indicated a predominance of particles representative of mineral dust, fly ash and metallic elements (DeMott et al. 2003). Furthermore, TEM analyses of particle morphologies and elemental compositions indicated that although particles of anthropogenic origin contributed significantly to the IN population, mineral dust sources were likely responsible for 80% of all such particles.

4. FUTURE WORK: SPRING 2004 STUDY

New studies during April and May 2004 will be done to sample free tropospheric air from the mountaintop site during what is expected to be the peak transport season for Asian dust particles to the site in the Western U.S. (VanCuran and Cahill, 2002). Figure 6 confirms the typical increase in soil dust concentrations at the site in spring compared to

concentrations closer to the annual minimum during the first study. Table 1 lists the suite of measurements for the next study. Included will be an additional aerosol mass spectrometer (AMS) with improved capabilities to quantify sulfate and organic particle content (Jimenez et al. 2003), improved size resolved composition with both mass spectrometers, new measurements of particle hygroscopicity, gas phase chemistry to correlate with IN measurements. Daily fine and coarse particle aerosol analyses will also be obtained from an IMPROVE (Interagency Monitoring of Protected Visual Environments) particulate monitoring network filter sampler.

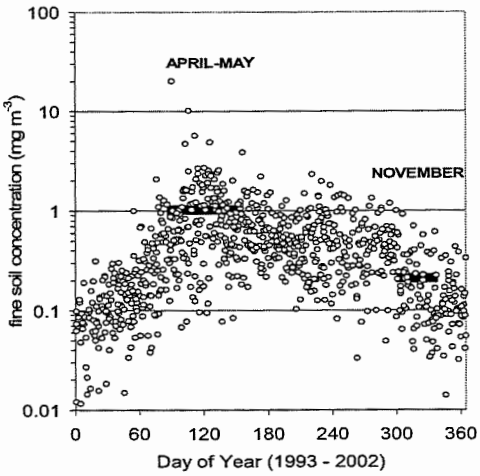

Figure 6 Annual cycle of fine soil dust at an IMPROVE network site located 10 km northwest of the study site and at approximately the same elevation. This indicates the expected difference between dust concentrations in the previous (November) and planned (April to May) study periods.

Table 1. Measurement Suite for 2004 Study

MEASUREMENT	INSTRUMENT
IN concentration	Continuous flow diffusion chamber
Aerosol and IN chemistry	AMS PALMS TEM grid collections
Bulk aerosol mass and chemistry	IMPROVE filters (24 hours integrated)
Water uptake (size resolved)	HTDMA
CCN	Thermal gradient diffusion chamber
Aerosol particle size	DMA (12 to 350 nm) OPC (100 to 2000 nm) APC (540 to 20000 nm)
Gas Phase	SO_2 O_3 CO

5. ACKNOWLEDGEMENTS

This research was supported by the U.S. NSF grants ATM0071321, ATM0124927, ATM0334228 and NOAA base funding. Any opinions, findings, conclusions, or recommendations expressed in this publication are those of the authors. Special thanks to Brian Jesse and David Rogers for assistance during this study.

6. REFERENCES

DeMott, P.J., D.J. Cziczo, A.J. Prenni, D.M. Murphy, S.M. Kreidenweis, D.S. Thomson, R. Borys and D.C. Rogers, 2003: Measurements of the concentration and composition of nuclei for cirrus formation. *Proc. Natl. Acad. Sci.*,**100**,14655-14660.

Chen, Y., P.J. DeMott, S.M. Kreidenweis, D.C. Rogers and D.E. Sherman, D.E., 2000: Ice formation by sulfate and sulfuric acid aerosol particles under upper tropospheric conditions. *J. Atmos. Sci.* **57**, 3752-3766.

Cziczo, D.J., D.M. Murphy, P.K. Hudson and D.S. Thomson, 2004a: Single particle measurements of the chemical composition of cirrus ice residue during CRYSTAL-FACE. *J. Geophys. Res.*, **109**, D04201, doi:10.1029/2003JB004032, 2004.

Cziczo, D.J., P.J. DeMott, S.D. Brooks, A.J. Prenni, D.S. Thomson, D. Baumgardner, J. C. Wilson, S. M. Kreidenweis, and D.M. Murphy, 2004b: Observations of organic species and atmospheric ice formation. *Geophys. Res. Lett.*, submitted.

Cziczo, D.J., P.J. DeMott, C. Brock, P.K. Hudson, B. Jesse, S.M. Kreidenweis, A.J. Prenni, J. Schreiner, D.S. Thomson, and D.M. Murphy, 2003: A Method for Single Particle Mass Spectroscopy of Ice Nuclei. *Aerosol Sci. and Technol.*, **37**, 460-470.

Haag, W. et al., 2003: Freezing thresholds and cirrus cloud formation mechanisms inferred from in situ measurements of relative humidity. *Atmos. Chem. Phys.*, **3**, 1791–1806.

Jimenez J.L. et al., 2003: Ambient aerosol sampling with an aerosol mass spectrometer, *J. Geophys. Res.*, **108**, 8425, doi: 10.1029/2001JD001213.

Kärcher, B. and U. Lohmann, 2003: A parameterization of cirrus cloud formation: Heterogeneous freezing, *J. Geophys. Res.*, **108**, 4402, doi: 10.1029/2002JD003220.

Koop, T., B.P. Luo, A. Tsias, and T. Peter, 2000: Water activity as the determinant for homogeneous ice nucleation in aqueous solutions. *Nature*, **406**, 611-614.

Meyers, M.P., P.J. DeMott, and W.R. Cotton, 1992: New primary ice nucleation parameterizations in an explicit cloud model. J. Appl. Meteor., 31, 708-721.

Vancuren, R.A. and T.A. Cahill, 2002: Asian aerosols in North America: Frequency and concentration of fine dust. *J. Geophys. Res.*, **107**, doi: 10.1029/2002JD002204.

HAILSTONE SIZE DISTRIBUTION IN ATMOSPHERIC SAHARAN DUST OUTBREAKS

J. Dessens[1], J.L. Sánchez[2], C. Berthet[1] and R. Fraile[2]

[1]ANELFA, Toulouse, France
[2]Universidad de León, Spain

1. INTRODUCTION

In southwestern France, atmospheric Saharan dust outbreaks are often accompanied with severe hailstorms. This situation may be due to the thermodynamic conditions observed in Saharan air masses, among which the presence of a very dry air layer at mid-level and of a rapid flow at upper level. However, the high concentration in aerosol dust could also have an effect on the microphysical processes leading to hail production (Rosinski and Kerrigan, 1969; Dessens and Fournier d'Albe, 1988). Recent works have concluded that the atmospheric content in dust or smoke aerosol has a significant effect on rain precipitation processes (Rosenfeld, 1999, 2000), which implies that it can thus also affect the formation of hail. A day-of-the-week variability of hail found in the polluted area around Toulouse enhances this hypothesis (Dessens et al., 2001).

The present study uses data collected from a large hailpad network for 15 years in the area of southwestern France bordered by the Atlantic to the west and by the Pyrenees to the south. During this period, several major dust outbreaks have occurred, some of them accompanied by hailstorms. The mean hailstone size distributions measured during these events are compared to distributions from similar hailstorms not developing in Saharan air masses.

2. SELECTION OF DATA

In relation with the large-scale hail suppression project of the Association Nationale d'Etude et de Lutte contre les Fléaux Atmosphériques (ANELFA), a hailpad network has been set up in southwestern France. The hailpad material, calibration, and data processing are described in Dessens et al. (2001), and a preliminary climatology of hail on the first 14 years is given in Fraile et al. (2003). In each hail season, a few hail days are also days of typical Saharan dust outbreak, as revealed by an unusually hazy sky associated with a warm flow from the south, then by red dust deposit or red rain (Dessens and Pham Van Dinh, 1990). Six major hail days among them have been selected according to the following criteria:

- the dust outbreak is evident, and it is confirmed by airmass trajectories,
- the number of point hailfalls recorded on the hailpad network is larger than 20. Such a sample allows to compute a representative mean size distribution for the day.

The selected days are given in Table 1. For comparisons'sake, six other major hail days having developed in air masses not coming from Africa have also been selected, among a much larger number of hail days (Table 2).

TABLE 1. Major hail days with Saharan dust outbreak.

Date	Hailstorm type	Largest hailstones measured, observed
6 July 1989	2 long traveling supercells	2.4 cm, 8 cm
23 July 1989	1 supercell	4.1 cm, 7 cm
8 August 1992	several traveling storms	3.2 cm, 8 cm
28 June 1993	2 major supercells	3.2 cm, 7 cm
25 July 1996	1 severe local storm	3.4 cm
27 May 1999	1 90 km long hailstreak	3.3 cm

TABLE 2. Major hail days without Saharan dust outbreak.

Date	Hailstorm type	Largest hailstones measured, observed
21 June1993	2 supercell south of the Pyrenees	3.6 cm, 6 cm
14 August 1993	several frontal storms	2.4 cm, 6 cm
18 June 1994	several damaging cells	4.0 cm, 5 cm
2 July 1995	3 traveling storms	4.0 cm
2 July 1998	1 hailstreak, 140 x 5 km	3.3 cm
7 May 1999	1 supercell south of the Pyrenees	4.5 cm

Corresponding author's address: Jean Dessens, ANELFA, 52 rue Alfred Duméril, 31400 Toulouse, France; E-Mail: jean.dessens@anelfa.asso.fr

In the last column of each table, the first number given is the diameter of the largest hailstones measured by hailpads, and the second is that of hailstones observed in the area and reported by newspapers. Meteorological information and detailed observations on the 12 major hail days are given in the annual reports of the ANELFA.

Except for their airmass origin, both samples are similar. They are composed of the major hail days having occurred during the 15-year period. However, the dust outbreak days are warmer than the other ones, the mean 0°C level being respectively at 3.8 and 3.2 km, which could induce some differences in the hailstone melting between the 0°C isotherm level and the ground.

3. HAILSTONE SIZE DISTRIBUTIONS

The daily hailstone size distributions are given in Fig. 1 for the dust outbreak cases, and in Fig. 2 for the control days. The curves are drawn in the usual manner. For example, a number of 1000 m^{-2} cm^{-1} hailstones for a diameter D = 1.0 cm corresponds to 20 hailstones of diameter between 0.9 and 1.1 cm measured on a hailpad of 0.1 m^2.

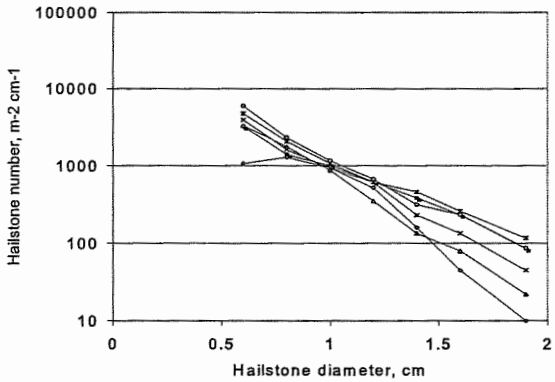

Fig. 1. Hailstone size distributions for six major hail days with Saharan dust outbreaks.

The distributions of the two samples appear to be similar for diameters of 1.4 cm and above, but the number of small hailstones is lower for the dust cases. However, it is difficult to apply the statistics to such small samples. The exponential distribution can be computed from the mean hailstone numbers in each range of diameters:

$N_D = 20{,}000\ e^{-3.0\,D}$ with dust
$N_D = 78{,}000\ e^{-3.8\,D}$ without dust

where N_D is the number of hailstones (in m^{-2} cm^{-1}) of diameter D (in cm).

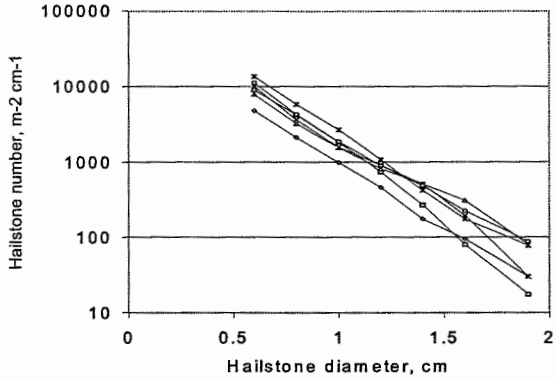

Fig. 2. Same as Fig. 1 for six major hail days without dust outbreak.

The number of large hailstones is about the same in both samples, but there are about three times more small hailstones in the "no dust" cases.

It is interesting to compare these distributions to those computed on a large sample of hailfalls stratified according to the days of the week (Dessens et al., 2001):

$N_D = 79{,}000\ e^{-3.7\,D}$ for weekends
$N_D = 179{,}000\ e^{-4.7\,D}$ for weekdays.

The distributions for the "no dust" cases are the same as for weekends, which is normal since the "no dust" cases have been selected among hail days occurring in non polluted air masses of Atlantic origin. The dust effect appears to be exactly opposite to the pollution effect, decreasing the slope of the curve instead of increasing it.

4. CONCLUSION

When the six hail days with Saharan dust outbreaks are compared to hail days without dust, the hailstone size distribution appears unchanged for the upper part of the distribution (above D = 1.4 cm), but there seems to be a large deficit in smaller hailstones for the dust cases. This result recalls the observation that, when short rainfalls occur under altocumulus embedded in Saharan dust aerosol, they are

made of very large drops without any small drops. Two explanations can be suggested:

- small raindrops, as well as small hailstones, evaporate in the warm, dry air often associated with large dust outbreaks,
- dust aerosol acts as giant condensation nuclei rather than as ice-forming nuclei, resulting in a large number of drops which collect the cloud water at the expense of smaller drops.

Until a larger sample of hail days with dust outbreaks is available, a firm conclusion is not possible. Physical measurements inside as well as under the clouds are necessary to understand the effect of dust aerosol on rain and hail formation and the role of melting during the fall of hailstones. However, this preliminary study suggests that a strong concentration of desert dust in thunderstorms does not significantly affect the severity of hailfalls, since it only contribute to a decrease in the number of small hailstones.

REFERENCES

Dessens, J., and E.M. Fournier d'Albe, 1988: The origin of air masses leading to severe hailstorms in southwestern France. Annalen der Meteorologie, 2, 452-454.

Dessens, J., and Pham Van Dinh, 1990: Frequent Saharan dust outbreaks north of the Pyrenees: A sign of climatic change? Weather, 45, 327-333.

Dessens, J., R. Fraile, V. Pont and J.L. Sánchez, 2001: Day-of-the-week variability of hail in southwestern France. Atmos. Res., 59-60, 63-76.

Fraile, R., C. Berthet, J. Dessens and J.L. Sánchez, 2003: Return periods of severe hailfalls computed from hailpad data. Atmos. Res., 67-68, 189-202.

Rosenfeld, D., 1999: TRMM observed first direct evidence of smoke from forest fires inhibiting rainfall. Geophys. Res. Lett., 26, 3105-3108.

Rosenfeld, D., 2000: Suppression of rain and snow by urban and industrial air pollution. Science, 287, 1793-1796.

Rosinski, J., and T.C. Kerrigan, 1969: The role of aerosol particles in the formation of raindrops and hailstones in severe thunderstorms. J. Atmos. Sci., 26, 695-715.

hail size distribution
occuring during Saharan
hail event

ICE FORMATION IN A BIOMASS BURNING CLOUD: MODEL SIMULATIONS OF DROP FREEZING IN IMMERSION AND CONTACT MODES

K. Diehl[1]*, M. Simmel[1], and S. Wurzler[2]

[1]Institute for Tropospheric Research, Leipzig, Germany
[2]North-Rhine-Westphalia State Environment Agency

1. INTRODUCTION

Biomass burning is one of the main sources of atmospheric aerosol particles. By the fire induced convection soils from the ground as well as burnt and unburnt vegetation parts are transferred into the atmosphere. Therefore, particles from biomass burning consist of biogenic, pyrogenic, and soil dust components with a high insoluble fraction between 80 and 95 % (e.g., Feingold et al., 2001, Guyon et al., 2003). A typical phenomenon in biomass burning clouds is the suppression of warm rain. It is caused by the large amount of small particles which lead to the formation of a high number of small drops in biomass burning clouds. The formation of precipitation from those by collision and coalescence is hardly possible. Therefore, the only other way to initiate precipitation from biomass burning clouds might be the ice phase (Rosenfeld, 1999).

In the temperature range between 0 and -35°C ice is mostly formed in the atmosphere by heterogeneous freezing, i.e., with the participation of insoluble particles. The freezing of supercooled drops can take place by two processes: immersion and contact freezing. In both processes large drop sizes are preferred. Immersion freezing is a function of the logarithm of the drop volume, i.e., the smaller the drop the lower the freezing temperature (Pruppacher and Klett, 1997). Contact freezing is restricted by the collision between the supercooled drops and the potential ice nuclei. The collision kernel (Kerkweg et al., 2003) shows highest values for large drops and particles. Thus, the small drop sizes in biomass burning clouds might prevent freezing whereas, on the other hand, the large insoluble fraction of biomass burning particles would favor the formation of ice by heterogeneous freezing.

Typical atmospheric ice nuclei are biological particles, minerals, and soot. An important point is that these insoluble particles show significantly different ice nucleating efficiencies (Pruppacher and Klett, 1997). Some of them, e.g., biological particles, can be active at rather warm temperatures, others only at rather low temperatures. Because of the release of latent heat the initiation of the ice phase can have dramatic effects on the vertical cloud dynamics so that the cloud can reach higher altitudes with lower temperatures where even more ice can be formed. The onset of freezing is a crucial point in mixed phase clouds. The different ice nucleating abilities of various insoluble particles have a significant impact on heterogeneous ice formation. Therefore, the modelling of mixed phase clouds requires to carefully describe the onset of freezing and to consider the different ice nucleating abilities of various insoluble particles. By estimating their characteristic effects on ice formation and, thus, on the vertical cloud dynamics it can be distinguished which components of the biomass burning particles are more important for ice formation than others. In the present study numerical simulations were carried out to show the effects of different ice nucleating abilities of various insoluble particles.

2. METHODS

For the numerial simulations a cloud model based on the linear discrete method (Simmel et al., 2002) was employed which describes the cloud microphysics and the interactions between aerosol particles and hydrometeors. It is an adiabatic air parcel model with entrainment and a sectional description of the microphyics. The insoluble and soluble fractions of the aerosol particles can be varied. The model includes the following processes: the growth and shrinking of aerosol particles by water vapor diffusion, the nucleation of drops, the condensation and evaporation of drops, the collision and coalescence of drops as well as impaction scavening of aerosol particles. Regarding the cold microphysics, the freezing of drops in immersion and

*Corresponding author's adress: Karoline Diehl, Institute for Tropospheric Research, Permoserstr. 15, 04318 Leipzig, Germany; E-mail: diehl@tropos.de

contact modes was included as a primary ice forming process, followed by the growth of the frozen drops by the deposition of water vapor, and as a secondary ice forming process the collision between supercooled drops and the formed ice particles. For the present model simulations a two dimensional description of the microphysics was selected which improves the treatment of drop freezing. A one dimensional microphysics is a function of the drop size only. This implies that equal sized drops can contain only equal sized aerosol particles and, thus, show the same freezing behavior. However, in reality equal sized drops can contain different sized particles which may lead to various concentrations of soluble material in the drops and, due to that, to various freezing temperatures of the drops (e.g., Koop et al., 2000). A two dimensional description of the microphysics spans a field of drop and aerosol particle sizes and allows that equal sized drops contain different sized aerosol particles which may lead to different freezing behaviors.

For drop freezing in immersion and contact modes new approaches were used which consider the different ice nucleating efficiencies of various insoluble particles as biological particles (bacteria, leaf litter, pollen), minerals (montmorillonite, kaolinite) and soot particles. They were based on the results of laboratory experiments (Hoffer, 1961; Pitter and Pruppacher, 1973; Levin and Yankofsky, 1983; Diehl and Mitra, 1998; Diehl et al., 2001; Gorbunov et al., 2001, Diehl et al., 2002). For immersion freezing the approach for the freezing rate due to insoluble particles was coupled with the freezing point depression due to the soluble fraction of the aerosol particles (Diehl and Wurzler, 2004). For contact freezing the approach for the numbers of frozen drops was combined with the collision kernel according to Kerkweg et al. (2003). Furthermore, a condition for the dryness of the particles was assumed.

The model simulations were carried out with initial conditions which are typical for biomass burning situations. Two different dry aerosol particle number distributions were selected: for the parcel a young biomass burning aerosol (Helsper et al., 1980), for the environment a haze aerosol (Reid et a., 1998). The vertical profiles were taken from calculations with a regional model for an area in Indonesia with biomass burning (Langmann, pers. comm.). For the present simulations a strongly convective profile was chosen. The soluble fraction of the aerosol particles was set to a value of 0.1. With these inititial conditions several model runs were undertaken: the warm case without drop freezing, the following cases with different insoluble particles. For these cases it was assumed that the insoluble fraction of the particles was of one sort. Immersion and contact freezing were investigated separately first to clarify their different effects, afterwards coupled.

3. RESULTS AND CONCLUSIONS

1. The freezing point depression can be neglected for biomass burning situations because of the low soluble fraction of the aerosol particles. The molalities of the liquid drops which were formed before the onset of freezing were below 0.05 mol/kg. The freezing point depression for solution drops of these concentrations is less than 0.1°C.

2. Drop freezing via immersion or contact modes led to different numbers of ice particles due to the freezing mechanisms. In immersion freezing lower temperatures effected the freezing of more and more drops. Furthermore, the onset of freezing started at significantly different model times, i.e., different temperatures for various insoluble particles. Thus, the numbers of frozen drops were highly dependant on the sort of particles and differed one or two orders of magnitude from each other.

On the other hand, in contact freezing a lower temperature could not effect more frozen drops when a collision between the supercooled drops and the potential ice nuclei was not possible. But the onset of freezing started at rather similar model times and temperatures for various insoluble particles. Therefore, at warmer temperatures the numbers of frozen drops could be higher than in immersion freezing but they did not increase further for lower temperatures.

3. Comparing the liquid and the ice water contents effected by immersion and contact freezing the differences became more evident. In immersion freezing the liquid water content dropped down for biological particles while in turn the ice water content increased what means it came to a glaciation of the cloud by the freezing of liquid drops for biological material only. In contact freezing, however, the liquid water content dropped down, too, while in turn the ice water content increased for all particles. That means that only very small liquid drops remained and indicates that the glaciation of the cloud was ongoing by the transfer of water vapor from the liquid to the frozen drops.

4. These differences in the freezing mechanisms led to different effects on the vertical cloud dy-

namics. In immersion freezing only the biological particles were able to form a sufficient amount of ice to effect the vertical cloud dynamics, in contact freezing this was possible for all particles. In the warm case, the cloud top height reached around 9 km with a temperature of approximately -23°C, for cases including the ice phase the cloud top height could be increased to more than 14 km with temperatures below -40°C.

5. Model simulations with combined immersion and contact freezing showed which process was more important for which particles. In Figure 1 the liquid and frozen drop numbers are given as functions of model time. The cases for the insoluble particles are marked by different linestyles which are labeled in the diagram. Freezing set in at similar model times between 500 and 600 s (corresponding with temperatures between 0 and -10°C) for all particles which was the influence of contact freezing. For later model times between 700 and 800 s (corresponding with lower temperatures between -15 and -25°C) the frozen drop numbers started to increase for the biological particles due to immersion freezing. However, this increase was decelerated by the deposition of water vapor from the liquid drops to the frozen drops so that the liquid drops became smaller requiring lower temperatures for freezing.

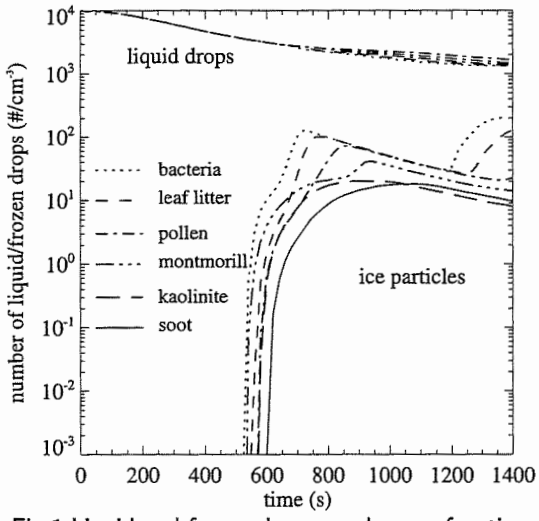

Fig.1 Liquid and frozen drops numbers as function of model time for different cases.

This was reached at model times later than 1200 s (corresponding with temperatures lower than -40°C). Montmorillonite particles which are very efficient in contact but not in immersion freezing benfit from immersion freezing at model times later than 900 s where the frozen drop numbers started to increase, too. Kaolinite and soot particles could not increase the frozen drop numbers at later model times.

As can be seen from Figure 2 where the liquid and ice water contents are given as functions of model time the glaciation of the cloud was established for all particles but at significantly different model times and temperatures between 750 s (corresponding with -15°C) for bacteria and 1200 s (corresponding with less than -40°C) for soot.

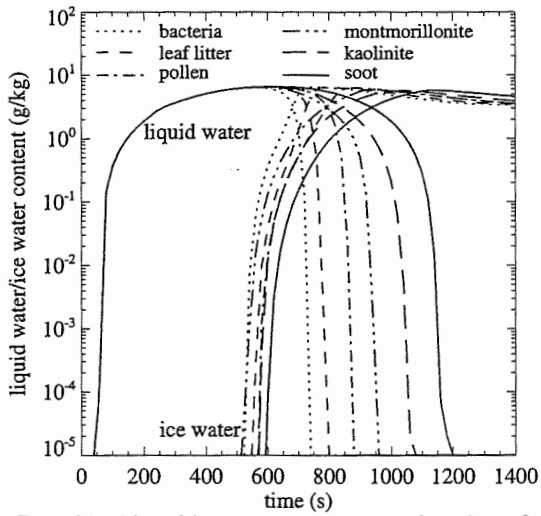

Fig.2 Liquid and ice water contents as function of model time for different cases.

According to the amounts of ice produced by the different particles the vertical updraft of the cloud was accelerated mostly by biological particles and fewest by soot.

6. From these results one can conclude that immersion freezing can be neglected for kaolinite and soot particles whereas contact freezing is dominant for these particles. For biological particles inversely immersion freezing is dominant. For montmorillonite particles both freezing processes are similarly important.

7. These results confirm that the formation of precipitation via the ice phase in biomass burning clouds should be possible. Important for this is the role of the biogenic components of the particles. They could initiate ice formation at rather warm temperatures availing the cloud to reach higher altitudes with lower temperatures where then also other ice nuclei can be active. The Bergeron-Findeisen process can be expected as an essential mechanism

for the formation of precipitation-sized ice particles because of the growth of frozen drops by water vapor deposition.

4. ACKNOWLEDGEMENTS

These studies were supported by the Ministry for Research and Education of the Federal Republic of Germany under the AFO 2000 joint research project EFEU.

5. REFERENCES

Diehl, K., and S. K. Mitra, 1998: A laboratory study of the effects of a kerosene burner exhaust on ice nucleation and the evaporation rate of ice crystals. Atmos. Environ., **32**, No.18, 3145–3151

Diehl, K., S. Matthias–Maser, S.K. Mitra, and R. Jaenicke, 2001: Wind tunnel studies of the ice nucleating ability of leaf litter and pollen in the immersion and contact mode. Proc. EGS XXVI General Assembly, Nice, France.

Diehl, K., S. Matthias–Maser, S.K. Mitra, and R. Jaenicke, 2002: The ice nucleating ability of pollen. Part II: Laboratory studies in immersion and contact freezing modes. Atmos. Res., **61**, 125–133.

Diehl, K., and S. Wurzler, 2004: Heterogeneous drop freezing in the immersion mode: Model calculations considering soluble and insoluble particles in the drops. J. Atm. Sci., in review.

Feingold, G., A. A. Remer, J. Ramaprasad, and Y. J. Kaufman, 2001: Analysis of smoke impact on clouds in brazilian biomass burning regions: an extension of Twomey's approach. J. Geophys. Res., **106**, D19, 22907–22922.

Gorbunov, B., A. Baklanov, N. Kakutkina, H.L. Windsor, and R. Toumi, 2001: Ice nucleation on soot particles. J. Aerosol. Sci., **32**, 199–215.

Guyon, P., B. Graham, J. Beck, O. Boucher, E. Gerasopoulos, O.L. Mayol-Bracero, G.C. Roberts, P. Artaxo, and M.O. Andreae, 2003: Physical properties and concentration of aerosol particles over the Amazon tropical forest during background and biomass burning conditions. Atm. Chem. Phys., **3**, 1951–967.

Helsper, C., H. J. Fissan, J. Muggli, and A. Scheidweiler, 1980: Particle number distribution of aerosols from testfires, J. Atmos. Sci., **11**, 439-446.

Hoffer, T.E., 1961: A laboratory investigation of droplet freezing. J. Meteor., **18**, 766–778.

Koop, T., L. Beiping, A. Tsias, and T. Peter, 2000: Water activity as the determinant for homogeneous ice nucleation in aqueous solutions. Nature, **406**, 611–614.

Kerkweg, A., Wurzler, S., Reisin, T., and Bott, A., 2003: On the cloud processing of aerosol particles: An entraining air parcel model with two-dimensional spectral cloud microphysics and a new formulation of the collection kernel. Quart. J. Roy. Meteor. Soc., **129**, 1–18.

Langmann, B.: Calculations with REMO, MPI Hamburg, Germany, pers. comm.

Levin, Z., and S.A. Yankofsky, 1983: Contact versus immersion freezing of freely suspended droplets by bacterial ice nuclei. J. Clim. Appl. Met., **22**, 1964–1966

Pitter, R.L., and H.R. Pruppacher, 1973: A wind tunnel investigation of freezing of small water drops falling at terminal velocity in air. Quart. J. Roy. Meteor. Soc., **99**, 540–550.

Pruppacher, H.R., and J.D. Klett, 1997: Microphysics of Clouds and Precipitation. 2nd ed., Kluwer Academic Publishers

Reid, J. S., P. V. Hobbs, R. J. Ferek, D. R. Blake, J. V. Martins, M. R. Dunlap, and C. Liousse, 1998: Physical, chemical, and optical properties of regional hazes dominated by smoke in Brazil, J. Geophys. Res., **103**, 32059–32080.

Roberts, G. C., A. Nenes, J. H. Seinfeld, and M. O. Andreae, Impact of biomass burning on cloud properties in the Amazon Basin, Journal of Geophysical Research, **108**, D2, 10.1029/2001JD000985.

Rosenfeld D., 1999: TRMM Observed First Direct Evidence of Smoke from Forest Fires Inhibiting Rainfall. Geophys. Res. Lett., **26**, 3105–3108.

Simmel, M., T.Trautmann, and G. Tetzlaff, 2002: Numerical solution of the stochastic collection equation - Comparison of the linear discrete method with other methods. Atmos. Res., **61**, 135–148.

modeling of diff. ice formation methods

SENSITIVITY OF CONTINENTAL LOW-CLOUDS MICROPHYSICAL PROPERTIES TO CHANGES IN AEROSOL NUMBER CONCENTRATION

R. Dupuy and P. Laj

Laboratoire de Météorologie Physique, OPGC, University of Clermont-Ferrand, France

1. INTRODUCTION

Quantification of the indirect radiative forcing of aerosol on climate through change in cloud number size distribution (better known as the Twomey effect (Twomey, 1991)) is a major source of uncertainty in Global Climate Models (GCM). The present uncertainty is in the range of 0 to -1.5 W m^{-2} and arises mostly from the poor representation of cloud scale processes in GCMs. In particular, the fraction of aerosol particles activated to droplets (CCN) is often derived from semi-empirical relationships between aerosol (or sulphate) mass or number and cloud droplet concentration (Boucher and Lohmann, 1995) or by prognostic relationships between CCN and supersaturation of water vapour. Both approaches commonly tend to overestimate droplet number concentration and do not consider possible artefacts such as the presence of soluble gases or organic material on aerosol particles.

The effect of increased aerosol concentration on cloud microphysics has been documented in a number of studies (Twohy et al., 1995, Leaitch et al., 1992). However, one of the difficulties of relating observed changes in aerosol properties to changes in cloud microphysics and albedo is the implicit assumption that the liquid water path (LWP = cloud liquid water content –LWC- x cloud height –h-) be constant. This assumption is very difficult to control and is seldom verified due to feedback mechanisms affecting cloud height (Ackerman et al., 2000, Han et al., 1998). As a consequence, the ideal methodology to relate change in cloud microphysics to change in aerosol concentration implies performing observations either at constant LWP (Feingold et al., 2003) or at constant height within clouds.

Corresponding author's address: Paolo Laj, LaMP-OPGC, University of Clermont-Ferrand, 24, avenue des Landais, 63177 Aubière Cedex, France, E-Mail: P.Laj@opgc.univ-bpclermont.fr

2. MEASUREMENTS

In this study we observed the relationships between aerosol number concentration (N_{CN}) and cloud effective radius (R_{eff}), commonly used in the parameterization of cloud optical characteristics, at the puy de Dôme cloud station (Central France, 48°N, 2°E, 1465 m asl) during winter and spring of 2000 and 2001. A total of 20 cloud events were analyzed representing a period of more than 250 hours of cloud sampling.

Measurements of total particle concentration (N_{CN}) were performed using a TSI 3010 particle counter (CPC) sampling behind a whole air inlet. The whole air inlet samples both particles and evaporated cloud droplets. The droplet number (N_d) - corresponding to the CCN number concentration N_{CCN} for LWC < 0.5 g.m^{-3} - is derived from a PMS Fast Forward Spectrometer Probe (FSSP). The cloud effective radius (R_{eff}), commonly used in the parameterization of cloud optical properties, is computed directly from the size distribution of droplets.

In addition, a particle volume monitor (PVM Gerber) provides cloud LWC. An additional CPC TSI-3010, connected to an interstitial inlet (50% cut-off = 5µm), measures unactivated interstitial aerosol concentration (N_{INT}). All measurements are performed using a time resolution of 1 Hz. Whole air and RJI inlets have been detailed previously (Sellegri et al., 2003a) and a complete description of the instrumental deployment at the site is provided by Sellegri et al. (2003b). The fraction of aerosols activated to CCNs in clouds (F_{Np}) is derived using N_d and N_{INT} :

$$F_{Np} = \frac{N_d}{N_d + N_{INT} - \Delta N} = \frac{N_d}{N_{CN}}$$

where ΔN accounts for the fraction of droplets smaller than 5µm, as measured by FSSP.

rel° b/n aerosol and cloud # after taking out interstitial aerosol conc^n

3. SAMPLE CLASSIFICATION

Sellegri et al. (2003a) classified the air mass types at Puy de Dôme based on their aerosol mass content and analyses of back-trajectories. In this study, a similar approach using aerosol number concentration leads to a similar classification of air masses corresponding to Modified Maritime (MM) type for N_{CN}< 700 cm^{-3}, Continental (CL) for 700 cm^{-3}<N_{CN}< 2200 cm^{-3} and Polluted (PL) for N_{CN}> 2200 cm^{-3}. Modified Maritime air masses are advected to Puy de Dôme during westerly conditions (distance to the Atlantic Ocean is 500 km) while continental air masses originate from Northern Europe. In contrast, PL air masses correspond to specific conditions where CL air masses are mixed with urban plumes from the large industrial areas of Northern France and Benelux.

To account for the changes of F_{Np} with LWP, we assumed no entrainment of dry air into the cloud. Thus, the lifting of droplets is adiabatic, leading to a linear relationship between LWC and h.. Under this assumption, LWC is indicative of height from the cloud base, and we performed a second sample classification on the basis of the LWC. Four LWC classes are considered: shallow clouds -sampled near the cloud base- for LWC < 0.1 g m^{-3}, medium-thin and medium-thick clouds with LWC values in the range of 0.1<LWC<0.2 g m^{-3} and 0.2<LWC<0.3 g m^{-3} respectively, and thick clouds where LWC> 0.3 g m^{-3}. The two classifications with CN and LWC lead to 12 different categories. Thin clouds forming in PL air masses contain the lowest number of samples, accounting for less than 1 hour of sampling. All other categories are represented by a sampling period of more than 2 hours which reaches 42 hours for the most common category.

4. ANALYSIS

The frequency distributions of the CCN fractions for all 12 categories are presented in Figure 1 showing large variations among categories. The computed F_{Np} values are statistically different (at the 99% confidence level) for each one of the categories. The average aerosol partitioning F_{NP} is calculated for each category and shown in Figure 2. The CCN fraction varies significantly with respect to both LWC and N_{CN}. The positive correlation between N_{CCN} and LWC results from the N_{CCN}-LWC relationship in thin clouds, that is close to cloud base. There, entrainment of sub-saturated air and variability of the super-saturation can lower R_{eff}.

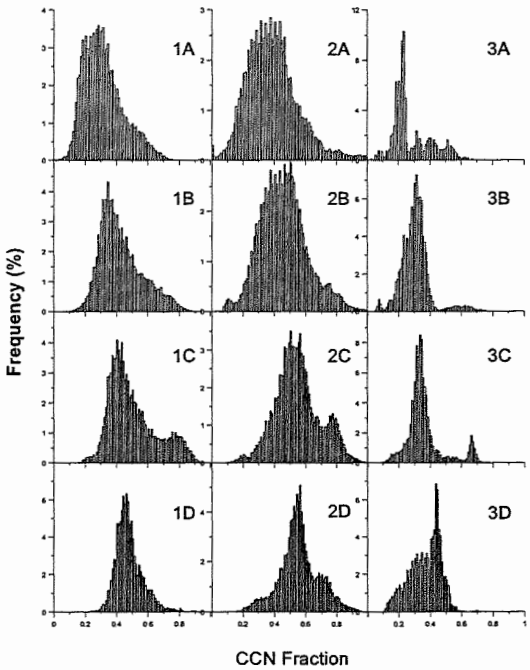

Figure 1 : Frequency distribution of the CCN fraction for the 12 classes of samples: Modified Maritime (1), Continental (2) and Polluted (3) and thin (A), medium-thin (B), medium-thick (C) and thick (D) clouds.

As expected, F_{Np} is the lowest for PL air masses (CCN accounts for 33 ± 11 % of all particles > 10 nm). Surprisingly, F_{Np} is larger during continental conditions (49 ± 16 %) than during MM conditions (40 ± 15 %). These values are in the range of those measured in previous studies (Gillani et al., 1995, Chuang et al., 2000) although direct comparison is rather difficult because very few studies considered the large variety of clouds measured in this study. Such a low scavenged fraction is a direct consequence of the elevated numbers of particles, especially those in the Aitken mode, and of the presence of hydrophobic material onto the aerosols.

Unexpectedly, the CCN fraction is lower for MM air masses than for CL air masses regardless of LWC. This is not seen in any previous studies (Snider and Brenguier, 2000, Gillani et al., 1995, Martinsson et al., 2000). This finding is not the result of the presence of finer particles in MM air masses than in CL air

masses, as indicated by the aerosol size distribution monitored at the station.

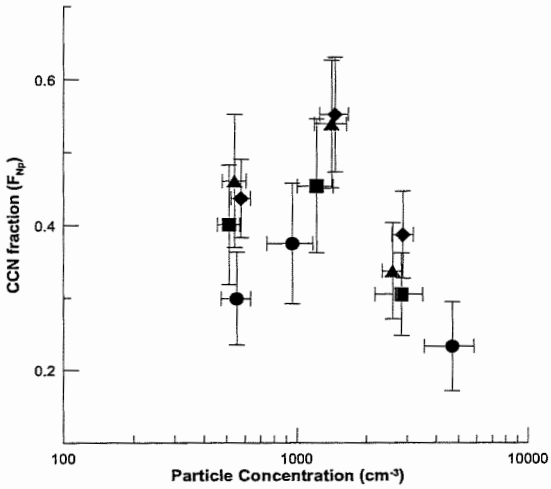

Figure 2 : variations of the CCN fraction of N_{CN} (F_{Np}) as a function of N_{CN} concentration for the 3 classes of air mass types – Modified Maritime (N_{CN}<1000), Continental (1000<N_{CN}<2000) and Polluted (N_{CN}>2000) – and at the 4 heights corresponding to thin (circle), medium-thin (square), medium-thick (triangle) and thick (diamond) clouds. Uncertainties correspond to one standard deviation of the mean.

Instead, it may be a direct consequence of the chemistry of aerosol particles. As mentioned above, MM air masses contain the largest fraction of organic material. We propose that this organic material limits the activation of aerosol particles and, consequently, the number of cloud droplets. This is consistent with Sellegri et al. (2003b) showing that, at Puy de Dôme, the organic particles are poorly scavenged in clouds. The origin of the organic material remains unclear. Recent measurements performed on the marine atmosphere revealed the presence of hydrophobic organic material (M.C. Facchini, personal communication) that could explain the limited particle activation. Another hypothesis, in agreement with Feingold and Chuan (2003), is that particle activation limitation arises from deposition of low-volatility organic material onto aerosol surfaces during the inland advection of marine air masses. This hypothesis is supported chemical analyses of particles showing that the mass fraction of organic matter increases with remoteness of the air mass (40% for MM down to 24% for PL) (Sellegri et al., 2003a)

This limitation has direct consequences for microphysics of clouds as seen in Figure 3. The variations of R_{eff} as a function of N_{CN} concentration at constant LWC have been computed for the four LWC classes. The relationship between R_{eff} and N_d (Raga and Jones, 1993) is also shown on the graph for different values ofLWC. This graph provides a direct estimate of the sensitivity of continental clouds microphysical properties to changes in aerosol number concentration. As expected, R_{eff} decreases with increasing N_{CN} at a rate that is close to that derived using a parameterisation proposed by Raga and Jones (1993) and corresponds, on average, to 2 µm between MM and PL cases. Note that the calculated dR_{eff}/dN_{CN} would have appeared much lower without the sorting of samples with respect to LWC.

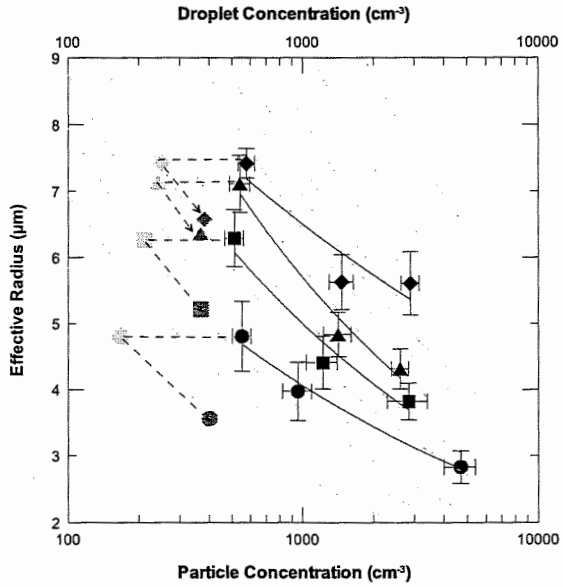

Figure 3: variations of R_{eff} as a function of N_{CN} concentration for the 3 classes of air mass types- Modified Maritime (N_{CN}<1000), Continental (1000<N_{CN}<2000) and Polluted (N_{CN}>2000) – and at the 4 heights corresponding to thin (circle), medium-thin (square), medium-thick (triangle) and thick (diamond) clouds. Iso-LWC are fitted with a power law [$Ln(R_{eff})$= A $ln(N_{CN})$ +B]. Grey lines are the relationship between R_{eff} and N_d at constant LWC for LWC varying from 0.05 mg m^{-3} to 1.8 mg m^{-3} and k=0.71. Light grey symbols correspond to the number of droplets measured in the marine cases while dark grey symbols correspond to number of droplets measured in the marine cases assuming F_{Np}=0.7.

5. CONCLUSIONS

The sensitivity of R_{eff} to change in N_{CN} (dR_{eff}/dN_{CN}) appears to be higher at low N_{CN} values. This is a direct consequence of the limited fraction of particles activated in MM air masses, leading to higher R_{eff} values. In order to quantify the effect of activation limitation on cloud microphysics, we estimated R_{eff} for an ideal Modified Maritime case where 70% of CNs are activated to droplets (F_{Np} = 0.7 at S=1%). Under this assumption, the change in R_{eff} ranges from -0.5 to -1 µm as respect to the measurements in MM air.

The limitation of the number of activated particles, and its subsequent impact on cloud microphysics, is significant. Marine aerosols affected by transport over the continents can lead to enhancement of R_{eff} in clouds. The reduction of N_d as respect to a theoretical marine case (F_{Np}=0.7 and S=1%) leads to the hypothesis that dR_{eff}/dN_{CN} may be higher than expected due mainly to the enhanced availability of CCNs and the (partial) suppression of the activation limitation in CL air masses. It is difficult to assess the regional extent of this effect until the elucidation of the nature of the chemical species involved in hygroscopic growth limitation.

6. ACKNOWLEDGMENTS

Authors acknowledge financial support from CNRS under the PNCA-INSU program, *Ministère de la Recherche et de la Technologie* under ACI-Jeune Cheurcheur to P. Laj, and the scientific council of Région d'Auvergne. Authors wish to thank J.-L Brenguier for useful discussions

7. REFERENCES

Ackerman, A. S., O. B. Toon, J. P. Taylor, D. W. Johnson , P. V.Hobbs, and R. J. Ferek, 2000: Effects of Aerosols on Cloud Albedo: Evaluation of Twomey's Parameterization of Cloud Susceptibility Using Measurements of Ship Tracks. J. Atmos. Sc. 57, 16, 2684-2695.

Boucher, O. and U.Lohmann, 1995: The sulfate-CNN-cloud albedo effect. A sensitivity study with two general circulation models, Tellus, 47B: 281-300.

Chuang, P.D., D., Collins, H. Pawloska, J. Snider, H. Jonsson, J.-L., Brenguier, R., Flagan, J. Seinfeld, 2000: CCN measurements during ACE-2 and their relationship to cloud microphysical properties, Tellus B, 52, 843-867.

Feingold, G. and P.D. Chuang, 2002: Analysis of the influence of film-forming compounds on droplet growth: implication for cloud microphysical processes and climate, J. Atmos. Sci., 59, 2006-2018.

Feingold, G., W. L. Eberhard, D. E. Veron, M. Previdi, 2003: First measurements of the Twomey indirect effect using ground-based remote sensors, Geophys. Res. Lett. 30, 6, 20-1-20-4,

Gillani, N.V., S.E. Schwartz, W.R. Leaitch, J.W. Strapp, G.A. Isaac, 1995: Field observation in continental stratiform clouds: partitioning of cloud particles between droplets and unactivated interstitial aerosols, J. Geophys. Res., 100, D9, 18687-18701,.

Han, Q., W.B. Rossow, J. Chou, and R.M. Welch, 1998: Global survey of the relationships of cloud albedo and liquid water path with droplet size using ISCCP, J. Climate, 11: 1516-1528,

Ji, Q. and G.E.Shaw,. 1998: On supersaturation spectrum and size distributions of cloud condensation nuclei, Geophys., Res. Lett. , 25(11): 1903-1906,

Jones, A., D.L. Roberts, and A.Slingo, 1994: A climate model study of indirect radiative forcing by anthropogenic aerosols, Nature, 370: 450-453,

Leaitch, W.R., G.A. Isaac, J.W. Strapp, C.M., Banic, H.A. Wiebe, 1992: The relationship between cloud droplet concentration and anthropogenic pollution: observation and climatic implication, J. Geophys. Res. , 97, 2463-2474,.

Martin, G.M., D.W. Johnson, and A. Spice, 1994: The measurement and parameterization of effective radius of droplets in warm stratocumulus clouds, J. Atmos. Sci., 51(13), 1823-1854,

Martinsson, B.G., G. Frank, S.-I. Cederfelt, O. H. Berg, B. Mentes, G.Papaspiropoulos, E. Swietlicki, J. Zhou, M. Flynn, K. N. Bower, T. W. Choularton, J. Mäkelä, A. Virkkula, R., Van Dingenen. 2000: Validation of very high cloud droplet number concentrations in air masses transported thousands of kilometers over the ocean, Tellus, 52B(2): 801-814,

McFarquhar, G.M., and A.J. Heymsfield, 2001: Parameterizations of INDOEX microphysical measurements and calculations of cloud susceptibility: applications for climate studies. J. Geophys. Res., 106, D22, 28675-28698,.

Pruppacher, H. R., and J. D. Klett, 1997: Microphysics of clouds and precipitation, Kluwer Academic Publishers, second edition,

Raga, G.B., and P.R. Jonas, 1993: Microphysical and radiative properties of small cumulus clouds over the sea. Quart. J. Roy. Meteor. Soc., 119, 1399-1417,.

Sellegri, K., P. Laj, F. Peron, R. Dupuy, M. Legrand, S. Preunkert, J-P. Putaud, H. Cachier, G. Ghermandi, 2003a: Mass balance of free trospopheric aerosol at the Puy de Dôme (France) in winter. J. Geophys. Res., 108-D11, 4333, doi: 10. 1029/2002JD002747.

Sellegri, K., P. Laj, R. Dupuy, M. Legrand, S. Preunkert, J-P. Putaud, H. Cachier, 1991: Size-dependent scavenging efficiencies of multi-component atmospheric aerosols in clouds. J. Geophys. Res., 108-D11, 4334, doi:10.1029/2002JD002749, 2003b.

Twomey, S., Aerosol, clouds and radiation, Atmos. Envir., 24A(11), 2435-2442.

SMOKE INTERACTIONS WITH CLOUDS

G. Feingold[1], H. Jiang[2] and J. Y. Harrington[3]

[1]NOAA Environmental Technology Laboratory, Boulder, CO 80305, USA
[2]CIRA, Colorado State University/NOAA, Fort Collins, CO 80523, USA
[3]Penn State University, University Park, Pennsylvania, USA

1. INTRODUCTION

The interaction between smoke aerosol and clouds presents interesting challenges from the perspective of aerosol-cloud-radiative feedbacks. Hansen et al. (1997) were the first to show that absorbing aerosol tends to diminish cloudiness. Recent satellite studies support this result by showing that smoky regions in the Amazon tend to be devoid of clouds (Koren et al., 2004). The problem has many interesting facets. From a radiative-dynamic perspective, dense smoke aerosol warms the boundary layer, cools the surface and acts to stabilize the boundary layer. Feedbacks to surface fluxes will also occur. From the microphysical perspective, the very large concentration of drop nucleation sites (order 1,000s - 10,000s cm^{-3}) means that droplets grow in a supersaturation-limited environment and surface-tension, chemical, and kinetic effects may be important in determining their fate. For example, Feingold et al. (1991) predicted that at sufficiently high aerosol loadings, large droplets may grow at the expense of smaller ones because small droplets don't have sufficient soluble material to survive. In addition, absorbing aerosol embedded inside droplets tends to evaporate them. Therefore, although there seems to be strong evidence for reduced cloudiness in regions of heavy loading of absorbing aerosol, the relative importance of the various processes involved is still not clear. To address this we have modified our large eddy simulation (LES) model to incorporate all of the abovementioned processes. Here we present a model description and first results. In our conference presentation we will focus on the feedbacks between the microphysical, dynamical and radiative components and attempt to delineate the primary reasons for smoke suppression of clouds.

2. MODEL DESCRIPTION

The model is a large eddy simulation based on the Regional Atmospheric Modeling System but with numerous changes and additions (e.g., Feingold and Kreidenweis, 2002). It includes a size-resolved representation of aerosol and cloud drops; aerosol are resolved in 14 size-bins over the range 0.04 μm; 7 μm with both mass and number calculated in each bin. Similarly, drops are resolved into 25 size-bins, with drop mass, drop number, as well as aerosol mass accounted for in each bin (Feingold et al. 1996). This configuration requires prognostic equations for 104 scalars. The model includes an 8-band coupled radiation model (Harrington et al. 2000). For the purposes of this study, the model has been upgraded to include the effects of a radiatively-active aerosol. Smoke aerosol particles are assumed to consist of a mix of soot and ammonium sulfate. Their optical properties (extinction and single scattering albedo ω_0) are calculated based on this composition and the ambient relative humidity. For the case to be presented ω_0 is about 0.90 at a wavelength of 0.47 μm. Off-line calculations for water vapour uptake by particles are performed assuming an 85% insoluble/15% ammonium sulfate mix (D. Collins, personal communication) and stored for access during simulations. Particles are assumed to be at equilibrium with their environment, except for the largest particles (> 0.1 μm) which are at 0.97 of their equilibrium sizes. Heating rates associated with smoke aerosol embedded inside droplets are calculated based on Conant et al. (2003) and these are coupled to the condensation/evaporation equation and the equation for prediction of supersaturation following Harrington et al. (2000). For completeness, Kelvin and solute corrections to the supersaturation field experienced by droplets are also included. These terms can become important at extremely large aerosol loadings when cloud supersaturation is low.

It should be noted that the microphysical details of smoke aerosol transition to droplets can be studied in greater detail using a Lagrangian parcel model (Feingold et al. 2001) but the latter is not able to represent the dynamical/radiative feedbacks as in the LES. The current model strives to represent the various dynamical, microphysical and radiative components with reasonable balance.

3. RESULTS

The simulation is initiated using a sounding based on one measured on September 26th 2002 at 15:00 UTC in Ji Parana (Fig. 1) during the Smoke, Aerosols, Clouds, Rainfall and Climate (SMOCC) field

Corresponding author's address: Graham Feingold, NOAA Environmental Technology Laboratory, Boulder, CO, 80305, USA; E-Mail: graham.feingold@noaa.gov.

need to add dependence of aerosol optical properties on relative humidity

do I need to add an effect of condensation on the calculations that are performed.

What sort of temperature perturbation is added in?

Do I need to add in temporal evol^n of aerosol?

experiment in Brazil. The large eddy simulation is set up with a domain size of 5600 m in the horizontal and 3500 m in the vertical. The horizontal grid size is 80 m and the vertical grid is 50 m. Both 2-d and 3-d simulations have been performed but only 2-d simulations will be presented here. The model is initiated with a random temperature perturbation at the first time step with a maximum/minimum of +/- 0.2°. Surface fluxes are fixed for the duration of the 4 hour simulation; the sensible heat flux is 90 Wm^{-2} and the latent heat flux is 250 Wm^{-2}. The sounding produces small cumulus clouds of between 500 m and 1000 m depth. Cloud bases are at approximately 1300 m. Cloud liquid water paths are on the order of 100 gm^{-2} (but as high as 700 gm^{-2}) for individual clouds; domain averaged values vary from ~ 30 g m^{-2} to 300 g m^{-2}.

The initial smoke aerosol profile has a lognormal distribution with number concentration N_a = 2000 cm^{-3}, median radius r_g=0.1 mm and geometric standard deviation σ = 1.5. The profile is constant in the first 1000m, and thereafter drops exponentially to 200 cm^{-3} at 3000m. The total aerosol optical depth (dry) is ~0.25.

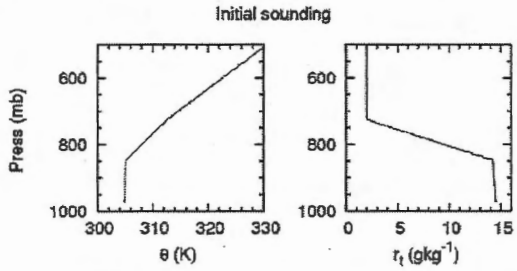

Figure 1: Initial potential temperature θ and total water vapour mixing ratio r_t profiles used for simulations

3.1 Base case and sensitivity simulations

We present a "base case" simulation for which aerosol is not allowed to interact with radiation, i.e., the aerosol is inert, except with regards to its interaction with the clouds. We then compare a simulation which does allow the aerosol to interact with the radiation by changing the atmospheric profile of heating rates.

Figure 2 shows time series of a number of domain averaged fields including domain averaged LWP (cloudy and cloud free areas), maximum root-mean-square velocity, cloud top and cloud fraction. Starting from a quiescent atmosphere, it takes about 50 min for turbulence to develop and for clouds to form. Cloud top varies significantly, depending on the height of penetrating convection. The first cloud event is remarkably similar in both cases. By the second cloud event (t~110 min) the simulations begin to differ; the sensitivity run has higher LWP, but lower cloud fraction. By the third main convective event the differences are much more marked. For the base case, we notice a strong convective event at about 180 min but only a weak event in the sensitivity run at ~ 215 min. Cloud fraction is approximately 30% for the base case but noticeably reduced for the sensitivity run for most of the 4 h simulation. Similar tests were performed for varying input conditions (aerosol profiles and ω_b. In all cases the same trend for reduced cloud

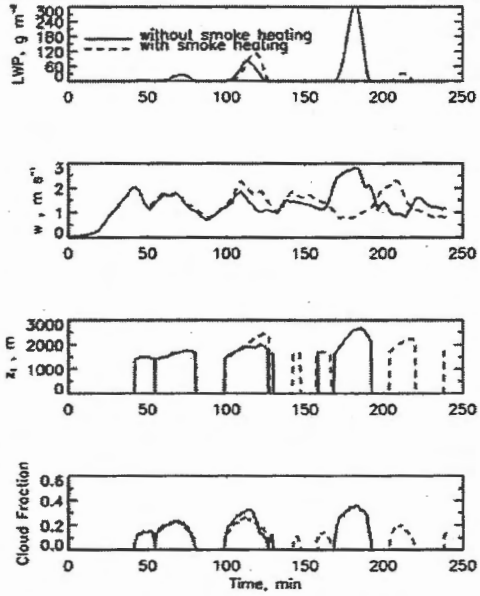

Figure 2. Time series of various parameters for the base case (without smoke heating) and the sensitivity run (with smoke heating): (a) domain averaged liquid water path LWP, (b) w, a measure of turbulence, (c) cloud top, z_t, and (d) cloud fraction.

fraction was observed, particularly at lower ω_b.

3.2 Heating Rate profiles

Analysis of the domain averaged profiles of heating rates reveals typical profiles associated with cloudy boundary layers, with warming through the boundary layer and a vertically confined cooling at cloud top (Figure 3). The absorbing aerosol in the sensitivity study generates higher heating rates throughout the boundary layer.

typical

3.3 Convective Pumping of Smoke

Figure 4 shows a comparison between the initial profile of smoke and the profile after 200 min for the base case simulation. The figure shows how the deepening boundary layer, aided by clouds has removed the strong gradient in smoke evident in the initial profile and transported a significant amount of smoke to heights above 2000 m (see also Andreae et al. 2004). We note that at these high aerosol

see how aerosols change depending on process

better job of treating 1st & 2nd indirect effect

simul^ns where aerosols interact and are not allowed to interact

concentrations, precipitation does not form so that the reduction in aerosol in the lowest 1000 m is purely due to convective redistribution. We also note that the ability of the model to track aerosol particles within drops and then regenerate them upon evaporation enables us to depict the convective transport of aerosol in a realistic manner.

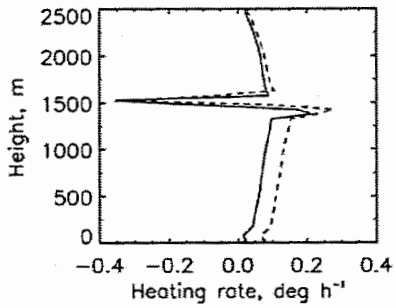

Figure 3. Domain-averaged heating rate profiles for base case (solid line) and sensitivity run (dashed line).

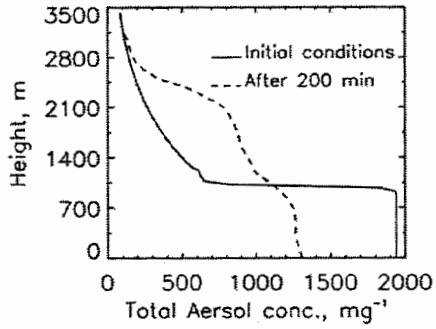

Figure 4. Domain-averaged smoke concentration profiles: initial conditions (solid line) and base case after 200 min (dashed line).

4. Discussion and Summary

We have presented first results of smoke interaction with clouds in a coupled large eddy simulation. The model includes size resolved treatment of aerosol and cloud microphysics, tracking of aerosol inside droplets, and a radiatively-active aerosol that feeds back to model dynamics. These initial simulations show that:

- Absorbing aerosol tends to suppress cloudiness. Cloud fractions in all simulations that include coupling of the effects of absorbing smoke particles are reduced relative to simulations that neglect this coupling;
- Heating rate profiles associated with the absorbing aerosol in the cloudy boundary layer are in agreement with the calculations of Koren et al. (2004)
- Small convective clouds are very effective at redistributing smoke to the free troposphere.

We note that the suppression of cloudiness occurred in these simulations even though the surface fluxes were fixed. In reality, surface fluxes will change in response to the smoke. Future work will examine more closely the relative importance of surface fluxes, as well as the various other parameters affecting cloud evolution in the presence of thick smoke.

5. Acknowledgements

We thank a NASA Interdisciplinary Science grant for supporting this work.

6. References

Andreae, M. O., D. Rosenfeld, P. Artaxo, A. A. Costa, G. P. Frank, K. M. Longo, M. A. F. Silva–Dias, 2004: Smoking rain clouds over the Amazon. *Science, 303, 1337-1342.*

Conant, W. C., A. Nenes, and J. H. Seinfeld, 2002: Black carbon radiative heating effects on cloud microphysics and implications for the aerosol indirect effect 1. Extended Köhler theory. *J. Geophys. Res.*, **107**, 4604, 10.1029/2002JD002094

Feingold, G., S. M. Kreidenweis, B. Stevens, and W. R. Cotton, 1996: Numerical simulation of stratocumulus processing of cloud condensation nuclei through collision-coalescence. *J. Geophys. Res.*, **101**, 21,391-21,402.

Feingold, G., L. A. Remer, J. Ramaprasad, and Y. Kaufman, 2001: analysis of smoke impact on clouds in Brazilian biomass burning regions: An extension of Twomey's approach. *J. Geophys. Res.*,**106**, 22,907–22,922.

Feingold, G., and S. M. Kreidenweis, 2002: Cloud processing of aerosol as modeled by a large eddy simulation with coupled microphysics and aqueous chemistry. *J. Geophys. Res.*, **107**, 4687, doi:10.1029/2002JD002054.

Hansen, J., M. Sato, and R. Ruedy, 1997: Radiative forcing and climate response *J. Geophys. Res.*, **102**, No. D6, p. 6831.

Harrington, J. Y., G. Feingold, and W. R. Cotton, 2000: 2000: Radiative impacts on the growth of a

population of drops within simulated summertime Arctic stratus. *J. Atmos. Sci.*, **57**, 766-785.

Koren, I., Y. J. Kaufman, L. A. Remer, and J. V. Martins, 2004: Measurement of the effect of Amazon smoke on inhibition of cloud formation, *Science*, **303**, 1342-1345.

need to consider effect of clouds on aerosol?

INVESTIGATION OF THE ICE NUCLEATION ABILITY OF TWO DESERT DUST AEROSOL SAMPLES AT -50C

P. R. Field[1], R. J. Cotton[1], O. Möhler[2], M. Schnaiter[2], M. Krämer[3], P. Connolly[4], A. J. Heymsfield[5]
1. Met Office, Exeter, UK. 2. Forschungszentrum Karlsruhe, IMK-AAF, Karlsruhe, Germany 3. Forschungszentrum Julich, ICG, Jülich, Germany 4. UMIST, Manchester, UK 5. NCAR, Colorado, USA

1. INTRODUCTION

The accurate representation of ice cloud in numerical weather and climate models relies upon a quantitative understanding of the ice nucleation process. In September 2003 a campaign carried out at the AIDA cloud chamber facility in Germany investigated the nucleation of ice on re-dispersed dust samples taken from Asia and the Sahara.

The AIDA was instrumented with a suite of pressure, temperature, water vapour and optical scattering instrumentation as well as optical particle counting probes including a small ice detector (SID), cloud particle imager (CPI) and video ice particle sampler (VIPS).

In this contribution we will present observations from cloud chamber expansions carried out at -50C where two distinct ice nucleation events were repeatedly observed to occur at two discrete ice supersaturations on subsequent expansions for both of the dust samples considered.

2. GENERAL METHOD

The cylindrical AIDA aerosol vessel is 7m high and 4m in diameter. The aerosol chamber is located within a larger chamber that acts as a thermal buffer and provides control of the initial temperature within the aerosol vessel. A fan within the aerosol vessel ensures well mixed conditions with sample temperatures within the volume agreeing to 0.3K

Ice nucleation experiments are started just below ice saturation inside the aerosol chamber. This is achieved by cooling the chamber to 273K, evacuating the vessel to 0.01 hPa, flushing twice with synthetic air, adding water vapour and filling the vessel to atmospheric pressure with synthetic air. Finally, the vessel is cooled to the starting temperature of the experiment.

To simulate the adiabatic cooling of rising air parcels the pressure within the chamber is reduced with a rate controllable mechanical pump from 1000 hPa to 800 hPa over typical pumping periods of 5 minutes. The cooling in the aerosol vessel is not purely adiabatic: the aerosol vessel wall temperatures remain approximately constant throughout the expansion and as a consequence there is a heat flux from the vessel wall into the chamber. Similarly, during the cooling the vapour pressure above the ice on the wall is greater than the vapour pressure in the chamber and a vapour flux into the chamber also occurs.

Before the candidate aerosol is added to the chamber a control run is made with the background conditions in the chamber. Once complete the candidate aerosol is added and then characterised with standard aerosol sampling intrumentation. Several expansions are carried out on the same candidate aerosol sample at different pump speeds (cooling rates) throughout the course of a day. More details about the AIDA chamber and the experimental procedures can be found in Möhler et al. (2003).

3. EXPERIMENTS AT -50C

Two samples of desert dust obtained from Asia and the Sahara were used. The samples were dry re-dispersed producing aerosol distributions with a size range between 0.2 and 2 μm. Several expansions were carried out on each sample using different cooling rates. Figure 1 and 2 show a compilation of results from two experiments using the two samples. In the top panel the gas temperature within the chamber shows a cooling of 6C over the course of the expansion. The second panel shows the gas pressure in the chamber and decrease is equivalent to a vertical motion in the atmosphere of 3.5 m s^{-1}. In the third panel particle size from the Small Ice Detector (SID) and the Droplet Measurement Technologies Cloud Droplet Probe (CDP). In particular the SID data show the growth of particles at two distinct times during the expansion: 60s and 210s. The CDP mean size is in agreement with the SID data showing an initial increase in size associated with the first nucleation event followed by a decrease in the mean size as many more smaller ice crystals are formed during the second nucleation event. The fourth panel shows the ice concentrations during these events indicating two step-like increases: a small increase for the first event and a much larger one for the second event. The final panel shows the relative humidity with respect to ice (RHi) and water (RHw) estimated from a Tunable Diode Laser hygrometer. This data suggest that the first and second nucleation events occurred when the chamber was at ~105% RHi and ~85% RHw, respectively. We have identified the onset of ice nucle-

[1] Corresponding author: Paul Field, Met Office, FitzRoy Road, Exeter, Devon, EX1 3PB, UK.

desert dust shows 2 distinct nucleation modes in cloud chamber experiments

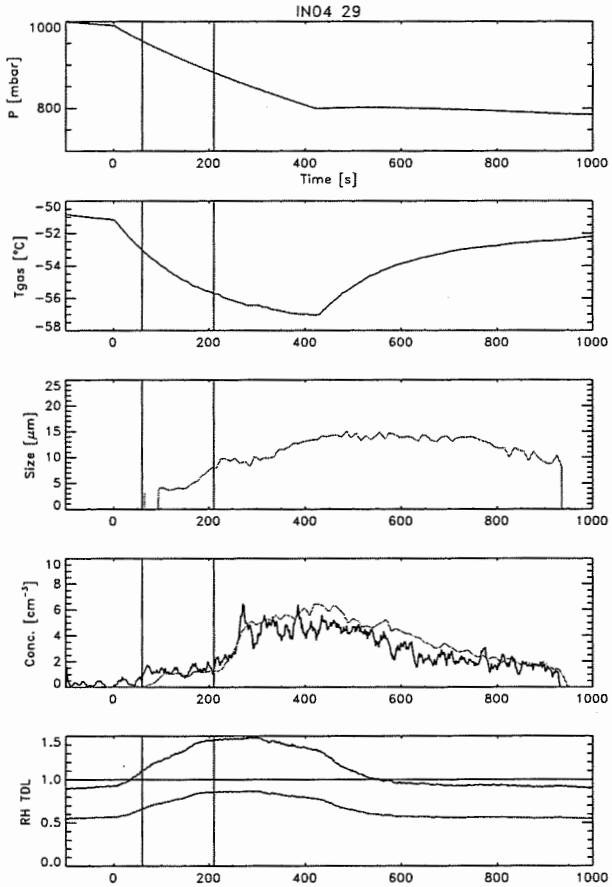

Figure 1: Experiment 29 using Asian dust. Top panel: gas pressure in the aerosol vessel. 2nd panel: gas temperature in the aerosol vessel. 3rd Panel: Particle sizes detected by SID (dots) and a mean particle size detected by the CDP (grey line). 4th panel: particle concentrations from SID (black) and the CDP (grey). Relative humidity estimated from a Tunable Diode Laser hygrometer. The upper line is RHi and the lower line is RHw. The vertical lines in each plot represent the onset of the first and second nucleation mode.

ation for the other experiments carried out with these aerosols at -50C. The actual point at which ice nucleation occurs is subject to some uncertainty which we estimate to be ±5%. The uncertainty arises from the time picked to represent the onset of ice nucleation. Relative humidities were also estimated from a cooled mirror device (MBW) that measures vapour plus condensed water and so will become unreliable when the ice water content becomes significant. These are preliminary data and we hope to reconcile them and reduce the uncertainty in the near future. Nevertheless, the results show that the TDL indicates the first nucleation event for both aerosols to occur between 3 and 13% supersaturation with respect to ice (9 and 22 % for the MBW) and is well below water saturation. The TDL indicates that the second ice nucleation event takes place at between 81 and 86% RHw (86 and 92% for the MBW) or around 140% RHi.

Initial aerosol concentrations for these experiments were 25 (29) and 32 (42) cm^{-3} The maximum concentration of ice crystals formed is ~20±5% of the initial aerosol concentration. From the slowest expansions the deposition nuclei represent ~6% of the aerosol population for the Asian dust sample and ~2% for the Saharan dust sample.

Experiments at other temperatures were also carried out during this campaign and are reported on in this issue by Möhler et al.(2004).

4. INTERPRETATION

First of all we assume that the first nucleation event is deposition ice nucleation for both aerosols. Deciding upon the cause of the second nucleation event is more difficult and we have to choose between two

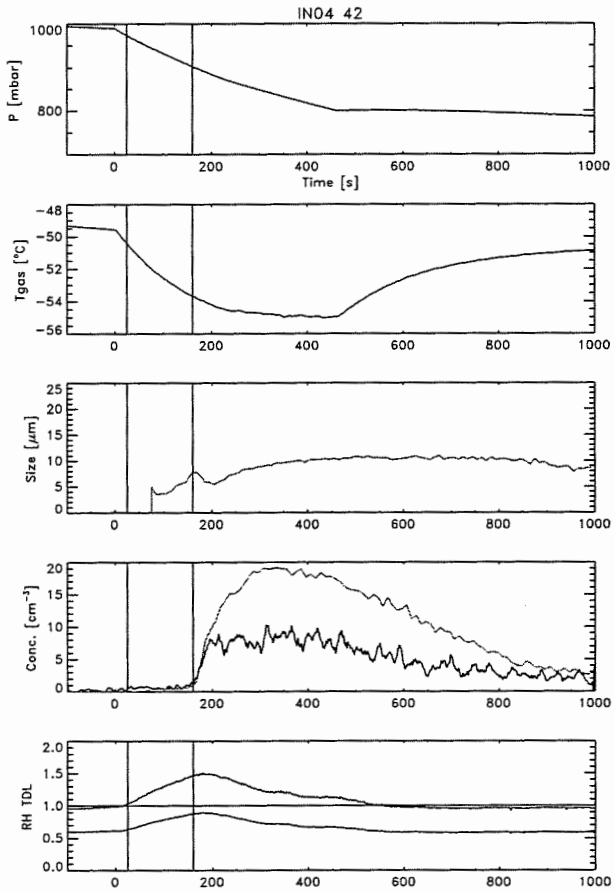

Figure 2: Experiment 42 using Saharan dust. Top panel: gas pressure in the aerosol vessel. 2nd panel: gas temperature in the aerosol vessel. 3rd Panel: Particle sizes detected by SID (dots) and a mean particle size detected by the CDP (grey line). 4th panel: particle concentrations from SID (black) and the CDP (grey). Relative humidity estimated from a Tunable Diode Laser hygrometer. The upper line is RHi and the lower line is RHw. The vertical lines in each plot represent the onset of the first and second nucleation mode.

possibilities: i) a second deposition mode at 140% RHi; ii) homogeneous freezing of haze formed on hydrophylic sites on the dust particles. It seems unlikely that two seperate dust samples should both display dual deposition nucleation activity at the same critical humidities, but we are not able to fully reject this hypothesis. Instead we have used a parcel model to investigate the homogeneous freezing of haze hypothesis. The model used is a modified adiabatic parcel model that includes heat and vapour fluxes from the AIDA aerosol chamber walls and is described in more detail in this issue by Cotton et al. (2004). Figure 3 shows a comparison between the model and observations from an experiment using the Asian dust sample. The model has been forced to produce ice by deposition nucleation at 105% RHi up to a maximum concentration of 2 cm^{-3} to reproduce the first nucleation event. The second nucleation event is due to homogeneous nucleation of haze. In the model we specified a size distribution for the haze forming ammonium sulphate particles which were allowed to grow and eventually freeze. An initial log-normal ammonium sulphate size distribution with a dry mode radius of 7 nm, a width of $\sigma = 1.8$ and a concentration of 30 cm^{-3} was used. The model reproduces the humidity trajectory and both the ice concentrations and particle sizes throughout the experiment, comparing well with the SID and CDP data. The success of the modelling suggests that the second nucleation mode through homogeneous freezing is a realistic possibility. However, it should be noted that the dust particles in the aerosol chamber are much larger than the ammonium sulphate distribution used in the model. This would imply that any soluble matter would likely exist

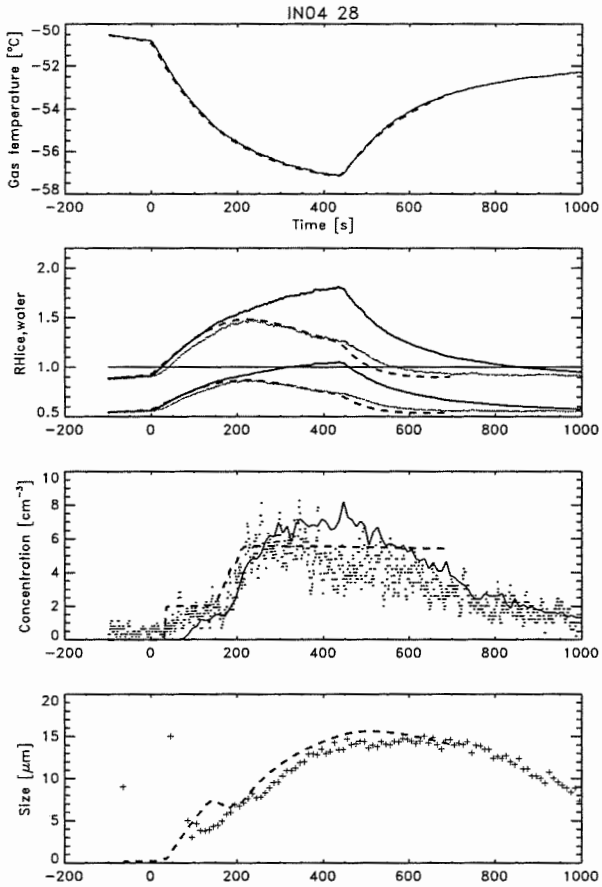

Figure 3: Results from a modified adiabatic parcel model. Top panel: gas temperature (solid) and model temperature (dashed). 2nd panel: relative humidity from the tunable diode laser hygrometer (black solid), a cooled mirror device that measures vapour+condensed water (grey) and the model value (dashed). The upper curves are RHi and the lower curves are RHw. 3rd panel: ice particle concentrations from the SID (black solid), the CDP (grey) and the model (dashed). Bottom panel: particle sizes from SID (dots) a mean particle size from the CDP (+) and a mean particle size from the model (dashed).

as discrete sites on the larger dust particles.

5. CONCLUSION

The AIDA cloud chamber has been used to investigate the nucleating ability of dust from Asia and the Sahara at -50C.

Two discrete nucleation events at different critical relative humidities were observed for both dust samples.

For both dust samples, the first nucleation event at ~105%RHi is thought to be deposition ice nucleation.

For both dust samples, the second nucleation effect could be explained by homogeneous freezing of haze forming at hydrophylic sites on the dust, but a second deposition nucleation mode cannot be yet ruled out.

6. REFERENCES

Cotton R. J. et al. Parcel modelling of ice nucleation in AIDA. Conf. Proc., ICCP, Bologna, 2004.

Möhler O., Stetzer O., Schaefers S., Linke C., Schnaiter M., Tiede R., Saathoff H., Krämer M., Mangold A., Budz P., Zink P., Schreiner J., Mauersberger K., Haag W., Karcher B. and Schurath U., 2003. Experimental investigation of homogeneous freezing of sulphuric acid particles in the aerosol chamber AIDA. Atmos. Chem. Phys., 3, 211-223.

Möhler O. et al. Formation, growth, and habit of ice crystals nucleated on desert dust aerosol. Conf. Proc., ICCP, Bologna, 2004.

PRECIPITATION INFLUENCE ON PARTICULATE MATTER DISPERSION IN COSENZA (ITALY)

M.Filice[1], P.De Luca[1], A. Nastro[1]

[1] Dipartimento di Pianificazione Territoriale, Università degli Studi della Calabria, Arcavacata di Rende - 87036 Rende (CS),Italy.

1.INTRODUCTION

Particulate matter in atmosphere has been studied to determine urban and environment impact [4]. The evaluation of pollution on urban environment is a very interesting tasks due to possible relations between the increase of the cardiovascular illness and the high density of vehicular traffic [3]. Recently epidemiologic studies have found out an association between particulate matter concentration and negative effects on the health [5].

The actual normative [2] considers particulate matter as particles with a diameter lower than 10 micrometers (PM10) or lower than 2.5 micrometers (PM2.5). The penetration of particles in the human body can favour rising up of the respiratory illness [1].

The particulate matter concentration is an important parameter to evaluate the degree of typical urban pollution and to determine strategies of reduction of the polluted emissions.

Effective methods for removing particulate matter have not been devised so far, but different studies have shown that the analysis on the meteorological parameters permits to evaluate the processes of dispersion and reduction of the pollution.

The aim of this work is to study the effect of the meteorological parameters, in particular rainy precipitation, on the dispersion of the PM10. Moreover, the particulate matter need to be investigated, also in the presence of rain, by chemical-physics techniques, such as Electronic Microscopy (SEM) and Atomic absorption (A.A.).

Corresponding author's address: Pierantonio De Luca, Dipartimento Pianificazione Territoriale- Università degli Studi della Calabria- Arcavacata di Rende- 87036 Rende- (CS) Italy;
Email: p.deluca@unical.it

2. EXPERIMENTAL

2.1 Analysis of the Zone

The area monitored is Cosenza, a urban centre of the south Italy. It is a middle-small city with 100.000 inhabitants. It is characterized by numerous commercial activities and by a middle volume of vehicular traffic that reaches peaks in nearness of the opening and closing of the commercial activity. Indeed the air pollution in Cosenza is mainly due to vehicular traffic.

This city is located in the centre of a valley surrounded by a mountainous chain, called Sila. In condition of calm of the wind and in absence of rainy precipitation there are static conditions that hamper the dispersion of the pollution and especially of the particulate matter.

2.2 Sampling

Generally, there are two methods used to investigate the degree of urban pollution: models and measures. This study treats a series of measures computed in open air performance.

Particulate matter sampler and the container devoted to picking up rain were situated at height of about 3 m, nearby an area used as public parking in the centre of the city. Simultaneously samples of particulate and rain were picked up both in sunny days and in rainy days, with an interval of 11 hours.

The sampling was effectuated by a vacuum pump. The breathed air passes through a filter of middling cellulose ester (MCE) with a rate of 20 lit./min. The rain samples, reported as mm/m^2, were picked up exploiting a cylindrical container with a diameter of 10 cm. Meteorological data, in synoptic scale, were acquired by national meteorological service.

2.3 Analytical Techniques

influence of rain on removing particulate matter

To characterise the particulate reduction during the rain precipitation it is necessary to consider two parameters: the concentration of particulate and their chemical composition [8].

The concentrations of particulate were obtained by gravimetric methods that expected a double weighing and a double conditioning of the filters [7]. The conditioning was performed treating the filters for two hours and at 100°C; subsequently filters were subjected to a dryer for another two hours. The filters were weighed before and after exposure. The morphology and the size of the particulate were studied by Electron Microscopy (SEM) JEOL Stereo Scan 360 [6]. The presence of some elements was investigated by atomic absorption SHUMADZU AA-660. The rain samples were measured and reported as function of particulate matter.

3. RESULTS AND DISCUSSION

3.1 Particulate Matter and Rain Relationship

11-hours samplings were conducted in different periods during the autumn 2002. They were carried out in working days, with and without rain and in condition of low wind. This method was used to reduce the influence of the traffic variable and the wind in the processes of particulate dispersion.

The sampling without rain was carried out to evaluate the weekly average concentration during the autumn. The sampling in rainy days permitted to determine the relations between rainfall and particulate matter concentration (see figure 1).

Table 1 shows some statistic parameters of PM concentration values. We observe that in rainy days particulate concentration decreases about the 70% with respect to the typical middle of the period. The higher the amount of rain (mm/m^2), the lower the particulate concentration. Moreover, there are peaks of concentration in days without rain.

	Max	Min	Average	Standard dev.
Sunny days	127.91	71.86	25.45	94.07
Rainy days	57.42	12.41	16.37	30.13

Table 1 - Statistical parameters of PM concentration values (μg/m^3) in autumn 2002.

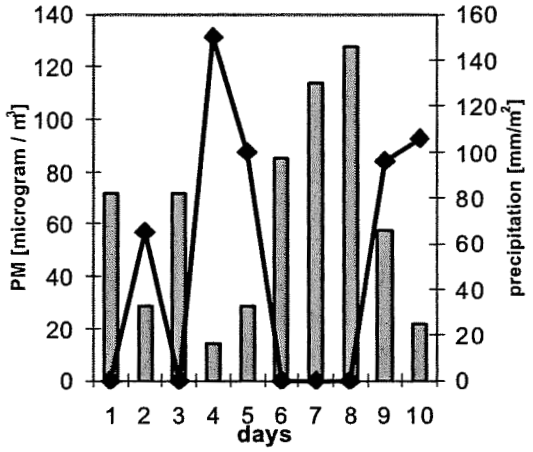

Figure 1 - Particulate matter concentration and rainfall relationship during autumn 2002.

3.2 Size Ditributions

The analysis carried out by electronic microscopy (SEM) shows the presence of a substrate with size about 1 micrometers and named PM1. On this substrate particels are visible with size mayor and named PM10 and PM2.5.

Figure 2 and figure 3 show the distribution of particulate in sunny and rainy days respectively. The amounts of PM10 and PM2.5 increase in rainy days.

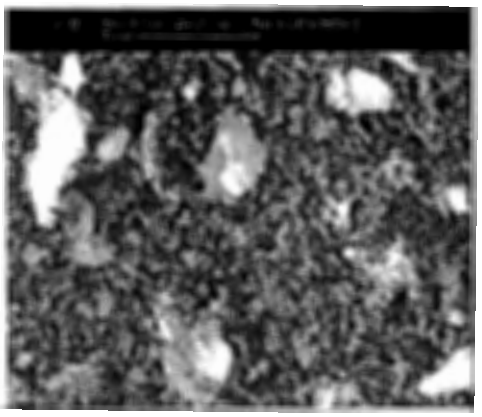

Figure 2 - An example of micrograph of MCE filter in sunny day.

Figure 4 and figure 5 show the density of PM10 and PM2.5 both in sunny days and in rainy days. This density was determined by an electronic microscopy and by counting the particles of PM10 and PM2.5 on an area of a filter of 926 μm^2.

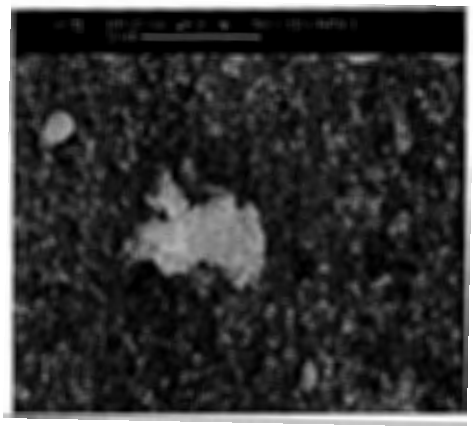

Figure 3 - An example of micrograph MCE filter in a rainy day.

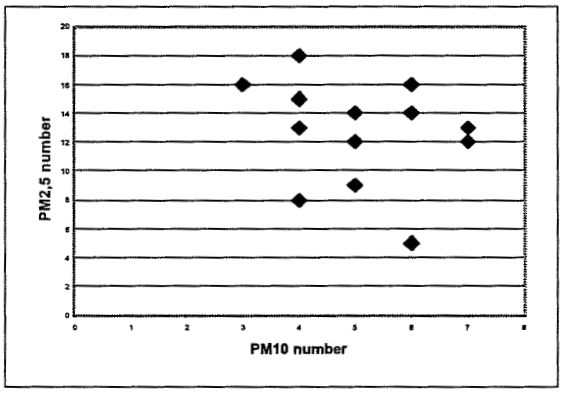

Figure 4 - Density PM10/PM2.5 on area of 926 μm^2 in a sunny day.

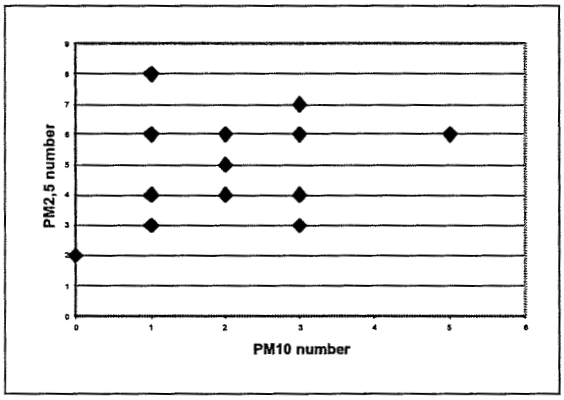

Figure 5 - Density PM10/PM2.5 on area of 926 μm^2 in a rainy day.

3.3 Chemical Composition

The particulate in atmosphere can contain toxic matters that represent a real problem for public health [10]. Element and metal found in traces represent a non negligible factor, thus they have to be monitored continuously.

Since the samples have a low weight, i.e. a few micrograms, methods having high sensibility and precision are needed. The atomic absorption conjugates these requirements [9].

To carry out analysis by atomic absorption different solutions were prepared by first destroying the filter of cellulose with few drops of sulphuric acid (98%) and 2.5 ml of nitric acid (65%). The resulting solution was heated to remove exceeding traces of acid, and subsequently it was take to a given volume.

Table2 reports the concentration of some elements in the samples collected. We observe that the proportion of some element on total weight sample is more low in rainy days.

Element	Sunny days [%]	Rainy days [%]
Na	23	12.4
K	3.79	3.79
Fe	2.24	3.64
Ca	19.44	16.04

Table 2 - Comparison of some elements on total weight sample.

4. CONCLUSION

Experimental results have shown that rain affects both the concentration and the nature of particulate matter in atmosphere. In particular, in rainy days, the concentration of both PM2.5 and PM10 decrease, but the latter decreases more rapidly. Moreover, we have observed a chemical variation in rainy days, and that amount of precipitation and chemical/physical particulate characteristics are strictly related.

5. REFERENCES

[1] Baeza-Squiban S., Bonvallot V., Boland S., Marano F., 1999: Airborne particles evoke an inflammatory response in human airway epithelium. Activation of transcription factors. Cell Biology and Toxicology; 15, 375-380.

[2] European Council 1999: Air quality daughter directive 1999/30/CE .

[3] Grima R., Micaleff A., Colls J., 2001: External contribution to urban air pollution, Environment Monitoring and Assessment 73, 291-314.
[4] Harrison R.M.,Ping Shi J., Jones M.R, 1999: Continous mesaurements of aerosol physical properties in the urban atmosphere, Atmospheric Environment, 33, 1037-1047.
[5] Izzotti A., Parodi S., Quaglia A., Farè C., Vercelli M., 2000: The relationship between urban airborne pollution and short-term mortality: Quantitative and qualitative aspects, European Journal of Epidemiology, 16, 1027-1034.
[6] Keywood M.D., Ayers G.P., et al., 1999: Relationship between size segregated mass concentration data and ultrafine particle number concentration in urban areas, Atmospheric Environment, 33, 2907-2913.
[7] Marcazzan G.M., Vaccaio S., Valli G., Vecchi R.,2001: Characterisation of PM10 and PM2,5 particulate matter in the ambient air of Milan (Italy), Atmospheric Environment, 35, 4639-4650.
[8] Raes F., R.Van Dingenen R.,Putaud J.P., Physical and chemical characteristics of particulate matter in urban, rural and background conditions in Europe, 2000: Workshop on particulate matter.
[9] Rizzio E., Gravieri G., Gallarini M., 2000: Some analytical problems ancountered for trace elements determination in the airborne particulate matter of urban and rural areas, The Science of the Total Environment 256, 11-22.
[10] Sègala C., Healtth effect of Urban Outdoor Air Pollution in children. Current Epidemiological Data, 1999: Pediatric Pulmonology, Supplement 18:6-8.

THE ROLE OF THE AEROSOL PARTICLE CHARACTERISTIC ON DRIZZLE FORMATION

I. Geresdi[1] and R. M. Rasmussen[2]

[1]University of Pecs, Hungary
[2]National Center for Atmospheric Research, Boulder, CO USA

1. INTRODUCTION

It is becoming increasingly evident that aerosol particles play an important role in the processes leading to precipitation formation. A number of studies have shown that the chemical composition and size distribution of the aerosol particles are important to the number and size of cloud droplets activated from cloud condensation nuclei (CCN) in a cloud, which in turn has an impact on the formation of precipitation (e.g. French et al., 2000). Bulk microphysical schemes typically do not simulate the activation of the CCN and the time evolution of the drop spectra, and as a result detailed microphysical schemes have been used to investigate these processes.

In this study we investigate the effect of the aerosol composition (soluble fraction of aerosol particles), shape of the size distribution, and the presence of the giant nuclei on drizzle formation. In order to perform these simulations we extended the model presented in Rasmussen et. al, 2002 to simulate the evolution of aerosol particles into water drops during diffusional growth. The dynamical framework chosen is a 2D bell shaped mountain with 1 km height and 100 km half width. Airflow past the barrier is assumed to have a constant wind speed of 15 m/s and to be neutrally stratified. Maximum updrafts with this configuration are 10 cm/s.

2. MODEL DESCRIPTION

The microphysics used in the current model is based on that presented in Rasmussen et al, 2002 with the addition of an improved treatment of water drop formation on CCN particles. This is achieved by adding 40 size bins to keep track of aerosol particles, with the 20th bin coinciding with the first bin used for water drops and ice particles. The first bin for the aerosol particles starts at a mass of 3.0477 10^{-20} kg (about 0.015 μm in radius), with mass doubling at the bin edges. Similar to Feingold et al. (1996), the concentration (N_k) and the mass (M_k) of the water drops and haze particles are calculated in every bin as well as the total mass of the aerosol particles inside the drops in the k-th mass category ($M_{a,k}$). The readers are referred to Geresdi and Rasmussen, 2004 for more details about microphysics of the model.

The initial size distributions of the aerosol particles used in the calculation was given by the lognormal size distributions suggested by Jaenicke (1988). We assumed that all the aerosol particles have the same soluble fraction independent of size, and that the soluble fraction consists of ammonium sulfate. Initially the aerosol particles were distributed in the first 27 bins, between radii of ~0.0015 μm and ~8.0 μm. Maritime (MARITIME), rural continental (CONT-A), urban (CONT-B) and extreme urban (CONT-C) type size distributions were used (Fig 1).

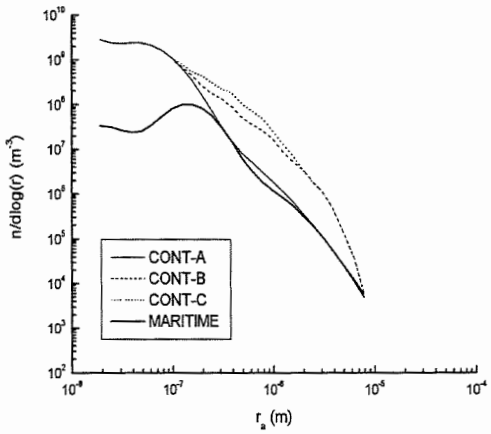

Fig. 1. Initial aerosol size distributions. The solid lines give the size distributions typical of rural continental and maritime air masses (Jaenicke 1988) The dashed and dotted lines denote urban and extreme urban aerosol size distributions, respectively. For the GIANTOFF cases the size distributions were truncated at 1.5 μm.

Corresponding author address: István Geresdi, University of Pécs, Pécs, Hungary; e-mail: geresdi@ttk.pte.hu

To investigate the effect of giant nuclei, the size distributions were truncated at 1.5 μm. This implies that the concentration of giant nuclei is about 0.3 cm^{-3} in the case of MARITIME and CONT-A aerosol size distributions.

3. RESULTS

Table 1. summarizes the simulations performed in this study. Cases with different size distributions and soluble fractions are emphasized, as well as cases with and without giant nuclei.

Table 1. Summary of the simulations.

	Type of the size distribution	Soluble fraction	Giant nuclei
M01GOFF	MARITIME	0.1	no
M10GOFF	MARITIME	1.0	no
M01GON	MARITIME	0.1	yes
M10GON	MARITIME	1.0	yes
CA01GOFF	CONT-A	0.1	no
CA10GOFF	CONT-A	1.0	no
CA01GON	CONT-A	0.1	yes
CA10GON	CONT-A	1.0	yes
CB10GON	CONT-B	1.0	yes
CC10GON	CONT-C	1.0	yes

Fig. 2 shows the time evolution of the maximum water mixing ratio (Fig 2a, and Fig 2b) and the maximum drizzle mixing ratios (Fig 2c and Fig 2d) for the various cases. Significant difference between the GIANTON and GIANTOFF cases was found only for the simulations where the size distribution of the aerosols is CONT-A and the soluble fraction is 1.0, (in the other cases the effect of the presence of giant nuclei was negligible, as in the case of MARITIME aerosol size distribution and soluble fraction of 0.1). When the solubility fraction is 1.0, drizzle formation starts later (from one-half to one hour), and reaches the maximum value of 0.11 g/kg more slowly (about two hours). The slower formation of drizzle in this latter case could be explained by the difference in the number concentration of the activated aerosol particles for the two solubility fractions.

The effect of the giant nuclei on drizzle formation in the current case is shown in Fig 3, which shows the time evolution of the relative difference in the domain maximum drizzle mixing ratios between the GIANTON and GIANTOFF cases. The presence of the giant nuclei results in earlier formation of drizzle drops, but this effect remains relatively large for only very small drizzle mixing ratios and decreases very quickly as drizzle mixing ratio increases. The effect of giant nuclei lasts for a longer time period (about one hour) only in the case CONT-A aerosol size distributions with soluble fraction of 1.0 (the case with the highest number of activated aerosol particles except for the urban and extreme urban size distributions). This result suggests that the very earliest drizzle drops from a cloud will likely be formed on giant nuclei, while the later, more intense drizzle will be due to the collision-coalescence process. Recent observations of drizzle by John Hallett off the California coast by John Hallett (personal communication) found the earliest drizzle drops to contain giant salt nuclei, consistent with this result.

4. SUMMARY

This study has investigated how the characteristics of aerosol particles affects drizzle formation in stably stratified layer clouds. A new technique was developed to simulate the evolution of water drops from wet aerosol particles. The detailed microphysical model was incorporated in the MM5 mesoscale model and two dimensional cloud simulations over a bell shaped mountain performed. The results of the simulations show:

1. Stably stratified clouds with weak updraft (< 10 cm/s) can form drizzle relatively rapidly for the maritime size distributions with any aerosol particle solubility, and for continental size distributions with highly insoluble particles due to the low number of activated CCN (< 100 cm^{-3}) as a result of low supersaturation achieved in these types of clouds (< 0.1 % typically).
2. Drizzle is suppressed in stably stratified clouds with weak updraft (< 10 cm/s) for highly soluble urban and extreme urban size distributions. These distributions had sufficiently increased numbers of water drops to mitigate drizzle formation and are

way of putting aerosol activation into MM5 looks at influence on drizzle formation?

characterized by significant increases of the aerosol concentration for particles larger than 0.1 μm. Thus, drizzle formation may be suppressed near urban areas.

3. The presence of giant nuclei has a minor effect on the drizzle formation. It was found that giant nuclei only enhances drizzle formation when the CCN concentration is relatively high and only during the early stages of the cloud formation when the collision – coalescence process has not established itself yet. Our simulations show that the CCN concentration should be higher than 100 cm^{-3} for giant nuclei to have an effect. This result agrees well with that of Feingold et al. 1999, who found a significant effect on drizzle formation in stratocumulus clouds only when the CCN concentration was above 150 cm^{-3}, and no effect when the CCN concentration was less than 50 cm^{-3}. The effect of the giant nuclei was only important in the first half of the simulation prior to the onset of collision coalescence. It was shown that the reduction of CCN concentration due to the lower solubility of the aerosol particles has a much stronger effect on drizzle formation than the giant nuclei.

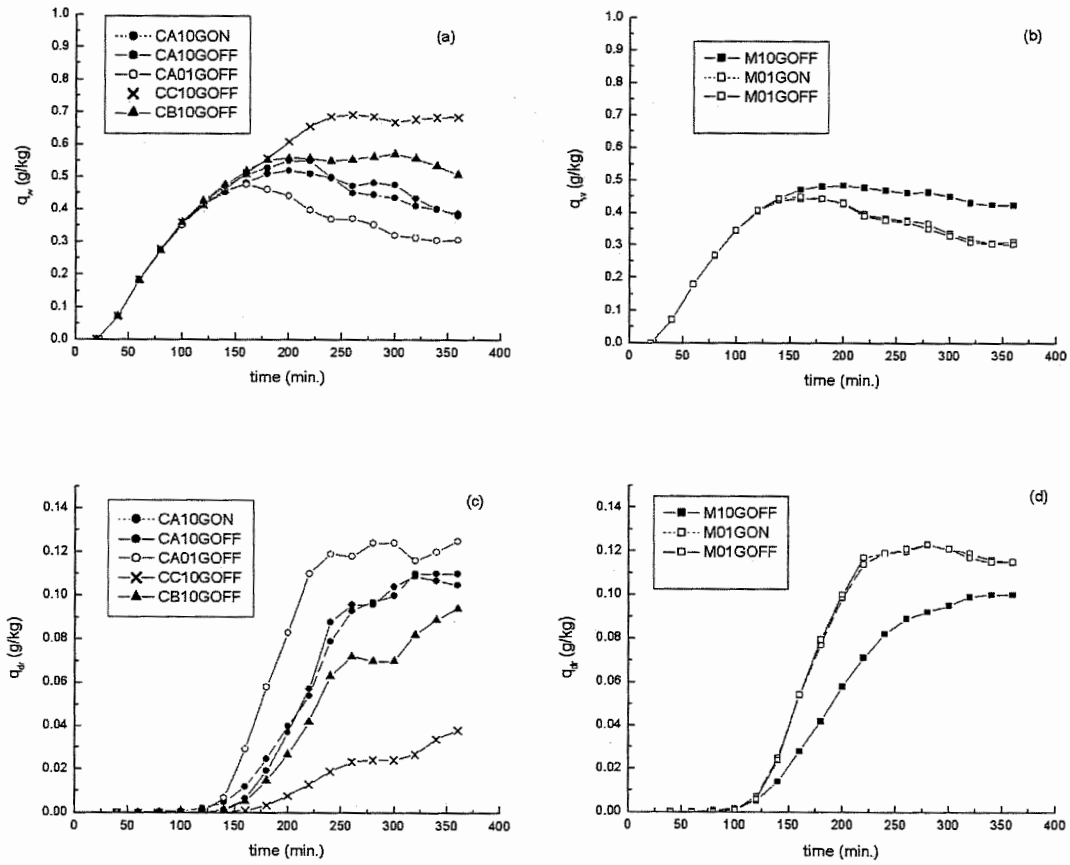

Fig. 2. Time evolution of the domain maximum cloud water mixing ratio (panel a and b) and drizzle mixing ratio (panel c and d) for simulations using the continental and maritime type aerosol particle size distribution

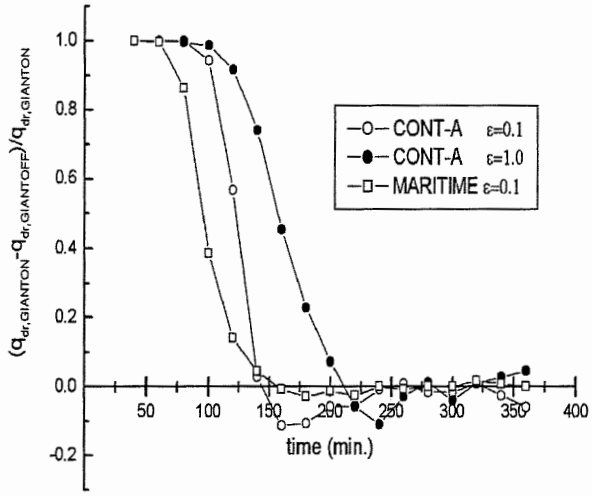

Fig. 3. The relative difference between the domain maximum drizzle mixing ratio of the GIANTON and the GIANTOFF maritime and continental simulations as a function of model time.

Acknowledgement

This work was supported by the Hungarian Scientific Research Fund under grant T043010. This research is also in response to requirements and funding by the Federal Aviation Administration (FAA). The view expressed are those of the authors and do not necessarily represent the official policy of the FAA.

References

Feingold, G., S. M. Kreidenweis, B. Stevens and W. R. Cotton 1996: Numerical simulations of stratocumulus processing of cloud condensation nuclei through collision-coalescence J. Geophys. Res., 101, 21,391-21,402

French, J. R., G. Vali and R. D. Kelly, 2000: Observation of microphysics pertaining to the development of drizzle in warm, shallow cumulus clouds, Q. J. R. Meteorol. Soc, 126, 415-443

Geresdi, I. and Rasmussen, R. 2004: Freezing drizzle formation in stably stratified layer clouds: Part II. The role of giant nuclei and aerosol particle size distribution and solubility (submitted to the J. Atmospheric Science)

Jeanicke, R., (1988): Aerosol physics and chemistry. in Landolt Boernstein: Zhalenwerte und Funktionen aus Naturwissenschaften und Tecnik, vol. 4b, edited by G. Fischer, pp. 391-457, Springer –Verlag, New York.

Rasmussen, R, M., Geresdi, I., Thompson, G., Manning, K., and Karplus, E., 2002: Freezing drizzle formation in stably stratified layer clouds: The role of radiative cooling of cloud droplets and cloud condensation and ice nuclei. J. Atmos. Sci. , 59, 837-860

SEPARATION BETWEEN CLOUD SEEDING AND AIR POLLUTION EFFECTS

A. Givati and D. Rosenfeld

Institute of Earth Sciences, the Hebrew University of Jerusalem, Israel

1. INTRODUCTION

The Enhancement of precipitation due to cloud seeding operations has been suggested in many studies around the world in the last several decades. On the other hand an opposite effect, suppression of rain and snow due to urban and industrial air pollution was just recently documented and quantified. Rosenfeld (1999, 2000) have shown that urban and industrial air pollution suppresses precipitation-forming processes in convective clouds. The suppression affects warm rain processes, as well as ice precipitation (Rosenfeld, 2000; Borys et al, 2000, 2003, Andreae et al 2004). Givati and Rosenfeld (2004) quantified the rainfall losses over hills downwind of major coastal urban areas in California and Israel, which amounts to 15 – 25% of the annual precipitation. The suppression occurs mainly in the relatively shallow aerographic clouds within the cold air mass of cyclones. Borys et al. (2003) showed that addition of as little as 1 μg m-3 of anthropogenic sulfate aerosol to a clean background can reduce orographic snowfall rate at the Colorado Rocky Mountains by up to 50% in a single storm. In Israel, two cloud seeding experiments where carried out during the period of 1961–1975 by aircraft seeding of silver iodide in northern and central Israel (Gabriel, 1967, Gagin, and Neumann, 1974,1981, Gabriel and Rosenfeld 1990). The experiments indicated a significant enhancement of 13%-15% in rain amounts for northern Israel. Since 1975 the seeding in northern Israel is operational. Nirel and Rosenfeld (1995) found only 6% enhancement for the period of 1975-1990 with less statistical significance then the previous seeding period. They also identified a decreasing trend in the historical target/control ratio. When they extrapolated the trend to the operational seeding period, the operational seeding effect was 11%.

In terms of clouds microphysical effects, cloud seeding and air pollution are the two opposite sides of the same coin. Both are manifestation of the same sensitivity of clouds to human activities. It seems that clouds respond correspondingly to what we add them. The results that are presented in this paper show for the first time the opposite effects of human impacts on clouds.

Corresponding author's address: Daniel Rosenfeld, Institute of Earth Sciences, The Hebrew University of Jerusalem, Jerusalem 91904, Israel.
E-Mail: daniel.rosenfeld@huji.ac.il

2. THE STUDY AREA AND METHODOLOGY

In order to separate the cloud seeding and the air pollution effects this study focused on the original control and target seeding areas in northern Israel. The pollution source is air pollution that arrives to this area from the Haifa bay, densely populated area (over one and a half million peoples) that contains power stations, a refinery and many industrial factories.

The first step was to quantify the combined effects of air pollution and seeding, without attempting to separate them. As was done in California and central Israel (Givati and Rosenfeld, 2004), highly correlated pairs of hills / coast rain gauges where selected. In order to achieve a good representation of the control and the target areas, clusters of rain gauges where actually selected. The stations in each cluster where selected according to the principles of geographical homogeneous and equal precipitation measuring periods. The main response parameter that is used is the annual time series of Ro. Ro is defined as the ratio between the rain gauges measured precipitation amounts at the hills, which where the target areas in the experiments, and at the upwind lowland, which used as control areas. Northern Israel was divided into six sub targets areas and three sub control areas, as was done in the cloud seeding experiments (see fig. 1).

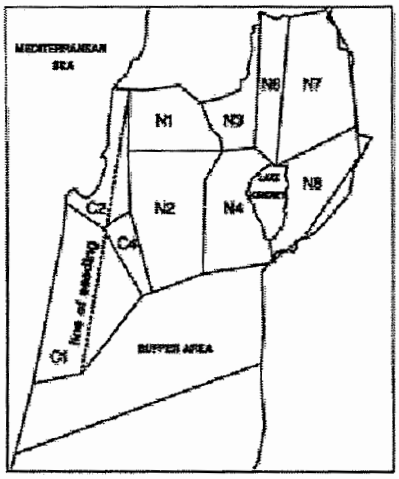

Figure 1: The partition of north Israel for cloud seeding target (start with N) and control (start with C) sub-areas during the Israel-2 cloud seeding experiment (1969-1975). The broken line is the seeding line during Israel-1 (1961-1967) experiment.

The next step after quantifying the combined effects in northern Israel was analyzing separate time series under seeded and unseeded conditions.
The years between 1950 and 1960 are the pre experimental years and so considered as non seeded period. The years between 1975 until today are the operational period and so considered as seeded. During the period of 1961 – 1975 (Israel 1 and 2 experiments) some of the days where seeded and some unseeded, at a random allocation that was inherent to the experiment. The separate time series contain daily precipitation amounts (from November to April each year).

3. RESULTS AND DISCUSSION

3.1 Trend of decreasing orographic enhancement

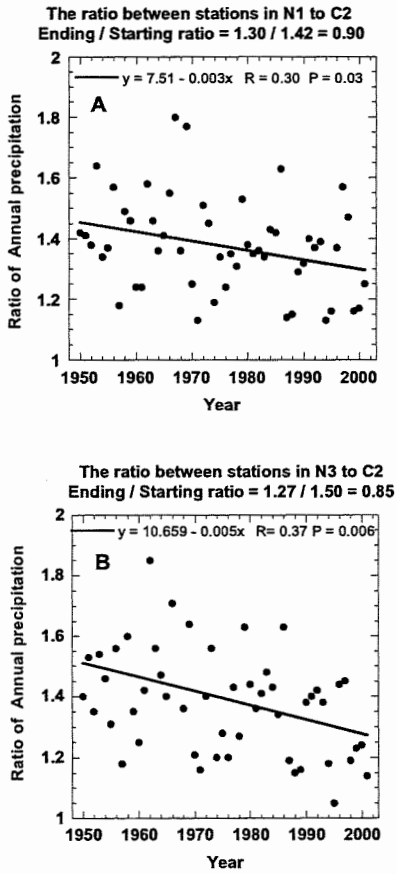

Fig. 2: Overall change in the target/control annual ratio of precipitation during the last 54 years, for a cluster of rain gauge cluster at elevations of 600 to 800 m in sub-area N1 (upper panel), and for a cluster at elevation of 750-950 m at sub-area N3 (lower panel). Note the statistically significant decrease of 10%-15% in the ratios with respect to C2 control area.

Fig. 2 displays the time series of Ro (the ratio of target-control annual rainfall) for the hilly clusters of N1 (A) and N3 (B) against the plain cluster of C2 (see locations in fig. 1). The hilly clusters are located downwind to the pollution sources in the bay of Haifa. It can be seen in the figure that a decreasing trend of 10%-15% in the Ro occurred along the years in those target areas. The decrease is statistically significant. This decrease in Ro is similar to the one that was found in hilly areas in central Israel and California (Givati and Rosenfeld, 2004). The cluster of stations in the areas of N2, N6 and N8 are low elevation areas and an orographic enhancement does not exist between them and the coast clusters. Respectively to the absence in the orographic enhancement, no significant trend in the Ro occurred in those areas along the years.

3.2 Separating pollution and seeding effects

Fig. 3 shows the trend lines under seeded (the broken line and empty points) and unseeded (the solid line and full points) conditions for the ratio between the clusters of stations in N1 (A) and N3 (B) against the plain cluster of C2. Both the seeded and the unseeded trend lines in both clusters decrease along the years but the broken line that represent the ratio under seeded conditions is shifted upward with respect to the solid line (that represents the unseeded condition). Note that the ending Ro in 1975 under the seeded conditions is higher than the ending ratio under unseeded conditions at this year. During the randomized seeding period of 1961-1975 the target/control ratio increased by 12.4% in N1 and by 14.4% in N3 (The calculation for the distance between the lines was made for the year 1975, in witch was the last year of Israel 2 experiment). Adding the years before 1961 to the unseeded regression and the years after 1975 to the seeded regression did not change much the regression lines. The regressions shown in Fig. 2 are for these full seeded and unseeded datasets. Implementation of the Student T test (linear statistical test for deference between groups) shows that the differences between the seeded and unseeded regression trend lines are significant at the level of 0.03% for N1 and at 0.07% for N3. This means that without cloud seeding the precipitation amount in those two target areas would have been 12 to 14% less of what they are today, or a loss of about 100 mm/year in areas with annual precipitation amount near 800 mm.

The increase in the orographic enhancement factor due to cloud seeding does not fully compensate the continuing decrease due to air pollution. Cloud seeding for rain enhancement is aimed at accelerating the conversion of cloud droplets into precipitation particles, whereas air pollution has exactly the opposite effect: suppression the coalescence of cloud droplets into raindrops and the forming of ice hydrometeors. This means that there is at least a potential of 14% for rain enhancement in order to

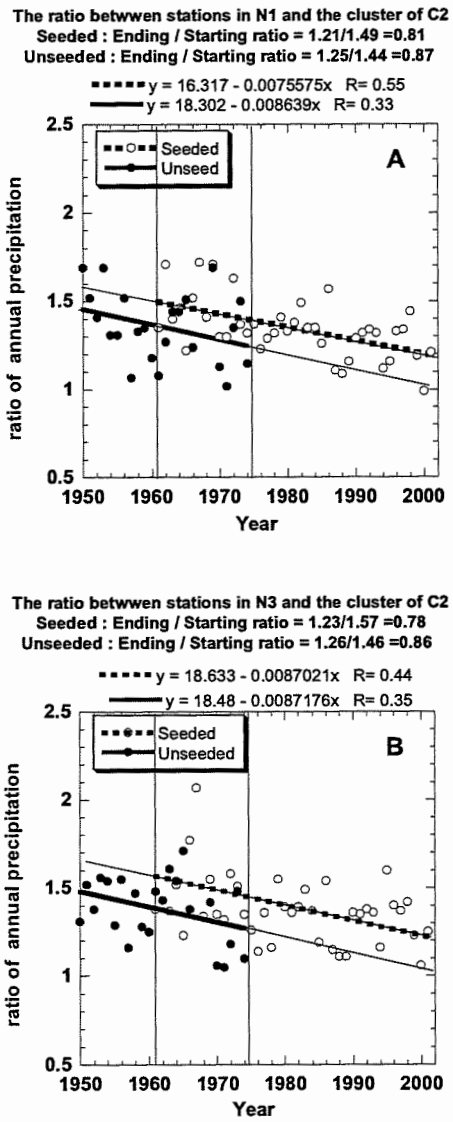

Fig. 3: change in the target/control annual ratio of precipitation during the last 54 years for the seeded (broken line and empty points) and unseeded (solid line and full points), between stations in the targets areas of N1 in the upper panel (western upper Galilee) and N3 in the lower panel (upper Galilee) to the control area C2 (northern coast). The seeded trend line is shifted upward with respect to the unseeded line by 12.4% in N1 and by 14.2% in N3.

restore to the values of the natural ratio that was in the early 50's. Fundamentally, Cloud seeding can increase precipitation amount above that natural values, as was actually done in the randomized cloud seeding experiments. After all, this was the original purpose of these experiments.

No significant trend in the Ro under seeded and unseeded conditions was found between low elevation clusters (N2, N6 and N8) to the control areas of C2 and C4. The ratio was stable along the years since the 50's until today. The effect of cloud seeding and air pollution is more limited there due to the lack of orographic component. This strengthens the suggestion that orographic clouds are the most susceptible for precipitation enhancement due to cloud seeding and to precipitation suppression due to air pollution.

4. CONCLUSIONS

The results that are presented in this paper are showing for the first time the opposite effects of human interference in precipitation processes. The effect of growing urban and industrial air pollution since the 50's caused a decrease in the ratio in the orographic enhancement factor between hilly areas and plain areas upwind from them (as was found in central Israel and other areas in the world). Without the air pollution no trend would have occurred in the ratio (as was found in pristine areas in Israel and other places in the world). Shallow and short-living orographic clouds are particularly susceptible to such impacts. Cloud seeding with sliver iodide was found to enhance the precipitation especially where the orographic enhancement factor was the largest. Likewise, the pollution effects reduced the precipitation by the greatest amount at the same regions. The meaning of that is that statistical evaluations of seeding efficacy on orographic precipitation without taking into account the pollution effects will lead to erroneous results and misleading conclusions. This fact can explain why such models that estimated the seeding effects in northern Israel based on historical comparisons (Niral and Rosenfeld, 1995) showed decrease in apparent seeding effect along the years.

5. ACKNOWLEDGEMENTS

This research was partially funded by the Eshkol foundation of the Israeli ministry of Science.

6. REFERENCES

Andreae, M. O., D. Rosenfeld, P. Artaxo, A. A. Costa, G. P. Frank, K. M. Longo, and M. A. F. Silva-Dias, 2004: Smoking rain clouds over the Amazon. *Science*, **303**, 1337-1342.

Borys, R.D., D.H. Lowenthal,D.L. Mitchell, 2000, The relationships among cloud microphysics, chemistry, and precipitation rate in cold mountain clouds, Atmos. Environ., **34**, 2593-2602.

Borys, R.D., D. H. Lowenthal, S. A. Cohn, and W. O. J. Brown, 2003: Mountain and radar measurements of anthropogenic aerosol effects on snow growth and snowfall rate. Geophys. Res. Lett., **30** (10), 1538, doi: 10.1029 /2002GL016855.

Gabriel, K.R., 1967, The Israeli artificial rainfall simulation experiment,Statistical evaluation for the period 1951-1965. Proc. Fifth Berkley symp. Math. Statistic and Probability , Vol **5** , Weather modification L.M. Lecam and J. Newman, Eds, University of California press, 91 -114.

Gabriel R. K. and D. Rosenfeld, 1990: The second Israeli Rainfall Stimulation Experiment: Analysis of precipitation on both targets, Journal of Applied Meteorology, **29**, 1055-1067.

Gagin, A., and J. Neumann, 1974: Rain stimulation and cloud physics in Israel, in: W.N. Hess (Editor), Weather and climate modification, Wiley, New York, pp.454 - 494.

Gagin, A., and J. Neumann, 1981: The second Israeli randomized cloud seeding experiment: Evaluation of the results. J. Appl. Meteor., **20**, 1301-1321.

Nirel R. and D. Rosenfeld, 1995: Estimation of the effect of operational seeding on rain amounts in Israel. J. Appl. Meteor., **34**, 2220-2229.

Rosenfeld, D., 1999: TRMM observed first direct evidence of smoke from forest fires inhibiting rainfall, Geophys. Res. Lett , **26**, 3105 -3108..

Rosenfeld, D., 2000: Suppression of rain and snow by urban air pollution. Science, **287**, 1793-1796.

Borys, R.D., D. H. Lowenthal, S. A. Cohn, and W. O. J. Brown, 2003: Mountain and radar measurements of anthropogenic aerosol effects on snow growth and snowfall rate. *Geophys. Res. Lett.*, **30**(10), 1538, doi: 10.1029 /2002GL016855.

Lahav R., D. Rosenfeld, 2004: The search for the optimal size of hygroscopic seeding particles. 14th International Conference on Clouds and Precipitation. Bologna, Italy, 18-23 July 2004.

Rosenfeld D., Y. Rudich and R. Lahav, 2001: Desert dust suppressing precipitation -- a possible desertification feedback loop. *Proceedings of the National Academy of Sciences*, **98**, 5975-5980.

need to take into
account air poll^n effects
on amount of orographic clouds
which are changing by pollution

SIMULTANEOUS AIRCRAFT OBSERVATION OF AEROSOL AND CLOUD DROPLET CONCENTRATIONS

T. Harimaya[1], A. Homma[1], A. Sasaki[1] and Y. Ishizaka[2]

[1] Division of Earth and Planetary Sciences, Hokkaido University, Sapporo, 060-0810, Japan
[2] Hydrospheric Atmospheric Research Center, Nagoya University, Nagoya, 464-8601, Japan

1. INTRODUCTION

Global cooling caused by the increase of aerosols is an important process in global climate change as well as in the greenhouse effect of CO_2. Atmospheric aerosols exert both a direct and an indirect force on climate. The indirect force is that man-made cloud condensation nuclei, through changes in cloud microphysics, would potentially modify cloud albedo. This indirect forcing was proposed first by Twomey (1977) and called the Twomey effect. The Twomey effect plays an important role in maritime stratus, which covers a wide area and has a long lifetime. Sulfate aerosols play an important role because they increase the most likely cloud condensation nuclei, which are thought to promote the indirect effect (Leaitch et al., 1992). There is a great deal of uncertainty in our understanding of this effect and accurate estimates have not yet been obtained, because cloud droplet forming and chemical processes are combined in a complicated way. Namely, further understanding in the role of clouds is necessary to accurately estimate the global climate change. The purpose of this study is to clarify the relationship between aerosol concentration and cloud droplet concentration.

2. OBSERVATIONAL AND ANALYTICAL PROCEDURES

Aircraft observations were carried out during the periods of December 10-19, 1999 and November 28-December 6, 2000. The purpose of these observations was to clarify the role of clouds on the transportation and transformation of air pollution materials which flow from the East Asiatic Continent to the Sea of Japan. Penetrating and horizontal flights were carried out in the interior and under the base of the stratocumulus and cumulus clouds which form over the Sea of Japan. Penetrating flights were carried out at only one height, because clouds were not very thick.

Observational areas were off the Oki Islands, Japan. In 1999 four flights were carried out and each lasted three hours in flight time. Two of the flights took place during a northwest monsoon on December 17 and 19. In 2000 three flights were carried out on December 2, 3 and 5. The weather conditions for the flights in 2000 did not include the northwest monsoon, as in the 1999 flights.

The data were obtained using B-200 aircraft. The B-200 aircraft is equipped to measure GPS latitude, GPS longitude, altitude, flight speed and flight attitude. Also, a CCD camera recorded the clouds. Particle counters (RION KC-01C; KANOMAX TF-500) and an aircraft microphysics probe (Gerber Scientific Inc. Model PVM-100A) instruments were used to obtain the data on aerosol concentration and cloud droplet concentration, respectively. The particle counter can obtain the aerosol concentrations at more than 0.3, 0.5, 1.0, 2.0 and 5.0 μm in diameter, respectively. The aircraft microphysics probe can obtain the liquid water content, surface area and effective radius of the droplet size spectrum. Therefore, the cloud droplet concentration was calculated from the liquid water content and effective radius under the assumption that the shape of a cloud droplet is a sphere.

3. RESULTS

3.1 Selection standard for analyzing object

Selection standards were set up to select the clouds suitable to analysis from the observed clouds as follows;

(1) clouds without precipitation,
(2) clouds for which aerosol concentration data were obtained during horizontal flights under

Corresponding author's address:
Toshio Harimaya, Division of Earth and Planetary Sciences, Graduate School of Science, Hokkaido University, Sapporo, 060-0810, Japan;
E-Mail: harimaya@taiki.ep.sci.hokudai.ac.jp

the cloud base.

In the case of precipitation, it is difficult to find an accurate relationship between aerosol concentration activated at the cloud base and cloud droplet concentration due to reduction of cloud droplets collected by rain drops. Therefore, our analysis is limited to the clouds without precipitation. Clouds with or without precipitation were judged by the pilot report. In order to correspond the cloud droplet concentration with aerosol concentration under the cloud base, we selected the clouds with simultaneous measurements of both cloud droplet concentration and aerosol concentration.

After selecting an object of study, we identified each cloud. It was difficult to judge the rift in the cloud by only data of the liquid water content and cloud droplet concentration for the stratocumulus. Therefore, we confirmed the cloud aspect and the rift in the cloud using the picture taken by the CCD camera. When we could not confirm a cloud due to an unclear picture, we used the data of the liquid water content and cloud droplet concentration as confirmation. For example, we judged that cloud A and cloud B were separate, if there was a distance of more than 2km between the two. Based on the method mentioned above, we judged synthetically. Using the above method, we identified twenty cloud samples.

After identification of the clouds, the maximum value of cloud droplet concentration for each cloud was determined as representative values. The aerosol concentration, which corresponded with the cloud droplet concentration, was obtained by averaging the data obtained under the cloud base.

3.2 Horizontal structure of cloud represented by cloud droplet concentration and liquid water content

It is possible to evaporate the cloud droplets and reduce the concentrations and radii of cloud droplets at the edge region by mixing them with the outer air. In order words, it is thought that the cloud droplet concentrations observed at the edge region are possibly lower than the original concentrations. It is considered that cloud droplets are not affected very much by mixing and they keep adiabatic liquid water content at the central region. The cloud droplets in the central region are thought to reflect the cloud droplet concentration generated at the cloud base. But, actual observation is not necessarily always possible in the central region. So, we tentatively adopt the maximum values of cloud droplet concentration as representative values. Here, geometric center is not necessarily always correspond to the position with maximum value. It is for this reason that this phenomenon may be explained by non-uniform entrainment. In these cases, maximum values were also adopted as representative value.

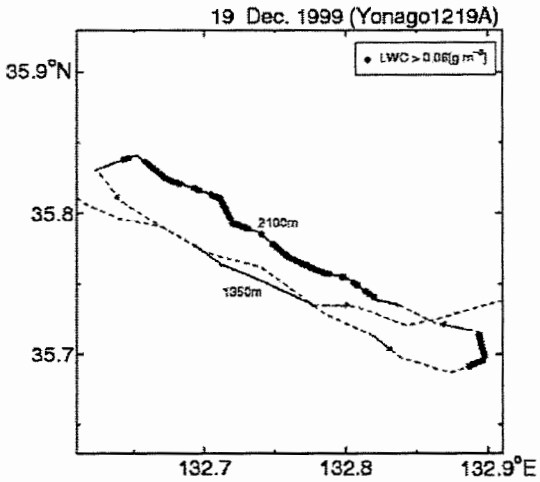

Fig. 1 Magnified flight courses: December 19, 1999 (Yonago 1219A).

Figure 1, which depicts the flight on December 19, 1999 (Yonago 1219A), shows the positions where the aerosols and cloud droplets were observed. The magnified flight course is described by connecting the positions corresponding to every 30 sec. The big shaded areas represent the positions detecting cloud droplet. The thick solid line indicated by 1,350 m is the division due to the horizontal flight. An aerosol concentration of more than 0.3 μm in diameter was constant in this division, so we adopted the mean value of these as the aerosol concentrations under the cloud base.

The thick solid line indicated by 2,100 m in Fig. 1 is the division formed by the penetrating flight. The spatial distribution of the cloud droplet concentration and liquid water content in the division is represented in Fig. 2. It is seen that the three patterns have a large value in the central portion and small values at both edges. We believed from this characteristic that this flight penetrated three clouds. We also confirmed this fact from the pictures taken by the CCD camera. The representative values of cloud droplet concentration are shown by the large dot on each solid line.

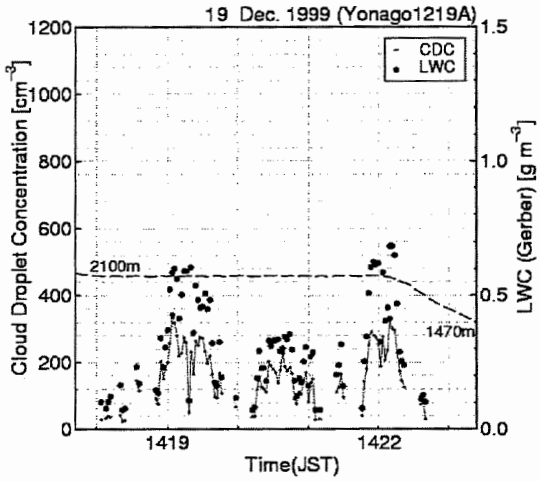

Fig. 2 Spatial distribution of cloud droplet concentration and liquid water content described by time for December 19, 1999 (Yonago 1219A).

3.3 Vertical structure of cloud represented by cloud droplet concentration and liquid water content

Generally speaking, supersaturation reaches a maximum near position above the cloud base and decreases with the increase of height. Cloud droplets are formed above the cloud base and their concentrations are determined by the maximum supersaturation near the cloud base. A portion of the cloud droplets may possibly evaporate by entrainment and mixing during the rise of air parcel with the cloud droplet. In the center region, it is thought that the updraft is strong and entrainment is weak. Therefore, the liquid water content in the region is thought to be nearly adiabatic. The region keeps the maximum cloud droplet concentration formed near the cloud base. If air parcel rises in the center of the cloud, the cloud droplet concentration at each height is expected to be equal to the concentration formed near the cloud base.

If the aircraft penetrates a cloud at several heights or the aircraft penetrates a cloud by ascending and descending flights, we can describe the vertical distribution of the cloud droplet concentration and liquid water content. Such a case is shown and the vertical structure is characterized as follows.

It is seen in Fig. 3 that the cloud droplet concentration shows nearly equal value despite the height, and liquid water content increases with increasing height on December 19, 1999 (Yonago 1219B). This shows that the cloud droplets continue to grow, keeping an equal concentration as they rise. Therefore, this case is not thought to be affected much by entrainment. Because the cloud droplet concentration has a maximum value at a in this cloud, this value was regarded as the representative value.

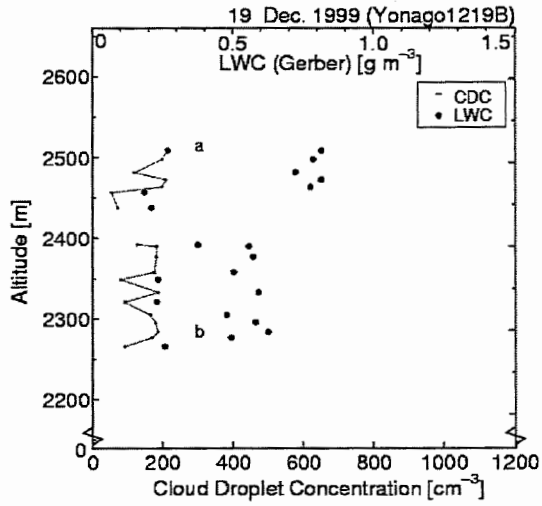

Fig. 3 Vertical distribution of cloud droplet concentration and liquid water content for December 19, 1999 (Yonago 1219B).

4. DISCUSSION

4.1 Calculation of adiabatic liquid water content

If air parcel rises, keeping the adiabatic process, the cloud droplets formed at the cloud base remain equal in concentration and increase in liquid water content. But, actual cloud droplets change in size and concentration by mixing and entrainment, and so the liquid water content does not always increase with the increase in height. Therefore, many methods have been tried to extract data that are not affected by entrainment. In order to estimate the deviation from the adiabatic process, we calculated the adiabatic liquid water content by assuming that the air parcel rises adiabatically from cloud base to the observation height, and compared the observed value with the calculation value. Then, we adopted the height of cloud base reported by the copilot and performed the abovementioned calculation. We calculated the liquid water content at the observation height, adding the each liquid water content of every 100 m in depth, as estimated by the moist adiabatic lapse rate from the cloud base to the observation height.

4.2 Relationship between aerosol concentration and cloud droplet concentration

When we compared the observation values with the calculated values of the adiabatic liquid water content at the observation height, three points were fairly smaller than adiabatic liquid water content. So we regarded these three points as non-adiabatic liquid water content and excluded them. Hereafter, we use the data of the 17 points mentioned above, and the 4 points obtained by aircraft observation at the Tane Island and the Hachijyo Island in order to discuss.

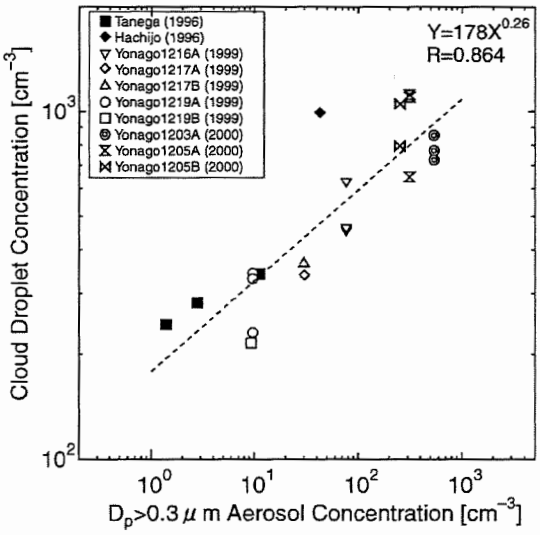

Fig. 4 Relationship between aerosol concentration and cloud droplet concentration.

Figure 4 shows the relationship between the aerosol concentration and cloud droplet concentration. It is seen in Fig. 4 that the cloud droplet concentration has a tendency to increase with increasing aerosol concentration. The dotted line indicates a regression line to all data, with the correlation coefficient of 0.864. It is seen from the regression formula that the rate of increase of the cloud droplet concentration becomes less steep in large aerosol concentrations than in small aerosol concentrations. Here, it is seen that the cloud droplet concentration is larger than the aerosol concentration, because it is thought that even the aerosols less than 0.3 μ m in diameter are activated and form cloud droplets in observed clouds.

5. CONCLUSIONS

relation of droplet # & aerosol conc

Aircraft observations were carried out off the Oki Islands, Japan during the periods of December 1999 and December 2000. We analyzed about five day's worth of data containing aerosol concentration and cloud droplet concentration.

In order to closely examine the relationship between the aerosol concentration under a cloud base and the cloud droplet concentration in the same cloud, we selected clouds without precipitation and obtained the aerosol concentration data during horizontal flights under the cloud base. It is thought that the cloud droplet concentration decreases due to the collection by rain drops, and aerosol concentration changes with height. We selected twenty cases satisfying these standards, and represented the horizontal and vertical structures of clouds by cloud droplet concentration and liquid water content. During horizontal penetrating flights, we measured the maximum values in the cloud droplet concentration and liquid water content at the center portion of the cloud. During ascending and descending flights, we observed that cloud droplet concentration shows nearly equal value despite the change in height, and the liquid water content increases with increasing height. These results reflect the fact that cloud droplets are formed at the cloud base and grow with the increase in height, maintaining the same concentration. Therefore, penetration exactly at the center portion of a cloud was confirmed to be important.

We selected further data which are close to the adiabatic liquid water content. As a result, it was seen that the cloud droplet concentration has a tendency to increase with increasing aerosol concentration. The relationship was represented by the regression formula $Y = 178X^{0.26}$ with 0.864 as the correlation coefficient. It was also confirmed that the rate of increase of the cloud droplet concentration in large aerosol concentrations is less steep than in small aerosol concentrations.

REFERENCES

Leaitch, W.R., G.A. Isaac, J.W. Strapp, C.M. Banic and H.A. Wiebe, 1992: The relationship between cloud droplet number concentrations and anthropogenic pollution: observations and climatic impactions. J. Geophys. Res., **97(D2)**, 2463-2474.

Twomey, S., 1977: The influence of pollution in the shortwave albedo of clouds. J. Atmos. Sci., **34**, 1149-1152.

PO VALLEY NUCLEATION EVENTS: A SIGNIFICANT SOURCE OF CCN

L. Hiltunen[1], J. Joutsensaari[1], M. C. Facchini[2], F. Cavalli[2] and A. Laaksonen[1]

[1]Department of Applied Physics, University of Kuopio, Finland
[2]Istituto di Scienze dell'Atmosfera e del Clima, Consiglio Nazionale, Bologna, Italy

1. INTRODUCTION

Atmospheric nucleation events have received increasing attention as a potentially important source of aerosol particles affecting climate (Kulmala et al. 2004). The first continuous long-term measurement of nucleation events was started in the beginning of 1996 at a Boreal forest area in Finland, where new particle production has been observed 50-70 times per year (Mäkelä et al 1996). Since then, other continuous measurements have been started at various locations. However, it is still unclear whether the yield of particles having radiative effects is substantial enough to affect the climate on global or regional scales. To have direct radiative effects, the freshly nucleated particles must grow to sizes larger than 100 nm in diameter, and to be able to act as cloud condensation nuclei they must reach at least the size of 50 nm. Here we show that nuclation events occur extremely frquently in the Po Valley region in Italy, and produce an important fraction of ambient particles larger than 50 nm, and affects the concentrations as large as 200 nm in diameter.

2. MEASUREMENTS

Particle size distribution measurements between 3 and 500 nm were started at the San Pietro Capofiume measurement station on March 24, 2002. The measurements are carried out using a twin Differential Mobility Particle Sizer (DMPS) system. The system consists of two DMPS's, the first measuring particle size distributions between 3-20 nm and the second between 20-500 nm. One measurement cycle lasts for ten minutes. Here, we discuss data obtained until 20 July, 2002, i.e. from a period of 119 days. However, there was 11 days from which we have no data due to instrument failure, leaving us 108 days for analysis.

To summarize, our data shows 50 nucleation event days, 40 non-event days, and 18 days during which an event may or may not have taken place. This is in stark contrast to the Boreal nucleation data, which shows on avarage roughly one event per week annually. Furthermore, the Boreal data shows a maximum in nucleation event frequency during the spring months and a pronounced minimum during the summer months (June-August), whereas no such variation can be detected from our data. The ratios of event days to non-event days were 7:1 in March, 12:10 in April, 12:12 in May, 7:12 in June and 12:5 in July.

A striking feature of many of the Po Valley nucleation events is the large sizes the particles grow to. The growth often takes place in two sequences: the largest particles reach the 50 nm size range within about 3-4 hours from the beginning of the event, and after that the mode of nucleated particles stays relatively stable until the evening, after which the second growth period takes place. The latter growth period is very probably due to semivolatile gases (possibly organic), which become condensable when the temperature drops in the evening. By midnight the largest particles can reach diameters of 200 nm and larger.

3. RESULTS

To determine the yield of possible CCN from nucleation events, we have calculated the increases in concentrations of particles in 50-500 nm, 100-500 nm, and 200-500 nm size ranges on nucleation event days. The particle concentration in a given size range usually shows a minimum just before the nucleation event start or slightly after (due to mixing of cleaner air from above in the morning), and a maximum when the nucleated particles or a fraction of them have grown enough. The concentration increases in the given size ranges were simply determined from the differences at the minima and at the maxima. Altogether 31 nucleation events from 62 days were analyzed in this way (on the rest of the 108 days there have been problems with the measurement system such that although we were able to determine whether or not an event took place, we could not determine the concentration differences reliably).

	yield of particles/cc	annual yield of particles/m^2
50-500 nm	137 000	2.7×10^{14}
100-500 nm	51 000	1.0×10^{14}
200-500 nm	11 000	2.1×10^{13}

Table 1 shows the particle yields from these 62 days in the different size ranges. We have also calculated what the numbers would be at an annual level per 1 square meter of Earth's surface assuming that the nucleation takes place in the surface layer up to the altitude of 1000 m, and that during the rest of the year

Corresponding author's address: Ari Laaksonen, Department of Applied Physics, University of Kuopio, P.O.Box 1627, FIN-70211 Kuopio, Finland; EMail: ari.laaksonen@uku.fi.

the nucleation event frequency drops by a factor of 5. Radke and Hobbs (1976) have estimated that on the Global level, the total annual CCN production from primary natural and anthropogenic sources is on the order of 10^{14} m^{-2}, which is very similar to the figure we calculate for 50-500 nm particles, i.e. 2.7×10^{14} m^{-2}. It can be concluded that nucleation events are indeed a strong regional source of CCN in the Po Valley area. Whether or not a similar conclusion holds for larger areas remains to be answered.

4. REFERENCES

Kulmala M, Vehkamäki H., Petäjä T, Dal Maso M., Lauri A., Kerminen V.-M., Birmili W., McMurry P.H., 2004: Formation and growth rates of ultrafine atmospheric particles: a review of observations. J. Aerosol Sci., **35**, 143-176.

Mäkelä J.M., Aalto P., Jokinen V., Pohja T., Nissinen A., Palmroth S., Markkanen T., Seitsonen K., Lihavainen H., Kulmala M., 1996: Observations of ultrafine aerosol particle formation and growth in boreal forest. Geophys. Res. Lett. ., **24**, 1219-1222.

Radke L.F., Hobbs P.V., 1976: Cloud condensation nuclei on the Atlantic seaboard of the United States. Science, **193**, 999-1002.

LONG-TERM, WINTERTIME CLOUD DROPLET, CONDENSATION NUCLEUS AND PRECIPITATION MEASUREMENTS IN THE NORTHERN COLORADO ROCKIES, USA

Edward E. Hindman1[1], Randolph D. Borys and Douglas H. Lowenthal[2]

[1]Earth and Atmospheric Sciences Department, The City College of New York, NYC, NY, 10031, USA
[2]Desert Research Institute and the University of Nevada, Reno, NV, 89512, USA

1. INTRODUCTION

Simultaneous cloud droplet physical and chemical measurements and condensation nucleus (CN) measurements have been made almost every winter for the past 21 years at 3250 m MSL Storm Peak Laboratory (SPL) in the northern Colorado Rockies (Borys and Wetzel, 1997; Hindman, 2001). During this period, the global average temperature increased about 0.3C most likely due to increased absorption of terrestrial radiation by anthropogenic gases (Mann, et al., 2003). The concurrent aerosol particle emissions were expected to increase cloud droplet number-concentrations, increasing cloud reflectivity and offsetting a portion of the global warming (Liepert, 2002).

Short-term investigations at SPL have identified polluted cloud episodes in which this "aerosol effect" has been detected (Borys, et al., 2000, 2003; Hindman, et al., 2002). However, the long-term record has revealed decreasing droplet number concentrations and CN concentrations and increasing mean droplet sizes and pH values through the winter of 1999/00 (Ponce and Hindman, 2001). These trends may reflect decreased upwind USA aerosol particle emissions and/or wetter winters. The data from the four recent winters are incorporated here to determine if these trends continue and if so, determine their significance.

2. MEASUREMENTS

Cloud droplet spectra were measured first using a cloud-gun (CG) (Hindman, 1987) and, then, using a Forward Scattering Spectrometer Probe (FSSP) (Cerni, 1983). The cloud droplet number concentration (N), mean droplet diameter (D_{bar}) and liquid water content (LWC) were calculated from these spectra using standard methods.

Hindman and Borys (1998) cross-calibrated the CG and FSSP instruments during the winter of 1994/95. The FSSP values have been transformed using the calibration to the corresponding CG values to produce consistent data. The LWC cross-calibration is used here to adjust the FSSP LWC values: $LWC_{FSSP} \sim 3.45^* LWC_{CG}$. The CG values are reported for the winters of 1983/84 through 1994/95 and the FSSP-adjusted values are reported thereafter.

A cloud "sieve", which looks like a scientific tennis racquet, developed by Hindman, et al. (1992) was used to collect supercooled cloud droplets during the cloud droplet spectra measurements. The resulting ice deposits were melted shortly after collection and the pH of the cloud water was immediately measured using a standard pH meter.

CN measurements were made irregularly during the cloud droplet spectra measurements prior to the winter of 1991/92 using a hand-operated Gardner counter. Thereafter, measurements were made using an automatic TSI Condensation Particle Counter (Keady, et al., 1986). The Gardner and TSI instruments were cross-calibrated January 1993 (Hindman and Borys, 1998). The Gardner data have been scaled to equivalent TSI values to produce consistent data. The CN concentrations are interstitial since cloud droplets were unable to enter the instruments and evaporate as discussed by Lowenthal, et al. (2002).

Twenty-four hour snowfall water-equivalent measurements were obtained daily in the morning through all the 21 winters. The measurements were made by personnel of the Steamboat ski area at 2767 m MSL Thunderhead Lodge about 2 km upwind of SPL. The snowfall measurements that encompassed the SPL cloud measurements were extracted from these records and averaged.

The SPL measurements were obtained at 3- to 4-hour intervals during cloud events which most frequently lasted 4-8 hours and occasionally lasted 36 to 48 hours (Hindman, 1986). The measurements were obtained primarily over 2- to 3-week periods during the winter months of December and January.

3. RESULTS

The cloud droplet, pH, CN and precipitation measurements for each winter were averaged and the results are listed in the Table 1. Linear-regression analyses were performed on these values to illustrate any trends through the 21-year period.

Table 1

Average values from the SPL 21-winter record: number of samples (n), droplet number concentration (N), mean diameter (D_{bar}), liquid water content (LWC), pH, CN and snowfall water-equivalent precipitation

Winter	Year	n	N (cm^-3)	Dbar (um)	LWC (g/m^-3)	pH	CN (cm^-3)	Ppt. (mm)	
1983-84	1	8	312	8.2	0.086	4.10	2542	28	
1984-85	2	106	249	8.1	0.087	4.21	5365	18	
1985-86	3	31	499	7.2	0.134	3.44	3662	2.8	
1986-87	4	14	306	7.6	0.089	3.87	100	3.2	
1987-88	5	27	224	7.9	0.063	3.82	658	20	
1988-89	6	10	261	6.0	0.037	3.99	4710	9.2	
1989-90	7	28	199	12.8	0.230	4.22	800	7.8	
1990-91	8	45	313	7.9	0.098	4.32	7756	0.33	
1991-92	9	37	231	6.5	0.039	4.37	1311	9.5	
1992-93	10	104	214	7.5	0.053	4.93	883	13	
1993-94	11	90	273	7.4	0.060	4.87	1551	13	
1994-95	12	55	212	7.7	0.059	4.96	1463	16	
1995-96	13	8	143	8.0	0.040	4.30		9.7	
1996-97	14	33	125	7.1	0.038	4.42	1374	11	
1997-98	15	57	68	10.7	0.034	4.50	786	4.1	
1998-99	16	33	165	9.7	0.039	5.56	834	19	
1999-00	17	29	205	9.0	0.055	5.64	866	11	
2000-01	18	31	193	10.1	0.090	4.61	1445	11	
2001-02	19	19	108	11.5	0.067	4.24	1174	7.8	
2002-03	20	21	144	9.6	0.068	4.40	1086	7.9	
2003-04	21	4	139	6.7	0.022	3.96	1415	0	
		790	54	0.7	0.045	0.54	1422	2.2	Stdev
			21	0.4	0.019	0.13	430	2	StError
			218	8.5	0.071	4.52	1965	11	Average
CG			CG-equiv. values	CG-equiv. values	CG-equivalent values		TSI-equivalent values		
FSSP									

The cloud droplet N, D_{bar} and LWC average values are plotted as a function of year in Fig. 1. The results of the linear regression analyses also are plotted; the significance levels (P) of the correlation coefficients (R) were produced following standard methods (eg. Snedecor, 1956). It can be seen in the figure, the trend of decreasing droplet number concentrations and increasing mean droplet diameters reported by Ponce and Hindman (2001) continued through the 2003/04 measurements.

Corresponding author's address: Prof. Ward Hindman, Earth and Atmospheric Sciences Department, The City College of New York, New York City, NY, 10031 USA; e-mail: hindman@sci.ccny.cuny.edu

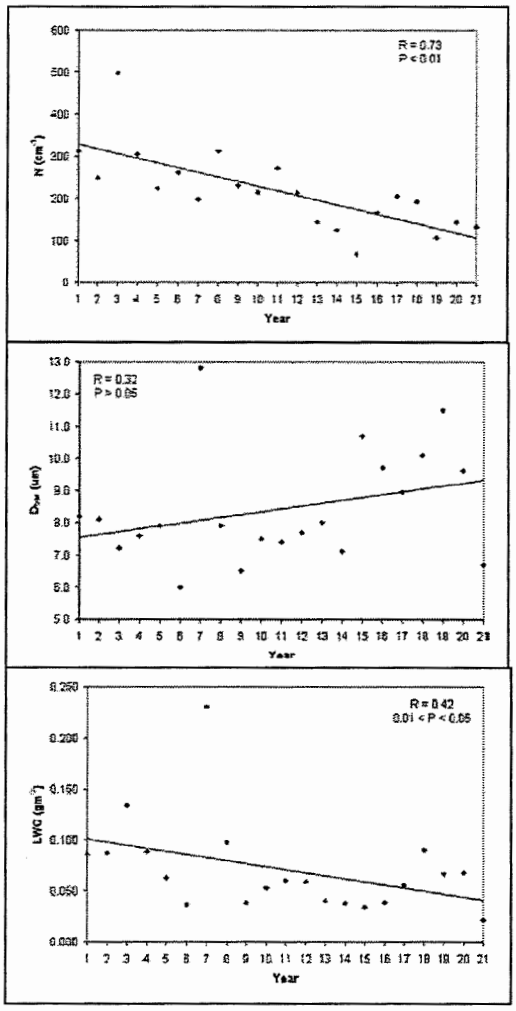

Figure 1. Cloud droplet number concentrations (upper), cloud droplet mean diameter (middle) and cloud droplet liquid water content (lower) as a function of year at SPL. Year 1= winter 1983/84 and year 21= winter 2003/04.

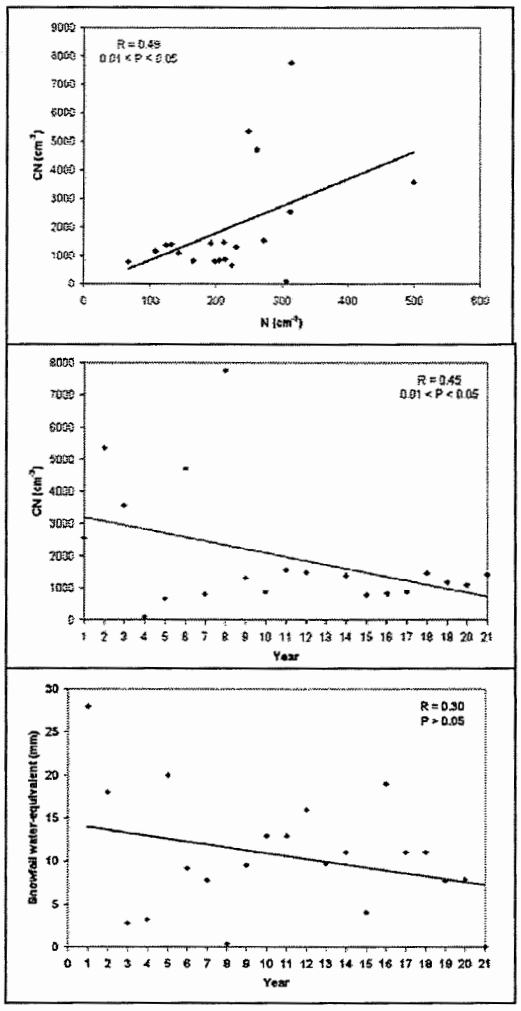

Figure 2. Cloud droplet pH (upper), interstitial CN (middle) and snowfall water-equivalent precipitation (lower) as a function of year at SPL. Year 1= winter 1983/84 and year 21= winter 2003/04.

Further, the trend of decreasing LWC reported by Hindman and Borys (1998) continued. The trend in the N values is statistically significant at the 1% level while the trend in the D_{bar} values is not statistically significant. The trend in the LWC values is statistically significant between the 1 and 5% levels.

The cloud droplet pH, CN and water-equivalent precipitation values are plotted as a function of year in Fig. 2. The results of the linear regression analyses also are plotted. It can be seen in the figure, the trends of increasing cloud droplet pH and decreasing CN concentrations reported by Hindman and Borys (1998) continued through the 2003/04 measurements. A trend of decreasing precipitation through the 21-year period is apparent. The trends in the pH and CN values are statistically significant between the 1 and 5% levels while the trend in the precipitation values is not statistically significant.

4. DISCUSSION

The cloud droplet N, D_{bar} and LWC trends in Fig. 1 are mutually consistent. The decrease in N by a factor of 1.8 and the increase in D_{bar} by a factor of 1.5 produce an expected decrease in LWC by a factor of 1.2. The measured decrease was a factor of 2. The difference between the factor of 1.2 and 2 is reasonable considering the scatter in the data. Further, the decrease in precipitation over the 21-year period (Fig. 2), although not statistically significant, is consistent with the decrease in LWC. A decrease in LWC would decrease the amount of cloud water collected by falling snow. This "riming" of snow crystals adds significantly to the amount of wintertime precipitation at SPL as demonstrated by Borys, et al. (2003). Thus, the large decrease in cloud droplet number concentrations and smaller increase in mean droplet diameters has led to a slight decrease in cloud liquid water content values.

The trend of increasing pH values, although weakly significant due to small values in recent winters, is consistent with the decreasing concentrations of CN and N. A weak relationship between CN and N at SPL, reported by Hindman and Murchison (1998), is confirmed in the 21-year record (see Fig. 3). Further, a weak relationship exists between pH and N and between CN and pH (Fig. 3). Thus, decreased CN concentrations, and most likely CCN concentrations as well, led to decreased droplet number concentrations which, in turn, led to larger droplets and larger pH values. The gradually

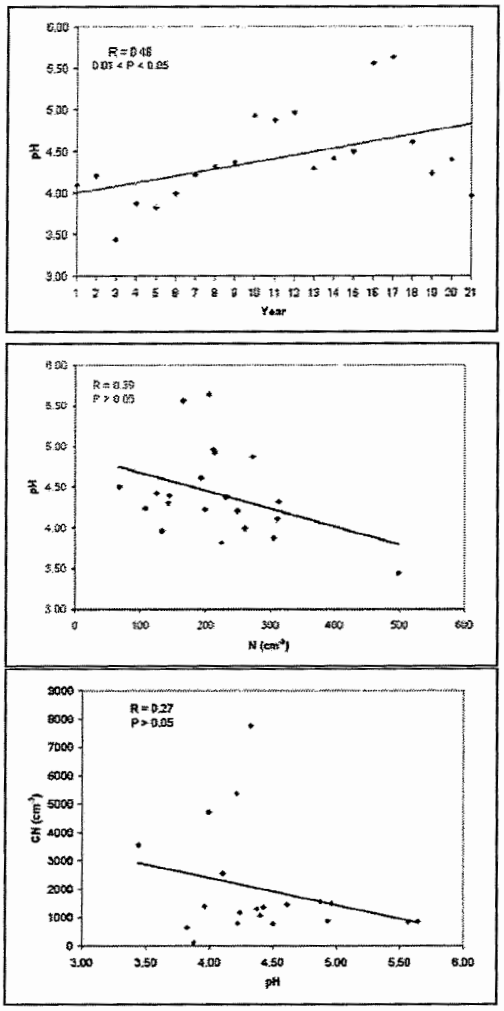

Figure 3. Average cloud droplet number concentrations (N) versus interstitial condensation nucleus concentrations (CN) (upper), cloud water pH versus N (middle) and CN versus pH (lower) at SPL for the winters of 1983/84 through 2003/04.

cleaner air at SPL over the 21-year period has produced less acidic cloud water pH values; a finding also reported from Europe (eg. Herckes, et al., 2002). Further, Ponce and Hindman (2001) reported snow pH values likewise increased at SPL between the winters of 1983/84 and 1999/2000.

The wintertime condensation nucleus concentrations at SPL decreased over the 21-year period along with a decrease in precipitation (Fig. 3). It was expected that CN concentrations would decrease with increasing precipitation due to increased precipitation scavenging of aerosol particles. The opposite appears to have occurred as illustrated in Fig. 4; the CN concentrations are not related to the amounts of precipitation.

Thus, the gradually cleaner air at SPL appears to have been due to reduced emissions and not to precipitation scavenging. For example, using the Interagency Monitoring of PROtected Environments (IMPROVE) data, Ponce and Hindman (2001) reported that $PM_{2.5}$ concentrations upwind of SPL reduced during December and January of 1988 through 2000. Hence, the effect of pollution-derived aerosol particles on clouds and precipitation at SPL reported by Hindman, et al. (2002) and Borys, et al. (2003) appear to occur infrequently. The precipitation suppression due to air pollution on the west

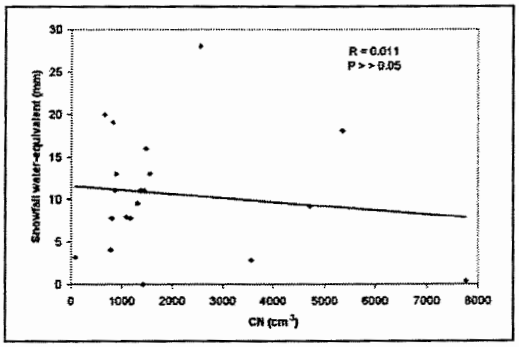

Figure 4. Average snowfall water-equivalent precipitation versus interstitial condensation nucleus concentrations (CN) at SPL for the winters of 1983/84 through 2003/04.

coast USA reported by Givati and Rosenfeld (2004) appears to have not reached northwestern Colorado according to the long-term records at SPL. The reduction in precipitation during the cloud samples collected at SPL over the 21-winter period was most likely related to large-scale meteorological factors and not air pollution.

One effect of global warming may be a rise in cloud base height if the warming decreases average relative humidity (RH); it is RH that is important in determining cloud base. If the warming raises average cloud base height, this would have the effect of lowering average LWC at a fixed height like SPL.

We employed a Skew T diagram to roughly estimate the effect. At 700 mb (typical SPL station pressure), the saturated mixing ratio is 4 g/kg at -4C and 5 g/kg at -1.5C or a rate-of-change of 0.4g/kg/C. So, a 0.3C change in temperature would require 0.12 g/kg more water to maintain saturation. We measured a 0.05 g/m^3 (0.06 g/kg) decrease in LWC over the 21-year period (Fig. 1). This decrease is on the order of that expected from a 0.3 C increase in temperature.

The effect of a 0.3C increase in temperature on cloud base height is estimated as follows. If the saturated lapse rate is about 5C/km, then 0.3C would correspond to a height change of (0.3/5)1000m or about 60m. A 60m increase in average cloud base height seems reasonable. Thus, the decreased LWC values may be a measure of the warming. In contrast, Chernykh, et al. (2001) report a lowering trend in cloud base height in recent years.

Finally, it needs to be determined if a warming of 0.3C occurred in the SPL 21-year record. This investigation is underway.

5. CONCLUSIONS

Over the 21-winter record at SPL, the large decrease in cloud droplet number concentrations and the small increase in mean droplet diameters is consistent with a slight decrease in cloud liquid water contents and amounts of precipitation. The gradually cleaner air at SPL over the period has produced less acidic cloud water pH values; a finding also reported from Europe. The gradually cleaner air appears to have been due to reduced aerosol particle emissions and not to precipitation scavenging. Hence, the effect of pollution-derived aerosol particles on clouds and precipitation at SPL appears to be infrequent. The reduction in precipitation measured during the cloud samples collected at SPL over the period was most likely related to large-scale meteorological factors and not air pollution.

6. ACKNOWLEDGEMENTS

EH received support from PSC-CUNY Awards, NOAA-CREST and NSF-AMP. The Steamboat Ski and Resort Corp. provided in-kind support; Jeff Hirschboeck of the ski patrol faithfully provided the snowfall data.

7. REFERENCES

Borys, R. D., and M. A. Wetzel, 1997: Storm Peak Laboratory: a research, teaching and service facility for the atmospheric sciences. *Bull. Am. Meteor. Soc.*, **78**, 2115-2123.

Borys, R. D., D. H. Lowenthal and D. L. Mitchell, 2000: The relationships among cloud microphysics, chemistry and precipitation rate in cold mountain clouds. *Atmos. Environ.*, **34**, 2593-2602.

Borys, R. D., D. H. Lowenthal, S. A. Cohn and W. O. J. Brown, 2003: Mountaintop and radar measurements of anthropogenic aerosol effects on snow growth and snowfall rate. *Geophys. Rsh. Ltrs.*, **30**, p.1538.

Cerni, T., 1983: Determination of the size and concentration of cloud drops with an FSSP. *J. Clim. Appl. Meteor.*, **22**, 1346-55.

Chernykh, I. V., O. A. Alduchov and R. E. Eskridge, 2001, Trends in low and high cloud boundaries and errors in height determination of cloud boundaries. *Bull. Amer. Meteor. Soc.*, **82**, 1941–1947.

Givati, A. and D. Rosenfeld, 2004: Quantifying precipitation suppression due to air pollution. *J. Appl. Meteor.*, in press.

Hindman, E. E., 1986: Characteristics of supercooled water in clouds at mountaintop sites in the Colorado Rockies. *J. Clim. Appl. Meteor.*, **25**, 1271-1279.

Hindman, E. E., 1987: A "Cloud-Gun" primer. *J. Atmos. Ocean. Tech.*, **4**, 736-741.

Hindman, E. E., E. C. Carter, R. D. Borys, D. L. Mitchell, 1992: Collecting supercooled cloud droplets as a function of droplet size, *J. Atmos. Ocean. Tech.*, **9**, 337-353.

Hindman, E. E. and R. D. Borys, 1998, Long-term cloud droplet measurements for climate-change studies. *World Res. Rev.*, **10**, 569-576.

Hindman, E. E., and M. Murchison, 1998: Condensation nuclei and cloud droplets. In *Ppts. Conference on Cloud Physics - 14th Conf. Planned and Inadvertant Wea. Modif.*, Am. Meteor. Soc., Boston, 283-286.

Hindman, E. E., 2001: The cloud catchers. *Weatherwise.*, **54**, 30-36.

Hindman, E. E., M. C. Meyer, S. D. Gedzelman and T. J. Bandosz, 2002: Acidic cloud episodes in the northern Colorado Rockies: Inadvertent weather modification? *J. Weather Modif.* (ISBN 0739-1781), **34**, 18-30.

Herckes, P., H. Wortham, P. Mirabel and M. Millet, 2002: Evolution of the fogwater composition in Strasbourg (France) from 1990 to 1999. *Atmos. Rsh.*, 64, 53-62.

Keady, P. B., F. R. Quant and G. J. Sem, 1986: A condensation nucleus counter for clean rooms. In *Proc. Institute Environmental. Science Annual Technical Meeting*, pp. 445-451.

Liepert, B., 2002: Observed reductions of surface solar radiation at sites in the US and worldwide. *Geophys. Rsh. Ltrs.*, **29**, 1421-1433.

Lowenthal, D. H., R. D. Borys and M. A. Wetzel, 2002: Aerosol distributions and cloud interactions at a mountaintop laboratory. *J. Geophys. Rsh.*, **107**, p. 4345.

Mann, M., et al., 2003: On past temperatures and anomalous late-20th Century warmth. *EOS*, **84**, 256-257.

Ponce, F. N. and E. E. Hindman, 2001: Wintertime cloud water pH increased between 1984 and 2000 in the northern Colorado Rockies. In *Ext. Abs. Second Intl. Conf. on Fog and Fog Collect.*, 61-64, (ISBN 0-9683887-1-X).

Snedecor, G. W., 1956: *Statistical Methods*, The Iowa State Univ. Press, 534 pp.

shows how cloud droplet pHs are changing

Reexamination of the influences of carbonaceous chemicals on cloud drop activation

Wei-Chun Hsieh and Jen-Ping Chen

Department of Atmospheric Sciences, National Taiwan University

1. Introduction

Carbonaceous contents may affect the capability of cloud condensation nuclei (CCN) to activate into cloud drops in many ways. Black carbon (BC) may retard the growth of droplets by the mechanism of radiative heating (Conant et al., 2002; Nenes et al., 2002). Nonvolatile insoluble organic compounds that reside on drop surface in the form of a monolayer film may cause a significant decrease in water accommodation coefficient, thus retarding the diffusion growth of droplets (Feingold and Chuang, 2003). Soluble organic compounds decrease the water activity as well as the surface tension of droplets, both result in the enhancement of drop growth. (Facchini et al., 1999). All these mechanisms are most active during the activation stage and may thus influence the number concentration of cloud drops, as well as many microphysical and radiative processes that are strongly dependent of them. In this study we examine the first two effects, namely the BC heating effect and the condensation retardation by film-forming compounds (FFCs), using an adiabatic parcel model with detailed microphysics.

2. Method

We adopt the detailed microphysical parcel model of Chen and Lamb (1994), which applies a multi-component particle framework that categorize particles (either in cloud or aerosol phases) into many size bins according to their water and solute contents. In order to resolve the fine variations in cloud drop activation, we applied 160 solute bins with a mass ratio of 1.1 between neighboring bins. For the water component, 45 bins with a bin-sizing ratio of 2 were applied.

Under the assumption of adiabatic ascent, aerosol and cloud particles in the air parcel are allowed to evolve naturally according to explicit physics. As our goal is to understand the changes in cloud drop number concentration due to the existence of carbonaceous material in CCN, the model simulations will emphasize on the activation stage of cloud formation. So our theoretical analysis will focus on the following condensation growth equation:

$$\frac{dm}{dt} = \frac{4\pi \cdot r \cdot D_v' \cdot f_v}{R_v} \cdot \left(\frac{e_a}{T_a} - \frac{e_{sw}(T_d, r, a_w)}{T_d}\right) \quad (1)$$

Corresponding author address: Jen-Ping Chen, Department of Atmospheric Sciences, National Taiwan University, Taiwan 10671, R.O.C.
Email: jpchen@webmail.as.ntu.edu.tw

where m and r are the mass and radius of the drop, D_v' is the diffusion coefficient with correction of gas kinetic effect, f_v is the ventilation coefficient, R_v is the water vapor gas constant, T_a and T_d are the ambient and drop temperatures, e_a is the ambient vapor pressure, and $e_{sw}(T_d, r, a_w)$ is the saturation vapor pressure over the surface of the drop that has a water activity of a_w. In this equation, T_d is directed influenced by the black-carbon heating effect, and D_v' is influenced by the FFCs as discussed below.

3. Effects of BC heating

The effect of BC on cloud drop activation is treated by adding a radiative heating term in the condensation equation. We first derive the modified condensation formula and transform the effect into the Köhler equation to demonstrate the BC heating effect on a single particle. The parcel model then is used to evaluation the effects on a population of aerosols.

In equation (1) the drop temperature can be determined from the energy balance equation:

$$L \cdot \frac{dm}{dt} - 4\pi \cdot r \cdot k_a' \cdot f_h \cdot (T_d - T_a) + Q = 0 \quad (2)$$

where L is the latent heat of evaporation, k_a' is the thermal conductivity of air with gas-kinetic effect correction, and f_h is the heat ventilation coefficient. The three terms represent latent heat release, heat conduction and other heat sources (Q) such as BC radiative heating. By combining (1) and (2) with some rearrangement and simplifications, the growth equation can be transformed into a form commonly seen in textbooks (cf. Pruppacher and Klett, 1997, p. 511):

$$\frac{dm}{dt} \approx \frac{4\pi \cdot r}{A_D + A_K} \cdot (S_a - S_d) \cdot (1 - B) \quad (3)$$

where

$$A_D = \frac{R_v T_a}{D_v' f_v e_{sw}(T_a, \infty, 1)}, \quad (4)$$

$$A_K = \left(\frac{L}{R_v T_a} - 1\right) \frac{L}{k_a' f_h T_a}, \quad (5)$$

S_a is the ambient saturation ratio, $S_d = S_w(T_a, r, a_w)$ is the saturation ratio of the drop with surface temperature the same as in the ambient, and

$$B = Q \cdot \frac{\left(L/R_v T_a - 1\right)}{(S_a - S_d) 4\pi r k_a' f_h T_a} \quad (6)$$

represents the BC heating effect.

The theoretical basis of cloud drop activation is the Köhler equation, which describes the equilibrium vapor pressure over a drop surface as influenced by the solute and curvature effects. Divide this surface vapor pressure by the saturation vapor pressure over a flat water under the same temperature one will get the S_d in (6). This Köhler theory can be written as:

$$S_d = a_w \cdot \exp\left(\frac{2\sigma}{\rho_w R_v T_a r}\right), \qquad (7)$$

where σ is the surface tension between water and air, and r_w is the water density. Heating by BC absorption will raise the drop temperature and alter S_d. By ignoring the latent heating term in 2, the temperature difference is derived as:

$$\Delta T \equiv T_d - T_a = \frac{Q}{4\pi \cdot r \cdot k_a' \cdot f_h}. \qquad (8)$$

By applying the Clausius-Clapeyon equation, the saturation ratio of heated droplet is

$$S_d' = S_d \cdot \exp\left(\frac{L}{R_v}\frac{\Delta T}{T_a(T_a+\Delta T)}\right) \approx S_d \cdot \left(1+\frac{L}{R_v}\frac{\Delta T}{T_a^2}\right) \qquad (9)$$

The exponential term represents the BC heating effect on drop saturation ratio. Such "heated" Köhler curves are plotted in Figure 1 for CCN with dry radii of 0.1, 0.3 and 1 μm, each contains 50% BC. One can see that the critical saturation ratio is elevated significantly. This phenomenon may hinder the growth and activation of droplets as discussed in Conant et al. (2002).

The actual situation is a bit more complicated because the drop should also be heated by latent heat release during growth. One can modify (3) to get:

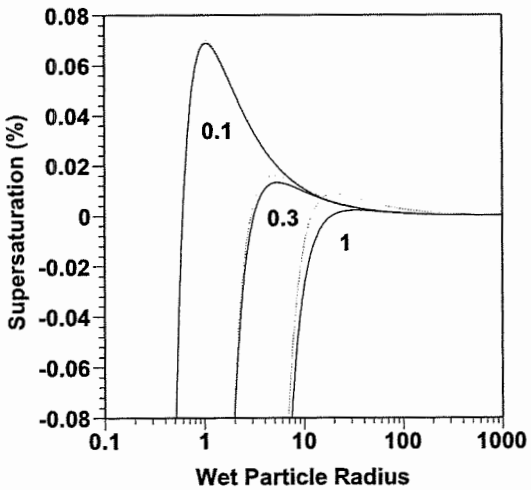

Figure1: Effect of BC heating on the Köhler curves for particles with dry radii of 0.1, 0.3 and 1 μm. The solid lines are for unheated, and the dashed lines are for heated droplets. Particles with larger dry radius contain more BC, thus has stronger heating effect.

complete treatment of particle growth

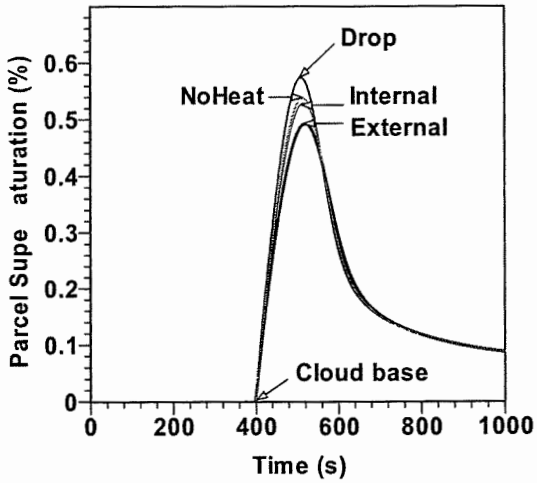

Figure 2: Development of supersaturation in air parcel for four BC heating scenarios. Marine aerosol distribution is applied and BC mass content is 50%.

$$\frac{dm}{dt} = \frac{4\pi \cdot r}{A_D + A_K} \cdot (S_a - S_d') \qquad (10)$$

where

$$S_d' = S_d \cdot \left(1 + B \cdot \frac{S_a - S_d}{S_d}\right) \qquad (11)$$

Comparing with (9), this formula shows that the BC heating effect on the capability of CCN activation into cloud drops is modulated by latent heating whenever the droplet is growing (i.e., $S_a > S_d$).

Nenes et al. (2002) evaluated the BC heating effect by considering four heating scenarios: no heating (NO), heat drop only (DH), externally mixed BC (XM; BC reside outside of CCN), and internally mixed BC (IM). We performed a similar test by implementing the above analysis into our model. For BC heating we adopted the radiative heating algorithm of Toon and Ackerman (1981). The initial air parcel properties are identical with those in Nenes et al. (2002) except that maritime type aerosol distribution from Whitby (1978) is used.

Figure 2 shows the evolution of cloud supersaturation in a parcel with 0.25 m/s updraft. The variation of maximum supersaturation is similar to those of Nenes et al. (i.e., DH > NO > IM > EM), but the delay of cloud formation for the EM scenario is not obvious in our simulation. The DH scenario has the highest supersaturation because BC heating hinders the growth of drop and thus increases supersaturation (hereafter called the "drop-heating effect"). Heating of BC with a thick liquid shell is stronger that that without. So the air heating in IM scenario should be stronger than in the XM scenario. Note that, the changes in maximum supersaturation become less obvious when the aerosol distribution is of continental type, because much more drops are activated to consume the excess water vapor. In the IM scenario,

BC heating also raises the air temperature, which in turn reduces supersaturation (hereafter called the "air-heating effect") by increasing the saturation vapor pressure. However, drops in the XM scenario are not directly heated by BC, so they grow much faster than those in the IM scenario do. That is why the maximum supersaturation is lower in the XM scenario. So one would expect more cloud drops in the IM scenario.

The relative strength of saturation enhancement or reduction by drop-heating effect to that by air-heating effect depends on the total mass fraction of BC and their distribution among aerosols. We found that the maximum saturation ratio can be either enhanced or depressed for different BC scenarios, which means that net influence of BC heating on cloud drop number concentration can be either positive or negative, a conclusion different from that of Nenes et al. (2002).

4. Effect of FFCs on drop growth

Within one mean free path close to the drop surface, the transport of water vapor is considered to proceed not by diffusion but by the gas kinetic process. This "vapor jump effect" is traditionally included in the mass growth equation by using the modified diffusion coefficient D_v' in Eq. (1), which has a full form of:

$$D_v' = D_v \Big/ \left[\frac{D_v}{\alpha r(\upsilon/4)} + \frac{r}{(r+\lambda)} \right] \qquad (12)$$

where D_v is the original diffusion coefficient of water vapor, α is the mass accommodation coefficient, υ is the mean thermal velocity, and λ is the vapor jump distance (one mean free path). The FFCs retard drop growth through their influence on α. Earlier studies (e.g., Feingold and Chuang, 2002) often assume that the effect of FFC on α occur only when the surface coverage by FFC exceeds a threshold value. So the value of α is either 0.035 (for pure water) or ~10^{-5} (for full FFC coverage). However, by reexamining the experimental data in relevant articles (e.g., Archer and La Mer, 1955; Rubel and Gentry, 1985; Seaver et al., 1992), we conclude that the effect should still exist under partial coverage. Based on molecule flux theory we developed a new, simple method to describing the relationship between α and FFC coverage.

To a first-order approximation, one may assume the FFCs affect water vapor flux only over the portion of drop surface that covered by them. Thus from the microscopic point of view, the total water vapor flux of the drop surface can be expressed as

$$\left.\frac{dm}{dt}\right|_{total} = \theta \left.\frac{dm}{dt}\right|_{\alpha_H} + (1-\theta) \left.\frac{dm}{dt}\right|_{\alpha_W} \qquad (13)$$

where θ is the FFC fractional coverage, and α_H (=10^{-5}) and α_W (=0.035) are the mass accommodation coefficients over the surface with and without FFC (assuming hexadecanol in this study), respectively. By combining (12) with (13) we have

$$\frac{1}{1+1/\alpha_T\beta} = \frac{\theta}{1+1/\alpha_H\beta} + \frac{1-\theta}{1+1/\alpha_w\beta} \qquad (14)$$

where

$$\beta \equiv \frac{\upsilon}{4} \frac{r^2}{D_v(r+\lambda)}. \qquad (15)$$

and α_T is the overall accommodation coefficient. We found that such a relationship fits well with the experimental data of Rubel and Gentry (1984), as shown in Fig. 3. Note that some FFCs may transform into a "solid" state when the surface coverage is close to unity. So one may switch the value of α_H from 2×10^{-4} to 10^{-5} when the coverage exceeds a threshold value (0.975 in this study).

To test the effect of FFC coverage on cloud drop growth and activation, we assumed three types of FFC contents in aerosol particles. The first and second types (hereafter referred to as FFC-1 and FFC-2, respectively) follow Feingold and Chuang (2002): (1) the mass of FFC is proportional to the particle surface area; (2) the mass of FFC is proportional to the particle mass. These FFCs are presumably non-volatile, so their mass in each particle do not change with time. Then the coverage of FFC can be expressed as (Rubel and Gentry, 1984)

$$\theta = n_H \sigma_H / (4\pi r^2) \qquad (16)$$

where n_H is the total number of FFC molecules, and σ_H (=20.2Å^2) is the effective area per hexadecanol molecule. Note that σ_H varies slightly with the total coverage, but we ignored this secondary effect here. We also would like to test the situation of gas adsorption of volatile FFC, in which case the coverage is determined solely by the gas-phase vapor pressure of FFCs. So, for the third type of FFC content (FFC-3), we assume the coverage is a fixed value.

Figure 4 shows the development of supersaturation in an ascending air parcel for three types of FFCs contents comparing with the FFC-free case (FFC-0).

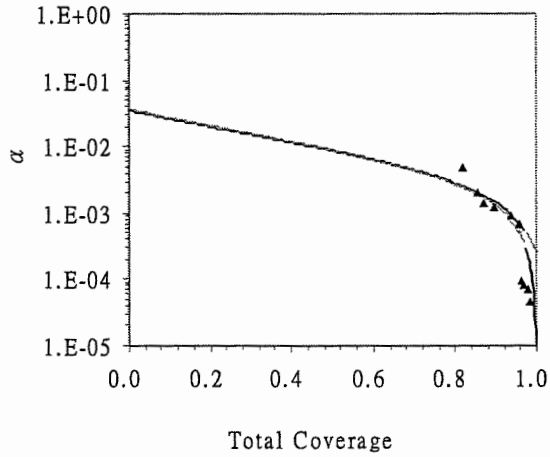

Figure 3: Overall mass accommodation coefficient as a function of FFC coverage. The upper curve is for α_H = 2×10^{-4} (for liquid state) and the lower curve is for α_H = 10^{-5} (for "solid" state). Filled triangles are the experimental data from Rubel and Gentry (1984).

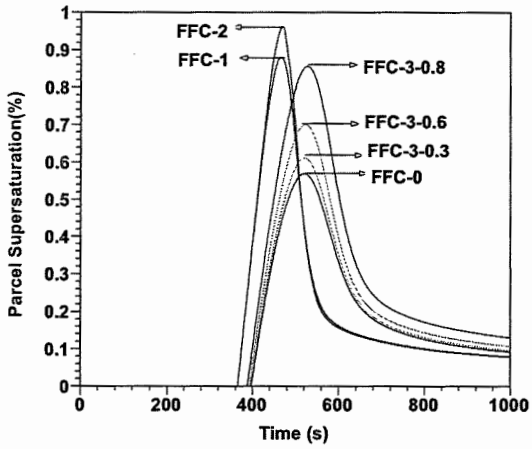

Figure 4: Supersaturation development for four types of FFC content. For FFC-3, three values of overall coverage are given for comparison. The aerosol size distribution is maritime type.

The setting of air parcel properties is the same as those in section 3, except that a continental aerosol type is used. The total FFC mass is 5% of the total aerosol mass for both FFC-1 and FFC-2 scenarios, in which a large portion of the aerosols are initially fully covered by FFC. In Fig. 4, we can see that all types FFC coating raised cloud supersaturation due to retardation of the condensation process. The effect of FFC on supersaturation in the FFC-2 scenario is stronger than that in the FFC-1 scenario because the larger aerosols that are more likely to be activated into cloud drops contain more FFC. In the FFC-3 scenario, particles consume water vapor faster because none of them are fully covered. Also, as the coverage decreases the maximum supersaturation becomes lower as expected. Note that the FFC effect on cloud drops weakens with time for FFC-1 and FFC-2 (but not for FFC-3) because the FFC coverage decreases as drops grow. It is noteworthy that a low amount of FFCs is enough to induce significant change of cloud properties even when the FFC surface coverage is only partial. Also, the effect is stronger for maritime aerosol situation when there are fewer drops to take up water vapor.

The effect of FFC on the maximum supersaturation certainly influences the number concentration of cloud drops. Our simulations generally show an increase in cloud drop number concentration due to the FFC effect. This result is different than those shown by Feingold and Chuang (2002). The difference stems mainly from the effectiveness of FFC under partial coverage that specified in this study.

5. Conclusion

Our simple model simulations suggest that the effect of BC heating on cloud drop activation is dependent on the mass fraction of BC as well as their mixing state within aerosols. The heating on individual drops inhibits drop growth and enhance air supersaturation, but the heating on air reduces supersaturation. The net effect can be either positive or negative. So there exist great uncertainties in estimating the effect of BC on cloud drop number if the total and fractional mass of BC and their state of mixing are not clearly known.

A simple method for modeling the effect of FFCs on water accommodation coefficient suggests that FFC coating on aerosols may increase cloud supersaturation due to retardation of the condensation process. This also means more aerosols can be activated into cloud drops. The effect of FFCs on cloud drop number concentration may be greatly underestimated if one ignores the influence under partial coverage. Currently we still have very poor understanding of the possible candidate of atmospheric FFC species, as well as the species-dependent mass accommodation coefficient.

poor understanding of growth

6. Reference

Archer, R.J., and V.K. La Mer, 1955: The rate of evaporation of water through fatty acid. *J. Phys. Chem.*, 59, 200-208.

Chen, J. P. and D. Lamb, 1994: Simulation of cloud microphysical and chemical processes using a multicomponent framework. Part I: Description of Microphysical Model. *J. Atmos. Sci.*, 51, 2613-2630.

Conant, W. C., A. Nenes, and J. H. Seinfeld, 2002: Black carbon radiative heating effects on cloud microphysics and implications for the aerosol indirect effect, 1, Extended Köhler theory. *J. Geophys. Res.*, 107, doi:10.1029/2002JD002094.

Facchini, M. C., M. Mircea, S. Fuzzi, and R. J. Charlson, 1999: Cloud albedo enhancement by surface-active organic solutes in growing droplets. *Nature*, 401, 257-259.

Feingold, G. and P. Y. Chuang, 2002: Analysis of the Influence of Film-Forming Compounds on Droplet Growth: Implications for Cloud Microphysical Processes and Climate. *J. Atmos. Sci.*, 59, 2006-2018.

Nenes, A., W. C. Conant, and J. H. Seinfeld, 2002: Black carbon radiative heating effects on cloud microphysics and implications for the aerosol indirect effect, 2, Cloud microphysics. *J. Geophys. Res.*, 107, doi:10.1029/2002JD002101.

Pruppacher, H.R., and J.D. Klett, 1997: *Microphysics of Clouds and Precipitation*. Kluwer Academic Publishers.

Rubel, G. O. and J. W. Gentry, 1984: Measurement of the kinetics of solution droplets in the presence of absorbed monolayers: Determination of water accommodation coefficients. *J. Phys. Chem.*, 88, 3142-3148.

Toon, O.B., and T. P. Ackerman, 1981: Algorithms for the calculation of scattering by stratified spheres. *Appl. Opt.*, 20, 36573660.

Whitby K. T., 1978: The Physical characteristics of sulfur aerosols. *Atmos. Environ.*, 12, 135-159.

ON THE ROLE OF THE GIANT AND SUPER-GIANT PARTICLES IN THE FORMATION OF CONVECTIVE PRECIPITATION AND HAIL

B. A. Kamalov

Fergana centre of weather modification, Namangan, Uzbekistan

Works on influence on the hail processes are being carried out in many countries already more than 30 years. Nevertheless the problem is so complicated, that till now there is no common opinion about its efficiency both in theoretical, and in the experimental plan.

At present the influence on the hail processes is carried out by clouds seeding by particles AgI of sub – micron sizes, in hope for creation of the grains in competition with the natural ones for the super – cooled liquid drops or the acceleration of the precipitation formation.

Up to the end of 70s of the last century, AgI was dispersed in the majority of the hail – protection services of the former USSR, in the cloud using the missile Elbrus – 2. In its centre, filled with the explosive, the briquette with AgI (70-100g) was put. During the explosion of an explosive, 1g of AgI produced 10^{12} of particles. By the results of the field measurements it was found out that with such dispersion of AgI by Elbrus – 2 explosives in the atmosphere, only less than 20% of the particles had a diameter more than 0,1 μm, about 1% - more than 0,2 μm while the particles with the diameter more than 1 μm were negligible (Khorguani, 1984).

Later, for the purpose of AgI saving, we changed for the use of pyrotechnical compounds with 1 – 3% content of AgI. Such compounds produce 10^{15} particles from 1g of AgI, i.e., the volume of one dispersed particle has decreased, in average, 1000 times in comparison with the former case. As it is known, with such particles it is required 3 – 4 times supersaturation for the water vapor condensation, which is not observed in nature. That is why, with the injection of such fine particles into a cloud, the effect should be zero. Such particles can be covered with water, but they will not grow further (Mazin, 1983).

At the same time many researchers point out the leading role of the giant and super -gian particles in the formation of the grains of convective precipitation and hail. At high temperature values (-6 ° – -8° C) the giant and super – giant aerosol particles act as iceforming nuclei. The experiments show that after entering the cloud the super – giant aerosol particles are quickly covered by water and transform into drops. Precipitation elements can be fast formed by the gravitational coagulation with small cloud elements. As Stepanov et al. (1990) note, even at 0° to – 5° C big drops (diameter 2 – 3 mm) are formed on super – giant particles in the deep cumulus clouds that make a significant contribution to the total liquid – content of a cloud.

The role of particles in the sizes up to 100-200 μm during formation of precipitation and hailstones was investigated by Rosinski (1974). Studying a microstructure of the aerosol particles contained in drops of precipitation and hailstones, collected at a surface of the ground during passage of the hail process, it was defined, that drops of precipitation are formed on particles of d>70 μm as a result of gravitational coagulation with cloudy drops, and particles d<70 μm are washed away by already formed elements of precipitation

It is necessary to note that with growth of the sizes of particles from 0,1 up to 100 μm the relative ice-forming activity raises on 4-5 orders (Berezinsky, 1986). Thus, the larger the particle on is, the larger the area of a soluble part is, that is, on them, alongside with the active centers of freezing, there are also centers of condensation. The executed chemical analyses show that the share of soluble substances in large particles is rather high and by weight exceeds 20 % (Andreev, 1968).

The concentration of super – giant particles in a cloud is 2 – 3 orders more the concentration of a hailstone while the concentration of giant particle is comparable with concentration of precipitation drops. The concentration of ice – producing nuclei is rather high as well – in the conditions of Central Asia at 3500 m their concentration is 40 – 80 per liter.

Corresponding author's address: Bakhodyr A. Kamalov, Fergana centre of weather modification 22 Navoi str. 716008 Namangan, Uzbekistan, E-mail: uzhymet@meteo.uz

experiments of AgI on hail growth

As it was shown, the giant and super – giant aerosol particles are high – temperature ice – producing nuclei and have a high concentration in a cloud. As the growth of a cloud particles and precipitation particles is mainly due the coagulation, the artificial hail – grains formed on AgI particles are probably not able to affect the growth of the natural hail – grains up to the moment when their sizes can be comparable. To reach such sizes is difficult because there is a high probability that they can be entrained by the larger natural cloud particles. This is proved by the measurements of M.Tlisov, which demonstrate that Ag particles in the hailstone layers from the seeded cloud are one order higher than in the hail – grains.

Table

Concentration of aerosol particles in layers and germs of hailstones.

Types of layers and of germs of hailstones	d_2 μm	d>0,5 μm		d<4 μm		d<10 μm		d>30 μm		d>60 μm	
		$nx10^6$ cm^{-3}	%	$nx10^6$ cm^{-3}	%	$nx10^6$ cm^{-3}	%	$nx10^4$ cm^{-3}	%	$nx10^4$ cm^{-3}	%
July 17											
Dry growth	4,6	7,5	100	5,7	76	7,4	98,7	3,3	0,4	0,15	0,02
Wet growth	10,7	4,3	100	2,6	60,5	4,0	93,0	4,6	1,1	0,20	0,047
The mixed growth	9,2	2,8	100	1,9	67,9	2,6	92,9	3,7	1,3	1,10	0,39
Germ-graupel	5,3	4,4	100	2,8	63,6	4,2	95,5	0,26	0,1	-	-
Germ-drop	8,6	4,3	100	2,7	62,8	4,0	93,0	3,7	0,9	1,30	0,3
July 22											
Dry growth	5,2	5,3	100	3,6	67,9	5,2	98,1	0,87	0,16	-	-
Wet growth	11,8	2,3	100	1,5	65,2	2,1	91,3	4,60	2,00	0,2	0,09
Germ-graupel	4,5	4,8	100	3,5	72,9	4,7	97,9	0,37	0,08	-	-
Germ-drop	8,2	4,9	100	2,9	60,4	4,7	95,9	2,55	0,52	0,1	0,02

In the table the data on concentration of aerosol particles in layers and germs hailstones, dropped out 17 and 22 July, 1978 in Krasnodar region (Russia), borrowed of (Tlisov et al., 1984). They characterize two hails processes-the first without seeding, the second with seeding.

The average sizes of aerosol particles in both cases are identical. In a case without seeding the maximum size of hailstones reached 2 sm., with seeding 3,5 sm. One big distinction between these cases of a hail fall is that in a case with seeding the quantity of aerosol particles of d>60μm on one order is less than in a case without seeding. Thus, in a case with seeding the germinal drops contained larger particles which size reached 260 μm. Probably, small number of particles of d>60 μm and their larger sizes have resulted in larger size of the dropped out hailstones and more intensive hail in a case with seeding.

Apparently, researches show a predominating role of giant and super giant particles in formation of germs convective precipitation and hailstones. Such particles are marked in sufficient number and on high (up to 5 km and more) altitudes. As growth of cloudy particles and particles of precipitation occurs mainly due to coagulation, in prevention of a hail it is difficult for a big success of clouds seeding with sub-micron particles of AgI.

The hypothesis of the acceleration of the precipitation formation with the aim of the mitigation of hail-damage due to the above-mentioned reasons is also problematic. Here it is necessary to mention that the acceleration of precipitation formation results (by the opinion of the authers) in some suppression of the updraught. And this should give rise to some decrease of precipitation. However, it is not observed. For example, in Gissar valley of Tadjikistan and on Northern Caucasus in result of hail suppression seeding the increase of precipitation at 10-20% is marked, and in Moldova it was impossible to establish any appreciable influence of hail cloud seeding on quantity of precipitation.

In Uzbekistan influence of convective clouds seeding on precipitation was investigated by comparison of the data on tested territory with the data on four control territories (Kamalov et al., 1985). Thus precipitation in tested territory are well correlated with precipitation in control territories. Factor of correlation is 0,78-0,93. The analysis of received data given by various

statistical ways specifies the absence of any directed changes of the sums of precipitation in result of convective clouds seeding. . Thus, this also the reason why the hypothesis about the acceleration of precipitation formation is still doubtful (Kamalov, 2001).

The reported success of the hail-suppression measures is determined, probably by:

- temperature rise with the growth of the first crystals as result of AgI particles entering the hail-grains
- dynamic effect of the missiles and shells explosion.
- acting as a reagent of the products of liquidation of the missiles and shells.

Taking all above mentioned into account, we can make a conclusion that it is more rational to conduct a cloud seeding by the ready coagulation centres for the mitigation of hail-damage.

References

1. Andreev B. G., Lavrinenko R. F., 1968: Some data about chemical composition of the Central Asia atmospheric aerosols. Meteorology and Hydrology, - 4. 63-69.

2. Berezinsky N. A., Stepanov G.V., Khorguany V. G., 1986: Dependence of ice-forming properties of a natural aerosol from the sizes of particles. VGI Proceedings, v, 63, 28-32.

3. Kamalov B. A., Sabaev V. V., Usmanov I., 1985: Evaluation of hail protection effect on the precipitation regime in Fergana valley. SANII Proceedings, 100(181), 56-75.

4. Kamalov B.A., 2001: Some questions of influences on hydrometeorological processes. Theses of reports the All-Russia conference on physics of clouds and active influences on hydrometeorological processes, VGI, Nalchik, 20-21.

5. Khorguani V. G., 1984: Microphysics of hailstone generation and growth.- Gidrometeoizdat, Moskov.-187 p.

6. Mazin I. P., Shmeter S. M., 1983, Clouds, Their Structure and Formation.- Gidrometeoizdat Leningrad.- 279 p.

7. Rosinski J., 1974: Role of aerosol particles in formation of precipitation. J. Rev. of Geophys. Space Physics. Vol. 12, I, 129-133

8. Stepanov G.V. etc., 1990: Super giant particles in powerful - cumulus clouds. VGI, Proceedings, 81, 115-123.

9. Tlisov M. J., Berezinsky N. A., 1984: Spectrum of sizes and ice-forming properties of aerosol particles contained in hailstones. Meteorology and Hydrology, 3, 50-55.

ON THE PRECIPITATION FORMATION IN DESERT AND NEAR-DESERT REGIONS

B. A. Kamalov

Fergana center on weather Modification Namangan, Uzbekistan.

As it is known, at present the desertification process affects the life of more than 300 mln people. About 1 bln of people living in more than 100 countries, are subjected to the menace of drought. In this conditions the advance of the deserts is going on, which depends not only on the climate but anthropogenic changes, as well. According to the evaluations, the velocity of the deserts advancing reaches 60 000 km ^{2} per year.

In 1977 the International Plan of Activities to Combat Desertification was adopted. A lot of plans and strategies on the environment monitoring and nature resources management were worked out. However, there is no sensible effect observed, and the problem of the land degradation is being more and more acute in the whole world which was stated by UNEP in 1991. The appearance of Convention to Combat Desertification is proving it, but this Convention will fail if the main attention will not be paid to the primary reasons of desertification process (both anthropogenic and climatic ones).

The anthropogenic reasons of desertification are known. They are such as the extensive cattle grazing, cutting of woods, ploughing of the land without necessary water needed for irrigation, land salinization with the extra irrigation and bad drainage, etc. These factors facilitate the effect of the wind and water erosion.

The climatic factors of desertification are presented by the extremely low amount of precipitation. Such situation in the desert areas is determined by the downdroughts of the air in the desert belt of the Earth caused by the trade-wind circulation prevailing during the year. There is also an opinion that the reason of such down-droughts is the increased albedo of the deserts.

Not contradicting such explanations of desertification I would like to note the following.

As it is known, the deserts and near-desert regions are characterized by abundance of dust. The huge places covered by sand and loess, dryness of climate and frequent en occurrence of strong winds, causing dust storms, create the conditions for entry in to atmosphere of a large amount of soil-erosive aerosol. According to the conducted researches this aerosol has a considerable fraction of solutes and consequently is the active nucleus of condensation.

The analysis of aerosols in Central Asia demonstrates, that in arid aerosol the content of gigantic aerosol particles increased by an order, that was confirmed in the Soviet-American experiment on investigation of arid aerosol. Even in regions, which are a little distant from desert, for example, near neighborhoods of Namangan such situation is remained. Namangan is in the northern part of the Fergana valley, and surrounded on all sides by high (4000-5000 m a.s.l.) mountains and only in west by narrow mountain pass it appears on the plains of Central Asia. This town is relatively removed from the famous desert Kyzylkum. But, in spite of this, the measurements made there, showed the increased concentration of gigantic aerosols: the particles with the size of 1 $\mu m < r < 16$ μm in a surface layer of air were 2-3 cm^{-3}, increasing up to 10 cm^{-3} (Khusanov G. H etc., 1974). The results of Soviet-American experiment have shown, that in arid aerosol the increase of the contents of large aerosol particles d>3-4 μm is accompanied by decrease in 5-10 times of the contents of fine d<1 μm particles. Thus the function of distribution of particles by size has a mode in the range of 40-50 μm. In spectra of the areas and volumes of particles the basic mode is displaced in the range of 60-70 μm (Smirnov V. V., 1992). The increased content of aerosol particles is marked as well at altitudes. It concerns also ice nucleus. For example, over the Kashkadarya valley at altitudes up to 3000 m a.s.l. the concentration of ice nucleus is 10-20 particles per liter (Abdukarimov etc., 1988).

Now researches show the significant role of giant and super-giant particles in formation of germs of precipitation. Easily to itself to present, that at various concentration of such particles the

Corresponding author's address: Bakhodyr A. Kamalov, Fergana centre of weather modification 22 Navoi str. 716008 Namangan, Uzbekistan, E-mail: uzhymet@meteo.uz

various conditions for growth of cloudy particles are created: independent coagulation growth is possible only up to some critical concentration of giant and super-giant particles. At concentration exceeding critical, the particles impede each other and, hence, growth of cloudy particles up to the sizes of particles of precipitation's is hampered, and in some cases is not reached at all.

The increased concentration of gigantic aerosols in desert and near-desert regions creates here the limitations in coagulation growth of cloud particles as a result of which the capability of occurrence of precipitation particles is restricted. Therefore in these regions it is more expedient to increase the precipitation, probability, not by cloud seeding, but on the contrary, by the cleaning of atmosphere from nucleus of condensation up to an optimal level.

References

1. Abdukarimov A. T., Vychuzhanina M. V., Mirochnichenko V. I., Parshutkina I. P. 1988, Ice nucleus measurements in the Kashkadarya river basin // CAO Proceedings. - №171. - p.14-18.
2. Smirnov V. V. 1992, Characteristics of disperse of structure of arid aerosol // "Soviet-American experiment on study of arid aerosol"- Cankt-Peterburg – p. 143-154.
3. Khusanov G.H., Petrenchuk O. P., Drosdova V. M. 1974. Chemical composition of aerosols in some area of Central Asia // GGO Proceedings. - №314. – p. 192-220.

THE CITY INFLUENCE ON PRECIPITATION IN CENTRAL ASIA

B. A. Kamalov

Fergana centre weather modification Namangan, Uzbekistan

As it is known, precipitation increase and modification in the city in comparison with environmental territory is the result of tree main reasons:

1.The city appear to be island of warmth, which leads to more intensive vertical air movement-the main condition of precipitation formation.

2. Air dynamics roughness of the city structure creates "barrier" effect.

3. Intensive pollution of the atmosphere above the city in comparison with environmental territory.

It is necessary to mention that practically all studies in this field emphasize the increase of precipitation amount in the urban areas comparing with the rural areas, or depending on the growth of the towns. However, such conclusions are somewhat doubtful because the available data are not very significant from the point of view of statistics. Regardless this point, the researches keep to the opinion of the importance of the urban effect on precipitation. The present work considers the study of this problem in the conditions of the Central Asian towns which are located near the deserts and subjected to their influence.

The results of studies of the change of precipitation amount in Tashkent, Namangan and other Central Asian towns located near the deserts reveal that the increase of the annual precipitation totals is rather rapid – 1 mm per year in average. Such trend is significant at 99% - level. However, such trend is similar to the annual precipitation totals recorded at the rural meteostations. This proves that precipitation increase in the Central Asian urban areas is caused, mainly by the common climatic factors, and the urbanization impact is rather smoothed in such case. In Tashkent the decrease of the number of days with the thunderstorms is being recorded, while in many studies their increase is noted (Landsberg, 1981, Glazyrin G. E. , 1991). What is the reason?

Table 1

Mean – monthly air temperature (^{0}C)

Month	Ashgabat		Mary	
	Urban area	Suburban area	Urban area	Suburban area
I	1.0	0,9	1,3	1,7
II	4.3	4,3	4,5	5,1
III	9.8	9,4	9,7	9,8
IV	16,4	16,4	16,9	17,1
V	22,8	23,1	23,2	23,6
VI	27,3	28,3	27,6	28,1
VII	29,3	30,6	29,6	30,0
VIII	27,7	28,9	27,7	27,9
IX	22,6	23,3	21,9	22,6
X	15,3	15,8	15,0	15,6
XI	8,4	8,1	8,3	8,9
XII	3,7	3,5	3,7	3,5
year	15,7	16,1	15,8	16,1

Corresponding author's address: Bakhodyr A. Kamalov, Fergana centre of weather modification 22 Navoi str. 716008 Namangan, Uzbekistan, E-mail: uzhymet@meteo.uz

First is was decided to ascertain the existence of the effect of the "heat island" and it was recognized that such effect does not exist in the Central Asian always. As it is presented in the Reference books on climate, the air temperature

in the urban areas is sometimes less than in the rural ones. It is demonstrated in Table 1 where the data on the mean – monthly air temperature in Ashgabat and Mary towns and in their surroundings are presented.

There are different opinions concerning the temperature regime of the biggest cite of the Central Asia – Tashkent (with population of more than 2 mln people and area about 300 km^2). Meteorological observations were started in Tashkent observatory since 1867 while since 1876 they are carried out on a permanent site. In the beginning this observational site was situated on the periphery of Tashkent but now it appeared to be just in its centre. The population of the cite was increased more than 15 times during the passed period.

After the study of the temperature regime variation in Tashkent, T. Sarymsakov et al. (1949) and E. Sofiev (1978) did not found out any systematic changes. G. Glazyrin (1982), when analyzing the air temperature trend by the data up to 1980, did not also found out them. But when he compared the date on the air temperature recorded at Tashkent meteostation and Dalversin station which is located 100 km to the south from Tashkent, he made a conclusion that the city has the warming effect (G. Glazyrin, 1991). However, to my mind, it is not reliable to compare the data taken at Dalversin station which is rather far from Tashkent.

With the aim of getting more correct results about the urban effect on the air temperature in Tashkent we used the data presented in two climatic reference books, taking the records of the stations located in the vicinity of Tashkent city. In one of them the mean-monthly values of the air temperature averaged up to 1960 are presented, while in the second one the date averaged up to 1980 are given. Their comparison is presented in Table 2 beneath.

Table 2

Air temperature values and their difference using the information of two reference books (^0C)

Meteo stations	Mean-yearly air temperature			Mean-winter (XII-II) air temperature			Mean summer (VI-VII) air temperature		
	To 1980	To 1960	Diffe rence	To 1980	To 1960	Diffe rence	To 1980	To 1960	Diffe rence
Bozsu	13.5	13.2	0.3	2.4	2.2	0.2	25.3	25.4	-0.1
Kaunchy	13.1	12.8	0.3	1.2	1.2	0.0	25.5	25.4	0.1
Kokaral	12.9	12.7	0.2	1.2	0.7	0.5	25.1	25.7	-0.6
Cyrdarya	12.9	12.6	0.2	1.1	0.6	0.5	25.4	25.3	0.1
Tashkent	13.5	13.3	0.3	2.4	2.3	0.1	25.6	25.5	0.1

These results do not give the ground to make a conclusion about the air temperature increase in Tashkent comparing with its neighborhood, which is probably explained by the green cover of the city and not very high heating during the winter. By the results of investigations conducted by B. Aizenshtat and L. Lukina (1982) the green plants cause the decrease of the mean-daily air temperature on 1.4-4.7 (^0C) in summer. They occupy about 40% of the whole surface area of Tashkent. Such features are characteristic for the Central Asian towns, that is why it is doubtful to ascertain the heating effect of the town resulting in precipitation increase.

As a rule, the impact of the atmospheric pollution on precipitation increase in the urban areas is related to the vast amount of the condensation nuclei which are emitted by the city traffic and industrial enterprises into the atmosphere. At the same time, the nearby location of the deserts results in the abundance of dust in the atmosphere of the urban areas located close to the deserts. Besides, the major part of these dust particles is hygroscopic and their sizes are somewhat bigger then the industrial emissions. We can suspect that the impact of the atmospheric pollution of the urban areas in the vicinity of deserts on precipitation formation is negligible.

References

Aizenshtat B. A., Lukina L. P., 1982: Bioclimate and mikroclimate of Tashkent.-Gidrometeoizdat, Leningrad.-128 p.

Glazyrin G. E., 1982: Climate of Tashkent by the data of the regular meteorological observations. Proc. of SANII v.94 (175), 85-93

Glazyrin G. E. et al., 1991: Secular trend of Tashkent climate. News of the Uzbekistan Geographic society, 17, 18-24.

Landsberg H. E., 1981: Yhe urban climate.- Academic Press, New York London Toronto Sydney San Francisco.-247 p.

Sofiev E. I., 1978: On the secular variability of the air temperature in Tashkent. Proc. of SANIGMI v. 57(138), 79-82.

Sarymsakov T. A. et al. 1949: On the long-term stability of the temperature regime in Central Asia. Reports of Ac. of Science of Uzbekistan. 4, 17-22.

PARAMETRIZATION OF WATER-SOLUBLE VOLUME FRACTION OF ATMOSPHERIC AEROSOL

K. Kandler[1], B. Busch[2], and L. Schütz[1]

[1]Institute for Physics of the Atmosphere, Johannes Gutenberg-University, Mainz, Germany
[2]Institute for Inhalation Biology, GSF-Research Center, Oberschleißheim, Germany

1. INTRODUCTION

The hygroscopicity of atmospheric aerosol is an important parameter for calculations of aerosol-cloud interactions, aerosol radiative properties and aerosol deposition in the lung. Thus, since decades many measurements have been performed to investigate hygroscopic properties.
These measurements were made by different methods under strongly varying conditions. In earlier work (Busch et al., 2002; Kandler, 2003), measurements with a single set of methods covering a wide size range of aerosol particles were performed at different places to gather information about characteristic hygroscopic properties of different aerosol type (i. e. urban or rural). To compare these measurements independently of humidity values, the parameter "water-soluble volume fraction" was used in this compilation.
The measurements show a very inhomogeneous behavior depending on time and place of measurement. To use such inhomogeneous data in radiative transfer or cloud models, it is often neccessary to parametrize it into more simple relationships.

2. METHODS

A set of two methods was used to measure hygroscopicity of atmospheric particles in the range of 50 nm to 4 µm: the well known "Hygroscopic Tandem Differential Mobility Analyzer" (HTDMA; for details see Busch et al., 2002) and the "Soluble Fraction of Large and Giant Particles" (SoFA) method (Eichel et al, 1996; Busch et al., 2002).
The HTDMA measures growth fractor of particles as a function of relative humidity, from which – knowing the chemical composition of aerosol particles – the water-soluble volume fraction can be well determined (Swietlicki et al., 1999). With the SoFA method the water-soluble volume fraction can be measured directly.
Additionally to these measurements, data for this compilation was taken from: Winkler (1974), Ochs and Gatz (1980), Okada (1983), Sekigawa (1983), Fuzzi et al. (1988), Winkler (1988), Alofs et al. (1989), Svenningsson et al. (1994), Brunnemann et al. (1996), Eichel et al. (1996), Kasahara et al. (1996), Khlystov et al. (1996), McInnes et al. (1996), Svenningsson et al. (1997), Sprengard-Eichel (1998), Ferron et al. (1999), Lee et al. (1999), Swietlicki et al. (1999), Zappoli et al. (1999), Naoe and Okada (2001), Okada and Hitzenberger (2001), Zhou et al. (2001), Weingartner et al. (2002).
Data show, that there exists usually a maximum of water-soluble volume fraction ε in the accumulation range (100 nm < d < 1 µm). Thus, an logarithmic normal distribution was used for data parametrization:

$$\varepsilon(d) = \varepsilon_0 + \varepsilon_v \cdot \exp\left[-\left(\frac{\log\left(d/d_0\right)}{\sigma_{log}}\right)^2\right]$$

with d particle diameter and ε_0, ε_v, d_0, σ_{log} parameters of the fit function (see Table 1).

3. RESULTS

The hygroscopicity measurements were classified into four aerosol types according to place and investigated air mass: maritime, urban, continental and free-tropospheric.
Parameters calculated for different aerosol types can be found in Table 1 together with the correlation coefficient. Figure 1 shows the results of the parametrization together with the measured data.
As a common feature a maximum of water-soluble volume fraction in or near the accumulation range can be found. This maximum can be explained by the high residence time of these particles: the longer the residence time, the higher the probability of particles being cloud-processed and thus having high soluble volume fraction. In maritime aerosol type this maximum is less pronounced. This may be explained by the production of soluble large particles (sea-salt). In average, maritime and free-tropospheric aerosol types show the highest water-soluble volume fractions, which is expected due to their

Corresponding author's address: Konrad Kandler, Institut für Physik der Atmosphäre, Johannes Gutenberg-Universität, 55099 Mainz, Germany
E-Mail: kzk@gmx.de

formation processes. The high variability of the maritime values may be due to a bias, because for these measurements in the past the greatest number of different analytical methods was used. It has to be mentioned, that aerosol particles of one size are not necessarily uniform in hygroscopicity: at one size there can exist separate modes or a spectrum of particles with different hygroscopicity in an external mixture (earliest works by Winkler, 1969; Covert et al., 1972). However, the amount of data available is not sufficient for a parametriztaion due to its high variability. A compilation on this topic was made by Kandler (2003).

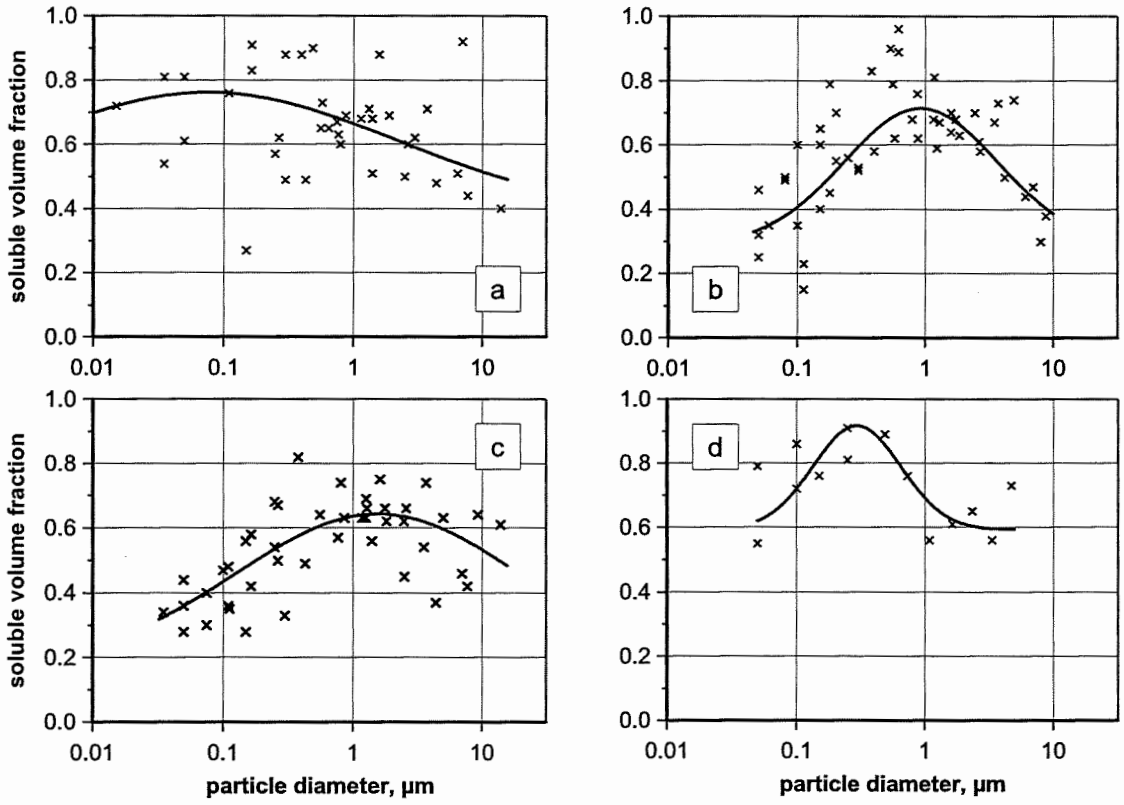

Figure 1: Measured soluble volume fraction ε and its parametrization for maritime (a), urban (b), continental (c), and free-tropospheric (d) aerosol type

aerosol type	ε_0	ε_v	d_0, µm	σ_{log}	r	*range, µm*
maritime (a)	0.39	0.37	0.076	2.02	0.16	$0.01 < d < 16$
urban (b)	0.29	0.42	0.93	0.85	0.73	$0.05 < d < 10$
continental (c)	0.16	0.48	1.56	1.58	0.71	$0.03 < d < 16$
free tropospheric (d)	0.59	0.32	0.30	0.48	0.69	$0.05 < d < 5$
total	0.42	0.26	0.90	0.79	0.46	$0.01 < d < 16$

Table 1: Parameters for calculation of average soluble volume fraction ε (see equation), correlation coefficient r and applicable particle size range (diameter)

4. CONCLUSIONS

The average water-soluble volume fraction of atmospheric aerosol particles was investigated. Together with a comprehensive literature review this data was classified into four different aerosol types. The so classified data was parametrized as a function of particle size using a logarithmic

measure hygroscopicity of diff aerosol fractions

normal distribution function. It can now be used as a simplified input parameter for various model calculations.

5. ACKNOWLEDGEMENT

This work was supported by the BMBF (German federal ministy of Education and Research) under grant AFS-07AF112.

6. REFERENCES

Alofs, D. J., Hagen, D. E., and Trueblood, M. B., 1989: Measured spectra of the hygroscopic fraction of atmospheric aerosol particles. J. Appl. Meteorol., 28, 126 – 136.

Brunnemann, G., Ten Brink, H. M., Dlugi, R., Kins, L., and Kos, G. P. A., 1996: Comparison of aerosol composition and size distributions at Petten (the Netherlands) and Hohenpeissenberg (southern Germany) for northwesterly and easterly air masses. J. Aerosol Sci., 27, S115 – S116.

Busch, B., Kandler, K., Schütz, L., Neusüß, C., 2002: Hygroscopic properties and water soluble volume fraction of atmospheric particles in the diameter range from 50 nm to 3.8 µm during LACE 98. J. Geophys. Res., 107 D, LAC 2-1 – LAC 2-11.

Covert, D. S., Charlson, R. J., Ahlquist, N. C., 1972: A study of the relationship of chemical composition and humidity to light scattering by aerosols. J. Appl. Meteor., 11, 968 – 976.

Eichel, C., Krämer, M., Schütz, L., and Wurzler, S., 1996: The water-soluble fraction of atmospheric aerosol particles and its influence on cloud microphysics. J. Geophys. Res., 101, 29499 – 29510.

Ferron, G. A., Karg, E., Busch, B., and Heyder, J., 1999: Hygroscopicity of ambient particles. J. Aerosol Sci., 30, S19 – S20.

Fuzzi, S., Orsi, G., Nardini, G., Facchini, M. C., McLaren, S., McLaren, E., and Mariotti, M., 1988: Heterogeneous processes in the Po valley radiation fog. J. Geophys. Res. D, 93, 11141 – 11151.

Kandler, K., 2003. Hygroskopische Eigenschaften atmosphärischer Partikel in kontinentalen Luftmassen. Dissertation, University of Mainz. http://archimed.uni-mainz.de/pub/2003/0023

Kasahara, M., Park, J. H., and Yamamoto, K., 1996: Characterization of atmospheric aerosols separated by particle size and water solubility using PIXE analysis. Nucl. Instrum. Meth. B, 109/110, 471 – 475.

Khlystov, A., Kos, G. P. A., Ten Brink, H. M., Kruisz, C., and Berner, A., 1996: Activation properties of ambient aerosol in the Netherlands. Atmos. Environ., 30, 3281 – 3290.

Lee, C.-T., Lin, N.-H., Hsu, W.-C., Chang, Y.-L., and Chang, S.-Y., 1999: Local circulation and aerosol water-soluble ions - a case study in Taiwan during Mei-Yu season. Chemosphere, 38, 425 – 443.

McInnes, L. M., Quinn, P. L., Covert, D. S., and Anderson, T. L., 1996: Gravimetric analysis, ionic composition, and associated water mass of the marine aerosol. Atmos. Environ., 30, 869 – 884.

Naoe, H. and Okada, K., 2001: Mixing properties of submicrometer aerosol particles in the urban atmosphere - with regard to soot particles. Atmos. Environ., 35, 5765 – 5772.

Ochs, H. T. and Gatz, D. F., 1980: Short communication on water solubility of atmospheric aerosols. Atmos. Environ., 14, 615 – 616.

Okada, K., 1983: Volume fraction of water-soluble material in individual aerosol particles. J. Aerosol Sci., 14, 301 – 302.

Okada, K. and Hitzenberger, R., 2001: Mixing properties of individual submicrometer aerosol particles in Vienna. Atmos. Environ., 35, 5617 – 5628.

Sekigawa, K., 1983: Estimation of the volume fraction of water soluble material in submicron aerosols in the atmosphere. J. Meteor. Soc. Japan, 61, 359 – 366.

Sprengard-Eichel, C., 1998: Die wasserlösliche Fraktion atmosphärischer Aerosolpartikel: Anteil und Zusammensetzung im Radiusbereich 0.2 bis 2.0 µm. Dissertation, University of Mainz; Shaker Verlag, Aachen.

Svenningsson, B., Hansson, H.-C., Martinsson, B., Wiedensohler, A., Swietlicki, E., Cederfelt, S. I., Wendisch, M., Bower, K. N., Choularton, T. W., and Colvile, R. N., 1997: Cloud droplet nucleation scavenging in relation to the size and hygroscopic behaviour of aerosol particles. Atmos. Environ., 31, 2463 – 2475.

Svenningsson, B., Hansson, H.-C., Wiedensohler, A., Noone, K., Ogren, J., Hallberg, A., and Colvile, R., 1994: Hygroscopic growth of aerosol particles and its influence on nucleation scavenging in cloud: Experimental results from Kleiner Feldberg. J. Atmos. Chem., 19, 129 – 152.

Swietlicki, E., Zhou, J., Berg, O. H., Martinsson, B. G., Frank, G., Cederfelt, S. I., Dusek, U., Berner, A., Birmili, W., Wiedensohler, A., Yuskiewicz, B., and Bower, K. N., 1999: A closure study of sub-micrometer aerosol particle hygroscopic behaviour. Atmos. Res., 50, 205 – 240.

Weingartner, E., Gysel, M., and Baltensperger, U., 2002: Hygroscopicity of aerosol particles at low temperatures. 1. New low temperature H-TDMA instrument: Setup and first applications. Environ. Sci. Tech., 36, 55 – 62.

Winkler, P., 1969: Untersuchungen über das Größenwachstum natürlicher Aerosolteilchen mit der relativen Feuchte nach einer Wägemethode. Ann. Meteorol., 4, 134 – 137.

Winkler, P., 1974: Die relative Zusammensetzung des atmosphärischen Aerosols in Stoffgruppen. Meteorol. Rdsch., 27, 129 – 136.

Winkler, P., 1988: The growth of atmospheric aerosol particles with relative humidity. Physica Scripta, 37, 223 – 230.

Zappoli, S., Andracchio, A., Fuzzi, S., Facchini, M. C., Gelencser, A., Kiss, G., Krivacsy, Z., Molnar, A., Meszaros, E., Hansson, H.-C., Rosman, K., and Zebühr, Y., 1999: Inorganic, organic and macromolecular components of fine aerosol in different areas over Europe in relation to their water solubility. Atmos. Environ., 33, 2733 – 2743.

Zhou, J., Swietlicki, E., Berg, O. H., Aalto, P. P., Hämeri, K., Nilsson, E. D., and Leck, C., 2001: Hygroscopic properties of aerosol particles over the central Arctic ocean during summer. J. Geophys. Res. D, 106, 32111 – 32123.

AEROSOL IMPACTS ON PRECIPITATION FROM CONVECTIVE CLOUDS

A. Khain*, D. Rosenfeld and A. Pokrovsky
The Hebrew University of Jerusalem, Jerusalem, Israel

1. INTRODUCTION

Observations (e.g., Rosenfeld 1999; 2000; Andrea et. al 2004) show effects of aerosol particles on droplet spectra and precipitation formation. Some of these effects were numerically simulated by Khain et al. (1999; 2001) using the two-dimensional spectral microphysics Hebrew University Cloud Model (HUCM). Detailed investigation of raindrop formation in ascending cloud parcels (Segal et al 2004) showed that the spectrum of cloud condensational nuclei (CCN) can be divided into three ranges: CCN with radii $r_{CCN} < 0.01\ \mu m$ are not usually activated and do not influence the cloud microphysical structure; CCN of the intermediate size with $0.01\ \mu m < r_{CCN} < \sim 1\ \mu m$ are usually activated and give rise to droplet formation. An increase in the concentration of CCN of this size leads to an increase in the droplet concentration and slower diffusional growth. Droplet spectra become narrower and the height of the collisions needed for triggering increases. This leads to a delay in raindrop formation (Andrea et al 2004, Khain et al 1999). The last, CCNs with $r_{CCN} > \sim 1\ \mu m$ give rise to formation of largest droplets, which foster raindrop formation at lower levels. A delay or acceleration in raindrop formation does not automatically lead to a decrease or increase in the accumulated rain. The physical mechanisms, through which aerosols influence accumulated rain, are discussed below.

2. NUMERICAL MODEL

Simulations were performed using the HUCM, whose microphysics is based on solving an equation system for eight size distribution functions of water drops, plate, columnar and branch-type ice crystals, graupel, snowflakes and hail/frozen drops, as well as aerosol particles (AP). Each size distribution is described using mass grids containing 33 bins. The model includes processes like the transport of AP and cloud hydrometeors, droplet and ice nucleation, secondary ice production, freezing/melting, diffusion growth/evaporation, drop-drop, drop-ice and ice-ice collisions. The model also includes the effects of collision breakup, as well as of turbulence on collision rate. Khain and Sednev (1996) and Khain et al (2000) describe the model in more detail.

3. AEROSOL EFFECTS ON PRECIPITATION

3.1 Unstable continental conditions

Simulations of cloud development under unstable conditions in Texas during summertime (Rosenfeld and Woodley 2000) were performed for a continental-type CCN (C_case) (the CCN concentration at 1% of supersaturation was 1260 cm^{-3}), as well as for microphysically maritime CCN (M_case) (the CCN concentration was about 100 cm^{-3}). Rain rates as the functions of time and x-coordinate are shown in Fig. 1.

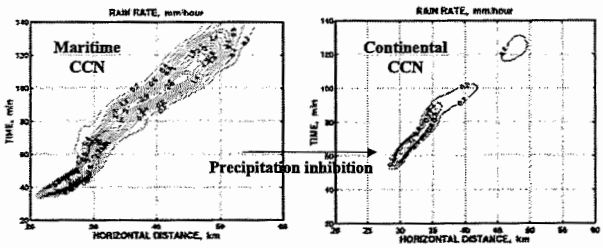

Fig.1. Rain rates in simulations under unstable continental conditions.

One can see a significant decrease in precipitation amount in clouds that developed in smoky (continental CCN) air. The difference in precipitation can be attributed to the following. When CCN concentration is low (M_case), raindrops and large graupel form at comparatively low levels, fall down and reach the surface without a significant evaporation. In C_case, high concentration of small droplets (up to 1000 cm^{-3}) arises by nucleation. These droplets have low collision efficiency, as well as low freezing rate. As a result, they reach the level of homogeneous freezing (about 9.5 km) and give rise to formation of ice crystals with concentration of several hundred per cm^{-3}. These crystals, as well as small graupel and snowflakes formed at higher levels spread over a large area and sublimate, and do not contribute to the precipitation. Droplets falling from higher levels also experience higher evaporation. As a result, the increase in CCN concentration decreases the precipitation efficiency of clouds that develop in strong unstable low humidity air.

3.1 Single maritime clouds

Aerosol effects on clouds and precipitation under maritime (as well as under comparatively wet and not extremely unstable conditions) are more complicated and are highly affected by vertical wind shear and air humidity.

The development of single clouds was triggered by 5 min of heating within the zone of the 0.5 km width in the surface layer. By varying the heating intensity, single clouds of different top height were simulated. The cloud evolution was simulated up to the cloud dissipation. **Fig. 2** shows the dependence of accumulated rain on the cloud top height (determined by the 10 dBz level) of convective clouds in three sets of simulations with the GATE (day 261) temperature profile (Ferrier and Houze, 1989). In the first set no wind shear (NO WS) was assumed. In the second set (with a weak wind shear, WS) the wind speed

*Communicating author: Alexander Khain, The Institute of Earth Sciences, The Hebrew University of Jerusalem, Givat Ram, Jerusalem 91904, Israel, email: khain@vms.huji.ac.il

increases from 0.4 ms^{-1} at z=0 km to 5 ms^{-1} at z=9 km. Above z=9 km the wind speed was assumed equal to 5 ms^{-1}. In both cases air humidity was quite high, with ~90% in the lower 2 km layer and about 50-60% in the middle troposphere. The third set of simulations was similar to the second one except the humidity was decreased by 10% in the lower 2 km layer (RH=80%) and by about 20-25% in the middle troposphere. Each set of the experiments consisted of experiments with maritime CCN (M_case) and continental CCNs (C-case). Initial CCN size distributions were similar to those used for the simulations of clouds under continental thermodynamic conditions.

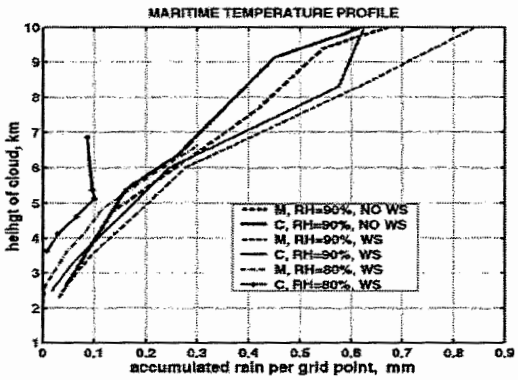

Fig.2 Dependences of accumulated rain on cloud depth under different conditions in case of maritime (GATE, 261 day) temperature profile.

One can see that a) single clouds that developed in M_cases produce larger amounts of accumulated rain. To produce the same rain amount, clouds that developed in C-case, should be higher; b) wind shear, and especially, the air humidity significantly change the accumulated rain amount, as well as the relationship between the rain amounts in C- and M-cases. At the same time, sensitivity of the accumulated rain to the CCN concentration under comparatively stable maritime temperature conditions is smaller than that under unstable continental conditions; c) while in all sets of simulations the accumulated rain monotonically increases with the cloud top height in M_cases, in C_cases with a non-zero wind shear, precipitation stops growing, beginning with a certain cloud top height.

The physical explanation *of the lower precipitation efficiency in single clouds developed in microphysically continental CCN conditions* can be derived from the analysis of vertical profiles of convective heating/cooling. **Fig.3** shows such profiles plotted for two clouds that developed in simulations with no wind shear. First cloud developing in C_case reaches the top height of 9 km. Second cloud that develops in M_case, reaches the maximum top height of 6.5 km. According to Fig. 2, these clouds produce comparable accumulated rain amounts. These profiles were obtained by averaging of heating/cooling in the horizontal direction over the computational area (64 km) and over time of simulation (4 hours). Dashed and dashed-dotted lines corresponding to positive values of latent heat release reflect contribution of condensation, freezing and deposition. Similar lines, but corresponding to negative values of latent heat release, reflect cooling caused by the droplet evaporation, ice melting and ice sublimation. Thick and thin solid lines show profiles of net convective heating for continental and maritime CCN, respectively. The squares (integrals) formed by these solid lines reflect the total atmospheric heating due to phase transitions and are a measure of the precipitation amount.

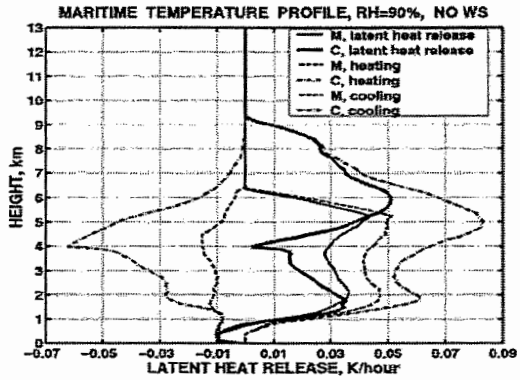

Fig.3 Vertical profiles of convective heating, cooling and net heating calculated under continental and maritime CCN. The clouds chosen produced nearly similar precipitation amounts.

The increase in the CCN concentration leads to a strong increase in heating both due to the increase in diffusion growth and due to more intense droplet freezing. At the same time, the cooling in the C_case is larger as compared to the M-case because of the larger droplet evaporation and ice sublimation. The higher droplets evaporation and ice sublimation in the C_case can be attributed to the following. In the C_case raindrops and ice particles are smaller than in the M_case and ascend to higher levels. Besides, they have smaller sedimentation velocity, As a result, the time duration of their sedimentation is longer. The detrainment of liquid and ice particles at upper levels leads to the fact that ice particles and drops falling from higher levels tend to sediment through a comparatively dry air. At the same time, in the M_case raindrops form at lower levels, and fall down through the vertically narrow layer of cloudy wet air (or in the close vicinity of the cloud). As a result, the evaporation (and cooling) in the maritime aerosol case is much lower as compared to the continental CCN case. The net heating in the C_case is extended to higher levels. The minimum in the net heating at ~4 km in the C_case is related to the cooling caused by the melting of ice (mainly graupel). No such minimum is seen in the profile of net convective heating in the M_case simulation indicating a smaller contribution of melted rain in the last case. *The higher loss in the precipitating mass by the drop evaporation and ice sublimation is the main cause of the lower precipitation efficiency of clouds developed in the continental CCN case.*

Another example of latent heat release profiles for clouds developed in case of upper level wind shear in the C_ and

effect of precip on latent heat rel

role of secondary cloud form^n from surface level convergence & dissipation

M_case is shown in Fig. 4. These clouds reached the same top heights (about 10 km), but have quite different accumulated rain (see Fig. 2).

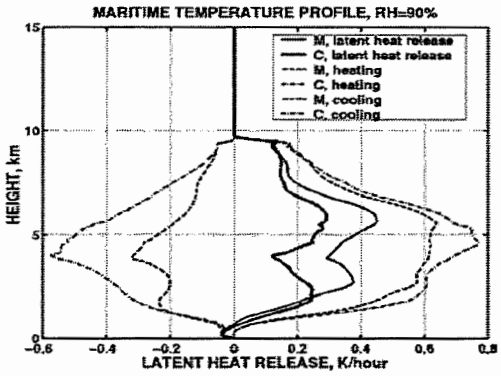

Fig. 4. Vertical profiles of convective heating for clouds developed in continental and maritime aerosols in case of a comparatively weak wind shear.

Stronger wind at upper levels moves water droplets and ice downwind fostering their fall through dry air and their evaporation and sublimation. Since water droplets and ice particles ascend to higher levels in C_cases, *wind shear leads to higher loss in precipitation for C-cases.* We believe that this is the reason, why in the presence of wind shear the precipitation amount in C_ cases does not increase with cloud top height (beginning with a certain cloud depths): a significant fraction of hydrometeors ascending above certain level evaporate and do not contribute to precipitation. This can explain results of some simulations with high wind shears at upper levels (not shown), when the growth of cloud top height in C_cases was accompanied by a decrease in precipitation amount. The decrease in precipitation with a decrease in humidity (Fig.2) is explained by the increase in the loss in precipitation by evaporation and sublimation. This loss is higher in clouds that develop under continental aerosol conditions. A comparatively low sensitivity of precipitation in M_cases to both wind shear and humidity is related to the formation of raindrops at low levels and to their fall within wet air in, or in the close surrounding of the cloud.

3.3 Dynamical aerosol effects

We sew in section 3.2 that the sensitivity of precipitation to CCN is closely related to effects of CCN on cloud dynamics. Below, we present another examples of the dynamical effects.

Since the instability of the maritime atmosphere is comparatively low, deep maritime convective clouds are often forced by surface level convergence caused by dissipating clouds. As a result, formation of secondary clouds turns out to be dependent on the properties of primary clouds. In section 3.2 primary clouds were forced by an initial heating within a comparatively narrow area of the subcloud layer. Besides, the wind shear was weak. As a result, these clouds did not produce secondary clouds either in the M_ and C_cases. As the width of the convection triggering zone was successively increased from 2 km to 4 km, the primary clouds became wider and the maximum vertical velocity increased. Besides, the wind shear was also increased to that measured at 261 day of the GATE (~ 7m/s per 5 km in the middle troposphere). **Fig. 5** shows that in the C_case experiments the strengthening of the primary cloud leads to formation of a secondary cloud (seen by the formation of new vertical velocity maximum). At a certain stage, this secondary cloud gives rise to *squall-line formation.* Note that secondary clouds formed in corresponding M_case simulations were much weaker and did not develop into a squall line. This effect can be attributed to the following. Figs. 3 and 4 show that convective heating by condensation and freezing significantly larger in C_cases than in M-cases. Because of wind shear transporting cloud hydrometeors downwind, cooling due to

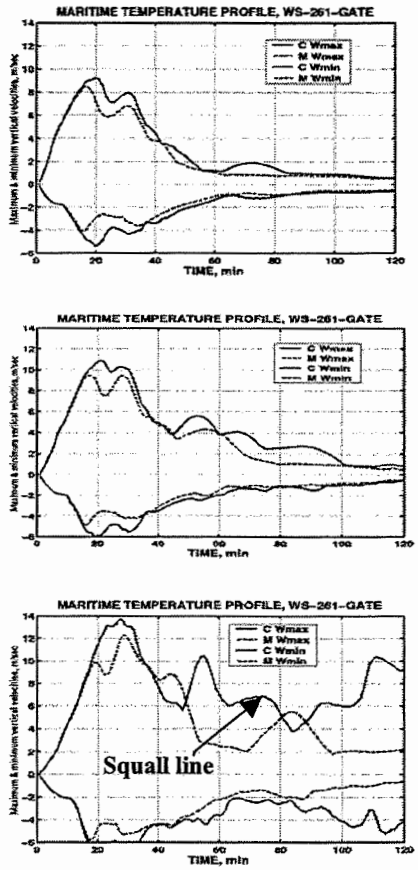

Fig. 5. Maximal updrafts and downdrafts in clouds developed using the GATE profiles under continental and maritime aerosol conditions. The development of secondary clouds in experiments with a successive increase in the intensity of the first cloud.

good to plot the vertical profile of latent heat release

evaporation and sublimation takes place at some distance from the cloud updraft. This spatial shift between heating and cooling is accompanied by a decrease in the loading in the updraft zone (in contrast to M_cases, where raindrop can fall through cloud updraft). These factors lead to formation of dynamically induced vorticity that increases both vertical updrafts and downdrafts in clouds arising within microphysically continental aerosol. As a result, the maxima of updraft and downdraft vertical velocity are larger in the C_case clouds than in M_case clouds (Fig. 5).

Fig. 6 shows precipitation rate in both the M-Case and C-case in simulations when the GATE (261 day) sounding was used, and the first cloud was triggered by a surface layer heating within the area of the 4 km width.

Profiles of convective heating suggest (not shown) a significant precipitation rate, as the heating significantly exceeds the cooling. We attribute the increase in the precipitation efficiency to an increase in the relative humidity within the area of the squall line and to a significant increase in cloud cover (squall line is accompanied by significant melted rain falling from startiform clouds behind the line).

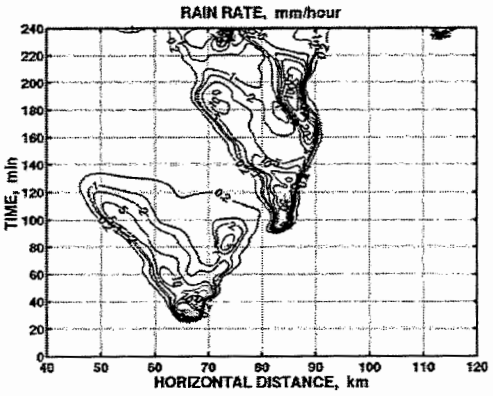

Fig. 6 Precipitation rate in M-Case and C-case in simulations when GATE (261 day) sounding in case of squall line formation

4. CONCLUSION

A two dimensional spectral microphysics cloud model is used for the investigation of aerosol effects on cloud dynamics, microphysics and precipitation. It is shown that a) increase in concentration of CCN with radii (0.01 $\mu m < r_{CCN} < \sim 1\ \mu m$) drastically decreases precipitation from clouds developed under unstable dry continental conditions; b) an increase in the CCN concentration decreases precipitation from individual maritime clouds (and, as follows from supplemental simulations, under intermediate continental conditions) as well. This decrease is, however, smaller than in case of unstable continental conditions and highly depends on wind shear and air humidity. The reduction of the precipitation efficiency with the increase in the CCN concentration is caused by the increase in the loss of precipitation during sedimentation through a deep layer of dry air. An increase in the CCN concentration increases the intensity of convection and fosters the formation of squall lines. In this case precipitation rate significantly increases, indicating non-linear effects in the cloud-aerosol interaction. The area covered by clouds also increases with the increase in the concentration of CCNs of intermediate size. The increase in cloud intensity, as well as the cloud top height should foster the lightening formation, and, possibly, other dangerous meteorological phenomena. These aerosol effects need a special consideration.

Acknowledgments

The study was performed under support of the Israel Ministry of Science (German-Israel collaboration in Water Resources, grant WT 0403), by the Israel Water Company (Shaham) as well as by EU project SMOCC.

References

Andreae, M. O., D. Rosenfeld, P. Artaxo, A. A. Costa, G. P. Frank, K. M. Longo, and M. A. F. Silva-Dias, 2004: Smoking rain clouds over the Amazon. *Science*, **303**, 1337-1342.

Ferrier, B.S. and R.A. Houze 1989: One-dimensional time dependent modeling of GATE cumulonimbus convection. J. Atmos. Sci., 46, 330-352.

Khain A., A. Pokrovsky, and I. Sednev, 1999: Some effects of cloud-aerosol interaction on cloud microphysics structure and precipitation formation: Numerical experiments with a spectral microphysics cloud ensemble model. Atmos. Res., 52, 195-220.

Khain, A. P., M. Ovtchinnikov, M. Pinsky, A. Pokrovsky, and H. Krugliak, 2000: Notes on the state-of-the-art numerical modeling of cloud microphysics. Atmos. Res. 55, 159-224.

Khain, A.P., D. Rosenfeld, and A. Pokrovsky, 2001: Simulation of deep convective clouds with sustained supercooled liquid water down to –37.5 C using a spectral microphysics model. Geophys. Rev. Lett., 3887-3890.

Rosenfeld, D., 1999: TRMM observed first direct evidence of smoke from forest fires inhibiting rainfall. Geophys. Res. Lett., 26, 20, 3105.

Rosenfeld, D, 2000: Suppression of rain and snow by urban and industrial air pollution. Science, 287 (5459), 1793-1796.

Rosenfeld D, and W. Woodley, 2000: Deep convective clouds with sustained supercooled liquid water down to –37.5C. Nature, 405, 440-442.

Segal, Y., A. Khain, and M. Pinsky, 2004: Effects of atmospheric aerosol on precipitation in cumulus clouds as seen from 2000-bin cloud parcel microphysical model: sensitivity study with cloud seeding applications. Quart. J. Roy. Met. Soc, 130B(587), 561-582

RESPONSE OF THE COUPLED CLIMATE SYSTEM TO INDIRECT AEROSOL FORCING

J.E. Kristjánsson[1], T. Iversen[1], A. Kirkevåg[1] and Ø. Seland[1]

[1]Department of Geosciences, University of Oslo, P.O.Box 1022 Blindern, N-0315 Oslo, Norway

1. INTRODUCTION

According to the Intergovernmental Panel on Climate Change (IPCC) current estimates of the warming effect of anthropogenic greenhouse gases are quite well known (Houghton et al., 2001). Much more uncertainty is attributed to the role of anthropogenic aerosols. The aerosols affect climate *directly* by reflecting and absorbing solar radiation, and to a lesser extent, through absorption and emission of longwave radiation. They also affect climate *indirectly* by altering the amount and size of cloud condensation nuclei (CCN) in the atmosphere. The different types of aerosols present in the atmosphere have different physical and chemical properties. In this study the focus will be on sulfate, which occurs naturally in the atmosphere due to emissions of DMS by algae in the ocean. More importantly, however, SO_2 emissions by human activities subsequently lead to the formation of SO_4 aerosols by oxidation or wet phase processes. Sulfate aerosols are excellent CCN, and hence contribute greatly to the indirect effect, while at the same time contributing to the direct effect through the reflection of solar radiation.

Some previous studies investigating the climate response to indirect aerosol forcing have either used aerosol fields obtained from off-line simulations (Rotstayn et al., 2000), precluding interactions between changes in climate parameters and the aerosols and their precursors. Other studies have used an interactive life cycle of aerosols (Williams et al., 2001; Rotstayn and Lohmann, 2002), but the importance of this refinement has not been investigated in detail. In this study, we will focus on differences between the results of simulations with on-line vs. off-line chemistry and transport calculations. The purpose is to understand better possible feedbacks between changes in the climate system on the one hand and aerosol sources and sinks on the other.

The next section reviews our aerosol treatment, and describes the setup for the experiments that follow. The main results of these experiments, and their interpretation is presented in section 3. Finally, section 5 presents a summary and the preliminary conclusions of this study.

2. MODEL AND EXPERIMENTAL SETUP

Corresponding author's address: Jón Egill Kristjánsson, Department of Geosciences, University of Oslo, P.O.Box 1022 Blindern, N-0315 Oslo, Norway; E-mail: j.e.kristjansson@geo.uio.no.

The basic model tool for the experiments is a modified version of the atmospheric global climate model NCAR Community Climate Model version 3 (CCM3; Kiehl et al., 1998), coupled to a slab ocean model. CCM3 is a state-of-the-art global climate model, run at T42 spectral truncation and with 18 levels in the vertical. The modifications to the CCM3 consist of: a) The introduction of a prognostic cloud water scheme, following Rasch and Kristjánsson (1998); b) Replacing the simple aerosol scheme in CCM3 with a detailed aerosol scheme, described by Iversen and Seland (2002), Kirkevåg and Iversen (2002) and Kristjánsson (2002). Background aerosols, consisting of sea salt, mineral and water-soluble non-sea salt particles are prescribed and size distributed. These size distributions are then modified by adding natural and anthropogenic sulfate and black carbon (BC) into an internal mixture, brought about by condensation, coagulation in clear and cloudy air, and wet-phase chemical processes in clouds. A normally minor fraction of sulfate and BC is externally mixed, produced by clear-air oxidation followed by nucleation, and by emission of primary particles. Starting from emissions of sulfate precursor gases (SO_2, DMS), sulfate particles (SO_4) and black carbon (BC), chemical reactions, transport and deposition are computed at every grid point. The largest emission sources are fossil fuel combustion, biomass burning and industrial releases. In the present study, the aerosol forcing modules are allowed to interact with the dynamics of the climate system, enabling calculations of the response to the aerosol forcing. The coupling of the CCM3 to a slab ocean model is described in detail in Kiehl et al. (1996). The purpose of using a slab ocean model is to obtain a realistic thermal inertia for the climate system on multi-decadal time scales.

details of how modified black carbon calc.

3. RESULTS

3.1 Sulfate chemistry and transport

First, in Figures 1a-b we show the horizontal distribution of the vertically integrated sulfate amount in the on-line simulations. The upper panel is for pre-industrial aerosols only, while the lower panel includes anthropogenic sulfate. As seen here and in Table 1, some 80% of the sulfate in the simulation with all aerosols is anthropogenic. The largest concentrations are found over SE Asia and North America, with high values also over Europe,

investigate how important it is whether aerosols ratified in the equations

Mexico, the Middle East and central Africa. Another noticeable feature is the fact that in general the concentrations are much higher over the Northern than the Southern Hemisphere, including the polar regions, where there are negligible emissions of aerosols or aerosol precursors.

a)

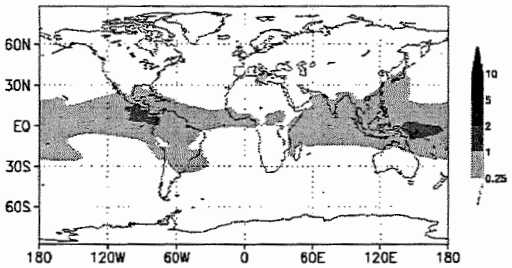

b)

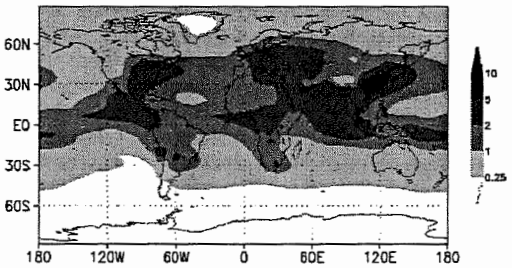

Figure 1: Sulfate column burdens in mg m^{-2}: a) Natural aerosols only; b) Natural and anthropogenic aerosols are considered.

	Aq. SO_4 prod. (%)	SO_2 dep. (%)	SO_4 burden (Tg(S))	SO_4 lifetime (days)
Off-line Natural	43.9	45.3	0.11	3.3
Off-line Change	**+0.2**	**-4.6**	**+0.41**	**+0.2**
On-line Natural	43.6	45.0	0.11	3.4
On-line Change	**+3.6**	**-7.3**	**+0.49**	**+0.4**

Table 1: Contributions from various terms to the globally averaged budgets of SO_2 and SO_4 in the four simulations described in the text.

We note from Table 1 that in the case of natural aerosols, there is a rather small sensitivity to running the life-cycle scheme for sulfate on-line. When anthropogenic aerosols are added, however, large differences are found between off-line and on-line simulations. Deposition of SO_2 (precursor for sulfate) is considerably reduced, while at the same time aqueous phase production of sulfate is significantly enhanced. As a result, the SO_4 burden is increased by almost 20%, and SO_4 lifetime is increased by almost 10%. These changes come about partly as a result of the cooling effect which the aerosols cause, through their influence on clouds. The cooler climate has less precipitation (Table 2, 2nd line), which reduces wet deposition of SO_2 and SO_4. Hence SO4 concentrations are increased, e.g., through wet phase processes (Table 1) and its overall impact on climate is enhanced. Thus, a positive feedback is established between the sulfur cycle and changes in climate caused by the indirect forcing of sulfate aerosols. This positive feedback is most clearly seen in the difference in aerosol induced cooling from 1.4 K in the off-line simulations to 2.1 K in the on-line runs. The rightmost column of Table 2 suggests that changes in cloud droplet size play an important role in this regard.

	Temp. (°C)	Precip. (mm/day)	LWP (g m^{-2})	r_e (μm)
Off-line Natural	13.9	2.90	41.2	10.81
Off-line Change	**-1.4**	**-0.11**	**-0.8**	**-0.67**
On-line Natural	14.7	2.95	42.2	11.15
On-line Change	**-2.1**	**-0.15**	**-1.3**	**-1.03**

Table 2: Global averages of key quantities in the four simulations described in the text.

3.2 Climate changes

The temperature changes just mentioned are shown in more detail in Figures 2a-b. Due to ice-albedo feedback the cooling is largest in the polar regions (Williams et al., 2001), even though the negative forcing is most pronounced in mid-latitudes of the Northern Hemisphere (Kristjánsson, 2002). Another noticeable feature is the much stronger cooling in the Northern Hemisphere than in the Southern Hemisphere. Finally, we note that in the on-line simulations the cooling is enhanced practically everywhere.

Figure 3a shows the change in precipitation resulting from the indirect effect from the off-line simulations, while Figure 3b shows the corresponding result from the on-line simulations. In both figures a noticeable feature is the southward displacement of the ITCZ, due to the interhemispheric differences in cooling seen in Figure 2. We also note the general reduction in precipitation caused by the overall colder climate. The differences between Figures 3a and 3b are most clearly seen in the subtropical regions of both hemispheres. These regions are characterized by shallow low clouds, which, due to the clean background marine aerosol are particularly sensitive to changes in CCN concentrations.

In order to visualize the changes in atmospheric circulations that the indirect effect

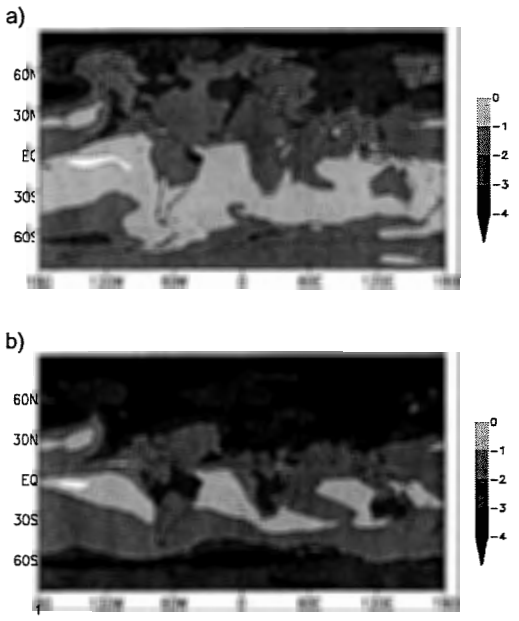

Figure 2: Temperature changes due to indirect forcing: a) Off-line simulations; b) On-line simulations.

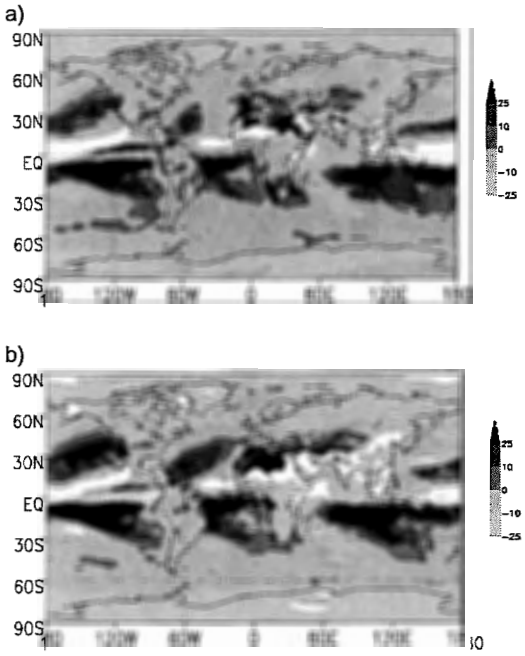

Figure 3: Changes in precipitation rate (mm day^{-1}) due to indirect forcing: a) Off-line simulations; b) On-line simulations.

causes, we show in Figure 4 the change in sea-level pressure from the on-line simulations. A strong pressure increase over the Arctic and adjacent land areas is found. This increase is most pronounced in the autumn (not shown). Apparently, the ice-albedo feedback associated with the Arctic region causes a strengthening of the Siberian high, and a similar effect is seen over the Canadian Arctic. This in turn leads to drier and colder winters over the continents, contributing to the reduction in precipitation mentioned above, in connection with Table 2.

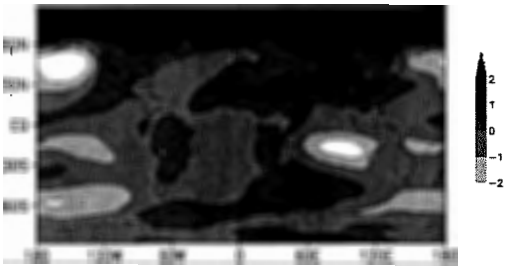

Figure 4: Changes in sea-level pressure (hPa) due to indirect forcing in on-line simulations.

4. SUMMARY AND CONCLUSIONS

Results from multi-decadal equilibrium simulations of the response to indirect aerosol forcing have been presented. The simulations were carried out using an atmospheric GCM coupled to a slab ocean. A special emphasis has been put on the differences between simulations in which the sulfate life-cycle scheme was run on-line, as compared to off-line simulations.

In the off-line simulations, results similar to those previously reported by e.g., Rotstayn and Lohmann (2002) and Williams et al. (2001) were found, e.g., a southward displacement of the ITCZ, and a maximum cooling in the Arctic, despite the forcing being most negative at mid-latitudes of the northern hemisphere. In the on-line simulations, a considerably stronger cooling effect was found. This was seen to be attributed to a positive feedback between the sulfate life-cycle and changes in climate. The colder and drier climate caused by the aerosol cooling leads to a reduced scavenging of sulfate aerosols and its precursor gases, while production of sulfate through wet phase processes is enhanced. Consequently, sulfate burden and sulfate lifetime are increased, and the overall (cooling) effect of sulfate on the climate system is enhanced.

5. Acknowledgments

This study was supported by the Norwegian Research Council through the RegClim project. Furthermore, this work has received support of the Norwegian Programme for Supercomputing through a grant of computer time. Helpful discussions with Jens Debernard, Lars Petter Røed and Philip J. Rasch are greatly appreciated.

6. REFERENCES

Houghton, J. T., Ding, Y., Griggs, D. J., Noguer, M., van der Linden, P. J., Dai, X., Maskell, K., and Johnson, C. A. (eds.), 2001. *Climate Change 2001: The Scientific Basis*. Contribution of Working Group I to the Third Assessment Report of the Intergovernmental Panel on Climate Change. Cambridge University Press, 881 pp.

Iversen, T., and Seland, Ø., 2002. A scheme for process-tagged SO_4 and BC aerosols in NCAR-CCM3. Validation and sensitivity to cloud processes. *J. Geophys. Res.* **107**, (D24), 4751, doi:10.1029/2001JD000885.

Kiehl, J. T., Hack, J. J., Bonan, G. B., Boville, B. A., Briegleb, B. P., Williamson, D. L., and Rasch, P. J., 1996. *Description of the NCAR Community Climate Model (CCM3)*. NCAR Technical Note, NCAR/TN-420+STR, 152 pp.

Kiehl, J. T., Hack, J. J., Bonan, G. B., Boville, B. A., Williamson, D. L., and Rasch, P., 1998. The National Center for Atmospheric Research Community Climate Model: CCM3. *J. Climate*, **11**, 1131-1149.

Kirkevåg, A., and Iversen, T., 2002. Global direct radiative forcing by process-parameterized aerosol optical properties. *J. Geophys. Res.* **107**, (D20), 4433, doi:10.1029/2001JD000886.

Kristjánsson, J. E., 2002. Studies of the aerosol indirect effect from sulfate and black carbon aerosols. *J. Geophys. Res.* **107**, (D15), 4246, doi:10.1029/2001JD000887.

Rasch, P. J., and Kristjánsson, J. E., 1998. A comparison of the CCM3 model climate using diagnosed and predicted condensate parameterisations. *J. Climate*, **11**, 1587- 1614.

Rosenfeld, D., Lahav, R., Khain, A., and Pinsky, M., 2002. The role of sea spray in cleansing air pollution over ocean via cloud processes. *Science*, **297**, 1667-1670.

Rotstayn, L. D., Ryan, B. F., and Penner, J. E., 2000. Precipitation changes in a GCM resulting from the indirect effects of anthropogenic aerosols. *Geophys. Res. Lett.*, **27**, 3045-3048.

Rotstayn, L. D., and Lohmann, U., 2002. Tropical rainfall trends and the indirect aerosol effect. *J. Climate*, **15**, 2103-2116.

THE SEARCH FOR THE OPTIMAL SIZE OF HYGROSCOPIC SEEDING PARTICLES

Ronen Lahav and Daniel Rosenfeld
The Hebrew University of Jerusalem, Jerusalem, Israel

1. ABSTRACT

It is well known that large concentrations of small aerosols, such as produced by smoke and air pollution, can suppress coalescence and precipitation. Our observations have shown giant salt CCN (e.g., sea spray) restore the precipitation from such polluted clouds (Rosenfeld et al., 2002).

Aircraft and satellite microphysical observations in Israel and adjacent areas show that hygroscopic seeding of clouds occurs naturally by sea spray, but the effect diminishes quickly with distance inland.

Cloud simulations and observations show that hygroscopic seeding is most effective with 2-4 μm diameter particles. This is larger than can be produced currently with hygroscopic flares, but smaller than can be produced with other methods, such as spray and powder seeding. The calculations also show that the mass that needs to be dispersed for such "optimal" seeding is larger than can be delivered by current flare technology, but starts to be feasible with spray seeding, and most practical with powder seeding.

The large apparent positive impact of the sea spray on the precipitation prompted us to imitate nature and do it artificially. Under the framework of the Israeli rain enhancement program, experiments with spray seeding applied to clouds inland Israel have shown that warm rain occurred in the clouds, which behaved as measured in natural clouds closer to the coastline at the same time. This new technique of hygroscopic seeding was done by spraying concentrated brine from the Dead Sea in a very high pressure from an agricultural sprayer. Preliminary results show early formation of large raindrops and somewhat wider cloud drop size distribution in the seeded clouds, in accordance with the theoretical expectations. The small concentrations of the seeding-induced raindrops suggest that the concentrations of seeded particles was too small. Increasing the number concentrations can be achieved by getting closer to the optimal size for hygroscopic seeding, using powder technology.

2. BACKGROUND

Artificial hygroscopic seeding has been done in a wide range of particle sizes, but the concentrations were constrained by the amount of material that could be carried by the aircraft and by its rate of dispersion into the clouds (Silverman and Sukarnjanaset, 2000). Hygroscopic flares appeared to be an attractive option (Mather at al., 1997, Bruintjes, 1999), but the problem with such technique is that it produce mostly sub-micron large CCN (Cooper et al., 1997). Their calculations showed that the sub-micron particles of the South African hygroscopic flare did not contribute to the enhanced coalescence. If this is true, only about 30% of the flare mass was in particles that were sufficiently large for enhancing the coalescence and precipitation.

Further calculations (Segal et al., 2004b) showed that a wide range of optimal diameter exists between 2 and 5 μm. Because dispersion of such particles at large seeding rates is not yet technologically feasible with flares, the next best thing that we could think of was to develop a new seeding method that imitates what nature does with sea spray (Rosenfeld et al., 2002).

3. SPRAY SEEDING

An agricultural spray aircraft was fitted with high-pressure pump and nozzles, designed for high capacity spraying of small drops. Concentrated Dead Sea brine, containing 500 g salt l^{-1}, was sprayed at a rate of 12 liters per minute. The carrying capacity of the aircraft is about 700 liters, which translates to a dry salt seeding rate of about 6 kg min^{-1} for a total duration of 1 hour. This mass-seeding rate is equivalent to 24 hygroscopic flares burning simultaneously, but the flares would last for only four minutes.

The size distribution of the spray was measured with the Israeli research aircraft flying in the plume of the seeder aircraft at a distance covered by less than 2 seconds of flight time. In view of the short distance and dry atmosphere (~60% relative humidity), the sprayed particles had not changed much between dispersion and measurement.

The spray seeding was tested in Israeli clouds on several case studies. Here we describe a couple of cases. On 25 February 2002 experimental spray seeding took place in northern Israel over the western lower Galilee. The seeder circled just below cloud base at 2500 feet and a cloud physics aircraft penetrating the seeded and adjacent similar unseeded clouds at various levels above cloud base. The distance in time and space from the spray seeding coordinates was used to identify the potentially seeded cloud volumes. The cloud physics aircraft was equipped with a CAS cloud droplet and aerosol spectrometer (0.3-50

Corresponding author's address: Daniel Rosenfeld, Institute of Earth Sciences, The Hebrew University of Jerusalem, Jerusalem 91904, Israel.
E-Mail: daniel.rosenfeld@huji.ac.il

μm), a precipitation particle imager OAP-2DC (25-800 μm), and KING and DMT hot wire liquid water content probes. In addition, temperature, pressure and GPS navigation parameters were recorded. Cloud tops reached 9000 feet, at -3.5°C. Very light rain showers occurred from these clouds from all-warm-rain processes. Mean cloud pass droplet concentrations > 2 μm were about 450 cm^{-3} for both unseeded and seeded clouds. The proximity to the sea (10 to 40 km) likely added a background of natural sea spray particles at unknown concentration. The surface wind over sea was about 15 knots. From visual inspection, white caps did not occur at the sea surface of the coastal waters. The near cloud-base spectra of the seeded and unseeded clouds were similar, but they deviated with altitude such that the DSD of the seeded clouds widened somewhat faster than the unseeded clouds (see Figure 1). Raindrops of 0.4 to 0.8 mm diameter appeared in the seeded clouds at 7900 feet, starting at 10 minutes after initial seeding. After additional 7 minutes the seeder aircraft reported the first raindrops falling through cloud base. These raindrops became "large" (by the appearance of the impacts on the seeded windshield of the seeder aircraft) after additional 4 minutes. The seeding was terminated after 25 minutes because the cloud drifted out of the area where air traffic control allowed flight. The unseeded clouds developed small raindrops of about 200 micron just at their tops near 9000 feet.

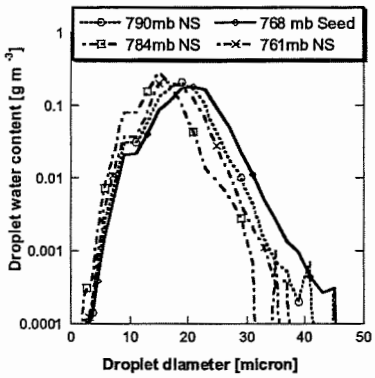

Figure 1: Normalized drop size distributions from full cloud passes of spray-seeded (bold line) and not seeded (broken lines), done at height of 7700 feet (5200 feet above base), on 25 February 2002 in north Israel.

A second spray seeding flight took place on 19 April 2002 in lower eastern Galilee farther away from the sea. Unfortunately, the FSSP100 cloud droplet spectrometer undercounted grossly, probably due to salt contamination from the previous flight, when it was flown in the wake of the sprayer. Cloud tops reached 9500 feet at the –2°C isotherm, for a cloud depth of 1.5 km, and the clouds produced no natural rainfall. Subsequently, up to 0.5 mm drops in concentrations of up to 4 $liter^{-1}$ were observed. The maximum total precipitation particles observable by the 2DC instrument reached 28 $liter^{-1}$. No raindrops and only a few 2DC dots (the smallest resolved drizzle particles) were observed in the non-seeded cloud clusters, which were sampled around the seeded small cloud cluster.

4. MODEL SIMULATION

The NaCl equivalent dry particle size distribution of the spray is given in Figure 2, along with the particle size distribution of the SA hygroscopic flares and the background concentrations that were used by Cooper et al. (1997) in their model simulations. The simulated cloud had a base height of 700 m, a temperature of 21°C, and a cloud base updraft of 2 m s^{-1}. The updraft accelerated to about 10 ms^{-1} near the 5 km level and there leveled off. The model-simulated rainfall flux (with respect to the rising air) and the drop effective radii are presented in Figures 3 and 4, respectively.

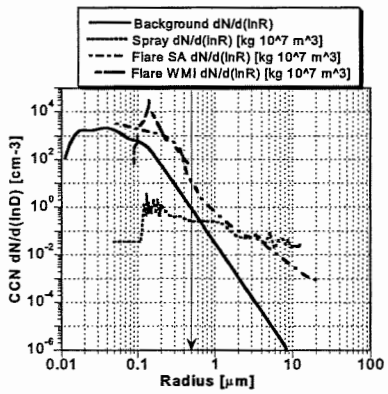

Figure 2: Size distribution of CCN in dry NaCl equivalent, for a spray of Dead Sea brine, SA hygroscopic flares, a hypothetical flare that produces only sub-micron particles, and the background CCN (bold). The concentrations are calculated for 1 kg of dry material diluted in 10^7 m^3 of air.

The calculation assumed that the dry mass of 1-kg seeded particles was diluted in 10^6, 10^7 or 10^8 m^3 of air well below cloud base. The results show the following:

Background aerosols started to develop precipitation (R>2 mm/hr) at a height of 5.5 km. Seeding with the South African flares at a dilution of 1-kg in 10^8 m^3 lowered the rain onset slightly from 5.5 to 5.3 km. Increasing the concentration of the flare effluent to 1-kg in 10^7 m^3 had a much larger effect and lowered the rainfall onset to 4700 m. Further increase of the concentration to 1-kg in 10^6 m^3 did not result in additional enhancement of the precipitation. This means that the concentration of 1-kg in 10^7 m^3 is already near the optimum.

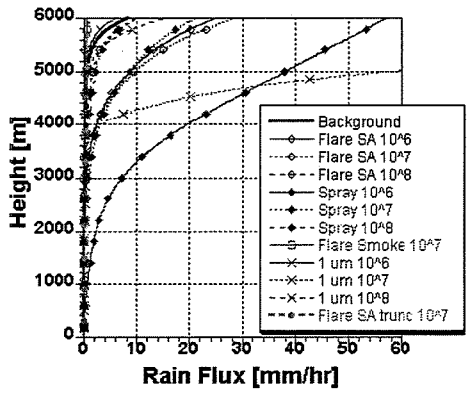

Figure 3: Simulated rain flux for clouds containing the background CCN as assumed for the simulations by Cooper and Bruintjes (1997) and in addition, the dry NaCl equivalent of spray of Dead Sea brine, South African hygroscopic flares, the SA flare with particle truncated at diameters > 1-μm, and a hypothetical flare that produces only 1-micron particles.

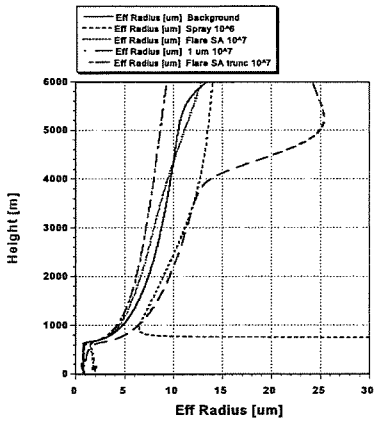

Figure 4: Simulated effective radius of cloud droplets, for clouds containing the background CCN (bold) as assumed for the simulations by Cooper et al. (1997) and in addition, the dry NaCl equivalent of a spray of Dead Sea brine, SA hygroscopic flares, and the South African flare with particles truncated at diameters > 1μm and a hypothetical flare that produces only 1-micron particles.

Truncating all the particles with diameters > 1μm at the "optimal" concentration of 1-kg in 10^7 m^3 resulted in a strong suppression of the precipitation compared to the background. Its effect was similar to the hypothetical smoke flare. According to Figure 4 the truncated distribution created a cloud with reduced droplet sizes with respect to the background. Even the "optimal" concentration of the un-truncated flare reduced the droplet size in the lower part of the cloud. This suggests that the smaller flare particles still nucleated and that they actually caused the cloud to produce more droplets at its base. The raindrop-embryo effect, produced by the super-micron flare particles, was mainly responsible for the rain enhancement, and it worked against the suppressing effect of the smaller particles. If sub-micron particles do not contribute to the apparent seeding effect, it is worthwhile to see what would be the result for a flare with a narrow distribution near 1-μm, which Cooper et al., (1997) have shown would produce optimal results. Here again, at a dilution of 1-kg in 10^8 m^3 only a slightly positive effect was noted, but it was dramatically increased when the concentration increased to 1-kg in 10^7 m^3. According to Figure 3, the rainfall enhancement occurred due to the size increase of the cloud-base droplets, which coalesced into drizzle and then continued their growth to raindrops at a height of 3.9 km. Increasing the concentration further, resulted in a return to near background precipitation, probably due to excessive concentrations of 1μm CCN, which already constituted the bulk of the cloud droplets.

Increasing the spray concentration to 1-kg in 10^6 m^3 to simulate the real situation enhanced the rain flux further, even beyond the composition of the "optimal flare" of 1μm particles, at least initially in the clouds. The rain started forming at a height of < 2 km, but its development with height was slower than for the "optimal flare" of 1μm particles. The large advantage of the 1μm "optimal" device is that it converts most cloud water quickly to drizzle and rainfall between 4 and 5 km, leading to very efficient precipitation in clouds that exceed this depth, whereas the spray seeding would leave most of the water still in the form of cloud droplets. The large number of drizzle particles can also recalculate into the cloud more easily and spread the seeding effect to cloud portions that are not seeded directly. However, dispersion of 1-μm salt particles in sufficient quantities for cloud seeding is still an unresolved technological challenge. Furtehrmore, 1 μm is still smaller than optimal, as shown next.

5. SALT POWDER SEEDING

Segal et al. (2004b) tested a large combination of sizes and concentrations for the maritime, Mediterranean and Texas clouds using the parcel model to obtain an answer to this question. They showed that a wide optimal size-range occurs between 2 and 5 microns diameter. This optimal size enhances rainfall even in maritime clouds in contrast to the action of even the best of the hygroscopic flares. The required mass was only 1 kg to 10^8 to 10^9 m^3. No over-seeding is possible.

The next challenge was the production of such particles. This cant be done currently with flare and spray technologies. We found the solution with a world-patented method for processing salt (NaCl) powder to these sizes, with anti-clumping additives. An example of such material shown if Figs. 5-6.

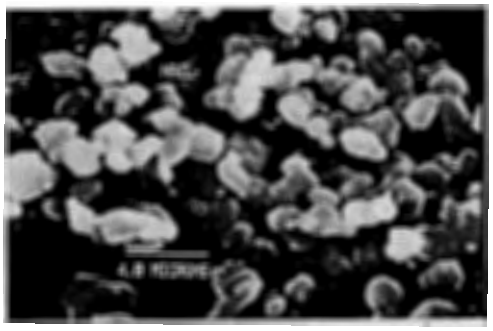

Figure 5: Scanning electron microscope image of the salt powder.

Hundreds kg of salt were milled to specification of diameter between 2 and 5 μm and field tested by dispersing from an agricultural duster aircraft. The experiment took place on 24 December 2003 in Megido airstrip at northern Israel, at 60% relative humidity. The deliquescence point of NaCl is 75%. The airplane made low dusting passes over the measuring instruments, which consisted of a Welas optical aerosol spectrometer (see Fig. 6) and filters. The dispersion rate was about 7.5 kg km^{-1}. If this material were to disperse uniformly in 1 km^3 of cloudy air, the salt concentration would be nearly optimal according to the model calculations discussed earlier. The dispersal rate can be controlled by the pilot to be smaller or higher, as desired.

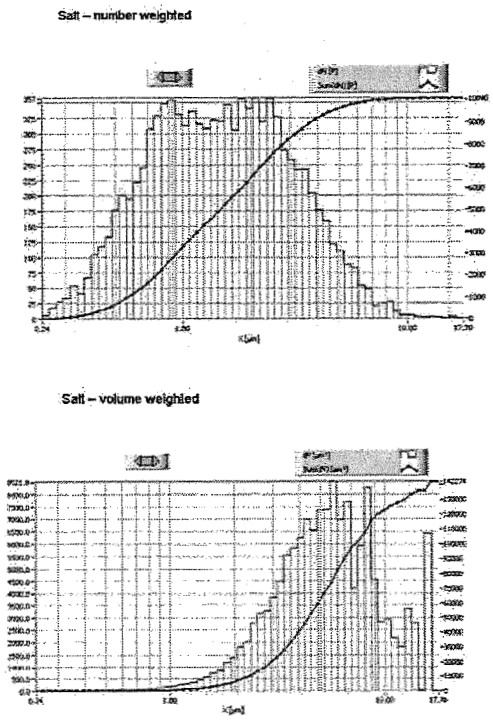

Figure 6: Particle size distribution of the salt powder after it was dispersed from the aircraft. Background concentrations are negligible. The abscissa is the particle diameter, and the left ordinate is the concentration density by numbers on the top panel [dN/dln(D)], and by volume on the bottom panel [dV/dln(D)]. The right ordinate provides the negative of the cumulative distribution of the particles.

The results seemed very encouraging. The next step is testing in clouds, and monitoring the effects with the cloud physics aircraft. Hopefully preliminary results of that will be available to show in the Bologna conference.

6. SUMMARY

Experiments of artificial addition of sea spray to clouds inland have shown that warm rain has returned to the clouds, which behave as natural clouds closer to the coastline. Both observations and simulations show that the spray seeding produced particles that were much larger than the optimal size .This led us to continue the search for the optimal size. Guided by the model results we developed an efficient and economically viable mean of hygroscopic seeding using an aircraft which disperse salt powder in diameters of 2-5 micron under the cloud base.

7. ACKNOWLEDGMENTS

This research is funded by the Israeli Water Commission. We Thank Electrical Mechanical Services for facilitating the field operations. We also thank CHIMNIR, an Israeli aviation company, for their highly professional services.

8 . REFERENCES

Bruintjes, B. T., 1999: A review of cloud seeding experiments to enhance precipitation and some new prospects. *Bull. Amer. Met. Soc.*, **80** (5): 805-820.

Cooper, W. A., R. T. Bruintjes, and G. K. Mather, 1997: Calculations pertaining to hygroscopic seeding with flares. *J. Appl. Meteor.*, Boston, MA, **36**(11): 1449-1469.

Khain A. P., D. Rosenfeld and A. Pokrovsky, 2001: Simulating convective clouds with sustained supercooled liquid water down to -37.5°C using a spectral microphysics model. *Geophys. Res. Lett.*, **28**, 3887-3890.

Mather, G. K., D. E Terblanche, F. E Steffens, and L. Fletcher, 1997: Results of the South African cloud-seeding experiments using hygroscopic flares. *J. Appl. Meteor.*, Boston, MA, **36**(11): 1433-1447.

Rosenfeld D., R. Lahav, A. P. Khain, M. Pinsky, 2002: The role of sea-spray in cleansing air pollution over ocean via cloud processes. *Science*, **297**, 1667-1670.

Silverman B. A., and W. Sukarnjanaset, 2000: Results of the Thailand Warm-Cloud Hygroscopic Particle Seeding Experiment. *J. Appl. Meteor.*, **39**, 1160-2000.

Segal, Y, A. Khain,M. Pinsky and D. Rosenfeld, 2004b: Effects of hygroscopic seeding on raindrop formation as seen from simulations using a 2000 bin spectral cloud parcel model. *Atmospheric Research* (in press).

model results look best suit for seeding, Nba tried to develop Lahuga

ADDING SALT TO MINERAL DUST PARTICLES AND THE INTERACTION WITH CLOUDS – A CASE STUDY FROM THE MEIDEX CAMPAIGN

Z. Levin[1], A. Teller[1] ,E. Ganor[1] and Y. Yin[2]

[1]Department of Geophysics and Planetary Sciences, Tel-Aviv University, Tel-Aviv, Israel
[2]Institute of Mathematical and Physical Sciences, University of Wales Aberystwyth, Wales, UK

1. INTRODUCTION

The Mediterranean Israeli Dust Experiment, MEIDEX, was designed to investigate the vertical characteristics of mineral dust in the Mediterranean region. The campaign was carried out between 16 January and 1 February 2003 and involved remote sensing from the shuttle Columbia in its STS-107 flight, and simultaneous in situ measurements from an airplane and from the ground. For details see http://luna.tau.ac.il/~peter/MEIDEX/home.htm.

Unfortunately, the space shuttle flight ended in disaster and the loss of the crew and the shuttle. Although some of the data was transmitted to ground and some was recovered after the accident, the space shuttle data from the dust storm reported here was lost. Therefore, here we report only on the results from airborne measurements that were performed during the research flight of 28 January when the Eastern Mediterranean region was affected by a Saharan dust storm.

We investigated the potential effects of particles that were measured in a dust storm over the Mediterranean Sea on precipitation in this region. The investigation consists of analysis of the particles size, concentration and chemical composition as measured from an airplane. These were compared with other data from MODIS and with AERONET measurements from a station in Nes Ziona, just east of the flight track. These data was used as initial conditions for simulations of cloud development using our 2D numerical cloud model with detailed treatment of the cloud microphysics [Yin et al. (2000)].

2. THE MEASUREMENTS AND INSTRUMENTATION

On January 27th –28th 2003 a dust storm that originated in western Africa passed over the southeastern corner of the Mediterranean Sea. This dust storm was followed by heavy precipitation on the western coast of Israel and southern Lebanon on January 29th.

Corresponding author's address: Zev Levin, Department of Geophysics and Planetary Sciences, Tel-Aviv University, Tel-Aviv, Israel; E-Mail: zev@hail.tau.ac.il

On the morning of January 28th a research flight was conducted at about 20–100 km from the southeast coast of the Mediterranean Sea.

Figure 1 shows a map of the measurement area of the flight including the location of Nes-Ziona AERONET station and schematic representation of the dust storm based on MODIS image.

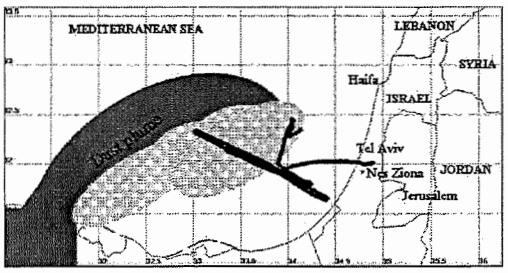

Figure 1 – Flight track on January 28th 2003 research flight. The gray and the lightly shaded areas represent heavy (AOT ~ 1–5) and mild dust loading (AOT <1), respectively

Aerosol Optical Spectrometers, AOS, consisting of PCASP-100 (0.1-3 μm, Equivalent Optical Diameter, EOD) and FSSP-100 (3-16 μm, EOD) were mounted on the King Air airplane. An isokinetic sampling system for collecting aerosols on filters and on various substrates inside a single stage impactor was set up. Big particles (>2 μm) were collected with a newly designed system mounted on the top of the plane, which collected particles by direct impaction on electron microscope grids for analysis of the elemental composition of single particles [Pardes et al. (1992) and Levin et al. (1996)]. Temperature and GPS were also measured.

Our in situ measurements were compared with AERONET data recorded at Nes Ziona (34.47 E, 31.55 N) and with images and analysis from the MODIS satellite.

3. RESULTS

A back trajectory analysis based on NOAA HYSPLIT model revealed that a dust plume, originating from northwestern Africa, entered the eastern Mediterranean region shortly before the

measurements started. A MODIS satellite image from 11:00 UT on January 28th also shows the dust plume pass over the Nile river delta on its way to the Mediterranean Sea as shown schematically in Figure 1.

The airplane performed aerosol measurements at different altitudes in the dust storm from about 150 m above the sea to about 3 km height.

3.1. Concentrations and size distributions

Figure 2 shows the vertical profile of the aerosol size distribution retrieved from the measurements of the optical counters. The figure shows that large concentrations of coarse particles were present up to about 3000 m above the sea while the highest concentrations were found up to about 2 km. Three size modes were measured up to about 500 m– one mode at ~ 0.2 μm, a second one at ~ 0.8 μm and a third at ~ 2 μm. The results revealed that the coarse particles concentrations decreased from about 30 particles/cm3 near the sea surface to about 1 particle/cm3 at altitudes above 2000 m.

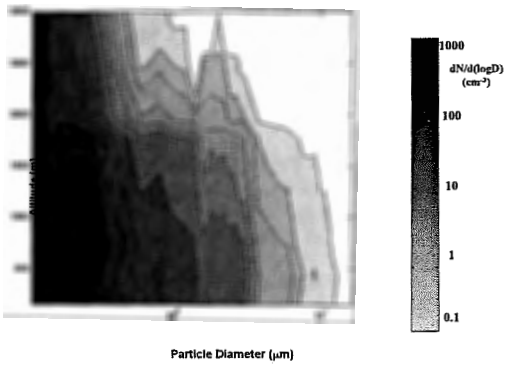

Figure 2 – Vertical profile of aerosol size distribution

3.2. Chemical analyses of single particles

Samples from four altitudes (500, 1000, 1500 and 2000 m) were chosen from the flight for quantitative elemental and morphological analysis using a SEM-EDS based on the calibration of Levin et al. (1996). The samples were collected on Thermanox substrate. Since Thermanox contains carbon, the present method could not identify the carbon. Quantitative estimation of the mass of nitrogen could not be obtained due to the proximity of its peak to that of carbon in the x-ray spectrum.

The analyzed particles were divided into 4 groups based on their chemical composition [Ganor et al. (1998)].

1. Sea salt aerosols – containing sodium and chloride (NaCl), sometimes together with Ca, Mg and/or K.
2. Sulfate and nitrate particles – containing only sulfur (possibly sulfuric acid (H_2SO_4), ammonium sulfate $(NH_4)SO_4$, or ammonium bi sulfate (NH_3HSO_4)), only sodium (sodium-nitrate ($NaNO_3$)), or Na and S (sodium-sulfate (Na_2SO_4)).
3. Mineral dust particles – containing Al, Si, Ca, and Fe.
4. Mixed aerosols – containing mixtures of sea salt and mineral dust.

The particles were also classified based on size as fine (<1 μm) and coarse (>1 μm).

560 particles were analyzed for their elemental composition, 200 of them were smaller than 1 μm while 360 were larger then 1 μm.

Table 1 shows the fractions by number of occurrence of each group in its own size category.

	≤ 1000 m		> 1000 m	
	fine	**coarse**	**fine**	**coarse**
Sea salt	0.43	0.13	0.10	0.10
Mineral dust	0.39	0.47	0.50	0.34
Sulfate and nitrate	0.12	0.04	0.35	0.47
Sea salt + mineral dust	0.06	0.36	0.05	0.08

Table 1 – Classification of individual particles

At low altitudes up to 1000 m above the sea, which corresponds to the height of cloud bases, the most prominent aerosol types were sea salt, minerals and aggregates of mineral dust and sea salt. The particles above 1000 m were mostly minerals and air pollution particles (sulfate and nitrates).

Most aerosols were internally mixed. Since the hygroscopicity of the particles is determined by the amount of the soluble material as well as by the exact location of the soluble material in the particle (imbedded or on the surface), it is important to determine the morphology and the approximate location of the soluble component.

X-ray mapping for some of the particles revealed that elements were dispersed non-uniformly on them, meaning that many of the particles were aggregates of NaCl with minerals or aggregates of air pollution with minerals.

3.3. Comparison with AERONET

Using the data from the AOS we calculated the height integrated volume distribution over the dust layer. We assumed that above the storm the contribution of the coarse aerosols was negligible and that the concentration of the fine particles decayed exponentially with height. Good correlation was found between these calculations and the AERONET retrievals based on the combined

spherical and spheroid inversion algorithm [Dubovic and King, (2000)].

3.4. The potential effects of dust and salt on clouds and precipitation

We used our TAU 2D numerical cloud model [Yin et al. (2000)] to estimate the possible effects of the mineral dust aerosols on clouds and on precipitation. This is a detailed microphysical model that uses the Spectral Method of Moments [Tzivion et al. (1987) and Reisin et al. (1998)] for calculating the growth of water drops and ice particles. The model is used with 300 m height resolution and 300 m lateral resolution.

The measured size distribution and chemical composition of the aerosols up to an altitude of 1000 m above the sea were used as initial conditions for nucleation. Using the SEM-EDS analysis (Table 1), we evaluated the fraction of aerosols that could serve as CCN. The types of aerosols that were used as CCN were therefore, sea salt and the mixed aerosols, which are treated as CCN due to the contribution of NaCl to their solubility. The particles entered the clouds and nucleated drops based on the supersaturation and critical diameter from Kohler theory. The drops grew by condensation and then by collision-coalescence. As the cloud developed vertically, reaching subfreezing temperatures, ice began to form by freezing of cloud drops containing efficient ice nuclei, IN, primarily those containing mineral particles. The large ice particles eventually began to descend, melting on their way down.

In order to study the potential role of dust and sea salt aerosols on cloud and rain formation, including the effect of ice nuclei concentrations, we ran the model in 3 scenarios with different size distributions as initial conditions. These size distributions were based on the measurements from the airplane. We assumed that the fine particles could serve as CCN while varying in the different scenarios the concentrations of the CCN in the coarse fraction.

The number of ice crystals was parameterized based on the approximation of Meyers et al. (1992). However, when dust particles entered the clouds we assumed that the Ice Nuclei, IN, concentration increased by a factor of 10 above the approximation of Meyers et al. (1992). This increase is due to the higher efficiency of mineral dust as IN as compared to other natural IN in the atmosphere [Pruppacher and Klett (1997)].

Table 2 describes the different aerosol characteristics that were used as initial conditions in the model.

Scenario No.	Name	Fine particles concentration (#/cc)	Coarse particle concentration (#/cc)	Ice nuclei enhancement factor
1	Dust, IN enhancement	900	15	10
2	Dust, no IN enhancement	900	15	1
3	No dust	900	0	1

Table 2 - Aerosol characteristics that were used as initial conditions for TAU 2D model of cloud development

Figure 3 shows the total amount of rain that fell from a cloud that was affected by cloud condensation nuclei composed of mineral dust coated with sea salt (with or without IN enhancement). It is compared with the amount of water that fell out of a cloud that was allowed to grow in the same environmental conditions, but was not affected by the dust particles. The total rain is computed assuming that the cloud depth is 1 km, as was done in Yin et al. (2000).

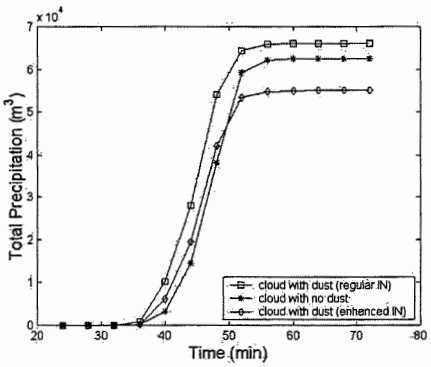

Figure 3 – Contribution of dust to total precipitation in a cloud. The initial condition of aerosol size distribution were based on the airplane measurements

We can see that the effect of the giant CCN in the form of dust particles coated with sea salt initiates the precipitation earlier and also enhances the amount of precipitation by about 10%. These changes are primarily due to the rapid drop growth by collection caused by the wider distribution of the CCN particles. The rapid development of the larger drops forms precipitation size drops at lower altitudes and starts the rain process earlier. In addition, this rapid growth at the lower levels of the cloud prevents some of the smaller drops and the few ice crystals that exist at higher levels from growing.

By comparison, the cloud that was not affected by mixture of dust and salt, having mostly smaller

CCN, produced rain less effectively with lower amounts. This is because the smaller CCN produced much smaller cloud drops, which needed much longer time to grow to become precipitation size. In this case more drops and ice crystals reach the upper parts of the cloud, leading to spreading of the released latent heat over a much larger vertical extent. In addition, many of these water droplets and ice crystals evaporated before having a chance to fall as precipitation.

Figure 3 also shows that, at least under the temperature profiles found in the Mediterranean region, inclusion of the effects of higher ice crystals production by dust particles tends to reduce the growth rate of the ice, delays the initiation of the rain and causes about 20% reduction in the total rainfall amount, as compared with the case having dust and salt as only giant CCN. These results are in agreement with those of Yin et al. (2000).

4. SUMMARY

In summary, the effect of the aerosols on the clouds is highly complex. Normally, increasing the concentrations of small CCN increases the droplet concentrations, reduces their size, delays the initiation of the rain and reduces the rainfall amount. On the other hand, introducing a few large CCN aerosols such as dust coated with sea salt or sulfate, leads to enhanced precipitation as shown here and in other works [Feingold et al. (1999), Yin et al. (2000), Wurzler et al. (2000)].

Since some of the mineral dust particles can act as effective IN, the amount of ice in the cloud could increase. Our results show that the enhanced concentrations of ice in the clouds in our region, delays the initiation of the rain and reduces the rainfall amounts by as much as 20% as compared to the case with giant CCN and no enhancement of ice.

5. ACKNOWLEDGMENTS

This work was sponsored by the Israeli Space Agency. It is dedicated to the brave astronauts on board the Columbia who gave their lives during the MEIDEX project.

6. REFERENCES

Dubovik, O. and M. D. King, 2000: A flexible inversion algorithm for retrieval of aerosol optical properties from Sun and sky radiance measurements, J. Geophys. Res., 105, 20673–20696.

very complex effects from obs'ns and simul'ns

Feingold, G., W. R. Cotton, S. M. Kreidenweis, and J. T. Davis, 1999: Impact of giant cloud condensation nuclei on drizzle formation in marine stratocumulus: Implications for cloud radiative properties. J. Atmos. Sci., 56, 4100-4117.

Ganor, E., Z. Levin and R. Van Grieken, 1998: Composition of individual aerosol particles above the Israelian Mediterranean coast during the summer time, Atmos. Environ., 32, 1631–1642.

Laird N. F., H. T. Ochs III, R. M. Rauber, and L. J. Miller, 2000: Initial Precipitation Formation in Warm Florida Cumulus. J. Atmos. Sci., 57, 3740-3751.

Levin, Z., E. Ganor, and V. Gladstein, 1996: The effects of desert particles coated with sulfate on rain formation in the eastern Mediterranean, J. Appl. Meteorol., 35, 1511–1523.

Meyers, M. P., P. J. DeMott, and W. R. Cotton, 1992: New primary ice-nucleation parameterizations in an explicit cloud model. J. Appl. Meteor., 31, 708–721.

Pardes, D., Z. Levin, and E. Ganor, 1992: A new method for measuring the mass of sulfur in single aerosols particles, Atmos. Environ., 26A, 679–680.

Pruppacher, H.R., and J.D. Klett, 1997: Microphysics of Clouds and Precipitation, 1954 pp., Kluwer Acad., Norwell, MA.

Reisin, T., Y. Yin, Z. Levin and S. Tzivion, 1998: Development of giant drops and high reflectivity cores in Hawaiian clouds: Numerical simulation using a kinematic model with detailed microphysics. Atmos. Res. 45, 275–297.

Tzivion, S., G. Feingold, and Z. Levin, 1987: An efficient numerical solution to the stochastic collection equation, J. Atmos. Sci., 44, 3139–3149.

Wurzler, S., T. G. Reisin and Z. Levin, 2000: Modification of mineral dust particles by cloud processing and subsequent effects on drop size distributions. J. Geophys. Res. 105, 4501–4512.

Yin, Y., Z. Levin, T. G. Reisin, and S. Tzivion, 2000: The effect of giant cloud condensation nuclei on the development of precipitation in convective clouds - A numerical study, Atmos. Res., 53, 91–116.

ANALYSIS OF THE EFFECTS OF ATMOSPHERIC ICE NUCLEI CONCENTRATIONS ON RADIANT PROPERTIES OF COLD CLOUD

Li Juan[1], Mao Jietai[1], You Laiguang[2], Hu Zhijin[2]

[1]Department of Atmosphere, Institute of Physics, Peking University, Beijing China
[2]Chinese Academy of Meteorological Science, Beijing, China

1. INTRODUCTION

Cloud can influence global radiative balance to a large extent. Its radiative force is very important to climate change (Baker, 1997; Twomey, 1984). Atmospheric aerosols can play an important role as CCN (Cloud Condensation Nuclei) in the microphysical process of warm cloud. They can influence cloud precipitation and cloud radiative properties directly and indirectly. Nowadays, many scientists have done a lot of research on climate change caused by numerical concentration changes of CCN, such as the studies of Twomey, Ramamatha, Harrison, Alkezweny, Rosenfeld, Steven, Kaufman and Richard (Twomey, 1984; Ramamatha, 1988; Harrison, 1990; Alkezweny, 1993; Rosenfeld, 2000; Steven, 2002; Kaufman, 1997; Richard, 2003). But their works are mainly of the studies of warm cloud.

In fact, cold cloud can also be very important to global radiative balance. With the changes of numerical concentration of atmospherical aerosol, IN (Ice Nuclei) concentration also changes. In 1963, 1995 and 1996, You Laiguang observed concentration of IN in the suburb of Beijing using BIG mixed cold-cloud-chamber (You Laiguang, 2002). He found that concentration of IN in the suburb of Beijing increased a lot. At -20℃, it had increased for about 15 times.

In fact, IN can be very important to cloud radiant properties. When temperature is lower than -35℃, formation of ice mainly relies on heterogeneous nucleation. When numerical concentration of IN changes, microphysical properties of cold cloud will change and radiative properties of cloud may also change. Thus, we pay much attention to IN for they may change radiative properties of cold cloud.

Because synchronous observation of numerical concentration of IN and ice particles in cloud is very difficult in reality, we can not verify the influence of IN concentrations on properties of ice particles easily. In this thesis, CAMS (Chinese Academy of Meteorological Science) 3-D cloud model is used in the research for it contains very detailed microphysical process of cloud (Hu Zhijin, 1987). Its horizontal grid is 0.7 km and vertical grid is 1.2 km. It considers supersaturation of vapor and variation of atmospheric temperature in ice nucleation process.

2. NUMERICAL SIMULATIONS USING 3-D CLOUD MODEL

Corresponding author's address: Li Juan, Department of Atmosphere, Institute of Physics, Peking University, Beijing 100871, China; E-Mail: lijuan@pku.org.cn.

In this part, one precipitation process is simulated as an example. Sounding data is from June, 10.1996. At that day, relative humidity on ground is 33 percents and height of zero degree level is 4km. In this simulation, IN concentration is assumed to increase 5 and 10 times. The two increased IN concentration are used in simulations respectively.

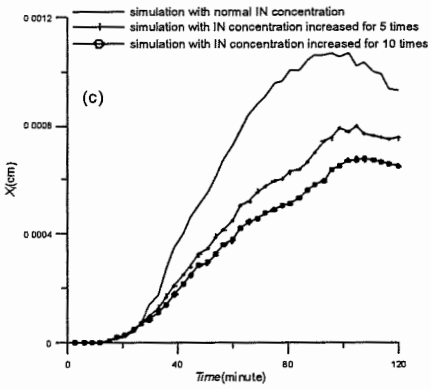

Fig. 1 IN nucleation velocity in simulated cloud with normal IN concentration, simulated cloud with IN concentration increases for 5 times and simulated cloud with IN concentration increases for 10 times

Fig. 1 is IN nucleation velocity in simulated cloud with normal IN concentration, simulated cloud with IN concentration increases for 5 times and simulated cloud with IN concentration increases for 10 times. Fig. 2 is content of ice particles in the three simulated cloud. Fig. 3 is dimension parameters of ice particles in the three simulated cloud. These figs show that when IN concentration increases, IN nucleation are enhanced, ice content increases and sizes of ice particles are smaller. The trends of changes are the same when IN concentration increases for 5 and 10 times. What is more, the difference between them is small. The simulation results show that when IN concentration increases, properties of simulated cloud will have some changes. These changes are that ice content increases, size of ice decreases and length of lengthways section of simulated cloud increases.

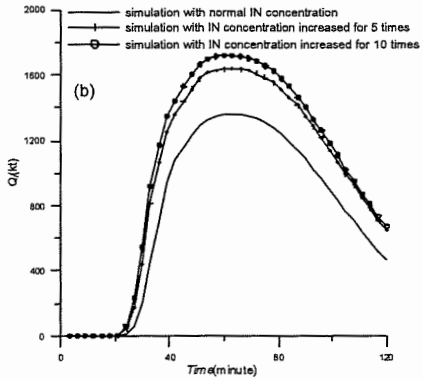

Fig. 2 content of ice particles in simulated cloud with normal IN concentration, simulated cloud with IN concentration increases for 5 times, simulated cloud with IN concentration increases for 10 times

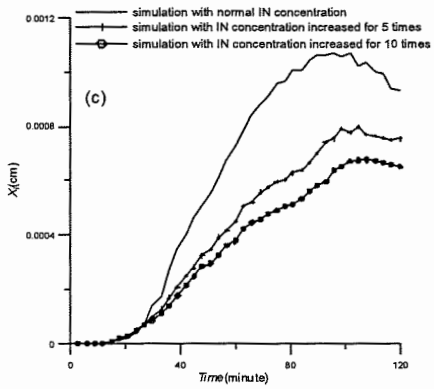

Fig.3 dimension parameters of ice particles in simulated cloud with normal IN concentration, simulated cloud with IN concentration increases for 5 times, simulated cloud with IN concentration increases for 10 times

From just one simulation we know that when IN concentration increases, properties of simulated cloud will have some changes. These changes are that ice content increases, size of ice decreases and length of lengthways section of simulated cloud increases. To demonstrate the conclusion to be universal, 18 more simulation are conducted. For the reason that trends of change are the same when IN concentration increases for 5 and 10 times, simulation with just increasing for 5 times is chosen.

Fig.4 shows proportions of maximal ice

content Q_i in the simulated cloud before and after IN concentration increases for 5 times. Moreover, it shows proportions of dimension parameters x_i in the simulated cloud before and after IN concentration increases for 5 times. In 90 percents cloud, ice content increases and the ice particles are smaller after IN concentration increases. The reason maybe is that more IN in the cloud will add the number of ice particles. In conclusion, these numerical simulations showed that in most simulated cloud, cloud top heightened, content of ice particles increased and size of them decreased when IN concentration increased. Analysis of these simulations showed that when numerical concentration of IN increased, macroscopical and microcosmic properties of cold cloud changed.

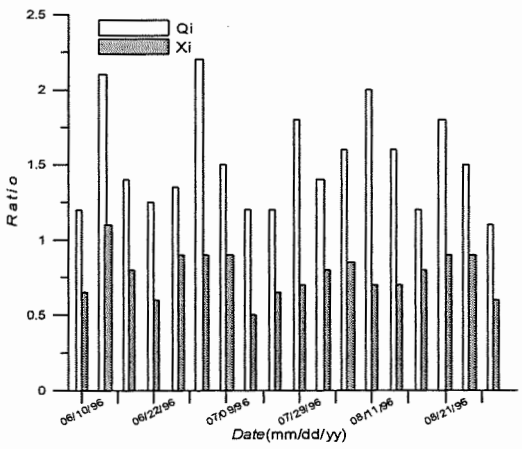

Fig. 4 ratio of maximal ice content (Q_i) in the simulated cloud before and after IN concentration increases for 5 times. Ratio of maximal dimension parameters (x_i) in the simulated cloud before and after IN concentration increases for 5 times increases for 5 times

3. SIMULATION WITH RADIATIVE MODEL

Simulations with 3-D cloud model show that when IN concentration increases, macroscopical and microscopical physical process will change. The next work is to study the changes of the radiant properties of cloud due to its physical changes. For the reason that this cloud model can not compute radiative properties of cloud, some qualitative analysis is done by using radiative models.

Numerical simulation of 3-D cloud model shows that, microphysical characteristics of 95 percents simulated cloud changes when IN concentration increases. Size of ice particles diminishes and ice content increases. In this part, libRadtran (Ping Yang, 2000) radiative model are used to show the changes of radiant properties of cold cloud due to the changes of microphysical properties. LibRdadtran model considers six kinds of ice shapes. These shapes include solid-column, hollow-column, rough-aggregate, rosette-4, rosette-6 and plate. The simulations shows that cloud reflectance which is composed of ice particles of various shapes will decrease when effective radius of cloud particles increase. What is more, cloud reflectance will increase in spite that the cloud is composed of different shape of ice particles when IWC increases. The trend is the same although the curves are a little different due to the different ice shape.

When cloud top is broadened, cold cloud amount is added. The simulation with 3-D cloud model shows that when IN concentration increases, area of cloud top is larger in most simulations. In some simulation, area of the cloud top can even be doubled. Thus, cold cloud amount will be larger and the radiative force of cloud will be much more significant.

4. CONCLUSION

With more and more human activities, numerical concentration of IN had increased a lot in atmosphere in some places. From the simulations with radiative models and 3-D cloud simulations, the conclusion is that concentration

of IN can change macroscopical and microscopical physical properties of cloud, and then change its radiant properties. When numerical concentration of IN increase, cloud reflectance will increase and vice versa. That is, IN will also influence the climate indirectly by take an active part in cold cloud microphysical process.

3-D convective cloud model was used in the research, so the results maybe have some limitation. For the reason that sheet cloud have similar microphysical process to convective cloud and its updraft velocity is smaller, we assumed that when IN concentration increased, microphysical properties of sheet cloud will also change but macroscopical properties may not change obviously. That is, radiative properties of sheet may also change. This work will be done later.

5. ACKNOWLEDGEMENTS

Many thanks to Mrs. Zhang Qiang who worked in Beijing Meteorological Bureau for offering me sounding data observed in 1996 from June to September to do the research.

6. REFERENCES

Alkezweny, A. J., et al. 1993: Measurements of cloud-droplet size distribution in polluted and unpolluted stratiform clouds. J. Appl. Meteor., 32(1), 106-115.

Baker, M. B., 1997: Cloud Microphysics and Climate. Science, 276, 1072-1078.

Rosenfeld, 2000: Suppression of Rain and Snow by Urban and Industrial Air Pollution. Science, 10(287), 1793-1796.

Harrison, E. F., 1990: Seasonal Variations of Cloud Radiative Forcing Derived From the Earth Radiation Budget Experiment. J. G. R., 95, 18687-18703.

Hu Zhijin, He Guanfang, 1987: The numerical simulations of microphysical process in the cumulonimbus. (1) Model with microphysical process. Acta. Meterologica. Sinica, 45(4), 467-483.

Paul Ricchiazzi, 1998: SBDART, A Research and Teaching Software Tool for Plane-Parallel Radiative Transfer in the Earth's Atmosphere. Bulletin of the Amer Mete Society, 79(10), 2101-2114.

Ping Yang, 2000: Parameterization of the scattering and absorption properties of individual ice crystals. J. G. R., 105(D4), 4699-4718.

Ramanathan V, et al, 2001: Aerosols, climate and the hydrological cycle. Science, 294, 2119-2124.

Ramamatha V, et al., 1988: Cloud Radiative Forcing and Climate, Results from the Earth Radiation Budget Experiment. Science, 243, 57-63.

Richard A. Kerr, 2003: Making Clouds Darker Sharpens Cloudy Climate Models. Science, 300, 1859-1860.

Steven Sherwood, 2002: A Microphysical Connection among Biomass Burning, Cumulus Clouds, and Stratospheric Moisture. Science, 295, 1272-1275.

Twomey S, et al, 1984: An assessment of the impact of pollution on the global cloud albeto. Tellus, 36B, 356-366.

Wylie D.P., et al, 1994: Four years of global cirrus cloud statistics using HIRS. J.Climate, 7, 1972-1986.

Kaufman, et al., 1997: The Effect of Smoke Particles on Clouds and Climate Forcing. Science, 12(277), 1636-1639.

You Laiguang, 2002: The study of the characteristics of the change of the numerical concentration of atmospherical ice nuclei in Beijing in 30 years. Acta. Meterologica. Sinica., 60(1),101-108.

model examining effect of ambient aerosols

REVIEW AND IMPLICATION OF WMO AND IUGG RECOMMENDATIONS CONCERNING THE EFFECT OF AEROSOL POLLUTION AND BIOMASS BURNING ON PRECIPITATION

Roland List

Department of Physics, University of Toronto, Toronto, Ontario, M5S 1A7, Canada

1. INTRODUCTION

In May 2003 I addressed the Congress XIV of the World Meteorological Organization about the increasing feeling in the science community about the importance of the issue of rainfall changes due to pollution. My intervention was based on the literature as well as a series of papers represented at the 8th WMO Scientific Weather Modification Conference, Casablanca, Morocco, 7.-12. April 2003. The driving thought was that a likely reduction of precipitation by pollution would lead to a loss of fresh water resources for the developing world. In such countries there is little possibility to circumvent the devastating problems of less precipitation because technology can not be as readily applied as in the developed world; lack of know-how and financial resources are the reasons. There was another point. Biomass burning through forest fires, cooking fires, charcoal production, heating with wood and dung produces haze over large regions of Africa, Asia and the Americas. This creates air loaded with excessive amounts of CCNs (1000-10000 particles per cc and more). Those particles are normally very small. In case of a lack of large CCN this leads to clouds with many tiny droplets, too small to interact and start the precipitation process.

A great recent example of industrial pollution is found in Rosenfeld (2000) showing a pollution plume which originates in Adelaide and moves North East through the Australian continent. The radar of the TRMM satellite showed no rain in the plume, but precipitation in the surrounding, similar clouds. The characteristic droplet sizes at cloud top also remained small, whereas the ones in the unpolluted air were > 28 μm. A startling example of biomass burning is the thick band of forest fires visible during cloudless nights in the Sahel region south of the Sahara, as taken by a Satellite during the winter 1994-1995 (NOAA-NESDIS poster). Cloud Physicists are normally unaware of the scope and importance of biomass burning. Not many would know about the Safari2000 project covering Central and Southern Africa (Kanyanga,et al. 2003). This project has spawned large scientific studies involving also a newly setup tropical Ozone project.

Corresponding author: Roland List, Department of Physics, University of Toronto, Toronto, Ont. M5S 1A7, Canada; e-mail address: list@atmosp.physics.utoronto.ca

The reader may also remember the "old" paper by Jack Warner (1968) about the reduction of precipitation by sugar cane fires.

In the abstract of their paper in Science on *"Aerosols, Climate, and the Hydrological Cycle"* V. Ramanathan, P. J. Crutzen, J. T. Kiehl, and D. Rosenfeld (Science, 2001) answer this question as follows: *"Human activities are releasing tiny particles (aerosols) into the atmosphere. These human-made aerosols enhance scattering and absorption of solar radiation. They also produce brighter clouds that are less efficient at releasing precipitation. These in turn lead to large reductions in the amount of solar irradiance reaching Earth's surface, a corresponding increase in solar heating of the atmosphere, changes in the atmospheric temperature structure, suppression of rainfall, and less efficient removal of pollutants. These aerosol effects can lead to a weaker hydrological cycle, which connects directly to availability and quality of fresh water, a major environmental issue of the 21st century."* [Underlining by R. List]

These "global" findings were recently supported by numerical model calculations (Lieper et al., 2004). At the local scale, Givati et al., (2004) have shown a 15-25% decrease of precipitation for areas downwind of major costal areas in California and Israel.

It is clear that pollution in general is the big factor, not just biomass burning. Why the particular focus on biomass burning? The reason is simple. While we should not loose sight of the overall effect, the biomass burning aspect is a sub-problem of limited scope. It may be worthwhile to deal with this aspect first because the issues are better defined and its solution may be easier and achieved faster than the general one. There is also the aspect of funding of an assessment process and, at a later stage, the funding of an international research program. Funding may become possible if the focus is on major issues of the *developing world* which affect societies and are of importance to the living conditions and economies through the availability of *fresh water resources*.

For Cloud Physics such an assessment, when followed by an international program, will provide funding in many areas for unbiased research relevant to the understanding of the precipitation process. This may introduce new purpose and excitement into the field, and provide a step for recognition that the basic physics of precipitation is also important to climate modeling.

With this introduction the following statement by WMO Congress XIV and the resolution by IUGG are self-explanatory.

2. THE WMO CONGRESS DECISION AND THE IUGG RESOLUTION

CGXIV Pink on Pollution Plumes affecting Rainfall

"3.3.5.4. Congress noted with concern the new additional evidence, also presented at the 8th WMO Scientific Conference on Weather Modification, that was pointing to an apparent substantial reduction of the rainfall efficiency of clouds by plumes of smoke caused by biomass burning (agricultural practices, forest fires, cooking and heating) and industrial processes. Congress also noted the evidence that such non-raining clouds could regain their raining ability once they moved over oceans or large bodies of water (such as the Aral Sea) because sea-salt was then mixed into the clouds and overrode the detrimental effect of the smoke particles. Therefore, Congress recommended CAS to establish an ad-hoc Group on Biomass Burning and Smoke Plumes in general, charge it to prepare a summary report for information of the Members, addressing relevant issues such as (1) the climatology of smoke and weather active aerosol (Cloud Condensation Nuclei or CCN) plumes, (2) the in situ and remote measurement of CCN and cloud droplet concentrations, (3) strategies to reduce biomass burning and hence the density of smoke plumes, and (4) the seeding procedures and evaluation methods to re-establish raining ability of clouds affected by smoke plumes, and CAS to report to Fifteenth Congress.

On July 10, 2003 IUGG passed a resolution in support of the WMO action:

"IUGG,
Considering *Biomass burning from agricultural practices, household consumption and wildfires produces substantial quantities of aerosol particles that can increase small cloud droplet number concentration.*
Realizing *that higher concentrations of small cloud droplets affect their coalescence and the formation of precipitation and thus the water supply.*
Welcoming *the recognition of the potential effect of all aerosol sources on precipitation by Congress XIV of the World Meteorological Organization, WMO, in May 2003 and its projected actions focused on biomass burning plumes.*
Urges *the scientific community to undertake systematic studies of the impact of biomass burning aerosol on precipitation formation on all scales. Feedback effects on climate as well as the competing effects of industrial fine particle aerosols and natural coarse particle aerosols such as sea salt and soil dust should be included.*
Recommends *that a body be established to undertake an international program of study and assessment of the rain related effects of biomass burning in collaboration with WMO and other international organizations.*

1. *that this body creates a mechanism to assemble the scientific evidence needed to lay the groundwork for a UN sponsored conference on pollution effects on precipitation and hence water supply.*
2. *that this body reports in the IUGG Newsletters and the GA in 2007 on the step taken and the progress made."*

The dialog has been started toward the setup of "AN ASSESSMENT OF AEROSOL EFFECTS ON PRECIPITATION". Professor Peter Hobbs, USA, has agreed to be the leader (if officially asked) and will be assuming full control of the process. This includes establishing the purpose and scope of the Assessment, the direction and content of the Assessment, and the specialists involved in producing the final document.

3. MAIN QUESTIONS

Some of the questions to be addressed might involve:

- The effect of aerosol pollution, including biomass burning, on precipitation; state of the art;
- The climatology of the weather-active aerosol and cloud droplets (inventory);
- The remote sensing of weather-active aerosol, droplets and raindrops;
- Modeling of global, regional and cloud scale effects of pollution;
- Natural seeding and development of seeding concepts.

The latter point addresses also seeding of "quasi" stable clouds which would not rain without interference – contrary to present day seeding of convective clouds which attempts to enhance an ongoing rain process.

A key issue will be to lay down assessment criteria. When is a firm conclusion possible? In science it is normally necessary to have a confirmation by another independent researcher or group for any finding to be acceptable. With the complexity of the problems at hand it can be suggested that any statement be based on observations and measurements, needs to be confirmed by numerical models and physical understanding. Are there any other elements which have to be concurrently fulfilled?

For the case of biomass burning there is a need to establish if local and regional effects have a larger-scale climatological impact.

4. WORK PLAN

In its statement the WMO asked for the establishment of an "*ad hoc group on Aerosols and Biomass Burning.* For simplification and within IUGG this group will be called "Panel. The members of the Panel will be selected at the recommendation of its leader, Prof. Peter V. Hobbs, by the President of the WMO Commission of Atmospheric Sciences (CAS) in concurrence with the IUGG. The Panel will consist of scientific leaders in the various topics that relate to the Assessment and experts from developing countries where increasing levels of pollution are becoming chronic. Their contributions will be discussed by e-mail, reviewed by other experts in relevant topics, and incorporated into interim reports. These reports will be presented at special symposia at the *International Conference on Clouds and Precipitation* in Bologna in July 2004, the *International Global Atmospheric Chemistry* conference, IGAC of IGBP, in Christchurch, New Zealand, in September 2004, and at the *IAMAS Assembly in Beijing*, August 2005.

The Assessment Report will be finalized at a Workshop of the *Panel* in November/December 2005 where all contributions will be considered and evaluated. The Assessment will be submitted to the IUGG, WMO and ISCU by March 2006. *[from IUGG Application to ICSU.]*

Acknowledgments. I am grateful for the continuing support by the Meteorological Service of Canada and the National Science and Research Council of Canada and the helpful discussions with Prof. Ulrike Lohmann, Dr. Len Barrie, Prof. Urs Baltensperger, Dr. George Isaac, Prof. Peter Hobbs and Prof. Zev Levin.

REFERENCES

Givati, A., D. Rosenfeld, 2004: Quantifying precipitation suppression due to air pollution. *J. Appl. Meteor.*, in print.

Kanyanga, J.K., M.T. Freiman, H.J. Annegarn, R.J.Swap, 2003: River of smoke: synoptic analysis of biomass burning smoke and haze over southern Africa during SAFARI 2000 campaign. Proc. 8th WMO Sci. Wather Modif. Conf., Casablanca, Morocco, 7-12 April, 2003. WMO Rep.No. 39, 397-400.

Liepert, B.G., J. Feichter, U. Lohmann and E. Roeckner, 2004: Can aerosol spin down the water cycle in a warmer moister world? *Geophys. Res. Letters*, in print.

Ramanathan, V., P.J.Crutzen, J.T. Kiehl and D. Rosenfeld, 2001: Aerosols, climate, and the hydrological cycle. Science, 294, 2119-2124.

Rosenfeld D., 2000: Suppression of Rain and Snow by Urban and Industrial Air Pollution. *Science*, **287** (5459), 1793-1796.

Warner, J., 1968: A reduction of rainfall associated with smoke from sugar-cane fires. An inadvertent weather modification? *J. Appl. Meteor.*, 7, 247-251.

OVERVIEW OF AEROSOL-CLOUD INTERACTIONS IN THE CLIMATE SYSTEM

Ulrike Lohmann

[1] Department of Physics and Atmospheric Science, Dalhousie University, Halifax, N.S., B3H 3J5, Canada.

1. INTRODUCTION

The anthropogenic component of sulfate and carbonaceous aerosols has substantially increased the global mean aerosol burden from pre-industrial times to the present-day and can influence the climate in different ways. Some aerosols exert an indirect effect by acting as cloud condensation nuclei (CCN) and thereby affecting the initial cloud droplet number concentration, albedo, precipitation formation, and lifetime of warm clouds. For a constant liquid water path, a higher cloud droplet number causes an increase in cloud albedo (cloud albedo effect). Reductions in precipitation efficiency due to more but smaller cloud droplets slow down the precipitation formation and increase cloud lifetime (cloud lifetime effect). The cooling from both indirect effects has been estimated by climate models to be -1 to -4.4 W m^{-2} in the global mean (e.g., Anderson et al., 2003). Thus, it is still very poorly constrained and is an important source of uncertainty in projections of future climate change.

2. MECHANISMS OF INDIVIDUAL AEROSOL EFFECTS ON CLOUDS

2.1 Aerosol effects on warm stratiform clouds

The IPCC Third Assessment Report concluded that the first indirect aerosol effect (Twomey effect) amounts to 0 to -2 W m^{-2} in the global mean. The Twomey effect refers to the enhanced reflection of solar radiation due to the more but smaller cloud droplets in a cloud whose liquid water content remains constant (Twomey, 1959). In addition, the more but smaller cloud droplets reduce the precipitation efficiency and therefore enhance the cloud lifetime and hence the cloud reflectivity, which is referred to as the second indirect aerosol or cloud lifetime effect (Albrecht et al. 1989). Absorption of solar radiation by black carbon leads to a heating of the air, which can result in an evaporation of cloud droplets. It is referred to as semi-direct effect (Hansen et al. 1997). This warming can partially offset the cooling due to the indirect aerosol effect (e.g., Lohmann and Feichter, 2001). Both the cloud lifetime effect and the semi-direct effect involve feedbacks because the cloud lifetime and cloud liquid water content change. Therefore they were not included in the radiative forcing bar chart of the IPCC (2001) assessment.

2.2 Evidence from observational data

Feingold et al. (2003) used various observations at the Atmospheric Radiation Measurement program (ARM) site in Oklahoma to estimate the indirect aerosol effect from the partial derivative of the logarithm of cloud droplet radius with respect to the logarithm of the aerosol extinction. Defined in this way, the indirect aerosol effect can be compared to its estimates from satellite retrievals. They find that the indirect effect at the ARM site is larger than estimated from the Polarization and Directionaly of the Earth Reflectance (POLDER) satellite data by Bréon et al. (2002). As, however, pointed out by Rosenfeld and Feingold (2003) that could stem from problems with the POLDER satellite retrievals because POLDER misses clouds wiht variable cloud top heights in its field of view. POLDER is also biased to thinner, less turbulent clouds.

Penner et al. (2004) combined ARM data together with a Lagrangian parcel model at the ARM sites in Oklahoma and Alaska to provide observational evidence of a change in radiative forcing due to the indirect aerosol effect. On the other hand, long-term observations with satellites over China show evidence for the semi-direct effect, i. e. a reduction in planetary albedo that can be attributed to absorbing aerosols (Krüger and Graßl, 2004). Non of these techniques is, however, able to estimate the anthropogenic indirect aerosol effect globally.

2.3 Climate model estimates of these indirect aerosol effects

Climate model estimates of the second indirect aerosol effect and the semi-direct aerosol effect are at least as uncertain as of the first indirect effect.

*Corresponding author's address: Ulrike Lohmann, Dept. of Physics and Atmospheric Science, Dalhousie Univ., Halifax, N.S. B3H 3J5, Canada; e-mail: Ulrike.Lohmann@Dal.Ca, URL: http://www.atm.dal.ca/~lohmann

Kristjánsson (2002) concluded that the Twomey effect is three times as important as the cloud lifetime effect whereas Lohmann et al. (2000) simulated a cloud lifetime effect that is 40% larger than the Twomey effect. Lohmann and Feichter (2001), Kristjánsson (2002) and Penner et al. (2003) concluded that the semi-direct effect is only marginally important at the top of the atmosphere in the global mean whereas Jacobson (2002) suggests that the climatic effect of black carbon is strongly positive. The importance of black carbon, however, is via its absorption of solar radiation within the atmosphere that leads to a large negative forcing at the surface (Ramanathan et al. 2001; Lohmann and Feichter, 2001).

Lohmann and Lesins (2002) constrained these three indirect aerosol effects by taking the difference in the slope of the cloud droplet effective radius-aerosol index relationship between the POLDER satellite data and the ECHAM general circulation model results into account. This reduced the total global mean aerosol effect from -1.4 W m^{-2} to -0.85 W m^{-2}. Liu and Daum (2002) esimated that the magnitude of the first indirect aerosol effect can be reduced by 10% - 80% by including the influence that an increasing number of cloud droplets has on the shape of the cloud droplet spectrum (dispersion effect). Taking this dispersion effect into account, Peng and Lohmann (2003) could reduce the global mean indirect aerosol effect from -1.4 W m^{-2} to -1.2 W m^{-2}.

2.4 Aerosol effects on large-scale mixed-phase clouds

Lohmann (2002) showed that if, in addition to mineral dust, a fraction of the hydrophilic soot aerosol particles is assumed to act as contact ice nuclei, then increases in aerosol concentration from pre- industrial times to present-day pose a new indirect effect, a "glaciation indirect effect", on clouds. Here increases in contact ice nuclei in the present-day climate result in more frequent glaciation of clouds and increase the amount of precipitation via the ice phase reducing global cloud cover. Hence more solar radiation is absorbed so that the traditional solar indirect aerosol effect on water clouds is at least partly offset.

2.5 Aerosol effects on convective clouds

Rosenfeld (1999, 2000) and Rosenfeld and Woodley (2000) analyzed aircraft data together with satellite data to show that pollution aerosols suppress precipitation. This hypothesis was confirmed by a modeling study with a cloud resolving model by Khain et al. (2001) who showed that aircraft observations of highly supercooled water in convective clouds can only be reproduced if large concentrations of small droplets exist but not if the cloud is rather clean. Taking these results to the global scale, Nober et al. (2003) evaluated the sensitivity of the general circulation to the suppression of precipitation by anthropogenic aerosols by implementing a simple warm cloud microphysics scheme into convective clouds. They found large instantaneous local aerosol forcings reducing the warm phase precipitation. Beyond one timestep, feedbacks within the climate system cannot be ignored and, hence, no estimates on aerosol forcings on convective clouds can be given. On the other hand, Menon et al. (2002) showed that absorbing aerosols over China change the atmospheric stability and vertical motion by heating the air and with that affect the large-scale circulation and the hydrological cycle.

2.6 Aerosol effects on cirrus clouds

Lohmann et al. (2003) studied the increase of the aerosol and ice crystal number concentrations after the Mt. Pinatubo eruption and showed that it crucially depends on the assumed aerosol size distribution. Effects from the Mt. Pinatubo eruption on clouds and climate considering only homogeneous freezing of ice crystals are small. Hence, Kärcher and Lohmann (2003) developed a parameterization for heterogeneous immersion freezing of cirrus clouds. They concluded that if only one type of ice nuclei with freezing saturation ratios > 1.3-1.4 triggers cirrus formation, then the influence of aerosols on cirrus clouds is still small. However, a much stronger indirect aerosol effect on cirrus clouds is possible if several ice nuclei types with different freezing thresholds compete during the freezing process.

2.7 Aerosol effects on the hydrological cycle

Even though anthropogenic aerosol effects on the hydrological cycle involve feedbacks within the climate system and are therefore not considered a forcing in the "classical" sense, they pose a "forcing" on the hydrological cycle and therefore will be discussed here. By increasing aerosol and cloud optical depth, human emissions of aerosols and their precursors cause a reduction of solar radiation at the surface. In order for the surface energy balance to reach a new equilibrium state, the latent and sensible fluxes have to adjust. As evaporation has to equal precipitation on the global scale, a reduction in the latent heat flux leads to a reduction in precipitation. As shown in model simulations by Liepert et al. (2004) and Feichter et al. (2004) despite an increase in greenhouse gases, increases in optical depth due to the direct

soot increases amount of pollution from the indirect ice phase.

and indirect anthropogenic aerosol effects can cause a reduction in evaporation and precipitation. This mechanism then explains the observations of decreased pan evaporation over the last 50 years by Roderick and Farquhar (2002). On a more regional scale, along the same line of arguments, Rotstayn and Lohmann (2002), hypothesized that the indirect effect of sulfate aerosols by cooling especially the North Atlantic sea surface temperature is partially responsible for the Sahel drought.

2.8 Aerosol effects on the snowfall rate

Observations by Borys et al. (2003) in midlatitude orographic clouds show that for a given supercooled liquid water content, both the riming and the snowfall rates are smaller if the supercooled cloud has more cloud droplets as, for example, caused by anthropogenic aerosols. Lohmann (2004) studied the climatic implication of this effect in global climate model simulations by replacing the constant riming efficiency with a size-dependent one appropriate for planar crystals and aggregates, respectively. In the model simulations that use a size-dependent riming collection efficiency, the pollution induced decrease in cloud droplet size causes a decrease in the riming rate in stratiform clouds despite larger liquid water contents in polluted clouds. Contrary to the above mentioned observations in all model simulations the snowfall rate increases as shown in figure 1 because of feedbacks in the climate system: Anthropogenic emissions of aerosols and their precursors increase the aerosol and cloud optical thickness which reduces the solar radiation at the top of the atmosphere and the surface. This is turn causes a cooling in Northern Hemisphere midlatitudes that favors precipitation formation via the ice phase.

3. SUMMARY

Highlights of these various aerosol effects on water, mixed-phase and ice clouds in terms of their radiative impact and their impact on the hydrological cycle will be presented at the conference.

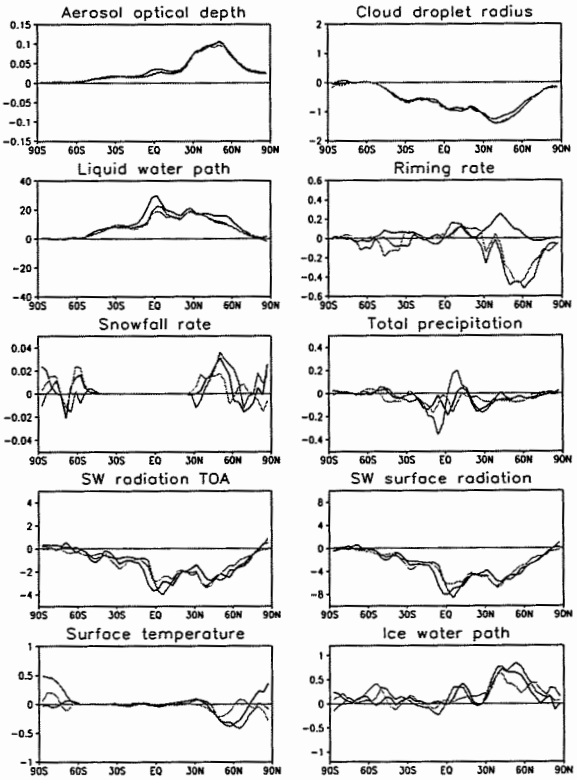

Figure 1: Zonal, annual mean changes in aerosol optical depth, effective cloud droplet radius averaged over all liquid water cloud layers [μm], liquid water path [g m^{-2}], vertically integrated riming rate [mg m^{-2} s^{-1}], snowfall rate [mm d^{-1}], total precipitation [mm d^{-1}], shortwave (SW) radiation at the top of the atmosphere (TOA) and at the surface [W m^{-2}], surface temperature [K] and ice water path [g m^{-2}] between pre-industrial and present day times for the control simulation with a constant riming efficiency (black line), and the simulations with size dependent riming efficiencies appropriate for planar crystals (red line) and aggregates (green line). In the pre-industrial simulations emissions of sulfate and carbonaceous (black carbon and organic carbon) aerosols from fossil fuel and biomass burning are set to zero. All simulations were conducted in T30 horizontal resolution (3.75°× 3.75°) and 19 vertical levels after an initial spin-up of three months using prescribed climatological sea surface temperatures and sea ice extent.

References

Albrecht, B. A., Aerosols, cloud microphysics, and fractional cloudiness, Science, 245, 1227-1230, 1989.

Anderson, T. L., R. J. Charlson, S. E. Schwartz, R. Knutti, O. Boucher, H. Rodhe, and J. Heintzenberg, Climate forcing by Aerosols - a hazy picture, Science, 300, 1103-1104, 2003.

Borys, R. D., Lowenthal, D. H., Cohn, S. A. and Brown, W. O. J. 2003. Mountaintop and radar mea-

surements of anthropogenic aerosol effects on snow growth and snowfall rate, Geophys. Res. Lett. 30, doi: 10.1029/2002GL016855.

Bréon, F.-M., D. Tanré, and S. Generoso, Aerosol effect on cloud droplet size monitored from satellite, Science, 295, 834–838, 2002.

Feichter, J., E. Roeckner, U. Lohmann and B. Liepert, Nonlinear aspects of the climate response to greenhouse gas and aerosol forcing, J. Climate, in press, 2004.

Feingold, G., W. L. Eberhard, D. E. Veron, and M. Previdi, First measurements of the Twomey indirect effect using ground-based remote sensors, Geophys. Res. Lett., 30, 1287, 2003.

Hansen, J., M. Sato, and R. Ruedy, Radiative forcing and climate response, J. Geophys. Res. 102, 6831-6864, 1997.

Jacobson, M. Z., Control of fossil-fuel particulate black carbon and organic matter, possibly the most effective method of slowing global warming, J. Geophys. Res. 107, doi: 10.1029/JD001376, 2002.

Kärcher, B. and U. Lohmann, A parameterization of cirrus cloud formation: Heterogeneous freezing, J. Geophys. Res. 108, 10.1029/2002JD003220, 2003.

Khain, A. P., D. Rosenfeld and A. Pokrovsky, A., Simulating convective clouds with sustained supercooled liquid water down to -37.5°C using a spectral microphysics model, Geophys. Res. Lett. 28, 3887-3890, 2001

Kristjánsson, J. E., Studies of the aerosol indirect effect from sulfate and black carbon aerosols, J. Geophys. Res., 107, doi: 10.1029/2001JD000887, 2002.

Krüger, O. and H. Graßl, H., Albedo reduction by absorbing aerosols over China, Geophys. Res. Lett., 31, doi: 10.1029/2003GL019111, 2004.

Liepert, B., J. Feichter, U. Lohmann, and E. Roeckner, Can aerosols spin down the water cycle in a warmer and moister world? Geophys. Res. Lett. 31, in press, 2004.

Liu, Y. and P. H. Daum, Indirect warming effect from dispersion forcing, Nature 419, 580-581, 2002.

Lohmann, U., J. Feichter, J. E. Penner and W. R. Leaitch, Indirect effect of sulfate and carbonaceous aerosols: A mechanistic treatment. J. Geophys. Res. 105, 12,193- 12,206, 2000.

Lohmann, U. and J. Feichter: Can the direct and semi-direct aerosol effect compete with the indirect effect on a global scale? Geophys. Res. Lett. 28, 159-161, 2001.

Lohmann, U., A glaciation indirect aerosol effect caused by soot aerosols, Geophys. Res. Lett. 29, 10.1029/2001GL014357, 2002.

Lohmann, U. and G. Lesins, Stronger constraints on the anthropogenic indirect aerosol effect, Science, 298, 1012-1016, 2002.

Lohmann, U., B. Kärcher and C. Timmreck, Impact of the Mt. Pinatubo Eruption on Cirrus Clouds Formed by Homogeneous Freezing in the ECHAM GCM, J. Geophys. Res. 108, 10.1029/2002JD003185, 2003.

Lohmann, U., Can anthropogenic aerosols decrease the snowfall rate? J. Atmos. Sci., subm. to, 2004.

Menon, S., J. Hansen, L. Nazarenko, and Y. Luo, Climate effects of black carbon aerosols in China and India, Science, 297, 2250-2253, 2002.

Nober, F. J., H.-F. Graf, H.-F. and D. Rosenfeld, Sensitivity of the global circulation to the suppression of precipitation by anthropogenic aerosols, Global Planetary Change 37, 57-80, 2003.

Peng, Y. and U. Lohmann, Sensitivity study of the spectral dispersion of the cloud droplet size distribution on the indirect aerosol effect, Geophys. Res. Lett. 30, 10.1029/2003GL017192, 2003.

Penner, J. E., S. Y. Zhang and C. C. Chuang, Soot and smoke aerosol may not warm climate. J. Geophys. Res. 108, 10.1029/2003JD003409, 2003.

Penner, J. E., X. Dong and Y. Chen, Y., Observational evidence of a change in radiative forcing due to the indirect aerosol effect, Nature, 427, 231-234, 2004.

Ramanathan, V., P. J. Crutzen, J. T. Kiehl and D. Rosenfeld, Aerosols, climate and the hydrological cycle, Science, 294, 2119-2124, 2001.

Roderick, M. L. and Farquhar, G. D., The cause of decreased pan evaporation over the past 50 years, Science, 298, 1410-1411, 2002.

Rosenfeld, D., TRMM observed first direct evidence of smoke from forest fires inhibiting rainfall, Geophys. Res. Lett., 26, 3105-3108, 1999.

Rosenfeld, D., Suppression of rain and snow by urban and industrial air pollution, Science, 287, 1793-1796, 2000.

Rosenfeld, D. and W. L. Woodley, Deep convective clouds with sustained supercooled liquid water down to -37.5°C, Nature, 405, 440-442, 2000.

Rosenfeld, D. and G. Feingold, Explanation of discrepancies among satellite observations of the aerosol indirect effects, Geophys. Res. Lett., 30, doi: 10.1029/2003GL017684, 2003.

Rotstayn, L. D. and U. Lohmann, Tropical rainfall trends and the indirect aerosol effect, J. Climate 15, 2103-2116, 2002.

Twomey, S. A., The nuclei of natural cloud formation. Part II: The supersaturation in natural clouds and the variation of cloud droplet concentrations, Geofis. Pure Appl., 43, 227-242, 1959.

overview of diff. effects that aerosols can lead

good references on homo + heterogeneous nucl

CIRRUS CLOUD MICROPHYSICS AND ITS DEPENDENCY ON AEROSOL TYPE, TEMPERATURE, AND COOLING RATE

A. Mangold[1], M. Krämer[1], O. Möhler[2], R. Wagner[2], H. Saathoff[2], H. Teichert[3], V. Ebert[3]

[1] Institute for Chemistry and Dynamics of the Geosphere I (ICG-I), Research Center Jülich, Germany
[2] Institute for Meteorology and Climate Research, IMK-AAF, Research Center Karlsruhe, Germany
[3] Institute of Physical Chemistry, University of Heidelberg, Germany

1. INTRODUCTION

Cirrus clouds have a great influence on the water cycle of the upper troposphere and are of great importance for the global radiative balance. The order of magnitude of an anthropogenically caused radiative forcing of these clouds remains highly uncertain (IPCC, 1999). For a more accurate evaluation of this impact, a better understanding of the micropyhsical processes leading to cirrus formation and the resulting optical properties (e.g. ice crystal number concentration and size) is crucial.

Cirrus clouds may either form via homogeneous or heterogeneous freezing of aerosol particles or via a combination of both processes. Homogeneous freezing was investigated in various laboratory and field studies (e.g. Heymsfield and Miloshevich, 1993; Jensen et al., 1998; Koop et al., 2000; Möhler et al., 2003). Using the freezing nucleation rates of Koop et al. (2000), Kärcher and Lohmann (2002a,b) developed a microphysical parameterization of homogeneous freezing, showing that an increasing ice crystal number density in cirrus clouds can mainly be described as function of decreasing temperature and higher updraft velocity (i.e. higher cooling rate and higher ice supersaturation). They also stated that enhanced number concentrations of sulfate aerosols, occurring e.g. after volcanic eruptions, would not influence significantly the process of cirrus formation.

There are several laboratory and field studies investigating the heterogeneous freezing of ice nuclei like, e.g., soot and soot coated with sulfuric acid (DeMott et al., 1999), mineral dust immersed in aqueous ammonium sulfate particles (Zuberi et al., 2002) or crystallized ammonium sulfate (Zuberi et al., 2001). Kärcher and Lohmann (2003) provided a microphysical parameterization of the heterogeneous ice nucleation in the immersion mode. For intermediate updraft velocities a strong aerosol effect on cirrus properties is possible, probably also affecting the radiative properties of cirrus clouds. The presence of heterogeneous ice nuclei with freezing thresholds significantly below the homogeneous one would lead to a lower ice crystal number concentration. The heterogeneously formed ice crystals scavenge the available water vapor during their growth, thus limiting the peak relative humidity with respect to ice (RH_{ice}), and hindering homogeneous freezing. Up to now there are only few field studies examining the relationship between the microphysical cirrus formation processes and the resulting occurrence and optical properties of the cirrus clouds (e.g. the INCA field campaign, Ovarlez et al., 2002; or the CRYSTAL-FACE field campaign in 2002). However, complete data sets to describe the thermodynamics, aerosol system and relative humidity during cirrus formation are difficult to obtain with high time resolution and accuracy at field campaigns. Therefore, laboratory investigations under controled conditions are of high interest.

Here, we present results of laboratory measurements with high time resolution and accuracy of homogeneous and heterogenous ice nucleation, performed at the aerosol chamber AIDA of Forschungszentrum Karlsruhe, Germany under simulated atmospheric cirrus conditions. The experiments were conducted at temperatures between 224 and 190 K. Submicron-sized sulfuric acid (SA) and ammonium sulfate (AS) solution droplets were used during homogeneous freezing experiments, whereas submicron-sized pure soot and soot coated with sulfuric acid, and mineral dust (Arizona Test Dust, ATD) particles served as ice nuclei during heterogeneous freezing experiments. Results with regard to the ice water content, the ice crystal number concentration and mean size are presented.

2. ICE NUCLEATION EXPERIMENTS

2.1 AIDA Aerosol and Cloud Chamber Facility

The AIDA aerosol chamber is a large coolable and evacuable vessel of 84 m^3 which can be cooled down to 183 K. The pressure range covers 0.1 to 1000 hPa. Under constant wall and gas temperatures, ice saturation is maintained by a thin ice layer on the chamber walls. The ice supersaturation necessary for the nucleation of ice crystals is achieved by 'volume expansion' due to controlled pumping, usually from 1000 to 800 hPa, causing RH_{ice} to increase by up to 50 % min^{-1}.

The Lyman-α-fluorescence hygrometer FISH (Zöger et al., 1999) is used to measure the total water concentration (gas phase + condensed phase) at a time resolution of about 1 Hz via a heated inlet tubing. Simultaneously, the gas phase water concentration is selectively measured in situ by an absorption spectrometer (TDL), based on room temperature near infrared tunable diode lasers at 1370 nm and a 82 m White multi-path cell. Ice crystal number concentrations and mean sizes are retrieved using in situ multi-path FTIR extinction spectroscopy. Number concentrations and optical diameters of growing ice crystals are also determined with two optical particle spectrometers (PCS2000 and WELAS, Palas). The total aerosol number concentration is measured with a condensation

Corresponding author's adress: Alexander Mangold, Forschungszentrum Jülich GmbH, ICG-I, D-52425 Jülich, Germany, E-mail: a.mangold@fz-juelich.de

particle counter (CNC3010, TSI). For a more detailed description of the instrumentation, aerosol generation, error estimation, and the methods of AIDA ice nucleation experiments see Möhler et al. (2003) and Mangold et al., (2004).

2.2 Typical ice nucleation experiment

Figure 1 illustrates a typical ice nucleation experiment in the AIDA chamber. At the beginning, the pressure p and temperatures T are constant (see Fig. 1, upper panel, for the time evolution of pressure, gas, and wall temperature). The partial pressure of water vapor e_{gas} (Fig. 1, middle panel, dash-3dots-dashed line) is controlled by the saturation vapor pressure over ice of the slightly colder ice coated walls $e_{s,i,w}$ (Fig. 1, middle panel, dash-dotted line). With the start of pumping, e_{gas} starts to decrease almost linearly with decreasing total pressure. Due to the expansion cooling, the ice saturation pressure $e_{s,i,g}$ (Fig. 1, middle panel, dashed line) steeply decreases with decreasing gas temperature and therefore RH_{ice} increases (Fig. 1, middle panel, solid line). As soon as RH_{ice} exceeds the critical ice supersaturation RH_{ice_nuc}, ice crystals begin to form.

Because the wall temperature remains almost constant during the expansion, there is an increasing difference between $e_{s,i,w}$ and e_{gas}, causing a continuous flux of water vapor from the ice layer on the wall into the gas phase. After ice crystals have formed, they start to take up the excess water and grow as long as RH_{ice} is ≥ 100 % (Fig. 1, lower panel, stars). This additionally lowers e_{gas} and therefore increases the water vapor flux from the wall ice layer, resulting in a marked increase of the total water signal (Fig. 1, lower panel, dotted line). When pumping is stopped, the gas temperature starts to increase, RH_{ice} drops below 100 % and the ice crystals start to evaporate.

The ice water content (IWC) is directly obtained by subtracting the gas phase water vapor concentration from the total water concentration (Fig. 1, lower panel, small crosses). The IWC is also retrieved from the FTIR extinction spectra (Fig. 1, lower panel, open squares). The IWC peaks around the end of the pumping period.

The ice crystal number concentration (N_{ice}) reaches its maximum shortly after ice nucleation (Fig. 1, lower panel, triangles). Subsequently, the number concentration decreases continuously due to the ongoing pumping and ice particle sedimentation.

The experiments are performed at pumping rates (dp/dt) between −50 and −20 hPa min^{-1}. Note that during all AIDA experiments the pumping rate – and not the cooling rate (dT/dt) – is controlled. During the pumping period, a heat flux from the warmer walls to the cooler gas phase exists, which decreases the cooling rate with time of pumping. Therefore, the cooling rate at ice nucleation $(dT/dt)_{nuc}$ depends, besides the pumping rate, also on the onset time of ice nucleation.

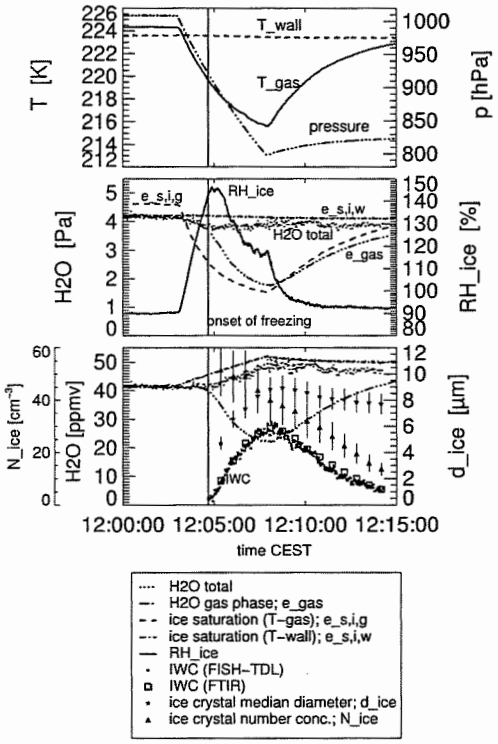

Figure 1: Time series of an AIDA ice nucleation experiment with sulfuric acid aerosol at 224 K; upper panel: total pressure, gas and wall temperature; middle panel: water vapor pressures and relative ice saturation; lower panel: water vapor mixing ratios, ice water content, ice crystal number concentration and median diameter. The lines explained in the legend refer only to middle and lower panel.

3. RESULTS AND DISCUSSION

3.1 Ice water content (IWC)

The IWC (Fig. 2, values refer to the maximum IWC for each experiment) is shown for a series of homogeneous and heterogeneous freezing experiments with different temperatures and aerosol types. The error is estimated to range between 10 and 15 %.

First, the good agreement between the IWC derived either from the difference between measurements of total and gas phase water (FISH-TDL) or from the FTIR extinction spectra should be noted. This applies not only to the maximum values, but also to the period of the dynamical growth and evaporation of the ice crystals (Fig. 1, lower panel).

Generally, the maximum IWC increases with increasing temperature, since there is more water vapor available for crystal growth at higher temperatures. This increase was nicely reproduced by both methods. The differences in the IWC at comparable temperatures but different aerosol types – most clear at the experiments around 205 K – may be due to different number concentrations, surface area densities, or habits of the formed ice crystals. The higher the ice crystal surface area density (i.e. the higher the ice

nucleation efficiency), the faster is the water vapor depletion of the gas phase and the earlier RH_{ice} decreases below 100 %, terminating the water vapor flux from the ice coated walls. This mechanism could explain the lower IWC values for the experiments with soot and mineral dust around 205 K and with soot, coated with sulfuric acid around 194 K.

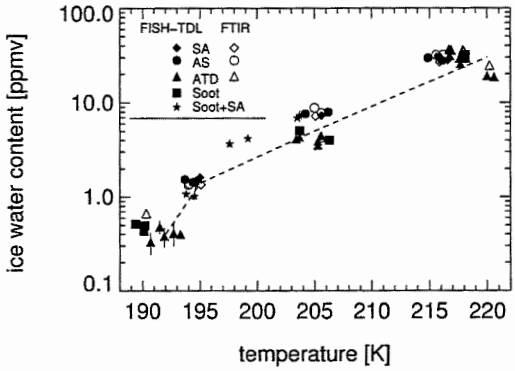

Figure 2: Maximum ice water content (IWC) of AIDA ice clouds for different aerosol types; SA = sulfuric acid (diamonds), AS = ammonium sulfate (circles); ATD = Arizona Test Dust (triangles); Soot (squares); Soot+SA = soot, coated with sulfuric acid (stars); filled symbols denote IWC retrieved from FISH-TDL data; empty symbols denote IWC retrieved from FTIR spectra.

3.2 Number concentration and mean size of ice crystals

The maximum number concentration (N_{ice_max}) and corresponding mean size (d_{ice}) of ice crystals measured during the homogeneous and heterogeneous freezing experiments at various temperatures are shown in Figure 3. All points refer to experiments with comparable pumping rates. The initial aerosol number concentrations (N_{ptcl}) were around 10000 cm^{-3} in the homogeneous freezing cases, around 3000 cm^{-3} in the coated soot cases and only a few hundred particles per cm^3 in the mineral dust experiments.

The dependency of N_{ice_max} on the cooling rate at homogeneous freezing processes is illustrated for SA and AS aerosol in Figure 4.

N_{ice_max} increases with decreasing temperature for both SA and AS aerosol, whereas AS produces distinctly more ice crystals than SA aerosol. Coated soot particles (Soot+SA) show similar values for N_{ice_max} as SA aerosol for all experiments shown here (Fig. 3), although compared to AS aerosol, distinctly less ice crystals are produced. This is mainly due to higher cooling rates at ice nucleation $(dT/dt)_{nuc}$ for the AS experiments. From Figure 4 it can be seen that at comparable temperatures higher cooling rates cause the formation of more ice crystals. Additionally, at lower temperatures significantly lower values for $(dT/dt)_{nuc}$ are sufficient to produce even higher ice crystal concentrations. At the Soot+SA experiments, the values for $(dT/dt)_{nuc}$ were comparable to the SA cases around 209 K and -1.2 K min for the 200 K case. The ice crystal sizes are much smaller at lower temperatures due to the larger ice crystal number concentration and the lower IWC.

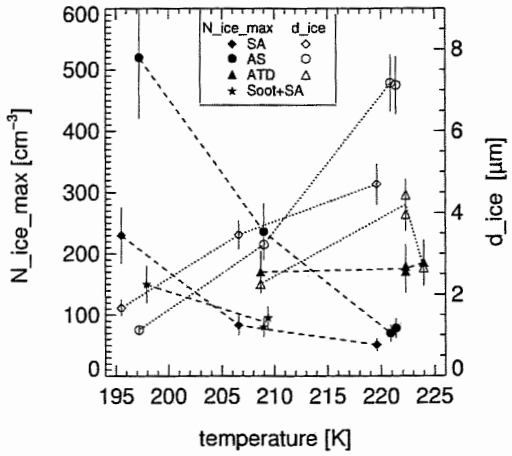

Figure 3: Maximum ice crystal number concentrations (N_{ice_max}; filled symbols) and corresponding median diameters (d_{ice}; empty symbols); SA = sulfuric acid (diamonds), AS = ammonium sulfate (circles); ATD = Arizona Test Dust (triangles); Soot+SA = sulfuric acid coated soot (stars); The dashed and dotted lines are only to guide the eye.

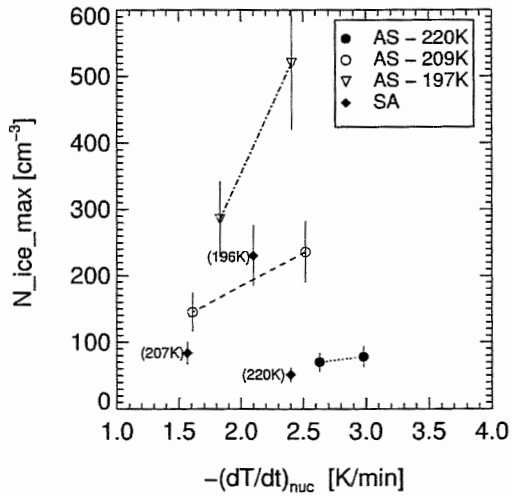

Figure 4: Dependeny of the maximum ice crystal number concentration (N_{ice_max}) on the critical cooling rate at ice nucleation $-(dT/dt)_{nuc}$ for AIDA experiments with AS = ammonium sulfate and SA = sulfuric acid aerosol at different temperatures.

In the observed temperature range, Arizona Test Dust (ATD) particles revealed the highest N_{ice_max}, that means the highest ice nucleation efficiency of the investigated aerosol types. Consequently, the size of the ice crystals is small. Compared to the experiments with AS, SA and Soot+SA aerosol, the fraction of ATD particles nucleating ice was about one order of magnitude higher. Additionally, there is no clear dependency of N_{ice_max} on temperature (Fig. 3). Note, however, that at 209 K, N_{ice_max} was limited by N_{ptcl} (180cm^{-3}).

4. CONCLUSION

Homogeneous and heterogeneous ice nucleation experiments at temperatures between 224 and 190 K were performed in the aerosol chamber AIDA with various aerosol types. The ice water content (IWC), the maximum number concentration of ice crystals (N_{ice_max}) and their corresponding mean size (d_{ice}) were investigated.

Ice water content: There is very good agreement between the IWC data retrieved from the difference between measurements of total water and interstitial water vapor and those retrieved from the FTIR spectra. Slight differences of the IWC between the aerosol types at comparable temperatures could qualitatively be explained by different ice surface aera densities or different amounts of water evaporating from the ice coated chamber walls during the experiments.

Homogeneous freezing: The experiments with sulfuric acid and ammonium sulfate solution droplets show that N_{ice_max} increases with decreasing temperature and higher cooling rates at ice nucleation. This dependency agrees very well with the parameterization by Kärcher and Lohmann (2002a). The higher values of N_{ice_max} at the AS experiments can mainly be explained by the higher cooling rates at the onset of freezing.

Heterogeneous freezing: Soot aerosol coated with sulfuric acid exhibited an ice nucleation efficiency comparable to SA aerosol. This may indicate that the heterogeneous freezing effect of the ice nuclei is at least partly masked by the sulfuric acid coating.

The mineral dust particles have been most efficient with respect to the ice crystal number concentration and almost all particles acted as ice nuclei. If N_{ice_max}, produced by mineral dust aerosol, is mainly limited by the number concentration of the particles themselves, this might imply that in the atmosphere the number of ice crystals produced via this pathway is less dependent on temperature or cooling rate (like for the homogeneous freezing mechanism). Thus mineral dust particles may indirectly affect the climate by changing the radiative properties of cirrus clouds. The high efficiency of mineral dust particles could have important implications for the parameterization of heterogeneous ice nucleation processes in atmospheric models.

ACKNOWLEDGEMENTS

We are grateful for the support and technical assistance by all staff members during the AIDA ice nucleation experiments, especially C. Linke, S. Büttner, O. Stetzer and M. Schnaiter. We are also grateful for the collaboration of C. Giesemann with the TDL instrumental setup and data retrieval. This work contributes to the German HGF project „Particles and Cirrus Clouds (PAZI)".

REFERENCES

DeMott, P. J., Y. Chen, S. M. Kreidenweis, D. C. Rogers, D. E. Sherman, 1999: Ice formation by black carbon particles. *Geophys. Res. Lett.*, **26**, 2429-2432.

Heymsfield, A. J., L. M. Miloshevich, 1993: Homogeneous ice nucleation and supercooled liquid water in orographic wave clouds. *J. Atmos. Sci.*, **50**, 2335-2353.

Intergovernmental Panel on Climate Change (IPCC), 1999: *Aviation and the Global Atmosphere*, in: J. E. Penner, D. H. Lister, D. J. Giggs, D. J. Dokken, M. McFarland (eds.), Cambridge University Press, 373pp.

Jensen, E. J., O. B. Toon, A. Tabazadeh, G. W. Sachse, B. E. Anderson, K R. Chan, C. W. Twohy, B. Gandrud, S. M. Aulenbach, A. Heymsfield, J. Hallett, B. Gary, 1998: Ice nucleation processes in upper tropospheric wave-clouds observed during SUCCESS. *Geophys. Res. Lett.*, **25**, 1363-1366.

Kärcher, B., U. Lohmann, 2002a: A parameterization of cirrus cloud formation: Homogeneous freezing of supercooled aerosols. *J. Geophys. Res.*, **107**(D2), 4010, doi:10.1029/2001JD000470.

Kärcher, B., U. Lohmann, 2002b: A parameterization of cirrus cloud formation: Homogeneous freezing including effects of aerosol size. *J. Geophys. Res.*, **107**(D23), 4698, doi:10.1029/2001JD001429

Kärcher, B., U. Lohmann, 2003: A parameterization of cirrus cloud formation: Heterogeneous freezing. *J. Geophys. Res.*, **108**(D14), 4402, doi:10.1029/2002JD003220.

Koop, T., B. Luo, A. Tsias, T. Peter, 2000: Water activity as the determinant for homogeneous ice nucleation in aqueous solutions. *Nature*, **406**, 611-614.

Mangold, A. R. Wagner, H. Saathoff, U. Schurath, C. Giesemann, V. Ebert, M. Krämer, O. Möhler, 2004: Microphysics of cirrus clouds formed by different types of aerosols: experimental investigation in the aerosol chamber AIDA. Submitted to Meteorol.Z.

Möhler, O., O. Stetzer, S. Schaefers, C. Linke, M. Schnaiter, R. Tiede, H. Saathoff, M. Krämer, A. Mangold, P. Budz, P. Zink, J. Schreiner, K. Mauersberger, W. Haag, B. Kärcher, U. Schurath, 2003: Experimental investigation of homogeneous freezing of sulphuric acid particles in the aerosol chamber AIDA. *Atmos. Chem. Phys.*, **3**, 211-223.

Ovarlez, J., J.-F. Gayet, K. Gierens J. Strōm, H. Ovarlez, F. Auriol, R. Busen, U. Schumann, 2002: Water vapour measurements inside cirrus clouds in Northern and Southern hemispheres during INCA. *Geophys. Res. Lett.*, **29**(16), 1813, doi: 10.1029/2001GL014440.

Zöger, M., A. Afchine, N. Eicke, M.-T. Gerhards, E. Klein, D. S. McKenna, U. Mörschel, U. Schmidt, V. Tan, F. Tuitjer, T. Woyke, C. Schiller, 1999: Fast in situ stratospheric hygrometers: A new family of balloon-borne and airborne Lyman-α photofragment fluorescence hygrometers. *J. Geophys. Res.*, **104**(D1), 1807-1816.

Zuberi, B., A. K. Bertram, T. Koop, L. T. Molina, M. J. Molina, 2001: Heterogeneous freezing of aqueous particles induced by crystallized $(NH_4)_2SO_4$, ice, and letovicite. *J. Phys. Chem. A*, **105**, 6458-6464.

Zuberi, B., A. K. Bertram, C. A. Cassa, L. T. Molina, M. J. Molina, 2002: Heterogeneous nucleation of ice in $(NH_4)_2SO_4$–H_2O particles with mineral dust immersions. *Geophys. Res. Lett.*, **29**(10), doi: 10.1029/2001GL014289

Experiments in chamber on homo + heterogeneous nucl.

EFFECTS OF AEROSOLS AND THERMODYNAMICS ON THE GLOBAL DISTRIBUTION OF TRMM-DERIVED WARM CLOUD PROPERTIES

T. Matsui[1], H. Masunaga[1], R. Pielke Sr.[1], and W.-K. Tao[2]

[1]Department of Atmospheric Science, Colorado State University, Ft. Collins, CO, 80523-1371, USA
[2]Laboratory for Atmospheres, NASA/Goddard Space Flight Center, Greenbelt, MD, 20771, USA

1. Introduction

Maritime low clouds, denoted hereafter as stratus, reduce the Earth's energy budget by approximately 15 (W/m²) in an annual average (Hartmann et al. 1992).

Stratus amount is, in particular, positively correlated with *lower-tropospheric static stability* (LTSS), defined as the potential temperature difference between the surface and the 700 (mb) pressure level (Klein and Hartmann 1993). Klein and Hartmann (1993) demonstrate that high LTSS represents a strong temperature inversion at the top of the atmospheric boundary layer, and the regional observations show that the stratus cloud is confined to the boundary layer in high LTSS, while extending their horizontal areal coverage.

Aerosols also control stratus properties by acting as cloud condensation nuclei (CCN) to form cloud droplets. A high concentration of aerosols overseed cloud droplets to generate highly concentrated, narrowly distributed cloud droplet spectra which increase the cloud albedo up to 30% (Twomey 1984). Narrowly distributed cloud droplet spectra prevent formulation of precipitation and could increase the cloud lifetime that further cools the Earth's surface (Albrecht 1989). This climatic impact of aerosols on cloud properties is called the aerosol indirect effect, which is one of the largest uncertainties in accurately describing the sensitivity of climate to changes in aerosol concentrations in the future.

Figure 1 exhibits a global distribution of seasonally-averaged LTSS (gray contours) derived from the NCEP/NCAR Reanalysis (Kalnay et al. 1996) and the seasonally-averaged aerosol index derived from the MODerate resolution Imaging Spectroradiometer (MODIS) (dark shaded) (Tanré et al. 1997). The aerosol index is better correlated than aerosol optical depth with the column aerosol concentration under some assumptions (Nakajima et al. 2001), and was derived from the aerosol optical thickness at 0.55 (μm) and Ångstrom exponent computed from 0.55 and 0.865 (μm). Different contributions from these two factors across the globe possibly influence the cloud microstructure. Objective of this research is to examine the sensitivity of the aerosol effect to the cloud properties on a global scale due to the background atmospheric thermodynamic structure.

Corresponding author's address: Toshihisa Matsui, Department of Atmospheric Science, Colorado State University, Ft. Collins, CO, 80523-1371, USA; e-mail:matsuit@atmos.colostate.edu, matsui@agnes.gsfc.nasa.gov

2. TRMM-derived Cloud Properties

A new algorithm using the Tropical Rainfall Measurement Mission (TRMM) Microwave Imager (TMI) and Visible/Infrared Radiance Imager (VIRS) provides the vertical structure of warm cloud (cloud top temperature > 273 K) microstructure by investigating two types of droplet effective radius (Re): shortwave-derived droplet size (Re (top)) and microwave-derived droplet size (Re (column)). This is because a VIRS-derived Re tends to be biased toward a cloud-top value due to strong absorption of the near-infrared band, whereas a TMI-derived Re is expected to be close to the value averaged over the cloud layer since microwaves can detect cloud droplets and raindrops without suffering from saturation within low maritime clouds (Masunaga et al. 2002).

3. Sensitivity of the Aerosol Indirect Effect

We performed a statistical analysis for the individual estimates of stratus, aerosol index, and LTSS. The three individual datasets are not precisely concurrent in time and space. We directly relate the daily 1-degree MODIS aerosol index, 0.25-degree TRMM cloud properties, and 2.5-degree LTSS from the NCEP/NCAR Reanalysis without spatial interpolation.

The means of Re (top) and Re (column) were derived with a given aerosol index (bins of 0.02) and LTSS (bins of 0.4 K) as can be see in Figure 2. The three-dimensional slope shows that high aerosol index and/or high LTSS lead to the smaller droplet size in both Re (column) and Re (top); i.e., a larger temperature inversion and higher concentration of aerosols inhibit cloud droplet growth. On the other hand, cloud droplet sizes are maximized in the pristine and less stable atmosphere.

For a fixed liquid water path, the relationship between Re and aerosol index is expressed as (e.g., Bréon et al., 2002)

$$\frac{d\log(\mathrm{Re})}{d\log(AI)} = \frac{\alpha}{3}, \qquad (1)$$

where AI is aerosol index, and α approximately relates the aerosol index to the number of cloud droplets (N_c) via $N_c \approx (AI)^{\alpha}$. The slope ($\alpha/3$) is a parameter that simply quantifies the magnitude of the aerosol indirect

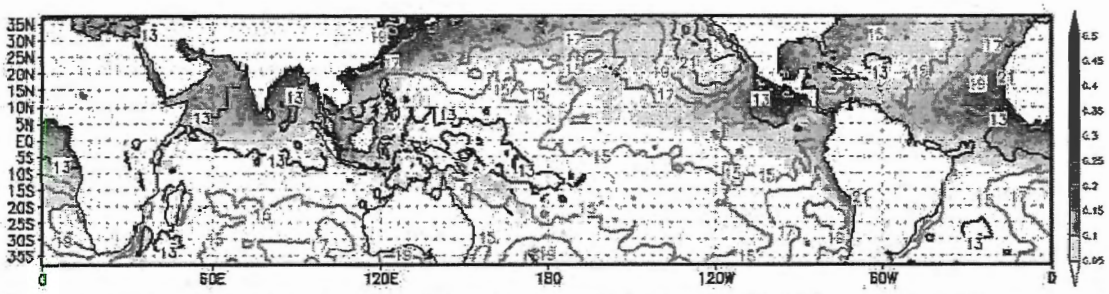

Figure 1. Global distribution of aerosol index (dark shaded) from the MODIS measurements and lower-tropospheric static stability (LTSS) (K) (gray contour) derived from the NCEP/NCAR Reanalysis averaged through March-May 2000. (From Matsui et al. (2004))

effect. Since the standard errors ($\sigma/\sqrt{n-2}$, where n and σ are the number of quasi-coincident measurements for each bin and is standard deviation, respectively) are generally larger for the bins of higher aerosol index due to the lack of the sample number, we derived the slope for an aerosol index > 0.25. Although our sampling and statistical processes are different from the previous studies in a strict manner, the slope of Re (top) averaged over a full range of LTSS ($\alpha/3$=0.069) is close to that derived from Bréon et al. (2002) ($\alpha/3$=0.085) and less than 50% of that derived from Nakajima et al. (2001) ($\alpha/3$=0.16). The slope of Re (column) is 0.222, which is three times larger than that of Re (top), and is close to that using a characteristic value, α = 0.7 (Charlson et al. 1992). Since the Re (column) is directly related to the cloud optical depth (Masunaga et al. 2002), the aerosol indirect effect and associated Earth's cooling effect could be greater than the estimation using cloud-top Re (-0.7 – 0.2 W/m²) (Nakajima et al. 2001).

The slopes of Re (column) averaged over the five bins of LTSS range from 0.12 to 0.32 (Table 1). In the same LTSS intervals, the slope of Re (top) range from 0.022 to 0.071. Those contain values derived over land and ocean (Bréon et al. 2002), suggesting that the difference in the slope between land and ocean could be explained by their background thermodynamic structure, in addition to the observational tendency of the specific sensor (Rosenfeld and Feingold 2003). Except for the lowest LTSS intervals (12.2 – 13.8), the slope of Re (column) and Re (top) generally decreases toward the higher LTSS (Table 1); i.e., a greater fraction of aerosols are converted into cloud droplets in the lower LTSS. This result is also physically reasonable, since a lower static stability permits a deeper atmospheric boundary layer and stronger updrafts to yield a higher supersaturation, which activate more CCNs thereby decreasing the droplet size (Feingold et al. 2003). However, the aerosol effect on the cloud albedo and associated Earth's radiation budget is not necessarily stronger in the convectively unstable atmosphere, since cloud areal coverage becomes very small in such regions (Klein and Hartmann 1993). The different slopes due to the LTSS also explain why the mean slope of Re (top) is smaller than Nakajima et al. (2001); our sampling number is biased toward the subtropical regions, where the LTSS is generally higher than the tropical region.

4. Conclusion

Our study demonstrates an important sensitivity of the aerosol effect on the cloud-precipitation process to the different static stability regimes through a simultaneous examination of the cloud-top and

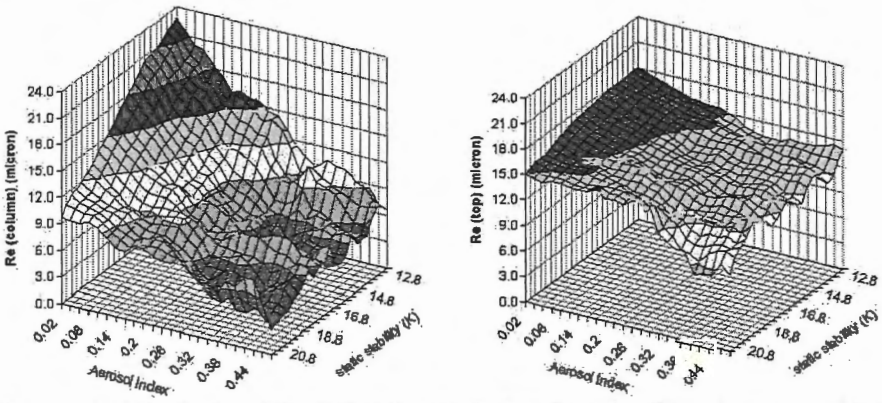

Figure 2. The mean of Re (top) and Re (column) were derived for sets with a given aerosol index (bins of 0.01) and low-atmosphere static stability (bins of 0.4 K) from May to March. (From Matsui et al. (2004))

Ranges of LTSS (K)		12.2 - 13.8	14.2 - 15.8	16.2 - 17.8	18.2 - 19.8	20.2 - 21.8
(α/3)	Re (top)	0.071	0.085	0.084	0.051	0.022
	Re (column)	0.19	0.32	0.27	0.20	0.12

Table 1. The slope (α/3) averaged over the five bins of the LTSS. (From Matsui et al. (2004))

columnar droplet effective radius. While the magnitude of its effect of cloud-top values reproduces the value reported in the previous studies, those of columnar values are greater than the previous studies, suggesting a possible underestimation of the aerosol indirect effect with using cloud-top droplet size. The cloud-aerosol interaction is clearly identified except where LTSS is so high that the cloud droplet growth is dynamically suppressed. *It is, therefore, important that the aerosol effect and static stability be simultaneously taken into account for diagnosing warm cloud properties on a global scale* (Matsui et al. 2004).

Acknowledgements. This work is funded by NASA CEAS Fellowship No. NAG5-12105, and NASA Grant No. NNG04GB87G. VIRS (1B01) and TMI (1B11) data were provided by NASA GSFC DAAC. NCEP/NCAR Reanalysis were provided by the NOAA CDC. The authors would like to thank Allen Chu at NASA/GSFC for providing the MODIS aerosol data and T.Y. Nakajima at NASDA/EORC for providing the GTR 4.1 packages. We also thank Dallas Staley for her professional editing.

References

Albrecht, B. A., 1989: Aerosols, cloud microphysics, and fractional cloudiness, *Science,* **245**, 1227-1230.

Bréon, F.-M., D. Tanré, and S. Generoso, 2002: Aerosol effect on cloud droplet size monitored from satellite, *Science,* **295**, 834-838.

Charlson R. J., S. E. Schwartz, J. M. Hales, R. D. Cess, J. A. Coakley Jr., J. E. Hansen, and D. J. Hofmann, 1992: Climate forcing by anthropogenic aerosols, *Science,* **255**, 423-430.

Feingold, G., W. L. Eberhard, D. E. Veron, and M. Previdi, 2003: First measurements of the Twomey indirect effect using ground-based remote sensors, *Geophys. Res. Lett.*. **30(6)**, doi:0.029/2003GL017967.

Hartmann, D. L., M. E. Ockert-Bell, and M. L. Michelsen, 1992: The effect of cloud type on earth's energy balance: Global analysis. *J. Climate,* **5**, 1281-1304.

Kalnay *et al.*, 1996: The NCEP/NCAR 40-year Reanalysis Project. *Bull. Amer. Meteor. Soc.*, **77**, 437-471.

Klein, S. A., and D. L. Hartmann, 1993: The seasonal cycle of low stratiform clouds. *J. Climate*, **6**, 1587-1606.

Masunaga, H., T. Y. Nakajima, T. Nakajima, M. Kachi, R. Oki, and S. Kuroda, 2002: Physical properties of maritime low clouds as retrieved by combined use of Tropical Rainfall Measurement Mission Microwave Imager and Visible/Infrared Scanner: Algorithm, *J. Geophys. Res.* **107(10)**, doi:10.1029/2001JD000743.

Matsui, T., H. Masunaga, R.A. Pielke Sr., and W-K. Tao, 2004: Impact of aerosols and atmospheric thermodynamics on cloud properties within the climate system. *Geophys. Res. Lett.*, **31**, doi:10.1029/2003GL019287, in press.

Nakajima, T. A. Higurashi, K. Kawamoto, and J. E. Penner, 2001: A possible correlation between satellite-derived cloud and aerosol microphysical parameters, *Geophys. Res. Lett.,* **28**, 1171-1174.

Rosenfeld, D., and G. Feingold, 2003: Explanation of discrepancies among satellite observations of the aerosol indirect effect, 2003: *Geophys. Res. Lett.* **30(14)**, doi;10.029/2003GL017684.

Tanré, D., Y. J. Kaufman, M. Herman, and S. Mattoo, 1997: Remote sensing of aerosol properties over oceans using the MODIS/EOS spectral radiance. *J. Geophys. Res.*, **102**, 16,971-16,988.

Twomey, S. A., M. Piepgrass, and T. L. Wolfe, 1984: An assessment of the impact of pollution on global cloud albedo, *Tellus,* **36B**, 356-366.

cloud amount highly correlated with amount of static stability, they are and cloud top considered during indirect studies

VARIATIONS OF CLOUD CONDENSATION NUCLEI AND CLOUD DROPLET NUMBER CONCENTRATION DUE TO THE REPRESENTATION OF SIZE DEPENDENT CHEMICAL COMPOSITION OF AEROSOL: A MODELLING STUDY

Mihaela Mircea, Maria Cristina Facchini, Stefano Decesari, Fabrizia Cavalli and Sandro Fuzzi

Istituto di Scienze dell'Atmosfera e del Clima, Consiglio Nazionale delle Ricerche, I-40129, Bologna, Italy

1. INTRODUCTION

Up until recently, cloud modeling studies have only considered bulk aerosol chemical composition, disregarding its size dependence. We used a one-dimensional (1-D) cloud parcel model to study the influence of different representations of aerosol chemical composition: size segregated and bulk, on cloud condensation nuclei (CCN) and cloud droplet number concentration (CDNC). The cloud model includes a detailed description of the activation process, and is therefore appropriate for exploring the influence of aerosol chemical composition on aerosol activation and droplet growth. The data used in this study are based on aerosol measurements carried out in the Po Valley (Italy) (Matta et al., 2003), and includes both inorganic and organic compounds as well as surface tension changes with the concentration of water soluble organic matter (Facchini et al., 1999).

2. THE PARCEL MODEL AND INITIAL CONDITIONS FOR PARCEL MODEL SIMULATIONS

The 1D cloud parcel model with explicit microphysics is based on the equations given by Pruppacher and Klett (1997), and Seinfeld and Pandis (1997), which govern the growth of a single droplet and of a droplet population, the vertical velocity, the temperature, pressure, water vapour mixing ratio, liquid water mixing ratio and saturation ratio inside the rising air parcel. The equilibrium saturation is computed with a modified form of the Köhler equation, as in Shulmann et al. (1996), and Mircea et al. (2002). The cloud droplet surface tension variation as a function of dissolved organic carbon concentration is computed as in Facchini et al. (1999). The initial aerosol size distribution is a sum of m (m=3÷4) superimposed log-normal functions with log D_g as independent variable. The aerosol size distribution function is modeled in the air parcel using a sectional representation.

The growth of the aerosol particles due to water vapor uptake is calculated on a moving grid to eliminate numerical diffusion (Jacobson, 1999). This means that during the simulations the aerosol particles keep their initial bin number, but their wet diameter varies due to water condensation or evaporation.

Corresponding author's address: Mihaela Mircea, Istituto di Scienze dell'Atmosfera e del Clima, Consiglio Nazionale delle Ricerche, Via Gobetti 101, 40129, Bologna, Italy. E-Mail: m.mircea@isac.cnr.it.

In all the simulations carried out in the present study, the air parcel starts rising at 98% relative humidity, 273 K and 800 mbar.

The aerosol number size distribution during winter in Po Valley is shown in Fig.1. The parameters of the multi-modal log-normal aerosol number size distribution are based on Putaud et al. (2002), Van Dingenen (unpublished data) and Balkanski et al. (2003).

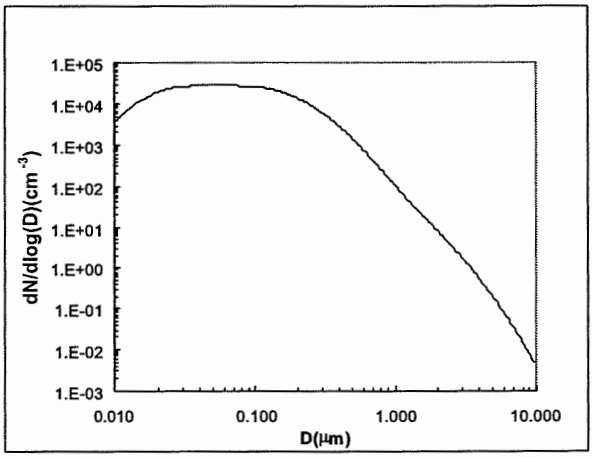

Fig. 1 Aerosol number size distribution in the Po Valley during the winter season.

The chemical composition of a representative aerosol sample for winter is shown in Fig.2.a(size segregated), b(bulk). The chemical composition of aerosol is derived from a five-stage low pressure Berner cascade impactor (LPI 80/0.05), which collects the aerosol segregated in the following size ranges: 1) 0.05–0.14 μm; 2) 0.14–0.42 μm; 3) 0.42–1.2 μm; 4) 1.2–3.5 μm; 5) 3.5–10 μm. Water soluble inorganic and organic components were analysed for each impactor stage, and a detailed characterisation of the water soluble organic compounds was also performed. More technical details on the analysis performed can be found in Matta et al. (2002).

The mass of the water soluble organic compounds (WSOC) was computed from measurements of the water soluble organic carbon content of the samples with a TOC liquid analyser, using a conversion factor from carbon mass to the mass of organic substances of 1.8. The WSOC conversion factor was derived from the results of chemical characterisation by functional group analysis, following the approach described in Decesari et al. (2000) and Fuzzi et al. (2001).).

size-segregated and cloud amount statistics are studied

According to the above approach, WSOC was separated into three main classes of compounds: neutral compounds (NC), mono-/di-acids (MDA) and polyacids (PA). In the model simulations, we represented the NC class of compounds with levoglucosan ($C_6H_{10}O_5$, ρ=1600 kg m^{-3}, van't Hoff factor=1), MDA compounds with succinic acid ($C_4H_6O_4$, ρ=1572 kg m^{-3}, van't Hoff factor=3) and PA compounds with fulvic acid ($C_{33}H_{32}O_{19}$ ρ=1500 kg m^{-3}, van't Hoff factor=5).

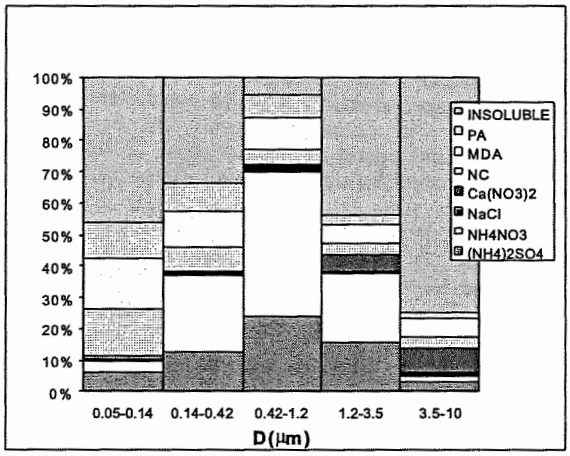

a)

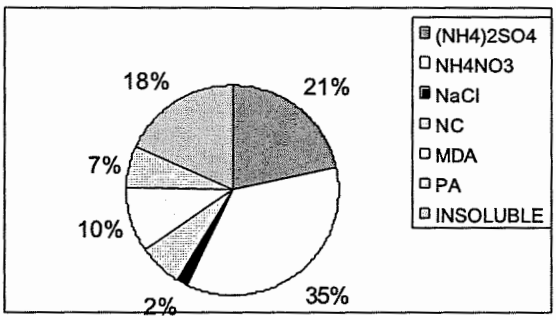

b)

Fig. 2. Size-segregated (a) and bulk (b) chemical composition of aerosol. INSOLUBLE indicates insoluble aerosol matter, NC are the neutral compounds, MDA is the class of mono-/di-acid and PA is the class of polyacids.

In order to transform the inorganic ionic species measured in the laboratory into the molecular form encountered in dry aerosol, we used the Aerosol Inorganic Model (AIM) (Wexler and Clegg, 2002). The inorganic compounds probably present in the dry aerosol were chosen on the basis of simulations made with AIM at low relative humidities (below 30%). The AIM model does not consider $Ca(NO_3)_2$ in its thermodynamic calculations. However, it was considered by us because we found a relevant concentration of Ca^{2+} in stages 4 and 5, and a large excess of NO_3^- not neutralized by Na^+ or NH_4^+. Since $Ca(NO_3)_2$ is soluble enough to be extracted with water, we consider its presence in dry aerosol to be plausible. We estimated that for the selected cases, the transformation of the ionic concentrations into molecular compound concentrations could cause an underestimation of soluble mass of aerosol below 10%.

The bulk aerosol chemical composition was calculated by summing the concentrations of inorganic and organic compounds at all impactor stages. The chemical composition was derived following the methodology described above, but starting from the sum of the measured ionic concentrations. Therefore, as a percentage of the total mass, the concentration of Ca^{2+} is negligible and the inorganic aerosol can be described only by $(NH_4)_2SO_4$, NH_4NO_3 and NaCl.

3. NUMERICAL SIMULATIONS

Here, we investigated the sensitivity of CCN and CDNC to the bulk and size-segregated chemical composition of aerosol samples.

CCN are defined as those aerosol particles which are capable of initiating drop formation at the observed atmospheric supersaturation (Pruppacher and Klett, 1997). According to Köhler's equilibrium theory, any particle with the critical supersaturation, S_c, smaller than the observed air supersaturation, and with size greater than the critical size, will grow into a cloud droplet. In this paper, we report as CCN all the particles with critical supersaturation lower than the parcel supersaturation (Pruppacher and Klett, 1997): this is a completely static approach that does not take into account the growth of aerosol particles due to condensation.

Usually, cloud microphysical studies consider as droplets all particles with diameter greater than a given value. At present, there is no fixed rule to define the minimum diameter of droplets; therefore, in some studies, the minimum value in the droplet spectrum is considered to be 0.2 µm (Flossman, 1998), while other studies count as droplets only particles greater than 2 µm (Feingold and Chuang, 2002). A diameter of 2 µm is also often used as a threshold diameter for cloud droplet in remote sensing. This value currently used seems to be a good threshold for separating clouds from aerosols, but it may certainly change, and its further definition depends on the future use of the clear/cloudy mask employed in optical retrievals. However, for the purposes of the present study, we consider as cloud droplets all particles with diameter greater than 2 µm.

4. INFLUENCE OF SIZE-RESOLVED CHEMICAL COMPOSITION OF AEROSOL COMPARED TO THAT OF BULK CHEMICAL COMPOSITION OF AEROSOL ON CCN NUMBER CONCENTRATION AND CDNC

Usually, the CCN number concentration is presented at the point of maximum air parcel supersaturation where, as seen in Fig. 3, the differences in supersaturation are greatest. From Table 1, it can be noted that at the point of maximum

supersaturation in the parcel, the size segregated chemical composition of the aerosol produces a decrease in CCN with respect to the bulk chemical composition of the aerosol, at all updrafts velocities considered in this study. For the case of an updraft velocity of 0.1 m/s, the decrease can be easily explained by taking two aspects into account: the air parcel maximum supersaturation for size segregated composition is lower than the air parcel maximum supersaturation for bulk composition (Table 1). In Fig. 4, it can be seen that for an aerosol particle of given size, the critical supersaturation computed with Köhler's theory is higher in the case of size segregated composition, than in the case of bulk composition. Considering the increase in critical supersaturation and the decrease in parcel supersaturation for size segregated composition with respect to bulk composition, as mentioned above, and the definition of CCN (see Section 3), it is obvious that the CCN number concentration is lower for size segregated as compared to bulk chemical composition.

For moderate and strong updrafts, the parcel supersaturation is higher for size segregated than for bulk composition, but not high enough to compensate the increase in critical s upersaturation shown in Fig. 4. Therefore, there is still a decrease in CCN number concentration due to the size segregated composition, but in a lower percentage, especially at high updrafts when the dynamics dominate the system.

A decrease in the CCN number concentration when considering a size segregated representation of aerosol chemical composition was also reported in the earlier work of Fitzgerald (1974); here, however, we prove that this decrease exists when measured aerosol data are used and when the presence of the organic compounds is taken into account.

In Table 2 we present CDNC for different updraft velocities and at 0.1 g/m^3 and 1 g/m^3 cloud liquid water content. As can be observed, at a given water content, the CDNC increases with the increase in the updraft velocity. Table 2 also shows that the CDNC does not always increase with the increase of liquid water content. At 1 m/s, one sees a decrease of the CDNC at a liquid water of 1 g/m^3 with respect to 0.1 g/m^3 It is explained by the fact that more of the water made available by the rising parcel is taken up on large particles at the expense of smaller ones.

Table 1. Changes in CCN due to the chemical composition at maximum supersaturation of the ascending air mass for different updraft velocities.

U (m s^{-1})	S_{max} % Bulk	S_{max} % Size-seg.	$(CCN_{size.seg}-CCN_{bulk})/CCN_{bulk}$ (%)
0.1	0.026	0.024	-21.0
1.0	0.105	0.112	-17.7
10	0.792	0.861	-6.4

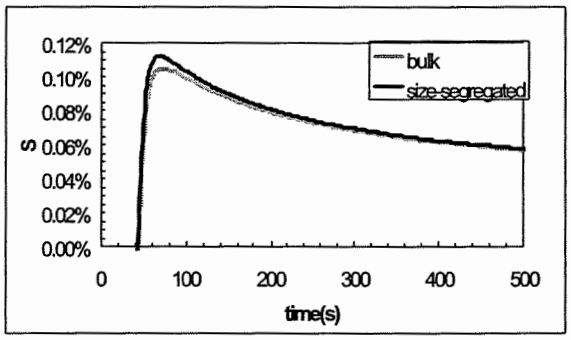

Fig. 3. Supersaturation (in percent) of air parcel versus time for a vertical velocity of 1 m/s. The black line corresponds to the simulation with size segregated chemical composition, the grey line to the simulation with bulk chemical composition.

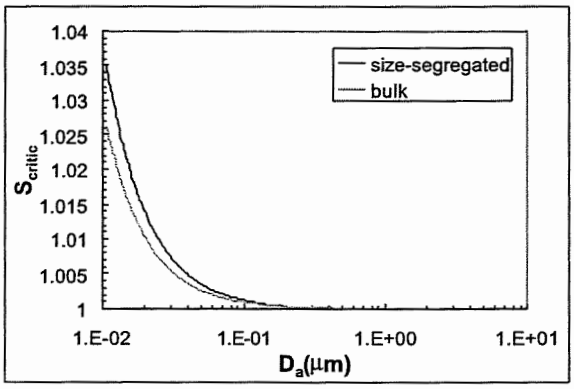

Fig. 4. CCN versus parcel supersaturation (in percent) for a vertical velocity of 1 m/s. The black line corresponds to the simulation with size segregated chemical composition, the grey line to the simulation with bulk chemical composition.

Table 2. CDNC(m^{-3}) for different liquid water values and different updraft velocity.

U (m s^{-1})	LWC=0.1 g m^{-3} Size seg.	LWC=0.1 g m^{-3} bulk	LWC=1 g m^{-3} size seg.	LWC=1 g m^{-3} Bulk
0.1	1.49×10^9	1.78×10^9	1.58×10^9	1.78×10^9
1.0	3.38×10^9	3.55×10^9	3.07×10^9	3.22×10^9
10	7.36×10^9	8.12×10^9	1.77×10^{10}	1.91×10^{10}

On the whole, it can be seen that the aerosol size segregated chemical composition determines a decrease in CDNC with respect to the bulk composition.

5. CONCLUSIONS

This work reveals a further "chemical effect" – size segregated chemical composition – which must be combined with the other chemical effects considered by Charlson et al (2001), and Nenes et al. (2002), where only bulk aerosol chemical composition is taken into account. The simulations with size-segregated chemical composition considered the aerosol internally mixed on each impactor stage, although, on the whole, it is an external mixture of aerosol particles of various chemical composition which is probably one of the most realistic descriptions of atmospheric aerosol possible at present.

Using the measured size-segregated chemical composition of the aerosol, we have shown that the detailed knowledge of chemical composition is very important for CCN number concentrations in weak and moderate updrafts, and for CDNC also in strong updrafts.

Overall, the results show that aerosol size-segregated chemical composition produces an important decrease in CCN number concentrations and CDNC, as compared to the one due to bulk chemical composition. However, at low and moderate updraft velocities, the influence of the size-segregated chemical composition is strongly influenced by kinetic effects (Nenes et al., 2001; Roberts et al., 2003). Thus, the combination of the updraft velocity and chemical composition is fundamental for predicting the CCN and CDNC. We therefore suggest the necessity of enhancing the knowledge of aerosol composition by both modelling and field studies, in order to improve further the parameterisations of aerosol-cloud interactions in global models.

6. REFERENCES

Balkanski, Y. , Bauer, S. E., van Dingenen, R., Bonasoni, P., Schulz, M., Fischer, H., Gobbi, G. P., Hanke, M., Hauglustaine, D., Putaud, J.-P., Stohl, A. and Raes, F., 2003: The Mt Cimone, Italy, free tropospheric campaign: principal characteristics of the gaseous and aerosol composition from European pollution, Mediterranean influences and during African dust events. Atmos. Chem. Phys. Discuss. 3, 1753-1776.

Decesari, S., Facchini, M.C. , Fuzzi, S. and Tagliavini, E., 2000: Characterization of water soluble organic compounds in atmospheric aerosol: a new approach. J. Geophys. Res. 105, 1481-1489.

Feingold, G. and Chuang, P.Y., 2002: Analysis of the influence of film-forming compounds on droplet growth: Implications for cloud microphysical processes and climate. J. Atmos. Sci. 59, 2006-2018.

Fitzgerald, J. W., 1974: Effect of aerosol composition on cloud droplet size distribution: a numerical study. *J.* Atmos. Sci. 31, 1358-1367.

Flossmann, A. I., 1998. Interaction of aerosol particles and clouds. J. Atm. Sci., 55, 879-887.

Fuzzi, S., Decesari, S., Facchini, M.C., Matta, E., Mircea, M. and Tagliavini, E., 2001: A simplified model of the water soluble organic component of atmospheric aerosol. Geophys. Res. Lett. 20, 4079-4082.

Facchini, M.C., Mircea, M., Fuzzi, S. and Charlson, R.J., 1999: Cloud albedo enhancement by surface-active organic solutes in growing droplets. Nature, 401, 257-259.

Jacobson, M.Z., 1999: Fundamentals of atmospheric modeling, Cambridge University Press, New York, 656pp.

Matta, E., Facchini, M. C., Decesari, S., Mircea, M., Cavalli, F., Fuzzi, S., Putaud, J.-P. and. Dell'Acqua, 2003: Chemical mass balance of size-segregated atmospheric aerosol in an urban area of the Po Valley, Italy. Atmos. Chem. Phys, 3, 623-637.

Mircea, M., Facchini, M.C., Decesari, S., Fuzzi S. and Charlson, R.J., 2002: The influence of the organic aerosol component on CCN supersaturation spectra for different aerosol types. Tellus 54B, 74-81.

Nenes, A., Ghan, S., Abdul-Razzak, H., Chuang, P. Y. And Seinfeld, J. H., 2001: Kinetic limitations on cloud droplet formation and impact on cloud albedo. Tellus 53B, 133-149.

Pruppacher, H.R. and Klett, J.D., 1997: Microphysics of clouds and precipitation, Kluwer Academic Publishers, Dordrecht, 955pp.

Putaud, J.-P, Van Dingenen *et al.*, 2002: A European Aerosol Phenomenology: physical and chemical characteristics of particulate matter at kerbside, urban, rural and background sites in Europe, JRC Report, EUR 20411 EN.

Roberts, G.C., Nenes, A., Seinfeld, J.H. and Andreae, M.O., 2003: Impact of biomass burning on cloud properties in the Amazon Basin. J. Geophys.Res. 108, doi:10.1029/2001JD000985.

Seinfeld, J.H. and Pandis, S. N., 1998: Atmospheric Chemistry and Physics, John Wiley&Sons, Inc., 1326pp.

Shulman, M.L., Jacobson, M.C., Charlson, R.J., Synovec, R.E. and Young, T.E. 1996: Dissolution behavior and surface tension effects of organic compounds in nucleating cloud droplets. Geophys. Res. Lett. 23, 277-280.

Wexler, S. A. and Clegg, S. L., 2002: Atmospheric aerosol models for systems including the ions H+, NH4+, Na+, SO42-,NO3-,Cl-, Br-, and H2O, J. Geophys. Res. 107, 10.1029.

HTDMA MEASUREMENTS AND THERMODYNAMIC MODELLING OF AQUEOUS AEROSOLS CONTAINING ORGANICS: A STUDY OF THE LETOVICITE AND MALEIC ACID SYSTEM

Mihaela Mircea[1], Maria Cristina Facchini[1], Stefano Decesari[1], Fabrizia Cavalli[1], Sandro Fuzzi[1], Jenny Rissler[2], Erik Swietlicki[2], Simon Clegg[3]

[1]Istituto di Scienze dell'Atmosfera e del Clima, Consiglio Nazionale delle Ricerche, I-40129, Bologna, Italy
[2]University of Lund, Division of Nuclear Physics, Sweden
[3]University of East Anglia, Norwich U.K.

1. INTRODUCTION

The water content of atmospheric aerosol controls particle size, density and refractive index, as well as its ability to sorb and react with ambient gases. The water uptake of inorganic aerosol is relatively well known from measurements and described by thermodynamic models, but that of mixed inorganic/organic aerosol is still under investigation. The complex chemical composition of the organic aerosol and the lack of thermodynamic data regarding the interaction between the inorganic-organic compounds within aerosol particles preclude the elaboration and testing of a general thermodynamic model at present. However, a practical approach for computing the thermodynamic properties of mixed inorganic/organic aerosols was recently proposed by Clegg et al., (2001), using the existing thermodynamic models for inorganic and organic solutions and taking into account the interaction between the ions and organic molecules. The present work compares the water uptake of mixed particles of letovicite and maleic acid as predicted by Clegg et al (2001) with that derived from HTDMA (Humidified Tandem Differential Mobility Analyser) measurements. The study is limited to the letovicite and maleic acid systems because it is the most representative for continental (urban/rural) aerosol. The applicability of the Zdanovski-Stokes-Robinson method to the letovicite/maleic acid system is also investigated using parameterizations for water activity of binary solutions derived from HTDMA measurements.

2. THEORY

The equilibrium growth of a soluble aerosol particles in HTDMA instrument can be described by the Köhler equation (1936) which was deduced on a thermodynamic basis.

Corresponding author's address: Mihaela Mircea, Istituto di Scienze dell'Atmosfera e del Clima, Consiglio Nazionale delle Ricerche, Via Gobetti 101, 40129, Bologna, Italy. E-Mail: m.mircea@isac.cnr.it.

The equation relates particle size, chemical composition and ambient humidity, considering the influence of both curvature and dissolved material on the equilibrium water vapour pressure. It has the following form:

$$\frac{e_D}{e_{sat,w}} = a_w \exp\left(\frac{4M_w\sigma_D}{RT\rho_w D}\right) \quad (1)$$

where e_D is the partial water vapour pressure over the droplet of diameter D, e_w is the saturation water vapour pressure over a flat water surface, a_w is water activity of the aqueous solution drop, M_w is the molecular mass of water, σ_D is the surface tension of the aqueous solution drop, R is gas constant, T is the ambient temperature and ρ_w is water density. The $e_D/e_{sat,w}$ represents the relative humidity (RH) inside the HTDMA. The eq. (1) was derived assuming that the drop is spherical and states that the saturation vapour pressure over the drop surface can be enhanced by the curvature effect (Kelvin's law) and depressed by the solute effect (Raoult's law).

Thus, knowing the value of RH inside the HTDMA instrument, one can theoretically compute the diameter of the particle, D, if one knows how to compute the surface tension, σ_D, and water activity, a_w.

To describe the surface tension changes of aqueous solution of letovicite, use was made of the empirical relation suggested by Hänel (1970) for electrolyte aqueous solutions:

$$\sigma_S = \sigma_0 + \beta m \quad (8)$$

where σ_0 represents the surface tension of pure water at the temperature of measurements and β is determined by fitting the measured data.

The variation of surface tension as a function of concentration of soluble carbon in moles l^{-1}, c, for maleic acid/water and letovicite/maleic acid/water systems is well described by the Szyszkowski-Langmuir equation (Langmuir, 1917) for organic aqueous solutions:

$$\sigma_s = \sigma_0 - \alpha T \ln(1+\beta c) \quad (9)$$

where T is the temperature (K). The two constants, α and β, are determined for each sample by fitting the measurements of surface tension and the corresponding concentration at fixed temperature with

the Szyszkowski-Langmuir equation. Symbol σ_0 represents the surface tension of pure water at the temperature of measurements, which was 72 mN/m for all measurements.

Depending on the way of calculating a_w, different forms of the eq. (1) can be found in literature. Often, the water activity of the droplet aqueous solution is computed as a function of the product between the practical or molal osmotic coefficient of the solution, Φ_s, and total number of ions of a salt molecule, ν, because it is a more exact form than the van't Hoff factor, i (Brechtel and Kreidenweis, 2000). In this case, the water activity of aqueous solutions for ionic compounds may be written (Robinson and Stokes, 1959):

$$a_w = \exp\left(-\frac{M_w \phi_s \nu m}{1000}\right) \quad (2)$$

where m is the solution molality.

By definition, the molality is the ratio between the number of moles of salt, n, and the kg of water:

$$m = \frac{m_s/M_s}{(\rho_s \pi D^3/6) - m_s} \quad (3)$$

For diluted solutions ($m_s << \rho_s \pi D^3/6$), and the molality becomes:

$$m = \frac{6m_s/M_s}{\rho_s \pi D^3} \quad (4)$$

A common assumption for diluted solutions in cloud and aerosol studies is Φ_s=1 (Pruppacher and Klett, 1997). Brechtel and Kreidenweis (2000) have shown that this assumption is not valid under most HTDMA measurement conditions and, even at critical diameter (the diameter corresponding to maximum saturation mixing ratio as given by Köhler type equations), the assumption give errors of 20% in predicting the maximum saturation mixing ratio. Therefore, an accurate description of water activity variations with solution composition needs a good parameterisation of Φ_s.

Clegg et al. (2001) proposed a first model for calculating Φ_s for solutions containing both inorganic and organic compounds:

$$\phi_s = 1 + (\phi' - 1)\left(\sum_i m_i\right)\Big/\left(\sum_j m_j\right) + (\phi'' - 1)\left(\sum_n m_n\right)\Big/\left(\sum_j m_j\right) + (\phi''' - 1) \quad (5)$$

where ϕ' is the osmotic coefficient contribution from ionic components, ϕ'' the contribution from organic solutes and ϕ''' is the contribution from ion-organic interactions. The m_i are the molalities of solute ions, m_n are the molalities of organic solutes and m_j are the molalities of all the solute species. The water activity in this case is defined as:

$$a_w = \exp\left(-\frac{M_w \phi_s \sum_j m_j}{1000}\right) \quad (6)$$

More details on the computations of ϕ', ϕ'' and ϕ''' can be found in (Clegg et al., 2001).

Another important parameter in the Köhler equation (1) is the surface tension, whose contribution has been neglected for aqueous inorganic solutions due to its small variation with the salt concentration. Recently, Facchini et al. (1999), Charlson et al. (2001), Nenes et al. (2002) have shown that the presence of organic compounds in solution significantly affects the surface tension of the droplets and, consequently, the Kelvin effect. Given the high concentrations/molalities experienced by particles in the HTDMA, the changes in surface tension will definitely be higher than at critical saturation and, therefore, we will take them into account in the next calculations.

The Zdanovski-Stokes-Robinson method (Stokes and Robinson, 1966) gives the solution molality for a specified water activity. Therefore, it can in principle be applied to any aqueous mixture. Knowing the values of the molalities of various single compound solutions at a specified water activity, it can be computed the overall concentration of the mixture.

The ZSR equation is:

$$\sum_j \frac{m_j}{m_{0j}(a_w)} = 1 \quad (7)$$

where m_j is the molality of j-solute in the multicomponent solution and $m_{0j}(a_w)$ is the molality of an aqueous solution of compound j with the same water activity as the multicomponent solution.

3. RESULTS AND CONCLUSIONS

The surface tensions of letovicite/water, maleic acid/water and letovicite/maleic acid/water systems were measured using a SINTECH (Berlin, Germany) PAT1 tensiometer for different molalities, and the data were fitted with eqs. 8 and 9.

Fig. 1 shows the molality of the letovicite/maleic acid aqueous mixture as a function of water activity, computed using the ZSR method (dashed line) and HTDMA measurements (circles). The binary parameterizations of molality as a function of water activity for letovicite and maleic acid were derived using the HTDMA data.

Fig. 1 also shows that the water activity computed with the osmotic coefficients of Clegg et al. (2001) are very close to the experimental results for the letovicite and maleic acid mixture.

These results prove that both theoretical approaches are able to describe the hygroscopic behaviour of multi-component aqueous aerosols, if adequate parameterisations for binary water activity or osmotic coefficient are available.

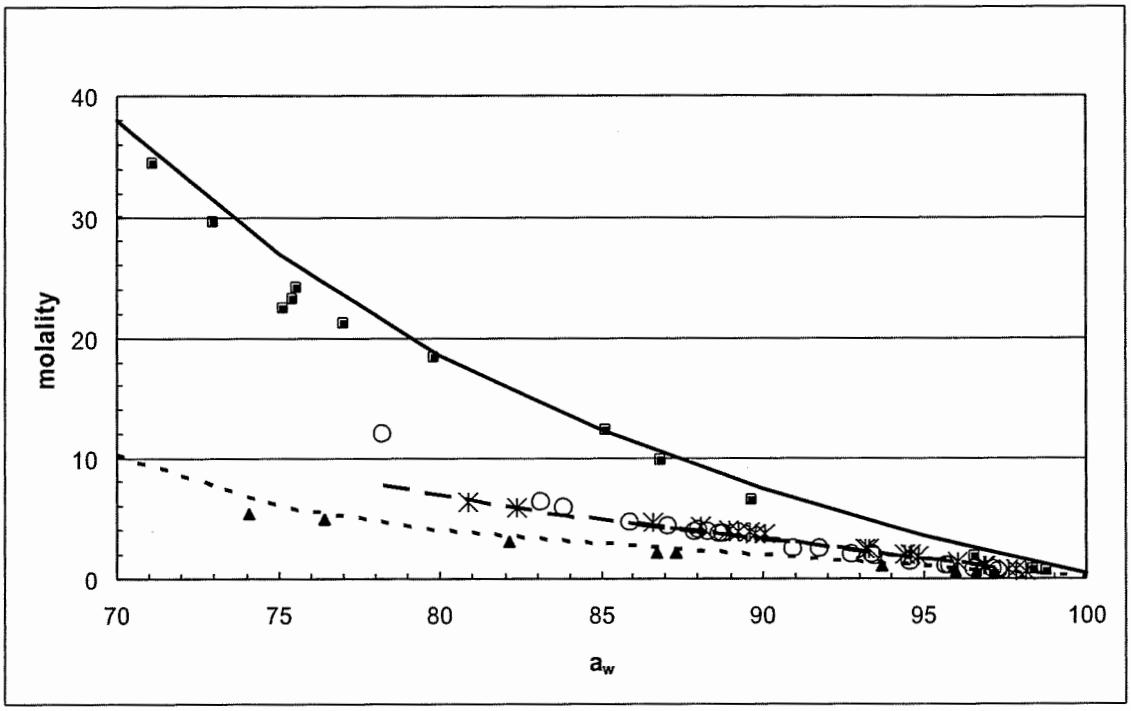

Fig. 1. Molality for total solute as a function of water activity. Squares and triangles represent HTDMA measured data for maleic acid and, respectively, letovicite. The solid line and dotted line are the parameterisations of molality as a function of a_w for maleic acid and, respectively, letovicite. Circles represent HTDMA measured data for letovicite and maleic acid, and dashed line is the molality of letovicite/maleic acid mixture computed using the ZSR method. Stars represent a_w computed with eq.(6), using a ϕ_s computed with eq. (5) (Clegg et al., 2001).

REFERENCES

Brechtel, F. J. and Kreidenweis, S.M., 2000: Predicting particle critical supersaturation from hygroscopic growth measurements in the humidified tdma. Part I: theory and sensitivity studies., J. Atmos. Science, 57: 1854-1871.

Charlson, R.J, Seinfeld, J. H., Nenes, A., Kulmala, M., Laaksonen, A. and Facchini, M.C., 2001: Reshaping the theory of cloud formation. Science, 292, 2025-2026.

Clegg, S.L., Seinfeld, J.H., and Brimblecombe, P., 2001: Thermodynamic modeling of aqueous aerosols containing electrolytes and dissolved organic compound. Journal of Aerosol Science, *32*, 713-738.

Clegg S.L., P. Brimblecombe and A.S. Wexler, 1998: A thermodynamic model of the system H-NH_4-SO_4-NO_3-H_2O at tropospheric temperatures, Journal of .Phys. Chem. A, 102, 2137-2154.

Facchini, M.C., Mircea, M., Fuzzi, S. and Charlson, R.J., 1999: Cloud albedo enhancement by surface-active organic solutes in growing droplets. Nature, 401, 257-259.

Hänel, G., 1970: Beitr.z.Phys.d.Atmos.,43, 119.

Köhler, H. 1936: The nucleus in the growth of hygroscopic droplets. Trans. Faraday Soc. 32, 1152-1161.

Langmuir, I., 1917: The constitution and fundamental properties of solid and liquids. II. Liquids. J. Amer. Chem. Soc. 39, 1848-1906.

Nenes, A., Charlson, R.J., Facchini, M.C., Kulmala, M., Laaksonen, A. and Seinfeld, J. H., 2002: Can chemical effects rival the first indirect effect? *Geophys.Res.Lett.* 29, doi:10.1029/2002GL015295.

Pruppacher, H.R. and Klett, J.D., 1997: Microphysics of clouds and precipitation, Kluwer Academic Publishers, Dordrecht, 955pp.Robinson, R.A. and R.H. Stokes, 1959: Electrolyte Solutions, 2d ed. Butterworth, 571pp.

Stokes, R.H. and R.A. Robinson, 1966: Interactions in aqueous nonelectrolyte solutions: I. Solute –solvent equilibria. Journal of Physical Chemistry, 70, 2126-2130.

FORMATION, GROWTH AND HABIT OF ICE CRYSTALS NUCLEATED ON MINERAL DUST AEROSOL

O. Möhler[1], R. Wagner[1], C. Linke[1], M. Schnaiter[1], H. Saathoff[1], A. Mangold[2], M. Krämer[2], V. Ebert[3], L. Schütz[4], P.R. Field[5], P.J. Connolly[6], and A.J. Heymsfield[7]

[1]IMK-AAF, Forschungszentrum Karlsruhe, Germany; [2]ICG-1, Forschungszentrum Jülich, Germany; [3]Physikalisch-Chemisches Institut, Universität Heidelberg, Germany; [4]Institut für Physik der Atmosphäre, Universität Mainz, Germany; [5]Met Office, Exeter, UK; [6]UMIST, Manchester, UK; [7]NCAR, Boulder, USA.

1. INTRODUCTION

Number concentration, size, and habit of ice crystals in clouds result from a complex interplay of ice initiation and ice multiplication processes, the dynamic partitioning of water between the interstitial vapor phase and the ice surface, as well as the crystal growth kinetics and thermodynamics. Aerosol particles play an important role as cloud condensation and ice nuclei. A quantitative understanding of the relation between aerosol properties and ice formation at typical cloud conditions is prerequisite for an improved description of the ice phase in numerical cloud, weather, and climate models.

In a recent campaign, we have concentrated on re-dispersed desert dust samples, motivated by the fact that several field studies (e.g. during Crystal-Face) have shown desert dust particles to act as efficient ice nuclei in the middle troposphere (DeMott et al. 2003). Expansion experiments were performed at different cooling rates and temperatures between 0°C and -70°C. The mineral dust particles with diameters between about 0.2 and 2 µm turned out to act as quite efficient deposition nuclei at relatively low ice supersaturations. In some experiments, two distinct modes of ice crystal nucleation occurred at different ice super saturations in the same aerosol sample. Experimental methods and ice nucleation results will be summarized in this contribution.

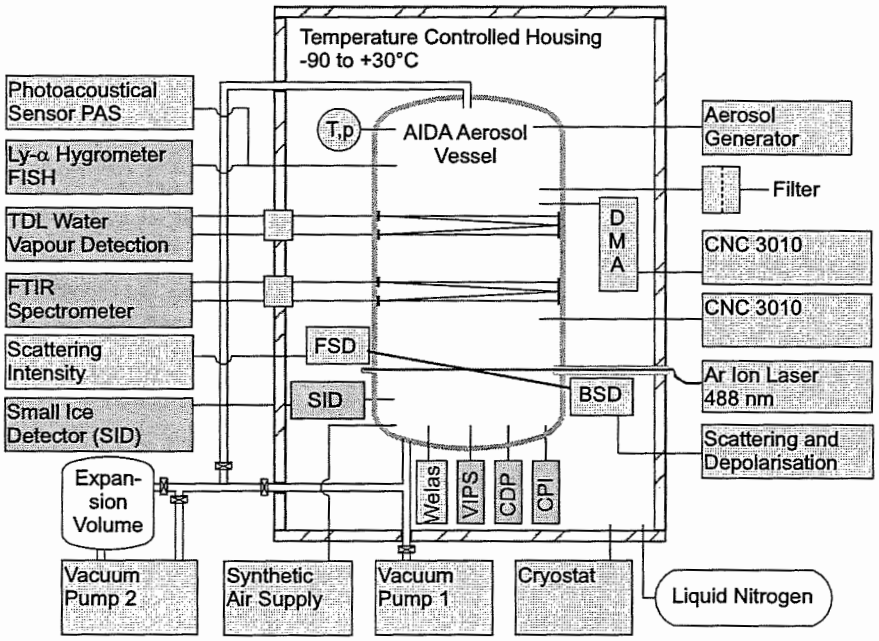

Figure 1: Schematic of the AIDA cloud chamber facility with instrumentation use for ice nucleation studies.

Corresponding author's address:
Ottmar Möhler, IMK-AAF, Forschungszentrum Karlsruhe, Postfach 3640, 76021 Karlsruhe, Germany;
Ottmar.Moehler@imk.fzk.de

2. METHODS

Using the large, moderate expansion aerosol and cloud chamber AIDA (Aerosol Interaction and Dynamics in the Atmosphere) of Forschungszentrum Karlsruhe (Fig. 1), we have investigated the formation, growth, habit, and optical properties of ice crystals nucleated on various aerosol samples. Experiments are started at atmospheric pressure, homogeneous temperature control, and almost ice saturated conditions maintained by ice coated chamber walls. Ice supersaturation is achieved by controlled pumping from about 1000 hPa to 800 hPa within a few minutes simulating cloud updraft conditions of about 1 to 5 m s^{-1} and corresponding cooling rates of about 0.5 to 4 K min^{-1}. Because the ice-coated chamber walls remain at almost the same temperature during expansion cooling, the time profiles of gas temperature and relative humidity are affected by heat and water vapor fluxes from the walls into the chamber volume which is well mixed with a fan. Even during strong pumping, the gas temperatures remain uniform within ±0.3 K. Heat and water vapor fluxes are also considered in cloud model studies using the AIDA results to investigate and improve the representation of ice formation and growth processes in numerical models (Field et al., 2004, this issue).

Water vapor partial pressure is measured by in situ tuneable diode laser absorption and total water concentration is measured with the FISH (fast in situ stratospheric hygrometer) instrument and a chilled mirror frost point hygrometer (Mangold et al., 2004). The formation of non-spherical ice particles is sensitively detected by measuring the intensity and depolarization of forward- and back-scattered laser radiation. The depolarization measurements are also used to relate the depolarization of the scattered laser light to the size and habit of ice crystals (Schnaiter et al., 2004, this issue). Ice particles are characterized with several optical spectrometer and imaging probes including (1) a novel optical particle counter Welas, (2) the optical cloud droplet probe (CDP) from UMIST, that operates like the FSSP probe, but is smaller in size, (3) the small ice detector (SID) instrument from the UK Met Office, the cloud particle imager (CPI) from UMIST, and the video imaging particle sizer (VIPS) from NCAR. Ice particle properties are also retrieved from in situ FTIR extinction spectra. First results of CPI habit analysis and growth model calculations are discussed by Connolly et al. (2004) in this issue.

Figure 2: Electron micrographs of dust particles used for the AIDA ice nucleation studies: Arizona test dust (ATD), Sahara desert dust (SD2), and Asian dust (AD1).

Figure 2 shows electron micrographs of the mineral dust samples used for the AIDA ice nucleation experiments. The samples include so-called Arizona test dust (ATD) and two surface dust samples taken from the Sahara desert close to Cairo, Egypt (SD2), and from the eastern Takla Makan desert in China (AD1). The latter sample was provided by the University of Mainz, Germany.

Size distributions of the mineral dust aerosols generated by dispersion of the dry samples and added to the AIDA chamber range from about 0.2 to 2 µm in particle diameter with mode diameters between 0.5 and 1.0 µm. First results of IR analysis of bulk sample size fractions with particle diameters less than 30 µm in cooperation with the University of Jena, Germany, show relatively large amount of quartz for ATD and of calcite for SD2. Further IR, EDX, and crystallographic measurements are underway to get more detailed information about the mineralogical composition of the dust samples, especially for the particles with diameters below 2 µm.

3. NUCLEATION ONSET RELATIVE HUMIDITY

At temperatures between 195 K and 242 K, all mineral dust aerosols show first ice formation to occur, probably by deposition nucleation, already at very low ice saturation ratios between nearly 1.0 and 1.2 (Fig. 3). The ice detection is sensitive to ice particle number concentrations of less than 1 cm^{-3} with diameters larger than about 0.2 µm. Because the aerosol number concentration was typically around 100 cm^{-3} or larger, the data points given in Figure 3 show the critical saturation ratios at which less than 1 % of the aerosol particles acted as ice nuclei. although the critical saturation is applicable to only a small fraction of the ice nuclei, the majority of the ice nuclei usually activate within further increase of the ice supersaturation by 10 to 30 %.

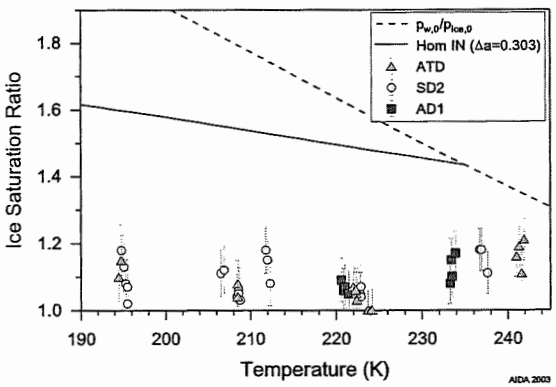

Figure 3: Threshold ice saturation ratios for deposition nucleation on three different mineral dust aerosols in the temperature range 195 to 242 K. Water saturation and homogeneous freezing thresholds are indicated by the dashed and solid lines.

Cal result of diff types of cloud habits on mineral dust particles

4. ICE PARTICLE NUMBER CONCENTRATIONS

In contrast to the nucleation onset, the formation rate of ice crystals seems to depend on the ambient temperature. Figure 4 shows the data sets of two expansion experiments with SD2 aerosol conducted at almost identical pumping speeds (i.e. cooling rates), but started at different temperatures of 223.5 K (IN04_41) and 214.0 K (IN04_45). The aerosol concentrations n_{ae} were 50 cm^{-3} and 40 cm^{-3}, respectively. The ice saturation ratio is almost identical in both experiments up to a peak value of about 1.45. Both the scattering intensity (panel 4) and the ice particle number concentration n_{ice} measured with the Welas probe (panel 5) show more ice crystals to occur at lower relative humidity for the experiment at the lower temperature (dashed lines). Also n_{ice} is somewhat larger for IN04_45 even though n_{ae} was less by about 20 %. The scattering intensity also increases with the total ice volume, therefore its maximum value is larger during IN04_41 because more water vapor is available for ice crystal growth during the experiment at the higher gas temperature.

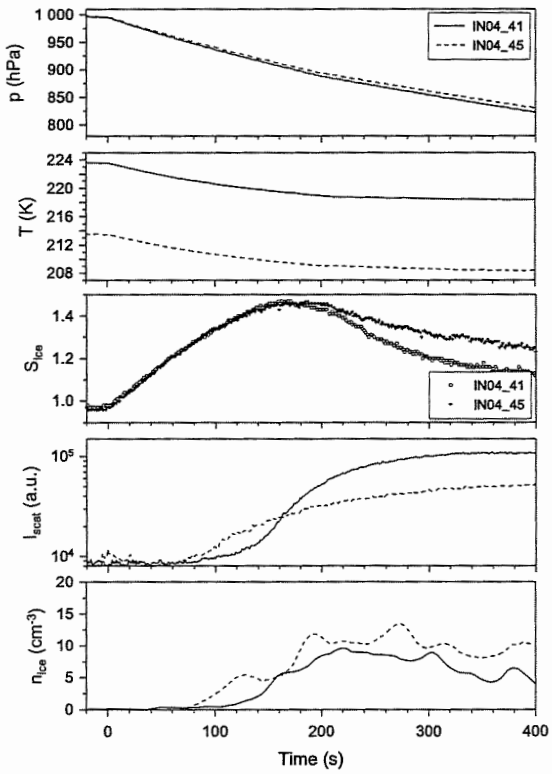

Figure 4: Time profiles of pressure, gas temperature, ice saturation ratio, scattering intensity at 176° scattering angle, and ice crystal number concentration measured with the Welas instrument during two ice nucleation experiments with mineral dust SD2 started at 223.5 K (IN04_41, solid lines, circles) and 214.0 K (IN04_45, dashed lines, triangles).

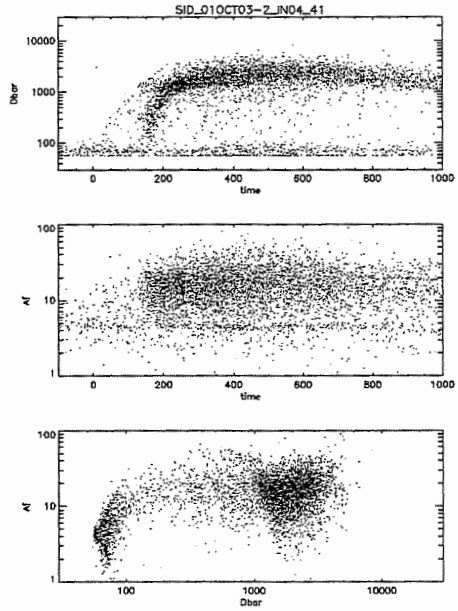

Figure 5: SID measurements during experiment IN04_41 started at 223.5 K.

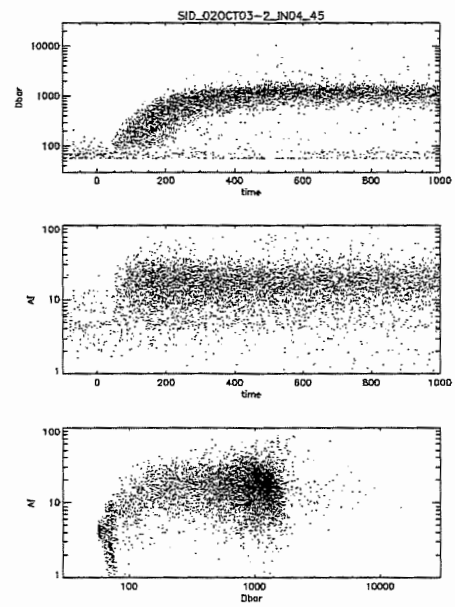

Figure 6: SID measurements during experiment IN04_45 started at 214.0 K.

Measurements with the SID probe also show the difference of the ice particle formation with time during experiments IN04_41 (Fig. 5) and IN04_45 (Fig. 6). The first panel shows the size parameter Dbar for individual particles, the second panel the a-sphericity parameter Af and panel 3 a scatter plot of both parameters. During IN04_41 (higher temperature), two branches of growing ice particles occur at different times, i.e. ice saturation ratios (cf. Fig. 4). This pattern is explained by model studies (Field et al., 2004, this issue) assuming two modes of ice nucleation being active at different ice saturation ratios. Most ice particles are activated at higher supersaturations. In contrast, the upper panel of Fig. 6 shows a more uniform pattern of ice crystal formation and growth during the period from 50 s (nucleation onset) to 150 s, when the peak relative humidity is reached.

5. ICE WATER CONTENT

Sequences of in situ FTIR spectra recorded in time intervals of 20 s are analyzed to get the temporal evolution of the number concentration and mean size of the ice crystals as well as the total IWC. Following the notation given by Arnott et al. (1997), the optical depth at a specific wave number is calculated as the sum of contributions from specific crystal size bins weighted by the number concentration of ice crystals in each size bin. The size bin–averaged extinction cross section is calculated at M = 107 wave numbers between 6000 and 800 cm^{-1} for N = 201 individual diameter size bins ranging from 0.1 to 30.1 μm (Mangold et al., 2004). The T-Matrix code (Mishchenko and Travis, 1998) was used for the calculations assuming randomly oriented cylindrical ice particles with an aspect ratio of 0.7. Fig. 7 shows the IWC retrieved from FTIR spectra to agree well with the IWC calculated from the difference of direct total (gas + ice) and gas-phase water measurements. The ice crystals were nucleated on SD2 particles at a temperature of 224 K.

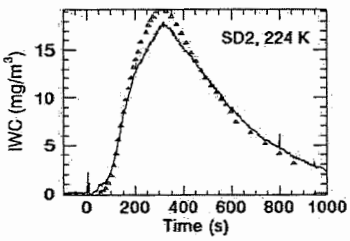

Figure 7: Comparison of ice water content (IWC) retrieved from FTIR extinction spectra (triangles) to the data from total water minus TDL gas-phase water measurements (solid line).

6. CONCLUSIONS

The nucleation and growth of ice crystals on two desert dust aerosol samples was investigated in the temperature range from 195 K to 242 K. Deposition nucleation occurred at low ice saturation ratios between 1.0 and 1.2, almost independent of temperature. First results indicate the formation rate of ice crystals at low ice supersaturations to increase with decreasing temperatures. The ice water content (IWC) from total minus gas-phase water measurements agrees well with data retrieved from FTIR extinction studies. Further data analysis will e.g. address comparison of size distribution and IWC from different optical (Welas, SID, CDP) and imaging (CPI, VIPS) probes. Further numerical model studies are also planned to test and improve concepts of formulating rate equations for heterogeneous ice nucleation.

7. REFERENCES

Arnott, W. P., C. Schmitt, Y. Liu, J. Hallett, 1997: Droplet size spectra and water-vapor concentration of laboratory water clouds: inversion of Fourier transform infrared (500-5000 cm-1) optical-depth measurement. Appl. Opt., 36, 5205-5216.

Connolly, P. J., P. R. Field, O. Möhler, A. J. Heymsfield, M. W. Gallagher, and T. W. Choularton, 2004: Simulations of ice crystal nucleation and growth: results from the AIDA cloud expansion chamber. *ICCP*, Bologna, Italy (this issue).

DeMott, P. J., K. Sassen, M. R. Poellot, D. Baumgardner, D. C. Rogers, S. D. Brooks, A. J. Prenni, and S. M. Kreidenweis, 2003: African dust aerosols as atmospheric ice nuclei. *Geophys. Res. Lett.*, **30**.

Field, P. R., R. J. Cotton, O. Möhler, M. Schnaiter, M. Krämer, P. Connolly, and A. J. Heymsfield, 2004: Investigation of the ice nucleation ability of two desert dust aerosol samples at -50°C. *ICCP*, Bologna, Italy.

Mangold, A., R. Wagner, H. Saathoff, U. Schurath, C. Giesemann, V. Ebert, M. Krämer, and O. Möhler, 2004: Microphysics of cirrus clouds formed by different types of aerosols: experimental investigation in the aerosol chamber AIDA. *Meteorol. Z. (submitted)*

Mishchenko, M.I., L.D. Travis, 1998: Capabilities and limitations of a current Fortran implementation of the T-Matrix method for randomly oriented, rotationally symmetric scatterers. J. Quant. Spectroscop. Radiat. Transfer, **60**, 309-324.

Möhler, O., et al., 2003: Experimental investigation of homogeneous freezing of sulphuric acid particles in the aerosol chamber AIDA. *Atmos. Chem. Phys.*, **3**, 211-223.

Schnaiter, M., S. Büttner, R. Wagner, C. Linke, O. Möhler, P. R. Field, and P. Connolly, 2004: Optical characterisation of ice crystals growing at simulated cirrus conditions. *ICCP*, Bologna, Italy.

MODELLING STUDIES OF CIRRUS CLOUDS OBSERVED DURING THE INCA CAMPAIGN, IMPLICATION FOR THE NUCLEATION MECHANISM.

M. Monier , W. Wobrock and A. I. Flossmann

Laboratoire de Météorologie Physique, OPGC, CNRS, Clermont Ferrand, France

1. INTRODUCTION

Due to the densification of the air traffic, a large amount of water vapour and aerosol particles are injected at the altitudes of cirrus clouds. Aircraft emissions may have caused observed long-term increases in cirrus occurrence frequency and amounts (Boucher, 1999) with a possible large impact on radiative forcing (IPCC, 1999). To quantify impact of aircraft rejection on cirrus cloud properties, we need to understand the formation mechanisms of cirrus clouds and how the size distributions and the composition of aerosols influence the formation of ice crystals. The flight campaign INCA (INterhemispheric differences in Cirrus properties due to Anthropogenic emissions) , an European project, took place in 2000 to provide comparable observations of "polluted" versus "natural" cirrus clouds.

The objective of the present work was to develop a detailed microphysics cirrus model based on the new observations of the INCA campaign, capable to simulate very high ice crystal concentrations in agreement with cirrus cloud observations. In addition, the model should be able to follow the chemical composition of wet aerosols and take into account the impaction of these aerosols by the ice crystals, in order to understand if the chemistry and the concentration of these wet aerosols are important for the formation mechanism of cirrus clouds.

2. MICROPHYSICS MODELLING DESCRIPTION

Our microphysical module is based on the warm microphysics model ExMix (*E*xternally *Mix*ed) developed by Wobrock et al. (2000). The number distribution of droplets $f_{wat}(m,m_{AP,N},x_i)$ is treated as a function of the total particle mass m, the dry aerosol mass $m_{AP,N}$, and the chemical composition x_i of the aerosol particle. In this study only one type of aerosol particles is treated and no external mixture. If $m \gg m_{AP,N}$ drops are present while for solution droplets m and $m_{AP,N}$ differ only by a factor of 3 or less. For $m = m_{AP,N}$, f_{wat} represents the dry aerosol particle distribution. The number distribution of ice crystals $f_{ice}(m,m_{AP,N},x_i)$ is given by the same variables. However, m represents the mass of the "solid" water. As above, only one species x_i of aerosol particles is treated for this study. Both number distributions f_{wat} and f_{ice} are calculated by the two following equations:

Corresponding author's address: A. I. Flossmann, LaMP, 24, avenue des Landais, F - 63177 Aubière; CEDEX; email:A.Flossmann@opgc.univ-bpclermont.fr

$$\frac{\partial f_{wat}(m,m_{AP,N},x_i)}{\partial t} = -\frac{\partial}{\partial m}\left[f_{wat}(m,m_{AP,N},x_i)\frac{dm}{dt}\bigg|_{wat}\right] - f_{wat}(m,m_{AP,N},x_i)\, J_{het/hom}$$

$$\frac{\partial f_{ice}(m,m_{AP,N},x_i)}{\partial t} = -\frac{\partial}{\partial m}\left[f_{ice}(m,m_{AP,N},x_i)\frac{dm}{dt}\bigg|_{ice}\right] + f_{wat}(m,m_{AP,N},x_i)\, J_{het/hom}$$

The first term on the right hand side describes the time evolution by vapour diffusion growth. The growth velocities $(dm/dt)_{wat}$ and $(dm/dt)_{ice}$ are used as given in Pruppacher and Klett (1997). The loss of wet aerosol particles due to their *nucleation* to form ice crystals is considered in the second term on the right hand side and appears as source terms for the ice crystals.

An important unresolved question is whether homogeneous or heterogeneous nucleation dominates the ice crystal formation. In an attempt to address this problem we have introduced these two mechanisms into the model.

For homogeneous nucleation the theoretical nucleation rate has the form of:

$$J_{hom} = 2N_c V_{sol}\left(\frac{\rho_{sol}kT}{\rho_{ice}h}\right)\left(\frac{\sigma_{ice/sol}}{kT}\right)^{1/2} exp\left[-\frac{\Delta F_{act}}{RT} - \frac{\Delta F_g}{kT}\right]$$

In this rate, the solution properties appear through density, surface tension, water activity and viscosity. Due to the variable chemical composition of the aerosol these parameters are mostly unknown and need to be parameterized. In order to study the sensitivity of the results with respect to the chosen parameterization, we have compared, for the case of sulfuric acid aerosol particles, different proposed parameterizations given in literature. These are taken from Tabazadeh et al. (2000), DeMott et al. (1997) and Koop et al. (2000), hereafter TAB, DEM and KOO. As to our knowledge no theoretical expression for the heterogeneous nucleation is available in literature, we use empirical approaches of Meyers et al. (1992) and DeMott et al. (1997) and DeMott et al. (1998) which are based on field or laboratory experiments, later on MEY, DEM97 and DEM98.

3. ICE CRYSTAL NUMBER CONCENTRATIONS.

Three parameterisations for homogeneous and heterogeneous nucleation respectively have been tested in the dynamical frame of an air parcel. The model results are compared with those of Lin et al. (2002). Following their recent comparative study on detailed cirrus models, we investigated the following

INCA ice crystal observations and relationship to other spaces

two scenarios: a cold air case, where the air parcel starts at 170 hPa, T = –60°C and RH_i = 100 %, and a warm case starting at 340 hPa, T = -40°C and RH_i = 100 %. The aerosol particle distribution was supposed to consist of a single mode log normal distribution with a total number of 200 particles cm^{-3}, a mean radius of 20 nm, and a standard deviation of 2.3. The formed ice crystals are assumed to be spherical.

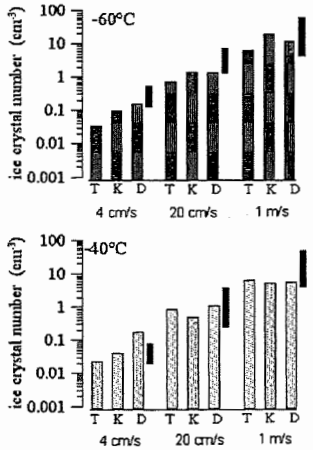

Fig. 1: Total number of ice crystals formed by homogeneous nucleation using different vertical updraft velocities and different nucleation rates from TAB (T), KOO(K), or DEM (D).

Fig. 1 presents the results for the modelled ice number concentration considering homogeneous nucleation only, for a vertical ascent of 800 m (in cold case in the upper figure and warm case in lower the figure). Each case was run for vertical wind speed of 4, 20, and 100 cm/s. For each case and each updraft speed the three different parameterisations for solution effects described in the previous section were compared. The elevated black bar for each case and each updraft velocity gives the range of the results found in Lin et al. (2002) for the same parcel studies. These authors compared 7 different detailed numerical cirrus models using one of the three parameterisations for homogeneous nucleation but each used their own parcel dynamics.

Fig. 1 shows that the number of ice crystals formed increases significantly with the intensity of the vertical wind. However, the influence of the air temperature on ice crystal production is less pronounced. From Fig 1, we can further argue that for mean and high updraft velocities the three parameterisations typically differ by a factor of 2, which is significantly lower than in the study of Lin et al. (2002). For low velocities however the discrepancy between the results can increase to a factor of 5 and more, which is in the same range as observed in Lin et al. (2002). These differences result from the size dependency of the nucleation rates, which vary significantly between the schemes TAB, KOO and DEM. To explain the lowering of ice crystal number variability for our study, we can argue that we used one numerical cloud model wherein only the rate of ice nucleation varied, while Lin et al. (2002) compared the results of seven different numerical cloud models in which each of them treated one (of the three) nucleation rate individually. However from our study, we can state that the choice of one parameterisation just matters for low updraft velocities and has less consequences for moderate to high vertical ascent.

To understand the impact of heterogeneous nucleation, we focused on the scenario of the warm case with a vertical velocity of 20 cm/s. Figure 2 shows the evolution of ice supersaturation, ice water content and ice crystal concentrations as a function of time (=altitude of the ascending air parcel). The comparison is done for homogeneous (Fig.2a) and heterogeneous nucleation individually and with homogeneous nucleation (Fig.2b).

We can see, in figure 2a, that for homogeneous nucleation the choice of the nucleation parameterisation does not change cloud base, which is, following Lin et al. (2002), the altitude at which the ice crystal number reach $1.l^{-1}$. The three schemes need at least 40% of supersaturation before forming ice, the maximum supersaturation varies only within 2%. Despite this small variability, the final variance in the number of crystals is quite important, with only 573 ice crystal per liter for KOO, 1020 for TAB, and 1280 for DEM. The time interval during which nucleation is active is short, the process becomes inactive within a few tens of meters.

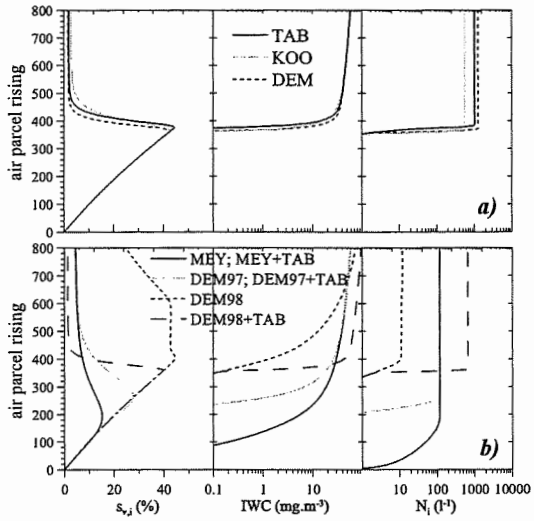

*Fig. 2: ice supersaturation (in %), total ice water content (in $mg.m^{-3}$) and ice crystal concentration (l^{-1}) as a function of altitude of ascending air parcel. Comparison of the different nucleation scheme for **a)** homogeneous nucleation only (TAB, KOO, DEM) **b)** heterogeneous nucleation alone and together with TAB (MEY, DEM'97, DEM'98).*

In Fig. 2b heterogeneous nucleation is considered. DEM98 parameterisation shows a different behaviour since it is inefficient to form ice crystals (only 12 per liter). For the two other parameterisations, nucleation is more active but final ice crystal concentrations

remain low compared to homogeneous nucleation case (117 per liter for MEY and 118 for DEM97). In both cases cloud base is lower than in Fig 2a. Cirrus cloud base is near the initial altitude for MEY and 200 m above for DEM97.

If we consider heterogeneous and homogeneous nucleations together, ice crystals formed primarily through heterogeneous process will, by vapour diffusion, prevent an increase of ice supersaturation to values needed homogeneous nucleation. That's why the curves for MEY and DEM97 stay the same, in Fig.2b, whether or not the TAB approach is simultaneously considered. But, for the DEM98 parameterisation, which was shown really inefficient to form ice crystals, the threshold for homogeneous nucleation in ice supersaturation could be reached. However, even though the number of ice crystals formed by heterogeneous nucleation is very small, they are sufficient to lower the maximum ice supersaturation from 44.5% (for TAB only) to 39.8% (for DEM98 and TAB). The final number in ice crystals is hence lower considering both nucleation mechanisms together (659 ice crystals l^{-1}) than considering homogeneous nucleation alone (1020 ice crystals l^{-1}).

During the INCA campaign the typical range of ice crystals concentrations observed ranged between 1.000 to 10.000 ice crystals per liter. From our theoretical modelling, we can conclude that the most efficient nucleation process to get high concentration of ice crystals is the homogeneous nucleation considered alone. This statement is in agreement with the conclusions of Lin et al. (2002). Indeed, the number of crystals formed by the heterogeneous nucleation parameterizations used is at least one order of magnitude smaller. If we consider the two processes together, the regime of homogeneous nucleation will never be reached since the ice crystals formed at lower supersaturation by heterogeneous nucleation consume the water vapour. In addition, even if heterogeneous nucleation scheme allows the homogeneous nucleation to be reached the ice crystal concentrations are then lower. Consequently, in order to explain the INCA measurements by the used model approaches homogeneous nucleation needs to be active alone. One can further argue, from Fig. 1, that ice crystal concentrations as high as found in the INCA measurements were only modeled for vertical velocities between 20 and 100 cm/s. This is not consistent with the falcon measurements since they typically range from 10 to 15 cm/s. But, Gierens et al. (2003) have shown that considering an accommodation coefficient of non-unity and in varying this coefficient as a function of time of crystal growth, they can get ice crystal number in agreement with the INCA campaign for vertical velocities commonly sampled.

4. CONSEQUENCES FOR RESIDUAL PARTICLES.

Another helpful method for the assessment of the different parameterisations for nucleation mechanisms is the analysis of measurements of the particle residuals stemming from cirrus ice crystal spectra. The modelling concept for ice crystals treats explicitly the nucleus mass $m_{AP,N}$ and therefore allows calculations of the residual particle spectra.

Results for the three different schemes for homogeneous nucleation TAB, KOO, and DEM are displayed for the warm case with w = 20 cm/s in Fig 3a. Large particles nucleate at lower supersaturation than small particles, thus, most large particles serve as ice nuclei while the small ones nucleate only slightly or not at all. KOO parameterisation contrasts from the other two since the incorporation of mostly large particle is less pronounced. For the DEM and TAB approach this effect is so strong that we can even define a sort of cut-size diameter for aerosol freezing, roughly 200 nm with a sharp transition in this study case.

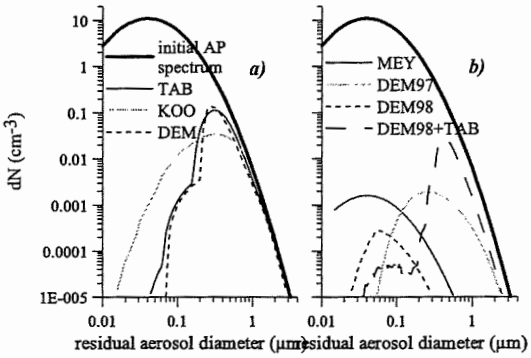

Figure 3: *Modelling results for number distribution of residual particles using a log normal distribution for the ambient aerosol particle spectrum.* ***a)*** *for the homogeneous nucleation rates* ***b)*** *for the heterogeneous nucleation rates only and for DEM98 heterogeneous together with the TAB homogeneous parameterisation.*

Fig 3b provides the equivalent results for the three heterogeneous nucleation parameterisation DEM97, DEM98 and MEY. The preference to nucleate large particles remains only visible for the DEM97 approach as the soot surface and the effective temperature are considered. The MEY parameterisation nucleates all particle size with the same efficiency as the nucleation rate only depends on the ice supersaturation. A size dependency for the heterogeneous nucleation rate for DEM98 also exists by the use of effective temperature, however this cannot be easily detected in Fig 3b due the low nucleation efficiency.

As explained in the previous section, if homogeneous and heterogeneous nucleation are active together in the air parcel, MEY and DEM97 results will not differ from heterogeneous only case. On the contrary, for a combination of DEM98 with one of the homogeneous schemes (TAB in the figure), both rates for nucleation become visible through two maxima in the residual spectra.

Measurements of ambient and residual aerosol particles were performed by Ström et al. (2001) during the INCA campaign. Fig. 4a shows results from 31 March and 29 sept. of both residual and ambient

particle spectra. The measurements suggest that the capacity of an aerosol particle to be an ice nucleus is independent of its size. The result of 31 march indicate that only 0.1% of the present aerosol particles nucleated and form ice crystals, which is very low. The results of 29 sept. show a bigger incorporation of 1%, which is more typical of the whole campaign (Johan Ström, personal communication).

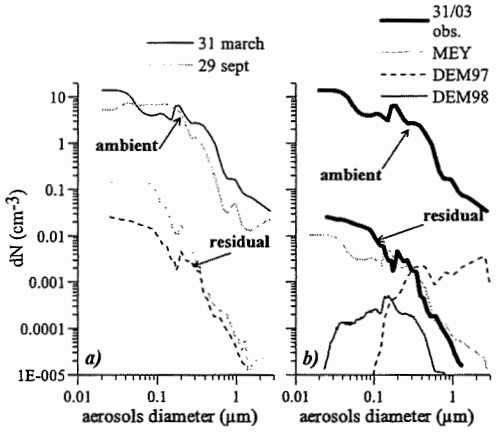

***Fig. 4:** a) Ambient and residual aerosol spectra observed the 31/03 and the 29/09. **b)** Comparison for the 31/03 with modeling results assuming nucleation to be heterogeneous.*

A comparison of the homogeneous nucleation model results for the ice crystal residual particles (Fig. 3a) with those measured during the INCA experiment in cirrus clouds (Fig. 4a) points out a dramatic discrepancy in the shape of the size dependency. Observations in cirrus clouds for the northern and southern hemisphere do not confirm a stronger nucleation efficiency for the larger aerosol particles but show rather a size independent nucleation efficiency. All three nucleation schemes, then, strongly overestimate the nucleation of large aerosol particles while the nucleation of the small ones is completely absent. A possible explanation for the discrepancy with the observation could be that not homogeneous but heterogeneous nucleation dominated during INCA. Similar to the above performed air parcel simulation for w = 20 cm/s and $T = -40$ °C, we studied the same three schemes for heterogeneous nucleation but with the observed aerosol spectrum given in Fig 4a. The modelling results are also displayed in Fig 4b for the 31 march. Similar to the homogeneous nucleation the parameterisations for heterogeneous nucleation DEM97 and DEM98 deviate from the observational results as these two approaches also consider a size dependency. However, it is surprising how well the MEY approach agrees with the observed crystal residual aerosol spectra. In this study, this parameterization is constraint in its maximum capacity of ice crystals production. The results for 29 sept are not displayed since DEM97 and DEM98 still deviate from observational results and MEY is not efficient enough to produce ice crystals.

From our results we can, therefore, only conclude that perhaps the 31 march the ambient aerosol have properties comparable to the one sampled by Meyers et al. (1992). We can also conclude that, in the others flight samplings, only homogeneous nucleation can explain the total ice crystal concentration but is unable to reproduce the behaviour of the residual aerosol to be incorporated in the ice phase.

5. CONCLUSIONS

We have developed a cirrus cloud detailed microphysics model, which describes the evolution of both solution droplet and ice crystal size distributions and follows individually their aerosol content. With this powerful tool, we have been able to study how the interactions between these microphysics processes control ice crystal concentration, size distribution, and aerosol content.

We have shown, on the one hand, that to get ice crystal concentrations as high as observed during the INCA campaign, homogeneous nucleation has to be considered alone. Nevertheless to get these concentrations at observed velocities, the accommodation coefficient should be adapted (Gierens et al., 2003). In other hand, we have shown that assuming nucleation as homogeneous strongly overestimates the ability of large aerosol particles to form ice crystals. It also strongly underestimates the ability of small aerosol particles to form ice crystals. These two limitations for the homogeneous nucleation to reproduce ice crystal concentration and more severely residual aerosol spectra could be explained by the work of Ettner et al. (2004). They observed freezing of sulfuric acid solution droplets with density commonly encountered in the upper troposphere and see the instantaneous ejection of the particular content of solution droplets on the surface during freezing. Ice crystals are then at the first stage surrounded by debris from the droplet content. These debris pieces could cause the lowering of the water accommodation coefficient for small ice crystals. Moreover, the numerous small aerosol particles found in ice crystal could be the remainder of larger particles dissolved and ejected in several parts from droplets during the freezing process.

6. REFERENCES

Boucher, 1999: *Nature*, **397**, 30–31
DeMott et al., 1997: *JGR*, **102**, 19575-19584
DeMott et al., 1998: *GRL*, **25**,1387-1390
Ettner et al., 2004: *ACPD*
Gierens et al., 2003: *JGR*, **108**, 4069-4073
IPCC, 1999: University Press, Cambridge, 373p
Koop et al., 2000: *Nature*, **406**, 611-615
Lin et al., 2002: *JAS*, **59**, 2305-2319
Meyers et al., 1992: *JAM*, **31**, 708-721
Pruppacher and Klett , 1997: Kluwer Academic, 954p
Tabazadeh et al., 2000:*GRL*, **27**, 1111-1114
Wobrock et al., 2001: *Atmos. Res.*, **58**, 231-265

Improved Methodology for the Combined Spectroscopic and Chromatographic Investigation of Water-Soluble Organic Compounds in Atmospheric Aerosols and Fog

F. Moretti[1], E. Tagliavini[1], S. Decesari[2]
[1] Dipartimento di Chimica "G. Ciamician", Alma Mater Studiorum Università di Bologna, 40126, Italy
[2] Istituto di Scienze dell'Atmosfera e del Clima, Consiglio Nazionale delle Ricerche, Bologna, 40129, Italy

1. INTRODUCTION

Aerosol particles play a major role in many processes of atmospheric physics and chemistry. When climatic changes are the topic under investigation, the outstanding role is probably constituted by the ability of aerosols to act as cloud condensation nuclei (CCN), thus determining the number, size and reflectivity of clouds.

The composition of aerosol and fog/cloud water is extremely complex, but water soluble organic compounds (WSOC) represent a very important fraction that determines some crucial features of aerosols. They are still poorly known. We have achieved recently a breakthrough in the knowledge of WSOC by the introduction of H NMR spectroscopy as an analytical tool and Ion Chromatography as an operative separation tool.

Exploiting such methodology we firstly obtained qualitative and quantitative structural information from the overall atmospheric WSOC but, at the same time, we realized that information from non-hydrogenated functional groups (like carboxilyc acids or ketones) is missing and their amount must be inferred indirectly (Fuzzi et al., 2001).

We present here an improved methodology for the complete investigation of water–soluble aerosols and fog/cloud water, based on the parallel ^{1}HNMR spectro-scopic investigation in D_2O and ^{1}HNMR in organic solvent ($CDCl_3$) after suitable chemical derivatization. We have chosen the methylation of carboxylic acids with diazomethane as target transformation for the crucial role of carboxylates in determining the solubility and surfactant capabilities of WSOC.

2. EXPERIMENTAL

Aerosol samples were collected using a high-volume system with a cut-off of 10 μm and equipped with glass-fiber filters (Whatman), in a kerbside site in Bologna (44°, 32' N; 11°, 19' E) from March to November 2003. The aerosol samples underwent multiple extraction with deionized water in an ultrasonic bath. The extracts were combined and filtered to isolate the WSOC. An aliquot of the extract was injected onto a glass-column packed with DEAE Sephadex gel (Pharmacia) and fractionated by step-wise elution with water, NH_4HCO_3 0.08M, and NH_4HCO_3 1M. The recovered fractions were assigned to neutral compounds (NC), mono-/di-carboxylic acids (MDA) and polyacids (PA), respectively. The original extracts and the isolated chromatographic fractions were analysed by means of: a) liquid-TOC analysis to determine the total WSOC concentration; b) ^{1}HNMR in deuterium oxide for WSOC functional group characterisation (Decesari et al., 2000). NMR spectra were obtained at 600 MHz with a Varian Inova 600 spectrometer. The PRESAT sequence was adopted to suppress the signal arising from HDO. Sodium 3-(trimethilsylyl-)-2,2,3,3-d_4-propionate (TSPd_4) was added as internal standard.

A derivatization method for total carboxylic acids of WSOC was set-up implementing the heterogeneous methylation reaction with diazomethane originally developed by Thorn (1989) for freshwater fulvic acids. Briefly, the WSOC solutions were first acidified with 1M HCl and dried under vacuum. The dried samples were suspended in CH_2Cl_2 in an ultrasonic bath, and freshly prepared diazomethane solution in ether was therefore added:

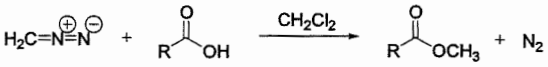

After the completion of the reaction, the samples were dried again, redissolved in $CDCl_3$ and subjected to ^{1}HNMR analysis using $(TMS)_4Si$ (TTMS) as internal standard. The band arising from methylated carboxylic groups is readily detectable between 3.2 and 4.4 ppm of proton chemical shift. The fraction of WSOC which did not react with the diazomethane was subsequently recovered in D_2O and analysed by ^{1}HNMR under the same experimental conditions adopted for the original aerosol water-extract.

A full WSOC characterisation performed according to the above methodology was obtained for sample G13102003, collected on 13 Oct 2003. The results discussed in the following section refer to this specific sample.

3. DISCUSSION

The average WSOC air concentrations during the collection of sample G13102003 is 2.03 ugC/m3, as determined by TOC analysis of the water extract. Such WSOC loading is close to the mean concentrations previously measured in Bologna during the cold

Corresponding author's address: Emilio Tagliavini, Dipartimento di Chimica "G. Ciamician", Alma Mater Studiorum Università di Bologna, via Selmi 2, 40126, Italy; E-Mail: emilio. tagliavini@.unibo.it.

season, during which WSOC account for approximately 50% of aerosol TC in PM10 (Matta et al., 2003). The ^{1}HNMR spectrum of the water extract of G13102003 reported in Figure 1 shows the same main functional groups already identified in the samples from Bologna on the basis of the non-exchangeable hydrogen atom composition (Matta et al., 2003). By assigning a C/H stechiometric ratio specific for each functional group, the derivation of the average chemical structure of WSOC expressed in moles of C per cubic meters is straighforward (Table 1). From the table it can be seen that WSOC in G13102003 are mainly aliphatic in character, with extended saturated C-H moieties. On the other hand, the identified functional groups by ^{1}HNMR add up to only 60% of total water-soluble carbon, being the rest uncharacterised. The unaccounted carbon may be associated to tetra-substituted carbon atoms (R_4C), polynuclear aromatics and to carbonlys which do not possess non-excangeable hydrogen atoms (COO^-, $R_2C=O$).

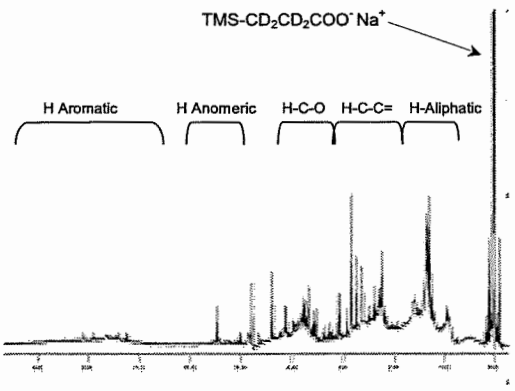

Figure 1. 1HNMR spectrum in D_2O of sample G13102003, with the intervals of chemical shift attributable to the different functional groups evidenced.

The contribution of carboxylic groups to the water-soluble carbon unaccounted by the direct ^{1}HNMR analysis was estimated by the derivatisation procedure described in the previous section. The results are included in the carbon budget of sample G10132003 reported in Table 1. The table shows that carboxylic groups account for 60 nanomoles of C per cubic meters, i.e. 10% of the "missing" carbon. Another fraction of 56 nmolC/m3, correspondent to 25% of WSOC, remains uncharacterised by the available techniques.

To our knowlegde, the concentrations of COOH groups reported in Table 1 are the first measurements of total carboxylic groups performed on atmospheric aerosol samples. The observed contribution of COOH groups to the water-soluble carbon is lower than the previous estimates which were based on the ^{1}HNMR features of underivatised samples (Fuzzi et al., 2001). However, the composition reported in the previous work referred to samples collected in a rural area 40 km distant from Bologna, where the aerosol may possess a more aged/oxidised character than that in a kerbside site.

Functional groups	μmoli H/ m^3	H/C ratio	μmoli C/ m^3
Identified on the underivatised sample:			
C-H	0.053	1,8	0.029
H-C-(C=)	0.049	1,8	0.027
H-C-O	0.022	1,1	0.020
O-CH-O, H-C=C	0.001	1	0.001
H-Ar	0.013	0,4	0.033
Identified on the methylated sample:			
COOH	0.017	3	0.006
Unaccounted C:			
			0.056

Table 1 Functional group composition of sample G13102003. H/C ratios for functional groups identified in the underivatised sample are assumed according to indications of Fuzzi et al. (2001). Notice that the μmol H/m^3 of the methylated sample refer to the moles of hydrogen of methylating agent which have reacted with the carboxylic acids in the sample.

The chromatographic fractions of the water extract of sample G13102003 were characterised according to the same procedure adopted for the unfractioned samples, and the resulting COOH concentrations in neutral compounds, mono-/di-acids and polyacids are reported in Table 2. As expected from the chromatographic behaviour, the MDA and PA fractions recover most of the COOH functionalities. However, the contribution of the carboxylic groups to the carbon budget of each fraction indicates that the COOH groups are not significantly enriched in PA compared to MDA. This finding support the previous ^{1}HNMR data suggesting that the MDA and PA differ mainly in their average molecular weight rather than in their functional group budget (Decesari et al., 2001). Therefore, these results indicate that PA isolated on DEAE columns are not extensively oxidised low-molecular weight compounds (e.g. tricarballic acid), while provide further support to the HULIS (humic-like substances) hypothesis.

Fractions	nmolC /m3	%WSOC	COOH (nmol C/m3)
NC	9	26	0.7
MDA	12	35	3.5
PA	5	15	0.8

Table 2 Air concentrations and total carboxylic contents of each of the three chromatographic fractions of WSOC. NC: neutral compunds; MDA: mono-/di-acids; PA: polyacids.

4. CONCLUSIONS

The present study reports first measurements of total carboxylic acids (as moles of COOH groups) in the water-soluble fraction of organic aerosols. These data improve the functional group characterisation already established on the basis of the ^{1}HNMR analysis of underivatised samples which was essentially limited to the functional groups carrying non-exchangeable hydrogen atoms. Our data suggest that the carboxylic content of urban aerosol is substantially lower than previously expected, whereas a high content of saturated aliphatic moieties can be detected. Therefore, the observed WSOC composition determined for an aerosol sample collected at a kerbside site is characteristic of poorly hygroscopic organic material.

The proposed methodology for a quantitative and specific methylation of COOH groups demonstrates the potential of extending the ^{1}HNMR analysis to the oxygenated functional groups by means of derivatization reactions. Beside methylation of carboxylic groups, other techniques can be developed for the determination of carbonyls and phenols, which are also believed to contribute to the most polar species occurring in organic aerosols in different environments. Improving the accuracy and specificity of the functional group characterisation of WSOC is a necessary step for a correct parameterisation of the effects of organic compounds on the ability of aerosol particles to absorb water and to act as CCN.

5. REFERENCES

Decesari, S., M.C. Facchini, S. Fuzzi, and E. Tagliavini, 2000: Characterization of water-soluble organic compounds in atmospheric aerosol: A new approach. J. Geophys. Res. 105, 1481-1489.

Decesari, S., M.C. Facchini, E. Matta, F. Lettini, M. Mircea, S. Fuzzi, E. Tagliavini, and J-P. Putaud, 2001. Chemical features and seasonal trend of water soluble organic compounds in the Po Valley fine aerosol. Atmos. Environ. 35, 3691-3699.

Fuzzi, S., S. Decesari, M.C. Facchini, E. Matta, M. Mircea, E. Tagliavini, 2001. A simplified model of the water soluble organic component of atmospheric aerosols. Geophys. Res. Lett., 28, 4079-4082.

Matta, E., M.C. Facchini, S. Decesari, M. Mircea, F. Cavalli, S. Fuzzi, J-.P. Putaud, A. Dell'Acqua, 2003. "Mass closure on the chemical species in size-segregated atmospheric aerosol collected in a urban area of the Po Valley, Italy" Atmos. Chem. Phys., 3, 623-637.

Thorn,K.A.,Nuclear-magnetic-resonance spectroscopy investigations of fulvic and humic acids from the Suwannee River. in U.S.G.S. report 87-557, 1989. Humic substances in the Suwannee River, Georgia: Interactions, properties, and proposed structures., Averett, R,C., Leenheer, J.A., McKnight, D.M. Thorn, K.A., editors, Denver, US.

MICROPHYSICAL AND CHEMICAL CHARACTERISTICS OF CLOUD DROPLET RESIDUALS AND INTERSTITIAL PARTICLES IN CLEAN CONTINENTAL CLOUDS

K.J. Noone[1], A. Targino[1], G. Olivares[2], L.M. Russell[3], D.S. Covert[4], J.A. Ogren[5], S. Borrmann[6], F. Drewnick[6], J. Schneider[6], S. Henseler[6], N. Hock[6], S. Weimer[6]

[1]Department of Meteorology, Stockholm University, S-10691 Stockholm, Sweden
[2] Institute of Applied Environmental Research, Stockholm University, S-10691 Stockholm, Sweden
[3]Scripps Institution of Oceanography, UCSD, La Jolla, CA 92093-0221 USA
[4]Department of Atmospheric Sciences, University of Washington, Seattle, WA 98195, USA
[5]Climate Monitoring and Diagnostics Laboratory, NOAA, Boulder, CO 80305, USA
[6]Institute of Atmospheric Physics, University of Mainz, D-55128 Mainz, Germany

1. INTRODUCTION

The effect of clouds on the Earth's radiative balance remains the largest uncertainty in our current understanding of climate. Since clouds start their lives as aerosol particles, understanding the interactions between aerosols and clouds is necessary before we will be able to develop a reliable predictive capability for describing cloud properties and the climatic effects of clouds.

A number of studies have shown that not all of the available aerosols in the atmosphere actually form cloud droplets [*Gillani et al.*, 1991; *Glantz and Noone*, 2003; *Hallberg et al.*, 1994; *Leaitch et al.*, 1992; *Noone et al.*, 1992]. Determining which particles do and do not form cloud droplets for different kinds of clouds is the first step in understanding and developing parameterizations for the processes controlling aerosol scavenging in clouds. While the inorganic composition of cloud droplets has been extensively investigated, there are relatively few direct measurements of organic species in droplets e.g., [*De Bock et al.*, 2000; *Facchini et al.*, 1999; *Noone et al.*, 2000; *Novakov and Penner*, 1993; *Russell et al.*, 2000]. As the measurement technology for organic aerosols advances, we are beginning to realize that organics can play a very important role in cloud droplet formation.

An experiment to determine the microphysical and chemical interactions between aerosols and cloud droplets was carried out during July 2003 at Mt. Åreskutan in central Sweden. The aim was to compare and contrast the properties of interstitial and scavenged particles to better understand the processes determining the uptake of particles into cloud droplets.

The project – called *Sources and Origins of Atmospheric Cloud Droplets* (SOACED) – was an international cooperative effort by groups from Sweden (Stockholm University), Germany (University of Mainz) and the United States (Princeton University, University of Washington, NOAA).

Corresponding author's address: Kevin J. Noone, Department of Meteorology, Stockholm University, S-10691 Stockholm SWEDEN; E-Mail: zippy@misu.su.se.

2. HYPOTHESES AND QUESTIONS

The experiment was designed to attempt to test several hypotheses about aerosol/cloud interactions. The hypotheses concerned the chemical, physical and optical properties of aerosols, and how these properties influence scavenging.

The hypotheses are:

1. Organic compounds are a substantial fraction of the aerosol that forms cloud droplets, both in terms of number and mass;
2. Accumulation-mode particles control the number population of cloud droplets in the clouds at this site;
3. The optical properties of the scavenged and interstitial aerosol in clouds are measurably different.

A number of questions needed to be addressed in order to test these hypotheses. For instance:

- What are the size distributions of the scavenged (droplet residual) and unscavenged (interstitial) aerosols in the clouds?
- What is the chemical composition of the residual and interstitial aerosol?
- What are the optical properties (scattering and absorption coefficients) of the residual and interstitial particles?

In addition to these questions, we also wanted to examine the variability of the aerosol properties at the site during the month of observations, and attempt to relate the chemical and microphysical properties of the aerosol to source regions as determined by analysis of back trajectories.

size distributions and compositions in clean clouds

3. EXPERIMENTAL DESCRIPTION

We sampled droplets and interstitial particles simultaneously in clouds using two complementary inlet systems. Cloud droplets larger than roughly 5μm diameter were sampled using a land-based Counterflow Virtual Impactor (CVI) system [*Noone et al.*, 1988; *Ogren et al.*, 1985]. Interstitial particles smaller than 5μm diameter were sampled with a radial impactor. Similar instrumentation (described in the following sections) was attached to both of these inlets to measure the physical, chemical and optical properties of the residual and interstitial particles

3.1 CVI Inlet

Figure 1 is a schematic diagram of the instrumentation attached to the CVI inlet.

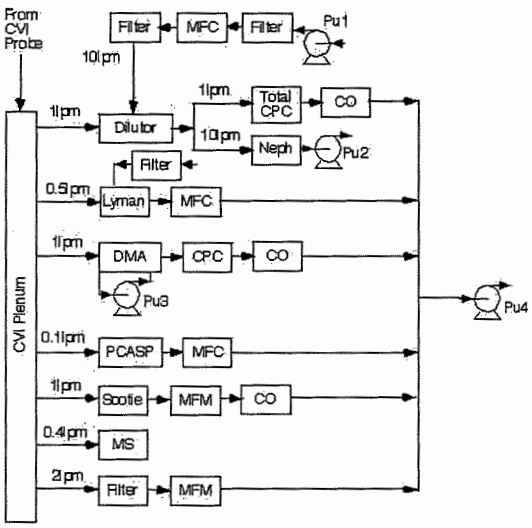

Figure 1. Flow diagram of the instrumentation attached to the CVI inlet. MFC – mass flow controller; CPC – TSI 3010 condensation particle counter; Neph – TSI 3563 integrating nephelometer; Lyman – Lyman-α hygrometer; DMA – differential mobility analyzer; PCASP – PMS passive cavity optical particle counter; Sootie – aerosol absorption photometer; MS – Aerodyne aerosol mass spectrometer.

The combination of instrumentation allowed us to characterize the size distribution of residual particles from 0.016 to 8.9μm diameter, to measure the scattering and absorption coefficients at blue, green and red wavelengths, and to determine the chemical composition of the particles as a function of size.

3.2 Interstitial Inlet

A complementary set of instrumentation was attached to the interstitial inlet (shown in Figure 2). The combination allowed us to directly compare the properties of the scavenged and interstitial aerosol.

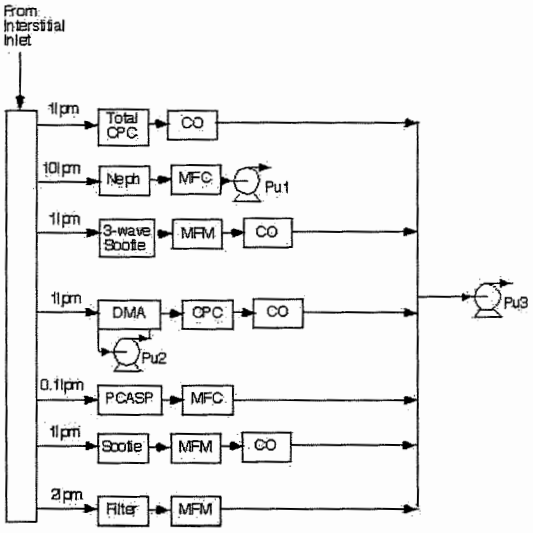

Figure 2. Flow diagram of instrumentation attached to the interstitial inlet. Notation as in Fig. 1.

Sampling cloud-free air with both inlets allowed us to compare the instrumentation during the experiment. The PCASPs were calibrated in the laboratory prior to the experiment. The nephelometers were routinely calibrated with CO_2 and particle-free air.

4. EXAMPLE RESULTS

Even though July 2003 was anomalously warm and dry, a number of cloud events were captured. An event at the end of the month (26-29 July) was particularly interesting. Analysis of five-day back trajectories for this period indicated that the air arriving at the site came from the north Atlantic region, and traveled over the Ireland and the UK on its way to Mt. Åreskutan.

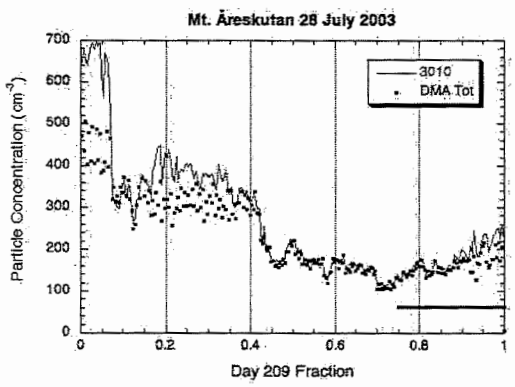

Figure 3. Time series of particle concentration from the interstitial inlet.

Figure 3 shows a time series of particle concentrations from the interstitial inlet for day 209 (28 July) 2003. The solid line is particle concentration above 10nm diameter from the interstitial TSI 3010 CPC, and the dots are the integrated concentration from the interstitial DMA, which was coupled to a second 3010 CPC. The difference between DMA total and 3010 concentrations is an indication of the concentration of accumulation-mode particles. Observer logs indicate that cloud was intermittent at the site from midnight on the 28th (zero in Fig. 3). Drizzle started at about 02:00 (ca. 0.1 in Fig 3), and particle concentrations dropped sharply. The fraction of accumulation-mode particles dropped at this time. Drizzle became rain at approximately 04:00 (0.2 in the figure). Interstitial particle concentrations continued to decrease, and the accumulation-mode particles were completely removed from the interstitial reservoir between roughly 09:30 (0.4) and 21:30 (0.9). Accumulation-mode particles began to reappear in the interstitial reservoir at about 21:30 (0.9). Drizzle had stopped at this time, and the cloud, while still present, was relatively thin.

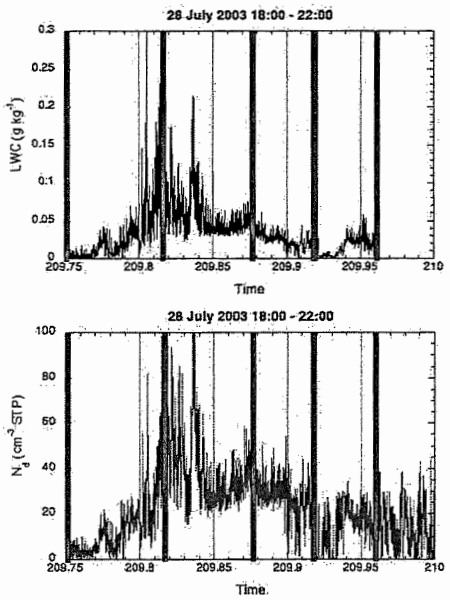

Figure 4. Time series of liquid water content and residual particle number concentrations (corresponding to droplet number concentration above 5μm diameter) from the CVI system. The vertical bars indicate periods when baseline measurements were being taken.

Figure 4 shows a time series of liquid water content (LWC) and droplet number above 5μm diameter (N_d) from the CVI system for the period 18:00 – 22:00, indicated with a heavy bar in Figure 3. Particles below the accumulation-mode size dominated the residual particles for the period up to about 209.8 (ca. 19:00). At this time, both LWC and N_d increased. At the same time, the residual particle size distributions became broader, and contained both accumulation-mode and Aitken-mode particles.

5. DISCUSSION

Drizzle appeared to have played an important role in modulating the concentration of accumulation-mode particles during this period. During the period of drizzle at the start of the time series, accumulation-mode particles were absent from both the interstitial and scavenged reservoirs. As droplet number and LWC increased, the accumulation-mode particles made a reappearance in the scavenged reservoir, but remained absent from the interstitial reservoir. When drizzle stopped towards the end of the period, the accumulation-mode particles reappeared even in the interstitial reservoir. Hypothesis 2 above appeared to have been false for this period, as accumulation-mode particles did not appear to control the number of droplets – particularly during periods of drizzle or rain.

Further analysis for this period will be focused on examining the size distributions of the interstitial and residual particles, and their chemical and optical properties.

6. REFERENCES

De Bock, L.A., P.E. Joos, K.J. Noone, R.A. Pockalny, and R.E. Van Grieken, Single Particle Analysis of Aerosols Observed in the Marine Boundary Layer during the Monterey Area Ship Tracks Experiment (MAST) with Respect to Cloud Droplet Formation, *J. Atmos. Chem.*, *37*, 299-329, 2000.

Facchini, M.C., S. Fuzzi, S. Zappoli, A. Andracchio, A. Gelencsér, G. Kiss, Z. Krivácsy, E. Mészáros, H.-C. Hansson, T. Alsberg, and Y. Zebühr, Partitioning of the organic aerosol component between fog droplets and interstitial air, *J. Geophys. Res.*, *104* (D21), 26,821-26,832, 1999.

Gillani, N.V., P.H. Daum, S.E. Schwartz, W.R. Leaitch, J.W. Strapp, and G.A. Isaac, An observational study of the efficiency of activation of accumulation-mode particles in warm continental stratiform clouds, in *Fifth International Conference on Precipitation Scavenging and Atmospheric-Surface Exchange Processes*, Richland, WA, USA, 1991.

Glantz, P., and K.J. Noone, Scavenging efficiencies of aerosol particles in maritime stratocumulus and cumulus clouds, *Quart. J. Roy. Meteor. Soc.*, in press, 2003.

Hallberg, A., K.J. Noone, J.A. Ogren, I.B. Svenningsson, A. Flossmann, A. Wiedensohler, H.-C. Hansson, J.

Heintzenberg, T. Anderson, B. Arends, and R. Maser, Phase partitioning of aerosol particles in clouds at Kleiner Feldberg, *J. Atmos. Chem.*, *19*, 107-127, 1994.

Leaitch, W.R., G.A. Isaac, J.W. Strapp, C.M. Banic, and H.A. Weibe, The Relationship Between Cloud Droplet Number Concentrations and Anthropogenic Pollution: Observations and Climactic Implications, *J. Gepohys. Res.*, *97* (D2), 2463-2474, 1992.

Noone, K.J., J.A. Ogren, A. Hallberg, J. Heintzenberg, J. Ström, H.C. Hansson, B. Svenningsson, A. Wiedensohler, S. Fuzzi, M.C. Facchini, B.G. Arends, and A. Berner, Changes in Aerosol Size and Phase Distributions Due to Physical and Chemical Processes in Fog, *Tellus*, *44B* (5), 489-504, 1992.

Noone, K.J., J.A. Ogren, J. Heintzenberg, R.J. Charlson, and D.S. Covert, Design and calibration of a counterflow virtual impactor for sampling of atmospheric fog and cloud droplets, *Aerosol Sci. Tech.*, *8*, 235-244, 1988.

Noone, K.J., E. Ostrom, R.J. Ferek, T. Garrett, P.V. Hobbs, D.W. Johnson, J.P. Taylor, L.M. Russell, R.C. Flagan, J.H. Seinfeld, C.D. O'Dowd, M.H. Smith, P.A. Durkee, K. Nielsen, J.G. Hudson, R.A. Pockalny, L. De Bock, R.E. Van Grieken, R.F. Gasparovic, and I. Brooks, A case study of ships forming and not forming tracks in moderately polluted clouds, *Journal of the Atmospheric Sciences*, *57* (16), 2729-2747, 2000.

Novakov, T., and J.E. Penner, Large contribution of organic aerosols to cloud-condensation-nuclei concentrations, *Nature*, *365*, 823-826, 1993.

Ogren, J.A., J. Heintzenberg, and R.J. Charlson, In-situ sampling of clouds with a droplet to aerosol converter, *Geophys. Res. Lett.*, *12* (3), 121-124, 1985.

Russell, L.M., K.J. Noone, R.J. Ferek, R.A. Pockalny, R.C. Flagan, and J.H. Seinfeld, Combustion Organic Aerosol as Cloud Condensation Nuclei in Ship Tracks, *J. Atmos. Sci.*, *57* (16), 2591-2606, 2000.

EFFECTS OF CLOUD SCAVENGING ON AEROSOL SINGLE-SCATTERING ALBEDO

J.A. Ogren[1], E. Andrews[1,2], D.S. Covert[3], and K.J. Noone[4]

[1]Climate Monitoring and Diagnostics Laboratory, NOAA, Boulder, CO 80305, USA
[2]Cooperative Institute for Research in Environmental Sciences, University of Colorado, Boulder, CO 80305, USA
[3]Department of Atmospheric Sciences, University of Washington, Seattle, WA 98195, USA
[4]Department of Meteorology, Stockholm University, S-10691 Stockholm, Sweden

1. INTRODUCTION

The magnitude, and even the sign, of the climate forcing by aerosol particles is strongly dependent upon the aerosol single-scattering albedo, which is the fraction of the aerosol light extinction that is due to scattering. Long-term monitoring at a variety of surface sites reveals a systematic decrease in aerosol single-scattering albedo as the aerosol loading decreases, i.e., aerosols are "blacker" in the cleanest air (Delene and Ogren, 2003). One hypothesis for this behavior is that clouds preferentially scavenge scattering aerosols more effectively than absorbing aerosols, which is what would be expected if the absorbing component of the aerosol is dominated by hydrophobic black carbon and the scattering component is dominated by hygroscopic species like sulfates. If the clouds precipitate, the aerosol that remains after the cloud dissipates will be enriched in black carbon relative to the water-soluble species that often dominate aerosol light scattering.

As a test of this hypothesis, measurements of aerosol light scattering and absorption were made during July 2003 at Mt. Åreskutan in central Sweden. Identical instruments for measuring aerosol light scattering and light absorption were operated downstream of two complementary inlets. A counterflow virtual impactor (CVI) provided samples of cloud droplet residuals, i.e., the aerosol particles that remain when a cloud droplet evaporates, and a radial impactor provided a sample of the interstitial particles smaller than the cloud droplets sampled by the CVI. The interstitial inlet was also used to sample ambient aerosols during cloud-free periods. Additional details of the field campaign are given in Noone et al. (2004, this conference).

2. EXPERIMENTAL APPROACH

The size cuts of the CVI and the radial impactor were both set to 5 μm diameter, i.e., all particles larger than this cut size were assumed to be cloud droplets and all smaller particles were called interstitial. Measurements of particles from both inlets were made at low relative humidity so that they could be directly compared. Aerosol light scattering coefficient was measured with an integrating nephelometer (Model 3563, TSI, Inc., St. Paul, USA) and light absorption coefficient was measured with a filter-based light photometer (Model PSAP, Radiance Research, Seattle, USA). All the measurements reported here are at a wavelength of 550 nm. Nephelometer data were corrected for truncation errors following the procedures recommended by Anderson and Ogren (1998) and the PSAP data were adjusted using the procedures recommended by Bond et al. (1999). Cloud liquid water content (LWC) was measured with a Lyman-alpha hygrometer in the CVI, and cloud extinction coefficient was estimated every minute using a digital camera ("cloudcam") that viewed a range of black and white targets.

The cloudcam system was developed as a simple and inexpensive approach to monitoring the presence or absence of clouds when the site was unattended. The CVI system was only operated while the site was attended, which generally was daily between 0900-1700 local time. The nephelometer and PSAP operated continuously, however, creating the need for an independent measurement of clouds. Five targets consisting of black and white squares were set up at distances of 11-93 m from the station, and a digital camera (model QuickCam Pro 4000, Logitech, Inc., Fremont, USA) recorded images of the targets once per minute. Figure 1 shows the scene in clear air and then one minute later when dense cloud suddenly enveloped the site. The visibility, calculated from the contrast between the black and white areas in the two visible targets in the cloudy image, was 40 m, consistent with the fact that the third target 55 m away is not visible. Although not a precise measurement of the extinction coefficient, the cloudcam allowed detection of clouds nearly 24 hours a day under the special lighting conditions in July in northern Sweden.

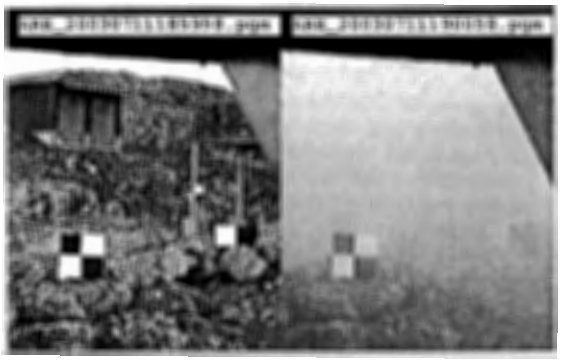

Figure 1: Cloudcam targets in clear and cloudy air.

Corresponding author's address: John A. Ogren, NOAA R/CMDL1, 325 Broadway, Boulder, CO 80305, USA; E-Mail: John.A.Ogren@noaa.gov

do clouds scavenge scattering aerosols more than absorbing aerosols? - make assumption of $\tilde{\omega}_0$ in Sweden to answer these questions

3. RESULTS

Aerosol concentrations were generally low during the month, and dropped to near or below the detection limits of the nephelometer and PSAP (0.1-0.2 Mm^{-1}) when clouds were present. Figure 2 shows the variability of the aerosol light scattering coefficient and the cloud light extinction coefficient during the study period. Variations of scene illumination (sun angle, high clouds, building shadows) and other factors (shifting targets, non-black targets) prevented the cloudcam from detecting cloud extinction coefficients below about 20 km^{-1}.

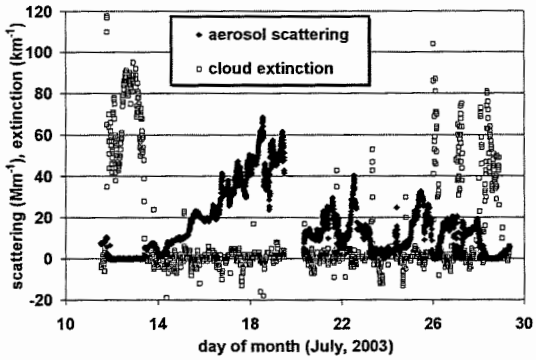

Figure 2: Variation of aerosol light scattering (closed symbols) and cloud light extinction (open symbols) during July, 2003.

The very low aerosol scattering and absorption coefficients in interstitial air indicate near-complete scavenging of all optically-important particles by the cloud droplets. For the purpose of this analysis, the key question is whether the few remaining particles were relatively enriched in absorbing material. Figure 3 shows the variation in aerosol single-scattering albedo, calculated as the aerosol light scattering coefficient divided by the sum of the scattering and absorption coefficients. Periods when the cloud extinction coefficient was above 20 km^{-1} are indicated by solid blocks along the abscissa. Values of single-scattering albedo larger than unity are physically impossible, and indicate the difficulty of measuring this quantity when the primary measurements are at or near their detection limits. Nevertheless, it is clear that the majority of in-cloud observations have single-scattering albedos that are substantially lower than the observations made in cloud-free air. This is particularly true for the observations on July 26 and 27, when the intersitial aerosol light scattering and absorption coefficients were slightly higher than during the cloudy periods at the beginning and end of the study.

- very small amount not scavenged, but appears absorbing cons are high

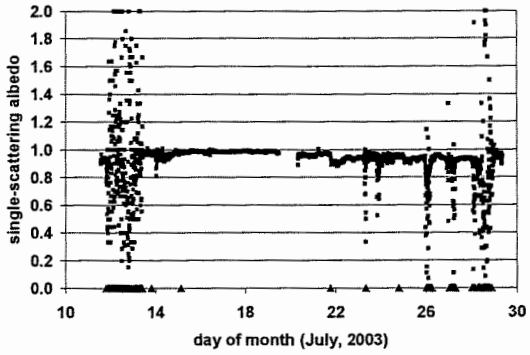

Figure 3: Variation of aerosol single-scattering albedo during July, 2003. Periods when clouds were detected by the cloudcam are indicated by the black triangles along the abscissa.

4. CONCLUSIONS

Both absorbing and scattering aerosols were nearly completely scavenged by the clouds encountered during the study. The very low in-cloud aerosol loadings preclude drawing firm conclusions from the interstitial aerosol measurements alone. However, the bulk of the evidence supports the hypothesis that light scattering aerosols are more efficiently scavenged by clouds than light absorbing aerosols, which would yield lower single-scattering albedos in air that has been scavenged by precipitating clouds.

5. ACKNOWLEDGEMENTS

This work was supported by the International Meteorological Institute at Stockholm University and the NOAA Aerosol-Climate Interactions Program.

6. REFERENCES

Anderson, T. L., and J. A. Ogren, 1998: Determining aerosol radiative properties using the TSI 3563 integrating nephelometer. *Aerosol. Sci. Tech.*, **29**, 57-69.

Bond, T. C., T. L. Anderson, and D. Campbell, 1999: Calibration and intercomparison of filter-based measurements of visible light absorption by aerosols. *Aerosol Sci. Tech.*, **30**, 582-600.

Delene, D. J., and J. A. Ogren, 2003: Variability of aerosol optical properties at four North American surface monitoring sites. *J. Atmos. Sci.*, **59**, 1135-1150.

Noone, K. J., A. Targino, G. Olivares, L. M. Russell, D. S. Covert, J. A. Ogren, S. Borrmann, F. Drewnick, J. Schneider, S. Henseler, N. Hock, and S. Weimer, 2004: Microphysical and chemical characteristics of cloud droplet residuals and intersitial particles in clean continental clouds. *Proceedings of the 14th International Conference on Clouds and Precipitation*, Bologna, Italy, July 2004.

SAHARAN DUST AS ICE NUCLEI

R.G. Oraltay[1], N. Fersiz[1] and J. Hallett[2]

[1]Marmara University, Eng. Faculty,
Environmental Eng. Dept. 34722 İstanbul, TURKEY
[2] Desert Research Institute, Reno, NV 89512-1095, USA

1. INTRODUCTION

An estimated amount of 60-200 million tons of Saharan dust is released into the atmosphere per year (Prospero and Carlson, 1972; Jaenicke and Schütz, 1978). Observation of red rain events in Europe (e.g. Spain, Italy) and in the Middle East (e.g. Israel, Turkey) indicates very effective scavenging processes are taking place (Prodi and Fea, 1979; Avila and Penulas, 1999; Kubilay, et. al., 2000). Most of the research on Saharan dust has been devoted to transport pathways and estimation of the dry/wet deposition fluxes (Guerzoni and Chester (Eds.), 1996; Ganor and Foner, 2001). Fluxes are related to the removal rates. History of the particles may affect their nucleation characteristics as in the case of sulfate coated desert particles (Levin et al., 1996). However, laboratory studies on the nucleation and other scavenging processes of the Saharan dust are too limited (Prodi and Oraltay, 1992). Furthermore, in spite of the nutrient characteristic of the minerals contained in Saharan dust (Guerzoni et al., 1999; Saydam and Senyuva, 2002) most of the research was focused on the determination of the chemical composition (Ganor and Foner, 1996) and any biological process is not included on the ice nucleating ability. In this work, we investigated ice nucleation properties of the Saharan dust in the laboratory.

2. EXPERIMENTAL

Dust particles were placed on a temperature controlled substrate in a cold box (Fig. 1). Supersaturation was obtained by maintaining temperature difference between the inner walls of the cold box and the substrate. Three sets of supersaturations were obtained this way: 10, 20 and 30% (± 1) with respect to ice, being underwater saturation, around water saturation and above water saturation respectively. Particles were monitored via a computer connected microscope-camera. Temperature of the substrate was determined with the first observation of the ice crystals. The number of nucleated particles was also recorded.

Corresponding author's address: Riza G. Oraltay. Marmara Univ., Engineering Faculty, Environ. Eng. Dept. 34722 Goztepe, Istanbul-Turkey.E-Mail: gurcan@marmara.edu.tr

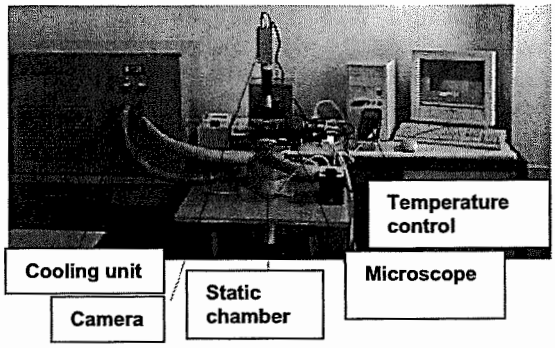

Figure 1. Experimental setup.

3. RESULTS AND DISCUSSION

In the first set of experiments, ice nucleation temperature of Saharan dust particles were determined at ice supersaturations of 10, 20 and 30%. Fig. 2 exhibits the number of particles acting as ice nuclei as a function of temperature at these supersaturations. About thousand particles were taking into account. A critical temperature of -12°C was obtained for all cases, but with the observation of increasing number of ice nuclei with increasing supersaturation.

Sahara dust as ice nuclei

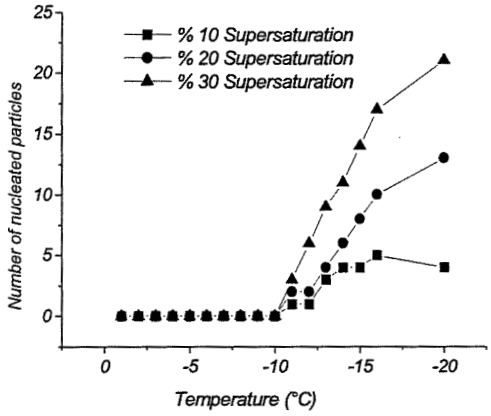

Figure 2. Number of untreated particles (out of thousand) acting as ice nuclei as a function of temperature.

Experiments were performed with also Saharan dust irradiated by $_{60}$Co, aiming the elemination of any biological activity leading to ice nucleation. In this case, critical temperature was suppressed about three degrees, -16°C, -15°C and -14°C for ice supersaturations of 10, 20 and 30% respectively.

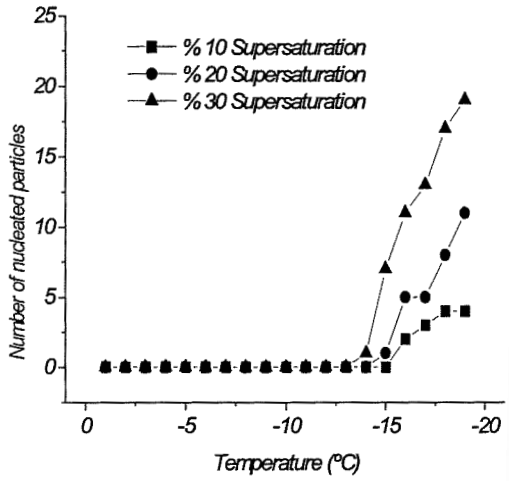

Figure 3. Number of $_{60}$Co treated particles (out of thousand) acting as ice nuclei as a function of temperature.

In addition to the experiments described above, we checked ice nucleation of supercooled water films by particles. The results were consistent with those shown above. To illustrate the difference of nucleation by normal Saharan dust and $_{60}$Co irradiated dust, two sets of photographs are given in Fig. 4 and Fig. 5. Normal Saharan dust is shown in Fig 4. The water film is cooled from -12 (Fig. 4a) to -15°C (Fig. 4b), indicating a clear increase in the number of nucleated particles. Fig. 5 shows the situation at -17°C for irradiated dust particles. Although temperature is much lower, any considerable nucleation does not take place.

Preliminary results suggest that, bacterial activity may be playing a role in the enhancement of the ice nucleation ability of the Saharan dust particles. In all supersaturations studied, at temperatures below -12°C natural Saharan dust particles were effective ice nuclei. In the case of irradiated particles, the critical temperature below water saturation (10% supersaturation

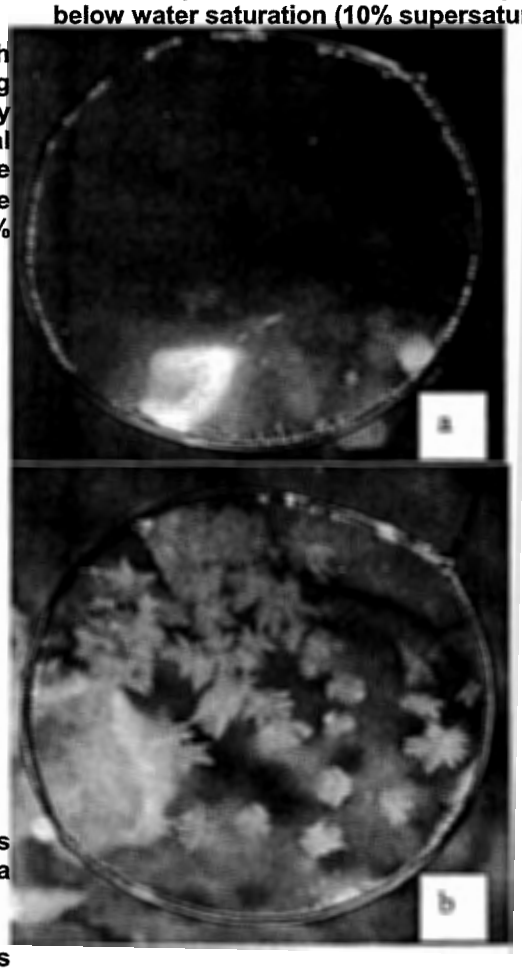

Figure 4. Normal Saharan dust: a)T= -12°C, b) T = -15°C

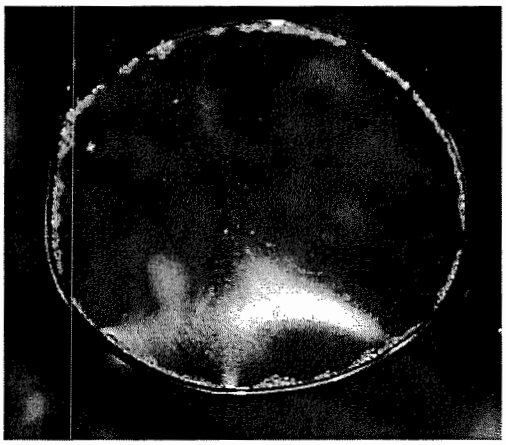

Figure 5. Irradiated Saharan dust T=-17°C

with respect to ice) was four degrees lower (T_c=-16°C). Comparison of the results to the previous mineral nucleation studies shows that current critical temperature of -12°C is higher than those obtained by Roberts and Hallett (1968): for water subsaturation, the critical temperature ranges between -17° and -28°C for different naturally occurring substances. In the case of irradiated dust, suppression of the critical temperature to -16°C shifts our sample closer to the range mentioned above-possibly because of the elimination of the biological activity.

Nucleation studies of desert dust obtained from different regions and characterization of the particles by crystallographic techniques are underway. Furthermore, remote sensing data on the field observations are being analyzed to investigate the link between Saharan dust transfer and heavy precipitation events in Turkey.

4. ACKNOWLEDGEMENTS

This work has been supported by a grand from Scientific and Technical Research Council of Turkey, project number YDABCAG-199Y19 and a TOKTEN/UNISTAR visiting grand.

5. REFERENCES

Avila, A., and J. Penulas, 1999: Increased frequency of Saharan rains over northeastern Spain and its ecological consequences. The Scien. of the Total Environ., 228, 153-156.

Ganor, E., and H.A. Foner, 1996: The mineralogical and chemical properties and the behaviour of aelian Saharan dust over Israel. The Impact of Saharan Dust Across the Mediterranean, 163-172, Kluwer Acad.

Ganor, E., and H.A. Foner, 2001: Mineral dust concentrations, deposition fluxes and deposition velocities in dust episodes over Israel. J. Geophys. Res., 106, 18341-18437.

Guerzoni, S., and R. Chester (Eds.), 1996: Impact of Desert Dust Across the Mediterranean, 389 pp., Kluwer Acad.

Guerzoni, S., Chester, R., Dulac, F., Measures, C., Migon, C., Molinaroli, E., Moulin, C., Rossini, P., Saydam, C., Soudine A., and P. Zieveri, 1999: The role of atmospheric deposition in the biogeochemistry of the Mediterranean Sea. Progress in Oceanography, 44, 147-190. Norwell, Mass

Jaenicke, R., and I. Schütz. 1978: A comprehensive study of physical and chemical properties of the surface aerosols in the Cape Verde Islands region. J. Geophys. Res., 83,3585-3599.

Kubilay, N., Nickovic, N., Moulin, C., and F.Dulac, 2000: An illustration of the transport and deposition of mineral dust onto the eastern Mediterranean. Atmos. Environ., 34, 1292-1303.

Levin, Z., Ganor, E., and V. Gladstein, 1996:The effects of desert particles coated with sulfate on rain formation in the Eastern Mediterranean. J. of Appl. Meteor. , 35, 1511-1523.

Prodi, F., and A. Fea, 1979: A case of transport and deposition of Saharan dust over the Italian peninsula and Southern Europe. J. of Geophys. Res., 84, 6951-6960.

Prodi, F., and R.G. Oraltay, 1992: Scavenging of aerosol particles by growing and evaporating ice crystals: Assessing the role of competitive processes. Precipitation Scavenging and Atmosphere Surface Exchange, Schwartz, S.E. and W.G.N. Slinn (Eds.), Vol.1, 75-86, Hemisphere Pub. Corp..

Prospero, J.M., and T.N. Carlson, 1972: Vertical and areal distribution Saharan dust over the western equatorial North

Atlantic, J. Geophys. Res., 77, 5255-5265.

Roberts F., and J. Hallett, 1968: A laboratory study of the ice nucleating properties of some mineral particles, Quart. Jour. of Royal Met. Soc., 94, No. 399, 23-34.

Saydam, A.C., and H.Z. Senyuva, 2002: Deserts: Can they be the potential suppliers of bioavailable iron? Geophys. Res. Letters, Vol.29, No 11, 19-1-3.

SAHARA DUST IMPACT ON PRECIPITATION IN SEVERE STORM EVENTS OVER WEST – CENTRAL MEDITERRANEAN AREA.

M. Pasqui[1,2], B. Gozzini[1,2] and F. Pasi[1,2]

[1] Institute of Biometeorology, National Research Council, Florence, Italy.
[2] Laboratory of Meteorology and Environmental Analysis Tuscany Region, Sesto Fiorentino, Italy.

1. INTRODUCTION

Aerosols particles plays a fundamental role on a wide number of atmospheric processes ranging from climate to micrometeorology dynamics, from rain formation and evolution to weather forecasting, from bio-chemical cycling to remote sensing application. Furthermore aerosols forcing is acting on those atmospheric phenomena both in a direct way and a indirect way: the former way is related to the reflection and absorption of solar radiation, and thus changing the atmospheric energy budget, while the latter is related in changing (both in size and concentration) cloud formation and evolution. Aerosols formation, dynamics, along with their distribution, both at regional and global scale, has been studied since so far using satellite and "in situ" measurements or specific field campaigns in several areas on the Earth. One of the most interesting area worldwide is the north Africa and the Mediterranean basin with its peculiar aerosol source – sink and concentration dynamics, see for detailed studies: Moulin et al. (1998), Israelevich (2002), Prospero et al. (2002).

From a meteorological point of view one of the main interesting aspects is represented by the cloud formation and dynamics along with the consequent rain formation. This is a critical point especially from a modelling point of view because aerosols, as the cloud condensation nuclei (CCN), act as an indirect forcing on the precipitation produced by microphysics schemes within the numerical weather prediction models (NWP), see Khain (2001) and Ramanathan (2001). Operational direct ingestion of observed CCN three dimensional distribution in the microphysical schemes in NWP is difficult, but under development. While indirect tuning driven by observed proxy field, based on the TOMS *Aerosol Index* (AI), is used within the Regional Atmospheric Modelling System (RAMS) at the Laboratory for Meteorology and Environmental Analysis (LaMMA – CNR – IBIMET). Our goal is the possibility of a specific setting of the initial CCN concentration of cloud droplets in RAMS according to the observed AI values. In order to explain our strategy we present a sensitivity study for the microphysical initialization in which a selection of severe rain events, occurred in West – Central Mediterranean sea, were analysed with respect to the CCN concentration and size distribution.

Corresponding author's address: Massimiliano Pasqui, Laboratory for Meteorology and Environmental Analysis, Institute of Biometeorology, Sesto Fiorentino, Italy, I-50154; E-Mail: pasqui@lamma.rete.toscana.it.

2. AEROSOL OVER THE MEDITERRANEAN SEA

Numerous works on the Sahara desert aerosols sources, sinks and transport over the Mediterranean region has been published since 70's. In particular the TOMS aerosols index was used to determine the behaviour and evolution of dust in this area. Several aerosols sources were pointed out in the north – west and north – central Africa which could be primary responsible for dust transport over sea to the Europe or over the Atlantic Ocean. As shown in Moulin et al (1998), Israelevich (2002) and Prospero et al (2002) the aerosols transport could be summarised as following: just a few dust sources provide and maintain the aerosols reservoir over the North Africa regions while synoptic circulation over Mediterranean sea determines and drives their transport. Three major situation were found to be responsible for Sahara dust transport over the Mediterranean basin:

- In the *spring* the Sharav cyclones, which move eastward along the North African coast carry dust in the eastern part of the basin.
- In *summer* highs over west – central Africa carry dust over west – central part of the basin, preventing from its propagation on the east part.
- From *late summer* to fall cyclones from the Atlantic carry dust on the west central part of the basin.

All these results are based on the extensive analysis of the TOMS aerosols index, AI, which, using a spectral contrast of two ultraviolet channels (340 and 380 nm), provides a wide used detection technique on a daily basis as illustrated in Herman et al (1997) and Torres et al (2002) at 1°x1.25° of horizontal resolution (http://toms.gsfc.nasa.gov). Such AI values are proportional to dust load mainly at altitudes higher than 1 km above the ground.

3. THE REGIONAL ATMOSPHERIC MODELING SYSTEM

3.1 RAMS general description

The Regional Atmospheric Modeling System, RAMS, has been used operationally at La.M.M.A. (http://www.lamma.rete.toscana.it), the regional meteorological service of Tuscany (Italy) since 1999. The latest RAMS version, 5.05, is used for this study as part of a pilot data assimilation technique developed in collaboration with the Institute of Biometeorology of National Research Council (http://www.ibimet.cnr.it), Pasqui (2000), Meneguzzo (2004), Meneguzzo (2002), Pasqui (2002), Soderman (2003), Pasqui (2004).

RAMS and its predecessors have been developed since the early '70s essentially as a research tool; nowadays it's widely used both for research and operational forecast purposes in many meteorological centres around the world. Since early '90s a large number of improvements have been introduced from both the physical (new numerical schemes) and the computational point of view (the parallel computing design). A general description of the model can be found in Pielke et al. (1992), while a technical description can be found on the ATMET web site (http://www.atmet.com).

Today RAMS represents the state-of-the-art in the atmospheric numerical modelling and it is continuously improved on the basis of a multi-disciplinary work both at Colorado State University and at several research and operational centres worldwide. Only few peculiar features of RAMS are shortly described below, leaving the details to the direct reading of the reference papers.

The physical package of the model describes a number of atmospheric effects: a two-way interactive nested grid structure, an atmospheric turbulent diffusion processes according with the Mellor-Yamada scheme, a cloud microphysics parameterization, modified Kain-Fritsch type cumulus parameterization, the Harrington radiative transfer parameterization short and long wave scheme and the Land Ecosystem Atmosphere Feedback scheme (LEAF-3) for soil – vegetation – atmosphere energy and moisture exchanges, described in Walko et al. (2000).

3.2 RAMS microphysics scheme

Among all the physical packages within RAMS a brief description of the microphysical scheme is provided here because concerns the proposed sensitivity study. The representation of cloud and precipitation microphysics in RAMS includes the treatment of each water species (cloud water, rain, pristine ice, snow, aggregates, graupel, hail) as a generalized Gamma distribution see Pielke et al. (1992).

The RAMS 5.05 employs a second–moment scheme for parameterization of cloud microphysics. It uses a generalized gamma size-spectrum and introduces ice–liquid mixed phase hydrometeor categories for ice crystals and a sophisticated heterogeneous nucleation parameterizations. The scheme predicts concentration and mass mixing ratios of eight forms of water categories: vapour, cloud water droplets, rain, pristine ice, snow, aggregates, graupel, and hail. Only the cloud droplets are assumed small enough to move with the air. All other categories fall down according to the environmental conditions and their specific dynamics. The only two categories which could nucleate from the vapour are cloud droplets and pristine ice. The remain categories are build from existing hydrometeors and, once formed, may grow by vapour deposition as well. Pristine ice, which is defined as relatively small crystals may continue its growth only by vapour deposition. The snow category is defined as consisting of relatively large ice crystals, which have grown by vapour deposition and riming. Aggregates are defined as ice particles that have formed by collision and coalescence of pristine ice, snow, and/or other aggregates. Aggregates, as snow, are allowed to retain their identity with moderate amounts of riming. Pristine ice, snow and aggregates are all low-density ice particles, having a relatively low mass and fall speed for their diameter. Graupel is an intermediate density hydrometeor assuming to be approximately spherical in shape. According to the assumptions, it is formed by moderate to heavy riming and/or partial melting of pristine ice, snow or aggregates. Graupel is allowed to carry up to only a low percentage of liquid. If the percentage becomes larger, by either melting or riming, a graupel particle is re-categorized as hail. Hail in the model is a high-density hydrometeor, which is assumed to be formed by freezing of raindrops or by riming or partial melting of graupel. Hail is allowed to carry any fraction of liquid water up to, but not including, 100%. In this case, a hail particle is re-categorized as water. Hydrometeors in each category are assumed to conform to a generalized gamma distribution, in which the shape of the distribution is determined by a special parameter n which may be any real number larger than or equal to 1. It controls the relative amount of smaller vs. larger hydrometeors in the distribution. When $n=1$, the Marshal – Palmer distribution is obtained, in which the number concentration decreases monotonically with diameter throughout the size spectrum. The larger the value of n, the more narrowly distributed the spectrum is and the distribution peaks at a larger diameter.

The scheme allows hail to contain liquid water and contains the description of the homogeneous and heterogeneous ice nucleation, and the ice size change by means of vapour deposition and sublimation.

A very efficient solution technique for the stochastic collection equation and a new technique for the prediction of sedimentation or precipitation of hydrometeors, which allows the definition of the fall velocity on the basis of the gamma size distribution, has been implemented by using a "look-up" table computed at the initial step, for a detailed description of the RAMS microphysical – precipitation scheme see Walko et al. (1995) and Meyers (1997).

4. CASE STUDIES

The proposed experiments were run in order to infer a better understand of aerosols impact on precipitation produced by RAMS NWP model and to provide a few guidelines for CCN initialisation within an operational framework as well. In order to do this we performed a sensitivity analysis and comparison of several very – high resolution RAMS simulation from selected severe rain episodes including a MAP storm occurred in Italy (Sep, 1999), a flood on Southern Spain (Jun, 2000) and a flash flood in Southern France (Sep, 2002), all of that evaluated in the framework HYDROPTIMET INTERREG Project. Such events were characterised by different conditions of environmental aerosols load and dynamics, in particular during the MAP case a dust plumes from Sahara was advected over southern European coast, causing high levels of aerosols concentrations, while the other two episodes were characterized, respectively, by moderate and low aerosols concentrations.

All simulations have been performed using a two nested and three nested grids configurations ranging from 8 – 2 km and 32 – 8 – 2 km horizontal resolution. The vertical structure of the grids is described by 36 model levels with a telescopic resolution ranging from 50 m, in the lowest layer, up to 1000 m in the upper part of the domain using a grid stretching factor of 1.125. The soil textural classes are represented by 11 levels down from 0.05 cm to 150 cm and using the FAO Soil dataset for a more accurate computation of the turbulent fluxes at the surface along with topography and vegetation coverage, at 1km of resolution, coming from USGS dataset. Weekly averaged sea surface temperature were from NOAA satellites at 4 and 9 km of horizontal resolution. Initial and boundary data for the mesoscale simulation were provided by the ECMWF global model with a time resolution of six hours.

5. PROPOSED CCN INITIALISATION STRATEGY

The evaluated case studies represent a sort of "test bed" for the calibration of RAMS microphysical scheme and a suitable choice of initial parameters and settings.

In details we define three different dust load concentration, namely *low / moderate / high*, with respect to the TOMS AI observed values categorised as follows: *Low* = *AI* < 0.7, *Moderate* = 0.7 < *AI* = 1.8, *High* = *AI* > 1.8 over the interest area. These conditions are direct linked with the CCN concentration. For each reference dust load condition we selected "the best choice", of microphysical parameter settings for the RAMS simulation, obtained through the analysed case studies simulations. Such strategy was then use for the operational runs.

Because not only the CCN concentration has a direct impact on precipitation additional tests were performed with the shape size distribution for each hydrometeors categories as well. Two different choice of the *n* parameter, controlling how the size spectra narrow is, were studied: a simple Marshall – Palmer (***n*** =1 for all the species) and a set of gamma shape distributions (***n*** in tab.1).

The prognostic equation for rain droplet number concentration was set for all the simulations, thus the mean droplet diameter is diagnosed from the prognosed mixing ratio and number concentration.

Following different specific suggestions appeared on microphysics characterization of cloud and rain formation studies, Krichak (2000), Khain (2001), Ramanathan (2001) and Lensky (2003), Masmoudi (2003), and through the specific analysis of the selected cases we present the three final sets of initial parameters for each species selected, for the RAMS cloud – precipitation scheme in tab.1.

	Low	Moderate	High	*n*
CPARM	*0.1e8*	*0.3e8*	*0.3e9*	*4*
RPARM	*0.1e-2*	*0.1e-2*	*0.1e-2*	*5*
PPARM	*0.1e-2*	*0.1e-2*	*0.1e-2*	*5*
SPARM	*0.1e-2*	*0.1e-2*	*0.1e-2*	*5*
GPARM	*0.1e-2*	*0.1e-2*	*0.1e-2*	*5*
HPARM	*0.5e-2*	*0.1e-2*	*0.1e-3*	*5*

Tab.1: Settings for the microphysics RAMS variables according to the observed aerosols concentration inferred by the TOMS AI for each hydrometeor species: cloud, rain, pristine ice, snow, graupel and hail form top to bottom.

6. FUTURE DEVELOPMENTS

Ingestion of real three dimensional aerosols concentration in an operational NWP model is difficult mainly because of direct measurement lack ness. But several dust loading analysis and forecasting system are available over the Mediterranean Sea (see for example http://forecast.uoa.gr). In the near future we will work on the automatic choice of the microphysical parameters and on the possible dust load evaluation from Meteosat Second Generation and/or MODIS satellites estimates.

7. ACKNOWLEDGEMENTS

This work was supported by several different projects: LaMMA – Tuscany Region (DOCUP project founded by EU) and HYDROPTIMET – INTERREG Project. We are also grateful to Dr. F. Meneguzzo, Dr. G. Messeri, Dr. C. Tei and Dr. Robert L. Walko for their useful help.

8. REFERENCES

Herman, J. R., P. K. Bhartia, O. Torres, C. Hsu, C. Seftor, and E. Celarier, 1997: Global distributions of UV-absorbing aerosols from Nimbus 7/TOMS data, J. Geophys. Res., 102, 16,911-16,922.

TOMS aerosol, looking at how aerosols affect rain

Israelevich P. L., Z. Levin, J. H. Joseph, and E. Ganor, 2002: Desert aerosol transport in the Mediterranean region as inferred from the TOMS aerosol index, J. Geophys. Res., 107 (D21), 4572.

Khain A. P., D. Rosenfeld and A. Pokrovsky, 2001: Simulating convective clouds with sustained supercooled liquid water down to -37.5°c using a spectral microphysics model. Geophysical Research Letters 28, 3887-3890.

Krichak, S.O. Levin, Z., 2000: Mesoscale Simulation of Life Cycle of Cloud Microphysics During Hazardous Weather Conditions in the Southeastern Mediterranean Atmospheric Research, 53, 63-89.

Lensky, M. I., and D. Rosenfeld, 2003: Satellite-based insights into precipitation formation processes in continental and maritime convective clouds at nighttime. J. Appl. Meteor, 42, 1227-1233. Highlighted in the Bulletin of American Meteorological Society, 84, September 2003, p. 1196.

Masmoudi M., Chaabane M., Tanre D., Gouloup P., Blarel L. and Elleuch F. 2003: Spatial and temporal variability of aerosol: size distribution and optical properties, Atmospheric Research, 66, 1-19.

Meyers, M. P., R. L. Walko, J. Y. Harrington, W. R. Cotton, 1997: New RAMS cloud microphysics parameterization. Part II: The two-moment scheme. Atmos. Res., 45, 3-39.

Meneguzzo, Pasqui, Menduni, Messeri, Gozzini, Grifoni, Rossi and Maracchi, 2004: Sensitivity of meteorological high-resolution numerical simulations of the biggest floods occurred over the Arno river basin, Italy, in the 20th century, Journal of Hydrology, in Press

Meneguzzo, F., Menduni, G., Maracchi, G.,Zipoli, G., Gozzini, B., Grifoni, D., Messeri, G.,Pasqui, M., Rossi, M., and C.J. Tremback, 2001: Explicit forecasting of precipitation: sensitivity of model RAMS to surface features, microphysics, convection, resolution. In: Mediterranean Storms. 3rd Plinius Conference 2001. Ed. by: R. Deidda, A. Mugnai, F. Siccardi. GNDCI Publ. N.2560, ISBN 88-8080-031-0, 79-84.

Moulin, C., et al., 1998: Satellite climatology of African dust transport in the Mediterranean atmosphere, J. Geophys. Res., 103, 13,137–13,143, 1998.

Pasqui et al. 2000: Performances of the operational RAMS in a Mediterranean region as regards to quantitative precipitation forecasts. Sensitivity of precipitation and wind forecasts to the representation of the land cover. Proceedings of "4th RAMS Users Workshop", Cook College - Rutgers University. , 22-24 May 2000, New Jersey, USA.

Pasqui et al. 2002: Historical severe floods prediction with model RAMS over central Italy. 5th RAMS Users Workshop, Santorini, Greece.

Pasqui M., Tremback C.J., Meneguzzo F., Giuliani G. and Gozzini B., 2004: A soil moisture initialization method, based on antecedent precipitation approach, for regional atmospheric modeling system: a sensitivity study on precipitation and temperature. 18th Conf. on Hydrology, AMS, Seattle.

Pielke, R. A. & Coauthors, 1992: A comprehensive meteorological modelling system-RAMS. Meteor. Atmos. Phys., 49, 69– 91.

Ramanathan, V., P. J. Crutzen, J. T. Kiehl, and D. Rosenfeld, 2001: Aerosols, Climate and the Hydrological Cycle. Science 294, 2119-2124.

Soderman, D., F. Meneguzzo, B. Gozzini, D. Grifoni, G. Messeri, M. Rossi, S. Montagnani, M. Pasqui, A. Orlandi, A. Ortolani, E. Todini, G. Menduni, and V. Levizzani, 2003: Very high resolution precipitation forecasting on low cost high performance computer systems in support of hydrological modeling. Prepr. 17th Conf. on Hydrology, AMS, Long Beach.

Torres, O., P.K. Bhartia ,J.R. Herman, A. Sinyuk, P. Gionoux and B. Holben, 2002: A long term record of aerosol optical thickness from TOMS observations and comparison to AERONET measurements, J. Atm. Sci..

Walko, R. L., W. R. Cotton, M. P. Meyers, and J.Y. Harrington, 1995: New RAMS cloud microphysics parameterization. Part I: The single-moment scheme. Atmos. Res., 38, 29–62.

Walko, R.L., L.E. Band, J. Baron, T.G.F. Kittel, R. Lammers, T.J. Lee, D. Ojima, R.A. Pielke, C. Taylor, C. Tague, C.J. Tremback, and P.L. Vidale, 2000: Coupled atmosphere-biophysics-hydrology models for environmental modeling. J. Appl. Meteor., 39, 931-944.

HIGH-RESOLUTION SENSITIVITY STUDY OF AEROSOL-CLOUD INTERACTIONS IN MARINE STRATUS CLOUDS

Irena T. Paunova and Henry G. Leighton

Atmospheric and Oceanic Sciences, McGill University, Montreal, Quebec, H3A 2K6, Canada

1. INTRODUCTION

It is generally agreed that cloud effects are responsible for some of the most fundamental uncertainties in current climate models and that the improvement of their representation should be among the top priorities in future model developments. There is also a consensus among the scientific community that cloud microphysical processes are mostly responsible for the existing large uncertainty of the possible indirect impacts of anthropogenic aerosols resulting from feedbacks on clouds and radiation. In order to reduce this uncertainty it is necessary to understand the processes involved.

The study aims to investigate the interaction between the anthropogenic aerosols and cloud and rain with the Mesoscale Compressible Community (MC2) model on the cloud scale. The present work, however, only presents a study of the response of the cloud properties to the indirect effect of aerosols on a regional scale. We expect to reveal want is understood and what is missing in our effort to simulate the indirect aerosol-cloud interaction.

2. CASE STUDY

We examined a case of single-layered marine stratus cloud that occurred on 1 September 1995 over the North Atlantic near the coast of Nova Scotia (Bay of Fundy). The cloud was observed during the Radiation, Aerosol, and Cloud Experiment (RACE) from 1720Z to 1910Z, which is 0120 to 0210 EST, by Twin Otter and Convair aircraft (flight F13C) operated by the National Research Council of Canada. This cloud had been influenced by anthropogenic pollution coming off the eastern coast of North America (Banic et al., 1996). In-situ aircraft measurements of aerosol and cloud microphysical properties taken during the RACE experiment and satellite imagery were used to verify the model simulations.

3. MODEL DESCRIPTION

3.1 Cloud Processing of Aerosol in MC2 Model

To ensure a realistic treatment of the aerosol indirect effects two explicit parameterizations were combined in the MC2 model, which is a limited area model offering a physically-based and fully interactive treatment of clouds and radiation. The Abdul-Razzak et al. (2000), AG00, nucleation parameterization allows one to explicitly model the cloud droplet nucleation process as a function of horizontally and vertically varying updrafts. In this parameterization, several externally and internally mixed aerosol species compete as cloud condensation nuclei (CCN). The Cohard and Pinty (2000), CP00, parameterization includes a prognostic treatment of cloud and rain water mass and number concentration and a link between the cloud droplet number concentration (CDNC) and precipitation rates, which allows a realistic representation of the cloud lifetime effect. Advection of aerosol and scavenging of aerosol by clouds were also included in the model. This allows us to simulate the response of the stratus cloud properties to variations in ambient aerosol concentrations. The in-cloud production of sulfate by oxidation is an important source of interstitial aerosol after the cloud evaporates but is of less importance for the cloud itself and therefore is omitted in this study.

3.2 Simulation Setup

A 36-hr simulation at 50-km resolution was generated from 12Z 21 August to 0Z 2 September 1995 using initial and boundary conditions from the Canadian Meteorological Center regional analysis data. Subsequently, a series of one-way nested runs were carried out at 25, 15, and 3 km using the results from the coarser resolution run as initial and boundary conditions for the nested run (Fig. 1).

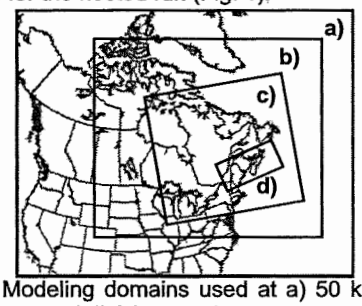

Figure 1: Modeling domains used at a) 50 km, b) 25 km, c) 15 km, and d) 3 km resolution.

At 50 km resolution, the convective and condensation processes were represented by the Kuo (1974) cumulus and the Sundqvist et al. (1989) stratiform parameterization and at 25 and 15 km resolution by the Fritsch and Chappel (1980) convective parameterization and the Kong and Yau (1997) explicit condensation scheme. Here we present results only from the 15 km simulation.

Corresponding author's address: Irena T. Paunova, Department of Atmospheric and Oceanic Sciences, McGill University, Montreal, Quebec, H3A 2K6, Canada; E-Mail: irena@zephyr.meteo.mcgill.ca.

explicit microphysics give better agreement with cloud statistics

comparison w/ soundings

The 15 km simulation was rerun with the CP00 double-moment microphysical parameterization and two cloud nucleation schemes, an empirical nucleation parameterization (Cohard et al., 1998) following Twomey's analytical approach (Twomey, 1959) for four-parameter CCN activity spectrum and the AG00 explicit nucleation scheme. This was the first time that the AG00 explicit nucleation scheme had been tested at this resolution.

Three experiments were compared. Experiment E842 used the empirical nucleation parameterization, where the CCN activity spectrum was derived using a size-resolving nucleation model and assuming a sulfate aerosol with number concentration 842 cm^{-3} (Fig. 2a). Experiments S1200 and M1200 used the explicit nucleation scheme. In experiment S1200 the initial aerosol consisted of sulfate particles with a number concentration of 1200 cm^{-3} (Fig. 2b) and in experiment M1200 the initial aerosol consisted of an external mixture of sulfate and sea-salt particles with a number concentration of 1200 cm^{-3} and 10 cm^{-3}, respectively (Fig. 2c). The initial aerosol size distribution was selected to fit the size distribution observed during the RACE flight F13C by Passive Cavity Aerosol Spectrometer Probe (PCASP) (0.14-2.75 μm in diameter) and by Fast Scattering Spectrometer Probe (FSSP) (1.31-28.58 μm in diameter). To ensure that relatively dry particles were sampled the values of FSSP counter were taken at relative humidity below 85%. The case represents a very polluted situation with aerosol number concentration reaching 1500 cm^{-3} close to the ground (Fig. 2d). For simplicity, the initial aerosol was assumed to be horizontally and vertically uniform.

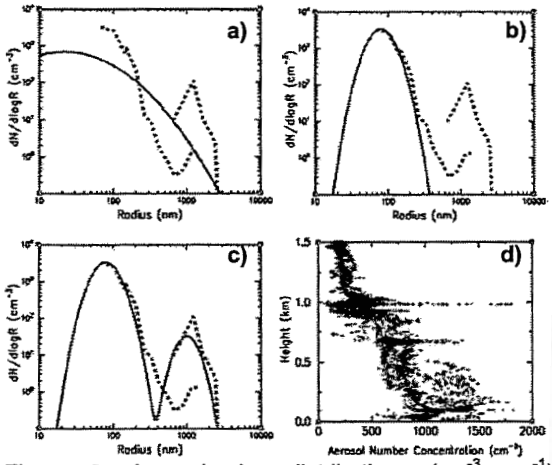

Figure 2: Aerosol size distributions (cm^{-3} nm^{-1}) observed during the RACE flight F13C by PCASC and FSSP counter (dashed lines) and superimposed log-normal size distributions used in a) E842, b) S1200, and c) M1200 experiment (solid line). d) Vertical profile of aerosol number concentration (cm^{-3}) during the RACE flight F13C.

To account for the effect of the small-scale variation of the updraft velocity on cloud nucleation at this resolution a subgrid-scale correction determined by the turbulent transport was added to the grid-mean vertical velocity following the approach of Lohmann et al. (1999). In simulations at cloud scale, the updraft velocity will be resolved explicitly and applying this correction will not be necessary.

4. MODELING EXPERIMENTS

4.1 RACE 1 September 1995 Marine Stratus Cloud

The occurrence of the RACE stratus cloud was associated with the passage of an upper-level ridge from 0Z to 18Z, which gave rise to deep large-scale mid-tropospheric subsidence, a typical formation mechanism for stratus clouds. At the lower levels, the cloud was associated with warm temperature advection caused by south-westerly winds.

A summary of the observed and simulated cloud properties is presented in Table 1.

	LWC ($g\ m^{-3}$)	CDNC (cm^{-3})	Base (m)	Thickness (m)
F13C	0.4-0.8	200-500	665-850	262-545
E842	0.3	25-30	560-1040	270-540
S1200	0.4-0.6	100-350	670-860	172-300
M1200	0.5-1.0	100-350	600-860	220-550

Table 1: Summary of the observed, RACE flight F13C, and simulated, E842, S1200, and M1200 experiments, stratus-cloud properties.

The numerical simulations with explicit cloud nucleation, S1200 and M1200, reproduced the aircraft and satellite observed cloud horizontal structure and position (Fig. 3). Similarly to the satellite image of the cloud, in the simulations with explicit nucleation the cloud extended from the land over the Bay of Fundy forming a clear boundary between the cloudy and the clear region over the Bay. The horizontally inhomogeneous structure of the cloud evident from the satellite image was only roughly simulated by the

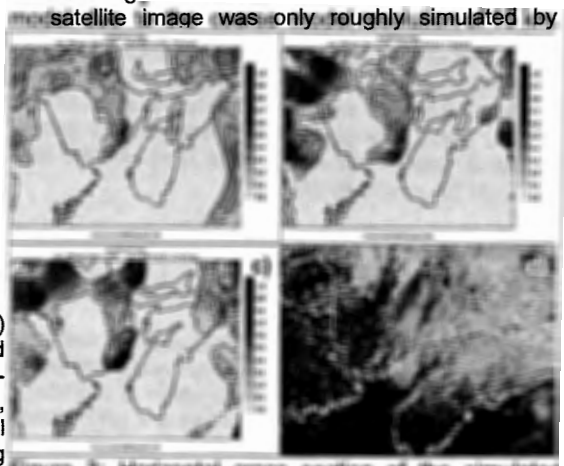

Figure 3: Horizontal cross section of the simulated cloud LWC ($g\ m^{-3}$) at 1040 m altitude for a) E842, b) S1200, and c) M1200 experiments. d) NOAA14 satellite visible image at 18Z on 1 September 1995.

Cloud scale simulations (~3 km resolution) are expected to improve this. In the simulation with empirical nucleation, E842, no cloud formed over water.

The vertical structure of the cloud was also reasonably simulated in all three simulations given the horizontal resolution (Fig. 4 and Fig. 5). In the simulations with explicit nucleation, the simulated cloud base and thickness reproduced very closely the observed cloud base and thickness. In the E842 simulation, the cloud position varied too much in vertical, southwestern end of the cloud was too high and the northeastern end was too low.

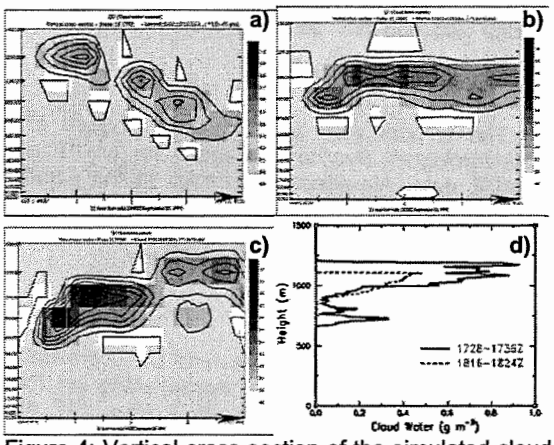

Figure 4: Vertical cross section of the simulated cloud LWC (g m^{-3}) for a) E842, b) S1200, and c) M1200 experiments. d) Vertical profiles of LWC observed around 1730Z (solid line) and 1820Z (dashed line) during the RACE flight F13C.

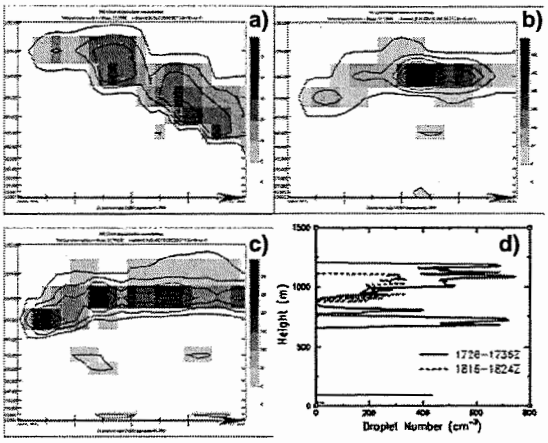

Figure 5: Vertical cross section of the simulated CDNC (cm^{-3}) for a) E842, b) S1200, and c) M1200 experiments. d) Vertical profiles of CDNC observed around 1730Z (solid line) and 1820Z (dashed line) during the RACE flight F13C.

Including explicit cloud nucleation improved also the simulated cloud liquid water content, LWC, (Fig. 4) and droplet number concentration, CDNC, (Fig. 5). In the simulation with empirical nucleation, E842, the cloud LWC, 0.3 g m^{-3}, compared reasonably with the observations, 0.4-0.8 g m^{-3}, but the CDNC was greatly under predicted, 25-30 cm^{-3} vs. 200-500 cm^{-3}. In the simulation with explicit nucleation, M1200, the cloud LWC, 0.4-1.0 g m^{-3}, and CDNC, 100-350 cm^{-3} compared best to the observed values.

Atmospheric soundings in the Bay of Fundy at 12Z, 6 hours prior to the occurrence of the cloud, show a very deep dry mid-tropospheric layer associated with subsidence, which is consistent with the typical formation mechanism of stratus clouds. Atmospheric soundings at 18Z in the cloud over water and over land are presented in Figure 6 and 7. All three simulations captured the capping inversion at the cloud top but the cloud top cooling was exaggerated. Due to the lack of vertical resolution, the simulations did not exhibit the sharp discontinuity of the sounding observed by aircraft. Over water and over land the below-cloud layer in all simulations was too warm and close to the surface it was too humid. In the E842 simulation, the below-cloud layer was also too dry giving rise to a higher cloud base. Overall, the M1200 sounding agreed best with the aircraft sounding.

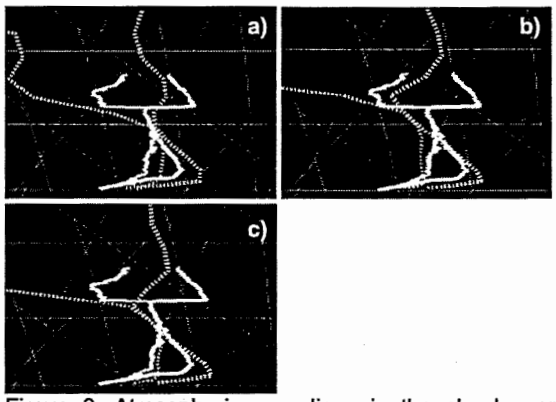

Figure 6: Atmospheric soundings in the cloud over land, observed (solid line) at 1730Z and simulated for a) E842, b) S1200, and c) M1200 experiment (dashed line) at 18Z.

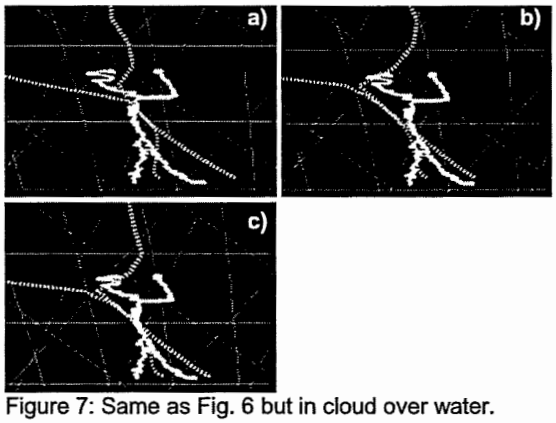

Figure 7: Same as Fig. 6 but in cloud over water.

4.2 Competition Between Sea-Salt and Sulfate Aerosol

In the previous section we demonstrated that including explicit cloud nucleation improved the simulated stratus cloud properties. In order to investigate the importance of the shape of the aerosol size spectrum (one-mode vs. multiple modes) for simulating cloud properties in a polluted atmosphere, it is insightful to study the sensitivity of the clouds and precipitation to changes in the aerosol spectrum. For this purpose we compared the cloud and precipitation patterns in S1200 and M1200 experiments associated with the low-pressure systems located upstream and downstream of the 1 September RACE stratus cloud. The comparison was done at 6Z, which is 12 hours prior to the time of the aircraft observations when the systems were most strongly developed.

In conditions of high sulfate number concentration (1200 cm^{-3}), the coarse sea-salt particles in the M1200 experiment competed for water vapor with the sulfate particles, which decreased the maximum supersaturation. This reduced the sulfate number activated in the M1200 experiment by 50-200 cm^{-3}, leaving more sulfate aerosol in the gas-phase (Fig. 8a). As a result, the droplet number concentration in this experiment decreased by 100-300 cm^{-3} (Fig. 8b), which enhanced the cloud autoconversion and accretion processes leaving less water in the cloud phase (Fig. 8c) more water in the rain phase (Fig. 8d) and initiating rain approximately 3 hours earlier than in the S1200 experiment.

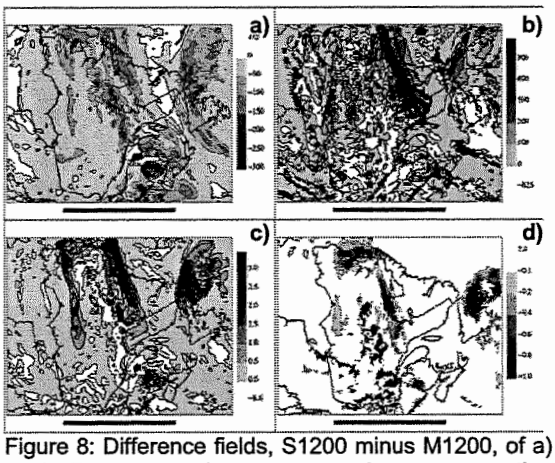

Figure 8: Difference fields, S1200 minus M1200, of a) vertically integrated aerosol number concentration (cm^{-3}) at 6Z, b) vertically integrated CDNC (cm^{-3}) at 6Z, c) cloud water path (g m^{-2}) at 6Z, and d) 1-hr rain accumulation (mm) at 1Z.

5. CONCLUSIONS

Simulations were conducted with the Canadian MC2 model at 15 km resolution to investigate the dependence of cloud properties on the atmospheric aerosol for a marine stratus cloud observed on 1 September 1995 during the RACE experiment. We demonstrated that after including explicit nucleation, the simulated cloud position and structure and most notably the simulated cloud water content and droplet number concentration were closer to the observed values compared to a simulation with an empirical treatment of nucleation. Furthermore, in sensitivity experiments we demonstrated that the shape of the aerosol spectrum has an important impact on the CDNC, cloud LWC and the timing and efficiency of rain formation at the regional scale.

In order to check if our findings are valid at cloud scales a higher-resolution modeling study is necessary. In addition, to study the effect of the cloud on the post-cloud aerosol size distribution, in-cloud sulfur oxidation must be included in the model.

6. ACKNOWLEDGEMENTS

The authors wish to thank Mark Couture of the Meteorological Service of Canada for providing the RACE data, Alexander Trischenko of the Canadian Space Agency for providing the satellite data, and Jason Milbrandt of McGill University for providing the code of the CP00 microphysical scheme.

6. REFERENCES

Abdul-Razzak, H., S.J. Ghan, and C. Rivera-Carpio , 2000: A parameterization of aerosol activation. Part II. Multiple aerosol types. *J. Geophys. Res.*, **105**, 6837–6844.

Banic, C. M., W. R. Leaitch, H., G. A. Isaac, M. C. Couture, 1996: Transport of Ozone and sulfure to the North Atlantic atmosphere during the North-Atlantic Regional Experiment. *J. Geophys. Res.*, **101**, 29091-29104.

Cohard, J.-M. and J.-P. Pinty, 2000: A comprehensive two-moment warm microphysical bulk scheme. Part I: Description. *Quart. J. Roy. Meteor. Soc.*, **126**, 1815-1842.

Cohard, J.-M., J.-P. Pinty, and C. Bedos, 1998: Extending Twomey's Analytical Estimate of Nucleated Cloud Droplet Concentrations from CCN spectra. *J. Atmos. Sci.*, **55**, 3348-3356.

Sundqvist H., E. Berge, and J.E. Kristjiansson, 1989: Condensation and cloud parameterizationstudies with a mesoscale numerical weather prediction model. *Mon. Wea. Rev.*, **117**, 1641-1657.

Fritsch J.M., and C.F. Chappel, 1980: Numerical prediction of convective driven mesoscale pressure system. Part I: Convective parameterization. *J. Atmos. Sci.*, **37**, 1722-1733.

Kong, F.-Y., and M.K. Yau, 1997: An explicit approach of microphysics in MC2. *Atmos.-Ocean*, **35**, 257-291.

Kuo, H.L., 1974: Further study on the parameterization of the influence of convection on large-scale flow. *J. Atmos. Sci.*, **31**, 1232-1240.

Lohmann, U., N. McFarlane, L. Levkov, K. Abdela, and F. Alberts, 1999: Comparing different cloud schemes of a single column model and using mesoscale forcing and nudging technique. *J. Clim.*, **12**, 438-461.

PREDICTION AND OBSERVATION OF AEROSOL PROCESSING BY A CUMULUS: EVIDENCE FOR PARTICLE REMOVAL AND NUCLEATION IN CLOUDS

Justin R. Peter[1,2], Steven T. Siems[1], Jørgen B. Jensen[3], John L. Gras[4], Yutaka Ishizaka[5], and Jörg Hacker[6]

[1]School of Mathematical Sciences, Monash University, Clayton, Australia
[2]Advanced Study Program, NCAR, Boulder, CO, USA
[3]Atmospheric Technology Division, NCAR, Boulder, CO, USA
[4]CSIRO, Division of Atmospheric Research, Aspendale, Australia
[5]Hydrospheric Atmospheric Research Center (HyARC), Nagoya University, Nagoya, Japan
[6]Flinders University/Airborne Research Australia, Adelaide, Australia

1. INTRODUCTION

In this paper we analyze airborne observations of cloud processing of aerosol by a cumulus. In particular we focus on two problems concerning the aerosol size distribution and its modification via cloud processes.

(1) *Changes in the aerosol size distribution due to in-cloud processes.* During the processing of an air parcel by a cloud, both the aerosol's size and composition are modified via various in-cloud processes. First, a fraction of the aerosol particles are activated and grow into cloud droplets, a process known as *nucleation scavenging*. Upon cloud evaporation, the aerosols are returned from the dissipating cloud droplets back to the sub-saturated atmosphere. If the only process occurring within cloud were that of nucleation scavenging then the aerosol detrained from the cloud would have the same properties as the aerosol originally ingested into the cloud. However, other cloud processes can modify the aerosol distribution. Cloud droplets can scavenge water-soluble trace gases, such as sulfur dioxide thereby increasing the size of the aerosol after evaporation of cloud droplets. Also, the unactivated fraction of aerosol, interstitial in the cloud can diffuse to cloud droplets, again increasing the size of the aerosol distribution. Cloud droplets may also coalesce within cloud decreasing the aerosol number concentration while increasing the size of the aerosol. If precipitation falls from the cloud, then there will be a loss of aerosol particles in cloudy air.

(2) *New particle formation in the region of a cloud.* Another climate-relevant modification of the aerosol size distribution can occur due to generation of ultra-fine aerosol in the vicinity of clouds. Several field experiments have observed new particle formation either in the outflow of clouds (Wiedensohler et al. 1997) or above cloud top (Weber 2001). Fresh particles are thought to be nucleated when gaseous precursor species, sulfur dioxide (SO_2) and dimethyl sulfide (DMS) are present in sufficient concentrations. Under conditions of high relative humidity, low pre-existing surface area and low temperatures, SO_2 and DMS will oxidize with hydroxl radicals to form sulfuric acid (H_2SO_4). New particles are then formed via homogeneous bi-molecular nucleation of H_2SO_4 and H_2O.

Corresponding author's address: Justin R. Peter, National Center for Atmospheric Research, P.O. Box 3000, Boulder, CO 80307-3000; E-Mail: justinp@ucar.edu.

2. EXPERIMENTAL DETAILS

2.1 Synoptic Situation

Satellite observations (Fig. 1) taken at 11:31 Japanese Standard Time (JST is UTC + 9 hours) revealed an isolated, thin, curved band of cumulus clouds to the south of the island of Shikoku and to the east of Kyushu. The cumulus band was in a near steady state, having held a consistent vertical structure for at least two hours before the observational period. The cloud band was observed to be heading nearly due south, and maintained an extent of roughly 200 km from north to south over the course of the day.

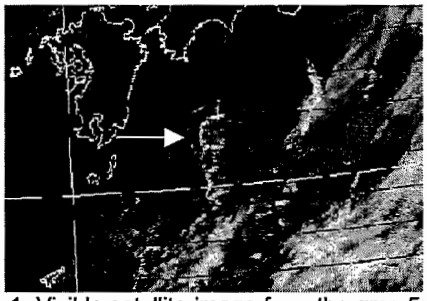

Figure 1. Visible satellite image from the gms-5 visible spectrum satellite taken at 0330 UTC (12:30 JST). A cloud band associated with a cold front is seen at the eastern edge of the image. The Cu system examined was the horseshoe shaped feature near the center of the image, indicated by the arrow.

2.2 Flight Paths

The Airborne Research Australia (ARA) King Air spent approximately two hours on station, encountering the cloud just after 12:00 JST at 133.1° E, 30.5° N. The aircraft drifted with the prevailing wind over this time in order to maintain a Lagrangian view of the cumulus band. The flight path allowed for a

see how aerosols are modified by cloud processes in cumulus

many diagrams measured and observed aerosol spectra

series of six horizontal legs perpendicular to the cloud band and two soundings on the upwind side of the cumulus. Flight legs were flown roughly along an east-west heading. Fig. 2 presents a two dimensional projection of the flight path (horizontal flight legs are numbered) and sketches where the cumulus band was encountered. The left-hand side of the diagram is to the west of the cloud band, in the upwind air. The term upwind is used with reference to the wind direction in the free troposphere. Though not strictly true in the boundary layer, the term upwind is adopted to refer to observations obtained to the west of the cumulus band. The King Air approached the air mass on the downwind (right-hand) side and departed the region with the ascent sounding on the upwind side.

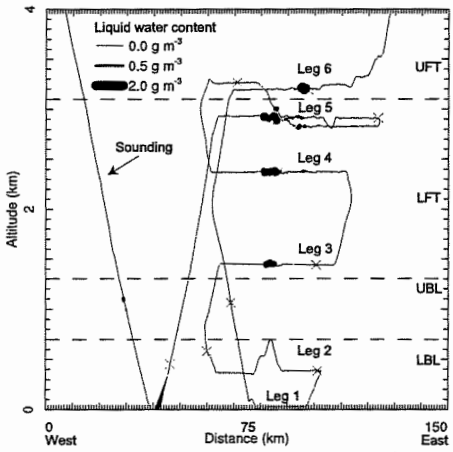

Fig. 2 Projection of the flight path onto the vertical plane The flight path has been corrected for advection by 1.5 ms^{-1} towards west. The aircraft entered the picture at the top right hand and exited at the top left. The heavier portions indicate the liquid water content as measured with the FSSP probe. LBL- lower boundary layer; UBL- upper boundary layer; LFT- lower free troposphere; UFT- upper free troposphere.

3. MIXING ANALYSIS

Fig. 3 shows a thermodynamic diagram (Paluch 1979) for flight Leg 3, using two parameters that are conserved for adiabatic motions where there is no precipitation; the total water mixing ratio (Q_{tot}) and wet equivalent potential temperature (θ_q). Total water mixing ratio includes water vapor, liquid water and precipitation. The advantage of using θ_q and Q_{tot} is that they mix linearly, or in the case of θ_q nearly linearly (Paluch 1979).

The direct measurement of cloud base air in Fig. 3 is marked with a large "+" sign and is located toward the top of the figure. The values of θ_q and Q_{tot} from the far upwind sounding are shown for all measurements above cloud base height; the labels along the sounding θ_q , Q_{tot} curve indicate pressure level. The dots on Fig. 3 represent 1-second averages of the thermodynamic state of the cloud free air from Leg 3, extending 6 km upwind and 11.5 km downwind of the cumulus band.

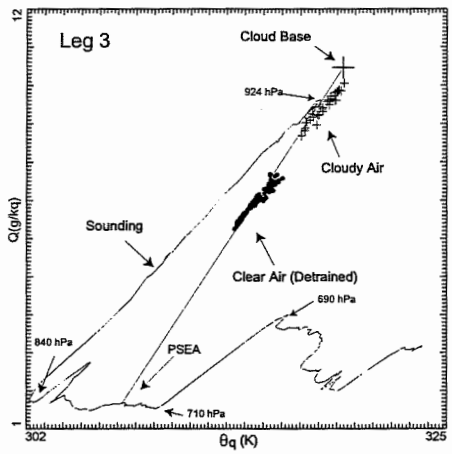

Figure 3. Mixing diagram for flight leg 3. Cloud base, sounding, cloudy air and clear air points are labeled. In-cloud and clear air points are 1-second values. The primary source of entrained air (PSEA) is indicated where the line of best fit between cloud base and the clear air measurements intersect the sounding.

Crosses represent 1-second data obtained from cloudy air. In this context, cloudy air was defined as having a LWC ≥ 0.5 gkg^{-1}, as measured by both the King and FSSP probes. Sub-saturated patches within the cloud were excluded utilizing high rate (64 Hz) liquid water data. In this manner, all 64 samples (measured with the King probe) within a 1 Hz interval were excluded if at least one had a LWC ≤ 0.1 gkg^{-1}. Clear air was considered as having a LWC ≤ 0.01 gkg^{-1} with the additional constraint that all 64 samples determined from the high rate data had a LWC ≤ 0.01 gkg^{-1}. In Fig. 3 there is a striking linearity of both in-cloud and clear air points, indicating linear mixing of sub-cloud and environmental (upwind) air. When cloudy or detrained θ_q, Q_{tot} samples form a highly linear pattern as shown in Fig. 3, then we can determine the Primary Source of Entrained Air (PSEA) (Jensen et al., 1985). The PSEA is determined from the point at which the line of best fit through either the cloudy or clear air points and the cloud base point intersects the sounding. The line of best fit through the clear air points and cloud base is shown in Fig. 3 and indicates a PSEA for the clear air of about 2100 m. It should be noted that the PSEA is not a single narrow level but rather an entrainment region located around the PSEA, however the strong linearity exhibited in Fig. 3 of both the in-cloud and clear air measurements precludes significant mixing from levels other than the PSEA.

The fraction of cloud base air F, in each cloudy sample or clear air sample can then be estimated as (Jensen et al., 1985),

$$F \approx \frac{1}{2}\left(\frac{\theta_q - \theta_{q,e}}{\theta_{q,b} - \theta_{q,e}} + \frac{Q - Q_e}{Q_b - Q_e}\right) \quad (1)$$

where subscript *e* refers to environmental air and *b* refers to cloud base air. The average value of the fraction of cloud base air in clear detrained air, (F_{clr}), is F_{clr}=0.66 (see Fig. 3).

4. COMPARISON OF PREDICTED AND OBSERVED SPECTRA

Based on the mixing argument presented in the previous section, the aerosol spectrum in the downwind air can be predicted by taking into account mixing of sub-cloud and entrained air. Assuming that the aerosol only undergoes nucleation scavenging within cloud, the aerosol subsequently detrained from cloud will mix in similar proportions to the air, as determined by the conserved variables Q_{tot} and θ_q. The aerosol size distribution in the detrained air obtained in this manner will be termed the *predicted* spectra. After using mixing analysis to predict the detrained aerosol spectrum, we compare the predicted and observed detrained aerosol spectra to examine: (1) cloud droplet scavenging of aerosol; and (2) Brownian coagulation of ultra-fine nuclei to cloud droplets within cloud. A model of Brownian coagulation is constructed to ascertain the contribution of the processes to the discrepancy between the predicted and observed aerosol number size distributions. In the case of Brownian coagulation of aerosol to cloud droplets, the comparison of the spectra observed to that predicted by mixing, coupled with numerical calculations of aerosol loss, is used to examine evidence of particle production.

Fig. 4 shows particle size distributions as determined by the TSI-3025, TSI-3010 and ASASP probes for sub-cloud, upwind and downwind clear air regions relative to the cloud band. The sub-cloud spectrum was obtained from the westerly level portion of Leg 2. Though not shown, analysis of the dynamics from leg 2 indicated that the boundary layer in-flow to the cloud was from this region. The detrained spectrum is from the cloud free horizontal portion east of the cloud band in Leg 3, and corresponds with the time representing clear air points on Fig. 3. The upwind spectrum is taken from the portion of the ascent corresponding to the source of entrained air as determined from the mixing diagram (Fig. 3). The concentrations from the three regions are also indicated in Fig. 4. The detrained spectrum is seen to be of an intermediate concentration with respect to the entrained and sub-cloud spectra. This is due to the fractional mixing of sub-cloud and entrained air, induced by convection.

The spectra exhibit similar shapes, however differences are apparent in the number concentrations for each of the regions. The number concentrations of both the entrained and detrained spectra are consistently lower than the concentrations of the cloud base spectra, except for particles larger than approximately 0.8 μm.

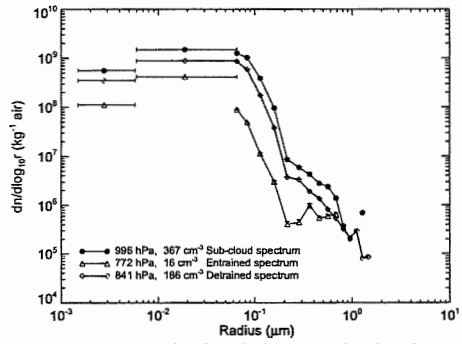

Figure 4. Spectra obtained from sub-cloud, upwind (entrained) and downwind (detrained) for Leg 3. The aerosol number concentrations as measured by the ASASP are indicated. The pressure level from which each distribution was sampled is also given.

4.1 Prediction of the Aerosol Size Distribution due to Mixing

To investigate the contribution of mixing of sub-cloud and upwind air to the observed spectrum downwind, the mixing arguments of Section 3 were employed. The detrained air is comprised of an average fraction *F*=0.66 of sub-cloud air detrained and 1-*F*=0.34 of environmental air entrained from upwind of the cumulus band. Here we make a comparison of the observed spectra with that predicted by mixing. The analysis is restricted to Leg 3, where we are confident of the reliability of the thermodynamic measurements and thus of the mixing fractions.

Assuming that the downwind spectra contain a mixture of cloud base and upwind aerosol, with mixing fractions determined by the F-fraction, and that the aerosol only undergo nucleation scavenging, a bin-by-bin comparison of the spectra predicted by mixing and that observed can be made. If the concentration of aerosol in bin *i* is denoted n_i then,

$$n_{i,pre} = F(n_{i,s}) + (1-F)n_{i,e} \quad (2)$$

where the subscripts *pre*, *s* and *e* indicate predicted, sub-cloud and entrained concentrations respectively.

The ratio of the predicted to the observed spectra is shown in Fig. 5. The error bars represent the addition of percentage uncertainties for each size bin. It is seen that the observed spectrum is consistently less than that predicted by mixing, except for the first size bin of the ASASP. Had only nucleation scavenging occurred, the aerosol population after cloud evaporation would return to its original form, and we would expect the ratio in each bin to be unity. This is not the case however, and the ratio less than unity shows that a significant fraction of the aerosol particles were

scavenged, through either coagulation or precipitation removal.

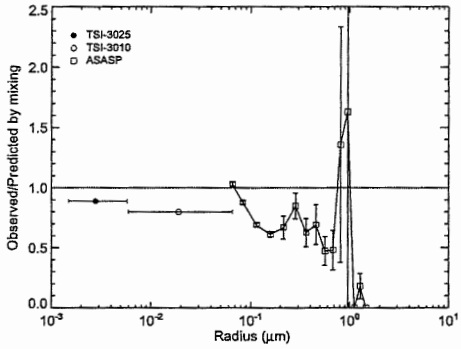

Figure 6. Comparison of the observed spectrum and the predicted spectrum. The spectrum predicted by mixing is given by $n_{i,pre} = Fn_{i,b} + (1-F)n_{i,e}$, where $n_{i,b}$ and $n_{i,e}$ represent the number of aerosol in each size class of the sub-cloud and entrained spectra respectively. The fraction of cloud base air is given by F.

The overall reduction (the average of the ratio for the TSI-3025, TSI-3010 and first six size classes of the ASASP) is approximately 30%. Observations of drizzle rate in-cloud during Leg 4 revealed a rate of 0.07 mm hr^{-1}, indicating that such a large loss of aerosol is unlikely to be due to precipitation scavenging. Coalescence scavenging, possibly enhanced by turbulent collection (e.g. Pinsky 1999) is a plausible candidate for the overall reduction of aerosol.

4.2 Interstitial scavenging of ultra-fine particles by cloud droplets

A simple model was used to determine if diffusional loss of ultra-fine particles to cloud droplets could account for the observed decrease in particles observed by the TSI-3025 and TSI-3010. The term ultrafine refers to the particles sizes located between the two CN counters i.e. 1.3 nm $\leq r_p \leq$ 6 nm. Interstitial aerosol particles are assumed to collide with cloud droplets and are removed from cloud interstitial air. The rate of such removal is governed by coagulation theory. Let $n_a(r_p,t)$ and $n_d(x,t)$ represent the aerosol and cloud droplet number distributions, respectively. The loss rate of aerosol particles per unit volume of air due to diffusional loss to cloud droplets is determined by,

$$\frac{-\partial n_a(r_p,t)}{\partial t} = n_a(r_p,t)\int_0^\infty K(r_p,t)n_d(x,t)\,dx \qquad (3)$$

where $K(r_p,x)$ is the collection coefficient and $n_a(r_p,t)$ and $n_d(x,t)$ are the aerosol and cloud droplet number distributions respectively. If the scavenging coefficient does not vary with time (i.e. if the drop distribution that the aerosol are diffusing to is stationary) then the number of aerosol $n_a(r_p,t)$ remaining after a time t, will be,

$$n_a(r_p,t) = n_a(r_p,0)\exp[-\Lambda(r_p,t)] \qquad (4)$$

where $\Lambda(r_p,t)$ is the scavenging coefficient and is given by the integral in Eq. (3). Equations (3) and (4) were solved with the assumption of a constant droplet size distribution. The droplet size distribution, $n_d(x,t)$ used was that measured by the FSSP during the cloud penetration of Leg 3. The results of the calculation are shown in Fig. 6. The series of dotted curves represent the fraction of particles scavenged by diffusion to cloud droplets. Curves are shown for times ranging from 10 minutes to one hour at ten-minute intervals, representative of a potential cloud lifetime. It can be seen that most, if not all of the ultra-fine particles should be removed by Brownian diffusion. The fact that any ultra-fine particles are being observed in the detrained cumulus air is indicative of particle nucleation.

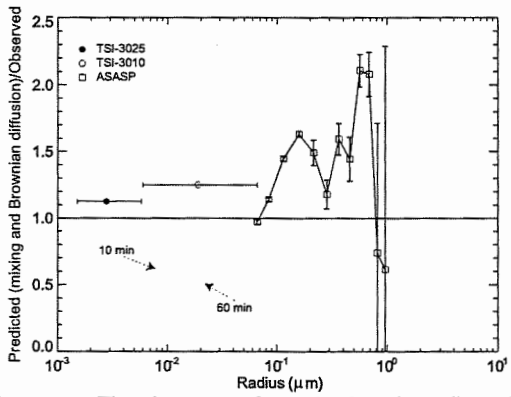

Figure 6. The inverse of Fig.5, but including the predicted spectrum due to loss of ultra-fine particles measured by the TSI counters. The majority of these particles should have been scavenged by cloud droplets, but there is still a measurable amount of these particles, albeit less than predicted by mixing.

3.8 References

Jensen, J., P. Austin, M. Baker, and A. Blyth, 1985: Turbulent mixing, spectral evolution and dynamics in a warm cumulus cloud., J. Atmos. Sci., 42, 173-192.

Paluch, I., 1979: The entrainment mechanism in Colorado cumuli., J. Atmos. Sci., 36, 2462-2478.

Pinsky, M., A. Khain, and M. Shapiro., 1999: Collision of small drops in a turbulent flow. Part 1: Collision efficiency, problem formation and preliminary results., J. Atmos. Sci., 56, 2585-2600.

Why cloud free air in marine stratus areas

AEROSOL AND POCKETS OF OPEN CELLS

M. D. Petters[1], Jefferson R. Snider[1] and Ian C. Faloona[2]

[1]Department of Atmospheric Science, University of Wyoming, Laramie, WY 82071, USA
[2]Department of Land, Air and Water Resources, University of California, Davis, CA 95616-8627, USA

1. INTRODUCTION

Factors determining the cloud fraction over regions where low-lying marine stratiform clouds dominate are one critical component for understanding the global climate system. Pockets of seemingly cloud-free air embedded in these clouds have been described by Stevens et al. (2004). These were named Pockets of Open Cells (POCs) and characterized as "coherent and long-lived" features that are "reminiscent of open cellular convection" and are "coupled to the development of precipitation". Because regions of POCs are of large areal extent, long-lived, and shown to be associated with an overall reduction in cloud fraction, these features require further investigation.

Here, our objectives are twofold: 1) we present an analysis of the vertical structure of the marine boundary layer (MBL) in the core regions of the pockets, and 2) suggest that there is a relationship between that structure and aerosol microphysical properties.

2. BRIEF REVIEW

Low-lying marine stratocumulus clouds form in the summer over the subtropical oceans. There, the boundary layer is typically structured in two layers, a below-cloud layer and a cloud-layer. The top of the cloud layer, and the boundary layer, is defined by a strong capping inversion separating the MBL from the free troposphere (FT). There has long been speculation that a subset of the aerosol, the cloud condensation nuclei (CCN) can play a critical role in the formation (Hegg, 1999), lifetime (Albrecht, 1989), and dissipation (Ackerman et al., 1993) of these clouds. These authors focused on connections between CCN, the generation of drizzle, and CCN scavenging in marine stratocumulus. One important effect of drizzle production is the reduction in the height-integrated cloud liquid water content, commonly known as the cloud liquid water path (LWP). Where the LWP is reduced, infrared (IR) radiative cooling rates are small and MBL dynamics may be altered (Stephens, 1978; Nicholls, 1984). These feedbacks are evident in the model developed by Ackerman et al. (1993) which demonstrates a mechanism for a stably-stratified stratocumulus layer to collapse and the cloud transition to a sea fog. Stevens et al. (1998), in their simulation of drizzling and non-drizzling stratocumulus, show that drizzle stabilizes the boundary layer via its action on the budgets of heat and water substance. The models of Stevens et al. (1998) and Ackerman et al. (1993) focus on the dynamical response of the MBL to changes in CCN. Contrast this to the study by Hegg (1999), who used a parcel model to illustrate that when CCN are very low they modulate shortwave (SW) cloud optical depth by shunting droplets into drizzle mass during the early stages of condensational growth. As a consequence, ascending parcels loose appreciable LWC before they reach the inversion.

Corresponding author's address: Markus D. Petters, Dept. 3038, 1000 E. University Ave. Laramie, WY 82071, USA; E-Mail: petters@uwyo.edu

3. DATA AND INSTRUMENTATION

Our data was collected within the remote subtropical eastern Pacific MBL on July 11, 2001 (RF2). At that day, the NCAR C-130 conducted a nocturnal Lagrangian study of the evolution of the Dynamics and Chemistry of Marine Stratocumulus clouds (DYCOMS-II, Stevens et al., 2003). The flight employed a stepped circular flight pattern conducted both in the MBL and FT. The centerpoints of the circle were repositioned using C-130 wind data acquired during the previous circle. During RF2, the repositioned centerpoints lagged positions computed from post-flight calculations of the wind. Although this was unintentional and introduced complications to our analysis, it allowed us to obtain a more complete picture cloud and aerosol characteristics during the late evening of July 10 and morning of July 11 (all times presented here are UTC, and LT = UTC - 8 h).

We utilize data from an array of probes that were deployed on the NCAR C-130 to measure: updraft velocity (w, Rosemount Model 1221F1VL, mean w was forced to zero over one circle), downwelling IR irradiance ($F_{IR\downarrow}$, Eppley PIR pyrgeometer), Aitken mode particles ($0.01 < D < 0.13$ μm, radial differential mobility analyzer: RDMA) accumulation mode particles (ACM, $0.1 < D < 3.0$ μm, DMT SPP-200), condensation nuclei (CN, TSI 3760), cloud condensation nuclei (CCN, see Petters et al., this issue), potential temperature (θ, derived from Rosemount Type 102 temperature (T) and Ruska Model 7885 pressure), cloud droplet number concentration (CDNC, $1.0 < D < 47.0$ μm, DMT SPP-100), downward viewed

vertical structure of marine boundary layer and how influences aerosols & microphysics

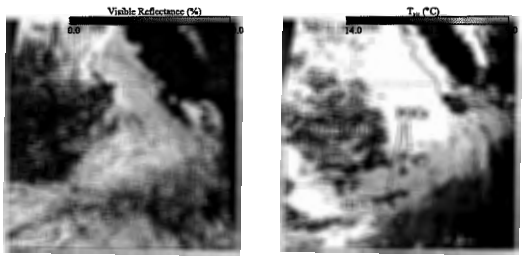

Figure 1. GOES-10 visible reflectance on July 10, 1800 UTC (left panel) and T_{b11} on July 11, 1300 UTC (right panel, adapted from Stevens et al. (2004)). The circle (left panel) corresponds to the position of the air thought collocated with the C-130 on July 11, 1300 UTC based on a finite-difference extrapolation from that point of collocation (left panel) and the flight circle corresponding to the time of the satellite data (right panel).

radiative temperature (T_H, Heimann KT19.85), altitude (z, GPS), radar reflectivity factor (Z, University of Wyoming 95 GHz Cloud Radar, WCR), and relative humidity (RH, derived from T, and General Eastern 1011B dew-point temperature).

Satellite brightness temperature at 11 μm wavelength (T_{b11}) was obtained from channel 5 of the geostationary operational environmental satellite (GOES-10, 4x4 km) or channel 5 of the NOAA-12 polar orbiting advanced very high resolution radiometer (AVHRR, 1x1 km).

3.1 Data Processing

CCN and ACM In the measurement community, CCN are defined as particles that activate to form cloud droplets when subjected to a fixed, or systematically-varying, water supersaturation within a droplet growth chamber. Here, we will utilize ACM, obtained from the DMT SPP-200, as a surrogate for CCN. The utilization of ACM is motivated by our need for CCN data at a rate substantially larger than those provided by the two UWyo CCN instruments (0.03 Hz) and justified because measured CCN concentrations (0.48% supersaturation) are generally consistent with aerosol size and chemistry data (Petters et al., this issue).

Aerosol Measurements Due to unrealistically high spectral densities encountered in the the fist channel of the SPP-200 instrument we disregarded these data. Data from the SPP-200 and RDMA instruments was utilized to construct a composite aerosol size spectrum (see Petters et al., this issue). When Aitken mode particles were present, concentrations derived from integrated composite size spectra underestimated those observed by the TSI 3760 by 40%. We attribute this to wall losses of small particles in the RDMA instrument.

Liquid Water Shattering Aerosol data (RDMA, SPP-200, and CN) concurrent with the observation of drizzle or cloud droplets (± 1 s), are suspect due to liquid water shattering and are excluded from the data.

WCR Due to power leakage, we removed the first three range gates of the radar reflectivity data. The data was thresholded five standard deviations above the mean noise level and interpolated onto a regular time-altitude grid (25 Hz x 20 m).

4. RESULTS

Figure 1 shows satellite data prior and during the research flight. The visible reflectance image demonstrates, that where open cells dominate, cloud fraction is reduced. During the night, increased values of T_{b11} indicates that the same area is transparent to IR radiation originating at the sea surface. The T_{b11} image also shows the POCs embedded in the stratiform cloud layer. Closer examination reveals that the POCs consist of several core and wall regions. The former are seemingly cloud-free and the latter are composed of cloud and often drizzle extending to the sea surface.

4.1 *In Situ* Data

Figure 2 shows a summary of C-130 data acquired below-cloud and in-cloud. The 9 bottom-left panels are in azimuth coordinates (Φ, degrees) around the 60 km circle. Here, $\Phi = 0°$ indicates the most northern point on the C-130 circle and larger values of Φ progress clockwise from that reference point. Core regions of the pockets (cores) are detected by decreased $F_{IR\downarrow}$ during the below-cloud segment (bottom-left panels). In the cores, turbulence is vigorous, ACM concentrations are reduced, and CN concentrations are enhanced.

During the in-cloud segment (middle-left panels), cores are detected by increased T_H. Here, we employ θ as tracer of FT air and CDNC to determine whether or not it is cloudy. Observe the increase in θ at $30° < \Phi < 110°$. These increases are thought due to the presence of FT air that altitude of the circular flight segment. Contrast this to the POCs region ($260° < \Phi < 355°$), where θ is steady, suggesting that these cores are a feature generated within the MBL and are not a consequence of an encroachment of free tropospheric air into the MBL. Turbulence is reduced in the vicinity of some cores ($\Phi \approx 280°$), but updraft velocities exceeding 0.3 m s^{-1} persist in others. Reduced turbulence intensities are consistent with the absence of radiative cooling and latent heat release due to condensation in the cores.

The top-left panels are an inset of the in-cloud data from the POCs region. Observe the correlation at fine scales and at lower resolution, between the T_H and the WCR reflectivity time-versus-height data. Also observe that some cores are characterized by weak WCR reflectivity values below. At flight level, cores are cloud-free (CDNC = 0 cm^{-3}) and ACM is generally below 40 cm^{-3}. In two cores (130340 - 130400 and 130550-130610 UTC) ACM is < 2 cm^{-3}. Contrast the

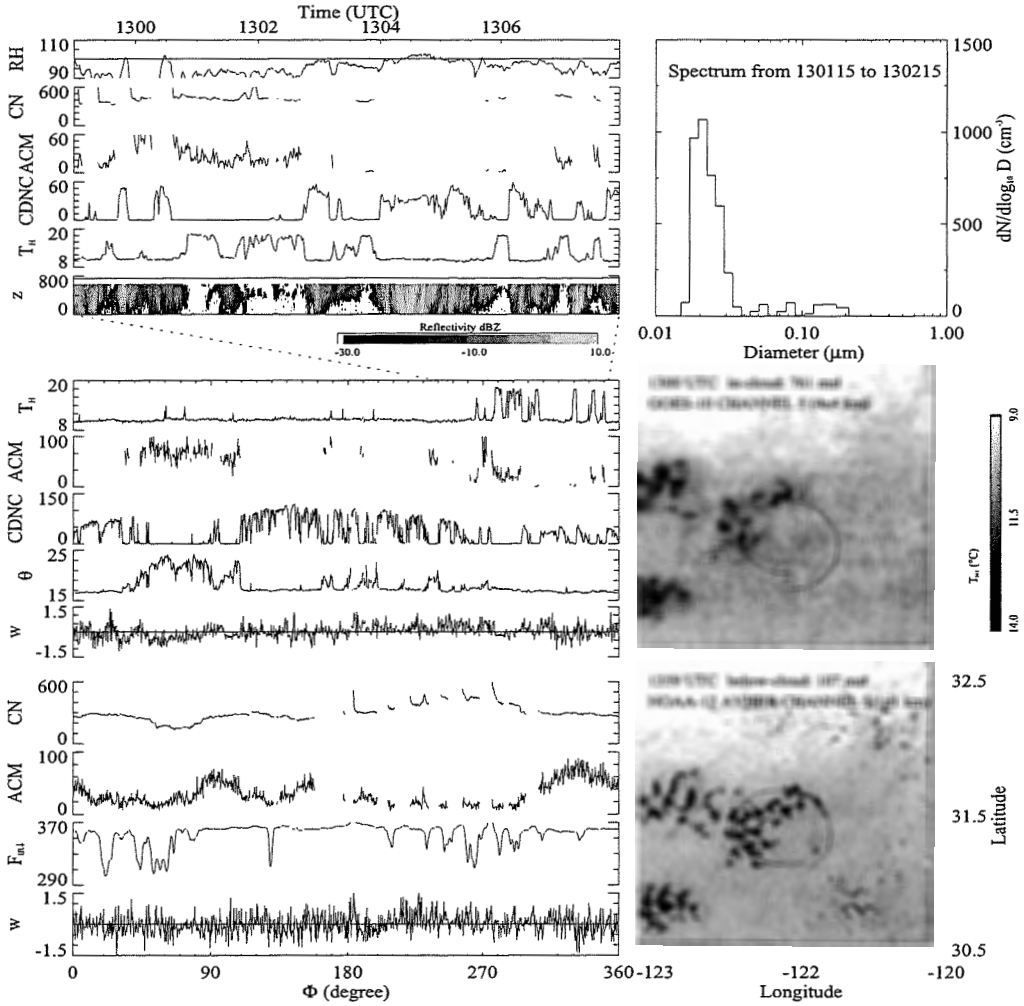

Figure 2. C-130 data corresponding to the below-cloud circle (1330-1400 UTC, bottom panels), in-cloud circle (1255-1325 UTC, middle panels), and the northwest quadrant of the in-cloud circle (top panels). The right panels show T_{b11} (°C) form the NOAA-12 AVHRR (bottom-right panel), T_{b11} form the GOES-10 satellite (middle-right panel), and the particle composite size spectrum (upper-right panel). Times in the right panels indicate the time of the satellite data (bottom-right and middle-right panel) and acquisition time range of the composite size spectrum (upper-right panel). On the satellite images, the flight track is superimposed and the aircraft indicates the position of the C-130 at the time of the satellite image. The units are w (m s^{-1}), $F_{IR\downarrow}$ (W m^{-2}), ACM (cm^{-3}), CN (cm^{-3}), θ (°C), CDNC (cm^{-3}), T_H (°C), z (msl), RH (%). The 6 upper-left panels are an inset of the in-cloud data (260° < Φ < 355°) with the corresponding times (UTC) indicated at the top. The image in the lowest of these panels is time-versus-height WCR reflectivity (dBZ) and the horizontal line indicates the C-130 flight level. The white color corresponds to data below the noise threshold (Section 3.1).

low ACM (0-40 cm^{-3}) to the large CN ($\approx$ 400 cm^{-3}) in the cores. Large CN-to-ACM ratios indicate the presence of Aitken mode particles, an assertion confirmed by the composite size spectrum shown in the upper-right panel. Furthermore, note that in the cores the air is slightly subsaturated at flight level. Observe, that adjacent to the cores, the droplet concentrations are below 60 cm^{-3} and that the radar reflectivities extend to the sea surface.

To summarize, the observations describe the cores as a MBL composed of three layers. These layers are: 1) a below-cloud layer, 2) a thin cloud layer, and 3) a "third" layer sandwiched between the cloud-top and the top of the MBL. In the below-cloud layer, ACM are low, turbulence is vigorous and CN are enhanced. The cloud-layer is characterized by weak WCR reflectivities. In the third layer cloud droplets are not observed, ACM concentrations are low, CN-to-ACM ratios are

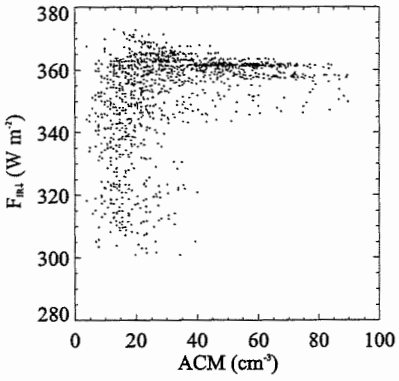

Figure 3. Scatterplot of ACM concentration and $F_{IR\downarrow}$ for the below-cloud data shown in Figure 2.

large, turbulence intensities are reduced, and the air is slightly subsaturated. The fact that aerosol properties in-cloud (1259-1307 UTC, ACM < 40 cm^{-3}, and CN $\approx$ 400, in-cloud POCs region) agree with those below cloud ($200 < \Phi < 300$, below-cloud POCs region) indicates that the air is well-mixed through the three layer boundary layer.

5. DISCUSSION

Curious is the observation of Aitken mode particles in the MBL. The observations show that CN-to-ACM ratios (an indicator for Aitken mode particle concentration) are large everywhere below-cloud and also large in the cores in-cloud. But in the wall regions and elsewhere in-cloud, CDNC is generally below 100 cm^{-3}. This suggests that the Aitken mode particles do not contribute to the cloud droplet concentrations. Parcel model calculations confirm that if the Aitken mode was composed of NaCl, droplet concentrations should be much larger than those observed. Thus we believe that the Aitken mode particles are non-hygroscopic. Furthermore, the origin of these particles appears to be within the MBL because we did not observe Aitken mode particles in the FT. Other investigators reported particle growth rates of 0.005 - 0.01 $\mu m\ h^{-1}$ for freshly nucleated particles in the MBL. From these observations we conclude that the Aitken mode particles we document could have been formed between 1500 and 2100 UTC on the previous day (July 10) in the MBL.

Figure 3 suggests that there is an important connection between aerosol microphysical properties and the three layer MBL structure. Where ACM concentrations are below 40 cm^{-3}, $F_{IR\downarrow}$ is decreased. This observation is consistent with data obtained in the core regions of the pockets in the third layer, where ACM concentrations are below 40 cm^{-3} as well. Our observations are also in accord with model results (Hegg, 1999) showing that decreasing CCN concentration modulate decreasing LWP and SW optical depth. If these pockets are indeed the consequence of low ACM concentrations, then small perturbations of the aerosol (e.g. anthropogenic pollution or increases in wind speed) may destroy the pockets and dramatically increase the cloud fraction over these regions.

During the daytime, the third layer may be a favorable environment for homogeneous particle nucleation. There, the actinic flux is large, ACM concentrations are low, and the relative humidity is large, especially close to cloud-top. This may explain the observation by Hegg et al. (1991), who show thin layers of elevated CN-to-CCN ratios close to the diffuse tops of coastal stratocumulus observed in the morning hours over the northeast Pacific.

6. CONCLUSIONS

We demonstrate that in core regions of pockets of open cells the marine boundary layer is divided into three layers. We assert that this third layer is the consequence of low ACM concentrations and that it may be a favorable environment for homogeneous particle nucleation in the MBL.

7. REFERENCES

Ackerman, A. S., O. B. Toon, and P. V. Hobbs, 1993: Dissipation of marine stratiform clouds and collapse of the marine boundary layer due to the depletion of cloud condensation nuclei by clouds. *Science*, **262**, 226–229.

Albrecht, B. A., 1989: Aerosols, cloud microphysics, and fractional cloudiness. *Science*, **245**, 1227–1230.

Hegg, D. A., 1999: Dependence of marine stratocumulus formation on aerosols. *Geophys. Res. Lett.*, **26**, 1429–1432.

Hegg, D. A., R. J. Ferek, P. V. Hobbs, and R. R. Lawrence, 1991: Dimethyl sulfide and cloud condensation nucleus correlations n the northeast pacific ocean. *J. Geophys. Res.*, **96**, 13,189–13,191.

Nicholls, S., 1984: The dynamics of stratocumulus: aircraft observations and comparisons with a mixed layer model. *Quart. J. Roy. Metor. Soc.*, **110**, 783–820.

Petters, M. D., J. R. Snider, C. Twohy, and J. Anderson: this issue, Prediction of cloud condensation nuclei from particle physiochemical data.

Stephens, G. L., 1978: Radiation profiles in extended water clouds. I:Theory. *J. Atmos. Sci.*, **35**, 2111–2122.

Stevens, B., W. R. Cotton, G. Feingold, and C. Moeng, 1998: Large eddy simulations of strongly precipitating, shallow, stratocumulus-topped boundary layers. *J. Atmos. Sci.*, **55**, 3616–3638.

Stevens, B., D. H. Lenschow, G. Vali, et al., 2003: Dynamics and Chemistry of Marine Stratocumulus-DYCOMS-II. *Bull. Amer. Meteor. Soc.*, **84**, 579–593.

Stevens, B., G. Vali, K. Comstock, R. Wood, M. C. Zanten, P. H. Austin, C. S. Bretherton, and D. H. Lenschow, 2004: Pockets of open cells (POCs) and drizzle in marine stratocumulus. *submitted*.

PREDICTION OF CLOUD DROPLET NUMBER CONCENTRATION FROM CLOUD CONDENSATION NUCLEI DATA

M. D. Petters[1] and Jefferson R. Snider[1]

[1]Department of Atmospheric Science, University of Wyoming, Laramie, WY 82071, USA

1. INTRODUCTION

One of the classical problems in cloud physics is the prediction of cloud droplet number concentration (CDNC) from cloud condensation nuclei (CCN) data. Early studies focused on cumulus clouds and relied on below-cloud measurements of CCN and in-cloud measurements of updraft velocity (w) and CDNC (e.g Twomey and Warner, 1967; Fitzgerald and Spyres-Duran, 1973). Below-cloud CCN and in-cloud w were used to compute predicted CDNC and make comparisons to those measured in cloud. These early studies were plagued by small sample sizes and the assumption of fixed vertical velocity. Renewed interest in the problem has derived from concerns that increased below-cloud CCN may increase the cloud albedo (Twomey, 1977). Marine stratocumulus clouds are most susceptible to this effect, so recent studies focused on this cloud-type (Yum et al., 1998; Snider and Brenguier, 2000). Additional problems arise in these clouds because the mean w is negligible and droplets activate in turbulent eddies. Most problematic is that individual observations of CDNC are not necessarily the consequence of the collocated updraft velocity. Hence, one problem is to find the appropriate set of updraft velocities to model the distribution of CDNC. This is augmented by the problem that the temporal evolution of droplet spectra is typically associated with a decrease in CDNC. Some droplets are removed via the collision-coalescence process while others are lost via evaporation as the result of mixing of warm and dry free tropospheric (FT) air with cloudy air at cloud-top (entrainment).

Here, our objective is to evaluate the degree to which measurements of droplet number concentration in quasi-adiabatic regions of marine stratocumulus are consistent with predictions based on vertical velocity frequency distributions and CCN data.

2. DATA AND INSTRUMENTATION

Our data was collected over the remote subtropical eastern Pacific ocean between July 10 and July 25, 2001. During that time the NCAR C-130 conducted a nocturnal Lagrangian study of the evolution of the Dynamics and Chemistry of Marine Stratocumulus clouds (DYCOMS-II, Stevens et al., 2003). Seven flights employed a stepped circular flight pattern conducted both in the marine boundary layer (MBL) and FT. The centerpoints of the circles were repositioned using C-130 wind data acquired during the previous circle. These flights are summarized in Table 1.

Here we utilize measurement from two UWyo static thermal gradient diffusion instruments (CCN104 and CCN108) deployed on the C-130. The instruments operated behind a solid diffuser inlet (SDI) and sampled CCN concentration at four supersaturations (0.11%, 0.24%, 0.48%, and 1.03%). A detailed discussion of the calibration of these instruments can be found in Petters et al. (this issue). Here we use the post-project concentration calibration and ignore the slight differences in the effective chamber supersaturation between the two counters. A robust technique for correcting the observations of cumulative CCN for transmission loss has not been developed. Rather laboratory-based measurements of transmitted fraction as a function of NaCl dry size (Petters et al., this issue) were used to estimate this loss. Here, the implemented correction factors are 1.02, 1.04, 1.07, and 1.13 corresponding to 0.11%, 0.24%, 0.48%, and 1.03% effective supersaturation, respectively.

Accumulation mode aerosol (ACM) was measured by a DMT SPP-200 (PCASP) aerosol size spectrometer. Aitken mode aerosol was measured by a radial differential mobility analyzer (RDMA). Data from the RDMA and PCASP was combined to produce a composite size spectrum. Petters et al. (this issue) present a detailed discussion of the quality of the RDMA and PCASP data as well as the construction of the composite size spectrum.

CDNC are measured by a DMT SPP-100 (FSSP-100) cloud droplet probe or the fast-FSSP (Brenguier et al., 1998). When both probes where available conc-

Table 1. Summary of the seven entrainment flights.

Flight	Date	Night	CCN[1] (cm^{-3})
RF1	07/10	yes	145 ± 32
RF2	07/11	yes	60 ± 24
RF3	07/13	yes	251 ± 95
RF4	07/17	yes	204 ± 47
RF5	07/18	yes	192 ± 41
RF7	07/24	yes	127 ± 34
RF8	07/25	no	138 ± 49

[1]Concentration of particles active at 0.47% water supersaturation.

Corresponding author's address: Markus D. Petters, Dept. 3038, 1000 E. University Ave. Laramie, WY 82071, USA; E-Mail: petters@uwyo.edu

how well predict cloud droplet number from w and CCN data C-130 & DYCOMS II

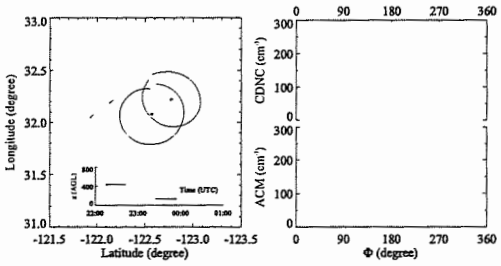

Figure 1. Time-height diagram and plane view of the flight track during RF8 (left panel), mean observed wind speed and direction (arrows), and ACM (cm^{-3}) and CDNC (cm^{-3}) vs. azimuth coordinate (Φ, degrees) around the circle (right panel).

entrations derived from the FSSP-100 were in good agreement with those from the fast-FSSP. Preliminary analysis shows that droplet number concentrations compare reasonably with residual concentrations obtained from a counterflow virtual impactor (C. Twohy, personal communication).

Updraft velocity was measured by Rosemount Model 1221F1V1 gust probe mounted at the aircraft radome. A bias of up to $0.3\ m\ s^{-1}$ is reported for this instrument (Brown, 1993). We remove this bias by forcing the mean of w to zero for constant-altitude segments conducted within the MBL.

3. METHOD

The Lagrangian stepped circular flight pattern shown in Figure 1 yielded a unique data set that allowed us to connect the time series of ACM below-cloud with the time series of CDNC in-cloud. This is achieved by a transformation to azimuth angle coordinates. Here, $\Phi = 0°$ indicates the most northern point on the C-130 circle and larger values of Φ progress clockwise from that reference point. The data generally show an excellent correlation between ACM below-cloud and CDNC in-cloud (Figure 1, right panel). This motivated us to adopt the following procedure for the CCN-to-CDNC closure: 1) we project the time series data onto an azimuth grid, 2) we subset the data into regions where below-cloud ACM concentrations are reasonably uniform, 3) we obtain the activation spectrum, $A(s)$, and the fitted coefficients for that particular region (Section 3.1), 4) we calculate the distribution of CDNC (Section 3.2), 5) we determine the observed distribution of CDNC in quasi-adiabatic regions limited to the azimuth subset (Section 3.3), and 6) compare the frequency distribution of observed CDNC to the frequency distribution of predicted CDNC .

3.1 CCN Activation Spectrum

Representation The CCN activation spectrum, $A(s)$, is the cumulative number of particles that "activate" (i.e., start growing kinetically) at an environmental supersaturation (s). Here, we utilize two descriptions of $A(s)$, the Twomey spectrum ($A(s) = C \cdot s^k$, Twomey, 1959) and the Cohard spectrum ($A(s) = C_c \cdot s^{k_c} \cdot F(\mu, k_c/2, k_c/2 + 1; -\beta s^2)$, Cohard et al., 1998). Here, $F(a, b, c; x)$ is the hypergeometric function, s is in %, and C, k, C_c, k_c, μ, and β are fitted coefficients. The Twomey representation has been criticized for predicting unrealistic concentrations when the spectrum is extrapolated to either large or small values of s (Johnson, 1981). Figure 2 illustrates this effect for data obtained below-cloud during RF5. The divergence between the Twomey activation spectrum and the predicted CCN activation spectrum based on aerosol physicochemical data (Petters et al., this issue) is obvious. This discrepancy is diminished when utilizing the Cohard spectrum which yields a reasonable description of $A(s)$ at both small and large values of s.

CCN Sampling Uncertainty One problem that has received little attention in the literature is the degree of certainty to which the CCN activation spectrum can be determined, given the uncertainties of the CCN measurement. Typically 10-60 data points obtained at 2-4 values of effective chamber supersaturation are used to calculate the best-fit coefficients (e.g., $\{C, k\}$). Consider that these data are snapshots taken from an atmosphere where aerosol concentration varies both randomly and systematically (Figure 1). This variability is augmented by sampling uncertainty due to small sample volume in the CCN instrument. To what degree then, does this best-fit reflect the underlying CCN statistics? To answer

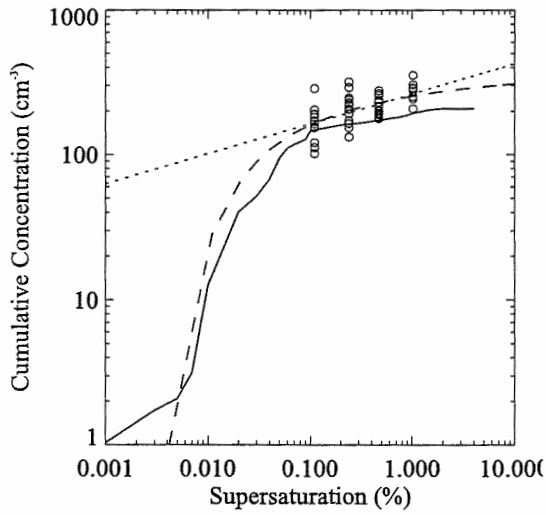

Figure 2. CCN activation spectrum constructed from UWyo CCN data below-cloud during RF5 (circles), Twomey spectrum (dotted line, $C = 263\ cm^{-3}$ and $k = 0.21$), Cohard spectrum (dashed line, $C_c = 2.38 \cdot 10^{11}\ cm^{-3}$, $k_c = 4.5$, $\mu = 2.37$, and $\beta = 28160\ \%^{-2}$), and CCN activation spectrum modeled from particle physicochemical data (solid line, Petters et al., this issue)

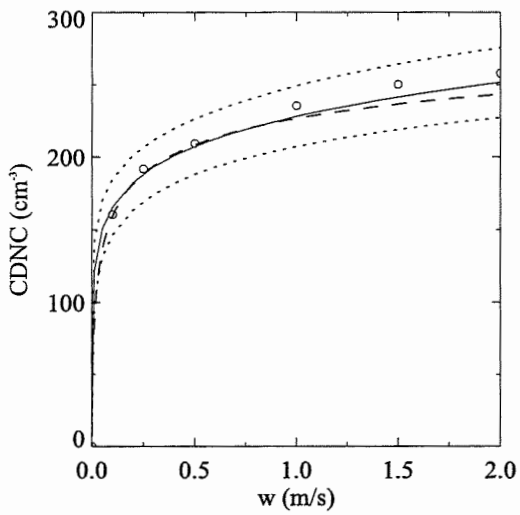

Figure 3. Prediction of CDNC based on the CCN activation spectra shown in Figure 2: Twomey model (solid line), upper and lower bound due to CCN uncertainty (dotted line), Cohard model (dashed line), parcel model ($\alpha = 0.04$) based on Twomey spectrum.

this question we developed a method that estimates the bivariant distribution of C and k. From this distribution we construct a lower and an upper bound estimates of the Twomey model prediction. A manuscript describing the details of this method is in preparation.

3.2 Calculating CDNC

Analytical Approximations In an ascending parcel, the environmental supersaturation is generated in proportion to w, and reduced in proportion to the number of active particles and their growth rate. With the assumption of Maxwellian droplet growth, analytical approximations that solve for the maximum supersaturation of the parcel exist for both the Twomey spectrum (Equation 1) and the Cohard spectrum (Equation 2).

$$s_{\max}^{k+2} \leq \left[\frac{\Psi w^{3/2}}{kCB(k/2, 3/2)}\right] \quad (1)$$

$$s_{\max}^{k_c+2} \cdot F(\mu, \tfrac{k_c}{2}, \tfrac{k_c+3}{2}; -\beta s_{\max}^2) \leq \left[\frac{\Psi w^{3/2}}{k_c C_c B(k_c/2, 3/2)}\right] \quad (2)$$

Here, $s_{\max}$ is the maximum supersaturation, Ψ is a thermodynamic parameter (see Cohard et al., 1998), and $B(x, y)$ is the complete beta function. Because Equations 1 and 2 are couched as inequalities they provide an upper limit for $s_{\max}$. Inserting $s_{\max}$ into $A(s)$ yields an estimate for CDNC.

Parcel Model Kelvin and Raoult effects as well as diffusion-kinetic (DK) theory are not included in these analytic expressions for CDNC (see Zou and Fukuta, 1999). Here we use a parcel model (Snider et al., 2003) to address the combined effects of Kelvin, Raoult, and DK theory on the predicted CDNC. This is achieved by initializing the parcel model with the Twomey activation spectrum and setting the condensation coefficient (α) to 0.04, a lower estimate of its value. Note that for $\alpha = 1$, CDNC obtained from the parcel model is in good agreement with CDNC derived from Equation 1 (Snider et al., 2003). Lowering α results in a retarded condensation rate, increased environmental supersaturation, and hence increased predicted CDNC.

In summary, we compare three separate predictions of CDNC as a function of w (Figure 3), 1) the analytic approximation based on the Twomey activation spectrum (solid line), including an upper and lower bound estimate due to CCN sampling uncertainty (dashed lines), 2) the analytic approximation based on the Cohard activation spectrum (dashed line), and 3) the parcel model prediction based on the Twomey activation spectrum and $\alpha = 0.04$ (circles). Figure 3 shows that all the model descriptions are circumscribed by the CCN uncertainties.

Quasi-Adiabatic Selection Our CDNC sampling procedure rejects data associated with drizzle (DMT SPP-2D 25 > 10 $L^{-1} \pm 1$ s) or from regions that were subadiabatic. An adiabatic liquid water content (ALWC) threshold was derived using average cloud base altitude determined from slantwise soundings performed by the C-130. Only data satisfying LWC (Gerber PVM-100) > ALWC were accepted. A consequence of this selection was a narrowing of the frequency distribution of observed CDNC. The utility of this conditional sampling strategy is obvious, since neither entrainment nor collision/coalescence is captured in our calculation of predicted CDNC.

Vertical Velocity Frequency distributions of updraft velocity were obtained from the in-cloud data segments. Here we only considered positive w values coincident with conditionally sampled droplets. A sensitivity analysis revealed that predicted distributions of CDNC were very similar when utilizing below-cloud values of positive w.

4. RESULTS

Figure 4 shows conditionally sampled and predicted frequency distributions of CDNC. Note that the Twomey model and Cohard model predictions are very similar. At low values of CDNC (< 120 mg^{-1}), the models capture the distribution of measured values.

Table 2. Moments of the CDNC distribution for RF5

Moment	O†	LT	T	UT	C	PM
μ‡	146	140	156	172	152	161
σ	22	24	25	26	31	29

†O: Observed, LT: Lower bound Twomey model, T: Twomey Model, UT: Upper bound Twomey model, C: Cohard Model, PM: Parcel model ($\alpha = 0.04$), units are mg^{-1}
‡ μ: mean, σ: standard deviation

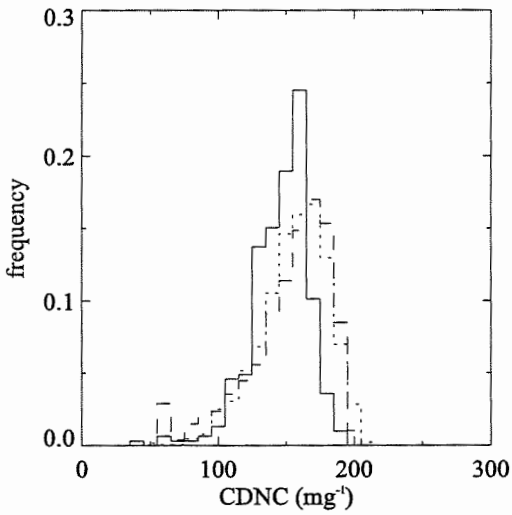

Figure 4. Frequency distribution of conditionally sampled CDNC during RF5 (solid line), predicted CDNC based on Twomey model (dashed line), and predicted CDNC based on Cohard model (dashed line).

At larger values, predictions slightly exceed the observations. Table 2 summarizes the moments of the CDNC distributions. These results show that the mean CDNCs of models, and also of the observation are circumscribed by the CCN sampling uncertainty bounds. Furthermore, all models slightly overestimate the width of the observed CDNC distribution.

5. DISCUSSION AND CONCLUSIONS

The overprediction of CDNC at large values is the consequence of the model predictions at large w. This can be traced back to the CCN activation spectra shown in Figure 2. Over the supersaturation range defined by $0.1 < s < 1.0$ the slope of the activation spectrum functions derived from the CCN data is larger than the slope indicated by the CCN activation spectrum modeled based on particle physicochemical data. We performed calculations (results not shown) that demonstrate that a reduction in the slope of the CCN activation spectrum can account for the disparity between the right tails of the CDNC distributions as well as the discrepancy between the predicted and the observed widths of the distributions. Why do those slopes not agree? In part this may be attributable to the transmission correction. This correction is more pronounced at larger supersaturation (smaller particle size). Hence an overestimation of transmission loss steepens the slope of the CCN activation spectrum. But, model runs without the transmission correction applied (Section 2), showed very similar results. Alternatively, the difference between the slopes may also be explicable by the CCN sampling uncertainty. This is corroborated by our results that show that the uncertainty in CDNC due to CCN sampling uncertainty circumscribes the observation and model predictions.

6. REFERENCES

Brenguier, J.-L., T. Bourrianne, A. A. Coelho, J. Isbert, R. Peytavi, D. Trevarin, and P. Wechsler, 1998: Improvements of the droplet size distribution measurements with the fast-FSSP (forward scattering spectrometer probe. *J. Atmos. Oceanic Technol.*, **15**, 1077–1090.

Brown, E. N., 1993: Measurement uncertainties of the NCAR air motion system. NCAR technical note, Research Aviation Facility, Atmospheric Technology Division, National Center for Atmospheric Research, Boulder, CO.

Cohard, J.-M., J.-P. Pinty, and C. Bedos, 1998: Extending Twomey's analytical estimate of nucleated droplet concentration from CCN spectra. *J. Atmos. Sci.*, **55**, 3348–3357.

Fitzgerald, J. W. and P. A. Spyres-Duran, 1973: Changes in cloud nucleus concentration and cloud droplet size distribution associated with pollution from St. Louis. *J. Appl. Meteor.*, **12**, 511–516.

Johnson, D. B., 1981: Notes and correspondence. analytical solutions for cloud drop concentration. *J. Atmos. Sci.*, **38**, 215–218.

Petters, M. D., J. R. Snider, C. Twohy, and J. Anderson: this issue, Prediction of cloud condensation nuclei from particle physiochemical data.

Snider, J. R. and J.-L. Brenguier, 2000: Cloud condensation nuclei and cloud droplet measurements during ACE-2. *Tellus*, **52B**, 828–842.

Snider, J. R., S. Guibert, and J.-L. Brenguier, 2003: Aerosol activation in marine stratocumulus clouds: 2. Köhler and parcel theory closure studies. *J. Geophys. Res.*, **108**, doi:10.1029/2002JD002692.

Stevens, B., D. H. Lenschow, G. Vali, H. Gerber, A. Bandy, B. Blomquist, J.-L. Brenguier, C. S. Bretherton, F. Burnet, T. Campos, S. Chai, I. Faloona, D. Friesen, S. Haimov, K. Laursen, D. K. Lilli, S. M. Loehrer, P. M. Szymon, B. Morely, M. D. Petters, D. C. Rogers, L. Russell, V. Savic-Jovcic, J. R. Snider, D. Straub, J. Szumowski, H. Takagi, D. C. Thorton, M. Tschudi, C. Twohey, M. Wetzel, and M. C. Zanten, 2003: Dynamics and Chemistry of Marine Stratocumulus-DYCOMS-II. *Bull. Amer. Meteor. Soc.*, **84**, 579–593.

Twomey, S., 1959: The nuclei of natural cloud formation, Part II: The supersaturation in natural clouds and the variation of cloud droplet concentration. *Geofis. Pura Appl.*, **43**, 243–249.

— 1977: The influence of pollution on the shortwave albedo of clouds. *J. Atmos. Sci.*, **34**, 1149–1152.

Twomey, S. and J. Warner, 1967: Comparison of measurements of cloud droplets and cloud nuclei. *J. Atmos. Sci.*, **24**, 702–703.

Yum, S. S., J. G. Hudson, and X. Yonghong, 1998: Comparison of cloud microphysics with cloud condensation nuclei spectra over the summertime Southern Ocean. *J. Geophys. Res.*, **103**, 16,625–16,636.

Zou, Y.-S. and N. Fukuta, 1999: The effect of diffusion kinetics on the supersaturation in clouds. *Atmospheric Research*, **52**, 115–141.

PREDICTION OF CLOUD CONDENSATION NUCLEI FROM PARTICLE PHYSICOCHEMICAL DATA

M. D. Petters[1], Jefferson R. Snider[1], Cynthia Twohy [2], and James R. Anderson[3]

[1]Department of Atmospheric Science, University of Wyoming, Laramie, WY 82071, USA
[2]College of Oceanography and Atmospheric Sciences, Oregon State University, OR 97331-5503, USA
[3]Department of Mechanical and Aerospace Engineering, Arizona State University Tempe, AZ 85287-6106, USA

1. INTRODUCTION

A subset of atmospheric particles, the cloud condensation nuclei (CCN), provide conditions favorable for water to condense at small values of vapor supersaturation. Cloud droplet number concentration, a critical determinant of cloud albedo, can be predicted based on updraft and the cumulative CCN concentration as a function of vapor supersaturation. The latter is referred to as the CCN activation spectrum. Early predictions of the CCN activation spectrum applied Köhler theory with particle mass derived from the particle size and parameterizations of the activation properties of either NaCl or $(NH_4)_2SO_4$ (Junge and McLaren, 1971, and references therein). More recent studies incorporate particle solubility (Bigg, 1986), particle chemistry (Liu et al., 1996; Chuang et al., 2000; Snider et al., 2003), or particle hygroscopic growth factor (Covert et al., 1998; Dusek et al., 2003). The bulk of these studies show that predicted CCN concentrations systematically exceed those measured directly by CCN instruments. This is in part due to the limited understanding of the chemical composition and mixing state of the particles.

Our objective is to evaluate whether or not there is consistency between CCN concentrations by by the University of Wyoming (UWyo) static thermal gradient diffusion instrument and those derived from particle size spectra and particle chemical composition and mixing state.

2. METHOD AND INSTRUMENTATION

Our data was collected within the remote subtropical eastern Pacific marine boundary layer (MBL) on July 18, 2001 (RF5). At that day, the NCAR C-130 conducted a nocturnal Lagrangian study of the evolution of the Dynamics and Chemistry of Marine Stratocumulus clouds (DYCOMS-II, Stevens et al., 2003). The data presented here was obtained between 9:45 - 10:05 UTC corresponding to $\approx$ 1:00 a.m. local time, and sampling was conducted $\approx$ 200 km west of San Diego, CA. At that time the C-130 sampled below a thin stratocumulus cloud deck. There, wind speeds were moderate ($\approx$ 10 m s^{-1}) and drizzle was not encountered. Backtrajectories calculated from the HYSPLIT4 model did indicate that the MBL airmass was "remote marine". The assertion that the air was not influenced by sources from the North American continent is corroborated by low and horizontally uniform carbon monoxide data.

Corresponding author's address: Markus D. Petters, Dept. 3038, 1000 E. University Ave. Laramie, WY 82071, USA; E-Mail: petters@uwyo.edu

2.1 Particle Chemistry

Size segregated single particle chemical composition was obtained from filter samples obtained via the low turbulence inlet (Huebert et al., 2000). The data are organized in 9 size channels with channel minimum particle diameters ranging from 0.04 μm to 2.44 μm. Single particle analysis was performed on a set of 100 particles utilizing transmission electron microscopy (TEM, lower two channels) and a set of 933 particles utilizing scanning electron microscopy (SEM, upper channels). Sizes measured microscopically are assumed to correspond to non-hydrated sizes and represent upper bound estimates because we did not account for spreading on the grid. The SEM- and TEM-derived data set convey the external mixing state of the particles by stratifying the particles into 10 composition categories: non reacted, partially reacted, and completely reacted seasalt, sulfate, organic carbon, crustal, industrial, soot, unresolved carbon, and other salts.

2.2 Particle Composite Size Spectra

Seven composite size spectra were obtained from upscans of a radial differential mobility analyzer (RDMA, 0.01 < diameter (D) < 0.13 μm), operated downstream of a solid diffuser inlet (SDI), and a wing mounted DMT SPP-200 (PCASP) particle size spectrometer (0.09 < D < 3 μm). Chemically bonded water did not contribute significantly to the particle size because measurements indicated 35% relative humidity in the RDMA instrument and the PCASP was operated with the deicing heater activated. The relationship between electrical mobility and particle D assumed temperature T = 20 °C and pressure P = 822 hPa in the annular space between the electrodes. During RF5, below-cloud, T was 26 °C and P was 920 hPa.

Table 1. Composite size spectra data quality

Time	CN[1] (cm^{-3})	A[2]	B[3]
09:49:13	397	1.09	0.90
09:51:57	390	0.95	0.95
09:54:41	415	1.17	0.96
09:57:25	386	1.02	1.01
10:00:09	382	0.74	0.97
10:02:53	397	0.78	0.96
10:05:37	408	0.97	1.02

[1] TSI 3710 CN concentration
[2] PCASP-to-RDMA spectral density ratio in the overlap region
[3] CN-to-integrated-composite-spectrum concentration ratio

Because of unrealistically high spectral densities in the first channel of the PCASP we only utilize PCASP measurements with $D > 0.1$ μm. For the composite size spectra, the RDMA was preferred in the overlap region ($0.1 < D < 0.13$ μm). Condensation nucleus (CN) concentrations from a TSI 3760, comparisons of spectral densities in the overlap region, and comparisons of integrated concentrations derived from the composite size spectra to the CN concentration are summarized in Table 1. The data indicate reasonable ratios of PCASP-to-RDMA spectral density in the overlap region and reasonable CN-to-integrated-composite-spectrum concentration ratios.

2.3 CCN Instruments

Two UWyo static thermal gradient diffusion instruments (CCN104 and CCN108) were deployed on the C-130. The instruments operated behind the SDI and sampled CCN concentrations at four temperature gradients corresponding to ≈ 0.10% (I), 0.24% (II), 0.48% (III), and 1.03% (IV) applied water supersaturation within the instrument (chamber supersaturation). Pre-project and post-project concentration calibrations of the instruments were performed (Delene and Deshler, 2000). Average concentrations reported by the two CCN instruments were in good agreement (Table 2). One exception was the lowest chamber supersaturation. This appears to be the consequence of a shift in the calibration of the CCN108 instrument or an incorrect pre-project calibration. Because the post-project calibration yielded good agreement with the CCN104 instrument at the lowest supersaturation and had little effect on all other counts we utilize the post-project calibration for the subsequent analysis.

The chamber supersaturations were obtained from

Table 2. Comparison of CCN104 and CCN108 between 09:45 and 10:05 UTC utilizing pre-project and post-project calibration.

SS[1]	CCN104 (cm^{-3})		CCN108 (cm^{-3})		CCN104/ CCN108	
	pre	post	pre	post	pre	post
I	179	172	108	167	1.66	1.03
II	192	210	159	177	1.21	1.19
III	193	217	178	204	1.08	1.06
IV	266	273	243	251	1.09	1.09

[1]chamber supersaturation, see text for details.

Table 3. Fitted coefficients for laboratory calibrations of activation efficiency and particle mobility equivalent diameter for NaCl and $(NH_4)_2SO_4$.

SS[1]	CCN104		CCN108	
	α	β	α	β
		NaCl		
0.10 (0.12)	54.1	−5.43	77.5	−7.10
0.24 (0.23)	66.6	−3.85	33.7	−1.98
0.48 (0.50)	183.6	−6.53	55.5	−1.96
1.03	435.0	−9.52	–	–
		$(NH_4)_2SO_4$		
0.11 (0.12)	32.5	−4.57	37.1	−4.83
0.25 (0.21)	146.4	−11.47	29.9	−2.64
0.53 (0.57)	145.3	−7.04	101.3	−4.65
0.99	385.5	−12.26	–	–

[1]chamber supersaturation corresponding to the 50% particle activation diameter. Number in parenthesis indicate values for CCN108.

laboratory studies that challenged the instrument with varying mobility selected particles of known composition (Snider et al., 2003). This calibration yields the chamber activation function, the fraction of particles that activate within the chamber as a function of particle mobility equivalent dry diameter (D_{me}). The activation function (F) is fitted to a two parameter function from which the 50% particle activation D_{me} can be inferred.

$$F = \Psi(x) \tag{1}$$

Here, F is the fraction of particles activated in the chamber, $\Psi(x)$ is the normalized Gaussian integral, $x = \alpha D_{me} + \beta$, D_{me} is in μm, and α and β are fitted coefficients. Under the assumption that D_{me} equals the particle sphere equivalent diameter, the chamber supersaturation can be inferred from α, β, and parameterizations of Köhler theory (Tang and Munkelwitz, 1994). Table 3 summarizes the coefficients α and β for NaCl and $(NH_4)_2SO_4$ particles.

The CCN instruments sampled downstream of 15 ft conductive tubing (TSI-3001904, 3/8" inner diameter) at a flow of 8.0 alpm. In a post-project laboratory experiment we recreated these conditions to evaluate wall losses as a function of NaCl particle mobility equivalent dry diameter. For laminar flow, wall loss depends on the particle diameter, the length of the tubing, and the flow rate. We found $T(D_{me}) = 99.67 + 0.083 D_{me}^{-1.29}$, where T is the particle transmission through the tubing in %. To compare concentrations observed by the CCN to those predicted we convolute the composite size spectra with $T(D_{me})$ before converting to predicted CCN concentrations.

2.4 Predicting CCN concentrations

For the purposes of this study we regroup the particle composition categories into three model categories: NaCl (non reacted, partially reacted, completely reacted seasalt), $(NH_4)_2SO_4$ (sulfate), and insoluble

Table 4. Percent of particle by number and size channel obtained from Scanning Electron Microscopy (SEM) and Transmission Electron Microscopy (TEM) particle analysis

Particle Composition	TEM		SEM							Model Category
	0.04†	0.11	0.26	0.37	0.48	0.63	0.83	1.14	2.44	
NR[1] - Seasalt	0	0	19.1	31.2	38.0	43.2	55.8	77.9	95.9	NaCl
PR[2] - Seasalt	0	0	52.9	57.5	53.1	55.5	38.7	19.1	0.0	NaCl
CR[3] - Seasalt	0	8	23.5	10.0	8.0	1.3	3.7	2.2	0.0	NaCl
Sulfate	36	46	0.0	0.0	0.0	0.0	0.0	0.0	0.0	$(NH4_2)SO_4$
Organic Carbon	12	21	0.0	0.0	0.0	0.0	0.0	0.0	0.0	Insoluble
Crustal	27	2	0.0	0.0	0.0	0.0	0.0	0.0	0.0	Insoluble
Industrial	21	4	0.0	0.0	0.0	0.0	0.0	0.0	0.0	Insoluble
Soot	0	19	0.0	0.0	0.0	0.0	0.0	0.0	0.0	Insoluble
Unresolved Carbon	0	0	4.4	1.2	0.9	0.0	1.8	0.8	4.1	Insoluble
Other Salt	3	0	0.0	0.0	0.0	0.0	0.0	0.0	0.0	Insoluble

†channel minimum particle diameter (μm)
[1]non reacted, [2]partially reacted, [3]completely reacted

(remaining categories). Although it is not strictly correct to associate seasalt with pure NaCl, and sulfates with pure $(NH_4)_2SO_4$, the error introduced by this assumption is expected to be small. The association between the remaining categories and insoluble material is more problematic. While soot and crustal particles are expected to be water insoluble, questions remain about the hygroscopicity of the organic carbon and industrial particles. Our understanding of the chemical composition, as well as the overall hygroscopic behavior of these categories is very limited. We expect that some of the particles classified as insoluble do contribute to the CCN (see Prenni et al., 2003, and references therein), therefore our predicted CCN concentrations are a lower bound estimate.

The predicted CCN concentrations, at a particular chamber supersaturation, are calculated by a set of convolutions. First we convolute the transmission corrected size spectrum with the model categories (Table 4) to obtain two component (NaCl and $(NH_4)_2SO_4$) particle size spectra. In this convolution we assume that the composition of particles with $D < 0.04$ μm is identical to those with $0.04 < D < 0.11$ μm. Second we convolute the two component size spectra with the particular activation function corresponding to the instrument and applied supersaturation (Table 3). Finally we compare the calculated concentration to CCN concentrations observed coinciding with the time interval of the RDMA scan.

Note that our description models particle concentrations that are expected to activate in the CCN instrument at a controlled particular differential temperature setting. This approach is appealing because it provides a mapping between the particle size spectrum and activated CCN without the need to invoke supersaturation. After the consistency between the two is established, predicted CCN activation spectra (based on particle size and composition) can be constructed.

3. RESULTS

Table 4 shows the result from the TEM and SEM single particle analysis. At smaller sizes ($D < 0.11$ μm), sulfate, crustal, soot, and organic carbon particles dominate. Conversely at $D > 0.26$ μm seasalt particles dominate. These include seasalt particles that reacted with sulfate or nitrate. Our results are consistent with particle composition in remote marine boundary layers (O'Dowd and Smith, 1993).

Figure 1 shows the average composite size spectrum between 09:45 and 10:05 UTC. The shading indicates the component spectra after the convolution of the particle size spectrum with the model components presented in Table 4. The particle size spectrum shows two modes, a narrow accumulation mode and a wide Aitken mode. Approximately 60% of the particles are larger than 0.1 μm.

Predicted-to-observed CCN ratios are shown in Table 5. The data show that measured CCN concentrations slightly exceed those predicted based on our model assumptions.

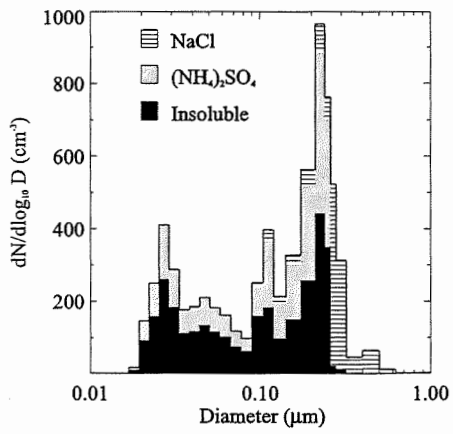

Figure 1. Average composite particle size spectrum convoluted with the three model categories of chemical composition. See text for details.

Table 5. Predicted-to-observed CCN ratios

SS	CCN104		CCN108	
	R†	n‡	R	n
I	0.92	2	0.66	2
II	0.75	2	0.60	1
III	0.81	2	0.98	2
IV	0.74	1	0.71	3
Overall	0.81	7	0.75	8

†mean predicted-to-observed ratios utilizing the post-project concentration calibration
‡number of CCN samples

4. DISCUSSION

The presented comparison between predicted and observed CCN concentrations needs to be evaluated critically. Our weakest assumptions are the model categories prescribing the particle chemical composition. Two major objections can be raised: 1) particles in any of the three categories may actually be internally mixed and 2) some fraction of the particles within the insoluble category may contribute to the CCN. The latter will increase the predicted CCN concentration. Indeed when assuming that all particles are composed of NaCl or $(NH_4)_2SO_4$ predicted-to-observed ratios range from 1.4-1.6. We note, that the predicted-to-observed CCN ratios are very sensitive to the size resolution of the particle composition. The effect of internal mixtures (e.g. NaCl with 10% soot) is opposite. In that case, the particle hygroscopic mass decreases and therefore predicted CCN concentrations at fixed chamber supersaturation decrease as well.

Potential biases in the CCN measurement have been addressed here. Particle concentrations entering the CCN instrument have been adjusted for non-ideal transmission. Furthermore we presented the pre-project and post-project calibrations. Note that concentrations derived from the post-project calibration are generally 10% higher than those derived from the pre-project calibration. Had we used the pre-project calibration, the predicted-to-observed ratios would indicate values that are 10% larger than those shown in Table 5.

Not addressed is the effect of variable temperature and pressure in the RDMA instrument. Future work will incorporate a sensitivity study of these effects on particle diameter and the predicted CCN concentration.

5. CONCLUSIONS

We present comparisons between CCN concentrations predicted based on particle size spectra and particle chemical composition and those measured by two UWyo CCN instruments during a 20 min segment on July 18, 2001 in the MBL over the remote subtropical eastern Pacific Ocean. The particles were externally mixed with sulfate, crustal, soot, and organic carbon dominating at the smaller particle size range and non reacted plus reacted seasalt dominating in the larger particle size range. Our results demonstrate, that detailed information about the particle composition and mixing state is necessary to achieve better agreement between predicted and observed CCN concentrations.

6. REFERENCES

Bigg, F. K., 1986: Discrepancy between observation and prediction of concentrations of cloud condensation nuclei. *Atmos. Res.*, **20**, 81–86.

Chuang, P. Y., D. R. Collins, H. Pawlowska, J. R. Snider, H. H. Jonsson, J.-L. Brenguier, R. C. Flagan, and J. H. Seinfeld, 2000: CCN measurements during ACE-2 and their relationship to cloud microphysical properties. *Tellus*, **52B**, 843–867.

Covert, D. S., J. L. Gras, A. Wiedensohler, and F. Stratman, 1998: Comparison of directly measured CCN with CCN modeled from the number-size distribution in the marine boundary layer during ACE 1 at Cape Grim, Tasmania. *J. Geophys. Res.*, **103**, 16,597–16,608.

Delene, D. J. and Deshler, 2000: Calibration of a photometric cloud condensation nucleus counter designed for deployment on a balloon package. *J. Atmos. Oceanic Technol.*, **17**, 459–467.

Dusek, U., D. S. Covert, A. Wiedensohler, C. Neussüs, D. Weise, and W. Cantrell, 2003: Cloud condensation nuclei spectra derived from size distributions and hygroscopic properties of the aerosol in coastal southwest portugal during ACE-2. *Tellus*, **55B**, 35–53.

Huebert, B. J., S. G. Howell, D. Covert, A. Clarke, and J. R. Anderson, 2000: Passing efficiency of a low turbulence inlet (PELTI). Technical report, NSF, huebert@soest.hawaii.edu.

Junge, C. and E. McLaren, 1971: Relationship of cloud nuclei spectra to aerosol size distribution and composition. *J. Atmos. Sci.*, **28**, 382–390.

Liu, P. S. K., W. R. Leaitch, C. M. Banic, S.-M. Li, D. Ngo, and W. J. Megaw, 1996: Aerosol observations at Chebogue Point during the 1993 north atlantic regional experiment: Relationships among cloud condensation nuclei, size distribution, and chemistry. *J. Geophys. Res.*, **101**, 28,971–28,990.

O'Dowd, C. D. and M. H. Smith, 1993: Physicochemical properties of aerosols over the northeast Atlantic: Evidence for wind speed related submicron sea-salt aerosol production. *J. Geophys. Res.*, **98**, 1137–1149.

Prenni, A. J., P. J. DeMott, and S. M. Kreidenweis, 2003: Water uptake of internally mixed particles containing ammonium sulfate and dicarboxylic acids. *Atmospheric Environment*, **37**, 4243–4251.

Snider, J. R., S. Guibert, and J.-L. Brenguier, 2003: Aerosol activation in marine stratocumulus clouds: 2. Köhler and parcel theory closure studies. *J. Geophys. Res.*, **108**, doi:10.1029/2002JD002692.

Stevens, B., D. H. Lenschow, G. Vali, et al., 2003: Dynamics and Chemistry of Marine Stratocumulus-DYCOMS-II. *Bull. Amer. Meteor. Soc.*, **84**, 579–593.

Tang, I. N. and H. R. Munkelwitz, 1994: Water activities, densities, and refractive indices of aqueous sulfates and sodium nitrate droplets of atmospheric importance. *J. Geophys. Res.*, **99**, 18,801–18,808.

MICROTOPS OBSERVATIONS OF COLUMNAR AEROSOL OPTICAL DEPTH, OZONE AND WATER VAPOR OVER GADANKI (13.5^{0}N, 79.2^{0}E)

Y. Jaya Rao[1], P. C. S. Devara[1], Atul Kumar Srivastava[1], Y. Bhavani Kumar[2] and D. Narayana Rao[2]

[1] Indian Institute of Tropical Meteorology, Dr. Homi Bhabha Road, Pune, India
[2] National MST Radar Facility, P O Box:123, Tirupati, India.

1. INTRODUCTION

Aerosols in the atmosphere play key role in the Earth's climate system through radiative forcing. They influence the solar radiation both directly through scattering and absorption of solar radiation, and indirectly by acting as condensation nuclei for formation of clouds and haze. Aerosols produced from different sources, including natural and anthropogenic origin, redistribute in the atmosphere through long range transport processes. Thus, atmospheric winds play very important role in transportation and re-distribution of aerosols in the atmosphere. The characteristics of aerosols over different environments have been reported by Jaya Rao et al (2001). In the present study, an attempt has been made to monitor the characteristics of aerosols and also variability of columnar ozone and water vapor over an unpolluted continental tropical station, using multi-channel solar radiometer.

2. OBSERVATIONS

MICROTOPS, a compact, portable and multi-channel solar radiometer, has been operated, for the first time, at National MST Radar Facility (NMRF), Gadanki, a tropical Indian station to study the characteristics of aerosols, ozone and water vapor. Observations carried out during the period February 28 – March 15, 2003 are reported here. Detailed descriptions of MICROTOPS and some results for a tropical urban station, Pune have been reported by Devara et al (2001). This instrument consisted of Sun photometer that provides columnar AOD at 380, 440, 500, 675, 870 nm and Ozone monitor which provides columnar ozone and water vapor by making use of differential absorption technique and also AOD at 1020 nm. MICROTOPS has the capability to make instantaneous measurements with high time resolution. Such measurements have been carried out at NMRF, a remote continental station with complex terrain features, during clear sky conditions. MICROTOPS has also been operated at a near by urban station, Tirupati (which is about 35 km from Gadanki in North-East direction) to examine the influence of anthropogenic activity on characteristics of aerosols, ozone and water vapor.

Corresponding author's address: Dr Y Jaya Rao, PM&A Division, Indian Institute of Tropical Meteorolgy, Dr.Homi Bhabha Road, Pune 411008, INDIA. E-Mail: jrao@tropmet.res.in.

3. SPECTRAL DISTRIBUTION OF AEROSOL OPTICAL DEPTH AND AEROSOL SIZE DISTRIBUTION

Figure 1 shows spectral distribution of Aerosol Optical Depth (AOD) observed during February 28 – March 12, 2003. The last panel of this figure (12 Mar 2003) shows the spectral distribution of AOD for Tirupati. Day-to-day variation of AOD is clearly evident from this figure. Though experiments have been conducted under clear sky conditions, it is observed that magnitudes of AOD, particularly for 380, 440 and 500 nm, show large on March 5, 7 and 8, 2003, suggesting the presence of optically thin clouds/haze.

Figure 2 shows the day-to-day variation of AOD for different optical channels. Significant day-to-day variation in AOD for all optical channels is clearly evident from this figure. Such variation is large for optical channels with shorter wavelengths as compared to that of optical channels with longer wavelengths. AOD for all optical channels show its maximum on March 8, 2003. The variation in AOD clearly indicates the variability in aerosol loading over Gadanki. The spectral distribution of AOD has been used to derive Aerosol Size Distribution (ASD) by making use of the inversion technique suggested by King (1982). Figure 3 shows the day-to-day variation of ASD. The ASDs over Gadanki show

by and large power-law distribution on different days. However, bi-modal distribution is observed on March 11, 2003 suggesting the enhanced loading of coarse-mode particles on this particular day. The ASD for Tirupati showed power-law distribution.

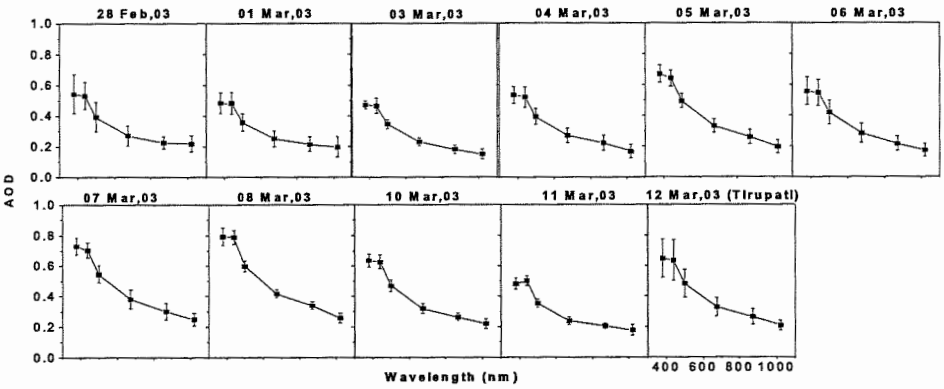

Figure 1: Spectral distribution of AOD for different days observed by MICROTOPS. Spectral distribution of AOD observed at Tirupati, an urban station, is shown in the last panel.

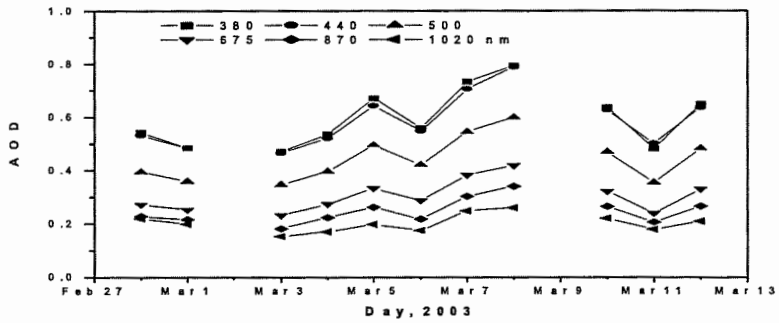

Figure 2: Day-to-day variation of AOD for different optical channels

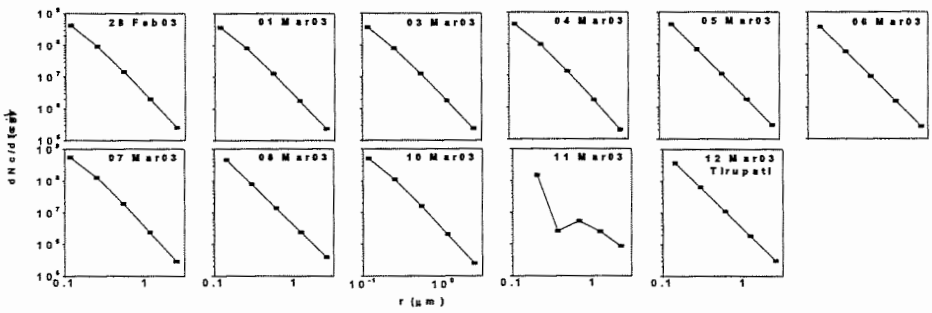

Figure 3: Day to day variation of Aerosol Size Distribution derived from spectral distribution of AOD.

4. TEMPORAL VARIATION OF AEROSOL OPTICAL DEPTH AND AEROSOL SIZE DISTRIBUTION

Though the mean ASD on different days shows power-law distribution, a close examination of ASD for individual days suggests possible dominant contribution of small size particles to the size distribution, there by ASD tending towards mono-modal distribution. The capability of MICROTOPS to make high resolution measurements has been used to study the temporal variations of AOD and ASD. Such a study is very significant to understand the variability of aerosol loading. Figure 4 shows the temporal variation of AOD for optical channels 380, 500 and 1020 nm. Significant temporal variation of AOD for different days can be noticed from this figure.

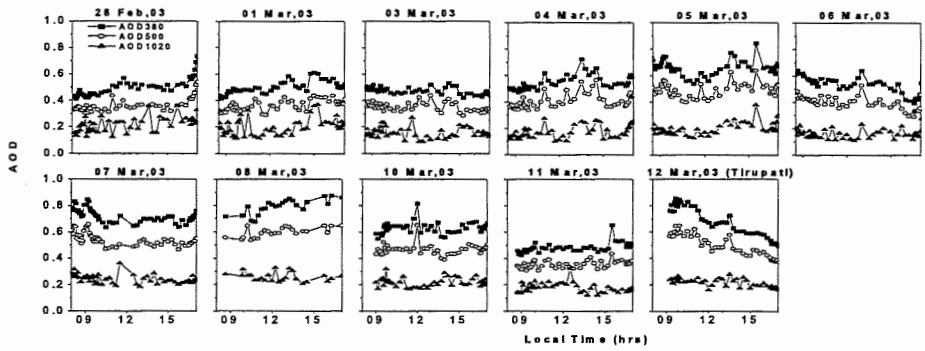

Figure 4: Temporal variation of AOD observed on different days by MICROTPS. The last panel shows temporal variation observed at Tirupati.

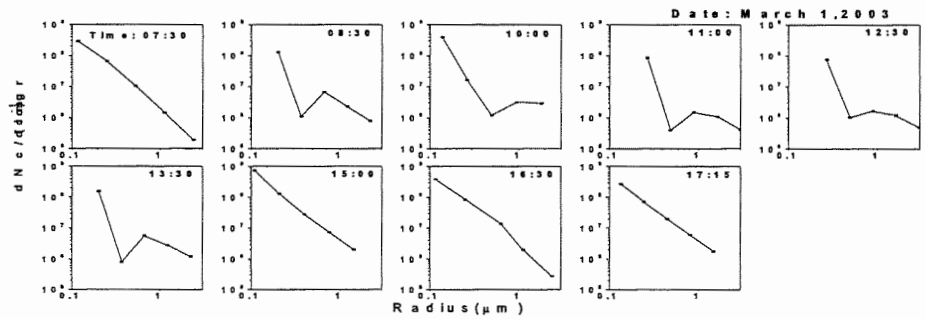

Figure 5 Hourly variation of ASD observed on March 1, 2003.

The temporal variation of AOD for Tirupati, observed on March 12, 2003 is quite different as compared to that observed for Gadanki on March 11, 2003. AODs, particularly for 380 nm and 500 nm, for Tirupati showed their maximum in the morning and then decreased as the day progressed. MICROTOPS observed temporal variation of AOD for different optical channels has been utilized to study the temporal variation of size distribution. Hourly means of AOD for different optical channels have been utilized for this purpose. Figure 5 shows the typical hourly variation of ASD observed on March 1, 2003. Time shown in each panel corresponds to the starting time for that hour. Significant variation of ASD with time is clearly evident from this figure. The ASDs show combination of mono- and bi-modal distributions indicating the enhanced loading of coarse-mode particles during 0830 - 1330 Hrs. The hourly variation of ASD for different days also showed similar features.

5. COLUMNAR OZONE AND WATER VAPOR

In addition to the aerosol measurements, MICROTOPS also provides columnar ozone and water vapor by making use of differential absorption of irradiance at 315, 330 and 340 nm for ozone and 940 and 1020 nm for retrieving the water vapor. MICROTOPS observed columnar ozone has been compared with that of Total Ozone Mapping Spectrometer (TOMS). Figure 6 shows comparison of ozone measured from MICROTOPS and TOMS.

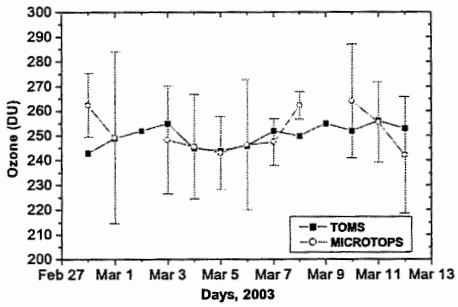

Figure 6: Comparison of columnar ozone measured independently by MICROTOPS and TOMS.

A good comparison, by and large, can be noticed between two independent techniques to measure columnar ozone. TOMS observations of ozone also show well within the standard deviation observed from MICROTOPS. High resolution measurements of columnar ozone and water vapor from MICROTOPS have been used to study the temporal variation of those parameters.

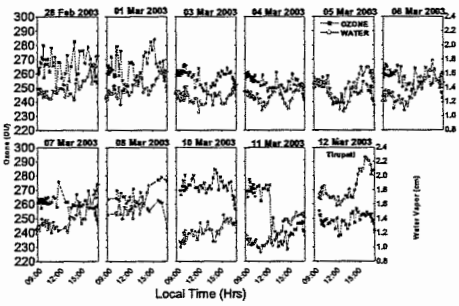

Figure 7: Temporal variation of columnar ozone and water vapor observed by MICROTOPS

Figure 7 shows temporal variation of ozone and water vapor for different days observed by MICROTOPS. Variations in ozone and water vapor, by and large, show opposite trend. An interesting feature of sudden fall in ozone concentration can be noticed on March 11, 2003 at about 12 noon and then continued till the end of observations on this day. Enhancement in water vapor during this period is also clearly evident from this panel.

6. CONCLUSIONS

High time resolution measurements of aerosols, ozone and water vapor have been carried out using MICROTOPS at a remote continental tropical station in India. Results show significant spectral as well as day-to-day variations of aerosol optical depth for different optical channels. Aerosol size distributions show, by and large, power-law distribution for this remote station. Significant temporal variation of AOD has also been noticed indicating variability of aerosol loading. Hourly variations of aerosol size distribution clearly show significant change in aerosol size distribution over a day. A good comparison has been noticed between MICROTOPS and TOMS observations of ozone. The temporal variations of columnar ozone and water vapor show by and large opposite trends.

7. ACKNOWLEDGEMENTS

Authors wish to express their thanks to the Director, Indian Institute of Tropical Meteorology, Pune for his keen interest and encouragement. The research work has been supported by the Indian Space Research Organization (ISRO), Department of Space, Government of India under RESPOND program.

REFERECNES

Devara et al., 2001: Some features of columnar aerosol optical depth, ozone and precipitable water content observed over land during the INDOEX-IFP 99, Meterologische Zeirschiriff, 10, 901-908.

Jaya Rao Y., et al., 2001: Atmospheric aerosol characteristics over different environments, In. Advances in Atmospheric Chemistry (Eds., P. C. S. Devara and P. Ernest Raj), pp 107-110.

King, M.D. 1982: Sensitivity of constrained linear inversions to the selection of the Lagrange multiplier, J. Atmos. Sci., 39, 1356-1369.

AEROSOL IMPACTS ON PRECIPITATION FROM CONVECTIVE CLOUDS: IN SITU AND REMOTE SENSING OBSERVATIONS

D. Rosenfeld

Institute of Earth Sciences, The Hebrew University of Jerusalem, Israel

1. FROM SHIP TRACKS TO PYRO-CB

1.1 Ship Tracks

The impact of anthropogenic pollution aerosols on cloud microstructure has become obvious with the discovery of the ship tracks, soon after Multispectral satellite images became available from the AVHRR onboard the NOAA satellites (Coakley et al., 1987). Shortly after that discovery, in situ aircraft measurements of ship tracks in marine stratocumulus clouds provided the first evidence that effluents from ship stacks change cloud microstructure by redistributing their water into a larger number of smaller droplets (Radke et al., 1989). Albrecht (1989) suggested that the drizzle, which normally occurs in marine stratocumulus clouds in clean air, would be inhibited from the clouds with reduced droplet size, thereby increasing the cloud water content and longevity. Satellite measurements of the relations between cloud drop effective radius and precipitation radar echoes have shown that convective clouds start precipitating at $r_e > 14$ μm (Rosenfeld and Gutman, 1994). In situ measurements in marine stratocumulus confirmed this threshold (Gerber, 1996). Further support for the 14 μm threshold was given by coalescence simulations (Rosenfeld et al., 2002).

1.2 Pollution Tracks Over Land

The attention of the cloud physics community during the first decade after discovery of the ship tracks was focused at the interactions of anthropogenic aerosols with marine clouds. Clouds over land were assumed to be already "continental". This was the decade of the great experiments of the marine stratocumulus, with extensive cloud physics campaigns. All that has started to change with the discovery of "pollution tracks" in the order of magnitude deeper (2 - 3 km) stratocumulus and cumulus clouds over land (Rosenfeld and Lensky, 1998; Rosenfeld, 2000). They showed that, at least in certain circumstances, anthropogenic emissions can create ship track like features in clouds well inland, and that these features are devoid of precipitation whereas adjacent thermodynamically similar clouds precipitate readily. This demonstrated that anthropogenic sources of CCN often change the clouds to be considerably more microphysically "continental" than the less affected natural background clouds over the continent. Furthermore, the pollution tracks were evident well inland mainly in the least inhabitant areas of the world, such as Australia and Canada, but not in places such as well inland USA or Europe. This supports the suggestion that the background concentrations of CCN are already dominated by anthropogenic emissions, and that cloud microstructure and precipitation properties are far removed from the natural state. Furthermore, these changes affect not only to slow down the warm rain processes, but also to inhibit the ice precipitation processes, as shown by remote sensing (Rosenfeld, 2000) and in situ (Borys et al., 2003) measurements.

Corresponding author's address: Daniel Rosenfeld, Institute of Earth Sciences, The Hebrew University of Jerusalem, Jerusalem 91904, Israel.
E-Mail: daniel.rosenfeld@huji.ac.il

1.3 Suppressed precipitation in deep convection

The Tropical Rainfall Measuring Mission satellite (TRMM) was launched in late 1997 and provided us with capabilities of observing both cloud microstructure and precipitation with its suit of instruments that include VIS/IR radiometer, passive microwave, radar and a lightning detector. TRMM measurements were used to demonstrate how smoke from burning tropical rain forests suppresses the precipitation in tropical clouds that their tops do not exceed the -10°C isotherm level, which is near 6.5 km msl in the tropics. This suggests that warm rain processes were suppressed to the extent that precipitation were initiated mainly by ice processes. These precipitation suppression effects were documented for Indonesia (Rosenfeld, 1999) and for the Amazon (Rosenfeld and Woodley, 2003). Not only smoke was capable of having such effects on tropical clouds, but also the heavy urban air pollution of Manila (Rosenfeld and Lensky, 1998) and the mixed urban and biomass burning aerosols over southern India (Rosenfeld et al., 2002). In situ aircraft measurements of aerosols and cloud drop size distributions (CDSD) (Andreae et al., 2004) have validated the satellite inferences about the role of smoke in suppressing the coalescence in deep tropical clouds.

1.4 Pyro-Cb: Pollution Tracks in the Anvils

A pyro cloud is defined as a cloud that feeds directly on the heat and smoke of an active fire. Very intense fires provide occasionally sufficient heat to create a convective cloud that develops all the way to the

tropopause, and even overshoot. Such a cloud is named here a pyro-Cb. Satellite measurements show that the r_e of cloud top particles in pyro-Cb often do not exceed the precipitation threshold of 14 μm even in the anvils (Fig. 1), whereas Cb clouds in the ambient air show well developed mixed phase precipitation although coalescence is suppressed in these highly micorphysically continental clouds, as inferred by the satellite methodology of Rosenfeld and Lensky (1998). Such small ice particles in convective elements are most probably formed because there is no effective mechanism to freeze the small cloud droplets before passing through the homogeneous freezing isotherm of -38°C. Such homegenous freezing of nearly adiabatic deep convective elements in microphysically highly continental clouds has been documented by aircraft measurements in West Texas (Rosenfeld and Woodley, 2001). Therefore, with the even more extreme microphysically continental nature of the pyro Cb, homogeneous freezing of the small cloud drops is the likely explanation for the extremely small r_e of the anvils of the pyro Cb. Under such circumstance there is also no effective mechanism for converting most of the cloud water into hydrometeors, so that precipitation from pyro-Cb is highly suppressed, even though their depth is the greatest possible. This lack of precipitation from Pyro Cb has been confirmed with radar measurements, for two cases in Canada and in the USA.
In situ aircraft measurements in tropical pyro clouds confirm the extreme extent of suppression of coalescence in these clouds (Andreae et al., 2004).

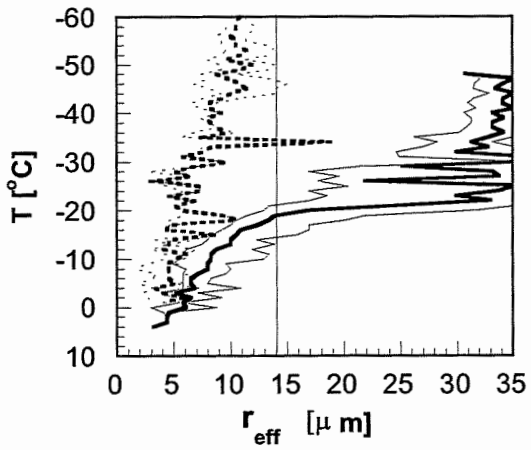

Figure 1: T-r_e relations of pyro-Cb (broken lines for the 15, 50 and 85 percentile lines) and ambient continental clouds (solid lines for the same percentiles) in Chisolm, Canada, from NOAA/AVHRR overpass at 29 May 2001, 00:00 GMT. Note the much smaller re of the pyro cloud, which did not exceed the precipitation threshold of 14 μm even at the coldest temperatures.

2. THE MIXED EFFECTS OF DESERT DUST

Desert dust originates typically as large (i.e., > 1 μm) mineral particles with little soluble content (Rosenfeld et al., 2001), so that the CCN activity is similar to much smaller soluble aerosols, which contribute to the microphysical "continentality" of clouds. Because of the large sizes of the dust aerosols, their small CCN activity cannot match that of even moderate concentrations of smoke aerosols. Therefore, the coalescence suppression effects would be evident mainly on the background of maritime air mass, as documented by Rosenfeld et al. (2001). Very large concentrations of dust particles can occur in very heavy dust storms. But in such case also the size of the dust particles becomes quite large, some well exceeding 10 μm. Such large dust particles can start the coalescence processes merely by their dry size, as they fall and collide with the rest of the cloud drops. Indeed, satellite observations of clouds in very heavy sand storms in the Middle East support this suggestion.

The dust particles that do not come directly from the source areas become coated with sulfates, probably due to cloud processing, and so potentially serving as giant CCN in subsequent cloud generations, and so enhancing coalescence and precipitation (Wuzler et al., 2000). Similar effect is caused by sea salt that is added to the dust particles (Schneider et al., 2004). In spite of these effects, both satellites and in situ measurements show that clouds forming in dust-free air over the east Mediterranean produce precipitation faster than clouds in nearby dusty air mass

Whatever effect of suppressing precipitation that the desert dust might still have is reversed at temperatures colder than -11°C, where the ice nucleating activity of the dust comes into effect (Rosenfeld and Farbstein, 1992). This has been documented in Israel with both satellite and in situ measurements (Rosenfeld et al., 2002).

3. SEA SALT RESTORING PRECIPITATION

Most sea salt aerosols form giant CCN that are capable of enhancing coalescence and precipitation, especially from polluted microphysically continental clouds. This process was documented over the Indian Ocean in clouds with very large pollution aerosol concentrations that came from SE Asia, using the TRMM satellite (Rosenfeld et al., 2002). The minimum cloud depth for precipitation decreased to 3 km, in line with the theoretical model calculations based on the measured aerosol population.

Situations of sea salt seeding clouds over land were observed over the desiccated bed of the Aral Sea. Winds blew the material from the dry seabed as salt dust storms that seeded the ambient microphysically continental clouds. The response of the clouds was a fast growing of cloud drop r_e with height, well beyond

the precipitation threshold (Rudich et al., 2002). The significance of these results becomes apparent when comparing with the opposite effect of a mineral desert dust interacting similarly with clouds (Rosenfeld et al., 2002).

What happens when large concentrations of mineral dust, smoke and salt mix together and ingested into the clouds? An opportunity to observed this occurred at the 1991 Gulf war (Rudich et al., 2002). Heavy smoke from the burning oil wells was mixed with salt from the brines that mixed with the oil. Some desert dust was likely to be in this environment, but not in sufficient quantities to be identified. The smoke and salt have opposite effects. It is questionable how many large salt particles remained in the heavy smoke after reaching the cloud level, but apparently there was insufficient quantity for making the clouds having larger r_e than the ambient clouds at their base. The smoky clouds remained with very small re up to about –20°C to -30°C, but glaciated thereafter at temperatures that are significantly higher than the pyro Cb. The heterogeneous freezing is evidence for a mixed phase zone in the cloud, where mixed phase precipitation do form. Is this difference between pyro clouds and the oil well clouds due to the added salt?

4. SMALL AND GIANT CCN

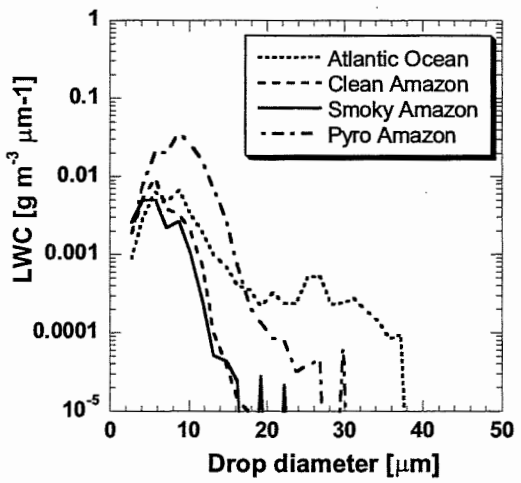

Figure 2: Cloud base drop size distributions exactly at cloud base (i.e., ground is barely visible from the aircraft) for clouds over the Atlantic Ocean, in the pristine clouds over western Amazon, in smoky clouds there, and in a pyro cloud. The pass through the pyro cloud was higher above the base, because base was not recognizable due to the smoke. Note the wide tail over the ocean, and its absence in the continental clouds.

The aircraft measurements within a wide range of conditions in the SMOCC campaign in Brazil (Andreae et al., 2004) provided additional information of the respective roles of small and giant CCN. According to Fig. 2, the shapes of the CDSD at the very base of the clouds were not distinguishable between the smoky and pristine clouds. In contrast, there was a very wide tail of large droplets at the base of the clouds over ocean. The tail developed quickly into raindrops, as evident from Fig. 4a of Andreae et al. (2004), whereas in the clean clouds over the Amazon the rain formed a little higher in the cloud due to the broadening of the main mode of the CDSD (Fig. 4b of Andreae et al., 2004). The pyro cloud had far smaller and fewer drops in the tail, which suggest far smaller activity of giant CCN than in ordinary maritime aerosols. This was manifested in the total lack of observations of warm rain in the smoky and pyro clouds, in line with the satellite observations. These results are in line with the observations of the impact of sea salt restoring the precipitation, by doing natural hygroscopic seeding with super-micron salt particles (Rosenfeld et al., 2002).

5. SIGNIFICANCE OF THE OBSERVATIONS

The recent satellite and in situ observations presented here and elsewhere demonstrate that the great sensitivity of clouds and precipitation to anthropogenic aerosols is not confined to the marine stratocumulus, but rather applicable to a large fraction of the convective clouds over land. Furthermore, the convective clouds over land are even more susceptible to the suppression effects of the pollution aerosols than clouds over ocean, because over ocean the sea salt giant CCN seed the clouds naturally and restore the precipitation even when high concentrations of small pollution aerosols exist.

This large sensitivity has many implications.

- Precipitation efficiency of convective clouds over land is often strongly dependent on anthropogenic aerosol emissions, usually to the detriment.
- The other side of the same coin is the potential to enhance precipitation by imitating the way nature does hygroscopic seeding (Lahav and Rosenfeld, this conference).
- Climate implications are that aerosols have strong effects on convective cloud lifetime over land (aerosol indirect effect of the second kind), whereas until now this effect was sought in marine stratiform clouds.
- Dynamic feedbacks of the precipitation effects are probably very large, as already suggested by model simulations (Khain et al., Kelman et al., this conference).

The most important implication is on the sensitivity of precipitation and water availability on our actions or defaults, as demonstrated by Givati and Rosenfeld

(2004). After all, water availability is the most important environmental property to our livelihood.

6. ACKNOWLEDGEMENTS

This research was funded by the Israeli ministry of Science and Technology, The Israeli Space Agency.

7. REFERENCES

Albrecht, B. A., 1989: Aerosols, cloud microphysics, and fractional cloudiness. *Science*, **245**, 1227–1230.

Andreae, M. O., D. Rosenfeld, P. Artaxo, A. A. Costa, G. P. Frank, K. M. Longo, and M. A. F. Silva-Dias, 2004: Smoking rain clouds over the Amazon. *Science*, **303**, 1337-1342.

Schneider J, Borrmann S, Wollny AG, Blasner M, Mihalopoulos N, Oikonomou K, Sciare J, Teller A, Levin Z, Worsnop DR, 2004: Online mass spectrometric aerosol measurements during the MINOS campaign (Crete, August 2001). *Atmospheric Chemistry and Physics*, **4**, 65-80.

Borys, R.D., D. H. Lowenthal, S. A. Cohn, and W. O. J. Brown, 2003: Mountain and radar measurements of anthropogenic aerosol effects on snow growth and snowfall rate. *Geophys. Res. Lett.*, **30**(10), 1538, doi: 10.1029 /2002GL016855.

Coakley, J. A., R. L. Bernstein, and P. R. Durkee, 1987: Effects of ship-stack effluents on cloud reflectivity. *Science*, **237**, 1020–1022.

Gerber, H., 1996: Microphysics of marine stratocumulus clouds with two drizzle modes. *J.* Atmos. Sci., 53, 1649-1662.

Givati A. and D. Rosenfeld. Quantifying precipitation suppression due to air Pollution. In Press, *Journal of Applied meteorology*.

Kelman G., D. Rosenfeld, A. Khain, 2004: Changing the latent heat release from convective clouds due to aerosol-precipitation interactions constituting Latent Heat Forcing as a new concept in climate change. 14th International Conference on Clouds and Precipitation. Bologna, Italy, 18-23 July 2004.

Khain A., D. Rosenfeld and A. Pokrovsky, 2004: Aerosol impacts on precipitation from convective clouds. 14th International Conference on Clouds and Precipitation. Bologna, Italy, 18-23 July 2004.

Kelman G., D. Rosenfeld and A. Khain, 2004: Changing the latent heat release from convective clouds due to aerosol-precipitation interactions constituting Latent Heat Forcing as a new concept in climate change. 14th International Conference on Clouds and Precipitation. Bologna, Italy, 18-23 July 2004.

Lahav R., D. Rosenfeld, 2004: The search for the optimal size of hygroscopic seeding particles. 14th International Conference on Clouds and Precipitation. Bologna, Italy, 18-23 July 2004.

Radke, L. F., Coakley, Jr., J. A., & King, M. D. (1989). Direct and remote sensing observations of the effects of ships on clouds. *Science*, **246**, 1146-1149

Rosenfeld D., 1999: TRMM Observed First Direct Evidence of Smoke from Forest Fires Inhibiting Rainfall. Geophys. Res. Lett., 26, No. 20, 3105.

Rosenfeld D., 2000: Suppression of Rain and Snow by Urban and Industrial Air Pollution. *Science*, **287** (5459), 1793-1796.

Rosenfeld D. and H. Farbstein, 1992: Possible influence of desert dust on seedability of clouds in Israel. *J. Applied Meteorology*, **31**, 722-731.

Rosenfeld, D., and G. Gutman, 1994: Retrieving microphysical properties near the tops of potential rain clouds by multispectral analysis of AVHRR data. *J. Atmos. Res.*, **34**, 259-283.

Rosenfeld D., R. Lahav, A. P. Khain, M. Pinsky, 2002: The role of sea-spray in cleansing air pollution over ocean via cloud processes. "Research Article" in *Science*, **297**, 1667-1670.

Rosenfeld, D. and M.I. Lensky, 1998: Space-borne based insights into precipitation formation processes in continental and maritime convective clouds. *Bull. Amer. Meteor. Soc.*, **79**, 2457-2476.

Rosenfeld D. and W. L. Woodley, 2000: Convective Clouds with Sustained Highly Supercooled Liquid Water Down to –37.5°C. *Nature*, **405**, 440-442.

Rosenfeld D. and W. L. Woodley, 2003: Closing the 50-year circle: From cloud seeding to space and back to climate change through precipitation physics. Chapter 6 of "Cloud Systems, Hurricanes, and the Tropical Rainfall Measuring Mission (TRMM)" edited by Drs. Wei-Kuo Tao and Robert Adler, 234pp., p. 59-80, *Meteorological Monographs*, **51**, AMS.

Rosenfeld D., Y. Rudich and R. Lahav, 2001: Desert dust suppressing precipitation – a possible desertification feedback loop. *Proceedings of the National Academy of Sciences*, **98**, 5975-5980.

Rudich Y., D. Rosenfeld, O. Khersonsky, 2002: Treating clouds with a grain of salt. *Geoph. Res. Let.*. **29** (22), doi:10.1029/2002GL016055, 2002.

Wurzler S, Reisin TG, Levin Z., 2000: Modification of mineral dust particles by cloud processing and subsequent effects on drop size distributions. *J. Geophys. Res.* **105** (D4): 4501-4512.

THE EFFECT OF AEROSOL CHEMICAL COMPOSITION ON CLOUD DROPLET NUMBER

K. E. Ross[1], S. J. Piketh[1] and R. T. Bruintjes[2]

[1]University of the Witwatersrand, Johannesburg, Wits 2050, South Africa
[2]National Center for Atmospheric Research, Boulder, Colorado, 80307, USA

1. INTRODUCTION

Organic aerosol particles are an important component of the atmospheric cloud condensation nuclei (CCN) reservoir, but there is currently a poor understanding of the way in which they participate in the activation process and consequently influence cloud droplet spectra. Approximately twice as many accumulation mode aerosols act as CCN over southern Africa during the burning season than during the wet season. It is hypothesised that the increased efficiency is due to the input of organic compounds derived from biomass burning. A cloud parcel model with explicit microphysics has been employed in this study to assess the sensitivity of cloud droplet activation to aerosol chemical composition.

2. DATA AND METHODS

The empirical relationship between aerosol and CCN concentration over southern Africa has been determined using measurements collected from an airborne platform during the burning season (August/September 2000) and the mid-wet season (January 1999). Accumulation mode aerosol size distribution was measured with a Passive Cavity Aerosol Spectrometer Probe (PCASP-100X; Particle Measuring Systems (PMS) Inc.) during the burning season campaign and with an Active Scattering Aerosol Spectrometer Probe (ASASP-100X; PMS Inc.) during the wet season campaign. CCN concentrations were recorded using a static thermal-gradient diffusion chamber (University of Wyoming, model 100A).

A one-dimensional adiabatic cloud parcel model developed at the National Center for Atmospheric Research in Boulder, Colorado (Cooper *et al.*, 1997) has been used to investigate the effect of aerosol chemical composition on cloud droplet formation and properties. Calculations simulate cloud droplet activation and simultaneous condensation and coalescence during the adiabatic ascent of a closed parcel. Surface tension, van't Hoff factor (a measure of the number of ions into which a molecule dissociates) and solution density are computed as a function of molality. Aerosol chemical composition is specified as one of three inorganic or three organic aerosol types, with a variable insoluble volume fraction.

Table 1: Properties of the organic compounds at 293 K

Compound	Mole-cular weight	Solubility (g/100g H_2O)	Density (g cm^{-3})	Van't Hoff factor
Ammonium sulphate $(NH_4)_2SO_4$	132.14	75.7	1.769	
Glutaric acid[1] $C_5H_8O_4$	132.12	116	1.424	1
Pinic acid[2] $C_9H_{14}O_4$	186.21	>8.46	0.8	1
Pinonic acid[2] $C_{10}H_{16}O_3$	184.24	0.786	0.64-0.71	1

[1]Cruz and Pandis, 1998
[2]Raymond and Pandis 2003

Low molecular weight dicarboxylic acids have been identified as one of the major water soluble organics in aerosols in both polluted and unpolluted areas. Three dicarboxylic acids of varying solubilities have been selected for this study (Table 1). The critical supersaturation of the less soluble compounds was taken to be the greater of the peak of the conventional Köhler curve and the initiation peak of the deliquescence, where droplet radius corresponds to the volume equivalent radius of the initial dry solute particle (Hori *et al.*, 2003). A van't Hoff factor of one was assumed for all the organic compounds since they are weak acids and no

Corresponding author's address: Kristy E. Ross, Climatology Research Group, University of the Witwatersrand, Private Bag 3, Wits, 2050, South Africa; E-mail: kristy@crg.bpb.wits.ac.za

experimental results are available. The depression in droplet surface tension as a function of organic carbon concentration measured by Shulman *et al.* (1996) was used.

The aerosol size distributions used to initialise simulations are averages of all measurements collected during the burning season and wet season, expressed as a multimodal lognormal distribution (Table 2). Only particles with diameter greater than 0.1 μm are considered. The total concentration of accumulation mode aerosols was 960 cm^{-3} in the burning season and 900 cm^{-3} in the wet season.

Table 2: Parameters of the lognormal aerosol size distributions

Lognormal parameter	Burning season	Wet season
N_1 (cm^{-3})	1164.0	1380.0
D_1 (μm)	0.16	0.12
Log(σ_1)	0.20	0.19
N_2 (cm^{-3})		13.5
D_2 (μm)		0.5
Log(σ_2)		0.11
N_3 (cm^{-3})	1.2	2.0
D_3 (μm)	1.0	1.0
Log(σ_3)	0.52	0.52

3. AEROSOL-CLOUD DROPLET RELATIONSHIP OVER SOUTHERN AFRICA

More than twice as many particles with diameter greater than 0.12 μm are CCN in the dry season (up to 77% at 0.36% supersaturation), than in the wet season (34% at 0.28% supersaturation), as seen in the scatterplots of CCN concentrations and simultaneously measured accumulation mode aerosol concentrations (Figure 1). The difference in supersaturation at which the CCN were measured does not account for such a large seasonal difference. The input of organic compounds to the atmosphere is highly seasonal, occurring mainly as a result of biomass burning in the late dry season from July to September, and provides a better explanation. It is likely that the soluble organic particles and potassium salts emitted by savanna fires (Gao *et al.*, 2003; Li *et al.*, 2003) are efficient CCN. Organic compounds generally depress surface tension and so lower critical supersaturation. Organic compounds may also condense or agglomerate on the surface of non-hygroscopic nuclei and enable them to activate. The fact that the CCN: aerosol ratio is highest in the tropics, where biomass burning is most intense, supports the notion that organic particles are responsible for the high CCN activation efficiency. Furthermore, it seldom rains during the burning season, and anticyclonic conditions frequently prevail, resulting in very stable conditions and a high incidence of recirculation. As a result, aerosol residence time over the subcontinent is prolonged at this time of year, giving more opportunity for mixing and coagulation. The accumulation mode aerosol is skewed to larger sizes in the burning season than in the wet season (Figure 2), indicating coagulation. The good correlation between aerosol and CCN concentrations (>0.65) is evidence of a well-mixed airmass.

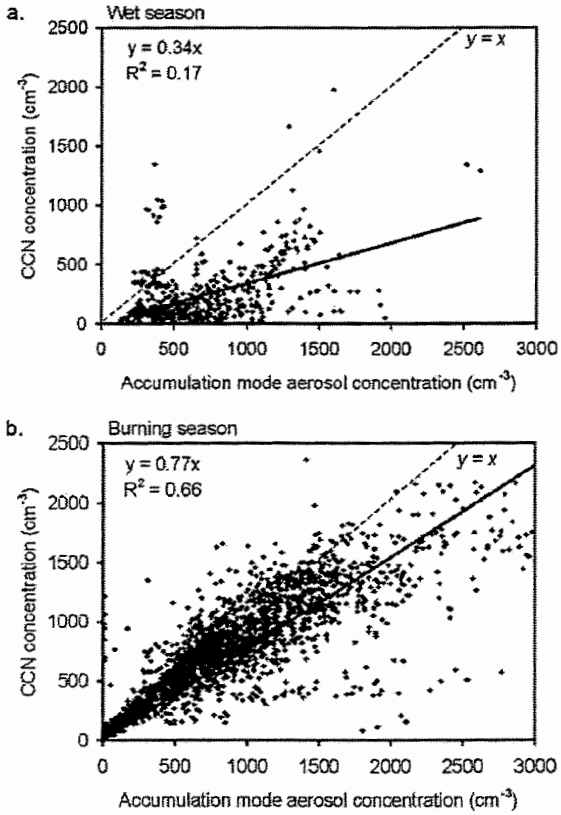

Figure 1: Relationship between CCN concentration and total accumulation mode aerosol concentration (diameter > 0.12 μm), a. in the mid-wet season (January 1999; CCN concentrations measured at a supersaturation of 0.28%) and b. in the burning season (August/September 2000; CCN concentrations measured at 0.36% supersaturation). The solid line is the best least squares linear fit and the dashed line indicates a 1:1 relationship.

During the wet season, most of the submicron aerosol loading is derived from industrial activities. The CCN:aerosol ratio is lowest over the industrialised Highveld, suggesting that the aerosols emitted by industries are non-hygroscopic. The lower proportion of aerosols activated in the wet season may also be attributed to the washout of soluble material, leaving predominantly insoluble particles behind.

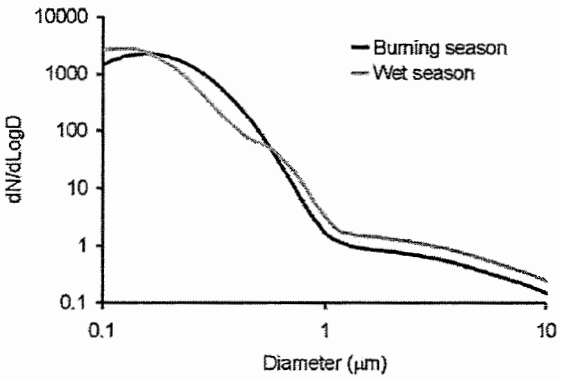

Figure 2: Average aerosol size distributions recorded with a PCASP during the burning season and an ASASP during the dry season

4. ACTIVATION OF ORGANIC AEROSOLS

It appears that organic particulate matter plays a key role in increasing the proportion of aerosols able to be activated over southern Africa in the late dry season. A cloud parcel model with explicit microphysics is used to further investigate the activation of organic compounds, both as pure particles, and mixed with insoluble aerosol particles. Three organic compounds are considered: glutaric acid, which is highly soluble, pinic acid, which is moderately soluble, and pinonic acid, which has very low solubility. Ammonium sulphate is used a reference.

The activated proportion of accumulation mode aerosols is primarily determined by the solubility of the compound. All the glutaric acid particles are activated at cloud base; pure glutaric acid is even more effective as a CCN than ammonium sulphate. A smaller percentage of the pinic acid particles are activated (70% in the burning season), and an even smaller proportion of the low solubility pinonic acid particles are activated (42%), due to the reduction of the Kelvin effect. Peak supersaturations are higher for the less soluble compounds (0.92% for pinic acid and 0.45% for pinonic acid, compared to 0.38% for glutaric acid). Supersaturation was controlled by the adiabatic ascent of the parcel under realistic temperature and dewpoint conditions (Cooper *et al.*, 1997) for these simulations.

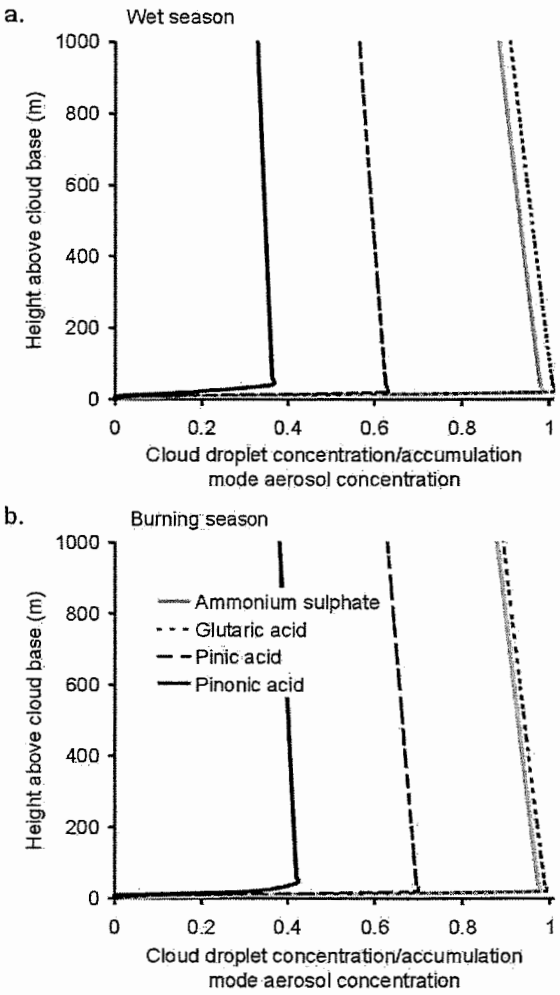

Figure 3: The ratio of cloud droplet to accumulation mode aerosol concentration with height above cloud base in a. the wet season and b. the burning season

The different aerosol size distributions in the two seasons affect the proportion of aerosols activated for the less soluble compounds: only 63% of pinic particles and 36% of pinonic particles are activated in the wet season (as opposed to 70% and 42% in the burning season) because the accumulation mode distribution is skewed to smaller sizes.

Organic compounds often condense onto or coagulate with other aerosols, and are found as

mixtures rather than as pure substances in the atmosphere. The in-situ measurements indicate that a large number of aerosol particles found in the atmosphere over southern Africa in the wet season are not hygroscopic. Calculations have been performed to gauge the extent to which organic inclusions can promote the activation of non-hygroscopic particles. In order to eliminate the effect of dynamics and varying supersaturations on cloud droplet number and better simulate conditions in the chamber of the CCN counter, the parcel model was run at a constant supersaturation of 0.36%. The average burning season aerosol size distribution was used for all runs.

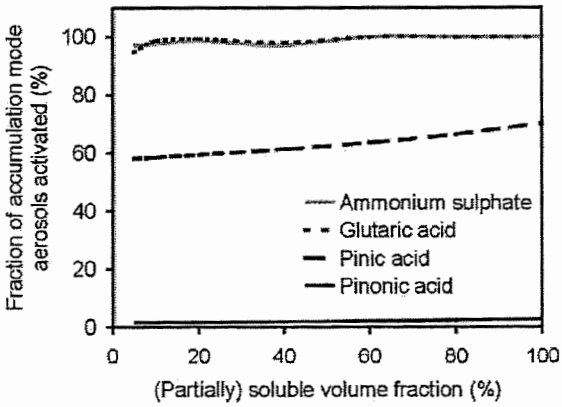

Figure 4: The fraction of accumulation mode aerosols activated as a function of the volume fraction of organic compound or ammonium sulphate. The remaining volume fraction is insoluble.

Soluble compounds are extremely effective in changing the activation potential of an insoluble particle. Even when comprising only 5% of the volume of otherwise insoluble particles, glutaric acid allows 94% of all accumulation mode aerosols to be activated at a supersaturation of 0.36%. Organic compounds with low solubility, such as pinonic acid, have very little influence on the number of particles activated, since they are not efficient CCN. Pinic acid increased the proportion of particles activated from 58% to 70% as its contribution to the total volume of the particles increased from 5% to 100%.

5. CONCLUSION

Results of the calculations described above show that soluble organic compounds, either as pure particles or internally mixed with non-hygroscopic aerosols, are highly effective CCN. Even an inclusion or coating of a moderately soluble organic compound, such as pinic acid, on an otherwise insoluble particle, is sufficient to significantly increase the insoluble particle's ability to act as a CCN. The combination of increased input of soluble organic compounds to the southern African atmosphere during the burning season, and prolonged residence times and associated coagulation and reaction of organic compounds with non-hygroscopic aerosols due to recirculation, atmospheric stability and absence of washout, accounts for the significantly higher proportion of aerosols acting as CCN over southern Africa in the late dry season compared to the wet season.

6. ACKNOWLEDGMENTS

This research was conducted while Kristy Ross was supported by a postdoctoral fellowship from the National Research Foundation in South Africa. Funding was also provided by the Water Research Commission and Eskom, South Africa. The National Center for Atmospheric Research is operated by the University Corporation for Atmospheric Research under the sponsorship of the National Science Foundation.

7. REFERENCES

Cooper, W. A., R. T. Bruintjes and G. K. Mather, 1997: Calculations pertaining to hygroscopic seeding with flares. *J. Appl. Meteor.*, 36, 1449-1460.

Cruz, C. N. and S. N. Pandis, S. N., 1998: The effect of organic coatings on the cloud condensation nuclei activation of inorganic atmospheric aerosol. *J. Geophys. Res.*, 103, 13,111-13,123.

Gao, S., D. A. Hegg, P. V. Hobbs, T. W. Kirchstetter, B. I. Magi and Sadilek, M., 2003: Water-soluble organic components in aerosols associated with savanna fires in southern Africa: Identification, evolution and distribution. *J. Geophys. Res.*, 108 (D13), 8491, doi:10.1029/2002JD002324.

Hori, M., S. Ohta, N. Murao and S. Yamagata, 2003: Activation capability of water soluble organic substances as CCN. *Aer. Sci.*, 34, 419-448.

Li, J., M. Pósfai, P. V. Hobbs and P. R. Buseck, 2003: Individual aerosol particles from burning in southern Africa: 2. Compositions and aging of inorganic particles. *J. Geophys. Res.*, 108 (D13), doi:10.1029/2002JD002310

Raymond, T. M. and S. N. Pandis, 2003: Formation of cloud droplets by multicomponent organic particles. *J. Geophys. Res.*, 108 (D15), doi: 10.1029/2003JD003503.

Shulman, M. L., M. C. Jacobson, R. J. Charlson, R. E. Synovec and Young, T. E., 1996: Dissolution behaviour and surface tension effects of organic compounds in nucleating cloud droplets. *Geophys. Res. Letters*, 23, 227-280.

SPATIAL AND SEASONAL VARIATIONS OF CLOUD CONDENSATION NUCLEI AND AEROSOLS IN THE UNITED ARAB EMIRATES

V. Salazar[1], R. Bruintjes[1], D. Breed[1], T. Jensen[1], S. Piketh[2], A. Al Mandoos[3], A. Al Mangoosh[3] and K. Ross[2].

[1]National Center for Atmospheric Research, Boulder Colorado, USA
[2]University of Witwatersrand, Johannesburg, South Africa
[3]Department of Water Resources Studies, Abu Dhabi, United Arab Emirates

1. INTRODUCTION

The last decade has seen an increase in studies on the role of aerosol particles in altering the Earth's climate. Several field projects have collected in-situ measurements of aerosol particles, CCN, cloud droplets, trace gases and state parameters in different parts of the world. The data collected during these campaigns has highlighted the complexity of aerosol effects on the atmosphere and the climate.

Aerosols have relatively short lifetimes, typically on the order of a week, and so their effect on the Earth's radiation balance is highest near major source regions (Kiehl and Briegleb, 1993). The wide range of estimates given for the different natural sources of aerosols reflects the uncertainty of the assumptions upon which these estimates are made. For example, a comparison of sources can be misleading because their contribution to the aerosol general budget depends on the different methods of transport, removal, and chemical transformation of a specific geographical region. Ross et al. (2003) showed how anthropogenic aerosol emissions significantly enhanced CCN concentrations immediately downwind of industrial biomass burning in southern Africa, demonstrating how the spatial distribution of CCN is controlled by the location of aerosol sources, atmospheric transport, chemical transformation, and removal mechanisms.

In the same context, the processing of particles through clouds can increase the mass of soluble material, making those aerosol particles more efficient CCN (Yin et al., 2002). These changes in the particles typically occur through processes like coagulation, sedimentation, aqueous phase chemical reactions and evaporation of drops (Wurzler et al., 2000). The ingestion of these modified particles into other clouds influences the development of precipitation and optical properties, especially in continental type of clouds.

Recent work has demonstrated the importance of large mineral dust as a natural source of atmospheric aerosols (Rosenfeld et al., 1996). Observations by Levin et al. (1996) in the Eastern Mediterranean region showed that sulfate particles are present in most aerosol particles, suggesting that mineral dust might be coated with sulfate as well as with other soluble substances (Fonner and Ganor, 1992). The specific type of coating on the particles could enhance the ability of mineral dust to act as cloud condensation nuclei.

Corresponding author's address: Vidal Salazar, National Center for Atmospheric Research, Research Applications Program, P.O. Box 3000 Boulder Co. 80307, USA; E-Mail: vidal@ucar.edu

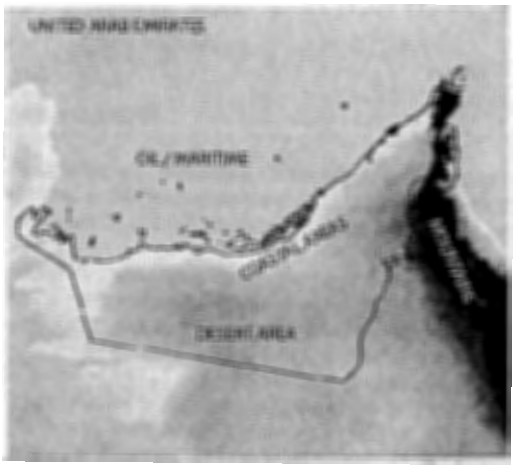

Figure 1. Regions of the United Arab Emirates delimited according to topography, land use and aerosol sources.

This paper presents results from airborne aerosol sampling conducted over the United Arab Emirates (UAE) in the winter (January-April) and summer (June-September) of 2001 and 2002 during the "Feasibility Study for the Augmentation of Rainfall in the United Arab Emirates" field project. Measurements of trace gases, aerosol characteristics and cloud physics were carried out in order to characterize the nature of the atmospheric constituents over the UAE. The aerosol and CCN characteristics are presented to explore the differences between various regions of the UAE, delimited by their surface characteristics and their ability to generate or modify the aerosol population. Seasonal variability as well as spatial differences are examined.

2. CLIMATOLOGICAL BACKGROUND OF THE UNITED ARAB EMIRATES

An introduction to the climate of the United Arab Emirates by Boer (1997) describes the UAE as hyperarid, with slightly higher mean annual temperatures than the rest of the Arabian stations.

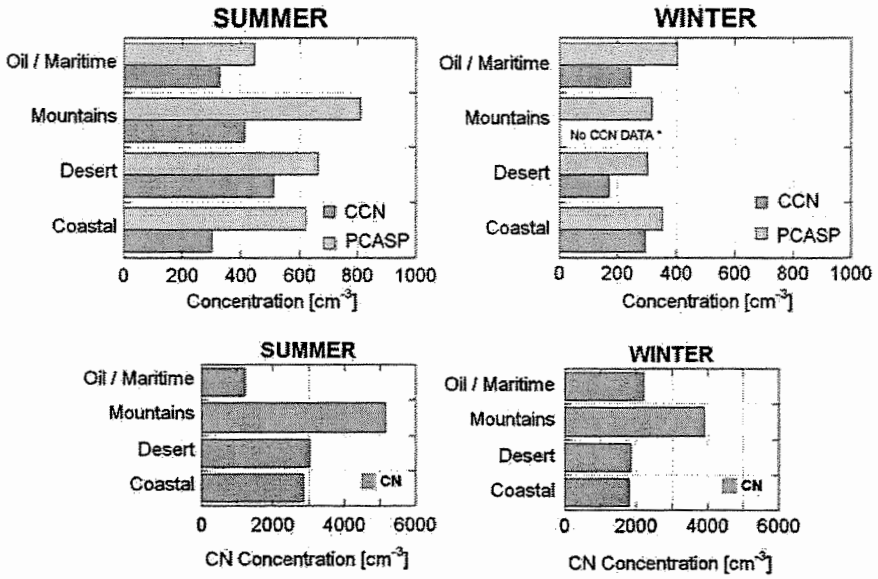

Figure 2. Spatial and seasonal variations in vertically integrated averages of PCASP, CCN and CN concentrations, recorded between 1000 m and 4000 m ASL during winter and summer. CCN concentrations were recorded at a supersaturation of 0.3%. Zones are delimited as in Figure 1.

Winter and summer conditions are delineated by distinctly different meteorological regimes. Winter months are characterized by dry stable conditions with a strong influence of the mid-latitude westerly flow, which occasionally brings rain producing westerly troughs and frontal systems. During the summer time, the UAE region is mostly under the influence of weak upper-level tropical easterly flow with moisture advected from the Gulf of Oman and the Arabian Sea. The UAE area has been divided into four regions based of topography, land cover and anthropogenic sources (Figure 1). These regions are represented by: 1) Coastal region (This includes major oil refineries, major urban centers like Abu Dhabi and Dubai, cement plants and industrial centers in general.); 2) Desert region (This includes the vast desert areas of the UAE, some agricultural activities and minor urban centers like the Liwa Oasis in the south.); 3) Oil / Maritime region (This includes both clean and polluted areas over the Persian Gulf and some major oil fields like Zirku Island and Das Island.), and 4) the Mountain region to the east and into Oman.

3. INSTRUMENTATION

A Piper Cheyenne II (in 2001) and a Beechcraft King Air 200 (in 2002) were used for air chemistry sampling, aerosol and cloud physics investigations. The instrumentation measured trace gases (SO_2, O_3, and NO_x), aerosol concentrations and size distributions, and cloud droplet and particle spectra. This paper highlights measurements from the cloud condensation nuclei counter (University of Wyoming CCNC-100A), an aerosol spectrometer (PCASP-100X), and a condensation particle counter (TSI 3760A). The CCN counter is a thermal diffusion chamber device and was operated in both single supersaturation mode (typically at 0.3% SS) and supersaturation spectra mode (0.3 to 1.0% SS). The PCASP measures primarily accumulation mode aerosols in the size range of 0.1 to 3.0 μm diameter, while the CN counter measures concentrations of aerosols roughly 0.01 – 1.0 μm (nucleation mode and accumulation mode).

4. SEASONAL VARIATIONS

4.1 Summer

Figure 2 summarizes the CCN, CN, and PCASP concentrations over the different regions for the two seasons. In general, higher concentrations from all three instruments exist in nearly all regions during the summer. PCASP concentrations vary from >800 cm^{-3} in the Mountain region to ~450 cm^{-3} in the Oil/Maritime region. The CCN concentrations are not drastically different between regions, with slightly higher concentrations in the Desert region (>500 cm^{-3}) and lower background concentrations (~300 cm^{-3}) over the coastal and maritime areas. CN concentrations are highest in the Mountain region (>5000 cm^{-3}), moderate and comparable in the Coastal and Desert regions (~3000 cm^{-3}), and lowest in the Oil/Maritime region (~1000 cm^{-3}).

4.2 Winter

Vertically averaged winter PCASP concentrations

Table 1. Summary of averaged CCN, CN and PCASP characteristics for the different regions of the UAE. The CN and PCASP data were averaged over the time it took to obtain each CCN spectra (~4 min). The C/CN average ratio is calculated using the C value of each CCN spectra and the averaged concentration of CN for each CCN spectra.

Region	CCN spectra characteristics						CN [cm^{-3}]		PCASP [cm^{-3}]		C/CN [cm^{-3}]	
	C		*k*		Altitude							
	Average	σ	Average	σ	Average	σ	Average	σ	Average	σ	Average	σ
						Summer						
Coastal	988	*	0.46	*	4017	*	*	*	*	*	*	*
Desert	839	220	0.56	0.33	1054	1161	4598	2603	816	77	0.24	0.18
Mountains	909	603	0.51	0.30	2764	947	4907	4640	1074	1577	0.29	0.23
Arabian Sea	1266	330	0.46	0.37	434	322	7640	7205	1092	*	0.34	0.20
Oman Coastal	956	353	1.02	0.59	304	0	6515	5443	1296	473	0.19	0.12
						Winter						
Coastal	1042	599	0.33	0.19	1959	1341	4752	4639	802	639	0.45	0.32
Desert	2540	*	0.99	*	847	*	14148	*	524	*	0.18	*
Oil / Maritime	1231	*	0.21	*	906	*	9258	*	934	*	0.13	*
Mountains	1540	*	0.52	*	1271	*	4280	*	795	*	0.36	*

* Not enough data to compute

are below 400 cm^{-3} for all the regions, with the highest concentrations (similar to summer conditions) over the Oil/Maritime region. The highest CCN concentrations are found in the Coastal and Oil/Maritime regions (~300 cm^{-3}), which are not much different than summer conditions. CN concentrations are high over the mountains (~4000 cm^{-3}) but around 2000 cm^{-3} over the rest of the UAE. This trend is the same as for the summer but with slightly lower concentrations.

5. CCN CHARACTERISTICS

The CCN characteristics of the air sampled over the different regions of the UAE are shown in Table 1.The concentrations were recorded approximately every 40 seconds at a set of sequential supersaturations between 0.3 and 1.0% to obtain CCN spectra of the form $N_{CCN}=CS^k$ (Twomey et al. 1968), where N_{CCN} is the total CCN concentration at a supersaturation S.

CCN characteristics have been classified as maritime or continental with respect to the C and k values of the CCN spectra. Hegg and Hobbs (1992) reported k values of 0.5 to 0.6 for clean maritime air and 0.5 to 0.9 for continental conditions, with C values ranging from 125 to 1000 cm^{-3} for the maritime air versus 600 to 5000 cm^{-3} for continental air.

5.1 Maritime region

Measurements of CCN in the Oil/Maritime region (Table 1) resulted in a C value of 1231 cm^{-3} (k=0.21) during the winter, with too few measurements in the summer to construct a meaningful average. These values are comparable to the measurements taken on one flight just off shore of Oman over the Arabian Sea (C=1266 cm^{-3}, k=0.46). These C and k values are consistent with a polluted maritime environment or maritime CCN with a strong influence of anthropogenic aerosols (Pruppacher and Klett, 1997). The CCN concentrations are considerably higher than the marine concentrations reported by Hudson et al. (1998) and in Pruppacher and Klett (1997), where the mean for maritime CCN at 1% SS was 100 cm^{-3}. The k values in the UAE maritime region are slightly lower than those found by Twomey and Wojciechowski (1968) – 0.21 versus 0.5. Also shown in Table 1 is the ratio of C divided by the CN concentration. Pruppacher and Klett (1997) summarized maritime observations of this parameter that ranged between 0.3 and 1.0. The maritime regions of the UAE showed ratios as low as 0.13 (winter) which in turn might indicate a contribution of non soluble particles to the CCN activity.

5.2 Continental regions

Continental CCN conditions would be expected to be sampled in the Desert and Mountain regions. The Desert region showed concentrations of CCN (1% SS) of 2540 cm^{-3} during winter and 839 cm^{-3} during summer, with k values of 0.99 and 0.56 respectively. The Mountain region had similarly high values of C and k during both seasons. The Coastal region also has high C values (1042 and 988 cm^{-3}) with slightly lower, more transitional k values (0.33 – 0.46). However, the Coastal region also has a sampling bias in that low level flights were restricted and hence sampling occurred at higher altitudes in more mixed or diluted conditions. The C/CN ratios summarized by

Pruppacher and Klett (1997) for continental type of conditions were between 0.025 and 0.14. The desert regions of the UAE show ratios as high as 0.18 during winter and 0.24 during summer indicating the presence of particles, such as sea salt, that are highly active as CCN.

6. DISCUSSION

Vertically averaged concentrations of CCN, PCASP and CN reflect the winter-summer transition in the UAE area. While almost all the regions in both seasons display enhanced aerosol concentrations, there are subtle but significant differences. Concentrations during the summer are generally higher due to a number of factors. An obvious one is the deeper mixed layer caused by the high surface temperatures and increased convection. Surface sources therefore can contribute through a deeper layer of the atmosphere. High concentrations throughout the regions during the summer also suggest long atmospheric residence times and a potentially greater contribution from transport of pollution from local urban centers, oil fields, Asia or Europe.

During the summer months, the UAE is under the influence of weak easterly flow, which is usually modified by mesoscale features such as the land-sea breeze. These flows are particularly important for transport into the Mountain region. A strong sea breeze can transport desert dust mixed with sea salt and oil-produced aerosols into the mountains from the west and northwest, while the high concentrations measured over the Arabian Sea (Gulf of Oman) suggest that aerosols are being transported by the easterlies from the sub-Asian continent.

In the oil/maritime region (over the Arabian Gulf), a more stable boundary layer may cause a smaller variation from season to season in the aerosol concentrations (CN, CCN and PCASP). The small differences in concentrations could be attributed to the natural variability of the land-sea breeze during both winter and summer - either bringing desert dust into the gulf region (decreasing CCN concentrations and increasing PCASP counts) or transporting polluted maritime air on shore (increasing CCN activity and lowering PCASP concentrations), sometimes mixing with urban air as an additional complexity.

One possible scenario for the seasonal differences in CCN properties could involve higher ocean temperatures (in the summer), which generally produce more dimethylsulfide, which in turn might make more CCN particles (Hudson et al., 1998). During the winter time, the measurements were usually taken at low altitudes or just above the boundary layer, so the high *k* values might be caused by small particle production (Hudson et al., 1998; Hudson and Xie, 1999). Alternatively, higher *k* values may be due to the stably stratified layers characteristic of the winter months. They inhibit mixing of air of different ages and different sources, preventing the coagulation and condensation processes that will increase the size of the particles and hence decrease the value of *k* (Hudson and Xie, 1999).

7. ACKNOWLEDGMENTS

This research was sponsored by the Department of Water Resources Studies, Office of H.H. the President in the UAE. The aircraft and technical support was provided by Weather Modification Inc. of Fargo, ND. NCAR is sponsored by the National Science Foundation.

8. REFERENCES

Boer, B., An introduction to the Climate of the United Arab Emirates. J. Arid Enviro., 35, 3-16, 1997.

Fonner, D., and E. Ganor, The chemical and mineralogical composition of some urban atmospheric aerosols in Israel, Atmos. Environ., Part B, 26, 125-133, 1992.

Hegg, D.A., and Hobbs, P.V., Cloud condensation nuclei in the marine atmosphere. Deepak Publishing, Hampton, VA, 181-192, 1992.

Hudson J. G., Xie Y., Soo Yum S., Vertical distributions of cloud condensation nuclei spectra over the summertime Southern Ocean. J. Geophy. Res., 103, D13, 1998.

Hudson J. G., Xie Y., Vertical distributions of cloud condensation nuclei over the summertime northeast Pacific and Atlantic Oceans. J. Geoph. Res., 104, D23, 1999.

Kiehl, J. T., and B.P. Briegleb, The relative roles of sulfate aerosols and greenhouse gases in climate forcing. Science, 260, 311-314, 1993.

Levin, Z., Ganor, E. and Gladstein, V., The effects of desert particles coated with sulfate on rain formation in the eastern Mediterranean. J. Appl. Meteor., 35, 1511-1523, 1996.

Pruppacher, H. R. and Klett, J. D. 1997. Microphysics of Clouds and Precipitation. Kluwer Dordecht.

Rosenfeld, D. and Nirel, R., The interaction of desert dust and the southern margins of rain cloud systems in Israel. J Appl. Meteor., 35, 1502-1510, 1996.

Ross, K. E., Picket, S.J., Bruintjes, R.T., Burger, R.P., Swap, R.J. and Annegran H.J., Spatial and seasonal variations in CCN distributions and the Aerosol-CCN relationship over southern Africa. J. Geophy. Res., 108, D13, 8481, 2003.

Twomey, S. and Wojciechowski, T.A. 1968. Observations of the geographical variation of cloud condensation nuclei. J. Atmos. Sci. 26, 684-688.

Wurzler, S., T. G. Reisin, and Z. Levin, Modification of mineral dust particles by cloud J. Geophy. Res., 105, 4501-4512, 2000.

Yin, Y., Wurzler, S., Levin, Z. and Reisin, T. G., Interactions of mineral dust particles and clouds: Effects on precipitation and cloud optical properties. J. Geophy. Res. 107, D23, 4724, 2002.

SIMULATION OF EFFECTS OF NATURAL AND SEEDING HYGROSCOPIC PARTICLES ON MICROPHYSICS OF ASCENDING CLOUD PARCELS

Y. Segal, A. Khain, M. Pinsky and D. Rosenfeld
The Hebrew University of Jerusalem, Israel

1. INTRODUCTION

Artificial droplet spectrum broadening in the Eulerian cloud models may mask aerosol effects. In this study, a precise cloud parcel model with a movable 2000 bin mass grid is used for investigation of effects of natural and seeding hydroscopic aerosols on droplet spectrum evolution and rain formation under different atmospheric conditions.

2. MODEL AND EXPERIMENT DESIGN

The spectral microphysics cloud parcel model is described by Pinsky and Khain (2002) and Segal et al, (2004a). The model equation system includes the diffusion growth equation used for non-activated nuclei and water droplets, the stochastic kinetic equation for droplet collisions, equations for supersaturation, vertical velocity and the temperature of the ascending parcel. The acceleration of cloud parcel velocity is determined by the buoyancy and the drag force. To describe size distribution of both non-activated nuclei and droplets within the radius range of $0.01\mu m$–$2000\mu m$ grid of masses containing 2000 bins was used. To eliminate artificial droplet spectrum broadening, the mass of each bin changes with time (height) according to the equation of diffusion growth. The time step of 0.001 s was used to calculate the diffusion growth of drops and aerosol particles. Such a small time step is necessary to simulate adequately the growth of the smallest aerosol particles, so that separation between non-activated nuclei and the growing droplets is simulated explicitly by solving the equation for the diffusion growth. Drop growth by collisions is calculated using a time increment of 0.5 s. The flux of drops leaving a cloud parcel (rain flux) was calculated using the terminal fall velocities of droplets, as well as the velocity of parcel updraft. The flux, integrated all over the period of the cloud parcel ascent, provides the evaluation of the total rain amount falling down from the parcel.

The initial spectrum of dry natural CCN was represented by a superposition of three lognormal distributions (Hobbs et al., 1985, Respondek et al., 1995) as:

$$\frac{dN}{d\ln r_n} = \sum_{i=1}^{3} \frac{n_i}{\sqrt{2\pi}\log\sigma_i \ln 10} e^{\left(-\frac{\left(\log\frac{r_n}{R_i}\right)^2}{2(\log\sigma_i)^2}\right)}$$

where n_i is the maximum number concentration in the *i-th* mode, R_i and σ_i are the mean radius and the width of the *i-th* aerosol mode. Radii and R_i the values of σ_i were chosen correspondingly R_1=0.006μm, log(σ_1)=0.3, R_2=0.03μm, log(σ_2)=0.3 and R_3=0.3μm, log (σ_3)=0.396. Simulations were performed for three thermodynamic conditions: a) maritime convection (Ferrier and Houze, 1989); intermediate convection, exemplified by the sounding of the Eastern Mediterranean rainy season, and c) continental convection, exemplified by the Midland/Texas sounding data of 13 August 1999 (Rosenfeld and Woodley, 2000). In different simulations we changed the concentration of aerosol particles belonging to different modes.

3. RESULTS OF EFFECTS OF NATURAL AEROSOLS

Results of simulations are described in detail by Segal et al (2004a). The results show that all aerosol particles playing the role of cloud condensational nuclei (CCN) can be separated into three size ranges: a) small aerosols with radii below ~0.01 μm do not activate even in strong updrafts. These particles are transported by cloud motions as a passive scalar; b) CCN of intermediate size with radii ranged between 0.01 μm and 1 μm nucleate and give rise to droplet formation. An increase in concentration of these CCN leads to the increase in droplet concentration and slows the diffusion growth. As a result, raindrop formation takes place (if any) at higher levels. This leads, as a rule, to a decrease in the amount of parcel rain felt during the parcel ascend; c) large CCN with radii larger 1 μm. The droplets formed at these CCN are larger than other droplets in droplet spectrum and attain sizes needed for collision triggering first. An increase in the concentration of these CCN lowers the collision triggering level and increases (as a rule) the parcel rain. The sensitivity of droplet concentration and parcel rain to the concentration of intermediate size CCN (under maritime thermodynamic profile) is shown in Figure 1.

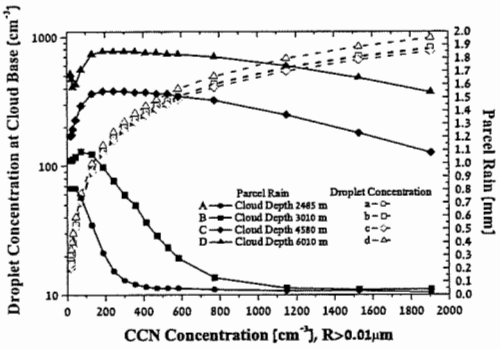

Figure 1. Dependence of droplet concentration and parcel rain on CCN concentration.

Fig. 1 shows that the increase in CCN concentration leads to a sharp decrease in parcel rain from

comparatively low depth cloud parcels. The larger the clouds depth is, the higher CCN concentration should be to inhibit precipitation.

Decrease in precipitation from deep cloud parcels begins to be significant at CCN concentration exceeds about 800 cm^{-3}. Note that the ratio between droplet concentration (equal to the concentration of activated CCN at cloud base) and the total concentration of CCN (or the CN concentration) obtained in the calculations agrees well with the results obtained in ASTEX-maritime and FIRE-maritime cases (see Table 6 in Yum and Hudson 2002). For instance, in maritime ASTEX the concentration of activated CCN at 0.6% (Nccn) and CN concentrations (Ncn) were 131 cm^{-3} and 241 cm^{-3}, respectively. According to Fig. 1 at Ncn of 241 cm^{-3}, the droplet concentration at cloud base is close to 130 cm^{-3}. Note that the maximum of super saturation at the cloud base in the simulations is close to 0.5-0.6%. Thus, droplet concentration at cloud base should be close to that of activated CCN.

Figures 2a-b show rain enhancement factor as the function of cloud parcel depth attained by the increase in concentration of large CCN under maritime (a), Mediterranean (b) conditions, respectively.

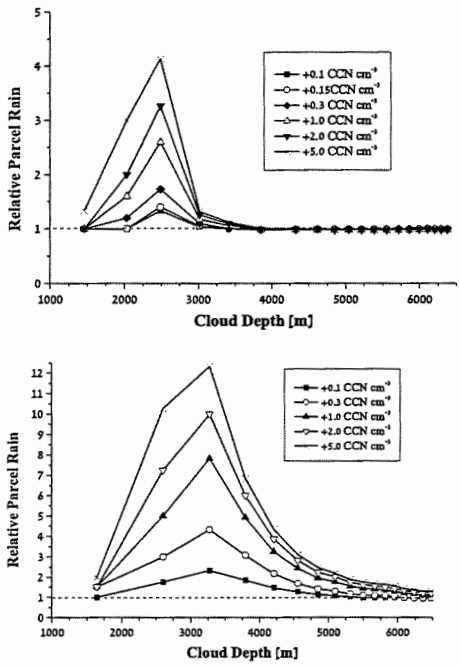

Figure 2a,b . Rain parcel increase as the function of cloud parcel depth and concentration of large CCN.

One can see that rain amount in maritime cloud parcels with significant cloud depth are not sensitive to large CCN. These parcels produce a high concentration of large drops by droplets collisions and thus realize their precipitation potential.

In case of Mediterranean thermodynamic conditions maximum rain enhancement is attained for cloud parcels of 3.5 km depth increases by a factor of 12 in case 5 cm^{-3} large CCN are added into the CCN size spectrum. It should be noted that rain enhancement depends non-linearly on the concentration of large CCN. In the particular case the major rain enhancement is achieved when additional large CCN concentration is equal to 1 cm^{-3}. Further increase in large CCN concentration leads to a relatively weak increase in the rain amount. An increase in precipitation largely depends on cloud depth.

Comparable effects of small and large CCN concentration variations on raindrop formation are investigated using as an example cloud parcels formed under the maritime sounding. Calculations were conducted within a wide range of small CCN concentrations (and respectively, a wide range of droplet concentrations) and with the concentration of large CCN ranging from 0.1 cm^{-3} to 1.0 cm^{-3}.

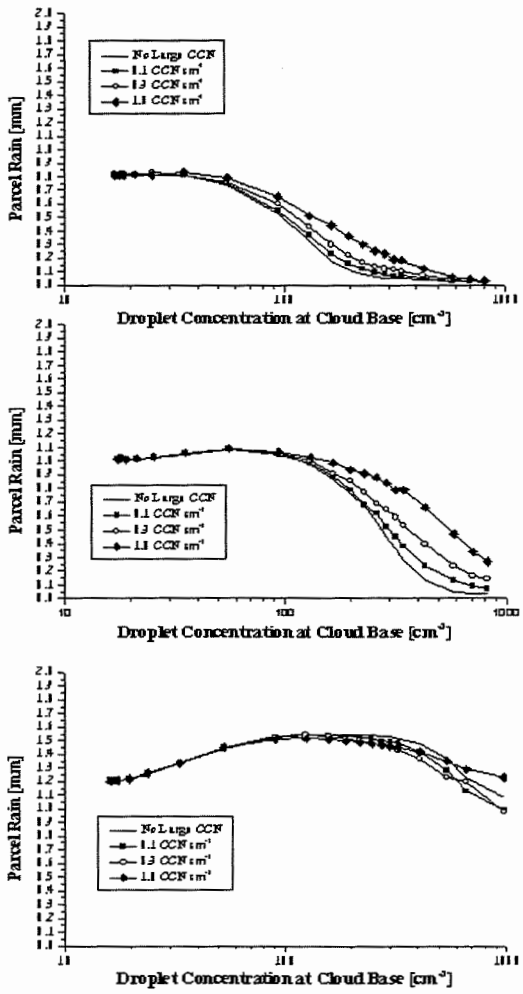

Figures 3a-c. Parcel rain as the function of droplet concentration

Figs. 3a-c show the dependencies of rainfall from an ascending cloud parcel as a function of droplet

concentration under different concentrations of large CCN for cloud parcel depths of 2485 m, 3010 m and 4600 m, respectively. The effect of large CCN becomes significant when further increase in the droplet concentration (or increase in the concentration of small CCN) leads to precipitation reduction. Deep maritime cloud parcels (Fig. 3c) are not very sensitive to the concentration of either small or large CCN. Some precipitation reduction takes place only when the droplet concentration becomes very high, exceeding 1000 cm^{-3}.

3. HYDROSCOPIC SEEDING SIMULATIONS

3.1 Simulations of seeding with hydroscopic flares

In simulations of cloud hygroscopic seeding (Segal et al, 2004b) with commercial hygroscopic flares only the CCN belonging to modes 1 and 2 were used in the *natural* CCN size spectrum. The measured particle size distributions of the various available hygroscopic flares and those approximated using log-normal distribution (1) are shown in Fig. 4. Parameters of the log-normal distributions used to approximate measured size spectra are presented in Table 1.

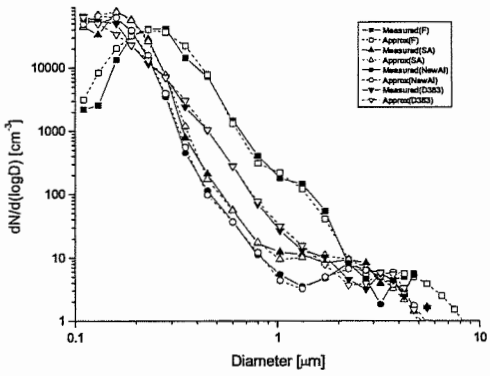

Figure 4. Size distributions of particles in different flares (Salazar et al. 2001) and their approximations.

flare	R_1	log (σ_1)	R_2	log(σ_2)	R_3	log (σ_3)
F	0.12	0.15	0.45	0.15	1.9	0.18
SA	0.075	0.125	0.17	0.17	0.85	0.22
N	0.07	0.125	0.13	0.22	1.2	0.18
D	0.033	0.28	0.1	0.27	1.75	0.08

Table 1 Parameters of log-normal distributions approximating the measured spectra.

The results of the simulations of a continental cloud parcel are shown in Fig. 5. Under continental conditions, only the French flare leads to a significant enhancement of parcel rain. This effect is attained, however, at a very large (possibly impractical) concentration of seed reagent.

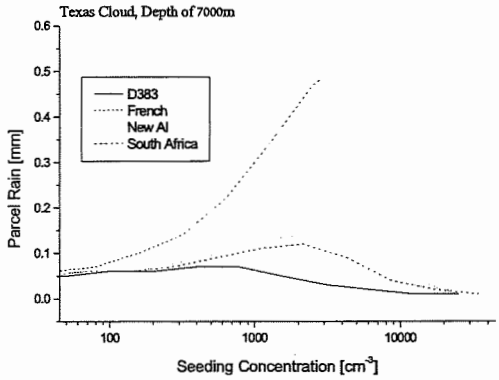

Figure 5. Parcel rain as the function of concentration of seed particles for different flares. Thermodynamic conditions are continental.

This comparatively low seeding effect can be attributed to the existence of a large concentration of small CCN in the hydroscopic flares. The French flare produces higher effect since it contains larger fraction of large seed particles.

The seeding of a maritime cloud parcel with hygroscopic flares suppresses coalescence and precipitation amount (Fig. 6) because the seeding increases droplet concentration in maritime clouds. The French flare is the least suppressive under maritime conditions, and is the best of all in Texas, because it contains larger fraction of large CCN than other flares. As was shown above, these CCN tend to decrease precipitation.

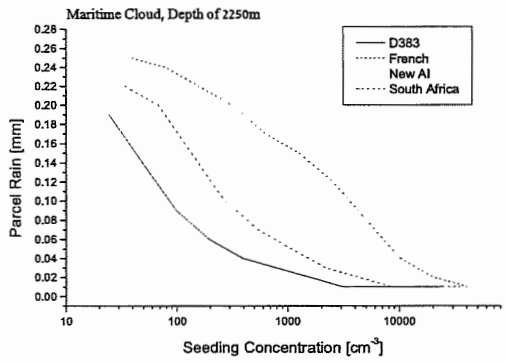

Figure 6. Parcel rain as the function of concentration of seed particles for different flares. Thermodynamic conditions are maritime.

3.2 Seeding with "optimal" reagent

Simulations show also that a significant rain enhancement effect could be attained by elimination of CCN with radii below
1.0 μm from the size distributions of commercial flares. At the same time seeding with giant CCN is obviously unpractical because of too large mass required. Thus simulations were performed aimed at the finding an optimum size of seed particles.

Simulations of cloud seeding of maritime, Mediterranian and continental cloud parcels with an "idealized" monodisperse reagent indicated the existence of the optimum size of seed particles (2 - 2.5 μm), which produces the maximum rain enhancement at a given mass of reagent (Figures 7 and 8). The utilization of the optimum reagent increases precipitation even in case of maritime clouds.

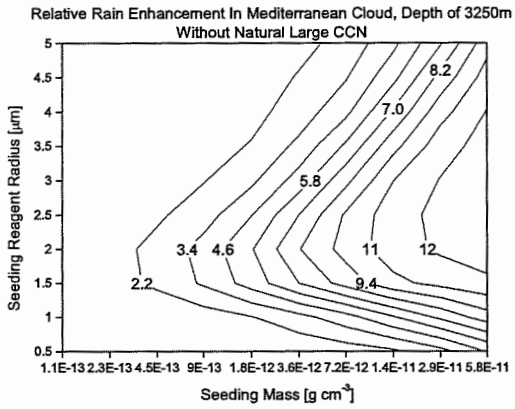

Figure7. Rain enhancement factor as the function of seeding mass and size of seed particles for intermediate conditions.

Figure 8. Rain enhancement factor as the function of seeding mass and size of seed particles for the

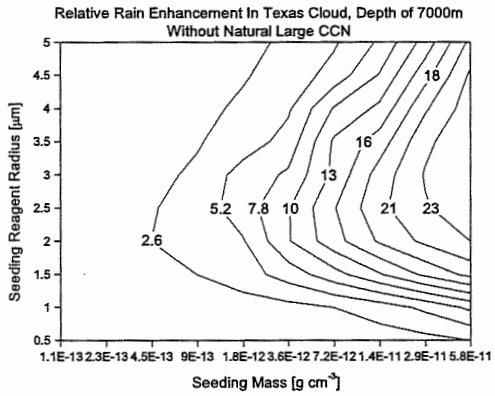

continental conditions.

It should be noted that the results shown in figures 7 and 8 were obtained in case of no large natural CCN. Large natural CCN decrease the rain enhancement factor, since they compete with seed particles producing natural rain drops. An example of this competition is shown in Figure 9, where the existence of large natural CCN is assumed.

One can see that in spite of significant decrease, rain enhancement still remains significant.

4. CONCLUSIONS

Effects of natural and seeded aerosols on the droplet spectrum formation and precipitation formation in ascending cloud parcels are investigated. It is shown that these effects are different for clouds of different height. Under each thermodynamic condition, there is a range of cloud heights, in which the sensitivity is maximal. Simulations of hygroscopic seeding showed that the efficiency of most commercial flares is quite limited. This can be attributed to the presence of a lot of small aerosol particles in their size spectra. The simulations showed that there exists an optimum size of seed particles (2-2.5 μm) providing maximum rain enhancement under given mass of seed reagent. The utilization of the optimum reagent allows one to get significant rain enhancement using quite reasonable reagent mass.

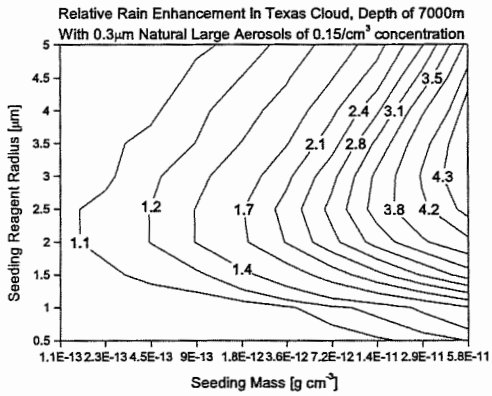

Figure 9. The same as in Figure 8, but in presence of large natural CCN.

Acknowledgments: The study was performed under support of the Israel Ministry of Science (German-Israel collaboration in Water Resources, grant WT 0403) as well as by the Israel Water Company (Shaham).

References

Pinsky, M., A. P. Khain, 2002: Effects of in-cloud nucleation and turbulence on droplet spectrum formation in cumulus clouds. *Quart. J. Roy. Met. Soc.*, 128, 1-33.

Salazar V., Hernandez-Carrillo, N., Roelof T. Bruintjes, 2001. Calculation of the effect of seeding material from hygroscopic flares on the collision-coalescence process and the development of rainfall in clouds. 15th Conference on Planned and Inadvertent Weather Modification, AMS.

Segal, Y., A. Khain, and M. Pinsky, 2004a: Effects of atmospheric aerosol on precipitation in cumulus clouds as seen from 2000-bin cloud parcel microphysical model: sensitivity study with cloud seeding applications. *Quart. J. Roy. Met. Soc.*, 130b (587), 561-582

Segal, Y, A. Khain, M. Pinsky and D. Rosenfeld, 2004b: Effects of hygroscopic seeding on raindrop formation as seen from simulations using a 2000 bin spectral cloud parcel model. *Atmospheric Research (in press).*

FINGERPRINTING CLOUD CONDENSATION NUCLEI

G. E. Shaw[1]

Geophysical Institute, University of Alaska, Fairbanks, AK 99775, USA

1. INTRODUCTION

John Aitken determined that droplets of water condense on nuclei: "vapour condenses on dust suspended in the air, because the dust particles form free surfaces at which the condensation can take place". A century later Sean Twomey (1974) pointed out that the albedo of clouds (and hence climate) will modulate in response to changes in Cloud Condensation Nuclei (CCN) brought about by changing atmospheric pollution. A critical parameter in assessing the "Twomey Effect" is the supersaturation spectrum, N(S), the number of drops potentially nucleated as a function of applied supersaturation, S. The number of drops actually nucleated in a cloud at the small supersaturations reached during cloud activation is a nonlinear function of N. But in practice N can be measured (though with some difficulty), and incorporated into climate models. In carrying out such a program it is mandatory to try and understand the nature of the CCN.

In this paper we discuss experiments that cast light on the physics and chemistry of CCN.

2. A PRELUDE: UNIV ALASKA CCN INSTRUMENT

All experiments used a special type of instrument we developed for measuring the CCN. It is a flow-through thermal diffusion chamber (Ji et al., 1998) in which known and small vapor supersaturation is maintained in the center of the chamber between the moistened hot and cold plates.

FIGURE 1. The University of Alaska's cloud condensation nucleus remover (CCNR).

The dirty air flows in a thin horizontal ribbon in the central region of the chamber, where the supersaturation is small, known, adjustable, and once when set is constant over the flow residence time of the chamber that can arbitrarily be set to as long as required.

Corresponding author's address: Geophysical Institute, 903 Koyukuk Drive, P.O. Box 757320, Fairbanks, Alaska 99775-7320, E-Mail: gshaw@gi.alaska.edu

Particles satisfying the condition of passing over the top of the Köhler curve nucleate and fall out of the flow onto the cold bottom of the chamber. By differencing the input and dried output of the flow-through chamber, one can not only determine the number of CCN and by suitable experimentation, certain chemical and physical properties of the CCN. We call the instrument the Cloud Condensation Nucleus Remover or CCNR

3. EXPERIMENTS

3.1 Using CCNR to Deduce Size of CCN

One can deduce not just the number of particles nucleated at a given supersaturation with the CCNR, but also *the size distribution* of the *nucleated* particles by differencing the input and output *size distributions* to the flow chamber. We have done just this using a Scanning Differential Mobility Analyzer. For the case when particles are simple and soluble salts all of one size, such as can be generated in the laboratory, the number of CCN would be zero low S then abruptly rise at the "critical" supersaturation S_{crit}, as shown below for a narrow distribution of lab-generated ammonium sulphate.

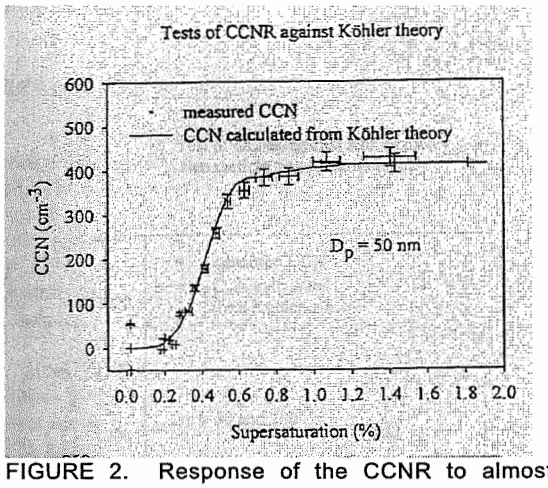

FIGURE 2. Response of the CCNR to almost-monodisperse ammonium sulphate aerosols.

Most of the non-abrupt behavior in the above is due to the small, but finite spread of the aerosol size distribution used. In practice there is some smearing also introduced by the instrumental transfer function but this can be made insignificant by proper instrument design, though at the expense of instrumental resolution time.

Atmospheric aerosols, even those pre-selected to be all of one size (in a narrow range) often are found to be non ideal and to behave differently because of nonhomogenities in composition, states of mixing and due, possibly, to surface-active agents. We deduced the fraction of soluble aerosols by fitting observed to calculated supersaturation spectra. An example from experiments during ACE 2 in Portugal is shown below:

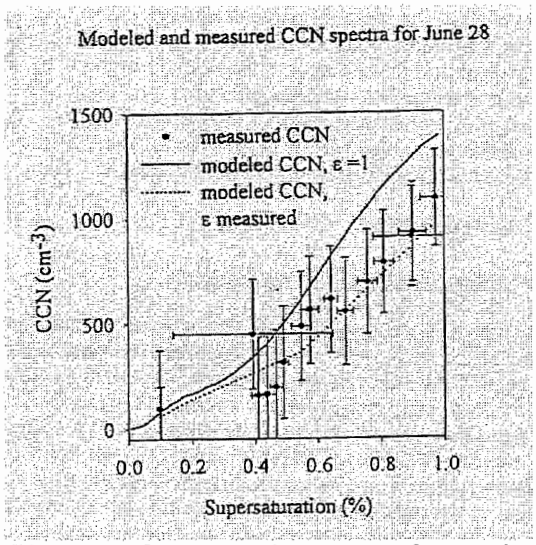

FIGURE 3. Supersaturation spectra of atmospheric aerosols measured in the ACE 2 experiment in Portugal. The top solid curve was generated from aerosol size distribution assuming soluble salt. The dotted curve is computed using measured soluble fraction of particles.

3.2 Using The CCNR in conjunction with Electron

Experiments are being conducted to derive the state of mixing and composition of the atmospheric aerosols nucleated in the CCNR. The idea is to impact the aerosols on surfaces, then analyze individual particles with transmission electron microscopy. Once again, it is necessary to subtract the entering and "surviving" fraction of particles to deduce the chemical and mixing characteristics of the nucleated particles.

To test this new technique we sampled aerosols from a mountain top site on Mt Lemmon, (altitude 3000 m) in southern Arizona, collecting Gobi desert dust aerosols and aerosols from "clean" areas of the Pacific. This project is ongoing, but we are finding some surprises: particles of aluminum silicates, for example, nucleate at lower supersaturations than predicted for insoluble particles, suggesting that the particles may be coated with liquid films.

3.3 Using The CCNR in Conjunction With Heat Treatment

Aerosols found in the free atmosphere are thermodynamic stable solid and liquid phase products produced from gas phase reactions in the atmosphere, or solid products from geology or sea salt evaporates.

Assuming for the moment that the state of mixing for these particles is external, important information relating to their composition, on a per particle basis, can be derived by investigating thermodynamic behavior as a function of temperature. We do this by exposing the particles to an elevated temperature field for a known amount of time, note the reduction in particle diameter, and from this deduce the equilibrium vapor pressure, at that temperature. Equilibrium vapor pressure of the aerosol substance is derived by modeling the particle shrinkage using Maxwellian diffusion theory (Twomey, 1971). This is practical to do even when equilibrium vapor pressures are too small to measure directly. It is a sensitive technique. Information thereby gained can sometimes be used to clarify the sources of particles. One can derive specific chemical composition from the thermodynamic vapor pressure-temperature relation.

We have improved on previous experiments by confining the "dirty" sample air to flow in the centerline of a more general filtered airflow in laminar flow regime. The flow velocity for the particles and thus the time exposed to the elevated temperature is therefore well defined. Using this well-defined-residence time heating, we have successfully deactivated quasi monodisperse particles which were previously activated within the CCNR device, sometimes passing the activation to higher supersaturation in accordance with the increase of vapor pressure due to the Kelvin effect. However, some aerosols require an even higher supersaturation, suggesting the presence of thin, hydrophilic films which were evaporated in the heating process. Using such techniques it is possible not only to deduce the partial vapor pressure of aerosol compounds, but details about the internal states of mixing.

3.4 References

Ji, Q., G. Shaw and W. Cantrell, A new instrument for measuring cloud condensation nuclei: Cloud Condensation Nucleus Remover, J. Geophys. Res., **103**, 28,013-28,019, 1998.

Twomey, S., The nuclei of natural cloud formation (parts 1 and 2) Geofisica pura el Applicta, **43**, 227-250, 1959.

Twomey, S., The evaporation of submicron aerosol particles, J. Recherches Atmos., 93-99, 1971

Twomey, S., Pollution and the planetary albedo, Atmos. Env., **8**, 1251-1256, 1974.

INTEGRATING PHOTOCHEMICAL-AEROSOL-CLOUD PROCESSES INTO A ONE DIMENSIONAL ATMOSPHERIC BOUNDARY LAYER MODEL

C.-J. SHIU[1] ,J.-P. CHEN[1], and S. C. LIU[2]

[1]Department of Atmospheric Sciences, National Taiwan University, Taipei,106, Taiwan, R.O.C.
[2]Research Center for Environmental Changes, Academia Sinica, Taipei, 115, Taiwan, R.O.C.

1. INTRODUCTION

Aerosols can perturb the atmospheric environment and climate through a direct effect of scattering and absorption of atmospheric radiation and an indirect effect via interacting with clouds. Besides the perturbations induced by the purely scattering aerosol such as sulfate aerosols, those induced by strongly absorbing aerosols e.g. soot particles are also of considerable interests (Hansen et al., 1997). Although the importance of radiative effects of aerosol on climate change has been widely recognized, relatively little efforts have been dedicated to the investigation of aerosol impacts on the evolution of atmospheric boundary layer. Due to the computational expenses, the aerosol and cloud processes in models like GCMs tend to be oversimplified or somewhat unrealistic in certain aspects. Therefore, in this study we attempt to develop a one-dimensional (1-D) model by combining a modified atmosphere-plant-soil coupling model (MCAPS model, Chang et al., 1999; Yu, 2000) with a multi-bin and multi-component aerosol and cloud model (Chen, 1992). For the evaluation of radiative effects, we apply the Fu and Liou radiation module (Fu and Liou, 1992, 1993; Fu et al., 1997), with consideration of aerosol optical characteristics based on the Mie theory (Toon and Ackerman, 1981). In addition, a 1-D photochemical model is applied to calculate the sources of precursors for aerosol nucleation (Trainer et al, 1987). This self-consistent 1-D composite model is useful in the investigation of several interesting issues. Our focus is primarily on the role of aerosols and clouds in the evolution of atmospheric boundary layer, such as the observed decrease of diurnal temperature range (DTR). In the initial stage of this study we perform a preliminary test by using prescribed aerosol and cloud properties to emphasize several important issues regarding to boundary processes. More realistic aerosol and cloud will be included shortly.

2. MODEL SETUP

2.1 Initial and boundary conditions

Corresponding author's address: Chein-Jung Shiu, Department of Atmospheric Sciences, National Taiwan University, Taipei, 106, Taiwan; E-Mail: cjshiu@earth.sinica.edu.tw

The control run is under clear sky conditions with the solar orientation given as July 15, 25°N. Radiative forcing of aerosols as well as cloud formation are turned off. The vertical wind profile is fixed, and there exists a large-scale subsidence of 0.7 cm/s above 2 km. A bare soil surface (sandy loam, saturated at 0.435) is applied without any canopy (vegetation coverage), and the surface albedo is set at 0.2. The field capacity and air-dry values are assumed to be 0.195 and 0.114, respectively. Soil moisture below surface was held constant and soil water contents were 0.20 and 0.22 in two layers.

2.2 Inclusions of aerosols and clouds

The aerosol effect is estimated by assuming a dry aerosol optical depth (AOD) of 0.5 in the visible wavelength. The extinction coefficients and asymmetric factors are set as those for sulfate aerosols (d'Almeida et al., 1991). Single scattering albedo (SSA) of the purely scattering and strongly absorbing aerosols is taken as 1.0 and 0.8, respectively, for the solar flux; SSA of 0.2 is taken for the thermal flux. In addition, the swelling of aerosol according to ambient humidity is also considered. The mixing state of aerosols can be of importance as well for the evaluation of radiative forcing. Here, we tested the three types of mixture state for soot and $(NH_4)_2SO_4$ as described in Jacobson (2000): 1) internal mixing, 2) core with shell, and 3) external mixing. The optical properties of the mixing aerosols are calculated using the algorithm of Toon and Ackerman (1981) .

The impacts of clouds on the diurnal temperature are evaluated by means of prescribed clouds at different heights. Three levels (i.e. low, middle, and high) of clouds are tested with assumed effective radius (r_e) and liquid water content (LWC). For low clouds: height = 2~2.5 km, r_e = 5.89 μm, LWC = 0.22 g/m^3; Middle clouds: height = 4~4.5 km, r_e = 10 μm, LWC = 0.3 g/m^3; High clouds: height = 6~7 km, r_e = 41.54 μm, IWC = 4.7e-3 g/m^3. Other values of r_e and LWC are also applied for sensitivity test on surface radiation budget.

3. RESULT AND DISCUSSION

3.1 Cloud forcing

Figure 1 shows that low and middle clouds tend to decrease the daytime temperature while increase the nighttime temperature. The magnitude of the

temperature change caused by clouds can be more than 3°C. Such significant asymmetric change of diurnal temperature can be one of the possible causes associated with the decrease of DTR observed in most of the stations over Taiwan.

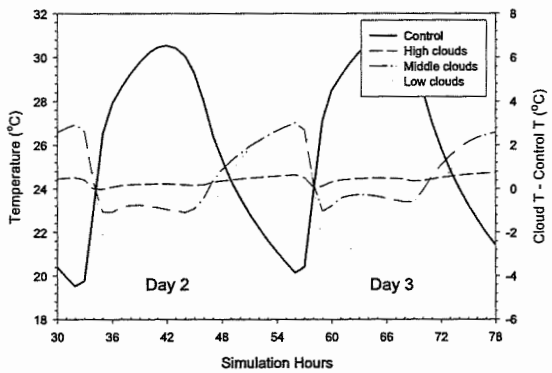

Figure 1. Impacts of clouds at different heights on the diurnal temperature at 2 m above the surface.

The high clouds increase the near surface temperature by about 0.5°C during both daytime and nighttime, suggesting that the longwave effect dominates. When we increase the thickness of high clouds by 2 km, the increase of nighttime temperature may exceed 1°C while the daytime temperature increase is still less than 0.5°C (not shown). The effects of middle and low clouds are much more significant than the high clouds during nighttime, where up to 2.5 and 3°C warming may be expected. But during daytime, the cloud forcing becomes a cooling effect, with a magnitude of about 1°C for middle clouds and 3°C for low clouds. Apparently, all three types of clouds have the potential of reducing DTR. However, actual clouds can be far more complicated than the assumed ones, especially when the clouds contain ice particles. In the near future, our self-consistent model should be able to provide insight into the complicated feedback mechanisms associated with the DTR changes.

3.2 Aerosol forcing

The direct radiative effect of aerosol is first evaluated under clear-sky conditions. We tested three different optical properties (SSA = 1.0, 0.9, and 0.8) with prescribed aerosols as described in Section 2.2. Figure 2 shows the aerosol-induced changes in the air temperature at 2m above the surface. Purely scattering aerosol (SSA = 1.0) tends to induce cooling and decrease daytime air temperature by about 0.5°C, except for the large decrease in the early morning. Strongly absorbing aerosols (SSA = 0.8) appear to warm up the air by as much as 0.5°C during daytime. It is interesting to note that a significant decrease of air temperature in the early morning can be found in the three prescribed aerosols. The stronger the absorbing effects, the larger the decrease in air temperature is. Although the reduction in the radiative heat flux is relatively small in the early morning, the largest temperature decrease occurs during this time because the atmospheric boundary layer is shallow and the temperature is sensitive to the change in the sensible heat flux. In the early morning, the soil temperature is sensitive to the radiative flux because the sensible and latent heat fluxes are very small and a large fraction of radiative flux is used to warm the surface skin. The larger the absorption of aerosols, the smaller the available radiative flux received. That is the reason why different SSA gives different results. A reduction in the sensible heat flux would also result from the stabilization of boundary layer air due to air heating by the strongly absorbing aerosols. In addition, a net warming or net cooling depends not only on the SSA, but also on aerosol vertical profile, surface properties (e.g., surface albedo, Bowen ratio), and meteorological conditions. In spite of the remaining uncertainty, it can be deduce that aerosols should have significant impacts on DTR. Clearly, the direct radiative effect of aerosols could also be one of major contributors to the observed DTR.

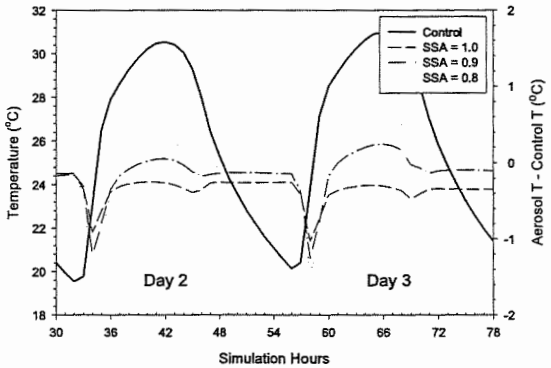

Figure 2. Impacts of aerosols on air temperature at 2 m above the surface.

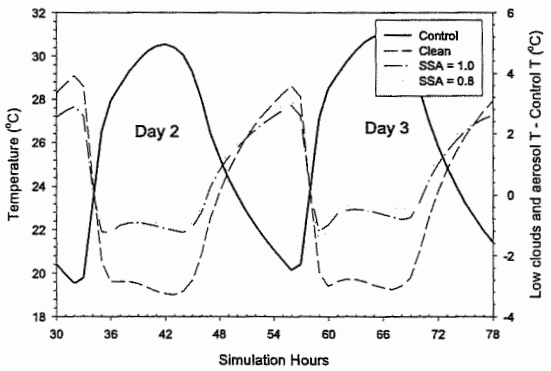

Figure 3. Impacts of aerosols with low clouds on air temperature at 2 m above the surface.

The effects of aerosol on surface radiation budgets are further tested for different cloud covers. As shown

in Figure 3, under the coverage of low clouds, the aerosol radiative effects on nighttime temperature are much smaller than that on daytime temperature by a factor of 3 to 4. It is interesting to note that the cooling of daytime temperature by low clouds with aerosols is smaller (by 2°C) than that without aerosols. Also, the temperature difference between purely scattering and strongly absorbing aerosols is not very significant. This result implies that the multiple scattering of aerosols under cloudy sky can be an important process and should be carefully considered in relevant calculations.

The radiative effects of aerosols are more prominent under high clouds as shown in Figure 4. With strongly absorbing aerosols, the atmosphere tends to heat up more during daytime and the effect even extends through most of the night except during the early morning hours. On the other hand, the purely scattering aerosols tend to reduce that with aerosols. Due to the stabilization of the boundary layer by aerosols, significant cooling in the morning hours can be found for both absorbing and non-absorbing aerosols. Evidently, the chemical compositions are very crucial in the determination of aerosol forcing. Although the impacts of middle clouds with aerosols are not shown here, it is logical to imagine that the patterns of temperature perturbation of middle clouds should be somewhat between low and high clouds (more similar with patterns of low clouds).

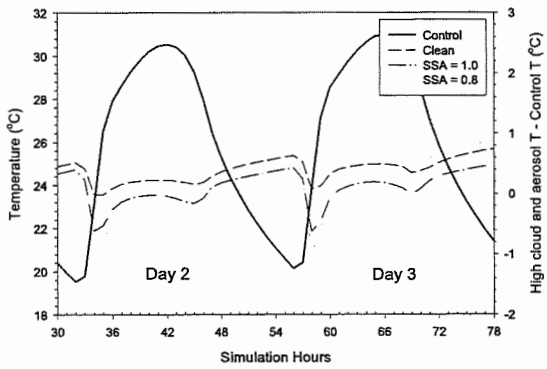

Figure 4. Same as Fig. 3 except for high clouds

Based on the above simulations, the radiative perturbation of aerosols on DTR is evident. The results shown here are more or less similar to the findings of Hansen et al., (1995) who concluded that the observed DTR over continental areas are more likely caused by a combination of radiative forcing from tropospheric aerosols and cloud cover. According to our 1-D simulation, it is worthy of further emphasizing the role of absorbing aerosols in the climate change issues.

3.3 Mixing state of aerosols

The mixing state of aerosols appears to be an influencing factor too as shown in Figure 5. The size distribution and chemical compositions of aerosols can be very complicated and variable in the ambient air, thus, in order to simply the conditions, only mono-dispersion soot (0.2 μm in radius, 500 cm^{-3} of number concentration) and $(NH_4)_2SO_4$ (0.5 μm in radius. 500 cm^{-3} of number concentration) are mixed together to demonstrate the impacts on temperature. Although the patterns of temperature variation are similar for different mixture states, the magnitude can be rather different. A difference of up to 1°C in daytime temperature and about 0.5°C in nighttime temperature may be produced. The highest difference comes from an external mixture, and the weakest from core with shell. This result might be associated with the procedures that are applied to include in the radiative forcing of aerosols in 1-D model and the methods that are used to evaluate the composite refractive index of the mixing aerosols. Therefore, more realistic ways are needed to evaluate the optical properties of aerosols that are size and composition dependent.

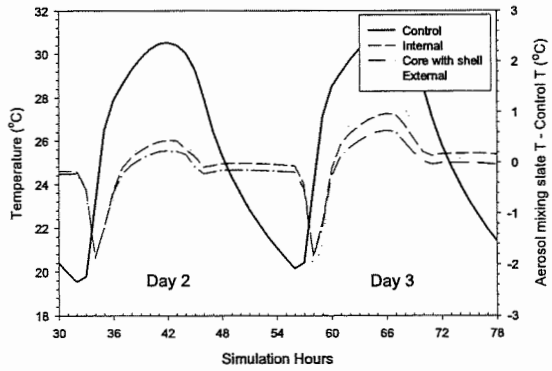

Figure 5. Impacts of mixing state of aerosols on the diurnal temperature at 2 m above the surface.

Actually, the vertical profile of aerosols is also important as revealed by such 1D model simulation (not shown here). In situ measurements of aerosol compositions and optical properties accompanying with lidar observation of vertical profile can be very helpful in the verification of the simulations conducted by this composite 1-D model.

4. CONCLUSIONS

From the sensitivity tests of aerosol and cloud impacts on the diurnal temperature change, it is obvious that low and middle clouds can significantly decrease daytime temperature while increase nighttime temperature, resulting in a decrease of DTR. Aerosols of different compositions and mixing states may also induce significant temperature perturbation. In the near future, when our atmospheric boundary layer model is fully coupled with a photochemical-aerosol-cloud model, the complex feedback processes of aerosol, cloud and climate can be better addressed. Although so far the impacts of aerosols and clouds on the observed DTR change over Taiwan and other

areas remain unresolved, we believe that by combining more observations with detailed simulation with such a 1-D model can be very helpful toward understanding the physical and chemical processes that govern the energy budget in the atmospheric boundary layer.

5. ACKNOWLEDGEMENT

The authors would like to thank Dr. Hongbin Yu, who kindly provided us the MCAPS model. The work is supported in part by the Theme Research Proposal to Academia Sinica entitled "Particulate Matter and its Environmental Impacts in Taiwan", and the Research Center for Environmental Changes, Academia Sinica, Taiwan, R.O.C.

6. REFERENCES

Chang, S. D., D. Hahn, C.-H. Yang, D. Norquist, and M. Ek, 1999: Validation study of the CAPS Model land surface scheme using the 1987 Cabauw/PILPS dataset. J. Appl. Meteorol., 38, 405-422.

Chen, J.-P., 1992: Numerical simulation of the redistribution of atmospheric trace chemicals through cloud processes. Ph.D. dissertation. Pennsylvania State University.

d'Almeida, G. A., P. Koepke, and E. P. Shettle, 1991: Atmospheric aerosols: global climatology and radiative characteristics. A. Deepak Publishing, Hampton, VA, USA.

Fu, Q., and K.-N. Liou, 1992: On the correlated k-distribution method for radiative transfer in nonhomogeneous atmosphere. J. Atmos. Sci., 49, 2139-2156.

Fu, Q., and K.-N. Liou, 1993: Parameterization of the radiative properties of cirrus clouds. J. Atmos. Sci., 50, 2008-2025.

Fu, Q., K.-N. Liou, M. C. Cribb, T. P. Charlock, and A. Grossman, 1997: Multiple scattering parameterization in thermal infrared radiative transfer. J. Atmos. Sci., 54, 2799-2812.

Hansen, J., M. Sato, and R. Ruedy, 1997: Radiative forcing and climate response. J. Geophys. Res., 102, 6831-6864.

Hansen, J. M., M. Sato, and R. Ruedy, 1995: Long-term changes of the diurnal temperature cycle: implications about mechanisms of global climate change. Atmospheric Research, 37, 175-209.

Jacobson, M. Z., 2000: A physically-based treatment of elemental carbon optics: Implications for global direct forcing of aerosols. Nature, 27, 217-220.

Toon, O. B. and T. P. Ackerman, 1981: Algorithms for the calculation of scattering by stratified spheres. Appl. Opt. 20, 3657-3660.

Trainer, M., E. Y. Hsie, S. A. Mckeen, R. Tallamraji, D. D. Parrish, F. C. Fehsenfeld, and S. C. Liu, 1987: Impact of natural hydrocarbons on hydroxyl and peroxy radicals at a remote site. J. Geophys. Res., 92, 11879-11894.

Yu, Hongbin, 2000: Radiative Effects on the Environment in China. Ph.D. Dissertation, 226pp. Georgia Institute of Technology.

WARM MICROPHYSICS IN AN OROGRAPHIC CLOUD AND PROCESSING OF AEROSOL PARTICLES

M. Simmel[1,*], K. Diehl[1], and S. Wurzler[1,2]

(1) Leibniz Institute for Tropospheric Research (IfT), Leipzig, Germany
(2) North Rhine-Westphalia State Environment Agency, Essen, Germany

1 INTRODUCTION

In the atmosphere cloud droplets are generated via heterogeneous nucleation. A certain part of the aerosol particles (AP) serves as cloud condensation nuclei (CCN) for the drop formation. As most of the clouds do not precipitate these AP are released during the evaporation process of the cloud decay. This leads to modified AP size distributions and chemical compositions inducing changed radiation and condensation properties (e.g., Wurzler et al. 2000; Feingold and Kreidenweis 2002).

Formation, development, and decay of a non-precipitating orographic cloud are simulated in order to understand the dynamical and microphysical processes involved. An adiabatic air parcel model using sectional microphysics is employed in three versions:

- 1d fixed bin model (1FBM): a one-dimensional discretization of the particle spectrum according to a fixed water mass grid
- 1d moving bin model (1MBM): a one-dimensional discretization of the particle spectrum according to a fixed aerosol mass grid, but with a moving water grid
- 2d fixed bin model (2FBM): a two-dimensional discretization of the spectrum according to fixed water and aerosol mass grids

At the expense of additional computational cost the use of 2FBM version has several advantages compared to 1FBM:

- drops of one size can have different amounts of aerosol mass (influencing the condensation properties)
- external AP mixtures can be represented
- the AP distributions are better prevented from numerical diffusion

As microphysical processes the models consider growth/shrinking of AP as well as nucleation and growth/evaporation of drops. Impaction of AP and collision-coalescence of drops are described using the Linear Discrete Method (Simmel et al. 2002) and the kernel of Kerkweg et al. (2003) in the fixed bin models 1FBM and 2FBM. For the cases investigated these processes turned out to be negligible due to the small drop sizes and short cloud lifetimes. Therefore, the 1MBM could be applied, too, and the results of the three models are compared.

2 MODEL INITIALISATION

All data for the model simulations are taken from the field experimental campaigns FEBUKO 2001 and 2002. Model initialisation data such as temperature, relative humidity, AP size distributions, etc. were measured at a valley station upwind of the cloud. Dynamical and microphysical model results are compared to experimental findings at two more stations: one at the mountain top (in cloud) and one downwind of the mountain (cloud free). Measured horizontal wind speeds are used to estimate transport times and – in combination with the orography – vertical velocities.

3 RESULTS

3.1 Overview

Fig. 1 shows modeled drop numbers and liquid water contents (LWC) for a selected day of the FEBUKO 2001 campaign for the standard model configuration (see Tab. 1) calculated with the 1FBM. The two parameters are anti-correlated. This is due to the orography which is rather shallow in the valley but becomes steeper towards the mountain top. Therefore, a smaller LWC representing a higher cloud base is connected with higher updraft velocities and more

*Corresponding author's address:
Martin Simmel, Leibniz Institute for Tropospheric Research, Permoserstr. 15, 04318 Leipzig, Germany,
E-mail: simmel@tropos.de

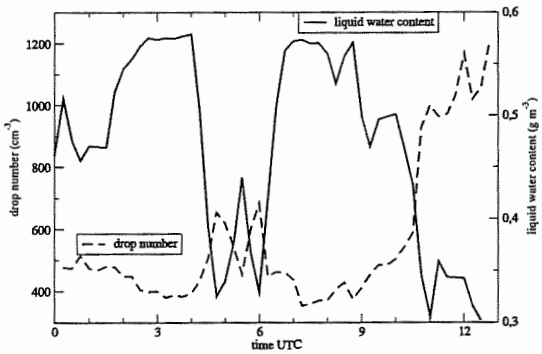

Figure 1: *Time series of drop number (dashed line) and liquid water content (solid line) at the hill station for the standard case.*

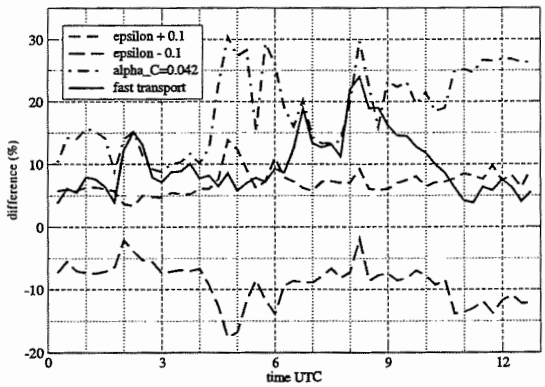

Figure 2: *Time series of drop number sensitivities vs. changes in soluble fraction ϵ, water accomodation coefficient α_C and transport time compared to the standard case.*

supersaturation leading to higher drop numbers if activation takes place in this region. Values of about 400–500 cm^{-3} were observed during the measurements which means that modeled drop numbers are realistic when LWC of about 0.45 g m^{-3} and more are reached. The strong fluctuations and extremely high drop numbers (> 700 cm^{-3}) are not observed in nature which suggests that in reality the air follows a more gentle updraft motion near the mountain top than in the model.

3.2 Model sensitivities

Model sensitivities against the three parameters transport time, soluble particle fraction ϵ, and water accomodation coefficient α_C are investigated using 1FBM (see Tab. 1 for parameter configurations of the different runs). Fig. 2 gives the influence of the parameter variations on drop number and summarizes the deviation from the standard case. For the description of cloud processing the drop number is a crucial parameter because chemical reactions and uptake of soluble gases occur mainly in drops and leave interstitial particles rather unchanged. Additionally, the activation process responds sensitively on changes in the microphysical and dynamical conditions.

As expected, a faster transport (see Tab. 1, case FAST; Fig. 2, solid line) from the valley to the mountain top (starting with a horizontal wind speed of 4 m/s instead of 2 m/s for the standard case) leads to higher drop numbers due to higher supersaturations reached. The difference to the standard case results ranges from 5–25 %.

case	wind speed	ϵ	α_C
standard	2 m/s	as measured	1
EPS+	2 m/s	meas. +0.1	1
EPS-	2 m/s	meas. −0.1	1
ALPHA	2 m/s	as measured	0.042
FAST	4 m/s	as measured	1

Table 1: *Parameter configurations for the investigation of the model sensitivities.*

For the standard case, ϵ was derived from the size-resolved chemistry measurements and averages a value of about 0.5–0.6, ranging from 0.2 for the smallest particles to 0.8 for the potential CCN. Variations in ϵ by ± 0.1 (see Tab. 1, cases EPS+ and EPS-) lead to changes in drop number up to 15 % in the model (see Fig. 2, dashed lines). Higher ϵ values result in higher drop numbers as well as lower maximum supersaturations and vice versa.

In cloud modeling a rather long list of α_C values ranging from about 0.01 to 1 is discussed (Pruppacher and Klett 1997; Kreidenweis et al. 2003). Fig. 2 (dot-dashed line) shows the impact of this coefficient (0.042 vs. 1 for the standard case, see Tab. 1, case ALPHA) on drop number. The use of a small α_C results in an increase of up to 30 % in drop numbers due to the stronger limitations on phase transfer. This induces higher supersaturations which enable smaller AP to activate.

All sensitivities shown lead to deviations from the standard case in the same order of magnitude. They are far from being constant for each of the parameters investigated but highly depend on the specific conditions. Therefore, the microphysical behavior for changes in certain parameters cannot be easily parameterized. This underlines the importance of a detailed description of the microphysical processes for the treatment of cloud processing.

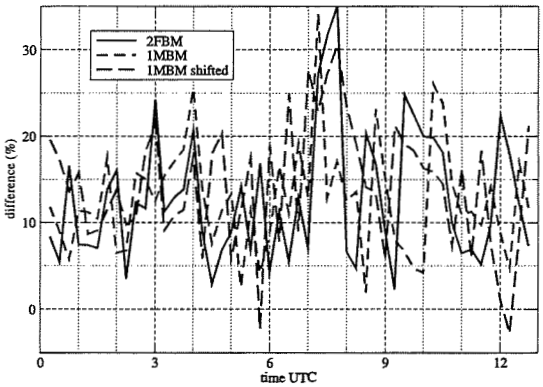

Figure 3: *Time series of drop number differences for 2FBM (solid line) and the 1MBM (dashed lines) for the standard case compared to 1FBM.*

3.3 Different model versions

The differences between the three model versions are investigated for the standard case like in Fig 1. Generally, higher drop numbers are calculated by 2FBM (solid line) and 1MBM (dashed lines) compared to 1FBM (Figure 3). In both model types, all particles belonging to a certain bin are either activated or not activated, whereas in 1FBM partial bin activation is possible. This leads to the problem of the initial grid choice which is arbitrary but can cause rather different results for 2FBM and 1MBM. This is demonstrated for 1MBM: the two results shown are obtained by only slightly shifting the aerosol grid at initialisation time. This small purely numerically induced shift without any microphysical meaning can result in differences up to 20 %. Like for the microphysical sensitivities in Fig. 2, the differences highly vary for each specific set of initial conditions.

3.4 Selected size distributions

Fig. 4 compares mass (isolines) and number (shaded areas) size distributions for a high (top) and a low (bottom) cloud base obtained from the 1FBM runs at 11 and 9 UTC, respectively. The lower cloud base (higher LWC) corresponds to earlier drop formation, less and, therefore, larger drops, and longer drop lifetimes as well as larger cutoff AP sizes for activation. For a higher cloud base (top), vertical velocity and supersaturation are much higher leading to a sharp activation profile with a large gap between non-activated interstitial particles and activated drops. This gap is also present but much less pronounced for the more gentle activation process at the lower cloud base (bottom).

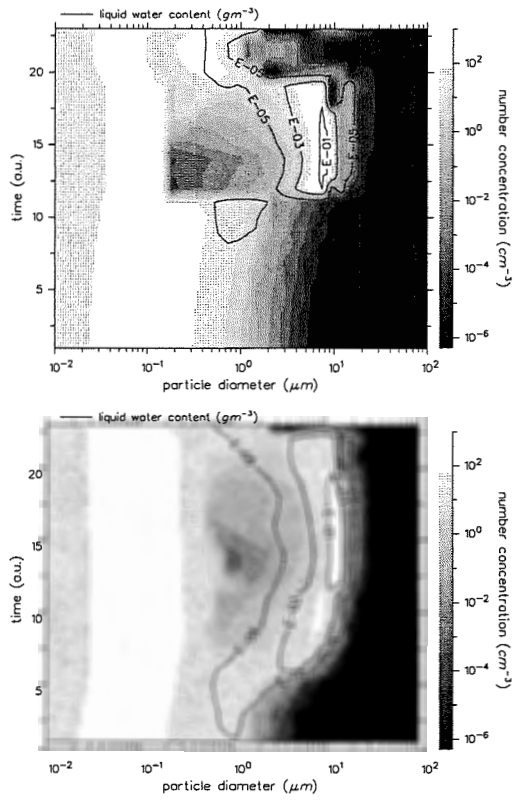

Figure 4: *Liquid water content (isolines) and particle/drop number concentration (shaded areas) size distributions for a complete mountain passage for high (top) and low (bottom) cloud base.*

4 CONCLUSIONS

The influence of various microphysical parameters and the choice of model version was investigated for a warm orographic cloud situation. Drop number was chosen as main parameter for the comparison due to its sensitivity on the one hand but also due to its importance for further processes such as cloud processing and precipitation formation (which did not take place in our case study).

The activation process and the number of drops nucleated are very sensitive to the updraft velocity and, therefore, to the position of the cloud base in complex terrain. A deviation in the soluble fraction ϵ of ± 0.1 which lies in the range of uncertainty and can occur easily when ϵ is estimated from experimental findings with partly unspecified components may lead to differences of up to 15 % in drop numbers. The choice of the water accomodation coefficient α_C which is still under discussion is crucial for the micro-

physical results and, therefore, the cloud processing.

The use of models with a fixed aerosol mass grid (here 1MBM and 2FBM) in principle suffers from the problem that the choice of the grid is arbitrary but highly influences the results. This can only be solved by increasing the resolution. The error in drop numbers can be estimated by the particle numbers of the bins in vicinity of the activation gap which can be as high as 100 cm^{-3} or more. For 2FBM this problem is of minor importance when external mixtures of AP are used as often observed instead of internal AP mixtures as they were applied here.

Acknowledgements

This work is part of the joint research project MODMEP *(Modelling of tropospheric multiphase processes)* which is carried out in cooperation with the joint research project FEBUKO *(Field investigations of budgets and conversions of particle phase organics in tropospheric cloud processes)*.

MODMEP and FEBUKO are supported by the German Federal Ministry of Education and Research (BMBF) in the framework of AFO 2000 (projects 07ATF40 and 07ATF01). Further information on these projects can be found via `http://projects.tropos.de:8088/afo2000g3/`

References

Feingold, G. and S. M. Kreidenweis (2002). Cloud processing of aerosol as modeled by a large eddy simulation with coupled microphysics and aqueous chemistry. *J. Geophys. Res. 107*(D27). 4687.

Kerkweg, A., S. Wurzler, T. Reisin, and A. Bott (2003). On the cloud processing of aerosol particles: An entraining air parcel model with two-dimensional spectral cloud microphysics and a new formulation of the collection kernel. *Q. J. R. Meteorol. Soc. 129*, 1–18.

Kreidenweis, S. M., C. J. Walcek, G. Feingold, W. Gong, M. Z. Jacobson, C.-H. Kim, X. Liu, J. E. Penner, A. Nenes, and J. H. Seinfeld (2003). Modification of aerosol mass and size distribution due to aqueous-phase SO_2 oxidation in clouds: Comparison of several models. *J. Geophys. Res. 108*(D7). doi:10.1029/2002JD002697.

Pruppacher, H. R. and J. D. Klett (1997). *Microphysics of clouds and precipitation.* Kluwer Academic Publisher.

Simmel, M., T. Trautmann, and G. Tetzlaff (2002). Numerical solution of the stochastic collection equation – Comparisons of the linear discrete method with other methods. *Atmos. Res. 61*, 135–148.

Wurzler, S., T. G. Reisin, and Z. Levin (2000). Modification of mineral dust particles by cloud processing and subsequent effects on drop size distributions. *J. Geophys. Res. 105*(D4), 4501–4512.

EFFECTS OF THE AEROSOL ON THE OPTICAL PROPERTIES OF CLOUDS

Sabina Stefan[1], Gabriela Iorga[2]

[1] University of Bucharest, Faculty of Physics, Dept. of Atmospheric Physics, Bucharest, Romania
[2] University of Bucharest, Faculty of Chemistry, Dept. of Physics, Bucharest, Romania

1. INTRODUCTION

The aerosol number or mass concentration is a key parameter in studies of radiative effects. Higher aerosol concentrations in atmosphere increase the cloud albedo, and, in turn, lead to a higher value of indirect forcing. This is called the first indirect effect of aerosol or "albedo effect" on climate and it is a result of the cloud droplet number concentration (CDNC) dependency on aerosol number concentration.

Based on an analysis of simulated indirect aerosol effect and the observed surface radiation, Penner et. al. (2004) carried out a study on cloud optical depth determined by the aerosol characteristics. This study has shown the significant influence of the indirect aerosol effect on radiative fluxes.

Also, Iorga and Stefan (2004) have shown for a marine aerosol consisting of pure ammonium sulfate and a rural aerosol, consisting of a mixture of ammonium sulfate and mineral dust, that optical properties of clouds are strongly correlated with the characteristics of aerosols.

In the present work we will study the sensitivity of cloud albedo to changes in CDNC in connection to the changes in liquid water content (LWC) and the cloud droplet effective radius (r_{eff}). The CDNC and r_{eff} were calculated for various types of aerosol using the parameterizations proposed by Abdul-Razzak (1998, 2000) and Liu and Daum (2000), respectively.

The aerosol types used in this study were rural and urban as continental aerosol and marine aerosol. The size distributions of these aerosol types were derived from measurements (Whitby,1978; Hoppel and Frick, 1990; Jaenicke, 1988). Also, the chemical composition of the aerosol is based on measurements reported in literature, which show that the continental aerosol contains 15-30% sulfate, while marine aerosol contains somewhat more (30-60%), and clearly most of the sulfate for both types of aerosol can be found in the accumulation mode.

Corresponding author's address: Sabina Stefan, University of Bucharest, Faculty of Physics, Department of Atmospheric Physics, P.O. Box MG-11, 76900 Bucharest, Romania; E-Mail: sabinastefan@hotmail.com.

The percent of 15-30% sulfate assures that fine particles aerosols at common humidity are hygroscopic ones and they behave as optically ideal droplets. In this respect we have carried out a study for optical and microphysical cloud properties starting from the three modes obtained from a lognormal fit of the measurements of aerosol size distributions by Whitby (1978), Hoppel and Frick (1990) and Jaenicke (1988).

2. THEORETICAL CONSIDERATIONS AND DATA USED

Global climate models rely on parameterisations to account the sub-grid processes of aerosol-cloud interaction and cloud formation. Our purpose is to test the sensitivity of cloud optical properties to the aerosol characteristics by using different aerosol types.

The aerosol number size distribution is assumed to be described by a lognormal distribution:

$$\frac{dn_r}{d\ln r} = \sum_{i=1}^{3} \frac{n_{r,i}}{\sqrt{2\pi}\ln\sigma_i} \exp\left(-\frac{[\ln(r/r_{m,i})]^2}{2(\ln\sigma_i)^2}\right) \quad (1)$$

where $n_{r,i}$, $r_{m,i}$ and σ_i are the total number concentration, geometric mean radius, and geometric standard deviation of aerosol mode i, respectively. The modes are: i = 1 nucleation mode, i = 2 accumulation mode and i = 3 coarse mode.

The fraction of activated aerosol particles as function of supersaturation S_m, for the aerosol mode "i" is computed using the Abdul-Razzak et al. (1998, 2000) parameterizations. Their parameterisations pertain to the cloud droplets formation from an aerosol population in a parcel of air rising adiabatically. We have assumed that the cloud condensation nuclei (CCN) predicted by Abdul-Razzak parameterization may become cloud droplets at a supersaturation of 1%.

The cloud droplet effective radius was parameterized as a "1/3" power law of the ratio between the cloud liquid water content and the cloud droplet number concentration (Martin et al., 1994; Lacis and Hansen, 1974) with some pre-factors which are dependent of spectral dispersion of droplet size distribution. We have used for these pre-factors the parameterization proposed by Liu and Daum (2000):

$$PF = 62.04 \cdot \frac{\left(1+2d^2\right)^{2/3}}{\left(1+d^2\right)^{1/3}} \quad (2)$$

where the d signifies the spectral dispersion of droplet size distribution ($d = \frac{\sigma}{\bar{r}}$). We have assumed that the spectral dispersion of the aerosol number size distribution characterizes the CDNC size distributions and we have considered only the values of the spectral dispersions corresponding to the accumulation ranges of the various aerosol types.

The asymmetry factor computed for visible and near-infrared ranges of the solar part of electromagnetic spectrum (Fouquart and Bonnel, 1980): the visible (0.25÷0.68 μm), and near infrared (0.68÷4.0μm), as it is considered in the ECHAM GCM model, where the single scattering properties of clouds are derived from Mie theory and the results fitted to the spectral resolution of the radiation model (Boucher and Lohmann, 1995).

We have computed the cloud optical depth, τ, using the formula:

$$\tau = \frac{3}{2} \cdot \frac{LWP}{\rho \cdot r_{eff}} \quad (3)$$

where *LWP* is the liquid water path (the product between *LWC* and the cloud geometrical thickness).

The cloud albedo, *A*, was computed taking into account the two-stream approximation of a nonabsorbing, horizontally homogeneous cloud (Lacis and Hansen, 1974) as a function of the cloud optical depth and the asymmetry factor, considering the cases of the marine, urban and rural aerosol.

The chemical composition of the rural aerosols is assumed to be a mixture of ammonium sulfate (75%) and mineral dust (25%) as appeared in Bott (2000). The corresponding coefficients of the aerosol number size distributions are shown in Table 1.

Table 1. Modal parameters of number size distributions for rural aerosols.

	$n_{r,i}$ (cm^{-3})	r_i (μm)	$\log\sigma_i$
W	1000	0.008	0.20
	800	0.034	0.32
	0.72	0.460	0.34
J	6650	0.007	0.225
	147	0.027	0.557
	1990	0.042	0.266

The Table 2 contains the modal parameters of the urban aerosols as given by Whitby (1978) and Jaenicke (1988).

Table 2. Modal parameters of number size distributions in the case of urban aerosol.

	$n_{r,i}$ (cm^{-3})	r_i (μm)	$\log\sigma_i$
W	$2120 \cdot 10^3$	0.006	0.240
	$37 \cdot 10^3$	0.031	0.297
	4.9	0.540	0.328
J	$9.93 \cdot 10^4$	0.006	0.245
	$1.11 \cdot 10^3$	0.007	0.666
	$3.64 \cdot 10^4$	0.025	0.337

The marine aerosols are assumed to consist of pure ammonium sulfate for the aerosol size distributions of Hoppel and Frick (1990) (HF) and Jaenicke (1988) (J). The marine aerosols of Whitby (1978) (W) consist of 61% of $(NH_4)_2SO_4$ and 39% NaCl. The coefficients appearing in Eq.(1) are given in Table 3.

Table 3. Modal parameters of number size distributions for a marine aerosol.

	$n_{r,i}$ (cm^{-3})	r_i (μm)	$\log\sigma_i$
HF	100	0.027	0.25
	120	0.105	0.11
	6	0.210	0.45
W	340	0.005	0.20
	60	0.035	0.30
	3.1	0.310	0.43
J	133	0.004	0.66
	66.6	0.133	0.21
	3.1	0.290	0.40

3. RESULTS AND DISCUSSIONS

Further, the cloud droplet effective radius was computed for different aerosol types at different liquids water content and for different pre-factors.

The Figure 1a shows the dependence of cloud droplet effective radius on CDNC for two values of LWC (liquid water content: 0.05g/cm^{-3} and 0.15g/cm^{-3}), for continental stratiform clouds formed in air masses characterized by rural aerosol.

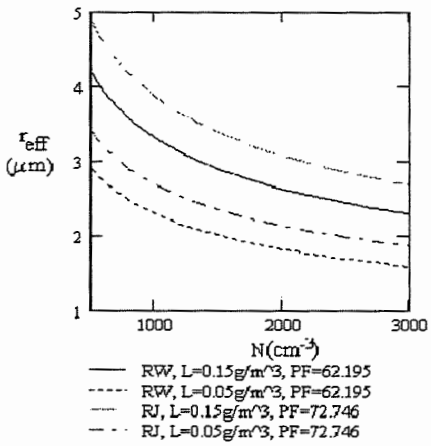

Fig.1a. Cloud droplet effective radius as a function of CDNC for rural air masses.

The Fig. 1b shows the dependence of cloud droplet effective radius on CDNC for the same two values of *LWC* like in Fig. 1a but for continental stratiform clouds formed in air masses characterized by urban aerosol. From Fig 1a and b it can be seen that the cloud droplet effective radius is lower for urban that for the rural aerosol.

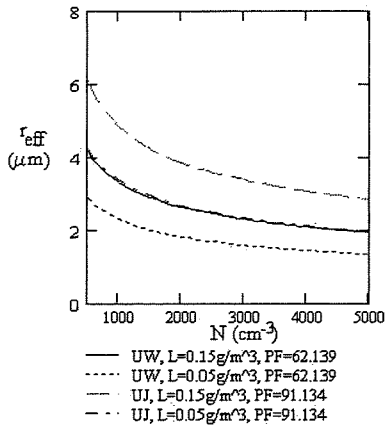

Fig.1b. Cloud droplet effective radius as a function of CDNC for urban air masses.

The most probable values for effective radius for continental stratiform clouds lie in the range 2 ÷ 4μm.

The dependence of cloud droplet effective radius on CDNC, considering two values for liquid water content of 0.1 g/m^3 and 0.3 g/m^3, is shown in Figure 2, for maritime air mass characterized by aerosol size distribution of HF, J and W.

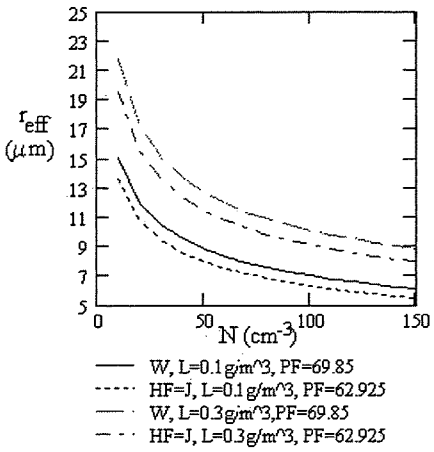

Fig.2. Cloud droplet effective radius as a function of CDNC for marine air masses.

For the maritime case, results show, for the same liquid water content the effective radius range is between 6 and 12μm, depending on the CDNC value. An increase of liquid water content leads to higher values for effective radius from about 9 to about 19μm. For larger values than 150 cm^{-3} of CCN, the values of r_{eff} are the same, closed on 4 μm. The values are similar with those measured by Hahn et al. (1995).

In the next computations of cloud parameters were taken into account only the situations where the values of cloud liquid water path were below 150 g/m^2, thus only non-precipitating stratiform clouds were considered. Figure 3 shows the optical thickness as a function of cloud droplet effective radius and LWP, for a cloud with geometrical thickness of 500 m.

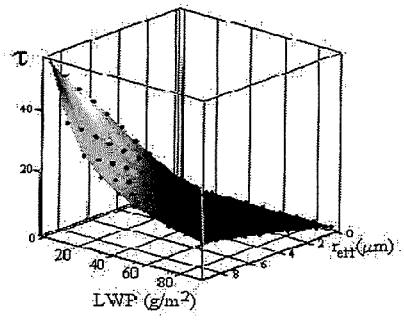

Fig. 3. Cloud optical depth as a function of LWP and cloud droplet effective radius from 0 to 10 μm

Han et al. (1998) reported that for optically thick clouds (τ > 15) over most of the world, cloud albedo increases with decreasing r_{eff}, and LWP decreases as r_{eff} decrease; for optically thin clouds (τ < 15) over oceans and tropical rain forest areas, they report that cloud albedo decreases with the decrease r_{eff}, while most continental areas albedo increase as r_{eff} decrease

It is important to observe that value of 15 for τ limits two ranges of dependences, in agreement with the results of Hann et al. (1998). This result becomes more clearly from a simultaneous analysis of Fig. 3 and Fig. 4, containing the results for cloud albedo. Fig 4 shows results for maritime clouds; in the case of continental clouds we have found a similar correlation. The higher albedo values for the visible range than those for the near infrared and the increase of albedo with the decrease of r_{eff} for both spectral ranges can be observed. The contrast between the albedo values obtained for the considered spectral ranges is much more reduced in the case of continental clouds than in the case of marine clouds.

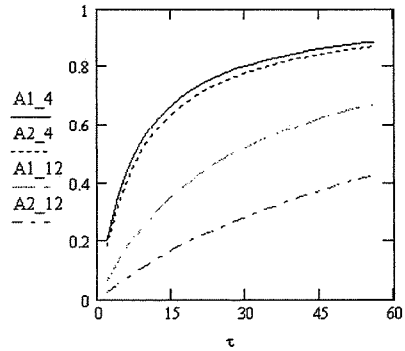

Fig.4. Dependence of cloud top albedo on optical thickness for values of r_{eff} of 4 and 12 μm, for visible (A1) and near-infrared ranges (A2)

Pertaining to the variation of albedo function of optical thickness, Figure 4 proves that τ = 15 can be considered as a separator value for two areas with different dependences; we have found an inverse correlation between A and r_{eff} for the entire considered range of τ but the curve slopes are different.

Sensitivity of cloud albedo, dA/dlnN, is shown in Fig. 5a for two values of effective radius (1μm and 4μm) and for 12μm and 4μm in Figure 5b, in visible spectral range.

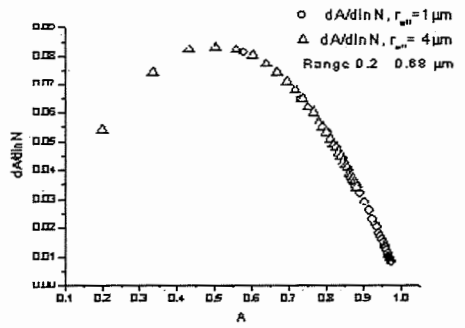

Fig. 5a. Sensitivity of cloud albedo in the visible range for continental stratiform clouds of effective radius of 4 and 1 μm

The sensitivity of cloud albedo to changes in cloud droplet number concentration has maximum values in the range 0.3 ÷ 0.7, as Charlson et al. (1992) predicted.

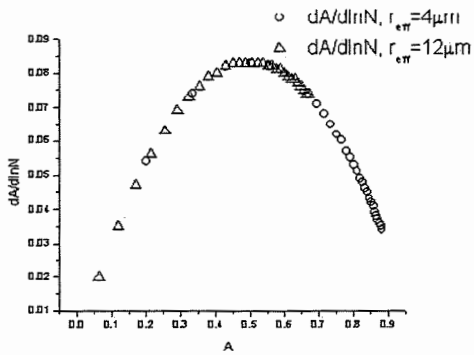

Fig. 5b. Sensitivity of cloud albedo in the visible range for maritime stratiform clouds of effective radius of 4 and 12 μ

A small flat range of sensitivity when albedo varies from 0.43 to 0.53 was observed (Fig. 5b) in the case of maritime clouds but only for the visible range. In this case, the sensitivity reaches its maximum values for all cloud albedo values between 0.43 and 0.53.

For continental clouds, for both spectral intervals, and for the near infrared in the case of maritime clouds, the sensitivity reaches its maximum (a single point) for the value of cloud top albedo of 0.5. In these later cases, an increase in cloud droplet number concentration of 1% leads to an increase of ~ $8.4 \cdot 10^{-4}$ in cloud albedo and in the case of maritime clouds in the visible range an increase of 1% in CDNC determine a increase of ~ $8.3 \cdot 10^{-4}$.

Acknowledgements

Sabina Stefan was supported by CERES3-105 VARICLIM grant of Romanian PNCDI.

References

Abdul-Razzak, H., Ghan, S.J., and Rivera-Carpio, C., 1998: A parameterization of aerosol activation, 1. Single aerosol type, J. Geophys. Res., 103, 6123-6132;

Abdul-Razzak, H., and Ghan, S.J., 2000: A parameterization of aerosol activation, 2. Multiple aerosol type, J. Geophys. Res., 105, 6837-6844;

Boucher, O., Lohmann, U., 1995: The sulfate-CCN-cloud albedo effect: A sensitivity study with two general circulation models, Tellus 47B, 281-300;

Bott, A., 2000: A numerical model of the cloud-topped planetary boundary layer: influence of the physico-chemical properties of aerosol particles on the effective radius of stratiform clouds, *Atmos. Res.*, 53, 15-27;

Fouquart, Y., Bonnel, B., 1980: Computations of solar heating of the Earth's atmosphere: a new parameterization, Beitr. Phys. Atmos., 53;

Han, Q., Rossow, W. B., Chou, J., Welch, R. M, 1998: Global survey of the relationships of cloud albedo and liquid water path with droplet size using ISCCP, *J. Climate*, 11; Hoppel, W.A. and Frick, G.M., 1990: Submicron aerosol size distributions measured over the tropical and south Pacific, Atmos. Environ, 24A, 645-659;

Hoppel, W.A, and Frick, G.M., 1990: Submicron aerosol size distributions measured over the tropical and South Pacific, Atmos. Environ., 3, 645-659;

Iorga, G., Stefan, S.,2003: Effects of microphysics on the cloud albedo in climate models (submitted to Global and Planetary Change);

Jaenicke, R., 1988: Aerosol physics and Chemistry, in Landolt-Boernstein (Ed.), Zahlenwerte und Funktionen aus Naturwissenschaften und Technik, Vol. 4b, Springer, 391-457;

Lacis, A.A., Hansen, J.E., 1974: A parameterization for the absorption of solar radiation in the Earth's atmosphere, J. Atmos. Sci., 31.

Liu, Y., Daum, P.H., 2000: Which size distribution function to use for studies related to effective radius, Extended abstract for presentation at the 13th International Conference on cloud and precipitation, Reno, NV, 14-18 August;

Martin, G.M., Johnson, D.W., Spice, A., 1994: The measurement and parameterization of effective radius of droplets in warm stratocumulus clouds, *J. Atmos. Sci.*, 51, 13;

Penner, J.E., Dong, X., Chen, Y., 2004: Observational evidence of a change in radiative forcing due to the indirect aerosol effect, Nature, 427, 231-234;

Whitby, K.T., 1978: The physical characteristics of sulfur aerosol, Atmos. Environ., 12, 135-159.

STUDIES OF THE AEROSOL INDIRECT EFFECT IN NCAR CAM2.0

Trude Storelvmo[1] and Jon Egill Kristjansson[1]

[1]Department of Geosciences, University of Oslo, Oslo, Norway

1. INTRODUCTION

The increase in global mean aerosol burden since pre-industrial times represents the least understood climate forcing within climate studies [Lohmann et al., 2000]. It is common to divide this forcing into two components, namely the direct and indirect effect of aerosols. The direct aerosol effect refers to a radiative forcing due to absorption and reflection of solar radiation by aerosols. This forcing is usually estimated to represent a negative forcing, although quantitatively uncertainty is high. Even more uncertainty is however associated with the indirect effect of aerosols [Penner et al., 2001]. This effect is caused by an increase in cloud condensation nuclei (CCN) concentration that comes about because of the hygroscopicity of certain anthropogenic aerosols. The aerosol indirect effect can be divided further into at least two parts: The Radius Effect represents an increase in cloud albedo due to smaller and more numerous cloud droplets; The Lifetime Effect represents an increase in cloud albedo due to less efficient precipitation release, and hence increased cloud volume [Kristjansson, 2002]. The significant uncertainty associated with the aerosol indirect effect is illustrated by the survey of 9 different climate model estimates conducted by Penner et al. [2001]. They found the estimates of the total indirect effect forcing (including both the radius and lifetime effects) to vary between -1.1 and -4.8 W/m^2.This was the motivation for the initiation of the COMBINE (Combined Observational and Modeling Based Study of the Aerosol Indirect Effect) project in March 2003. The observational part of this 3-year project involves analyses of data from the MODIS instrument onboard the TERRA (EOS AM) and AQUA (EOS PM) satellites. The aim of the modeling part of the project is to investigate the indirect effect of aerosols using the National Center for Atmospheric Research Community Atmosphere Model Version 2.0 (NCAR CAM2.0). considered, i.e. sulfate and black carbon aerosols.

Corresponding author's address: Trude Storelvmo, Department of Geoscience, Section for Meteorology and Oceanography, University of Oslo, P.O. Box 1022, Blindern N-0315, Oslo, Norway.

In addition, calculations of the indirect effect of organic carbon will shortly be included in the model.

Two types of anthropogenic aerosols are currently Here we present the preliminary results from the modeling aspect of the COMBINE project.

2. METHODOLOGY

The modeling aspect of the COMBINE project is a continuation of the work presented in Kristjansson [2002]. The work included the implementation of a module for calculations of the aerosol indirect effect into the National Center for Atmospheric Research Community Climate Model Version 3 (NCAR CCM3). The same module has now been implemented in NCAR CAM2.0 and will in the future serve as a platform for further development.

In this aerosol module, concentrations and vertical distribution of sulfate and black carbon are obtained from a life cycle model developed by Seland and Iversen, [2000]. Monthly averaged fields from three dimensional life-cycle model runs are fed into the module, which is developed for calculations of both the direct and the indirect effect of aerosols. In addition to natural and anthropogenic sulfate and black carbon, three different background aerosols are treated:

- *A continental background*, consisting of a water-soluble and a dust-like mode.
- *A maritime background*, consisting of three sea-salt modes and a long-range transported mineral mode .
- *An arctic background,* consisting of a sea-salt mode and a mineral mode.

The sulfate and black carbon aerosols are added to the background using a method described in detail in Kirkevåg et al.,1999. Based on knowledge of the hygroscopicity of the aerosols and the grid box supersaturation, the number of activated CCN can then be calculated. However, it is difficult to obtain a reasonable estimate of the supersaturation in a GCM grid box.

Currently, the approach is simply to prescribe the supersaturation depending on cloud type. The assumed supersaturations are slighthly lower than observed values for each cloud type. The cloud droplet number concentration would otherwise be overestimated due to the fact that microphysical sinks in cloud droplet number are not accounted for. These crude approaches will be significantly improved within the COMBINE project, as

will be described in section 4. At this point, only the indirect effect of water clouds (i.e. clouds in the lower troposphere) has been accounted for. An attempt to parameterize the indirect effect of ice clouds will be carried out in the later stages of the COMBINE project. To calculate both the radius- and lifetime effects as radiative forcings,three parallel calls are made to the radiation- and condensation schemes of the model at every time step. One is for advancing the model, the other two are diagnostic calls. They correspond to microphysical properties based on natural aerosols and all (natural + anthropogenic) aerosols, respectively. The anthropogenic aerosols introduce smaller cloud droplets and increased amounts of cloud water, and hence a stronger negative radiative forcing. The difference between given parameters in the two diagnostic calls gives us a quantitative measure of these effects. The results presented in the following section are new and so far unpublished.

3. PRELIMINARY MODEL RESULTS.

In this section, the results from a 3-year model run is presented. The 3-year run was started after one year of model spin-up, which should be sufficient in this case. The run has been conducted for two sets of aerosol data obtained from from the aerosol module of Iversen and Seland, [2002].
The data sets are calculated by running the module for the IPCC A2 scenario [Penner et al., 2001] for 2000 with and without anthropogenic aerosols. Figure 1 shows the anthropogenic change in cloud droplet number concentration (CDNC) for the lowest model level.

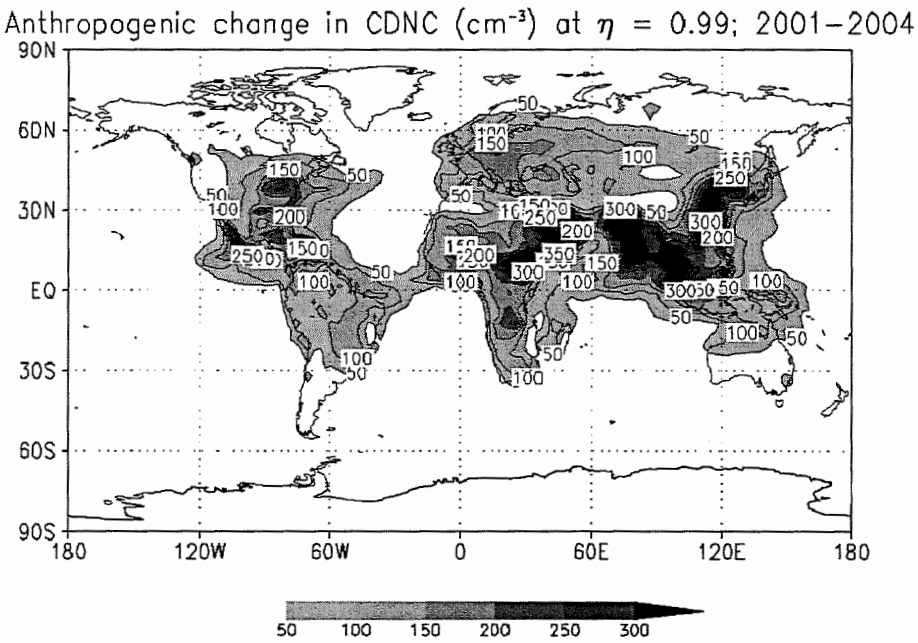

Figure 1: Anthropogenic change in cloud droplet number concentration.

As expected, we find the highest values over SE Asia, Central Europe and eastern North America. The signature of biomass burning in Central Africa and parts of South America can also be seen. In Figure 2 we show the reduction in cloud droplet size due to anthropogenic aerosols.
Reductions are again found over expected areas, SE Asia representing the strongest change of more than 3 μm. In global average, the cloud droplet size is 10.29 μm, as can be seen from Table 1.
Also evident is the difference between the Northern Hemisphere and the Southern Hemisphere, the first average being >1 μm smaller than the latter.
A similar difference between the hemispheres can be found for the cloud liquid water path (LWP) (see Table 1, no figure shown). Cloud water and droplet size changes

are comparable with those found in Kristjansson,[2002], although both changes are slightly smaller. Figure 3 shows the indirect effect of anthropogenic aerosols, while global averages are given in Table 1. As expected, the Northern Hemisphere represents the strongest negative radiative forcing of –1.29 W/m^2, while the global average is -0.91 W/m^2. This is a somewhat weaker forcing than expected, compared to Penner et al., [2001] and Kristjansson, [2002]. The deviation from the indirect effect presented in Kristjansson, [2002], can probably be explained by several factors. One is that the anthropogenic change in cloud droplet size and LWP is somewhat smaller in this study. In addition, the amount of cloud water in NCAR CAM2.0 is significantly larger (about 50 %) than in NCAR CCM3. Consequently, the radiative forcing will be less sensitive to a relatively small change in LWP.

Table 1. Area and Annual Averages of Key Quantities from 3-year model run.

	Indirect Effect, W/m^2	r_{ev},μm	LWP g/m^2	Δr_{ev},μm	ΔLWP g/m^2
Global	-0.91	10.29	65.4	-0.51	1.46
NH	-1.29	9.73	65.9	-0.76	2.18
SH	-0.53	10.88	64.9	-0.25	0.74

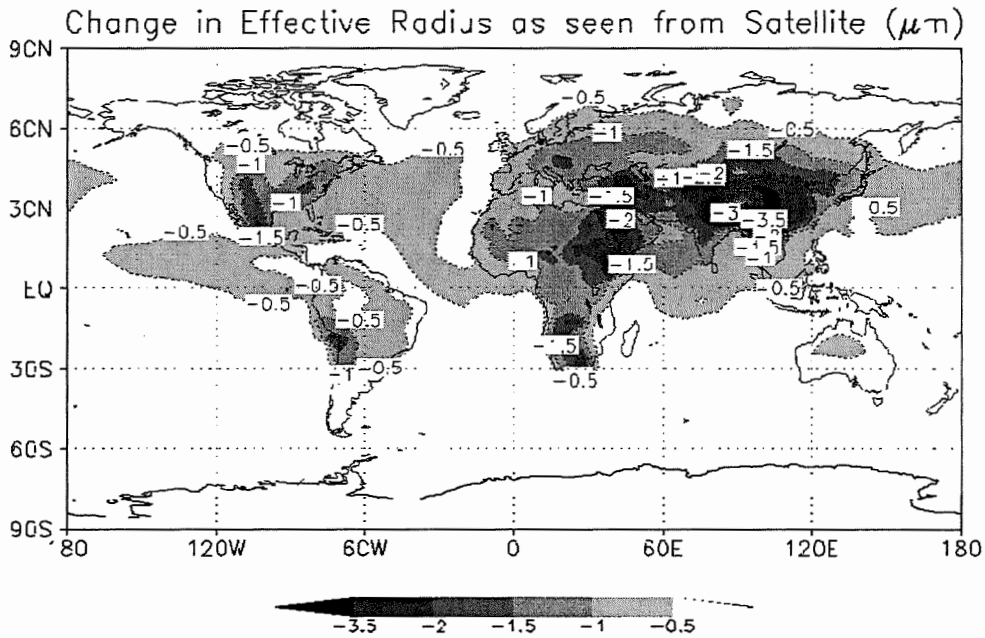

Figure 2. Changes in cloud droplet size (r_{ev}) due to anthropogenic aerosol emissions, 3-year model run.

4. CONCLUSION & FUTURE PLANS

As already mentioned, a major simplification is made by simply prescribing the supersaturation in each grid box. In addition, microphysical sources and sinks of cloud droplets are only crudely accounted for. This will be significantly improved by introducing a continuity equation for cloud droplet number concentration. The nucleation term in this equation will be calculated using a parameterization of the subgrid scale variation in vertical velocity, and hence supersaturation, accounting for the natural variability found in real clouds [Abdul-Razzak and Ghan, 2000]. Future work within the COMBINE project will also include an attempt to parameterize the indirect effect of ice clouds.

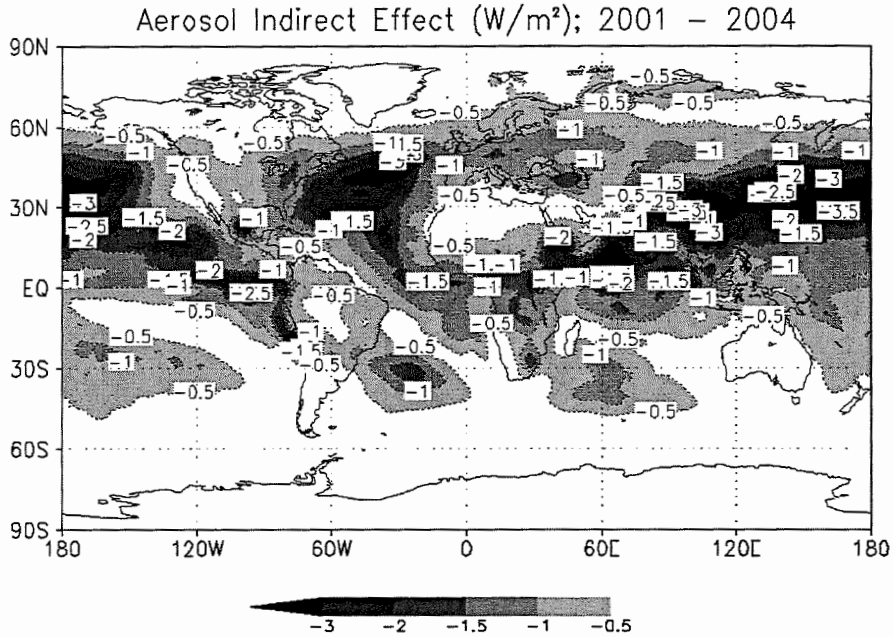

Figure 3. Simulated indirect effect of aerosols in 3-year model run.

AKNOWLEDGEMENTS

The work presented here has been supported by the Norwegian Research Council through the COMBINE project. Thanks to Alf Kirkevåg, Øyvind Seland and Steve Ghan for help and cooperation.

REFERENCES

Abdul- Razzak, H. and S. Ghan, 2000: A parameterization of aerosol activation , 2. Multiple aerosol type., *J. Geophys. Res., 105,* 6837-6844.

Kirkevåg, A. and T. Iversen, 2002: Global direct radiative forcing by process-parameterized aerosol optical properties. *J. Geophys. Res., 107* (D20), 4433, 10.1029/2001JD000886.

Kristjansson, J. E., 2002: Studies of the aerosol indirect effect from sulfate and black carbon aerosols, *J. Geophys. Res., 107* (D20), 4246, 10.1029/2001JD000887.

Lohman, U., J. Fleichter, C. C. Chuang and J. E. Penner, 2000: Indirect effect of of sulfate and carbonaceuous aerosols: A mechanistic treatment, *J. Geophys. Res., 104,* 9169-9198.

Iversen , T. and Ø. Seland (2002) A scheme for process-tagged SO_4 and BC aerosols in NCAR CCM3. Validation and sensitivity to cloud processes. *J. Geophys. Res., 107* (D24), 4751, 10.1029/2001JD000885.

Penner, J. E., Andreae, M. Annegarn, H. Barrie, L. Feichter, J., Hegg, D., Jayaraman, A., Leaicht, R., Murphy, D., Nganga, J. and Pitari, G., Aerosols, their direct and indirect effects, Chapter 5 (pp. 289-348) in: *Climate change 2001: The scientific basis.* Contribution of working group I to the Third Assessment Report of the Intergovernmental Panel on Climate Change. Cambridge University Press.

ANALYSIS OF CLIMATE CHANGE BY AEROSOL DIRECT AND INDIRECT EFFECTS WITH AEROSOL TRANSPORT-RADIATION MODEL

Toshihiko Takemura[1] and Toru Nozawa[2]

[1]Research Institute for Applied Mechanics, Kyushu University, Kasuga, Fukuoka, 816-8580, Japan
[2]National Institute for Environmental Studies, Tsukuba, Ibaraki, 305-8506, Japan

1. INTRODUCTION

A change in the aerosol loading in the atmosphere is assumed to cause climate change through the direct and indirect effects. The direct effect is that aerosol particles scatter and absorb the solar and thermal radiation. The indirect effect is that an increase in the aerosol loading causes a decrease in the cloud droplet size acting as cloud condensation nuclei, leading to an increase in the cloud albedo (first indirect effect) and an increase in the cloud lifetime (second indirect effect). The semi-direct effect is also discussed, which the atmosphere is stabilized by radiative absorption of aerosol particles such as black carbon so that cloud is suppressed. The Third Assessment Report of the Intergovernmental Panel on Climate Change (IPCC 2001) estimated that the radiative forcing due to anthropogenic aerosols is –0.5 W m^{-2} with an uncertainty of a factor of 2 for the direct effect and from 0 to –2.0 W m^{-2} without a plausible value for the first indirect effect. The second indirect effect could not be estimated because of much little confidence. These suggest that there is a larger uncertainty in the evaluation of the aerosol radiative forcing, especially of the indirect effect.

Global aerosol models are ones of the principal tools for analyzing the climate response to the aerosol direct and indirect effects. The past modeling studies for estimating the indirect effect, however, used the simple parameterization that the cloud droplet number concentration is diagnosed only from the aerosol particle number or mass concentrations because it was difficult to treat cloud microphysical processes in global models. It includes arbitrary fitting to observations, which results in one of the main reason for the uncertainty in the evaluation of the indirect effect. Then, in this study, a parameterization on the cloud-aerosol interaction considering cloud microphysical processes is introduced into a global aerosol model, which includes effects of the updraft velocity, solubility of aerosol particles, and curvature of cloud droplets. The climate change due to the aerosol direct and indirect effects is also analyzed with this parameterization.

Corresponding author's address: Toshihiko Takemura, Research Institute for Applied Mechanics, Kyushu University, 6-1 Kasuga-koen, Kasuga, Fukuoka 816-8580, Japan; E-mail: toshi@riam.kyushu-u.ac.jp

2. MODEL DESCRIPTION

The global aerosol transport-radiation model, SPRINTARS (Spectral Aerosol Radiation-Transport Model for Aerosol Species), is driven by the atmospheric general circulation model (AGCM) of Center for Climate System Research (CCSR)/University of Tokyo, National Institute for Environmental Studies (NIES), and Frontier Research System for Global Change (FRSGC) (Numaguti et al. 1995). The model simultaneously treats the main tropospheric aerosols, that is, carbonaceous (black and organic carbons), sulfate, soil dust, and sea salt, and the precursor gases of sulfate, that is, sulfur dioxide and dimethylsulfide. The aerosol transport processes include emission, advection, diffusion, sulfur chemistry, wet deposition, and gravitational settling. The radiation scheme in CCSR/NIES/FRSGC AGCM (Nakajima et al. 2000) is extended for the aerosol direct effect that is related with scattering and absorption by aerosol particles depending on the refractive index, size distribution, and hygroscopic growth of each aerosol component and for the aerosol indirect effect that is a change in the cloud albedo with a change in the aerosol particle number concentration. Global distributions of aerosol concentrations and optical parameters simulated by SPRINATRS are in reasonable agreement with ground-based, aircraft, and satellite observations (Takemura et al., 2002, 2003). The detailed description for SPRINTARS is in Takemura et al. (2000, 2002).

The parameterization for diagnosing the cloud droplet number concentration N_c is based on the Köhler theory (Ghan et al. 1997; Abdul-

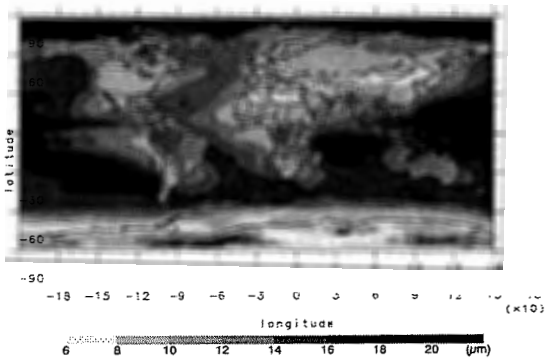

FIG. 1. Annual mean distributions of the simulated cloud droplet effective radius at cloud top above 273K.

Razzak et al. 1998):

$$N_c = \frac{N_a}{1+\left[f_1\left(\frac{AN_a\beta}{3\alpha\omega}\right)^2 + f_2\frac{2A^3N_a\beta\sqrt{G}}{27Br_m^3(\alpha\omega)^{3/2}}\right]^b}, \quad (1)$$

where N_a is the aerosol particle number concentrations, B is the solute effect, and f_1, f_2, and b depend on the aerosol size distribution, which are different among aerosol components. A is the curvature effect of cloud droplets. ω is the updraft velocity as a function of the turbulent kinetic energy. With Equation (1), the cloud droplet effective radius r_{eff} and precipitation rate P are calculated for estimating the aerosol first and second indirect effects, respectively:

$$r_{eff} = k\left(\frac{3}{4\pi\rho_w}\frac{\rho l}{N_c}\right), \quad (2)$$

$$P = -\frac{dl}{dt} = \frac{\alpha\rho l^2}{\beta + \gamma\frac{N_c}{\rho l}}, \quad (3)$$

where ρ is the air density, ρ_w is the water density, and l is the cloud water mixing ratio. These parameterizations are adapted to stratus water cloud.

SPRINTARS is coupled with the mixed layer ocean in this study. Only the calculation of the radiative forcing is carried out with the atmospheric model using the prescribed sea surface temperature and sea ice according to the definition. The horizontal resolution of the triangular truncation is set at T42 (approximately 2.8° by 2.8° in longitude and latitude) and the vertical resolution is 20 layers. The emission data of anthropogenic aerosols and precursors produced by our research group is used. The two equilibrium experiments are run for different scenarios that are present and pre-industrial aerosol emissions. Each experiment is integrated for thirty years and analyzed for last ten years. The concentrations of greenhouse gases are fixed to the 2000 level in both experiments.

3. RESULTS AND DISCUSSION

Figure 1 shows the global distribution of the cloud droplet effective radius at cloud top at the temperature above 273 K. It is good agreement quantitatively between them simulated by SPRINTARS and retrieved from satellites such as AVHRR (Kawamoto et al. 2000), which is small radii over land in contrast to large them over ocean. A change in the radius is calculated to be especially large over densely populated and biomass burning regions in comparison between the pre-industrial and present runs. The

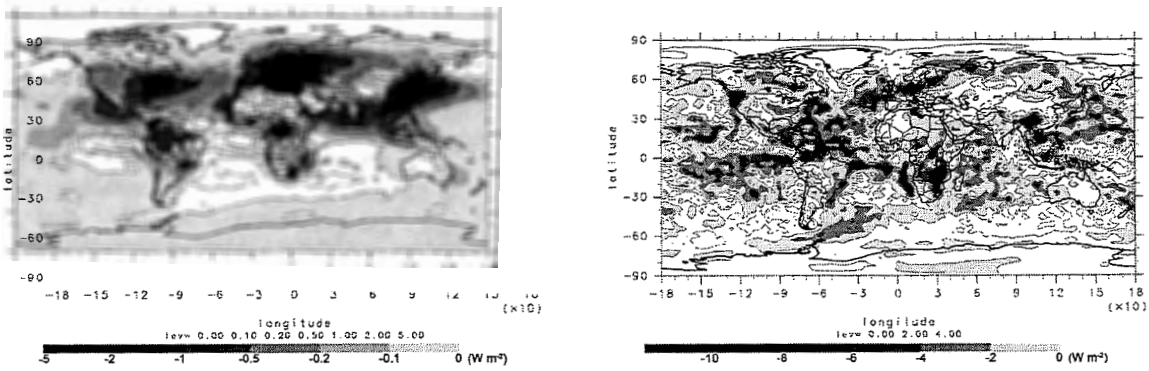

FIG. 2. Annual mean distributions of the simulated aerosol radiative forcings of the direct (left) and indirect (right) effects at the tropopause.

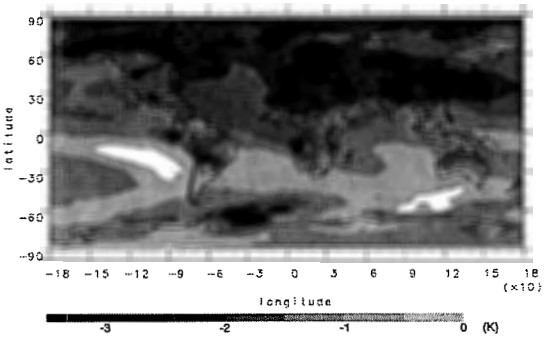

FIG. 3. Annual mean distributions of the simulated change in the surface air temperature due to anthropogenic aerosols.

simulated cloud water content and precipitation are also reasonable agreement with satellite observations, which is related with the aerosol second indirect effect (not shown).

Figure 2 shows the direct and indirect radiative forcings at the tropopause due to anthropogenic aerosols. The direct one is generally negative especially Asia, Europe, and North America. Absorption of the solar radiation by biomass burning aerosols, however, enhanced by lower cloud than aerosols, leading to the high positive forcing. The indirect one is negative over regions where anthropogenic aerosols largely increase though it is a slightly positive over remote regions from anthropogenic influences. The global mean radiative forcing is calculated to be –0.14 W m^{-2} for the direct effect and –0.78 W m^{-2} for the indirect effect.

The experiments coupled with the mixed layer ocean can simulate changes in meteorological field due to aerosols. Figure 3 shows the surface air temperature change from 1850 to 2000 by the aerosol direct and indirect effects. Its decrease is remarkable in the mid-latitudes of the Northern Hemisphere. The global mean change is –1.0 K, on the other hand, it is estimated to be +2.3 K due to anthropogenic greenhouse gases by the same model. The result indicates that it is important to consider the aerosol effects for evaluating climate change. The transient experiments with the ocean-atmosphere coupled model including the on-line SPRINTARS by the CCSR/NIES/FRSGC group also shows a reasonable agreement with observations for a change in the surface air temperature from 1850 to 2000.

ACKNOWLEDGEMENTS

We thank the contributions to the development of the CCSR/NIES/FRSGC GCM. This study is supported by the APEX project of the Core Research for Evaluational Science and Technology of the Japan Science and Technology Agency, and the Kyousei 1 and 2 projects of the Research Revolution 2002 of the Ministry of Education, Culture, Sports, Science and Technology of Japan.

REFERENCES

Abdul-Razzak, H., S. J. Ghan, and C. Rivera-Carpio, 1998: A parameterization of aerosol activation 1. Single aerosol type. *J. Geophys. Res.*, **103**, 6123–6131.

IPCC (Intergovernmental Panel on Climate Change), 2001: *Climate Change 2001: The Scientific Basis*. T. Houghton et al., Eds., 896 pp., Cambridge University Press.

Ghan, S. J., L. R. Lenug, R. C. Easter, and H. Abdul-Razzak, 1997: Prediction of cloud droplet number in a general circulation model. *J. Geophys. Res.*, **102**, 21 777–21 794.

Kawamoto, K., T. Nakajima, and T. Y. Nakajima, 2001: A global determination of cloud microphysics with AVHRR remote sensing. *J. Climate*, **14**, 2054–2068.

Nakajima, T., M. Tsukamoto, Y. Tsushima, A. Numaguti, and T. Kimura, 2000: Modeling of the radiative process in an atmospheric general circulation model. *Appl. Opt.*, **39**, 4869–4878.

Numaguti, A., M. Takahashi, T. Nakajima, and A. Sumi, 1995: Development of an atmospheric general circulation model. *Climate System Dynamics and Modeling*, T. Matsuno, Ed., Center for Climate System Reseacrh, University of Tokyo, 1–27.

Takemura, T., H. Okamoto, Y. Maruyama, A. Numaguti, A. Higurashi, and T. Nakajima, 2000: Global three-dimensional simulation of aerosol optical thickness distribution of various origins. *J. Geophys. Res.*, **105**, 17 853–17 873.

Takemura, T., T. Nakajima, O. Dubovik, B. N. Holben, and S. Kinne, 2002: Single scattering albedo and radiative forcing of various aerosol species with a global three-dimensional model. *J. Climate*, **15**, 333–352.

Takemura, T., T. Nakajima, A. Higurashi, S. Ohta, and N. Sugimoto, 2003: Aerosol distributions and radiative forcing over the Asian Pacific region simulated by Spectral Radiation-Transport Model for Aerosol Species (SPRINTARS). *J. Geophys. Res.*, **108**(D23), 8659, doi:10.1029/2002JD003210.

THE IMPACT OF AEROSOLS ON CLOUD AND PRECIPITATION PROCESSES: CLOUD-RESOLVING MODEL SIMULATIONS

Wei-Kuo Tao[1], X. Li[2], A. Khain, J. Simpson[1], D. Johnson[2] and L. Remer[1]

[1]Laboratory for Atmospheres, NASA/Goddard Space Flight Center, Greenbelt, MD, 20771, USA

[2]Goddard Earth Sciences and Technology Center, University of Maryland, Baltimore County, Baltimore, MD

[3]Department of Atmospheric Science, Hebrew University of Jerusalem, Jerusalem, Israel

1. INTRODUCTION

Cloud microphysics is inevitably affected by the smoke particle (CCN, cloud condensation nuclei) size distributions below the clouds. Therefore, size distributions parameterized as spectral-bin microphysics are needed to explicitly study the effects of atmospheric aerosol concentration on cloud development, rainfall production, and rainfall rates for convective clouds.

Recently, a detailed spectral-bin microphysical scheme was implemented into the Goddard Cumulus Ensemble (GCE) model. Atmospheric aerosols are also described using number density size-distribution functions. A spectral-bin microphysical model is very expensive from a computational point of view and has only been implemented into the 2D version of the GCE at the present time. The model is tested by studying the evolution of deep tropical clouds in the west Pacific warm pool region and summertime convection over a mid-latitude continent with different concentrations of CCN: a low "clean" concentration and a high "dirty" concentration. The impact of atmospheric aerosol concentration on cloud and precipitation will be investigated.

2. MODEL DESCRIPTION AND CASE STUDIES

2.1 GCE Model

The model used in this study is the 2D version of the GCE model. Modeled flow is anelastic. Second- or higher-order advection schemes can produce negative values in the solution. Thus, a Multi-dimensional Positive Definite Advection Transport Algorithm (MPDATA) has been implemented into the model. All scalar variables (potential temperature, water vapor, turbulent coefficient and all five hydrometeor classes) use forward time differencing and the MPDATA for advection. Dynamic variables, u, v and w, use a second-order accurate advection scheme and a leapfrog time integration (kinetic energy semi-conserving method). Short-wave (solar) and long-wave radiation as well as a subgrid-scale TKE turbulence scheme are also included in the model. Details of the model can be found in Tao and Simpson (1993) and Tao *et al.* (2003).

2.2 Microphysics (Bin Model)

The formulation of the explicit spectral-bin microphysical processes is based on solving stochastic kinetic equations for the size distribution functions of water droplets (cloud droplets and raindrops), and six types of ice particles: pristine ice crystals (columnar and plate-like), snow (dendrites and aggregates), graupel and frozen drops/hail. Each type is described by a special size distribution function containing 33 categories (bins). Atmospheric aerosols are also described using number density size-distribution functions (containing 33 bins). Droplet nucleation (activation) is derived from the analytical calculation of super-saturation, which is used to determine the sizes of aerosol particles to be activated and the corresponding sizes of nucleated droplets. Primary nucleation of each type of ice crystal takes place within certain temperature ranges. A detailed description of these explicitly parameterized processes can be found in Khain and Sednev (1996) and Khain *et al.* (1999, 2001).

2.3 Case Studies

Two cases, a tropical-oceanic squall system observed during TOGA COARE and a midlatitude-continental squall system observed during PRESTORM, will be used to examine the various partitioning methods. The June 10-11, 1985 PRESTORM case has been well studied (e.g., Johnson and Hamilton 1988; Rutledge *et al.* 1988; Tao *et al.* 1996; Lang *et al.* 2003). The PRESTORM environment was fairly unstable but relatively dry with a lifted index of -5.37 and a Convective Available Potential Energy (CAPE) of 2300 J/kg. The February 22, 1993 TOGA COARE squall line has also been well studied (Jorgensen *et al.* 1997; Trier *et al.* 1996, 1997; Wang et al. 1996). The CAPE and lifted index are moderately unstable, 1776 J/kg and -3.2, respectively.

A stretched vertical coordinate was used in the model with 31 grid points. There were 1024 horizontal grid points; the central 872 had a fixed 750 and 1000 m resolution for TOGA COARE and PRESTROM, respectively. The outer grids were stretched. Radiation was included, and a low-level cold pool was used to start the system.

3. RESULTS

3.1 Rainfall and Its Characteristics

Corresponding author's address: W.-K. Tao, Code 912, NASA GSFC, Greenbelt, MD 20771, USA; E-Mail: tao@agnes.gsfc.nasa.gov

The rainfall amounts and the their stratiform percentage for TOGA COARE and PRESTORM clean and dirty cases are shown in Table 1. For the TOGA COARE case, a dirty environment (high CCN) produced more rainfall and less stratiform rain (or light precipitation) than did the clean (low CCN) environment. The simulated convective organization is quite different between these cases even though the same thermodynamic and horizontal wind shear was used for initialization. For the high CCN case, the simulated convection is stronger and penetrates at high altitude compared to the low CCN case. Consequently more small cloud ice and large snow/graupel are produced in high CCN case. In addition, the CCN case sometime acquires multicellular characteristics (up-shear tilt and multi-updrafts). Unicellular (erect) convection is generally simulated in the low CCN case. Tao *et al.* (1995) and Ferrier *et al.* (1996) found that less rainfall was simulated in unicellular convection compared to the multicellular.

On the other hand, the PRESTORM case showed a slight decrease in rainfall in the dirty environment. Both environments led to multicellular structures as observed. Both cases showed a bright band in the stratiform region as observed. The CAPE and horizontal wind shear are much larger in PRESTORM than in TOGA COARE. The aerosol concentration does not have a major impact on the organization and precipitation for the PRESTORM case. In addition, ice processes are more important in the PRESTORM case than the TOGA COARE case. Rainfall originates mainly through the melting of large ice species in the PRESTORM environment (Tao *et al.* 1995).

	TOGA Clean	TOGA Dirty	Prestorm Clean	Pretorm Dirty
Rain rate Mm/day	17.1	23.0	32.8	31.9
Stratiform %	59	30	28	46

Table 1 Domain-averaged surface rainfall amounts and stratiform percentage for both the TOGA COARE and PRESTORM cases after 12 h of integration.

These model results indicate that high CCN (pollution) case does not suppress precipitation for convective systems in either tropical oceanic (less unstable and moist) or mid-latitude continental (unstable, dry) environments. These results are not in agreement with recent observations indicating that biomass burning could suppress cloud and rainfall processes. However, the model results did show that low CCN concentrations produce rainfall at the surface sooner with less cloud water mass aloft. Also the total rainfall is reduced for high CCN during the first 60-90 minutes of model integration.

3.2 Cloud Drop Size Distribution

Because the spectral-bin model explicitly calculates and allows for examination of both the mass and concentration of species for each size category, a detailed analysis of the instantaneous size spectrum can be obtained for the two cases. Since the low CCN case produces fewer droplets, larger sizes develop due to greater condensational and collection growth, leading to a broader size spectrum in comparison to the high CCN case. This result is consistent with a finding based on TRMM satellite data (Rosenfeld, 2000).

4. References

Ferrier, B.S., S. Simpson, and W.-K. Tao, 1996: Factors responsible for different precipitation efficiencies between midlatitude and tropical squall simulations. Mon. Wea. Rev., 124, 2100-2125.

Johnson, R.H., and P.J. Hamilton, 1988: The relationship of surface pressure features to the precipitation and airflow structure of an intense midlatitude squall line. Mon. Wea. Rev., 116, 1444-1472.

Jorgensen, D.P., M.A. LeMone, and S.B. Trier, 1997: Structure and evolution of the 22 February 1993 TOGA-COARE squall line: Observations of precipitation, circulation, and surface energy fluxes. J. Atmos. Sci., 54, 1961-1985.

Khain, A. P., and I. Sednev, 1996: Simulation of precipitation formation in the Eastern Mediterranean coastal zone using a spectral microphysics cloud ensemble model. *Atmos. Res.*, 43, 77-110.

Khain, A. P., A. Pokrovsky, and I. Sednev, 1999: Some effects of cloud-aerosol interaction on cloud microphysics structure and precipitation formation: Numerical experiments with a spectral microphysics cloud ensemble model. *Atmos. Res.*, 52, 195-220.

Khain, A. P., M. Ovtchinnikov, M. Pinsky, A. Pokrovsky, and H. Krugliak, 2000: Notes on the state-of-the-art numerical modeling of cloud microphysics. *Atmosph. Res.*, 55, 159-224.

Lang, S., W.-K. Tao, J. Simpson, and B. Ferrier, 2003: Modeling of convective-stratiform precipitation processes: Sensitivity to partitioning methods. J. Appl. Meteor., 42, 505-527.

Rosenfeld, D., 2000: Suppression of rain and snow by urban and industrial air pollution. *Science*,287,1793-1796.

Rutledge, S.A., R.A. Houze Jr., M.I. Biggerstaff, and T. Matejka, 1988: The Oklahoma-Kansas mesoscale convective system of 10-11 June 1985: Precipitation structure and single-doppler radar analysis. Mon. Wea. Rev., 116, 1409-1430.

Tao, W.-K., and J. Simpson, 1993: The Goddard Cumulus Ensemble Model. Part I: Model description. *Terrestrial, Atmospheric and Oceanic Sciences*, 4, 35-72.

Tao, W.-K., J. Scala, and J. Simpson, 1995: The effects of melting processes on the development of a tropical and a mid-latitudes squall line. *J. Atmos. Sci.*, 52, 1934-1948.

Tao, W.-K., S. Lang, J. Simpson, C.-H. Sui, B. Ferrier, and M.-D. Chou, 1996: Mechanisms of cloud-radiation interaction in the tropics and midlatitudes. J. Atmos. Sci., 53, 2624-2651.

Tao, W.-K., J. Simpson, D. Baker, S. Braun, D. Johnson, B. Ferrier, A. Khain, S. Lang, C.-L. Shie, D. Starr, C.-H. Sui, Y. Wang and P. Wetzel, 2003: Microphysics, Radiation and Surface Processes in a Non-hydrostatic Model, *Meteorology and Atmospheric Physics*, 82, 97-137

Trier, S.B., W.C. Skamarock, M.A. LeMone, D.B. Parsons, and D.P. Jorgensen, 1996: Structure and evolution of the 22 February 1993 TOGA-COARE squall line: numerical simulations. J. Atmos. Sci., 53, 2861-2886.

Wang, Y., W.-K. Tao, and J. Simpson, 1996: The impact of a surface layer on a TOGA COARE cloud system development. Mon. Wea. Rev., 124, 2753-2763.

5. Acknowledgements

This work is mainly supported by the NASA headquarters' Atmospheric Program and NASA TRMM Mission. The authors are grateful to Dr. R. Kakar at NASA headquarters for his support of this research. Acknowledgement is also made to the NASA/GSFC for computer time used in this research.

SCAVENGING OF CONDENSATION NUCLEI IN CLOUDS: DEPENDENCE OF SIGN OF ELECTROSCAVENGING EFFECT ON DROPLET AND CCN SIZES

Brian A. Tinsley

University of Texas at Dallas, Richardson, Texas, 75083-0688, USA

1. INTRODUCTION

The effect of electric charge on the collection efficiencies for scavenging of aerosol particles by droplets was extensively modeled in the 1970s and 1980s by Pruppacher and his group. The interpretation of this work was that only in well developed thunderstorms would the amount of charge on the droplets and the particles they were scavenging be great enough to affect cloud microphysical processes. In recent years it has been realized that even in weakly electrified clouds such as marine stratocumulus the amount of electrical charge is sufficient to affect contact ice nucleation and CCN concentrations (Tinsley et al., 2001). Here we consider the dependency of the sign of the electroscavenging effect on the sizes of the droplet and CCN, and the implications for cloud processing of aerosol particles.

2. CLOUD CHARGING

Measurement of droplet charge in non-thunderstorm clouds have shown charges of ~ 100e ($e = 1.6\times10^{-19}$C) (Pruppacher and Klett, 1997, sec. 18.4; MacGorman and Rust, 1998, ch.2, Bead et al. 2004). The source of this charge, especially for ice-free clouds of relatively large horizontal extent, appears to be the ionosphere-earth current density (J_z) which is the return current in the global electric circuit (Bering et al 1998). The conductivity (σ) is about an order of magnitude lower in clouds than in clear air at the same altitude (Pruppacher and Klett, 1997), and the flux of J_z through the conductivity gradients at cloud boundaries generates positive space charge at cloud tops and negative space charge at cloud bases. The electric field $E = Jz/\sigma$ and the vertical gradient in conductivity is $dE/dz = J_z d/dz(1/\sigma)$. The space charge ($\rho$) is given by Poisson's equation $\nabla\cdot E = \rho/\varepsilon_o$ so that $\rho = \varepsilon_o J_z d/dz(1/\sigma)$.

Aerosol particles and cloud droplets collect this space charge. A process that can produce the more highly charged aerosol particles is the evaporation of some of the charged droplets, e.g., with mixing at cloud boundaries.

Corresponding author's address: Brian A. Tinsley, MSFO22, UT Dallas, Box 830688, Richardson, TX 75083-0688, USA, E-mail: Tinsley@UTDallas.edu

The evaporation residues retain the droplet charge, which decays on a time-scale of tens of minutes down to a lower charge, determined by the amount of space charge present and the particle radius (Tinsley et al. 2000). Aerosol particles are independently charged to this level by the attachment of air ions directly from the space charge, as will be discussed later.

3. ELECTROSCAVENGING

The effect on collision efficiencies of the charges on the aerosol particles and on the droplets has most recently been modeled by Tinsley et al. (2000, 2001). The scavenging for same-sign charges (q) on particles as charges (Q) on droplets will be the normal situation when space charge is present. For particle radii small compared to droplet radii the electrical force F is given by $F = C[(Kr + 1)/r^3 - r/(r^2 - 1)^2]$ where $K = Q/q$ and $C = q^2/(4\pi\varepsilon_o A^2)$ where A is the droplet radius and a is the particle radius and $r = a/A$ (Tinsley et al., 2000). For Q and q of the same sign the first term on the RHS is a long range repulsion while the second term is the short range attraction due to the image force that is independent of the sign of Q/q and increases rapidly as the particle approaches the droplet surface and r tends to 1.

The numerical integration of trajectories shows that for droplets of radii about 10 μm and greater the long range repulsion is unable to prevents the particles with radii greater than about 0.1 μm being carried, by the flow around the falling droplet, close enough to the droplet surface so that the short range attraction ensures collection. For the smaller particles with higher mobility, with the smaller droplets with smaller fall speeds, the long range repulsion keeps the particle out of range of the image force and can reduce the collection efficiency well below that would otherwise be due to collection by phoretic processes and Brownian diffusion.

Figure 1 is a plot of collection efficiencies for droplets of 1.5, 3, 6 and 12 μm radii respectively, with charge Q of 50e, interacting with charged aerosol particles with charges q of 0, 1, 2, 5, and 10e, with the curves labeled by the particle charge. The upper four panels are for Q and q of the same sign, and the lower panels are for them of opposite sign. There is little effect of particle density for radii below 0.5 μm; the upper panels are for 1000 kg/m^3 and the lower panels are for 2000 kg/m^3 as can be seen in the curves for 0e.

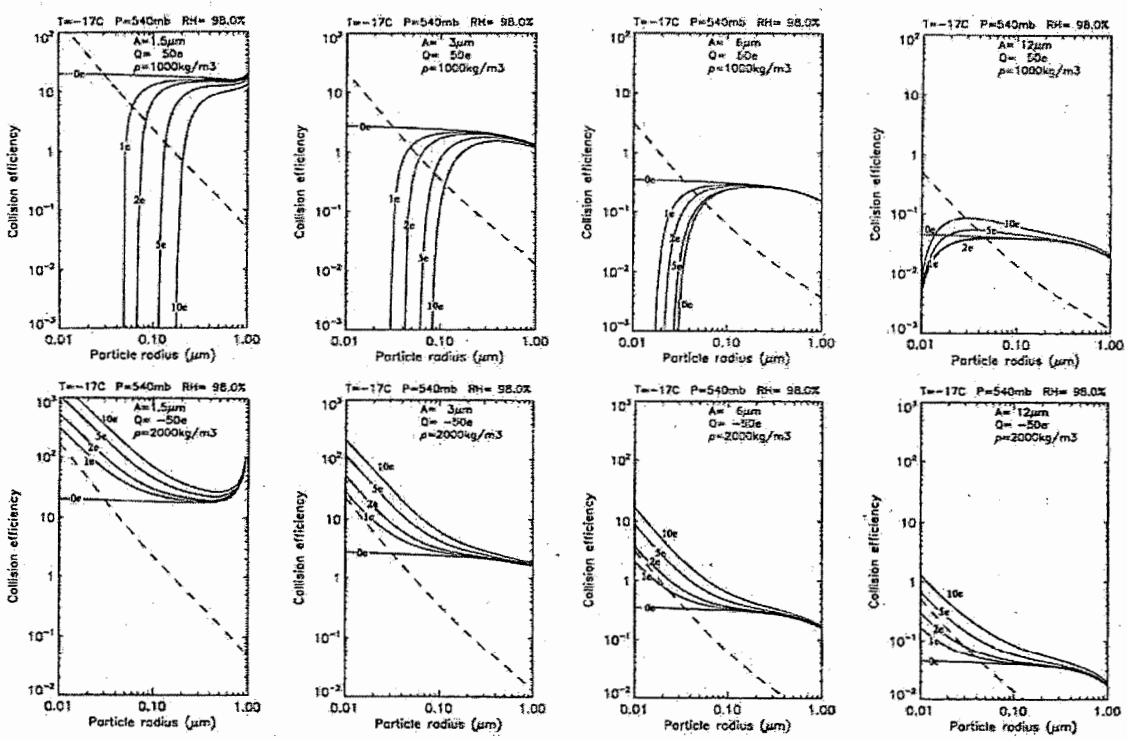

Figure 1. Variation of collision efficiency as a function of particle radius for four different droplet radii A. The top four panels are for droplet charge Q and for particle charge q of like sign; the bottom four panels are for Q and q of opposite sign. The curves are labeled by particle charge q. The atmospheric pressure, temperature, and relative humidity are 540 hPa, -17° C and 98% respectively. The curves for 0e show the effect of phoretic forces alone. The collection efficiencies for Brownian diffusion are calculated separately and are shown as dashed curves.

The calculated collision efficiencies are a combination of phoretic scavenging and electroscavenging. The collection efficiency due to Brownian diffusion is calculated separately (Pruppacher and Klett, 1997). The droplet charge of 50e is consistent with the measurements of Beard et al. (2004).

4. APPLICATIONS TO CLOUDS

In order to determine the magnitude of the electrical enhancement or reduction of the scavenging of CCN, to produce the indirect aerosol effect, or of scavenging of aerosol particles in general, relevant to cloud processing of aerosol and gases, it is necessary to determine the distribution of charge q on the aerosol particles. There is little observational or theoretical information available. For monodispersive aerosol of radius a the equilibrium charge distribution is given by Harrison and Carslaw (2003) as:

$N_j/N_o = (x)^j \sinh(\lambda j)(\exp(-\lambda j^2))/(\lambda j)$, where N_j is the concentration of particles with j elementary charges, and; N_o the concentration of uncharged particles; $\lambda = e^2/(8\pi\varepsilon_o kTa)$ where T is the absolute temperature. The charge distribution is related to the space charge ρ by the parameter x. For a concentration n^+ of positive ions and n^- of negative ions the space charge $\rho = (n^+ - n^-)e$, and it corresponds to a positive conductivity $n^+\mu^+$ and a negative conductivity $n^-\mu^-$, where μ^+ and μ^- are the mobilities of the positive and negative ions. Then $x = (n^+\mu^+)/(n^-\mu^-)$.

This equation implies that for a plausible negative space charge accumulation at cloud base, say giving x=0.3, and temperatures corresponding to the middle troposphere (256K) about 70% of the particles of radius 0.05 μm are negatively charged with a mean charge of about –1e. For a = 0.1μm the percentage is ~80% with mean charge about -2e; for a = 0.2 μm it is ~97% with mean charge about –4e, and for a = 0.5μm it is ~99.9% with mean charge about –9e.

The actual atmospheric aerosol size distributions are far from monodispersive. The results from Pueschel et al. (1994) for maritime air far from land show concentrations of particles falling steeply with increasing radius, e.g. with more than three orders of magnitude concentration decrease for radii increasing from 0.05μm to 0.5μm. The effect of this on the charge distributions has not been evaluated, but if they remain similar to monodispersive distributions then a high percentage of the particles would remain

negatively charged.

The effect of aerosol charge, and therefore space charge, on the scavenging of aerosol particles also depends on the droplet size distribution in the cloud. For the base of the marine stratus cloud in Figure 2-13 of Pruppacher and Klett (1997) the mean droplet radius in the distribution is near 4 μm, increasing to about 10μm at the top of the cloud. With reference to Figure 1here, and in view of the preponderence of aerosol particles with radii less than 0.1μm, one might expect that at cloud base the effect of space charge, for x = 0.3, would be a reduction in the phoretic and Brownian scavenging rates by a non-negligible amount.

4. COMPLEXITIES TO BE CONSIDERED

The electrically induced processes in clouds are likely to be even more complex than the above description would imply, as there are strong time dependencies present. The charging time to produce the space charge is of order 10 minutes, with the production beginning with the initial stages of cloud formation as updrafrs produce cooling and increased relative humidity. The formation of droplets from activated CCN lowers the conductivity due to attachment of air ions, and the increasing conductivity gradient begins to generate space charge. The reduction of conductivity in fog and pre-fog conditions has been reviewed by Dolezalek (1963).

The formation of charged droplets quickly scavenges the charged aerosols (and ions) of opposite sign (as illustrated in the lower row of panels of Figure 1) so that there is a positive feedback on the developing conductivity asymmetry. Whether the rate at which this occurs is fast enough to prevent equilibrium charge distributions from forming is not yet determined.

Overall, it seems possible that there are significant effects on aerosol and CCN concentrations from electroscavenging of aerosol particles at cloud bases, whether charged directly by space charge or as charged residues from evaporated droplets when mixing is present. For the aerosol particles of CCN size it seems that the net effect would be an increase in CCN concentration with increasing space charge, as particles are preserved from being lost by other scavenging processes. This could lead to macroscopic cloud and precipitation changes by the indirect aerosol effect. However, much cloud modeling work is needed to test this possibility.

5. SCAVENGING OF ICE FORMING NUCLEI

With larger aerosol particles, with radii in the range 0.1 μm to 1 μm, the relatively large charge on them and their lower mobility can result in an increase rather than a decrease in scavenging rates, relative to phoretic and Brownian rates, especially where the mean droplet radius is ~ 10 μm and greater. For cloud tops where the temperature is below freezing the scavenging of ice-forming nuclei can occur. Larger aerosol particles are more likely to be effective IFN than smaller ones, on account of the greater surface area for ice nucleation sites, and larger droplets are more likely to be present near cloud tops. For these conditions it seems likely that the rate of electroscavenging leading to contact ice nucleation will increase with increasing space charge (see Tinsley et al 2001).

Acknowledgements

This work has been supported by NSF grants ATM-0308523 and ATM-0240827

References

Beard, K. V., H. T. Ochs, J. S. Naul and C. H. Twohy, 2004: Aircraft measurements of high average charges on cloud drops in stratiform clouds, unpublished manuscript, 7 pp.

Bering, III, E. A., A. A. Few, J. R. Benbrook, 1998: The global electric circuit, Physics Today, 51, 24-30.

Dolezalek, H., 1963: The atmospheric electric fog effect, Rev. Geophys., 1, 231-282.

Harrison, R. G., and K. S. Carslaw, 2003: Ion-aerosol-cloud processes in the lower atmosphere, Rev. Geophys, 41(3), 2-1 – 2-26.

MacGorman, D. R., and W. D. Rust, 1998: The Electrical Nature of Storms, Oxford Univ. Press, Oxford.

Pruppacher, H. R., and J. D. Klett, 1997: Microphysics of Clouds and Precipitation, 2nd. Rev. edn., Kluwer Academic Publishing, Dordrecht.

Pueschel, R. F., J. M. Livingston, G. F. Ferry and T. E. DeFelice,1994: Aerosol abundances and optical characteristics in the Pacific Basin free troposphere, Atmos. Env., 28(5), 951-960.

Tinsley, B. A., R. P. Rohrbaugh, M. Hei and K. V. Beard, 2000: Effects of image charges on the scavenging of aerosol particles by cloud droplets and on droplet charging and possible ice nucleation processes, J. Atmos. Sci., 57, 2118-2134.

Tinsley, B. A., R. P. Rohrbaugh and M. Hei, 2001: Electroscavenging in clouds with broad droplet size distributions and weak electrification, Atmos. Res., 59-60, 115-135

MODELLING THE HYGROSCOPIC PROPERTIES OF AEROSOLS

David Topping[1], Gordon McFiggans, Hugh Coe, Michael Cubison

Department of Physics, University of Manchester Institute of Science and Technology (UMIST), PO Box 88, Manchester, M60 1QD, United Kingdom.

1. INTRODUCTION

The ability to predict the water content associated with aerosol particles is an important factor in reducing the uncertainties associated with climate change. However there are varying levels of complexity with which one calculates the water content associated with the aerosol, and of course, the presence of organic species complicates matters greatly. It is the purpose of this study to present results from a newly developed thermodynamic equilibrium model that treats mixed inorganic/organic systems. Such results are then compared with hygroscopic growth measurements derived from a HTDMA instrument and similar measurements from mixed inorganic/organic systems. In this respect, building on previous studies, it will be able to assess our ability to model these atmospherically important systems.

2. METHODS

The level of complexity with which one models the hygroscopic properties of aerosols is largely determined by the way in which the nature of the solute/solute and solute/solvent interactions are treated in solution. The ability to deal with such interactions is of vital importance. Indeed, the predicted water content associated with an aerosol particle is extremely sensitive to the accuracy of the many techniques available. In light of this, a framework has been developed which allows many options to be explored and the ability to incorporate the most accurate techniques available.

2.1 MODELLING FRAMEWORK

A thermodynamic model centred on a direct minimisation of the Gibbs free energy has been developed. The Gibbs energy minimum is found using an algorithm based on sequential quadratic programming and adjusted energies of formation, similar to those used by Ansari and Pandis (1999). The model employs the numerical algorithm FFSQP (Fast Fortran Sequential Quadratic Programming) (Zhou et al 1997). The way in which one calculates the water content however is dictated by the method chosen for treating non-ideality in solution.

2.2 INORGANIC FRACTION

Calculating activity coefficients of solution components using empirical mixing rules often result in the use of similar mixing rules to calculate the aerosol water content, with the disadvantage that interactions between solution components are not treated directly. Semi-empirical models provide a more fundamental approach to dealing with non-ideality by treating interactions explicitly. In this respect the module employs the activity model of Clegg et al (1992a,b), which circumvents some of the concentration limitations of the molality based Pitzer model (Pitzer 1986). This more accurate way of calculating the water content associated with the inorganic fraction provides a robust framework on which to deal with the more complex organic fraction. For example, although accurate and widely used, the ZSR mixing rule does not have to be employed whilst treating the inorganic fraction. This allows the effect of multiple solutes on individual water absorption characteristics to be treated explicitly in the model.

2.3 ORGANIC FRACTION

To calculate activity coefficients in multi-component organic systems the UNIFAC model is employed (Fredenslund et al 1975). Group contribution methods such as UNIFAC allow one to treat a wide range of organic species where data would be otherwise lacking. Despite problems associated with various species of atmospheric importance, revised parameters are now available which improve activity coefficient predictions significantly (e.g. Saxena and Hildemann 1997). This will also allow an analysis of how well UNIFAC can deal with organic aerosols following previous studies.

2.2 TREATING MIXED ORGANIC/INORGANIC SYSTEMS

It is widely recognised that organic species play an important role in determining the hygroscopic properties of aerosols. The crux of the problem lies in how one treats the interactions taking place between the organic and inorganic components in solution. The framework described above was designed specifically to calculate the water content in mixed inorganic/organic systems. In light of this, a separate activity model is used to deal with the non-ideality of the organic fraction. In this manner, the contributions from both the inorganic and organic fraction are assumed to be independent of each other. Using this method, the inorganic and organic fractions contribute to the total water content using an approach analogous to the ZSR relationship, whilst the separate contributions are dealt with on a more complex level. Despite this, an additional feature of the framework described above allows one to deal with inorganic/organic interactions using the techniques such as that proposed by Clegg et al (2001) when important interaction parameters become available.

3 HYGROSCOPIC SPECTRUM

Finally, one must deal with the effect of particle size on the equilibrium water content of aerosols through treatment of the Kelvin effect. This physical characteristics is that which separates aerosol science from more basic equilibrium problems. In addition, it is very significant in determining the hygroscopic properties of aerosols in both the sub and super-saturated humid environments. In the sub-saturated environment, the equilibrium model described above is housed within an iterative scheme that finds the solution pertaining to the new definition of equilibrium given by the simple Kohler equation. In this manner, various surface tension models and density mixing rules can be used and analysed. One can then compare model results with measurements derived from the HTDMA instrument (e.g. figure 1). It is also possible to expand the model to treat the hygroscopic properties in the super-saturated humid environment. The numerical treatment however is somewhat different, given the sensitivities of equilibrium at high relative humidity, whilst the new definition of equilibrium given by the simple Kohler equation is still used.

4. CONCLUSIONS

A thermodynamic equilibrium model has been developed in order to calculate the water content associated with mixed inorganic/organic atmospheric aerosols. Comparisons with the simple ZSR rule indicate that for mixed inorganic species of atmospheric importance, the more complex model can reproduce measured water uptake behaviour better up to higher solution molalities. Building on this, the model can be expanded to include organic species by using a separate activity model that treats non-ideality in mixed organic systems (UNIFAC). After treating the Kelvin effect, model predictions can then be compared with hygroscopic growth measurements derived from a HTDMA instrument for both inorganic and organic systems.

REFERENCES

Ansari A.S., Pandis S.N., Prediction of multicomponent inorganic atmospheric aerosol behaviour. Atmos Env 33 (1999) 745-757.

Clegg S.L.,Pitzer S.P. Thermodynamics of multicomponent, miscible, ionic solutions: Generalised Equations for symmetrical electrolytes. J. Phys. Chem. (1992a), 96, 3513-3520.

Clegg S.L.,Pitzer S.P. and Brimblecombe P. Thermodynamics of multicomponent, miscible, ionic solutions. 2. Mixtures including unsymmetrical electrolytes. J. Phys Chem. (1992b), 96, 9470-9479.

Clegg S.L., Seinfeld J. H., and Brimblecombe P. (2001). Thermodynamic modelling of aqueous aerosols containing electrolytes and dissolved organic compounds. Aerosol Science 32 , 713 – 738.

Pitzer K.S., Simonson J.M., Thermodynamics of multicomponent, miscible, ionic systems: Theory and Equations. (1986). J. Phys. Chem. 1986, 90, 3005-3009.

Fredenslund A., Jones R.L. and Prausnitz J. M., Group-Contribution Estimation of Activity Coefficients in Nonideal Liquid Mixtures. (1975) AIChe Journal (Vol 21, 6).

Zhou, J.L., Tits A.L.,and Lawrence C.T., (1997) *User's Guide for FFSQP Version 3.7 : A Fortran Code for Solving Optimization Programs, Possibly Minimax, with General Inequality Constraints and Linear Equality Constraints, Generating Feasible Iterates*, Institute for Systems Research, University of Maryland,Technical Report SRC-TR-92-107r5, College Park, MD 20742.

THE IMPACTS OF SAHARAN DUST ON FLORIDA CONVECTION

Susan C. van den Heever and William R. Cotton

Department of Atmospheric Science, Colorado State University, Fort Collins, CO 80523, USA

1. INTRODUCTION

Unusually high aerosol concentrations were observed on 28 and 29 July during the CRYSTAL-FACE (Cirrus Regional Study of Tropical Anvils and Cirrus Layers – Florida Area Cirrus Experiment) field program conducted by the National Aeronautics and Space Administration (NASA) over the Florida peninsula during July 2002 (Jensen et al., 2004). These have been attributed to the penetration of Saharan dust over the peninsula during this time (DeMott et al., 2003; Sassen et al., 2003). The presence of dust can have significant effects on the nucleation of ice and liquid water, which in turn may affect other microphysical, dynamical and optical properties of convective storm systems. The goal of the research presented here is thus to investigate the impacts that increasing the concentrations of ice forming nuclei (IFN), cloud condensation nuclei (CCN) and giant CCN (GCCN) may have on the characteristics of the convective and anvil stages of Florida convection, through the use of a cloud-resolving numerical model.

2. METHODS

2.1 Model Description

The Regional Atmospheric Modeling System developed at Colorado State University (RAMS@CSU) was chosen to achieve the goal stated above (Pielke et al., 1992; Cotton et al., 2003). Four nested grids were employed, the horizontal grid spacings of which were 40, 10, 2 and 0.5 km for grids 1 to 4, respectively. The location of these grids is shown in Figure 1. The fourth grid was moved in order to follow the developing anvils. A stretched 36-level grid was used in the vertical. RAMS was initialized at 12Z with 40km ETA data, and the simulations were performed for 12 hours. All the microphysical species (cloud water, rain, pristine ice, snow, aggregates, graupel and hail) in RAMS were activated, and both hydrometeor mixing ratios and number concentrations were predicted through the use of the two-moment bulk microphysics scheme (Meyers et al., 1997). CCN, GCCN and IFN concentrations are all considered prognostic variables in RAMS (Saleeby and Cotton, 2004).

Corresponding author's address: Susan C. van den Heever, Department of Atmospheric Science, Colorado State University, Fort Collins, Colorado, USA. Email: sue@atmos.colostate.edu

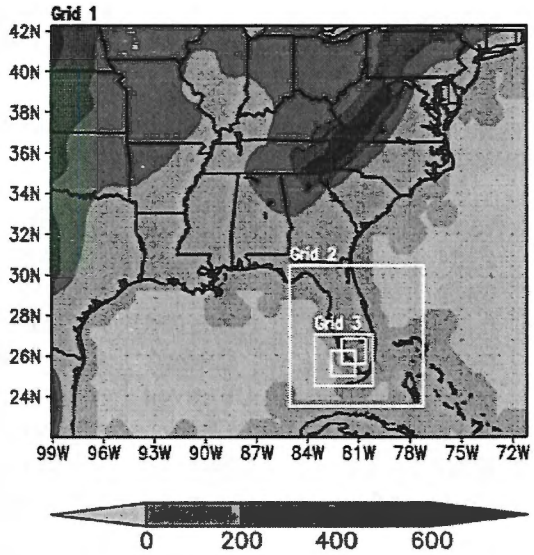

Figure 1: The topography (m) and location of grids 1 through 4 used in the simulations described in the text. Both locations of grid 4 are shown.

2.2 Experiment Design

Generalized vertical profiles of CCN, GCCN and IFN concentrations were obtained for 28 July (OBS), as well as for several "clean" days (CLN)

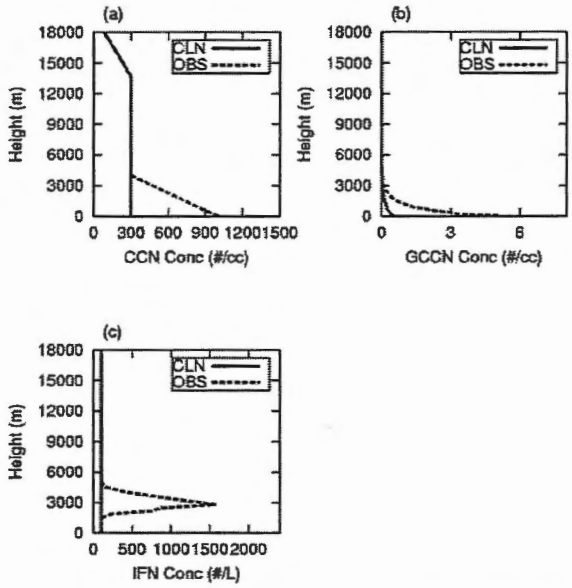

Figure 2: Generalized clean (CLN) and observed (OBS) vertical profiles of (a) CCN, (b) GCCN and (c) IFN concentrations used in the sensitivity tests described in the text.

Table 1: Aerosol characteristics of the conducted sensitivity tests

Name	CCN	GCCN	IFN
CLN	Clean	Clean	Clean
Exp2	Observed	Clean	Clean
Exp3	Clean	Observed	Clean
Exp4	Clean	Clean	Observed
Exp5	Observed	Observed	Clean
Exp6	Observed	Clean	Observed
Exp7	Clean	Observed	Observed
OBS	Observed	Observed	Observed

during July 2002 (Figure 2). These profiles, which were based on measurements made by Paul DeMott of the Colorado State University Simulation Laboratory during the CRYSTAL-FACE field campaign, were used to initialize the aerosol fields of the model. Eight different sensitivity tests were then performed in which the initial aerosol concentrations were varied independently and simultaneously (Table 1). A factor separation analysis (Stein and Alpert, 1993) was also conducted to determine which aerosol species has the predominant effect on various cloud properties and the surface precipitation.

3. RESULTS

The development and southwestward progression of the convective cores and their associated anvils are evident in the vertically integrated condensate fields (Figure 3). The simulated convection in the OBS case is a good representation of the actual storm systems that developed on 28 July (not shown), although the modeled systems move offshore slightly faster than the observed systems did. The anvil in the CLN case covers a greater area than in the OBS case, but is not as well-organized as in the latter simulation.

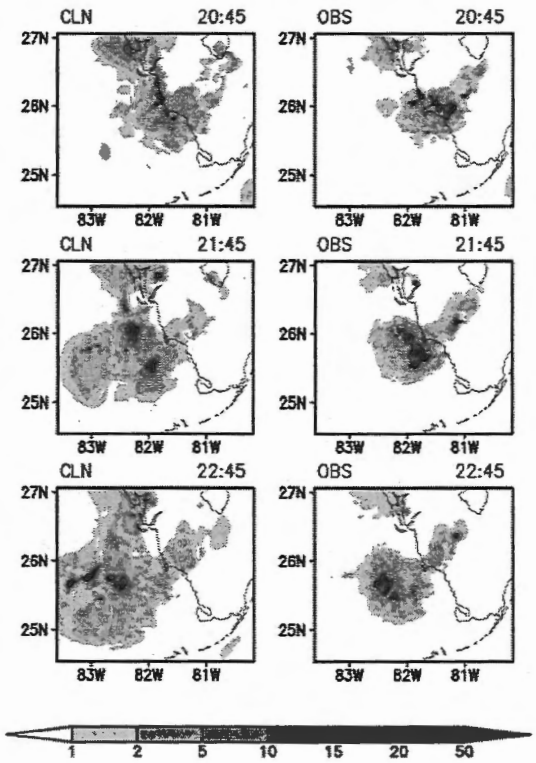

Figure 3: Vertically integrated condensate (mm) for the CLN (left column) and OBS (right column) sensitivity tests. The indicated times are UTC.

Vertical profiles were taken through the maxima of the vertically averaged (averaged between ~9 and 14 km for the ice variables, and from the surface to ~6 km for all the other variables) mixing ratios and vertical velocity at 15 minute intervals for the entire simulation. The results from 20:45 UTC are shown here, and are representative of the trends that occurred throughout the entire simulation (Figure 4). It is apparent from these vertical profiles that the updrafts are consistently and significantly stronger in the OBS case compared with those in the CLN case. The anvils associated with the stronger updrafts in the OBS case are deeper and contain more ice mass than in the CLN case. The graupel and hail mixing ratios at mid-levels are greater in the OBS simulation, although little, if any of these species reaches the ground in either case. Increasing the aerosol concentrations also increases the amount of cloud water and rain that is produced.

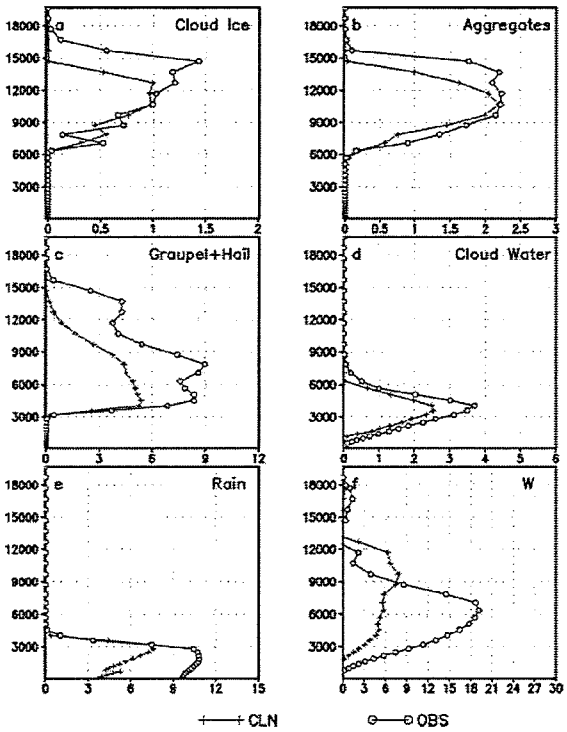

Figure 4: Vertical profiles of (a) cloud ice, (b) aggregates, (c) graupel+hail, (d) cloud water and (e) rain mixing ratios ($g.kg^{-1}$), and (f) vertical velocity ($m.s^{-1}$) for the CLN (+) and the OBS (o) cases at 20:45 UTC. The ordinate is height (m).

The 12-hour accumulated volumetric precipitation at the surface (acre-feet) is shown in Table 2 for each sensitivity test. It is apparent from these totals that more precipitation is produced in the OBS case compared with the CLN case, although the surface precipitation maximum (mm) is greater in the CLN case (not shown). It is interesting to note that the greatest volumetric precipitation is produced in Exp3, the sensitivity test in which only the observed GCCN concentrations were employed. The factor separation analysis performed on the volumetric precipitation demonstrates that GCCN have a significantly greater effect on the total surface precipitation (+48 acre-feet), compared with CCN (+1 acre-feet) and IFN (-1 acre-feet), the latter of which actually reduces the precipitation, although weakly so. The factor analysis also indicates that the contributions solely due to the interactions between CCN and IFN (-5 acre-feet), between GCCN and IFN (-15 acre-feet) and between CCN and GCCN (-76 acre-feet) are negative, and thus reduce the total surface precipitation.

Table 2: The 12-hour accumulated volumetric precipitation (acre-feet) for each sensitivity test

RANK	RUN	Volumetric Precipitation (acre-feet)
1	Exp3	925
2	OBS	923
3	Exp7	908
4	Exp2	878
5	CLN	877
6	Exp4	876
7	Exp6	871
8	Exp5	848

4. CONCLUSIONS

Increasing the concentrations of CCN, GCCN and IFN in cloud-resolving simulations have been found to increase the maximum updraft speeds, the depth, organization and longevity of the anvil,

and the mixing ratios of both liquid water and ice hydrometeor species. The 12-hour accumulated volumetric precipitation also increases with increasing aerosol concentrations, although the surface precipitation maximum is greater in the clean air case. A factor separation analysis indicates that GCCN have the greatest effect on the volumetric precipitation, whereas increases in CCN have only a weak positive influence, and increases in IFN concentrations tend to decrease the volumetric precipitation, albeit weakly. Finally, the contributions to the volumetric precipitation solely due to the interactions between CCN and IFN, CCN and GCCN, and GCCN and IFN are negative.

5. ACKNOWLEDGEMENTS

Paul DeMott and Anthony Prenni of the Colorado State University Simulation Laboratory are acknowledged for providing us with the clean and observed aerosol profiles from the CRYSTAL-FACE field campaign. This research was funded by NASA under contract NAG5-11507.

6. REFERENCES

Cotton, W.R., R.A. Pielke Sr., R.L. Walko, G.E. Liston, C.J. Tremback, H. Jiang, R.L. McAnelly, J.Y. Harrington, M.E. Nicholls, G.G. Carrio, and J.P. McFadden, 2003: RAMS 2001: Current status and future directions. *Meteor.. Atmos. Phys.*, **82**, 5-29.

DeMott, P.J., K. Sassen, M.R. Poellet, D. Baumgardner, D.C. Rogers, S. Brooks, A.J. Prenni, and S. M. Kreidenweis, 2003: African dust aerosols as atmospheric ice nuclei. *Geophys. Res. Lett.*, 30, 10.1029/2003GL017410.

Jensen, E., D. Starr, and O.B. Toon, 2004: Mission investigates tropical cirrus clouds. EOS, 85, 45-50.

Meyers, M.P., R.L. Walko, J.Y. Harrington, and W.R. Cotton., 1997: New RAMS cloud microphysics parameterization. Part II: The two-moment scheme. *Atmos. Res.*, **45**, 3-39.

Pielke, R.A., W.R. Cotton, R.L. Walko, C.J. Tremback, W.A. Lyons, L.D. Grasso, M.E. Nicholls, M.D. Moran, D.A. Wesley, T.J. Lee, and J.H. Copeland, 1992: A comprehensive meteorological modeling system – RAMS. *Meteor. Atmos. Phys.*, **49**, 69-91.

Sassen, K., P.J. DeMott, J.M. Prospero, and M.R. Poellet, 2003: Saharan dust storms and indirect aerosol affects on clouds: CRYSTAL-FACE Results. *Geophys. Res. Lett.*, 30, doi:10.1029/2003GL017371.

Saleeby, S.M., and W.R. Cotton, 2004: A large-droplet mode and prognostic number concentration of cloud droplets in the Colorado State University Regional Atmospheric Modeling System (RAMS). Part I: Module descriptions and supercell test simulations. *J. Appl. Meteor.*, 43, 182-195.

Stein, U., and P. Alpert, 1993: Factor separation in numerical simulations. *J. Atm. Sci.*, 50, 2107-2115.

study Venian
could perform
for hurricanes

THE LEIPZIG AEROSOL CLOUD INTERACTION SIMULATOR: DESCRIPTION AND FIRST RESULTS

Heike Wex, Frank Stratmann, Alexei Kiselev, and Jost Heintzenberg

Institute for Tropospheric Research, Leipzig, Germany

1. INTRODUCTION

The effect of atmospheric aerosol particles on the formation of clouds is still not completely understood. Thus the influence of the anthropogenic change of the atmospheric aerosol on properties of clouds such as cloud optical properties, lifetime and precipitation behavior remains unclear. Performing measurements on clouds is a difficult task, due to spatial and time variations of clouds and due to their irregular appearance. Modeling the growth from aerosol particles to cloud droplets, on the other hand, poses other problems, as models are far from being complete. Some quantities that still need to be determined or confirmed are e.g. the osmotic coefficient, which accounts for the non-ideal behavior of solution droplets in equilibrium with the surrounding relative humidity, and particle/droplet growth laws, vapor diffusion coefficients (Pruppacher & Klett (1997)) and vapor accommodation coefficients (e.g. Kreidenweis *et al.* (2003), Fladerer & Strey (2003)) for the growth of particles in super-saturated environments. Laboratory measurements are needed for the determination of the different quantities in question. Therefore, the Leipzig Aerosol Cloud Interaction Simulator (LACIS, Stratmann *et al.* (2004)) has been developed and applied to measure both, particle/droplet equilibrium sizes for sub-saturated conditions and the size of activated and grown droplets for super-saturated conditions.

2. EXPERIMENTAL SETUP

LACIS (see Figure 1) consists of a laminar flow tube with thermostated walls into which cloud condensation nuclei of well-defined size, composition and number concentration are introduced at adjustable relative humidity levels. Depending on the relative humidity level at the LACIS inlet and on the temperature of the LACIS wall, saturation levels inside LACIS maybe adjusted over a wide range from almost zero to maximum super-saturations of several percent. The length of the LACIS flow tube is 1 m.

Aerosol particles are generated with an atomizer (manufactured by TSI 3010, TSI Inc., St. Paul, Minnesota, USA). So far, particles were generated from solutions of either sodium chloride or ammonium sulfate or from PSL particles suspended in water. The generated aerosol particles are dried and

Corresponding author's address: Heike Wex, Institute for Tropospheric Research, Permoser Strasse 15, 04318 Leipzig, Germany, E-Mail: wex@tropos.de.

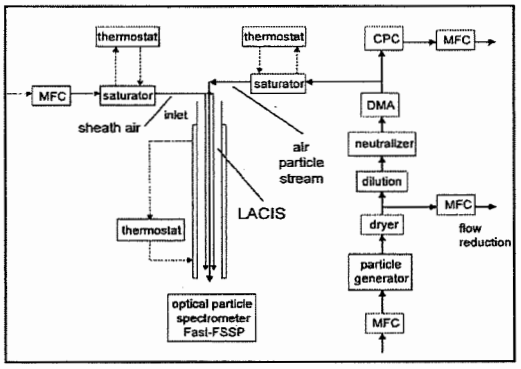

Figure 1: LACIS setup.

the aerosol flow is reduced. The remaining aerosol then passes through a dilution system and through a neutralizer and a differential mobility analyzer (DMA, Knutson & Whitby (1975)), which extracts a quasi-monodisperse fraction of aerosol particles. The number concentration of the aerosol is measured with a condensation particle counter (CPC, manufactured by TSI 3010, TSI Inc., St. Paul, Minnesota, USA) downstream of the DMA. During experiments, the particle number concentration is kept at values of 100 to 500 cm^{-3}. The remaining aerosol flow is led through a saturator where it is saturated with water vapor. The humidified aerosol and particle free sheath air which has also been humidified are combined in the LACIS head. Both flows are humidified at the same saturator temperature, i.e. their dew point temperature is equal. The combined flows then reach the LACIS flow tube, where particles grow depending on the relative humidity in the flow tube, which depends on the dew point temperature of the flows and on the LACIS wall temperature.

At the LACIS outlet, the size of the grown particle/droplet is measured optically. These measurements were made with either a Fast-FSSP (Brenguier *et al.* (1998)) or with a newly developed single particle optical counter (Kiselev *et al.* (2004)). The new counter consists of a Xenon arc lamp, which provides white light. The light beam is shaped and illuminates the particle beam through a small slit in the LACIS flow tube, with the light beam being perpendicular to the particle beam. The light scattered by the particles is collected with two elliptical mirrors for scattering angles from about 10° to 50° in the forward direction and is passed on to two photomultipliers. The position and shape of the signals of the two photomultipliers are compared, and this

procedure allows to include only those droplets in the evaluation, which are passing through the center of the measuring volume. PSL particles of different sizes from 300 nm to 1500 nm are used for the calibration of the optical counter to determine the response function of the instrument. For the determination of the size of grown aerosol particles/droplets, the refractive index of the solution is derived by accounting for the dissolved mass of the dry salt particle.

3. FINE PARTICLE MODEL

To describe the coupled fluid flow, heat/mass transfer and particle/droplet dynamical processes taking place in LACIS, FLUENT 6 (Fluent, 2003) together with a modified version of the Fine Particle Model (FPM, Wilck *et al.* (2002), Particle Dynamics (2003)) was utilized. This numerical model solves the momentum and the heat and mass transport equations of the water-vapor-air mixture and moment equations describing the particle/droplet dynamical processes. It accounts for molecular and thermal vapor diffusion, includes vapor condensation on the LACIS walls, and particle/droplet transport due to diffusion, thermo-phoresis and sedimentation and particle/droplet growth/shrinkage due to condensation/ evaporation. The model features different expressions regarding the determination of critical properties such as the vapor diffusion coefficient, carrier gas heat conductivity, and osmotic coefficient. Also different particle/droplet growth laws have been implemented.

With this numerical model, particle/droplet sizes as function of position in LACIS can be calculated. Comparing modeled and measured values, expressions for e.g. material and/or thermodynamic properties and growth laws used in the simulations can be evaluated and verified or, if needed, improved.

4. MEASUREMENTS AT SUB-SATURATION: THE INFLUENCE OF THE OSMOTIC COEFFICIENT

Comparisons of measured and modeled growth rates were made for sodium chloride and for ammonium sulfate particles with a dry size of 200 nm, with the growth rates being the factor by which the dry diameter of a particle has to be multiplied with to obtain the equilibrium diameter it grows to at a certain relative humidity. The measurements of the equilibrium sizes of the particles were performed with the newly developed optical counter. For the measurements, the relative humidity in LACIS was set to values between 86 % and 98.5 %. Measurements repeated on three days were averaged and for a relative humidity up to 97 % the repeatability of the derived growth factors was better than 2 %. At a relative humidity of 98.5 % it was 4 %.

The equilibrium sizes of the particles also were calculated with the FPM. For a first set of calculations, the osmotic coefficient was set to one, i.e. an ideal solution for the droplets was assumed. In a second and third set, the osmotic coefficient was used following

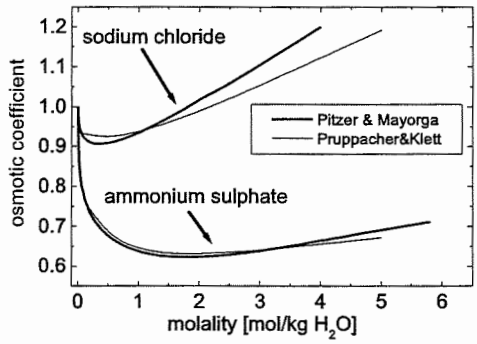

Figure 2: Osmotic coefficients for NaCl and $(NH_4)_2SO_4$ based on Pitzer & Mayorga (1973) and on Pruppacher & Klett (1994).

a parameterization derived from Pitzer & Mayorga (1973) and from Pruppacher & Klett (1997), respectively (Figure 2). For both substances, the shape of the curves of the osmotic coefficient is similar for the two different parameterizations, but the osmotic coefficient for sodium chloride is close to one for low molalities up to 4 mol/kg, whereas it is closer to 0.6 to 0.7 for ammonium sulfate in this molality range.

Growth rates were also derived from measurements by Tang (1996) for sodium chloride and Tang & Munkelwitz (1994) for ammonium sulfate, and were also used in a comparison of measured and modeled values. All growth rates derived with the different methods described above are shown in Figure 3.

For NaCl the difference between the results of the model simulations using the two different osmotic coefficients as shown in Figure 2 is smaller than 1 %. The deviation between all three different model approaches and the measurements derived from Tang (1996) and those from LACIS is smaller than 3 %.

The remarkable feature in the comparison of the different values for the $(NH_4)_2SO_4$ growth rates is the displacement of the results of the simulations performed with an osmotic coefficient of one, which assumes the droplet to behave like an ideal solution. The results of this simulation exceed the results from the two model simulations with the more realistic osmotic coefficients, the data from Tang & Munkelwitz (1994), and the LACIS measurements by 10 % to 15 %, whereas the results of the latter 4 methods differ from each other by only 0.5 % to 4 %. The deviation between the two model simulations with the different osmotic coefficients is less than 3 %.

The molality of the droplets examined in these experiments is lower than 4 mol/kg. As stated above (see Figure 2), for these molalities the osmotic coefficient for NaCl is close to one, whereas it takes values of 0.6 to 0.7 for $(NH_4)_2SO_4$. This explains the large deviation of the model simulation assuming ideal behavior for $(NH_4)_2SO_4$. Thus, when modeling the growth of different aerosol particles, the deviation of the solution from ideal behavior has to be taken into account.

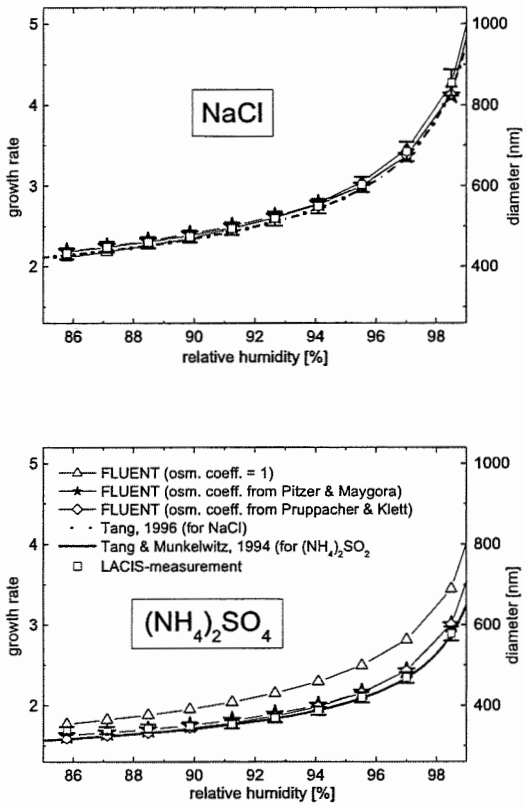

Figure 3: Comparison of measured and modeled growth rates and equilibrium diameters for NaCl and $(NH_4)_2SO_4$ particles with a dry diameter of 200 nm at different relative humidities.

5. MEASUREMENTS AT SUPER-SATURATION

For experiments with LACIS performed at super-saturation the particles/droplets become activated and grow to larger sizes. One example of the profile of the relative humidity in the flow tube simulated with the FPM can be seen in Figure 4. The super-saturation reaches a maximum value at 30 cm to 40 cm into the flow tube, with super-saturations of 0.9 % to 6.2 %, and converges toward unity further downstream. Aerosol particles grow, depending on the saturation. The simulated particle sizes resulting from the saturation profiles shown in Figure 4 is depicted in Figure 5. At the entrance of the LACIS flow tube, particles are in equilibrium at the relative humidity that results from the dew point temperature of the aerosol and sheath air flow and from the temperature of the LAICS head. A few centimeters into the flow tube the cold temperatures of the wall (e.g. 3.3 °C for Figure 4) start to influence the temperature at the center axis of LACIS, and the relative humidity, i.e. the saturation, increases. With a small delay in time, due to kinetic effects, particles start to grow and do so until after the saturation decreases again. Due to this decrease of the saturation particles start to shrink towards the end of the flow tube. In the example shown in Figure 5, for a saturator temperature of 21.75 °C the particles reach a new equilibrium.

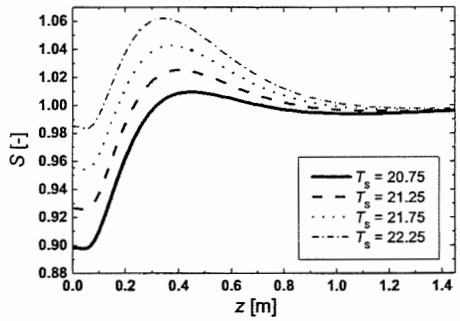

Figure 4: Profile of the saturation at the center axis of LACIS for a wall temperature of 3.3 °C and different dew point temperatures at the saturators, simulated with the FPM.

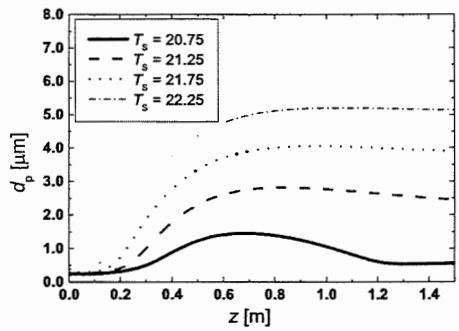

Figure 5: Profile of the size of the grown aerosol particles/droplets at the center axis of LACIS, simulated with the FPM according to super-saturations depicted in Figure 4.

First measurements at super-saturation conditions were performed with NaCl or $(NH_4)_2SO_4$ particles with a dry diameter of 100 nm at LACIS wall temperatures of 2 °C. The particle/droplet size was measured with the Fast-FSSP at the LACIS outlet through a glass window in the tubing. LACIS was completely sealed to allow measurements at different stable system pressures of 1000 mbar and 700 mbar.

The comparison of measured and modeled sizes of the particles/droplets at the outlet is shown in Figure 6. Good agreement between measurement and model within the range of measurement uncertainty was found. Nevertheless, measured data are on average 4 % smaller than the simulated values. Parameters in the model such as the mass accommodation coefficient for water, the diffusion coefficient of water-vapor in air and the heat conductivity were taken from literature (Pruppacher & Klett (1997)) and are afflicted

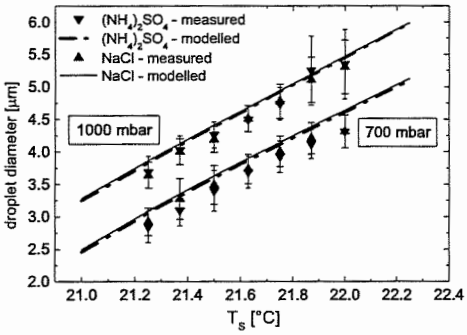

Figure 6: Comparison of measured and modeled particle/droplet sizes for the growth of salt particles with a dry size of 100 nm for different system pressures and for different super-saturations.

with uncertainties. Sensitivity studies of the uncertainty of the modeled particle growth with respect to these parameters will have to be examined in the future (Stratmann *et al.* (2004)).

6. ACKNOWLEDGEMENTS

The authors thank F. Brechtel for providing his code for the calculation of the Tang & Munkelwitz (1994) and Tang (1996) growth rates.

7. REFERENCES

Brenguier, J. L., Bourrianne, T., Coelho, A. A., Isbert, J., Peytavi, R., Trevarin, D., and Wechsler, P., 1998: Improvements of droplet size distribution measurements with the Fast-FSSP. *J. Atmos. Oceanic Technol.*, **15,** 1077-1090.

Fladerer, A. and Strey, R., 2003. Growth of homogeneously nucleated water droplets: a quantitative comparison of experiment and theory, *Atmos. Res.*, **65**, 161-187.Fluent, 2003.

FLUENT 6 Users Guide. Fluent Inc., Lebanon NY.

Kiselev, A., Wex, H., and Stratmann, F., 2004. Development of a single particle optical counter for in-situ measurements of aerosol particle condensational growth. accepted by *J. Aerosol Sci.,* **S1**.

Knutson, E. O. and Whitby, K. T., 1975: Aerosol classification by electric mobility: apparatus, theory, and applications. *J. Aerosol Sci.*, **6,** 443-451.

Kreidenweis, S. M., Walcek, C. J., Feingold, G., Gong, W., Jacobson, M. Z., Kim, C.-H., Liu, X., Penner, J. E., Nenes, A., and Seinfeld, J. H., 2003. Modification of aerosol mass and size distribution due to aqueous-phase SO2 oxidation in clouds: comparison of several models, *J. Geophys. Res.*, **118**, D7, AAC 4: 1-12.

Particle Dynamics, 2003. *FPM 1.0.1 Users Guide*. Particle Dynamics GmbH, Leipzig, Germany.

Pitzer, K. S. and Mayorga, G. ,1973. Thermodynamics of electrolytes. II. Activity and osmotic coefficients for strong electrolytes with one or both ions univalent, *J. Phys. Chem.*, **77**, 2300-2308.

Pruppacher, H. R. and Klett, J. D., 1997. *Microphysics of Clouds and Precipitation.* Kluwer Academic Publishers, Dordrecht, The Netherlands.

Stratmann, F., Kiselev, A., Wurzler, S., Wendisch, M., Heintzenberg, J., Charlson, R. J., Diehl, K., Wex, H., and Schmidt, S., 2004. Laboratory studies and numerical simulations of cloud droplet formation under realistic super-saturation conditions, accepted by *J. Atmos. Oceanic Technol.*.

Stratmann, F., Wex, H., and Kiselev, A. 2004. Modelling particle/droplet activation and growth in LACIS: A sensitivity study regarding material properties and operational parameters, accepted by *J. Aerosol Sci.*, **S1**.

Tang, I. N. and Munkelwitz, H. R., 1994. Water activities, densities, and refractive indices of aqueous sulfates and sodium nitrate droplets of atmospheric importance, *J. Geophys. Res.*, **99**, D9, 18801-18808.

Tang, I. N., 1996. Chemical and size effects of hygroscopic aerosols on light scattering coefficients, *J. Geophys. Res.*, **101**, D14, 19245-19250.

Wilck, M., Stratmann, F., and Whitby, E. R., 2002. A fine particle model for FLUENT: description and Application, in *Proc. 6th International Aerosol Conference*, Taipei, Taiwan.

CORRELATION BETWEEN NUMBER OF THUNDER-DAYS AND DURATION OF THUNDERSTORM ACTIVITY IN EASTERN GEORGIA

A.G.Amiranashvili [1], B.Sh. Beritashvili[2] , I.P. Mkurnalidze[2]

[1]Institute of Geophysics of Georgian Academy of Sciences, Tbilisi, 0193, Georgia
[2] Institute of Hydrometeorology of Georgian Academy of Sciences, Tbilisi, 0112,Georgia

1. INTRODUCTION

Georgia is one of the thunderstorm active regions of the world. The average annual number of thunder-days in some regions here exceeds 50. The investigation of thunderstorm processes in Georgia counts more than 70 years and the results of this research are presented, in particular, in a number of publications, Kurdiani (1935), Gunia, (1960), Amiranashvili et al., (2003). In this work the data on statistical features of number of thunder-days and thunderstorms duration through the warm period of the year in Eastern Georgia are presented.

2. METHODS

Twenty-year data (1955-1974) of visual and audio observations on the number of thunder days (X) and thunderstorms duration (Y) for 35 meteorological station in Eastern Georgia through the warm season of the year (April-October) are analyzed. Stations are located in six different climatic zones, the detailed classification of which is given by Lominadze and Chirakadze, (1971). The short description of these zones, the list of weather stations, their coordinates and elevation are given below (accordingly N.L. , E.L. and m above s.l.).

Zone 5 – Upper and lower Kartli Valley with foothills. Temperate damping is decreasing to the East. The mean annual temperature is in the range 10-13°C. The type of climate - moderately arid subtropics with the temperature cold winter and highly warm summer. The stations – Tbilisi (41.7; 45; 403),Bolnisi (41.5; 44.7; 534), Samgori (41.7; 44.9; 549), Mukhrani (41.9; 44.6; 550), Gori (42; 44.1; 588), Khashuri (42; 43.6; 690), Akhalgori (42.1 44.5; 760), Sagarejo (41.7; 45.3; 802), Tskhinvali (42.2; 44.; 862), Dusheti (42.1; 44.7; 922), Gombori (41.9; 45.2; 1085), Tianeti (42.1; 45; 1099)

Zone 6 – Alazani Valley with foothills. The region is characterized by temperature damping slightly decreasing from north-west to the south-east. Mean annual temperature 11-13°C. Type of climate – weakly moisturized subtropics. The stations – Tsnori (41.6; 46.1; 223), Lagodekhi (41.8; 46.3; 362), Gurjaani (41.8; 45.6; 410), Kvareli (42; 45.8; 449), Akhmeta (42; 45.2; 567), Telavi (41.9; 45.5; 568), Signakhi (41.6; 45.9; 795).

Zone 7 – The Iori Upland with adjacent steppes. The region is arid and abundant of warmth. The average annual temperature makes 10-12°C. Type of climate – arid subtropics with high moistre deficit and high continentality. The stations – Gardabani (41.5; 45.1; 300), Shiraki (41.4; 46.3; 555), Dedoblis-Tskaro (41.5; 46.1; 800).

Zone 10 – Piedemont and mid-mountain area of Eastern Great Caucasian Range. Mid-mountain area is characterized by moderate damping. The average annual temperature is 7-8°C. Type of climate – temperate damp with moderate cold winter and chilly summer. The stations – Pasanauri (42.4; 44.7; 1070), Djava (42.4; 43.9; 1109).

Zone 14 – Southern slopes of Meskheti and Trialeti ridges. The region is moderately damp with pronounced of vertical zonality of climate. The mean annual temperature is in the range of 4-9°C. Type of climate – mountainous, moderately damp. The stations – Borjomi (41.8; 43.4; 789), Tetri-Tskaro (41.6; 44.5; 1140), Manglisi (41.7; 44.4; 1194), Dmanisi (41.3; 44.2; 1256), Abastumani (41.8; 42.8; 1265), Kodjori (41.7; 44.7; 1338), Bakuriani (41.7; 43.5; 1665).

Corresponding author's address:
Avtandil Amiranashvili, Geophysics Institute of Georgian Academy of Sciences, 1., M. Aleksidze Str., Tbilisi 0193, Georgia; E-mail:.
Avto_Amiranashvili@excite.com
Avto_Amiranashvili@hotmail.com

Zone 15 – The southern part of South Georgian Highland. The region is poor of precipitation and has clearly expressed continentality. The mean annual temperature is 3-9°C. Type of climate – arid mountainous. The stations – Akhaltsikhe (41.6; 43; 982), Tsalka (41.6; 44.1; 1457), Akhalkalaki (41.4; 43.5;1716), Efremovka(41.2;43.8;2112).

3. RESULTS

The results are presented in Tables 1-2.

Table 1

Statistical characteristics of the number of thunder days and thunderstorms durations.

Station	Number of thunder-days				Thunderstorm duration			
	Max	Min	Mean	St. Dev	Max	Min	Mean	St. Dev
Tbilisi	42	17	29.2	7.5	92.9	19.3	52.2	17.9
Bolnisi	53	29	41.7	7.2	254.8	75.1	153.9	49.1
Samgori	38	12	25.1	7.1	98.1	12.2	38.4	23.6
Mukhrani	53	21	38.1	8	248.8	84	155.5	40
Gori	44	19	30.3	7.2	207.2	45.6	96.2	39.2
Khashuri	50	23	35.3	7.4	193	79.4	127.4	33
Akhalgori	31	10	19.5	5.6	69	17	35.8	17.2
Sagarejo	46	22	33.3	6.9	103.3	28.6	61.6	19
Tskinvali	31	13	23.6	5.2	102.8	30.8	60.3	13.2
Dusheti	71	29	44.9	10.6	170.2	67.3	118.1	31.2
Gombori	39	15	29.1	7.4	100.1	14.9	50.3	24.2
Tianeti	57	22	38.7	8.2	185.3	51.1	97.5	31.6
Tsnori	47	23	31.5	6.1	139.8	38.8	76.6	23.6
Lagodekhi	63	29	48	8.3	218.1	80.5	142.4	33.9
Gurjaani	47	20	40	6.9	177.1	56.1	114.3	32.4
Kvareli	42	17	31.6	6.9	127.2	21.3	59.6	26.6
Akhmeta	51	8	26.1	11.6	150.7	10	54.1	39.7
Telavi	66	29	45.9	10.2	179.2	75.5	119.2	31.8
Signakhi	49	27	38	6.8	160.3	57.9	90.2	29.4
Gardabani	41	16	28.7	6.1	136.8	47.3	83.5	23.9
Shiraki	37	20	28.6	5	122.9	26.2	56.8	25
Dedoblis-Tskaro	47	22	34.6	6.5	167.4	46.5	100.8	27.7
Pasanauri	63	23	40.5	8.9	194.1	66.7	107.5	36
Djava	51	18	30.1	8	56.4	9.4	25.3	11.9
Borjomi	56	25	36.9	7.9	74.5	19.8	40.9	12
Tetri-Tskaro	53	32	42.4	6.4	193.2	70.9	135.8	32.1
Manglisi	55	28	40.2	8.5	246.9	62.4	142.1	59.2
Dmanisi	41	14	29.9	6.6	63.8	8.5	30.9	13.6
Abastumani	71	32	44.5	9	175.6	38.6	96.9	34.1
Kojori	31	14	21.1	4.6	38.5	11	22.4	8.1
Bakuriani	75	27	39.8	9.9	272.9	110.2	156.2	36.3
Akhaltsihe	80	34	51.8	10	209.1	60.8	128.5	42.9
Tsalka	42	20	30.7	6.5	85.2	23.6	50.5	16.9
Akhalkalaki	75	31	49.8	8.6	317.2	147.4	202.9	41.3
Efremovka	85	35	51.1	12.6	231.1	84.7	124.2	37.7

Table 1(continue)

Zones	Number of thunder-days				Thunderstorm duration (hours)			
	Max	Min	Mean	St. Dev	Max	Min	Mean	St. Dev
Zone 5	46	19	33	7	152	44	87	29
Zone 6	51	20	36	7	151	40	87	28
Zone 7	42	19	31	6	142	40	81	26
Zone 10	57	21	35	9	125	38	67	24
Zone 14	55	25	36	8	152	46	89	28
Zone 15	71	30	46	9	211	79	127	29
Eastern Georgia	54	22	36	8	156	48	90	28

Table 2

Coefficients a and b in linear and power regression equations relating thunderstorm duration with the number of thunder days. R^2 – coefficient of determination between Y and X.

Station	$Y = aX + b$			$Y = aX^b$		
	a	b	R^2	a	b	R^2
Tbilisi	1.56	6.77	0.42	1.35	1.076	0.59
Bolnisi	2.85	35.1	0.18	5.87	0.866	0.21
Samgori	2.8	-32	0.71	0.23	1.556	0.72
Mukhrani	3.46	23.5	0.48	7.53	0.828	0.52
Gori	4.63	-43.9	0.72	0.937	1.348	0.72
Khashuri	3.5	4.13	0.62	4.325	0.946	0.59
Akhalgori	1.94	-1.97	0.41	1.735	0.997	0.42
Sagarejo	1.94	-2.825	0.50	1.603	1.035	0.50
Tskinvali	2.27	-5.61	0.49	2.015	1.061	0.58
Dusheti	2.68	-2.05	0.82	2.263	1.038	0.81
Gombori	2.225	-14.4	0.46	0.369	1.437	0.56
Tianeti	2.94	-16.2	0.58	2.069	1.048	0.53
Tsnori	3.35	-29.1	0.74	0.876	1.29	0.69
Lagodekhi	3.15	-8.65	0.59	2.142	1.081	0.64
Gurjaani	3.43	-12.6	0.53	2.047	1.109	0.61
Kvareli	3.15	-39.8	0.67	0.133	1.753	0.76
Akhmeta	3.1	-26.5	0.81	1.078	1.168	0.62
Telavi	2.23	16.7	0.52	3.267	0.937	0.59
Signakhi	3.1	-27.4	0.52	1.193	1.182	0.55
Gardabani	2.67	7.03	0.46	6.357	0.761	0.37
Shiraki	3.27	-36.6	0.42	0.377	1.476	0.37
Dedoblis-Tskaro	3.24	-11.15	0.58	2.676	1.018	0.46
Pasanauri	3.15	-19.8	0.61	2.384	1.023	0.53
Djava	1.41	-17	0.90	0.085	1.66	0.88
Borjomi	1.24	-4.95	0.67	0.645	1.146	0.66
Tetri-Tskaro	3.7	-21.2	0.55	1.23	1.251	0.56
Manglisi	6.42	-116	0.84	0.159	1.828	0.85
Dmanisi	1.23	-5.76	0.35	0.36	1.293	0.48
Abastumani	3	-36	0.62	0.507	1.376	0.58
Kojori	1.04	0.47	0.35	0.771	1.093	0.42
Bakuriani	3.065	9.25	0.71	7.025	0.8	0.64
Akhaltsihe	3.23	-37.8	0.56	1.409	1.136	0.48
Tsalka	2.2	-16.8	0.72	0.401	1.405	0.79
Akhalkalaki	3.77	15.1	0.62	7.303	0.849	0.58
Efremovka	2.6	-9.1	0.76	2.871	0.955	0.72
Eastern Georgia	2.85	-11.2	0.81	2.016	1.063	0.79

The table 1 demonstrate statistical features of number of thunder-days and thunderstorm duration for separate stations, climatic zones and the territory of Eastern Georgia as a whole. In the table 2 values of coefficients a and b in linear and power regressions equations are given, which determine the relation between thunderstorm duration and number of thunder-days in the form of $Y = aX + b$ and $Y = aX^b$ for each weather station and for the territory of Eastern Georgia in general. Relevant values of determination factors are presented as well.

As it could be seen from the table 1, the maximum number of thunder-days is observed at the station of Efremovka (85 days) while maximum duration of thunderstorm activity is registered at the station of Akhalkalaki (317 hours). The minimum number of thunder-days is observed in Akhmeta (8 days), and minimum duration of thunderstorms – in Dmanisi (8.5 hours).

According to climatic zones maximum values of both number of thunder days and thunderstorm duration is recorded in the zone 15, and the minimum values of both examined parameters – in the zones 5-10.

Table 2 shows that at the majority of stations, according to both linear and power regression equations, sufficiently high values of determination coefficient are derived. The relatively low values of factors by linear equations are obtained at the stations of Dmanisi and Kojori, and by power equations – at Shiraki and Gardabani stations. By both equations low values of determination factor are registered at the Dmanisi station.

It ought to be mentioned that table 2 data allow to choose the kind of regression equation for each station. E.g., for the stations of Tbilisi and Gombori the relation between thunderstorm duration and number of thunder-days is better fit by power equation, while for the stations Akhmeta, Dedoplis-Tskaro and Akhaltsikhe – by linear equation.

So, in Eastern Georgia the number of thunder-days and thunderstorm duration are widely different for separate stations. The relation between these thunderstorm parameters is satisfactorily described both by linear and power regression equations. The obtained results can be used in the development of regional climatic models, in the construction of lightning-protection systems for the different important objects in the region, etc.

4. REFERENCES

Kurdiani, I. G., 1935: On the Thunderstorms and the Hailfalls in Kakheti, Tbilisi, Georgian Geographical Society, 1-60, (in Russian)

Gunia, S.U.,1960: Thunderstorm processes under Transcaucasia's "Condutions, Leningrad, Gidrometeoizdat, 1-153 (in Russian).

Amiranashvili, A.G., Amiranashvili C.A., Beritashvili B.Sh., Mkurnalidze I.P., Chumburidze Z.A., 2003: Some Characteristics of a Thunderstorm Activity in Georgia, Proc. 12th Int. Conf. on Atmospheric Electricity, Versailles, France, 9-13 June 2003, vol. 2, 711-714.

Lominadze, V.P., Chirakadze G.I.(Eds.) , 1971: Climate and Climate Resources of Georgia, Leningrad, Gidrometeoizdat, 363-375 (in Russian).

SPATIAL-TEMPORARY CHARACTERISTICS OF NUMBER OF DAYS WITH A HAILS IN THE WARM PERIOD OF YEAR IN GEORGIA

A.G.Amiranashvili[1], V.A. Amiranashvili[1], A.G.Nodia[1],
T.V.Khurodze[2], A.F.Toronjadze[2], T. Bibilashvili[3]

[1]Institute of Geophysics of Georgian Academy of Sciences, Tbilisi, 0193, Georgia
[2]Institute of computational mathematics of Georgian Academy of Sciences,Tbilisi,0193,Georgia
[3] Tbilisi State University , Tbilisi, 0128, Chavchavadze Av. 3, Georgia

1. INTRODUCTION

Georgia is known by its hail activity. The annual number of days with a hails in some regions here exceeds 20. At some meteorological stations of the Georgia the observations of the number of days with a hail are conducted since 1891. However, for the greatest number of meteorological stations series of continuous observations covers period from 1941 through 1990.

The investigation of hailstorm processes in Georgia counts more than 70 years and the results of this research are presented, in particular, in a number of publications: Kurdiani (1935), Gigineishvili (1960), Gagua (1980), Amiranashvili et al. (2000). In this work the results of researches of the spatial-temporary characteristics of number of days with a hails in a warm season of year in Georgia are presented.

2. METHODS

The observations over the hail events at 122 meteorological stations in period 1941-1990 were analyzed. The meteorological stations on territory of Georgia are located approximately in regular intervals (in Western Georgia – 81 stations, in Eastern Georgia – 41 stations) .Range of heights H is from 2 up to 2197 m above sea-level, latitude φ - from 41.2° up to 43.4° North and longitudes λ - from 40.03° up to 46.33° East .

Corresponding author's address: Avtandil Amiranashvili, Geophysics Institute of Georgian Academy of Sciences, 1., M.Aleksidze Str., Tbilisi 0193, Georgia; E-mail: Avto_Amiranashvili@excite.com
Avto_Amiranashvili@hotmail.com

The subject of research is the average characteristics of the hail events for each station in three periods of time: general- for 1941-1990, 1- for 1941-1965 and 2- for 1966-1990 (accordingly N, N1, and N2).

The presence of trend was evaluated according to Student's criterion with significance level not worse than 0.1.

3. RESULTS

The statistical characteristics of the number of days with a hails for 122 meteorological stations of Georgia in three periods of time are presented in Table 1.

In the period from 1941 till 1990 years on average at all stations the quantity of the hail events was 1.27.

In the first period the quantity of the hail events for these stations on average was 1.54, and in second period the quantity of the hail events decreased up to 1.0.

Occurrence of number of days with a hails trends in Georgia (1966 -1990 in comparison with 1941-1965) are presented in Table 2.

Thus, in territory of Georgia in the second period of time in comparison with first period as a whole, so in its western and eastern parts predominantly the negative trend of the number of days with a hails was observed (Table 1 - 2).

By height of locality the quantity of the hail events grows up and for a range of heights from 2 up to 2197 m above sea level in the specified periods of time satisfactorily is approximated by the following linear equations:

Table 1

The statistical characteristics of the number of days with a hails for 122 meteorological stations in three periods of time

Parameter \ Period	1941-1990	1941-1965	1966-1990
Mean	1.27	1.54	0.99
Min	0.04	0.04	0
Max	5.6	7.24	6.08
St Dev	1.31	1.6	1.2

Table 2

Occurrence of number of days with a hails trends in Georgia (1966 -1990 in comparison with 1941-1965)

Region \ Trend	Negative (%)	Positive (%)	No (%)
Western Georgia	50.6	14.8	34.6
Eastern Georgia	58.5	4.9	36.6
Whole territory	53.3	11.5	35.2

N = 0.0017H + 0.08 (coefficient of correlation is 0.77);
N1 = O.0021H + 0.11 (coefficient of correlation is 0.76);
N2 = 0.0014 H + 0.05 (coefficient of correlation is 0.67).

The spatial distribution of quantity of the hail events in three specified periods of time satisfactorily is approximated by the following equations of multiple regression :
N = - 0.0962 φ + 0.0975 λ + 0.00164 H (multiple coefficient of correlation is 0.78);
N1 = - 0.125 φ + 0.127 λ + 0.00197H (multiple coefficient of correlation is 0.77);
N2 = - 0.0671 φ + 0.0679 λ + 0.00131H (multiple coefficient of correlation is 0.67).

The possible reasons of the negative trends of the number of days with a hails in Georgia can be the climate warming and the anthropogenic pollution of the atmosphere increase.

4. REFERENCES

Kurdiani, I. G., 1935: On the Thunderstorms and the Hailfalls in Kakheti, Tbilisi, Georgian Geographical Society, 1-60, (in Russian)

Gigineishvili, V.M.,1960: Hailfalls in Eastern Georgia , Leningrad, Gidrometeoizdat, 1-123 (in Russian)

Gagua, V.P., 1980: Hail, in: Dangerous Hydrometeorological Phenomena in the Caucasus, Edited by G.G. Svanidze and Ya.A. Tsutskiridze, Leningrad, Gidrometeoizdat, 137-150(in Russian)

Amiranashvili, A.G., Amiranashvili V.A., Doreuli R.I., Khurodze T.V., Kolesnikov Yu.M., 2000: Some Characteristics of Hail Processes in the Kakheti Region of Georgia, Proc. 13th Int. Conf. on Clouds and Precipitation, Reno, Nevada, USA, 14-18 August 2000, vol. 2, 1085-1087.

INFLUENCE OF THE ANTHROPOGENIC POLLUTION OF THE ATMOSPHERE AND THUNDERSTORMS ON THE PRECIPITATIONS REGIME AND THEIR CHEMICAL COMPOSITION IN ALAZANI VALLEY CONDITIONS

A.G.Amiranashvili[1], V.A. Amiranashvili[1], L.L. Bachiashvili[2], T. Bibilashvili[3], G.D. Supatashvili[3]

[1]Institute of Geophysics of Georgian Academy of Sciences, Tbilisi, 0193, Georgia
[2]Institute of Hydrometeorology of Georgian Academy of Sciences,Tbilisi,0112,Georgia
[3]Tbilisi State University , Tbilisi, 0128, Chavchavadze Av. 3, Georgia

1. INTRODUCTION

Earlier work presented the results of the investigations of the chemical content of precipitation from thunderstorm and non-thunderstorm clouds in conditions of Alazani valley in Kakheti region of Georgia, Abesalashvili et al., (1996).

In this work the influence of an anthropogenic pollution of the atmosphere was estimated by comparison of the data about a mode of precipitations and their chemical structure during the weekdays and weekends.

2. METHODS

The data on daily quantity of precipitations and thunderstorms are taken from meteorological station Telavi.

The measurement of precipitation's chemical structure (pH, $NH4^+$, $NO3^-$, Ca^{2+}, $SO4^{2-}$) was made in Ruispiri, which is located in 6 km from Telavi.

The array station is located in 60 km to east from the powerful source of an anthropogenic pollution of the atmosphere, from city Tbilisi. The data of a warm season (1967-1970) were analyzed, when the general level of atmosphere's pollution was much lower than in present.

Chemical analyses of precipitation samples were carried out by the method Supatashvili,(1971, 1973) with measurement error not more than ±10%.

Corresponding author's address: Avtandil Amiranashvili, Geophysics Institute of Georgian Academy of Sciences, 1., M.Aleksidze Str., Tbilisi 0193, Georgia;
E-mail: Avto_Amiranashvili@excite.com
Avto_Amiranashvili@hotmail.com

The estimation of difference between the investigated parameters was evaluated according to Student's criterion with significance level not worse than 0.2.

3. RESULTS

Data of the chemical content of precipitation and daily-mean value of precipitation from thunderstorm and non-thunderstorm clouds in week-days and weekend are presented in Table 1-2.

In particular, the following results are submitted:

- As a whole, in days with thunderstorms the contents of all specified chemical components, except pH, in precipitations was higher, than per days without thunderstorms. But the difference in the contents of these chemical components in precipitations between weekdays and weekends was not observed.
- In precipitations in days with a thunderstorm in weekdays, in comparison with weekends the raised contents of $SO4^{2-}$ was registered. The difference in the contents of $SO4^{2-}$ in precipitations in days with a thunderstorm in comparison with precipitations in days without thunderstorms is even higher (accordingly 7.3 , 5.15 and 4.6 mg/l).
- As a whole in days with thunderstorms the average daily quantity of precipitations is higher, than per days without thunderstorms (8.2 and 4.6 mm accordingly). In week-days the daily quantity of precipitations was higher, than in weekends as an in days with or without thunder-storms

It should be noted that in the region of investigated the radar reflectivity maximum and hailfall intensity in week-days is also higher than in weekend.

Table 1

Chemical content of precipitation from thunderstorm and non-thunderstorm clouds (mg/l) in week-days and weekend

Atm. Cond.	1. Rain without thunderstorm			2. Rain with thunderstorm		
Parameter	Mean	St. dev	No of samp.	Mean	St. dev	No of samp.
pH	6.43	0.64	127	6.44	0.64	68
$NH4^+$	0.37	0.64	127	0.65	1.0	68
$NO3^-$	1.47	1.51	127	1.99	1.52	68
Ca^{2+}	2.49	2.67	127	3.01	2.05	68
$SO4^{2-}$	4.71	3.6	127	6.68	3.76	68
Atm. Cond.	3. Rain with thunderstorm (week- days)			4. Rain with thunderstorm (weekends)		
pH	6.42	0.7	49	6.5	0.48	19
$NH4^+$	0.74	1.135	49	0.43	0.49	19
$NO3^-$	1.94	1.49	49	2.11	1.64	19
Ca^{2+}	3.0	2.11	49	3.05	1.98	19
$SO4^{2-}$	7.28	4.06	49	5.15	2.28	19
Atm. Cond.	5. Rain without thunderstorm (week- days)			6. Rain without thunderstorm (weekends)		
pH	6.4	0.66	94	6.51	0.61	33
$NH4^+$	0.36	0.56	94	0.42	0.82	33
$NO3^-$	1.51	1.6	94	1.34	1.22	33
Ca^{2+}	2.3	2.29	94	3.01	3.53	33
$SO4^{2-}$	4.6	3.37	94	5.03	4.21	33

Table 2

Daily-mean value of precipitation from thunderstorm and non-thunderstorm clouds in week-days and weekend (mm)

Parameter	Atmospheric condition (according Table 1)					
	1	2	3	4	5	6
Mean	4.61	8.24	8.98	6.79	5.18	3.01
St. dev	7.65	10.45	10.84	9.58	8.33	5.02
No of samp.	191	151	100	51	141	50

The reasons of the specified variability of a mode of precipitations and their chemical structure for thunderclouds and non-thunderclouds is the anthropogenic pollution of the atmosphere.

4. REFERENCES

Abesalashvili, L.Sh., Amiranashvili A.G., Supatashvili G.D., 1996: Results of Rain Chemical Content Investigation in Alazani Valley, Proc. 12th Int. Conf. on Clouds and Precipitation, Zurich, Switzerland, 19-23 August 1996, vol. 2, 1066 -1069.

Supatashvili, G.D., Karsanidze N.K., 1971: Determination of the Microelements in the Natural Waters, Proc. of Tbilisi State University, A1(137), 161-163, (In Russian).

Supatashvili, G.D., 1973 : Some Regularity the Formation of Chemical Composition of Atmospheric Precipitations in Georgian SSR. Proc. of the Institute of Oceanology of the USSR A Sc. N63, 72-92, (in Russian).

RAINFALL VARIABILITY OVER THE MEDITERRANEAN REGION AND ITS LINKAGE WITH LARGE SCALE FEATURES

M. Baldi, F. Cesarone, G.A. Dalu, G. Maracchi, F. Meneguzzo

Institute of Biometeorology – National Research Council, Via Nizza 128, 00198 Roma, Italy

1. INTRODUCTION

Several Authors identified different climate subregions in the Mediterranean in each season, and the occurrence of the Mediterranean Oscillation is evident between West and East sub-basins (Conte, 1989). Precipitation and SLP fields in the Eastern basin are correlated with this Mediterranean Oscillation. A decrease of the mean precipitation has been detected in the last few years (Brunetti et al. 2001, 2004), although some very intense events occurred. During winter a fundamental role is played by NAO index, which, deflecting the trajectory of the Atlantic storms towards the Mediterranean or towards the North Europe, therefore, it plays a major role in the precipitation patterns over the Region. Moreover, temperature analysis over the last 40 years in the Mediterranean shows a clear warming, following the pattern over the North Hemisphere and the NAO index fluctuations in winter. During summer a role is played, in the western basin, by the West African Monsoon, while the Eastern basin is influenced by the Asian Monsoon and transverse circulation. The SLP field in the Eastern Mediterranean is inversely correlated to the Sahel and Asian precipitation indices, while the SLP field in the Western Mediterranean is positively correlated to these two indices. In this paper we analyzed the precipitation dataset of Climatic Research Unit of University of East Anglia (CRU-UEA) over the Mediterranean basin during 1900-1998, and some possible mechanisms of interaction with larger scale features.

2. METHODOLOGY

The data used are the monthly precipitation CRU dataset for global land areas from 1900 to 1998, gridded at coarse resolution (2.5° latitude by 3.75° longitude).

Corresponding author's address: M. Baldi, IBIMET-CNR, Via Nizza 128, 00198 Roma, Italy; email: m.baldi@ibimet.cnr.it

The Mediterranean basin (30°N-50°N) is divided into two sub-basin: the West 10° W-15° E, and East from 15° W-40° E. In addition, we examine the Central basin defined from Sardinia-Corsica to the Otranto channel (8° E-19°E). We derived the mean precipitations averaging 97 grid points over the Mediterranean (45 points in the West basin, and 52 in the East, 23 in the Central).

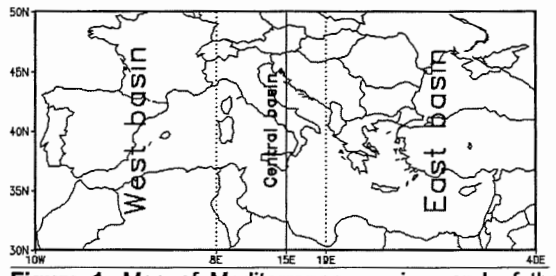

Figure 1. Map of Mediterranean region, and of the three sub-basins.

In order to detect only the long term trends and variability, avoiding high frequency fluctuations, we applied a 20 years mobile average, and a linear fit. The possibility of rainfall variability during the 1900-98 period has been analized using a *coefficient of variability (CV)*:

$$CV = \frac{a \cdot \tau}{c} \cdot 100$$

where a is annual precipitation variability $[mm/year]$, τ is available time range (99 years) and c linear trend intercept. The results are listed in Table 1. In order to detect changes in the characteristics of precipitations we defined two classes of events: dry and wet, as follows: a wet event is an event in which the precipitation is more intense than normal of one or more standard deviations, and a dry event if it is less intense than normal precipitation of one or more standard deviations.

We find that precipitation trends of annual average over the whole basin, and in each sub-basin, are decreasing, and this decrease is more evident going from west to east. It is interesting to note that precipitation mean of wet events over Mediterranean basin describe a positive trend both annually and seasonally, in particular

during the warm season (JJA), when the wet events occurring are more intense. Moreover, we can observe that this findings is true mainly for West basin. Vice versa, dry events are less dry, but they are more frequent in the last half century.

TOTAL	M CV (%)	W CV (%)	C CV (%)	E CV (%)
ANNUAL	-3.7	-2.0	-3.0	-4.7
DJF	-2.9	7.0	-6.0	-9.9
MAM	-2.9	-5.3	-5.1	-0.4
JJA	-0.4	0.7	0.0	-1.9
SON	-5.7	-7.4	0.5	-1.9
WET	M CV (%)	W CV (%)	C CV (%)	E CV (%)
ANNUAL	4.4	5.8	2.9	0.7
DJF	5.8	8.1	-2.5	8.7
MAM	4.7	-1.9	-0.3	4.3
JJA	9.7	28.1	-2.6	-3.7
SON	2.6	-6.3	1.7	-5.0
DRY	M CV (%)	W CV (%)	C CV (%)	E CV (%)
ANNUAL	0.8	2.2	-0.5	1.1
DJF	-4.7	-13.4	0.1	-16.4
MAM	8.2	15.4	4.5	9.4
JJA	9.2	0.1	5.4	-3.5
SON	-5.2	-13.1	11.8	14.9

Table 1. Annual and seasonal ***CV*** over the different basins.

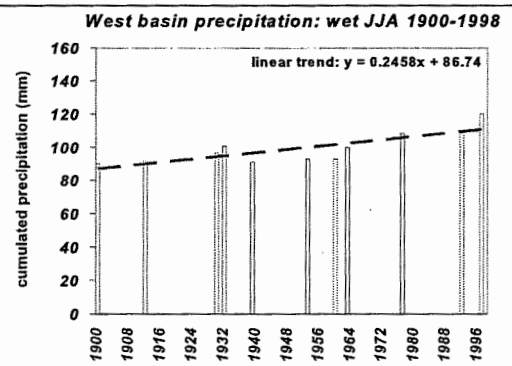

Figure 2. West basin cumulated precipitation in summer in the wet events from 1900 to 1998.

In the West basin the winter precipitation are increasing and tend to be more intense. In winter, dry events are both more frequent and dry (decrease of -13.4%). Characteristics of rainfall are changing in fall, while the usual fall features are moving towards winter and summer. In fact, during fall the precipitation is decreasing and the dry events are more frequent and dry in the last half century, while the strength of "wet" summer precipitation is increasing (CV=28.1%) (Figure 2). In the Central basin during fall there is an increase in dry events, which are more intense (i.e. dry events are less extreme, CV=11.8%) and frequent. Moreover, rain data show that winter precipitation is decreasing as well as the frequency and intensity of "wet" winter. So, it seems that the rainfall are occurring more in winter than in fall. The East basin is drier than the other basins. In fact, annual and seasonal precipitation mean describe a negative trend, mainly in winter (Figure 3: CV=-9.9%). But in this season there is an increase in extreme dry event (CV=-16.4%). During fall, negative trend of wet events and positive trend of dry events are not supporting any hypothesis of a marked trend.

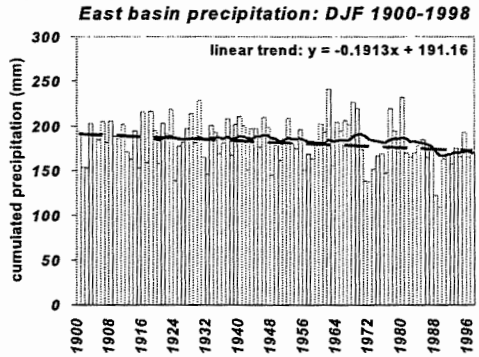

Figure 3. East basin cumulated precipitation in winter from 1900 to 1998.

3. CONNECTIONS TO LARGE SCALE ATMOSFERIC PROCESSES.

The NAO is most pronounced in amplitude and areal coverage during winter (DJF) and strongly influences the wintertime climate of the Northern Hemisphere. Changes in the mean circulation patterns over the North Atlantic are accompanied by pronounced shifts in the storm tracks and associated synoptic eddy activity. These changes affect the transport and convergence of atmospheric moisture and are directly tied to changes in regional wintertime precipitation. Drier-than-normal conditions occur during high NAO index winters over much of central and southern Europe, the Mediterranean countries, and west North Africa. At the same time, wetter-than-normal conditions occur from Iceland trough to Scandinavia.

In Figure 4, the correlation between NAO index and the cumulated precipitation in the Mediterranean during winter show an inverse linear connection (-81%).

It is well known that changes in low-frequency patterns are associated with changes in storm activity and shifts in the storm tracks (Chang *et al.*, 2001; Hoskins *et al.*, 2002): there is a strong connection between the seasonally averaged NAO and storm activity, which has its maximum amplitude around midwinter (Figure 5).

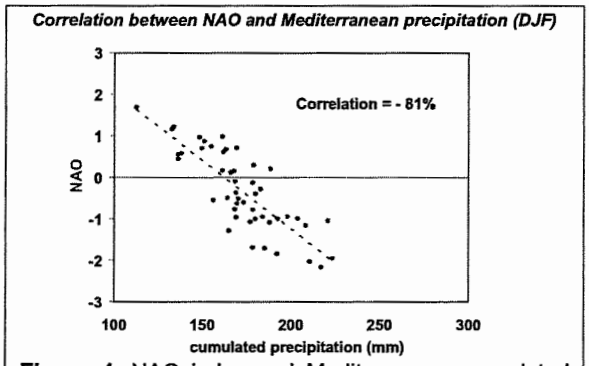

Figure 4. NAO index and Mediterranean cumulated precipitation during winter in the last half century.

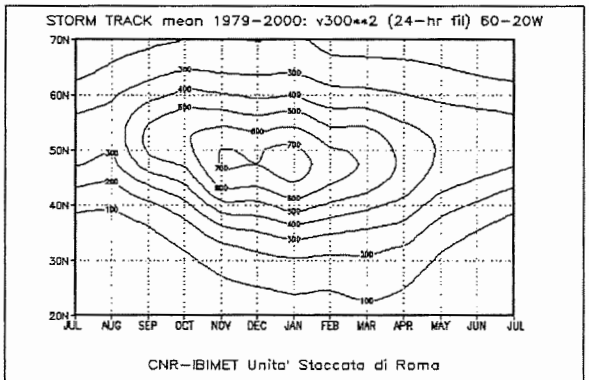

Figure 5. Latitude-time section of the monthly amplitude storm activity averaged from 1979 to 2000.

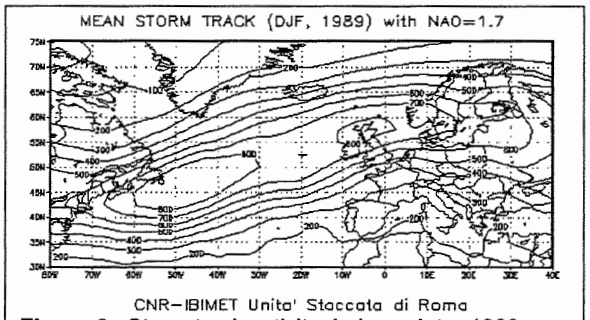

Figure 6. Storm track activity during winter 1989 over 80W-40E lon and 30N-75N lat.

To diagnose storm track strength, we used the 300 mb meridional winds variance, computed using a 24-h difference filter, denoted by v^2 $[m^2/s^2]$, and calculated as follows:

$$v^2 = \overline{[v_{(t+24h)} + v_{(t)}]}$$

where the overbar denotes an average over all available observation times. As an example, we show the storm activity of a specific winter (DJF 1989: Figure 6) when a strong NAO tilts the storm track towards North Europe (Marshall *et al.*, 2001). We find that the precipitation of this winter is lower than mean values of about three standard deviations. The structure of the 925 hPa geopotential height field confirms the influence of pressure dipole (Azores High, Iceland Low) on storm track direction (Figure 7).

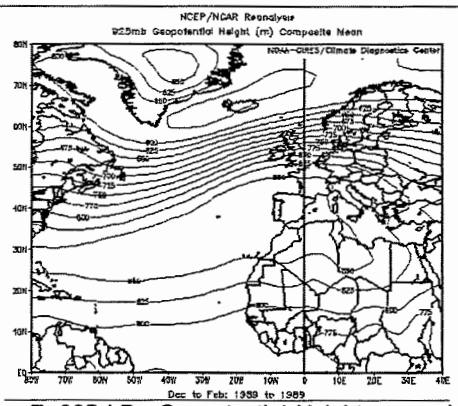

Figure 7. 925 hPa Geopotential Height mean during winter of 1989.

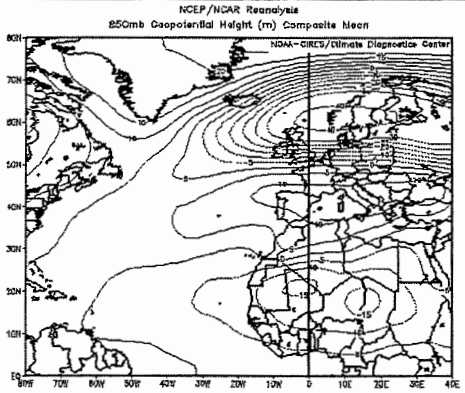

Figure 8. 850 hPa Geopotential Height composite anomaly for dry and wet summer.

During summer, the southward advection of anticyclonic air in the Atlas region is accompanied by subsidence and high pressure, reinforced by the Rossby waves generated by the African monsoon, influencing the summer precipitation in the Mediterranean region.

Figure 8 shows the pressure anomalies between dry and wet configurations. We find that there is a positive anomaly on Mediterranean basin, because of a wide and strong high pressure region over Azores, and a negative anomaly on west Africa, in connection with a reinforcement of the West African monsoon.

As an example we compared precipitation map over the Mediterranean (GPCP dataset)

with storm track and geopotential height at 850 hPa for summer 1997, showing a remarkable connection between those fields (Figure 9).

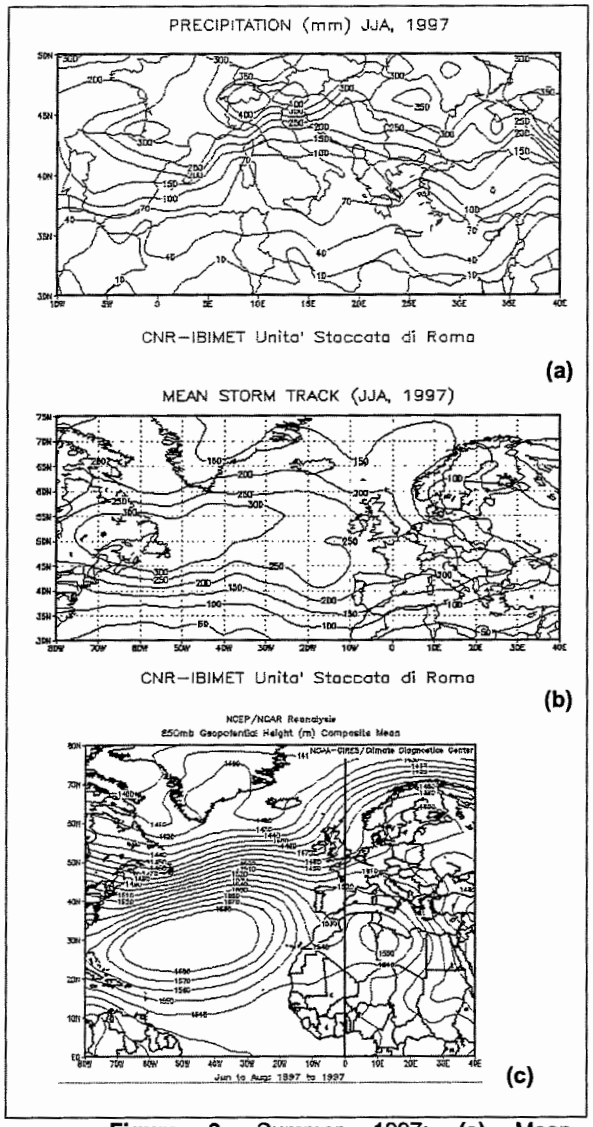

Figure 9. Summer 1997: **(a)** Mean Precipitation map (GPCP); **(b)** Storm track; **(c)** Average geopotential height at 850 hPa

4. CONCLUSIONS

We examined the cumulated precipitation from CRU-UEA dataset for the period 1900-1998 in the Mediterranean basin, and the West, East, and Central sub-basins separately. Precipitation trends are observed annually and seasonally, although they cannot be quantified due to the low resolution of dataset. Moreover, focusing on wet and dry events, we detected changes in frequency and/or intensity of rainfall. We found that the variability of the annual average over the whole basin, and in each sub-basin, is within one standard deviation. However, when examined seasonally, there is a trend towards drier autumns and wetter winters, while summer can be wetter or drier than the seasonal average, with a steeper trend in the last half century. The Central basin is generally wetter than the West basin, while the East basin is 20% drier than the West basin.

The Mediterranean basin is located in southern part of the westerly atmospheric flow, therefore during winter rainfall variability is strongly correlated to the NAO index: a strong positive or negative NAO tilts the storm tracks towards North or South Europe, respectively, affecting precipitation patterns. During summer, the rainfall in the East basin is related to the Asian monsoon, and rainfall in the West is related to the position and strength of the Azores anticyclone and to the West Africa monsoon.

Acknowledgements

Authors thank the Italian Space Agency for financial support under the ASI-MeditRain Project.

REFERENCES

Brunetti, M., M.Colacino, M.Maugeri, T.Nanni, 2001: Trends in the daily intensity of precipitation in Italy from 1951 to 1996. Int. J. Climatol., 21, 299-316.

Brunetti, M., M.Maugeri, F.Monti, T.Nanni, 2004: Changes in the daily precipitation frequency and distribution in Italy over the last 120 years. J. of Geophys. Res., 109, D05102.

Chang, E.K.M., S.Lee, K.L.Swanson, 2002: Storm track dynamics. J. Clim., 15, 2163-2183.

Conte M., A. Giufrida, S. Tedesco, 1989: Paper presented at Conference on Climate and Water, Vol. 1 (Publications of the Academy of Finland 9/89), pp. 121-137.

Hoskins B.J., K.Hodges, 2002: New perspectives on the Northern Hemisphere winter storm tracks. J. Atmos. Sci., 59, 1041-1061.

Marshall, J. *et al.*, 2001: North Atlantic climate variability: phenomena, impacts and mechanisms. Int. J. Climatol., 21, 1863-1898.

SATELLITE RAINFALL ESTIMATION USING A FEED FORWARD NEURAL NETWORK : IMPROVEMENTS AND LIMITATIONS

J.C. Berges[1] and F. Chopin[2]

[1]PRODIG Université Paris1, Paris, 75005 France
[2]Laboratoire de Météorologie Dynamique IPSL/CNRS Ecole Polytechnique, Palaiseau,91128 France

1. METHODOLOGY AND DATA SET

It is well known that improvement of satellite rainfall estimation, especially over land surfaces, is one of the main issues for environment monitoring. Famine early warning system, desert locust operations and flash flood monitoring require continuous rainfall information at a scale as fine as possible.

Most of satellite methods are using IR data or MW data (GPI, GSCAT) or a combination of datasets from different radiometers (AGPI, probability matching methods...). It has been shown that the synergy of information deduced from all the available sources improve the rainfall estimation. The exploitation of the data provided by SEVIRI on board Meteosat-8 satellite will increase the information dedicated to rainfall estimation. In addition, the Global Precipitation Mission (GPM) will in the future, supply more active and passive microwave data to estimate the precipitation rate. To take advantage of these new datasets, a robust method utilising a multi-source and multi-frequency algorithm is necessary.

Our experimental database combines geostationary satellites (Meteosat and GOES) and low orbiting satellite (TRMM) observations

Two geographical zones are considered: West Africa during the 1998, 1999 and 2000 rainfall periods and South America from December 10th 1998 to January 11th 1999. The TRMM data used is the 3G68Land dataset, which provides the outputs of three different algorithms on a 0.1° x 0.1° grid: the 2A12, the 2A25 and the 2B31. In this abstract, the results of the 2A25 algorithm which uses the precipitation radar of TRMM will be applied.

Corresponding author's address:
Jean Claude Berges, PRODIG Université Paris1, 191 rue saint Jacques 75005 Paris, France.
E-Mail : Jean-Claude.Berges@univ-paris1.fr
Franck Chopin, Laboratoire de Météorologie Dynamique IPSL/CNRS, Ecole Polytechnique, 91128 Palaiseau Cedex France
E-Mail : chopin@lmd.polytechnique.fr

2. NETWORK DESIGN AND IMPLEMENTATION

The general frame of geostationary based rainfall estimation method is a regression issue: to assess a rainfall intensity function on satellite data referring to an other data source. This data source is more directly related to rainfall but gets a poorer spatial and temporal coverage. Dealing with non linear regression technique a widespread method is a three layers feed forward neural network. Figure 2.1 is a graphical representation of such a network. Assuming that node transfer function get some basic properties, as the logistic function we use, and that the hidden layer is large enough, it has been demonstrated (Funahashi, 1989) that any continuous function could be approximated by such a network. Each link in this figure is a weight to be assessed. It clearly appears that the number of coefficients to be assessed is directly related to nodes number and is far more important than in linear regression. Once weights have been estimated on the learning dataset, in order to get differences between estimated and reference values as low as possible, this network can be computed on any geostationary image.

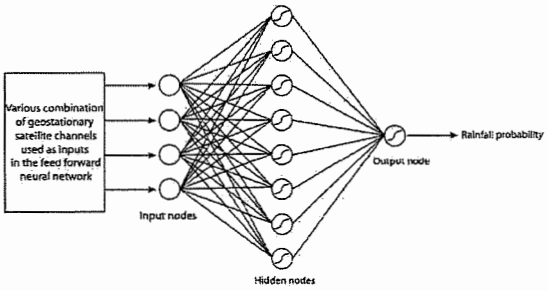

Figure 2.1: Feed forward network representation

Input nodes are composed from various satellites channel combinations. GOES estimator uses a four input nodes model (IR, WV, IR local variance and split window) whereas Meteosat estimator is based on a six input nodes model (IR, WV, IR local variance, WV local variance IR temporal difference and WV temporal difference). Output reference values are extracted from TRMM precipitation radar 3G68 product. We code rainfall presence as a binary value. Output of this network, values between 0 and 1, will be interpreted as rainfall probability. Usually, the hidden nodes number is a tradeoff between overtraining (getting too much) and accuracy (getting too few). As the records number in the learning dataset is much larger than input nodes number, the network architecture can be easily designed with enough hidden mode to get a smooth retrieval (15 for each dataset).

The weights assessment phase has been carried out using standard on line learning method. As we were using a learning set of co-registred geostationary and TRMM pixels the results look as erratic: slight changes in learning data base produced completely different weight sets. This behaviour is linked with spatial coherence image which makes neighbouring pixels usually correlated. As following elements from learning set did not compensate their random dispersion but reinforce their common patterns the last dataset image were grossly overweighed. To correct this artefact, input dataset has been scrambled and image contiguous pixels were separated when ingested in estimation algorithm. Avoiding use of batch learning method makes estimation phase faster.

This simple modification greatly enhances stability and estimations from similar datasets do not show global discrepancy. Anyway, as we are using non-linear methods, robustness is a serious issue. To enhance results stability we use a bagging method as proposed by Breimann (1994). Various estimations are carried out from slightly modified basic datasets and corresponding results are aggregated. The basic dataset is modified by random elimination and replacement on 5% of input records. The same reason than previously makes the random selection to operate on track basis and not on pixel basis. On our database, results quickly converge and a set of 5 random sampling looks as sufficient.

3. NN RESULTS

When the estimation is accomplished, the network has to be computed for every satellite slot on our interest period. Figure 3.1 is a resulting rainfall probability image (dark grey levels correspond to the higher probability).

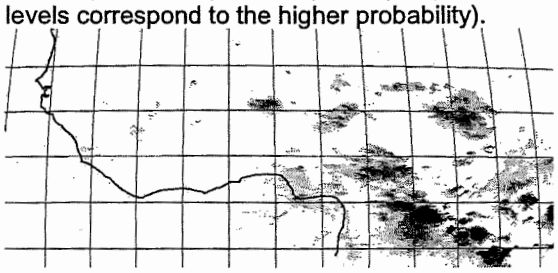

Figure 3.1 : Rainfall probability image over West Africa

Main patterns are close from those extracted in the corresponding 10.7µm channel. Network coefficients analysis shows that this input gets the more important weight. In order to assess neural network enhancement on a mono channel estimation procedure we computed stratified biases on GOES dataset.

Table 1 contains mean of absolute value biases on partition classes. Four partitions are considered: 1° latitude, 1° longitude, ½ hour within a day and day. They are compared with the best simple IR threshold procedure and IR alone probability matching. As it could be expected neural network performs always better than probability matching and probability matching is better than simple threshold.

	Day	½ Hour	1° Long.	1° Lat.
IR. Thr	0.034	0.058	0.036	0.024
Prob. Mat.	0.030	0.046	0.030	0.023
Neur. Net.	0.023	0.030	0.014	0.018

Table 1 : mean of absolute value biases on four partition classes for three procedures.

When applying neural network to classification procedure, a common practice is to balance input dataset. But, if we modify our learning set by records duplication to get the same number of rainy and non rainy inputs, we grossly over-estimate rainfall probability because mean rainfall probability would be close from 50%.

A direct neural rainfall estimation could be obtained extracting directly rain intensity from 3G68 grid cells to get reference output values. Unfortunately obtained estimations do not match well with input data as area of high rainfall

intensity do not appear. On most of resulting images higher intensity is below 1 mm/h.

An alternative method should be to estimate rainfall class instead of rainfall intensity. But process efficiency decreases quickly as rain threshold increases. On each dataset we have estimated probability to get rainfall intensity above a given value, then correlations between estimated and reference data have been computed. Figure 3.2 shows R^2 values on the two datasets. The same threshold effect can be observed on each curve.

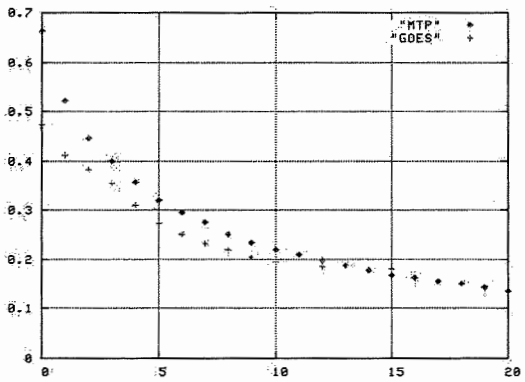

Figure 3.2 : R^2 values on the GOES and Meteosat datasets for different threshold (mm/h)

This behaviour may be linked to the nature of input nodes. Infrared channel images are more closely related to cloud properties than to rainfall intensity. Whereas deep convection areas can be fairly well identified on multispectral imagery which is corroborated by radiative transfer model results, the relationship with rainfall intensity is only statistically based. Although on coarse scale rainfall amount and rainfall duration are obviously correlated, there is no evidence of such a link at the event scale.

An other difficulty arises from the actual rainfall intensity distribution. On GOES dataset, whereas 13% of pixels are indicated as rainy by TRMM/PR, only 5% are associated with rainfall intensity above 1mm/h and 0.8% with intensity above 5 mm/h. The rainfall intensity distribution of Meteosat dataset is very similar as it appears from figure 3.3. These figures are close to a stretched exponential distribution which could suggest an unstable mean estimator. This statistical property could explain the best performances of estimation methods based on actual data compared with those based on climatology. The very same distribution explains why we don't get any benefit from restricting rainfall intensity estimation to rainy pixels. It has to be quoted that these distributions differ from those obtained from ground radar analysis (Nzeukou, 2002) which are log-normal. This discrepancy could be explained by an instrument bias, the strong attenuation by water droplets in horizontal propagation, and by a sampling effect.

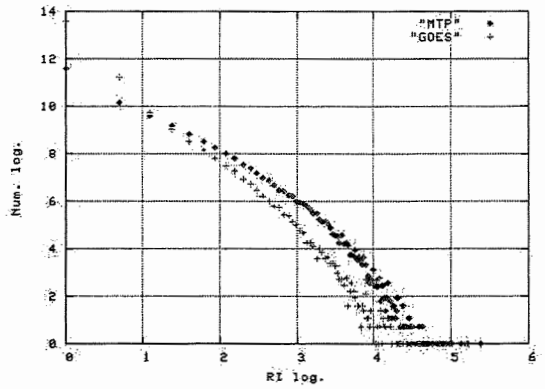

Figure 3.3 : log scale rainfall distribution with GOES and Meteosat datasets

4. TOWARD AN OPERATIONAL PROCEDURE

Because of these limitations linked with rainfall distribution, we propose a two step procedure: first to assess rainfall probability by a feed forward neural network as described above, then to use a probability matching formula for rainfall intensity estimation.

$$I_e = I_p \cdot P_r \qquad (4.1)$$

The estimated rainfall intensity I_e is the product between a potential rainfall intensity I_p and the rainfall probability P_r. Actual computation of this potential intensity, is based on an other estimator of actual rainfall intensity. This estimator is more directly related to rainfall but does not allow a follow up of phenomena as fine as geostationary satellite images. Raingauge datasets, microwave satellites based information, or gridded synthesis data like GPCP will be considered as rainfall intensity estimator.

From the previous relation we define a downscaling step in time and space. This step allows to evaluate the potential rainfall intensity in a cell grid area for a stated period. For a cell A and a period T, the downscaling formula used is :

$$\iint_{AT} ms(a,t) I_r(a,t)\,da\,dt = I_p(A,T) \cdot \iint_{AT} ms(a,t) P_r(a,t)\,da\,dt \qquad (4.2)$$

ms is the data presence mask. It differs according to the dataset used as the reference rainfall intensity I_r in the neighbourhood A during the period T. I_p is the potential rainfall intensity and P_r represents the rainfall probability. This formula is similar to the one defined by Nzeukou et al. (2004).

The 4.2 formula allows to obtain an estimated rainfall intensity with the geostationary image resolution in space using a potential intensity calculated on a stated period. The estimated rainfall at time *t* and at the position *a* can be computed with the upscaling formula:

$$I_e(a,t) = I_p(A,T) \cdot P_r(a,t) \qquad (4.3)$$

From previous formula rainfall amount on any period and area can be computed from integration at the scale of geostationary data.

A key issue in this method is setting the integration area and period (*A* and *T*) and this is mainly dependent on reference dataset type. As stated before, datatasets used as rainfall intensity estimators will be continuous gridded or instantaneous. Grid data gets a continuous coverage but at a much coarser resolution than geostationary. This coarse resolution acts as a lower boundary for integration box size. Instantaneous data extracted from low orbiting satellite can get a spatial resolution close from geostationary but operates a sampling in time and space. For these data, box integration size depends both on sensor coverage and on actual frequency of rainfall events. Setting box size is a tradeoff, too small would not get significant estimation and too large would result in an excessive smoothing. We propose as an heuristic to select a neighbourhood size large enough in any cells. Figure 4.1 represents the rainfall accumulation over Brazil from December 10th 1998 to January 11th 1999 (darker grey levels correspond to the higher rainfall intensity).

It has to be quoted that, even with gridded data, integration area have to be a sliding window. A fixed box would produce boundary artefacts annihilating downscaling benefits.

5. CONCLUSION

Splitting estimation algorithm in two steps avoids introduction of local correction parameters to match with high rainfall intensity patterns. Upscaling rainfall on geostationary resolution allows to match with any final product grid size.

The proposed method is a frame to design Meteosat–8 based rainfall estimator. It can be tuned according to operational environment which is defined by expected accuracy and available input data on time.

References

Breimann L., 1994 : Bagging predictors, Tech. rep., 421,Dept. of Stat., University of California, Berkeley.

Funahashi K. I., 1989 : On the approximate realisation of continuous mapping by neural networks, Neural Networks, 2,182-192.

Nzeukou A. and Sauvageot H., 2002 : Distribution of rainfall parameters near the coast of France and Senegal, J. Appl. Meteor., 41, 69-82.

Nzeukou A., and Sauvageot H., 2004: Raindrop size distribution and radar parameters at Cap Verde, J. Appl. Meteor., 43, 90-105.

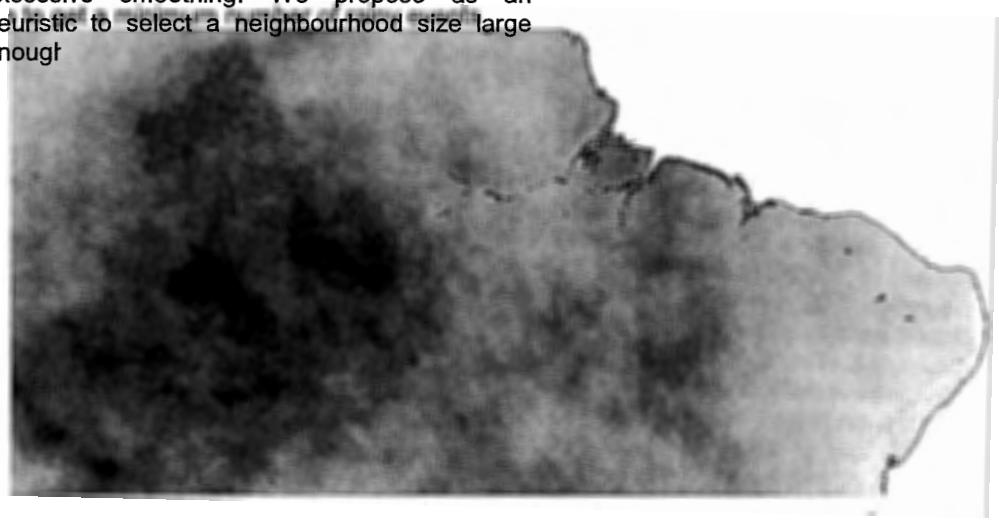

Figure 4.1 : raining accumulation over Brazil from December 10th 1998 to January 11th 1999

NORTH ATLANTIC OSCILLATION AND RAINFALL IN CONTINENTAL SPAIN

Amaya Castro[1], Luisa Miguélez[1], Vera Lucia Fonseca[2] and Roberto Fraile[1]

[1] Departamento de Física. Universidad de León. 24071, Spain
[2] Universidade Caxias do Sul. Caxias do Sul, Brazil

1 INTRODUCTION

The study of the North Atlantic Oscillation (NAO) dates back to the beginning of the 20th century, when Walker observed the pressure oscillations in each hemisphere and suggested the existence of the two most important oscillations known today. Over time, the southern oscillation has received more attention, probably due to the dramatic consequences of El Niño, a phenomenon associated to this oscillation. However, in the past few years there has been a considerable increase in the number of studies devoted to the NAO. Its consequences are certainly less spectacular than those of the southern oscillation, but they are of more interest in our area.

The strong positive trend of the NAO detected over the past 30 years has led to numerous studies. The most outstanding anomalies were registered from the winter in 1989 (Hurrell 1995; Walsh 1996; Thompson y Wallace 1998; Watanabe y Nitta 1999), when positive values in the NAO index were then recorded.

One of the climatic consequences observed in the NAO are regional changes in the precipitation models (Hurrell 1995; Hurrell y van Loon 1997; Dai et al. 1997).

Current studies on global climatic change carried out by the IPCC (2001) show that during the 20th century the average annual rainfall has increased between 7% and 12% in zones between 30°N and 85°N, while it tends to decrease in latitudes around 30°N. Bearing in mind these data, the questions that arise are the following: is the NAO the cause of these changes in the rainfall in Western Europe? Is there a way to forecast the total amount of rain using the NAO index?

The aim of this paper is to analyze the influence of the NAO on the rainfall regime in Spain. Linear correlations have been established between monthly rainfall data and monthly NAO indices for different months. Several combinations have been considered. Similar correlations have been established with seasonal rainfall data and seasonal NAO values, again in various combinations.

Author's address: Roberto Fraile, Departamento de Física, Facultad de CC Biológicas y Ambientales, Univ. de León, 24071 León, Spain; E-Mail: robertofraile@unileon.es

2 DATABASES

2.1 Rainfall

This study has been carried out in the Spanish part of the Iberian Peninsula, i.e. continental Spain (Fig. 1). The data of monthly rainfall from 325 meteorological stations were used (a density of one rainfall station per 2000 km²). The data were in electronic format and were provided by the National Institute for Meteorology in Spain for the period between 1961 and 1998.

Fonseca (2002) has described in detail the procedure followed to complete the precipitation data in those stations where some of these data were missing. It has also been demonstrated that the rainfall series of the stations used for this paper were homogeneous (Fonseca, 2002).

Apart from the monthly rainfall series, the four seasonal series were also added (spring, summer, fall and winter), as well as the annual rainfall series. Thus, seventeen rainfall series were analyzed for each meteorological station (12 monthly, 4 seasonal and 1 annual series). All in all, 5,525 series were used for this study.

2.2 North Atlantic Oscillation

The NAO index is traditionally defined as the normalized pressure difference at sea level between a station on the Azores and one on Iceland. This index takes on different values depending on the stations used to calculate it. In this case it has been calculated using the data from Ponta Delgada and Stykkisholmur.

Fig. 1. Location of the 325 meteorological stations used.

The necessary data to establish the NAO index have been kindly provided by James W. Hurrell (*Climate Analysis Section* from the *National Center for Atmospheric Research*, in Boulder, Colorado). These data were also used to establish the average seasonal and annual NAO. The units used for the NAO index are hPa.

3 METHODOLOGY

Two procedures were followed to obtain the results: on the one hand, the linear regressions between the rainfall series and the NAO were studied; and on the other hand, contour maps were drawn for every individual study, in order to represent the spatial correlations and facilitate the interpretation of the results.

3.1 Linear regressions between rainfall series and NAO

Linear regressions of four types were carried out depending on the number of variables involved:

- $y = ax + b$ between, for example, a monthly NAO *(variable x)* and the rainfall during that month *(variable y)*.
- $z = ax + by + c$ between, for example, the NAO for two consecutive seasons (variables x e y) and the rainfall in the following season (variable z);
- $w = ax + by + cz + d$ between, for example, the NAO for three consecutive seasons (variables x, y, z) and the rainfall in the following season (*variable w*).
- $v = ax + by + cz + dw + e$ between the NAO for two consecutive seasons (variables x, y) and the rainfalls of those two consecutive seasons (variables z, w) in order to forecast the rainfall in the following season (variable v).

Once the constants that define the linear equation have been calculated (*a, b, c* or *d*) what we have is, depending on the case, a sort of 'rainfall forecast' for the following month, season or year, if the NAO values are known beforehand (and for the rainfall in previous months or seasons, if they were also taken into account).

In each linear regression, simple or multiple, the correlation coefficient *R* was calculated with an explained variance of R^2. The significant correlations for $\alpha = 0.05$ were selected and the meteorological stations that fulfill this condition were represented on maps.

3.2 Spatial distribution of rainfall – NAO correlations

Areas with similar R^2 have been represented on maps drawing contour lines with the same correlation between rainfall and NAO. These lines were drawn employing the correlation data with the temporal series from every one of the 325 meteorological stations. The Kriging interpolation method has been used to draw the maps (Isaaks and Srivastava, 1989). The lines in Fig 2 and the following figures delimit the geographical areas affected in a similar way by the North Atlantic Oscillation in their monthly, seasonal or annual rainfalls. The sections below describe the most important results found in continental Spain with respect to the relationship between each of the 17 temporal series analyzed and the NAO index from different points of view.

4 RESULTS

Only the results for those linear correlations with statistically significant results will be commented upon.

4.1 Correlation between monthly NAO and monthly rainfall

In October and November (top line in Fig. 2) there is a statistically significant correlation in wide areas of Spain.

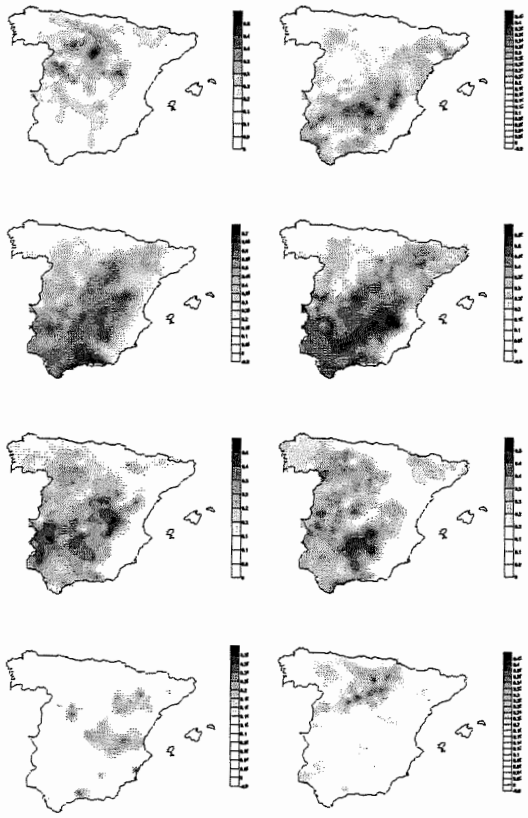

Fig. 2 From left to right and from top to bottom, spatial distribution of the correlation coefficients squared (R^2) between monthly NAO and the corresponding monthly rainfalls from October (top left-hand corner) to May (bottom right-hand corner).

Nevertheless, in October there is a considerable lack of correlation in the West and part of the south of the Iberian Peninsula. In November there is no significant correlation in the western coast and in the north of the Peninsula.

It was noted that the zones with a good correlation grow monthly until they reach a maximum area in the winter months: December, January, February and March. It is in these months that the NAO effects can be most clearly detected in the north-Atlantic coasts. Therefore, it comes as no surprise that this influence is especially noticeable in Spain during the winter months. It is noteworthy that there is no significant correlation in any of the Spanish coasts (see 2nd and 3rd lines in Fig. 2).

A significant correlation has also been found in the spring months, but the areas affected by the NAO are much smaller. No significant trend can be detected in the summer.

4.2 Correlation between seasonal NAO and seasonal rainfall

The results show that the NAO indices in winter and spring correlate very well (although with a negative correlation) with the rainfalls in those two seasons. This good correlation can be found in the whole of the Iberian Peninsula except for the eastern coast and the far northern coast. However, this does not happen in summer and fall.

4.3 Correlation between annual NAO and annual rainfall

It has been noted that the annual rainfall is significantly correlated with the annual NAO index in areas located in the southern plateau of the Peninsula. There is also a significant correlation in some isolated points in the north.

4.4 Correlation between seasonal NAO and rainfall in the following season

The authors considered the possibility of forecasting the rainfall recorded in a particular season according to the NAO index for the preceding season. However, no clear relationship between these two variables was found, indicating that the NAO index is not a good rainfall forecaster in this sense.

4.5 Correlation between the NAO of two consecutive seasons and the rainfall in the following season

Forecasting the rainfall of a particular season by using the NAO indices of the two previous seasons is only acceptable in the case of fall rain by using NAO indices for spring and summer. However, this was only found to be applicable to a small part of the Iberian Peninsula: a strip less than 300 km wide going from the Central Pyrenees to the north of Extremadura.

4.6 Correlation between the NAO indices of three consecutive seasons and the rainfall in the following season

The correlations of the NAO indices of three consecutive seasons to forecast the rainfall in the following season are not good in most of the meteorological stations in Spain. There are only significant correlations in a few small areas. This means that the NAO indices of the three previous seasons do not generally help in forecasting the rainfall in the following season.

4.7 Correlation between monthly NAO and the rainfall in the following month

As in the case of seasons, no significant correlations were found between the monthly NAO index and the rainfall in the next month. This means that the monthly rain forecast by using the NAO index of the previous month is not useful, except in the months of February, March, November and January in small isolated zones.

Anyway, it is again the case that the best correlations occur in the winter months.

4.8 Correlation between monthly rainfall + monthly NAO and the rainfall of the following month

The correlations based on monthly rainfall plus the monthly NAO index are useful to forecast the rainfall of the next month in several months of the year, especially in January, February and March. (Fig. 3).

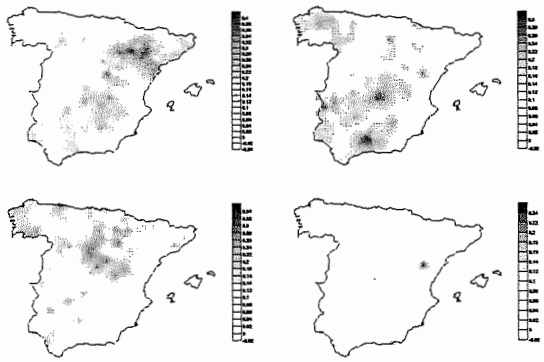

Fig. 3 Spatial distribution of the correlation coefficients squared (R^2) between monthly rainfall plus monthly NAO and the rainfall of the following month. From left to right and from top to bottom, the figures illustrate the correlations between rainfall in December and NAO in December with the rainfall in January, and so on. The last correlation refers to March and April.

The correlations are not good in the spring and summer months, though. The reason for this may lie in the fact that most of the rainfall in those months, particularly in the summer, is of convective origin. In consequence, there is no correlation between the formation of storms and the NAO in those months.

4.9 Correlation between seasonal rainfall + seasonal NAO and the rainfall in the following season

In general, there are no significant correlations in enough places to produce a reliable forecast of the rainfall in a particular season.

4.10 Correlation between rainfall for two seasons + NAO for two seasons and rainfall in the following season

The forecasts of monthly rainfalls based on NAO indices plus rainfalls for the two previous seasons are good, especially in the case of fall precipitation (Fig. 4).

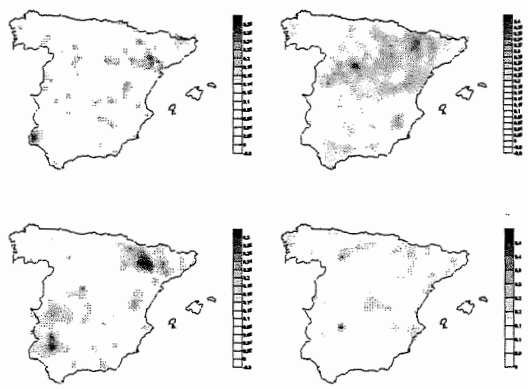

Fig. 4 Spatial distribution of the correlation coefficients squared (R^2) between the rainfall in two consecutive seasons plus the NAO indices in those seasons and the rainfall in the following season. From left to right and from top to bottom, the figures represent the correlation of winter and spring rainfalls plus winter and spring NAO indices with summer rainfalls; the correlation of spring and summer rainfalls plus spring and summer NAO indices with fall rainfalls; the correlation of summer and fall rainfalls plus summer and fall NAO indices with winter rainfalls; and finally, the bottom right-hand figure represents the correlation of fall and winter rainfalls plus fall and winter NAO indices with spring rainfalls.

5 CONCLUSIONS

- The NAO considerably affects rainfalls in the Iberian Peninsula, especially in winter and summer. It affects annual rainfalls as well.
- There are generally few possibilities of forecasting monthly rainfalls with linear models in Spain using the NAO index of the previous month.
- It is very difficult to forecast the evolution of the NAO index. Nevertheless, the NAO index may be used, together with data from recent rainfalls, to suggest reliable forecasts of the amount of seasonal precipitation, especially fall precipitation.

6 ACKNOWLEGEMENTS

The authors are grateful to Dra. Noelia Ramón for translating the paper into English and to Dr. James W. Hurrell for the NAO index data. The study was supported by the Consejería de Educación y Cultura, Junta de Castilla y León (Grant LE67/04).

7 REFERENCES

Dai, A., I.Y. Fung, and A.D. Del Genio, 1997: Surface observed global land precipitation variations during 1900-88. J. Climate, 10, 2943-2962.

Fonseca, V.L., 2002: Análise especial e temporal das tendencies das precipitacoes na Espanha Peninsular. Ph. D. Thesis. Universidad de León, 342 pp.

Hurrell, J.W., 1995. Decadal trends in the North Atlantic Oscillation: regional temperatures and precipitation. Science, **269**, 676-679.

Hurrell, J.W. and H. van Loon, 1997: Decadal variations in climate associated with the North Atlantic Oscillation. In: Climate Change. Proc. Int. Workshop on Climatic Change at High Elevation Sites, Wengen, Switzerland.

IPCC. 2001: Climate Change 2001: The Scientific Basis. Contribution of Working Group I to the Third Assessment Report of the Intergovernmental Pannel on Climate Change [Houghton, J.T., Y. Ding, D.J. Griggs, M. Noguer, P.J. van der Linden, X. Dai, K. Maskell, and C.A. Johnson (eds.)]. Cambridge University Press, Cambridge, United Kingdom and New York, NY, USA, 881 pp.

Thompson D.W.J. and J.M. Wallace, 1998: The Arctic Oscillation signature in the wintertime geopotential height and temperature fields. Geophys. Res. Lett. **25**, 1297-1300.

Isaaks, E.H. and R.M. Srivastava, 1989: An introduction to Applied Geostatistics. Oxford University Press, NY, 561 pp.

Walsh, J.E. 1996. Recent decrease of sea level pressure in the central Arctic. J. Climate 9, 480-486.

Watanabe, M. and T. Nitta, 1999: Decadal changes in the atmospheric circulation and associated surface climate variations in the Northern Hemisphere winter. J. Climate, 12, 494-510.

CONTRIBUTION OF CHANGES IN SEA SURFACE TEMPERATURE AND AEROSOL LOADING TO THE DECREASING PRECIPITATION TREND IN SOUTHERN CHINA

Yanjie Cheng[1], Ulrike Lohmann[1], Junhua Zhang[1], Yunfeng Luo[2], Zuoting Liu[3], Glen Lesins[1]

[1] Department of Physics and Atmospheric Science, Dalhousie University, Halifax, NS, B3H 3J5, Canada.

[2] National Natural Science Foundation of China, Beijing, China

[3] Guangdong Meteorological Administration, Guangzhou, China

1. INTRODUCTION

During the last few decades, heavy flooding has frequently occurred in Eastern and Southern China during summer. Recent studies attributed this trend to the increasing aerosol loading in China (Menon et al., 2002; Xu, 2001). Climate model simulations suggest that flooding in Southern China can be caused by absorbing aerosols, such as black carbon, which absorbs sunlight, heats the air, and hence alters the atmospheric stability and vertical motion, leading to more convective precipitation in Southern China (Hansen et al., 2000; Jacobson, 2001; Menon et al. 2002).

The SST is also important for regional precipitation variations. In early summer, after the onset of the South China Sea monsoon in mid-May, Southern China enters its main rainy season. The precipitation reaches its maximum during May and June every year. Previous studies found that wet anomalies usually appear in Southern China during El Niño episodes (Dai and Wigley, 2000). Climate modeling studies recently showed that the cold SST in the East Pacific Ocean together with above-normal SST in the Indian and West Pacific Ocean caused mid-latitude droughts in the Northern Hemisphere in 1998-2002 (Hoering and Kumar, 2003).

Although most regions in Southern and Eastern China suffer from heavy flooding in the summer, a region near the South China Sea experienced a drought trend in early summer during the last 40 years (Fig. 1). In this study, we will investigate the role of SST versus aerosol loading for the regional climate change with emphasis on the drought region in Southern China in early summer.

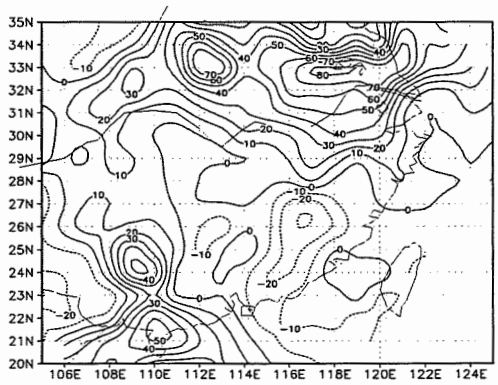

Fig. 1 Normalized precipitation trend [%] from the 1960s to the 1990s in Eastern and Southern China in the early summer (May and June) {Calculated as (1990s-1960s) /1960s×100%}.

Corresponding author's address: Yanjie Cheng, Department of Physics and Atmospheric Science, Dalhousie University, Halifax, NS, B3H 3J5, Canada; Email: ycheng2@dal.ca.

2. DATA

- Monthly precipitation data (1961.1- 2000.12) observed at 75 stations from the Chinese National Meteorology Center.
- Monthly low level cloud cover (LCC) and visibility data observed from 35 surface observation stations
- Annual mean aerosol optical depth (AOD) data, 4 stations in Southern China 1961-1990 from surface solar radiation observations (Luo et al., 2001).
- Monthly global sea surface temperature data from the extended reconstructed COADS data (Smith and Reynolds, 2002),
- Air temperature, wind and specific humidity, and 500-hPa geopotential height reanalysis data from the (NCEP/NCAR) (Kalnay et al., 1996)

3. A POSSIBLE EFFECT OF AEROSOLS ON LOW LEVEL CLOUD COVER AND PRECIPITATION

In China, 80% of power generation originates from coal combustion. Therefore, sulfur dioxide emissions have significantly increased in the last 20 years (Xu, 2001). This trend is reflected in an increase in AOD accompanied by a decrease in visibility in this region as shown in Fig. 2a. AOD increased by about 40% in the last 30 years. In contrast, visibility decreased by about 50% in the last 40 years. AOD and visibility are negatively correlated from the 1960s to the 1990s with a correlation coefficient r=-0.72, which is significant at the 99.9% confidence level. Because AOD data is only available at 4 stations in this region, we use visibility as a surrogate for AOD in this study. Fig. 2b shows that in early summer visibility and LCC are negatively correlated with LCC having increased over the last 40 years. The spatial distribution of these trends is shown in Fig. 3a and Fig. 3b.

AOD and LCC are increasing, but visibility and precipitation are decreasing in this region, suggesting that the aerosol indirect effect may be an important factor in this region. That is, increasing aerosol loading may increase the cloud droplet number concentration and hence decrease the cloud droplet effective radius in liquid water clouds. This will act to suppress the warm rain formation in polluted clouds and increase their lifetime as discussed in studies by Lohmann and Lesins (2002), Kaufman et al. (1997) and Ramanathan et al. (2001). However, dynamical factors may contribute as well and this will be discussed next.

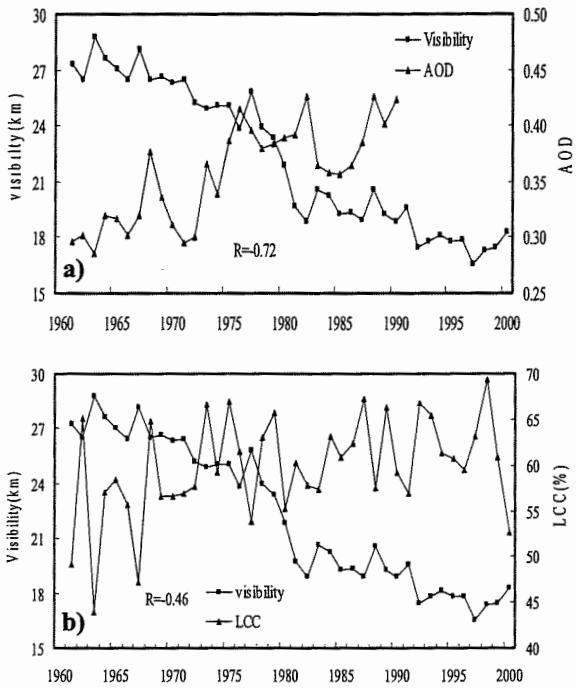

Fig. 2 a) Visibility and AOD annual variations in Southern China (no AOD data are available after 1990); b) low level cloud cover and visibility variations from all stations in early summer (May and June) during 1961-2000.

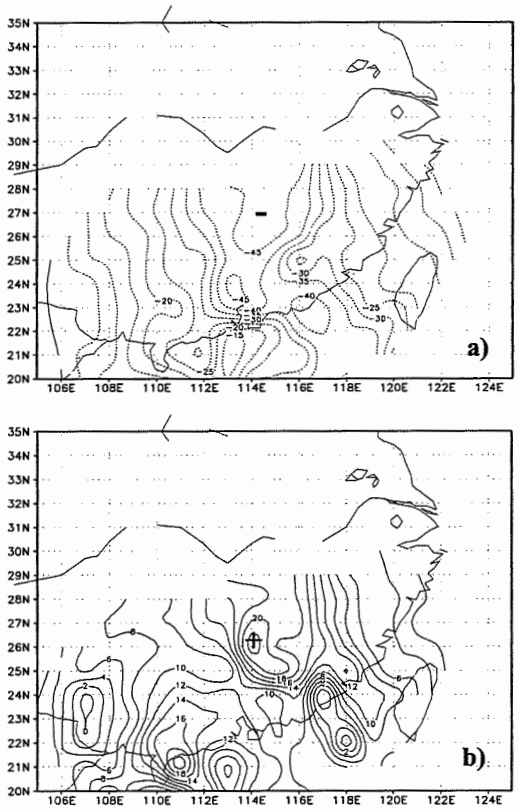

Fig. 3 a) Change in visibility (%) and b) LCC (%) in Southern China in early summer, calculated as (1990s-1960s)/1960s×100%.

4. EFFECT OF SST ON PRECIPITATION AND LOW LEVEL CLOUD COVER

The SST in the South China Sea and in the northeastern part of the Indian Ocean has increased by about 0.2-0.4°C in early summer during the last 40 years. A similar spatial distribution is reflected in the 1000-hPa air temperature field over the ocean, with a strong cooling region located over the continent from 70-120°E, 35-45°N. It is not exactly clear what caused this cooling, but the increase in frequency and strengths of sandstorms in spring and early summer in the 1990s may be one possible reason. Angell (1981) demonstrated that during warm SST conditions the subtropical high in the Northern Hemisphere strengthens and its center moves southward. During the last 40 years, the west Pacific subtropical high (WPSH) has strengthened and extended further westward over the continent in the 1990s. Similar result was found by Nan & Li (2003). The 850-hPa wind vector and general circulation have adjusted to the weakened temperature contrast between the ocean and the continent. This weakened the southwesterly monsoon circulation over the South China Sea and Southeastern China. Also, the convergence region associated with the main rain belt in the drought region of Southern China weakened from the 1960s to the 1990s. Instead a divergence anomaly region has appeared in the east of the drought region in the Southeastern China. In addition, the specific humidity decreased at levels below 800-hPa over the center of the drought region, because less moisture was transported into this region from the ocean during southern China's main rainy season in early summer.

Because less moisture is transported to Southern China as the SST warmed and the specific humidity decreased below 800-hPa in the last 40 years, LCC should have decreased instead of increased in Southern China. Therefore, the increase in LCC in the drought region suggests that increasing aerosols levels may have reduced the precipitation efficiency of low level clouds (the indirect aerosol lifetime effect), thereby causing the increase in LCC. However, the temperature in this region increased more above 950-hPa than below resulting in a stabler boundary layer. This promotes longer-lived, less precipitating stratus clouds instead of shorter-lived, more precipitating convective clouds. Thus, if this change in temperature originates from

investigate role of SST, aerosol loading and how about observations

of the static stability in assessing the amount of cloud cover — have to assess what to look

dynamical changes alone, then aerosols may not play a role.

On the other hand, what has caused the precipitation to increase in Eastern China north of 28°N as shown in Fig. 1? This part of China is located in the northern part of the WPSH. Although the specific humidity in this region decreased here as well during the last 40 years, the strengthened convergence anomaly in this region with moisture flux from south over the drought region led to more precipitation in early summer.

ACKNOWLEDGEMENTS

The authors thank Moses Iziomon, Peter Klages and Maheswar Rupakheti at Dalhousie University for their helpful comments and suggestions. This work is supported by the Modelling Clouds and Climate (MOC2) program funded by the Canadian Foundation for Climate and Atmospheric Sciences (CFCAS) and the Natural Sciences and Engineering Research Council (NSERC) and the Meteorological Service of Canada (MSC).

REFERENCES

Angell, J. K., 1981: Comparison of variation in atmospheric quantities with sea surface temperature variations in the equatorial eastern Pacific, *Mon. Wea. Rev.*,109, 230-243.

Dai, A. T. and M. L. Wigley, 2000: Global patterns of ENSO-induced precipitation, *Geophy. Res. Letters*, 27, 1283-1286.

Hansen, J., M. Sato, R. Ruedy, A. Lacis and V. Oinas, 2000: Global warming in the twenty-first century: An alternative scenario. *Proc. Natl. Acad. Sci.*, USA 97, 9875-9880.

Hoering, M., and A. Kumar, 2003: The Perfect Ocean for Drought, *Science*, 299, 691-694.

Jacobson, M. Z., 2001: Strong radiative heating due to the mixing state of black carbon in atmospheric aerosols, *Nature*, 409, 695-697.

Kalnay, E. et al., 1996: The NCEP/NCAR 40-Year Reanalysis Project. *Bull. Amer. Meteor. Soc.*, 76, 437-471.

Kaufman, Y. J., and R. S. Fraser, 1997: The effect of smoke particles on clouds and climate forcing, *Science*, 277, 1636-1639.

Lohmann, U. and G. Lesins, 2002: Stronger constraints on the anthropogenic indirect aerosol effect, *Science*, 298, 1012-1016.

Luo, Y., D. Lu, X. Zhou, W. Li and Q. He, 2001: Characteristics of the spatial distribution and yearly variation of aerosol optical depth over China in the last 30 years, *J. Geophys. Res.*, 106, 14501-14513.

Nan S., J. Li, 2003, The relationship between the summer precipitation in the Yangtze River valley and the boreal spring Southern Hemisphere annular mode, *Geophy. Res. Letters*, 30, 2266-2269.

Menon, S., J. Hansen, L. Nazarenko and Y. Luo, 2002: Climate Effects of Black Carbon Aerosols in China and Indian, *Science*, 297, 2250-2253.

Ramanathan, V., P. J. Crutzen, J. T. Kieh, D. Rosenfeld, 2001: Aerosols, Climate, and the Hydrological Cycle, *Science*, 294, 2119-2124.

Smith, T.M. and R. W. Reynolds, 2002: Extended reconstruction of global seas surface temperatures based on COADS data 1854-1997, *J. Climate*, Submitted.

Xu, Q., 2001: Abrupt change of the mid-summer climate in central east China by the influence of atmospheric pollution, *Atmos. Environ.*, 35, 5029-5040.

ANALYSIS OF HEAVY RAINFALL IN VERY HIGH TEMPORAL RESOLUTION IN ITALY DURING LAST 10 YEARS

Edmondo Di Giuseppe Domenico Vento Stanislao Esposito Chiara Epifani

Ufficio Centrale di Ecologia Agraria, Rome, 00186, Italy

1. INTRODUCTION

Data survey's methods determine somehow scientific analyses. The extending spread of new technological techniques over meteorological stations has made it possible to have high temporal resolution data and to collect them automatically.

This paper attempts to characterise Italy's precipitation framework according to 10 minutes data resolution. Moreover, we investigate heavy rainfalls' trend. By this purpose, time series data of precipitation surveyed by RAN (*Rete Agrometeorologica Nazionale)* have been used. Available data sets are from 1993 to 2003 and it is necessary to underline that the shortness of the period won't permit to do a rigorous statistical analysis, nevertheless it provides an important information in order to explain climatological features, especially extreme events and, above all, it concerns high temporal resolution data extended to the whole country.

2. DATA AND METHODS

The RAN' s network is composed at present by 33 automatic stations and it is managed by *Sistema Informativo Agricolo Nazionale (SIAN)* and by *Ufficio Centrale di Ecologia Agraria* (UCEA). We take 20 stations which can provide almost complete time series data of precipitation from at least 1993 to 2003. These stations are located all over Italy (fig. 1).

Data have been grouped into 3 different time-lag: 10, 60 and 180 minutes. Following analyses have been performed on each of them.

At first step, we consider average features of precipitation phenomenology examining monthly average's trend (total of monthly precipitation to number of rainy days per month).

Corresponding author's address:
Edmondo Di Giuseppe, Ufficio Centrale di Ecologia Agraria, via del Caravita 7/A, 00146, Rome, Italy. E-Mail:edigiuseppe@ucea.it

Fig. 1 20 stations of automatic of RAN

As an example, we graphed *Monsampolo*' s data in 10 minutes time-lag (fig. 2). For the sake of simplicity, we define:

- Prec(h) =precipitation data referred to *h* (time-lag resolution: 10, 60 or 180 minutes)
- n =# of available rainy (>1mm) h data
- Prec(i,j) = $\sum_h prec(h)_{i,j}$

  i =month, *j* =year

As a consequence, we have:

1. monthly average of precipitation

$$\text{MAP} = \frac{\sum_h prec(h)_{i,j}}{n_h(i,j)}$$

2. average of monthly precipitation

$$\text{AMP} = \frac{\sum_j prec(h)_i}{\sum_j n_h(i)}$$

3. average of precipitation's monthly cumulated quantity

$$AMC=\frac{\sum_j prec(h)_i}{\sum_j i}$$

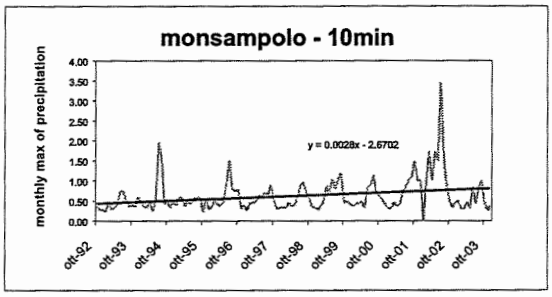

Fig. 2 Monthly averages of precipitation's trend (MAP)

Similarly, we calculate precipitation's average for all the 12 months over time series' length, so that we have January's mean of precipitation over 1993 to 2003, February's mean of precipitation over 1993 to 2003, etc. Having distributions for 10, 60 and 180 minutes scale, we normalise obtained values in order to compare them to average value of monthly cumulated quantity of precipitation (AMC) (fig. 3).

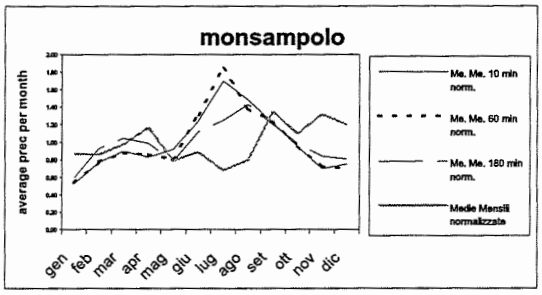

Fig. 3 Average of monthly precipitation (AMP)

At second step, we investigate heavy rain that usually constitutes a significantly smaller fraction of the precipitation events and totals in extratropical regions. A number of 250 data has been used as threshold which determines events to be included in a 90th and 98th percentile range for each station and in order to make possible comparisons between stations and between time's scales. We distribute those "rare" events over time series' length (fig. 4).

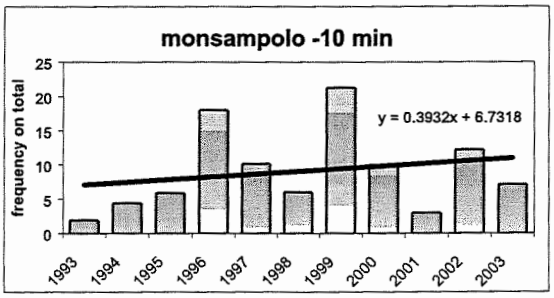

Fig. 4 Extreme events' distribution (98th percentile)

Linear regression has been run to model heavy precipitation events' trend both for frequency and yearly maximum of precipitation (fig. 5).

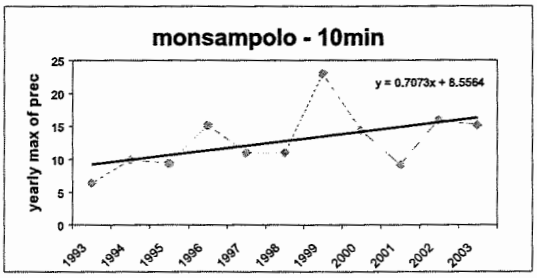

Fig. 5 Yearly maximum of precipitation's trend

Mann-Kendall's statistic test has also carried out to verify trend's significativity. As we would have expected, test doesn't have a positive confirm, having very short time length data sets. We shall leave out other details for the sake of brevity, but if we refer to further factors, as well as comparing trends over the whole area, we shall have general indications about the phenomenology under consideration.

A third part of this work considers probability distribution of 180 minutes' extreme events conditioned by 10 minutes'probability distribution.

3. RESULTS

In general, results show an intrinsic variability basically due to the shortness of data sets' time length and to climatological differences of places where automatic stations are located. Nevertheless, it is worth noticing some common features. The principal results are as follows:

1) precipitation's monthly averages (AMP) have a similar distribution for short time-lags (10 and 60) and meaningfully different compared to average value of precipitation's monthly cumulated quantity (AMC) (fig. 3). In

particular, values are higher during summer when short and heavy rainfall are supposed to be originated from changeable phenomena. Furthermore, 180 minutes extreme events' distribution follows the general climatic course according to its peculiarity of precipitation's phenomenology.

2) higher average values of precipitation seem to be gathered at the last part of the period showing an increasing trend even tough it is not quite solid. This is true for the most of the stations.
3) heavy rainfalls' trend reveal increases both in frequency and yearly maximum values. Obviously, the sample analysed can't provide evidence for a statistically significant increase, besides these results haven't a spatial meaning because of the low number of stations under consideration. Nevertheless, we cannot ignore that 2/3 of stations show an increase.
4) significant relation between 10, 60 and 180 minutes scales is showed by observations of extreme events. More work is needed to establish this entirely, but it appears that empirical analyses seem to support heavy rainfall' s persistence from 10 minutes until 3 hours.

4. SUMMARY

Of particular interest, from both practical and theoretical considerations, are the analyses of precipitation change. This work can be considered as a small contribution to this study, in particular for extreme events. We also think it might be interesting to consider links between this phenomenology, that is still not so known, and human activity.

5. ACKNOLEDGMENTS

This work has developed within the context of Research's project "*CLIMAGRI - Cambiamenti Climatici e Agricoltura*" – Research 1.2 Study on the possible variations in the structure of meteorological data and of Italian rainfall regimes - financed by *Ministero delle Politiche Agricole e Forestali* (D.M. 639/7303/2003). We thank Roberto Epifani for his support and Massimiliano Pasqui for his helpful suggestions.

6. REFERENCES

Brunetti M., Maugeri M., Nanni T., 2001: Changes in total precipitation, rainy days and extreme events in North Eastern Italy. Int. J. Climatol., ., 861–871.

Brunetti M., Buffoni L., Maugeri M., Nanni T., 2000: Precipitation intensity trends. in Northern Italy Int. J. Climatol. 20: 1017–1031

Karl TR, Knight RW, Plummer N. 1995. Trends in high-frequency climate variability in the twentieth century. Nature 377: 217–220.

Yu B, Neil DT. 1991. Global warming and regional rainfall: the difference between average and high intensity rainfalls. Int. J. Climatol., 11: 653–661.

PERSISTENCE OF WET AND DRY SPELLS IN ITALY. FIRST RESULTS IN MILANO FROM 1858 TO 2000.

Chiara Epifani[1], Stanislao Esposito[1], Domenico Vento[1]

[1]Central Office of Crop Ecology, Rome, 00186 Italy

1. INTRODUCTION

The meteorological phenomenon "precipitation" can be analyzed through many different features: its physical (rain, snow, hail) or its quantitative (extreme events, cumulated values during different periods of time) or its qualitative features (persistence). So the climatic characterization of precipitation should be considered in different framework. Variability is the main precipitation characteristic so, try to find some systematical variation elements combined to climatic variations, it's very difficult.

The purpose of the present work is to investigate a specific precipitation feature: its persistence.

Many studies has been carried out in order to determine the most suitable probability model: Gabriel and Neumann (1962) among others, have found that sequences in daily rainfall occurences can be described by a simple Markov chain model. De Arruda (1980) showed that for tropical regions, the truncated negative binomial model is more efficient than Markov chain, nevertheless for wet days the Eggemberger-Polya distribution provides a good fit to observed data of Uccle (Berger and Goossens 1982).

Considering a wet day as one with ≥1,0 mm of rain, the purpose of the present work is to investigate:

a. the best probability model which is able to fit the observed data and to catch interactions between the typology of one day and the adjacent ones.
b. if the identified theoretical model is able to catch eventual different features of the spell distribution between two periods: the last 30 year series compared to the previous secular period, in order to give a further contribute to climatic change problems.

Corresponding author's address: Chiara Epifani, Central Office of Crop Ecology, Rome, 00186 Italy; E-Mail: cepifani@ucea.it

2. MATERIALS AND METHODS

A ultra secular series (from 1858 to 2000) of daily rainfall data collected from the Brera Observatory Milan, Italy, was analyzed both in its annual and seasonal aggregations (considering the cold season from October to March and the warm season from April to September) taking into account that Italian climate presents a clear seasonal variability.

It has been already said, we consider a wet day (W) as one where the precipitation is ≥1,0 mm and, obviously, dry day (D) the one where there's not precipitation or is not > 1,0 mm, so each data set is organized in sequences of W and D.

A wet spell is a sequence of wet days and it begins and ends the day after and the day before a dry day, so, for example, a 4 days wet spell is identified with DWWWWD and these kind of sequences form the annual and the two seasonal sets.

A VISUAL-BASIC program is used to count systematically the dry and wet spell, their total number, their mean length and their distribution according to their length for annual as well for seasonal aggregation. When a spell overlaps a seasonal change (that is, it includes the 31st of March and the 1st of April or the 30th of September and the 1st of October) it is considered in its whole, up to its modality change even if it reaches the following season and we included it in the season in which it develops longer.

The sample gives the observed frequency of dry (wet) spell of *i* length (where *i* goes from 1 to the longest spell). The *i* length spell can be considered as a casual variable and its probability density, which can be calculated with theoretical model, is to compare to empiric frequency: if the difference between the theoretical and the empirical values falls within a predetermined range (significance test), we assume the theoretical model goodness of fit.

The first theoretical model, that has been used to describe the empirical data, is the Bernoulli

model and the priori probabilities are calculated with the Binomial law. In this case, as the test results show, the Binomial law is a inadequate fitting model because it requires the data independence. Therefore, others theoretical models that consider data dependence, must be analyzed.

Several kind of models have been used to describe dry and wet spells frequencies of occurrences considering the climatic features of the different countries. We have tested:

- the Eggenberger-Polya model;
- the truncated negative binomial model;
- the logaritmic model;
- the exponential model (that can be applied only to wet spells);
- the Markov chain of order one and higher than one.

The χ^2 test for goodness of fit was employed as the significance test for every model, assuming the level of significance equal to 5% (α = 0,05).

Later, we divide each season in two periods the 1°(1858-1970) and the 2°(1971-2000) and the *p(i)* distribution calculated for the 1° period is compared to the one calculated for the 2° period.

The statistics hypothesis that both the samples belong to the same universe (it means unchanged climatic conditions) and the alternative hypotesis that they don't belong to the same universe (that is, a climatic change that concerns this specific aspect of precipitation) is evaluated.

First of all, sample mean and variance of the 1° and the 2° period are compared using t-Student and F-Fisher tests. We have to underline that these results are only indicative because these tests suppose the almost normality of the samples, condition which is not realized.

A more decisive evidence is achieved applying to the 2° period (the 30-year series) the Eggemberg-Polya model calculated with the parameters derived from the 1° period. In this case, if the model don't fit to the observed data, it'll mean that in the last 30 years, climatic scene is changed.

3. RESULTS

Tables 1_a and 1_b give the usual statistics parameters of wet and dry days distribution.

Main characteristic of D and W spell during wintertime				
		D		W
Total number of days		22545		7470
General probability		0.751		0.249
Number of spells		3364		3365
Mean lenght of spells (days)		6.70		2.22
Standar deviation (days)		7.99		1.61
Max lenght (days)		80		14

Tab 1_a

Main characteristic of D and W spell during summertime				
		D		W
Total number of days		17236		4973
General probability		0.776		0.224
Number of spells		2897		2897
Mean lenght of spells (days)		5.95		1.72
Standar deviation (days)		5.99		1.11
Max lenght (days)		64		13

Tab 1_b

The first phase of this work, shows that Eggemberg-Polya and truncated negative binomial models are more efficient than the other in fitting observed data, for wet and dry spell and for annual and seasonal aggregations. The other models fit only one phenomenon typology (Markov chains, logaritmic model, the exponential model that can be applied only to wet spells) or don't fit at all (logarithmic model) (examples in Tab 2 and 3, Fig 1)

Considering that the truncated negative binomial model needs three parameters (mean, variance and the empirical frequency of the 1 day spell) while Eggemberg-Polya needs only two parameters (mean and variance), we consider the latter as the theoretical model that can be more easily used.

MILANO - wet spells during wintertime							
length of spells (days)	observed frequency	thoretical frequency					
		Binomial	Markov 1	E. & P.	B.N.T.	LOG	EXP
1	1437	472.4	1515.9	1483.3	1437	1788.7	1558.8
2	930	117.6	833	854.8	857.7	680.8	836.6
3	471	29.3	457.7	471.8	480.7	345.5	449.0
4	235	7.3	251.5	256.6	263	197.2	241.0
5	132	1.8	138.2	138.5	141.8	120.1	129.3
6	68	0.5	75.9	74.4	75.7	76.2	69.4
7	42	0.1	41.7	39.9	40.1	49.7	37.3
8	24	0.0	22.9	21.3	21.2	33.1	20.0
9	11	0.0	12.6	11.4	11.1	22.4	120.7
10	7	0.0	6.9	6.1	5.8	15.3	5.8
>= 11	8	0.0	8.4	6.9	6.3	36	7.1
chi-square value			18.3	11.5	11.9	251,1	23.0
c. s. 95% level			19.7	19.7	18.3	19.7	19.7

Tab 2

MILANO - dry spells during summertime								
length of spells (days)	observed frequency	thoretical frequency						
		Binomial	Markov 1	Markov 2	Markov 3	E. & P.	B.N.T.	LOG
1	582	112.7	487.0	582	582	603.0	582	940.3
2	406	87.5	405.1	373.6	406	411.9	422.5	444.6
3	305	67.9	337.0	313.3	303.1	318.3	327.1	280.3
4	268	52.7	280.4	262.8	255.0	255.4	260.9	198.8
5	219	40.9	233.2	220.4	214.5	208.7	211.7	150.4
6	190	31.7	194.0	184.8	180.4	172.4	173.8	118.5
7	160	24.6	161.4	155.0	151.8	143.5	143.8	96.1
8	117	19.1	134.3	130.0	127.7	120.0	119.7	79.5
9	78	14.8	111.7	109.0	107.4	100.8	100.1	66.8
10	106	11.5	92.9	91.4	90.4	84.9	84.0	56.9
11	71	8.9	77.3	76.6	76.0	71.6	70.8	48.9
12	69	6.9	64.3	64.3	63.9	60.6	59.7	42.4
13	53	5.4	53.5	53.9	53.8	51.3	50.5	37.0
14	39	4.2	44.5	45.2	45.2	43.5	42.8	32.5
15	30	3.2	37.0	37.9	38.1	37.0	36.3	28.7
16	36	2.5	30.8	31.8	32.0	31.4	30.9	25.4
17	22	2.0	25.6	26.7	26.9	26.7	26.3	22.6
18	19	1.5	21.3	22.4	22.7	22.8	22.4	20.2
19	20	1.2	17.7	18.7	19.1	19.4	19.1	18.1
20 - 24	60	2.9	52.8	57.0	58.4	61.7	61.0	67.0
25 - 29	24	0.8	21.0	23.6	24.6	28.1	28.0	41.2
30 - 39	14	0.3	11.7	13.9	14.7	18.8	19.1	43.4
>= 40	9	0.0	2.2	2.9	3.2	5.2	5.5	37.2
chi-square value			64.8	34.2	29.1	26,6	25,9	433,7
c.s. 95% level			31.4	30.1	28.9	31.4	30.1	31.4

Tab 3

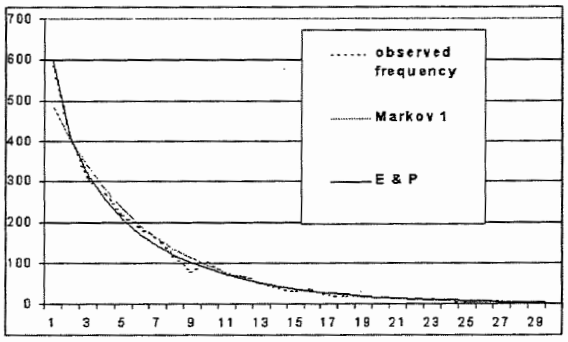

Fig 1 Dry spells on summertime: comparison among observed data and the results of Markov 1 and Eggemberg-Polya models.

The second phase of the work shows that the last 30–year series and the secular series:

- have not differences among the wet spells distributions;(Tab 4_a and 4_b)

Wet spells summertime					
length of spells (days)	observed freq. 1° per.	E. & P. 1° per.	observed freq. 2° per.	E. & P. 2° per.	E. & P. 2° with 1°
1	1348	1352.5	334	334.4	333.5
2	583	570.6	137	134.8	140.7
3	221	236.2	56	58.0	58.2
4	107	97.2	25	25.4	24.0
5	36	39.9	11	11.3	9.8
6	21	16.3	6	5.0	4.0
>= 7	8	11.3	4	4.1	2.8
χ^2 c s. 95% level=9,5		cq=4.9		cq=0.3	cq=1.9

Tab 4_a

Wet spells wintertime					
length of spells (days)	observed freq. 1° per.	E. & P. 1° per.	observed freq. 2° per.	E. & P. 2° per.	E. & P. 2° with 1°
1	1141	1180.1	296	301.8	290.0
2	741	681.6	189	175.0	167.5
3	387	379.6	84	92.7	93.3
4	186	208.8	49	47.6	51.3
5	110	114.1	22	24.1	28.0
6	56	62.2	12	12.0	15.3
7	37	33.8	5	6.0	8.3
>=8	42	40.2	8	5.8	11.3
χ^2 c s. 95% level=11,1		10,2		3,3	8,2

Tab 4_b

- there are significant differences among the dry spell distributions both in the wintertime and summertime (Tab 5), in particular:
  both seasons show an increase in dry spell mean duration, essentially due to a considerable increase (+ 50%) of the longest spells frequency (> 25 days) but also, even if less remarkable, due to a decrease (about -8%) of the shortest spells (from 1 to 3 days). (Tab 6)

Dry spells summertime					
length of spells (days)	observed freq. 1° per	E. & P. 1° per.	observed freq. 2° per	E. & P. 2° per.	E. & P. 2° with 1°
1	450	476.8	132	122.6	117.5
2	337	333.9	69	78.3	82.3
3	252	259.8	53	59.5	64.1
4	229	208.8	39	47.6	51.5
5	173	170.6	46	39.0	42.1
6	161	140.6	29	32.5	34.7
7	123	116.7	37	27.3	28.8
8	90	97.2	27	23.1	24.0
9	65	81.3	13	19.7	20.0
10	88	68.2	18	16.8	16.8
11	55	57.3	16	14.4	14.1
12	51	48.2	18	12.3	11.9
13	43	40.6	10	10.6	10.0
14	27	34.3	12	9.2	8.4
15	25	28.9	5	7.9	7.1
16	29	24.4	7	6.8	6.0
17	16	20.7	6	5.9	5.1
18	14	17.5	5	5.1	4.3
19	15	14.8	5	4.4	3.7
20-24	44	46.4	16	14.9	11.4
25-29	20	20.5	4	7.4	5.0
30-39	12	13.1	2	5.7	3.2
>= 40	5	3.3	4	2.0	0.8
χ^2 c s. 95% level=31.4		22.8		23.0	36.9

Tab 5

Probability of Dry Spells from 1 to 3 days	
1° period	p(D)= 0.461
2° period	p(D)= 0.455
Probability of Dry Spells > 25 days	
1° period	p(D)= 0.016
2° period	p(D)= 0.026

Tab 6

4. CONCLUSIONS

The Eggemberg-Polya model is able to describe the persistence of wet and dry spells in Milan in the annual and the seasonal aggregation. The application of this model has shown that climatic scene regarding this particular aspect of precipitation, has changed and that the occurrence of long period of absence of rainfall is higher than the past, at least for Milan station or for the climatic region that it represents.

The study of dry spell consist in an deeper study of the structure of dryness length and of its variation: these results seems to prove an increase of climate dry features in this region.

The extension of this application to other daily precipitation secular series will allow a better characterization of eventual climatic variation in our country and an deeper investigation on the eventual potentiality of this tool.

5. ACKNOWLEDGEMENTS

This work was conducted as part of the core program "CLIMAGRI – climatic change and agriculture" financed by Italian Ministry of Agriculture (D.M. 639/7303/2003).

The authors wish to thank M. Maugeri (Milan University, Italy) for providing Milan data and for his helpful suggestions.

6. REFERENCES

Gabriel, K. R. and Neumann, J 1962: A Markov chain model for daily rainfall occurence at Tel-Aviv. Quart. J. R. Met. Soc., 88, 90-95.

De Arruda, H. V. and Pinto, H. S. 1980: An Alternative Model for dry-spell probability analysis. Mon. Wea. Rev., **108**, 823-825.

Berger, A. and Goossens CHR., 1983: Persistence of wet and dry spells at Uccle (Belgium). J. Clim. **Vol 3**, 21-34.

CHANGES IN PRECIPITATION INTENSITY UNDER CLIMATE CHANGE CONDITIONS IN MAJOR CATCHMENTS IN EUROPE

Daniela Jacob, Katharina Buelow and Ralf Podzun

Max-Planck-Institute for Meteorology, Bundesstr. 53, 20146 Hamburg, Germany

1. INTRODUCTION

During the last 10 to 15 years extreme weather events seem to appear more often and sometimes intensified in Europe. The severe drought connected to a heat waves in summer 2003 covered large parts of southern and central Europe and led to local temperature anomalies in daily mean temperature of e.g. more than 10 K in Karlsruhe, Germany.

During the period of 1993 to 2003 more than 10 severe flooding events – 5 during summer periods - happened in different parts of Europe. Four of them have been titled as Century floods.

Extreme precipitation, defined as days with more than 30 mm precipitation, can lead to devastating land-slides and to summer flooding like the Elbe flooding in August 2002. This event was dominated by a so-called Vb-situation, in which low pressure systems were traveling from the Mediterranean sea to Eastern Europe, where extensive precipitation was observed.

As an example, observations of daily precipitation at the measurement site Hohenpeißenberg of the German Weather Service (DWD) show a clear positive trend. The number of days per year with extreme precipitation increased from 2.8 in 1879 to 5.2 today. Before 1953 only one day per year exceeded the 30 mm level, since 1953 this happens at least twice but not more often than 3 times a year. More than 89% of all cases are in April to September, 41% can be detected in June and July (Fricke and Kronier, 2001).

If the frequency of synoptic situations with the preference of extreme precipitation increases, higher precipitation values can be expected. Fricke (2002) analyzed the correlation between extreme precipitation and Großwetterlagen at the Hohenpeißenberg. He showed that the Vb-situation belongs to the group of synoptic situations which occurs more frequently in summer and which is clearly correlated to a significant increase of the number of days with more than 30 mm precipitation.

2. MODEL AND EXPERIMENTS

The three-dimensional hydrostatic climate model of the Max-Planck-Institute for Meteorology, REMO (REgional MOdel (Jacob, 2001)) was used to study the hydrological cycle over Europe, with special focus on the Elbe and Rhine drainage basins.

To address the reliability of climate change studies it is important to analyze a set of three regional simulations: for today's climate, control and future climate.

For all experiments REMO, version 5.1, using the physical parameterization schemes from the global climate model ECHAM4 of the Max-Planck-Institute for Meteorology (MPI-M) was run on 0.5° as well as on 0.16° horizontal resolution covering Europe. The analyzed experiments cover different lengths ranging from 10 years to 140. The very long experiment covering the period of 1960 to 2100 could only be performed on 0.5° horizontal resolution.

For today's climate REMO has been driven at the lateral boundaries by re-/analyses data from ECMWF, the so-called perfect boundaries, to investigate the quality of the REMO results through a detailed comparison against observations.

To investigate the influence of climate change on the hydrological cycle concentrations of greenhouse gases and sulphate aerosol are chosen according to IPCC (International Panel on Climate Change Scenario) scenario B2 (Houghton, 2001). Two more experiments are necessary: a control run and a scenario run. The difference between these results can be attributed to the climate change signal. Data from the MPI-M coupled global climate model system ECHAM4-OPYC3 have been used to drive REMO on 0.5° horizontal resolution, which in turn was used as lateral boundaries for REMO 0.16° horizontal resolution. The up-date frequency at the boundaries for all experiments was 6 hours and the output frequency for precipitation was hourly.

3. RESULTS

Comparing the observations (1979-1998) for Elbe and Rhine to the model results it is found that both are in very good agreement. The annual mean temperatures for the Elbe and Rhine drainage basins show positive trends in the observations and the model results. Both also show a decrease in the number of cold days (minimum temperature < 0°C).

The simulated precipitation can also be calculated realistically compared to observations (Jacob, 2001, Jacob et al., 2001). The monthly mean precipitation sum for the Elbe drainage basin over 20 years is 52.2 (53.3) mm/month in the model results (observations). The single monthly sums vary from 6.3 to 130.4

mm/month for the model results and from 3.3 to 123.3 mm/month in the observations. The mean annual precipitation sum calculated by REMO is 747.3 mm/year and observed is 640 mm/year. For this project we only received uncorrected precipitation observations. Due to the problem of under catch at precipitation observation stations the model results are always slightly higher, but therefore not automatically too high.

Within another project REMO results are compared to corrected observations from DWD (Milliez, 2003) and very good results are achieved. The following figure shows the precipitation intensity distribution for a sub-basin of the Rhine basin, Rhinefelden, which can be seen as a sub-basin with alpine character. It can not be expected that a grid point model of 18 km x 18 km grid lengths reproduces the extremes correctly. An underestimation is expected.

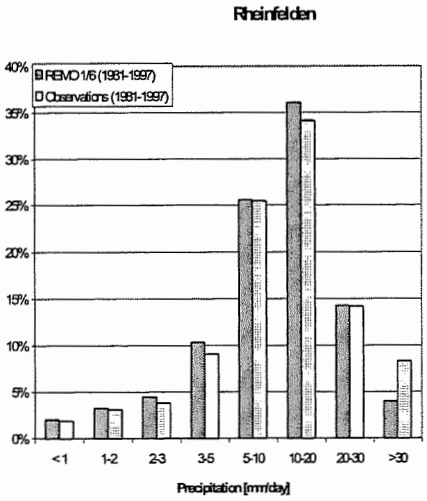

Figure 1: Observed (light) and simulated precipitation intensities (mm/day) Rheinfelden, a sub-basin of the Rhine basin for 1981 to 1997

Comparing the control period 1990-99 to the 3 decades between 2020 and 2049, a clear increase of surface temperature can be found. In the Elbe drainage basin the annual mean temperature increases from 9.5 °C in the control period to 11.2 °C in the last decade of the Scenario 2040-49. Especially during the winter the temperature increases by about 2 °C in the period from 1990-2049.

The monthly mean precipitation increases in the period of the scenario compared to the control period mainly during the winter. Looking at the annual horizontal precipitation distribution different results are found. In most parts of the Elbe river basin the mean annual precipitation increases, this is mostly pronounced during the period of 2030-39, with a precipitation increase of more than 20 % in some regions. The amount of days with precipitation intensity higher than 10 mm/day increases significantly in the period of the scenario compared to the control period.

For the Rhine basin an increase of the extreme precipitation (> 30 mm/day) can be seen in the two decades 2030 to 2050 (figure 2). The calculated signal is different in flat areas and alpine regions, which seems reasonable. In addition the signal changes with season. More details about this as well as the investigation within a few other European catchments will be shown during the poster presentation.

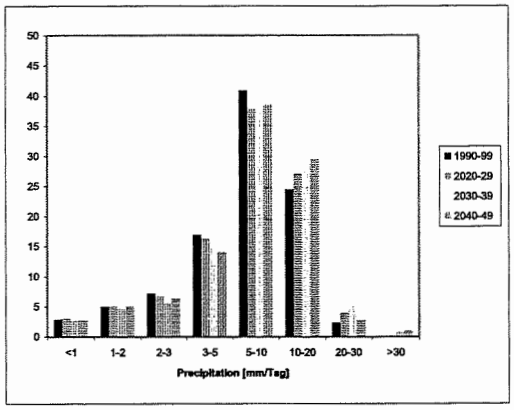

Figure 2: Simulated precipitation intensities (mm/day) for the Rhine basin 1990-99, 2020-29, 2030-39, 2040-2049 from left to right.

4. ACKNOWLEDGEMENT

Parts of the work has been carried out within the BMBF-funded project GLOWA-ELBE as well as within the KLIWA project, funded by three German water management agencies.

5. REFERENCES

Houghton, J.T et al., (2001): Climate Change 2001: The Scientific Basis, Contribution of Working Group I to the Third Assessment Report of the Governmental Panel on Climate Change, Cambridge University Press.

Jacob, D., (2001): A note to the simulation of the annual and interannual variability of the water budget over the Baltic Sea drainage basin, Meteorol. Atmos. Phys.77, p. 61-73.

Jacob, D., Van den Hurk, B.J.J.M., Andræ, U., Elgered, G., Fortelius, C. Graham, L. P., Jackson, S.D., Karstens, U., Koepken, Chr., Lindau, R., Podzun, R., Roeckel, B., Rubel, F., Sass, B. H., Smith, R.N.B., Yang, X. (2001) : A comprehensive model intercomparison study investigating the water budget during the BALTEX PIDCAP period, Meteorol. Atmos. Phys, 77, 19-43.

Fricke W. and M. Kronier (2001): Betrachtungen zum Klimawandel am Hohenpeißenberg. Klimastatusbericht, Deutscher Wetterdienst, http://www.ksb.dwd.de

Fricke, W. (2002): Hängen vermehrte Starniederschläge am Hohenpeißenberg mit veränderten Wetterlagen zusammen? Klimastatusbericht, Deutscher Wetterdienst, http://www.ksb.dwd.de

Milliez, M. (2003): Validation of today's climate simulation with the regional model REMO. Diplomarbeit am DEA Oceanologie, Meteorologie et Environnement, der Universite Pierre et Marie Curie

GLOBAL OCCURRENCES OF EXTREME PRECIPITATION AND THE MADDEN-JULIAN OSCILLATION: OBSERVATIONS AND PREDICTABILITY

Charles Jones[1], Duane E. Waliser[2], K. M. Lau[3] and W. Stern[4]

[1] ICESS, University of California, Santa Barbara, CA 93106, USA
[2] IPTA, State University of New York, Stony Brook, NY, USA
[3] Climate and Radiation Branch, Goddard Space Flight Center, NASA, Greenbelt, MD, USA
[4] Geophysical Fluid Dynamics Laboratory, Princeton University, Princeton, NJ, USA

1. INTRODUCTION

Extreme precipitation events are among the most devastating weather phenomena, since they are frequently followed by flash floods and sometimes accompanied by severe weather such as lightning, hail, strong surface winds and intense vertical wind shear. Consequently, extreme precipitation can cause significant impacts on societies with losses of human lives and property as well as disruption of infrastructure services

In this context, significant research emphasis has been given to identify relationships between low-frequency modes in the coupled ocean-atmosphere system and the occurrence of extreme precipitation (IPCC 2001). On interannual time scales, the El Niño/Southern Oscillation (ENSO) is the main mode of variability and several studies have found notable linkages relating ENSO and regional changes in the frequency of extremes in many locations around the world (e.g. Bell and Halpert 1997).

On intraseasonal time scales (roughly 20 to 90 days), the Madden-Julian Oscillation (MJO) stands out as the dominant mode of tropical intraseasonal variability and is most active in the boreal winter (Madden and Julian 1994). The influences of the MJO on the patterns of precipitation in the global tropics and in portions of the extratropics have been well documented. In addition, the MJO strongly influences the precipitation patterns associated with the monsoons in Asia–Australia, and moderately in North America and South America (Yasunari 1979; Lau and Chan 1986; Mo 2000; Nogués-Paegle et al 2000; Higgins and Shi 2001; Jones and Carvalho 2002).

The present paper has several objectives (Jones et al. 2004a). Although previous studies have provided some important understanding of the modulation of the MJO on regional frequencies of extreme precipitation, our current view of this modulation is still quite fragmented. All previous works have concentrated on the influence of the MJO on extreme precipitation over specific geographic locations.

Given the planetary scale of the MJO, the first objective of this study is to obtain a global of view of the slow eastward propagation of the MJO during boreal winter and the occurrence of extreme precipitation in the tropics and extratropics. The results are compared against quiescent periods of the MJO. The next issue addressed in this study relates to the current weakness that most general circulation models (GCM) have to adequately represent MJO properties (e.g. eastward propagation, period and phase speed, amplitude etc), as discussed in more detail in Waliser et al. (2003). In the second objective, we use a GCM that has been shown to have a fairly reasonable representation of the MJO (Waliser et al. 2003a) to investigate how realistic is the modulation of the model MJO on extreme precipitation events. This analysis is performed by comparing observed and model statistical properties of precipitation and the frequency of extremes. Finally, the third objective of this study investigates the modulation of the MJO on the predictability of extreme precipitation events, an issue with important operational applications.

Corresponding author's address: Charles Jones, ICESS, University of California, Santa Barbara, CA 93106, USA; E-Mail: cjones@icess.ucsb.edu.

2. SUMMARY AND CONCLUSIONS

The Madden-Julian Oscillation is the dominant mode of tropical intraseasonal variability and its role in the coupled ocean-atmosphere system has been noted in many previous studies. Indeed, previous work has identified clear signals relating the activity of the MJO and extreme precipitation over specific geographic locations. This paper first developed an observational analysis to obtain a global view of the relation between the slow eastward propagation of the MJO and occurrences of extreme precipitation during boreal winter. This task, which was addressed with GPCP data, was limited to pentads time resolution to ensure global coverage. The results show higher frequency of extremes in the Indian Ocean, Indonesia and western Pacific during periods of active MJO than quiescent episodes of the oscillation, which is consistent with anomalies of convective activity associated with the MJO. Moreover, the eastern part of South America exhibits unambiguous and robust signals of increased frequency of extremes during active MJO situations. Other regions with amplified occurrence of extremes associated with active MJO are located over northeast Africa, the Middle East and eastern China. Although the GPCP data analysis reveals higher frequency of extremes during active MJO only over some locations off the west coast of North America and parts of southern California, previous studies using surface station data have

related the MJO to high frequency of extreme precipitation over western North America. This discrepancy can be partially attributed to the low time and space resolution of the GPCP data, which may be unable to capture the effects of important topographic mesoscale circulations responsible for heavy precipitation in those locations. Nevertheless, the GPCP data analysis indicates that, on a global scale, the number extreme events during active MJO situations are about 40% higher than in quiescent phases of the oscillation.

As a second objective, this paper examined the degree to which the NASA GLA model, which has a relatively reasonable representation of the MJO (e.g. Waliser et al 2003), realistically simulates the precipitation variability and modulation of the MJO on extreme events. A straight comparison between statistics derived from observed (GPCP) and model (GLA) precipitation is hampered by the different time (and possibly space) resolutions of both data sets. Future improvements in satellite estimates of precipitation (Scofield and Kuligowski 2003) will facilitate the validation of model results. Nevertheless, there is a generally realistic representation by the GLA model of extremes in tropical convective regions associated with the MJO. The higher frequency of extremes in South America during active MJO than in quiescent cases is also reasonably well represented, although the model has difficulty in simulating the timing of the events. Extremes are more frequently observed in South America when the MJO convection is in the central Pacific, whereas the model suggests more extremes when convection is in the Indian Ocean or maritime continent. The GLA model also shows a strong signal in the frequency of extremes in the north Pacific and western coast of North America, which somewhat agrees with observational studies using station data.

Lastly, some previous work has also found that the MJO seems to modulate weather forecast skill in midlatitudes particularly during boreal winter (Lau and Chang 1992; Hendon et al. 2000; Nogués-Paegle et al., 1998; Jones and Schemm 2000; Ferranti et al. 1990). In the third objective of this study, we investigated the relationships between the MJO and the predictability of extreme precipitation. The statistical analysis indicates higher success in the prediction of extremes during active MJO than in quiescent situations in several areas in tropical Africa, Indian Ocean, Indonesia, western Pacific and South America. Additionally, extensive areas in the subtropical and midlatitude of the North Pacific, western North America and a large area in the North Atlantic Ocean, show increased predictability of extremes during active MJO. Overall, the predictability experiments indicate the mean number of correct forecasts of extremes during active MJO to be nearly twice the correct number of extremes during quiescent phases of the oscillation. These results raise encouraging perspectives for further improvements in weather forecasts on subseasonal time scales. Numerical weather prediction models with realistic representation of the MJO as well as empirical forecast models (Waliser et al. 1999; Lo and Hendon 2000; Mo 2001; Jones et al 2004b; Wheeler and Weickmann 2001; Wheeler and Hendon 2004) can potentially use the slow eastward propagation of the MJO to improve the prediction of extreme events at long lead times.

It is also important to recognize a number of caveats associated with the results derived from the numerical model used in this study. First, while the intraseasonal peak of equatorial wavenumber−1, upper-level velocity potential and zonal wind in the model is quite similar in terms of magnitude and frequency to observations, the model spectra has too much high-frequency (~days) variability for wavenumber−1. Relative to the MJO, this variability would be considered to be unorganized, that is, errant convective activity that may erode the relatively smooth evolution of the MJO. Second, the simulations were carried out with fixed climatological SST values. A previous study with this model showed that coupled SSTs tend to have an enhancing and organizing influence on the MJO, making it stronger and more coherent, which can potentially impact the occurrences of extreme precipitation in the extratropics. The third aspect is the fact that the model contains too little variability over the western Indian Ocean and southern Maritime Continent region. We are currently developing simulations similar to the ones presented here but with coupled SSTs as well as interannual variations

Acknowledgements

The authors would like to acknowledge the support of the following research grants. C. Jones: National Science Foundation (ATM-0094387) and NOAA Office of Global Programs CLIVAR – Pacific Program (NA16GP1019); D. E. Waliser: National Science Foundation (ATM-0094416) NOAA Office of Global Programs CLIVAR (NA16GP2021). The authors would like to thank the Climate Prediction Center (CPC/NCEP/NWS/NOAA) for making the GPCP data available.

References

Bell, G. D., M. S. Halpert, 1998: Climate Assessment for 1997. *Bull. Amer. Meteor. Soc.,* **79,** 1014-1014.

Ferranti, L., T. N. Palmer, F. Molteni and K. Klinker, 1990: Tropical-extratropical interaction associated with the 30-60 day oscillation and its impact on medium and extended range prediction. *J. Atmos. Sci.*, **47**, 2177-2199.

Hendon, H.H., B. Liebmann, M. Newman, J. D. Glick, and J. Schemm, 2000: Medium range forecast errors associated with active episodes of the Madden–Julian oscillation. *Mon. Wea. Rev.,* **128,** 69–86.

Higgins, R. W., and W. Shi, 2001: Intercomparison of the principal modes of interannual and intraseasonal variability of the North American monsoon system. *J. Climate,* **14**, 403-417.

IPCC, 2001: *Climate Change: The Scientific Basis. Contribution of Working Group I to the Third Assessment Report of the Intergovernmental Panel on Climate Change.* [Houghton, J. T., Y. Ding, D. J. Griggs, M. Nouguer, P. J. van der Linden, X. Dai, K. Maskell, and C. A. Johnson (eds)]. Cambridge United Kingdom and New York, NY, USA, 881 pp.

Jones, C., and L. M. V. de Carvalho, 2002: Active and break phases in the South American Monsoon System. *J. Climate*, **15**, 905-914.

_____, and J.-K. E. Schemm, 2000: The influence of intraseasonal variations on medium-range weather forecasts over South America. *Mon. Wea. Rev.*, **128**, 486–494.

_____, D. E. Waliser, K. M. Lau, and W. Stern, 2004a: Global occurrences of extreme precipitation events and the Madden-Julian Oscillation: observations and predictability. Submitted to *J. Climate.*

_____, D. E. Waliser, K. M. Lau, and W. Stern, 2004b: The Madden-Julian Oscillation and its Impact on Northern Hemisphere Weather Predictability. *Mon. Wea. Rev.* (in press).

_____, L. M. V. Carvalho, W. Higgins, D. Waliser, J-K. Schemm, 2004b: A statistical forecast model of tropical intraseasonal convective anomalies. *J. Climate* (in press).

Lau, K. M., and P. H. Chan, 1986: Aspects of the 40-50 Day oscillation during the Northern Summer as inferred from Outgoing Longwave Radiation. *Mon. Wea. Rev.*, **114**, 1354-1367.

Lo, F., and H. H. Hendon, 2000: Empirical Prediction of the Madden-Julian Oscillation. *Mon. Wea. Rev.*, **128**, 2528-2543.

Madden, R. A., and P. R. Julian, 1994: Observations of the 40-50 day tropical oscillation: A review. *Mon. Wea. Rev.*, **112**, 814-837.

Mo, K. C., 2000: Intraseasonal modulation of summer precipitation over North America. *Mon. Wea. Rev.*, **128**, 1490-1505.

_____., 2001: Adaptive Filtering and Prediction of Intraseasonal Oscillations. *Mon. Wea. Rev,* **129**, 802-817.

Nogués-Paegle, J., L. A. Byerle, and K. Mo, 2000: Intraseasonal modulation of South American summer precipitation. *Mon. Wea. Rev.,* **128**, 837-850.

Scofield, R. A., and R. J. Kuligowski, 2003: Status and outlook of operational satellite precipitation algorithms for extreme-precipitation events. *Wea. and Forec.*, **18**, 1037-1051.

Waliser, D. E.., C. Jones, J. K. Schemm and N. E. Graham, 1999: A Statistical Extended-Range Tropical Forecast Model Based on the Slow Evolution of the Madden-Julian Oscillation. *J. Climate*, **12**, 1918-1939.

_____, K. M. Lau, W. Stern, C. Jones, 2003: Potential predictability of the Madden-Julian Oscillation. *Bull. Amer. Meteo. Soc.*, 33-50.

Wheeler, M, and K. Weickmann, 2001: Real-time monitoring and prediction of modes of coherent synoptic to intraseasonal tropical variability. *Mon. Wea. Rev.*, **129**, 2677-2694.

_____, M.C., H.H. Hendon, 2004: An All-season Real-time Multivariate MJO Index: Development of an Index for Monitoring and Prediction. *Submitted to Mon. Wea. Rev.*

Yasunari, T., 1979: Cloudiness fluctuations associated with the Northern Hemisphere monsoon. *J. Met. Soc. Japan.*, **58**, 225-229.

PRECIPITATION IN THE MEDITERRANEAN REGION OBSERVED WITH TRMM MICROWAVE DATA

Martina Kästner and Jörg Steinwagner

German Aerospace Center, Oberpfaffenhofen, D-82234 Wessling, Germany

1. INTRODUCTION

Various climate models predict a decrease of precipitation in the future over many parts of the subtropics, particularly in the winter (Bolle, 2003). Therefore, it is essential to have not only climatological data from land but also from over the seas not covered by conventional observation networks but now be continuously monitored by low orbiting and geostationary satellites. Beneath operational retrievals of e.g. Grody (1991), Kummerow et al. (1996) or Wentz and Spencer (1998) some recent satellite rain retrievals in both the IR and the MW spectra are developed by Bauer (2001) using TMI estimates calibrated with PR, both onboard the TRMM satellite, Turk et al. (2002) using individual SSM/I and TMI overpasses to calibrate geo-IR precipitation estimates, Grose et al. (2002), Oh et al. (2002) and Kidd et al. (2003) among others.

The evaluation of passive microwave (PMW) precipitation algorithms which are directly linked to the 3-D structure of the precipitating system use measurements from different sensors on different satellites, like SSM/I on DMSP, TMI/PR on TRMM, or AMSU on NOAA. Passive MW techniques perform much better over the oceans than over land. The MW techniques are directly related to the hydrometeors through scattering and emission, but the low earth orbits and less frequent coverage hinders tracking of developing severe storms. While the daily course of precipitation is not easily obtained from TRMM data, IR-based techniques from geostationary satellites have been widely used due to the high revisit period. However, they have an inherent weakness regarding the physical relation between cloud top temperatures and underlying rain rate. Further, the rain characteristics vary with different climate regimes, hence, any developed method has to be validated against appropriate in situ measurements taken over the region of interest.

A cross-comparison of PMW and/or IR based algorithms with the Bologna local area model (BOLAM) in 0.25° lat-lon grid resolutions is performed for the Algerian flood in early November 2001. Although the validity of the results obtained is restricted to the case studies some general information could be extracted.

Corresponding author's address: Martina Kästner, DLR - DFD, Oberpfaffenhofen, D-82234 Wessling, Germany; E-Mail: martina.kaestner@dlr.de.

2. DATA

The Algerian severe weather event was used as a common case study for an inter-comparison of PMW, IR, combined MW/IR rainfall algorithms and the BOLAM model. The validation is performed for a severe weather event between 08 and 12 November 2001 on the Algerian coast and the Balearic Islands. The synoptic situation was characterised by strong surface winds and heavy rainfall. An intense upper-level trough pushed far to the south of Europe where a cut-off low developed. The METEOSAT-7 IR image (Fig. 1) shows the clouds with heavy rainfall on the Algerian coast. The rainfall started on late 9 Nov and ended the next day at about noon on 10 Nov, when 150 litres per m² within six hours were observed. Together with the cut-off low process heavy thunderstorms developed in a cyclogenesis over the Balearic Islands the next day. The precipitation was reported to be greater than 400 mm over two days, with a maximum of 68 litres per m² in six hours (Thomas et al., 2003).

Two processes intensified the convective development: 1) the cold maritime arctic air that crossed over the still 18° C warm Mediterranean Sea where it picked up moisture, destabilised, and met initially maritime subtropic air and 2) the strong surface winds blowing against the high mountains along the African coast (> 2300 m) caused intense orographic rainfall which led to the flooding disaster in Algiers with more than 750 deaths.

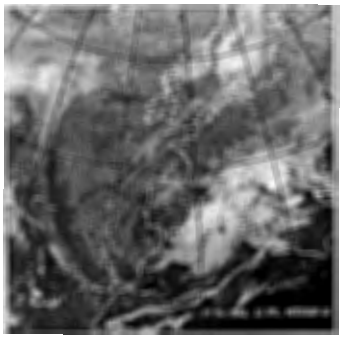

Fig. 1: METEOSAT-7 IR, 10 November 2001, 12 UTC. A = Algiers. (credit: EUMETSAT)

The input data for the used PMW algorithms (PATER, FDA) are the brightness temperatures (TB) of nine channels (10.7v,h, 19.4v,h, 21.3v, 37.0v,h, 85.5v,h GHz) with varying resolutions from 70 to 6 km from the TMI instrument onboard the low orbiting TRMM satellite. Fig. 2 shows differences of emission over water and over land for both polarizations and for different TMI channels. Over water, the rainy areas appear to be warmer than their surroundings, while over land they appear to be colder due to the high MW emission of land.

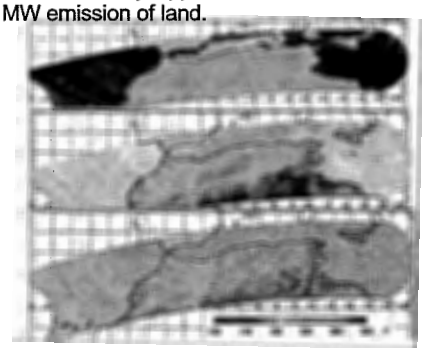

Fig. 2: TRMM TMI brightness temperatures for 19h (top), 19v (mid) and 85v (bottom) GHz channels (v = vertical, h = horizontal polarization), 10 November 2001, 00:25 UTC.

The used rain data are from 1) the BOLAM, a hydrostatic model in σ coordinates, feeded by ECMWF 6-hourly analyses (Buzzi et al., 2003), 2) the PMW satellite Frequency Difference Algorithm (FDA) of Kidd that uses the 19v and 19h GHz channels and relates their difference to the rain rate (RR), 3) the empirical Neural Rain Estimator (NRE), an operational rapid update geo-IR-based algorithm to diagnose half-hourly near-surface rainfall that uses features of the cloud top evolution and structure and information from a NWP model, 4) the Naval Research Laboratory (NRL) blended technique (Turk et al., 2002) that uses probability matching methods for dynamically-updated TB-RR lookup tables from time- and space-coincident IR and MW pixels of different satellites, and 5) the over-ocean satellite MW rainfall algorithm PATER (Bauer et al., 2001), a physical algorithm that uses only two empirical orthogonal functions instead of the nine TBs from the TMI channels basing on a database from several 3-D cloud model simulations including the melting layer. The latter algorithm has a stand-alone PMW component based on TRMM TMI (1B11) data and an optionally carefully co-located calibration part with PR (2A25) data (~5 km) downscaled to the lower TMI spatial resolution for the 10 GHz (~50 km).

3. INTER-COMPARISON OF RAIN RETRIEVALS

3.1 Method of Analysis

For the inter-comparison of several rain algorithms applied in the scope of the EURAINSAT project, continuous and categorical statistics were used within a common area extended from 15 W to 20 E and from 30 to 60 N in a common period from 09 to 11 November 2001 and with rain rates re-sampled into a 0.25° lat-lon grid (~28 km). TRMM and NRE data did not consistently cover the complete common area. The temporal coincidence was optimal for the different PMW algorithms, otherwise the temporal window was better than +/-15 min for comparisons with IR (NRL, NRE) and in most cases better than +/-90 min for comparisons with the independent model data, which have a 3-hourly temporal resolution. Comparisons were made for single orbits as well as for merged data within 3-h periods.

3.2 Results

Both PMW algorithms, PATER and FDA, rely on the same TMI orbit data and so it was expected that their comparison would result in a rather similar rainfall region and intensity. Both algorithms are assessed to be of equal quality in this heavy rainfall event, considering that the PATER algorithm is restricted to ocean surfaces and to events above 1mm/h rain intensity. The most successful comparison of PMW with other techniques was in this case the BOLAM model followed by the NRL blended MW/IR technique, both performed better than the IR technique.

Figures 3 to 7 show the RR from different retrievals for one special date (10 Nov 2001, 03 UTC).

Figure 3 shows three areas of heavy rainfall, one west of the Canary Islands, the biggest one is around Algiers, and one southeast of Sardinia. The three rain areas coincide very well with results of both MW algorithms. Even the rain intensities are similar except for the Sardinia area. FDA works over land and ocean (Fig.4), PATER exclusively over ocean. The low rain rates erroneously detected by PATER over the sea south of Sicily are attributed to strong desert aerosol also detected as aerosol fallout in Rome the next day. The rainy speckles over the Atlantic are due to cumulus convective showers within the cold air. Compared to both techniques, the BOLAM model rainfall (before nudging) shows wide agreement of the strong rain bands (Fig. 5). The rainfall intensities were rather similar; only the position of the rainfall had an error for the Sardinia area. On the other hand, the shower pattern over the Atlantic is not well matched and there are too many areas with light rain. The two IR-based algorithms, NRL and NRE (Fig. 6 and 7), give heavy rain areas over the Mediterranean Sea, but not at the correct position. The Algerian coast, where the maximum precipitation fell, is hardly classified as a heavy rain area. The combined MW/IR NRL algorithm shows a much better performance than the IR algorithm NRE alone.

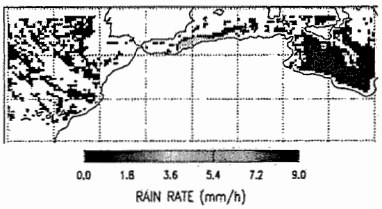

Fig. 3: PATER algorithm – MW

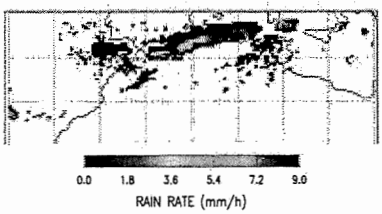

Fig. 4: FDA algorithm - PMW

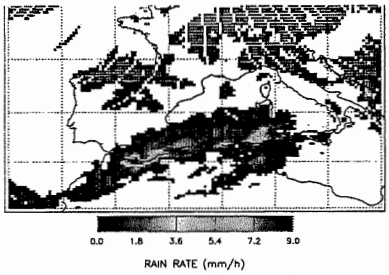

Fig. 5: BOLAM – model

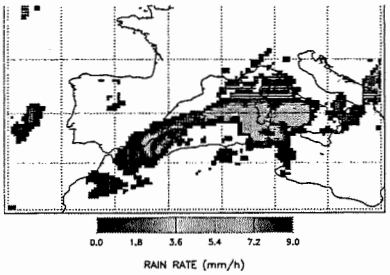

Fig. 6: NRL algorithm – combined IR-MW

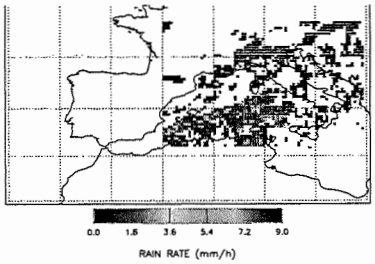

Fig. 7: NRE algorithm – IR

Overall it seems to be worthwhile to combine the high temporal resolution of IR with the better rainfall identification performance of MW techniques for monitoring purposes. The NRL algorithm or the now available TRMM 3B42RT products belong to this category. The MW pixel resolution makes a 0.25° lat-lon grid appropriate, but better spatial resolution is desired by the users.

A more comprehensive analysis of the categorical statistics of all possible combinations of the above mentioned algorithms within the period 08 to 13 Nov 2001 is given in Kästner (2003). The accuracy of all inter-comparisons is measured in terms of Heidke skill score that ranges from 0.61 (BOLAM vs. NRE), over respectable 0.78 (BOLAM vs. FDA), to optimal 0.82 comparing both PMW algorithms (PATER vs. FDA). The bias between PATER and NRL is small and again PATER performs best when compared with FDA, their bias is neglectable. Worthwhile to note that even in this heavy rain event only 10% of the gridded pixels are hits (rain/rain), whereas the majority (62%) is correct negatives (no-rain/no-rain), thus, the correct negatives dominate the statistics.

4. MONTHLY MEANS OF RAINFALL

The MW PATER algorithm over ocean by Bauer (2001) is applied to all available orbits that hit the Mediterranean region extending from 30°W to 40°E (Azore Islands to Israel) and 25°N to 40°N (Canary Islands to Sicily) in the winter rain period November 2002 till May 2003. The Mediterranean climate is characterized by winter rains and summer droughts. The strong difference between the wet winters and the dry summers is caused by the seasonal alternation of the dominance of cyclonic storms in winter and subtropical high pressure cells over the adjacent ocean in summer with subsiding maritime tropical air. Only in the European area, because of the Mediterranean Sea, the Mediterranean climate covers the wide area of 3.1 Mkm² while in most other regions it is confined to narrow coastal belts (Bolle, 2003).

Within the belt of the Mediterranean climate exists a strong gradient of the meteorological parameters, the precipitation ranges between 0 and 300 mm/month accumulated rainfall. For this study all available TRMM data of the Mediterranean belt and within one month contribute to the monthly mean RR given in mm/h. The single observation is instantaneous and some problems occur when averaging, nevertheless the gridded (0.25° lat-lon) monthly mean RR reveal some interesting features. When neglecting the averaging problems the evaluated RR can roughly be converted into accumulated rainfall by multiplication with a factor of 90, resulting from 3 orbits per day times 30 days per month, then the scale runs from 0 to 110 mm accumulated rainfall.

Figure 8 shows the geographical distribution and the temporal development in the rainy winter period 2002/2003 by selected months from November to May.

Within the Atlantic there is a west-east gradient towards the coasts of Africa and Spain, especially in January and May. Further, a gradient to the north is detectable over the Atlantic.

Over the Mediterranean Sea the high spatial variability even at relatively small scales is seen in every month. Maximum precipitation over the southern Mediterranean Sea occurred for this winter period in March 2003. The northern part of the Mediterranean Sea is outside the TRMM coverage.

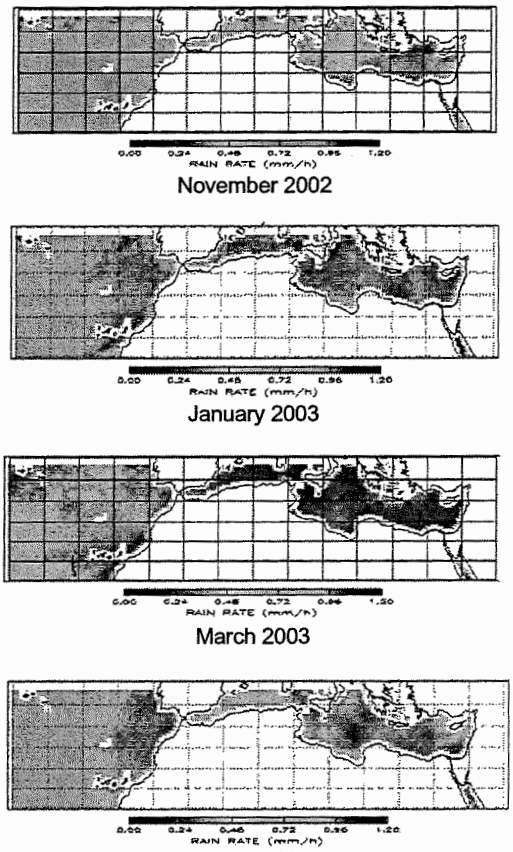

Fig 8: Geographical distribution of precipitation in the winter season 2002/2003 using the MW satellite rain retrieval PATER (Bauer, 2001)

ACKNOWLEDGEMENT

This research is funded by the EURAINSAT project, a shared-cost project (contract EVG1-2000-00030), co-funded by the Research DG of the European Commission within the RTD activities of a generic nature of the Environment and Sustainable Development sub-programme in the 5th Framework Programme.

REFERENCES

Bauer P, Amayenc P, Kummerow CD, Smith EA, 2001: Over–Ocean Rainfall Retrieval from Multisensor Data of the Tropical Rainfall Measuring Mission. Part II: Algorithm Implementation. *J. Atmos. Oceanic Technol.*, **18**, 1838-1855.

Bolle, H-J (ed.): *Mediterranean Climate – Variablility and Trends.* Berlin, Springer, 372 pp, 2003.

Buzzi A, D'Isidoro M, Davolio S, 2003: A case study of an orographic cyclone formation south of the Alps during the MAP-SOP. *Q. J. R. Meteorol. Soc.*, **129**, 1795-1818.

Grody NC, 1991: Classification of snow cover and precipitation using the Spacial Sensor Microwave/ Imager (SSM/I). J. Geophys. Res., **96**, 7423-7435.

Grose A, Smith EA, Chung H-S, Ou ML, Sohn BJ, Turk FJ, 2002: Possibilities and limitations for QPF using nowcasting methods with infrared geosynchronous satellite imagery. *J. Appl. Meteor.*, **41**, 763-785.

Kästner M, 2003: Inter-comparison of precipitation estimations using TRMM microwave data and independent data. In: Proc. 3rd GPM Workshop - Consolidating the Concept, Noordwijk, The Netherlands, 24-26 June 2003, AP-5. http://www.estec.esa.nl/conferences/03C06/

Kidd C, Kniveton D, Todd M, Bellerby T, 2003: Satellite rainfall estimation using a combined passive microwave and infrared algorithm. *J. Hydrometeorology*, **4**, 1088-1104.

Kummerow C, Olsen WS, Giglio L, 1996: A simplified scheme for obtaining precipitation and vertical hydrometeor profiles from passive microwave sensors. *IEEE Trans. Geosci. Remote Sens.*, **34**, 1213-1232.

Oh HJ, Sohn BJ, Smith EA, Turk FJ, Seo AS, Chung HS, 2002: Validating infrared-based rainfall retrieval algorithms with 1-minute spatially dense raingauge measurements over the Korean peninsula. *Meteor. Atmos. Physics*, **81**, 273-287.

Thomas W, Baier F, Erbertseder T, Kästner M, 2003: Analysis of the Algerian severe weather event in November 2001 and its impact on ozone and nitrogen dioxide distributions. *Tellus B*, **55B**, 993-1006.

Turk FJ, Ebert EE, Oh HJ, Sohn BJ, Levizzani V, Smith EA, Ferraro R, 2002: Validation of an operational global precipitation analysis at short time scales. In: Proc. 1st Worskshop Intern. Precip. Working Group (IPWG), Madrid, Spain, 23-27 Sept. 2002.

Wentz FJ and Spencer RW, 1998: SSM/I rain retrievals within an unified all-weather ocean algorithm. *J. Atmos. Sci.*, **55** (9), 1613-1627.

LATENT HEAT FORCING: A NEW CONCEPT IN CLIMATE CHANGE

Guy Kelman, Daniel Rosenfeld*, Alexander Khain

Institute of Earth Sciences, The Hebrew University of Jerusalem, Israel

1 INTRODUCTION

In considering the engines that drive changes in global climate, radiative forcing was considered as the only major component. However, one aspect has been overlooked so far: Because the air is transparent to sunlight at most wavelengths, most of the solar radiation is delivered to the atmosphere indirectly. Most ($\approx$ 77%) of the solar radiation reaching the surface is consumed to evaporate water and the energy is transported in the atmosphere as latent heat within the water vapor. Only when and where the reverse process occurs, i.e., precipitation back to the surface, the released latent heat of condensation causes a net warming of the air, decreases its density and so creates pressure gradients that propel the global circulation of the atmosphere [1].

Thus, convection and the formation of precipitation lead to the release of enormous amounts of latent heat. It has been recently shown that anthropogenic aerosols can have substantial effect on precipitation [3] [4] [8], and hence on the resultant latent heat release. We define here the anthropogenic induced changes in latent heating as *'latent heat forcing'*.

2 HUMAN ACTIVITIES

Smoke and pollution aerosols have been shown to suppress the coalescence, so that all condensates can ascend as cloud drops to above the zero isotherm level, where they form ice precipitation particles that release the extra latent heat of freezing aloft. The melting of the ice precipitation at lower levels takes back the latent heat of freezing, and so having two effects due to the suppression of drop coalescence: (i) The latent heat release is deposited higher in the atmosphere. (ii) Greater amount of heat is transferred from the lower to the upper troposphere for a given rain amount. This means that same percentage less precipitation can satisfy the radiative loss of the atmosphere. This leads to the same net loss of precipitation. In addition, the early development of warm rain suppresses the updraft. Therefore the delay in initiation of precipitation allows further invigoration of the convection, thus elevating the level of the detrained latent heat.

3 METHODS

3.1 The study area

The Amazon area has a vastly growing deforestation activity that employs a primitive technique of burning the logged trees in order to make room. During the dry season, several hundred thousand fires burn in the area, covering a large area with dense smoke. In the recent years, knowledge is accumulated via satellite imagery and field observations to assess and quantify the impact of this activity on the climate. The lastest large scale campaign made detailed measurements of physical and chemical properties of the aerosol in Brazil from the middle of the dry season to the beginning of the wet season (Sep-Nov 2002).

*Corresponding author's address: Daniel Rosenfeld, Institute of Earth Sciences, The Hebrew University of Jerusalem, Jerusalem 91904, Israel. E-Mail: daniel.rosenfeld@huji.ac.il

3.2 Modeling

In this research we deploy a 2-dimensional cloud Ensamble spectral (bin) model with explicit microphysics named HUCM. The model's unique feature is the coupling of aerosol distribution functions into the dynamics and thermodynamics stages of calculation [2]. in-situ observations have shown good correspondence with the model's calculations [5] [6]. The model's domain consists of $64kmX16km$ grid with $250m$ horizontal resolution and $125m$ along the vertical axis. Within we introduce CCN distribution functions to describe maritime and continental environments and thermodynamic conditions from soundings that correspond the exact day and time of in-situ observations from the LBA SMOCC field campaign [8]. Figures (1) and (2) show an example field of graupel number concentrations which are calculated at t=1500sec of the model run. The difference in cloud-top height are obvious as well as the horizontal extent in the two cases of instability.

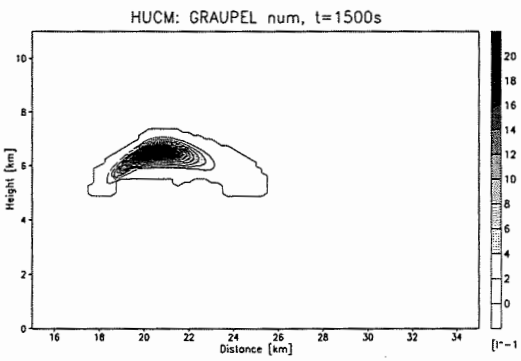

Figure 1: graupel number concentration MS (maritime stable conditions)

The model's results for 4 runs according to table (1) were then taken into a secondary stage of calculating heat fluxes. The work presented in this article reports the findings from these results.

3.3 Heat budgets

Latent heat release remaining in the atmosphere must be a unique function of the precipitation

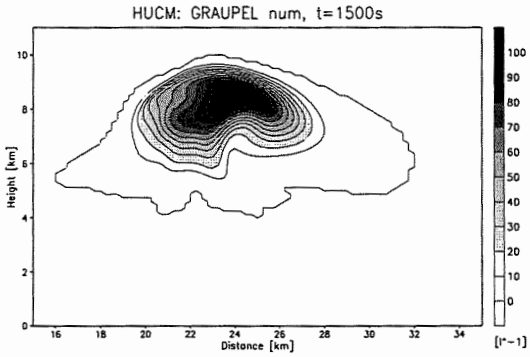

Figure 2: graupel number concentration MU (maritime unstable conditions)

Table 1: stability and aerosol conditions on Oct. 4, 2002: (i) stable sounding from Ji-Parana 18:00GMT; unstable sounding from Leticia - Peru 12:00GMT after providing for the solar heating (ii) continental (smoky) aerosols 3670 CCN at 1% supersaturation; maritime aerosols 225 CCN at 1%

	Maritime	continental
Stable	MS	CS
Unstable	MU	CU

amount reaching to the surface.

In order to calculate the latent heating, we have to account for all the components of the energy budget. The significant terms of the energy budget equation within the simulated fields are :

$$\frac{\partial \theta}{\partial t} + \frac{\partial u\theta}{\partial x} = C + \frac{\partial}{\partial t} k \frac{\partial \theta}{\partial z} \quad \left(\frac{^oK}{sec}\right) \qquad (1)$$

where,

+ first term denotes the heating rate.
+ second term denotes the heat flux through the lateral boundaries.
+ third term (C) denotes the latent heat release due to water phase changes.
+ fourth term denotes the turbulation generated moment at the surface. the k parameter (of

second order) is significant at the surface since $w(z = 0) = 0$. we add a similar calculation at the topmost level (there, the boundary is closed i.e. $w(z_{top}) = 0$)

Integration of this differential equation horizontally results in a time-dependent vertical profile of the heat flux. Further integration vertically and with time will result in the total heating that has occured in the domain in one run. In order to remove the inflow of mass from the left and right boundaries and from the surface heat flux (determined by the atmospheric conditions) we conducted another set of 4 'empty' runs, which, respectively generated a domain with the same atmospheric conditions but without the formation of clouds. The 'empty' runs were subtracted from the 'cloudy' runs, so that the resulting heat profiles would not account for heating that was not caused by cloud processes.

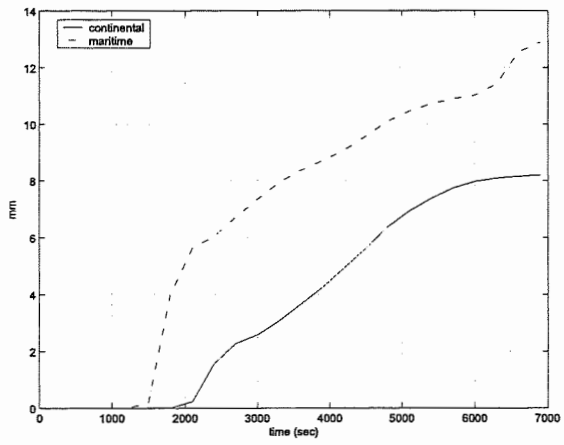

Figure 3: accumulated rainfall through runs CS and MS. The delay in precipitation onset in the continental cloud is obvious. This delay occures due to the dominance of ice precipitation processes.

4 VERTICAL HEATING PROFILES

According to the model's scheme, a calculation of rainfall amounts reaching the surface could be performed. Figure (3) shows large differences of precipitation amounts and distribution between the maritime and the smoky continental environments.

The amount of the net latent heating of the atmosphere throughout the run must equal to the equivalent energy stored in precipitation deposited on the surface. However, the vertical distribution of this latent heating can vary greatly, depending on the instablity and on the aerosols. This is shown in figures (4) and (5).

Figure (4) shows the effect of the aerosols suppressing warm rain and decreasing precipitation efficiency. Much of the unprecipitated condensates evaporate at the highest levels from ice crystals blowing off the anvils, and create evaporative cooling there, as can be seen at $H > 11km$ in figure (4). The greater released latent heat of freezing is manifested as excess heating at $6km < H < 11km$. The cooling due to melting appears at $3km < H < 5.5km$

Figure (5) shows the effect of instability for the same maritime aerosols. There was no excess cooling at the higher levels in the unstable run, probably due to the high precipitation efficiency in both stable and unstable conditions with maritime aerosols. Large heating excess at $H > 4.5km$ is compenstaed by equally large excess cooling at the lower levels. This is attributed to the fact that in the stable case, much of the rain is deposited without ever freezing, whereas in the unstable case, warm rain is lofted by the strong updrafts, freezes and releases the latent heat of freezing aloft, only to fall later and absorb that heat while melting at the lower levels.

5 CONCLUSIONS

In summary, increasing aerosols and instability have the same effect of greater upward transfer of heat for the same precipitation amount. this implies that greater precipitation amounts are required to compensate for the same radiative cooling of the atmosphere in more polluted and/or unstable atmosphere. Both parameters are affected by anthropogenic emissions and modification of surface properties. This constitutes the *latent heat forcing.*

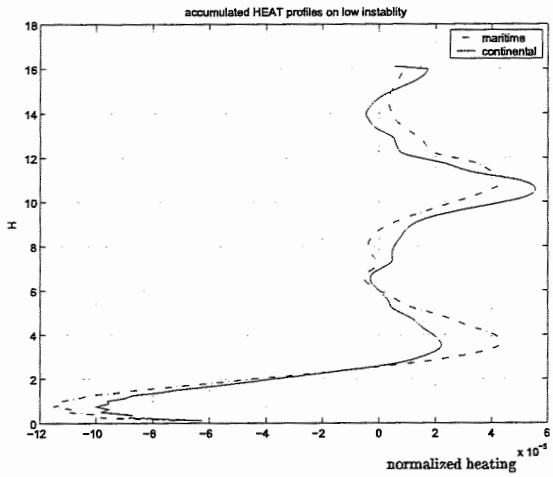

Figure 4: heating profiles of continental vs. maritime aerosols under stable atmospheric conditions, normalized by the total heat release.

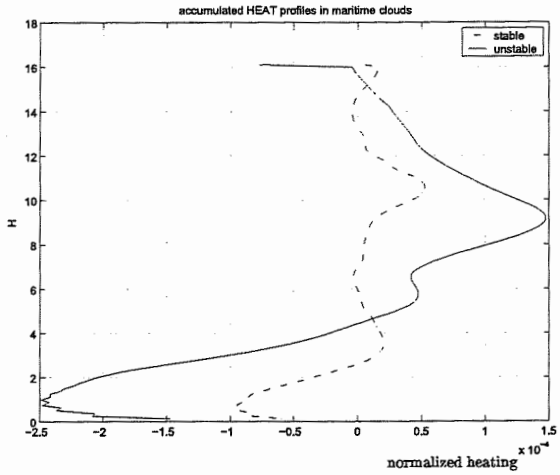

Figure 5: heating profiles due to clouds forming in maritime aerosols, in stable vs. unstable conditions, normalized by the total heat release.

6 ACKNOWLEDGEMENTS

This study was funded by the European Commission (Project SMOCC).

References

[1] Kasahara, A. and P.L.D., Dias, 1986: Response of planetary waves to stationary tropical heating in a global atmosphere with meridional and vertical shear. J. Atmos. Sciences 43 (18), 1893-1911

[2] Khain, A.P. and I., Sednev, 1995: Simulation of hydrometeor size spectra evolution by water-water, ice-water and ice-ice interactions. J. Atmos. Res. 36, 107-138.

[3] Rosenfeld D., 1999: TRMM Observed First Direct Evidence of Smoke from Forest Fires Inhibiting Rainfall. Geophys. Res. Lett., 26, No. 20, 3105.

[4] Rosenfeld D., 2000: Suppression of Rain and Snow by Urban and Industrial Air Pollution. Science, 287 (5459), 1793-1796.

[5] Rosenfeld D. and W. L. Woodley, 2000: Convective Clouds with Sustained Highly Supercooled Liquid Water Down to -37.5^oC. Nature, 405, 440-442.

[6] Khain A. P., D. Rosenfeld and A. Pokrovsky, 2001: Simulating convective clouds with sustained supercooled liquid water down to -37.5^oC using a spectral microphysics model. Geophysical Research Letters 28, 3887-3890.

[7] Rosenfeld D., R. Lahav, A. P. Khain, M. Pinsky, 2002: The role of sea-spray in cleansing air pollution over ocean via cloud processes. "Research Article" in Science, 297, 1667-1670.

[8] Andreae, M. O., D. Rosenfeld, P. Artaxo, A. A. Costa, G. P. Frank, K. M. Longo, and M. A. F. Silva-Dias, 2004: Smoking rain clouds over the Amazon. Science, 303, 1337-1342.

ROLE OF RELIEF AND DESERT IN FORMATION OF CLOUDS AND PRECIPITATION AT TIEN SHAN AND THE PAMIRS

Kurbatkin V. P.

Central Asian Research Hydrometeorological Institute (SANIGMI)
Tashkent, Uzbekistan

1. INTRODUCTION

Being a a closed region Central Asia gets water by the discharge of the rivers formed in the region mountains. Considerable areas are contented with the moisture brought by a precipitation. The precipitation is falling out over the natural pastures of mountains and deserts and also over the narrow band of foothills where it is possible to grow grain crops without watering.

It is evident that the precipitation is determined by the climate factors and by the physical and geographical environment of the region.

At conditions of plains and foothills the falling of atmospheric precipitation is basically related to frontal systems. 35-55 of such cases are occurred in a year. But there are regions in Tien Shan and the Pamirs mountain where those are observed 2-3 times more often.

Aim of presented work is to show role of relief and location of the region in the process of cloud and precipitation forming.

2 LOCATION AND RELIEF OF CENTRAL ASIA

The analyzed part of Central Asia is within the rectangular confined by 35^0 and 45^0 N and longitude 50^0 and 80^0 E. The region area is 1230 km^2. The considerable part of the region is flat with a slight slope to the north-west. In the east of the region there is the vast mountain massif known as the mountain system of Tien Shan and the Pamirs - Alay. In the south of the region from Caspian Sea to the spurs of Paropamise there are the mountain ridges of Copet-Dag which contribute to the north part of Turkmenian-Khorassan mountains. Further to the south boundary there is a wide meridionall lowering and next to that there is a slightly separated mountain system of Paropamise.

In the north of the region there is Khazakh small hills by which it is possible to draw the line of the region watershed from the more plain northern part. In the west of the region there is the Caspian Sea and near to it Caspian steppes. Thus, the region is open for the north flows and by considerable rate for the western flows. The intrusions of air masses move from the south along the Caspian Sea and along the rivers of Tedjen and Murgab through the above mentioned lowered part. In the east the region is blocked by a vast mountain system. Only significantly warmed air masses can cross the mountain systems. They are observed more often at the south of the region. And more seldom the monsoons penetrate through the Pamirs from the Indian Ocean.

Kurbatkin V. P. Central Asian Research Hydrometeorological Institute (SANIGMI) ,72 K. Makhsumov Str., 700052,Tashkent, Uzbekistan
E-mail:sanigmi@albatros.uz

3. BRIEF INFORMATION ABOUT THE PRECIPITATION

Over the region territory there is different quantity of precipitation fall over the plains, the total precipitation is 100-200 mm per a year, and over the foothills this quantity reaches the value of 1000 mm. According to the river discharge data the regions with the precipitation of 1500-2000 mm per a year can be distinguished. The East Pamirs is a dry region (the precipitation quantity in a year is 60-73 mm). There is a small precipitation fall in Central Tien Shan (270 -350 mm per a year), which amount in summer. In a yearly regime the precipitation falls irregularly. For Shahrysiabs situated in the central foothill part of the region and for Pskem situated in a plain open to air flows the yearly precipitation regimes are given in Table1.

Table 1

The average monthly value of a yearly precipitation norm (%)

Months							
1	2	3	4	5	10	11	12
Pskem							
11	12	14	13	8	9	11	13
Shahryslabs							
14	14	21	16	8	4	8	13

As one can see the precipitation falls in the region during the cold periods. The observed amount of precipitation falls during three months (February-April) when 40-50% of a yearly precipitation norm fall. According to Central Asia meteorologists data [Bugaev V. A., 1957, Nazarova T.Z.,1956, et. al.] the precipitation is, mainly caused by the cold fronts. Their energy source is the atmosphere baroclinicity in the boundary zone of two air masses and the energy of water phases transitions during the process of clouds and precipitation formation at the front, and it means that there will be a greater amount of high temperature warm masses and with higher temperature counteracts of the two air masses at the fronts. This regularity spreads both to an individual process and to the season. In winter between 30°-50° N a chain of polar climatology fronts is formed separating the zones with a prevalence of middle latitudes air over the zones with tropical air. In spring as snow melts and a stable snow

deposition is observed in the north these fronts displace to the north. What air masses form precipitation in the region?

4. AIR MASSES PENETRATING INTO CENTRAL ASIA

The first substantial work describing air masses including our region is the work of Bugaev B.A. and Georgio, B. A., 1940. Two air masses determining the overcast weather in the region are formed over Mediterranean area. They are tropical air mass and the air mass of the south region of the temperate latitudes. These air masses come into the region under the determined synoptic processes.

There are 15 synoptic processes over the region. In three of them tropical Mediterranean air mass comes into the region. These are intrusions of South Caspian and Murgab cyclones or a formation of wave activities over the mountains of the region. The temperate air of the south latitudes of Mediterranean area comes into Central Asia at one of the west kinds of intrusion. At other kinds of the west intrusion the temperate air of air masses formed over Atlantic Ocean or European area of Russia and Ukraine comes into the region. The amount of Mediterranean sea area masses intrusions into the region is given in Table 2.

Table 2

An average frequency of origination of individual synoptic processes

Type	Months					
	1	2	3	4	5	6
1	3.4	3.0	2.4	2.4	2.5	0.8
2	2.2	2.4	2.4	0.9	0.9	-
5	3.0	2.7	3.6	3.0	4.2	5.7
10	2.5	0.2	0.5	3.4	5.6	5.3
Type	Months					
	7	8	9	10	11	12
1	0.1	0.4	0.5	1.7	2.5	2.0
2	-	-	0.1	0.2	1.6	2.6
5	4.3	3.8	3.8	3.2	3.2	3.3
10	5.7	4.5	4.0	3.4	2.8	2.1

1 – South Caspian cyclone;
2- Murgab cyclone
5- North-west intrusion
10 – West intrusion

During the months with the greatest quantity of precipitation (February-April) tropical Mediterranean air flow penetrates thirty times into the region in average for many years, and the process itself lasts up to five days. Thus, during these months the tropical air is a rather frequent phenomena. But it doesn't always spread to the whole the region and its moisture frequently is not converted into precipitation. South cyclones breaks - through are realized by three trajectories [Bugaev V. A. et. al., 1957.]. And only those of them which bear this mass to the mountains give abundant precipitation.

In the presence of these air masses and Arctic air masses intrusion from Greenland or from Siberian sector of Arctic, the fronts with an abundant precipitation is formed over plains and foothills. In the time of the middle latitudes air intrusion from Western Siberia, Kazakhstan or European part of Russia which has been formed into a slow-moving cyclone, the fronts with light precipitation or without it is formed.

5. AIR MASSES FORMING OVER THE REGION

By the middle of the last century it has been known that two air masses which define in many respects the process of formation of cloud, are formed over the region. These are Turan air mass of the middle latitudes south belt (MT) in wintertime and Turan tropical one (TT) in summertime. MT is formed from an air mass incoming into the plain part of the region (the Turanian lowland) from north, west and north-east. This is Arctic or middle latitude air mass which is transformed into MT in mild weather (little-gradient field) and when the synoptic process known as the south-west periphery of anticyclone occurs. The period of the transformation lasts for 1.5-2 days during which the temperature rises by 2-5°, sometimes 5-8 ° daily. Then its rise is stopped and later on the temperature fluctuates insignificantly. If during the transformation period cold (arctic) air inflow continues the transformation process is protracted for 4-5 days. Warming up of air in this period of year is observed up to 2km altitude above sea level (a.s.l.). More often an isothermal process occurs there. Even at the Tashkent latitude over a snow cover due to a slight radiation from a snow surface at night and a slight warming up in the daytime owing to a high albedo of the surface, cooling of air mass does not become intensive and can not spread up to a kilometer altitudes. But in the plain part of Central Asia due to its geographical location there is not a stable snow cover, therefore the warmed Turan air mass from the middle latitudes differs by its temperature from the middle latitude air mass forming over a snow surface. As it is forming in a mild weather and often after a precipitation fall, the humidity in it may reach 90% by morning time. In daytime the absolute humidity is transferred to upper layers. From dry soils the aerosol lifting is possible in daytime. According to B. A. Ayzenshtat's investigations in summer and autumn in desert where the upper soil layer is dry, 86% of diurnal heat absorbed by soil is consumed for warming up of the air. In winter 10 million ha. of the desert are dry as well what facilitates to warm up the air over it up to high altitudes.

In warm period of a year (from the middle of May to the middle of September) under a little-gradient field over the plain Turan tropical air is formed from air masses invaded in previous period. It is strongly warmed up. The vertical temperature gradients at an altitude up to 4 km may reach 0.008° per 1m. At an altitude of 2-3 km a. s. l. the gradient is 0.009 ° per 1m. In winter time is is 0.007 and 0.008 per 1m respec-

tively. The relative humidity in the atmosphere is 35-50%. The specific humidity is presented in figure1.

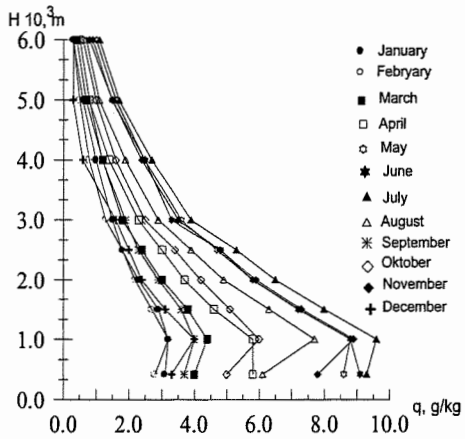

Fig. 1. Monthly average specific humidity in Turan air masses MT (October-April) and TT (May-September).

Thus the plain territory of the region and its desert part facilitate precipitation formation at foothills and mountains owing to warming up of the middle troposphere air, and its saturation by aerosols, moisture in daytime and preservation of moisture losses in the moisture-laden flow isolating it from contiguity to land surface at night.

6. THE SYNOPTIC PROCESS FORMED BY OROGRAPHY

In the list of 15 synoptic processes determining the weather in the region, the seventh type is "wave activity in the south and south-east of Central Asia" which is formed under impact of orography. In the known monograph it is [Bugaev V. A. et. al., 1957], described by M. A. Petrosyanz – a noted scientist in particular in the field of the study of cyclone activity over Central Asia. This type is described as a process when the cyclone waves, which displace along the mountain system are developed on the fronts of cold air mass intrusion having not large vertical extension (up to 2 km). At the same time the planetary upper-level frontal zone in free atmosphere is situated along latitudes and originates over the Mediterranean Sea. The temperature regime in the area of this weather type development fluctuates noticeably against the temperature corresponding to the intruded into cold air mass. This is the longest synoptic process in Central Asia, which lasts up to 7 days. There is a direct relation between wet months and years at foothills and a number of process occurrences.

Accumulated data allow giving more simple explanation of mountain impact on the process forming in contract to previous one. In wintertime a mountain wind is dominating in lower layers of the atmosphere on coming out from valleys and on the distance of dozens kilometers towards submountain plains direction. According to the observations at one of the Western Tien Shan plains in wintertime only in 5% of cases the mountain wind is not occurred in the lower of the mountain valley while it "is depressed" by a strong wind over mountain ridge. In the considered case "depression" is observed when the wind being at the mountain ridge level has a velocity of 15 m/s at condition of coincidence of its direction with the valley direction and a velocity of 20-25 m/s and more in the transversal direction. The same observations have shown that the mountain wind "is fed" by an airflow at mountain ridge area. In this weather type accompanied by heavy rainit is either the cold air mass (arctic) or the air of the southern middle latitude of Mediterranean, possibly transformed into tropical one. Obviously it is transformed by the mountain system (it is cooled down and possibly become wet). Therefore the mountain wind, which meet with an arctic air, forms a front (warm or cold depending on their temperature relation) on coming out from the valley. And the wet air mass passes over them. Three air masses have been registered in foothills under this type of weather conditions according to radiosonde and aircraft sounding data. The mountain system, forming a gravity wind, carries it out along valleys, going to the plain. The most strong flows form at eight largest river basins of the region and their main inflows on the plain. They determine the cyclonic waves in case of the cold air intrusion from north or north-west in a lower two-kilometer level of atmosphere and wet flow from west or south-west higher than that level occupying, at last, the middle troposphere.

7. RELIEF FORMS, CONTRIBUTING TO THE PROCESS OF CLOUD AND PRECIPITATION FORMING

7. 1. Over-basic surfaces of leveling

There are ancient peneplain surfaces or over-basic surfaces of leveling at the high ridges of Pamirs-Alai and Tien Shan Mountain. These zones have tens hundreds kilometers extension. They are well blown out at least when there are moderate winds. Based on the atmosphere properties, even under baroclinicity condition absence, a typical wind velocity is 10 m/s. Typical size of unevenness for West Pamirs is altitude of 900-2300 m. Based on the classical description of boundary layer of the atmosphere such surface roughness may be characterized by a 9-75 m value. This is confronted with the roughness of several mesozones on a greatly hilly plain and a big city. If increase of hilly surface to compare with the area of the horizontal projection of this territory it increases up to 45% for West Pamirs condition.

Under mountainous condition vertical temperature gradients must be close to those of free atmosphere. In this case under mild weather condition the wind velocity is 8-12 m/s, but may be 20-30 m/s. For these conditions the boundary layer altitude over such zones will be at least 800-2500 m. Some results are pre-

sented in table 3. Knowing that in first approximation a layer of extrusion may be accepted equal to 0.6-0.8 times boundary layer depth it is easy to estimate part of airflow kinetic energy suppressed by the relief.

Table 3

Atmosphere boundary layer height, m

γ 10^{-3}°/ m	Geostrophic wind velocity, m/s			
	10	12	15	20
5.0	1000	1211	1514	2019
6.5	1207	1448	1810	2414
8.0	1597	1916	2395	2874

This value ensures vertical currents in the boundary layer. For surface in the form of a square with a site of 50 km the vertical air flows in the boundary layer will be characterized by tens of centimeters per second (table 4). Under plain conditions from clouds having their a vertical extension of 2.5 km and when the vertical components of wind velocity are 2-3 times less, a considerable precipitation falls. For given parameters the conditions for precipitation formation are favorable. It is necessary to study humidity what is less than in plain. But large values of H and W may compensate humidity characteristics. From consideration of shape and size of these surfaces it is seen that W value fluctuation within one order is possible.

Table 4

Values of vertical component of wind velocity, 10^{-2} m/s

H, m	V_g, m/s				
	8	10	12	15	20
800	11	14	17	21	28
1000	14	17	21	26	35
1500	21	26	31	39	52
2000	28	35	42	52	69
2500	35	43	52	65	87
3000	41	52	62	78	104

7. 2. High-mountain slope of the valleys having non round cross-section

According to Schiller and Nlkuradse J. [according to Shlihting H., 1969] in non round tubes and channels in airflows secondary movements are observed. They are from the centre of the flow along bisector of angle where they diverge along their walls. Thus they form circulating curls. Similar circulations were registered during experimental investigations at the lower of Pskem valley (West Tien Shan) in wintertime [Kurbatkin V. P., 1984]. This fact allows to suppose that similar vertical movements along mountain slopes are possible in valleys having non round cross-section.

The main mountain ridges of Tien Shan and Pamirs are directed along latitudes. They are opened for west transport. The north faced slopes of these ridges are generally snow-covered. Then it may be assumed that moisture sublimation from air masses venting the valley is possible on these slopes. Bottom of Alai valley is characterized by a altitude of 3000 m a.s.l.. Zaalai ridge north faced slopes are snow-covered and its several peaks reach a altitude of 7000 m a.s.l. Preliminary estimation shows that precipitated moisture may be not less than a few tens of millimeters in a year at these slopes in zones of the ascended airflows.

8. CONCLUSION

Rough surface of the hollow type plain having general inclination toward north-west facilitates flowing of mountain and slope winds from the South, East and North. Interaction between north flow breaks and mountain winds gives strengthening of fronts at foothills. Protracted lift of air masses along an inclined meso-rough surface of plain and foothills promotes the same process. These processes are short-time one as cold air masses in mild weather even in wintertime are warming up for 2-3 days. Due to firstly south location of the region, secondary – stable snow cover absence, thirdly – availability of dust storms when it is not required to spend heat for evaporation even after precipitation fall. Accumulated in wintertime moisture the desert evaporates by plant transpiration in spring.

Continuous cold air inflow into lower layers promotes passing of wet, warm air masses from west over them without any moisture losses for condensation (sublimation) near the ground. Warm wet air masses tropical and Turanian origin coming to foothills, table-lands and a number of relief forms form clouds and precipitation. Processes of precipitation forming over them are strengthened by cold intrusions and mountain winds.

At Tien Shan and the Pamirs foothills can be simultaneously registered tree air masses with their own cloud systems. Possibly their accumulation into a single system having a number of crystals in its upper part sufficient for complete realization of moisture from wet warm air masses with the least moisture losses in cold subcloud layer. These situations facilitate falling out of abundant precipitation.

References

Bugaev V. A. and Georgio V.A., 1940, The air masses classification. M. and G., 12, 33-45.

Bugaev V. A., Georgio V. A., Kozik E.M. et. al., 1957. Synoptic processes of Central Asia , Tashkent: publ.by AS of UzSSR, 464.

Kurbatkin V. P., 1984 The empirical model of troposphere composition at the condition of mountain relief. Proc. SANIGMI , No.100(121), 21-31.

Nazarova T.Z.,1956,The influence of tropical origin air masses on spring-summer precipitation in Uzbekstan. Col. meteorology and hydrology in Uzbekistan, Tashkent.- Publ. by AS of UzSSR, 195-199.

Shlihting H., 1969, Boundary layer theory, Moscow: publ. by "Science",744.

MONTHLY PRECIPITATION ESTIMATE OVER WESTERN CHINA

Xiaoyang Liu[1] T. D. Diallo[1] Jietai Mao[1] Jiantong Li[2]

[1]Department of Atmospheric Science, Peking University, P. R. China
[2]Institute of Atmospheric Physics, Chinese Academic of Sciences, P. R. China

1. INTRODUCTION

Recently, there are many large scale precipitation datasets which cover more than 10 years. Two of them, GPCP (the Global Precipitation Climatology Project) and CMAP (the Climate Prediction Center (CPC) Merged Analysis of Precipitation) are widely used in climate analysis, numerical verifications and other investigation. GPCP dataset (Huffman et al, 1997) is developed by a group at the National Aeronautics and Space Administration Goddard Space Flight Center (NASA/GSFC) for the GPCP project in World Climate Research Program (WCRP) for the period from 1979 to present. Xie and Arkin (1996) take the gauge observations, multi-satellite estimates and the precipitation distributions from the National Centers for Environmental Prediction (NCEP) – National Center for Atmospheric Research (NCAR) reanalysis, and create the CMAP for the same period as for the GPCP product.

As a key component of the GPCP, the Global Precipitation Climatology Center (CPCC) in Germany has developed a sophisticated system of data selection, quality control, and objective interpolation for constructing gauge-based analyses over the global land areas (Rudolf 1993) from almost 7000 stations obtained from the Global Telecommunication System (GTS). The CMAP constructed a gauge-based analysis of global land precipitation by applying the same algorithm as the GPCC to over 6000 stations obtained from the version-1 dataset of the Global Historical Climatology Network (GHCN) of the NOAA National Climatic Data Center (NCDC) and the Climate Anomaly Monitoring System (CAMS) of NOAA/CPC.

In western part of China, there are only sparse gauge observations, and the geostationary satellite GMS positioned too east to use IR technology directly like GPI (the Global Precipitation Index) which is the main IR algorithm in both GPCP and CMAP satellite estimates. Since the average latitude is below 40 degree, the number of passing time of polar satellites is not as many as that at high latitude. So it is very difficult to estimate the precipitation accurately in this area. The error analysis of GPCP shows big relative uncertainty remained in this area. Most part of this area are deserts, so seldom gauge stations locate in this area and the amount of annual precipitation is no more than 100 mm. It is more difficult to measure and estimate precipitation when the GMS satellite positioned out side the suitable domain for GPI. This paper presents a modified GPI (named as WGPI) to estimate the monthly precipitation over west China with local climate precipitation and humidity data. Results show that WGPI has the similar accuracy as GPCP data set with more realistic structure.

2. DATA SOURCES

Corresponding Author's Address: Xiaoyang Liu, Department of Atmospheric Science, Peking University, Beijing, P. R. China, 100871
Email: xyliu@water.pku.edu.cn

Hourly GMS data used in this paper are received by the department of atmospheric sciences, Peking University, during 1996 to 2002. Several months lack of data due to different reasons. Only the channel of 10~11 micrometer is used in this research.

The disc of 41-factor climate data of China over 30 years (1961 to 1990) is used which is distributed by National Climate Data Center of China (NCDC) and total 649 surface stations included. Only several factors such as monthly relative humidity, monthly precipitation and raining days are used in this research.

The GPCP data set version 2 is downloaded from NASA/GSFC internet web.

3. ALGORITHM

Similar to GPI method, the WGPI can be expressed as following:

$$WGPI(\lambda,\varphi,m)=\int G(\lambda,\varphi,m)F_c(\lambda,\varphi,m)f(\lambda,\varphi,m)dt \quad (1)$$

Where λ• φ• m stand for longitude, latitude and month, G denotes local climate average precipitation rate (mm/hr), Fc denotes the cloud fraction where the temperature lower than the threshold (default 235K), f is the wetness modification function, $WGPI$ will be the integrated monthly precipitation. The basic idea of this method is to determine precipitation field structure with GMS satellite data and to correct the precipitation value with local climate data.

In order to get mean climate precipitation rate based on surface observations in 6 hour interval, an equation is introduced in each 2.5*2.5 grid as following:

$$G(\lambda,\varphi,m) = C*R_{month}(\lambda,\varphi,m)/(D_{rain}*4) \quad (2)$$

Where R_{month} and D_{rain} indicate monthly precipitation and raining days which can be read directly from the climate data disc, C is a transfer coefficient from 6 hour mean climate precipitation rate to 1 hour mean climate precipitation rate.

Generally, the precipitation lasts not as long as 6 hours. Based on 30 year climate data set, the 6 hour mean climate precipitation rate equals 3.0258mm/6hour over central China. And at the same area, the best result can be found by comparison GPI precipitation and GPCP data when 3 mm/hr is used in GPI. So the coefficient C can be calculated by C=3*6/3.0258≈6.0. For simplification, the C is used as a constant all over the western part of China in this research.

In WGPI, another wetness modification factor is also introduced which is in the form as:

$$f(\lambda,\varphi,m)=\begin{cases}(1+e^{b-cq(\lambda,\varphi,m)})^{-1} & q(\lambda,\varphi,m)<\bar{q}\\ ln(hq(\lambda,\varphi,m)-k) & q(\lambda,\varphi,m)\geq\bar{q}\end{cases} \quad (3)$$

Where b=2.7431• c=4.74• h=18.6• k=10.3 are statistic parameters• $q(\lambda,\varphi,m)$ is the monthly mean relative humidity (%) at each grid, $\bar{q}$ is the monthly mean relative humidity all over China. For western part of China, just the $q<\bar{q}$ is used due to its dry climate.

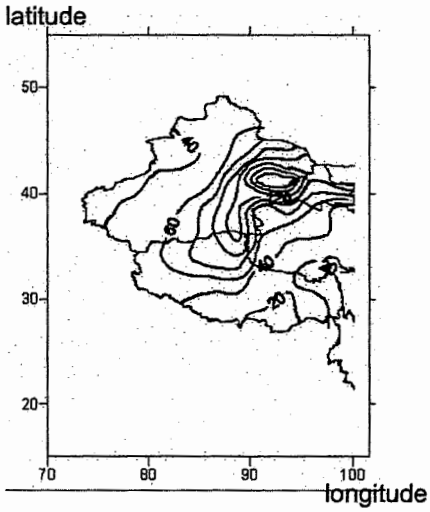

Fig 1• GPCP relative error distribution on June, 1998

4. DISCUSSION

In GPCP, the surface observations contribute most over western China continent. However, on 2.5*2.5 degree grid, only one or two surface gauges exist in the west of 100 degree east longitude. Some area even none of gauge exists and the value of precipitation should be interpolated. So some uncertainty could be included in the GPCP precipitation data. Since the monthly precipitation over western China is small, the absolute error of GPCP data is not large. But the relative error is remarkable. 40% are quite common, and more than 100% in the eastern part of XINGJIANG area also occur (Fig. 1).

Since the western China locates less than 100 degree east longitude, where is the continental climate area, and the satellite of GMS positioned the east of China. So the GPI is not suitable. The equation (2) is used to calculate the climate precipitation rate *G* which varies between 2.6 and 0.3. And the equation (3) acts as a modification of brightness temperature threshold (235K).

The accuracy of estimate can be increased

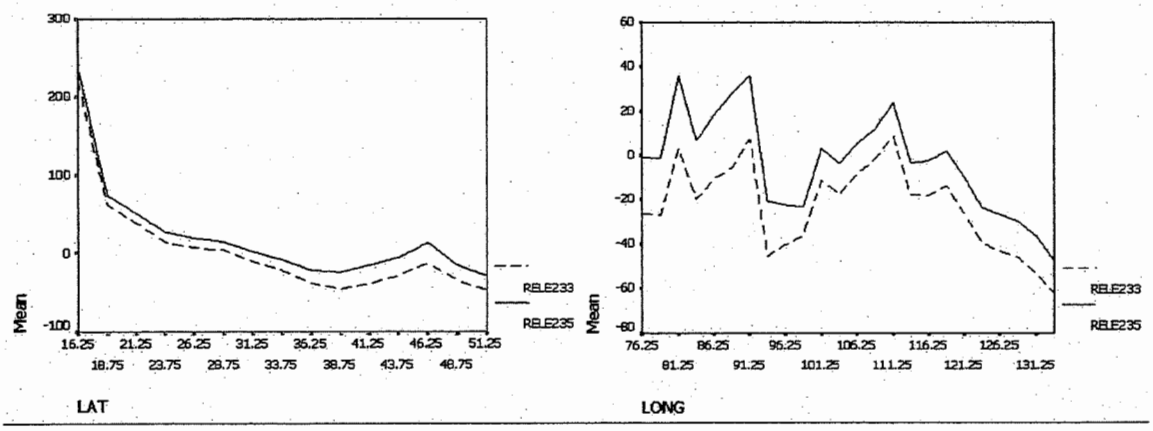

Fig. 2 MGPI mean relative error distribution along latitude (left) and longitude (right) with temperature threshold 233K (dashed) and 235K (solid) during Jun. and July, 1998 and 1999

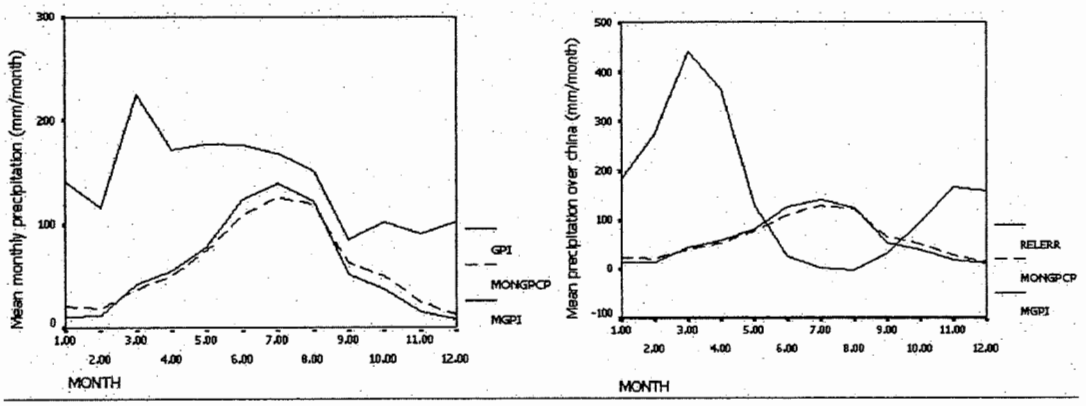

(a) (b)

Fig. 3• MGPI (lower solid lines) GPCP (dashed lines) monthly precipitation estimates over China. Upper solid lines (a) for GPI estimate, (b) for MGPI relative error

much higher when just replace the *G* in GPI with local *G* from equation (2) (refer to as MGPI). The mean relative error decreased from 200% of GPI (Figure neglected) to about 20% of MGPI (Fig. 2). And the correlation coefficient between GPCP and MGPI reached to 0.890 all over China.

By use of MGPI, the precipitation from 1996 to 2002 can be estimated. Fig. 3a shows the mean monthly precipitation distribution of GPI (upper line), GPCP (dashed) and MGPI (middle) over this period. The results of MGPI and GPCP are much similar. The Fig. 3b indicates the relative error distribution (upper line) which is quite high at less rain seasons.

Further modification to the GPI is the relative humidity factor. The results of GPCP,

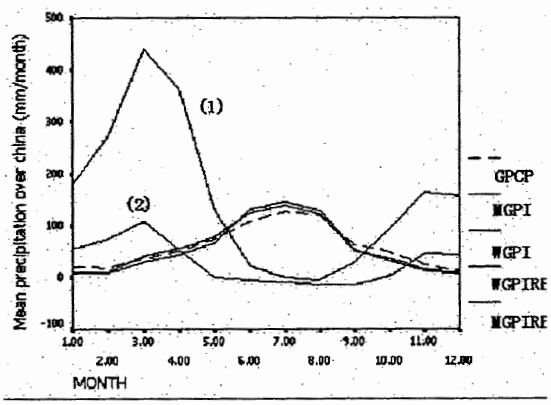

Fig. 4• WGPI,MGPI GPCP comparison

MGPI and WGPI are shown on Fig. 4 and the lines (1) and (2) stand for mean relative error of MGPI and WGPI, respectively. The estimates of them are very similar and the relative error of WGPI decreases below 100% and much lower than MGPI. Except 2 points, all of the grids have the relative errors less than 50% which is very close to the uncertainty of GPCP when applying the WGPI to estimate monthly precipitation on June, 1998.

5. CONCLUSIONS

From above discussion, it can be seen that the GPI is not suitable for the area of western China. But it can be still used effectively after some modifications.

The WGPI estimates monthly precipitation without any surface rain gauge data and reaches similar accuracy to GPCP. It is more useful for western China where fewer surface stations locate.

The WGPI estimates derived from real cloud coverage should be more realistic compared with those merely from interpolation.

GPI-like method is not suitable for warming precipitation, but it is not found any warming precipitation in all sampling data probably because of high altitude and moderate latitude.

So it is possible to get better precipitation estimate in the western part of China by combining the WGPI derived precipitation with surface gauge observations than that from GPCP which is combined by multi-satellite estimates and surface gauge observations.

6. ACKNOWLEDGEMENT

The authors would like to say thanks to Dr. Pingping Xie of NOAA/CPC, senior researcher Ping He and NCDC of China who supplied the climate data, and the NASA/GSFC, USA, who supplied GPCP combined data set version 2.

7. REFERENCES

Huffman, G. J., and Coauthors, 1997: The Global Precipitation Climatology Project (GPCP) combined precipitation dataset. Bull. Amer. Meteor. Soc., 78, 5-20.

Xie, P., and P. A. Arkin, 1996: Analysis of global monthly precipitation using gauge observations, satellite estimates and numerical model predictions. J. Climate, 9, 840-858.

A NEW SNOW GROWTH MODEL WITH APPLICATION TO RADAR PRECIPITATION ESTIMATES

D. L. Mitchell, A. Huggins and V. Grubisic

Desert Research Institute, Reno, Nevada, USA

1. INTRODUCTION

The use of moment conservation equations combined with moment expressions to predict the evolution of ice particle size spectra has resulted in favorable comparisons with observed evolution of size spectra (e.g. Mitchell 1988; Mitchell 1994), where snow growth model input consisted of the vertical profile of the ice water content (IWC) and temperature. Based on this success, it would be advantageous to adopt the same methodology in developing a microphysical scheme that is easily incorporated into cloud resolving models (CRM). That is, instead of using the IWC as an input parameter, use supersaturation, as this will be compatible with the existing framework of some CRMs. This was the approach taken by Bennedetti et al. (2003). Such a model framework may also allow investigations into complex processes such as the interplay between ice crystal habit, supersaturation and ice crystal nucleation rates (Mitchell and Chai 1998). In addition, such a model might find practical application in the estimation of snowfall rates below cloud base where radar's are often not able to "see". The reflectivity of the lowest radar echo could be used to initialize such a model, which would provide an estimate of snowfall rate at ground level.

This was precisely the motivation for the model described in this paper. While only run as a steady state height dependent model at this time, the model equations illustrate its potential for running in a 3-dimensional time dependent mode. But for radar applications, the steady state model is sufficient.

2. MODEL FORMULATION

The strategy here is to develop two coupled prognostic equations, one for dN/dt and another for dλ/dt, where N = particle number concentration and λ = slope parameter of a size distribution having a gamma form:

$$N(D) = N_o D^v \exp(-\lambda D) , \qquad (1)$$

where D = maximum dimension. The parameter v may be given a constant value for a given hydrometeor class. Both prognostic equations are general for any hydrometeor class (i.e. snow, rain, cloud droplets), and are functions of supersaturation, particle shape, and other factors. They are linked to the dynamics through the supersaturation development equation, generalized for mixed phase clouds (Chen 1994).

2.1. Particle number concentration

We begin with a form of the particle number density equation, similar to that in Mitchell (1994) but with the inclusion of a particle nucleation term:

$$\frac{\partial}{\partial t} n(m)dm = \left[\frac{\partial N}{\partial t}\right]_{Nucl} - \frac{\partial}{\partial z}\left\{[w - v(m)]\, n(m)\right\}$$

$$- \frac{\partial}{\partial m}\left[\frac{\partial m}{\partial t}\, n(m)\right]$$

$$+ \tfrac{1}{2}\int_o^m n(m-m')n(m')k(m-m',m')g(T)dm'$$

$$- n(m)\int_o^\infty n(m')k(m,m')g(T)dm' . \qquad (2)$$

The 1st term on the rhs of (2) gives the particle nucleation rate, the 2nd term the vertical advection dependence, the 3rd the particle mass growth rate dependence, the 4th the production of particles of mass m through aggregation, and the 5th the removal of particles of mass m through aggregation. The zeroth moment conservation equation with respect to mass is generated by multiplying all terms in (2) by $m^p dm$ and integrating over all m, where p = 0. Since this is for the zeroth moment (i.e. governing N), the mass growth term does not affect N, and the 3rd term is absent in this conservation equation. Nucleation for both cloud droplets and ice crystals can be expressed as

$$dN/dt = k\, C\, S^{k-1}\, dS/dt , \qquad (3)$$

Corresponding author address: David L. Mitchell, Desert Research Institute, 2215 Raggio Pkwy, Reno, NV 89512-1095, USA E-Mail: mitch@dri.edu

where C and k are constants and S = supersaturation over ice or water (e.g. Huffman 1973). Equation (3) has the constraint that only positive values are used. The remainder of the derivation follows the same methodology as in Mitchell (1994), resulting in the following time and height dependent solutions for N, where z is positive downwards:

$$\frac{\partial N}{\partial t} = k\,C\,S^{k-1}\,dS/dt - \frac{\pi\,a\,E\,I(v,b)\,N^2}{8\,\Gamma(v+1)\,\Gamma(v+1)\,\lambda^{2+b}} \quad (4)$$

and

$$\frac{\partial N}{\partial z} = \frac{bN}{\lambda}\frac{\partial \lambda}{\partial z} + \frac{\Gamma(v+1)\lambda^b}{a\,\Gamma(b+v+1)}\left[kCS^{k-1}dS/dt + \frac{\partial(wN)}{\partial z}\right] - \frac{\pi\,E\,I(v,b)\,N^2}{8\,\Gamma(b+v+1)\Gamma(v+1)\lambda^2} \quad (5)$$

where a and b are the fallspeed power law coefficients

$$v = a\,D^b\,, \quad (6)$$

Γ denotes the gamma function, w = cloud updraft, E = aggregation efficiency and I(v,b) is an integral solved by Gauss' hypergeometric function and is related to the rate of change in N due to aggregation. The 1st rhs term in (4) is the nucleation rate while the 2nd term is the aggregation rate, indicating $\partial N/\partial t$ is determined through the competing effects of these two processes. Regarding the height dependence of N, the 1st term on the rhs of (5) describes the dependence of $\partial N/\partial z$ on particle fallout, or vertical advection without an updraft. The prefactor of the 2nd term in (5) is the inverse of the number flux weighted fallspeed v_{Nf}, defined as

$$v_{Nf} = \int v(D)N(D)dD/\int N(D)dD$$

$$= a\,\Gamma(b+v+1)/\Gamma(v+1)\lambda^b\,. \quad (7)$$

The product of this prefactor and the 1st term in brackets gives the nucleation dependence of $\partial N/\partial z$, while the product of this prefactor and the 2nd term in brackets gives the updraft dependence of $\partial N/\partial z$. The 3rd term on the rhs gives the aggregation dependence.

The Lagrangian derivative dN/dt (neglecting the horizontal advection terms) is thus given by combining (4) and (5):

$$\frac{dN}{dt} = \frac{\partial N}{\partial t} + (v_{Nf} - w)\frac{\partial N}{\partial z} \quad (8)$$

2.2 Particle size

The slope parameter, λ, is a measure of particle size. For instance, the mean N(D) size is simply $(v+1)/\lambda$. The solution for λ also begins with Eq. (2), generating the second moment conservation equation with respect to mass by multiplying all terms by m^2dm and integrating over all m. The nucleation expression used in (2) by Lo (1983) had the form:

$$[\partial N/\partial t]_{Nucl} = c(t)\,\delta(m)dm \quad (9)$$

where δ is the dirac delta function. This simply indicates that ice embryos resulting from nucleation have very small mass relative to all other particles in the N(D), and are distributed over a very narrow mass or size range, as denoted by $\delta(m)$. Multiplying $[\partial N/\partial t]_{Nucl}$ by m^2dm to generate the second moment conservation equation results in a term $m_o^3/3$, where m_o corresponds to an ice embryo mass. This makes the nucleation term negligible relative to other terms in the second moment conservation equation, and one can ignore nucleation here.

Since we are no longer expressing diffusion or condensation growth in terms of IWC or LWC, but rather expressing this growth in terms of supersaturation, the mass growth equation for a particle is used here:

$$dm/dt = 4\,\pi\,C_s\,D\,D_v\,f_v\,(\rho_\infty - \rho_{vs})\,, \quad (10)$$

where C_s = particle shape factor, D_v = diffusion coefficient for water vapor, f_v = ventilation coefficient, ρ_∞ = ambient vapor density and ρ_{vs} = vapor density at saturation with respect to water or ice. For a stationary particle, f_v = 1.0 and (10) can be expressed as

$$dm/dt = f(T,p,S)D\,, \quad (11)$$

where T, p and S refer to temperature, pressure and supersaturation. In practice, f_v is evaluated for the entire N(D) as described in Mitchell (1994), and thus need not appear in (11). Using the same methodology as described in Mitchell (1994) but using (11) directly (without substituting the 1st moment conservation equation for f(T,p,S)), the time and height dependent solutions for the N(D) slope parameter are

$$\frac{\partial\lambda}{\partial t} = \frac{f(T,p,S)\lambda^{\beta}}{\beta\alpha}\left[\frac{\Gamma(v+2)}{\Gamma(\beta+v+1)} - \frac{2\Gamma(\beta+v+2)}{\Gamma(2\beta+v+1)}\right]$$

$$- \frac{\pi\, a\, E\, I(\beta,v,b)\, N}{4\beta\Gamma(2\beta+v+1)\Gamma(v+1)\lambda^{b+1}} \qquad (12)$$

and

$$\frac{\partial\lambda}{\partial z} = \left[\frac{a\,\Gamma(2\beta+b+v+1)}{\lambda^{b}}(2\beta+b)N - 2\beta\,\Gamma(2\beta+v+1)wN\right]^{-1}$$

$$\left\{\frac{\partial N}{\partial z}\lambda^{1-b}a\Gamma(2\beta+b+v+1) - f(T,p,S)N\lambda\,\frac{\beta\,2\Gamma(\beta+v+2)}{\alpha}\right.$$

$$\left. - \frac{\partial(wN)}{\partial z}\lambda\Gamma(2\beta+v+1) - \frac{\pi\, a\, E\, I(\beta,v,b)\, N^2}{4\Gamma(v+1)\lambda^{b+1}}\right\} \qquad (13)$$

where $I(\beta,v,b)$ is another integral solved by Gauss' hypergeometric function and is related to the rate of change of aggregation growth. The constants α and β refer to the mass-dimension power law corresponding to a given particle type:

$$m = \alpha D^{\beta}. \qquad (14)$$

Combining (12) and (13) gives the Lagrangian derivative for λ, where z is positive downwards:

$$\frac{d\lambda}{dt} = \frac{\partial\lambda}{\partial t} + (v_z - w)\frac{\partial\lambda}{\partial z}. \qquad (15)$$

Here v_z is the $(\text{mass})^2$ moment weighted fallspeed, given as

$$v_z = \int v(D)[m(D)]^2N(D)dD/\int[m(D)]^2N(D)dD$$

$$= a\,\Gamma(2\beta+b+v+1)/\Gamma(2\beta+v+1)\lambda^{b}. \qquad (16)$$

The first term on the rhs of (12) describes the influence of diffusional growth on $\partial\lambda/\partial t$, while the second term describes the effect of aggregation. Regarding (13), the first term on the rhs in brackets contains two terms within the brackets. The first is the downward N flux in the absence of an updraft, while the second is the upward N flux due to w in the absence of sedimentation. Collectively these terms help describe the impact of w on $\partial\lambda/\partial z$. Of the remaining terms (also in brackets), the first and third terms relate to sedimentation and updraft effects, respectively, while the second and forth terms describe the influence of diffusion and aggregation growth on $\partial\lambda/\partial z$. Note all these terms are divided by the first bracketed term. To better understand Eq. (13) physically, we let w = 0, which allows (13) to simplify to the following form:

$$\frac{\partial\lambda}{\partial z} = \frac{\lambda}{(2\beta+b)N}\frac{\partial N}{\partial z} - \frac{f(T,p,S)\lambda^{\beta+b}\,2\Gamma(\beta+v+2)}{\alpha\, a\,(2\beta+b)\,\Gamma(2\beta+b+v+1)}$$

$$- \frac{\pi\, E\, I(\beta,v,b)\, N}{4(2\beta+b)\,\Gamma(2\beta+b+v+1)\Gamma(v+1)\lambda}. \qquad (17)$$

The first term on the rhs of (17) describes the effect of vertical advection through particle sedimentation on $\partial\lambda/\partial z$. The second describes the effect of diffusion growth, while the third term describes the influence of aggregation. The impact of these processes on $\partial\lambda/\partial z$ in terms of the variables which describe them is now more apparent. One example may be worth pointing out. Although a nucleation term is not explicitly in this solution, $\partial N/\partial z$ and N (which appear in the fallout term) do depend partially on nucleation, as indicated in (5). If $\partial N/\partial z$ is positive with N increasing with decreasing height due to nucleation, then this will increase λ, as one would intuitively expect.

The horizontal advection terms will be similar to the time dependent solutions, as illustrated in Mitchell (1994).

2.3 Accretional growth

Past experience has taught that numerical stability is enhanced when the process of accretion growth (e.g. riming for snow) is dealt with as a separate prognostic equation (i.e. not derived simultaneously with the other processes from (2)). The λ dependence on accretion is described in Mitchell (1995) and the dependence of ice particle mass and fall speed constants on accretion is given in Mitchell (1990).

2.4 Supersaturation coupling

The governing equations for the size distribution, (8) and (15), are strongly coupled with supersaturation produced in the updraft through both particle nucleation and vapor diffusion growth. These processes determine the uptake rate of excess vapor, and thus determine the supersaturation level. The principal link between the microphysical scheme described above and the cloud dynamics is the supersaturation development equation (Chen 1994):

$$\frac{dS}{dt} = A_1 w - A_2\frac{dy_l}{dt} - A_3\frac{dy_i}{dt}, \qquad (18)$$

where

$$A_1 = S\left(\frac{L_v}{c_pT} - 1\right)\frac{M_a g}{RT}, \quad (19)$$

$$A_2 = S\frac{L_v^2}{c_pRT^2} + \frac{p}{e_s}, \quad (20)$$

$$A_3 = S\frac{L_v L_s}{c_pRT^2} + \frac{p}{e_s}, \quad (21)$$

and where L_v is the latent heat of vaporization, L_s is the latent heat of sublimation, c_p is the molar heat capacity of air at constant pressure, M_a is the molecular weight of air, g is the gravitational acceleration, R is the universal gas constant, p is the air pressure, and e_s is the saturation vapor pressure over liquid water at temperature T. The rate of change of y_L and y_I give the rates at which the cloud droplet and ice particle size distributions uptake excess moisture, respectively. For example, for $f_v = 1$,

$$\frac{dy_I}{dt} = \int_0^\infty \frac{dm}{dt} N(D)dD = \frac{(v+1)\, f(T,p,S)\, N}{\lambda}. \quad (22)$$

Note that N and λ in (22) come from (8) and (15), and are hence functions of particle shape. Also, f(T,p,S) depends on particle shape through C_s. In this way shape effects influence the rates of moisture uptake.

3. MODEL INITIALIZATION WITH RADAR

Derived from the fundamentals of Rayleigh scattering, the IWC can be expressed as

$$IWC = \alpha\, \Gamma(\beta+v+1)\, [\, g_w/g_i\,]\, Z_w\, \lambda^\beta / \Gamma(2\beta+v+1), \quad (23)$$

where

$$g_w/g_i = (\pi K_w \rho_i)^2 / (6\alpha K_i)^2, \quad (24)$$

$$K_i = |(m_i^2-1)/(m_i^2+2)|, \quad (25)$$

and

$$K_w = |(m_w^2-1)/(m_w^2+2)|, \quad (26)$$

where m_I and m_w are the real refractive index for water and ice, and ρ_i is the bulk density of ice. The term Z_w in (23) is the operational reflectivity factor used by the NWS, and is based on m_w and spherical drops. Therefore a term is needed to translate Z_w into Z_i, the reflectivity factor for ice particles. This is supplied in (23) by the ratio g_w/g_i, whereby Z_w units of mm^6/m^3 are converted to units of $cm^{2\beta}/m^3$. The slope λ in (23) corresponding to Z_w is estimated from temperature T following Ryan (2000), where T is based on sounding data. In this way the model can be initialized near cloud base with radar reflectivity and T, and used to estimate the snowfall rate at ground level.

Preliminary testing of the model predicts the evolution of size spectra very similar to those observed in frontal clouds, as well as providing physical insights regarding snow formation. Due to space limitations, these results will be presented at the meeting.

Acknowledgment: This research was sponsored in part by the NSF USWRP, the NOAA CSTAR and the DOE ARM programs.

4. REFERENCES

Bennedetti, A., G.L. Stephens, T. Vukicevic, 2003: Variational assimilation of radar reflectivities in a cirrus model. I: Model description and adjoint sensitivity studies. Q.J.R. Meteorol. Soc., **129**, 277-300.

Chen, J.-P., 1994: Predictions of saturation ratio for cloud microphysical models. *J. Atmos. Sci.*, **51**, 1332-1339.

Huffman, P.J., 1973: Supersaturation spectra of AgI and natural ice nuclei. *J. Appl. Meteorol.*, **12**, 1080-1082.

Lo, K.K., 1983: Growth processes of snow. Ph.D. dissertation, Massachusetts Institute of Technology, Report No. AFGL-TR-83-0105, 192 pp.

Mitchell, D.L., 1988: Evolution of snow-size spectra in cyclonic storms. Part I: Snow growth by vapor deposition and aggregation. *J. Atmos. Sci.*, **45**, 3431-3451.

Mitchell, D.L., 1990: Evolution of snow-size spectra predicted by the growth processes of diffusion, aggregation and riming. Preprints, Conf. on Cloud Physics, AMS, July 23-27, 1990, San Francisco, Calif.

Mitchell, D.L., 1994: A model predicting the evolution of ice particle size spectra and radiative properties of cirrus clouds. Part I: Microphysics. *J. Atmos. Sci.*, **51**, 797-816.

Mitchell, D.L.., 1995: An analytical model predicting the evolution of ice particle size distributions. Ph.D. thesis, University of Nevada, Reno. 171 pp.

Mitchell, D.L. and S.K. Chai, 1998: The potential dependence of ice nucleation rates on crystal shape. Preprints, Conference on Cloud Physics, 17-21 August 1998, Everett, Washington, 60-63.

Ryan, B.F., 2000: A bulk parameterization of the ice particle size distribution and the optical properties in ice clouds. *J. Atmos. Sci.*, **57**, 1436-1451.

CLIMATE OF CITIES URBAN HEAT ISLAND AND URBAN INDUCED PRECIPITATION,EFFECT ON HUMANITY.

O.F.OMIDIORA.

POLLUTION HAZARDS FREE ENVIRONMENTAL GROUP
EMMAUS CHRISTIAN SCHOOL, MAENZA(LT) ITALY

Introduction

A knowledge of the climate of cities, has many important applications, particularly in bioclimatology, the study of the relations of climate and life. For Example, in cities where pollution levels are becoming alarmingly high, it may be necessary to select new areas for industrial zoning on the basis of meteorological factors. City climate is an example of man- made local modification. The climate of cities has been considered by Geiger and Kartzar(260). Since much of the world's population lives in a built-up areas, the subject is of great importance. There is growing evidence, for example, that the urban environment contributes substantially to illness and morbidity, particularly in the case of respiratory diseases, published climate summaries may be used in three ways in the search for urban country weather relations. A rural and a city observing station may be compared, long-term record (20-50 years) may be analyzed for evidence of an effect of increasing, industrialization and population growth, Sunday and weekday climate averages may be compared, commercial and industrial activities are at minimum on Sunday.
Lansberg(261) emphasized two difficulties that arise in the identification of city climate by the above methods. In the first place, there are not many comparative records between city and country. Generally, such parallel services are available by accident rather than by design.
This is the case for the usually observed weather elements at a city station and an outlying airport.
Secondly the urban climate is frequently complicated by special orographic features such as lakes. It is then not always possible to isolate urban from other contributing factors. For these reasons there is increasing interest in special micro-meteorological studies of a city, although a complete energy balance estimate had yet to be attempted. There is a very real need for a detailed description of the heat, water vapor and pollution source strengths and emission heights throughout the urban area. Only then will it be possible to arrive at some reasonable estimate of the energy budget of a city.

Anthropogenic Heat And Water sources.

The Anthropogenic heat of a cities in a range of climates are based on estimate of energy life within a city from all sources (electricity, gas, coal, solar conversion, gasoline, wood etc.) for the purpose of space heating, manufacturing, transportation, lighting etc. The average anthropogenic heat flux density (QF) depends upon the average energy used by individuals on many factors including the affluence and nature of the economy and the need for winter space heating. It might be thought, therefore that the city-country temperature difference would be a maximum in winter when space heating requirement are greatest, particularly if there is snow in the suburbs but not in the center of the city.
Considerable amounts of water vapour are released when fossil fuels such as natural gas, gasoline, fuel oil, and coal are burnt. The use of water to absorb waste heat from power plant and other industrial processes also greatly enhances vaporization from cooling towers, cooling ponds rivers and lakes. In combination these provide a preferential source of vapour for the urban atmosphere(F). the importation of water to the city is necessary to meet demands from residential, industrial and other users. ultimately this water is lost from the system via evapotranspiration or runoff.

Omidiora Olakunle Francis
Emmaus Christian School Localita Farneta Snc 04010
Maenza LT Italy.
Email: wxboy2002@yahoo.ca

Water Balance

Considering the water balance of an urban building volume with that of a corresponding soil or soil- plant-air volume in the surrounding countryside. The water input to the urban system is greater because its precipitation is augmented by vapour(F) and the water in the city, for which there are no rural counterparts (if we ignore irrigation).The urban evapotranspiration on and sub surface storage (?S) are less than in the

rural situation. Evapotranspiration is expected to be reduced because of the removed of vegetation and its replacement relatively impervious materials.

Energy Balance

Comparing the energy balance of an urban building-air volume with that of a nearby rural soil-plant air volume, the daytime heat storage is therefore greater than in the case of a grass covered field. This is because pavement and concrete buildings have relatively high heat capacities (PC) and high conductivity (K) Finally the lack of evaporational cooling increases the energy available for sharing between QH and QG (Heat Flux) At night, the storage daytime heat is released from buildings and pavement, resulting in higher air temperatures than occur in the country.

Reliable energy balance for urban areas are only just becoming available. The example given in Fig 1.0 below is based on direct measurements of Q and QH, calculated ?QS and solution for QE as the residual in the energy balance. It is assumed that ?Qa is negligible and that QF is incorporated in the other terms. The data in Fig 1.0 are averages based on 30 days of summer observations at two cities in the greater Vancouver area. The rural site is an extensive area of grassland and the sub-urban one is in an area fairly uniform 1 or 2 stored housing (36% built, 64% green space) for the sub-urban (a) it shows that the turbulent sensible heat flux density QH is the primary means of dissipating, the day time net radiation surplus. Evapotranspiration QE is the next largest heat sink for the system showing that water is still readily available despite the waterproofing effect of urban development, sensible heat storage ?QS by the system is also a significant term in the balance. The apparent lag of the QH curve in Fig (!.0a) remains positive into the late evening (after sunset). This continued warming of the atmosphere by turbulent heat transport may be important in the growth of the urban heat Island that occurs in the same period Fig (2.0) Urban pack, especially if irrigated may act as "oases" because they are relatively anomalous moisture source in an otherwise generally dry area. These comments highlight the fact that the availability of moisture is one of the most important controls on urban climate. By comparing the sub-urban result with those gathered synchronously at the rural site (1.0b) it is accessed that the impact of urbanization upon the energy balance. This most easily achieved using Fig (1.0c) which shows the difference between the environments. In the daytime, the suburban net radiation probably the most important change is the lower evapotranspiration in the city leading to a preferential channeling of energy into sensible from (QH and ?QS), and therefore a warming of that environment. The sensible heat appears be put mainly into greater storage in the morning and released into the atmosphere in the late afternoon and evening.

There is greater urban heat storage due to the insulation provided by rural vegetation covers or the greater surface area for absorption impacted by urban geometry, or the reduced heat uptake due to the relative dryness of urban materials.

Two aspects of urban climate are particularly noteworthy because of their hidden implications, these are

1. The increase in temperature over urban areas (The so called heat Island phenomenon) and
2. The pollution of the city air. urban areas are much warmer than their rural environs particularly at nights.

Radiation Balance

The short-wave input (K =S+D) to urban areas is considerably altered in its passage through a polluted atmosphere. The attenuation of the incoming radiation depends upon the nature and amount of the pollutants. In a heavy industry or coal burning city (Energy Heat) K may be reduced by 10-20% in composition with its surrounding countryside .In less industrial cities where vehicles are the prime sources and photochemical pollution is dominant, the range is 2-10%.

The reflection of short wave radiation from building-air volume depends both on the Albedo of the individual reflecting surfaces and on their geometrical arrangement.

The Albedo of low latitude, cities is less certain but in mid latitude, it is expected that K will be less in the urban area compare with the surrounding countryside, but that this deficit is partially offset by a lower urban albedo. Therefore , except for snow- covered conditions, urban/rural net short wave radiation differences are not large. Ass we shall see later that the urban area is warmer than its environs at night, and as a result it emits more long wave radiation to the atmosphere(L) .The return long wave flux from the atmosphere (L) is also greater in the urban area because of the overlying pollution layer. This simple analysis therefore suggests that although Urbanization alters every component flux of the radiation budget, the net effect on urban/rural radiation differences is small.

City Temperature

The characteristics warmth of a city is called Urban Heat Island. The air in the urban canopy is usually warmer than in surrounding countryside. This urban heat Island effect is probably both the clearest and the best documented example of inadvertent climate modification. The exact form and size of this phenomenon varies in time and space as a result of meteorological, locational and urban characteristics.

Heat islands form most readily in calm weather, strong winds tend to disperse heat and the pollutant too. A windy day gives the city much the same weather as the surrounding country. Interference by high buildings makes the wind even gustier in the city with light winds, however, the buildings have the opposite effect. The air over the inner city is trapped by the obstacles and remains in the urban canyons. Pollutants accumulates and fog forms, the pollutants combine with the water or Ice droplets to form smog.
As cities have grown bigger, their heat Island have become more intense. The bigger the city, the bigger their heat island. For city dwellers this has been a real climatic change. In Paris France, for example, mean annual temperature rose almost 1°K between 1880 and 1965. Mean annual temperature in Tokyo, Japan, rose by 1.4°K between 1915 and 1970.
Studies of the urban Island phenomenon have been carried out mainly in cities in the Temperate regions. These studies indicate that the heat Island effect is greatest during Summer and early Autumn or clear nights when the wind speed is less than 5-6 m/s.
The net result of the energy exchange discusses in chapter one above and summarized is to create an urban heat Island, making the city a few degrees warmer than surroundings. The intensity of the heat Island is largely a function of building density and the amount of incorporated as would be expressed from energy considerations.
There is a general relationship between city size and heat island intensity.

Tu - r = Plog

Where Tu - r is the temperature of the urban and the rural area, is the population.

Hypothesized Causes Of The Urban Heat Island

The urban heat island phenomenon is caused by the following factors.

The thermal heat capacity and conductivity of urban surfaces which encourage the absorption of outgoing long wave radiation during the day and its re-emission by polluted urban atmospheric at night.
The addition of heat from combustion, space heating and metabolism in the human body as a result of over population.
Decrease loss of sensible heat due to the decrease in wind flow because of the frictional effect of city structures, reduces the exchange of warm city air with that of the cooler rural environ and affects evaporative processes which can produce cooling.
Decrease evaporation due to the removal of vegetation and the surface water proofing of the city, most of the energy will be used for warming the air. The dryness of the city surfaces is due to the removal of surfaces runoff by urban storage systems, lack of extensive vegetation cover and absence of swamps or water pools from which evaporation and transpiration can take place.
The green house effect of the pollution layer over city also aids the development of the urban heat island phenomenon. There is a reduction in terrestrial infra-red radiation to space at night so that energy is conserved within the city atmosphere below the polluted layer.

The Urban Heat Island Development In The Cities.

By comparing the low latitudes (Tropics) and the Temperate regions. The urban heat Island phenomenon is likely to be less developed in cities in the low latitudes, this is because of the prevailing high temperature which does not allow space heating, secondly, most cities in the tropics are not as industrialized or motorized as those in the temperate region. Level of air pollution can be expected to be
lower. This implies that more of the tropics are less paved and the storm water drainage is less efficient than those in the more development temperate region.
This means that less energy will be stored or radiated by the urban surfaces in the tropics. Similarly, more energy will be utilized for evaporation and transpiration with consequently less energy available for warming the air. Also, the urban heat Island size of cities in the tropics are generally smaller than those of the temperate region, the heat Island phenomenon is likely to be less developed in the tropics.

Consequences Of Urban Heat Island Phenomenon

Some consequences of the urban heat Island phenomenon are desirable, others are not desirable. One major desirable effects of the heat island phenomenon is that the need for space heating is less than in the cooler rural environments. There is also a decrease in the frequency and intensity of inversion conditions as a result of increased thermal and mechanical convection over cities. On the other hand, urban warmth is responsible for the earlier building and blooming of flowers and trees in the cities of temperate regions as well as the longer growing season compared to their rural surroundings the heating bills are lower, humidity is lower and there are fewer days with snow.
The heat Island phenomenon however, has an undesirable effect which greatly increased exposure to dangerous pollutants. In addition, the increased rainfall reduced sunlight, loss of visibility and intensified

summer heat provide a more depressing environment. These changes also create a greater need for artificial illumination and summer air- conditioning especially in the tropical cities which are already warm or even hot. Also the heat Island effect tends to speed up the process of chemical weathering of building materials.

Induced Urban precipitation

Considering a city as being composed of a series of inter linked micro climates certainly in calm conditions it is obvious that the temperature variations within a city can be clearly sensed by any urban dweller. For example during a summer afternoon in columbia, Maryland, USA, the temperature over a lawn was found to be 31°c where as a nearby car pack had a temperature of 44°c.

The influences on other elements of the climate by the heat Island, by providing a hot-spot convection can be enhanced, leading to an increase in cloudiness over an immediately down wind of the city may cause it to act as a barrier to the regional wind flow, forcing the air to rise. Furthermore there is increasing possibility of increased cloud amount.

These effects are suspected to being the agent responsible for increased precipitation down wind, and is known as the Induced Urban Precipitation.. However, the role of the regional climate in such enhancement must be stressed. Regional air flows must contain the necessary moisture and must be susceptible to the vertical motions induced by the city.

Estimates of precipitation enhancement by the city are difficult to obtain since it is difficult to extract the urban effects from the usual temporal and spatial precipitation variation. Most of information therefore, comes from cities in areas of relatively homogeneous terrain with a well marked prevailing wind direction.

Conclusion

As long as urban population continue to grow there are no obvious solutions to this problem of urban heat Island, the shift from the central city to the suburbs tends to off set the problem, but as urban areas merge, this may be only a temporary effect. One of the most important ways to cut down heat in the cities is to increase the proportion of its land surface where evaporation can occur (Myrup 1969) Widely dispersed urban parks, fountains, and green belts of trees and plants are esthetically pleasing. They play an equally important role in increasing evaporation and thus helping make cities liable in the summer especially in the tropics.

References

Arthur N. S (1997); Geography and Man's Environment

Ayoade J.O (1993); Introduction to climatology for the Tropics

Chambers F.M (1993); Climate change and Human impact on the Land scale

Gates D.M (1972); Man and his environment: Climate Harper and Row New York .

Goward S.N (1981); Thermal behavior of Urban Landscape and the urban Heat Island.

Griffints J.F; Man influences on nature

Henderson A; Contemporary Climatology

Lansburg H.E (1954); Bio-climatology of Housing Meterol; Monog 2, Nos 8 Arner, Metorol soc SL 98.

Landsburg H.E ; Introduction to Micro- Meteorology

Money D.C ; Climate And Environmental Systems

Oke T.R (1987); Boundary Layer Climate

Oke T. R (1973); City Size and the Urban heat Island Atmost. Environ pg 769- 799.

Oyediran O.O; Climate Of west Africa

THE CHEMISTRY OF PRECIPITATION IN THE AMAZON BASIN: A COMPARISON OF PRESERVED AND DISTURBED REGIONS

Theotonio Pauliquevis[1], Paulo Artaxo[1], Luciene Lara[2], Norbert Miekeley[3], Mariana Gouvea[1]

[1]Institute of Physics, University of São Paulo, Rua do Matão, Travessa R, 187, São Paulo, SP, CEP 05508-900, Brazil.
[2]Isotopic Ecology Lab - CENA/USP, Centro de Energia Nuclear na Agricultura, Universidade de São Paulo, Av. Centenario, 303, CEP 13400-970, Piracicaba, SP, Brazil.
[3]Departamento de Química, Pontifícia Universidade Católica do Rio de Janeiro, RJ, Brazil.

1. INTRODUCTION

The study of rainwater composition is important due to the fact that chemistry of precipitation reflects partially the composition of the atmosphere e.g. EPA (2001). Beyond that, it is an important sink of atmospheric compounds, connecting atmosphere and soil trough the hydrological cycle, playing an important role in the nutrients cycle e.g.: Charlson (1997)

The composition of rainwater is a consequence of two processes: the incorporation of water in the aerosols acting as Cloud Condensation Nuclei (CCN) and the washing of the below cloud aerosols during a rain event. Therefore the chemical profile of rainwater provides information about the concentration of gases and aerosols in the atmosphere.

In the study of the chemical composition of rainwater in Amazonia, it must be regarded the differences between pristine and disturbed areas. Central Amazonia is a relatively preserved area, representing the natural conditions of the rainforest. On the other hand, there are very disturbed regions like the southwest region of Amazonia, where the conversion of natural forest to pasture using biomass burning is intensive.

At pristine regions, the concentration of aerosol number is very low (~ 700#/cm^3) e.g.: Zhou (2003). The emission of Volatile Organic Compounds (VOC's) by the forest plays an important role in the formation of organic aerosols (by Gas Particle Conversion), which are very hygroscopic and efficient as CCN.

For disturbed areas (like the southwest region of Amazonia), extensive changes have deforested large areas. As an example, the state of Rondonia (highly impacted) converted 22,4% of natural forest to pasture in the last 20 years. In the conversion from forest to pasture biomass burning emits an enormous load of aerosols during the dry season (July - October). In this period the particle concentration reaches values as high as 30000#/cm^3 with an average concentration around 5000 – 15000 #/cm^3, and the highest black carbon concentrations reaches 30000 ng/m^3.

Under so different atmospheric conditions, the composition of rainwater is strongly influenced by the impact of biomass burning and rainwater composition gets enriched under such a situation by biomass burning associated compounds like sulfates, potassium, ammonium and dissolved organic carbon (DOC). The deposition rates were also much higher over disturbed areas, comparing e.g. Balbina in Central Amazonia and Rondonia, at southwest Amazonia. If the in-cloud or the below-cloud processes are dominant is matter of research yet. However, in this study, statistical analysis of the data from a disturbed site indicates that in-cloud processes are most important.

2. SAMPLING SITES AND CHEMICAL ANALYSIS DESCRIPTION

The geographical distribution of the sampling sites is shown in figure 1. Balbina represent the natural conditions of Amazonia, typical of pristine regions; Santarem, despite some logging activity, is quite free of a meaningful biomass burning influence and due to Santarem be the easter site of our network it suffers a greater influence of trade winds, carrying marine aerosols. Rondonia, at southwest of Amazonia, is strongly disturbed by human activities, with an

[1] Corresponding author address: Theotonio M Pauliquevis Junior (FAP), Rua do Matão, trav. R. num 187, CEP 05508-900 Sao Paulo SP Brazil; e-mail: theo@if.usp.br

intense biomass burning activity during the period from July though November. Then, among the three sites, Balbina is the most pristine followed by Santarem and Rondonia is representative of impacted areas.

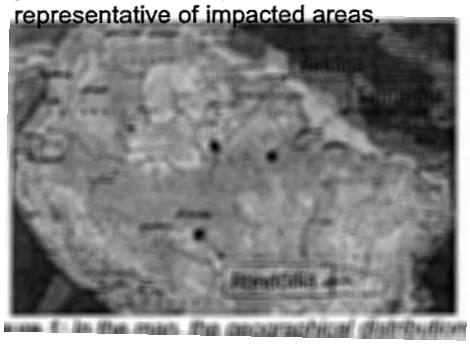

Figure 1: In the map, the geographical distribution of the three rainwater sampling sites in Amazonia operated in this study.

Besides the differences cited below, rain regime in Amazonia is under different influences for each region. In all sites the local convergence is very important, when large-scale conditions allows it, mainly during the wet season. At Balbina and Santarem, the movements of the Inter Tropical Convergence Zone (ITCZ) govern the wet/dry season regime and the penetration of instability lines from the east is also important for these sites. At Rondonia the wet/dry regime is governed by a climatological high-pressure system that, in the period from July to October, is over Central Brazil and regulates the timing of dry season in Rondonia. Cold fronts from the southwest Brazil also influence Rondonia rain production. The sampling period for each site correspond for one and half year to Balbina, a six-month period during the wet season in Santarem and a two three-months sampling period during intensive campaigns of the LBA Experiment: February – May of 1999 (wet-to-dry) and September – November of 2002 (dry to wet) – see table 1

Sampling site	Sampling period
Balbina	2000 and 2001 (2nd semester – dry season) -
Santarem	1st semester 2000 – wet season
Rondonia	March – May (1999) wet-to-dry Sept – Nov (2002) dry to wet

Table 1: sampling periods for each site

3. RESULTS

3.1 Balbina

The concentration of soluble compounds measured by Ionic Chromatography in Balbina during the wet and dry seasons is shown in figure 2.

The concentration of ions at Balbina presents few differences among dry and wet seasons. The typical precipitation amount for each season is about 1650 mm and 850 mm for wet and dry periods respectively, e.g. ANA (2002). This difference causes deposition rates higher during the wet season (v figure 2)

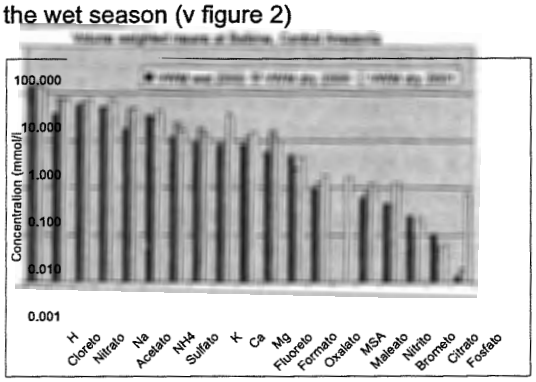

(a)

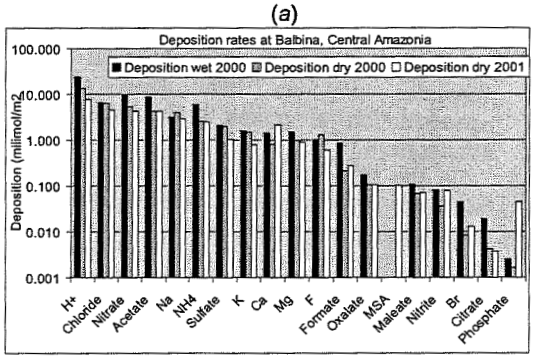

(b)

Figure 2: Average concentration (a) and deposition rates (b) of ions in Balbina, Central Amazonia

The most abundant ion is H^+, followed by nitrates, acetate and Chloride. Chloride specially is mainly connected to natural sources as Na (r^2 = 0.82) and some mineral acidity associated to HCl.

The acidity sources are a mixture of organic and mineral acids. There is a significant association between organic anions (acetate + formate) and H^+ (r^2 = 0.70) as well as mineral

anions (nitrate + sulfate + chloride) and H+ (r^2 = 0.61).

A Principal Component Analysis (PCA) performed with Balbina data showed the presence of five main sources: sea salt, sources of acidity, biogenic 1 (Phosphate and Calcium), biogenic 2 (Oxalate and Ammonium) and biogenic 3 (Citrate).

3.2 Santarem

Santarem is under similar conditions of Balbina, but that is closer to ocean than it. In fact, the marine originated ions shows greater values at Santarem than in Balbina.

The most abundant ion at Santarem (wet season) is H^+, followed by chloride, sodium, potassium and nitrate. The concentration of phosphate in Santarem is especially higher than in the other sampled sites.

	Deposition		Concentration	
	BALBINA	SANTAREM	Balbina	SANTAREM
H^+	25.31	10.17	14.46	10.76
Chloride	6.68	4.01	3.82	4.24
Nitrate	10.14	1.95	5.79	2.06
Acetate	8.90		5.08	
Sodium	3.24	3.30	1.85	3.49
Ammonium	6.07	1.11	3.47	1.18
Sulfate	2.15	1.28	1.23	1.35
Potassium	1.63	2.40	0.93	2.54
Calcium	1.47	1.38	0.84	1.46
Magnesium	1.51	0.86	0.86	0.91
Formate	0.89		0.51	
Oxalate	0.18		0.10	
MSA				
Maleate	0.1109		0.0633	
Nitrite	0.083		0.047	
Bromide	0.0456		0.0260	
Citrate	0.0194		0.0111	
Phosphate	0.0025	0.51	0.0015	0.54
HCO_3		0.48		0.51

Table 2: comparison between deposition rates and average concentration of ions at Balbina and Santarem, for the 2000 wet season (January – June). Units are milimol/m^2 for deposition rates and µmol/liter for concentrations.

Santarem presented about half the volume precipitation of Balbina (945 and 1750 mm respectively). Consequently a smaller deposition values for many compounds as nitrates (five times smaller), ammonium (six) and sulfate (two). The deposition of H+ is about half than in Balbina.

We also measured trace metals in Santarem rainwater, by ICP-MS (Inductively Coupled Plasma – Mass Spectrometry) technique. Performing a cluster analysis to all measured compounds (Ionic Chromatography and ICP-MS) we found three main sources: one, connected to rare earth elements (La, Ce, Pb, Ba), another to most of soluble compounds (Na (soluble), H+, Li, NO_3, NH_4, K (soluble), SO4 and U) and a third one with most of trace metals connected to soil ressuspension (Na (soluble + insoluble), Ni, K, (soluble + insoluble), Al, Fe, Ti, Rb, Cr, Mg (soluble), Ca (soluble), Cl, PO_4, Sc, Se, Ca (soluble + insoluble), Sr, Mg, Mn, Zn, As, Br and Cu).

3.3 Rondonia

Rondonia is the most impacted area among the sampled sites, with a biomass burning season from August to November.

For the wet season we performed analysis by Ionic Chromatography and ICP-MS. Comparing Rondonia and Balbina, it can be observed that there are few differences for wet season. However, performing PCA with the data set that includes Ionic Chromatography (soluble compounds) and ICP-MS (metals – soluble + insoluble fractions), it is possible to detect seven principal components: three from soil, two biogenic, two of anthropogenic activities. The existence of these anthropogenic sources even at wet season (when there is absence of biomass burning) demonstrates that the

intensive human occupation that the state of Rondonia suffered in the last 20 years caused changes in the environment that causes permanent influence on atmosphere during all the year.

The comparison of wet and dry seasons shows an enormous difference for concentration and deposition rates. The deposition rates were higher (twice in some cases) during dry than in wet (figure 3), despite the sampling period of wet season was almost twice of dry (3.5 and 2 months respectively) and precipitation amount was almost three times greater for wet (615 mm) than in dry season (229 mm). It is a clear consequence of the higher loading of gases and aerosols during the dry season.

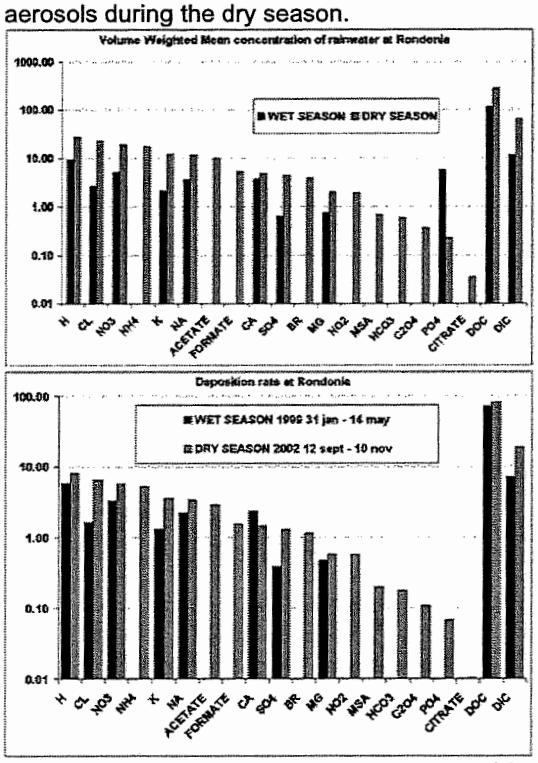

Figure 3: average concentration of compounds (a) and deposition rates for wet and dry season at Rondonia

Performing a cluster analysis in the rain VWM data and separating by event and not by element, we got two main groups whose most important feature was storm size. Performing a test of Analysis of Variance (ANOVA) in these samples, significant differences in concentrations were found for compounds associated with biomass burning as H^+, SO_4, NH_4, K, Cl and NO_3. These compounds were in a more concentrated situation for the larger storm size events, which means that in-cloud processes are dominant, and that these compounds are taking an important role in the cloud formation process.

4. CONCLUSIONS

The results of this work show how the fast land use changes in some regions in Amazonia have consequences in the deposition patterns in, through the comparison between pristine and disturbed area. The enhanced deposition rates at Rondonia dry season are a clear example that illustrates potential changes in nutrients cycling by wet deposition.

The results from Rondonia also show an enhancement of biomass burning compounds in high size storm rain events. It shows that these compounds are suffering a cloud processing, they are actuating as CCN, and changing the features of typical clouds in Amazonia.

5. REFERENCES

ANA, National Water Agency homepage http://www.ana.gov.br

Andreae, M. O. et al, 2004, "Smoking Rain Clouds over the Amazon" *Science* 27 February 2004; 303: 1337-1342

Charlson, R.J., Orians, G.H., Wolfe, G.V, Global Biogeochemical Cycles, Academic Press, 1997

EPA (Environmental Protection Agency), 2001, "Frequently asked questions about atmospheric deposition", EPA-453/R-01-009 September 2001

Roberts, G.C., et al, 2001, "Cloud condensation nuclei in the Amazon Basin: 'Marine' conditions over a continent?" *Geophysical Research Letters*, 28 (14), 2807-2810, 2001.

Zhou JC, et. Al, 2002, "Submicrometer aerosol particle size distribution and hygroscopic growth measured in the Amazon rain forest during the wet season", J. Geoph. Res. Atmospheres 107 (D20): Art. No. 8055 SEP-OCT 2002

PARAMETERIZATION OF THE NITRIC ACID EFFECT ON CCN ACTIVATION

S. Romakkaniemi, H. Kokkola and A. Laaksonen

Department of Applied Physics, University of Kuopio, Kuopio, Finland

1. INTRODUCTION

Previous cloud model studies have shown that trace gases like nitric acid (HNO_3) and ammonia (NH_3) can increase the cloud droplet number concentration (CDNC) significantly (Kulmala et al. 1993, Hegg 2000). This will reduce the mean cloud droplet size and so increase cloud albedo. The magnitude of the effect of trace gases on cloud condensation nuclei (CCN) activation can be calculated using a cloud parcel model, but to estimate the global albedo effect reliably, large scale models such as GCM's need to be used. Because the exact calculation of the trace gas effect is computationally demanding, the results obtained from parcel model simulations have to be parameterized into a form that can be used in the large scale models. In this study we are developing a simple parameterization for the HNO_3 effect on aerosol activation.

In the recent years many parameterizations for cloud droplet formation have been developed. The most straightforward parameterizations are based on direct measurements relating the number of condensation nuclei to the number of cloud droplets (Gultepe and Isaac 1999). Such parameterizations do not take into account any variation of the aerosol population or cloud forming dynamics. More sophisticated parameterizations include theoretical calculations combined with detailed numerical parcel model simulations (e.g. Nenes et al. 2003; Abdul-Razzak and Ghan 2002). These parameterizations take into account the dynamics and the size distribution of the aerosol population, but the role of other condensing gases than water is undetermined.

2. METHODS

The parameterization is based on numerical simulations, which are done with an air parcel model including detailed liquid phase thermodynamics and differential equations for adiabatic expansion and condensational growth of liquid particles (Kokkola 2003). Our strategy is to develop a parameterization which can be used to calculate the activated fraction F_x with x ppb of HNO_3 in the air, when the activated fraction without trace gases F_0 is known. The basic form of the parameterization is very similar to a parameterization previously presented by Laaksonen et al. (1998).

$$F_x = F_0 + (1 - F_0)\exp(f(C, T, F_0, V, dist))$$

where the function $f(C,T,F_0,V,dist)$ is a function of HNO_3 concentration C, temperature T, F_0, updraft velocity V, and aerosol distribution parameters. In this way the parameterization is independent of the method used to calculate F_0 and can be used in all models with varying level of sophistication.

3. RESULTS AND DISCUSSION

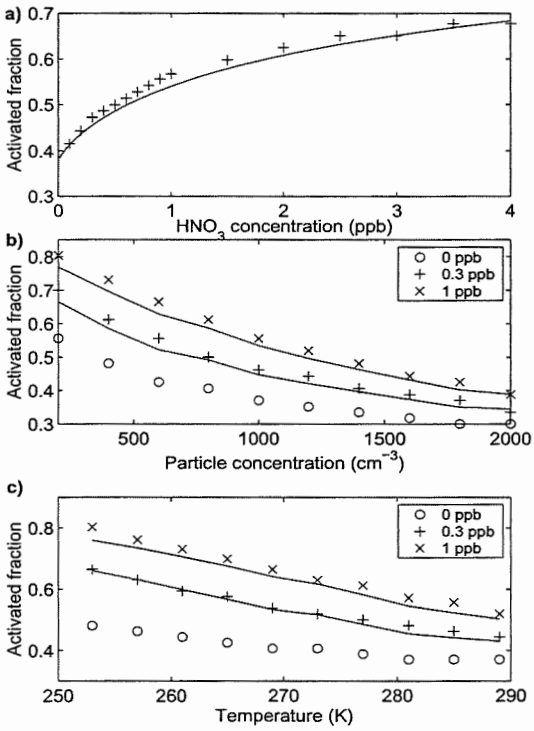

Figure 1: **a)** Activated fraction as predicted by parameterization (-) and cloud parcel model (+) as a function of HNO_3 concentration. **b)** Activated fraction as a function of particle concentration for three different HNO_3 concentrations and corresponding predictions by parameterization. **c)** Activated fraction as a function of temperature for three different HNO_3 concentrations and corresponding predictions by parameterization.

Corresponding author's address: Sami Romakkaniemi, Department of applied physics, University of Kuopio, P.O.Box 1627, 70211 Kuopio, Finland;
E-Mail: sami.romakkaniemi@uku.fi.

In Figure 1 we compare the prediction of the parameterization to the fraction of aerosol particles that activate given by our cloud model. In these simulations updraft velocity is 0.5 m/s. Aerosol size distribution is unimodal with 30 nm geometric mean radius and standard deviation of 1.7. Initial temperature in Figures 1a and b is 283 K. In Figure 1a the activated fraction is presented as a function of nitric acid concentration when particle concentration is 1000cm^{-3}. In Figure 1b the activated fraction is presented as a function of particle concentration for 0.3 ppb and 1 ppb of HNO_3 and in Figure 1c the activated fraction is presented as a function of initial temperature when particle concentration is 1000 cm^{-3}. It can be seen that in these cases the parameterization slightly underestimates the number of activated particles.

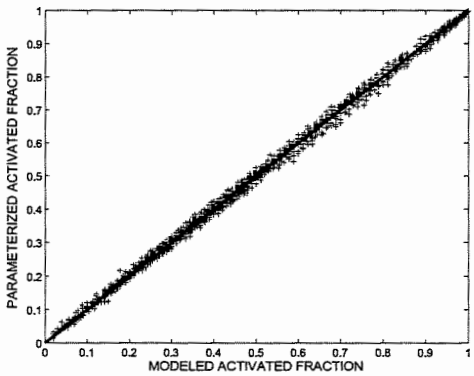

Figure 2: Activated fraction as predicted by new parameterization and by cloud parcel model.

In Figure 2 we compare the prediction of the parameterization with the fraction of aerosol particles that activate with 0.1-3 ppb of HNO_3 when the updraft velocity is varied between 0.1 m/s and 3 m/s, given by our cloud model. The comparison consists of more than 2000 box model simulations in the temperature and total pressure range from 253 K to 293 K and from 500 mbar to 1000 mbar, respectively. The aerosol distribution is lognormal and unimodal, number densities varying between 100 cm^{-3} and 6000 cm^{-3}, geometric mean radius varying between 5 nm and 150 nm, and standard deviation varying between 1.3 and 2.5.

Figures 1 and 2 show that we already have a good parameterization for a simple base case. The highest F to F_0 ratios in the simulations are over four and still all the points in figure 2 are very close to the 1:1 line. In the future, the parameterization will be extended to include more complicated (multimodal) distributions.

ACKNOWLEDGMENTS

This study was supported by the Academy of Finland

REFERENCES

Abdul-Razzak H and S. J. Ghan 2002: A parameterization of aerosol activation 3. sectional representation. J. Geophys. Res., **107**, 4026, doi:10.1029/2001JD000483.

Gultepe I. and G.A. Isaac 1999: Scale effects on averaging of cloud droplet and aerosol number concentrations: observations and models. J. Climate, **12**, 1268-1279.

Hegg D. A., 2000: Impact of gas-phase HNO_3 and NH_3 on microphysical processes in atmospheric clouds. Geophys. Res. Lett., **27**, 2201-2204.

Kokkola H., 2003: Model studies on the evolution of fogs and clouds in the presence of semi-volatile gases. Ph.D. thesis. Report series in aerosol science finnish association for aerosol research, Helsinki

Kulmala M., A. Laaksonen, P. Korhonen, T. Vesala, T. Ahonen, and J.C. Barrett 1993: The effect of atmospheric nitric acid vapor on cloud condensation nucleus activation. J. Geophys. Res., **98**, 22949-22958

Laaksonen, A., J. Hienola, and M. Kulmala 1998: Parameterization of the soluble trace gas effect on CCN activation. J. Aerosol Sci., **29**, Suppl. 1., 563

Nenes A and J. H. Seinfeld 2003: Parameterization of cloud droplet formation in global climate models. J. Geophys. Res., **108**, 4415, doi:10.1029/2002JD002911.

DIAGNOSTICS OF MESOSCALE AND SYNOPTIC STRUCTURE OF PRECIPITATION ASSOCIATED WITH ATMOSPHERIC CYCLONES

Irina Rudeva, Sergey Gulev, Olga Zolina

P.P.Shirshov Institute of Oceanology, RAS, 36 Nakhimovsky av., Moscow, 117218, Russia; *rudeva@sail.msk.ru*

1. INTRODUCTION

We analyse in this study the structure of mesoscale and synoptic-scale precipitation fields associated with mid-latitudinal cyclones over the North Atlantic and Western Europe, using observational data, available form the routine merchant ship observations over the ocean and from rain gauges over the continent. The main objective is to design composites of precipitation fields, co-located with the major structural elements of the propagating cyclones during their life cycle. Of a particular interest is to link the cyclone characteristics with the intensity of rainfall and to quantitatively describe the projections of atmospheric moisture transport over the Atlantic Ocean onto European precipiation variability. This will allow for the quantification of the projections of the North Atlantic climate variability onto European climate.

2. DATA AND PREPROCESSING

Cyclone tracks and characteristics of the cyclone life cycle (intensity, deepening rate, life time, propagation velocity) were obtained from the tracking of 6-hourly sea level pressure fields from NCEP/NCAR Reanalysis for the period from 1948 to 2002 (*Gulev et al. 2001, Zolina and Gulev 2002*). Tracking was carried out by the numerical scheme, searching the consequent locations of cyclone centers and accounting for the cyclone propagation through the dynamical interpolation. Besides the locations of the cyclone centers and central pressure, we also analysed the vorticity, pressure gradient and the other parameters which allow for the co-location of the cyclone structure with cloud and precipitation fields.

Over the mid-latitudinal North Atlnatic precipitation estimates were derived from the Voluntary Observing Ship (VOS) data using indirect information reported by VOS (past and present weather code, humidity, cloudiness). The VOS data were taken from the latest updates of the I-COADS (International Comprehensive Ocean-Atmosphere Data Set (Woodruff et al. 1998). Retrievals of the precipitation intensity from the weather code and meteorological observations were done according to the experimental relationships. Sampling density of the VOS observations over the North Atlantic Ocean for selected years and time periods allows for quite reliable description of synoptic-scale to meso-scale features of precipitation in the propagating synoptic transients. Figure 1 shows an example of VOS data points distribution for 06:00 UTC 26.03.94 overplotted with sea level (SLP) field for this moment.

Over European continent precipitation estimates were taken from the long-term station rain gauge observations, available from different collections of daily and higher resolution precipitation data sets. These collections consist of the KNMI European Climate Assessment data set, NCDC collection of station observations of precipitation and precipitation data from Russian Metoffice (*Zolina et al.* 2004). The best sampling density over the continent is available for the period starting from 1994 onwards. Transport of moisture by mean flow and atmospheric cyclones has been quantified using the method developed by *Ruprecht et al.* (2002) on the basis of reanalyses data.

3. RESULTS OVERVIEW

Ensembles of precipitation composites were performed for different typical cyclone life cycles over the mid-latitudinal ocean (for the well sampled cases and periods) and over the continent. Composites were designed by performing statistical analysis over precipitation and cloud cover fields for similar cyclones in different regions of the North Atlantic and over western Europe. In order to achieve an effective co-location the composites have been performed for the different stages of the cyclone development over the North Atlantic mid latitudes. Of a special importance on this stage was the definition and quantification of the cyclones are and its association with the local pressure gradients, vorticity and parameters of the cyclone life cycle.

The composites for the precipitation derived from the VOS data were then compared with those derived from the reanalyses in order to quantify to what extent the NWP (numerical weather prediction) products can adequately represent the mesoscale precipitation structure. We show in particular, that the relative comparability is higher over the oceans rather than over the continental Europe. On the other hand, it is still unclear whether this can be attributed to better skills of reanalyses to represent the precipitation structure over the ocean, or to a better quality of in-situ data over the continents.

For a number of typical cyclone types we estimated integral characteristics of water balance, resulting from the advection of atmsopheric moisture, precpitation and evaporation for different oceanic and continental

Corresponding author's address: Irina Rudeva, P.P.Shirshov Institute of Oceanology, RAS, 36 Nakhimovsky ave., 117218 Moscow, Russia, rudeva@sail.msk.ru

regions. These estimates also were derived from observational data and reanalyses and intercompared with each other.

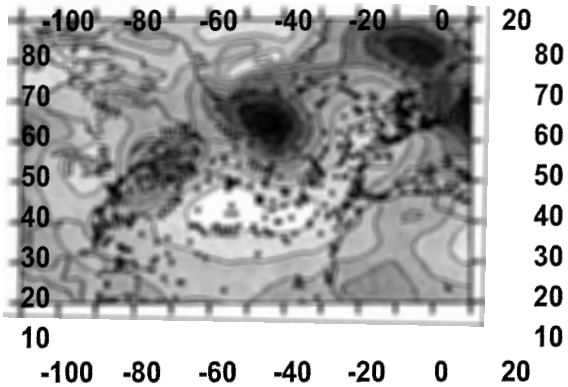

Figure 1. Spatial distribution of the VOS observations over the North Atlantic and the corresponding SLP field for 06:00 UTC 26.03.94.

Finally, we analysed interannual variability of the cyclone life cycle and associated precipitation patterns over the North Atlantic and Europe. This variability is considered in a view of the leading climate modes in the Atlantic-European sector (North Atlantic Oscillation and others). In particular, we tried to link changes in the Atlantic mid-latitudinal precipitation and the cyclone water vapour content over the North Atlantic with the statistical characteristics of precipitation over European continent during different phases of the North Atlantic Oscillation. Results show that although the NAO-related variability is largely responsible for the precipitation patterns associated with mid-latitudinal cyclones, there is a significant portion of variance, driven by processes, not associated with NAO. We also analysed the precipitation patterns and the moisture transport characteristics during periods of 1960s - 1970s and the last two decades and found that these periods demonstrate strong differences not only in the magnitude of the processes, but also in spatial patterns even under same (positive or negative) NAO phases, that might result form the NAO regime shift in the late 1970s.

4. ACKNOLEDGEMENTS

This study is supported by Russian Foundation for Basic Research (grant 02-56331) and the joint project "North Atlantic Oscillation: regional impacts on European weather and climate", funded by Folkswagen Stiftung (Hannover, Germany).

5. REFERENCES

Gulev, S.K., O.Zolina, and S.Grigoriev, Extratropical cyclone variability in the Northern Hemisphere winter from the NCEP/NCAR Reanalysis data, *Clim. Dynamics*, 17, pp. 795-809, 2001.

Ruprecht, E., S. S. Schroeder and S. Ubl, On the relation between NAO and water vapour transport towards Europe, *Meteorologische Zeitschrift*, 11, pp. 701-702, 2002.

Woodruff, S.D., H.F.Diaz, J.D.Elms, S.J.Worley, 1998: COADS Release 2 data and metadata enhancements for improvements of marine surface flux fields. *Phys. Chem. Earth*, 23, 5/6, 517-526.

Zolina, O., and S.K.Gulev, Improving accuracy of mapping cyclone numbers and frequencies, *Mon. Wea. Rev.*, 130, pp. 748-759, 2002.

Zolina, O., A.Kapala, C.Simmer, and S.K Gulev, 2004: Analyses of extreme precipitation over Europe from different reanalyses: a comparative assessment. *Global and Planetary Change*, submitted.

DETECTION OF CLIMATE CHANGE OVER NORTH-EAST OF I. R. OF IRAN USING HISTORICAL PRECIPITATION AND AIR SURFACE TEMPERATURE TREND'S PATTERNS

A. Shahabfar[1], J. B. Jamali[1, 2], A. Ramesh[1]

1. Climatological Research Institute (CRI), Mashhad, I. R. of Iran (P.O.Box: 91735-491)
2. I. R. of Iran Meteorological Organization (IRIMO), Tehran, I. R. of Iran.

1.Introduction

Several climatological studies shown that human activities such as urbanization, industrial developments have a great impact on changing of climatic parameters around the world, for example, exist of heat island over the large cities, increasing of global mean temperature, increasing of mean sea surface height... Based on the latest scientific assessment of the earth's climate system, Poland et al. (2001) have revealed that average global surface temperature has increased by about 0.6±0.2°C since the late 19th century. The Northern hemisphere experienced cooling during the period from 1946 to 1975, while the Southern hemisphere showed warming. They pointed out that the recent 1976-2000 warming was largely globally synchronous, but was more pronounced in the Northern hemisphere continents during winter and spring. Folland et al. (2001), assessing a large number of studies, have also indicated that analyses of mean daily maximum and minimum land surface air temperatures continued to support a decrease in the diurnal temperature ranges in many parts of the world. Minimum temperatures increased at nearly twice the rate of maximum temperatures during the period from 1990 to 1993.

Based on the results of previous studies (Shahabfar et al., 2003), based on annual number of freezing days, a general decrease was dominate in this climatologically parameter series over Mashhad city at the Khorasan Province for period of 1965-2002. In particular, in this industrial city was generally characterized by lower than long- term average number of freezing days conditions during the period between the late 1970s and early 2002.

2.Data and assessment of homogeneity

This study based on an updated temperature and precipitation data set consisting of monthly averages of the daily mean, daily maximum (day-time) and daily precipitation.

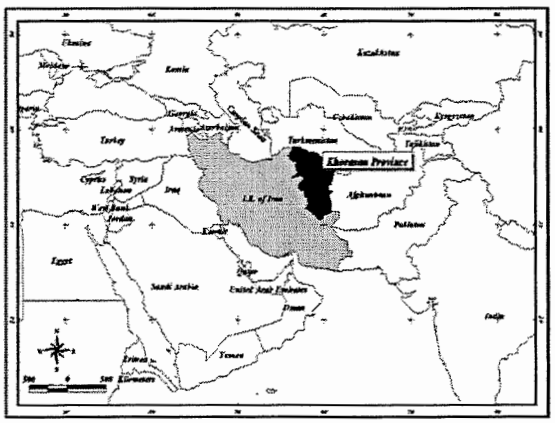

Figure 1. The geographical location of Khorasan province in the Middle – East

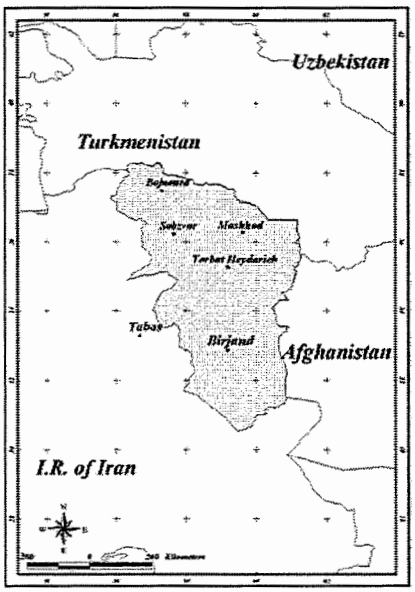

Figure 2. The spatial distributions of the locations of the synoptic stations in the Khorasan province.

Temperature and precipitation data have been observed and recorded by the I. R. of Iran

Meteorological Organization (IRIMO) since late 1950.

A total of 17 stations, were examined with respect to their length of record, geographical distribution over the Khorasan province and homogeneity. In order to detect homogeneity in mean annual and seasonal series, first a homogeneity analysis was performed by using the non-parametric Bartlet test for homogeneity was carried out of the means and variances of both 5 year sub–periods. This objective analysis was done not only detect in homogeneity (inconsistency) in the overall series, but also to examine whether the recent observations of about the last decade affected the consistency of the temperature and precipitation series. Second, the non-parametric Kendall serial correlation test was applied to the series to examine the nature and magnitude of the serial dependence from year – to – year variations, and / or abrupt changes in the series. The result of the Kendall test, when supported by information from both a station's history file and statistical and graphical time – series analysis, is very useful for deciding whether a statistical significant inhomogenity in a series (especially with a probability less than 0.01) arose from a non-climatological jump, from natural two-frequency fluctuations, or a strong persistence. A non – climatological jump in the mean of a series may result either from an abrupt change associated with relocation of a station or from steep trend (a rapid increase or decrease) in temperature and precipitation values because of different factors, such as urbanization (i.e. urban heat island or urban cooling effect respectively). Third, statistically significant in homogeneities from the Kendall test were checked by means of the additional information from our own station's history file and the plotted time – series to some extent. Time – series plots were prepared for both original temperature and precipitation with smoothed values and the u (t) and u′(t) values derived from the sequential analysis of the Mann-Kendall (M-K) test. Consequently, we have analyzed the updated date set of Khorasn province's mean, maximum and minimum temperature series and precipitation series of 17 stations for a large study period from 1972 to 2002. The scope of the paper is: (i) to give detailed information on the updated Khorasan Provinces temperature and precipitation data and homogeneity assessments of temperature and precipitation series; (ii) to assess the rapid urbanization in the North- East of I. R. of Iran; (iii) to reveal the nature and magnitude of the serial dependence and long- term trends, and the change points and significant warming (or cooling) periods in annual and seasonal mean, maximum and minimum temperature series and precipitation series of Khorasn province by using non-parametric tests; and (iv) to detect the linear trend rates per decade in the same temperature and precipitation series.

3.Methodology

The non-parametric M-K rank correlation test (Sneyers, 1990) was to detect any possible trend in temperature series, and to test whether or not such trends are statistically signification. A detailed assessment for testing of climatic data unevenly distributed in time and a comparison of methods for estimating the significance level of a trend can be found in a recent study performed by Huth (1999). The M-K test statistic u (t) is a value that indicates directions (or sign) and statistical magnitude of the trend in a series.

When the value of u (t) is significant at the 5% significant level, it can be decided whether it is an increasing or a decreasing trend depending on whether u (t)>0 or u (t)<0. A 1% level of significance was also taken into consideration. Partial and short – period trends, and a change point or beginning point of a trend in climatic series were investigated by using time – series plot of the u (ti) and u′(ti) values. In order to obtain such a time- series plot, sequential values of the statistics u (t) and u′(ti) computed from the progressive analysis of the M-K test. Following Sneyers (1990), this procedure is formulated as follows: first, original observations are replaced by their corresponding ranks yi, which are arranged in ascending order. Then, for each term yi, the number uk of terms yi preceding (i>j) is calculated with (yi>yj), and the test statistic ti is written as:

$$t_i = \sum_{k=1}^{i} n_k \qquad (1)$$

The distribution function of the test statistic ti has a mean and a variance derived by;

$$E(t_i)=i(i-1)/4 \quad \text{and} \quad var\,(t_i)=[i(i-1)(2i+5)]/72 \qquad (2)$$

Values of the statistic u (ti) are then computed as;

$$u(t_i) = [t_i - E(t_i)] / \sqrt{Var(t_i)} \qquad (3)$$

Finally, the values of u′(ti) are similarly computed backward, starting from the end of the series. With a trend, intersection of these curves enables the beginning of a trend in the series to

be located approximately. Without any trend, a time – series plot of the values u (ti) and u'(ti) shows curves that overlap several times. A moving average order 5 filters was used as a low – pass filter to investigate visually the characteristics of the long – period fluctuations in the series.

The non – parametric Kendall serial correlation test was chosen to determine randomness against the serial dependence (persistence) in temperature series (Alijani, 1998). Alijani advised use of the Kendall serial correlation test combine with M-K tests, because changes in climatic series seem, generally, to proceed in a manner rather than a linear or monotonic trend.

4.Summary and conclusions

The following gives a summary of the results and the main conclusion.

1) *Mean temperatures.* Year-to-year variations in annual mean temperatures series of Khorasan Province are generally characterized by Kendall coefficient. Significant warming trends from M-K test have shown up particularly at the highly urbanized stations of the northern regions. The significant warming trend rates from the least-squares linear regression vary between 0.51^{0}C to 1.1^{0}C.

Most spring mean temperature series show an increasing trend. Summer mean temperature series are mostly characterized by a statistically significant Kendall coefficient. Summer mean temperature series are shown a slight warming at many stations over the northern part of Khorasan Province, whereas the rest of the province has experienced a general cooling. Autumn mean temperatures have significantly increased at three stations. Significant warming trends are evident over the northern regions. Significant linear trend rates vary between 0.70^{0}C to 1.3^{0}C per decade.

2) Maximum temperature series. The observed low-frequency fluctuations in annual maximum temperature series of Khorasan Province are mostly associated with a significant Kendall Coefficient. A weak increasing trend shows up over the northern regions, and a decreasing trend is generally observed in the inner parts.

Year-to-year variability of spring maximum temperatures is mostly characterized by a significant positive serial correlation coefficient. Spring maximum temperature series have indicated an increase at many stations except those in the northern regions. Significant Kendall coefficients at the all of stations are a statistical indication of the observed low-frequency fluctuations in summer maximum temperature series. Summer maximum temperatures have increased at many stations and decrease at some stations. Warming trends are significant at four stations. Autumn maximum temperatures have increase over the study region.

3) Minimum temperature series. Year-to-year variations of annual minimum temperatures indicate mostly a significant serial dependence. Most of the rapidly urbanizing and already urbanized stations of Khorasan Province have experienced a night-time warming during the study period, and the warming trends at five stations are significant. The range of significant night-time warming rates is 1.84^{0}C to 0.25^{0}C per decade.

Year-to-Year variations of most spring minimum temperatures have shown a warming trend at majority of the Khorasan Province stations, three of which are significant. The significant night-time warming trends dominate mainly in the highly urbanized or rapidly urbanizing cities of Khorasan province, and significant warming rates lie within the range of 1.56^{0}C to 0.41^{0}C per decade.

Interannual variations of summer minimum temperatures series at the all of stations are characterized by a significant Kendall coefficient. As in spring, the summer temperatures have increased at the majority of the stations, most of which are located in the already urbanized or rapidly urbanizing cities. Warming trends are significant at five stations. The significant night-time warming rates are in the range of 0.07^{0}C to 1.9^{0}C per decade.

Autumn minimum temperatures series have shown a significant warming trend at four stations, many of which are located in the northern regions of the province. The range of significant warming rates is 0.60^{0}C to 2.8^{0}C per decade.

4) *Precipitation series.* Year-to-year variations in annual precipitation series of Khorasan Province are generally characterized by Kendall coefficient. Significant decreasing trends from M-K test have shown up particularly at the highly urbanized stations of the northern regions. The significant decreasing trend rates from the least-squares linear regression vary between -2.22 *mm* to 0.694 *mm* per decade.

Most spring precipitation series show a decreasing trend. Summer precipitation series are mostly characterized by a statistically significant Kendall coefficient. Summer

precipitation series are shown a slight drying at many stations over the northern part of Khorasan Province. Autumn precipitations have significantly decreased at four stations. Significant drying trends are evident over the northern regions. Significant linear trend rates vary between -3.13 *mm* to 1.24 *mm* per decade.

5) *Overall assessment.* According to this research summer minimum temperatures have generally increased at a larger rate than in spring and autumn minimum temperatures. On the other hand, night-time warming rates of spring and summer are generally stronger than those that exist in spring and summer daytime temperatures. Considering the significant increasing trends in annual, spring and summer temperatures, it is seen that night-time warming rates are stronger in the northern regions, which are characterized by the Khorasan province macroclimate type: a very hot and dry summer, a relatively hot, dray and late spring and early autumn and a moderate winter. We have seriously considered the strong warming trends in spring and summer and thus likely in annual minimum air temperatures. It is very likely that significant and very rapid night-time warming trends over much of the province can be related to the widespread, rapid and increased urbanization in Khorasan province, in addition to long-term and global effects of the human-induced climate change on air temperatures.

Acknowledgements

We would like to thank Prof. Alijani for his constructive recommendation, and to express our special thanks to I.R. of Iran Meteorological Organization (IRIMO) for giving some facilities.

References

1. Ben-Gai T. Bitan A. Manes A. Alpert P. Rubin S. 1999. Temporal and spatial trends of temperature patterns in Israel. Theoretical and Applied Climatology 64: 163-177.
2. Esteban-Parra MJ. Rodrigo FS. 1995. Temperature trends and Change points in the northern Spanish Plateau during the last 100 years. International Journal of Climatology 15: 1031-1042.
3. Ehteramian K.Shahabfar A.Nazemossadat M.2003: Prediction of Drought Condition by Using Normalized Difference Vegetation Index (NDVI) in I.R. of Iran, National conference of Geomatics83, Tehran, I.R.of Iran.
4. Folland CK. Karl TR. Christy JR. Clarke RA Gruza GV. Jouzel J. Mann ME. Oerlemans J. Salinger MJ. Wang S-W. 2001. Observed climate variability and change In Climate Change 2001: The Scientific Basis. Contribution of Working Croup I to the Third Assessment Report of the intergovernmental Panel on Climate Change. Houghton JT. Ding Y. Griggs DJ. Noguer M. van de Linden PJ. Dai X. Naskell K. Johnson CA (eds). Cambridge University Press: Cambridge: 99-181.
5. Huth R. 1999.Testing for trends in data unevenly distributed in time, Theorical and Applied Climatology 64:151-162
6. Maheras P. Xoplaki E. Davies T. Martin-Vide J. Bariendos M. Aleoforado MJ. 1999. Warm and cold monthly anomalies across the Mediterranean basin and their relationship with circulation: 1860-1990. International Journal of Climatology 19: 1697-1715.
7. Metaxas DA. Bartzokas A. Vitsas. A. 1991. Temperature fluctuations in the Mediterranean area during the last 120 Years. International Journal of Climatology 11: 897-908.
8. Proedrou M. Theoharatos G. Cartalis C. 1997. Variations and trends in annual and seasonal air temperatures in Greece determined from the ground and satellite measurements. Theoretical and Applied Climatology 57: 65-78.
9. Shahabfar A. Gharaei MS. Javdani KhN.2003: Study of Mashhad freezing day's fluctuations. The Third Regional Conference On Climate Change, Isfahan University, I.R.of Iran.
10. Turkes M.Sumer U.M.Demir I.2002.Re-evaluation of trends and changes in mean, maximum and minimum temperatures of Turkey for the period 1929-1999.International Journal of Climatology22: 947-977.
11. Sneyers F. 1990. On the statistical analysis of series of observations. World Meteorological Organization (WMO). Technical Note. NO. 143. Geneva: 192 pp.
12. WMO. 1966. Climatic change. World Meteorological Organization (WMO). Technical Note. No. 79. Geneva: 79 pp.

CHEMICAL COMPOSITION OF ATMOSPHERIC PRECIPITATION - INDICATOR OF CLIMATIC CHANGES OF ATMOSPHERE ON THE EXAMPLE OF TASHKENT PROVINCE

Smirnova T.Y.,Tolkacheva G.A.

Central Asian Hydrometeorological Research Institute (SANIGMI), Uzbekistan, Tashkent

The Central Asian region is one of the specific regions of Euro-Asia which is famous for an unique combination of the natural and climatic zones, mainly with the extremely continental climate, abundance of sun-shine days, loess soil cover which is a very considerable natural source of soil aerosol inflow into atmosphere.

Nowadays the study of chemical composition of atmospheric precipitation is an actual issue for monitoring of environmental pollution. The issues concerning revelation of the pollution starting points, pollution rate changes with time and the chemical composition of pollutants is worthy of special notice.

The scientific-technical revolution in XX century along with its tremendous positive effects on human being has exerted a negative contribution in environment pollution, including atmosphere air pollution.

As a result of this the atmosphere pollution with anthropogenic origin aerosols has increased.

The break of the ecological balance in the region caused by the drying processes in the Aral Sea was resulted in degradation of the ecosystems, climate change in the region. From the other hand, the availability of the developed agricultural and industrial complexes formed on the territory of Tashkent province, contributes to the environment pollution, as well.

The main anthropogenic atmospheric pollutants are oxides of sulfur, nitrogen, carbon, and solid particles of the diverse origin and composition. The main air pollutants on the territory of Tashkent province are the heat producing plants, construction industry, mining and chemical industries, transport complex and others.

The chemical composition of the total precipitation during a month is the integral characteristic which demonstrates the pollution of the boundary atmospheric layer. Following the dynamics of variations of this characteristic it is possible to study the influence of the general atmospheric circulation on the expansion of the green-house gases and aerosols over a certain territory.

Smirnova T.Y.,Tolkacheva G.A. Central Asian Hydrometeorological Research Institute (SANIGMI)

72, K.Makhsumov str., Tashkent, 700052, Uzbekistan, e-mail: sanigmi@albatros.uz

The aim of this study is to investigate a dynamics of the chemical composition of precipitation on the territory of Tashkent province; to define the changes in their composition which can help to identify the input of the green-house gases and aerosols into the regional climatic characteristics.

The following tasks were put and solved to reach the specified objective:

- The dynamics of the chemical composition of precipitation was studied at eight stations in the Tashkent province (Almalyk, Angren, Bekabad, Dukant, Kaunchi, Tashkent, Tyiyabuguz, Chirchik) with the analysis of the commonly accepted indices (pH, electric conductivity, ion sum (SO_4^{2-}, NO_3^-, Cl^-, HCO_3^-, Mg^{2+}, Ca^{2+}, Na^+, K^+, NH_4^+), the trends were determined.
- The possible relationships between the levels of the precipitation pollution by the green-house gases components and aerosols have been investigated (HCO_3^-, NO_3^-, Mg^{2+}, Ca^{2+})

The chemical composition of precipitation was investigated with the application of the techniques of the ion chromatography, atomic adsorption, photo-colormetry, microscoping and other ones /2/.

The long-term trends of the chemical composition of precipitation were studied with methods of mathematical statistics.

The chemical composition of precipitation depends on three main factors:

1. The ocean aerosols incoming into the atmosphere. The content of sodium, magnesium, chlorine and general inorganic carbon in meteoric water depends on the value of the incomings.
2. The industrial emissions of gaseous sulfur and nitrogen oxides and combustion products of coal and other kinds of fuel into atmosphere. Their concentration influents on pH value.
3. Dust incoming into atmosphere owing to wind erosion of soil and arid climate conditions.

Comparison the chemical composition of precipitation, collected on the background station and the above mentioned stations situated in the industrial zone (an athropogenic stress zone) has showed the change dynamics of its chemical composition and pH.

Component-wise change dynamics of mean annual values of the precipitation composition has been examined.

It is necessary to underline that the chemical composition of precipitation reflects influence of local anthropogenic sources of aerosol emission and it may serve as an indicator of regional and global atmosphere pollution. The trends of the precipitation mineralization have displayed a general increasing tendency and, as a consequence of that increasing the atmosphere pollution by natural and anthropogenic sources in the region as well.

The investigation of the possible changes in the chemical composition of precipitation for last 15 years revealed quantitative and quantitative changes of the basic components composition. The database of obtained results has been created.

The following changes of pH values have been examined using data from the above stations and the background complex monitoring station of the Chatkal reserve (Chatkal) for 5 years (1998-2002):

The falling of pH values has been observed at Chatkal for 5 years (1998-2002). At Tashkent the rise of pH values up to 2001 and falling of them have been revealed. At Angren an appreciable falling of pH values have been observed for last 5 years. At Kaunchi, Tyiyabuguz and Chirchik pH values have not changed considerably for last 5 years. At Bekabad pH values are largest, pH value equaled to 7.59 was observed in 2000. Thus the precipitation was near alkaline one. At Almalik pH values are least, pH value equaled to 5.03 was observed in 2002. Therefore the precipitation was closed to acid one.

The lowest mineralization of precipitation and maximal amount of that is at Chatkal. The maximal mineralization of precipitation and minimal amount of that is at Angren, Kaunchi, Bekabad and Tyiyabuguz. At Tashkent, Almalik and Chirchik a regularity is not revealed. The mineralization and the amount of precipitation are not significant at Tashkent. At Almalik the mineralization have decreased for 5 years. That amounts to 189.24 mg/dm^3 in 1998 and 57.36 mg/dm^3 in 2003 when under the same amount of precipitation in these years.

The emissions of compounds containing sulfur, nitrogen and carbon influence on the chemical composition of precipitation. The main source of sulfur dioxide incoming into atmosphere is the heat and power industry and that of nitrogen dioxide is transport. Availability free oxygen in atmosphere leads to sulfate and nitrate formation.

It is necessary to note that sulfate concentration in precipitation samples at Tashkent practically coincide with that at Chatkal for 5 years (within the limits 7.5 – 10.5 mg/dm^3). At Chirchik the concentration of sulfate is slightly higher in comparison with that at Chatkal and it almost have not changed for the period. At the same time the concentration at Kaunchi and Bekabad have large values. Maximums were observed at these stations in 2001. They amount 114.7 and 78.3 mg/dm^3 correspondingly. At Angren an increase in sulfate concentration in the precipitation samples have occurred for 5 years. In 2002 a maximum equal to 120.5 mg/dm^3 was registered. On the contrary at Almalyk a decrease in that has been observed. In 2002 a minimum equal to 19.9 mg/dm^3 was registered. At Tyiyabuguz an insignificant increase of sulfate concentration has been recorded for the period.

The changes in nitrate concentration in precipitation samples at Chatkal, Tashkent, Bekabad, Almalyk and Chirchik are insignificant and those have a tendency to decrease. At Angren changes in nitrate concentration have a tendency to increase. Nitrate concentration in precipitation samples at Tyiyabuguz is largest. A maximum value was observed in 2002 (55.5 mg/dm^3). Nitrate concentration in precipitation samples at Kaunchi is noticeably larger in comparison with that at Tashkent although these stations are situated close to each other. The obtained data testifies to local sources impact on nitrate incoming into atmosphere.

At Tyiyabuguz hydrocarbonate concentration in precipitation has tendency to increase for the period (1998-2002). High values of hydrocarbonate in precipitation at Tashkent and Kaunchi were observed in 2001 (28.21 and 41.65 mg/dm^3 respectively). At Angren and Bekabad hydrocarbonate concentration in precipitation is much larger in comparison with that in others cities. At Angren a maximum equal to 68.7 mg/dm^3 was observed in 2001 and at Bekabad in 2000 (88.08 mg/dm^3). At Almalyk and Chirchik hydrocarbonate concentration is higher than that in Tashkent. It points to a local atmosphere pollution. High hydrocarbonate concentration at Tashkent, Kaunchi, Angren, Bekabad and Tyiyabuguz via Chatkal testifies to impact of CO and CO_2 emissions from local sources in atmosphere where they transformed to hydrocarbonates. Maximal hydrocarbonat concentration at Chatkal (15.45 mg/dm^3) occurred in 2000.

Content of ion ammonium in atmosphere precipitation is unsignificant at these stations.

Analysis of contribution percentage of each component into pollution of atmosphere precipitation at the above stations have showed the following. At Tashkent the percentage of hydrocarbonats constitutes 35 %, at Kaunchi -20%, at Almalyk – 13%, at Chatkal – 29%. The percentage of nitrates is at Tashkent – 12%, at Kaunchi -15%, at Almalyk – 7%, at Chatkal – 16%.

Having analyzed obtained data on chemical composition of precipitation over Tashkent region it was revealed that local sources of atmosphere pollution have an impact on the chemical composition of precipitation. At considered stations the basic pollutants concentration in atmosphere precipitation is higher that at the back ground station.

REFERENCES

1. Report " Environment protection and use of natural resources of the Republic of Uzbekistan", 1993, 90

2. Management directive # 52.25.23-96, Method of measurements of mass concentration of fluorine, chloride, hydrocarbonate, nitrate, sulphate anions in atmospheric precipitation and surface water using the ion chromatography techniques. Tashkent, Glavgidromet, 1996, 21

3. A.O.Alekin, 1970, Fundamentals of Hydrochemistry, Leningrad, 132-135

CLOUD RESOLVING MODEL SIMULATIONS OF WATER AND ENERGY BUDGETS FOR THE INDIAN OCEAN REGION: EFFECTS OF AEROSOLS ON TRADE WIND CUMULI

Hailong Wang[1], Greg M. McFarquhar[1] and Wojciech Grabowski[2]

[1]University of Illinois, Dept. of Atmospheric Sciences, Urbana, IL, 61801, USA
[2]National Center for Atmospheric Research (NCAR), Boulder, CO, 80307, USA

1. INTRODUCTION

This study presents three-dimensional numerical simulations of effects of aerosols on trade wind cumuli over the Indian Ocean region. Trade wind cumuli are prevalent in the tropical maritime region and impact water and energy budgets directly and indirectly through their role as feeder systems for deep convection. Anthropogenic aerosols emitted into the atmosphere alter the Earth's radiative forcing and climate both through their direct radiative effect and indirect effects of increasing cloud albedo (Twomey 1974) and lifetime (Albrecht 1989). Aerosols containing black carbon (soot) may also reduce cloud cover and liquid water content through the absorption of solar radiation. This is known as the semi-direct effect (Hansen et al. 1997) and has a warming effect on climate by reducing the shortwave radiation scattered back to space by clouds.

The Indian Ocean Experiment (INDOEX) was a major field study aimed at understanding the regional and global climate forcing associated with the anthropogenic haze that spread over the tropical northern Indian Ocean during the winter monsoon. Extensive observations during INDOEX (Ramanathan et al. 2001) show that the haze was mainly in the boundary layer, in which trade wind cumuli with a low fractional coverage were embedded. The effects of aerosols on cloud properties were shown by Heymsfield and McFarquhar (2001). Using a large eddy simulation model, Ackerman et al. (2000) found a decrease of trade wind cumulus cloud cover and liquid water path when solar heating from soot was taken into account.

There is considerable uncertainty in estimates of indirect and semi-direct effects, which severely limits the ability to represent these processes in large-scale models needed to predict the global forcing associated with such processes. The purpose of this study is to better characterize the nature of semi-direct and indirect effects by conducting three-dimensional limited domain simulations of trade wind cumuli in the Indian Ocean region, where processes such as the effect of soot absorption can be represented in finer detail than possible in large-scale models. Because semi-direct effects should decrease cloud coverage and indirect effects increase the optical depths of existing cloud layers, the premise of the modeling simulations can be tested against observations of these quantities obtained during INDOEX. These observations come from a combination of in-situ and remote sensing observations.

Corresponding author's address: Hailong Wang, University of Illinois, Dept. of Atmospheric Sciences, 105 S. Gregory Street, Urbana, IL, 61801-3070, Email: hailong@atmos.uiuc.edu.

2. CLOUD RESOLVING MODEL SIMULATIONS

2.1 Model Description

The cloud resolving model used for this study is the Eulerian version of the three-dimensional, two-time-level non-hydrostatic Eulerian/semi-Lagrangian (EULAG) anelastic fluid model described by Smolarkiewicz and Margolin (1997). The model includes the moist precipitation thermodynamics of Grabowski and Smolarkiewicz (1996) and Grabowski (1999). The standard warm-rain parameterization of small-scale atmospheric thermodynamics (Kessler 1969) is used for warm-rain processes. Cloud droplet concentration is prescribed and different values are used for clean and polluted environments. The effective radius of cloud droplet is calculated interactively using the scheme and parameters proposed by McFarquhar and Heymsfield (2001). The δ-four-stream radiative transfer model (Liou et al. 1988, Fu and Liou 1992) is used to compute the broadband solar and infrared radiative properties of clouds, aerosol including soot, nongray gases, and air molecules.

The lateral boundary conditions are cyclic (double periodic). The model bottom is flat and free-slip (i.e. no surface friction). In order to minimize the gravity wave energy accumulation at the upper lid, and reflection from it, damping absorbers are employed in the vicinity of the model top boundary. The model takes initial sounding and sea surface temperature as inputs. Surface heat flux and moisture flux are thereby computed using the simplified Fairall et al.'s (1996) bulk formulae.

2.2 Experimental Setup

Simulations are performed in a numerical domain of 64X64X75 grid mesh with a uniform grid spacing of 100m in the horizontal and 40m in the vertical. A constant time step increment of 2.5s is used in all simulations. To save computational time but maintain

sufficient accuracy, radiative forcing is updated every 2.5 minutes in the model.

There are two series of simulations conducted in this study, sensitivity tests examining the dependence of predicted cloud fields to representations of varying processes and those examining diurnal evolution of the trade wind cumuli. All sensitivity simulations, in which the model is provided with constant external forcing, such as solar radiation and surface fluxes, are run for 6 hours, while simulations on diurnal evolution with varying external forcing are run for 30 hours. The model does not include any large scale forcing. To maintain a quasi-steady state of horizontal flow, temperature and moisture as observed in the initial sounding, a relaxation approach with a timescale of 1000s is applied starting from the middle of well-mixed layer up to the model top. This is a good strategy to perform sensitivity studies to examine how environmental parameters affect cloud formation and its properties because the simulations will not drift significantly from the observed conditions. To investigate the time evolution of cloud properties, the vertical profiles are allowed to vary with time because the solar radiation and surface fluxes have a diurnal variation.

The control experiment for sensitivity study (CONS) is done without soot in the environment. Four other experiments with soot above the cloud layer (SOOTA), within the cloud layer (SOOTW), below the cloud layer (SOOTB), and throughout the boundary layer (SOOTT) are then performed to study the effects of absorbing aerosols and their vertical distribution on cloud formation, development and dissipation. By using the observations of aerosols during INDOEX (Ramanathan et al. 2001) and Mie theory, the single scattering albedo and extinction coefficient of the absorbing aerosols at 0.55μm are computed as 0.889 and 0.124, respectively.

The control experiment for the diurnal evolution study (COND) is also conducted without soot. Another two experiments are performed. SOOTD aims to show how the semi-direct effect of soot suppresses the formation of clouds or desiccates the existing clouds. For comparison, the NOSUN run is identical to COND, except that the solar radiation is not considered.

3. CASE DESCRIPTION AND MODEL INITIATION

During INDOEX, there were 5 gradient flights when the NCAR C-130 made long low-level transits in and below cloud flying south from Male (4°11'N, 73°32'E) to approximately 7°S in order to depict the meridional variation of cloud properties. On the return leg to Male, the C-130 flew through the middle troposphere collecting solar and infrared radiometer data, and released dropsondes to sample the thermodynamic structure of the atmosphere at fine resolution. This provides the environmental profiles needed to initiate the CRM simulations. In the first phase of this study, a smoothed average profile based on 6 soundings within a temporal range of 2 hours on February 20, 1999, is used as the initial profile, as shown in Figure 1. A well-mixed layer, in which the air is quite humid, exists below 500m. Above this, a conditionally unstable layer extends all the way up to the top of model atmosphere. There is no inversion cap over the top of boundary layer, which allows the vertical development of trade wind cumuli. To see the effect of the inversion cap, simulations are also performed with individual soundings where weak inversions exist near the top of planetary boundary layer. A weak southeasterly wind is blowing over the whole model atmosphere.

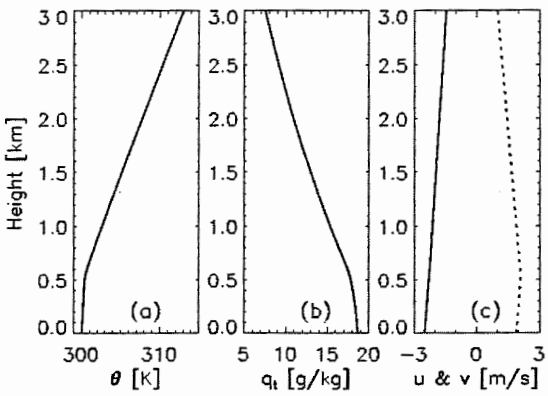

Figure 1 Initial profiles of (a) potential temperature [K], (b) total water mixing ratio [g/kg], and (c) horizontal wind speed [m/s](solid line for E-W component, dotted line for N-S component).

Sea surface temperature (SST) is estimated using retrievals from the Tropical Rainfall Measuring Mission (TRMM) Microwave Imager (TMI). Webster et al. (2002) show that the daily variation of SST over the Indian Ocean during April and May of 1999 is around 0.5°C. In this study the SST is set as constant for the entire simulation. Surface fluxes of heat and moisture for the sensitivity studies are set as $10Wm^{-2}$ and $100Wm^{-2}$, respectively. The Bowen ratio is thus 0.1, a typical value over the ocean. Surface fluxes for diurnal evolution simulations are calculated interactively in the model. Small amplitude random perturbations to the boundary temperature and moisture are applied at the start of the simulation to allow small-scale convective instabilities, and hence clouds, to develop.

4. SIMULATION RESULTS

As described in Section 2, several experiments are performed to investigate the sensitivity of cloud properties to the vertical distribution of absorbing soot and its heating effect. Figure 2 shows the temporal variation of the simulated domain-averaged cloud fraction and cloud liquid water path (LWP). After an approximately 1 hour spin-up time, a pronounced difference among various cases is seen indicating that the cloud fraction and LWP are sensitive not only to the concentration and absorption properties of aerosol, but also to its vertical distribution. Other sensitivity studies on surface fluxes of heat and moisture, thermodynamic profiles, horizontal wind, and radiative forcing will be shown in the conference presentation.

Figure 3 shows the temporal evolution of LWP and cloud fractional coverage for three other experiments simulating the diurnal evolution of cloud properties. The simulations start at local midnight. The model spin-up time is a little longer but ends before sunrise so that it does not affect the results. The simulated cloud fraction and LWP are very small in magnitude but close to values observed during INDOEX. There is a significant daytime reduction of cloud fraction and LWP for the control run (COND), which occurs partly through evaporation of existing clouds and partly through suppressing the formation of new cells. The absorption of solar radiation at cloud top may cancel the cloud-induced radiative cooling, enhance the environmental temperature, and accelerate the evaporation of cloud droplets. At the same time, solar heating increases the near surface air temperature and reduces surface heat flux, which plays an important role in cloud initiation. For comparison, results from the NOSUN run show that the cloud fraction and LWP are in a dynamical balance throughout the simulation. This shows that the daytime reduction of cloud is driven by solar radiation directly and indirectly through feedbacks. With the absorbing soot in the environment, the daytime reduction in cloud is further enhanced. The differences between cloud properties in the COND run and those in the SOOTD run indicate that the semi-direct effect is quite significant.

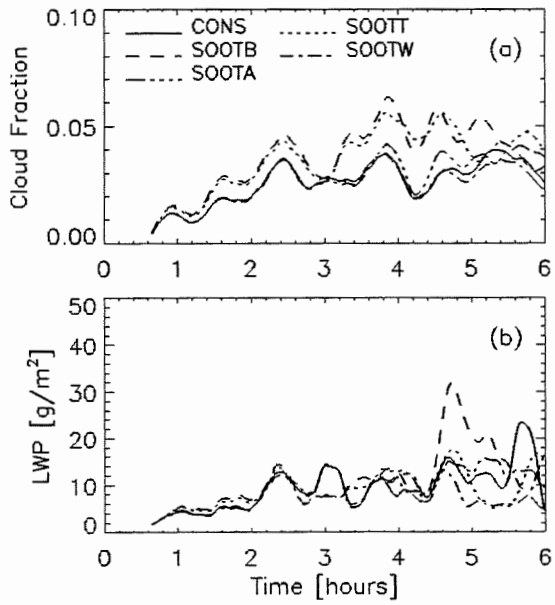

Figure 2 Simulated temporal variations of (a) domain-averaged cloud fraction, and (b) liquid water path averaged over cloudy columns. The curves have been smoothed over 20-minutes data points.

In order to illustrate how the simulated cloud fraction responds to the diurnal variation of solar radiation, the evolution of cloud fraction vertical distribution with two contour levels is given in Figure 4. A 2% contour is selected for display because it represents the outline of the distribution well, and the 4% contour is used to enclose the area where cloud occur more frequently. It can be seen that the cloud base height is near the top of the well-mixed layer (500m) and varies little with time, while the cloud top height changes a lot. During the daytime, cloud fraction is reduced at all levels but more significantly at cloud top, because of the heating and subsequent evaporation of clouds from absorption of solar radiation. The reduction of cloud fraction near cloud base is mainly contributed by the feedbacks from below, such as increase in the environmental saturation vapor pressure near cloud base and decrease in surface fluxes. After sunset, the cloud fraction increases quite rapidly.

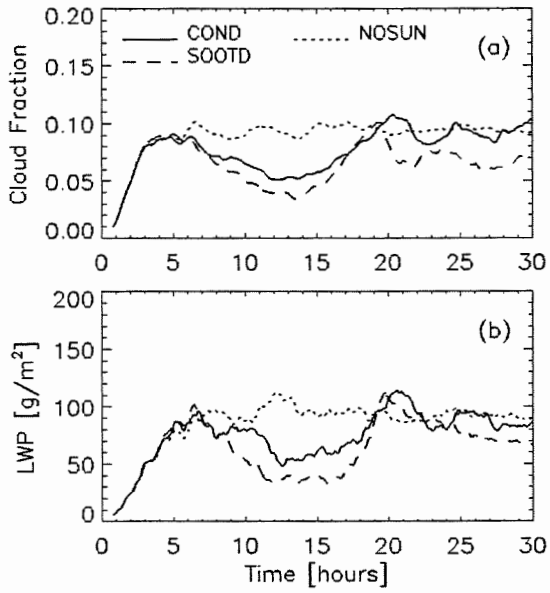

Figure 3 Simulated diurnal evolutions of (a) domain-averaged cloud fraction, and (b) liquid water path [g/m^2] averaged over cloudy columns. The curves have been smoothed over 3-hour data points.

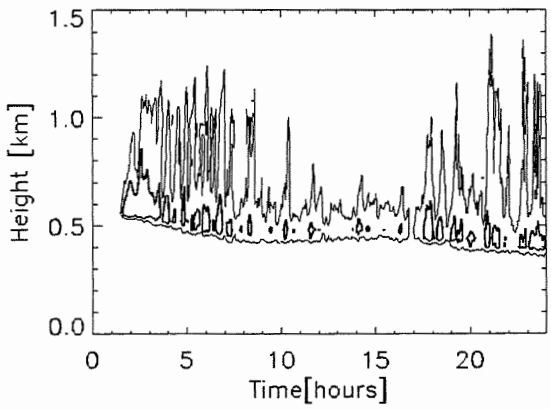

Figure 4 Simulated evolution of cloud fraction vertical distribution for the COND run. The thin solid line stands for 2% cloud fraction contour, while the thick solid line stands for 4% cloud fraction contour.

5. SUMMARY

In this study, the impact of absorbing soot in the formation and evolution of trade wind cumuli in the Indian Ocean region has been examined. Sensitivity studies show that cloud properties are sensitive not only to the concentration and absorption properties of aerosol, but also to its vertical distribution.

Simulations show that EULAG model can reasonably simulate the diurnal evolution of trade wind cumuli. The magnitude of the simulated cloud fraction is very close to observations obtained during INDOEX. The model results show that the semi-direct effect, caused by absorption of solar radiation by soot, has an important effect on cloud properties, and therefore, on the water and energy budgets of the simulated region. The findings of this study can ultimately be used to help develop parameterizations for indirect and semi-direct processes to General Circulation Models (GCMs), and hence estimate global water and energy budgets.

6. ACKNOWLEDGEMENTS

The National Aeronautics and Space Administration Global Water and Energy Cycle (GWEC) Research and Analysis Program, Michael Jasinski program manager, supported this research. The findings of this research do not necessarily represent the views of the agency. The dropsonde data were obtained from NCAR's Joint Office of Science Support (JOSS). TMI data and images are produced by Remote Sensing Systems and sponsored by NASA's Earth Science Information Partnerships (ESIP): a federation of information sites for Earth Science; and by NASA's TRMM science team.

7. REFERENCES

Ackerman, A.S., O.B. Toon, D.E. Stevens, A.J. Heymsfield, V. Ramanathan, and E.J. Welton, 2000: Reduction of tropical cloudiness by soot. *Science*, **288**, 1042-1047.

Albrecht, B.A., 1989: Aerosols, cloud microphysics, and fractional cloudiness. *Science*, **245**, 1227-1230.

Fairall, C.W., E.F. Bradley, D.P. Rogers, J.B. Edson, and G.S. Young, 1996: Bulk parameterization of air-sea fluxes for Tropical Ocean-Global Atmosphere Coupled-Ocean Atmosphere Response Experiment. *J. Geophys. Res.*, **101**, 3747-3764.

Fu, Q., and Liou, K.N., 1992: On the correlated k-distribution method for radiative transfer in nonhomogeneous atmospheres. *J. Atmos. Sci.*, **49**, 2139-2156.

Grabowski, W.W., 1999: A parameterization of cloud microphysics for long-term cloud-resolving modeling of tropical convection. *Atmos. Res.*, **52**, 17-41.

Grabowski, W.W., and P.K. Smolarkiewicz, 1996: On two-time level semi-Lagrangian modeling of precipitating clouds. *Mon. Wea. Rev.*, **124**, 487-497.

Hansen, J., M. Sato, and R. Ruedy, 1997: Radiative forcing and climate response, *J. Geophys. Res.*, ***102***, 6831-6864.

Heymsfield, A.J., and G.M. McFarquhar, 2001: Microphysics of INDOEX clean and polluted trade cumulus clouds. *J. Geophys. Res.*, **106**, 28653-28674.

Kessler, E., 1969: On the distribution and continuity of water substance in atmospheric circulations. Meteor. Monogr., No. **32**, *Amer. Meteor. Soc.*, 84 pp.

Liou, K.N., Q. Fu, and P.T. Ackerman, 1988: A simple formulation of the delta-four-stream approximation for radiative transfer parameterizations. *J. Atmos. Sci.*, **45**,1940-1948.

McFarquhar, G.M., and A.J. Heymsfield, 2001: Parameterizations of INDOEX microphysical measurements and calculations of cloud susceptibility: applications for climate studies. *J. Geophys. Res.*, **106**, 28 675-28 698.

Ramanathan, V., and 39 Co-authors, 2001: Indian Ocean Experiment: An integrated analysis of climate forcing and effects of the great Indo-Asian haze. *J. Geophys. Res.*, **106**, 28371-28398.

Smolarkiewicz, P.K., and L.G. Margolin, 1997: On forward-in-time differencing in fluids: An Eulerian/semi-Lagrangian nonhydrostatic model for stratified flows. *Atmosphere-Ocean Special*, **35**, 127-152.

Twomey, S., 1974: Pollution and the planetary albedo. *Atmos. Environ.*, **8**, 1251-1256.

Webster, P.J., E.F. Bradley, C.W. Fairall, J.S. Godfrey, P. Hacker, R.A. Houze, R. Lukas, Y. Serra, J.M. Hummon, T.D.M. Lawrence, C.A. Russell, M.N. Ryan, K. Sahami, P. Zuidema, 2002: The JASMINE pilot study. *Bull. Amer. Meteor. Soc*, **83**, 1603-1630.

Verifications of high-resolution long-term prediction by Japan Meteorological Agency – Nonhydrostatic Model (JMA-NHM) with the Spectral Boundary Coupling (SBC) method

K. Yasunaga[1], T. Kato[2], H. Sasaki[2], C. Muroi[2], K. Kurihara[2], and Y. Sato[2]

[1]Advanced Earth Science and Technology Organization, Tokyo, Japan
[2]Meteorological Research Institute / Japan Meteorological Agency, Tsukuba, Ibaraki, Japan

1. INTRODUCTION

Climate changes are coming to be recognized as critical factors which affect human life seriously. For several decades, possible climate changes have been investigated and discussed in the global aspects. Although global-scale climate changes have universal importance, they also have small-scale aspects which are deeply connected with serious disasters. Recently, the need for detailed information of the climate changes over a limited area (e.g., occurrences of severe phenomena such as heavy rainfall and gust, changes of hydrological cycle, a drain of water resources, frequencies of abnormally warm/cold weather) has exhibited a dramatic increase, because regional climate may drastically change even when the global climate slightly changes, and the regional climate changes will directly affect the living circumstances over the limited area.

A general circulation model (GCM) with coarse horizontal resolution of a few hundred kilometers has been used for climate simulations. While the GCM with the grid interval of a few hundred kilometers can resolve synoptic-scale disturbances, meso-scale disturbances, which are equally important to regional climate, cannot be resolved. Therefore, when the regional climate is particularly focused on, a climate model with horizontal resolution of 20 – 100 km that covers only a limited area of interest has recently been employed. Such regional climate model (RCM) is, however, still insufficient to examine regional climate, because horizontal scales of severe phenomena accompanied with strong vertical motions such as heavy rainfall are smaller than 20 – 100 km, and hydrostatic balance, which is generally assumed in most GCMs or regional climate models, is not satisfied in the severe phenomena. Accordingly, simulations by a nonhydrostatic model with high resolution of a few kilometers are urged to conduct a detailed investigation about regional climate.

The Meteorological Research Institute (MRI) and Numerical Prediction Division, Japan Meteorological Agency (JMA) have jointly developed a nonhydrostatic model (JMA-NHM). Now, the JMA-NHM is used for the short-term prediction (less than 1 day), and the good model performances are confirmed, especially for the prediction of heavy rainfall. Recently, the fastest super computer around the world (Earth Simulator, ES) has become available to the climate simulations. The ES's calculation speed is so fast that it enables us to use the JMA-NHM as a high-resolution nonhydrostatic regional climate model. Some improvements are, however, necessary to apply the JMA-NHM of a short-term prediction model to a long-integrated model. As one of some improvements, the sophisticated coupling method of the JMA-NHM with a GCM is introduced into the JMA-NHM.

There are some approaches to couple a RCM with a GCM. Traditionally, the method termed "lateral boundary coupling (LBC)" has often been used. In the LBC method, an inner model is joined with the one-way transfer of information from the outer low-resolution model at the lateral boundary, and numerical treatment near the boundary of a limited area model is generally required in order to remove spurious solutions as well as noise. According to Anthes et al. (1989), this can be accomplished by introducing Newtonian damping effects near the lateral boundary. In this paper, the LBC method implies the boundary coupling technique that includes the boundary relaxation method near the lateral boundary. When the LBC method is employed, the lateral boundary of an inner fine mesh model is adjusted only at the limited area around boundary to an outer coarse mesh model in real space. The concept of the LBC method is based on the idea that regional modeling is to solve an initial/boundary-value problem, and other information of the outer coarse model has no direct effects inside of the fine mesh model. Therefore, it is likely that the great difference between the two models appears over the inner area of the fine mesh model, unless the lateral boundary condition is precisely treated (Anthes et al. 1989).

Kida et al. (1991) proposed another coupling approach termed "the Spectral Boundary Coupling (SBC) method". The SBC method is the nesting technique in wave number space. In practice, the SBC method is to replace the large-scale fields (the long wave part) of a fine mesh model with the corresponding large-scale fields supplied externally from a coarse mesh model. Accordingly, the SBC method would inhibit the discrepancies between the phases and the positions of disturbances in the two models over the whole domain of interest, and the long-term integration could be conducted smoothly. The concept of the SBC method is based on the idea that regional modeling is to predict small-scale

Corresponding author's address: Kazuaki Yasunaga, Meteorological Research Institute, 1-1 Nagamine Tsukuba, Ibaraki, Japan; E-Mail: kyasunag@mri-jma.go.jp.

response to large-scale conditions ("downscaling" von Storch 1995) and that the large-scale field cannot be well reproduced within a limited area.

The SBC method works in wave number space, while the LBC method works in real space. Therefore, the SBC method can simultaneously used with the LBC method. Sasaki et al. (1995) and Sasaki et al. (2000) used the objectively analyzed fields instead of the forecasts of a GCM, and it was found that the limited area models for the regional climate simulation with horizontal resolutions of 40 km and 127 km well reproduced the objective analysis with a higher accuracy when the SBC method was employed together with the LBC method than when only the LBC method was used. The models are hydrostatic models, and the dynamical and physical frameworks of the two models are similar to those of a GCM or the model used for objective analysis in JMA. Such similarity is favorable to suppress noise when the long wave part is replaced in the SBC method. On the other hand, JMA-NHM is a nonhydrostatic model. JMA-NHM generally employs much finer resolution, and cloud microphysics is explicitly represented (No convective parameterization is used). Namely, the dynamical and physical frameworks of JMA-NHM are quite different from those of a GCM or the model used for objective analysis. Therefore, it is unknown that the SBC method also works well for the JMA-NHM.

In the present study, it is investigated that whether the long-term simulations by the high-resolution JMA-NHM show high performances when the SBC method is used. In order to evaluate performances of long-term integrations of JMA-NHM with the SBC Method, the JMA-NHM is also nested the objectively analyzed fields instead of the forecasts of a GCM.

In East Asia, summer monsoon starts from the south in May, and ends in July, extending to the north. The monsoon circulation forms rain/cloud zone with a stationary front across East Asia (from china to Japan), and a lot of rainfall is brought about in this season. The monsoon rainfall season over East Asia is identified as Baiu-season in Japan (Meiyu-season in China). From the point of view of water resources or natural disaster, it is especially important to examine how the position of the frontal zone and the intensity of the precipitation forming over the frontal zone are altered when green house gas concentrations steadily increase. Therefore, the goal of our group is to predict climate changes by the increase of greenhouse gas concentrations in Baiu-season around East Asia, making a use of the JMA-NHM. Taking our final object into consideration, the simulation period is set to be Baiu-season and the domain covering East Asia is employed, in order to evaluate the performances the JMA-NHM with the SBC method.

2. Model descriptions and experimental designs

2.1 Model descriptions

A nonhydrostatic regional climate model used in the present study is based on JMA-NHM. For the basic equations, fully compressible equations in terrain following coordinates on a polar stereographic projection map are employed. The model treats sound waves implicitly in the vertical direction and explicitly in the horizontal direction (HE-VI scheme). The modified second-order centered-difference advection scheme and leap-flog time differential scheme are used. Details of JMA-NHM are shown in Saito et al. (2001).

The horizontal grid size of the model is 5 km, and the domain covers 4000 km x 3000 km (Fig. 1). The model has 48 vertical layers with a finer resolution (20 m) near the surface and coarser resolution (920m) at the model top. Since the horizontal grid length of 5 km allows strong convective updrafts to be treated explicitly, no convective parameterization is used, and cloud microphysics is explicitly treated. The prognostic variables are horizontal wind components (u, v), vertical wind component (w), potential temperature (θ), pressure (p), turbulent kinetic energy (tke), mixing ratios of water substances (water vapor, cloud water, rainwater, cloud ice, snow, and graupel), and number densities of condensates (cloud water, rainwater, cloud ice, snow, and graupel). While ground temperature is predicted with a soil model, sea surface temperature is not. The JMA's objective analysis of SST is used instead of the prediction by an ocean model. The SST analysis by JMA is conducted once a day, and the horizontal resolution is 1 degree. Accordingly, the SST analysis is linearly interpolated into the grids of the NHM at each model time-step. Calculations of the surface fluxes are based on the Monin-Obukov similarity theory. The level-2.5 closure model is applied to represent the vertical turbulent diffusion. Rayleigh damping is imposed near the upper and lateral boundary.

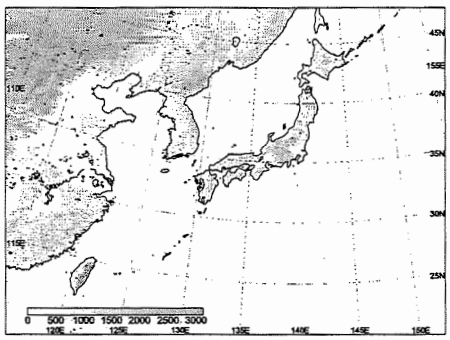

Fig.1 The model domain and orography.

2.2 Experimental designs

The regional analysis by JMA (RANAL) is utilized for the initial field, and for the boundary conditions with the LBC method and the SBC method in the simulation. The RANAL is operationally produced 4 times a day (00, 06, 12, 18 UTC), and covers East Asia with the resolution of 20 km in east-west and north-south directions. The RANAL is also linearly interpolated in time and space as well as the SST analysis.

Two experiments are conducted to evaluate performances of the SBC method. In one experiment, the LBC method is only employed, and in the other experiment, the LBC and SBC methods are simultaneously used. The former is called as the LBC experiment, and the latter as the SBC experiment, hereafter. In the two experiments, the integration starts at 21 May 2003, and ends at 30 Jun (40 days).

2.3 The SBC method

The procedure of the SBC method and some specified constants controlling the SBC method briefly described in this sub-section. More details are shown in Kida et al. (1991) and Sasaki et al. (1995).

First, the coarse mesh model fields and the fine mesh fields are individually expanded in a double-Fourier series horizontally after a certain time. Secondly, only long wave parts of the two models in the wave number space are transformed back to the real space. Thirdly, the grid data that belongs to the long wave part of the fine mesh model is subtracted from the total fields. As a result, the grid data that belongs to the short wave part of the fine mesh model is obtained. The long wave part of the coarse mesh model and the short wave part of the fine mesh model are finally coupled, and the time integration is continued. These cycles are repeated until the end of the time integration.

In the present study, the wave numbers which divide the large-scale and small-scale are $k = l = 6$ on $0 < x, y < \pi$, where k and l are wave numbers in x and y directions, respectively. As the time intervals of the SBC method, 20 minutes are adopted. The RANAL is provided every 6 hours, and in between, values are derived through linear interpolation. The SBC method is confined to higher altitudes (the height of 5 km is used in the present study), so that the flow at lower levels is free to adjust to local conditions. The SBC method applied to u, v and θ.

3. Results

3.1 Sea Level Pressure

On the 10th day of the integration (31 May), a depression is predicted in the SBC experiment close at the analyzed position (Figs. 2a-1 and 2b-1), although the value of the sea level pressure at the depression center (986 hPa) is slightly smaller than the analyzed value (990 hPa). On the other hand, in the LBC experiment, the depression is predicted apart from the analyzed position (Fig.2c-1), and the value at the center (996 hPa) is overestimated. On the 20th and 30th day, depressions predicted in the SBC experiment are also closer to the analyzed positions than in the LBC experiment (Figs.2a-2, 2a-3, 2b-2, 2b-3, 2c-2, and 2c-3). On the 30th and 40th day, anticyclones over the Pacific Ocean become much stronger in the LBC experiment than in the SBC experiment and analysis (Figs.2a-3, 2a-4, 2b-3, 2b-4, 2c-3 and 2c-4).

While the model bias of the domain-averaged sea level pressure frequently exceeds the value of 2 hPa in the LBC experiment, the bias is below the value of 1.2 hPa in the SBC experiment (Fig.3a). Moreover, much lager values of the Root Mean Square Error of the sea level pressure are found in the LBC experiment than in the SBC experiment (Fig.3b).

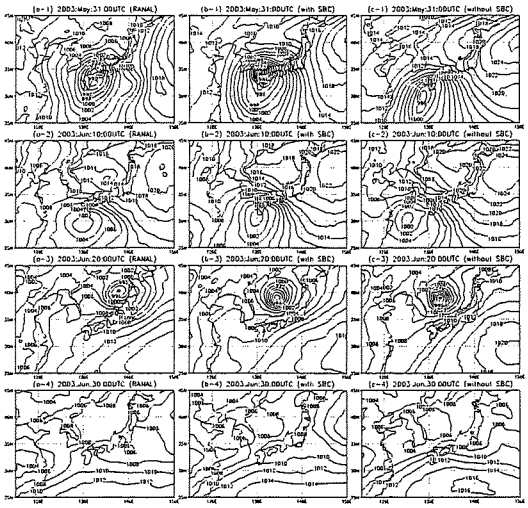

Fig.2 Analyzed and predicted sea level pressure patterns at 31 May (10th day), 10 Jun (20th day), 20 Jun (30th day), and 30 Jun (40th day) from the top. Panels in the left row are the objectively analyzed patterns. Panels in the middle and right rows are predicted patterns in the SBC and LBC experiments, respectively.

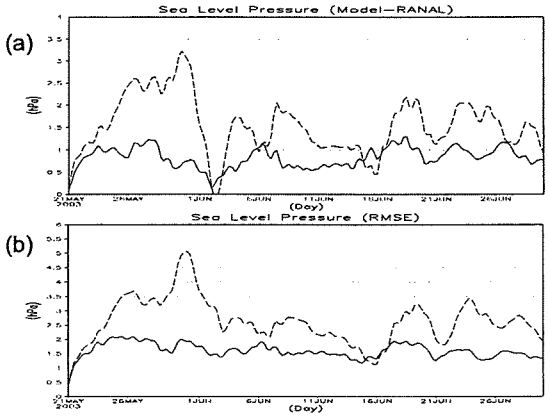

Fig.3 Time-series of (a) the model bias of the domain-averaged sea level pressure against the RANAL (predictions - RANAL), and (b) Root Mean Square Errors (RMSEs) of the predicted sea level pressure from the RANAL. Solid and dashed lines represent the results in the SBC and LBC experiments, respectively.

3.2 Rainfall

The SBC experiment reproduces more similar rainfall patterns to the GPCP than the LBC experiment

where heavy rainfall regions shift toward the north. It is thought that the shifts result from the stronger anticyclones over the Pacific Ocean in the LBC experiment (Figs. 2c-3 and 2c-4). The peaks of the rainfall amounts are generally weaker in both experiments than in the GPCP (Fig.4).

In order to statistically evaluate surface precipitation and surface temperature over Japan, the model domain around Japan is divided into 5 sub-regions (SW, KS, CJ, EJ, and NJ in Fig.5a), and the predictions are compared with the ground-based observations by JMA over each sub-region.

In the LBC experiment, the rainfall amounts accumulated during 30 days are overestimated over all regions except in the SW region. In the SBC experiment, the rainfall amounts are lower than in the LBC experiment except in the SW region, and agree with the analyzed values (Fig5b). RMSE of the rainfall over each region is also lower in the SBC experiment than in the LBC experiment. The differences of the RMSE between the two experiments become lager from the south to the north.

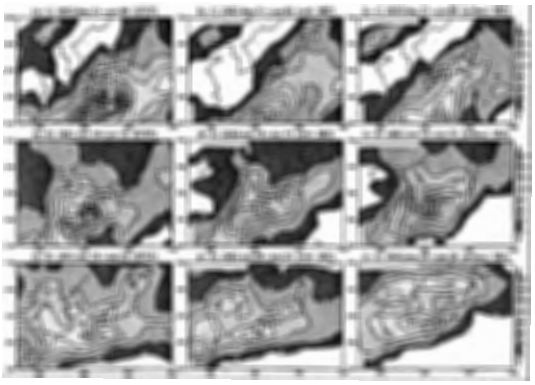

Fig.4 Rainfall patterns accumulated for 10 days (the upper panels: 31 May - 10 Jun, the middle panels: 10 Jun - 20 Jun, the bottom panels: 20 Jun - 30 Jun). Panels in the left row show the patterns from the GPCP. Panels in the middle and right rows represent the patterns predicted in the SBC and LBC experiments, respectively.

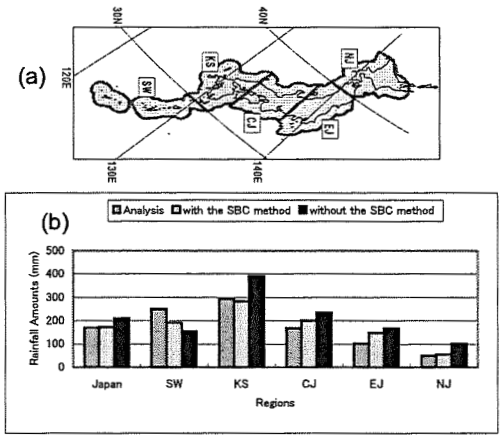

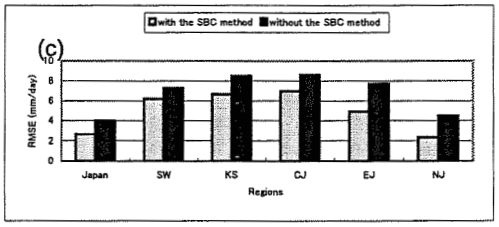

Fig.5 (a) coverage of each sub-region (see text), (b) accumulated rainfall amounts and (c) RMSE of rainfall from the analysis over Japan and each sub-region from the 11th to 40th day of the integration (30 days).

3.3 Surface temperature

A correlation coefficient is used as a statistic to evaluate the predicted surface temperature. Over all regions, correlation coefficients are lager in the SBC experiment than in the LBC experiment (Fig.6).

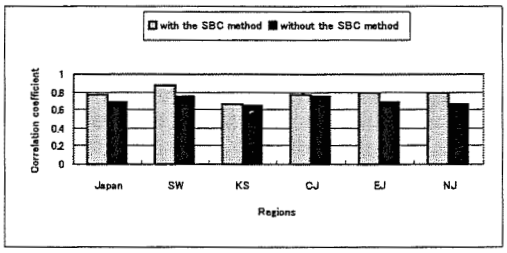

Fig.6 Correlation coefficients of the mode-predicted surface temperature to observations over each region.

4. Summary

In the SBC experiment, patterns of sea level pressure and surface precipitation are well reproduced, and statistics over Japan such as RMSEs of sea level pressure and surface precipitation, and correlation coefficients of surface temperature are all better than in the LBC experiment. Therefore, it can be concluded that the SBC method works well for the JMA-NHM.

5. References

Kida, H., T. Koide, H. Sasaki, and M. Chiba, 1991: A new approach to coupling a limited area model with a GCM for regional climate simulations. *J. Meteor. Soc. Japan*, **69**, 723-728.

Saito, K., T. Kato, H. Eito, and C. Muroi, 2001: Documentation of the Meteorological Research Institute / Numerical Prediction Division Unified No hydrostatic model. *Tech. Rep. of MRI.*, **42**, p133.

Sasaki, H., Y. Sato, K. Adachi, and H. Kida, 1995: The performance of long-term integration of limited area model with the spectral boundary coupling method. *J. Meteor. Soc. Japan*, **73**, 165-181.

Sasaki, H., Y. Sato, K. Adachi, and H. Kida, 1995: The performance and evaluation of the MRI regional climate model with the spectral boundary coupling method. *J. Meteor. Soc. Japan*, **78**, 477-489.

THE SPACE-TIME VARIATIONS OF THE THUNDERSTORM ACTIVITY OVER UKRAINE

T.N.Zabolotskaya, V.N.Podgurskaya and T.N.Shpital

Ukrainian Hydrometeorological Research Institute, Kiev, 03028, Ukraine

1. INTRODUCTION

At present the problem of global climatic change became one of the most major. The many-sided researches of this problem are realized in many countries. For example, in Ukraine the changes of surface temperature, precipitation amount (Voloschuk et al.,2002), cloud cover (Zabolotskaya et al.,2002), character of air-mass circulation (Martazinova et al.,1998) were estimated. To number of such problems can be related the contemporary changes of the thunderstorm activity. This information represents both scientific and practical interest.

The space-time variations of the thunderstorm activity were determined by comparing of two 30 years periods: 1936-1965 and 1961-1990. The number of thunderstorm days (N) and the thunderstorm duration (D) for month and warm half year (from April to September inclusive) were considered as characteristics. The tendency of thunderstorm duration changes was determined for 1961-2000.

2. CHARACTER OF THUNDERSTORM ACTIVITY

The character of thunderstorm activity was identical practically on all territory of Ukraine during both periods. At the beginning and the end of warm half year (April, September) the thunderstorm duration less than 1 hour was most probable (accordingly 43 and 37%). In May-August the thunderstorms became longer and the maximum frequency of duration was 1-2 hours (33-37%).

In general the thunderstorm frequency by D ≤ 2 hours in April was 80%; May, September – 70%; June-August – 60-65%. Exception was the border north-west and south-east regions. Here thunderstorms were longer: the maximum frequency of its duration was 2-3 hours. Besides, if on the large part of territory thunderstorms by D > 5 hours were observed in 5% cases then in these regions – about 20%.

3. ANALYSIS OF THUNDERSTORM ACTIVITY CHANGES

In period 1936-1965 the number of thunderstorm days for warm half year was 28 (σ = 3,5). But the regions were selected, where the thunderstorm frequency was more approximately on 10-20%: the border north-west (30 days), south-west (30-32), central regions (32-33), the border south-east (30-32) and Zakarpatiye (35). Also the regions were selected, where thunderstorms were less on 20-30%: the north (25 days), the steppe regions (24-25) and the narrow zone of coast (19-23). The mean duration of thunderstorms in this period was 65 hours (σ =18).The values D were varied from 40 to 110 (the higher values D were in regions with N_{max}).

In period 1961-1990 N was changed inessentially and was equal 27 days (σ=3). The spatial distribution conserved the same features as in previous period, but it became more smooth, as the values N_{max} decreased and N_{min} increased. These changes N in relation Ñ were 5-20%. The exception were Zakarpatiye and Karpaty. Here N_{max} became more expressed.

The mean thunderstorm duration in warm half year in second period was decreased on 10% and consisted of 59 hours (σ =15). The spatial distribution mainly conserved the same features as in period 1936-1965. The changes D mainly corresponded to changes N.

The analysis of thunderstorm duration changes for each concrete month was showed, that in second period practically on all territory of Ukraine the thunderstorm duration was increased in April on 0,5-1 hour especially on north-west, in Zakarpatiye and the mountain regions of Karpat and also in central steppe regions. In May the increasing

Tamara N.Zabolotskaya,
Ukrainian Hydrometeorological Research Institute, Kiev, 37 Nauki Av., 03028, Ukraine

of thunderstorm duration was conserved in the above named regions (except Zakarpatiye), on the remaining territory D was decreased. The same picture was in June, only area with hightened values was decreased and with reduced values was increased. In July the increasing of D was conserved only in mountain and central regions, that is the thunderstorm duration was decreased on a large part of territory. In August D was decreased everywhere (on 2,5 hour average). In September the large part of territory was enveloped by decreasing D , but also the increasing was observed in central and coastal regions. It is necessary to select Crimea, here for all warm half year the thunderstorm duration was above then in previous period.

The significance of differences of monthly means D was estimated by the Student's criterion. It was founded that the significant increasing of the thunderstorm duration was in April and decreasing in August (the significant level was 0,01). In July the differences were fixed at the significant level equal 0,1. In May, June, September the differences of the thunderstorm duration between two periods were no significant.

Since at present the climatic changes especially are appreciable, the change tendency of thunderstorm duration means for warm half year was estimated for period 1961-2000. The data of 37 stations were used. Figure 1 shows the distribution of linear trend coefficient on the territory of Ukraine. In northern regions, on south-west and south-east the steady decreasing of the thunderstorm duration is observed, at the same time on west, in center, on south and in Crimea the duration is increased. To regions where there is the decreasing or increasing of thunderstorm duration correspond the same changes of number of thunderstorm days.

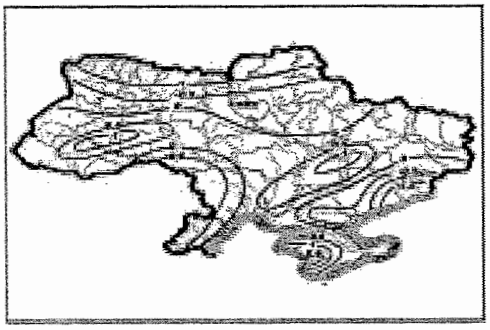

Figure 1. The distribution of linear trend coefficient on territory of Ukraine

The thunderstorms on Ukraine mainly are formed on atmospheric fronts, therefore such tendency of changes can be explained by changing of air-mass circulation character. The atmospheric fronts in warm period over Ukraine are conditioned by south-west and south cyclones (70%), less often by west and north-west (30%). The south-west and south cyclones are formed in the following regions: Italy, the Aegean sea, the Lower-Danube lowland, west of the Black sea, eastern regions of the Azov sea and Northern Caucasus. Since at present the Azore anticyclone is extended to east (Martazinova et al.,1998) perhaps it has an influence on frequency of a formation and a degree of development of these cyclones. It can supposed (fig.1),that at present the activity of north-west and south-west cyclones was decreased, but the activity of west (from the Hungarian lowland) and south (from the west part of the Black sea) cyclones was increased.

4. CONCLUSIONS

The mean number of thunderstorm days in second period (1961-1990) relative to first period (1936-1965) was decreased inessential (on 1 day). The thunderstorm duration was decreased on 6 hours (10%).

The significant increasing of thunderstorm duration was observed in April (on 0,5-1 hour) and decreasing in August (on 2,5 hour). The significant level was 0,01.

The tendency of thunderstorm duration changes during 1961-2000 indicates its decreasing in northern, south-west and south-east regions and increasing in west, south, in center and Crimea. The possible reason of such changes can be the change of air-mass circulation.

REFERENCES

Martazinova, V., and T.Sverdlik , 1998:
The large-scale atmospheric circulation of XX century, its changes and the contemporary state. Tr. Ukr. Met. Inst., 246, 21-27.

Voloschuk,V. S.Boychenko, S.Stepanenko, S.Bortnik, and P.Shischenko, 2002:
The global warming-up and the climate of Ukraine. Regional ecological and social-economic aspects. IPC. Kiev Univers., 116.

Zabolotskaya, T., V.Podgurskaya, and T.Shpital, 2002:
The space-time changes of cloud cover over Ukraine. Tr.Ukr.Met.Inst., 250, 100-106.

THE UNCOMMON STRONG PRECIPITATION AND THE POSSIBLE REASONS OF ITS FORMATION OVER UKRAINE

T.N.Zabolotskaya, V.N.Podgurskaya, T.N.Shpital

Ukrainian reseach hydrometeorological institute, 03028, Kiev, Ukraine

1. INRTODUCTION

The dangerous meteorological phenomena cause the considerable losses, but the most there are at the time of very strong precipitation especially when they are long and envelop of the large areas. It causes the intensive water flow and formation of floods. Such precipitation can classify as uncommon strong (USP) as frequently it falls more 100 mm for rain.

For investigation of reasons of the formation USP the observation period (1966-1995) was used on all territory of Ukraine (75 stations) during of May-September as 90% of all strong precipitation (>30 mm/24 hours) fall at this time (Logvinov et al.,1972). For analysis the cases were selected, when the daily precipitation amount was >50 mm.

2. RESULTS OF THE INVESTIGATION

Analysis of the data showed that USP fall in any region of Ukraine, but frequently (75% of all cases) in west, south-west and central regions. Approximation of number of provinces with USP by polynomial indicated on some cyclic recurrence of its formation: the increasing of frequency (on 45%) was in 1966-1974; the decreasing (on 45%) - in 1975-1987, then again the increasing but less essential (30%) – in 1988-1995.

The synoptical analysis of all cases showed that such precipitation were observed under conditions: a) the going out of southern and south-west cyclones (or its interaction with the wave cold front from west or north-west); b) the presence of the blocking process which apply the brake to cyclonic motion. Both the standing cyclone and the anomalous motion there were. Frequently the center of cyclone made "the looping" motion.

The types of blocking processes were different but most of all the cyclone was blocked by two anticyclones: from the west and the east, sometimes from the north and the east. Primary the general reason was conditioned by the intensive cyclogenes over West Siberia, which blocked the motion to east of anticyclone over Europe part of Russia and therefore the natural cyclonic motion.

Both the slow down motion and the standing of cyclone led to the change of its circulation. The quantitative estimation was made for 15 synoptical situations. So in cyclone the circular motion is nearly in the horizontal plane that the geostrophic vorticity (Ω) answer for such motion and it is proportional to the intensity of circulation. This parameter was calculated every three hours in the synoptical scale during all period of the being of cyclone over Ukraine. Then these values were compared with precipitation area and amount in frontal zones.

It was received that the values of geostrophic vorticity were increased to $\Omega>1\cdot10^{-4}$ 1/s just during of the blocking period. At this time the fall of uncommon strong precipitation was observed. The values $\Omega>1\cdot10^{-4}$ 1/s were kept during 24 hours in 70% of all cases and 36-48 hours – 30%. The values Ω_{max} were 1,02 - $3\cdot10^{-4}$ 1/s, but 1-1,5$\cdot10^{-4}$ 1/s – 60%, 1,51-2$\cdot10^{-4}$ 1/s – 15%,>2$\cdot10^{-4}$ 1/s – 25% of all cases. In each case the precipitation were long (24-48 hours); maximum amount in limits 100 mm was marked in 45% of cases, 101-150 mm – 40% and to 200 mm – 15%; precipitation covered the large areas (50-150 thousands km^2).

For example, on figures 1,2 are represented the time changes of the geostrophic vorticity and the precipitation amount in two synoptical situations: 2-4 July 1971 and 30 September 1995. In first case Ω_{max} was 2,12$\cdot10^{-4}$ 1/s, the values $\Omega>1\cdot10^{-4}$ 1/s were kept 48 hours; maximum precipitation amounts were equal 100 mm in Chernovzy province, 110 mm – in Ternopol province and 120 mm – in Vinniza province. The second case – the example of the "outburst" cyclogenes. Here Ω_{max} was equal $3\cdot10^{-4}$ 1/s. The anomalous motion of cyclone and its standing took place during 12 hours, for this time 60-70 mm of precipitation was falled. The cyclone was clutched with the west and the east of two anticyclones, but its power was so large

Tamara N.Zabolotskaya,
Ukrainian Hydrometeorological Research Institute, Kiev, 37 Nauki Av., 03028, Ukraine

that moving to the north the cyclone forced the western anticyclone to go down on the south.

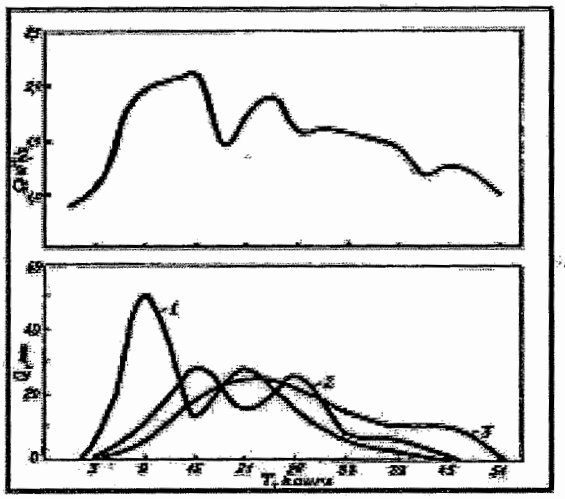

Figure 1. The time variation of geostrophic vorticity and precipitation amount. 2-4 July 1971; 1 – Vinniza province, 2 – Chernovzy province, 3 – Ternopol province

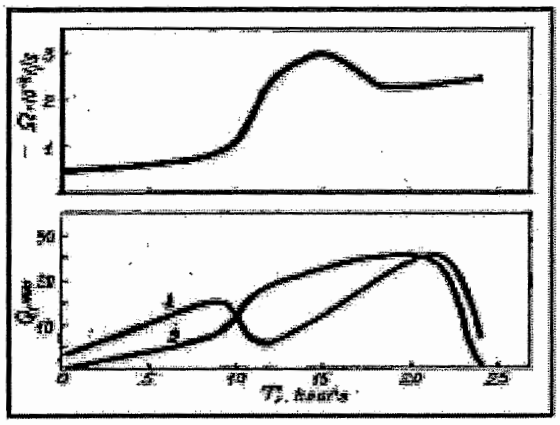

Figure 2. The time variation of geostrophic vorticity and precipitation amount. 30 September 1995; 1 – Kiev province, 2 – Cherkassy province

The southern and south-west cyclones moving on Ukraine are mainly young baric formations. Their distinctive features are following: a) the temperature asymmetry, b)the vertical extension of cyclonic circulation, c) the large velocity of motion. But if there is the blocking process then such cyclones become a quasi-stationary. Hence the new air masses (probably more dry air since the previous baric field was anticyclonic) are not drawn into cyclone, that is the moisture loss on evaporation are small. But the growth of geostrophic vorticity intensify the ordered ascensional velocity and the moisture air ascent. Because of the fall temperature the air masses become moist-labile and the additional favorable conditions are originated for its forced ascent over a large space and for a long time.

The corresponding calculations of the ordered ascensional velocity and the forced ascent were made by the pluviometric data over all strong precipitation area. The ordered ascensional velocity was in limits 5-10,5 cm/s, but the value 5-7 cm/s was dominated. The velocity of forced ascent was changed from 14 to 67 cm/s, but it was <20 cm/s (50% of cases), 21-30 cm/s – 40% and >30 cm/s – 10%.

Besides the energy of instability (as the characteristic of the present conditions for the development of free convection) and the equipotential temperature profile (as the characteristic of the potential instability) were estimated in each case. It was received that the conditions for the free convective development were only in four synoptical situations; in two - the such conditions were episode and in other nine situations the conditions for the free convective development were absent.

For precipitation formation it is necessary to have the reserves of moisture. In majority of synoptical situations (13 cases) the specific surface humidity was 9-13 g/kg; on level surface 700 mb – 5-6 g/kg, that is the precipitation formation layer was enough saturated. In two other situations the specific surface humidity was 5-6 g/kg but its value was conserved in all precipitation formation layer.

3. CONCLUSIONS

Analysis of 15 synoptical situations with the uncommon strong precipitation was shown that the primary reasons of its formation were: a) the blocking of cyclones and as a result the intensification of cyclonic circulation, b) the increase of the ordered ascensional velocity and the development of forced air ascent, c) the minimum of dew-point.

REFERENCES

Logvinov,K., V.Babichenko, and M.Kulakovskaya,1972:

The dangerous phenomena of weather on Ukraine. Tr. Ukr. Met. Inst.,110, 59-73.

DETERMINATION OF MESOSCALE AND SYNOPTIC-SCALE PRECIPITATION AND ITS IMPACT ON PRECIPITATION EXTREMES FROM THE SYNOPTIC STATION NETWORK OVER EUROPEAN CONTINENT

O.Zolina,[1] A.Kapala[1], C.Simmer[1] and S.K. Gulev[2]

[1] Meteorologisches Institut, Universitaet Bonn, Germany
[2]P.P.Shirshov Institute of Oceanology RAS, Moscow, Russia

1. INTRODUCTION

Continental-scale analyses of statistical characteristics of precipitation, based on daily station data, show typically very spatially noisy results, characterized by strong spatial inhomogeneity (e.g. Klein Tank and Koennen 2003, Zolina et al. 2004). This inhomogeneity is normally attributed to the impact of the meso-scale precipitation variability on the large-scale precipitation patterns. Typical spatial scales of convective precipitation range from several kilometers to several tens of kilometers, that is smaller than a typical resolution of the synoptic station network. Quantitative estimation of the convective component of precipitation and quantification of its impact onto the large-scale patterns is crucially important for the effective precipitation analysis. In particular, station-based validation of precipitation from reanalyses, which provide separate estimates of the stratiform and convective rainfalls, requires parameterization of convective precipitation in the station data. Ideally this task should be carried out on the basis of precipitation data of very high spatial and temporal resolution, which allows for the adequate description of the meso-scale precipitation component. Such data sets are only available for limited areas and time periods and still cannot be used for the continental scale analysis. The aim of this work is to use climatological European network of the long-term daily precipitation measurements for the quantification of mesoscale precipitation component.

2. EUROPEAN DAILY PRECIPITATION DATA

We used in this study daily precipitation data from different collections of station rain gauge measurements over European continent with a precision of 0.1 mm (Figure 1). The Royal Netherlands Meteorological Institute (KNMI) collection, known as European Climate Assessment (ECA) daily dataset (Klein Tank et al. 2002) consists of 208. Additionally we used the regional German Weather Service (DWD) collection. This data set covers well Germany and consists of 106. Collection of the NOAA National Climate Data Center (NCDC) provides observations at 888 stations in western Europe (except Germany) and covers the period from 1948 onwards. Finally we used also the collection of Russian Meteorological Service, which includes 1128 stations. For our purposes all data sets were merged. The merged data set consists of 2233 stations, 515 of which provide measurements for periods from 50 to 100 years and 203 for more than 100 years starting from the mid 19th century onwards. The data set still has a quite inhomogeneous spatial coverage with the highest station density in Central Europe and a considerable drop of the number of observational sites in Southeastern and Eastern Europe. However, it looks to be quite effective for estimation of sub-grid scale precipitation components. Thus, for 96% of locations the merged data set provides more than 20 neighboring stations within the radius of 300 km. In 30% of locations the number of the neighboring stations exceeds 40.

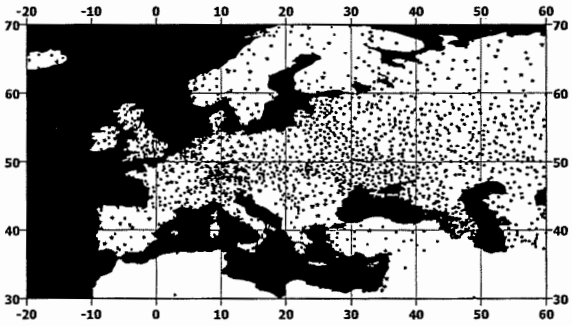

Figure 1. Locations of the precipitation stations in Europe. stars - KNMI collection; triangles – DWD collection; squares – NCDC collection; dotes – Russian Meteorological Service collection.

3. RESULTS OVERVIEW

3.1 Estimation of the spatial correlation scales from a synoptic network

In order to quantify spatial inhomogeneity of the characteristics of daily precipitation we first estimated correlation on synoptic and sub-synoptic time scales for different intrastational distances. Osborn and Hulme (1997) argued that effective correlation radius over European continent may change dramatically from several tens of kilometers in Alpine region in summer to several hundreds of kilometers over Northern continental Europe in winter. In order to estimate intrastaional correlation we analysed all

Corresponding author's address: Olga Zolina, Meteorologisches Institut, Universitaet Bonn, Bonn, auf dem Huegel 20, 53121 Germany; E-Mail: olga.zolina@uni-bonn.de.

available pairs of stations within 300 km radius around every of 2223 stations. Each pair provides an estimate of the correlation coefficient for a given intrastational distance and a given month. Then all estimates were grouped for the 10-km classes of intrastational distances and the mean correlation coefficients were derived for these classes. Figure 2 shows as example winter map of correlation coefficients corresponding to the spatial radius of 100 kilometers. Remarkably, the largest correlation of more than 0.9 is observed in Eastern Europe and Central Russia. At the same time, in the Alpine region, correlation decreases sharply, varying within the range of 0.2-0.6. Summer estimates of correlation are normally smaller than winter ones, that reflects a stronger impact of mesoscale variability on spatial inhomogeneity of daily precipitation.

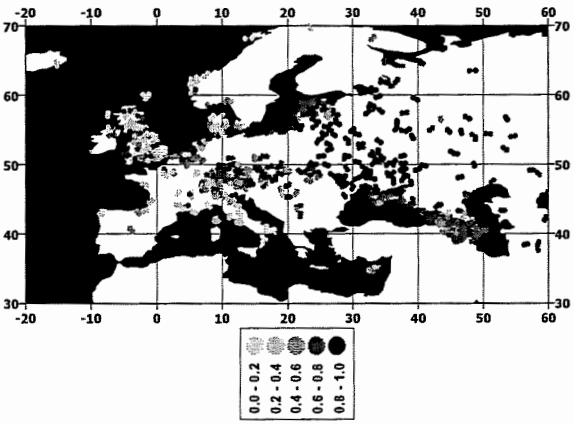

Figure 2. Correlation coefficient corresponding to the spatial radius of 100 km for January.

For most regions correlation exhibits exponential decreasing with increasing spatial radius. Typical values of the correlation coefficients for the classes 0-10 km and 10-20 km are 0.9-1.0 for the Northern continental Europe in winter and from 0.6 to 0.8 for mountain regions in summer. Exponential approximation of the correlation functions allows for the estimation of correlation at zero intrastational distance, which already gives a quantitative estimate of the percentage of variance which cannot be explained by large-scale spatial variability (for a given station network) and, thus, can be attributed to the mesoscale variability. Important assumptions in these speculations are the relative homogeneity of random observational errors of rain gauges and smaller (with respect to the convective precipitation component) magnitude of random observational erros.

4.2 Estimation of sub-grid scale precipitation component using semivariagram method

Our next step was to quantify mesoscale precipitation component using semivariagram approach, which is typically used for the analysis of random observational errors in instrumental measurements (e.g. Lindau 1995, Kent et al. 1999, Gulev et al. 2003). In this method the difference between measurements taken simultaneously in different locations is considered as a function of station-to-station distance. It is then extrapolated to zero distance, where spatial variability does not contribute to the total variance. Therefore, the latter should represent only the variance associated with mesoscale precipitation (error variance in the case of the use of semivariagrams for estimation of observational errors) σ_o^2, which has to be divided by two to get the squared measurement error $\varepsilon_m^2 = \sigma_o^2/2$. A polynomial fit is used to extrapolate the error to zero distance.

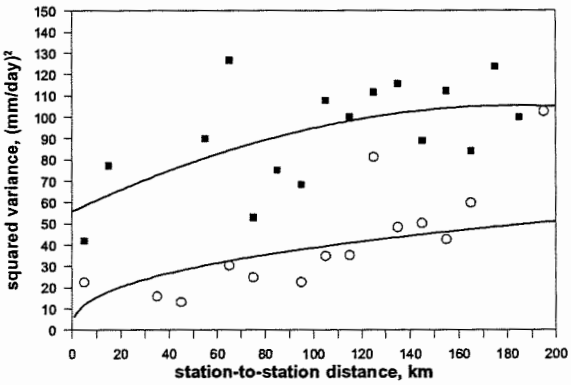

Figure 3. Summer semivariagrams for The Netherlands (open circles) and for the Swiss Alps (squares).

We analysed semivariagrams for different locations for winter and summer month. For most areas semivariagrams exhibit non-linear increase of the squared variance with station-to-station distance. Effective approximation of the semivarigrams implies 3rd order polynomial functions describing the behavior of squared variance with station-to-station distances. Figure 3 demonstrates semivariagrams derived for the summer season for the two station clusters: in The Netherlands, characterized by the flat homogeneous terrain and in Alpine region, where local orography implies strong mesoscale spatial variability of precipitation. Remarkably enough, estimates of convective precipitation component in the Netherlands give considerably smaller value than that observed in the Swiss Alps. Note, that the difference obtained (about 4 mm/day) cannot be attributed to the uncertainty associated with the random observational error whose typical magnitude ranges within 1 mm/day.

5. CONCUDING REMARKS

We analysed sub-synoptic and mesoscale variability of European precipitation as revealed from the daily synoptic network. It should be noted that the use of

daily data has some limitations, first of all associated with the fact that effective time-scale of convective precipitation lies within first hours (sometimes minutes) and cannot be fully accounted for by the observations used. On the other hand, daily precipitation measurements by the station rain gauges provide at present the only source of the continental scale massive precipitation data, used for climate assessments. Thus, our estimates, based on the same data, give quite valuable (if only partly incomplete) information about the intensity of mesoscale processes in different European regions. Further analysis should involve extensive validation of the proposed methodology using high resolution data from the local experiments specially designed for the analysis of mesoscale and sub-mesoscale variability of precipitation.

6. ACKNOWLEDGMENTS

This study is supported by the North Rhine-Westphalia Academy of Science under the project "Large Scale Climate Changes and their Environmental Relevance". We appreciate discussions with Pavel Groismann of NCDC (Asheville), Andreas Hense of MIUB (Bonn) and Vladimir Semenov of IFM (Kiel). DWD is also acknowledged for the provision of station data over Germany. We also benefited form the support of Russian Foundation for Basic Research (grant 02-56331).

7. REFERENCES

Gulev, S.K., V.Grigorieva, A.Sterl, and D. Woolf, 2003: Assessment fo the reliability of wave observations from voluntary observing ships: insights from the validation of a global wind wave climatology based on voluntary observing ship data. J. Geophys. Res. – Oceans, **108(C7)**, 3236, doi:10,1029/2002JC001437.

Kent, E. C., P. Challenor and P.K. Taylor, A Statistical Determination of the random errors present in VOS Meteorological reports. J. Atmosph. Oceanic Tech., 16, 905-914, 1999.

Klein Tank, A.M.G., and G.P. Koennen, 2003: Trends in indices of daily temperature and precipitation extremes in Europe, 1946-99. J. Climate, **16**, 3665-3680, 2003.

Klein Tank, A.M.G., and Coauthors, Daily dataset of 20th century surface air temperature and precipitation series for the European Climate Assessment. Int. J. Climatol., **22**, 1441-1453.

Lindau, R., A new Beaufort equivalent scale. Proceedings of the International COADS Winds Workshop, Kiel, Germany,1994. Ed. H.Diaz, H.-J.Isemer, NOAA-ERL, IFM (Kiel),232-252, 1995.

Osborn, T.J., and M.Hulme, 1997: Development of a relationship between station and grid-box rainday frequencies for climate model evaluation. J. Climate, **10**, 1885-1908.

Zolina, O., A. Kapala, C. Simmer, and S.K. Gulev, 2004: Analysis of extreme precipitation over Europe from different reanalyses: a comparative assessment. Global and Plan. Change, in print.

ANALYSIS OF EXTREME PRECIPITATION OVER EUROPE FROM DIFFERENT REANALYSES: A COMPARATIVE ASSESSMENT

O.Zolina,[1] A.Kapala[1], C.Simmer[1] and S.K. Gulev[2]

[1] Meteorologisches Institut, Universitaet Bonn, Germany
[2]P.P.Shirshov Institute of Oceanology RAS, Moscow, Russia

1. INTRODUCTION

The short-term variability of European precipitation is crucially important due to the strong social and economic impacts of extreme precipitation anomalies. Studies of precipitation variability over the European continent based on station data describe regional changes of both secular and interannual nature.

During the last decades the National Centers of Environmental Prediction (NCEP) together with the National Center for Atmospheric Research (NCAR) and the European Centre for Medium Range Weather Forecasts (ECMWF) produced dynamically consistent data sets for the needs of climate research, commonly known as reanalyses. These data sets provide an alternative source of daily (and higher resolution) precipitation data, which are, however, should be considered with caution due to poor skills of NWP models to simulate precipitation.

In this work we analyzed extreme precipitation for four major existing reanlayses (NCEP/NCAR, hereafter NCEP1, NCEP2, ERA15 and ERA40) over the European continent and compared them with station data. We quantify the extreme precipitation characteristics in every product and quantitatively assess the differences in the mean characteristics of precipitation extremes and their variability patterns. This allows us to identify the common characteristics and their spatial distribution in different data sets, which can be used for further validation of the reanalyses against observational data.

2. DATA AND PREPROCESSING

ECMWF ERA15 Reanalysis covers the period 1979-1993 and is based on the operational T106 atmospheric general circulation model (AGCM). The model uses the mass flux convection scheme by Tiedtke. The ECMWF ERA40 (1958-2001) system formulation used a T159 resolution AGCM and assimilated SSM/I radiances as well as ERS-1 and ERS-2 data.

NCEP1, covering the period from 1948 onwards, is based on the T62 operational NCEP model. Assimilation included, besides radiosondes, the dropsondes and pibals, marine and continental winds from different sources. NCEP2 reanalysis was run at the same resolution (T62) as NCEP1, covering the period from 1979 onwards. This product is free from many known biases and errors, which have been identified in the NCEP1. In particular, an incorrect parameterization of horizontal moisture diffusion has been corrected along with an unrealistically high oceanic albedo.

For the intercomparison we used the output from all reanalyses with 6-hourly temporal resolution, from which we derived daily precipitation. Available spatial resolution of the output was 1.92°×1.875° for NCEP1 and NCEP2 and somewhat higher in ERA reanalysis. The different spatial resolutions among the data sets were interpolated onto 2°×2° spatial resolution by the modified method of local procedures. Total precipitation values (when unavailable) were derived from the convective and stratiform components.

For a pilot intercomparison with station data we used daily precipitation measurements from the collection of the Royal Netherlands Meteorological Institute (KNMI), known as European Climate Assessment (ECA) daily dataset. It has been merged with the regional German Weather Service (DWD) collection. The merged data set consists of about 306 stations, 140 of which provide measurements for periods from 50 to 100 years and 45 for more than 100 years starting from the mid 19th century onwards. The data set has a quite inhomogeneous spatial coverage with the highest station density in Central Europe and a considerable drop of the number of observational sites in Southeastern and Eastern Europe. The precision of the most of rain gauges is 0.1 mm, and thus, daily precipitation from the rain gauge observations is reported with the accuracy of 0.1 mm. In order to provide comparability we set all daily precipitation sums smaller than 0.1 mm to zeros in the reanalyses time series. This resulted in the drop in the number of wet days by 5 to 30%. The largest differences are observed in NCEP1 and ERA15 in the Central and Eastern Europe. This ad-hoc correction changing estimates of the number of wet days and precipitation intensity, has a smaller impact on the mean precipitation values (from 1-3% for most locations).

3. STRATEGY AND METHODS

In order to quantify the characteristics of extreme precipitation we use the parameters of the Gamma-distribution of daily precipitation. The effectiveness of this distribution for the analysis of daily precipitation

Corresponding author's address: Olga Zolina, Meteorologisches Institut, Universitaet Bonn, Bonn, auf dem Huegel 20, 53121 Germany; E-Mail: olga.zolina@uni-bonn.de.

was demonstrated for both model and observational data by many authors (e.g. Groismann et al. 1999, Katz 1999, Semenov and Bengtsson 2002, Watterson and Dix 2003). The Gamma-distribution PDF is characterized by the two basic parameters, namely shape factor and scale factor. The shape parameter α is non-dimensional and determines the skewness of the Gamma PDF, shifting it to the left with small α values and to the right with high α values. The scale parameter β, which has the dimension of variable analysed, steers stretch and squeeze of the PDF.

Our strategy was to compute statistical characteristics (e.g. the parameters of Gamma distribution) and to analyse their climatological values and variability in the four reanalyses for the common period of overlap (1979-1993). Some comparisons were, nevertheless performed for a longer period (1958-2001) for NCEP1 and ERA40 reanalyses. Analysis of interannual variability was based on the estimation of linear trends in the statistical parameters and the leading empirical orthogonal functions (EOFs) for the shape parameter, scale parameter and percentiles of the Gamma-distribution.

4. RESULTS OVERVIEW

4.1 Statistical characteristics of heavy and extreme precipitation in different NWP products

Despite a general qualitative similarity of spatial patterns of the shape, quantitative differences between different products are strong. Among all four reanalyses ERA40 shows on average the highest shape parameter (largest probability of heavy rainfall) and ERA15 demonstrates the smallest shape factor, implying the smallest occurrence of precipitation extremes.

Comparisons of the scale parameter show that in general it closely follows the pattern of the precipitation intensity, implying pattern correlation of 0.83-0.95 with a maximum for ERA40 in summer and minimum for NCEP products in winter. Among the four reanalyses the highest scale parameter is observed in NCEP2 for both winter and summer and the smallest values of scale parameter are diagnosed by ERA40.

The occurrence of extreme precipitation depends on both scale and shape parameter. In order to assess the differences in the extreme precipitation diagnosed by the different products we estimated the precipitation values corresponding to 99% percentile of Gamma CDF. In Figure 1 we show spatial distribution of the precipitation corresponding to 99% percentile in ERA40 and NCEP2 for winter (Figures 1a,b) and summer (Figures 1c,d). In general they follow to the spatial distribution of mean precipitation, but exhibit a much larger range, varying from 5 to 25 mm/day in winter and growing up to 40 mm/day in NCEP2 in summer. NCEP gives slightly higher values than ERA in the winter season and much higher values during summer in accordance with generally higher mean precipitation in NCEP products. In winter ERA15 shows smaller 99% values than ERA40 over most of the eastern and southern European regions. At the same time, in Northwestern Europe the 99% percentile precipitation values are smaller in ERA40. In summer precipitation values for 99% percentile in ERA15 are almost everywhere higher in comparison to ERA40 with the largest differences observed over Scandinavia and in the Southern Europe. NCEP2 shows primarily higher than NCEP1 precipitation values for 99% percentile during both winter and summer with the highest difference of 10-15 mm/day during summer in the Southern Europe.

4.2 Interannual variability of statistical characteristics of European precipitation

We characterized secular changes in statistical characteristics of daily precipitation over Europe by the linear trends of the shape and scale parameters. Linear trends were computed for the common 43-year period (1958-2000) of ERA40 and NCEP1. In winter both products show significantly positive trends in the shape parameter over Western Scandinavia and Central and Southern Russia and significantly negative trends in Southwestern Europe (with however, stronger magnitude for NCEP1) for α. Trends of the opposite sign are locally observed in the Northeastern European Russia. Summer differences in the linear trend patterns are very pronounced in the Central and Southern Europe. ERA40 diagnoses continuous pattern of positive trends, while NCEP1 shows negative trends, implying a decrease of the probability of extreme precipitation in this product. Winter trend patterns in the scale parameter are quite consistent in both reanalyses, showing a north-south dipole trend pattern with the positive trends over the Northern Europe and primarily negative trends in the Central and Southern Europe. However, in summer strong differences in the trend estimates are observed over the Southern Europe, where ERA40 shows strong negative trends and NCEP1 diagnoses increasing β. Disagreement is also observed over Scandinavia, where trends are weakly positive in ERA40 and strongly negative in NCEP1. Large differences occur over the Alpine region (strongly negative trends in ERA and significant positive trends in NCEP).

Analysis of the correlations between the de-trended anomalies of the shape and scale parameters derived from the NCEP1 and ERA40 shows that during winter correlation for the shape parameter is higher than 0.5 in Northwestern Europe, along the main storm track area in the Eastern Europe, decreasing in the Northeastern and Southern Europe. In summer we observe a much lower level of correlation everywhere, first of all in Central and Southern Europe. For the scale parameter in winter a continuous pattern of very high correlation (above 0.7) is observed over the most European regions, except for the Mediterranean coast. In summer, correlation higher than 0.5 is only observed in Scandinavia, British Islands and Northeastern Europe.

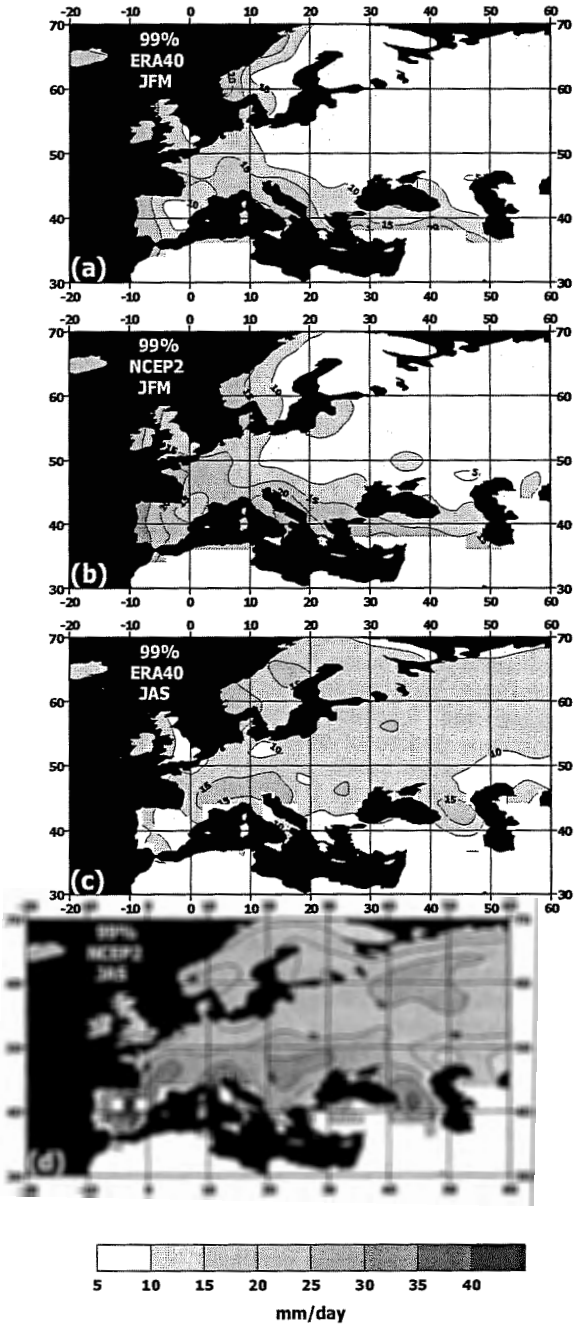

Figure 1. Precipitation values corresponding to 99% percentile (mm/day) in ERA40 (a, c) and NCEP2 (b, d) for winter (a, b) and summer (c, d).

We computed correlations between the NAO index and scale and shape parameters for the four data sets. We used for this purpose the NAO index based on Reykjavik and Ponta Delgada (Hurrell 1995) to keep it independent on reanalyses. Different reanalyses show qualitatively very comparable projections of the NAO onto the heavy precipitation characteristics. Figure 2 shows associated correlations for the winter season derived for the period 1979-1993 from ERA40 reanlayses data, which indicate the highest correlation level. Associated correlation pattern for the shape parameter is represented by a Northeast-Southwest dipole, which is very robust in all four reanalyses. NCEP2 shows correlation values which are very close to those diagnosed by ERA40. ERA15 and NCEP1 show 5 to 10% weaker correlation in comparison to ERA40. The NAO correlation with the scale parameter is also qualitatively consistent between the data sets, showing Northwest-Southeast dipole-like patterns with positive correlations in the Northern Europe and negative correlations in the Southern and Eastern Europe.

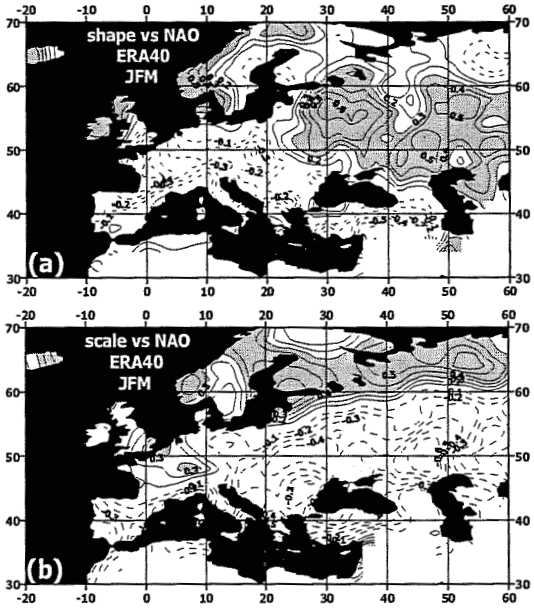

Figure 2. Associated correlation for the winter season between the NAO index and shape parameter (a) as well as between the NAO index and scale parameter (b) for the period 1979-1993, derived from ERA40 reanalysis. Areas of significant correlation are shaded.

4.3 Regional comparison with the station data

Comparison of precipitation statistics from reanlayses with observations is largely influenced by spatial inhomogeneity of station data and local impacts of mesoscale processes. This effect affects both comparisons of means and interannual variability patterns, especially in summer. Nevertheless, to the extent that it is possible to make comparative assessment using these very different data sources (NWP and stations), we can draw the conclusion that characteristics of extreme precipitation over Europe in NCEP products (especially NCEP2) are closer to the

stations data, than those of ECMWF products. However, this conclusion should be considered with caution and does not mean that precipitation in NCEP products is superior with respect to ERA in all other respects, such as global hydrological cycle characteristics, precipitation over oceans and others.

We analysed correlation between the de-trended anomalies of the shape and scale parameters, derived from the station data and ERA40 reanalysis. Anomalies of the scale parameter are considerably stronger correlated in the station data and in reanalyses, than the anomalies of the shape parameter. Winter correlation between the station data and reanalysis is 20 to 30% higher than that observed in summer. For the shape parameter correlation exceeds 0.5 in 32% of points in winter and in only 14% of locations in summer. At the same time for the scale parameter in winter 62% of points show the correlation higher than 0.5 and about 26% of points indicate correlation higher than 0.7. During summer for the scale parameter correlation higher than 0.5 is observed in 32% of locations and correlation higher than 0.7 is identified in less than 15% of points. This is in agreement with the strong impact of regional mesoscale variability on interannual variability during summer, mentioned above. The largest correlation during both seasons is observed over the Northeastern and Eastern Europe and the smallest in the Southern Europe and mountain regions, where the impact of spatial inhomogeneity considerably increases.

5. SUMMARY AND FUTURE WORK

We analysed statistical characteristics of European precipitation on the basis of four reanalyses data sets, widely used in climate studies and found remarkable differences in the shape and scale parameters of Gamma-distribution of daily precipitation, as well as extreme precipitation values. In general, NCEP products show higher values of extreme precipitation than ECMWF products. NCEP2 shows the highest estimates of precipitation extremes and ERA15 gives the smallest ones. The estimation of extremes in terms of long-term return values or return periods (e.g. Hennessy et al. 1997) will result in higher precipitation extremes, especially in summer, in NCEP products in comparison to ERA products and in NCEP2 compared to NCEP1. The diagnosed differences in the characteristics of gamma-distribution (shape and scale parameters) and extreme precipitation values between different NWP products may vary within 30-40% on average. This is larger than the differences in these characteristics simulated by climate models in greenhouse gas experiments (Hennessy et al. 1997, Semenov and Bengtsson 2002), which report normally the largest changes between the greenhouse gas experiments and the present climate to be within 10 to 20%. Thus, one has to be careful when choosing reanalysis data set for the description of what we term the present climate.

Further validation efforts should be focused on the detailed comparison of statistical characteristics of precipitation from reanalyses with station data. This comparison should involve analysis of mesoscale spatial variability and its impact on estimates of statistical characteristics (Osborn and Hulme 1997). Nevertheless, our comparison implies considerable underestimation of the heavy and extreme rainfalls in reanalyses products. Since the difference between statistical characteristics derived from the station data and from reanalyses is of the same order of magnitude or higher than the variations between different reanalyses, we can conclude that these deviations represent a robust signature. At the same time, temporal variations of the occurrence of extremes can be quite effectively diagnosed by reanalyses, at least in comparison to the moderate precipitation.

6. REFERENCES

Groismann, P.Y., and multi 1999: Changes in the probability of heavy precipitation:important indicators of climatic change. Clim. Change, **42**, 243-285.

Hennessy, K.J., J.M.Gregory and J.F.B. Mitchell, 1997: Chnages in daily precipitation under enhanced greenhouse conditions. Clim. Dyn., **13**, 667-680.

Hurrell, J.W., 1995: Decadal trends in the North Atlantic Oscillation: Regional temperatures and precipitation. Science, **269**, 676-679.

Katz, R.W., 1999: Extreme value theory for precipitation: sensitivity analysis for climate change. Adv. Water Resour., **23**, 133-139.

Osborn, T.J., and M.Hulme, 1997: Development of a relationship between station and grid-box rainday frequencies for climate model evaluation. J. Climate, **10**, 1885-1908.

Semenov, V.A. and L. Bengtsson, 2002: Secular trends in daily precipitation characteristics: greenhouse gas simulation with a coupled AOGCM. Clim. Dyn., **19**, 123-140.

Watterson, I.G. and M.R. Dix, 2003: Simulated changes due to global warming in daily precipitation means and extremes and their interpretation using the gamma distribution. J. Geophys. Res., **108**, 4379, doi:10.1029/2002JD002928.

7. ACKNOLEDGENEMENTS

This study is supported by the North Rhine-Westphalia Academy of Science under the project "Large Scale Climate Changes and their Environmental Relevance". We also benefited form the support of Russian Foundation for Basic Research (grant 02-56331).

INFLUENCE OF CLOUDINESS AND AEROSOL POLLUTION TRENDS ON THE TOTAL SOLAR RADIATION IN SOME NON INDUSTRIAL REGIONS OF GEORGIA

A.G. Amiranashvili[1], V.A. Amiranashvili[1] , K.A. Tavartkiladze[2]

[1]Institute of Geophysics of Georgian Academy of Sciences, Tbilisi, 0193, Georgia
[2]Institute of Geography of Georgian Academy of Sciences, Tbilisi, 0193, Georgia

1.INTRODUCTION

Earlier works presented the results of the investigations of the aerosol pollution and cloudiness effects on the radiation fluxes in Tbilisi, Amiranashvili et al., (2000a). In Amiranashvili et al.,(2000b) presented the results of the investigations of the spatial-temporary variations of total and lower layer cloudiness over the Georgian territory.

This work presents the results of the investigation of the aerosol pollution and cloudiness effects on the radiation fluxes in 5 non industrial regions of Georgia (Telavi, Tsalka, Anaseuli, Senaki, Sokhumi). The following parameters were considered: annual sums of direct (S), diffuse (D), total (Q) radiation, annual sums of long-wave radiation balance (Bg) and radiation balance (B), mean annual values of the aerosol optical depth of the atmosphere (τ_a), total (G) and lower (g) cloudiness. The data for 1954-1990 were analyzed. Unfortunately after 1990 data of actinometric observation are unreliable.

2. METHODS

The values of the aerosol optical depth of the atmosphere τ_a were determined using the data of actinometric observations on the direct incident solar radiation irradiance and the method Tavartkiladze (1989). In this paper the value of τ_a are presented for the wavelength $\lambda = 1$ mcm.

Corresponding author's address:
Avtandil Amiranashvili, Geophysics Institute of Georgian Academy of Sciences, 1., M.Aleksidze Str., Tbilisi 0193, Georgia;

E-mail:Avto_Amiranashvili@excite.com/
Avto_Amiranashvili@hotmail.com

Cloudiness (G and g) was determined visually at the meteorological stations using the standard methodology , Amiranashvili et al.,(2000b)

Actinometric observations of radiation fluxes were carried out according to the standard methodology , Tavartkiladze (1989).

3. RESULTS

The statistical characteristics of specified above parameters are presented in Table 1. Correlations among the investigated parameters (the minimum significant value of a correlation with the confidence level 95% amounts to ± 0.28) are presented in Table 2.

For the estimation of the effect of the aerosol optical depth of the atmosphere and total and lower cloudiness on radiation fluxes multiple regression equation were used. For example, for total radiation this equations have the following forms:

Telavi: $Q = -10652.5\,\tau_a - 464\,G + 55.9\,g + 8884.6$ MJ/m² (Multiple correlation coefficient is 0.9); Tsalka: $Q = -5367.4\,\tau_a - 97.8\,G - 180.8\,g + 6809.9$ MJ/m² (Multiple correlation coefficient is 0.4); Anaseuli: $Q = -9409.8\,\tau_a - 479.4\,G + 65.6\,g + 8213.9$ MJ/m² (Multiple correlation coefficient is 0.7); Senaki: $Q = -7913.7\,\tau_a - 44.7\,G - 395.8\,g + 7377.2$ MJ/m² (Multiple correlation coefficient is 0.67); Sokhumi: $Q = -12792.7\,\tau_a - 592.7\,G + 114\,g + 8774.5$ MJ/m² (Multiple correlation coefficient is 0.83).

In the variations of Q the shares of the τ_a , G and g respectively are: Telavi (25, 11 and 2 %), Tsalka (7, 2 and 7 %), Anaseuli (27, 15 and 4.5 %), Senaki (17, 1 and 11 %), Sokhumi (20, 12 and 5 %).

Table 1

Statistical characteristics of the investigated parameters in fife non industrial regions of Georgia in 1954-1990

Parame-ter	τ_a	MJ/m² per year					Amount	
		S	D	Q	Bg	B	G	g
Station	Telavi (41.9. N.L., 45.5 E.L., 568 m)							
Min	0.061	3571	1813	4229	-1842	1779	5.47	3.22
Max	0.176	5652	2516	5862	-1256	2885	6.65	4.83
Mean	0.107	4561	2176	4986	-1536	2295	6.01	4.02
Std. dev	0.036	551	160	428	134	242	0.31	0.409
Station	Tsalka (41.6 N.L., 44.1 E.L.,1457 m)							
Min	0.043	3647	2014	4354	-1758	1805	5.6	3.18
Max	0.113	5778	2868	5820	-1256	3190	6.78	5.07
Mean	0.067	4602	2347	5077	-1504	2237	6.2	4.24
Std. dev	0.0177	472	205	271	121	285	0.281	0.406
Station	Anaseuli (41.9 N.L., 42 E.L., 158 m)							
Min	0.054	2303	950	2734	-1884	1377	6.43	2.98
Max	0.177	5108	2441	5234	-670	2483	7.78	5.97
Mean	0.09	3913	1971	4311	-1231	2112	7.03	4.75
Std. dev	0.03	567	284	510	239	257	0.332	0.79
Station	Senaki (42.3 N.L., 42.1 E.L., 40 m)							
Min	0.057	2901	1160	3069	-1507	1499	5.63	2.37
Max	0.158	5401	2361	5443	-921	2876	6.93	4.93
Mean	0.087	4189	1832	4364	-1219	2179	6.25	3.54
Std. dev	0.027	724	299	547	166	309	0.294	0.659
Station	Sokhumi (43 N.L., 41 E.L.,116 m)							
Min	0.057	3458	1796	4312	-1717	2131	5.88	3.08
Max	0.163	5443	2491	5610	-1089	2943	7.02	4.4
Mean	0.092	4486	2185	4912	-1394	2424	6.53	3.66
Std. dev	0.0256	465	160	285	194	175	0.254	0.338

Table 2

Correlations among the investigated parameters (the minimum significant value of a correlation with the confidence level 95% amounts to ± 0.28)

Par.	Telavi			Tsalka			Anaseuli			Senaki			Sokhumi		
	τ_a	G	g	τ_a	G	g	τ_a	G	g	τ_a	G	g	τ_a	G	g
S	-.78	-.25	.06	-.40	-.52	-.08	-.60	-.60	-.12	-.77	-.60	.07	-.70	-.28	-.02
D	-.55	.05	.13	.13	.28	-.11	-.48	-.23	-.28	-.28	.05	.50	.38	.13	-.27
Q	-.85	-.09	.17	-.26	-.29	-.14	-.65	-.48	-.21	-.79	-.48	.28	-.50	-.13	-.18
Bg	.30	.37	.33	-.12	.48	.44	.39	.28	.08	.55	.26	-.30	.63	.22	.06
B	-.74	.04	.38	-.41	-.17	.13	-.66	-.55	-.28	-.74	-.52	.16	.09	.07	-.11

4. REFERENCES

Amiranashvili, A.G., Amiranashvili V.A., Khurodze T.V., Tavartkiladze K.A., 2000a: Influence of Cloudiness trends on the Total Solar Radiation in Tbilisi, Proc. 13th Int. Conf. on Clouds and Precipitation, Reno, Nevada, USA,14-18, August2000, vol.2,876-877.

Amiranashvili, A.G. Amiranashvili V.A., Gzirishvili T.G., Kolesnikov Yu.M., Tavartkiladze K.A., 2000b: Spatial-Temporary Variations of Total and Lower Layer Cloudiness over the Georgian Territory, Proc. 13th Int. Conf. on Clouds and Precipitation, Reno, Nevada, USA, 14-18 August 2000, vol. 2, 1159 - 1161.

Tavartkiladze, K.A., 1989: Modelling of the Aerosol Attenuation of Radiation and Atmospheric Pollution Control Nethods, Tbilisi, Metsniereba, 1-204, (in Russian).

AMELIORATION OF GLOBAL WARMING BY CONTROLLED ENHANCEMENT OF THE ALBEDO AND LONGEVITY OF LOW-LEVEL MARITIME CLOUDS

Keith Bower[1], Tom Choularton[1], John Latham[1,2] & Jalil Sahraei[1]

[1]Physics Department, UMIST, Manchester, UK
[2]MMM Division, NCAR*, Boulder, Colorado, USA

1. INTRODUCTION

Herein we describe research to submit to a more rigorous examination than hitherto the technique proposed by Latham (1990, 2002) for controlled enhancement of droplet concentrations in low-level maritime clouds, with corresponding increase in their albedo and longevity: thereby producing a cooling effect. Such clouds cover about one-third of the earth's oceanic surface. The technique involves dissemination at or close to the ocean surface of small seawater droplets which act as cloud condensation nuclei (CCN). Its central physics, which formed the basis of a number of studies (e.g. Twomey 1977; Charlson et al. 1987; Wigley 1989; Slingo 1990), is that an increase in droplet concentration N causes the cloud albedo to increase because the overall droplet surface area is enhanced; and can increase cloud longevity (tantamount to increasing cloudiness) because the growth of cloud droplets by coalescence to form drizzle or raindrops - which often initiates cloud dissipation - is slowed down since the droplets are smaller. In some circumstances, increasing N suppresses the production of rain. Calculations by above-mentioned workers indicate that a doubling of N in marine stratocumulus clouds, on a global basis, would be sufficient to produce a cooling which would more than compensate for the warming associated with doubling the carbon dioxide concentration. The associated change in top-of-cloud albedo is about 0.02. Also, there may be further cooling resulting from increased cloud cover. Advertent generation of sea-salt CCN at the ocean surface, thereby enhancing N, is basically a more efficient version of a process that happens naturally.

2. PRELIMINARY QUANTITATIVE CONSIDERATIONS

In the lower atmosphere there is an ample supply of natural CCN, in the sense that sufficient concentrations exist (at temperatures where condensation occurs in preference to ice nucleation) to initiate cloud formation when the relative humidity H achieves a value of about 100%. The advertent introduction of further, especially effective CCN – of characteristics selected to ensure that they are activated at significantly lower supersaturations S than the great majority of the naturally occurring ones - can, however, increase (or decrease) the droplet concentration N with a corresponding enhancement (or reduction) in cloud albedo. The number concentration of droplets in clouds over the oceans is characteristically 50-200 $cm.^{-3}$

Latham (2002) performed simplistic calculations in order to consider the requirements of a droplet production and dissemination technique which yields a value of N=400 $cm.^{-3}$. He assumed that the CCN particles advertently introduced into the atmosphere are seawater droplets containing a mass m of NaCl, and that they become distributed uniformly in concentrations N = 400 cm^{-3} over the entire area of the Earth to an altitude of 500m. If $m=10^{-14}g$ (dry radius r_d = 0.13μm) – corresponding to sea-salt droplets which would be activated at lower supersaturations than aerosol consisting of ammonium sulphate particles formed from dimethylsulphide produced at the ocean surface by planktonic algae, which are believed (e.g. Charlson et al. 1987) to be the dominant CCN over the oceans - we deduce that M = 2 $kg.km^{-2}$, which corresponds to 2.10^{17} km^{-2} seawater particles. Globally, the total mass of artificially introduced NaCl present in the atmosphere is 10^9 kg, and the corresponding number of droplets is 10^{26}. Latham calculated that to maintain the stipulated value of N, droplets need to be disseminated into the atmosphere at rates of about 6.10^{23} hr^{-1} (globally) or 10^{15} $hr.^{-1}$ $km.^{-2}$. Since the salinity of seawater is about 35 g/kg, the corresponding rates of dissemination of seawater (in the form of droplets of radius 0.4um containing a mass $m=10^{-14}g$ of NaCl) are 2.10^8 $kg.hr^{-1}$ (globally) or 0.3 $kg.hr.^{-1}$ $km.^{-2}$, which appears technologically feasible.

Wigley (private communication) incorporated the advertently produced changes in N into his 10-year climate model and concluded that they are equivalent to a cooling of about –3 W/m^{-2}, which is adequate to compensate for warming associated with a doubling of atmospheric CO2 concentration.

3. SENSITIVITY OF COMPUTED ALBEDO CHANGES TO CLOUD AND METEOROLOGICAL PARAMETERS

In this section we present more comprehensive and rigorous calculations designed to provide estimates of albedo-change (increase) δA resulting from the inoculation of shallow maritime clouds with sea-water droplets of number concentration N, for a wide range of values of salt-mass m, cloud-base temperature T, cloud thickness Z and updraught

Corresponding author's address: John Latham, National Center for Atmospheric Research, Boulder, CO, 80307; E-mail: latham@ucar.edu.
*NCAR is sponsored by the National Science Foundation

speed U. The changes in Albedo are calculated from the droplet number concentrations using the method described by Schwartz and Slingo (1996).

The CCN activity spectrum of the natural cloud, which we assume, in our calculations, to have been advertently inoculated with seawater aerosol, is a typical one measured in the ACE-2 experiment. The aerosol spectrum was characteristic of relatively clean air over the subtropical North Atlantic, the air being free of anthropogenic influence from Europe. It was measured at Punta del Hidalgo on the North coast of Tenerife. The number concentration of sea-salt CCN advertently added, ΔN, was varied from 0 to 1000 cm^{-3}, T from 10 to 25C, Z from 110 to 210m, U from 0.05 to 1.0 m/s, and salt-mass m from 10^{-12}g to 10^{-15}g. As illustrated in Table 1, in addition to values of δA, computations were also made of the droplet number concentration N in the adulterated cloud and the maximum supersaturation S(%) achieved in the adulterated cloud which, in these first results, was not assumed to be diluted by entrainment of environmental air.

	$m = 10^{-15}$g				$m = 10^{-12}$g			
	ΔN cm^{-3}				ΔN cm^{-3}			
	0	100	300	1000	0	100	300	1000
N (cm^{-3})	206	305	502	1190	206	280	458	1090
10S (%)	7.4	7.3	7.3	7.2	7.4	5.7	3.9	1.8
100 A	0	3.0	6.7	13.2	0	2.3	6.7	12.6

Table 1. Calculated values of total droplet number concentration N, maximum supersaturation S and albedo-increase δA, for specified values of salt-mass m and additional droplet concentration ΔN. T = 15C, Z = 110m, U = 1 m/s.

We see from these calculations that for all cases considered, in which the number concentration of CCN advertently introduced into the cloud has non-zero values, the albedo-increase exceeded 0.02, the value calculated by Charlson et al. (1987) as being required in order to produce a cooling sufficient to compensate for the warming associated with a doubling of the atmospheric CO2 concentration.

The calculated values of δA and N and are seen to be insensitive to salt-mass m over the four orders of magnitude considered. δA and N were found also to be insensitive to updraught speed U and cloud-depth Z. Some subtle dependencies of δA and N on m, U and Z were found (not discussed herein), which were not, however, of quantitative significance. δA and ΔN were found to increase slowly with cloud-base temperature T and very rapidly - as shown in Table 1 – with additional droplet concentration ΔN.

4. TECHNOLOGICAL CONSEQUENCES EMANATING FROM THE CALCULATIONS

The calculations presented in the preceding section demonstrate that the calculated albedo-changes are highly insensitive to the values of salt-mass m – and therefore seawater droplet-size. It follows that the choice of droplet size can therefore, to a considerable extent, be dictated by technological convenience. It follows also that, in terms of influencing values of albedo-change δA, there is no advantage to striving for monodispersity of the droplet spectrum: though we note that monodispersity is likely to enhance cloud stability and therefore longevity.

A further point is that since – as shown in Table 1 – values of δA can be achieved which are several times larger than the critical value of 0.02 (Charlson et al., 1987), the areal fraction of maritime stratocumulus clouds which needs to be adulterated in order to compensate for warming resulting from the burning of fossil fuels can be much lower than unity; therefore rendering less formidable the problem of achieving adequate lateral dispersal of advertently disseminated seawater CCN.

5. SOME ASPECTS REQUIRING FURTHER STUDY

We now outline various arguments and unresolved scientific questions which would need to be addressed before a definitive assessment of the idea considered herein can be made.

5.1 It was implicitly assumed in the foregoing calculations that all the particles disseminated at the ocean surface would be transported by turbulence to higher levels. This will clearly not be correct. Airborne measurements (Smith et al. 1993) together with estimates (Blanchard 1969) based on the reported global rate of creation of effective NaCl CCN at the ocean surface by bubble-bursting (10^{28} per year), both suggest that this loss factor - the fraction of the droplets created by bubble-bursting at the ocean surface that do not escape to higher levels - is not

greater than 0.9. If this is correct, the required mass dissemination rates reported previously need not be increased by more than a factor of ten; and thus remain modest. This issue requires more detailed attention.

5.2 Although recent work has enhanced our knowledge of the relationships between N and both precipitation development and cloud lifetime, further research is required in order to achieve an adequate quantitative understanding of these issues in relation to our specific goals. We also need further information as to the importance in precipitation development in maritime clouds - and therefore their longevity - of ultra-giant nuclei, UGN, particles of salt-water generated naturally at the ocean surface which, because they are large and contain NaCl, grow rapidly by collision and coalescence to form drizzle drops if they enter maritime clouds. The importance of these particles in rainfall initiation is in dispute. The influence of UGN on cloud albedo is unlikely to be significant.

5.3 Attention has been devoted to the question of whether naturally occurring sea-spray droplets make a significant contribution to the exchange of heat and water vapour between the oceans and the air. The conclusion from this work is that though the contribution may be significant in highly localised regions, such as in the vicinity of storms, it is secondary or negligible on a global basis. The seawater mass dissemination rates calculated herein correspond to heat and vapour fluxes much less than those naturally occurring, which are thus negligible in terms of the overall fluxes between ocean and air.

5.4 Clouds other than the low-level maritime ones central to our idea may be influenced by an advertent increase in the concentration of CCN. An undesirable feature of this possible effect is that we have little information regarding the overall radiative impact of changing the droplet concentrations in higher-level, often deeper clouds which are likely to contain significant quantities of ice. A reduction of the impact of advertently introduced CCN on other cloud types can be achieved by restricting dissemination to regions where low-level maritime clouds form, rather than employing it globally, as assumed in our simplistic calculations.

5.5 If the proposed technique was ever implemented on a global scale, changes in the Earth's temperature distribution would result. Consequently it would be vital to engage in a prior assessment of the associated climatological and meteorological implications, which might involve currently unforeseen feedback processes. Major problems of model formulation and testing would need to be addressed. Also, we would be attempting to neutralise the warming effect of vertically distributed greenhouse gases with a surface-based cooling effect, which could have consequences such as changes in static stability which would need careful evaluation. Possible changes in wind patterns and local visibility are among other issues that would need to be addressed.

5.6 It will be necessary to determine quantitatively - for all situations of significance - the factors influencing lateral dispersal of the droplets during their ascent from ocean surface to cloud base. This will dictate the number density of disseminators required. The environmental impact of the deployment of these devices on a global scale would have to be addressed. The possibility of utilising electrostatic forces to enhance the dispersal should be examined.

6. TECHNOLOGICAL CONSIDERATIONS

Latham (1990, 2002) envisaged two possible methods of creating and disseminating seawater droplets at the ocean surface, for which the required electrical power could in principle be provided by wave motion or sunlight. In both cases it was assumed that seawater droplets would be produced from a large number of disseminators, globally distributed over oceanic regions over which low-level clouds are prone to form, rather than from a small number of large-output devices.

The first method is atomisation. A virtue of this technique is that the droplet sizes could be controlled and the size distribution arranged to be essentially monodisperse, which would be advantageous from the point of view of delaying precipitation formation and thus increasing cloud longevity. Atomisers which can produce the required seawater particle sizes and dissemination rates are already commercially available. An alternative technique would be to create air bubbles below the ocean surface - perhaps by forcing air through porous pipes - whereupon they would rise to the surface and burst - just as happens in nature, with large numbers of seawater droplets ejected. A substantial proportion of the saltwater droplets so produced will be within the size (and associated salt-mass) range required to be effective as CCN in clouds. The airflow rates required for a level of bubble production sufficient to yield the necessary concentrations of N appear readily achievable. This technique suffers from two disadvantages arising from the fact that significant concentrations of UGN may be produced, which could facilitate rain formation and decrease the longevity of the clouds.

If this proposed technique were at some stage to be deployed operationally - i.e. on a global basis - it may prove viable to mount the droplet disseminators on floating rafts or derricks. The power required to operate them would be modest - of the order of watts - so it should be readily possible to provide it from sunlight or wave motion.

An alternative, and probably more promising technique of droplet dissemination involves spray turbines, as described by Salter (2002). A single spray turbine can atomise seawater at a rate of about 1 m^3/s, which means that very few would be required globally in order to disseminate droplets at the

required rate. However, problems of producing the optimal droplet sizes remain to be resolved.

Whichever dissemination technique is employed, satellite measurements of albedo and cloudiness could be fed back into a computer model to define adjustments to be made swiftly and remotely to dissemination rates, in order to produce the required cooling effect.

7. DISCUSSION AND CONCLUSIONS

No justification would exist for employing the large-scale installations described in the preceding section unless we have: (a), examined fully the scientific problems raised in Points 1 to 6 above (plus others); (b), resolved all salient technological questions regarding droplet dissemination and dispersal; (c), made much more detailed and rigorous calculations related to all aspects of the proposed technique. This would require the utilization of a full cloud/climate model with the microphysics treated explicitly. If this work justifies continuance, the next stage should probably be to perform a limited-area field experiment in which seawater CCN are introduced in a controlled manner into maritime stratocumulus, microphysical measurements are made below and within the clouds, and above-cloud radiative and cloudiness data are obtained.

Latham (2002) argued that it may be possible to harness the Earth's electric field to facilitate the transportation of NaCl droplets from the ocean surface to cloud base. This idea should be examined further.

We conclude by pointing out an ecologically attractive feature of this possible technique for amelioration of global warming. The only raw material required for this proposed technique is seawater, which will largely fall back into the oceans.

ACKNOWLEDGEMENTS

The authors are grateful to Dr Tom Wigley of NCAR for performing computations with his 10-year climate model, as described herein. Part of this work was performed while JL was in receipt of a Tyndall Visiting Fellowship.

REFERENCES

Blanchard, D.C., 1969: The oceanic production rate of cloud nuclei. *J. Rech. Atmos.* **4**, 1-11.

Charlson, R.J., J.E. Lovelock, M.O.Andreae, and S.G.Warren, 1987: Oceanic phytoplankton, atmospheric sulphur, cloud albedo and climate. *Nature* **326**, 655-661.

Latham, J., 1990: Control of global warming? Nature 347. 339-340.

Latham, J., 2002: Amelioration of Global Warming by Controlled Enhancement of the Albedo and Longevity of Low-Level Maritime Clouds. *Atmos. Sci. Letters.* (doi:10.1006/Asle.2002.0048).

Salter, S., 2002: Spray turbines to increase rain by enhanced evaporation from the sea. *Tenth Conf. Of Int'l Maritime Assoc. of the Mediterranean*, Crete.

Schwartz, S.E. & Slingo, A. (1996) in *Clouds, Chemistry and Climate-Proceedings of NATO Advanced Research Workshop*, eds. Crutzen, P. & Ramanathan, V. (Springer, Heidelberg), pp. 191-236.

Slingo,A., 1990: Sensitivity of the Earth's radiation budget to changes in low clouds. *Nature*, **343**, 49-51.

Smith, M.H., P.M. Park, and I.E. Consterdine, 1993: Marine aerosol concentrations and estimated fluxes over the sea. *Q. J. R. Met. Soc.* **119**, 809-824.

Twomey, S., 1977: Influence of pollution on the short-wave albedo of clouds. *J. Atmos. Sci.*, **34**, 1149-1152.

Wigley, T.M.L., 1989: Possible climate change due to SO2-derived cloud condensation nuclei. *Nature*, **339**, 365-367.

THE MICROSCALE STRUCTURE OF ENTRAINMENT-MIXING IN BOUNDARY LAYER CLOUDS

F. Burnet and J.-L. Brenguier

Météo-France/CNRS, CNRM/GAME, Toulouse, France

1. INTRODUCTION

For the numerical simulation of boundary layer clouds, a bulk parameterization of the microphysics (i.e. limited to the prognostic of the cloud and precipitating drops water mixing ratios) is generally sufficient. There are however key issues for which details on how the liquid water content (LWC) is distributed among droplets is crucial. The onset of precipitation is one of them, since coalescence is non-linearly dependent upon the maximum size cloud droplets can reach in the cloud layer. Radiative transfer is also a sensitive case. The cloud albedo is in fact determined by microphysical properties, namely the ratio of the total droplet surface to the total droplet volume, (Twomey, 1977), within the upper layer of the cloud. The CCN activation and entrainment-mixing processes at the cloud top however, that are responsible for the variability of the droplet spectrum, involve scales generally smaller than the model grid. It is therefore crucial to experimentally document this variability for the development of microphysical parameterizations.

2. THE DATA SET

The data analysed here were collected during the Dynamics and Chemistry of Marine Stratocumulus study held off the southern cost of California in July 2001 (DYCOMS-II, Stevens et al., 2003). Among other instruments, the research aircraft NCAR-C130 was equipped with the Fast-FSSP (Brenguier et al., 1998, Burnet and Brenguier, 2002) for measurements of the cloud droplet size distribution.

We focus in this paper on measurements collected during Flight 3, on July 12. The Sc sampled during this flight was unbroken, about 350 m thick, contained light drizzle, and was topped by a strong inversion in both liquid water potential temperature θ_l and total water mixing ratio q_t ($\Delta\theta_l = 9$ C and $\Delta q_t = 10$ g kg^{-1}). Figure 1 shows time series of 10 Hz measurements collected along the cloud top profiling circle of this flight, hereafter refered to as the porpoising section.

Corresponding author's address: Frédéric Burnet, Météo-France, CNRM/GMEI/MNPCA, 42 av. Coriolis, 31 057 Toulouse Cedex 01, France.
E-Mail: frederic.burnet@ meteo.fr

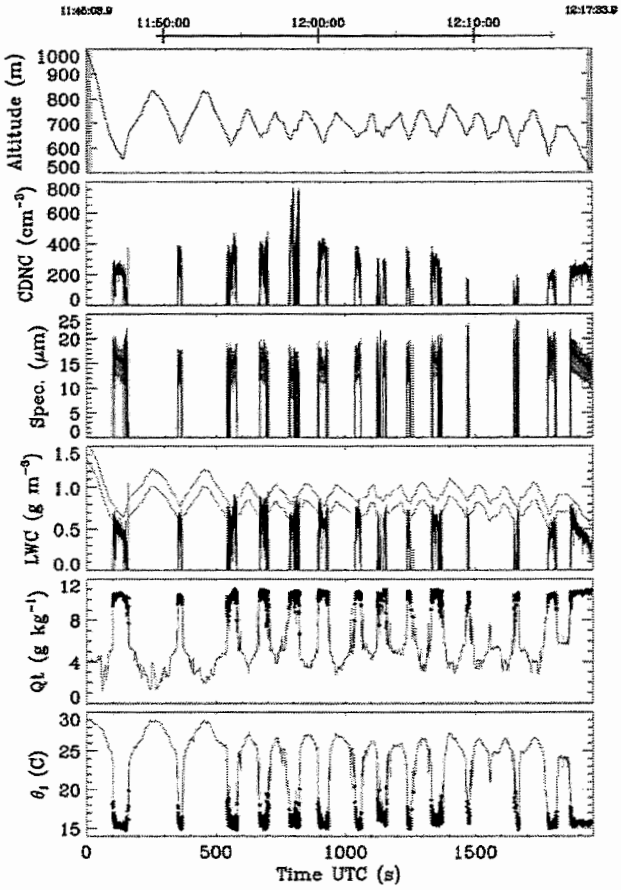

Fig. 1: Time series of the cloud top porpoising section of Flight 3, from top to bottom: aircraft altitude; droplet concentration; 10% percentiles of the droplet spectrum, with a thick line for MVD; LWC (black) and adiabatic LWC for a cloud base at 280 m and 370 m (grey); q_t ; and θ_l, with cloud samples marked by a thicker line.

3. DATA ANALYSIS

3.1 Thermodynamics

The effect of mixing on the droplet size distribution depends on the temperature and humidity properties of the entrained clear air. Figure 2 shows vertical

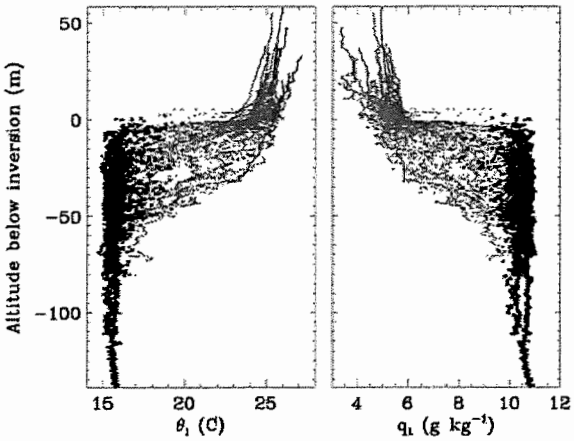

Fig. 2: Vertical profiles of θ_l (left) and q_t (right) for the 14 traverses of the porpoising section. The altitude is relative to the height of the inversion in each profile

profiles of θ_l and q_t for the 14 cloud top traverses of the porpoising section. In order to precisely estimate the thickness of the mixing layer, irrespective of possible large scale ondulations of the inversion level, the altitude scale of each profile has been translated with respect to a single reference altitude (the 0 coordinate on the Y axis), defined as the lowest altitude for which the variance of both θ_l and q_t is lower than 0.2. The frequency distribution of this reference altitude is plotted in the Figure 3.

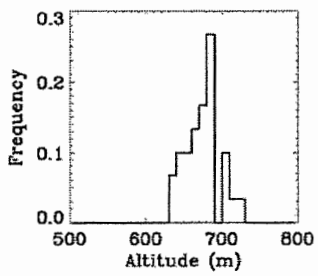

Fig. 3: Frequency distribution of the reference inversion level

Figure 2 reveals that mixing processes penetrate more than 70 m below the inversion, and that all kind of profiles can be observed from a very sharp transition of about 10 m thickness, to a smooth transition of 70 m. The θ_l / q_t diagram is represented in Figure 4, with the saturation curves at 935 and 950 hPa which are the pressure values at the top of the inversion and at cloud top, respectively. Frequency distributions of θ_l and q_t are plotted along the axis for the clear air samples (thick solid line) and the cloudy samples (filled in black).

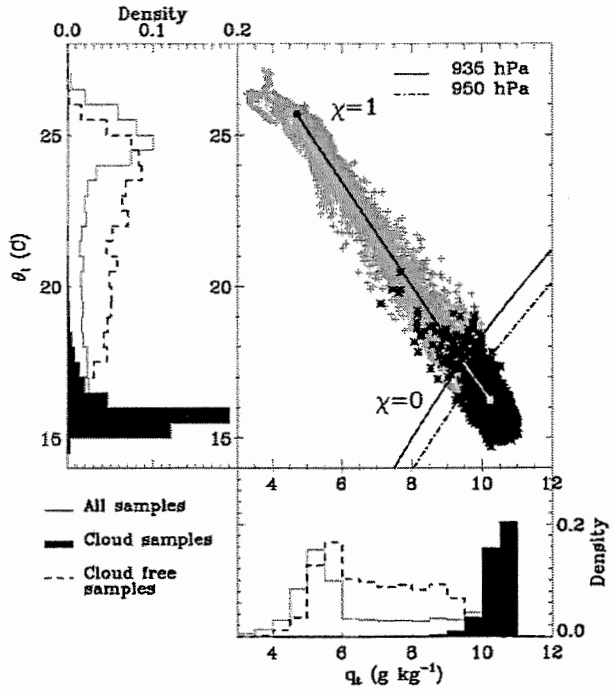

Fig. 4: Scatter plot of θ_l vs. q_t for the same data as in Fig. 2 with cloud samples in black. Saturation lines are shown for the cloud top altitude (P=950 hPa) and for the maximum height of the inversion level (P=935 hPa). Isobaric mixing between air from the free troposphere (T=20 C and U=30%) and cloudy air (T=12.25 C, LWC=0.7 g m^{-3}) is represented by the solid straight line. Frequency distributions of θ_l and q_t are shown along the two axis, for all samples, cloud and clear air samples separately

Most of the cloudy samples stay within the 935 hPa water saturation curve. Nevertheless, a few samples extend beyond the curve. It shall however be noted that our analysis is limited to 10 Hz samples, that is about 10 m horizontal resolution, while Gerber et al. (2002) have shown finer scale structures of the order of a meter. Condensed water beyond the saturation curve can thus be attributed to such fine scale heterogeneities.

The frequency distributions of both θ_l and q_t reveal that all possible mixing proportions of adiabatic (unmixed) cloudy air and clear air from the top of the inversion, have a similar frequency of occurence. These observations are consistent with a finite-thickness mixing layer in which clear air from the top of the inversion is progressively mixed with cloudy air. That also suggests that cloudy samples are not directly exposed to the warm and dry air from the top of the inversion, but rather to pre-moistened clear air. The impact on cloud microphysics is particularly sensitive to this feature.

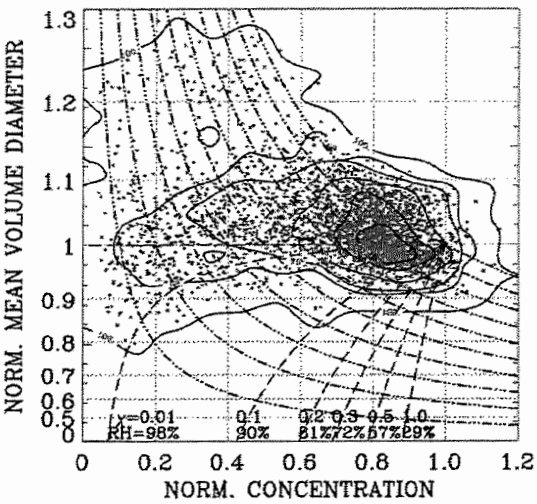

Fig. 5: Isocontours of the frequency distribution of the normalized MVD versus the normalized CDNC for cloud samples collected during the porpoising section. The dot-dashed lines are the isolines of LWC from 10% to 100% of the adiabatic value. The dashed lines represent the variation of MVD and CDNC during homogeneous mixing with entrained air taken along the 935 hPa mixing line of Figure 4 The proportion of cloudy air in the mixture is represented by the solid lines..

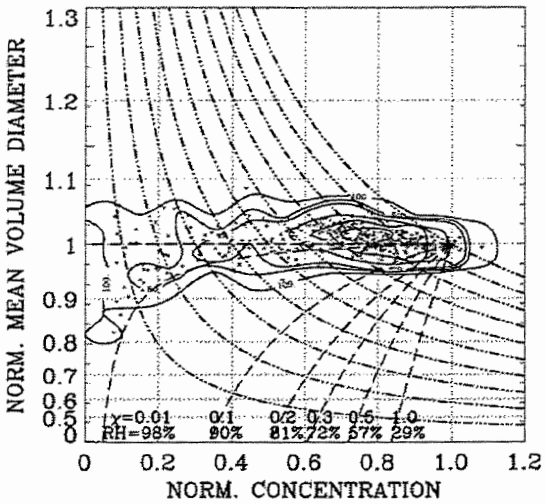

Fig. 6: Same as Figure 5 for the cloud samples collected during the 3rd zoom of the porposing section.

3.2 Microphysics

To examine the impact of the mixing processes on the droplet size distribution, we use the $\{N, \Phi^3\}$ diagram, that illustrates how a given LWC is distributed in terms of cloud droplet number concentration (CDNC) on the X axis, and mean volume diameter (MVD) on the Y axis. Both CDNC and MVD values are normalised to their adiabatic values (unmixed cloud volume), to account for the MVD increase with altitude. The dot-dashed-lines represent the ratio of the LWC values to the adiabatic value, from 100 % at the coordinate {1:1}, down to 10 %. The dashed lines correspond to different characteristics of the entrained air, that are taken along the isiobaric mixing line of Figure 4. Each one is labeled with its relative humidity *RH* and a scale varying from $\chi=0$ for pure cloudy air ($\theta_l = 10.5$ C and $q_t = 15.5$ g kg^{-1}), to $\chi=1$ for pure free tropospheric air ($\theta_l = 25.5$ C and $q_t = 5$ g kg^{-1}).

When cloudy air is mixed with clear air, CDNC decreases proportionnaly to the amount of entrained clear air. Therefore, the X axis scale for the normalised CDNC, also represents the proportion of cloudy air in the mixture, 1 for pure cloudy air, and 0 for entrained air only. The moister the entrained air, the lesser droplets are evaporated. If the entrained air is in fact just saturated, MVD remains constant. This tendency is illustrated by the χ isolines.

Microphysical data from the 14 cloud top profiles of Flight 3 are reported in Figure 5. Most of the diluted samples show MVD values comparable to the adiabatic one, with even a significant proportion of values greater than adaibatic. A possible explanation for such super-adiabatic values, is that the cloud base altitude (Z_o) or the adiabatic CDNC value at cloud base (N_o), that both determine the adiabatic MVD value at cloud top, are fluctuating. In fact previous circles with profiles through the whole cloud layer show that the cloud base altitude fluctuates between 280 and 370 m. CDNC also varies from 200 to 750 cm^{-3}. Since these CDNC variations are spatially coherent from one circle to the next one, they are likely to be due to large scale variations of the aerosol background and of the cloud condensation nuclei activation process rather than due to mixing processes. It follows that a unique set of N_o and Z_o values can not be selected as representative of the entire porpoising section.

N_o is therefore defined for each profile separately as the 98th percentile of the CDNC cumulative distribution. The same procedure is not applicable for Z_o because the profiles of the porpoising section do not reach the cloud base. A guess could be obtained by fitting the adiabatic LWC profile to the measured one. At this stage however, only variations of CDNC are accounted for in Figure 5. The expected increase of the adiabatic LWC, due to a lowering of the cloud base from 370 to 280 m is illustrated in the LWC panel of Figure 1. It is consistent with the 25 % Φ^3 increase with respect to the adiabatic that can be observed in Figure 5. Most of the profiles merged in Figure 5 do not show the same super adiabatic MVD values, when normalized separately, as shown in Figure 6 for one of them.

An interesting feature is the fact that most of the mixed cloudy samples are distributed along mixing lines corresponding to very low χ values, as if mixed cloudy samples were all resulting from the mixing of adiabatic cloudy air with free tropospheric air that has been pre-moistened by previous mixing events. This has been refered to by Baker et al. (1980) as heterogeneous mixing. When each profile is considered separately, even profiles corresponding to the sharpest transition in Figure 2, do not show the reduced MVD values that would reflect the mixing of adiabatic cloudy air with pure free-tropospheric air ($\chi = 1$).

4. SUMMARY

The analysis of a DYCOMS-II case study of non-precipitating stratocumulus, topped by a sharp inversion, reveals that entrainment-mixing penetrates the upper 70 m of the cloud layer. This mixing layer shows values of the liquid water potential temperature and total water mixing ratio that are linearly distributed between the adiabatic values at cloud top and the values characterizing the free troposphere. All possible mixtures show a similar frequency of occurence.

The examination of the CNDC versus MVD distributions in the cloudy samples exhibit features typical of heterogeneous mixing, that is a significant reduction of CDNC, while MVD remains almost unchanged. This feature is commonly attributed to a progressive mixing process during which the entrained air is pre-moistened by mixing events, until it becomes saturated, so that in the final step only CDNC is diluted while droplet sizes are not affected. The few profiles where cloud top was reaching the top of the inversion layer, and mixing of cloudy air with pure free-tropospheric air was expected, show the same heterogeneous mixing features. This observation suggests that the competition between turbulent mixing and droplet evaporation occurs at scales smaller than 10 m and that the heterogeneous mixing scheme is the most realistic parameterization of the process, when model grids are larger than this scale.

5. ACKNOWLEGMENTS

The authors acknowledge the contributions of the DYCOMS-II participants, and the support of Météo-France and CNRS/INSU/PATOM.

6. REFERENCE

Baker, M. B., R. G. Corbin, and J. Latham, 1980: The influence of entrainment on the evolution of cloud droplet spectra: I. A model of inhomogeneous mixing. *Quart. J. Meteor. Soc.*, **106**, 581-598.

Burnet F., and J. L. Brenguier, 2002: Comparison between standard and modified Forward Scattering Spectrometer Probes during the Small Cumulus Microphysics Study., *J. Atmos. Oceanic Technol.*, **19**, 1516-1531.

Brenguier, J. L., T. Bourrianne, A. Coelho, J. Isbert, R. Peytavi, D. Trevarin, and P. Wechsler, 1998: Improvements of the droplet size distribution measurements with the Fast FSSP., *J. Atmos. Sci.*, **15**, 1077-1090.

Gerber, H, Malinowski S. P., Brenguier J. L., and Burnet F., 2002: On the entrainment process in stratocumulus clouds, *Preprints, 11th Conf. On Cloud Physics*, Odgen, UT, AMS, paper JP7.6.

Pawlowska, H. , and J. L. Brenguier, 2000: Microphysical properties of stratocumulus clouds during ACE-2., *Tellus.*, **52B**, 868-887.

Stevens, B et al., 2003: Dynamics and chemistry of marine stratocumulus – DYCOMS-II., *Bull. Amer. Meteor. Soc.*, **84**, 579-593.

Twomey, S. 1977:The influence of pollution on the shortwave albedo of clouds. *J. Atmos. Sci.*, **34**, 1149-1152.

OPTICAL CHARACTERISATION OF ICE CRYSTALS GROWING AT SIMULATED CIRRUS CONDITIONS

S. Büttner[1], M. Schnaiter[1], R. Wagner[1], C. Linke[1], O. Möhler[1], P. R. Field[2], P. J. Connolly[3]

[1]Institute for Meteorology and Climate Research (IMK-AAF), Forschungszentrum Karlsruhe, Germany.
[2]Met Office, Exeter, UK.
[3]Atmospheric Physics Research Group, UMIST, Manchester, UK.

1. INTRODUCTION

Quantifying the role of cirrus clouds in the climate system requires the determination of the microphysical properties like size and habit of cirrus ice particles and their radiative properties in the infrared and visible region. Fundamental knowledge of scattering, absorption, and polarisation properties of ice crystals is also required for reliably retrieving ice particle properties of visible and subvisible cirrus clouds from remote sensing data.

Whereas cirrus clouds have been investigated in many field studies, yet there is little known about the aerosol effect on cirrus formation and on the relation between microphysical and optical ice crystal properties. Knowledge of this relation is e.g. crucial for LIDAR measurements of cirrus clouds that rely on backscattering and depolarisation of polarised laser light by ice crystals and aerosols.

In this contribution, we show results from an experimental study investigating, among other objectives, the depolarisation of laser light scattered by ice crystals of different size and habit. The ice crystals nucleated on mineral dust aerosol particles grew by vapour deposition at simulated cirrus conditions.

2. EXPERIMENTAL METHODS

Ice crystals are nucleated and grown in the aerosol chamber AIDA by the expansion cooling technique described by Möhler et al. (2003, 2004). The instrumental setup used for the ice nucleation studies is shown in Fig. 1 of Möhler et al. (2004) in this issue. Here, we concentrate on measurements of size, habit, and scattering properties of ice crystals nucleated on mineral dust particles (Arizona test dust, ATD) during AIDA expansion experiments at temperatures between 235 K and 260 K.

Ice particle size (d_{eq}) and habit (*roundness*, cf. Korolev & Isaac, 2003) are analysed with a Cloud Particle Imager (CPI, Spec. Inc.) for ice particles greater than about 30 µm:

$$d_{eq}=2\sqrt{\frac{Area}{\pi}}, \qquad \text{(Eq. 1)}$$

$$roundness=\frac{4Area}{\pi d_{max}^2}. \qquad \text{(Eq. 2)}$$

The projection area (*Area*), the maximum dimension (d_{max}) and the equivalent diameter (d_{eq}, Eq. 1) are determined from the individual ice particle images. For distributions of particle equivalent diameters, lognormal size distributions for the whole experiment are fitted. The median diameter of this distribution is denoted by d_{eq}^{mean}. The particle dimension perpendicular to d_{max} and the mean of its distribution are referred as *width* and $width^{mean}$, respectively. We use the term *roundness* as the average value over all individual ice particle images taken during one experiment.

For particle sizes smaller than 10 µm, ice crystal size distributions are measured with an optical particle counter (PCS 2000, Palas).

For the scattering and depolarisation measurements, an Argon$^+$-Laser (λ=488 nm) with vertical polarisation is directed horizontally through the chamber (Fig. 1). Scattering intensities are measured with photomultipliers (PMT) in the forward direction (4°), and polarisation resolved in the backward direction (176°). The mean depolarisation δ during ice particle presence in the chamber, which is typically 10 minutes is computed as:

$$\delta=\frac{I_\perp-I_\perp^{bg}}{I_\perp-I_\perp^{bg}+I_\parallel-I_\parallel^{bg}}, \qquad \text{(Eq. 3)}$$

where $I_\perp$, $I_\parallel$ denote the intensities in the channel perpendicular and parallel to the incident laser polarisation, and I^{bg} is the background signal in both channels.

Corresponding author's address: Simone Büttner, Forschungszentrum Karlsruhe, IMK-AAF, Postfach 3640, 76021 Karlsruhe, Germany, E-Mail: simone.buettner@imk.fzk.de.

Optical characteristics of laboratory grown ice crystals

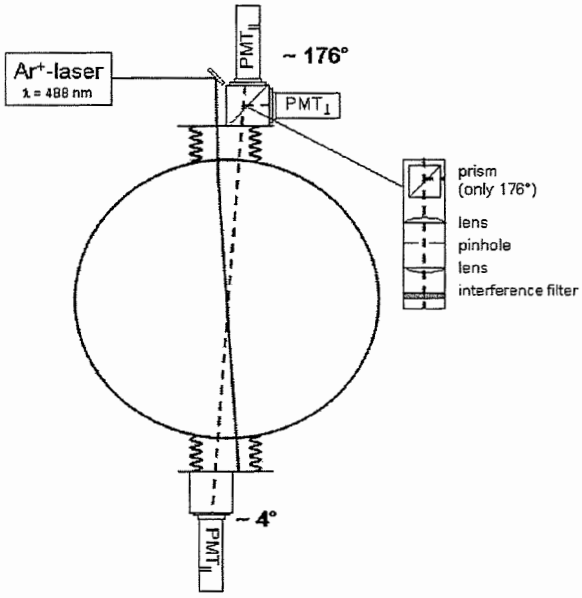

Fig. 1: Laser scattering device at the AIDA chamber.

3. RESULTS

In our experiments, ice particles with different sizes and crystal habits are formed at different temperatures and cooling rates. While in most experiments, crystal habits with roundness only slightly less than 1 are found, in some experiments highly aspherical particles are formed.

Connolly et al. (2004) classified ice crystals nucleated heterogeneously in the AIDA chamber according to the crystal habits. They suppose that the freezing mechanism has an influence on the predominant particle habit. With deposition nucleation, mainly elongated columns are present in the chamber, whereas immersion freezing favours polycrystalline plates.

Fig. 2 shows measured depolarisation vs. roundness, combined with some of the appropriate ice particle images. Accordingly to these images, there are bullet rosettes, columns, and bundles of columns present during the experiments. Hence, there is both a size and a shape distribution of ice particles present in the chamber.

From Fig. 2 it is interesting to see that ice crystals that have an obviously aspherical shape tend to be less depolarising than particles of about the same size, but with a more compact spherical shape. This result of a decrease in depolarisation with increasing asphericity is also shown in Fig. 3.

In contrast, for particles with small deviations from the spherical shape, the depolarisation increases monotonically with particle size (Fig. 3).

Since the ice particles observed in our experiments are much larger than the wavelength of the laser light used, these results apply to the geometric optics regime. Zakharova & Mishchenko (2000) found similar results for wavelength sized spheroids with the help of T-Matrix computations. They explain the behaviour of strongly elongated particles as follows: the scattering properties, especially the scattering matrix elements other than the phase function, are comparable to those of Rayleigh particles. The size of the minor axis, which in their calculations lies within the Rayleigh limit, determines these scattering properties, and therefore also the depolarisation.

Our results point out that a similar behaviour of lower depolarisation for higher asphericity might also be true in the geometric optics regime. Here, also the size of the minor axis of the particle seems to be responsible for the amount of depolarisation detected in light scattering experiments with ice crystals (Fig. 4). Please note that in Fig. 4 *width* is equal to the minor axis of the crystal only for specific particle shapes like needles or plates.

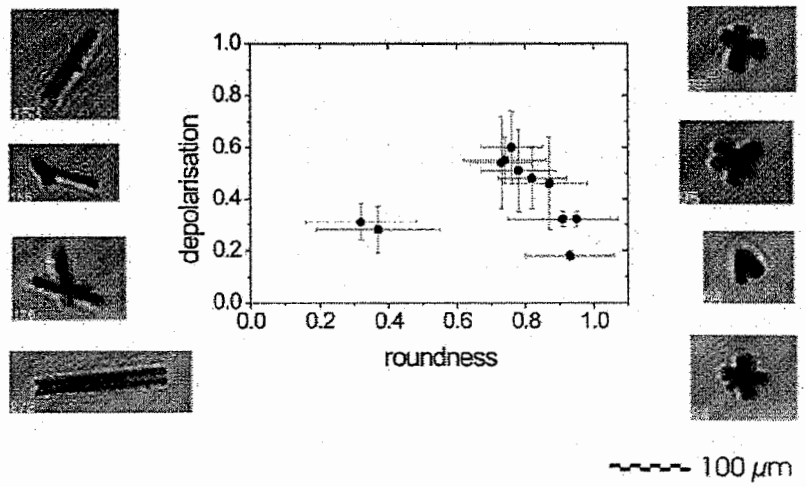

Fig. 2: Depolarisation against ice crystal roundness during heterogeneous ice nucleation experiments with mineral dust and appropriate ice particle images.

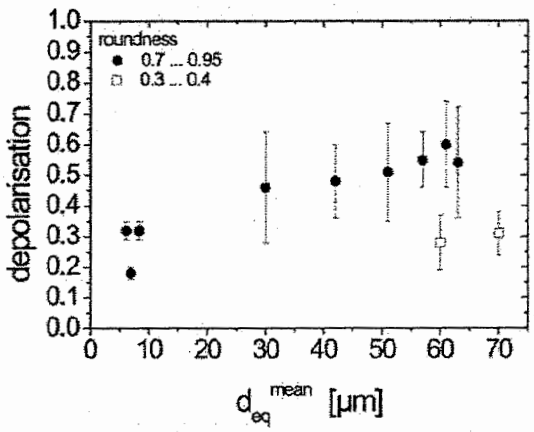

Fig. 3: Depolarisation against ice particle size for ice crystals with high and low roundness under the same conditions as in Fig. 2.

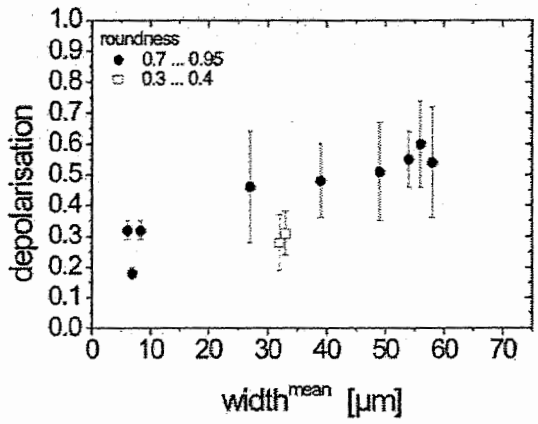

Fig. 4: Smaller dimensions of the particles (e. g. particle width) determine the amount of depolarisation.

4. SUMMARY

In the aerosol chamber AIDA, simultaneous measurements of ice crystal habit, size and depolarisation characteristics have been made for ice crystals nucleated and grown under simulated cirrus conditions. Ice nucleation occurs heterogeneously with mineral dust as seeding aerosol. The ice particles measured in the presented dataset have mean diameters between 6 µm and 70 µm.

The ice crystals exert both a shape and a size effect on the depolarisation measurements: For ensembles of particles with high roundness, there is an increase of depolarisation with size, whereas highly aspherical particles are characterised by a lower depolarisation compared to equal-sized crystals with higher roundness.

The latter observation might point to an extension of the theoretical predictions by Zakharova & Mishchenko (2000) to the geometric optics regime. They found similar results for wavelength-sized spheroids. These results have to be kept in mind in the interpretation of depolarisation measurements, e.g. LIDAR measurements.

5. REFERENCES

Connolly, P. J., P. R. Field, O. Möhler, S. Büttner, H. Saathoff, A. J. Heymsfield, M. W. Gallagher, T. W. Choularton, 2004: Simulations of ice crystal nucleation and growth: results from the AIDA cloud expansion chamber. This issue.

Korolev, A., G. Isaac, 2003: Roundness and aspect ratio of particles in ice clouds. J. Atmos. Sci., 60, 1795-1808.

Möhler, O., O. Stetzer, S. Schaefers, C. Linke, M. Schnaiter, R. Tiede, H. Saathoff, M. Krämer, A. Mangold, P. Budz, P. Zink, J. Schreiner, K. Mauersberger, W. Haag, B. Kärcher, U. Schurath, 2003: Experimental investigation of homogeneous freezing of sulphuric acid particles in the aerosol chamber AIDA. ACP, 3, 211-223.

Möhler, O., R. Wagner, A. Mangold, M. Krämer, V. Ebert, L. Schütz, P. Field, P. Connolly, A. Heymsfield, 2004: Formation, growth, and habit of ice crystals nucleated on desert dust aerosol. This issue.

Zakharova, N. T., Mishchenko, M. I., 2000: Scattering properties of needlelike and platelike ice spheroids with moderate size parameters. Appl. Opt., 39(27), 5052-5057.

detailed microphysics with time varying diurnal forcing and boundary layer

IFN/CCN AND CLIMATE

– looking at detrainment from the clouds

Gustavo Carrió, Hongli Jiang and William R. Cotton

Colorado State University, Fort Collins, Colorado

1. INTRODUCTION

The potential impact of intrusions of polluted air into the Arctic basin on sea-ice freezing/ melting rates and the surface energy budget is examined. We performed two series of multi-month cloud-resolving (CRM) simulations for the fall-winter and spring seasons during the 1997-1998 SHEBA field campaign. For that purpose, we implemented the Los Alamos National Laboratory sea-ice model (CICE) into the research and real-time versions of the Regional Atmospheric Modeling System at Colorado State University (RAMS@CSU). This new version of RAMS@CSU also includes a new microphysical module that considers the explicit nucleation of cloud droplets and a bi-modal representation of their spectrum. Aerosol profiles based on May 4 1998 observations were used to characterize the polluted upper layer. The 2-3 daily SHEBA soundings were utilized to provide time-evolving boundary conditions. Results indicate that the entrainment from above the inversion decreases the freezing rates and increases the melting rates when mixed-phase clouds are present. An opposite, although less important, effect can be associated with CCN entrainment when liquid-phase clouds prevail.

2. MODEL DESCRIPTION

The model used in this study is the 2-D CRM version of RAMS@CSU (Cotton et al., 2003). The new microphysical package (Saleeby and Cotton, 2003) shares the double moment microphysical framework of the previous scheme (Meyers et al., 1997) assuming that hydrometeor size spectra have a gamma distribution function and mass mixing ratio as well as number concentration of the hydrometeor species is predicted.

Corresponding author's address : Gustavo G. Carrió, Atmospheric Science Department, Atmospheric Science Bldg., Colorado State University, Fort Collins CO 80523, USA; E-Mail: carrio@atmos.colostate.edu

However, among other new features it explicitly considers the nucleation of cloud droplets via activation of CCN, and a bimodal representation of spectrum of liquid particles. The predicted microphysical categories also include the number concentration and mixing ratio of rain, pristine ice, snow, aggregates, graupel and hail, as well as the IFN and CCN concentration. This sea-ice model discretizes the sub-grid ice thickness distributions in different categories, considering their corresponding fractional areas as prognostic variables. Ice thickness categories are partitioned in a number of internal ice layers. For each thickness category, the surface and snow temperatures as well as the temperatures associated with the internal layer are also prognostic variables. The original version of CICE (Hunke and Lipscomb, 1999) was modified in its structure to allow module communication in an interactive multi-grid framework.

3. EXPERIMENT DESIGN

Fall-winter simulations were initialized on Oct 16 1997 with total simulation time of 180 days, while spring-summer numerical experiments covered the period May 1-July 31 1998. All these experiments have been performed in a two-dimensional (2-D) framework. Model domain was 5000m in the horizontal and approximately 3325m in the vertical. A constant horizontal resolution of 50m, a vertical resolution of 30m, and a timestep of 2s were used. The lateral boundary conditions were cyclic and the domain top is a rigid lid.

The 4 May aerosol profiles were used as a benchmark although IFN and CCN concentrations were assumed to be constant with altitude within the upper layer (at time=0). The simulations were initialized using different IFN and CCN profiles based on those observed within the upper layer. Conversely, the initialization profiles for all experiments assume "clean" concentrations of IFN and CCN (3 L^{-1}, 100cm^{-3}, respectively) with the boundary layer.

Only the initialization profiles corresponding to the control run assume "clean" IFN profiles for both layers. In order to efficiently isolate the effect of the entrained aerosols, a Newtonian relaxation technique (nudging) was applied to restore the polluted and clean aerosol concentrations above and below the current altitude of the inversion, respectively.

For both sensitivity tests, six ice thickness categories (with 4 internal layers) are considered to describe the sub-grid ice thickness distribution. The mass and energy-conserving remapping scheme of Lipscomb (2001) is used to transfer ice among categories. The SHEBA daily time series of divergence and shear rates were used to take into account the changes in thickness distribution associated with ice dynamics. Ice thickness was initialized with values of 1.5 and 2.41m for the fall-winter and spring-summer numerical experiments, respectively.

A summary of multi-month CRM runs that correspond to the results presented in this abstract in given in Table 1.

Table I

EXP	IFN	CCN
EC-C (control)	clean	clean
EC-1	clean	100% obs
E.50-C	50% obs	clean
E.50-1	50% obs	100% obs
E.75-1	75% obs	100% obs
E1-C	100% obs	clean
E.75-.75	75% obs	75% obs
E1-1	100% obs	100% obs
E.75-1	125% obs	125% obs

4. RESULTS

4.1 Melting season

We generated probability density functions (PDFs) of various microphysical variables associated with solid-phase particles for the entire 3-month period. Figure 1 gives the PDFs of total ice number concentration (Ni) and mean mass diameter (Di) of precipitation ice particles. Increasing IFN within the upper layer reduces the mode of Di and increases the frequency of large values of Ni. Substantial differences can also be observed between runs that consider enhanced IFN concentrations in PDFs of ice water path (IWP), total condensate path (TCP), and longwave down (LWDN) (not shown). The larger values of these quantities exhibit a monotonic behavior increasing their frequency when a more polluted upper layer is assumed.

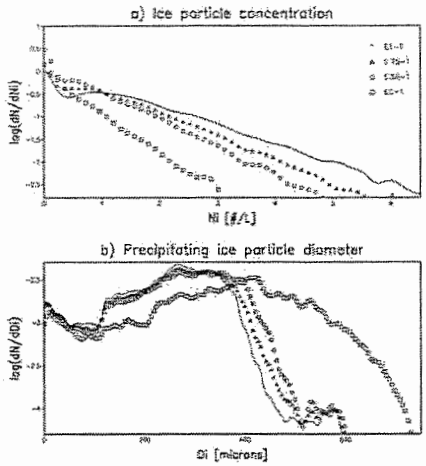

Figure 1. PDF's for Ni (a) and Di (b) .

The simulated longwave down (LWDN) is compared for the control run and the run that nudges the observed profiles in Figs. 2a. The percent differences of LWDN with respect to the control run have been computed using six-hour averages of horizontal mean values. The sign and magnitude of these LWDN differences vary in a monotonic manner when nudged IFN concentrations above the inversion increase (not shown). Scatter plots of LWDN differences against those corresponding to TCP are given in Fig. 2b. This scatter plot reveals an important degree of association between the changes in LWDN and TCP differences induced by the entrainment of IFN. Similar numerical experiments have been performed for a CCN concentration 50% higher, although the main results of Figs. 2 remained unaltered.

The differences of the simulated sea-ice thickness with respect to the control run are plotted in Fig. 3. Differences in this figure are negative for all experiments that consider enhanced IFN concentrations above the inversion, indicating larger melting rates compared to the control case. The largest (negative) differences correspond to the run that considers an upper layer with an IFN concentration associated with the observations

and a clean CCN profile (E1-C). Conversely, larger melting rates were obtained for run EC-1 that only takes into account CCN entrainment. The sign and the magnitude of these differences for these runs suggest that the CCN effect is opposite but less important than that associated with IFN entrainment.

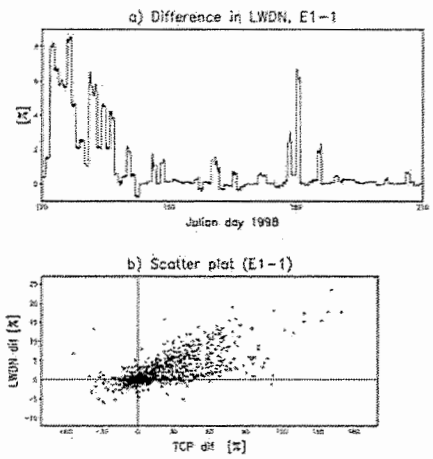

Figure 2. LWDN difference (a). Scatter plot for LWDN and TCP differences (b).

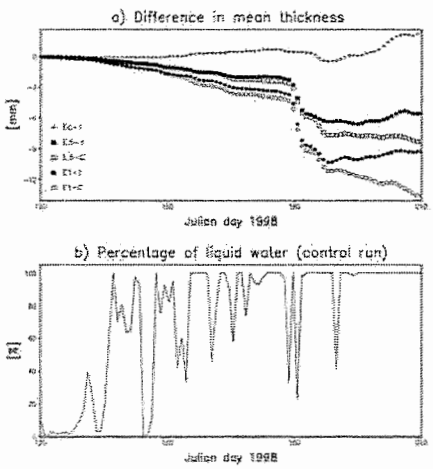

Figure 3. Ice thickness difference (a). Liquid water fraction for the control run (b).

4.2 Freezing season

Results corresponding to the 6-month period initialized on Oct 16 1997 exhibit a very similar behavior compared that of the spring-summer numerical experiments.

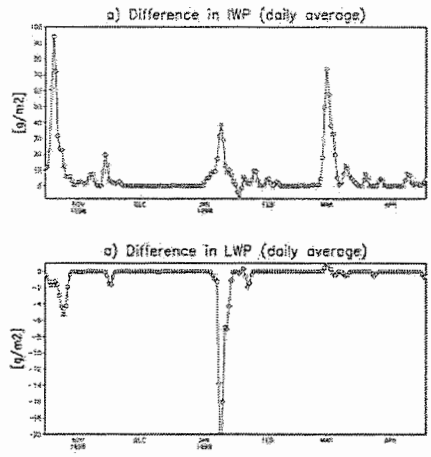

Figure 4. Ice thickness difference (a). Liquid water fraction for the control run (b).

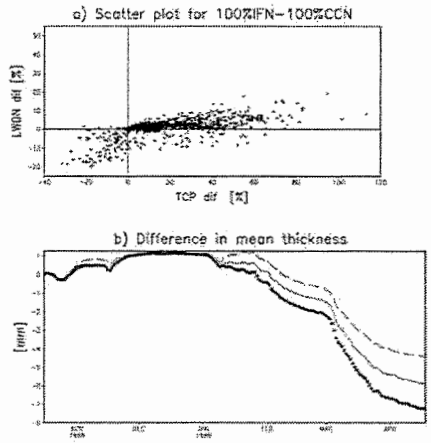

Figure 5. Scatter plot for LWDN and TCP differences for the run with observed profiles(a). Ice thickness difference (b), dashed lines, solid line and crosses denote 75%, 100%, and 125% observed.

When comparing experiment E1-1 with the control run in Fig. 4, positive and negative differences were obtained for IWP and LWP, respectively. It can be seen that differences in simulated mean ice thickness monotonically increase when a more polluted upper layer is assumed increasing the aerosol concentration above the boundary layer (see Fig 5). These negative differences indicate lower freezing rates due to aerosol entrainment from above the inversion.

5. CONCLUSIONS

The potential effect of major intrusions of polluted air into the Arctic basin on sea-ice melting/growth rates is examined. Two series of numerical experiments have been performed covering both freezing and melting season. Results indicate a significant impact on the microstructure of the simulated clouds.

When assuming polluted initial profiles within the upper layer, the liquid water fraction of the cloud monotonically decreases, the total condensate path increases, and LWDN tends to increase due to a significant increase in IWP path. Results corresponding to both series of multi-month CRM simulations that IFN entrainment of from polluted air overriding the inversion may have a significant impact on sea-ice freezing/melting rates when mixed phase clouds are present. Results also indicate that the CCN effect on sea-ice melting/freezing rates is opposite though less important than the IFN effect. We must await daily observations of IFN and CCN profiles before we can determine the total impacts of aerosol intrusions into the Arctic on climate. However, the results suggested by these multi-month CRM simulations may have important climatological implications since the extent and duration of sea-ice coverage not only effects regional climate but also global climate through ice-albedo feedbacks.

6. ACKNOWLEDGEMENTS

This research was supported by a University of Alaska Fairbanks Research contract UAF-00-0086/FP100092 (CSU 5-33422) and by a NSF grant #0215367. The authors also wish to thank Brenda Thompson for technical support.

7. REFERENCES

Carrió, G.G., Jiang, H, and W. R. Cotton, 2003: Impact of aerosol intrusions on the Arctic boundary layer and on sea-ice melting rates Part I: May 4 1998 case. Submitted to J. Atmos. Sci..

Cotton,W. R., R.A. Pielke, Sr., R.L. Walko , G.E. Liston, C.J. Tremback, H. Jiang, R. L. McAnelly, J. Y. Harrington, M.E. Nicholls, G.G. Carrió and J. P. Mc Fadden 2003: RAMS 2001: Current Status and future directions. Meteor. Atmos. Physics, 82, 5-29.

Harrington , Y.Y. , T. Reisin, W.R. Cotton, S. M. Kreidenweis, 1999:Cloud resolving simulations of Arctic stratus. Part II: Transition-season clouds. Atmos. Res., 51, 45-75.

Hunke, E. C., and Lipscomb, 1999: CICE: The Los Alamos se-ice model, documentation and software, version 2.0, Los Alamos National Laboratory,LA-CC-98-16, v.2.

Lipscomb, W. H, 2001: Remapping the Thickness Distribution of Sea-ice. J. Geophys. Res..Vol 106, 13989-14000.

Meyers, M. P. Walko, R. L., Harrington J. Y. , Cotton, W.R., 1997: New Rams cloud microphyisics parameterization : Part II. The two-moment scheme. Atmos. Res., 45, 3-39.

RADIATIVE IMPACT OF MIXING PROCESSES IN BOUNDARY LAYER CLOUDS

F. Chosson[1] , J.-L. Brenguier[1] and M. Schröder[2]

[1]Météo-France, CNRM-GMEI, Toulouse, 31057, France
[2]Institut für Weltraumwissenschaften, Freie Universität, Berlin, 12165, Germany

1. INTRODUCTION

The radiative properties of warm boundary layer clouds are mainly determined by the microphysical properties at cloud top, in a thin layer corresponding to the first few units of optical thickness. In particular, a key parameter is the ratio of the total droplet volume to the total droplet surface, or the droplet effective radius. In the most simplified radiative transfer models, the cloud is represented as a vertically and horizontally uniform layer (the so called plan-parallel model). More sophisticated models have been developed to account for the vertical stratification of the microphysics (Brenguier et al., 2000a, Schüller et al., 2003). The horizontal heterogeneity of the microphysical field is also an important feature to consider for radiative transfer calculations (the so-called heterogenous bias) (Cahalan et al., 1994). We examine here an additional contribution, namely the impact of entrainment-mixing processes on the microphysical properties of the upper cloud layer. This layer, which contributes the most to the cloud optical properties, is also strongly affected by the mixing of cloudy-air with the overlying dry and warm air from the free troposhere. The ratio of droplet volume to surface in mixed cloud volumes is significantly modified with respect to its adiabatic (unmixed) value at cloud top, and the modification is mainly dependent upon the thermodynamical properties of the entrained dry air.

In this study, we explore the effects of these mixing processes on the radiative properties of simulated cloud fields. The cloud structure is simulated with a 3D large-eddy simulation model (Meso-NH) of marine stratocumulus, with bulk parameterization of the microphysics. Introducing a realistic microphysical parameterization of the mixing processes, the cloud optical properties are then computed with a 3-D radiative transfer model. The impact of the mixing processes on retrieval techniques of cloud microphysical properties from satellite remote sensing of visible and near-infrared radiances is also investigated.

2. LES MODEL AND CASE STUDY DESCRIPTION

Meso-NH is a non-hydrostatic model that computes 3D dynamics, solar heating and longwave cooling at each grid point, using the ECMWF radiative scheme, surface (sea) fluxes and liquid water content (hereafter LWC) by saturation adjustment. The one and a half order turbulence closure is based on a prognostic equation of the subgrid scale turbulent kinetic energy.

In our simulation, the grid size is 50 m in both horizontal directions and varies from 10 m to 50 m in the vertical, with the finest resolution in the cloud and in the inversion layer. In order to avoid interactions between the cloud structures and the domain size, the horizontal domain dimension is set to 10 km for a 3h simulation time run. Periodic boundary conditions are used horizontally and the top of the domain reaches 1.5 km height.

The simulation is initialized using vertical profiles of liquid water potential temperature, total water mixing ratio and horizontal wind components, as measured with the Merlin IV research aircraft on July 9th over the north Atlantic, during the ACE-2 CLOUDYCOLUMN campaign, 1997 (Brenguier et al., 2000b).

3. CLOUD MODEL SIMULATIONS

After a 3 hours run, a thin stable and heterogeneous stratocumulus deck is obtained, that is illustrated in Figure 1 with the 3D 0.1g/kg LWC iso-surface over the simulation domain.

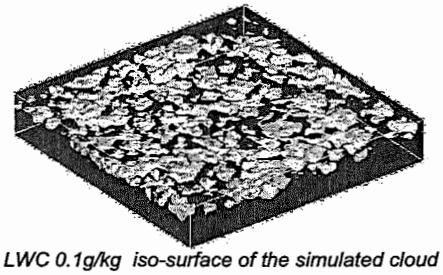

Fig.1. *LWC 0.1g/kg iso-surface of the simulated cloud field.*

Brenguier et al. (2003) calculated vertically stratified LWC statistics from series of ascents and descents through the cloud layer. The cloud layer is divided in five 30 m thick sub-layers above cloud base. Figure 2 shows the derived LWC probability frequency distribution (PFD) for the 9th July case (continuous line). The histogram represent the simulated LWC PFD. Statistics of the simulated LWC cloud field are in very good agreement with the measurements.

The geometrical thickness (*H*) of the simulated cloud is also statistically validated. As for the measurements, the cloud base (respectively top) is defined by as the 1% percentile (resp. 99%) of the

Corresponding author's address : Frédérick Chosson
Météo-France, CNRM/GMEI/MNPCA, 42 av. Coriolis
31057 Toulouse Cedex 01, France.
Email : chosson@cnrm.meteo.fr

cumulated frequency distribution of the cloudy grid box altitude. H is the difference between the cloud top and base altitudes. The model simulation (H_{sim}=145 m) and the measurements (H_{obs}=148 m) are also in good agreement.

The cloud field observed on July 9 shows a large variety of cloud structures, ranging from extended clear air areas to thick homogeneous cloud cells. Such a variability can be explained by the sharp inversion at cloud top. According to Deardorff (1980), the cloud was unstable with respect to cloud top entrainment. It appears that the simulated cloud structure is in fact particularly sensitive to the tuning of the moisture inversion strength.

At our disposal, we now have a large set of realistic simulated cloud fields, with different heterogeneous cloud structures and geometrical thicknesses.

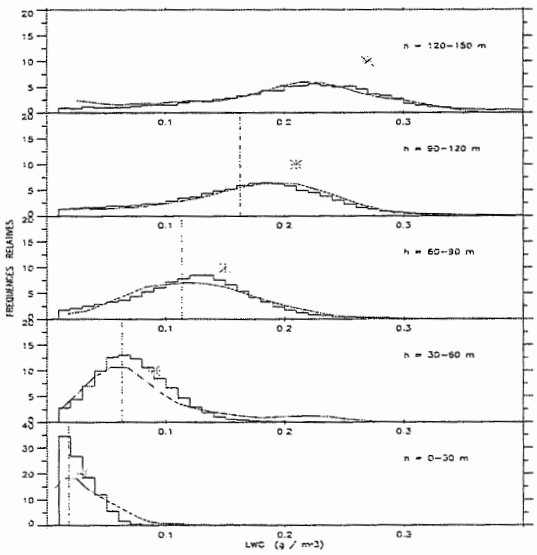

Fig.2. *LWC PFD in five 30 m thick layers above cloud base. Observed cloud (continuous line) and simulated cloud (histogram). The mean simulated LWC (vertical dashed line) and the adiabatic LWC value (star) at the middle of each layer are also shown.*

4. MICROPHYSICAL PROPERTIES

The Meso-NH LES simulations have been performed with a bulk parameterization of the microphysics, that is only the liquid water mixing ratio is predicted. Modelling radiative transfer however also requires information about the droplet size distribution (DSD) for deriving the extinction.

In quasi-adiabatic cloud columns, the DS can be approximated by using the β^2 scheme of Brenguier (1991), that has been further used by Schüller et al. (2003) for radiative transfer calculations.

4.1 The β^2 microphysical scheme

The β^2 scheme is based on three hypotheses:

– Cloud condensation nuclei (CCN) are activated at cloud base. In actual clouds, the CCN activation is in fact completed within the first 50 m of convective ascent. Secondary CCN activation following mixing is neglected. For the parameterization, an analytic description of the initial droplet size distribution (DSD) at cloud base is used, that only depends on the droplet number concentration (N).

– Droplet growth by water vapor diffusion, after activation is completed, is reduced to : $dr^2/dt = 2BS$ where r is the droplet radius, S is the water vapor supersaturation, and B is a coefficient function of temperature and pressure. It follows that the shape of the droplet surface distribution $n(r^2)$ remains unchanged and is simply translated by a quantity β^2 in the r^2 scale, when the altitude above cloud base h increases:

$$n(r^2,h,N) = n(r^2-\beta^2,0,N)$$

This shift value β^2 is thus a function of h and N.

– LWC is approximated by a linear function of height above cloud base : $LWC(h) = C_w\, h$ where C_w is a weak function of temperature and pressure. β^2, can then be calculated from LWC as a solution of:

$$LWC(h) = C_w h = 4/3\, \pi\rho_w \int r^3 n(r^2-\beta^2)dr^2$$

The effective radius (r_{eff}), defined as the ratio of the third to the second moment of the DSD is a function of β^2, N and of the mean surface radius at cloud base $r_{s\,base}^2$:

$$r_{effad}(h,N) = \frac{C_w\, h}{4/3\, \pi\rho_w N\,(r_{s\,base}^2 + \beta^2)}$$

4.2 Parameterization of mixing: introduction

The β^2 scheme is only valid in adiabatic cloud volumes. A significant part of the cloud layer however is affected by mixing with the overlying warm and dry air from the free troposphere, hence resulting in LWC values lower than the adiabatic reference. The effect of mixing on the DSD can be parameterized following either a heterogeneous or a homogenous mixing scheme (Baker, et al. 1980). In the homogeneous mixing scheme, it is assumed that turbulent mixing between the cloudy and the entrained clear air is faster than the characteristic time of droplet evaporation. All the droplets are therefore exposed to the same water vapour deficit and they are all evaporated according to $dr^2/dt = 2BS$, where S now represents a sub-saturation. In the heterogeneous mixing scheme, in contrast, turbulent mixing is assumed to be much slower than droplet evaporation. Some droplets that are exposed to subsaturated air are totally evaporated, until the entrained air is saturated. At this point, the remaining droplets are no longer affected by mixing.

The $\{N:\Phi^3\}$ diagramme (Burnet, Brenguier, 2000) illustrates the concept. The mean volume diameter (MVD) of a droplet spectrum is represented versus N. Both are normalized by their respective adiabatic values. The dot-dashed hyperboles represent the ratio

of LWC to the adiabatic reference, from 100 % for the isoline crossing the coordinate {1:1}, down to 10 %.

In the homogeneous mixing scheme, the ratio of N to its adiabatic reference (X axis) also represents the proportion of cloudy air in the mixture. N and MVD values resulting from homogeneous mixing between adiabatic cloudy air and entrained air are given by the intersection of the curve relative to the humidity of the entrained air (labeled from 10 to 100 % in the figure) and the proportion of cloudy air indicated on the X-axis. The horizontal line labeled 100, corresponds to homogeneous mixing with saturated entrained air, during which only N is diluted while droplet sizes remain unchanged.

The heterogenous mixing scheme is also represented by the line labeled 100 (constant MVD), but N shall be calculated explicitely as a function of the proportion of entrained air and its relative humidity.

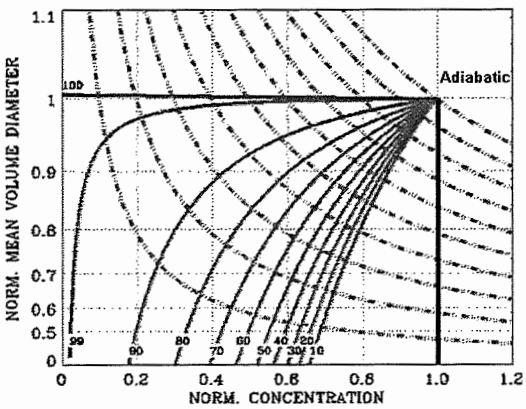

Fig.3. *MVD versus N. LWC isolines from 100 % to 10 % of the adiabatic reference (dot-dashed lines). Homogeneous mixing curves labeled with the relative humidity of the entrained air, from 10 to 100 %.*

4.2 Parameterization of mixing in LES simulations

In order to evaluate the impact of the mixing parameterization scheme on radiative transfer calculation, two extreme cases are tested. First, the model columns are considered separately (independent pixel approximation) and the adiabatic LWC is calculated in each grid box as a function of the altitude h above the average domain cloud base, as defined in Section 3. If the grid box LWC is greater or equal to the adiabatic value, r_{eff} is calculated using the β^2 scheme (r_{effad}).

If the grid box LWC is lower than the adiabatic value, two mixing parameterization schemes are applied.

On the one hand, we consider a heterogeneous mixing process, represented by the mixing line labeled 100 in Figure 3. It follows that:

$$r_{eff} = r_{effad}(h) \text{ and } N = N_{ad} \times LWC / (C_w\, h),$$

where LWC is the liquid water content in the grid box, and r_{eff} is the effective radius after mixing.

On the other hand, we consider an extreme homogeneous mixing process, corresponding to partial evaporation of the droplets without any dilution. It is represented in Figure 3 by the vertical mixing line. Even though such a case corresponds to an unreaslitic relative humidity of 0 %, it offers a very simplified way of approaching the 10 % *RH* homogeneous mixing case. It follows that:

$$r_{eff} = r_{effad}(h)\ (LWC/C_w\, h) \text{ and } N = N_{ad}$$

5. IMPACT ON RADIATIVE PROPERTIES

The optical thickness is then calculated by integration of the extinction over each model column separately. Overall the optical thickness derived with the homogeneous mixing scheme is always greater than the one of the heterogeneous mixing scheme. For example, the mean optical thickness of the cloud field presented in Figure 1 is 35% greater with the homogeneous scheme than with the heterogeneous one.

6. IMPACT ON SATELLITE RETRIEVAL SCHEMES

This preliminary analysis demonstrates that the mixing scheme has a significant impact on the simulated optical properties of a cloud field. We now investigate in more details the impact of the mixing scheme on the statistical properties of the radiance fields, that are used for retrieval of cloud microphysical properties from satellite remote sensing.

Schüller et al. (2003) developed such a technique for retrieval of droplet number concentration and geometrical thickness of stratiform boundary layer clouds, based on visible and near infrared measured reflectances.

Using the SHDOM radiative transfer model (Evans, 1998) and following the same approach as in Schüller et al., a look-up table of nadir reflectances at 754 nm and 1553 nm wavelengths is computed for a large set of adiabatic clouds, with varying droplet concentrations N and geometrical thicknesses H (using the β^2 microphysical scheme). SHDOM is then applied to the LES 3-D simulated cloud by assuming either a homogeneous or a heterogeneous mixing scheme.

Figures 4 to 6 show examples of the conditional distribution of reflectances at both wavelengths, with their respective frequency distributions plotted along both axis. The superimposed grid shows isolines of constant N and H, as derived from the look-up table of adiabatic clouds.

With the homogeneous mixing scheme (Figure 4), the conditional frequency distribution of reflectances is well distributed along the N isoline corresponding to the LES simulation ($N = 256\ cm^{-3}$). The cloud geometrical thickness over the simulated domain has a mean value of 100 m, with peak values up to 200 m. The figure however shows that the frequency distribution of reflectances extends up to values as high as 250 m. With a heterogenous mixing scheme (Figure 5), the conditional frequency distribution of reflectances is narrower, centered on slightly lower N values, and both reflectance frequency distributions show, at both wavelengths, lower reflectances than with the homogeneous mixing scheme.

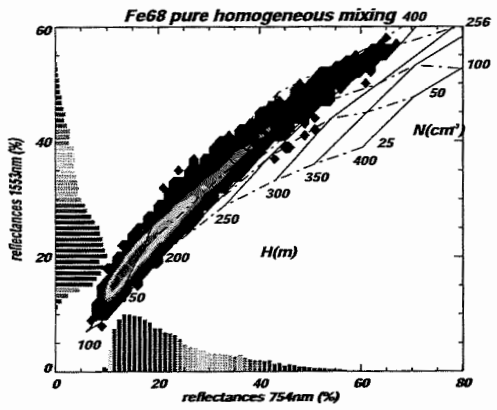

Fig.4. *Conditional frequency distribution of reflectances in near-infrared versus visible wavelengths, with a homogeneous mixing scheme. Reflectances corresponding to LWP < 5 g/m² are not represented.*

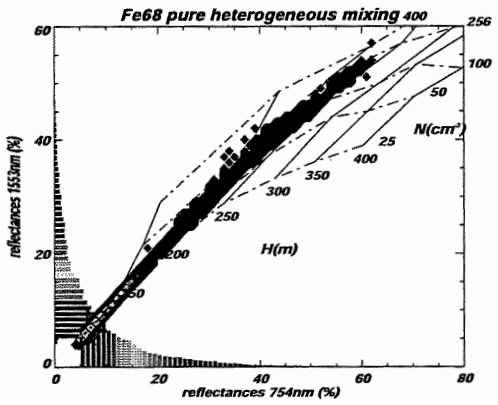

Fig.5. *Same as fig.4 with a heterogeneous mixing scheme.*

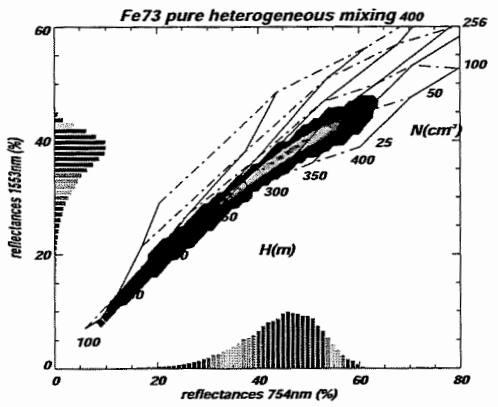

Fig.6. *Same as fig.5 with N=50 cm^{-3} and with a H mean value of 300 m, with peak values up to 400m.*

Figure 6 shows a simulation with a heterogeneous mixing scheme, *N=50 cm^{-3}* and a *H* mean value of *300 m*, with peak values up to *400 m*.
The conditional reflectance frequency distribution is well distributed along the *N=50 cm^{-3}* isoline, but the reflectance values at both wavelengths are significantly larger than in the previous case, showing that the increase in cloud geometrical thickness largely compensates the reduction of the droplet concentration.

7. CONCLUSION

This preliminary study reveals that the choice of a mixing parameterization scheme has a significant impact on the calculation of simulated cloud radiative properties. Simulations of the nadir reflectances in the visible and near-infrared channels, that are currently used for the retrieval of cloud microphysical properties from satellite remote sensing, demonstrate that the simulated frequency distributions of reflectance exhibit different features depending on the selected mixing scheme. These features will now be further explored for improving the satellite retrieval schemes.

8. REFERENCES

Baker, M.B., R.G. Corbin and J. Latham, 1980: The influence of entrainment on the evolution of cloud droplet spectra: Part I A model of homogeneous mixing. *Q.J.R.M.S.*, **106**, 581-598

Brenguier, J.L., 1991: Parameterization of the condensation process: a theoretical approach. *J.A.S.*, **48**, 264-282

Brenguier, J. L., H. Pawlowska, L. Schueller, R. Preusker, J. Fischer, and Y. Fouquart, 2000a : Radiative properties of boundary layer clouds: droplet effective radius versus number concentration. *J. Atmos. Sci.* **57**, 803-821.

Brenguier, J. L., Y. Chuang, Y. Fouquart, D. W. Johnson, F. Parol, H. Pawlowska, J. Pelon, L. Schüller, F. Schröder and J. R. Snider, 2000b: An overview of the ACE-2 CLOUDYCOLUMN Closure Experiment, *Tellus, **52B***, 814-826,.

Brenguier, J. L., H. Pawlowska, and L. Schüller, 2003: Cloud Microphysical and Radiative Properties for Parameterization and Satellite Monitoring of the Indirect Effect of Aerosol on Climate , PACE Topical Issue, *J. Geophys. Res.*, **108**, No. D15, 8632 10.1029.

Burnet, F. and J.L. Brenguier, 2000: Effect of entrainment and mixing on droplet spectral broadening. *Proc. 13th ICCP*, 144-147

Cahalan, R. F., W. Ridgway and J. W. Wiscombe, 1994b: Independent pixel and Monte Carlo estimates of stratocumulus albedo. J. Atmos. Sci., ***51***, 3776-3790,.

Deardorff, J.W., 1980: Cloud Top Entrainment Instability, *J.A.S.*, 37, 131-147

Evans, K.F., 1998: The Spherical Harmonics Discrete Ordinate Method for 3D Atmospheric radiative transfer, *A.M.S.*, 55,429-446

Schüller, L., J.L. Brenguier, H. Pawlowska, 2003: Retrieval of microphysical, geometrical and radiative properties of marine stratocumulus from remote sensing, *J. of Geophys. Research.*, 108, 8631, doi.10.29/2002JD002680

EVALUATION OF CLOUD AMOUNT TRENDS AND CONNECTIONS TO LARGE SCALE DYNAMICS

Todd D. Ellis*, Graeme L. Stephens, and David W. J. Thompson
Colorado State University, Fort Collins, CO

1. INTRODUCTION

Recent studies by Wielicki et al. (2002) and Chen et al. (2002) provide evidence of a decadal-scale trend in the cloud amount (cloud fraction) in the tropics. Wielicki et al. use data from the Earth Radiation Budget Experiment (ERBE, Barkstrom 1984) to demonstrate a decadal-scale upward trend in the tropical mean long wave (LW) flux time series since 1985. They argue that this trend must be reflected in changes in the cloud amount in the tropics. Chen et al. use International Satellite Cloud Climatology Project (ISCCP, Schiffer and Rossow 1983) data to show that there was an overall change in the cloud amount in the tropical and subtropical regions over the same time period. Figure 1 shows one representation of how the global cloud amount has changed in the last 20 years.

Changes in the global cloud amount may have important climatic implications. Chen et al. provides evidence that these changes were associated with changes in vertical motion from reanalysis data that could be associated with the tropical Hadley/Walker circulation. Furthermore, while there is debate on the mechanism by which clouds feedback on tropical sea surface temperatures, there is general agreement that such feedbacks do exist and that they are important for understanding the climate system and its variability (Miller 1997, Pierrehumbert 1995, Lindzen et al. 2001, Lin et al. 2002, and others).

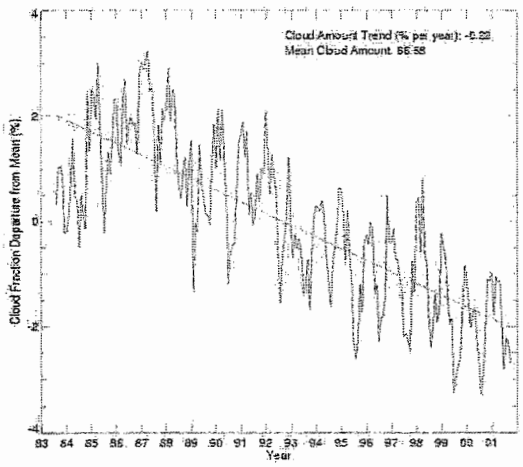

Figure 1: Time series of ISCCP D2 monthly mean cloud amount with the period mean removed. The total change from 1987 until 2001 is about 4%. The trend shown in green represents only that part of the data beginning in 1987.

*Corresponding authors address: Todd D. Ellis, Department of Atmospheric Science, Colorado State University, Fort Collins, CO, 80523; email: ellis@atmos.colostate.edu

However, there is still some debate over whether the global cloud amount trend shown in Figure 1 is physical, or if it is simply some artifact of the satellites or the processing algorithm. Additionally, little effort has been expended to examine this trend thoroughly. For example, it has yet to be determined what kinds of clouds are experiencing the changes, where these clouds are located, and whether or not the trends are more pronounced at certain times of the year. Furthermore, previous studies have not attempted to examine mechanisms that might be driving such changes either on the local or global scales. All of these issues should be addressed in order to characterize the nature of the cloud amount changes in the climate system. This will improve our ability to model them and to understand their impact on the climate system.

This manuscript will describe efforts to characterize the nature of the global cloud amount trend and its interaction with the Earth's climate. Section 2 of this manuscript will detail the data sets used in this study. Section 3 will detail the methodology employed to conduct this study to date. Section 4 will present some of the results obtained prior to the submission of this manuscript, and section 5 will present a discussion of remaining tasks and possible future studies. For the most current figures and complete results to date, the authors refer you to their website:
http://reef.atmos.colostate.edu/ellis/AMStalk.html

2. DATA USED IN THIS EXPERIMENT

2.1 Cloud datasets

In order to ensure that the cloud amount trends obtained are not simply artifacts of the peculiarities of a particular dataset, two different sources of cloud data are used. The primary source of this data is the ISCCP D2 monthly mean cloud data. This dataset provides information on total cloud amount, as well as cloud amounts for different types of clouds. For the purposes of this study, the following types of clouds are analyzed: low cloud (cloud top below 680 mb), middle cloud (cloud top between 680 mb and 440 mb), cirrus cloud (cloud top above 440 mb, cloud optical thickness less than 3.6), cirrostratus (cloud top above 440 mb, cloud optical thickness between 3.6 and 23), and deep convection (cloud top above 440 mb, cloud optical thickness above 23). These divisions are further described in Rossow and Schiffer (1999). The temporal coverage of this dataset is from July 1983 until September 2001, and the spatial resolution is 2.5° X 2.5°. Since this is the primary dataset used in this study, all of the other datasets were trimmed so that they also only span this time period.

The Cloud Archive User Service (CLAUS) 2.5° x 2.5° brightness temperature dataset (Hodges et al. 2000) was also employed to provide some independent verification of the cloud amount trend by taking advantage of the different algorithm employed in their processing of ISCCP B3 data. This time series only spans the years 1983-1993, however since it overlaps 7 years of the downward ISCCP trend, it is sufficient for independent verification of the trends in the ISCCP D2 dataset.

2.2 Atmospheric Data

In order to further verify the trends in cloud amount as well as to evaluate the coupling between the cloud amount and climate, two independent sources of reanalysis data are used in this study: the National Centers of Environmental Prediction (NCEP) – National Center for Atmospheric Research (NCAR) 40-Year Reanalysis data (Kalnay et al. 1996) and the European Centre for Medium-Range Weather Forecasting (ECMWF) 40-year Reanalysis (ERA-40, Gibson et al. 1996; Gibson et al. 1997). These datasets provide global fields of monthly mean 200 mb winds and divergence, 850 mb winds and divergence, sea level pressure, and 500 mb heights at 2.5° x 2.5° resolution.

Precipitation data was also obtained from two different sources: the Global Precipitation Climatology Project (GPCP, Huffman et al. 1996) and the Climate Prediction Center Merged Analysis of Precipitation (CMAP, Xie and Arkin 1997). Both datasets are a combination of satellite-derived precipitation estimates merged with surface observations; the primary difference between them being that CMAP also ingests numerical model output in its algorithm to generate precipitation fields. Both of these datasets are also available at 2.5° x 2.5° resolution.

The NOAA OI version 2 SST monthly dataset was used for all SST analysis (Reynolds et al 2002).

3. METHODOLOGY

The first part of this study involves characterizing the trends in the cloud amount (CA) data. First of all, upon inspection of Figure 1, it is apparent that the downward trend in CA begins in 1987. Therefore, in order to not diminish the slope of the CA trend, all trends are found by performing linear regressions only to the subset of data beginning in January 1987. In order to study how the CA trend varies with time of year, the time series is then partitioned into 12 subsets – one for each month – and then a linear regression was performed on each to describe the trends as a function of month. Finally, in order to study the types of clouds that are most affected by this trend, the clouds are separated into the five categories described in Section 2. Each was then studied to find how the total CA trend manifests itself as a function of cloud type.

The second and most important part of this study is the statistical verification of the ISCCP cloud amount trend by examining how it correlates with the reanalysis datasets. It is important to keep in mind that two independent datasets will show high correlations if both exhibit trends or variations of the same frequency regardless of whether the two datasets are physically related. Therefore, the following steps are taken to reduce this possibility. First of all, the downward linear trend in the cloud amount dataset is removed. The monthly climatology is then removed in order to eliminate any signatures of a seasonal cycle from the cloud amount data. The time series that remains simply describes the variance of cloud amount about the long-term trend and the long-term monthly climatological mean. This time series will hereafter be referred to as the detrended CA time series.

To study how this time series is related to changes in large-scale dynamics, reanalysis data is used to generate maps of regression coefficients for each field described in section 2. In order to create these maps, the following steps are taken. Anomaly maps are created by removing the monthly climatology from each of the 219 monthly maps of a given field. Using all of these maps, a time series that describes how the anomaly field changes is generated for each point on the map. The detrended CA time series is then regressed onto and correlated with each of these time series. The map of regression coefficients shows where, and by how much, the field changes with a positive change in cloud amount. The map of correlation coefficients shows how the time series at each point correlates with the detrended CA time series. Using a 2-tailed Student's t-test at the 95% confidence level and 217 degrees of freedom, this map is then used to determine which regression coefficients are statistically significant. Finally, by taking the inner product of the regression map with each time step of the corresponding anomaly maps, the result is an expansion coefficient time series that shows how strongly the anomaly field for that month reflects the pattern of the regression map. This time series is important because, if the field in question is indeed related to the detrended CA time series, then the expansion coefficient time series and the detrended CA time series should be highly correlated. This procedure is then repeated for each of the reanalysis fields listed in section 2.2

4. RESULTS AND DISCUSSION

Figure 2 shows the spatial distribution of the global cloud amount trend shown in Figure 1. Of particular interest are the centers of action located in the tropical Pacific Ocean near the dateline and the positive trend located over Indonesia. The magnitudes of these trends are among the largest on the map, and it will be shown that these two centers of action appear regularly in most of the remaining analysis. Therefore, it is safe to say that these trends are robust. The spatial pattern of the trend near the dateline suggests that the cloud amount trends are symmetric about the equator, which suggests changes in the ITCZ cloudiness. This pattern also shows a possible trend in the South Pacific Convergence Zone (SPCZ). The gradient in the CA trend located near 60° East longitude appears to be suspicious, and is most likely due to limb darkening near the edges of the satellite field of view. Figure 3 shows the zonal mean CA trend as a function of latitude and a contour plot of how the zonal mean CA trend varies with time of year. From this plot, it is apparent that the negative CA trend is concentrated in the tropics and is most strongly negative in the winter and early spring. The CLAUS data, shown in Figure 4, shows a pattern that reflects the bimodal pattern of Figure 2 in that the centers of action are located over Indonesia and near the dateline and they have opposite signs.

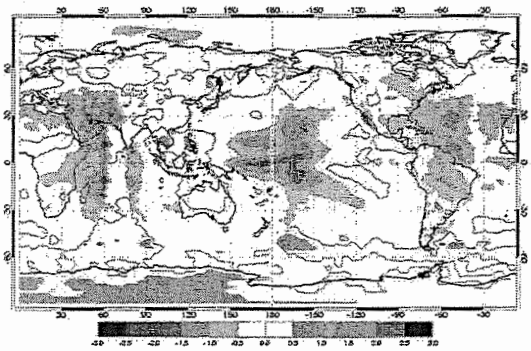

Figure 2: Map of ISCCP cloud amount trend for the years 1987-2001 as a function of spatial location. The map resolution is 2.5° x 2.5°. Contour units are in % cloud per year.

The CA trend manifests itself in different ways depending on cloud type, especially over the tropical Pacific. Low-level cloud shows only very slight trends, with a slightly negative trend over Indonesia and a near zero or slightly positive trend near the dateline. Middle clouds seem to change in a manner consistent with the patterns in Figure 2. Cirrus clouds appear to have the largest negative trend of all the cloud types over the tropical Pacific, but also show a negative trend over Indonesia. Stratocirrus clouds, however, seem to be strongly positive over Indonesia, but only slightly negative near the dateline. Deep convection also shows a weak negative trend on either side of the equator demonstrating that there may be a small change in the convection located in the ITCZ. These findings are not, however, obviously corroborated by brightness temperature trends from CLAUS data. There is an increase in brightness temperature over Indonesia, and a decrease near the dateline, neither of which obviously correspond to the changes as a function of cloud type. Further study is currently ongoing as to why this is the case. Figures for this portion of the study are available on the website.

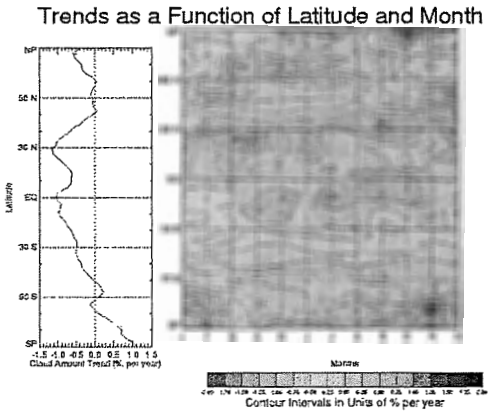

Figure 3: The zonal mean cloud amount trends as a function of latitude for the time period in Figure 2 (left), and as a function of latitude and month of year (right)

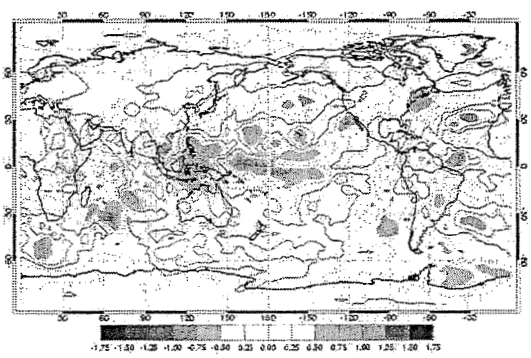

Figure 4: Map of CLAUS brightness temperature trends for the period 1987-1993 as a function of spatial location. The map resolution is 2.5° x 2.5°

Correlations to reanalysis fields are currently still being studied. However, some preliminary results seem to show evidence that there is a statistically significant correlation between changes in the tropical circulation and changes in cloud amount. For instance, for an increase in CA, there is evidence of increased 200 mb divergence and 850 mb convergence in the tropical Pacific near the dateline, and the opposite sign of both over Indonesia. Given this pattern, for an increase in CA it is likely that there is increased upward vertical motion over the tropical Pacific and decreased upward vertical motion over Indonesia. Increased 850 mb westerlies are also correlated with increased CA over the tropical Pacific. And not surprisingly, there is an increase in precipitation over the tropical Pacific near the dateline and there is a decrease in precipitation over Indonesia both of which correlate with an increase in the global CA. All of these features are statistically significant at the 95% level in all datasets. Therefore, there is ample reason to believe that the global cloud amount trend shown in Figure 1 is both real and robust. Since there are several figures for this portion of the study, the reader is directed to our website to examine the latest figures in support of these findings:
http://reef.atmos.colostate.edu/ellis/AMStalk.html.

5. REMAINING WORK

At this point, there are still several questions that need to be answered. First of all, it is important to examine the correlation between these CA trends and the El Nino – Southern Oscillation (ENSO) to examine how much of an effect ENSO has on the variability of cloud amount. The authors expect to see some correlation due to the fact that CA trends are significantly correlated with increased westerlies at low levels. Additionally, it would be instructive to study how the correlations with the reanalysis data vary as a function of time of year, especially since CA shows a strong seasonality. Therefore, the authors plan to generate maps similar to Figure 3 showing how the correlation and regression coefficients change as a function of latitude and time of year. Finally, since the data processing is nearly, but not yet complete, any examination of the possible climate feedbacks is premature at this time. However, by the start of the AMS conference, the authors hope to provide some insight into what, if any feedback mechanisms are detectable in the results of this study.

6. ACKNOWLEDGEMENTS

This work was partially funded by a one-year AMS Graduate Fellowship, and the authors are grateful for this support. The following sources also need to be acknowledged for their assistance in providing the data used in this study. The ISCCP data were obtained from the NASA Langley Research Center Atmospheric Sciences Data Center. CLAUS data were obtained via the British Atmospheric Data Centre. NCEP-NCAR Reanalysis data and CMAP data were provided by the NOAA-CIRES Climate Diagnostics Center, Boulder, Colorado, USA, from their web site at http://www.cdc.noaa.gov/. ERA-40 data were obtained via the ECMWF website. The authors' thanks go out to each of these groups for making their data available for this study. The GPCP combined precipitation data were developed and computed by the NASA/Goddard Space Flight Center's Laboratory for Atmospheres as a contribution to the GEWEX Global Precipitation Climatology Project. NOAA SST OI v.2 data were obtained via the LDEO/IRI Data Library. Finally, the authors would like to thank Dr. Christian Kummerow for his advice on which precipitation datasets would be appropriate for study.

7. REFERENCES

Barkstrom, B.R.: The Earth Radiation Budget Experiment (ERBE). *Bull. Amer. Meteor. Soc.*, **65**, 1170-1185.

Chen, J., B.E. Carlson, and A.D. Del Genio, 2002: Evidence for strengthening of the tropical general circulation in the 1990s. *Science*, **295**, 838-841.

Gibson, R., P. Kallberg, S. Uppala, A. Hernandez, A. Nomura, and E. Serrano, 1997: ERA description. ECMWF Reanalysis Project Report Series, Vol. 1, 86 pp. [Available from ECMWF, Shinfield Park, Reading RGZ 9AX, United Kingdom.].

Gibson, R., P. Kallberg, and S. Uppala, 1996: The ECMWF Re-Analysis (ERA) project. ECMWF Newsletter 73, 7–17. [Available from European Centre for Medium-Range Weather Forecasts, Shinfield Park, Reading, Berkshire RG2 9AX, United Kingdom.].

Hodges, K., D.W. Chappell, G.J. Robinson, and G. Yang, 2000: An improved algorithm for generating global window brightness temperatures from multiple satellite infrared imagery. *J. Atmos. And Ocean Tech.*, **17**, 1296-1312.

Huffman, G.J., and Coauthors, 1996: The Global Precipitation Climatology Project (GPCP) combined precipitation dataset. *Bull. Amer. Meteor. Soc.*, **77**, 5-20.

Kalnay, E.M., and Coauthors, 1996: The NCEP/NCAR Reanalysis Project. *Bull. Amer. Meteor. Soc.*, **77**, 437-471.

Lin, B., B.A. Wielicki, L.H. Chambers, Y. Hu, and K-M Xu, 2002: The iris hypothesis: a negative or positive feedback?, *J. Climate*, **15**, 3-7.

Lindzen, R., M.D. Chou, and A. Hou, 2001: Does the Earth have an adaptive iris?, *Bull. Amer. Meteor. Soc.*, **82**, 417-432.

Miller, R.L., 1997: Tropical thermostats and low cloud cover. *J. Climate*, **10**, 409-440.

Pierrehumbert, R., 1995: Thermostats, radiator fins, and the local runaway greenhouse. *J. Atmos. Sci.*, **52**, 1784-1806.

Reynolds, R.W., N.A. Rayner, T.M. Smith, D.C. Stokes, and W. Wang, 2002: An improved in situ and satellite SST analysis for climate. *J. Climate*, **15**, 1609-1625.

Rossow, W.B. and R.A. Schiffer, 1999: Advances in understanding clouds from ISCCP. *Bull. Amer. Meteor. Soc.*, **80**, 2261-2287.

Schiffer, R.A. and W.B. Rossow, 1983: The International Satellite Cloud Climatology Project (ISCCP) – the first project of the World Climate Research Project, *Bull. Amer. Meteor. Soc.*, **64**, 779-784.

Wielicki, B.A., and Coauthors, 2002: Evidence for large decadal variability in the tropical mean radiative energy budget. *Science*, **295**, 841-844.

Xie, P. and P.A. Arkin, 1997: Global precipitation: a 17-year monthly analysis based on gauge observations, satellite estimates, and numerical model outputs. *Bull. Amer. Meteor. Soc.*, **78**, 2539-2558.

SUPER-PARAMETERIZATION: GLOBAL CONTEXT FOR CLOUD-SCALE PROCESSES

Wojciech W. Grabowski[1], Marat Khairoutdinov[2], and David A. Randall[2]

[1] National Center for Atmospheric Research, Boulder, CO 80307 USA
[2] Colorado State University, Fort Collins, CO USA

1. INTRODUCTION: CLOUDS IN CLIMATE

Clouds play a fundamental role in the Earth's climate system through their impact on the Earth's radiation budget and their role in the water and energy cycles. As far the impact on radiation budget is concerned, this is best illustrated by globally- and seasonally-averaged top-of-the-atmosphere (TOA) shortwave and longwave cloud forcings. These forcings are defined as differences (separate for shortwave and longwave radiation) between the TOA radiative fluxes for the column with clouds and the fluxes for a hypothetical column from which all clouds have been removed. The longwave cloud forcing is positive (i.e., clouds warm the Earth in this part of the spectrum) and its magnitude is about 30 W m^{-2}. The shortwave cloud forcing, dominated by the reflection of solar radiation back to space, is negative (i.e., cooling effect) and approximately equal to –50 W m^{-2}. The overall impact of clouds on the climate system (a sum of the shortwave and longwave cloud forcings) is a net cooling of about 20 W m^{-2}. This number can be compared with climate forcings by greenhouse gases other than water vapor (such as carbon dioxide, methane, etc.) estimated at 2-4 W m^{-2} and the direct impact of atmospheric aerosols (about -1 W m^{-2}). The impact of clouds on water and energy cycles is obvious: precipitation develops inside clouds and associated latent heating is a footprint of microphysical processes once precipitation falls out.

At the same time, however, representation of clouds in large-scale models is challenging. This is because clouds are typically subgrid-scale horizontally (e.g., convective clouds) and often vertically (e.g., stratocumulus, cirrus). Moreover, clouds, unlike trace gases, are dynamically active with cloud microphysics and cloud dynamics strongly coupled at small scales. This microphysics-dynamics coupling is important for several reasons. First, moist processes span a wide range of spatial and temporal scales and are responsible for convection organization as highlighted by the mesoscale convective systems in the tropics and over midlatitude summertime continents. Secondly, cloud dynamics and cloud micro-physics are responsible for the formation of precipitation and development of cloud particle size distribution, which is important for the cloud-radiation interactions. These processes are relatively well understood at the cloud scale, but their global impacts remain ambiguous.

Arguably, a cloud-system-resolving atmospheric general circulation model (AGCM) is needed to quantify the role of cloud-scale processes in the climate system. Such a model, perhaps feasible on most powerful computers today (like the Earth Simulator at the Japanese Frontier Research System for Global Change) is about 5 to 6 orders of magnitude more computationally demanding than traditional climate models. Consequently, it is difficult to envision application of such a model to century-long climate change simulations in the near future. However, a different modeling approach, the cloud-resolving convection parameterization (CRCP), often referred to as the super-parameterization, was proposed recently to improve representation of cloud and mesoscale processes in contemporary AGCMs. In this paper, we briefly describe CRCP and illustrate its application to idealized and realistic climate simulations.

2. THE CLOUD-RESOLVING CONVECTION PARAMETERIZATION (CRCP)

CRCP was proposed by Grabowski and Smolarkiewicz (1999) and applied in idealized aquaplanet simulations by Grabowski (2001; 2003a) and to the climate system by Khairoutdinov and Randall (2001) and Khairoutdinov et al. (2004). The cornerstone is to apply a 2D cloud-resolving model in each column of a 3D large-scale model to represent subgrid-

Corresponding author's address: Wojciech Grabowski, National Center for Atmospheric Research, PO Box 3000, Boulder, CO 80307 USA; E-Mail: grabow@ncar.ucar.edu

scale processes. In the spirit of classical convection parameterization, which assumes scale separation between convection and large-scale flow, the cloud-resolving models from neighboring columns interact only through the large-scale dynamics.

The scientific basis for CRCP comes from numerous numerical studies of moist convection driven by observed large-scale conditions over a period of many days. These modeling studies demonstrate that a 2D computational framework results in cloud systems whose integral effects (including effects on surface and radiative processes) mimic both observations and 3D simulations. Thus, a 2D cloud-scale model inside each column of the 3D large-scale model should be capable of explicitly representing the interaction between moist convection and large-scale flow, convection organization, and the effects of convection on surface and radiative processes. CRCP is computationally expensive because the cost of running a large-scale model with CRCP is almost entirely due to cloud-resolving calculations. Moreover, limitations of the CRCP associated with the assumed scale separation between large-scale and cloud-scale dynamics have to be kept in mind. For instance, mesoscale convective systems are not capable of propagating from one model column into the neighboring one (see section 3 of Grabowski 2001 and Randall et al. 2003 for discussions).

In principle, one can include all relevant small-scale processes (radiative transfer, surface processes, boundary-layer processes, chemical processes, etc) into a dynamic framework of the cloud-scale model. As a result, a "super-parameterization" of these processes can be developed.

3. CRCP IN CLIMATE MODELING

The idealized simulations concern convective-radiative quasi-equilibrium on a constant-SST ("tropics everywhere") aquaplanet, with the same size and rotation as Earth. This problem was extensively discussed in Grabowski (2001, 2003a) and specific results presented here are discussed in detail in Grabowski (2003b). As far as the dynamics are concerned, the simulations feature spontaneous formation of coherent structures within the equatorial waveguide, with deep convection on the leading edge and strong surface westerly winds to the west, the westerly wind bursts. These coherent structures resemble the Madden-Julian Oscillation (MJO) observed in the terrestrial tropics. No large-scale organization of convection is present outside the equatorial waveguide.

Grabowski (2003b) discusses the impact of cloud microphysics on global convective-radiative quasi-equilibrium. The results suggest that cloud microphysics impact quasi-equilibrium temperature and moisture profiles substantially, but the relative humidity is only weakly affected. Small cloud and precipitation particles result in a climate that is warmer and moister. This is explained by the impact of cloud microphysics on the coupling between convection and surface exchange during the approach to quasi-equilibrium. When prescribed radiative cooling is used, the upper-tropospheric cloud fraction is much higher when cloud and precipitation particles are assumed small (see figure 1a). This is consistent with small sedimentation velocity for small cloud and precipitation particles. With the interactive radiation, however, the upper-tropospheric quasi-equilibrium cloud fraction is approximately the same for small and large cloud and precipitation particles (figure 1b). This is explained by the evolution (during the approach to quasi-equilibrium) of the of mean cloud fraction profiles as a results of cloud-radiation interactions, explicitly treated by the super-parameterization.

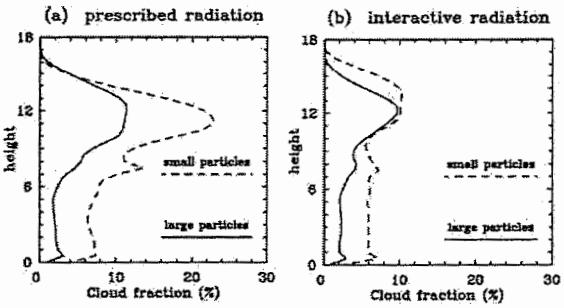

Figure 1. Quasi-equilibrium globally-averaged profiles of the cloud fraction for CRCP simulations of convective-radiative quasi-equilibrium on a rotating constant-SST aquaplanet applying (a) prescribed radiative cooling and (b) interactive radiation transfer model. Results from simulations that assume small (large) cloud and precipitation particles are shown using dashed (solid) lines.

Similar impact of cloud-radiative interactions is observed in simulations that apply CRCP in the atmospheric part of the Community Climate System Model, the Community Atmospheric Model (CAM), see Khairoutdinov et al. (2004). As an illustration, figure 2 compares the JJA (Jun, July, and August) low-level cloud fractions from two simulations driven by observed spatial and

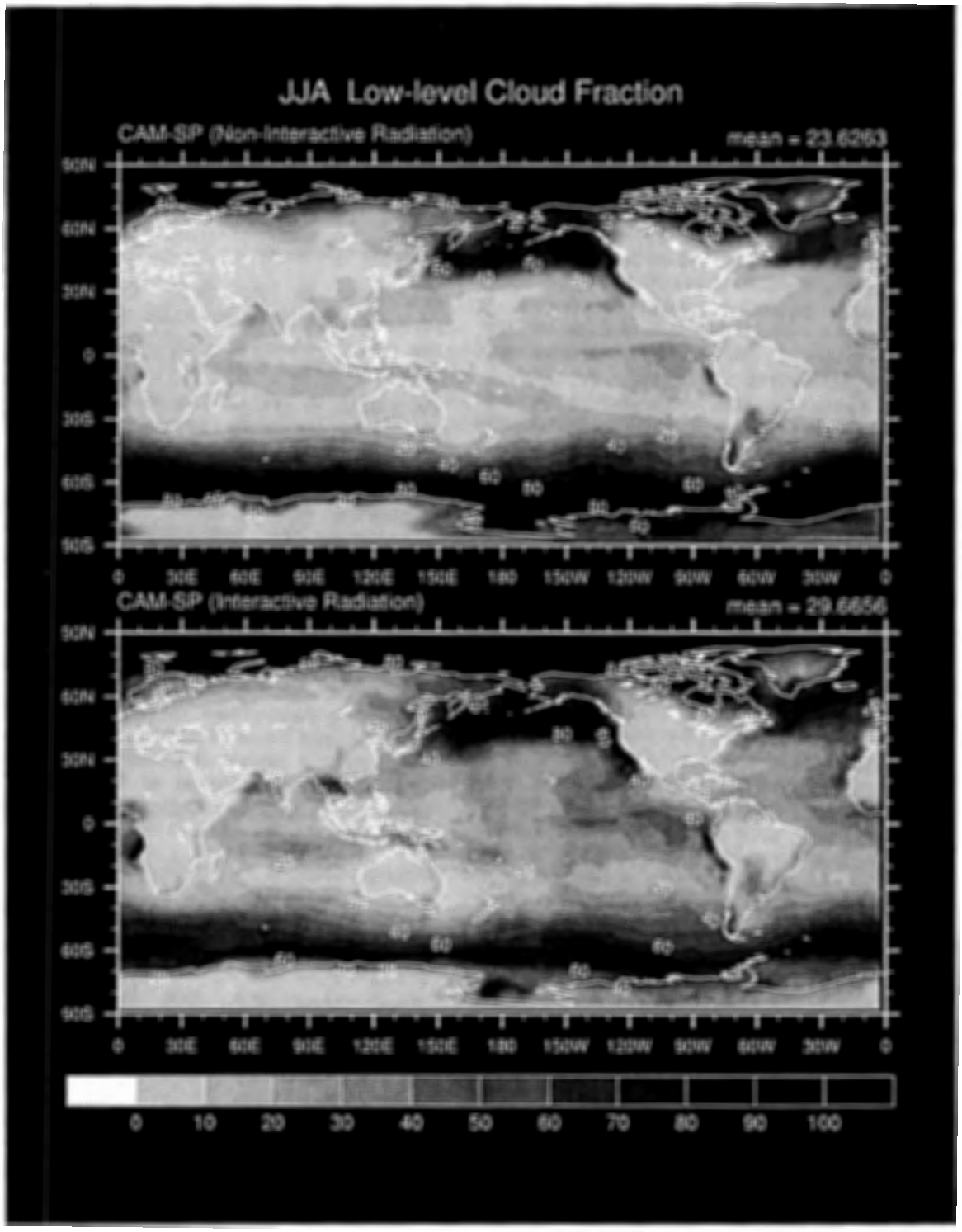

Figure 2. Geographical distribution of the mean cloud fraction due to low-level cloudiness for summer months (JJA) in CRCP CAM simulations applying radiation transfer model either on averaged CRCP fields (i.e., no small-scale cloud-radiation interactions; upper panel) or within CRCP domains (i.e., including small-scale cloud-radiation interactions; lower panel).

temporal distribution of the sea surface temperature. The first simulation uses only CRCP-averaged cloud information (such as cloud fraction, condensate mixing ratio, etc) in the radiative transfer (upper panel). The second simulation applies radiative transfer model within CRCP and hence allows for small-scale cloud-radiative interactions (lower panel). As Fig. 2 shows, the interactive radiation simulation results in more realistic values of low-level cloud fractions in the tropics and in the subtropics. In particular, subtropical low-level cloudiness along the west coasts of major continents is significantly improved. These regions are well known to exhibit unrealistic low-level cloudiness in standard AGCMs.

In summary, both idealized aquaplanet simulations and realistic climate simulations show importance of cloud-scale interactions between clouds and radiation, explicitly treated when radiative transfer is performed within CRCP. Such interactions are difficult (if not impossible) to capture in traditional climate models.

4. CONCLUSIONS

Clouds play a fundamental role in atmospheric general circulation. Traditional approaches to represent ("parameterize") clouds in large-scale models offer very limited framework to address the role of cloud processes in the Earth's climate and climate change. To move forward, global cloud-system-resolving models are needed. Unfortunately, such models are not expected to be practical for years, if not decades, to come. The super-parameterization allows cloud and mesoscale processes to be included in current models of weather and climate. It has already proven useful in the context of climate research. As far as numerical weather prediction is concerned, CRCP is unlikely to be a promising approach for traditional short-term and medium range forecasts where spatial resolutions of a few tens of kilometers are typically used. However, CRCP might prove useful for seasonal prediction, which is typically performed using models with low horizontal resolution, as in climate studies. Although large-scale models with CRCP use more than 99% of the computational cost for cloud-resolving calculations, such models are "embarrassingly parallel" and run efficiently on parallel computers with thousands of processors. CRCP offers an attractive compromise between a high-cost cloud-system-resolving global model, where all scales from cloud to global are resolved and coupled, and a low-cost traditional climate model, where representation of cloud-scale and mesoscale processes is questionable at best.

5. REFERENCES

Grabowski, W. W., 2001: Coupling cloud processes with the large-scale dynamics using the Cloud-Resolving Convection Parameterization (CRCP). J. Atmos. Sci., 58, 978--997.

Grabowski, W. W., 2003a: MJO-like coherent structures: Sensitivity simulations using the Cloud-Resolving Convection Parameterization (CRCP). J. Atmos. Sci., 60, 847--864.

Grabowski, W. W., 2003b: Impact of cloud microphysics on convective-radiative quasi-equilibrium revealed by Cloud-Resolving Convection Parameterization (CRCP). J. Climate, 16, 3463--3475.

Grabowski, W. W., and P. K. Smolarkiewicz, 1999: CRCP: A Cloud Resolving Convection Parameterization for Modeling the Tropical Convecting Atmosphere. Physica D, 133, 171--178. (Special Issue: Predictability: Quantifying Uncertainty in Models of Complex Phenomena, 18th Annual Conference of the Center for Nonlinear Studies, Los Alamos, NM, USA, 11-15 May 1998).

Khairoutdinov, M. F., and D. A. Randall, 2001: A cloud resolving model as a cloud parameterization in the NCAR Community Climate System Model: Preliminary results. Geophys. Res. Let., 28, 3617-3620.

Khairoutdinov, M.F., D.A. Randall, and C. DeMotte, 2004: Simulations of the atmospheric general circulation using a cloud-resolving model as a super-parameterization of physical processes. J. Atmos. Sci. (submitted).

Randall, D., M. Khairoutdinov, A. Arakawa, and W. Grabowski, 2003: Breaking the cloud-parameterization deadlock. Bull. Amer. Meteor. Soc., 84, 1547--1564.

THE EFFECT OF CLOUDS ON THE SHORTWAVE RADIATION BUDGET ON GLOBAL SCALE

G.P. Habilomatis and N. Hatzianastassiou

Laboratory of Meteorology, Physics Department, University of Ioannina, 45110 Ioannina, Greece

1. INTRODUCTION

Clouds cover about 67% of the Earth's surface (Rossow and Schiffer, 1999) and they are very important for climate and climate changes (Liou and Ou, 1989), since they affect profoundly the radiative budget of the Earth-atmosphere system, exerting thus a strong influence on temperature structure and general circulation of the atmosphere (Gupta et al.,1993). Clouds reflect about 30% of the incoming solar radiation at TOA (Wild et al., 1998), producing a cooling, while they present the escape of longwave (LW) radiation, producing a warming of the Earth-atmosphere system. The balance between the cloud impact on shortwave (SW) and LW radiation is subtle (IPCC, 2001), and may be altered by a change in any of a good number of parameters: cloud cover at different levels, cloud water content (for liquid water and ice) and cloud droplet (or crystal) equivalent radius, cloud asymmetry factor or single scattering albedo, which depend on cloud composition, and most notably on their phase. Thus, it is very important to be able to determine as accurately as possible the effect of clouds on SW and LW radiation, in order to asses their net climatic effect. The term cloud radiative forcing (CF), which is the difference between the cloud-free radiation budget climatology, F^{clear}, and the average over all scene types, F^{all}, (Eq.1) has been adopted to describe the effect of clouds on radiation.

$$CF = F^{clear} - F^{all} \qquad (1)$$

The CF defined at the top of atmosphere (TOA) is very important, since it represents the overall effect of clouds on surface-atmosphere system. Globally distributed values of CF can be obtained either with models or from satellite data. The former technique requires an appropriate representation of clouds in the models, in terms of various cloud properties. However, the highly parameterized cloud processes and interactions still represent one of the main uncertainties in climate modeling (Chen and Roeckner, 1997). A number of published works have given estimates of cloud forcings (e.g. Harrison et al., 1990; Stephens and Greenwald, 1991; Hartmann, 1993; Rossow and Zhang, 1995; Chen and Roeckner,1997;, Hatzianastassiou and Vardavas, 1999) which indicate a disagreement. Nevertheless, all studies show that the SW cloud forcing (SWCF) dominates the LWCF one. Another technique is to use satellite observations to infer the components F^{clear} and F^{all} of Eq.1, and hence CF values. Given the advance in satellite technology during the last decades, this technique became very attractive. Especially, the high instrument accuracy, and the improved spatial and temporal resolution of Earth Radiation Budget Experiment (ERBE, Barsktrom et al., 1989) provides valuable data to compute CF values. Gupta et al.(1993) used ERBE data to derive SWCF and LWFC values at both surface and TOA for the midseasonal months of April, July, and October 1985 and January 1986. Hartmann (1993) provided global distributions of CF values for seasons, based on two years data (1985-1986) from ERBE scanning instruments.

In this study, 5-year (1985-1989) data from ERBE-S4 scanner data are used to determine the SWCF at TOA. The SWCF values are computed from Eq.1 in terms of outgoing SW radiation at TOA. Mean values over the 5-year period are computed as well as mean hemispherical and global values, along with annual means, which all provide a valuable analysis of the effect of clouds on SW radiation on global scale.

2. THE DATA USED

The 5-year (1985-1989) mean monthly 2.5-degree equal angle SW (0.2-5 μm) data were taken from the ERBE S4 high-accuracy monthly scanner data products, distributed by the NASA Langley Research Center Atmospheric Sciences Data Center (ASDC). The ERBE S4 scanner data have been collected from scanning radiometers on the three ERBE satellites for combined satellite cases. The ERBE instruments were launched on the NASA Earth radiation Budget Satellite (ERBS), and the two National Oceanic and Atmospheric Administration (NOAA) polar orbiting satellites: NOAA-9 and NOAA10. The ERBE S4 data used in this study cover the time periods during which the scanners were operational: November 1984-February 1990 for ERBS; February 1985-January 1987 for NOAA-9; and November 1986-May 1989 for NOAA10. The NOAA-9 and the NOAA-10 satellites provide global coverage, while the ERBS provides coverage between 67.5° north and south latitude.

3. RESULTS AND DISCUSSION

The global distribution of SWCF values forcings averaged over the 5-year period (1985-1989) for the midseasonal months of January, April, July and October, are given in Figs. 1a-d. In January, clouds generally increase the reflected SW radiation at TOA,

Corresponding author's address: Dr. Nikos Hatzianastassiou, Laboratory of Meteorology, Physics Department, University of Ioannina, 45110 Ioannina, Greece; E-Mail: nhatzian@cc.uoi.gr.

by up to 200 W m-^{2} at pixel level, producing thus a strong cooling effect of the Earth-atmosphere system. The largest (negative) CF values are found along the storm track zone of Southern Hemisphere (50°-70°S), which is characterized by large low-level cloud amounts. Large CF values, up to –100 Wm^{-2} also occur along the Intertropical Convergence Zone (ITCZ) over tropical convective areas with high-level clouds, such as South America, South Africa and Indonesia (Fig.1a). In contrast, clouds decrease the outgoing SW radiation at TOA by up to 40 Wm^{-2} (planetary heating) over areas with high surface albedo, such as Greenland, Arctic Ocean and, especially, Antarctica. The decrease in outgoing SW radiation in these cases, is due to multiple scattering of solar radiation between clouds and highly reflected ice- or snow–covered surfaces underneath. Corresponding features appear also for April, July and October, but with SWCF values ranging from -170 to 40 Wm^{-2}. In general, SWFC values are modulated by insolation, whereas they are largest over areas with extensive cloud amounts, for example over the North Atlantic storm tracks in July. The SWCF values are generally larger over ocean than land areas, due to larger contrast between cloud and surface albedo values.

Figure 2 shows the time series of mean monthly SWCF values averaged over the north and southern hemispheres and over the globe. For the Northern hemisphere, SWCF varies between about –35 Wm^{-2} and –70 Wm^{-2}, while for the South Hemisphere it varies between -37 and –80 Wm^{-2}, roughly, with maximum values in summer, and minimum in winter for both hemispheres. The seasonal variations of the two hemispheres cancel out each other, so that the global mean SWCF has a much weaker seasonal variation, equal to about 10 Wm^{-2} (from –45 to –55 Wm^{-2}), showing primary and secondary maxima, in summer of southern and northern hemisphere, respectively. SWCF is found to decrease over the 5-year period, by 1.92 Wm^{-2} for the Northern Hemisphere, while it increases by 2.5 Wm^{-2} for the Southern one. However, on global scale, SWCF is found to have increased slightly, by 0.3 Wm^{-2}. These small tendencies have to be investigated in detail, to identify their sources. It is also very important to extend time series beyond 1990, by using either other satellite sources (though this is not very easy through

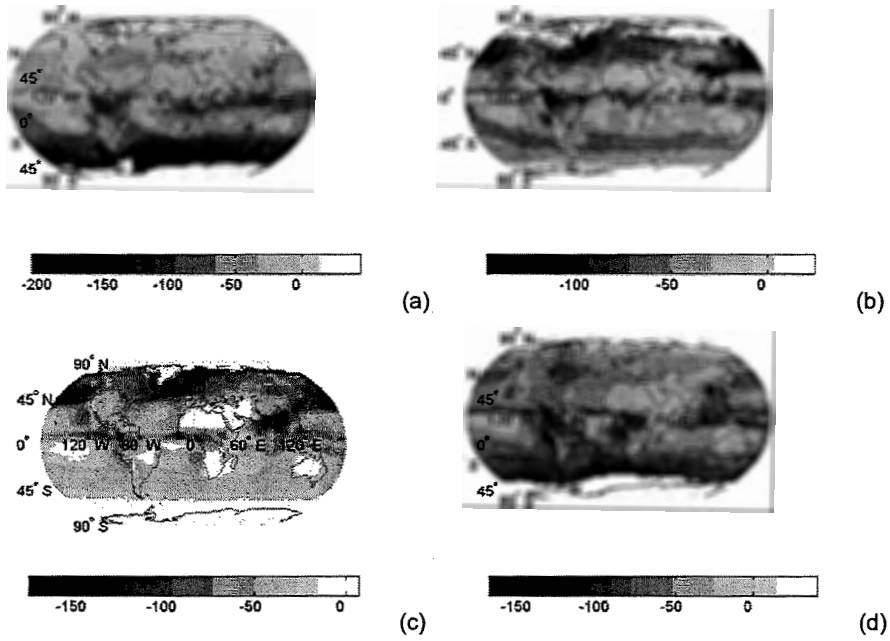

Figure 1. Global distribution of cloud radiative forcing at the top of atmosphere, averaged from 5-year (1985-1989) ERBE data, for the mid-seasonal months of (a) January, (b) April, (c) July and (d) October.

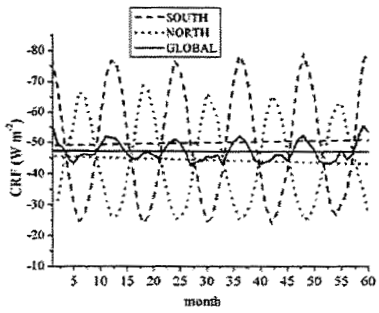

Figure 2. Time series (January 1985 to December 1999) of monthly mean cloud radiative forcing (CRF) at the top of atmosphere averaged over the globe and the two hemispheres, and associated linear trends.

the end of '90s due to lack of available continuous data) or by using accurate models.

The hemispherical and global averages of CRF (Fig.3b) show a significant seasonal variation, with summer maximum and winter minimum values. CRF ranges from –26 to –67 Wm^{-2} (annual amplitude of 41 Wm^{-2}) for the North Hemisphere, against –24 and –80 Wm^{-2} (annual amplitude as 56 Wm^{-2}) for the Southern one. The seasonalities of CRF hemispherical averages are opposite, so that the globally averaged CRF values have a small annual range, equal to 8.5 Wm^{-2}, with small local maxima in December and June.

Table 1. Year by year and 5-year (1985-1989) average annual mean cloud radiative forcing (in W m^{-2}) at the top of atmosphere for the northern (NH) and southern (SH) hemispheres and the globe. The interhemispherical differences (NH-SH) are also given.

	1985	1986	1987	1988	1989	1985-1989
NH	-45.6	-45.1	-43.3	-43.6	-43.8	-44.3
SH	-50.4	-49.5	-49.2	-49.6	-51	-49.9
NH-SH	4.8	4.4	5.9	6.0	7.2	5.6
GLOBE	-48	-47.3	-46.2	-46.6	-47.4	-47.1

The latitudinal and seasonal variation of the averaged CRF values over the 5-year period (1985-1989) are given in Figs. 3a,b. The mean annual 10-degree latitudinal averages of CRF vary between 14 and –93 Wm^{-2}, indicating a cooling of the Earth-atmosphere system, induced by clouds. Our absolute maximum CRF value is larger by about 20 Wm^{-2} than that (-75 Wm^{-2}) given by Hartmann (1993), but based on 2 years' (1985-1986) ERBE data. The largest radiative effect of clouds (cooling) is found between 40° and 70°S, where clouds increase the outgoing SW radiation at TOA by up to about 95 Wm^{-2}. There are also local maximum values in equatorial areas (of about -60 Wm^{-2}), and also in the northern mid latitudes, i.e over areas with large cloud amounts. Note that CRF decreases in magnitude poleward of 40°N and 60°S, reaching near zero values at the north pole, while the become positive (15 Wm^{-2}) in the zone 80°-90°S, i.e over Antarctica's plateau.

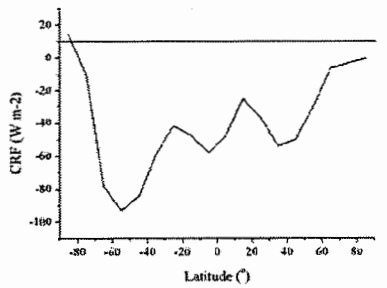

(a)

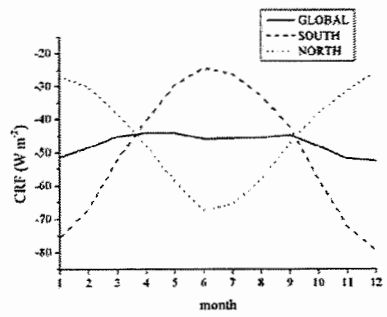

(b)

Figure 3. (a) Ten-degree latitudinal zonal variation of annual mean cloud radiative forcing (CRF) at the top of atmosphere, and (b) seasonal variation of cloud radiative forcing at the top of atmosphere, averaged over the globe and the two hemispheres.

Table 1 shows the computed hemispherical and global averages of mean annual CRF values for every year from 1985 to 1989, as well as for the whole 5-year period. The Southern hemisphere has systematically larger CRFs than the Northern one by 4.4 - 7.2 Wm^{-2}. The interhemispherical difference of CRF is found to increase during the period 1987-1989 with respect to 1984-1985, which is probably attributed (at least partly) to the shift from NOAA-9 to NOAA-10 satellite. Overall, based on the 5-year ERBE data, clouds are found to cool our planet by 47.1 Wm^{-2}, while they cool the North and South hemispheres by 44.3 and 49.9 Wm^{-2}, respectively. The corresponding values given by Hartmann (1993) from 2-year ERBE data, are equal to 48, 46 and 50 Wm^{-2}. In the future, it is planned to compute CRF values over more extended time periods reaching recent years, by using modelling techniques that have been already applied, but on a zonal mean basis (Hatzianastassiou and Vardavas, 1999), by using recent satellite data (e.g. ISCPP-D2, Rossow et al., 1996) which provide a global coverage.

4. REFERENCES

Barkstrom, B., Harrison, E., Smith, G., Green, R., Kibler, J., Cess, R., and ERBE science team, 1989: Earth Radiation Budget Experiment (ERBE) archival and April 1985 results, Bull. Am. RMeteorol. Soc., 70, 1254-1262.

Chen, C.-T., and Roeckner, E., 1997: Validation of the Earth radiation budget as simulated by the Max Planck Institute for Meteorology general circulation model ECHAM4 using satellite observations of the Earth Radiation Budget Experiment, J. Geophys. Res., 101, 4269-4287.

Gupta, S. K., Staylor, W. F., Darnell, W. L., Wilber, A. C., and Ritchey, N. A., 1993: Seasonal variation of surface and atmospheric cloud radiative forcing over the globe derived from satellite data, J. Geophys. Res., 98, 20671-20778.

Harrison, E. F., Minnis, P., Barkstrom, B. R., Ramanathan, V., Cess, R. D., and Gibson, J. J., 1990: Seasonal variation of cloud radiative forcing derived from the Earth Radiation Budget Experiment, J. Geophys. Res., 95, 18687-18703.

Hartmann, D. L., 1993: Aerosol-Cloud-Climate Interactions, Radiative effects of clouds on Earth's climate, International Geophysics Series, Vol. 54, P. Hobbs, Acad. Press Inc., 151-173.

Hatzianastassiou, N. and Vardavas, I., 1999: The net radiation budget of the Northern Hemisphere, J. Geophys. Res., 104, 27341-27359.

Intergovernmental Panel on Climate Change (IPCC): Climate Change 2001, The Scientific Basis, 881 pp., edited by J. T. Houghton et al., Cambridge Univ. Press, New York, 2001.

Liou, K. N. and Ou, S.-C., 1989: The role of cloud microphysicsl processes on climate: an assessment from a one dimensional perspective, J. Geophys. Res., 94, 8599-8607.

Rossow, W. B. and Zhang, Y.-C., 1995: Calculation of surface and top of atmosphere radiative fluxes from physical quantities based on ISCCP data sets 2. Validation and first results, J. Geophys. Res., 100, 1167-1197.

Rossow, W. B. and Schiffer, R. A., 1999: Advances in understanding clouds from ISCCP, Bull. Am. Meteorol. Soc., 80, 2261-2287.

Rossow, W. B., Walker, A. W., Beuschel, D. E. and Roiter, M. D., 1996: International Satellite Cloud Climatology Project (ISCCP). Documentation of new cloud datasets, 115 pp., Wold Meteorol. Org. Geneva.

Stephens, G. L. and Greenwald, T. J., 1991: The Earth's radiation budget and its relation to atmospheric hydrology: Observations of cloud effects, J. Geophys. Res., 96, 15311-15324.

Wild, M., Ohmura A., Gilgen H., Roeckner E., Giorgetta M. and Morcrette J.-J, 1998: The disposition of radiative energy in the global climate system: GCM-calculated versus observational estimates, Clim. Dyn., 14, 853-869.

SEASONAL VARIATIONS OF CLOUDS, AEROSOLS AND SHORTWAVE RADIATION OVER CHINA

Tadahiro Hayasaka[1], Kazuaki Kawamoto[1] and Jianqing Xu[2]

[1]Research Institute for Humanity and Nature, Kyoto 602-0878, Japan
[2] Frontier Research System for Global Change, Yokohama 236-0001, Japan

1. INTRODUCTION

The recent growth of economy in East Asian region is being watched with keen interest. It is pointed out from many of aerosol studies that aerosols have been increasing with an increase in energy consumption in this region, for example, fossil fuel consumption in China has increased factor of 2.5 since 1980. soil dust particles in spring season, in addition to the above aerosols, are also considered to be important related to land use change and desertification. These anthropogenic aerosols may give rise to the indirect effect on the earth's climate system.

In the present study, downward shortwave radiative flux (F_{SW}) on the surface around China for the period of 1984 -1995 are evaluated from ISCCP data and ground-based measurement data, and analyzed with cloud properties obtained from ISCCP data and those retrieved from satellite data by ourselves.

2. AEROSOL CHANGES DUE TO HUMAN ACTIVITIES

Since many of aerosol measurements had been carried out from the point of view of its influences on human health, there are not many studies on the long term monitoring available for climate studies. We reviewed about 200 papers for East Asia in order to evaluate current status of aerosol observational studies such as the optical depth, scattering coefficient, absorption coefficient, single scattering albedo, complex refractive index, mass concentration, number concentration, size distribution, vertical profile, horizontal distribution and chemical composition. Among them, as a result, it is valid to use direct solar radiation over the total wavelength in order to study long-term variability more than 20 years, since this kind of measurement has been conducted continuously with the same principle. Spectral measurements of direct solar radiation are also useful in the past few decades. According to the review, it is pointed out inland heavy industrial cities have large optical depths such as Chongqing and Chengdu (Luo et al., 2001). As for long-term trend, the aerosol optical depth had increased after 1960 all over China, and then seemed to be stable in 1980's. SO2 emission inventory by Streets and Waldhoff (2000), however, show an increasing trend still in 1980's and 1990's. On the other hand, the seasonal variation is different among the locations (Qiu et al., 2000). In big cities such as Beijing, aerosol optical thickness is large in spring and summer because of Yellow Sand storm and anthropogenic sulfate aerosols, whereas it becomes large in winter in rural aera such as Wulumuqi.

Corresponding author's address: Tadahiro Hayasaka, Research Institute for Humanity and Nature, Kyoto 602-0878, Japan; E-Mail: hayasaka@chikyu.ac.jp

3. CLOUD PROPERTIES

We used NOAA/AVHRR GAC data as well as ISCCP data to investigate cloud properties such as cloud amount, cloud optical thickness, and effective particle radius.

It is inferred from ISCCP cloud analyses that low-level cloud amount is more important in spring rather than optical thickness, while optical thickness as well as cloud amount is also important in summer. It is also found that spatial variations of these cloud properties change year to year.

We retrieved cloud amount, optical thickness and effective particle radius of low-level clouds from NOAA/AVHRR data, based on the reflection method (Nakajima and King, 1990). This method basiclly uses visible and near infrared channels, by comparing the data and theoretical calculations. In order to avoid the errors in the retrieval due to cloud inhomogeneity, data with scanning angle less than 25 degree were used (Iwabuchi and Hayasaka, 2002). Results of AVHRR analysis suggest that aerosols strongly affect not only cloud amount but also effective particle radius and optical thickness, for example, small cloud particles and large optical thickness are observed around Sichuan basin corresponding to aerosol optical thickness distribution. In autumn and winter, effective particle radius is smaller than summer. Low-level cloud system is affected by aerosols in boundary layer and thus aerosol indirect effects become more important.

4. SHORTWAVE RADIATIVE FLUX

It is difficult to estimate spatial and temporal variations of surface radiative flux in a wide area. We used the F_{SW} data set provided by NASA Langley Research Center, which are calculated from ISCCP data (Gupta, 2000?). Another data set calculated from ground based measurements of meteorological items were also used. The ground-based data were calculated from sunshine duration and water vapor measurements. ISCCP-based and ground-based radiation data are in general consistent with each other for monthly average values.

Figure 1 shows a typical distribution of F_{SW} which is calculated from ISCCP data It is found that F_{SW} over China has seasonal variations as follows. In spring and summer, large values of F_{SW} extend over desert and semi-desert area in the north part of China, whereas F_{SW} in the southern part is small. These properties are associated with front system. It is inferred from ISCCP cloud analysis that low-level cloud amount is more important in spring rather than optical thickness, while optical thickness as well as cloud amount is also important in summer. In autumn and winter, spatial variation of F_{SW} is small except for the minimum value around Sichuan basin where heavy aerosol loading is always observed.

5. SUMMARY

Shortwave radiative flux on the surface in East Asia were discussed, related to cloud and aerosol properties. In this region, it is suggested that indirect effect of aerosol is conspicuously observed in autumn and winter, particularly in the southern part of China.

Acknowledgements

We would like to thank Drs. P. W. Stackhouse Jr. and S. Gupta for providing surface radiation data set calculated from ISCCP data.

References

Gupta, S. K., N. A. Ritchey, A. C. Wilber, C. H. Whitlock, G. G. Gibson, and P. W. Stackhouse Jr., 1999: A climatology of surface radiation budget derivedfrom satellite data. *J. Climate*, **12**, 2691-2710.

Iwabuchi, H. and T. Hayasaka, 2002: Effects of cloud horizontal inhomogeneity on the optical thickness retrieved from moderate-resolution satellite data. *J. Atmos. Sci.*, **59**, 2227-2242.

Luo, Y., D. Lu, X. Zhou, and W. Li, 2001: Characteristics of the spatial distribution and yearly variation of aerosol optical depth over China in last 30 years. *J. Geophys. Res.*, **106**, 14501-14513.

Nakajima, T. and M. D. King, 1990: Determination of the optical thickness and effective particle radius of clouds from reflected solar radiation measurements. Part I: Theory. *J. Atmos. Sci.*, **47**, 1878-1893.

Qiu, J. and L. Yang, 2000: Variation characteristics of atmospheric aerosol optical depths and visibility in North China during 1980-1994. *Atmos. Environ.*, **34**, 603-609.

Streets, D. G. and S. T. Waldhoff, 2000: Present and future emissions of air pollutants in China: SO2, Nox, and CO. *Atmos. Environ.*, **34**, 363-374.

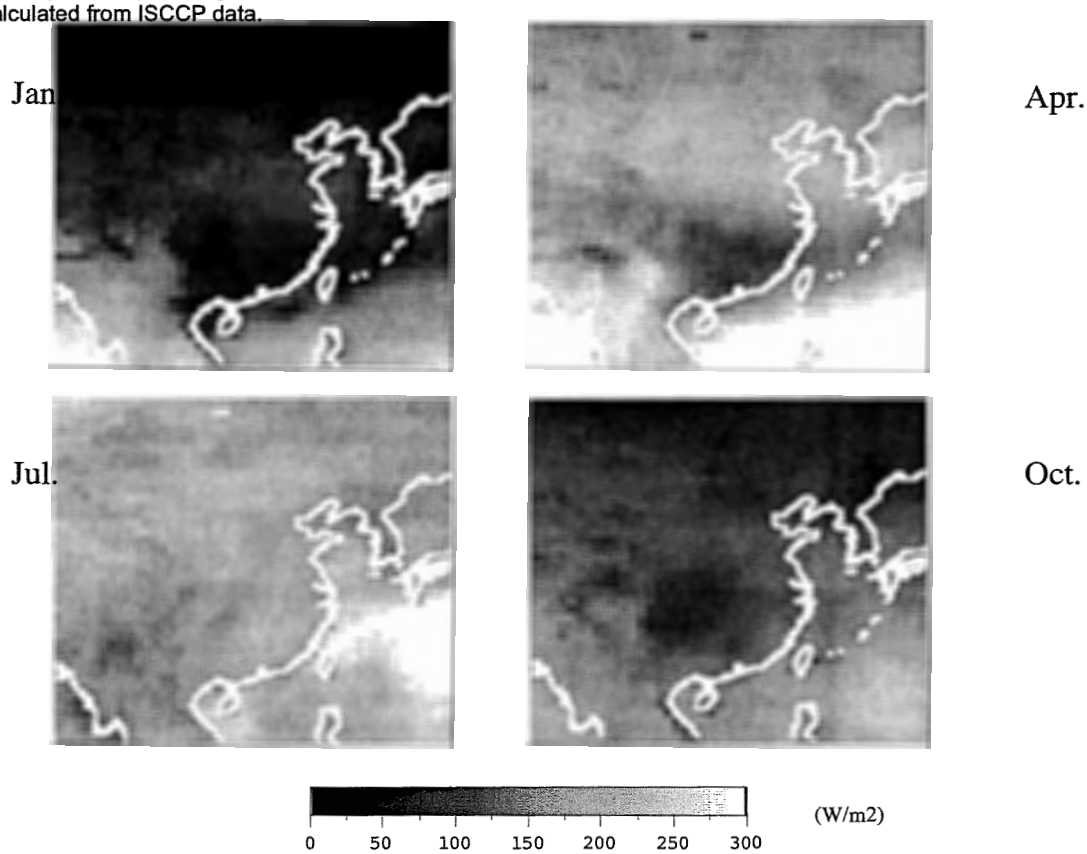

Fig. 1. Shortwave sueface radiative flux in 1995 over China estimated from satellite data.

ESTIMATION OF FRACTIONAL SKY COVER, CLOUD TYPE AND CLOUD FORCING EFFECTS AT TERRA NOVA BAY STATION (75°S) FROM BROADBAND RADIATION MEASUREMENTS.

C. Lanconelli[1], A. Lupi[1], M. Nardino[1,2], V. Vitale[1], P.Calzolari[1], F. Evangelisti[1], U. Bonafè[1], G. Trivellone[1] and D. Bortoli[1,3]

[1]Institute of Atmospheric Sciences and Climate (ISAC-CNR), Bologna, Italy
[2]Institute for Biometeorology (IBIMET-CNR), Bologna, Italy
[3]Geophysics Centre of Évora, Évora University, Évora, Portugal

1.- INTRODUCTION

Clouds exert a large influence on the earth's climate by virtue of their radiative properties both in the solar and thermal-infrared spectral regions, and because of their role in the hydrological cycle. Especially in the polar regions, clouds are known to act as a critical forcing factor on the radiation budgets at the top of the atmosphere and at the surface, Yamanouchi et al. (1984). Unfortunately, the lack of surface observations is one of the most severe impediments in determining the effects produced by clouds on the radiative balance, by realistically separating them from those induced by the cryosphere. Thus, observational data are crucial, especially in climatic areas where the sensitivity of the surface-atmosphere system to clouds is more pronounced in order to both improve the parametrization schemes to be inserted into climatic models and test their results.

The short-wave and long-wave radiation flux measurements performed in Antarctica (75°S) at the Italian station of Terra Nova Bay (TNB) during austral summer since 1999, were analysed in order to estimate cloud coverage and cloud type characteristics during the summer season and identify behaviour than can be considered as typical of the Ross Sea coastal region.

2.- MEASUREMENTS

All radiation measurements were carried out at the Icaro Camp site, located on the coast 2 km southward from TNB base (74° 43' S 164° 07' E). Accurate surface measurements of the four radiation balance terms were obtained by using a CNR-1 Kipp & Zonen radiometer, while simultaneous measurements of the diffuse and direct components of the incoming solar radiation flux were carried out by using a MFR-7 shadowband radiometer (YES Inc.).

Both instruments were placed at a height of about 2.5 meters above the surface to avoid the obstruction of Icaro Camp containers, so as to obtain a 2π field of view which was (i) almost free of obstacles toward the sea side for azimuth angles from 5° to 210°, where the reliefs were all lower than 5°, and (ii) without too prominent reliefs in the hinterland sector from 210° to 5°, where the angular height of obstacles varied between 5° and 7° from 210° to 280° azimuth angle, between 7° and 10° from 280° to 310°, and between 3° and 7° from 310° to 5°. The measurements continuously performed by the four CNR-1 sensors were separately sampled in 3-second time-intervals and stored in terms of average values calculated over 1-minute inter-vals together with the corresponding standard deviations. The MFR-7 spectral measurements were carried out with a frequency of one scanning every 20 seconds and then stored as average values obtained for 1-minute periods. The 10-minutes averages were also evaluated and stored.

Corresponding author's address: Christian Lanconelli, Institute of Atmospheric Sciences and Climate (ISAC-CNR), Via Gobetti, 101, I-40129 Bologna, Italy; E-mail: c.lanconelli@isac.cnr.it

3.- CLOUD AMOUNT AND CLOUD TYPE

Estimates of total cloud cover from solar radiation measurements can be obtained through proper parameterizations of the cloud effects on global and diffuse measured irradiances, Kasten et al. (1980), Long et al. (1999) or through automatic classification techniques, Calbo et al. (2001). Both methods require the evaluation of the downwelling global shortwave irradiance under clear sky conditions.

In order to evaluate clearness conditions at TNB, we made use of the algorithm proposed by
Long and Ackerman (2000) to identify, for the austral summers from 1999 to 2002, cloudless conditions Clear sky irradiances for 0° solar zenith angle were found to range between 1200 and 1280 Wm^{-2} over the whole data-set, being the 95% confidence interval between 1220 and 1250 Wm^{-2}. These results clearly indicate that during the summer season atmospheric trans-parency conditions along the Ross Sea coast are stable and slightly influenced by variations in water vapour and aerosol amounts.

Making use of these results, as well as of measured global and diffuse irradiances in 1 minute resolution, we evaluate a cloud cover index over 15 min time intervals, applying the two parametric algorithms cited above. Mean values from early November to early February were found, for both methods, to range between 0.4 and 0.55 from one year to the other, with standard deviations around 0.4. These results clearly indicate that heavy cloudy conditions can be frequently

found during summer, as a conse-quence of synoptic weather systems reaching the coastal area of TNB from northern latitudes.

Empirical parameters as well as regression relationships employed in the two algorithms were obtained for very different surface physical characteristics and surface-atmosphere radiative features. Therefore, in order to validate these methodologies for TNB and determine reliability of our results, we compared them with human observations regularly carried out each 6 hours by the TNB weather-office. Cover indexes values and synoptic observations were divided in four intervals, so as to obtain 16 different classes.

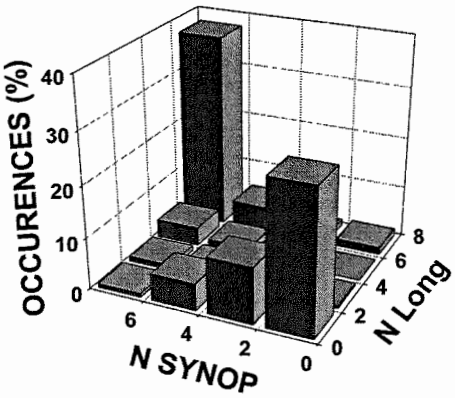

Figure 1 - Comparison of cover sky fractions in octas as obtained from human observations and the Long et al. (1999) estimation technique.

The results for the Long et al. (1999) estimation technique are given in Figure 1. As can be seen, clear sky and overcast conditions were quite well identified, while scattered clouds and intermediate conditions appear to be misclassificated. In particular, at TNB the Long et al. (1999) technique, with the settings we used, produces cloud amount estimates somewhat lower than those from observer reports when the total cloud cover ranges between 2 and 5 oktas. These results could of course be made to agree by adjustment of the limits and settings used in the Long et al. (1999) technique, but here we used the "typical" settings as suggested by the authors, which are based on a definition related to minimal radiative impact on te downwelling shortwave radiation (Long and Ackerman, 2000).

Other differeces could arise from the different location of human observations and radiation measurements and the complex orography of TNB area. Unfortunately, the data-set was not yet so wide to allow as to deeply investigate these features through a statistical analysis based on observed cloud type. Similar results were obtained for the the Kasten and Czeplack (1980) method.

Cloud type classification were obtained by using the Duchon and O'Malley (1999) criteria. The results are shown in Figure 2. As can be seen, the results indicate on a yearly base an occurrence frequency ranging between about 10% and 15% for all cloud classes identified by the procedure. Clear sky conditions were found to range between 26% to more than 40%. The relatively high percentage of cumulus clouds, and the fact that similar percentages were also found in the two measurement sites of Hells Gate (HG) and Nansen Ice-sheet (NIS), 20 km south TNB and 5 km and 15 km inside, respectively, Nardino et al. (2003), confirms that cloudiness in the TNB area is frequently related to cyclonic systems reaching the Antarctic coast from northern latitudes. On the contrary, since stratus clouds appear to be present with similar percentages above Icaro Camp and HG, and with very low percentage above NIS, this type of cloud seems to be mainly related to local meteorological conditions. The large number of cases in which the procedure did not allows us to identify cloud type or clear sky conditions, ranging between 18% and 30%, clearly suggest that further improvements are needed in the Duchon and O'Malley methodology, when it is applied to measurements carried out at the TNB observation site.

By using human observations recorded in the synop messages regularly compiled by meteo-office, we obtained an independent cloud classification for the summer season over the last ten years, based on 4 daily observations. To compare these results with those evaluated with the Duchon and O'Malley (1999) procedure, we reduced synop information to the 5 classes of the automatic procedure. Mean values for cirrus, cumulus, cum+cirrus, stratus and clear sky were found to be 10% ± 1.9%, 16% ± 7.4%, 11% ± 6.4%, 40% ± 10.9% and 27% ± 10.8%, respectively.

4.- SW AND LW CLOUD FORCING

The daily mean values of the surface radiation fluxes as obtained for three of the four measurement campaigns are plotted in Figure 3 as a function of the daily mean values of the cloud cover index *N*. As a function of the cloud amount only, cloud influence on the three components of the surface radiation budget presents a large variability up to more than 50%, as a consenquence of both cloud type influence and high variability of overall surface albedo during summer season.

An average measure of the dependence rates of the surface radiation budget components on the cloud amount can be given in terms of linear best-fit line. Such slope coefficient is expected to yield merely an estimate of the order of magnitude of the variation rate per unit variation of the cloud cover index, since in general the dependence features of radiation fluxes on *N* are very far from the linear regime, as pointed out by Bintanja et al. (1996), and shown by Figure 3. Slope coefficients were found to be equal to -234 Wm^{-2},

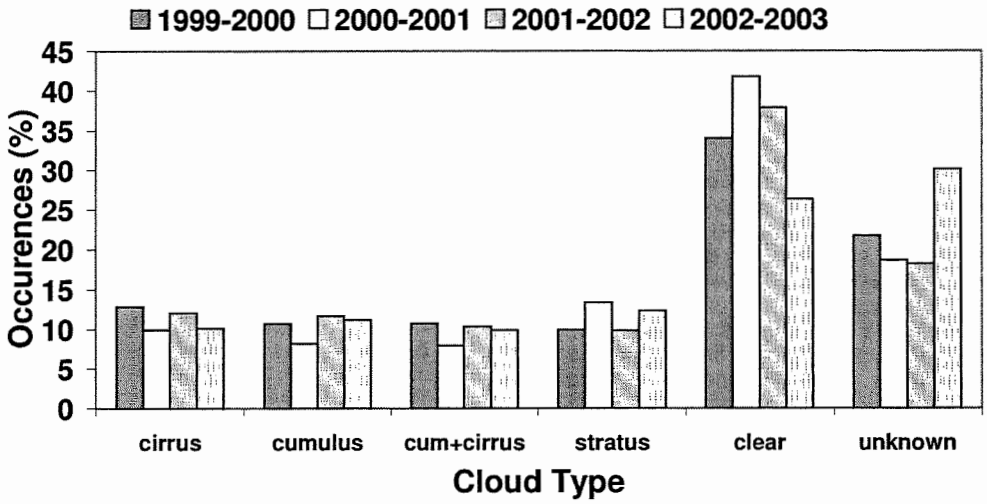

Figure 2 - Relative frequency histogram of cloud-type classes obtained for the four measurements campaigns by following the procedure proposed by Duchon and O'Malley (1999).

+121Wm^{-2} and -112Wm^{-2}, for net SW, net LW and net radiation, respectively. Differences with evaluations obtained at other Antarctic stations, Yamanouchi et al. (1995), Bintanja et al. (1996), can be mainly attributed to the high frequency, during summer, above TNB station of clouds with high liquid water content and to low values of surface albedo, usually ranging between 0.4-0.5.

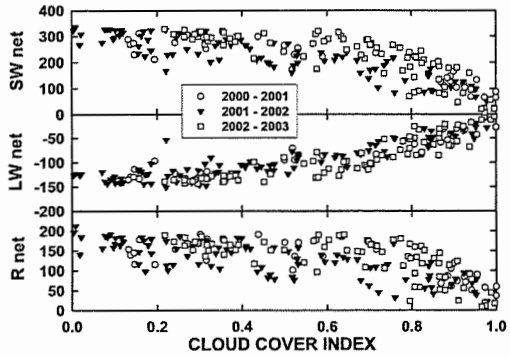

Figure 3 - Daily mean values of the three surface radiation budget components, net SW, net LW and net radiation fluxes versus the daily mean values of the cloud cover index for the last three measurement campaigns.

Making use of the clear-sky expected irradiances, obtained following the Long and Ackerman (2000) procedure, we evaluated the cloud effects on the shortwave fluxes. Daily (24 hour) average cloud effect results for the 2002-2003 measurement campaign are shown in Figure 4. With the exception of January 11, total shortwave cloud effect was always negative, ranging between 0 and -272 Wm^{-2}. All days the decrease in shortwave irradiance at the surface was due to attenuation of the direct component alone, partially compensated for by an increase in the diffuse irradiance. Also during severe storms, like those occurred January 20-24, diffuse cloud effect resulted to be positive. Daily average cloud transmittance was found to reach minimum values of 0.25, and frequently range below 0.5. For the four campaigns the total cloud effect averages were found to be -86 Wm^{-2}, -96 Wm^{-2}, -73 Wm^{-2} and -96 Wm^{-2}.

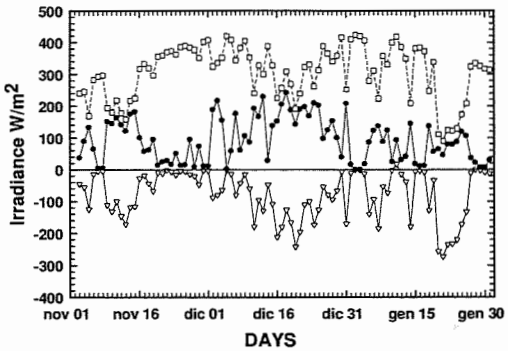

Figure 4 - Daily average total (open inverse triangle) and diffuse (black circle) shortwave cloud effect for 2002-2003 measurement campaign. Squares represent the total downwelling measured shortwave irradiance daily average.

5.- CONCLUSIONS

The present results clearly show that clouds can produce important radiative effects on the radiation balance terms at the surface, as measured in the coastal region of TNB. Overall cloud effect on the net radiation fluxes is negative, so that clouds contribute to cool the PBL during the summer season. This overall result, and the dependence features of such effects induced by the variations in the cloud cover conditions turn out to be strictly related to specific characteristics of this area, in particular to the low values assumed by the surface albedo during the summer season.

On the other hand, some of the variable dependence features of the surface radiation balance terms on cloud cover parameters can arise partially from unusual meteorological conditions, such as the particularly high values of temperature and/or relative humidity in the middle and high troposphere, favouring the formation of stratified clouds characterised by high optical density. These conditions should be responsible of the main part of the large variability observed during the summer season as well as of the large interannual variability. Thus, the present results are preliminary. An analysis carried out over longer measurement periods scheduled in several years should enable us to define more accurately and realistically the cloud radiative effects occurring in the TNB region and to investigate more deeply their time-variations during the local summer season.

6.- ACKNOWLEDGEMENTS

The authors wish to acknowledge Charles N. Long for providing the computational programme for clear sky identification and shortwave cloud effect calculations, with modifications for our input format. The Antarctic campaigns were funded by the PNRA (Italian National Programme for Antarctic Research).

7.- REFERENCES

Bintanja R. and M.R. Van den Broeke, 1996: The influence of clouds on the radiation budget of ice and snow surface in Antarctica and Greenland in summer. *Int. Jour. Climatol.*, **16**, 1281-1296.

Calbo, J., 2001: A Method for sky-condition classification from ground-based solar radiation measurements. *J. Appl. Meteor.*, **40**, 2193-2199.

Duchon C. E. and M.S. O'Malley, 1999: Estimating cloud type from pyranometer observations. *Jour. Appl. Meteor.*, **38**, 132-141.

Kasten F. and G. Czeplak, 1980: Solar and terrestrial radiation dependent on the amount and type of cloud. *Solar Energy*, **24**, 177-189.

Long, C.N., J.J. DeLuisi and J. Augustine, 1999: Estimation of fractional sky cover from broadband SW radiometer measurements. Preprints *10th Conf. on Atmospheric Radiation*, Madison, WI, Amer. Meteor. Soc., 383-386.

Long, C.N. and T.P. Ackerman, 2000: Identification of clear skies from broadband pyranometer measurements and calculation of downwelling shortwave cloud effects. *J. Geophys. Res.*, **105**, 15.609-15.626.

Nardino, M. and T. Georgiadis, 2003: Cloud type and cloud cover effects on the surface radiative balance at several polar sites, *Theor. Appl. Climatol.*, **74**, 203-215.

Yamanouchi T. and S. Kawaguchi, 1984: Longwave radiation balance under a strong surface inversion in the katabatic wind zone, Antarctica, *J. Geophys. Res*, **89**, 11771- 11778.

Yamanouchi T. and T.O. Charlok, 1995: Comparison of radiation budget at TOA and surface in the Antarctic from ERBE and ground surface measurements, *J. Climate*, **8**, 3109-3120.

SENSITIVITY STUDIES OF CIRRUS CLOUDS FORMED BY HETEROGENEOUS FREEZING IN THE ECHAM GCM

Ulrike Lohmann[1,*], Bernd Kärcher[2] and Johannes Hendricks[2]
[1] Department of Physics and Atmospheric Science, Dalhousie University, Halifax, N.S., B3H 3J5, Canada.
[2]DLR Institute for Atmospheric Physics, Wessling, Germany.

1. INTRODUCTION

Cirrus clouds can form by homogeneous and heterogeneous freezing at temperatures below 235 K. While homogeneous freezing of supercooled aqueous phase aerosol particles is rather well understood, understanding heterogeneous freezing is in its infancy. Koop et al. (2000) showed that nucleation rates of supercooled aqueous aerosol particles can be parameterized as a function of temperature and the water activity of the aerosol particles; the latter can reasonably well be approximated by the ambient relative humidity for the purpose of global model applications.

In the climate modeling framework, Lohmann and Kärcher (2002) started to account for cirrus formation by homogeneous freezing using a parameterization derived from theory and validated by adiabatic parcel model simulations (Kärcher and Lohmann, 2002a) employing the water activity concept by Koop et al. (2000). In the light of the findings described above, it is important to evaluate the global impact of heterogeneous freezing on cirrus cloud formation and lifetime. At the moment, we have no parameterization that can describe the observed competition between heterogeneous and homogeneous freezing so that the simulations described in this study will be limited to either pure homogeneous or heterogeneous freezing. It is, however, necessary to start with comparing pure homogeneous freezing with pure heterogeneous freezing in order to understand their differences in terms of cirrus cloud properties and their impact on cloud radiative properties. Only in this framework will we later on be able to understand the competition between homogeneous and heterogeneous freezing in a global modeling framework.

In this study we use the parameterization of heterogeneous freezing as described in Kärcher and Lohmann (2003). It is restricted to immersion freezing as the most likely heterogeneous freezing pathway for cirrus formation at temperatures below 238 K (DeMott et al., 1997). The exact nature (immersion mode or deposition mode) of the heterogeneous freezing process is not important for our sensitivity studies. The key factors controlling the impact of heterogeneous freezing in the model are the freezing threshold relative humidity and the total concentrations of available ice nuclei, both of which will be varied.

As for homogeneous freezing, immersion freezing is formulated in terms of the water activity such that the water activity is shifted towards smaller values for heterogeneous freezing. The shift may depend on temperature, as suggested by the experimental results of DeMott et al. (1999) and Zuberi et al. (2002) but could also depend on other variables required to characterize the heterogeneous freezing process (Kärcher and Lohmann, 2003). Our empirical approach has the advantage that (i) it reduces to homogeneous freezing for pure particles, (ii) is simple to comprehend and straight forward to apply and (iii) can be fitted to any experimental data. In most practical cases, the volume fraction of the immersed solid particle is not an important factor in determining the freezing threshold for mixed particles.

2. MODEL DESCRIPTION

The ECHAM4 general circulation model (GCM) (Roeckner et al. 1996) used in this study is described in Lohmann et al. (2003). Prognostic aerosol variables are the mass mixing ratios of sulfate, methane sulfonic acid, hydrophilic and hydrophobic organic carbon, hydrophilic and hydrophobic black carbon, sub- and supermicron dust, and sub- and supermicron sea salt. Transport, dry and wet deposition, and chemical transformations of the aerosols and gaseous precursors are calculated on line with the GCM.

We convert the mass of each aerosol component into a particle number concentration assuming that the size distribution of the total aerosol can be approximated as a four-mode lognormal distribution as described in Lohmann et al. (2003). The prognostic cloud

*Corresponding author's address: Ulrike Lohmann, Dept. of Physics and Atmospheric Science, Dalhousie Univ., Halifax, N.S. B3H 3J5, Canada; e-mail: Ulrike.Lohmann@Dal.Ca, URL: http://www.atm.dal.ca/~lohmann

variables are the mass mixing ratios of cloud liquid water and cloud ice for large-scale clouds and their number concentrations.

Cloud ice can originate from depositional growth during large-scale ascent or from detrainment of deep convective clouds. The homogeneous and heterogeneous nucleation rates of cirrus clouds formed by large-scale ascent requires that the grid box is supersaturated with respect to ice. This simplified assumption will not be necessary any longer once we incorporate a more sophisticated method to allow for subgrid scale fluctuation of temperature and humidity, which is not yet available in the case of cirrus clouds. In the case of detrainment, the detrained ice water is added to the ice water content of the large-scale ice clouds. The large-scale ice crystal number concentration is assumed to be unaffected. In case that detrainment occurs within a grid box that is not supersaturated, the detrained ice is sublimated and the ice crystal number concentration is set to a minimum value of 10^{-5} cm^{-3}.

In our reference simulation (simulation HOM), the number of newly frozen ice crystals N_i at temperatures below $-35°$ C is obtained from the parameterization of homogeneous freezing by Kärcher and Lohmann (2002b) that takes the effects of the aerosol size distribution on N_i into account. N_i is a function of the vertical velocity, temperature and supersaturation with respect to ice. The parameterization scheme considers a multimodal aerosol size structure, with an arbitrary number of modes each of which is characterized by a lognormal distribution. Consequently, the parameterization is called by ECHAM with the number mode radius of the freezing particles prior to freezing, along with a total number density and a geometric width for each mode. We consider a bimodal aerosol size distribution, consisting of an accumulation mode and a coarse mode as used in Lohmann et al. (2003) in accordance with observations (Dubovik et al. 2002). The accumulation mode aerosol consists of carbonaceous aerosols, sulfate species and submicron sea salt, i. e. comprises the two smallest size classes mentioned above. The coarse mode corresponds to our third size class consisting of supermicron sea salt and the smaller size dust. The largest size dust hardly reaches the upper troposphere and is therefore neglected for homogeneous freezing. Also, very fine sulfate particles present in the nucleation and Aitken mode size ranges are neglected here since such fine particles are of secondary importance for cloud formation. The mode radii and standard deviations in each of the two aerosol size modes are averaged from the corresponding size distribution parameters of each lognormally distributed aerosol species weighted by its total particle number concentration.

In ECHAM, we obtain the mesoscale updraft velocity w needed for ice crystal formation as the sum of the grid mean vertical velocity and a turbulent contribution expressed in terms of the turbulent kinetic energy (TKE) (Lohmann and Kärcher 2002:

$$w = \overline{w} + 0.7\sqrt{TKE} \tag{1}$$

While this is a crude approximation to account for subgrid-scale variability of the vertical wind, this choice of the turbulent contribution in conjunction with the underlying advective transport scheme leads to a reasonable representation of the relative humidity in ice-supersaturated regions and of grid-box averages of the total ice crystal number density in cirrus, as shown by Lohmann and Kärcher (2002) and Kärcher and Ström (2003).

All simulations were conducted in T30 horizontal resolution with 19 vertical levels and a 30 minute time-step over a period of 3 years after an initial spin-up of 3 months using climatological sea surface temperatures and sea ice extent. In the reference simulation HOM cirrus formation is based on homogeneous freezing including aerosol size effects (Kärcher and Lohmann (2002). To study heterogeneous freezing, we conduct two sensitivity studies. In the first scenario, we assume that all the aerosols available for homogeneous freezing, freeze effectively at 130% relative humidity with respect to ice (simulation HOM130%). That is, we only replaced the temperature dependent freezing threshold for homogeneous freezing by a constant value of 130% relative humidity. With that, this experiment represents an upper limit for the number of freezing nuclei. In the other simulation we assume that only soot and mineral dust trigger heterogeneous freezing as shown by experimental results of DeMott et al. (1999) and Zuberi et al. (2002) using the same freezing relative humidity of 130% (simulation HET130%). The freezing relative humidity of 130% is taken for simplicity. In principle, we could have employed the explicit temperature dependence found in DeMott et al. (1999) and Zuberi et al. (2002) but it is unclear how to extrapolate these values for black carbon outside their measured values. However, reducing the threshold freezing relative humidity to 105% or enhancing it to 150% changes the vertically integrated ice crystal number by only 1% because the limiting factor is the scarcity of the number of freezing nuclei. Thus, even taking the observed freezing thresholds would hardly change the results. Therefore, we will subsequently only concentrate on contrasting simulations HOM, HOM130% and HET130%.

3. RESULTS

The number concentrations of hygroscopic aerosols

that can freeze homogeneously in simulation HOM and the ice nuclei concentration from simulation HET130% are shown in Figure 1. It shows that the ice nuclei concentration amounts to between 0.1 and 5% of the hygroscopic aerosol number concentration in the zonal mean. The fraction is highest in the lower troposphere because the dust and black carbon number concentration decrease more rapidly with height than some of the aqueous species like sulfate and MSA that are formed by gas-to-particle conversion within the atmosphere. This figure also shows that the ice crystal concentration is limited by the number of ice nuclei at altitudes above 600 hPa. Recall that we assume that only black carbon and dust act as ice nuclei. In comparison, homogeneous freezing is only limited by the number of hygroscopic aerosols in the tropical upper troposphere where vertical velocities are large and the number of aerosols is small. Because of this limitation, ECHAM4 studies showed that the Mt. Pinatubo eruption enhanced the ice crystal number concentration formed by homogeneous freezing in this region (Lohmann et al., 2003).

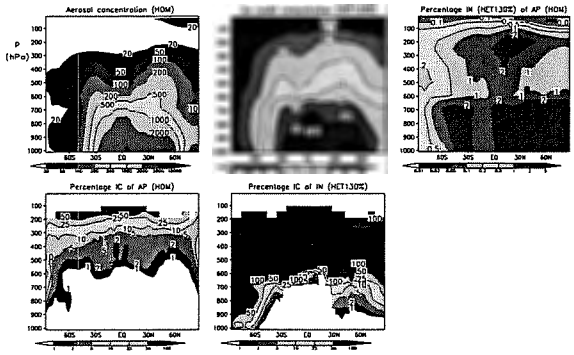

Figure 1: 3-year average of the annual zonal mean latitude versus pressure cross sections of (a) number concentration of hygroscopic aerosols in simulation HOM (cm^{-3}), (b) ice nuclei (IN) concentration consisting of mineral dust and black carbon (cm^{-3}) in simulation HET130%, (c) the fraction of IN to hygroscopic aerosols (AP) (%), (d) fraction of ice crystals (IC) in the cloudy part of the grid box to AP (%) in simulation HOM, and (e) fraction of IC in the cloudy part of the grid box to IN (%) in simulation HET130%. (a)-(c) are averages over cloudy and cloud-free periods.

The number of ice crystals formed by homogeneous and heterogeneous freezing in cirrus clouds in ECHAM is calculated from the difference of the newly formed ice crystals minus the previously existing ones. As shown in Figure 2, the highest ice crystal formation rates in simulation HOM are associated with topographically induced high vertical velocities over the Rocky Mountains, the Himalayas, Greenland and Scandinavia. Secondary maxima are found over midlatitude storm tracks and in anvil cirrus formed from deep convection where the relative humidity can be very high. If homogeneous freezing commences at 130%, then more ice crystals form and more water vapor is converted into cloud ice but the regional pattern remain similar. Most of the maxima simulated in HOM vanish in HET130% where the ice crystal formation rates is limited by the ice nuclei concentration. Here maxima are restricted to regions with high amounts of black carbon and/or dust such as South East Asia, Europe and Africa.

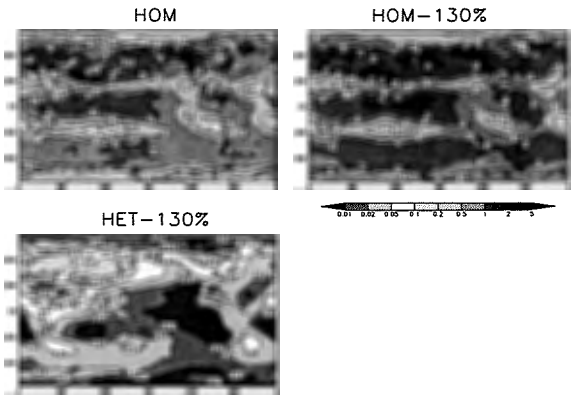

Figure 2: 3-year average of the annual mean vertically integrated number of newly formed ice crystals by homogeneous and heterogeneous freezing in cirrus clouds (particles cm^{-2} s^{-1}) including cloudy and cloud-free periods for the simulations HOM, HOM130% and HET130%.

The impact of the different nucleation schemes on the zonal mean ice crystal number concentration and ice water content is shown in Figure 3. The ice water content is averaged over cloudy and cloud-free regions and periods whereas the number of ice crystals is averaged only over cloudy regions and periods. Maxima in ice water content and ice crystal number concentrations in simulation HOM are associated with anvil cirrus outflow from deep convection in the tropics and with extratropical cyclones. Arctic ice clouds are also characterized by a high ice crystal number concentration of up to 2 cm^{-3} but at lower ice water contents. The vertically integrated ice crystal aggregation and accretion rate is not that much smaller in the Arctic than at midlatitudes (not shown) but the nucleation rate is smaller in the Arctic than in midlatitudes, so that the high ice crys-

tal concentrations are likely caused by advection from mid latitudes. Ice crystal number concentrations of this order of magnitude have been observed in the Arctic by the forward scattering spectrometer probe (FSSP) (Lohmann et al., 2001) but there is an ongoing debate as to how reliably ice crystal measurements can be inferred from the FSSP, as, for instance, discussed by Field et al. (2003).

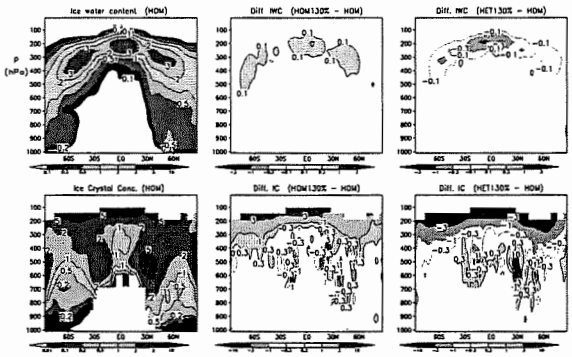

Figure 3: 3-year average of the annual zonal mean latitude versus pressure cross sections of ice water content (IWC) (mg kg^{-1}) including cloudy and cloud-free periods and ice crystal number concentrations (IC) (cm^{-3}) averaged only over cloudy periods for the simulation HOM, and the differences HOM130% - HOM, and HET130% - HOM. Areas with less than 1% of cloud occurrences are not shown.

When homogeneous freezing commences at 130% relative humidity with respect to ice, i. e. almost unlimited ice nuclei are assumed, then the number of ice crystals is increased by up to 3 cm^{-3} (Kärcher and Lohmann, 2002) and the ice water content is increased by up to 0.3 mg kg^{-1} in the zonal mean. If the number of freezing nuclei is limited by the number of dust and black carbon aerosols, the ice crystal number concentrations are lowered by more than 1 cm^{-3} in the upper troposphere. The largest decreases of more than 10 cm^{-3} occur in the tropics at 150 hPa. The fewer particles grow to larger sizes and with that increase the global mean precipitation rate and decrease the ice water content by up to 1 mg kg^{-1}.

References

DeMott, P. J., D. C. Rogers, and S. M. Kreidenweis, 1997: The susceptibility of ice formation in upper tropospheric clouds to insoluble aerosol components, *J. Geophys. Res.*, *102*, 19,575–19,584.

DeMott, P. J., Y. Chen, D. C. Rogers, S. M. Kreidenweis, and D. E. Sherman, 1999: Ice formation by black carbon particles, *Geophys. Res. Lett.*, *26*, 2429–2432.

Dubovik, O., B. N. Holben, T. F. Eck, A. Smirnov, Y. J. Kaufman, M. D. King, D. Tanre, and I. Slutsker, Variability of absorption and optical properties of key aerosol types observed in worldwide locations, *J. Atmos. Sci.*, *59*, 590–608, 2002.

Field, P. R., R. Wood, P. R. A. Brown, P. H. Kaye, E. Hirst, 2003: R. Greenaway, and J. A. Smith, Ice particle interarrival times measured with a fast FSSP, *J. Atmos Ocean. Techn.*, *20*, 249–261.

Kärcher, B. and U. Lohmann, 2002a: A parameterization of cirrus cloud formation: Homogeneous freezing of supercooled aerosols. *J. Geophys. Res.* **107**, 10.1029/2001JD000470.

Kärcher, B., and U. Lohmann, 2002b: A parameterization of cirrus cloud formation: Homogeneous freezing including effects of aerosol size, *J. Geophys. Res.*, *107*, doi: 10.1029/2001JD001429.

Kärcher, B., and U. Lohmann, 2003: A parameterization of cirrus cloud formation: Heterogeneous freezing, *J. Geophys. Res.*, *108*, doi: 10.1029/2002JD003220, 2003.

Kärcher, B., and J. Ström, The roles of dynamical variability and aerosols in cirrus cloud formation, *Atmos. Chem. Phys.*, *3*, 823–838, 2003.

Koop, T., Luo, B., Tsias, A. and Peter, T. 2000: Water activity as the determinant for homogeneous ice nucleation in aqueous solutions. *Nature* **406**, 611–614.

Lohmann, U., J. Humble, W. R. Leaitch, G. A. Isaac, and I. Gultepe, 2001: Simulations of ice clouds during FIRE.ACE using the CCCMA single column model, *J. Geophys. Res.*, *106*, 15,123–15,138.

Lohmann, U. and Kärcher, B. 2002: First interactive simulations of cirrus clouds formed by homogeneous freezing in the ECHAM GCM. *J. Geophys. Res. 107*, doi: 10.1029/2001JD000767, 2002.

Lohmann, U., B. Kärcher, and C. Timmreck, 2003: Impact of the Mt. Pinatubo eruption on cirrus clouds formed by homogeneous freezing in the ECHAM GCM, *J. Geophys. Res.*, *108*, doi: 10.1029/2002JD003185.

Roeckner, E., Arpe, K., Bengtsson, L., Christoph, M., Claussen, M., Dümenil, L., Esch, M., Giorgetta, M., Schlese, U. and Schulzweida, U. 1996. The atmospheric general circulation model ECHAM4: Model description and simulation of the present day climate. *Tech. Rep.* **218**, Max–Planck–Inst. für Meteorol., Hamburg, Germany.

Zuberi, B., A. K. Bertram, C. A. Cassa, L. T. Molina, and M. J. Molina, Heterogeneous nucleation of ice in $(NH_4)_2SO_4$-H_2O particles with mineral dust immersions, *Geophys. Res. Lett.*, *29*, doi: 10.1029/2001GL014289, 2002.

An Assessment of Multi-angle Imaging SpectroRadiometer (MISR) Stereo-derived Cloud Top Heights using Ground-based Millimeter-wavelength Cloud Radars

R. T. Marchand[1] and T. P. Ackerman

[1]Pacific Northwest National Laboratory, Richland, WA 99352, USA

1. INTRODUCTION

Clouds are of tremendous importance to climate because of their direct radiative effects and because of their role in atmospheric dynamics and the hydrological cycle. The value of satellite imagery in monitoring cloud properties on a global basis can hardly be understated. One cloud property that satellites are in an advantageous position to monitor is cloud top height. In this article we provide an assessment of stereoscopically derived cloud top heights produced from the Multi-angle Imaging SpectroRadiometer (MISR).

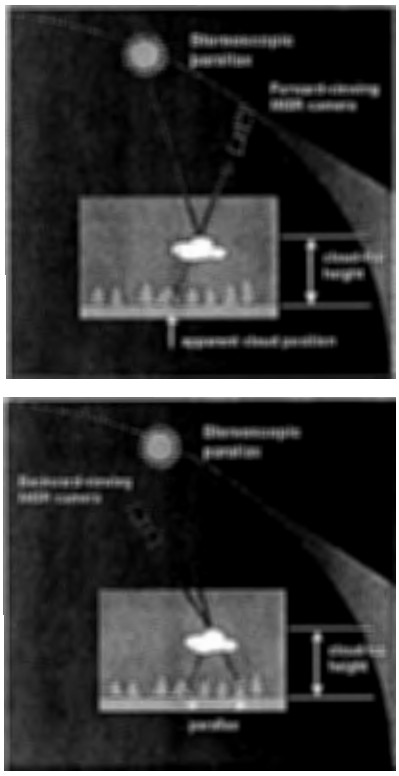

FIGURE 1 – Depiction of stereoscopic height retrieval.

Corresponding author's address: Roger Marchand, Pacific Northwest National Laboratory, P.O. Box 999, Richland, Washington, 99352, United States; E-Mail: roj@pnl.gov

MISR is one of five instruments on board the NASA EOS AM-1 or TERRA satellite, which was launched in December of 1999. This instrument consists of nine pushbroom (or line imaging) cameras, each of which makes high-resolution images (at approximately 275 meters) in four narrow spectral bands located at 443, 555, 670, and 865 nm. These cameras collect data at nine view angles (nadir plus 26.1, 45.6, 60.0, and 70.5 degrees forward and aft of the direction of flight) [Diner et al. 2002].

The MISR stereo-height retrieval is conceptually simply, as depicted in figure 1. An object located above the surface (such as a cloud) will appear in two different positions when viewed from two different angles. From the apparent change in position (or parallax) one can calculate the height of the object, and using multiple views one can estimate both the height and velocity. In the MISR algorithm, 3 cameras are used to estimate the velocity (which is assumed to be constant on a 70.5 km scale), after which 2 other cameras are used to obtain a 2.2 km resolution height field. We refer interested readers to Moroney et al. [2002] for further information.

Cloud top height retrievals are especially important for MISR because the derived height field is used to co-register the measured radiances. That is, the derived height field is needed to determine which radiances in the forward or aft views are coming from the same cloud or surface element observed in the nadir direction.

In this article we show the results of an ongoing comparison between ground-based millimeter-wave cloud radar and lidar measurements of cloud top and MISR stereo-derived cloud top height. This comparison is based on data from 3 radar systems located in the U.S Southern Great Plains (Lamont, Oklahoma), the tropical western pacific (Nauru Island) and the North Slope of Alaska (Barrow, Alaska). These radars are operated as part of the U. S. Department of Energy Atmospheric Radiation Measurement (ARM) program.

The MISR stereo height algorithm is performing largely as expected for most optically thick clouds. As with many satellite retrievals, the stereo-height retrieval has difficulty with optically thin clouds or ice clouds with little optical contrast near cloud top.

2. RESULTS

Among the best available independent data sources for evaluating MISR-retrieved cloud top heights are ground-based cloud radar and lidar systems. As part of MISR validation activities, we have been collecting and comparing MISR stereo-cloud top with ARM radar

and lidar observations (for all of the ARM sties). Shown below in figure 2 is one example of that comparison for the ARM site in Barrow, Alaska. In this figure each symbol represents one overpass of the ARM site where we have subdivided the overpasses into a number of categories:

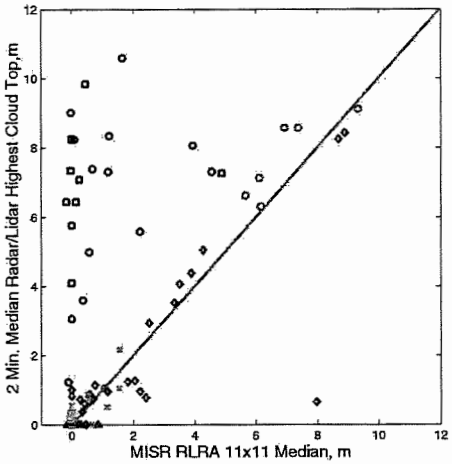

Figure 2 – Scatter plot of Radar/Lidar derived cloud top (median value for two-minutes surrounding satellite overpass) versus MISR stereo-derived cloud-top (median value for 11x11 pixel patch centered on ground site).

- Blue carats or blue diamonds = clear-sky or opaque cloud top, respectively.
- Red symbols = Thin cloud over surface. Squares mean NO hint of any cloud is visible in nadir imagery.
- Black symbols = Thin cloud over other clouds. MISR Cloud top height IS in good agreement with lower cloud tops.
- Green crosses = broken boundary layer clouds.
- Magenta circles = semi-opaque cirrus.

For opaque clouds (represented by the blue, green and magenta symbols) the MISR retrieval works well. Much of the error in the individual comparisons (for example the scatter in the blue diamonds near 1 km) is the result of error in the cloud velocity/wind-retrieval, which is used as input to the stereo-height retrieval. The MISR wind algorithm is currently being modified to include an additional wind quality assessment flag to detect when errors of > 500m may occur. We find that for optically thick clouds (for blue/green/magenta symbols) the Radar - MISR cloud top height difference is:

ARM North Slope of Alaska (NSA) Barrow Site:
Median = 177 m
Mean = 207 m
Std dev = 843 m

ARM Southern Great Plains (SGP) Site:
Median = 747 m
Mean = 710 m
Std dev = 1252 m

ARM Tropical Western Pacific (TWP) Nauru Site
Median = 107 m
Mean = -124 m
Std dev = 733 m

For the Barrow and SGP sites, the underestimate in MISR cloud top is largely a result of the image-matching-algorithm identifying contrast inside of a cloud with a diffuse and optically thin cloud top rather than the actual cloud top. (These clouds are represented by magenta symbols). If one removes these clouds from the above statistics, the mean and standard deviations are all less than about 500 meters.

Some clouds are too optically thin for the MISR stereo-algorithm to detect. These clouds are represented by the red and black symbols in figure 1. Many satellite retrievals have problems with thin clouds, and an important consideration in using the MISR stereo-results is to know how thin is thin?

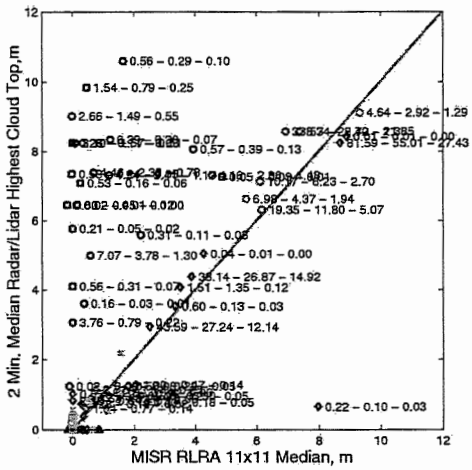

Figure 3 – same as figure 2, but with radar-based cloud optical depth (max – best – min value).

To answer this question we are examining retrievals of cloud optical depth from the ARM radar data. Figures 3 through 5 show scatter plots, similar to figure 1 expect that we label each overpass (symbol) with a minimum, a maximum and best-guess radar-retrieval for the cloud optical depth.

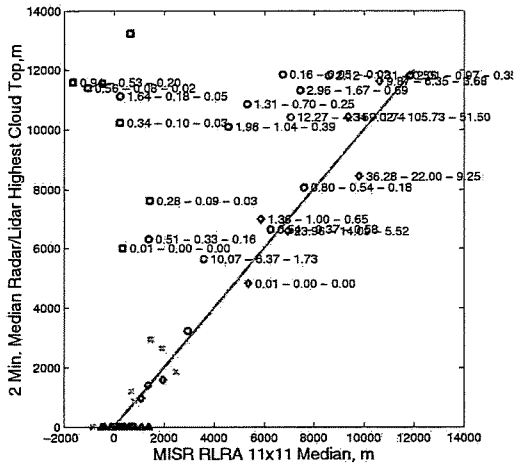

Figure 4 – same as figure 3, but for ARM Southern Great Plains (SGP) site.

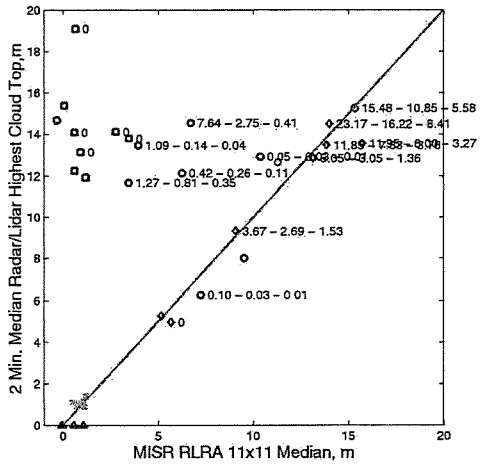

Figure 5 – same as figure 3, but for ARM Tropical Western Pacific (TWP) site at Nauru Island.

3. SUMMARY OF RESULTS

It is in the nature of the stereo-imaging technique at the heart of the MISR stereo-height retrieval to identify the location of points where contrast in the observed radiance imagery is generated. Having examined the overpass cases and retrieval results in detail we find that for opaque clouds with high contrast, the MISR retrieval is working very well (good to ~ 500m). For optically thick clouds (tau > ~ 5) but without well-defined contrast at cloud top, the MISR-stereo height tends to identify structures within the cloud, typically 500m to 1.5 km deep.

The MISR stereo routinely identifies features below optically thin (cirrus) clouds. The optical depth threshold at which the algorithm identifies the thin cloud rather than the underlying object depends on the contrast of the underlying feature. For the extreme case of very dark features (such as open water) near bright features (fresh snow) clouds with optical depth of at least 2, and perhaps as much as optical depth 5, can be missed. When boundary layer clouds such as stratocumulus and trade cumulus are present, cirrus clouds with optical depths up to approximately 1 are not detected. However, for cases without lower clouds, thin cirrus clouds with optical depths near 0.3 over heterogeneous land and even smaller optical depths over dark water are usually detected.

4. DISCUSSION/FUTURE ACTIVITIES

The above optical depth assessment is based on results from a cloud-radar reflectivity and Doppler velocity based retrieval technique. This technique is powerful in that it can be applied in most cloud conditions; unlike most other ground-based retrievals that require single layer and usually homogeneous clouds. However, the uncertainty in the optical depth retrieval is often sufficiently large to make determining the dividing line between thin and thick cirrus difficult. We are currently working to improve this retrieval technique in a number of ways, including estimating the cloud particle habit from the MISR multi-angle radiance pattern and including additional information (from radar wind profilers) on meso- to synoptic scale air motions (both major sources of uncertain in the current retrieval). We are also planning to supplement this retrieval with retrievals from other techniques when possible.

The MISR processing algorithms are also being improved and modified to include geometric and wind quality assessments flags. These flags should prove helpful in identifying outliers in the stereo-height retrieval. Evaluation and recommendations on using these quality flags is planned as part of MISR validation activities.

5. REFERENCES

Diner DJ, Beckert JC, Bothwell GW, Rodriguez JI, 2002: Performance of the MISR instrument during its first 20 months in earth orbit. IEEE transactions on geoscience and remote sensing, 40 (7): 1449-1466 JUL 2002

Moroney C, Davies R, Muller JP, 2002: Operational retrieval of cloud-top heights using MISR data. IEEE transactions on geoscience and remote sensing, 40 (7): 1532-1540 JUL 2002

shows that MISR cloud heights not doing too bad.

SINGLE-SCATTERING PROPERTIES OF MIXED-PHASE CLOUDS AT ARCTIC CLOUDS AT SOLAR WAVELENGTHS: IMPACTS ON RADIATIVE TRANSFER

Greg M. McFarquhar[1] and Stewart G. Cober[2]

[1]University of Illinois at Urbana-Champaign, Urbana, IL
[2]Meteorological Service of Canada, Downsview, Canada

1. INTRODUCTION

Although regions at poles are especially sensitive to climate change, large uncertainties in the response of the Arctic to climate perturbations exist. Complex feedback mechanisms involving sea ice, snow cover, and clouds must be better understood and characterized before large disagreements between general circulation model (GCM) simulations can be reduced and future predictions of climate change refined. A lack of comprehensive measurements of ice-ocean-atmosphere processes and cloud and radiation properties previously prevented research progress on feedback mechanisms. Recent observations obtained during the First International Satellite Cloud Climatology Project (ISCCP) Regional Experiment (FIRE) Arctic Clouds Experiment (ACE) and the Surface Heat Budget of the Arctic Ocean Experiment (SHEBA) can now be used to enhance our understanding of Arctic climate.

For Arctic clouds, Shupe et al. (2001) showed that retrieval techniques for all-ice and all-liquid clouds could be used only 34% of the time, suggesting mixed-phase or overlapping clouds were present at other times. Understanding the properties of mixed-phase clouds is therefore critical for the Arctic environment. These properties feedback on radiative budgets because modeled single-scattering properties of mixed-phase clouds differ substantially from those composed exclusively of liquid or ice particles (e.g., Sun and Shine 1995). Using direct measurements of single-scattering cloud properties from a cloud integrating nephelometer, Gerber et al. (2000) illustrated such differences finding larger values of asymmetry parameters (g) for mixed- and liquid-phase clouds than for ice-phase clouds. Not only do cloud radiative properties depend on the relative amounts of the phases, but also on the manner of spatial mixing (Sun and Shine 1994; Rotstayn et al. 2000).

In-situ measurements obtained during FIRE.ACE are used here to examine the nature of phase mixing and the contributions of water and ice to mixed-phase single-scattering and microphysical properties. The roles of water and ice in determining energy balance for this region are determined from radiative transfer simulations performed using calculated single-scattering properties.

Corresponding Author: Prof. McFarquhar, University of Illinois, Dept. of Atmospheric Science, 105 S. Gregory Street, Urbana, IL, 61801.

2. IN SITU OBSERVATIONS

Instruments on board the National Research Council (NRC) Convair-580 (CV580) aircraft were used to collect microphysical data during FIRE.ACE in April 1998 (Cober et al. 2001a, b). The CV580 was equipped with several Particle Measuring Systems, Inc. probes that were used to measure the drop and ice crystal particle size distributions (PSDs) including a two-dimensional cloud (2DC) probe for PSDs between 125 and 800 μm, a two-dimensional precipitation probe (2DP, 800 to 6400 μm), a two-dimensional grey probe (2DG, 125 to 1600 μm), and two forward scattering spectrometer probes (FSSP-096, 3.5 to 45.5 μm and FSSP-124, 5 to 95μm). Water content was measured with a SkyTech Research, Inc. Nezvorov LWC/ total water content (TWC) probe (Korolev et al. 1998), and a King LWC probe. A Rosemount icing detector was used to determine icing rate and to identify the presence of supercooled water drops. The FSSP and 2D probes covered the drop spectrum from 1 to 6400 μm and the ice crystal spectrum from 100 to 6400 μm, from which properties of the PSDs could be determined.

Data from all in-cloud penetrations were analyzed at 30-s resolution to identify cloud phase and to determine PSDs. Cloud regions were identified as liquid, mixed or glaciated using a combination of observations from several instruments including the 2DC, 2DP, FSSPs, RID, King LWC and Nevzorov LWC/TWC probes. From the in-cloud observations during FIRE.ACE, 33% were identified as mixed-phase, 16% as liquid-phase, and 51% as ice-phase. The relative percentage of liquid, mixed and glaciated conditions is somewhat sensitive to the threshold mass content used to define cloud. The temperatures of mixed-phase clouds ranged from –33°C to –4.8°C, of the liquid-phase clouds from –20.5°C to –1.7°C, and of the ice-phase clouds from –44°C to –3.5°C.

3.BULK MIXED-PHASE PROPERTIES

To calculate mass and single-scattering properties, estimates of PSDs for liquid and ice-phase particles, as well as of mass and projected area of such particles are required. These are determined using from the 2D probes, the Nezvorov probe, and the FSSP. Although the FSSP cannot be typically used quantitatively for glaciated conditions (e.g., Cober et al 2001b showed that FSSP channels larger than 30 μm diameter were heavily biased by responses to ice crystals whenever the ice

crystal concentration for crystals larger than 125 μm exceeded approximately 1 L^{-1}), examination of the FIRE.ACE data showed that the FSSP PSDs in mixed-phase clouds had peaks in number concentration between 5 and 15 μm and number concentrations not significantly differing from PSDs measured in liquid clouds. The mass concentrations estimated from these distributions, assuming spherical water particles with density 1 g cm^{-3}, are reasonable when compared against bulk estimates of liquid water from the Nezvorov probe. However, FSSP PSDs measured in glaciated clouds or in clouds with ice concentrations exceeding about 2 L^{-1} (only 10% of cases) exhibit broad distributions, not representative of super cooled drops. Thus, it appears the FSSP adequately characterizes the distributions of water drops for most mixed-phase clouds.

The PSDs for ice clouds are estimated from the 2D data, with the 2DC used for particles with X dimension (maximum diameter of the particle in the time direction parallel to the aircraft motion) between 125 and 800 μm, and the 2DP for X dimension larger than 800 μm. Figure 1 shows examples of images collected in mixed-phase events, which although exhibiting tremendous variability, showed liquid drops larger than 100 μm in only 4 of the 30-s observations during FIRE.ACE.

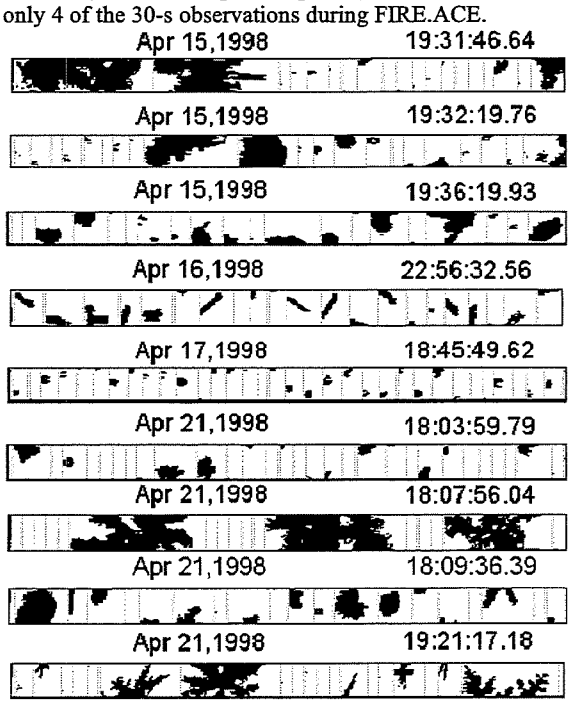

Figure 1: Crystals imaged by 2D probes in conditions identified as mixed-phase by Cober et al. (2001b) algorithm

Estimates of particle mass (m) and projected area (A) are required to calculate single-scattering properties of ice particles measured by the 2D probes. Boudala et al. (2002a) compared mass contents from various m-D and A-D relations against measurements from the Nezvorov probe from several field campaigns, and suggested that Cunningham's (1978) m-A relations best characterized the measured mass contents. However, because most crystals shadowed one end element of the photodiode array, reconstruction techniques that assume circular symmetry were used to estimate area, giving relatively large uncertainties in area, and hence in derived masses following Cunningham (1978).

Thus, a modification was made to calculate mass. An automatic shape classification algorithm sorted the 2D images according to whether the images had circular, irregular, dendritic, or needle shapes, and corresponding areas of the dendrites, needles, and irregular crystals are then estimated from the crystal models that are ultimately used to determine their single-scattering properties. These areas are used to estimate mass following Cunningham (1978). Integration over the size distribution then gives total mass concentrations, and bulk single-scattering properties are computed by weighting scattering properties in a library of such properties (Yang et al. 2000) by number concentration and scattering cross-section.

4. BULK SCATTERING PROPERTIES

Figure 2 shows frequency distributions of extinction coefficient, β_{ext}, calculated from in-situ observations, with different line types representing mixed-, liquid- and ice-phase clouds; for ice clouds, calculations both with and without contributions due to small crystals measured by the FSSP are shown. As expected, β_{ext} for water and mixed-phase clouds are larger than those for ice clouds, even when small ice crystals are assumed to have the concentrations measured by the FSSP.

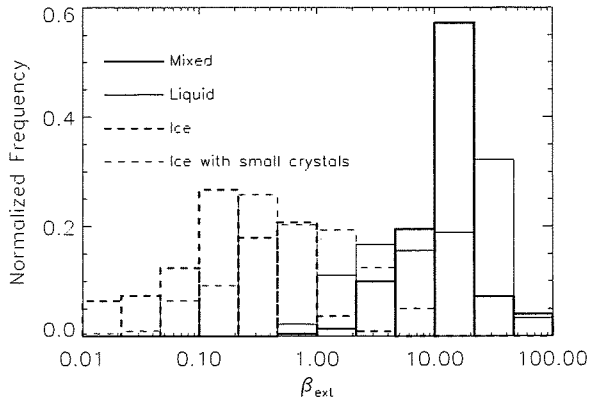

Figure 2: Normalized distribution of frequency of occurrence of β_{ext} for mixed-phase, liquid-phase, and ice-phase clouds with and without the contributions of small ice crystals measured by the FSSP. Curves are normalized so that total number of occurrences for each cloud type is 1.

For mixed-phase clouds, water droplets dominate the contributions to extinction, as shown in Figure 3. Asterisks represent the fractional contribution of liquid to β_{ext} that would be predicted by the Boudala et al.

(2002b) parameterization scheme, and are substantially lower than for the measurements. This discrepancy occurs because the parameterization scheme is derived from measurements over all phases of clouds, including clouds composed solely of water and ice.

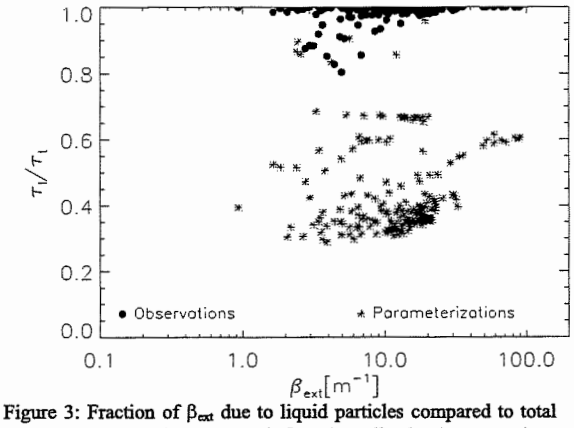

Figure 3: Fraction of β_{ext} due to liquid particles compared to total β_{ext} as function of total β_{ext} for all cloud penetrations identified as mixed-phase. Circles represent calculations using observed PSDs, asterisks represent calculations using the Boudala et al.(2002) parameterization of liquid fraction as described in text.

Figure 4 shows the normalized frequency of occurrence of asymmetry parameter, g, calculated from the observations for 4 broad bands commonly used in large-scale models. Different line types represent g for mixed-, liquid-, and ice-phase clouds, and values that would be obtained for parameterization schemes typically used in large-scale models (i.e., g is a weighted mixture of ice and water g values, where the weight is a function of total water content and temperature). For the two bands at the lowest wavelengths (λ) especially, with the greatest fraction of solar energy, the distributions of g for mixed-phase and liquid-phase clouds are similar. However, they are substantially different from distributions for ice-phase clouds and modeled mixtures. Implications of such differences on radiative fluxes are discussed next.

5. RADIATIVE FLUXES

To investigate whether differences in single-scattering properties between observed and parameterized mixed-phase clouds are large enough to impact estimates of cloud radiative forcing and fluxes predicted at the top of the atmosphere and surface, simulations are performed using a plane parallel radiative transfer model (developed by A. Macke 1994) to compute top of the atmosphere radiative flux. Separate simulations were performed for each 30-s observed PSD, which was assumed to exist uniformly throughout a horizontally and vertically homogeneous 1 km thick cloud, with β_{ext} estimated from the observed PSD. For the first set of simulations, the scattering phase function (P(Θ)) and single-scattering albedo (ω_0) for the cloud were computed by combining the observed PSD with Yang et al.'s (2000) scattering library as previously described. For the second set of simulations, 1 km thick clouds with the same β_{ext}, were again used as input, but P(Θ) and ω_0 were calculated by combining ice–water fractions estimated from the Boudala et al. (2002b) large-scale parameterization (using total water content and temperature of the observed PSD as input) with the Yang et al. (2000) library.

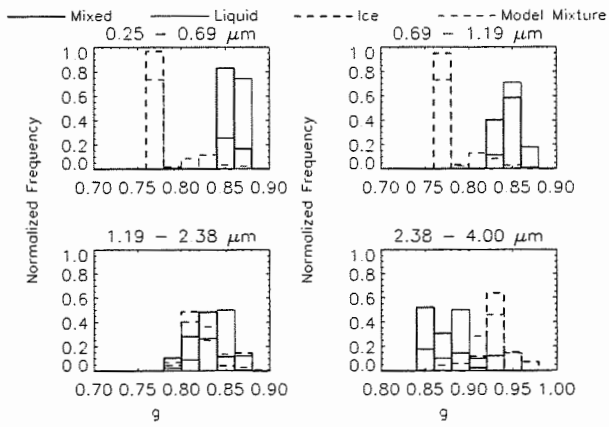

Figure 4: Normalized frequency distributions of g for 4 broadbands commonly used in large-scale models. Different line types correspond to frequency distributions for mixed-phase, liquid-phase, and ice-phase clouds, and for calculations of g using the Boudala et al. (2002) parameterization of liquid water fraction.

Figure 5 compares broadband albedos for 0.25 to 0.69 μm, computed for the 2 sets of simulations. The average albedo calculated using the observed PSDs was 0.80, 6% lower than 0.85 computed for the parameterized PSDs, showing water droplets play a larger role in determining the single-scattering properties of the observed clouds than of the parameterized clouds, where ice plays a larger role. Differences were even larger for wavelength bands in the near infrared (figure not shown).

Although differences in Fig. 5 are informative, a more important climate issue is how to represent single-scattering properties of mixtures of phases over large spatial scales. Over scales of 100 km, all of mixed, ice, and water-phase clouds exist. To test the performance of the Boudala et al. (2002b) scheme over such averages, the plane parallel model is used to simulate top of the atmosphere fluxes using all FIRE.ACE clouds as input, including ice- and liquid-phase clouds. Simulations using single-scattering properties computed using parameterized mixtures of water and ice are also conducted. The simulations depicted in Fig. 4 represent a subset of these simulations as they were performed only for clouds identified as mixed-phase.

When comparing average albedos for observed and parameterized PSDs over all phases for Arctic conditions, differences in average albedo were less than 5% for the 0.25 to 0.69 μm band. Differences were

larger for longer wavelengths. The lack of difference is partially attributed to the high surface albedos used to describe the snow covered surface; when a lower surface albedo of 0.4 was assumed, differences in average albedos for simulations based on observed and parameterized PSDs, increased to approximately 5%.

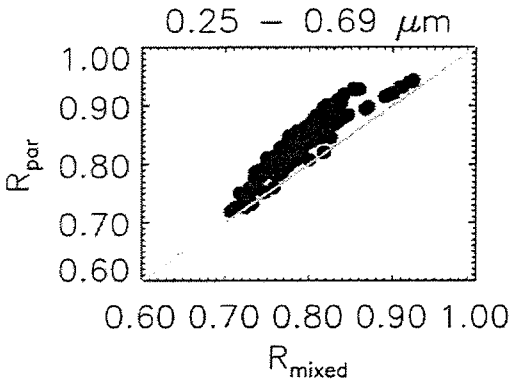

Figure 5: Albedo computed using plane-parallel model assuming 1 km thick cloud and single-scattering properties determined using observations of mixed-phase clouds on horizontal axis versus albedo determined from parameterizations of these observations on vertical axis. Each point represents calculations from 30-s time averaged PSD.

Differences in average albedos noted above would be more significant if particular phases clumped or clustered because water and ice have different effects on radiation; distributions of phases also determined cloud impacts on radiation. Analysis of FIRE.ACE data shows that the phases are typically clustered, meaning that if a PSD was mixed-phase, the neighboring PSD is more likely to be mixed as well. In fact, over 90% of the 30-s averaged PSDs identified as mixed-phase occurred either before of after another mixed-phase distribution. A larger dataset and more physical understanding of the nature of mixed-phase clouds is needed.

6. SUMMARY

In-situ observations on the sizes, shapes, and phases of cloud particles obtained during FIRE.ACE have been used to investigate the single-scattering properties of Arctic mixed-phase clouds. Consistent with previous studies, mixed-phase clouds are seen to occur frequently and supercooled water droplets dominate their mass contents. This study has focused on examining the relative roles of water and ice in determining the single-scattering properties of mixed-phase clouds. Radiative transfer simulations, conducted with a plane parallel model, have been used to investigate whether conventional parameterizations, predicting the mixing of water and ice in temperature ranges where mixed-phase clouds exist, accurately predict the radiative fluxes associated with such clouds. Although substantial differences from such parameterizations are noted on a local scale, differences on larger scales may or may not be significant depending on the nature of the clustering between phases. Observations to be obtained during the Mixed-Phase Arctic Cloud Experiment (M-PACE) will be used to further investigate these issues and to better determine the vertical structure and origin of Arctic mixed-phase clouds.

7. ACKNOWLEDGMENTS

This research was supported by the Department of Energy Atmospheric Radiation Measurement Program (ARM) under contract number DE-FG03-02ER63337. The findings do not necessarily represent the views of DOE ARM. Cloud microphysical data collected by the CV580 were obtained from the NASA Langley Research Center Atmospheric Sciences Data Center. Codes and a database from Ping Yang and Andreas Macke were used.

8. REFERENCES

Boudala, F.S., G.A. Isaac, Q. Fu, and S.G. Cober, 2002a: Parameterization of effective ice particle size for high-latitude clouds. *Int. J. Climatol.*, **22**, 1267-1284.

Boudala, F.S., G.A. Isaac, S.G. Cober, Q. Fu, and A.V. Korolev, 2002b: Parameterization of liquid fraction in terms of temperature and cloud water content in stratiform mixed phase clouds. 11th Conf. Cloud Physics., *Amer. Meteor. Soc.*, Ogden, UT, 2.5.

Cober, S.G., G.A. Isaac, and J.W. Strapp, 2001a: Characterizations of aircraft icing environments that include supercooled large drops. *J. Appl. Meteor.*, **40**, 1984-2002.

Cober, S.G., G.A. Isaac, A.V. Korolev, and J.W. Strapp, 2001b: Assessing cloud-phase conditions. *J. Appl. Meteor.*, **40**, 1967-1983.

Gerber, H., Y. Takano, T.J. Garrett, and P.V. Hobbs, 2000: Nephelometer measurements of the asymmetry parameter, volume extinction coefficient, and backscatter ratio in Arctic clouds. *J. Atmos. Sci.*, **57**, 3021-3034.

Rotstayn, L.D., B.F. Ryan, and J.J. Katzfey, 2000: A scheme for the calculation of the liquid fraction in mixed-phase stratiform clouds in large-scale models.

Shupe, M.D., T. Uttal, S.Y. Matrosov, and A.S. Frisch, 2001: Cloud water contents and hydrometeor sizes during the FIRE Arctic clouds experiment. *J. Geophys. Res.*, **106**, 15015-15028.

Sun, Z., and K.P. Shine, 1994: Studies of the radiative properties of ice and mixed-phase clouds. *Quart. J. Roy. Meteor. Soc.*, **120**, 111-137.

Sun, Z., and K.P. Shine, 1995: Parameterization of ice cloud radiative properties and its application to the p. *J. Climate*, **8**, 1874-1888.

Yang, P., K.N. Liou, K. Wyser, and D. Mitchell, 2000: Parameterization of the scattering and absorption properties of individual ice crystals. *J. Geophys. Res.*, **105**, 4699-4718.

EVALUATION OF THE MULTI-SCALE MODELING FRAMEWORK USING DATA FROM THE ATMOSPHERIC RADIATION MEASUREMENT PROGRAM

Mikhail Ovtchinnikov[1], Thomas P. Ackerman[1], Roger T. Marchand[1], and Marat Khairoutdinov[2]

[1]Pacific Northwest National Laboratory, Richland, Washington, 99352, USA
[2]Colorado State University, Fort Collins, Colorado, 80523, USA

1. INTRODUCTION

One of the goals of the Atmospheric Radiation Measurement (ARM) program is to provide long-term observations for evaluating and improving cloud and radiation treatment in global climate models. Unfortunately, the traditional parametric approach of diagnosing cloud and radiation properties for gridcells that are tens to hundreds kilometers across from large-scale model fields is not well suited for comparison with observed time series at selected locations. A recently emerging approach called the multi-scale modeling framework (MMF) has shown promise to bridge the scale gap. MMF consists of a two-dimensional cloud system resolving model (CSRM) embedded into each grid column of the Community Atmospheric Model (CAM), thereby computing cloud properties at a scale that is more consistent with observations. Here, we present a comparison of data from two ARM sites, one at the Southern Great Plains (SGP) in Oklahoma and one at Nauru island in the Tropical Western Pacific (TWP) region, with output from both CAM and MMF.

2. MODEL AND OBSERVATION DESCRIPTION

The MMF model setup is described in detail by Khairoutdinov and Randall (2001) and only briefly summarized here. The CAM has 26 layers in the vertical (stretched grid) and T42 horizontal (spectral) resolution, which corresponds to grid size of 2.8° x 2.8°. Thus, each gridcell represents an area of approximately 300 x 300 km^2 in the tropics. The CSRM has 64 columns at 4 km spacing and 24 layers in vertical coinciding with the lowest 24 CAM levels. Time steps are 1 hour for CAM and 20 seconds for CSRM.

Two sets of model runs are analyzed in this study: one using climatological sea surface temperatures (SSTs) and another using the observed SSTs for the year of 1999. Each set consists of a CAM run with standard cloud and radiation parameterization as well as a MMF run. Each simulation covers a period from October to the end of the following year. However, in order to allow for model spin up and to prevent seasonal bias, only one full year (January through December) is analyzed meaning that the first fall season is excluded from consideration. In this study, we look only at the yearly statistics, although we realize that there are important aspects of seasonal and diurnal variability that need to be addressed in the future.

Observations are taken at the TWP site located at the island of Nauru (0.521°S, 166.916°E) and the SGP Central Facility located at (36.617°N, 97.50°W). Cloud fraction statistics are derived from vertically pointing millimeter wave (35 GHz) cloud radar observations. Precipitation rates on the ground are measured by an optical rain gauge at the TWP site and by electrically heated, tipping bucket precipitation gauge at the SGP site.

For the TWP site, we use three years worth of data from November 1, 1998 through October 31, 2001. For that period, the radar data are available 64% of the time. For the SGP site, we use four years worth of data from 1 September 1998 through 31 August 2002 when the radar data are available 84% and precipitation data 93% of the time. There could be a small bias introduced by missing observations, especially for cloud fraction at the TWP site.

Obviously, comparison of the climatological SST set of runs with the runs for the real SST for the single year does not allow for comprehensive study of the inter-annual variability in model simulations. Nevertheless even this limited analysis can provide an initial assessment of model strengths and weaknesses and identify potential problem areas for future research.

3. RESULTS

3.1 Cloud Fraction

Cloud fractions (CF) analyzed here are determined as follows. For any model column, the CAM CF is taken as predicted by the cloud parameterization and averaged over one or three hours, as indicated below. In the MMF, the domain (spatial) CF at any time is defined as the ratio of the number of cloudy columns to the total number of columns. Similarly to the CAM CF, the MMF CF used here is averaged over the same three hour period. Although time averaging is used in the analysis, both these CFs are instantaneously defined for a prescribed area. In contrast, CF derived from the vertically pointing cloud radar is defined only for a time series as the ratio of the observations with a

Corresponding author's address: Mikhail Ovtchinnikov, Pacific Northwest National Laboratory, P.O. Box 999, Richland, Washington, 99352, USA; E-Mail: mikhail@pnl.gov.

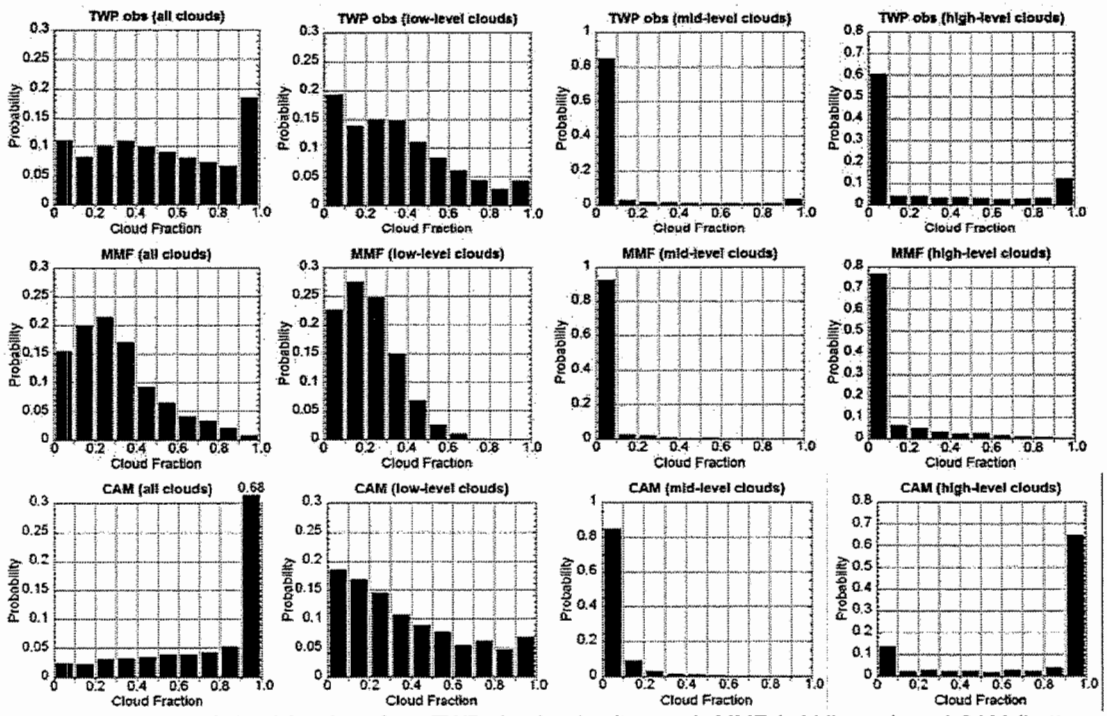

Fig. 1. Histograms of cloud fractions from TWP cloud radar (top row), MMF (middle row), and CAM (bottom row). Four columns from left to right show cloud fractions for all, low, middle, and high-level clouds, respectively.

Table 1. Parameters of total CF distribution for TWP

	TWP	MMF	CAM
Mean	0.55	0.30	0.84
Median	0.53	0.27	0.99
Std Dev	0.33	0.21	0.27

Table 2. Parameters of total CF distribution for SGP

	SGP	MMF	CAM
Mean	0.48	0.22	0.31
Median	0.43	0??	0??
Std Dev	0.43	0.34	0.43

return signal exceeding a specified threshold to the total number of observations over that period. In order to mimic such observations, a temporal CF was also computed for a single column of MMF.

Table 1 and Fig. 1 present a comparison of model predicted CF from the runs with climatological SSTs with radar derived CF at TWP site. Compared to observations, CAM greatly overpredicts overcast conditions, while the MMF simulation lacks this regime. Note that the latter discrepancy could be, at least partially, due to sampling differences as the overcast condition over the CSRM domain could not be observed as often as over the ARM site. The CAM CF on the other hand is clearly unrealistic since an overcast condition over a larger area (as in a CAM gridcell) must also be observed at any location within this area.

Comparison of cloud fractions for low (below 700 mb), middle (between 700 and 400 mb), and high (above 400 mb) level clouds reveals that the overcast conditions in the CAM run are primarily due to high-level (cirrus) clouds. This known shortcoming of the traditional cloud scheme is corrected, and perhaps overcorrected in the MMF run, in which overcast conditions are extremely rare in any 3-hour period.

Comparison of the low-level cloudiness is less conclusive. There are at least two complicating factors. First, small cumulus clouds, which are a prominent feature in the tropics, are not well resolved on the 4-km CSRM grid. Second, radar derived cloud statistics could be contaminated by the island effect, which will be most pronounced in low-level cloud observations.

Table 2 shows a comparison of observed and model predicted CF at the SGP site. Both MMF and CAM models underpredict the cloud amount at all levels, the only exception being the familiar overprediction of overcast high-level clouds in the CAM run. The positive bias in high-level cloudiness in CAM, although moderate in this case, partially compensates for the lack of low clouds and results in a total CF that is closer to observations than the CF from the MMF.

The MMF framework allows us to explore the effects of various definitions of cloud fraction. Fig. 2 illustrates that CF calculated spatially for the CSRM domain differs significantly from temporal (over 3-hour interval) CF for the CSRM column. The effect is dominated by the difference in the low-level CF while the changes in the mid- and high-level statistics are

negligible (not shown). The result is to be expected due to the generally smaller horizontal extent of low-level clouds. A second sensitivity test addresses the issue of determining the cloud boundary. For that the CF was computed for the CRM column using two cloud thresholds:

(1) IWC > 0.0165 g m^{-3} or LWC > 0.136 g m^{-3}, and

(2) IWC > 0.0042 g m^{-3} or LWC > 0.038 g m^{-3}.

The first threshold corresponds to radar reflectivity of ~ -30 dBZ and the second to ~ -40 dBZ. Once again the change affects primarily low-level clouds but the effect is small (Fig. 3). Cloud fraction derived from radar observations is much more sensitive to the radar reflectivity threshold than this simulation predicts.

3.2 Precipitation

Precipitation is one of the major components of the water cycle. Prediction of both the total amount and distribution of intensity of precipitation is important.

Table 3. Total annual precipitation at TWP site (mm). Model values are averaged over 4 neighboring points.

	TWP obs	MMF	CAM
Climate	637	677	1309
Year 1999	358	286	826

Table 4. Total annual precipitation at SGP site (mm). Model values are averaged over 4 neighboring points.

	SGP obs	MMF	CAM
Climate	878	478	431
Year 1999	1031	407	319

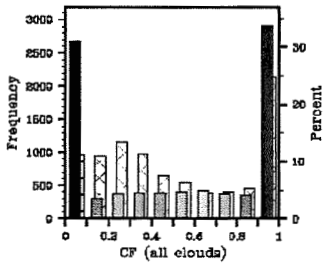

Fig. 2. Histograms of temporal (foreground) and spatial (background) cloud fraction for 1999 from MMF run.

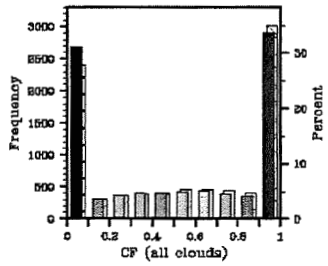

Fig. 3. Histograms of cloud fraction for 1999 from MMF run for -30 dBZ (foreground) and -40 dBZ (background) thresholds.

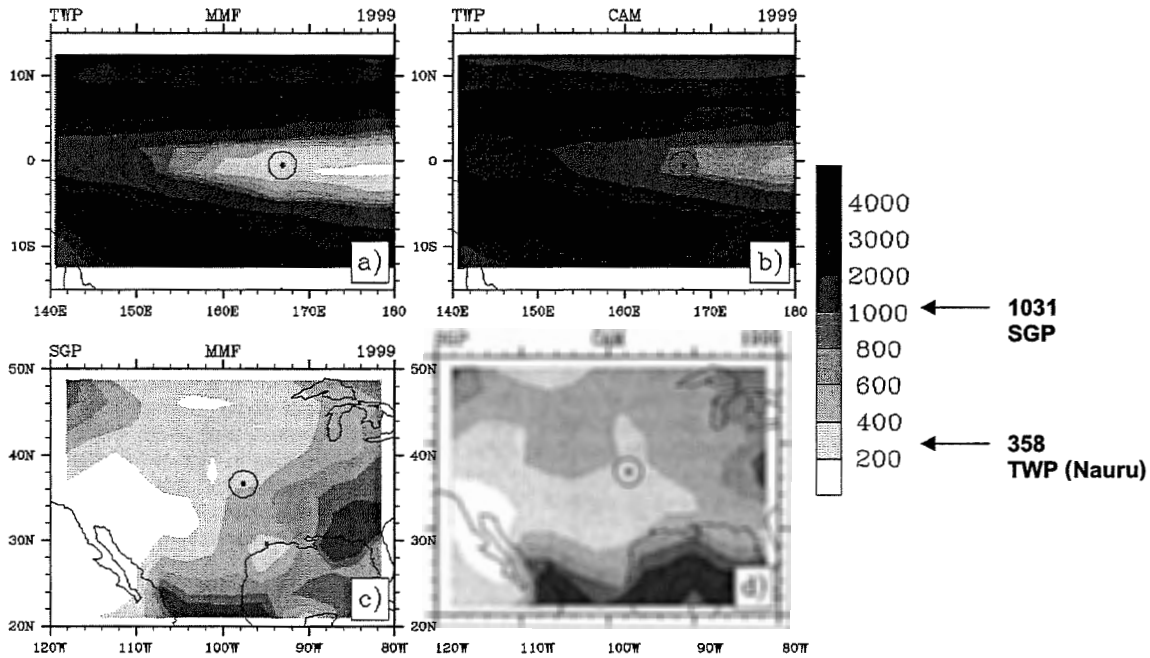

Fig. 4. Total annual precipitation amount (mm) as predicted by MMF (left column) and CAM (right column) for TWP (top row) and SGP (bottom row) regions for 1999. Locations of the two ARM sites and observed precipitation amounts for these sites are also indicated.

In the standard CAM setup, the total precipitation analyzed here includes both convective (subgrid) and stratiform (resolved) components, which are predicted separately. In the tropics, the effect of stratiform precipitation is minimal, while in mid-latitudes both components can be important. There is no such division in the MMF because all precipitation comes from explicitly resolved clouds.

Table 3 and Fig. 4a,b summarize the total annual precipitation amount from TWP observations and MMF and CAM runs with both climatological and 1999 SSTs. The observed annual precipitation in 1999 is only 358 mm or 55% of the 1998-2002 average of 637 mm. This is consistent with 1999 being a La Niña year of medium strength. The MMF simulations are in close agreement with observations both in annual precipitation amount and in predicting a relatively dry 1999 year. In the two CAM simulations, the precipitation is overestimated by a factor of two or more although the relative reduction for the year 1999 compared to climatology is still captured.

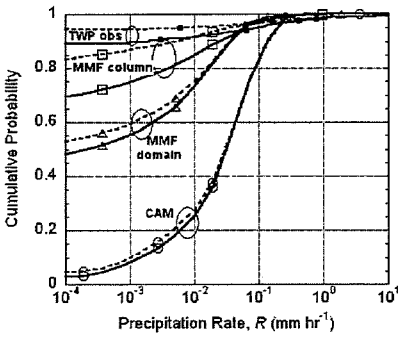

Fig. 5. Cumulative probability distributions of one (dash) and three-hour (solid) average precipitation rates from observations and models for 1999 runs.

Direct comparison of precipitation rate distributions is difficult because they are dominated by different spatial averaging (Fig. 5). Observations represent point measurements with no spatial averaging, MMF/CSRM column statistics represent an area of 4x4 km^2, MMF/CSRM domain statistics correspond to a strip of 64 columns (area of 256 x 4 km^2), and the standard parameterization provides mean values for the CAM grid (roughly 300 x 300 km^2). In general, we should expect larger extremes and more variability in local (point) measurements than in the CSRM strip, which in turn should be more variable than the parameterization representing CAM grid-cell properties.

For the northern Oklahoma region, La Niña years generally correlate with drier than normal conditions. In 1999, however, a notable positive precipitation anomaly was observed at the SGP site (Table 4) with total precipitation for the year exceeding the multi-year average by 15%. Verifying that this anomaly is not an instrumental artifact, the increased precipitation for the region in 1999 is also confirmed by the three Oklahoma Mesonet stations surrounding the central facility (not shown).

The model fails to produce enough precipitation in the area, regardless of the cloud treatment (Table 4 and Fig. 4c,d). Both MMF and CAM runs predict only about half of the observed annual precipitation amount in all simulations. Moreover, in contrast to observations, both models show 1999 as the drier year compared to climatology by 20 to 25%.

4. CONCLUSIONS

Two sets of one year long global simulations are considered: one using climatological sea surface temperatures (SST) and another using 1999 SST. Each set includes a run with MMF as well as a CAM run with conventional cloud and radiation treatment. Time series of cloud fraction and precipitation intensity are statistically analyzed. For the TWP site, parameters of frequency distributions of these variables from MMF run are shown to be more consistent with observation than those from the CAM run. For the SGP, the improvements are marginal. By explicitly resolving clouds, the MMF framework notably improves the realism of the prediction of precipitation and cloud amount in the tropics.

There are several possible reasons for the apparent lack of improvement in MMF predictions for the SGP region compared to the TWP region. First of all, although the convection is still the primary source of precipitation in the SGP, the large scale dynamical forcing is much more complicated and important in mid-latitudes compared to the tropics. Exchanges between CAM columns and the surface as well as interactions among these CAM columns are handled on a large scale and are not affected much by the embedded CSRMs. The east-west orientation of CSRMs may also be a more important factor at the SGP site, where precipitation is driven primarily by the northward transport of moisture from the Gulf of Mexico. Finally, at least some part of the precipitation in the SGP region is in the form of snow, which introduces more uncertainty in both simulations and observations.

5. ACKNOWLEDGEMENTS

This research was supported by the Laboratory Directed Research and Development Program at PNNL.

6. REFERENCES

Khairoutdinov, M. F., and D. A. Randall, 2001: A cloud resolving model as a cloud parameterization in the NCAR Community Climate Model: Preliminary results. *Geophys. Res. Lett.*, **28**, 3617-3620.

CONVECTIVE ORGANIZATION IN A RADIATIVE-CONVECTIVE EQUILIBRIUM CLOUD RESOLVING MODEL - RADIATIVE AND MOISTURE FEEDBACKS

Lyle .A. Pakula and Graeme .L. Stephens and Marat Khairoutdinov
Colorado State University, Fort Collins, Colorado

1. INTRODUCTION

The concept of radiative and convective equilibrium (RCE) has proven to be a useful paradigm for understanding the Earth's climate system (Stephens, 2004). Past RCE Cloud Resolving Modelling studies have had varying model domain sizes together with varying levels of sophistication of both cloud microphysics and the coupling of radiation to cloud processes as well as the initial conditions, such as wind shear, thermodynamic sounding, surface drag, and sea surface temperatures, making it difficult to draw general conclusions about the equilibrium reached and the relation of this equilibrium to the real atmosphere. One feature that looms as an important aspect of the RCE is the importance of the coupling of water vapor to convection, one sustaining the other via some kind of mutual feedback system (Grabowski and Moncrief, 2000, Tompkins, 2000, Tompkins and Emanuel, 2000, Fuchs and Raymond, 2002).

This paper describes two RCE-CRM experiments that show how a coupling between water vapor, shallow clouds (congestus and cumulus) and an inversion around the freezing level combine to produce radiative and dynamical feedbacks important to the eventual equilibrium reached. These feedbacks operate in a mode that is consistent with the three phases in the cycle of tropical convection observed by Stephens et al. (2004).

2. EXPERIMENT SETUP

The Radiative-Convective Equilibrium experiments were conducted using the new three-dimensional cloud-resolving model (CRM) developed at Colorado State University (CSU), based on the model of Khairoutdinov and Randall (2003). Incorporated into this model was the radiative transfer model developed at CSU referred to as BUGSrad (Stephens et al, 2001).

All experiments were conducted on a 2D grid of 8192 points, at 2.4 km grid spacing covering roughly 20,000km in the horizontal. Vertical structure is resolved using a stretched grid of 65 points with a boundary layer resolution as fine as 50m near the surface, increasing to 500m by 5km and then constant to the top of the atmosphere at 27 km. The Coriolis parameter was set to zero with a free-slip lower oceanic boundary (SST of 300K) and time step of 10s. A gravity-wave absorber in the upper 1/3 of the domain was active with a Rayleigh damping applied to the horizontal momentum and temperature fields, with a relaxation coefficient of 2 hours. The lateral boundaries were periodic. All runs were initialized with the 00 GMT 5 December 1992 TOGA COARE sounding with zero mean wind in the vertical. The standard NCAR tropical ozone sounding was used. An initial small-amplitude randomized disturbance was introduced into the temperature field to initiate convection and all surface fluxes are interactive, that is they are wind-speed dependent.

Two different model configurations were adopted. The first experimental setup imposed a prescribed radiative cooling profile and is hereafter referred to as the "Prescribed Radiation" experiment, or PR. The second experiment, referred to as "Interactive Radiation" (IR), allowed radiation feedbacks to occur through radiative heating that varies column-by-column with changes in clouds. BUGSrad was applied to each column at 5 minute intervals with constant solar insolation (no diurnal cycle).

2.1 REPRESENTED SCALES

The cloud-resolving framework, over a large domain, represents atmospheric scales from the smaller convective scale, to the scale of individual MCSs, to the broader synoptic scale. During the initial stages of integration, random small scale, shallow convection developed throughout the domain. These clouds are much akin to common tropical shallow cumulus and cumulus congestus clouds and, although ineffectual on their own, by their massive coverage are shown to have a significant role hydrologically and dynamically.

Mesoscale Convective Systems (MCSs) represent the next scale up and travel in both directions. Despite the inherent symmetry in the model setup (no rotation or preconditioning), the model preferentially develops stronger MCSs in one direction purely as a consequence of initial chaotic perturbations and wave-wave interactions.

The largest scale of variability is hereafter referred to as the synoptic scale. Although the model begins

*Corresponding author address: Lyle A. Pakula, Department of Atmospheric Science, Colorado State University, Fort Collins, CO 80523; e-mail: lyle@atmos.colostate.edu.

at rest, synoptic scale motions develop in the model arising from gravity waves that are stimulated by the developing MCSs. These gravity wave features propagate across the domain in both directions interacting with convection producing important feedbacks that govern the mode by which the radiative convective equilibrium is established. For this short paper, the topic of MCS-synoptic wave-wave interactions, the reader is referred to the complete article of Pakula et al. (2004).

3. THE PR EXPERIMENT

During the initial spin-up period, the domain is populated everywhere by shallow, random convection and the water vapor content is high. After about 10 days, the convection becomes more organized into fewer, more massive MCSs that propagate inconcert with the synoptic waves. The precipitable water field also has a wave like structure but regions appear with higher and lower values that are locked into the same area for long periods, creating an 'alley' type of appearance in Hovmoller diagrams.

These alleys are attributed to cold pools generated by MCSs. The cool, dry perturbation in the MCSs wake produce enhanced surface fluxes due to their large temperature and moisture difference to air unaffected by an MCS. As the stable cold pool recovers, it is able to generate higher precipitable water values that eventually form boundary layer conditions more favorable for convection and the cycle repeats itself. These higher precipitable water traces then drift with the low-level mean flow, creating the 'alley' type of appearance (also seen in CAPE and CIN fields).

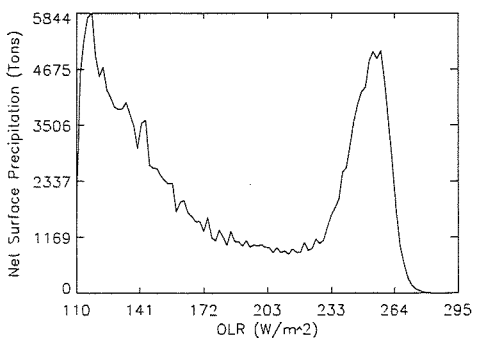

Figure 1: Relationship between OLR and 10 day accumulated precipitation

4. THE IR EXPERIMENT

The IR experiment starts off looking very similar to the PR experiment, but after some 20 days, nearly all fields exhibit a more pronounced almost quasi-stationary alley-like appearance, except the 200mb wind field. The cause of this organizational change from the PR experiment is primarily due to the influence of radiation in creating more cumulus and congestus type clouds (referred to herein as shallow clouds). These clouds are found to coexist with an inversion around the freezing level, the combination of which leads to several feedbacks that maintain the areas favorability for convection. The importance of these clouds has been shown in the observational study of Johnson et al. (1999) and have recently been suggested in TRMM data as a source of precipitation in the tropics (Boccippio et al, 2003, Nesbitt et al, 2000). In this regard, the IR experiment creates a more realistic trimodal distribution of convection as well as bimodal distribution of precipitation (Fig. 1).

4.1 MOIST DOMES

The meandering high precipitable water regions are referred to as moist domes because the higher water vapor mixing ratios extend only up to the top of the inversion, making a dome-like appearance.The moist dome capped by this inversion is likened to a bubbling pot, with shallow convection constantly mixing the entire layer. Cloud top radiative cooling, which approach -15 K/day at the top of these congestus clouds, clearly plays a significant role in the formation and maintenance of this inversion as there was no such inversion in the PR experiment. Furthermore, the detrainment and mixing from these bubbling clouds enhances the water vapor up to the inversion, resulting in stronger long-wave cooling at that height, further strengthening the inversion. The near saturated moist dome enables the shallow convection to precipitate very efficiently to the surface (e.g. Fig 1) providing the mechanism for the radiative-convective equilibrium balance in this lower-layer.

The inversion above the moist dome proves to be fundamental to the maintenance of the dome itself, as well as to the regulation of convection and vertical structure of synoptic waves. The inversion layer stratifies the atmosphere from subsidence disturbances by preventing vertical mixing. Furthermore, small scale wave disturbances, generated by the abundant shallow convection, have the stochastic affect of destroying a synoptic waves vertical structure. Thus, the combination of stratification and buffering from synoptic disturbances protects the domes moisture.

Finally, the shallow clouds provide the fundamental source for moisture and instability through Wind Induced Surface Heat Exchange (WISHE). This is

emphasized in Fig. 2, which provides the integrated surface fluxes over the last 10 days of equilibrium and shows definitively that shallow convection is the source for all moisture. The large amounts of latent heat released by shallow convection, in conjunction with the tropical inversion, induces the build up of higher levels of moisture and CAPE under the dome.

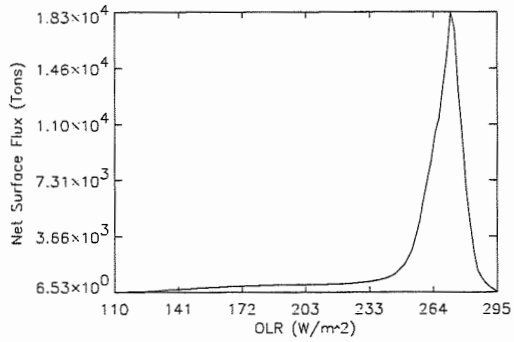

Figure 2: Relationship between OLR and 10 day accumulated surface fluxes

4.2 PHASES OF DEEP CONVECTION

The last 15 days of the IR model run were analyzed in terms of a simple two-layer atmosphere. Layer 1 is the atmosphere below the melting level tropical inversion, and layer 2 refers to the region between the inversion and the tropopause. Given these layers, the domain was then divided into moist and dry regions with the transition between these regions chosen to be 42mm based on observations of precipitation in the model. The precipitable water field was smoothed to a 200km scale to average out local effects of convection. These regions were then tracked as they formed and decayed using complete model captures at half hour intervals. A typical region would be of an order 1000km wide. Fig 3 demonstrates conceptually how the moist domes and deep convection interact, drawing on the observations of this compositing method. In a manner similar to that proposed by Stephens et al (2004), three phases to a convective event can be identified, the pre-conditioning phase, the convective phase and then the recovery phase.

One of the most significant factors in the preconditioning phase is the presence of shallow convection. The initial lack of high clouds promotes stronger cooling in the lower level but this cooling decreases in concert with increasing shallow convection and higher clouds through this period. This warming and the increase in shallow cloudiness produce positive feedbacks on boundary layer instability as previously discussed. Free tropospheric cooling in the clear skies of the upper-layer also increases instability. The combination of these mechanisms causes CAPE to build to a maximum value before convection as conjectured by Stephens et al (2004). Several hours before the onset of deep convection, the congestus clouds start to penetrate into and through the inversion, reducing CIN and moistening the mid levels.

The CAPE build up is not the trigger for deep convection but merely a signal for pre-conditioning. With the aid of a passing synoptic wave, the congestus clouds deepen and the convective phase begins. This coincides with a sharp rise in surface precipitation, layer 2 cloudiness and a sharp decrease in layer 1 cloudiness. This is the deep convective gravity wave signal spreading across the moist dome, shutting down shallow convection while promoting deep and stratiform convection on the meso-scale. Low-level water vapor is steadily transferred into the upper layer with only a minimal loss to precipitation as moisture operates on a longer time scale than that of a single convective event. Net column radiative cooling rates decrease from longwave warming by extensive high clouds. As the MCS propagates along and consumes the moist dome instability, CAPE is steadily removed and CIN is generated by trailing cold pools, stratiform precipitation and dynamic wave subsidence.

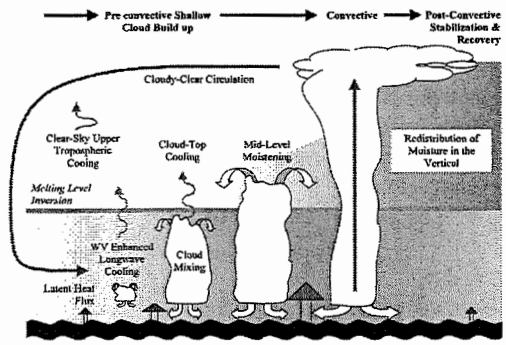

Figure 3: Conceptual cartoon of how moist domes form, are maintained and combine with deep convection

Stratiform precipitation continues to diminish but the stabilizing affect of increased net column heating, due to mid-level and high clouds, signals the stabilization and recovery phase. This stabilization completely removes the low-level clouds, causing precipitation to slide off to much lower values than that prior to deep convection. The latent heat flux is also severely shutdown due the the lack of shallow clouds to fuel winds and mix down drier air from above. For recovery to begin, these mid-level and high clouds

must be removed by either advection or a synoptic subsidence disturbance and allow shallow clouds to reform in the lower-layer and start the cycle again.

5. MOIST DOME GROWTH RATE

To understand the time scale of moist dome feedbacks, we consider the precipitable water (w) as a proxy measure of the moist domes and examine the flux balance for growth of (w);

$$\frac{d}{dt}(w) = \text{LHF} - \text{Sfc. Precip. Flux}$$

From the equilibrium results discussed thus far, three regimes of importance emerge and are analysed by the follwing OLR filter; clear-sky ($> 285\ W/m^2$), shallow convection (285 - 230 W/m^2) and deep convection ($< 230\ W/m^2$). The moisture budget for last 15 days of the IR model run was composited and combined into regime growth rates (Fig 4). These growth rates were obtained by weighting the mean growth rates by their occurrence within the entire domain. Thus, Fig 4. should be interpreted as the net flux, per hour, across the entire domain owing to the contribution of each cloud regime to the total flux.

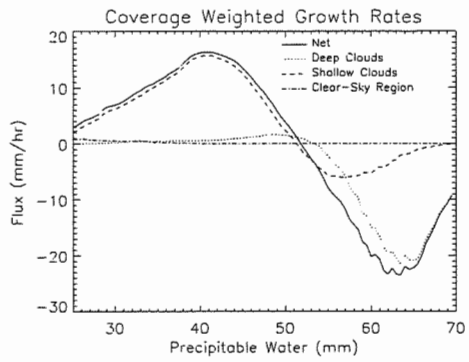

Figure 4: Growth rates of moist domes owing to deep convection (dotted), shallow clouds (dashed) and clear skies (dash-dot). The net growth rate of moisture is denoted by the solid line for refernce

This analysis reveals that the principal source of water up to 50 mm is the regime of shallow convection. Above this, water is lost principally from the deep convection regime, although shallow convection can also become too efficient and rain out excess water at higher w. It is also noteworthy that the precipitable water of the model never exceeds 50mm in non-deep convective regions. This result suggests that convection acts as a fundamental regulator of the atmospheric water content prohibiting runaway growth of water vapor.

6. SUMMARY AND CONCLUSIONS

As opposed to propagating convective regions in the PR, the deep convection and the coexisting precipitable water field become quasi-stationary in the IR experiment. The regions of higher precipitable water are thousands of kilometers wide and coincide with a near ubiquitous tropical inversion around the melting layer not found in the first experiment, except very near deep convection. Below this inversion, moisture builds forming 'moist domes' that produce conditions favorable to deep convection. These moist domes are dominated by shallow cumulus and cumulus congestus that produce significant hydrological, radiative and dynamical effects. Shallow convection appears to be a major contributor to the formation and maintenance of the inversion layer, the two combining to buffer the moist dome from erosion by synoptic wave disturbances. The moist domes create ideal conditions for deep convection and, through MCS-synoptic wave-wave interactions, MCSs preferentially form here. A further secondary circulation driven by cloudy clear-sky radiative heating differences also contribute to the maintenance of the moist dome and subsequent location of deep convection, which is found to undergo a cycle similar to that conjectured by Stephens et al. (2004), beginning with a pre-conditioning phase, followed by a deep convective phase and then a recovery phase. Thus, through their massive spatial and temporal coverage, enhanced WISHE and synoptic wave buffering, moist domes are robust and provide all the moisture in the model. Precipitation efficiency in these moist domes is found to prevent runaway moisture growth suggesting that convection regulates atmospheric water vapor.

7. REFERENCES

Khairoutdinov, M.F. and D.A. Randall, 2003; Cloud-resolving modeling of the ARM summer 1997 IOP: Model formation, results, uncertainties and sensitivities. *J. Atmos. Sci,* 60 pp. 607-625

Pakula, L.P, G.L. Stephens and M.F Khairoutdinov, 2004; Convective Organisation in a Radiative Cloud Equulibrium Model Radiative and Moisture Feedbacks. Submitted *J. Atmos. Sci,* 2004

Stephens, G.L, P.J. Webster, R. H. Johnson, R. Engelen and T. L'Ecuyer, 2004; Observational evidence for the mutual regulation of the Tropical Hydrological Cycle and Tropical Sea Surface Temperatures. to appear in *J. Climate*

RETRIEVAL OF MICROPHYSICS OF DRIZZLING WATER CLOUDS

N.A.J. Schutgens

National institute of Information and Communications Technology (NICT), Tokyo, Japan

1. INTRODUCTION

To understand monthly or yearly averaged radiative effects of clouds, it is important to understand cloud lifetimes, and hence the influence of the 2nd indirect aerosol effect. To obtain global datasets of cloud parameters, NASA is preparing the CloudSat/CALYPSO mission, while ESA/JAXA is considering the EarthCARE mission. Both missions employ a combination of active (radar and lidar) and passive (VIS and SWIR imager) remote sensing instruments. Cloud parameters will be retrieved simultaneously from these instruments, using the strengths of one instrument to overcome the weaknesses of another (sensor synergy). EarthCARE is particularly suited for this task, as all instruments are situated on the same platform. This ensures that all observations are co-located in time and space.

2. RETRIEVAL ALGORITHMS

The retrieval of the properties of drizzling clouds by present-day space-borne missions is difficult because:

1) observations by VIS and SWIR imagers (e.g. AVHRR, MODIS) do not penetrate below water clouds and are rather insensitive to a few large water drops,
2) observations by radars (TRIMM) are insensitive to small cloud drops.

This is exemplified in Figure 1 which shows cloud optical depth and radar reflectivity as observed for a bimodal particle size distribution.

We propose to use existing retrieval algorithms for imager and radar, but to interpret the retrieved data together and, if possible, use that to improve on the original retrievals.

For the imager data, which will consist of top-of-atmospere radiances at 660, 1600 and 2200 nm, we propose to use recently developed algorithms by Brenguier et al. (2000) or Chang & Li (2002. These algorithms are capable of retrieving limited profile information on R_{eff}. For the Doppler radar data we propose to use Frisch et al. (1995).

Corresponding author's address: Nick Schutgens, Cloud Profiling Group, NICT, 4-2-1 Nukui-kitamachi, Koganei, Tokyo, 184-8795, Japan; E-mail: schutgens@nict.go.jp

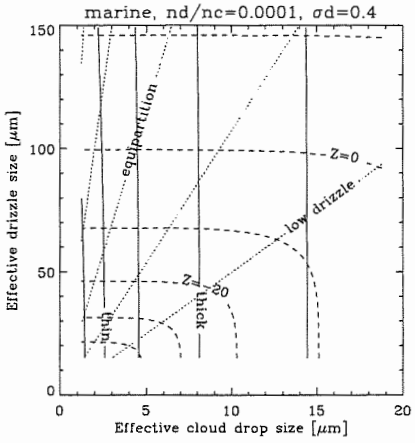

Figure 1 For a bimodal PSD, optical thickness (solid) and radar reflectivity (dashed) are shown.

3. VALIDATION

APEX-3 campaign data (airborne 95 GHZ radar and MODIS or GLI observations, as well as in-situ measurements) will be used to validate the combined algorithms. We will also use a software package specifically developed for simulating EarhCARE observations (Donovan et al. 2002). Together with LES models with explicit microphysics, this will enable us to explicitly quantify errors due to e.g. theoretical assumptions or EarthCARE sampling strategies.

Brenguier J-L, Pawlowska H, Schüler L, Preusker, R, Fischer J and Fouquart, Y, 2000: Radiative properties of boundary layer clouds: droplet effective radius versus number concentration. JAS 57, p. 821.

Chang FL and Li Z, 2003: Retrieving vertical profiles of water-cloud droplet effective radius: algorithm modification and preliminary application. J Geophys Res 108, p. 4763.

Donovan DP, Schutgens NAJ, Poiars Baptista JPV, Barker H, Blanchet J-P, Quante M, Skelton R, Testud J, Ferreira F, 2002: Active and passive synergetic cloud remote sensing from space: simulation of the EarthCARE mission. Proc 2nd int. workshop on space-based cloud radar and lidar, august 2002, Tokyo, Japan.

Frisch A.S., Fairall C.W. and Snider J.B., 1995: Measurement of stratus cloud and drizzle parameters in ASTEX with Kα-band Doppler radar and microwave radiometer. JAS 52, p. 2788.

VARIOUS APPLICATIONS ON TROPICAL CONVECTIVE SYSTEMS USING A GODDARD CUMULUS ENSEMBLE (GCE) MODEL

Chung-Lin Shie[1,2], Wei-Kuo Tao[1], and Joanne Simpson[1]

[1]Laboratory for Atmospheres
NASA/Goddard Space Flight Center, Greenbelt, MD 20771, USA
[2]Goddard Earth Sciences and Technology Center
University of Maryland, Baltimore County, Baltimore, MD 21250, USA

1. INTRODUCTION

The growing usage of cloud resolving model (CRM or cloud ensemble model-CEM) in recent years can be credited to its inclusion of crucial and physically relatively realistic features such as explicit cloud-scale dynamics, sophisticated microphysical processes, and explicit cloud-radiation interaction. On the other hand, impacts of the environmental conditions (for example, the large-scale wind fields, heat and moisture advections, as well as sea surface temperature) on the convective system can also be plausibly investigated using the CRMs with imposed explicit forcing.

In this paper, by basically using a 2D and 3D Goddard Cumulus Ensemble (GCE) model, three distinct studies on tropical convective systems are briefly presented. Each of these studies serves a special goal as well as uses a different approach. In the first study, which uses more of an idealized approach, an interesting relationship found between the quasi-equilibrium temperature and water vapor fields based on both model results and observations will be presented. For the second study, a handful of real tropical episodes (TRMM Kwajalein Experiment - KWAJEX, 1999; TRMM South China Sea Monsoon Experiment - SCSMEX, 1998) have been simulated such that several major atmospheric characteristics such as the rainfall amount and its associated stratiform contribution are investigated. In this study, the observed large-scale heat and moisture advections are continuously applied to the 2D and 3D model. The modeled cloud generated from such an approach is termed "continuously forced convection" or "continuous large-scale forced convection". A third study, which focuses on the respective impacts of atmospheric components on upper ocean heat and salt budgets, will be presented in the end. Unlike the two previous studies, this study employs the 3D GCE-simulated diabatic source terms (using TOGA COARE observations) - radiation (longwave and shortwave), surface fluxes (sensible and latent heat, and wind stress), and precipitation as input for the ocean mixed-layer (OML) model.

Corresponding author's address: Dr. Chung-Lin Shie, Code 912, NASA/GSFC, Greenbelt, MD 20771, USA; E-mail: shie@agnes.gsfc.nasa.gov.

2. MODEL

The 2D or 3D GCE model used in this study is an anelastic, nonhydrostatic model that has been broadly used to study cloud-radiation interaction, cloud-environment interaction, and air-sea interaction. The cloud microphysics include a two-category liquid water scheme (cloud water and rain), and a three-category ice microphysics scheme (cloud ice, snow and hail/graupel). The model also includes solar and longwave radiative transfer processes, and a subgrid-scale turbulence (one-and-a-half order of turbulent kinetic energy) scheme. A stretched vertical coordinate with finer/coarser grid resolution in the lower/upper layers as well as a uniform horizontal coordinate with cyclic boundary conditions is included in the model. The sounding derived large-scale temperature and moisture tendencies are imposed as the major forcing that drives the model. The model structure was detailed in Tao and Simpson (1993).

3. RESULTS

In the first study, Figure 1 shows a scatter diagram of domain-averaged water vapor ("Q" in unit of mm) vs temperature ("T" in unit of K) at the quasi-equilibrium states for the 16 2D GCE modeled simulations (at the end of 25-day of integration). The setups for these 16 (or 8 pairs) idealized GCE tropical simulated runs (either reaching or near statistically quasi-equilibrium states) can be categorized as follows. Six (3 pairs) runs of them are the same as those in Shie et al. 2003 that involve various model setups pertaining to two major components: the vertical wind shear pattern and the minimum surface wind speed used for surface flux computation (see details in Table 1a and Fig. 1 of Shie et al. 2003). These 3 pairs use one type of sounding setup. One other pair of runs have a similar model setup to that of the pair of runs "1M" and "1N" in Shie et al 2003 (also see their Table 1a) except for using a different sounding setup. The rest 4 pairs of runs all have a similar model setup with respect to the pair of "controlled" runs "4M" and "4N" in Shie et al. 2003, except that each pair of these 4 pairs possess an unique setup component, i.e., either in large-scale forcing (constant or variant), surface fluxes (constant or variant), radiations (constant or variant), or sea surface temperature (28.18 or 29.51 C), respectively. Similar to our previous studies (Tao et al. 1999 and Shie et al. 2003), the current 16 modeled experiments presented here have also shown an interesting quasi-

linear relationship. A slope value of dQ/dT (mm/K), i.e., 4.218 can be obtained by applying a built-in linear regression method (from the "KaleidaGraph" plotting package that generated this diagram) to the group of 16 data points (see dashed line). An idealized relationship that may plausibly represent the dQ/dT slope based on a simple thermodynamic concept will be elaborated in detail during the meeting.

In the second study that involves simulations of tropical field experiments, the GCE modeled results have shown promising features for both 2D and 3D. For example, the temporal variation of both 2D and 3D modeled rainfall has agreed fairly well with the observation that was diagnostically estimated from the combined radar and raingauge data (not shown here). Such a good agreement, we believe, is mainly attributed to the driving forcing -- the sounding derived large-scale temperature and moisture tendencies that were implemented into the model. However, both 2D and 3D simulated rainfalls have quantitatively shown a slight wet bias in all three episodes (Table 1). Overall, the 3D model has a slightly better performance than the 2D model in simulating both temporal evolution and total amount of rainfall. It is also found that the 2D model generates more stratiform-type rainfall, while the 3D model significantly favors convective-type rainfall. The commonly found larger vertical velocity (not shown) in the 3D simulations may account for this interesting feature. Moreover, based on the 3D model results, the clouds and cloud systems are generally unorganized and short lived in the KWAJEX episodes. This numerical finding has further been validated by radar observations that will be presented in the meeting.

Evolutions of the 2D modeled domain-average apparent heat source (Q1) and the sounding estimate for the August 29-September 13, 1999 episode are shown in Figure 2. The modeled Q1 qualitatively agrees well with the observed Q1 over the entire model domain (Figure 2a and 2b, respectively), as well as captures the typical convective (Figure 2c) and stratiform (Figure 2d) Q1 structures. Accordingly, a sole maximum heating is found around 500-550 mb in the convective profiles, while a maximum heating/cooling occurs in the upper (around 400mb)/lower (below the melting level) troposphere. A similar feature is also found in the other two episodes. On the other hand, the model simulations (Figure 2) also reasonably capture the typical structures of apparent moisture sink (Q2).

Table 2 lists the temperature, water vapor and static energy budgets of three KWAJEX episodes for both 2D and 3D model simulations. Regardless of the dimension, for all three episodes, the large-scale forcing and net condensation (sum of condensation, deposition, evaporation, sublimation, freezing, and melting of cloud) are the two major physical processes that account for the evolution of the budgets with surface latent heat flux and net radiation (solar and long-wave radiation) being secondary processes. Quantitative budget differences between 2D and 3D as well as between various episodes will be further discussed in the meeting.

In the third study, 3D GCE modeled surface quantities for three convective episodes during TOGA-COARE have been used as input forcing to drive the OML model. TOGA-COARE observations are used as initial and boundary conditions for the coupled model as well as to validate the model results. The three episodes studied are episode 1, December 10-17, 1992; episode 2, December 19-27, 1992; and episode 3, February 9-13, 1993. Episode 1 is prevailed by easterly, while episodes 2 and 3 evolve in the system mainly associated with strong westerlies. A series of sensitivity simulations have been performed for each episode to study the impact by the individual input forcing on upper ocean heat and salt budgets. A series of time evolution of horizontal mean mixed layer temperature ("T"), depth ("h"), and 3-m salinity ("S") for the three episodes will be presented in the meeting.

4. SUMMARY

The three studies presented in this paper have clearly shown the multiple and versatile functions that the GCE model (a CRM) may genuinely provide in tackling various tropical atmospheric and oceanic phenomena. In each of the three studies (idealized approach, real atmospheric field experiment simulation, as well as air-sea interaction study), the modeled results have generally captured certain genuine features.

5. REFERENCES

Shie, C.-L. , W.-K. Tao, J. Simpson and C.-H. Sui, 2003: Quasi-equilibrium states in the tropics simulated by a cloud-resolving model. Part 1: Specific features and budget analyses, *J. Climate*, **16**, 817-833.

Tao, W.-K., J. Simpson, C.-H. Sui, C.-L. Shie, B. Zhou, K. M. Lau, and M. Moncrieff, 1999: Equilibrium states simulated by cloud-resolving models. *J. Atmos. Sci.,* **56**, 3128-3139.

Tao, W.-K. and J. Simpson, 1993: The Goddard Cumulus Ensemble Model. Part I: Model description. *Terr. Atmos. Oceanic Sci.,* **4**, 35-72.

Table 1. Domain-average surface rainfall amount (mm day^{-1}) and stratiform percentage (%) of three KWAJEX episodes for both 2-D and 3-D model simulations, along with the respective rainfall observations (mm day^{-1})

	2-D Rainfall / Stratiform	3-D Rainfall / Stratiform	Rainfall Observations
Aug 7-Aug 12 1999	13.19 / 43.5	13.65 / 32.4	12.00
Aug 17-Aug 21 1999	12.94 / 43.3	12.85 / 31.3	11.06
Aug 29-Sep 13 1999	9.24 / 47.3	9.89 / 36.2	8.85

Table 2. (a) Temperature (C day^{-1}), (b) water vapor (mm day^{-1}), and (c) static energy (W m^{-2}) budgets of three KWAJEX episodes for both 2D and 3D model simulations. Net condensation is the sum of condensation, deposition, evaporation, sublimation, freezing, and melting of cloud. The first and third columns contain the local time change and imposed large-scale advective tendency of the respective quantity. The net radiative contribution of short wave heating and long wave cooling is shown in the fourth column of Table 2a.

(a)

2-D / 3-D	dT/dt (C day^{-1})	Net Condensation	Large-scale Forcing	Net Q_R	Sensible Heat Fluxes
Aug 7-Aug 12 1999	-0.72 / -0.80	3.47 / 3.54	-3.19 / -3.19	-1.07 / -1.25	0.08 / 0.10
Aug 17-Aug 21 1999	-0.37 / -0.68	3.32 / 3.25	-2.84 / -2.84	-0.91 / -1.17	0.06 / 0.08
Aug 29-Sep 13 1999	-0.29 / -0.43	2.37 / 2.50	-1.98 / -1.98	-0.78 / -1.08	0.10 / 0.14

(b)

2-D / 3-D	d(Qv) /dt (mm day^{-1})	Net Condensation	Large-scale Forcing	Latent Heat Fluxes
Aug 7-Aug 12 1999	-1.88 / -2.32	-13.50 / -13.95	9.61 / 9.61	2.01 / 2.03
Aug 17-Aug 21 1999	-5.34 / -5.13	-12.95 / -12.85	6.08 / 6.08	1.54 / 1.64
Aug 29-Sep 13 1999	-1.89 / -2.15	-9.24 / -9.89	4.84 / 4.96	2.51 / 2.78

(c)

2-D / 3-D	D(CpT+LvQv) (W m^{-2})	Net Condensation	Large-scale Forcing	Net Q_R	Sensible Heat Fluxes	Latent Heat Fluxes
Aug 7-Aug 12 1999	-136.3 / -158.9	5.58 / 0.79	-87.1 / -87.1	-121.9/-142.9	9.04 / 11.68	58.13 / 58.77
Aug 17-Aug 21 1999	-197.1 / -225.8	4.37 / 0.00	-148.6/-148.6	-103.6/-133.8	6.31 / 9.16	44.43 / 47.43
Aug 29-Sep 13 1999	-87.5 / -110.8	4.11 / 0.01	-86.1 / -83.4	-89.5/-124.0	11.22 / 16.06	72.76 / 80.48

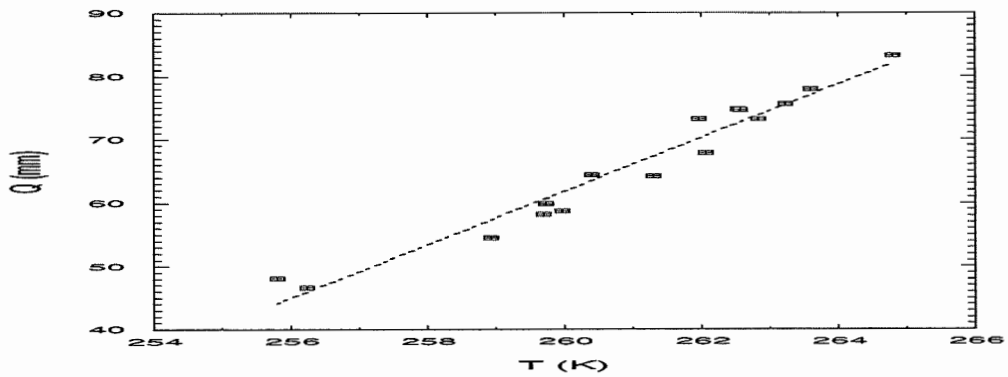

Figure 1. Scatter diagram of domain-averaged water vapor vs temperature at the quasi-equilibrium states (after 25 days of integration) for 16 numerical simulations. A slope value of 4.218 is obtained as a built-in linear regression method in the "KaleidaGraph" plotting package (used to generate this diagram) has been applied to the group of 16 data points (see dashed line).

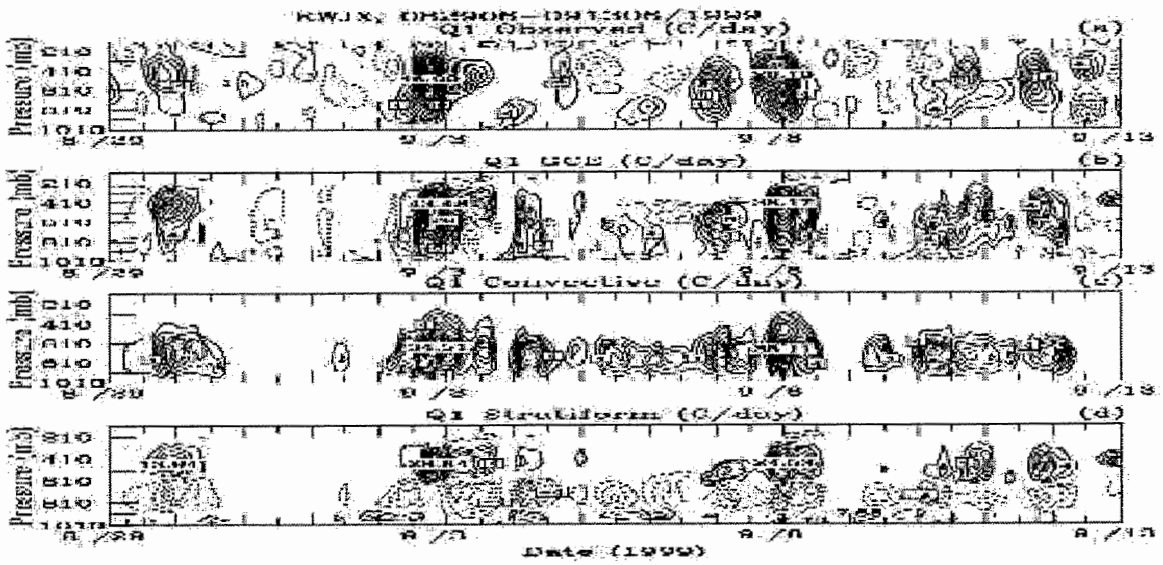

Figure 2. Evolution of the 2D domain-average apparent heat source (Q1) for the August 29-September 13, 1999 episode, (a) derived diagnostically from soundings (provided by Zhang et al. at State University of New York, Stony Brook), and simulated from the GCE model over (b) the entire region, (c) the convective region, and (d) the stratiform region. The contour interval is 2 C day^{-1} for each panel.

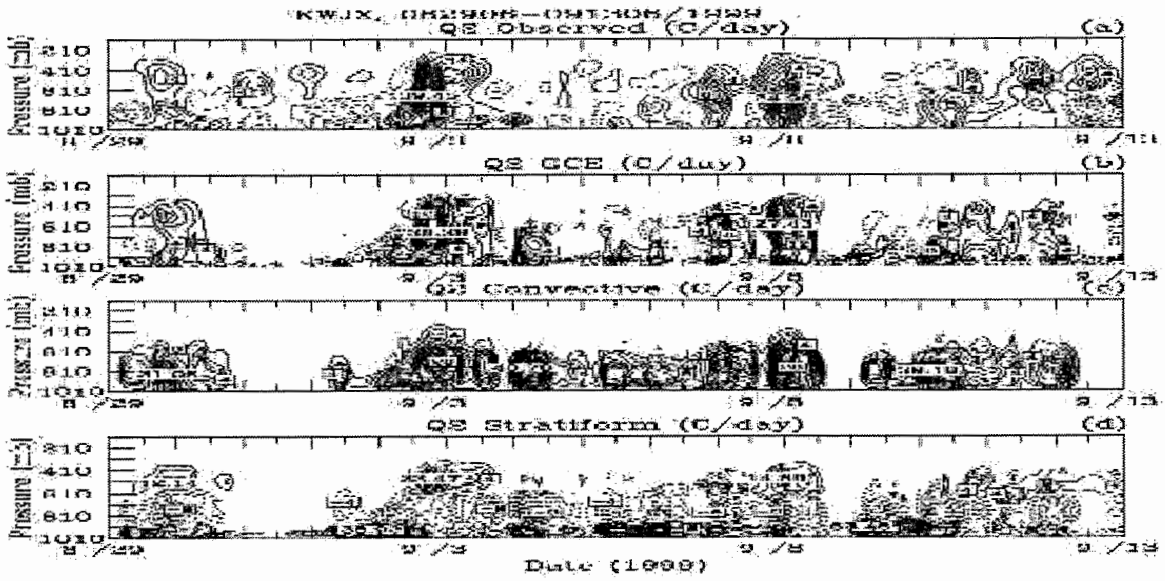

Figure 3. Same as Figure 2 except for the moisture (Q2) budget.

CLOUDS AND THE EARTH'S CLIMATE: AN OBSERVATIONAL STUDY OF CLOUD FEEDBACKS AND THE REGULATION OF THE HYDROLOGICAL CYCLE OF THE TROPICAL ATMOSPHERE

Graeme L Stephens[1] and Tristan L'Ecuyer[1]

[1]Department of Atmospheric Science, Colorado State University
Fort Collins, CO 80523-1371 USA

1. INTRODUCTION

The approximate balance between the radiative cooling of the atmosphere and latent heating associated with precipitation is fundamental to understanding how the earth's hydrological cycle might change in the context of climate change. This has been realized for some time and is the basis of the classical radiative-convective equilibrium assumption used as a paradigm for studying climate and climate interaction. As an illustration of the importance of this type of equilibrium, Stephens (2004) analyzed the outputs of several coupled climate model simulations to suggest that the range in predicted changes in precipitation is a direct consequence of the wide range in the contribution of clouds to the atmospheric radiative heating.

The study reported here builds on the study of Stephens et al. (2004) that suggests cloud radiation interactions exert an important influence on the way in which convection responds to produce this approximate quasi equilibrium. The study analyzes observations of the Madden-Julian Oscillation (MJO) to support the idea that the coupling between the SST, convection and radiation in the atmosphere may be an important characteristic of the oscillation. The MJO is characterized in this study in terms of three different data sources each offering slightly different capabilities and thus different insights into the nature of the MJO. TOGA COARE data provide a detailed localized view of the changing nature of convection, surface fluxes and the SST observed over a period of a few months. Climatological satellite data provide a broader and longer term perspective of the relation between precipitation, OLR, upper tropospheric humidity, and the SST over a period of several years. The analysis of new data sources derived from the Tropical Rainfall Measurement Mission (TRMM) (L'Ecuyer and Stephens, 2003) provide a more intimate view of the relationships between cloud, precipitation, and atmospheric radiative heating. Analysis of these three data sources provide a consistent picture of the coupling between the ocean, convection, and atmospheric heating creating a form of feedback between the ocean and atmosphere referred to as the humidistat feedback.

Results from large domain cloud resolving model experiments run to equilibrium (Pakula et al., 2004) further support the general ideas of the feedbacks.

2. FEEDBACK OVERVIEW

The observations referred to above were analyzed in such a way as to provide some degree of understanding of the nature of the coupling between the ocean, moist atmospheric thermodynamics, radiation and the dynamics of the tropical warm pool regions. The analysis suggests a feedback that regulates, in unison, the SSTs and hydrological cycle of these regions. This is not to suggest that we consider the MJO to be merely a consequence of thermo-dynamic/radiative feedbacks but that these feedbacks interact with and are organized by the dynamics of the MJO in ways that are not yet fully understood.

Stephens et al. (2004) refer to the feedback as the humidistat feedback and argue that it evolves in the three main phases as synthesized in Fig. 1. Cloud resolving model equilibrium simulations

Corresponding author's address: Graeme L. Stephens, Department of Atmospheric Science, Colorado State University, 1371 Campus Delivery, Fort Collins, CO 80523-1371; E-Mail: stephens@atmos.colostate.edu

also suggest that convection evolves in these three phases.

These phases of convection are:

The Destabilization Phase: This corresponds to a warming phase of SST, clearly evident the composite analysis of the data that will be shown in the presentation of this paper. This SST warming phase is induced by quiescent conditions of calm winds resulting in relatively low but non-negligible evaporation and (near) clear skies. These are conditions that favor strong solar heating exceeding 50 Wm^{-2} as the TRMM data source indicates and weak evaporative cooling of the upper ocean indicated by the exaggerated diurnal cycle detected by SST observations. The combination of SST warming and enhanced radiative cooling of the upper atmosphere associated with the lack of high clouds or reduced levels of IWP during this period favors a destabilization of the atmosphere which can be quantified by an observed sharp increase of convective available potential energy (CAPE) of the tropical column during these periods. It is also during this stage that shallow convection begins to increase resulting in a steady moistening of the low levels which plays a further role in conditioning the atmosphere for deep convection. The importance of this shallow convection has been confirmed in other studies including the model study of Pakula et al. (2004), see also the abstract of Pakula and Stephens (2004) presented in this meeting. That model study indicates the importance of cloud-top radiative cooling in forming the congestus-type convection that overall controls the water budget of the region. These conditioning processes do not, however, guarantee the subsequent outbreak of large-scale convection observed during the second phase of the cycle.

The convective phase: The convective phase follows the destabilization stage. The latter is superimposed on a dynamical setting of the MJO that exerts a fundamental control on the triggering of convection and its propagation eastward. The convection that develops is organized into large-scale cloud clusters or super-cloud clusters. The convective period is marked by strengthening of the lower level winds, subsequent increase in evaporation from the ocean and mixing of cold waters upwards into the oceanic mixed layer, heavy precipitation, a drying of the lower layers of the atmosphere and a substantial moistening of the upper troposphere. The envelope of deep convection eventually moves out of the region towards the east proposed to be a manifestation of convectively driven, moist equatorially trapped Kelvin modes. The SSTs cool throughout this period due to a combination of the stronger evaporation, enhanced ocean mixing and reduced solar heating of the ocean.

The restoring phase: Although there is not a distinct beginning to this phase it occurs with the propagation of the large-scale convective envelope or "supercluster" leaving the region filled with high level clouds associated with the residual moisture. These upper level clouds, maintained by the residual moisture, reduce the radiative cooling of the atmosphere through absorption of the infrared radiation emitted upwards from the warmer atmosphere and surface below. SST's continue to cool with solar radiation blanketed by these high clouds. The combination of SST cooling and the heating of the upper atmosphere by high clouds are major factors that lead to an increase of atmospheric stability and a decrease of CAPE and, together with conditions of strong shear, suppress convection. As the winds weaken and the thick upper level clouds dissipate to thin cirrus clouds, evaporation from the ocean surface is reduced and solar heating of the upper ocean mixed layer begins to increase bringing the cooling of the SSTs to an end and returning to the warming phase with the return of a strong diurnal cycle in SST.

3. CLIMATOLOGIES

The TRMM data source used in conjunction with other data to identify the feedback processes summarized in Figure 1 also provide a climatological estimate of the water and energy budgets of the tropical atmosphere. The annual mean energy budget over the tropical oceans in 1998 is summarized in Figure 2. Uncertainty estimates from a comprehensive set of sensitivity studies accounting for errors in all retrieval algorithms and all ancillary data products are also provided. Since it is not possible to determine the fraction of these errors that can be ascribed to random and systematic components, no reduction of noise through spatial and temporal averaging can be rigorously justified at this time.

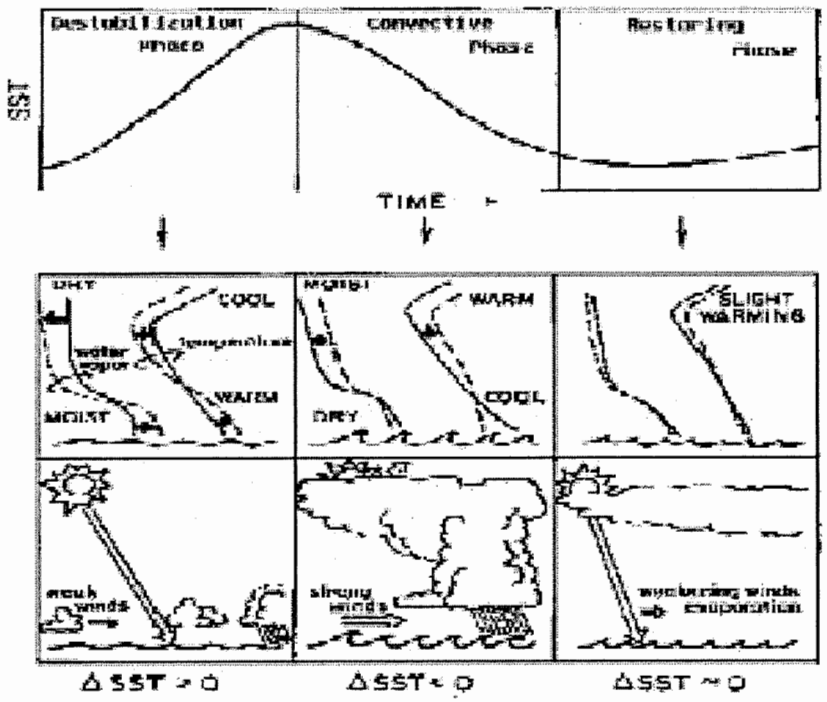

Fig 1. A schematic summary of the observational findings that lead to the concept of the humidistat feedback and its three principal phases. The cycle of SST, highlighted in the upper panel, is a simple depiction of the SST variation as a function of time as observed during TOGA COARE and in other data sources that will be described. This variation offers a reference for defining the three phases of the feedback. The second panel provides a schematic of how the atmospheric temperature and moisture change during these phases defined with respect to the SST cycle. Changes of cloud conditions and associated wind field and heating changes are indicated in the lower panel.

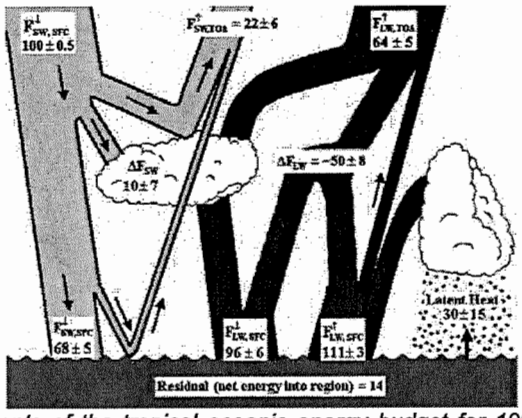

Fig. 2 Principal components of the tropical oceanic energy budget for 1998. All fluxes have been normalized by the mean solar insolation at the top of the atmosphere, 392 Wm^{-2}.

A schematic representation of the distribution of water among its primary atmospheric reservoirs over the same region and time period is presented in Figure 3. Ice and liquid water masses are derived from the algorithms by L'Ecuyer and Stephens (2003) the total mass of atmospheric water vapor is computed from TRMM microwave radiometer data augmented by ECMWF analyses. The accompanying uncertainty estimates derive from rigorous analysis of the source of each quantity and again provide an upper-bound on the accuracy of the products due to the lack of information regarding their breakdown into random and systematic components.

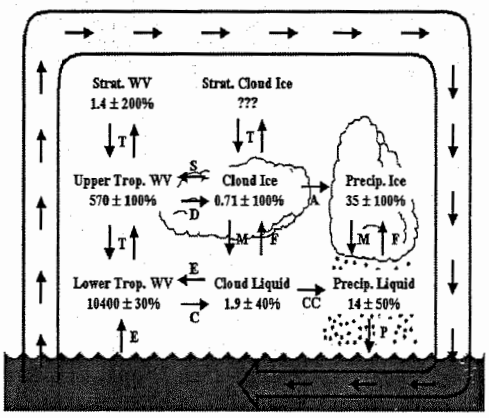

Fig. 3 Primary reservoirs in the hydrologic cycle over the tropical oceans for 1998. All water masses are in 10^{12} kg. The lower troposphere is defined to extend from the surface to 500mb, the upper troposphere from 500 to 200mb, and the stratosphere above 200mb. Arrows between reservoirs represent dominant pathways for exchange between them: evaporation (E), transport (T), condensation (C), deposition (D), sublimation (S), melting (M), freezing (F), aggregation (A), collision and coalescence (CC), and precipitation (P).}

4. ACKNOWLEDGEMENTS

This work has been supported in part by NASA research grants NAS5-99237 and Office of Biological and Environmental Research of the U. S. Department of Energy grant #DE-FG02-94ER61748 as part of the Atmospheric Radiation Measurement Program.

5. REFERENCES

Stephens, G. L., 2004: Cloud feedback in the climate system: a critical review. In Press: J. Climate.

Stephens, G. L., P. L. Webster, R. H. Johnson, R. Engelen, and T. S. L'Ecuyer, 2004: Observational evidence for the mutual regulation of the tropical hydrological cycle and tropical sea surface temperatures. In Press: J. Climate.

Pakula, L. A., G. L. Stephens, and M. Khairoutdinov, 2004: Convective organisation in a radiative-convective equilibrium cloud resolving model, Part I: Effects of radiative feedbacks. Submitted to: J. Geophys. Res.

Pakula, L. A., G. L. Stephens, and M. Khairoutdinov, 2004: Convective organisation in a radiative-convective equilibrium cloud resolving model – Radiative and Moisture Feedbacks. 14th International Conference on Clouds and Precipitation, Bologna, Italy, 18-23 July 2004.

L'Ecuyer, T. S., and G. L. Stephens, 2003: The tropical ocean energy budget from the TRMM perspective, Part I: Algorithm and uncertainties. J. Climate., 16, 1967-1985.

THE ROLE OF SHALLOW CONVECTION IN THE WATER AND ENERGY CYCLES OF THE ATMOSPHERE

K. von Salzen, Norman A. McFarlane, and Michael Lazare

Canadian Centre for Climate Modelling and Analysis, Meteorological Service of Canada, Victoria, British Columbia, V8W 2Y2, Canada

1. INTRODUCTION

Shallow convection plays an important role in the global water and energy cycles of the atmosphere. Considerable fluxes of moisture at the top of the subtropical planetary boundary layer (PBL) are associated with updrafts in shallow cumulus clouds and compensating fluxes of dryer free tropospheric air in the vicinity of shallow cumuli (e.g. Riehl et al. 1951; Nitta and Esbensen 1974). It has been hypothesized that the release of latent heat through re-condensation of water vapour detrained from shallow cumulus clouds leads to important dynamical feedbacks between shallow and deep convection in the tropics (e.g. Johnson and Lin 1997).

The main goal of this study is to determine the impacts of shallow convection on global water and energy cycles, with emphasis on the effects of shallow convection on clouds and radiation. A version of the fourth generation atmospheric general circulation model (hereafter referred to as AGCM4) that is currently under development at the Canadian Centre for Climate Modelling and Analysis (CCCma) is used in this study. A new parameterization of the bulk effects of transient shallow cumulus clouds (von Salzen and McFarlane 2002) is used to represent the effects of shallow convection in AGCM4.

2. MODEL DESCRIPTION

2.1 General

The model version used in this study is based on CCCma AGCM3 (McFarlane et al., manuscript in preparation for *Atmos.-Ocean*). The spectral representation currently used in AGCM4 corresponds to a 47 wave triangularly truncated (T47) spherical harmonic expansion. The vertical region is spanned by 35 layers from the surface to about 1 hPa.

The cloud microphysics scheme of Lohmann and Roeckner (1996), which accounts for cloud water and cloud ice as separate prognostic variables, is used. The scheme has been modified to include the semi-empirical cloudiness parameterization of Xu and Randall (1996) and the parameterizations of autoconversion and accretion by Khairoutdinov and Kogan (2000).

An interactive sulphur cycle is included in the model based on the approach by Lohmann et al. (1999). In the model, sulphate aerosols affect clear-sky radiative transfer directly and indirectly via the first and second indirect effect in stratiform clouds.

Radiation calculations in AGCM4 are based on the correlated k-distribution method for gaseous transmission (Li and Barker 2002). The radiative effects of cloud overlap, cloud infrared scattering, and cloud subgrid-scale variability (Barker 1996; Li and Barker 2002) are also included in the model.

2.2 Deep Convection

The cumulus parameterization of Zhang and McFarlane (1995) is used to represent the effects of deep convection (hereafter denoted by ZM) in the model. The ZM-parameterization is a bulk mass flux scheme which includes a representation of convective scale motions. It is designed to account for the effects of penetrative convection and downdrafts produced by evaporation of rain. As a modification of the original approach, the ZM-parameterization in AGCM4 is applied only to cumulus cloud ensembles with maximum cloud top heights above the ambient freezing level as predicted by the parameterization. This effectively limits the application of the parameterization to cumulonimbus and cumulus congestus types of clouds. The closure condition for deep convection is that the convective available potential energy (CAPE) is consumed at an exponential rate by the cumulus clouds.

2.3 Shallow Convection

The effects of shallow convection are parameterized following von Salzen and McFarlane (2002). In the parameterization, parcels of air are lifted from the PBL into the layer above the PBL. Shallow cumulus clouds are formed once the parcels reach the level of free convection (LFC), at which the parcels become positively buoyant. Above the LFC, the parcels are modified by entrainment of environmental air into the ascending top of the cloud and also by organized entrainment at the lateral boundaries of the cloud. The

Corresponding author's address: Knut von Salzen, Canadian Centre for Climate Modelling and Analysis, Meteorological Service of Canada, University of Victoria, Box 1700 STN CSC, Victoria, BC, V8W 2Y2, Canada; E-Mail: knut.vonsalzen@ec.gc.ca.

cloud-top mixing produces horizontal inhomogeneities in cloud properties and vertical fluxes which are parameterized using joint probability density distributions of total water and moist static energy. The growth phase is followed by rapid decay during which the air within the cloud is completely detrained into the environment.

For implementation of the approach in AGCM4, the cloud base closure condition proposed by Grant (2001) is used. This diagnostic approach is based on a simplified turbulent kinetic energy (TKE) budget for the convective boundary layer.

3. RESULTS

3.1 Experimental Design

A control simulation (CTL) and a number of sensitivity tests have been performed with the model in order to study the sensitivity of the model results to the parameterization of shallow convection (von Salzen et al., manuscript submitted to *Climate Dyn.*). The simulations have been performed for 5-year periods for climatological sea surface temperatures. In the following, results of simulation NOSC, which does not include any explicit parameterization of shallow convection, are compared to results of CTL.

3.2 Mixing and Clouds

The removal of the parameterization of shallow convection from AGCM4 produces substantial increases in zonal mean cloud amounts in simulation NOSC. Typical increases in zonal mean cloud amounts are on the order of 20% in the subtropics. Further analysis of the model results shows that differences in cloud amounts between NOSC and CTL are predominantly associated with large increases in the amounts of low clouds in or above the PBL over the subtropical oceans. The most significant changes in cloud amounts occur in a layer between about 950 hPa and 850 hPa. The increases in cloud amounts are directly related to the removal of the parameterization of shallow convection which strongly reduces the vertical mixing and increases the relative humidity in the lower troposphere in simulation NOSC.

3.3 Hydrologic Cycle

Changes in cloud amounts also lead to substantial changes in precipitation rates. Increases in the amounts of stratiform clouds coincide with increases in annual and global mean stratiform precipitation rates of 0.3 mm/day. On the other hand, convective precipitation rates are generally reduced, although the changes are smaller than those for stratiform precipitation (Table 1).

The simulated increases in convective and decreases in stratiform precipitation rates occur predominantly over the subtropical oceans and give evidence for direct feedbacks between convective and stratiform clouds in these regions. However, changes in cloud amounts and precipitation rates are only relatively weak in the ITCZ. Hence it appears that feedbacks between cloud processes in the ITCZ and between the ITCZ and adjacent regions are less important for the simulated cloud amounts and precipitation rates than direct feedbacks between different types of subtropical cloud systems.

Table 1. Annual and global mean water budgets (units: mm/day). E denotes surface evaporation, P_c and P_s denote precipitation associated with convective, respectively stratiform clouds.

Simulation	E	P_c	P_s	$E-(P_c+P_s)$
CTL	2.79	1.55	1.26	-0.02
NOSC	2.88	1.34	1.56	-0.02
NOSC-CTL	0.09	-0.21	0.30	0.00

In simulation NOSC, reduced vertical mixing of moisture and increased removal of moisture by stratiform precipitation in the lower troposphere causes substantial drying of the free troposphere. As a consequence, the global mean precipitable water decreases from 23.3 mm in CTL to 20.6 mm in NOSC. The increased free tropospheric dryness in the sensitivity tests is not favourable to the formation of deep convection. This leads to an overall reduction in latent heating and precipitation from deep convection in NOSC relative to CTL.

3.4 Energy Balance

Changes in the hydrologic cycle are associated with changes in the energy cycle of the atmosphere in simulation NOSC. The dominant change is a strengthening in shortwave cloud forcing in the subtropics on the order of -20 W/m^2 which results from the increases in the amounts of stratiform clouds in and above the PBL.

The most significant changes between the annual and global mean energy balances in NOSC and CTL are the increases in the reflected solar flux at top of the atmosphere and a similar reduction in solar heat absorbed by the ground (Table 2).

Table 2. Annual mean energy budgets at the top of the atmosphere (units: W/m^2). Fluxes in the table are the incident solar flux F_i, outgoing longwave flux F_o, solar flux reflected from the atmosphere F_{ra}, solar flux reflected from the surface F_{rg}, and the net radiation flux F_{net}.

Simulation	F_i	F_o	F_{ra}	F_{rg}	F_{net}
CTL	341	-234	-82	-25	0.52
NOSC	341	-232	-93	-25	-8.78
NOSC-CTL	0	1.3	-10.8	0.2	-9.31

If interpreted as a linear climate forcing, the simulated change in the radiative forcing of the atmosphere due to the effects of shallow convection is about 3% of the total energy input into the

atmosphere, which is a non-trivial amount if compared to greenhouse gas and aerosol forcings.

Changes in the radiative fluxes and circulation lead to reductions in zonal mean temperatures on the order of about 1.2 K in the upper free troposphere and smaller decreases in zonal mean temperature in other parts of the troposphere in simulation NOSC.

4. CONCLUSIONS AND OUTLOOK

The results of this study give evidence for strong and more or less localized interactions between shallow convection and other types of clouds in the subtropics. The main role of shallow convection in the simulations is to increase the transport of moisture from the subtropical PBL to the free troposphere. The removal of shallow convection from the AGCM leads to moistening in and above the PBL and drying in the lower and mid free troposphere over the subtropical oceans. The associated large amounts of stratiform clouds in the lower subtropical atmosphere give rise to large changes in the water and energy budgets of the atmosphere.

Although it is well established that the processes that cause deep and shallow cumuli to form, grow, and decay are different in nature, it may not be straightforward to represent transitions from shallow to deep convective regimes and feedbacks between these regimes in an AGCM if two conceptually different closures are used for shallow and deep convection as done in this study. Future studies are under way to investigate this issue in more detail.

The simulated changes in the energy and water budgets due to shallow convection are based on the current climate and feedbacks between the atmosphere and ocean have been ignored in this study. Non-linear feedbacks between ocean and atmosphere are likely important factors which may cause a different sensitivity of the climate system for changes in the treatment of shallow convection if accounted for in the model. However, the main features of the simulated response to parameterized shallow convection are likely robust and can be expected to be also of importance in coupled simulations of the climate system.

5. ACKNOWLEDGEMENTS

This study has been funded by the Meteorological Service of Canada with additional support from the NSERC-CFCAS project Modelling of Clouds for Climate (MOC2).

6. REFERENCES

Barker, H. W., 1996: A parameterization for computing grid-averaged solar fluxes for inhomogeneous marine boundary layer clouds. Part I: Methodology and homogeneous biases. J. Atmos. Sci., **53**, 2298-2303.

Grant, A. L. M., 2001: Cloud-base fluxes in the cumulus-capped boundary layer. Quart. J. Roy. Meteor. Soc., **127**, 407-421.

Johnson, R. H., and X. Lin, 1997: Episodic trade wind regimes over the western Pacific warm pool. J. Atmos. Sci., **54**, 2020-2034.

Khairoutdinov, M., and Y. Kogan, 2000: A new cloud physics parameterization in a large-eddy simulation of marine stratocumulus. Mon. Wea. Rev., **128**, 229-243.

Li, J., and H. W. Barker, 2002: Accounting for unresolved clouds in a 1D infrared radiative transfer model. Part II: Horizontal variability of cloud water path. J. Atmos. Sci., **59**, 3325-3342.

Lohmann, U., and E. Roeckner, 1996: Design and performance of a new cloud microphysics scheme developed for the ECHAM general circulation model. Climate Dyn., **12**, 557-572.

Lohmann, U., K. von Salzen, N. McFarlane, H. G. Leighton, and J. Feichter, 1999: Tropospheric sulphur cycle in the Canadian general circulation model. J. Geophys. Res., **104**, 26,833-26,858.

Nitta, T., and S. Esbensen, 1974: Heat and moisture budget analyses using BOMEX data. Mon. Wea. Rev., **102**, 17-28.

Riehl, H., T. C. Yeh, J. S. Malkus, and N. E. LaSeur, 1951: The northeast trade of the Pacific Ocean. Quart. J. Roy. Meteor. Soc., **77**, 598-626.

von Salzen, K., and N. A. McFarlane, 2002: Parameterization of the bulk effects of lateral and cloud-top entrainment in transient shallow cumulus clouds. J. Atmos. Sci., **59**, 1405-1429.

Xu, K.-M., D. A. Randall, 1996: A semiempirical cloudiness parameterization for use in climate models. J. Atmos. Sci., **53**, 3084-3102.

Zhang, G. J., and N. A. McFarlane, 1995: Sensitivity of climate simulations on the parameterization of cumulus convection in the CCC-GCM. Atmos.-Ocean, **3**, 407-446.

CLOUD OBJECT MODELING AND OBSERVATIONS FOR CLIMATE STUDIES

Kuan-Man Xu[1], Bruce A. Wielicki[1], Takmeng Wong[1], and Lindsay Parker[2]

[1]NASA Langley Research Center, Hampton, VA, USA
[2]Science and Application International Corporation, Hampton, VA, USA

1. INTRODUCTION

One of the largest uncertainties in the climate system is cloud feedback. Current climate models continue to struggle to accurately model cloud feedbacks. One of the persistent problems is the difficulty of comparing cloud observations with climate models to the accuracy requirement of climate sensitivity studies. Achieving a statistically significant sampling of observing cloud feedbacks without the influence of weather "noises" requires a minimum of a month of data over a region, and often up to a year. This is because significant cloud feedbacks can result from changes in global mean cloud properties as small as 1% per decade, or regional change of 1% per year. Use of classic gridded monthly or annual mean cloud data invariably includes a wide range of atmospheric states and cloud conditions. It then becomes very difficult in this time-averaged Eulerian view to diagnose which type of cloud is being poorly represented in climate models. This diagnosis is crucial to improve these models' representation of cloud processes.

On the other hand, a Langragian approach, called the "cloud object" approach, groups instantaneous cloud objects by cloud-system type, independent of where and when the cloud-system type occurs. Simulation of these cloud objects is also performed, driven by the matched atmospheric state data. This approach offers two advantages: it reduces cloud variability by grouping data from the same cloud-system type and it reduces sampling noises by combining results from a wide range of geographic regions. Because of its large sample size, the combined results can be stratified according to some measures of atmospheric states such as sea surface temperature (SST) so that the partial derivatives between radiative fluxes and atmospheric variables can be obtained to study cloud feedbacks from observations and model simulations. This study presents the basic methodology and some preliminary results of the cloud object approach.

Corresponding author's address: Dr. Kuan-Man Xu, Mail Stop 420, NASA Langley Research Center, Hampton, VA 23681, USA, k.m.xu@larc.nasa.gov

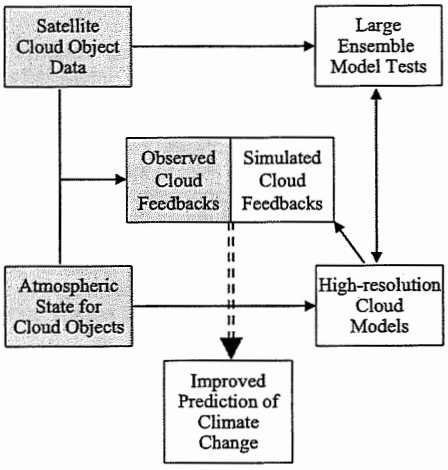

Fig. 1: *A schematic of the approach for cloud object observation and modeling to understand cloud feedbacks.*

2. A NEW METHODOLOGY

Analysis of observational data and high-resolution modeling are integrated in the new cloud object approach to improve the understanding of cloud feedbacks (Fig. 1). In order to reach climate accuracy, satellite data from the Earth Observing System (EOS) are analyzed to generate large ensembles of cloud objects for different cloud-system types. The atmospheric state is matched to each cloud object. The grand mean statistics of observed cloud objects are stratified according to some independent measures of atmospheric states to study cloud feedbacks.

The atmospheric state is also used to drive the simulations of high-resolution cloud models. The statistics of the simulated cloud objects are vigorously compared with those of satellite observations for large ensembles of cloud objects so that systematic errors can be identified and further improvements to the high-resolution cloud models can be made without the need of arbitrary model tuning. The simulated cloud feedbacks can be analyzed and compared with those from satellite cloud object analysis to further improve the high-resolution cloud model. Further testing of the

improved cloud models can be performed by embedding them into a global climate model for selected seasonal and interannual simulations. This revolutionary method of climate modeling is called the "Multi-scale Modeling Framework" or "super parameterization" (Khairoutdonov and Randall 2001). Once these tests are passed, decadal climate prediction can be performed to improve the prediction of climate change.

3. ANALYSIS OF CLOUD OBJECTS

A cloud object is defined as a continuous region composed by individual cloud pixels that satisfy a set of physically-based cloud-system selection criteria. Due to the limited width of satellite swath and the selection criteria, a cloud object can just include part of a cloud system. The limited width of satellite swath can truncate a cloud system. The selection criteria can break a large cloud system into several smaller cloud objects. A "region-growing" strategy based on imager-derived cloud properties is used to identify the cloud objects within a single satellite swath (Wielicki and Welch 1986). A key part of this task is to label the boundaries of an individual cloud object along the scan lines of satellite. Two scan lines are examined simultaneously to identify the boundary pixels of a large continuous cloud region. Assuming that pixels are square, a cloud pixel is flagged as a cloud edge pixel if one or more of its sides is adjacent to a clear pixel. A cloud object is uniquely determined if no cloud edge pixels are adjacent to another cloud object.

This study will examine only the cumulonimbus and its associated thick upper tropospheric anvils over the Pacific Ocean using TRMM data. Four criteria are used to define the tropical deep convection type: 1) the pixels must have 100% cloud fraction; 2) a minimum value of 10 for the cloud optical depth is used to eliminate thin anvil clouds; 3) the cloud top height must be greater than 10 km and 4) the cloud pixels must be located within 25° S and 25 °N of the Pacific Ocean. After individual cloud objects have been identified, grand mean statistics in terms of probability density functions (PDFs) are produced for a group of cloud objects as a function of SST, geographic location and size. A number of measured and retrieved variables is available from both the EOS-Terra and EOS-Aqua satellites. A few PDFs will be shown below to illustrate the sensitivity of cloud properties in tropical convection to change in SSTs and cloud object size ranges.

4. PRELIMINARY RESULTS

Figure 2 shows the number of tropical deep-convective cloud objects in the Pacific during January-August 1998. The numbers of cloud objects are obtained for five different SST ranges and three cloud-object size classes. The SSTs represent the values with the peak probability densities associated with individual cloud objects. The cloud-object size class is defined in terms of equivalent diameters of cloud objects. It appears that the distribution for the smallest cloud objects with equivalent diameters of 100-150 km is more Gaussian than that of the largest cloud objects. This suggests that higher SSTs are preferred by larger cloud objects during this period, even though the range of the SSTs is only 2 K.

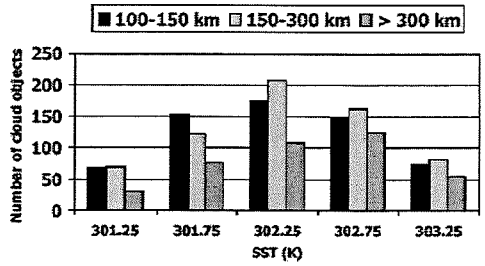

Fig. 2: *Number of cloud objects at different sizes and at different sea surface temperature (SST) ranges.*

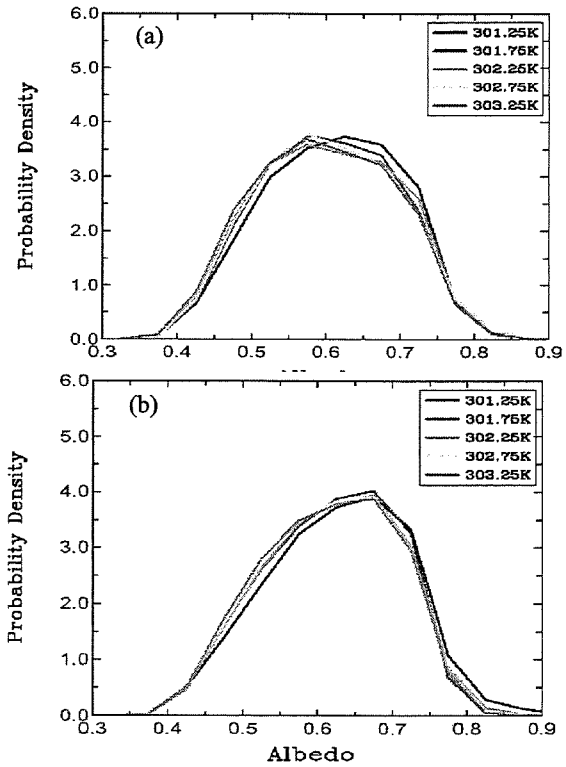

Fig. 3: *Probability density functions of the TOA albedo for (a) 100-300 km and (b) greater than 300 km size classes at five different SST ranges.*

Figures 3 to 7 show comparisons of grand mean PDFs for two size classes (100-300 km; and > 300 km) for TOA albedo, cloud optical depth, ice water path (IWP), outgoing longwave radiation (OLR) flux, and cloud top height. The two smallest size classes shown in Fig. 1 are combined into one (100-300 km). Many of these variables appear to have much greater differences between the size classes than between the SST ranges. The PDFs of OLR fluxes and cloud top heights (Figs. 6 and 7) show slightly greater differences among the SSTs than the rest of the variables. The PDFs of TOA albedos (hereafter, albedo) for both size classes are rather similar among the SSTs except for the lowest SST, in which the clouds are slightly more reflective (Fig. 3). For a given SST, the cloud objects with equivalent diameters greater than 300 km have much higher albedos than those with equivalent diameters between 100 and 300 km. In the small size class, the PDFs are more quasi-normal for all SSTs, while they are slightly skewed to higher albedos in the large size class. This feature is consistent with results of cloud optical depth (Fig. 4) and ice water path (Fig. 5). The cloud optical depths are distributed exponentially while the ice water paths are distributed lognormally for both size classes. The large size class, however, shows higher densities for large values of both variables. This can be more easily seen by comparing the

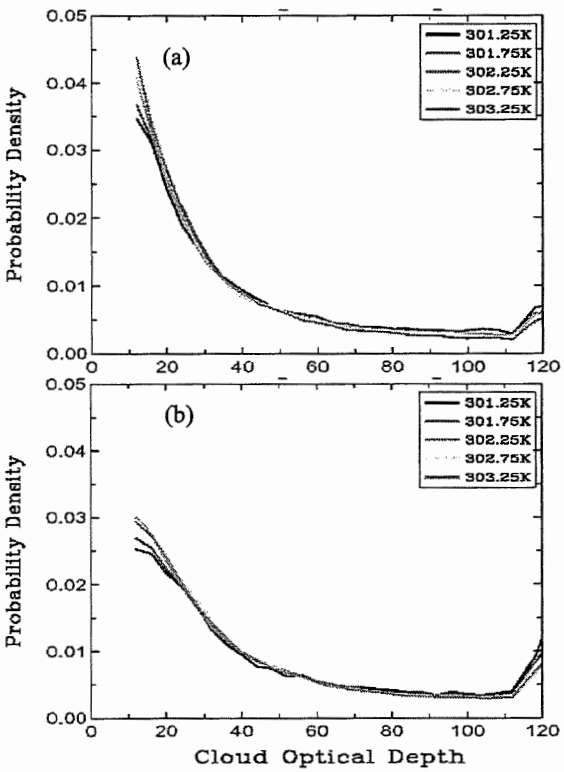

Fig. 4: *Same as Fig. 3 except for cloud optical depth.*

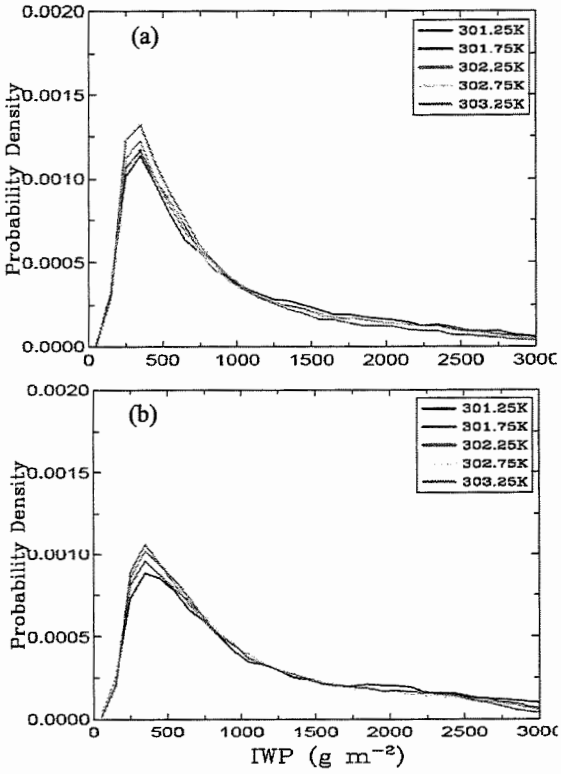

Fig. 5: *Same as Fig. 3 except for ice water path.*

peak densities for low values of both variables in Figs. 4 and 5. The peak densities are much lower for the large size class for all SSTs. An explanation for the differences between the two size classes is that more cumulonimbus cores with slightly thicker anvil clouds are present in the large cloud objects. The small cloud objects are more likely associated with slightly weaker cloud systems which have weaker cumulonimbus cores so that fewer pixels satisfy the selection criteria: cloud top heights greater than 10 km and cloud optical depths greater than 10.

Another interesting result appearing in Figs. 3-5 is that the cloud objects that occur over higher SSTs are slightly less reflective than those that occur over lower SSTs. The PDFs of cloud optical depth and ice water path are also respectively skewed towards lower values of cloud optical depth and ice water path for cloud objects that occur over higher SSTs, although the differences between SSTs are small compared to those between the size classes. This result may be related to the higher cloud tops of the cloud objects that occur over higher SSTs (Fig. 7). Relatively thin anvils are somewhat more abundant when cloud tops are higher. Cloud ice contents of anvil clouds peak well below 10 km. As their heights increase, cloud ice contents decrease and thus more pixels exist with small IWPs.

The OLR fluxes also show large differences between the two size classes (Fig. 6). The PDFs are skewed to the right of the peak PDF value (124 W m^{-2}) for the small size class, but less so for the large size class. This result is expected, based upon the differences in cloud optical and microphysical properties between the two size classes shown in Figs. 4 and 5. This is also related to the lower cloud tops for the small size class for a given SST (Fig. 7). The OLR PDFs are separated into two groups with two or three members each in both size classes. The OLR fluxes are lowers for higher SSTs. This result is not consistent with the fixed anvil temperature (FAT) hypothesis of Hartmann and Larson (2002). They hypothesized that the emission temperature of tropical anvil clouds will remain constant during climate change. It should be noted, however, that not all anvils are included in the PDFs shown in Fig. 6 because we restricted our examination to the thick anvil clouds. The dependence of the cloud top heights on the SST is much stronger (Fig. 7). The cloud tops are much higher for higher SSTs in both size classes, especially so in the small size class. These suggest that macrophysical properties of cloud objects are more sensible to change in SSTs.

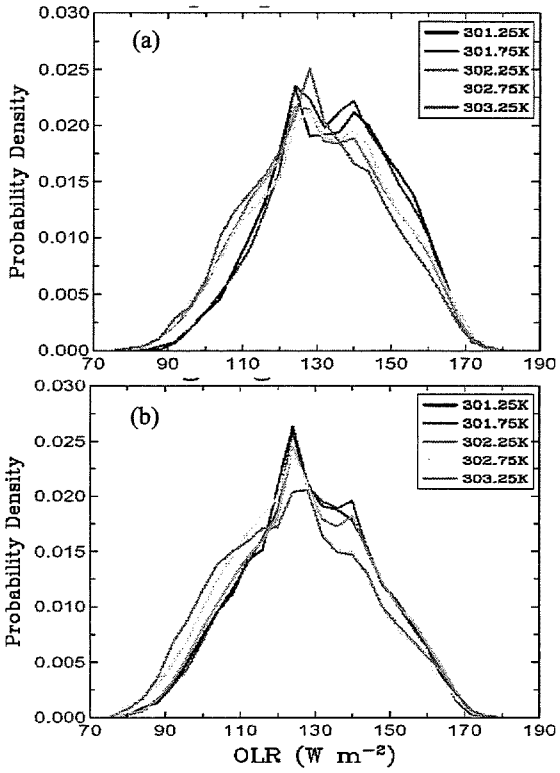

Fig. 6: *Same as Fig. 3 except for outgoing longwave radiative fluxes.*

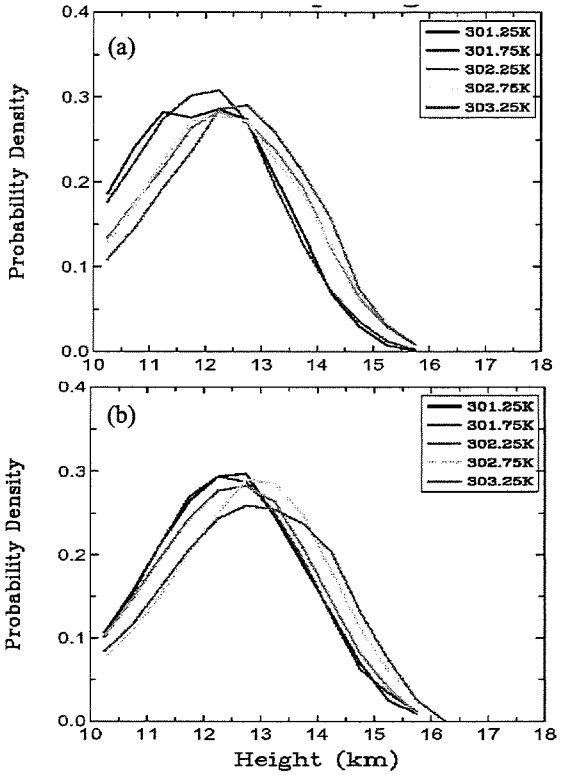

Fig. 7: *Same as Fig. 3 except for cloud top heights.*

5. CONCLUSIONS

This study has presented a new method for studying cloud feedbacks in the climate system through an integrated observational and modeling approach. Satellite data have been analyzed to produce large ensembles of cloud objects for different size classes and SSTs. The statistics of the observed cloud objects are analyzed to understand the sensitivity of cloud feedbacks. It has been found that the differences in the statistics are much greater between the small and large size classes of cloud objects than between different SSTs, especially in cloud microphysical and optical properties. Macrophysical properties show slightly stronger dependency on the SST. Further studies will be performed to compare statistics between observations and high-resolution cloud model simulations.

Acknowledgments: This research has been supported by NASA Interdisciplinary Study Program.

References

Hartmann, D. L., and K. Larson, 2002: An important constraint on tropical cloud-climate feedback. *Geophs. Res. Lett., doi:1029/2002GL015835.*

Khairoutdinov, M., and D. A. Randall, 2003: *Geophys. Res. Lett.,* **28,** 3617-3620.

Wielicki, B. A., and R. M. Welch, 1986: *J. Clim. Appl. Meteor.,* **25,** 261-276.

THE IMPORTANCE OF CLOUD DROP REPRESENTATION ON CLOUD PHOTOCHEMISTRY

Mary C. Barth[1], Roberto Cancel[2], Kristy Ross[1,3] and Si-Wan Kim[1]

[1]National Center for Atmospheric Research, Boulder, Colorado, USA
[2]SOARS/University Corporation for Atmospheric Research, Boulder, Colorado, USA
[3]University of the Witwatersrand, Johannesburg, Wits, South Africa

1. INTRODUCTION

Cloud chemistry, that is, both aqueous phase chemistry and the modification of gas-phase chemistry due to separation of reactants, can affect the production of important tropospheric oxidants. The influence of cloud chemistry on tropospheric oxidants is dependent on the pH of the drops, the liquid water content, and the chemical environment. Because pH varies across the cloud drop spectrum, the degree that cloud chemistry affects tropospheric oxidants is not obvious. For this study, a cloud parcel model is coupled with a gas-aqueous chemistry module to investigate whether the cloud drop representation affects the concentration of several chemical species that participate in ozone photochemistry or aerosol sulfate production. Results of simulations in which cloud drops activate on a cloud condensation nuclei (CCN) distribution are compared to results of a simulation in which a cloud drop population is assumed to have a single size.

2. MODEL DESCRIPTION

The cloud parcel model (Cooper *et al.*, 1997) represents cloud drop activation, condensation, and coalescence. The initial CCN distribution is obtained from aircraft observations measured in South Africa (Ross, 2003; Ross *et al.*, 2004). For particles <0.1 μm, the CCN distribution is represented by the empirical power law relation between number and supersaturation. For larger particles, the size distribution is represented by 3 lognormal equations. The evolution of the aerosol and cloud drop distributions is simulated using a sectional method with up to 256 bins (Cooper *et al.*, 1997).

The gas chemistry represents daytime chemistry of 22 chemical species, including ozone (O_3), nitrogen oxides, carbon monoxide, methane, hydrogen peroxide (H_2O_2), methyl hydrogen peroxide, formaldehyde (CH_2O), hydroxyl (OH) and peroxy radicals, sulfur dioxide (SO_2), sulfate (SO_4^{2-}), ammonia, and carbon dioxide. The aqueous chemistry module represents 18 chemical species. Reactions and reaction rates are those listed in Barth *et al.* (2003) with the addition of SO_2 oxidation by OH in the gas phase and by H_2O_2 and O_3 in the aqueous phase.

Corresponding author's address: Mary C. Barth, NCAR, P.O. Box 3000, Boulder, CO 80307-3000, E-mail: barthm@ucar.edu

3. CONDITIONS OF THE SIMULATIONS

The air parcel begins the simulation at cloud base where the pressure and temperature are 700 hPa and 286.15 K. Gas-phase chemistry is integrated for 600 s to allow the fast-reacting species to reach photochemical equilibrium. The parcel then rises with an initial updraft of 3 m s^{-1}. The updraft is modified by buoyancy-induced acceleration and reaches velocities of up to 9 m s^{-1} or so. While the parcel rises condensation is simulated, coalescence of drops is suppressed, and gas and aqueous chemistry are simulated. Ascent of the parcel is prevented by an artificial inversion placed at 550 hPa, which corresponds to about 1600 m above cloud base and 300 s after cloud drop activation. The parcel then remains at this level while condensation and cloud chemistry are simulated. After a total of 600 s of cloud chemistry (300 s of parcel rising and 300 s of parcel at inversion), the cloud drops are instantly evaporated, aqueous-phase species are volatized to the gas phase, and 900 s of gas-phase chemistry is calculated to complete the integration.

Two airmass scenarios are considered. The first represents a clean airmass, while the second represents a moderately polluted airmass. Initial concentrations of key species are listed in Table 1. The CCN distribution (Table 1), which is composed of ammonium sulfate, follows the power law relation between number and supersaturation (*S*). Photolysis rates are summertime, midlatitude values with a diurnal profile. It is assumed that the simulation begins at 11 a.m.

Table 1: Initial Concentrations of Chemical Species

	Remote Clean	Moderately Polluted
O_3	50 ppbv	75 ppbv
NO_x	125 pptv	1.25 ppbv
CO	100 ppbv	100 ppbv
CH_4	1.7 ppmv	1.7 ppmv
SO_2	10 pptv	1.0 ppbv
H_2O_2	1.0 ppbv	1.0 ppbv
CH_3OOH	0.2 ppbv	0.5 ppbv
CH_2O	0.5 ppbv	1.0 ppbv
HNO_3	1.0 ppbv	1.0 ppbv
CCN	230 $S^{0.72}$	1660 $S^{0.29}$

For each airmass scenario, two simulations are performed. The first calculates the aqueous-phase chemistry in each of the bins representing the cloud drop distribution. The second calculates the aqueous-phase chemistry assuming that the size of the cloud drops are 10 μm in radius, a common assumption in bulk-water microphysics parameterizations. The same total liquid water content is used for both simulations.

4. RESULTS

The liquid water content (LWC) calculated for both the remote clean conditions and the moderately polluted conditions are within 1% of each other (Figure 1). The cloud water mass (expressed in g m^{-3} μm^{-1}) as a function of diameter for 20 s, 60 s, and 300 s after cloud formation is shown in the inset of Figure 1. For moderately polluted conditions, the cloud water mass distribution peaks at smaller sizes than the remote clean conditions, yet has more water in the larger sized drops.

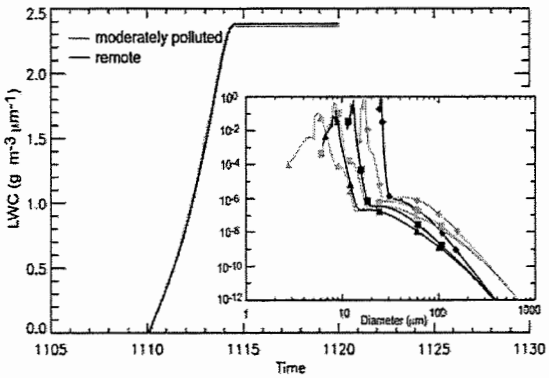

Figure 1. Liquid water content as a function of time for the remote clean and moderately polluted cases. The inset shows the cloud water mass distribution (g m^{-3} μm^{-1}) at 20 s (triangles), 60 s (squares), and 300 s (diamonds) for the remote clean (black) and moderately polluted (gray) cases.

The LWC-weighted pH of the cloud drop population is shown as a function of time (Figure 2) for the 4 simulations. In general the cloud drops are more acidic for the moderately polluted simulations compared to the remote clean simulations. When comparing the pH between the constant radius of the 10 μm simulation to the LWC-weighted pH of the cloud drop population simulation, the values are quite different until about 60 s after cloud drop activation. After this time, the pH values are essentially the same. Before t = 60 s, the pH of the cloud drops with constant radius of 10 μm is greater than the pH of the cloud drop population, showing the poor assumption of 10 μm cloud drop soon after drop formation. The 10 μm drops are more diluted than the drops activated from the CCN, resulting in less acidic cloud water.

The pH is shown as a function of cloud drop size in the inset of Figure 2 for the remote clean and moderately polluted cases. At t = 20 s, the pH values vary significantly with small drops having the smallest pH values. At t = 60 s, the pH of the small drops (<15 μm for remote clean, <8 μm for moderately polluted) has risen such that it is greater than the pH of drops that are somewhat larger in size. As the integration proceeds, the pH across the drop size distribution becomes more uniform. The pH range for the remote clean drop distribution at t = 300 s is 5.35 to 5.54, while the pH range for the moderately polluted drop distribution is 4.3 to 5.4 at t = 300 s.

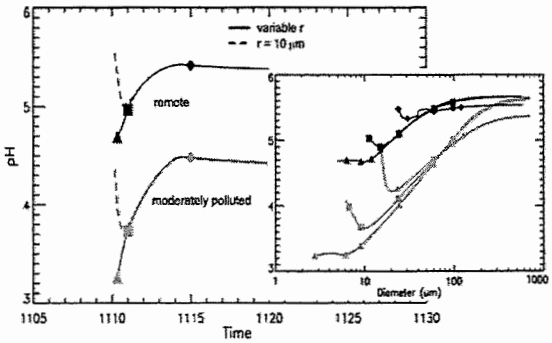

Figure 2. Same as Figure 1 except for pH.

To determine whether cloud drop size and pH of the drops affect the species' concentration, sulfate, hydrogen peroxide, formaldehyde, and formic acid are examined. These species are chosen because their aqueous-phase chemistry depends on pH.

Production of sulfate depends on pH because the reaction rate of S(IV) and O_3 depends strongly on pH. At pH>5.5 the reaction rate is large and is the dominant pathway for sulfate production. At lower pH values, the rate is small and sulfate production is dominated by the S(IV) + H_2O_2 reaction. Once the pathway for sulfate production is altered, the concentrations of H_2O_2 are affected. Thus, pH indirectly affects H_2O_2 concentrations.

One of the key oxidants in the aqueous phase is the superoxide anion (O_2^-). It rapidly reacts with HO_2 (aq) producing H_2O_2, and O_3 (aq) producing OH. At pH values above 4.5, more (O_2^-) is present than HO_2 allowing greater reaction rates to occur.

Formic acid also dissociates in the aqueous phase to form an equilibrium between the acid and formate ($HCOO^-$). Formate rapidly reacts with OH and causes total formic acid concentrations to reach a steady state between production by formaldehyde oxidation and destruction by OH. Above a pH of 3.8 (for T = 285 K), more formate is in the cloud drop than formic acid. Hence less formic acid is produced.

4.1 Remote Conditions

Under remote, clean conditions the chemical concentrations are predicted to be very similar (Figure 3) for both the situation where the cloud drop size distribution and the constant cloud drop radius of 10 μm are used. At ten minutes after cloud drop activation, the percent difference between the simulation with cloud drop size distribution and the simulation with constant drop size of SO_4^{2-}, H_2O_2, CH_2O, and HCOOH are 0.35%, 0.13%, 2.1%, and -1.9%, respectively. For these conditions the pH of the drop size distribution varies over only one pH unit (Figure 2) during the first minute after cloud drop activation and varies <0.2 pH units for the rest of the integration. Because the pH values are so similar between the two simulations, the predicted chemical concentrations are also very similar.

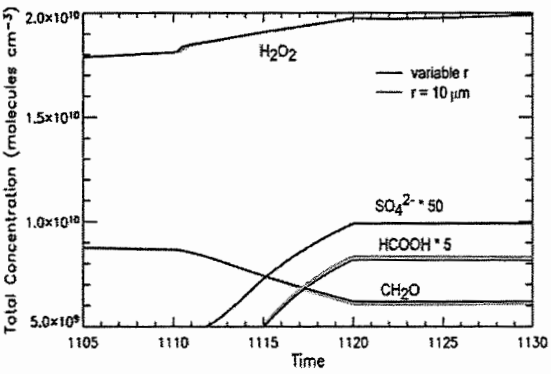

Figure 3. Total concentration (gas + aqueous phases) of SO_4^{2-}, CH_2O, H_2O_2, and HCOOH as a function of time for the remote clean case. Black lines are concentrations for when the cloud drop size distribution was considered. Gray lines are concentration for when the drop size was set to 10 μm.

Because so little SO_2 is present initially, H_2O_2 is not depleted by cloud chemistry, but instead is produced from the aqueous-phase reaction of hydro peroxy radical (HO_2) with its anion, superoxide (O_2^-).

4.2 Moderately Polluted Conditions

Under moderately polluted conditions, differences between the predicted chemical concentrations are noticed (Figure 4). More sulfate is produced when the cloud drop size distribution is included in the model than when a constant radius of 10 μm is used. There is approximately 2% more SO_4^{2-} for the simulation using a cloud drop size distribution after 10 minutes of cloud chemistry. This result follows that found in previous work (Hegg and Larson, 1990; Roelofs, 1993, Gurciullo and Pandis, 1997). As a consequence, H_2O_2 concentrations are also affected, because less H_2O_2 is consumed by S(IV) for the simulation when a constant radius is used for the cloud drops. After 10 minutes of cloud chemistry, there is 1.6% more H_2O_2 for the simulation with constant radius.

Formate is the major form of formic acid in the cloud drops for the simulation with a constant radius of 10 μm, because pH values are always greater than 3.8. Therefore the destruction of formate (and thus the total concentration of formic acid) is greater for this simulation compared to that in the simulation with the cloud drop size distribution, resulting in a greater total concentration of formic acid (~5% at time 1120) for the simulation where cloud drop size is considered than for the simulation where cloud drop size is held constant.

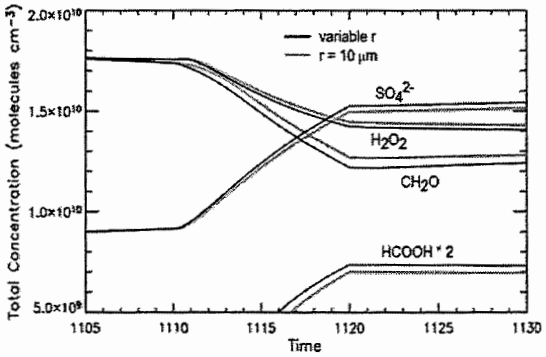

Figure 4. Same as Figure 3 except for the moderately polluted case.

The formaldehyde concentrations also differ for the two simulations. Because both formic acid and formaldehyde are oxidized in the aqueous phase by OH, the two reactions compete. When the faster-reacting formate reaction dominates because of more formate present in the cloud drops, less OH is available for reaction with CH_2O. Consequently CH_2O concentrations are greater for the simulation (~4.2% at time 1120) when the cloud drop radius is held constant when the pH is relatively high.

5. DISCUSSION

The results of the simulations described above indicate that the representation of the cloud drop size distribution has a minor effect on the prediction of cloud chemistry. Factors that contribute to this outcome include the cloud drop size distribution predicted, which may be linked to the simulated vertical velocities, and the absence of coalescence.

The simulations tend to predict narrow cloud drop distributions (Figure 1), which often occurs in cloud parcel models, but does not necessarily occur in nature. When the drops are distributed over a narrow size range, the drops are essentially of a single size. The cloud chemistry for the cloud drop size distribution simulations would then be expected to

respond in a fashion similar to the simulations where the cloud drops are set to a single size.

The vertical velocity predicted in these simulations is typical of cumulus clouds. To simulate more stratiform clouds, simulations are being performed with smaller vertical velocities that are held constant. Preliminary simulations under these conditions indicate that CH_2O-HCOOH chemistry is affected to a greater degree than shown here.

These simulations did not simulate coalescence of drops, which broadens the drop distribution to rain drop sizes. In doing so it would combine drops of different chemical composition resulting in different chemical characteristics. Simulations investigating the effect of coalescence will be pursued.

Lastly the simple chemistry scheme used for these simulations is likely to be inappropriate for moderately polluted or polluted conditions. In particular, gas-phase organic chemistry, which affects CH_2O, H_2O_2, and O_3 concentrations, should be represented. Preliminary simulations with a more complex chemistry mechanism show that the aqueous-phase chemistry is significantly influenced by the treatment of the microphysics.

ACKNOWLEDGMENTS

The National Center for Atmospheric Research is operated by the University Corporation for Atmospheric Research under the sponsorship of the National Science Foundation.

REFERENCES

Barth, M. C., S. Sillman, R. Hudman, M. Z. Jacobson, C.-H. Kim, A. Monod, and J. Liang, 2003: Summary of the cloud chemistry modeling intercomparison: Photochemical box model simulation, *J. Geophys. Res.*, **108**, 4214, doi:10.1029/2002JD002673.

Cooper, W. A., R. T. Bruintjes, and G. K. Mather, 1997: Calculations pertaining to hygroscopic seeding with flares, *J. Appl. Meteor.*, **36**, 1449-1469.

Gurciullo, C. S. and S. N. Pandis, 1997: Effect of composition variations in cloud droplet populations on aqueous-phase chemistry, *J. Geophys. Res.*, **102**, 9375-9385.

Hegg, D. A. and T. V. Larson, 1990: The effects of microphysical parameterization on model predictions of sulfate production in clouds, *Tellus*, **42B**, 272-284.

Roelofs, G. J. H., 1993: A cloud chemistry sensitivity study and comparison of explicit and bulk cloud model performance, *Atmos. Environ.*, **27A**, 2255-2264.

Ross, K.E., 2003: Aerosol-cloud interactions over southern Africa, unpublished PhD thesis, University of the Witwatersrand, Johannesburg, South Africa.

Ross, K.E., Piketh, S.J., Bruintjes, R.T. and Salazar, V., 2004: The effect of coarse mode aerosols on precipitation production efficiency, in preparation.

TRANSFORMATION AND CLOUD INTERACTION OF ATMOSPHERIC AEROSOLS

Hugh Coe[1] M. Rami Alfarra[1], J. D. Allan[1], K. N. Bower[1], M. Cubison[1], P. I. Williams[1], G. McFiggans[1], D. Topping[1], H. Coe[1], J. T. Jayne[2], M. R. Canagaratna[2], D. R. Worsnop[2], J. L. Jimenez[3], S. Fuzzi[4], M.-C. Facchini[4], S. Decesari[4], and A. Berner[5]

[1]Department of Physics, UMIST, Sackville Street, Manchester, M60 1QD, UK
[2]Aerodyne Research Inc., 45 Manning Road, Billerica, MA, USA
[3]University of Colorado, Boulder, CO, USA
[4]ISAC, Bologna, Italy
[5]University of Vienna, Vienna, Austria

1. INTRODUCTION

Large numbers of predominantly hydrophobic sub 100 nm aerosols are released from the urban environment that are composed primarily of organic material. On regional scales they are processed by mechanisms such as surface oxidation (which provides a feedback on photo-oxidant and radical production), condensation, coagulation, and reaction, and are transformed into larger and more hygroscopic particles. These changes to the water affinity subsequently affect the particles effectiveness as cloud condensation nuclei. Observations show that accumulation mode aerosol particles are composed of a mixture of inorganic salts such as ammonium sulphate and nitrate and organic material. In this paper we will use a range of measurements from recent field experiments to demonstrate the composition of aerosol in urban areas as a function of size, how this is modified as a function distance away from the source region, and its subsequent effect on the hygroscopic properties, and the ability of the particles to act as cloud condensation nuclei.

2. AEROSOL COMPOSITION

Measurements of aerosol composition have been made with an Aerodyne Aerosol Mass Spectrometer (AMS) and a range of offline methods after size resolved impactor collection. The AMS samples particles into vacuum through an aerodynamic lens, which focuses particles between 30 nm and 700 nm diameter into a narrow beam with close to 100 % efficiency. The particles are focused onto a heated surface and the non refractory fraction are flash volatilized in the region of maximum electron density of an electron impact ionizer. The ion fragments are then sampled by a quadrupole mass spectrometer. A mass spectrum of the submicron aerosol ensemble is retrieved that can be used to deliver the mass loadings of key components such as ammonium, sulphate, nitrate and organics. Mass size distributions of key species are obtained by chopping the particle beam and rapidly sampling the ion rate of key fragments rapidly. The detection of the ions relative to the phase of the chopper slit gives the particle size information.

Impactor samples were always analysed for inorganic ions, but often were also analysed using a range of other techniques including EC/OC, PAHs, water soluble organic carbon (WSOC), which was further segregated based on the functionality of organic fraction following the techniques developed by Decesari et al., (2000).

Figure 1 shows averaged size distributed organic mass loadings from an urban site in Canada, together with average mass spectra taken over the same period. The mass spectra are characteristic of particles observed in diesel exhausts. There is a clear bimodal distribution in both plots though the relative abundances of these modes are variable. Key fragments are used to identify characteristic organic components in the distribution. M/z 57 is characteristic of aliphatic chains typical of recent emissions; m/z 44 arises from CO_2^+ which arises from highly oxidised organic species; m/z 43 has contributions from both sources. The Canadian data show that aliphatic compounds dominate the smaller mode but have very little contribution to the accumulation mode organic mass, which is dominated by the oxidised fragments.

As the aerosol advect away from the source region the population changes. Figure 2 shows the organic size distributed mass loadings were obtained from a rural site in Canada and from the mountain site Jungfraujoch (3500 m asl) in the Swiss Alps. In these environments, away from local sources, the smaller mode is absent and the large accumulation is dominated by the m/z 44 and other oxidised organic fragments (not shown). The mass spectral signatures are ubiquitous and dominated by m/z 18 and 44, fragments arising from decarboxylation during the AMS vaporization process.

During the ACE-ASIA experiment impactor samples were analysed for the functionality of WSOC and showed that 75% of the water soluble organic material can be identified as mono, di or poly carboxylic acid compounds and this constituted much of the total organic mass. Laboratory measurements of Fulvic

Corresponding author's address: Hugh Coe, Physics department, UMIST, Sackville Street, Manchester, M60 1QD, UK; E-Mail: hugh.coe@umist.ac.uk.

Acid aerosol, an environmentally relevant polyacid shows a very similar mass spectral fingerprint with aged ambient mass spectra obtained from different sites (Figure 3). Smog chamber experiments have also shown that polymerization of secondary organic aerosols produce mass spectral fingerprints that are similar to processed aerosol. The high degree of correlation provides clear evidence that polyacidic compounds of this general type are significant in regional aerosol.

3. HYGROSCOPIC PROPERTIES

Figure 4 shows the growth factor (ratio of humid, 90%, to dry diameter) distributions for 27 nm, 89 nm, and 217 nm dry diameter particles as a function of time during recent sampling in central Manchester. Also shown are the average growth factor distributions during this period. At all sizes most particles show low growth factors, implying the particles are essentially hydrophobic, the larger sizes indicate a more hygroscopic mode that is intermittently present. These data support the AMS results showing large concentrations of aliphatic and aromatic hydrocarbons dominate the organic mass loading.A recent experiment was conducted 30 km east of London close to Chelmsford. The aerosol display hygroscopic properties that are highly variable and very dependent on wind direction and distance from source. Two clear periods have been identified: the first, south westerly advection from the large Greater London conurbation; the second, an anticyclonic period dominated by sea breeze circulations. The average growth factor distributions for 27 nm, 89 nm, and 217 nm dry diameter aerosol (figure 5) show that the aerosol in the London plume have a low growth factor mode similar to the urban data from Manchester but also display a larger and more hygroscopic mode. The data from the anticyclonic period show much broader hygroscopic modes that extend to larger GFs than observed in the London plume or central Manchester. This differences are clear in the chemical size distributions from the AMS measurements.

4. COMPARISONS WITH MODEL PREDICTIONS

These data will be compared with a newly-developed model of the evolution of atmospheric aerosol. A new thermodynamical model of multicomponent inorganic and organic aerosols has been developed at UMIST. A state-of-the-art inorganic ionic interaction model and the UNIFAC group contribution technique for organic compounds are combined to describe the water uptake of mixed aqueous aerosols. Particle curvature is accounted for with a variety of multicomponent surface tension and density formalisms. The model allows a continuous description of aerosol water affinity from the sub to supersaturated environment. This thermodynamic module has been incorporated into a time-evolving coupled model of aerosol microphysics and gaseous photochemistry. The gas phase VOC oxidation mechanism is a subset of the Master Chemical Mechanism (MCMv3) that has been tuned to predict the major contributors to secondary organic aerosol (SOA) formation based on 2D-GCxMS volatile organic compound (VOC) and (oxidised) OVOC precursor measurements. The condensable products have been lumped according to predicted vapour pressures and Henrys Law solubilities. The lumped semi-volatile components are allowed to partition into a measured multicomponent aerosol distribution. In the aqueous aerosol fraction the involatile organic fraction and the partitioning semi-volatile components are represented by compounds consistent with the groupings of water soluble organic compounds (WSOC) measured by the ISAC group (Bologna) and initialisations are constrained by Aerosol Mass Spectrometer (AMS) measurements. The non-aqueous aerosol fraction is constrained only by AMS measurements, but includes compounds shown likely to be formed by the MCMv3 but predicted to be of both low aqueous solubility and low vapour pressure. The model uses a sectional aerosol representation and explicit disequilibrium mass transfer to predict the evolution of the distribution.

Model results, initialised with measurements made in recently polluted conditions, will be presented and compared with measurements made at a location several hours downwind of any major pollution source. The measurements used for this initialisation and validation were taken during the UK Natural Environment Research Council (NERC) Tropospheric ORganic CHemistry (TORCH) experiment.

5. REFERENCE

Decesari, S., M.C. Facchini, S. Fuzzi, E. Tagliavini, 2000. "Characterization of water soluble organic compounds in atmospheric aerosol: A new approach". Journal of Geophysical Research, 105, 1481-1489.

6. ACKNOWLEDGEMENTS

This work was funded through NERC grants NER/A/S/2001/01135, GR3/12499, NER/T/S/2002/00494, and NER/A/S/2000/00442

7. FIGURES

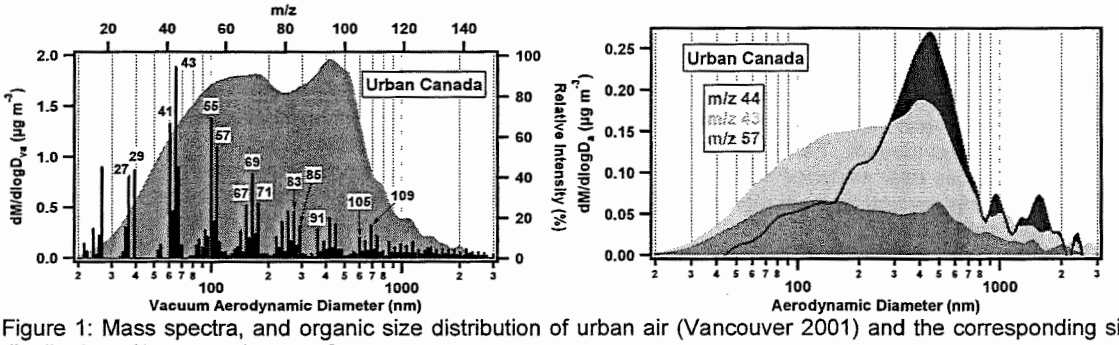

Figure 1: Mass spectra, and organic size distribution of urban air (Vancouver 2001) and the corresponding size distribution of key organic mass fragments

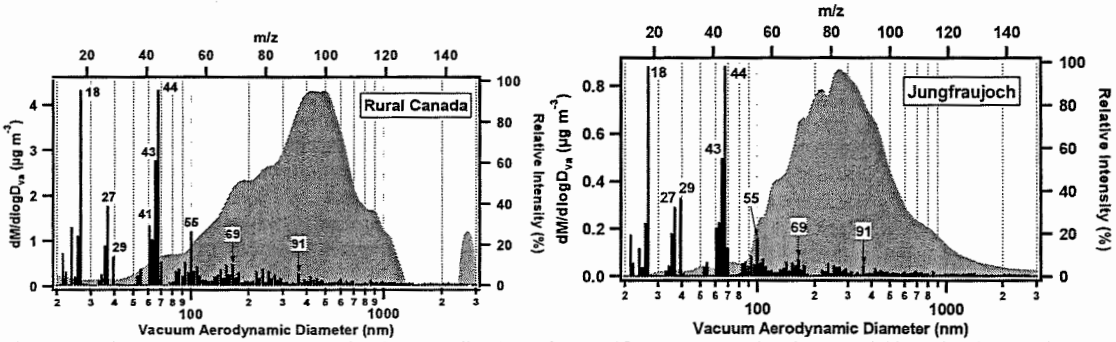

Figure 2: Mass spectra, and organic size distribution of rural (Canada) and background (Jungfraujoch) air.

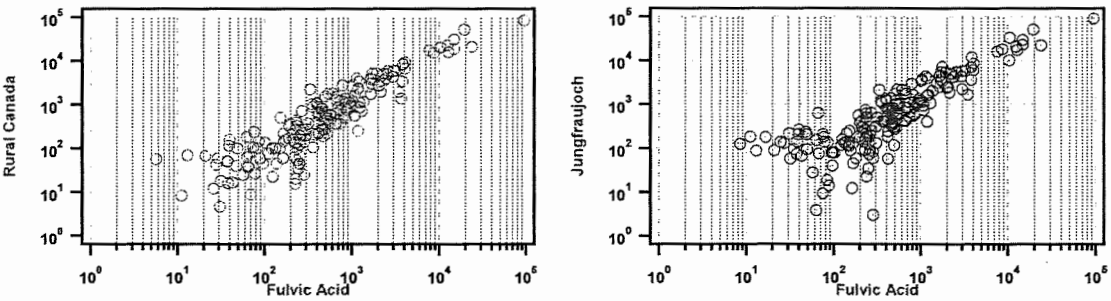

Figure 3: Correlation plots of m/z signal strengths between ambient data taken away from source and a laboratory generated Fulvic acid mass spectrum.

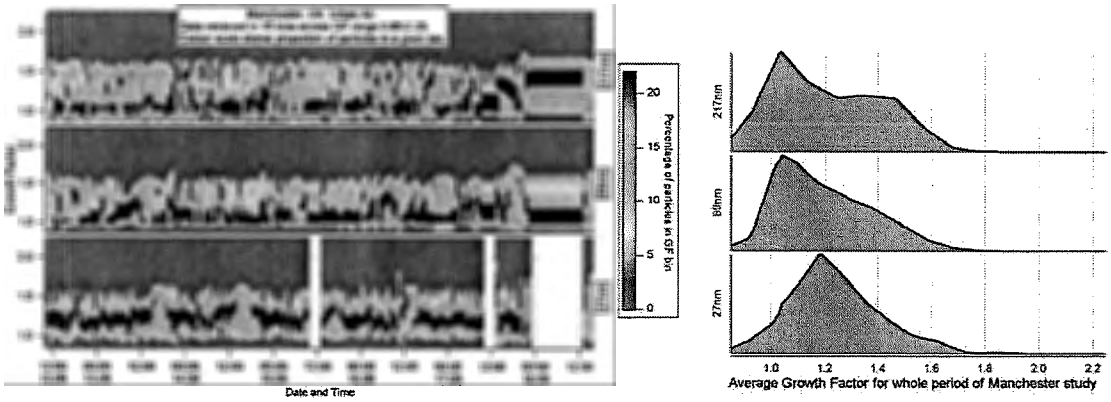

Figure 4: Time series and average growth factor distributions of aerosol sampled at Chelmsford, 30 km to the east of London during August 2003.

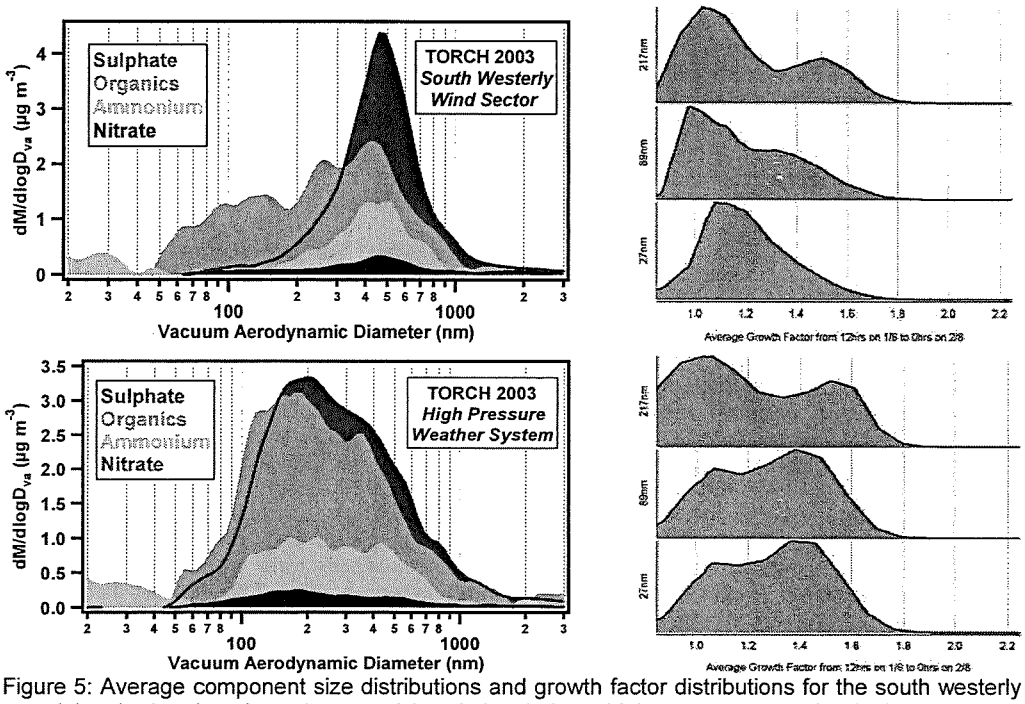

Figure 5: Average component size distributions and growth factor distributions for the south westerly wind sector containing the London plume (top panels) and also during a high temperature anticyclonic period.

The surface tension of fog water samples, cloud water, rainwater and deliquesced aerosols, and its linkage to the organic chemical composition

S. Decesari[1], M. C. Facchini[1], M. Mircea[1], F. Cavalli[1], and S. Fuzzi[1]

[1]Istituto di Scienze dell'Atmosfera e del Clima, Consiglio Nazionale delle Ricerche, Bologna, 40129, Italy

1. INTRODUCTION

Surface films on cloud droplets and deliquesced aerosols have a potential impact on the hygroscopic growth of aerosol particles and the nucleation of cloud droplets. Indeed, the films may act as a barrier to the absorption of water vapor, thus slowing down the growth of the particle (Feingold and Chuang, 2002). On the other hand, the surface tension lowering favors nucleation at a lower equilibrium critical supersaturation (Facchini et al., 1999). Quantifying the impact of such processes is challenging due to the absence of ST measurements on concentrated aqueous samples (solute mass fraction > 0.2 %), and on the structure and permeability of surface films.

It has been argued that surface films are essentially organic layers, a few nanometers thick, lowering the surface tension of samples compared to that of pure water. Fatty acids (FAs) are the most common organic compounds known to be surface-active, and are found in both aerosol and cloud/fog water samples by chemical analysis. However, systematic measurements of the surface tension effect of FAs on cloud water have suggested that in most cases fatty acids could not account for the observed lowering of surface tension (Seidl, 2000). Therefore, the actual molecular composition of the surface-active fraction of OC is still a matter of debate. Recently, it has been argued that also humic-like substances (HULIS), i.e. a fraction of OC not-characterized at the molecular level, may significantly contribute to the lowering of surface tension in fog water (Facchini et al., 2000). Clarifying the chemical nature of atmospheric surfactants is of major importance for understanding how films form and develop as a function of the aerosol water uptake. One key physico-chemical property of the surfactants governing film formation is their *water solubility*. The theory of surface films of soluble and insoluble surfactants is traditionally split in the literature (Adamson, 1990). The governing equations relate the surface tension lowering to the surface area, in the case of insoluble films, and to the surfactant bulk concentration (independent of the surface area), in the case of soluble films. Such theoretical approaches must be at the basis of any treatment of film formation in mycrophysical models describing the nucleation of cloud droplets. The available sets of ST measurements and surfactant chemical analyses do not allow an assessment of which of the two approaches is correct. In order to clarify this issue, we present the contribution of the results from a) novel dynamic ST measurements of atmospheric aqueous samples, and b) OC chemical characterization of aerosol/fog/rainwater samples by nuclear magnetic resonance (NMR) spectroscopy. The results of dynamic surface tension measurements are discussed extensively in the paper by Decesari et al. (2003). Here, we provide a selection of data from that paper, plus some new results obtained on samples collected during a recent field experiment (SMOCC). Furthermore, we focus on the link between the results of ST measurements and the organic composition of atmospheric samples provided by NMR, in order to derive conclusions on film structure and properties.

Corresponding author's address: Istituto di Scienze dell'Atmosfera e del Clima, Consiglio Nazionale delle Ricerche, Bologna, 40129, Italy; E-Mail: s.decesari@isac.cnr.it.

2. EXPERIMENTAL

Sample origin. Samples of cloud water and aerosol from polluted continental and marine environments were selected for dynamic surface tension measurements and NMR characterization. A fine aerosol (< 2.5 μm) was collected with a dichotomous high-volume sampler (HVDS) at a rural site in Brazil on 25-26 Sept. 2002 during the SMOCC field campaign. The PM3 samples were collected in Los Angeles during Oct 1993. Fog water was sampled at a rural site in the Po Valley (Italy) during Jan 2001 and Jan 2002 using an automatic active collector. Cloud water sampling was performed with an active size-segregated collector and a passive stainless-steel collector in Korea, April 2001, during the ACE-ASIA campaign.

ST measurements. Axialsymmetric drop shape analysis (ADSA) performed by a SINTECH (Berlin, Germany) PAT1 tensiometer was used to determine the surface tension on a drop of sample (Loglio et al., 2001). Each sample was analyzed at different surface areas and solute concentrations by progressively reducing the sample volume in a rotary evaporator prior to the ST measurements. Dynamic surface tension, i.e. the variation of ST as a function of time, was measured while sinusoidal variations (T = 20, 40, 80 and 240 s) of the surface area were induced. Automatic FT of dynamic ST profiles was adopted to derive the surface dilatational parameters. Details on the experimental apparatus and conditions can be found in the paper by Decesari et al. (2003).

Organic analysis. The chemical characterization of WSOC was performed by ^{1}HNMR spectroscopy at 400 MHz with a Varian Mercury spectrometer (Decesari et al., 2001). Samples of fog/rainwater and aerosol extracts were dried before redissolution in deuterated water containing 0.22 mM of Tsp-d_4 as internal standard. From 300 to 4000 scans were acquired for each sample, depending on the WSOC concentration.

3. DISCUSSION

The elasticity of surface films is the surface tension variation induced by a small perturbation of the surface area of the film. It is usually expressed by the dilatational elasticity modulus ε:

$$|\varepsilon| = - d\sigma / d\ln A$$

where σ is the surface tension and A is the area of the film. The dilatational elasticity modulus of the films on aqueous atmospheric samples is shown in Figure 1. Data are reported as a function of the surface pressure, π, of the film, i.e. the lowering of surface tension, calculated as the difference between the ST of pure water and that of the sample.

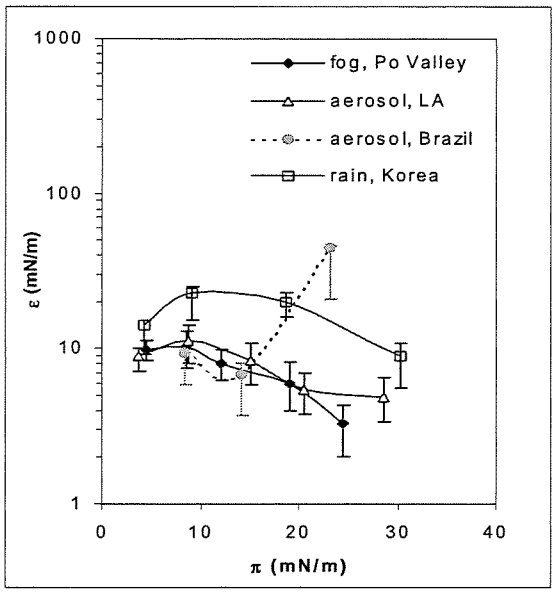

Figure 1. Elasticity modulus ε as a function of surface pressure π, obtained by relaxation experiments on a fog water sample from the Po Valley, the water-extract of a PM3 aerosol sample from Los Angeles (LA), the water-extract of a PM2.5 of an aerosol sample from Rondonia (Brazil), and from a rainwater sample from Korea.

The dilational elasticity modulus varies between 3 and 50 mN/m, with higher values obtained for the Korean rainwater sample and for the Brazilian aerosol extract, but at different surface pressure regimes. The elasticity of the samples from Korea, Los Angeles and the Po Valley show a maximum at ca. 10 mN/m of surface pressure, and then decrease slowly with π. However, the elasticity of the Korean sample is always two-threefold higher than that of the other samples. At low surface pressures, the Brazilian aerosol extract exhibits an elasticity comparable to that of the Po Valley fog and of the Los Angeles sample, whereas in the high π regime it increases to 50 mN/m. In order to interpret the above results in terms of the physico-chemical properties of the surfactants responsible of the measured ST lowering, commercial standards of insoluble (stearic acid) and water-soluble (sodium dodecyl sulfate, SDS) surfactants were subjected to the same method for dynamic ST measurements adopted for the sample. In addition, Suwannee River fulvic acid (solubility in water: ca. 4 g/100g_{H2O}) was analyzed as a model compound for HULIS (Fuzzi et al., 2001). Figure 2 summarizes the results obtained on standards.

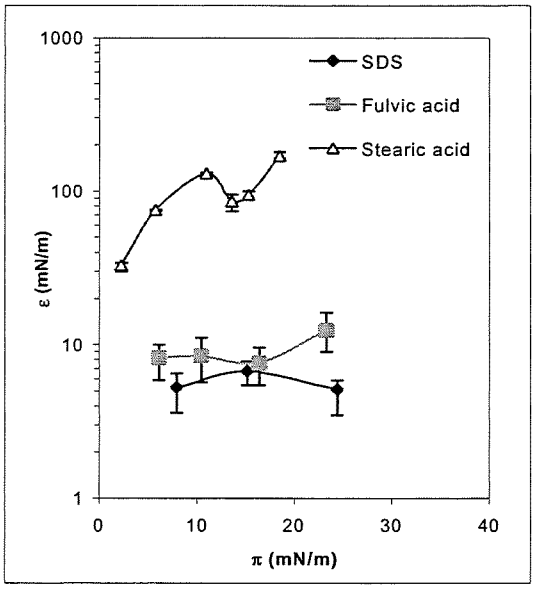

Figure 2. Elasticity modulus ε as a function of the surface pressure π, obtained by relaxation experiments on films of sodium dodecyl sulfate (SDS), Suwannee River fulvic acid, and stearic acid.

Notwithstanding the differences in molecular structure, surface films made of SDS or fulvic acid (FA) show similar elasticity properties. Conversely, surface layers of stearic acid show ε values one order of magnitude higher compared to the other two standards. Such differences must be attributed to the diffusional exchange of water-soluble surfactants (in the case of SDS and fulvic acid), which tends to compensate the changes in surface concentration induced by the dilation/compression of the film. The comparison of the results obtained on the samples with those provided by the standards suggests that this mechanism of diffusion between the surface film and the bulk aqueous phase occurs also in deliquesced aerosols, and fog/rain water. More precisely, the elasticity values obtained on the Po Valley fog samples and Los

Angeles aerosol extract are characteristic of water-soluble surfactants, whereas the results for the Korean sample still indicate water-soluble surfactants, but less soluble than FA and SDS. Finally, the behavior of the Brazilian sample is consistent with that of water-soluble surfactants, although the increase in elasticity at high surface pressures may indicate that the surfactant bulk concentration is approaching its saturation point. The process is also responsible for the increase in elasticity of the FA at surface pressure higher than 20 mN/m, when the FA bulk concentration reaches 3 g/100g_{H2O}, i.e. just below the saturation point.

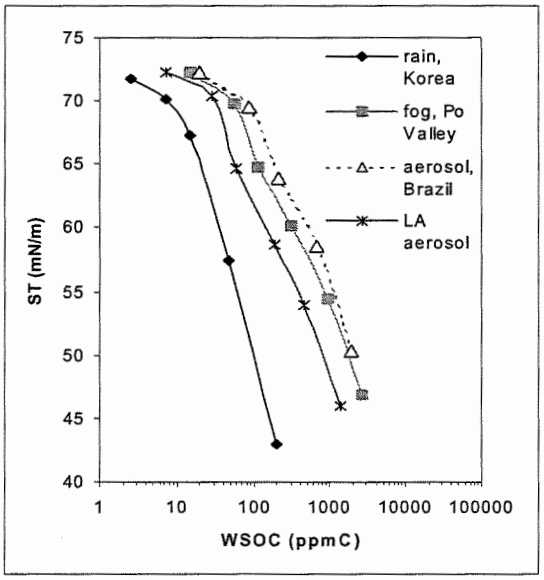

Figure 3. Surface tension (ST) versus bulk WSOC concentration (as ppm of carbon) measured for atmospheric aqueous samples: rainwater from Korea, fog water from the Po Valley, and water-extracts of a PM3 aerosol sample from Los Angeles (LA) and of a PM2.5 aerosol sample from Rondonia (Brazil).

On the other hand, in all π regimes, none of the samples showed elasticity values as high as those observed for stearic acid, indicating that completely insoluble surfactants were not responsible for the surface tension lowering measured on the samples. Furthermore, the analysis of other rheological parameters of the films on atmospheric samples, such as the dilatational viscosity, supports the interpretation based on water-soluble surfactants diffusing between the surface layer and the bulk solution (Decesari et al., 2003).

The surface tension of aqueous solutions of film-forming compounds is usually expressed as a function of their bulk solution, according to the Szyszkowsky equation:

$\sigma = \sigma_0 - \Gamma_{max} RT \ln(1+c/a)$

where σ_0 is the surface tension of pure water, Γ_{max} is the maximum surface excess, R is the gas constant, T the temperature, and 'a' is a constant characteristic of the surfactant. The above equation has already been used to fit the surface tension lowering as a function of the bulk WSOC concentration in fog water samples (Facchini et al., 1999). Figure 3 shows the ST lowering versus bulk WSOC concentration of the samples considered in the present study. Their behaviors are qualitatively similar, and also comparable to the case presented by Facchini et al. (1999): no transition to multiple layers or micellae regimes could be observed, and the surface concentration of surfactants mainly continued to increase asymptotically towards a maximum surface excess Γ_{max} of 1 - 3 molecules nm^{-2}. Despite this general behavior, the effect of WSOC on surface tension reveals a large quantitative variability among samples. The figure clearly shows that the WSOC in the Korean rainwater are more efficient in reducing the surface tension compared to those contained in fog water or in the Brazilian aerosol extract (the Los Angeles aerosol shows an intermediate behavior). Such differences must be attributed to actual differences in WSOC chemical composition.

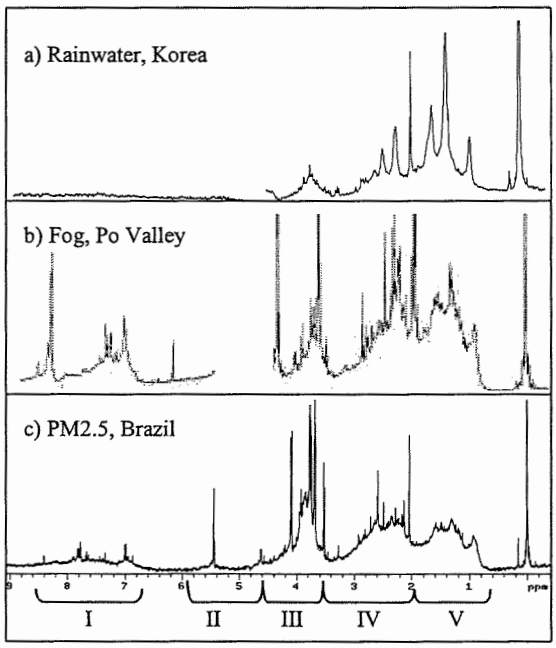

Figure 4. ^{1}HNMR spectra at 400 MHz of the water-soluble carbon fraction of: a) rainwater from Korea, b) fog water from the Po Valley, c) a PM2.5 aerosol sample from Rondonia, Brazil. The observed signals were attributed to five main categories of functional groups according to the scale of chemical shifts: I aromatic (Ar-H); II vinyl and acetals (H-C=, O-CH-O); III alcohols and ethers (HC-O); IV aliphatics bound to unsaturated carbon atoms (HC-C=C, HC-C=O), V saturated aliphatics (C-H). The peak at 0 ppm is due to the internal standard.

Figure 4 reports the ^{1}HNMR spectra of the Korean rainwater sample, the Po Valley fog, and the Brazilian aerosol extract (LA aerosol not analyzed). The analysis of the spectra provides the chemical

composition of WSOC in terms of major functional groups (Decesari et al., 2001). The samples from the Po Valley and Brazil are characterized by abundant aromatic moieties substituted with carbonyls and phenolic groups, whereas the band of aromatic hydrogen atoms is virtually absent in the Korean sample. The latter exhibits aliphatic groups, mainly associated with saturated C-H units, such as straight chains with terminal methyls. Conversely, the methylenic chains (peak at 1.3 ppm) are much less abundant in the samples from the Po Valley and Brazil. These samples contain other saturated aliphatic moieties, possibly alicyclic compounds, or C-H units in β position to electronegative atoms and double bonds. Furthermore, the C-H groups in α position to C=C and C=O (carbonyls and carboxyls) and bound to oxygen atoms (alcohols and ethers) are much more concentrated in the Po Valley and Brazilian samples than in the Korean sample. In brief, the ^{1}HNMR analysis of the WSOC in the Korean sample highlights the occurrence of compounds carrying large hydrophobic groups, while more polar species were found to dominate the WSOC composition in the other two samples. Therefore, a plausible explanation of the difference in surface-activity of the samples (Figure 3) is provided by the partly hydrophobic WSOC in the Korean sample, which enrich at the air/water interface even at low bulk concentrations. Conversely, the oxygenated species that account for the WSOC composition in the samples from the Po Valley and Brazil starting forming a surface excess only at bulk concentrations as high as 100 ppmC.

4. CONCLUSIONS

Atmospheric samples from different sources show rheological parameters of the surface films comparable with those of standards of water-soluble surfactants, such as fulvic acid and SDS. Therefore, on the basis of our set of samples, we can conclude that the principal contributors to film forming substances in cloud droplets and wet aerosols are WSOC, and that the Szyszkowsky equation, relating ST to the bulk composition of the sample, is appropriate for modeling the formation of surface layers on liquid droplets in the atmosphere. However, the different surface tension lowering observed in different samples at comparable WSOC concentrations indicates that the parameters of the Szyszkowsky equation (especially the term 'a') cannot be extrapolated to samples of unknown composition. Such differences in surface-activity of the samples are reflected by actual differences in WSOC chemical composition as determined by ^{1}HNMR analysis. In particular, it was found that WSOC carrying saturated straight chains, thus having a partially hydrophobic character, are responsible for the highest surface tension lowering measured on atmospheric samples. These findings provide further evidence that the bulk chemical composition of WSOC is the main factor controlling the formation of surface films on deliquesced aerosols and fog/cloud droplets.

5. ACKNOWLEDGEMENTS

The authors gratefully thank Patrick Chuang (University of California, Santa Cruz, CA, USA) and Michael Hannigan (University of Colorado, Boulder, CO, USA) for providing the samples from Los Angeles. Tom W. Choularton and Keith N. Bower (UMIST, Manchester, United Kingdom) are acknowledged for coordinating and performing cloud water sampling in Korea during the ACE-ASIA campaign. Finally, we extend thanks to Willy Maenhaut (Ghent University) for providing the samples from Brazil, collected during the SMOCC experiment. This work was partially financed by Agenzia 2000 of C.N.R..

6. REFERENCES

Adamson, A.W., 1990. Physical chemistry of surfaces, Wiley-Interscience, New York., USA.

Decesari, S., M. C. Facchini, M. Mircea, F. Cavalli, S. Fuzzi, 2003. Solubility properties of surfactants in atmospheric aerosol and cloud/fog water samples. J. Geophys. Res., 108, 4685, doi:10.1029/2003 JD003566.

Decesari, S., M.C. Facchini, E. Matta, F. Lettini, M. Mircea, S. Fuzzi, E. Tagliavini, and J-P. Putaud, 2001. Chemical features and seasonal trend of water soluble organic compounds in the Po Valley fine aerosol. Atmos. Environ. 35, 3691-3699.

Facchini, M.C., Mircea, M., Fuzzi, S., and Charlson, R.J., 1999. Cloud albedo enhancement by surface-active organic solutes in growing droplets, Nature, 401, 257-259.

Facchini, M.C., Decesari, S., Mircea, M., Fuzzi, S., and Loglio, G., 2000. Surface tension of atmospheric wet aerosol and cloud/fog droplets in relation to their organic carbon content and chemical composition, Atmos. Environ., 33, 4853-4857.

Feingold, G. and Chuang P.Y., 2002. Analysis of the influence of film-forming compounds on droplet growth: Implications for cloud microphysical processes and climate, J. Atmos. Sci., 59, 2006-2018.

Fuzzi, S., S. Decesari, M.C. Facchini, E. Matta, M. Mircea, and E. Tagliavini, 2001. A simplified model of the water soluble organic component of atmospheric aerosols, Geophys. Res. Lett., 28, 4079-4082.

Loglio, G., P. Pandolfini, R. Miller, A.V. Makievski, F. Ravera, M. Ferrari and L. Liggieri, 2001. 'Drop and Bubble Shape Analysis as Tool for Dilational Rheology Studies of Interfacial Layers', in 'Novel Methods to Study Interfacial Layers', Studies in Interface Science, Vol. 11, D. Möbius and R. Miller (Eds.), Elsevier, Amsterdam, pages 439-485.

Seidl, W., 2000. Model for a surface film of fatty acids on rain water and aerosol particles, Atmos. Environ., 34, 4917-4932.

POLAR NIGHT INVESTIGATION OF CHEMICAL COMPONENTS IN FRESH SNOW PARTICLES AND AEROSOL/GAS IN THE ATMOSPHERE AT NY-AELESUND

T. Endoh[1], T. Takahashi[2], T. Hayashi[2], I. Noguchi[3], S. Koga[4], N. Kurita[5], N. Tanaka[5], and M. Wada[6],

[1]Tottori University of Environmental Studies, Tottori
[2]Hokkaido University of Education, Sapporo,
[3]Hokkaido Institute of Environmental Science, Sapporo
[4]National Institute for Resources and Environment, Tsukuba
[5]Frontier Research System for Global Change, Tokyo
and
[6]National Institute of Polar Research, Tokyo

1. INTRODUCTION

It had been observed and marked that non-rimed snow crystals have preferentially higher concentration of NO_3^- ion than rimed snow crystals as reported by Takahashi etal. (1996). Such results are seen in coinciding to the results obtained in the laboratory experiments by Mitra etal. (1992) and Diehl etal. (1996). At that time, the component of NO_3^- in solid precipitation without frozen cloud droplets were considered to be taken by the atmospheric scavenging of an anthropogenic contamination of air in land breeze below cloud base. One of the reasons why they took place in these processes as their origin was thought that NO_3^- was brought in short range transport. To verify that, same kind of observation and sampling were carried out in a remote area, Moshiri (Japan) where environmental atmosphere was extremely clean like in the polar region. The concentration of NO_3^- in solid precipitation was however, observed not to be inthe lower level expected but in the considerably greater values. Therefore, these results made us to consider about the abilities of NO_3^- in solid precipitation participating in long range transport like as SO_4^{2-} ion. To examine and verify these hypotheses, this study was carried out at Ny-Ålesund (Spits Bergen) of the polar region as one of the most remote areas of the world.

Corresponding author's address: Tatsuo Endoh, Tottori University of Environmental Studies, Tottori 689-1111, Japan; E-mail: t-endoh@kankyo-u.ac.jp

2. METHODS

Solid precipitation particles were sampled with receiving directly as a natural snowfall with several clean-up containers in the center floor surrounded by a screening net wind-shelter avoiding not to be contaminated by drifting snow. Inside of the shelter, two instruments were installed i.e. a measuring system for snowfall rate with an electric balance and a recording system of snow particle shapes, sizes and species by a time lapse video microscopic camera. The environmental atmosphere was introduced from inlet pipes set in the outdoor and connected to a system commercially called low volume air sampler with a virtual filter at the diameter in 2 micron dividing into two size ranges i.e. fine and coarse particles.

3. RESULTS

An observational research had been carried out at the arctic, Ny-Ålesund (79oN, 12oE) as one of the most remote areas of northern hemisphere, from 16th December 1998 to 9th January 1999. Solid precipitation particles were sampled at and analyzed by means of mainly chemical methods with some isotopic ones. Atmospheric gaseous and particle materials in the environmental atmosphere were also sampled by a system of low volume air sampler. Although seven series of definite snowfall had

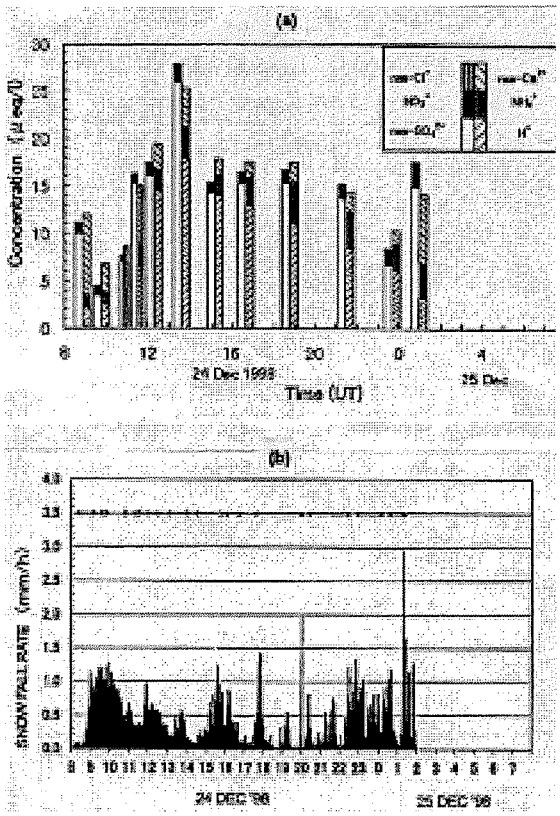

Fig.1. Temporal changes of (a) chemical components in solid precipitation and (b) snow fall rate in Ny-Å lesund in Case 1 for 24th-25th December 1998.

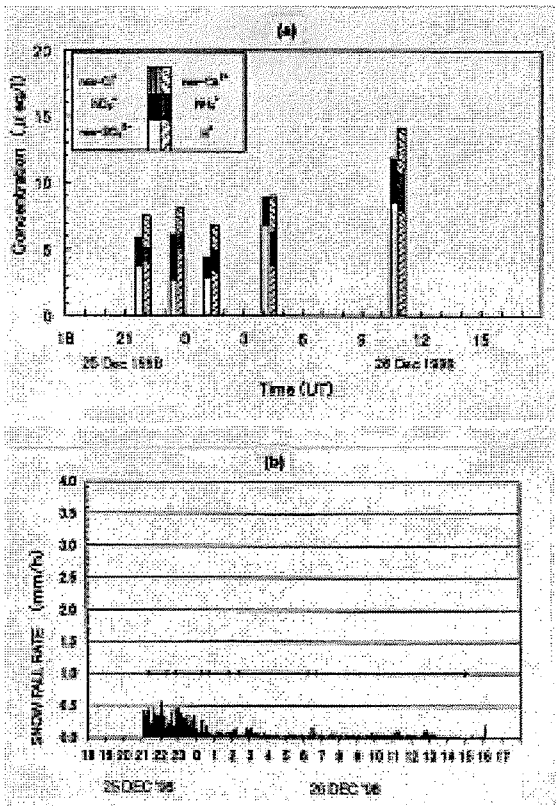

Fig.2. Temporal changes of (a) chemical components in solid precipitation and (b) snow fall rate in Ny-Å lesund in Case 2 for 25th-26th December 1998.

been observed for the observational duration, four characteristic cases are selected for discussion of this presentation as shown in Figs. 1, 2, 3 and 4. Over the whole duration of snow fall season over there, we had used to have almost rimed snow particles which had been observed to contain nss-SO_4^{2-} ions predominantly as shown as open columns in Figs.1a and 3a. Almost similar results were reported previously by Parungo etal. (1987) and Takahashi etal.(1996). In these cases, winds were almost all southeasterly wind which is thought to bring abundant vapor or a lot of super cooled cloud droplets. These cloud droplets are easily considered to intake SO_4^{2-} and provide it to rimed snow crystals. In very shorter period, non-rimed snow crystals were observed with north-westerly wind which were thought to bring no abundant cloud droplets as the relatively dryer air stream from sea ice covered ocean area where the supply of water vapor were not sufficient. Those samples of solid precipitation have been analyzed and revealed for them to contain much higher concentration of NO_3^- ions than the rimed snow crystals as shown in Fig.2a comparing with Figs.1a and 3a.

For the duration of a series of a long lasting snowfall in Case 3 shown in Fig 3a, rimed snow crystal were observed continuously over the whole duration. Predominant chemical component in cation were also remarked to be nss-SO_4^{2-} shown as open columns in Fig.3a as similar as in Fig.1a. In the

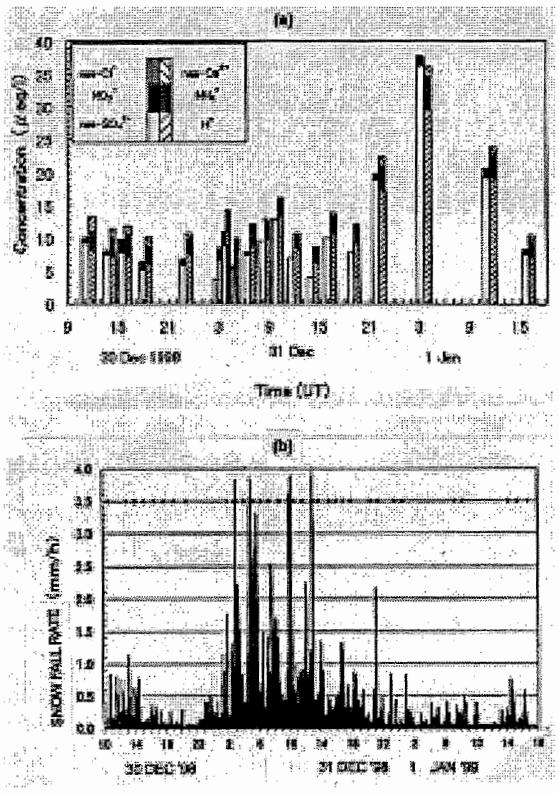

Fig.3. Temporal changes of (a) chemical components in solid precipitation and (b) snow fall rate in Ny-Ålesund in Case 3 from 30th December 1998 to 1st February 1999.

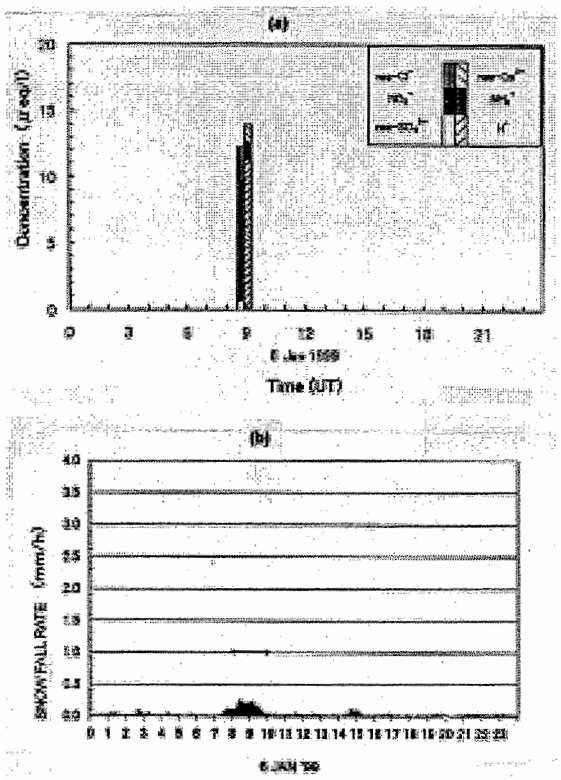

Fig.4. Temporal changes of (a) chemical components in solid precipitation and (b) snow fall rate in Ny-Ålesund in Case 4 on 6th February 1999.

same figure, it seems interesting that concentration of NO_3^- in snow particles shown as solid columns were seemed to decrease with the time lapse and finally to become vanished into lower values below the threshold of detection.

Another new finding was pointed out the highest concentration of NO_3^- detected in solid precipitation of this observation as shown by solid columns in Fig.4a. This precipitation was thought to be brought by an isolated cloud. It may be the most interesting remark that ion concentration in solid precipitation of are NO_3^- and H^+ are almost same values. These result means that the snow crystals obtained had to intake those ions as the shape of HNO_3 gas.

4. DISCUSSION

Since it was complete polar night, photo-chemical processes and existence of OH were not considered to be there. Only aqueous phase reaction is considered to take place there. Therefore, oxidization to SO_4^{2-} is corresponding to riming processes. Accordingly over there, if snow crystals are rimed, so that the snow crystals have preferentially higher concentration of SO_4^{2-}. Conversely when it is found that from chemical analysis, solid precipitation contains higher concentration of SO_4^{2-}, it may be expected to be composed of rimed snow crystal. Therefore, SO_4^{2-} ion in precipitation may be considered to be a kind of tracer of riming under such polar night. SO_2 is usually oxidized into SO_4^{2-} in two major chemical reaction as follows.

1. Gaseous phase chemical reaction.

OH ← photo-chemical reaction.

$SO_2 + OH \rightarrow HOSO_2$ (1)

$HOSO_2 + O_2 \rightarrow SO_3 + HO_2$ (2)

$SO_3 + H_2O \rightarrow H_2SO_4$ (3)

2. Aqueous phase chemical reaction.

SO_2 is solved easily into the liquid of cloud droplets and reach to some equilibrium state,

$SO_2 + H_2O = HSO_3^- + H^+ = SO_3^{2-} + 2H^+$.

$HSO_3^- + H_2O_2 \rightarrow SO_4^{2-} + H^+ + H_2O$ (4)

$SO_3^- + O_3 \rightarrow SO_4^{2-} + O_2$ (5)

Oxidization of NO_2 to NO_3^- are usually considered to be divided into daytime and nighttime processes as followings.

Daytime

$NO_2 + OH + M \rightarrow HNO_3 + M$ (6)

Nighttime

$NO_2 + O_3 \rightarrow NO_3 + O_2$ (7)

$NO_3 + NO_2 = N_2O_5$ (8)

$NO_3 + RCHO \rightarrow HNO_3 + RCO$ (9)

where the supply of water vapor were not sufficient. Those samples of solid precipitation have been analyzed and revealed for them to contain much higher concentration of NO_3^- ions than the rimed snow crystals as shown in Fig.2a comparing with Figs.1a and 3a.

For the duration of a series of a long lasting snowfall in Case 3 shown in Fig 3a, rimed snow crystal were observed continuously over the whole duration. Predominant chemical component in cation were also remarked to be nss-SO_4^{2-} shown as open Here, R is H or CH_3.

Here again, since it was complete polar night, OH is not considered to exist. Reaction of (6) may be thought not to occur. Oxidization processes to NO_3^- were considered to be limited to proceed in reaction (7) with O_3. In Case 3, noted depression of NO_3^- was observed in long lasting snowfall. If we had a sunrise in that morning there, such depression might not be found out.

5. CONCLUDING REMARKS

The remarked findings are summarized as followings.

(1) It may be also recognized and confirmed there that rimed and non-rimed snow crystals have predominantly higher concentration of SO_4^{2-} and NO_3^-, respectively with lower values than those in mid-latitude by one order.

(2) In a duration of such non-rimed snowfall, noted depressions of NO_3^- were observed in temporal changes of fine aerosols rather than those of gas (HNO_3) and coarse aerosols in the environmental atmosphere.

(3) On the other hand, it was observed that a considerably higher concentration of NO_3^- was detected in non-rimed solid precipitation, coexisting with H^+ ion with nearly equal concentration (New!!). It may be thought for non-rimed snow crystals to intake NO_3^- ion as HNO_3 gas in some absorption mechanisms.

(4) In the duration of a considerably long lasting snowfall, concentration of NO_3^- in solid precipitation was observed to decrease with time lapse up to almost limited value of detection.

(5) Summarizing over all concluding remarks, it may be speculated comprehensively that NO_3^- is seen as long range transport material since NO_3^- ion was observed in solid precipitation at such remote area.

References

Diehl K., Mitra S. K. and Pruppacher H. R., 1996: A laboratory investigation on uptake of SO_2, HNO_3 and HCl by 12th ICCP (Zurich), Proceedings of 12th ICCP(Zurich), 1047-1049.

Endoh, T., Takahashi, T., Noguchi, I., Kurita, N. and Tanaka, N.,1998: Investigation of origin of falling snow particle and its composition with chemical and isotopic analysis. Proceeding of AMS Conference on cloud physics(Everett), 245-248.

Mitra S. K. , Diehl C. and Puruppacher H. R 1992: A laboratory study of the uptake of SO_2 and HNO_3 by snow crystals., 11th Intl. Conf. on Cloud and Precipitation, 851-854.

Parungo F., Nagamoto C. and Madel R., 1987: A study of the mechanisms of acid rain formation. J. Atmos. Sci., 44, 3162-3174.

Takahashi, T., Endoh, T., Muramoto, K., Nakagawa and Noguchi, I. 1996: Influence of the growth mechanism of snow particles on their chemical composition. Atmospheric Environment, 30, 1683-1692.

EFFECT OF ARCTIC SULFURIC ACID AEROSOLS ON WINTERTIME LOW-LEVEL ICE CRYSTALS, HUMIDITY, AND TEMPERATURE OVER THE ARCTIC

E. Girard and A. Stefanof

Regional Climate Model Laboratory, Department of Earth and Atmospheric Sciences, University of Quebec at Montreal, Montreal, Quebec, Canada

1. INTRODUCTION

This study focuses on an indirect effect of aerosol on arctic wintertime cloud and climate, the dehydration-greenhouse feedback, which was originally formulated by Blanchet and Girard (1994). The process may be summarized as follows. Anthropogenic and biogenic activities produce sulphuric acid, a northward extension of the mid-latitude acid precipitation problem, that coats most of existing aerosols. The increased concentration of sulphuric acid decreases the saturation vapor pressure above aerosol and lowers the freezing point (e.g. Cziczo and Abbatt 1999). At cold temperatures, this process inhibits ice crystals production (Borys 1989, Bigg 1996) and favors the formation of fewer larger ice crystals instead of many smaller ones. In practice, it enhances formation of precipitating ice crystals to the expense of more persistent ice fog or stratus. 1-D simulations show (Girard and Blanchet 2001a,b; Girard et al. 2004) an increase of the water flux from the lower atmosphere to the surface leading to dehydration and reduction of the greenhouse atmospheric radiation due the strong effect of water vapor, primarily in the broad rotation band. The reduced greenhouse effect further promotes dehydration and cooling cycle. The process affects also the mid-latitude regions by increasing the production of available potential energy that feeds the intensity of our winter storms. A feedback is established between the enhanced circulation and the transport of anthropogenic aerosols from the mid-latitudes.

To verify whether the dehydration-greenhouse feedback is important or not, we proceeded in two steps: (1) The first simulations were done with the single-column version of the Northern Aerosol Regional Climate Model. This allows to understand all the physical processes and their interactions from a local point of view, that is without any feedbacks with the dynamics. (2) The second experiment was performed with the 3D Northern Aerosol Regional Climate Model (NARCM) over a grid that includes the Arctic and the sub-arctic regions. Interactions between the local perturbation of physical variables (produced by the dehydration-greenhouse feedback) and the circulation are allowed for.

Corresponding author's address: Eric Girard, University of Quebec at Montreal, C.P. 8888 Succursale Centre-ville Montréal (Québec) H3C 3P8 Canada E-Mail: girard.eric@uqam.ca.

In this paper, we first make a brief description of the model in section 2. Section 3 includes few results obtained with the single-column model followed in section 4 by the 3D model results. In this paper, we put the emphasis on 3D results since 1D results are extensively discussed in Girard et al. (2004).

2. MODEL DESCRIPTION

NARCM is a state-of-the-art model that was developed over the last decade. It is a limited-area non-hydrostatic model (*Caya and Laprise* 1999) with physical parameterization and a dynamic size-distributed aerosol scheme CAM (Canadian Aerosol Module). It simulates aerosol explicitly with 12 size bins from 0.005 to 20.48 μm (*Gong et al.* 2003). The aerosol module CAM (Canadian Aerosol Module) in NARCM is a size-segregated multi-component algorithm that treats five major types of aerosols: sea-salt, sulphate, black carbon, organic carbon and soil dust. It includes major aerosol processes in the atmosphere: production, growth, coagulation, nucleation, condensation, dry deposition, below-cloud scavenging, activation, a cloud module with explicit microphysical processes to treat aerosol-cloud interactions and chemical transformation of sulphur species in clear air and in clouds. Each of these aerosol processes is strongly dependent on particle size, thus requiring an explicit representation of the size distribution. Although still demanding in computer resources, the numerical solution was optimized to efficiently solve the complicated size-segregated multi-component aerosol system and make it feasible to be included in global and regional models. Application of CAM in the Canadian GCM have shown that CAM is able to predict relatively well aerosol size and concentration in marine and continental area (*Covert et al.* 1996). With proper anthropogenic emissions surrounding the Arctic, CAM is able to predict the spatial and temporal aerosol compositions and size distributions in the Arctic atmosphere. Surface processes are simulated with the Canadian Land Surface Scheme (CLASS) (*Verseghy* 2000). A simple thermodynamics model is used to simulate the temperature of sea ice. NARCM can be implemented at a range of grid resolutions (generally from 10-100 km) and a variety of domains.

The cloud microphysics schemes used in NARCM are Girard and Curry (***GC* 2001**) and Lohmann and Roeckner (1996) schemes. Both are two-moment microphysics schemes. In addition, the

scheme of GC has interactive aerosols. Both schemes are used in this study.

The *GC* (2001) scheme has six prognostic variables: the ice and liquid water contents, the number concentrations of water droplets and ice crystals, rain, and snow. The following microphysical processes are accounted for: nucleation, condensation, evaporation, deposition, sublimation, collision processes, heterogeneous and homogeneous freezing of water droplets, homogeneous freezing of interstitial haze droplets and Bergeron process. The GC scheme can either be used with prognostic aerosol or with prescribed aerosol. In this research, the former version is used. Aerosol size distribution and microphysical properties are provided by CAM. Supersaturation is free to evolve above the saturation point following a budget equation and is used with the CCN and IFN concentrations to determine the nucleation rate of water droplets and ice crystals. The prognostic determination of the number concentration for water droplets and ice crystals provides the mean diameter of ice crystals and water droplets assuming a lognormal cloud bimodal size distribution (one mode for each phase). Inclusion of the mean diameter of the cloud liquid droplets and ice crystals allows for a more physically based treatment of the condensation, evaporation, nucleation, deposition, sublimation, and freezing processes. Sophisticated parameterization of the heterogeneous freezing of cloud droplets allows for mixed-phase clouds at temperatures well below the freezing point. The GC scheme has been applied over Alert (NWT) for the period 1991-95 and over the Beaufort Sea and results show that the scheme is able to reproduce quite well complex mixed-phase clouds of the Arctic at temperatures as low as 240 K (*GC* 2001; Girard and Craciun, 2004; Girard et al., 2004). Other validation cases are however necessary to justify the inclusion into GCMs of complex microphysics scheme such as GC. The proposed research will give an opportunity to further validate the GC scheme.

The physics package of the single-column version of NARCM is identical to the 3D NARCM. The dynamical tendencies (for momentum, temperature, and humidity) are calculated using the Residual Iterative Method (Girard and Blanchet, 2001), which is a method that computes the dynamical tendencies at the lateral boundary of the column from available aerological soundings.

3. EXPERIMENT WITH THE SINGLE-COLUMN MODEL

Simulations of four cold seasons (from November to May) were performed over Alert (Canada) for the period 1991 to 1994. Aerosol observations near the surface were available at this arctic research station for this period and these were used for our simulations together with 12-hour aerological soundings. These observations were used to calculate the dynamical tendencies with the residual iterative method (Girard and Blanchet 2001). Three aerosol scenarios were considered for our simulations: (1) a natural aerosol case; (2) an acidic scenario that distinguishes form the latter by fewer ice nuclei concentration and lower homogeneous freezing temperature of haze particles. In this scenario, the decrease of ice nuclei and the amount to which the homogeneous freezing

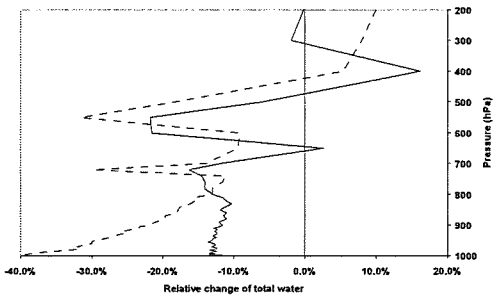

Figure 1: Relative total water change averaged over the 4 cold seasons of the very acidic scenario (dashed line) and the acidic scenario (full line) compared to the natural scenario (baseline case)

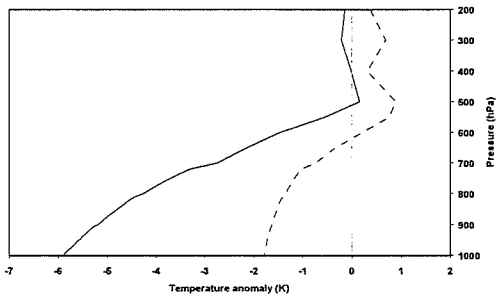

Figure 2: Temperature change averaged over the 4 cold seasons of the very acidic scenario (dashed line) and the acidic scenario (full line) compared to the natural scenario (baseline case)

temperature of haze particles is reduced is a function of the observed aerosol acidity; and (3) a very acidic scenario in which the decrease of ice nuclei and homogeneous freezing temperature is always applied whatever the aerosol composition.

Results show that the total water averaged over the four cold seasons (total water includes water vapor, liquid and ice water) decreases substantially in the two acidic cases below 500 hPa (see Figure 1). Due to the decrease of ice nuclei concentration, fewer ice crystals are nucleated (not shown). This leads to the formation of ice crystals with a larger diameter since the water vapor available to deposit on each ice crystal increases. Therefore, ice crystals are more efficient to precipitate and dehydrate the lower atmosphere. Figure 2 shows that the temperature vertical profile is modified in acidic scenarios with colder temperature near the surface and in the lower troposphere, thus reducing the greenhouse effect locally. This effect gradually decreases as we go upward in the atmosphere.

4. EXPERIMENT WITH THE 3D MODEL

NARCM was used to simulate the month of February 1990 over a domain that includes the Arctic and sub-artic regions north of about 45°N. This grid includes the main anthropogenic sources of aerosols in Europe. Initially, no aerosol is present. NARCM generate its own aerosols with natural and anthropogenic sources that are within the domain. The horizontal grid resolution of 100 km. A 1-month spin-up period is allowed for the adjustment of the atmosphere to its equilibrium. Sea ice temperature, sea ice concentration and sea-surface temperature are from the Atmospheric Model Intercomparison Project (AMIP) dataset. Lateral boundary conditions are from the National Center for Environmental Prediction (NCEP) reanalysis. A 2-month simulation is performed (from January 1st to March 1st) but only results for the month of February are analyzed.

The model is able to reproduce quite well the climate of the region with errors in the temperature of plus or minus 5°C close to the surface. These errors are maximum near the ice margin in the Barents Sea and Greenland.

The experiment consisted in comparing 2 simulations: (1) a baseline case in which ice nuclei concentration is not affected by acidic aerosols, and (2) an acidic case (the perturbed simulation) in which the ice nuclei concentration depends on the sulphate aerosol concentration. These two simulations correspond to scenario 1 and 2 respectively discussed previously for the single-column model.

Figure 3 shows the perturbation of the specific humidity at 1000 hPa that results from the effect of aerosol acidification on ice nucleation ability of aerosols (perturbed minus baseline). The lower atmosphere is drier over the Western and Central Arctic. The area covering the Barents Sea and the Greenland Sea is however wetter. The same dipole pattern appears in the perturbation of the downward longwave radiation at the surface (Figure 3). A decrease of up to 12 W m^{-2} in the Central and Western Arctic and an increase of up to 15 W m^{-2} east and north east of Greenland. Figure 3 also shows the corresponding temperature perturbation with negative values of up to –4°C in the Western and Central Arctic and +2°C over the Barents Sea. These perturbations seem to correspond to the sea-level pressure field change with a decrease of the Greenland Low of about 5 hPa and an increase of the mean sea-level pressure over the Eastern Arctic.

These results suggest a strong interaction between the enhance cooling of the lower atmosphere by the aerosol acidification and the circulation. Indeed, it seems that the dehydration-greenhouse feedback is effective over the cold area of the Arctic. Furthermore, the surface cooling is also gradually decreasing upward (not shown), corresponding to what was obtained with the single-column model (see Figure 2). This enhanced cooling increases the baroclinicity of the atmosphere, particularly between the Central Arctic and the Greenland Low. This enhanced circulation allows for a more efficient transport of anthropogenic aerosols from Europe to the Arctic, thus establishing a positive feedback between the dehydration of the lower atmosphere in the Arctic due to acidic aerosols and the circulation that brings even more acidic aerosols from mid-latitudes.

At the same time, the enhanced baroclinicity of the atmosphere favors the formation of more storms, precipitation, and cloudiness in the North Atlantic region compared to the reference case. That is why this region is warmer in the perturbed case compared to the reference case. Indeed, cloud cover and precipitation increases in the area covering Greenland and the North Atlantic (including the Western part of Europe). Consequently, the downward infrared radiation flux at the surface and the surface air temperature are also increased in this area.

5. DISCUSSION

The dehydration-greenhouse feedback is investigated using a 1D and a 3D regional climate model. The lower ability of anthropogenic sulphuric acid aerosols to nucleate ice is responsible for the initiation of the dehydration-greenhouse feedback. One-dimensional simulations at Alert during the period 1991-94 showed that the effect of changes in cloud characteristics by aerosol acidification results in larger cloud ice crystals forming in the lower troposphere and more effective ice crystal precipitation events. Consequently, we find an increase of the lower troposphere dehydration rate. Radiation calculation with the 1D climate model shows that cloud alteration produces a substantial surface cooling anomaly. Three-dimensional simulations indicate that the surface cooling in the Arctic initiate a feedback loop with the circulation. As a result, anthropogenic aerosol transport to the Arctic from mid-latitudes is more efficient and the lower atmosphere cooling due to the resulting decrease of ice nuclei (related to the increase concentration of sulphuric acid aerosol) is enhanced.

Further investigations with a full 3D model and more refined simulations (ensemble simulations and longer simulations) are required to assess the complex feedbacks between aerosols, cloud, radiation, sea ice and dynamic transport in order to further evaluate the impacts of the dehydration-greenhouse feedback on the arctic climate and its regional extend.

6. REFERENCES

Blanchet, J.-P., and E. Girard, 1994. Arctic greenhouse cooling. Nature 371, 383.

Bigg, E.K., 1996. Ice forming nuclei in the Arctic. Tellus 48B, 223-233.

Borys, R.D., 1989. Studies of ice nucleation by arctic aerosols on AGASP-II. J. Atmos. Chem. 9, 169- 185.

Caya, D. and R. Laprise, 1999: Mon. Wea. Rev., 127, 341-362.

Covert et al., 1996: J. Geophys. Res., *101* (D3), 6919-6930

Cziczo, D.J., and J.P.D. Abbatt, 1999. Deliquescence, efflorescence, and supercooling of ammonium sulfate aerosols at low temperature: Implications for cirrus cloud

formation and aerosol phase in the atmosphere. J. Geoph. Res. 104, 13 781-13 790.
Girard, E., and J.-P. Blanchet, 2001a. Simulation of Arctic diamond dust and ice fog and thin stratus using an explicit aerosol-cloud-radiation model. J. Atmos. Sci. 58, 1199-1221.
Girard, E., and J.-P. Blanchet, 2001b. Microphysical parameterization of Arctic diamond dust, ice fog and thin stratus for climate models. J. Atmos. Sci. 58, 1181-1198.
Girard, E., J.-P. Blanchet, and Y. Dubois, 2004: Effects of arctic sulfuric acid aerosols on wintertime low-level atmospheric ice crystals, humidity, and temperature at Alert, Nunavut., Atmos. Res. (under review)
Girard, E. and L. Craciun, 2004: Modelling of the wintertime mixed-phase clouds observed during SHEBA. (in preparation)
Girard, E., and J.A. Curry, 2001: Simulation of low-level tropospheric clouds during FIRE experiment in May 1998., *J. Geoph. Res.*, 106, 15139-15154.
Gong, S.L., L.A. Barrie, J.-P. Blanchet, K.v. Salzen, U. Lohmann, G. Lesins, L. Spacek, L.M. Zhang, E. Girard, H. Lin, R. Leaitch, H. Leighton, P. Chylek, and P. Huang, CAM: A Size Segregated Simulation of Atmospheric Aerosol Processes for Climate and Air Quality Models 1. Module Development, *J. Geoph. Res.*, 108, 2003.
Lohmann, U., and E. Roeckner, 1996: Clim. Dyn., 12, 557-572.

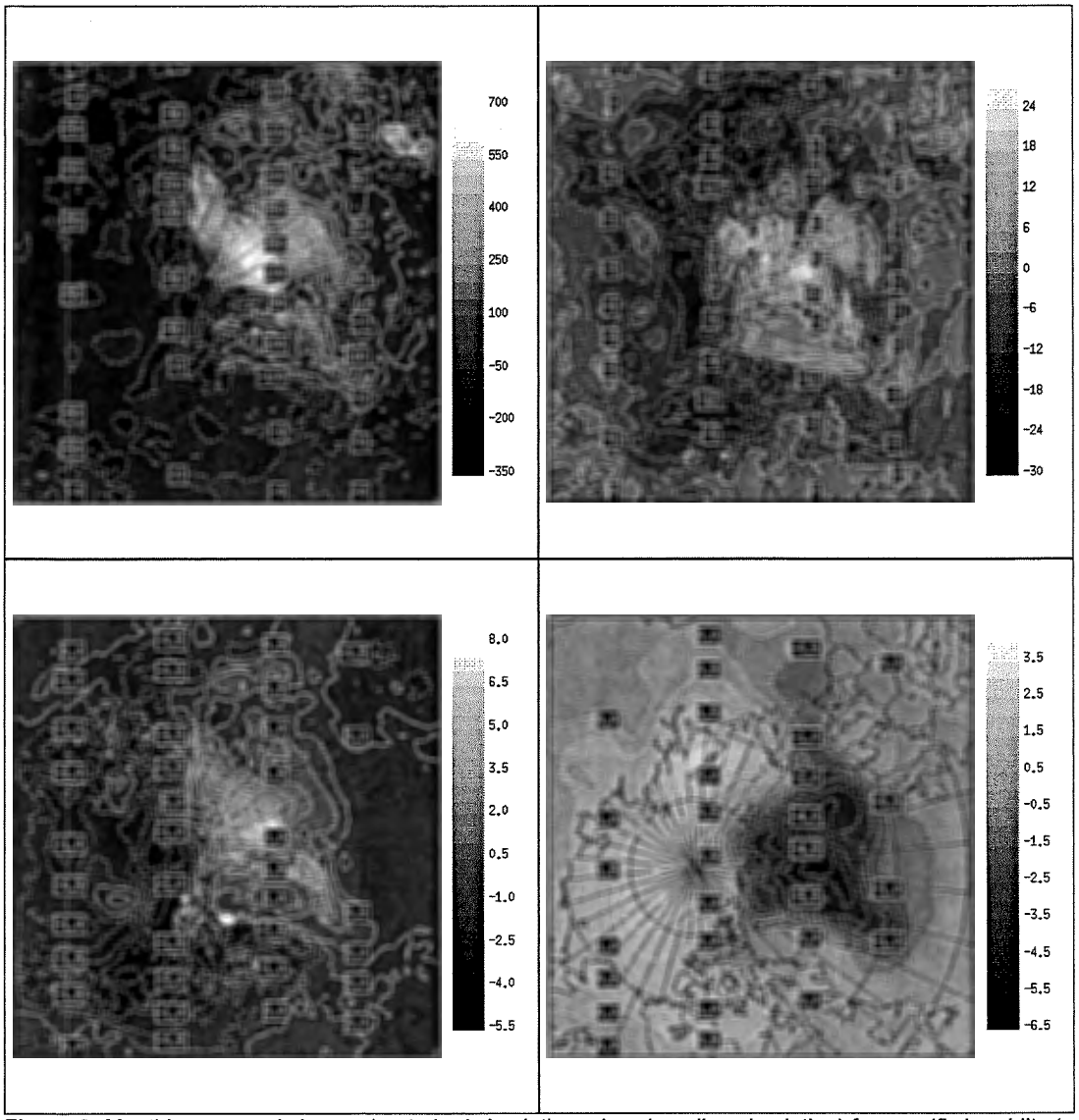

Figure 3: Monthly averaged change (perturbed simulation minus baseline simulation) for specific humidity (values are multiplied by) (upper left), downward longwave radiation at the surface in W m^{-2}(upper right), surface air temperature in K (lower left) and sea-level pressure in hPa (lower righ)

CLOUD PROCESSING OF GASES AND AEROSOLS IN A REGIONAL AIR QUALITY MODEL (AURAMS)

Wanmin Gong[1], Ashu P. Dastoor[2], Véronique S. Bouchet[3], Sunling Gong[1], Paul A. Makar[1], Michael D. Moran[1], Balbir Pabla[1], Sylvain Ménard[3], Louis-Philippe Crevier[3], Sophie Cousineau[3], and S. Venkatesh[1]

[1]Air Quality Research Branch, Meteorological Service of Canada, Downsview, Ontario, M3H 5T4, Canada
[2]Air Quality Research Branch, Meteorological Service of Canada, Dorval, Quebec, Canada
[3]Canadian Meteorological Centre, Meteorological Service of Canada, Dorval, Quebec, H9P 1J3, Canada

1. INTRODUCTION

Clouds play an active role in the processing and cycling of chemicals in the atmosphere. Gases and aerosols can enter cloud droplets through absorption/condensation (of soluble gases) and activation and impact scavenging (of aerosol particles). Once inside the cloud droplets these tracers can dissolve, dissociate, and undergo chemical reactions. It is known that aqueous-phase chemistry in cloud makes significant contribution to sulphate aerosol production in atmosphere. Some of the aqueous-phase tracers will be removed from the atmosphere when precipitation forms and reaches the ground. However, the majority of clouds are non-precipitating, and upon cloud dissipation and evaporation, the tracers, physically and chemically altered, will be released back to the atmosphere. Updrafts and downdrafts in convective clouds are also efficient ways of redistributing atmospheric tracers in the vertical. It is therefore important to represent these cloud-related physical and chemical processes when modelling the transport and transformation of atmospheric chemical tracers, particularly aerosols.

A new multiple-pollutant (unified) regional air-quality modelling system, AURAMS, with size- and chemical-composition-resolved aerosols is being developed at the Meteorological Service of Canada. In the current version of AURAMS, many of the cloud processes mentioned above are represented. In this paper we will examine the impact of the various cloud processes on modelled regional aerosols, based on model simulations of a one-week period during a major air-quality field campaign in eastern North America and sensitivity studies. Comparison with observations will also be discussed.

2. AURAMS AND ITS CLOUD PROCESSES

AURAMS consists of these primary components: an emissions processor; a meteorological driver model; and a chemical transport model closely coupled with a size-resolved (sectional) and chemically speciated aerosol module. Processes represented in the chemical transport model include emission, advection and diffusion, gas-phase chemistry, gas-to-particle conversion (including secondary organic-matter aerosol formation and multi-phase thermodynamics of the sulphate-nitrate-ammonia-water system), aerosol microphysics, cloud processing of gases and aerosols, wet and dry deposition, and sedimentation. In the following, we will briefly describe the representation of the various cloud processes in current AURAMS. For a detailed description of the model and the various components see Moran et al. (1998), Gong, S. et al. (2003), Zhang et al. (2002), Makar et al. (2003), Gong, W. et al. (2003).

Cloud processing of gases and aerosols in AURAMS currently includes aerosol activation (or nucleation scavenging), aqueous-phase chemistry, tracer scavenging and removal due to precipitation. The current representation of aerosol activation, inherited from the Canadian Aerosol Module, CAM (Gong, S. et al., 2003), is based on a simple empirical relationship between the aerosol number density and the number density of cloud droplets formed on the activated aerosols (CCN) as described in Jones et al. (1994). The bulk cloud water content from the meteorological driver model is distributed evenly amongst the activated aerosols, and the cloud droplet size is then determined for each activated aerosol size bin. The aqueous-phase chemistry mechanism in the present study is adapted from ADOM (Acid Deposition and Oxidant Model: Venkatram et al., 1988). It is focused on sulfur chemistry and includes non-equilibrium mass transfer of SO2, O3, H2O2, ROOH, HNO3, NH3 and CO2 and oxidation of S(IV) to S(VI) by dissolved ozone, hydrogen peroxide, organic peroxides and oxygen (in the presence of trace metals). The aqueous-phase chemistry is coupled with the size-resolved aerosol chemical components in AURAMS. Sulphate, nitrate, and ammonium are directly affected by the aqueous processes while the remaining aerosol components are indirectly modified due to the internally mixed aerosol assumption. Aqueous-phase chemistry modifies both aerosol mass and size distribution. The latter is addressed through "rebinning" (under the fixed-bin structure) ensuring conservation of both mass and number. Wet deposition in AURAMS considers the processes of tracer scavenging and transport by precipitation. The scavenging process includes both tracer transfer from cloud droplets due to the auto-conversion process and the direct impact scavenging of aerosol particles and

Corresponding author's address: Wanmin Gong, Meteorological Service of Canada, Toronto, Ontario, M3H 5T4, Canada; E-Mail: wanmin.gong@ec.gc.ca.

soluble gases by falling hydrometeors (liquid or solid). The parameterization of impact scavenging of aerosols by precipitation is based on Slinn and Slinn (1981) as in CAM (Gong, S. et al. 2003). The impact scavenging of soluble gases by precipitation is treated separately for irreversible and reversible scavenging. The irreversible scavenging of gases (e.g., H2O2, ROOH, HNO3 and NH3) is treated similarly as that of aerosols, i.e., through a parameterized scavenging rate, while for the reversible scavenging of gases (e.g., SO2 and CO2) an equilibrium assumption is used. Tracers captured in precipitation are removed from the atmosphere when the precipitation reaches the ground. However, part or all of the precipitation may evaporate before reaching the ground, in which case the tracers will remain in the atmosphere but will be vertically redistributed (see Gong, W. et al., 2003, for details).

3. MODEL SIMULATION OF AN EMEFS-1 CASE

3.1 Model setup

A simulation of regional oxidants and particulate matter (PM) over eastern Canada and the northeastern U.S. using AURAMS with cloud processes was conducted for the period of August 1 - 6, 1988. The actual simulation started from July 30, 1988, to allow for a 2-day model "spin-up". The model was run on a 85 x 105 x 28 grid with 42 km (true at 60°N) spacing in the horizontal. The 28 unevenly spaced vertical levels range from the surface to 25 km. AURAMS is driven, off-line at 900 s time interval, by the Canadian operational numerical weather forecast model (GEM) (Côté et al. 1998a,b). Emissions used for the simulation is based on the 1990 Canadian and U.S National Inventories. Bulk primary PM emissions included in these inventories are chemically and size segregated in AURAMS by primary emission source stream. Twelve size bins (logarithmically evenly distributed between 0.01 and 40 μm) are used and 8 aerosol composition categories (sulfate, nitrate, ammonium, organic carbon, elemental carbon, crustal material, sea salt and aerosol-bound water) are currently represented in AURAMS.

3.2 Results

The 6-day study period corresponds to a regional oxidant event over the eastern North America. A relatively dry stagnant high pressure system dominated the first half of the period, while a low pressure system moved into the region during the last two days accompanied by stronger flow, more clouds, and precipitation. Figure 1 shows the model simulated aerosol sulfate, nitrate, and ammonium concentration (μg m^{-3}), at 2.5 μm size-cut, at 15 m AGL averaged over the last 3 days of the simulation. High concentrations of PM2.5, over 100 μg m^{-3} in places (not shown), is simulated over the Ohio Valley extending to the St. Lawrence River Valley for this period, with sulfate being the dominant component. Particulate nitrate is suppressed over the high sulfate area, where it cannot compete with sulfate for limited ammonium available.

Figure 2 shows the hourly wet deposition fluxes of major ions (SO4=, NO3-, and NH4+, x10 μ-mole m^{-2} hr^{-1}) also averaged over the last 3 days of the simulation. The wet fluxes consist of two components, "rain-out" (i.e., cloud-to-rain conversion) and the "below-cloud" scavenging, which are "tagged" separately in the model. In the case of $SO4^{=}$, the wet deposition is mostly contributed from the "rain-out" component, whereas in the case of $NO3^{-}$ and $NH4^{+}$ the "below-cloud" component makes a significant contribution to the wet deposition from precipitation scavenging of gaseous HNO3 and NH3, which are assumed to dissociate readily in the liquid phase.

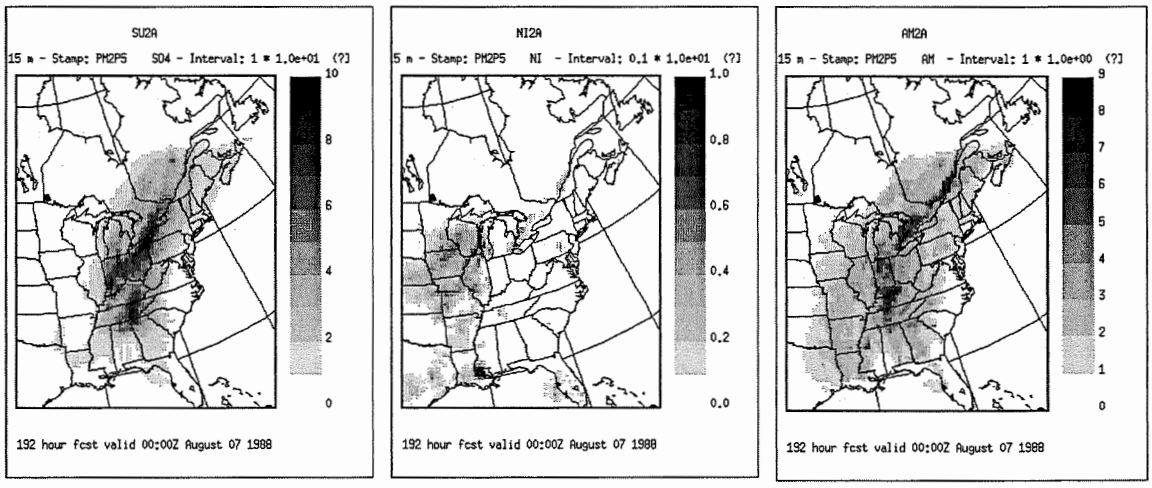

Figure 1. Simulated total and speciated aerosol concentrations: sulfate-2.5 (left), nitrate-2.5 (middle), and ammonium-2.5 (right), at 15 m (units in μg m^{-3}), averaged over August 4 – 6, 1988.

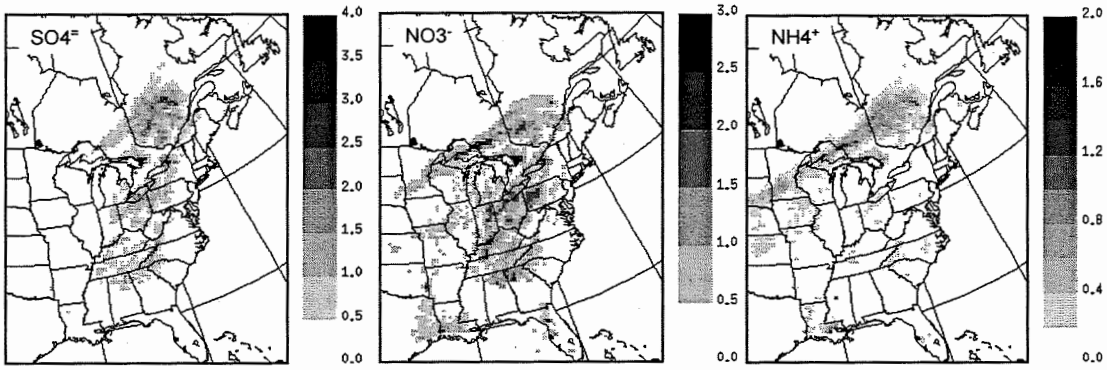

(a) (b) (c)

Figure 2. Modelled wet deposition fluxes (μ-moles m^{-2} hr^{-1}) of (a) $SO4^{=}$, (b) $NO3^{-}$, and (c) $NH4^{+}$, averaged over August 4 – 6, 1988.

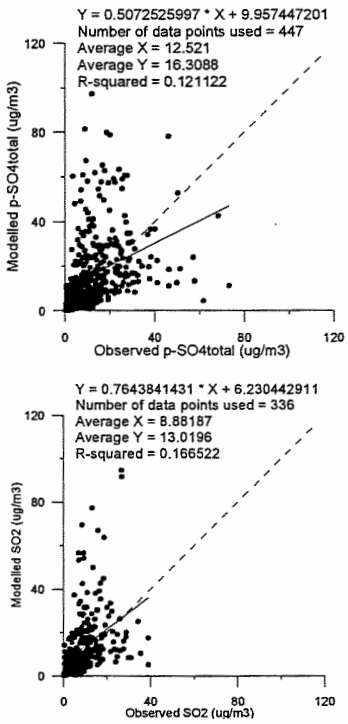

Figure 3. Scatter plot of modelled (24-hr average) vs. observed (filter) PM-SO4 (top) and SO2 (bottom), Aug. 1 – 6, 1988.

3.3 Comparison with observations

The simulation period was chosen to make use of the relatively extensive measurement data collected during the EMEFS campaign (Hansen et al, 1991). The data collected from the participating networks (McNaughton and Vet, 1996) include continuous-chemistry (O3), filter-chemistry (SO2, HNO3, NH3, particulate sulfate, nitrates, and ammonium), and precipitation-chemistry measurements. There were also detailed chemistry measurements at special sites as well as aircraft measurements. The extensive model evaluation of this period will be discussed elsewhere. Here we will only give a few examples of comparisons of model results against observations.

Figure 3 shows scatter plots of model vs. observation of SO2 and total PM-SO4 for the 6-day period. Model results are averaged over 24 hr in order to compare with the 24-hr filter measurements. Over-predictions are found both in SO2 and PM-SO4. Correlation is better for SO2. The causes for the over-prediction are being investigated including the possibility of under-prediction of wet scavenging (see below). The over-prediction in PM-SO4 is partially related to the over-prediction in SO2.

Figure 4 shows scatter plots for precipitation amount and $SO4^{=}$ concentration in precipitation. The latter depends critically on the former, i.e., model's ability to predict cloud and precipitation (location, timing, and amount). As seen the model generally under-predicted precipitation for this study period, which led to the under-estimation of wet fluxes (not shown) by the model.

4. IMPACT OF CLOUD PROCESSING ON REGIONAL PM

To have an idea of how important the in-cloud production of sulfate is in comparison to the gas-phase production on a regional scale, separate production rates were tracked during the simulation. Figure 5 shows the column-integrated sulfate production rates (μg m^{-2} hr^{-1}) averaged over Aug. 4 – 6, 1988. It is seen that the gas-phase sulfate production is mostly confined to the near-source region, while the aqueous-phase production (in-cloud) can be found farther downstream. This is in agreement with the findings in Barth et al. (2000), where various sources and productions for sulfate were tagged in their global model runs. However, in contrast to Barth et al. (2000) where the aqueous-phase production dominates (up to 80% globally and over 50% over eastern North America) the total sulfate production, on average only about 30% of the total sulfate production comes from aqueous-phase in this study. The difference can be partly attributed to the fact that the present analysis is based on a regional model simulation over a particular

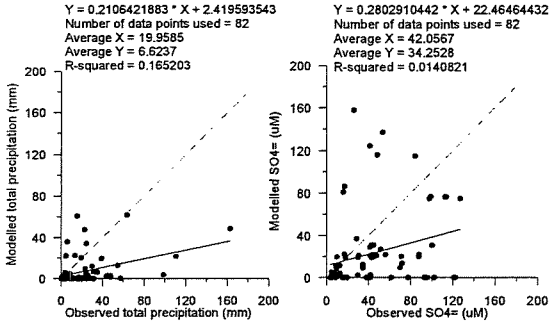

Figure 4. Scatter plot of modelled vs. observed precipitation amount and SO4= concentration in precipitation, averaged (weighted) over Aug. 1 – 6, 1988.

week compared to the analysis of annual average from Barth et al. (2000), which is based on a global model simulation over 4 years. However, it is also possible that the relatively low contribution from in-cloud production towards the total sulfate production shown here is due to the deficiency in current model parameterizations for some of the processes or to the processes not currently represented in the model (e.g., subgrid-scale convective tracer mixing).

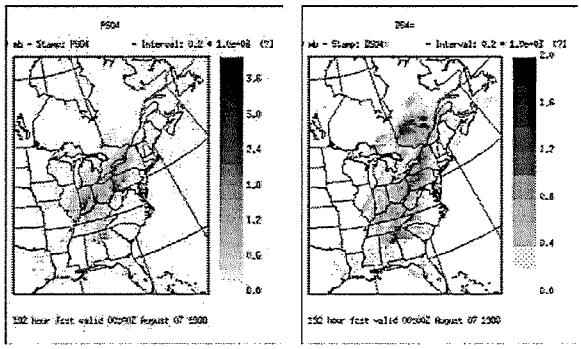

Figure 5. Column-integrated gas-phase (left) and aqueous-phase (right) sulphate production rates (μg m^{-2} hr^{-1}), averaged over Aug. 4 – 6, 1988

To further investigate the impact of aqueous-phase oxidation on regional PM, a sensitivity test was conducted where aqueous-phase oxidation was "turned off". An average of 30% decrease in surface PM-SO4 concentration was predicted compared to the base case (with aqueous-phase oxidation). This is consistent with the sulfate production analysis above. Greater impact is found at places under cloud farther away from the SO2 source region. The SO4= "rain-out" flux in this case is contributed solely by nucleation scavenging. Compared with the flux in the base case, the model indicates that close to 50% of the wet deposition of $SO4^{=}$ comes from in-cloud oxidation.

REFERENCES

Barth, M.C., P.J. Rasch, J.T. Kiehl, C.M. Benkowivitz, and S.E. Schwartz, 2000: Sulfur chemistry in the National Center for Atmospheric Research Community Climate Model: description, evaluation, features, and sensitivity to aqueous chemistry, *J. Geophys. Res.*, **105**, D1, 1387-1415.

Côté, J., Desmarais, J.-G., Gravel, S., Méthot, A., Patoine, A., Roch, M., and Staniforth, A., 1998a: The operational CMC-MRB Global Environment Multiscale (GEM) model. Part I: Design consideratios and formulation. *Monthly Weather Rev.*, **126**, 1373-1395.

Côté, J., Desmarais, J.-G., Gravel, S., Méthot, A., Patoine, A., Roch, M., and Staniforth, A., 1998b: The operational CMC-MRB Global Environment Multiscale (GEM) model. Part II: Results. *Monthly Weather Rev.*, **126**,1397-1418.

Gong, S.L., Barrie, L.A., Blanchet, J.-P., von Salzen, K., Lohmann, U., Lesins, G., Spacek, L., Zhang, L.M., Girard, E., Lin, H., Leaitch, R., Leighton, H., Chylek, P., and Huang, P., 2003: Canadian Aerosol Module: A size segregated simulation of atmospheric aerosol processes for climate and air quality models. 1. Module Development, *J. Geophys. Res.*, **108**. D1, 4007.

Gong, W., A.P. Dastoor, V.B. Bouchét, S. Gong, P.A. Makar, M.D. Moran and B. Pabla, 2003: Cloud processing of gases and aerosols in a regional air quality model (AURAMS) and its evaluation against precipitation-chemistry data, *Proceedings of the Fifth Conference on Atmospheric Chemistry: Gases, Aerosols, and Clouds*, 2.3 (CD-ROM), American Meteorological Society, Boston.

Hansen, D.A., K.J. Puckett, J.J. Jansen, M. Lusis, and J.S. Vickery, 1991: The Eulerian model evaluation field study (EMEFS), *in Proceedings of 7th Joint Conference on Applications of Air Pollution Meteorology with AWMA,* pp. 58-62, Am. Meteorol. Soc., Boston, Mass..

Jones, A., D.L. Roberts, and J. Slingo, 1994: A climate model study of indirect radiative forcing by anthropogenic sulphate aerosols, *Nature*, **370**, 450-453.

Makar, P.A., V.S. Bouchét, and A. Nenes, 2003 : Inorganic chemistry calculations using HETV – a vectorized solver for the SO_4^{2-}-NO_3^--NH_4^+ system based on ISOROPIA algorithms, *Atmos. Environment*, **37**, 2279-2294.

McNaughton, D.J. and R.J. Vet, 1996: Eulerian Model Evaluation Field Study (EMEFS): A summary of surface network measurements and data quality. *Atmos. Environment*, **30**, 227-238.

Moran, M.D., Dastoor, A.P., Gong, S.-L., Gong, W., and Makar, P.A., 1998: Conceptual design for the AES unified regional air quality modelling system (AURAMS), Internal Report, 100 pp., Air Quality Research Branch, Atmospheric Environment Service. [Now Met. Service of Canada]

Slinn, A.A. and W.G.N. Slinn, 1981: Modeling of atmospheric particulate deposition to natural waters. *In Atmospheric Pollutants in Natural Waters*, S.J. Eisenreich, Editor, Ann Arbor Sci., Ann Arbor, Michigan, 23-53.

Venkatram, A., P.K. Karamchandani and P.K. Misra, 1988: Testing a comprehensive acid deposition model. *Atmos. Environment*, **22**, 737-747.

Zhang, L., M.D. Moran, P.A. Makar, J.R. Brook and S. Gong, 2002: Modelling gaseous dry deposition in AURAMS – A Unified Regional Air-quality Modelling System. *Atmos. Environment*, **36**, 537-560, 2002.

LABORATORY STUDIES ON THE UPTAKE OF AMMONIA, BTEX AND ALKYLBENZENES BY ICE CRYSTALS

Ines Hoog[1], Subir K. Mitra[1], Elke Fries[2], Wolfgang Jaeschke[2], Stephan Borrmann[1]

[1]University of Mainz, Institute of Atmospheric Physics
[2]J.W. Goethe-University of Frankfurt am Main, Center for Environmental Studies

INTRODUCTION

Naturally occurring emissions and continuously rising levels of anthropogenic emissions are responsible for the presence of inorganic and organic trace gases and particles containing trace materials in the atmosphere. An important process affecting the fate of inorganic and organic compounds in the atmosphere is their removal by wet deposition. Rain and snow contain significant amounts of inorganic trace compounds detected as ions like SO_4^{2-}, NO_3^-, Cl^-, Na^+, K^+, NH_4^+. Ammonia, one of the most important trace gases found in continental rainwater is primarily released by natural sources (Warneck, 2000). The concentration of NH_3 in the atmosphere varies between 1 and 25 ppbv (Seinfeld, 1986). Because it is basic and also highly soluble in water, this compound plays a key role in the acid-base exchange process in cloud and rainwater. Aromatic compounds constitute an important part of the volatile organic compounds (VOCs) emitted from traffic as well as from solvent use and production. VOCs like benzene, toluene, ethylbenzene and xylene isomers (BTEX) as well as several alkylbenzenes (ABs) were found in rain water and snow samples at ppt- and ppb levels, respectively (Ligocki et al., 1985, Czuczwa et al., 1988). The processes leading to the uptake of the amounts of inorganic and organic compounds in rain and snow are not fully understood. Most of the precipitation falling to the surface at mid latitudes originates as ice in the troposphere. The uptake of inorganic compounds like SO_2, HNO_3 and HCl by growing and non growing ice crystals was studied already in the past (Johannson and Granat, 1986; Mitra et al., 1990a, 1990b; Diehl et al. 1995). Santachiara et al. (1998) have shown that significant amounts of NH_3 can be incorporated in growing ice crystals. However, little is known on the uptake of NH_3 by non growing ice crystals. Also there is little information on the uptake of organic compounds by ice crystals. In the atmosphere, VOCs are mainly present in the gas phase and the process of gas scavenging must be of primary importance. To clarify the uptake of inorganic and organic gases a series of experiments were conducted in a 2m by 2m walk-in cold chamber at the Institute of Atmospheric Physics, University of Mainz. We studied the uptake of BTEX and several ABs by adsorption on non-growing ice crystals as well as during the growth of ice crystals by vapor deposition. Due to the low water solubilities of the given organic compounds the direct condensation of vapor onto the solid phase is expected to be more important as an uptake mechanism than an uptake through the riming process. The uptake of inorganic and organic gases might also play a meaningful role in the atmospheric process. It has already been demonstrated that inorganic trace gases in ice crystals reduce their evaporation rates (Diehl et al., 1995) resulting in an increased lifetime of ice clouds. This might affect the earth's climate and climatic feedback (Stephens et al. 1990).

EXPERIMENTAL DETAILS

In a first series of experiments we examined the uptake of ammonia by non growing ice crystals. Dendritic ice crystals were grown by diffusion of water vapour in an ice supersaturated environment at –15 °C. After growth the crystals were put on teflon net placed in a 5 cm diameter horizontal flow tunnel located in the walk-in cold chamber. The crystals were exposed at a temperature of –2°C to an ice saturated air stream containing ammonia in desired concentrations. The concentration of ammonia in the air stream was set and maintained using a mass flow controller and was monitored continuously by a calibrated NOx, NOy, NH_3 chemiluminescence analyser (ANSYCO - NH30M). Exposure times were varied between 20 and 60 minutes. Subsequently the melt water of the crystals was analysed by ion chromatography with a Dionex DX 300 System to determine the NH_4^+ ion concentration. The standard deviation of the applied analytical method was 2 to 9 ppb. It was found that in addition to NH_4^+ ions, Na^+ and K^+ were present as background contamination. It is most likely, that these ions got incorporated into ice during crystal growth.

Second series of experiments were carried out to study the uptake of ammonium with polycrystalline ice pellets. Deionized water droplets were allowed to fall and freeze in liquid nitrogen producing polycrystalline ice pellets (Sommerfeld et al. 1986) with a mean diameter of about 3 mm. We exposed the pellets also for 20, 30, 40 and 60 minutes to ammonia–air mixtures with concentration of 0.2, 1.5, 2.5 and 5 ppmv. The exposed pellets were collected in 10ppm HCl solution to avoid loss of adsorbed ammonia during the melting process. The melt water of the pellets was also analysed by ion chromatography to determine the NH_4^+ ion concentration.

In a third series of experiments we studied the adsorption of BTEX and ABs by non-growing ice crystals. Dendritic snow crystals were generated by vapor diffusion in a crystal growth chamber. After generation the crystals were removed and put on different screen inserts installed in a vertical tube inside the walk-in cold room. The cold room temperature was maintained at -20 °C. Ice crystal growth as well as evaporation during experiments was avoided by ice saturating the carrier stream of precleaned external air (flow rate: 31 l min^{-1}). The carrier gas was mixed with various proportions of BTEX and AB vapours. The resulting gas concentrations in the exposition chamber ranged between 1 and 10 ppbv.

In a fourth series of experiments the uptake of BTEX and ABs was studied while the ice crystals were growing by vapor deposition at different temperatures and humidities. A continuous flow of pre-cleaned external air (31 l min^{-1}) was humidified by passing it through a vessel filled with water. Inside the walk-in cold chamber BTEX and AB vapours were added to the carrier air stream. The gas concentrations ranged from 0.6-10 ppbv. The airflow loaded with organic gases was passed through a heated input pipe into a specially constructed crystal growth tube where ice supersaturation permitted the deposition of ice from the vapor onto cooling fins.

To quantify the uptake concentrations, BTEX and ABs were determined in the melt water of ice crystals after each experiment. The applied analytical method was based on a pre-analysis concentration enhancement of VOCs by Solid-Phase-Micro-Extraction (SPME) followed by GC/MS-analysis. After a certain exposure time ice crystals were removed from the flow tube and transferred to a 20 ml vial. The sample volumes varied between 2.7 and 12.0 g and 5 µl of 1-Brom-2-Chlorethane (200 ng μl^{-1}) was added to each sample as an IS. The SPME apparatus consists of a 100 µm polydimethylsiloxane coating on a fiber that is mounted on a syringe needle. In the SPME-procedure the VOCs were allowed to adsorb into the bonded organic phase. The sample temperature during extraction was kept at 35 °C. Once adsorbed, VOCs were thermally desorbed from the coating by inserting the SPME-fiber into the injector of a Thermoquest 2000 GC kept at 260 °C. The fiber remained in the injector for 20 minutes. Peak detection and identification were carried out using a Thermoquest Voyager MS. The determination limits for the given compounds varied between 1-10 ng l^{-1}.

RESULTS AND CONCLUSIONS

In Figure 1, we show the concentration variation of NH_4^+ and the exposure time at 0.6 and 1,5 ppmv partial pressure of ammonia at a temperature of –2 °C. At 20, 40 and 60 minutes exposure time the ion concentrations of ammonium in melt water varied between 3 and 10 µg l^{-1}, 15 and 25µg l^{-1}, and 20 and 40 µg l^{-1}, respectively for 0.6 ppmv gas concentration. For 1.5 ppmv partial pressure the concentrations of ammonium were 12 and 23 µg l^{-1}, 18 and 20 µg l^{-1}, and 18 and 42 µg l^{-1}, respectively for the same exposure times. Our results demonstrate that for 20 minutes exposure time, the ion concentrations of ammonium were a little bit higher for 1.5 ppmv than for 0.6 ppmv partial pressure. For 40 and 60 minutes exposure time the concentration were rather similar for both partial pressures. Our results indicate that at temperatures near 0°C the amount of ammonia taken up by non growing ice crystals is small compared to that of other highly water soluble gases like HNO_3 and HCL in spite of the presence of a quasi liquid layer at these temperatures. It was expected that NH_3 behave more like HCl and other highly soluble gases but no dramatic uptake especially around 0°C was observed. In comparison to the experiment with growing crystals in presence of NH_3 with similar concentrations (Santachiara et al. 1998) the experiments showed an order of magnitude lower ammonia uptake for non growing crystals. Experiments to determine the uptake of ammonia during ice crystal growth and also by non growing crystals at other temperatures are currently being carried out.

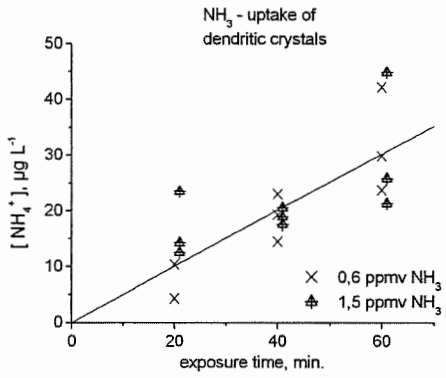

Figure 1. Variation of NH_4^+ ion concentrations in melt water of dendritic crystals with increasing exposure time for 0,6 and 1,5 ppmv ammonia concentration at temperature about - 2°C

Preliminary results of the experiments with ice pellets exposed 20, 30, 40 and 60 minutes with various concentrations of ammonia in air namely 0.2, 1.7, 2.5, and 5ppmv show no significant increase of NH_4^+ ion concentration in melt water. So it appears that contrary to the uptake of HCl and HNO_3 by ice pellets no significant uptake of ammonia takes place at a temperature of – 2°C.

The results from the experiments on the uptake of VOCs by non-growing ice crystals showed that adsorption of BTEX and ABs onto non-growing ice surfaces was insignificant. However, growing ice crystals scavenged significant amounts of BTEX and AB vapours. Variation of the concentrations of BTEX

and ABs in the melt water of ice crystals grown in an ice supersaturated environment by vapor deposition at -5 and -20 °C in the presence of VOC are shown in Figure 3. We obtained different shapes and sizes of ice crystals at different supersaturations generated by different temperatures. At temperatures near -5°C short columns occurred at relatively high supersaturations whereas at lower temperatures around -20°C we observed dendritic ice crystals. The uptake of BTEX with water solubilities higher than 180 mg l^{-1} by short columns was always higher with concentrations in melt water from 15 ng l^{-1} up to 135 ng l^{-1} than by dendrites with melt water concentrations between 6 ng l^{-1} and 23 ng l^{-1}. For less polar compounds like ABs with water solubilities lower than 100 mg l^{-1} we observed a better uptake by dendrites than by short columns with melt water concentrations from 49 ng l^{-1} to 120 ng l^{-1} and from 9 ng l^{-1} to 63 ng l^{-1}, respectively.

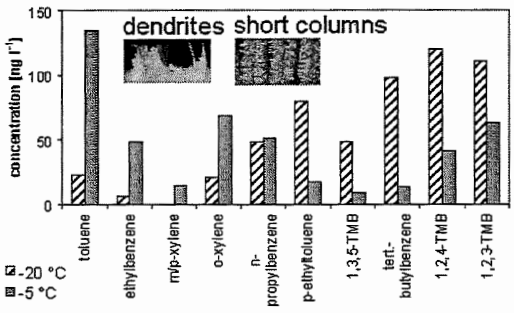

Figure 2. Concentrations of BTEX and ABs in the melt water of ice crystals grown by vapor deposition at -5 and -20 °C (TMB = trimethylbenzene).

The low uptake of the given BTEX and ABs by adsorption on non growing ice crystals indicates that below-cloud scavenging of organic gases by snow crystals can be neglected. Since much higher air concentrations would be required than those measured in the atmosphere equilibrium distributions argue also against below-cloud scavenging. The results of our study point at a significant uptake of BTEX and ABs by ice crystals during their growth from vapor deposition. This indicates that the tropospheric ice phase can be assumed to play a role in the removal processes of VOCs from the atmosphere. The extent of the uptake of VOCs must be dependent on temperature (implying crystal shape) as well as on the physical and chemical parameters of every single compound. Our findings indicate that scavenging of VOCs by tropospheric ice crystals may influence the long-range transport and atmospheric fate of such chemicals.

ACKNOWLEDGEMENTS

This research was funded by the German Science Foundation (DFG) through grant Mi 483/4-1, Ja 350/1-1 and supported by the University of Mainz, the Max-Planck-Institute for Chemistry in Mainz and the University of Frankfurt

REFERENCES

Beilke, S., and Georgii, H.W., 1968, Tellus, 20, 435 - 441

Czuczwa, J, Leuenberger, C., Giger, W. (1988) Seasonal and temporal changes of organic compounds in rain and snow. Atmos. Environ. 22, 907-916.

Diehl, K., Mitra, S.K., and Pruppacher, H.R., 1995: A laboratory study on the uptake of HNO_3 and HCl vapour by snow crystals and ice spheres at temperatures between 0 and -40 °C. Atmos. Environm., 29, 975-981.

Johannson,C., and Granat, L., 1986: An experimental study of the dry deposition of gasous nitric acid to snow. Atmos. Environm., 20, 1165 – 1170.

Ligocki, M.P., Leuenberger, C., Pankow, J. (1985) Trace organic compounds in rain II. Gas scavenging of neutral organic compounds. Atmos. Environ. 19, 1609-1617.

Mitra. S.K., Barth, S., and Pruppacher, H.R., 1990a: A laboratory study of the efficiency with wich aerosol particles are scavenged by snow flakes. Atmos. Environm. 24 A , No.5, 1247 -1254

Mitra. S.K., Barth, S., and Pruppacher, H.R., 1990b: A laboratory study on the uptake of SO_2 by snow crystals. Atmos. Environm. 24 A , No.9, 2307 -2312

Santachiara, G., et. al., 1998: Scavenging of SO_2 and NH_3 during growth of ice. Atmos. Res. 47 – 48, 209 – 217.

Seinfeld, J.H., 1986: Atmospheric chemistry and physics of air pollution. John Wiley, New York

Sommerfeld, R.A. and Lamb, D., 1986: Preliminary measurements of SO_2 adsorbed on ice. Geophys. Res. Lett., 13, 349-351.

Stephens, G. L., et al. 1990. The relevance of microphysical and radiative properties of cirrus clouds to climate and climatic feedback. Atmos. Sci. 47, 1742 – 1753.

Warneck, P., 2000: Chemistry of the natural atmosphere. second edition; Academic Press.

MICROPHYSICS OF PYROCUMULONIMBUS CLOUDS

Eric Jensen, Andrew S. Ackerman, Ann Fridlind

NASA Ames Research Center, Moffett Field, CA, USA

1. INTRODUCTION

The intense heat from forest fires can generate explosive deep convective cloud systems that inject pollutants to high altitudes. Both satellite and high-altitude aircraft measurements have documented cases in which these pyrocumulonimbus clouds inject large amounts of smoke well into the stratosphere (Fromm and Servranckx 2003; Jost et al. 2004). This smoke can remain in the stratosphere, be transported large distances, and affect lower stratospheric chemistry. In addition recent in situ measurements in pyrocumulus updrafts have shown that the high concentrations of smoke particles have significant impacts on cloud microphysical properties. Very high droplet number densities result in delayed precipitation and may enhance lightning (Andreae et al. 2004). Presumably, the smoke particles will also lead to changes in the properties of anvil cirrus produces by the deep convection, with resulting influences on cloud radiative forcing.

In situ sampling near the tops of mature pyrocumulonimbus is difficult due to the high altitude and violence of the storms. In this study, we use large eddy simulations (LES) with size-resolved microphysics to elucidate physical processes in pyrocumulonimbus clouds.

2. APPROACH

For this modeling study we use a 48-km square horizontal domain with uniform 500-m grid spacing. The vertical domain is 0–24 km with 375 km spacing. Boundary conditions are specified as rigid at the top and bottom and open at the horizontal faces. Cloud microphysical properties are treated with a size resolved scheme consisting of 32 size bins each for aerosols, droplets, and ice crystals spanning 5 nm–1 μm, 2 μm–1 cm, and 2 μm–3 cm, respectively. Algorithms used for processes such as nucleation, condensational growth, aggregation, breakup, and sedimentation are described by (Fridlind et al. 2004).

We focus here on the pyrocumulonimbus cloud system formed over the the Chisholm fire that occurred 28 May, 2001, in Alberta, Canada. Results from this case will be compared with simulations of pyrocumulus observed during the LBA-SMOCC campaign in Brazil. (Fromm and Servranckx 2003) documented the injection of large smoke cloud deep into the stratosphere by supercell convection associated with the Chisholm fire. Following (Winterrath et al. 2003), we specify the fire as a 10-km by 500-m source of heat, smoke particles, and water vapor, with fluxes of 300 kJ m^{-2} s^{-1}, 18.9 g H_2O m^{-2} s^{-1} and 100 CN/cm^{-2} s^{-1}, respectively. We use a nearby pre-storm sounding with a convective available potential energy (CAPE) of 350 J kg^{-1}. The thermodynamic instability in this case was clearly insufficient to generate a severe storm without heat input from the fire.

We describe below the overall evolution of the pyrocumulonimbus in the baseline simulation described above. Several sensitivity tests have been run to evaluate the importance of the different fire fluxes on the cloud evolution. We focus on the fire aerosol input impact on pyrocumulus processes and the resulting anvil properties.

3. RESULTS

The strong heat source specified drives a rapid buildup of explosive convection. Within 20 minutes, the peak updraft speeds exceed 40 m s^{-1}. Figure 1 shows a cross section of the storm perpendicular to the fire line at 50 minutes into the baseline simulation. The convection penetrates the tropopause (about 12 km) and injects large amounts of ice into the stratosphere up to as high as about 14 km.

Figure 2 shows the evolution of various cloud--system diagnostics for the baseline simulation and sensitivity tests with the fire water vapor and aerosol sources removed. For this pyrocumulonimbus case, the heat source from the fire dominates the dynamical evolution and bulk properties of the cloud. The source of water vapor from the fire does not change the cloud dynamics and increases the cloud ice water path (IWP) by only about a 25%. Similarly, the large source of smoke particles acting as CCN have no impact on the cloud dynamics and only minimal impact on LWP or IWP. How-

Corresponding author's address: Eric Jensen, NASA Ames Research Center, Mail Stop 245-4, Moffett Field, CA 94035; E-mail: ejensen@cirrus.arc.nasa.gov.

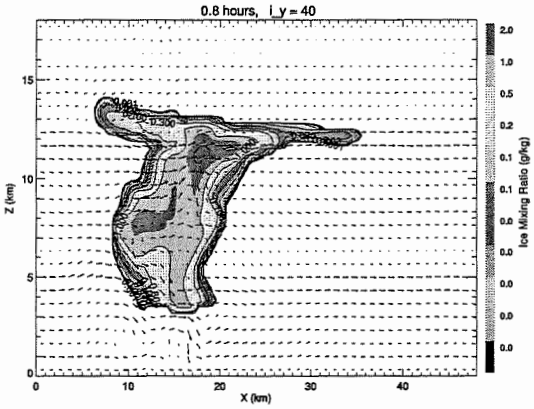

Figure 1: Condensed water content (g kg^{-1}) is plotted for on an x-z plane through the center of the model (perpendicular to the fire line) at 50 minutes into the baseline simulation.

ever, the smoke particles and water vapor source dramatically change the cloud microphysical properties. Peak ice concentrations increase by about an order of magnitude from $\simeq$20 cm^{-3} in the case with no smoke to $\simeq$200 cm^{-3} in the baseline simulation with the smoke particle source. Excluding the water vapor source reduces peak ice concentrations by about a factor of 5 compared to the baseline simulation.

Unexpectedly, neither the timing of precipitation onset or the magnitude of precipitation are substantially affected by the numerous smoke particles acting as CCN in the pyrocb. Precipitation is delayed only very slightly, and the cumulative precipitation is reduced by no more than about 50In analysis of pyrocumulus clouds over the Amazon, (Andreae et al. 2004) showed that warm rain was significantly delayed and reduced by biomass burning aerosols. The increase in droplet concentration limited droplet sizes and prevented precipitation development until ice formed in the updrafts. This effect is less important for the boreal Chisholm fire for two reasons: (1) The surface is much colder at high latitudes than in the tropics so the freezing level, 0°C, is reached at a lower altitude (about 3.2 km for the Chisholm case versus about 5 km in the deep tropics); (2) given the very strong updrafts in this pyrocb ($\simeq$40 m s^{-1}), the freezing level is reached within the updraft within 15 minutes, so precipitation associated with the ice phase occurs very quickly anyway.

The anvil ice crystal size distributions (Figure 3) are also dramatically altered by the fire particle and water vapor sources. With all of the fire

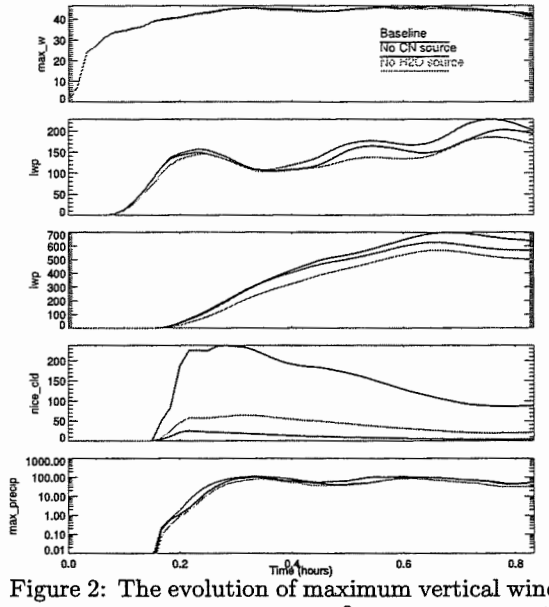

Figure 2: The evolution of maximum vertical wind speed, liquid water path (g m^{-2}), ice water path (g m^{-2}), anvil ice crystal concentration (cm^{-3}), and maximum precipitation rate (mm hr^{-1}). The water vapor source has very little effect on the cloud simulation. The fire aerosol source (smoke particles) has little impact on the bulk cloud properties or dynamics, but the anvil cirrus microphysical properties are strongly altered by the smoke particles

fluxes included (baseline case), anvil ice concentration is dominated by crystals smaller than 10 μm radius. Eliminating either the H_2O or particle source results in more than an order of magnitude reduction in average anvil ice concentration, and omitting the particle source increases the ice mode radius from $\simeq$ 6 μm to $\simeq$ 18 μm. In the baseline pyrocb simulation, the anvil crystals are significantly smaller than those observed in typical cumulonimbus anvils (Garrett et al. 2003).

REFERENCES

Andreae, M. O., D. Rosenfeld, P. Artaxo, A. A. Costa, G. P. Frank, K. M. Longo, and M. A. F. Silva-Dias (2004). Smoking rain clouds over the amazon. *Science 303*, 1337–1342.

Fridlind, A. M., A. S. Ackerman, E. J. Jensen, A. J. Heymsfield, M. R. Poellot, D. E. Stevens, D. Wang, L. M. Miloshevich, D. Baumgardner, R. P. Lawson, J. C. Wil-

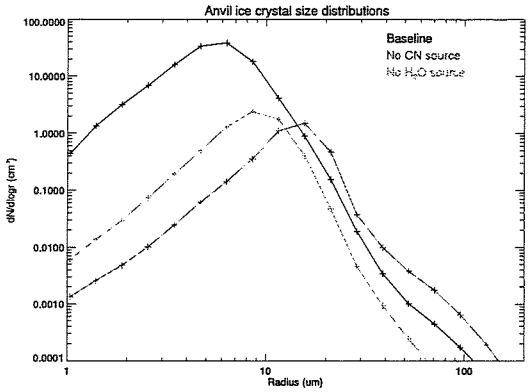

Figure 3: Horizontally averaged anvil ice crystal size distributions are plotted. We have excluded grid boxes with vertical wind speeds larger than 2 m s^{-1}.

son, R. C. Flagan, J. H. Seinfeld, H. H. Jonsson, T. M. VanReken, V. Varutbangkul, and T. A. Rissman (2004). Evidence for the predominance of mid-tropospheric aerosols as subtripical anvil nuclei. *Science 303*, in press.

Fromm, M. D. and R. Servranckx (2003). Transport of forest fire smoke above the tropopause by supercell convection. *Geophys. Res.Lett. 30*, doi:10.1029/2002GL016820.

Garrett, T. J., H. Gerber, D. G. Baumgardner, C. H. Twohy, and E. M. Weinstock (2003). Small, highly reflective ice crystals in low-latitude cirrus. *Geophys. Res.Lett. 30*, doi:10.1029/2003GL018153.

Jost, H.-J., K. Drdla, A. Stohl, L. Pfister, M. Loewenstein, J. P. Lopez, P. K. Hudson, D. M. Murphy, D. J. Cziczo, M. Fromm, T. P. Bui, J. Dean-Day, M. J. Mahoney, E. Richard, N. Spichtinger, J. Pittman, E. M. Weinstock, J. C. Wilson, and S. C. Wofsy (2004). Observations of mid-latitude forest fire plumes deep in the stratosphere. *Geophys. Res.Lett. 32*, in press.

Winterrath, T., J. Trentmann, C. Textor, M. Fromm, R. Servranckx, G. Mullendore, D. Rosenfeld, P. K. W. P. V. Hobbs, and M. O. Andreae (2003). Modeling of fire-induced supercell convection and transport of biomass burning aerosol into the stratosphere: The chisholm fire of 28 may, 2001. *EOS, Transactions, American Geophysical Union 84*, 0.

aerosols affect clouds
w physics and aerosols
but not the dynamics
measures

CHANGES IN ACIDITY OF OPENING RAINFALL AND THROUGHFALL IN RELATION TO CANOPY OPENNESS IN FORESTS

Katsuhiro Kikuchi and Yoshiaki Sasaki

Akita Prefecturral University, Akita, 010-0195, Japan

1. INTRODUCTION

Acid precipitation is an important aspect of conservation of the global environment. The effects of such acid precipitation on the forest ecosystem of Japan have fortunately not been realized until recently. However, almost all precipitation, including rainfall and snowfall in Akita prefecture, including Akita city, in Tohoku district of the main island of Japan, showed an acidity below pH 5.6. Most of the precipitation ranged between pH 5.0 and 4.0 and frequently fell below pH 4.0. It is therefore clear that the ecosystem, and of special note the Shirakami-Sanchi (Shirakami-Mountainous region) World National Heritage Area of Akita Prefecture, will be detrimentally affected by the continued accumulation of these acidic substances. This area is characterized by a primeval forest of beech trees (*Fagus crenata Blume* (*Fagaceae*)), as well as by heavy snowfall brought by northwesterly monsoon winds in the winter season, and by heavy rainfall in the summer season. At the foot of the mountains and plain of Akita prefecture, Japanese cedar (*Cryptomeria japonica* (*L. fil.*) *D.Don.*) is the most typical tree and has been nominated as the tree of Akita prefecture, Japan.

Numerous studies have been conducted in Japan to date. However, most of these were limited by their short periods of observation except in a few examples. Occasionally, they measured total amount of rainfall of a few or many times. Furthermore, as seen in the Proceedings of the Acid rain 2000 in Tsukuba, Japan (Satake, 2000, 2001 a, b, c), there were practically no reports of measurements of the one-to-one correspondence of the pH values of opening rainfall and throughfall, and of the relationship between the acidity of throughfall and canopy openness of trees.

For these reasons, we examined the relationship between the acidity of opening rainfall and throughfall of several kinds of trees continued to the previous year (Kikuchi *et al.*, 2000), including beech trees and Japanese cedar, and other broad-leaved trees, such as Fagus crenata, Quercus dentana and Aesculus turbinata, as well as coniferous trees, such as Pinus thunbergii and Pinus densiflora. In addition, we examined the relationship between the acidity of throughfall and canopy openness of oak trees. Furthermore, the neutralization effect of throughfall using a bundle of branches of beech trees was examined.

Corresponding author's address: Katsuhiro Kikuchi, Laboratory of Atmospheric and Hydrospheric Sciences, Faculty of Bioresource Sciences, Akita Prefectural University, Akita, 010-0195, JAPAN; E-mail: kikuchi_snow@akita-pu.ac.jp

2. SAMPLING SITES OF RAINFALL AND THROUGH-FALL

Two sampling sites of rainfall and throughfall were selected; one (A-site) is near the Akita campus of Akita Prefectural University in Akita city, and the other (E-site) is the ecosystem park in Ohgata village approximately 30 km north of Akita city. The main tree species at the A-site is Japanese black pine (Pinus densiflora), together with patch-like communities of oak trees. As well known, the dead leaves of oak trees do not fall easily compared with other deciduous broad-leaved species as winter approaches. It is, therefore, very favorable to measure the seasonal variation in acidity of throughfall in different tree species. At the A-site, sampling of the throughfall in an oak tree and two Japanese black pines was performed. At the E-site, sampling was performed in two beech trees, a keaki tree and a horse chestnut as representative broad-leaved trees, two Japanese cedars, and two Pinus thunbergii as representative coniferous trees.

3. MEASUREMENTS OF RAINFALL AND THROUGH-FALL pH AT A-SITE

Sampling and measurements of rainfall were carried out from April to December, 2002. Almost all the pH values of opening rainfall in this period remained in a range between pH 4.0 and 5.0, except in several cases that reached pH 3.4 and pH 5.6.

The one-to-one correspondence of the pH values of opening rainfall and throughfall in oak trees at the A-site is shown in Fig. 1. In this figure, closed and open circles indicate the pH values of the opening rainfall and throughfall in oak trees on each rainfall day. From the end of April to the beginning of May, the difference between pH values of the opening rainfall and throughfall in the oak trees was small. As the oak trees came into bud, however, the difference between these values became large from early May to June. From mid-June to the beginning of November, the difference between these values showed little change. From

mid-November to mid-December, however, the differences between these values became small and both values became equal except several samples.

Figure 2 shows a different form of the results described above. Here, the vertical axis shows the pH values of throughfall in oak trees and the horizontal axis shows the pH of opening rainfall. All data were divided into three-month periods, that is, from April to June (a), July to September (b), and October to December (c). The dashed lines that were obtained by the least mean square method in each (a), (b) and (c) panel showed a difference of 3 months, respectively. It was recognized that the distance between two lines in each panel became narrower from (a) to (c).

The one-to-one correspondence between the pH values of opening rainfall and throughfall in Japanese black pine trees at the A-site is shown in Fig. 3. Here, the pH values of the Japanese black pines are shown as open circles. Compared with the oak tree data shown in Fig. 1, the difference between the pH values of the opening rainfall and throughfall in Japanese black pines was clearly small. Presentation of the data as in Fig. 4 demonstrates that the separations between the two lines in each (a), (b) and (c) panel became narrower compared with the oak tree data as shown in Fig. 2. In addition, as with Fig. 2 the separations between two lines became successively narrower from (a) to (c). As seen clearly in panel (c) in Fig. 4, two lines were practically equal.

4. MEASUREMENTS OF RAINFALL AND THROUGH-FALL pH AT E-SITE

The measurements at E-site were begun from mid-May to the end of December, 2002. The difference between pH values of both samples of beech trees and opening rainfall showed a similar tendency to the results of oak tree from the A-site. Specifically, both data in December were almost coincidental. It is considered therefore that almost all the leaves of beech trees at this time had fallen off the branches except for a few leaves. Measurement results of pH values of opening rainfall and throughfall in Japanese cedar tree examined at E-site showed a similar tendency to the results of Japanese black pine from the A-site.

5. THE RELATIONSHIP BETWEEN THE ACIDITY OF THROUGHFALL AND CANOPY OPENNESS OF OAK TREES

As described previously, it was considered that the acidity of opening rainfall was neutralized by the throughfall. This tendency was most obvious from May to June but disappeared from November to December. It was therefore considered that the degree of neutralization may have been correlated with the life cycle of the trees. We therefore investigated the relationship between pH values of the opening rainfall and throughfall of oak trees, and the canopy openness of the oak trees. Canopy openness was determined by photographs taken with a fish-eye lens camera at a rate of several per month. The results are shown in Fig. 5. Here, the pH values are shown on the left-hand vertical axis, the percent canopy openness on the right-hand vertical axis, and the month in the horizontal axis. Photographs taken of typical months are indicated by arrows, namely, April, May, October and November, 2002. As clearly observed, the canopy openness correlated well with the difference between the pH values of the throughfall of oak trees and opening rainfall. This was particularly conspicuous in the transition from April to May and from October to November.

6. THE NEUTRALIZATION EFFECT OF THROUGH-FALL USING BRANCHES OF BEECH TREE

As suggested previously, the acidity of opening rainfall appeared to be neutralized by throughfall. To test their neutralization capacity, several beech tree branches were cut away, with official permission, and the branches divided into one branch, three branches and five branches, and the three and five branches were then bundled together with. These three specimens were hung from two parallel ropes at regular intervals, so as to maintain their balance, and were set up near the opening rainfall collection bucket in the Dakedai beech tree forest near the Shirakami-Sanchi World Natural Heritage Area. The results were shown in Fig. 6, demonstrate the corresponding pH values of 4.57 for the opening rainfall, of 4.81 for the throughfall of natural beech trees, pH 4.70, 4.68 and 4.80 for 1, 3 and 5 branches, respectively. It was therefore concluded that the effects of neutralization of throughfall corresponded to that of 5 branches in this experiment. The effects of 1 and 3 branches were nearly equal in this experiment. As the neutralization effect of throughfall was dependent on the number of rain drops that were in contact with the leaves for a length of time, the effect did not significantly differ between 1 and 3 branches in this experiment.

7. CONCLUSIONS

The results of this study indicate that the acidity of throughfall was lower than that of the opening rainfall in nearby areas. Furthermore, the acidity of throughfall from broad-leaved trees, such as beech (Fagus crenata), oak (Quercus dentana), keaki (Zelkova serrata), and horse chestnut (Aesculus turbinata) was lower than that of coniferous trees, such as Japanese cedar (Cryptomeria japonica), red pine (Pinus thunbergii), and Japanese black pine (Pinus densiflora). The decreased acidity of throughfall corresponded to

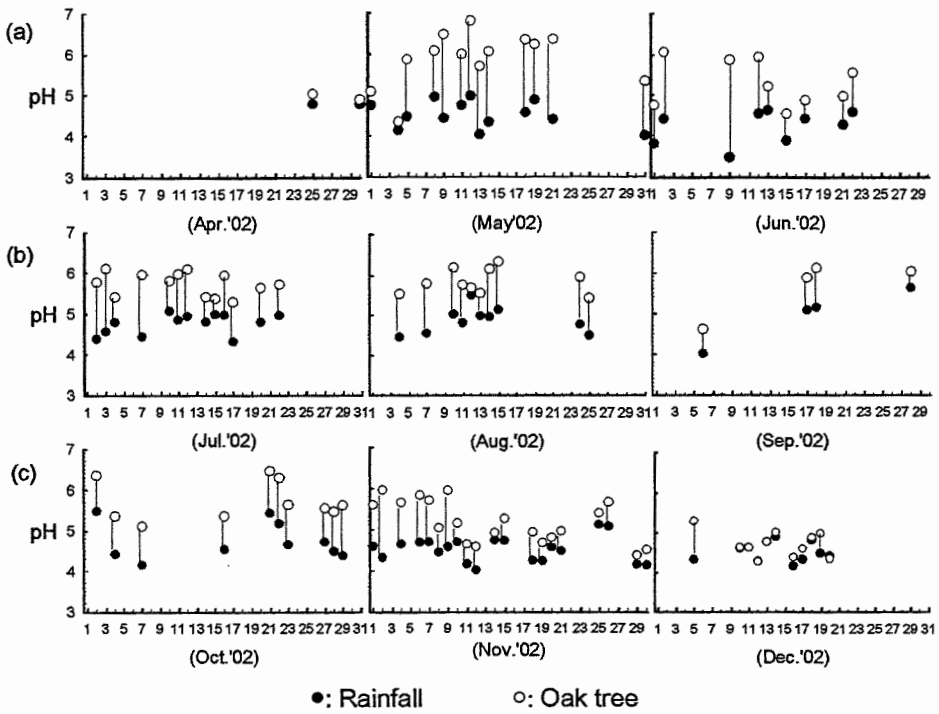

Fig. 1. pH values of throughfall in oak trees and rainfall at A-site.

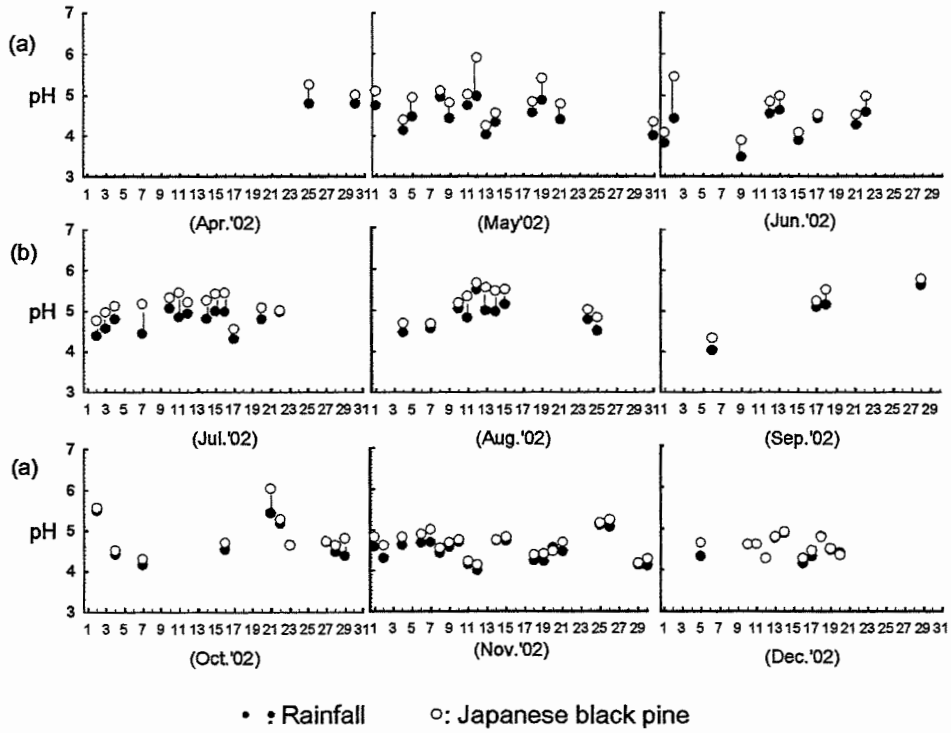

Fig. 3. pH values of throughfall in Japanese black pine and rainfall at A-site.

the lower values of canopy openness in the forest. We therefore conclude that broad-leaved trees, including beech trees, can effectively neutralize acid rainfall. Furthermore, in experiments of the neutralization effects of throughfall using bundled beech tree branches, the acidity of opening rainfall was found to correspond to the situation with five branches. Presumably, therefore, potassium ions in these broad-leaved trees (Kikuchi *et al.*, 2001) are able to neutralize the acidic depositions of raindrops on their leaves more effectively than leaves of coniferous trees.

8. References

Kikuchi, K., Katano, N. and Sasaki, Y., 2001: Do beech leaves neutralize acid rain ? IAMAS 2001, Abstract, Innsbruck, p. 61.

Satake, K., 2000: Abstract Book, 6th International Conference on Acidic Deposition, Kluwer Academic Publishers, 356 pp.

Satake, K., 2001a: Proceedings from the 6th International Conference on Acidic Deposition, Vol. I, Kluwer Academic Publishers, 186 pp.

Satake, K., 2001b: *ibid*, Vol. II, 187-922 pp.

Satake, K., 2001c: *ibid*, Vol. III, 923-1854 pp.

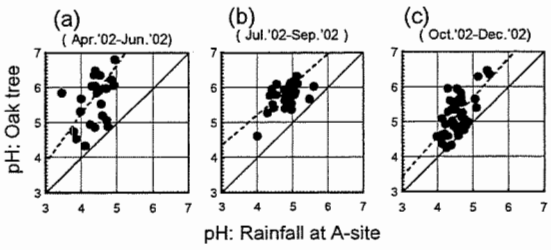

Fig. 2. Relationship between pH values of oak trees and rainfall at A-site. (a) April to June, (b) July to Sept., and (c) Oct. to Dec., 2002.

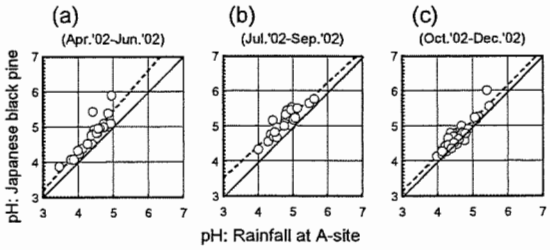

Fig. 4. Relationship between pH values of Japanese black pine and rainfall at A-site.

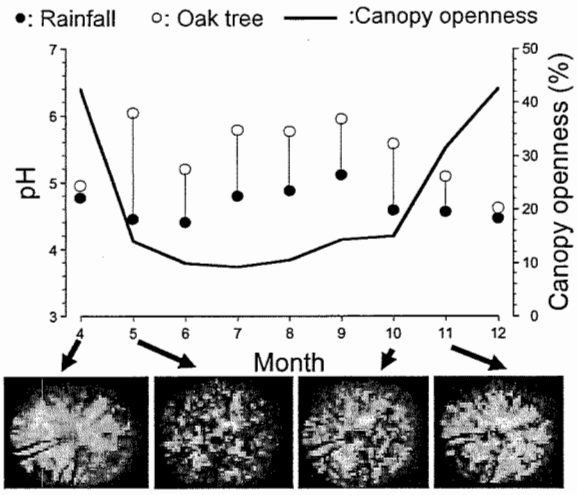

Fig. 5. Relationship between canopy openness, and pH values of throughfall of oak trees and rainfall.

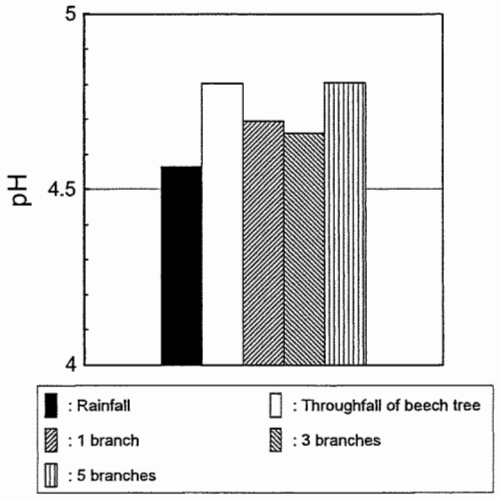

Fig. 6. pH values of rainfall, throughfall of beech tree and 1, 3 and 5 branches.

DROPLET EVAPORATION: THEORETICAL IMPLICATIONS OF RECENT DATA FOR BINARY NITRIC ACID SOLUTIONS

[1]Dennis Lamb, [1]Alfred M. Moyle, and [2]Huiwen Xue

[1]Meteorology Department, The Pennsylvania State University
University Park, Pennsylvania 16802, USA
[2]NOAA Environmental Technology Laboratory
Boulder, CO 80305, USA

1. INTRODUCTION

Cloud droplets continually respond to the changing environmental conditions within clouds by growing or shrinking in size. When the ambient saturation ratio exceeds unity, the "excess vapor" condenses onto the droplets, whereas in subsaturated conditions the droplets evaporate and transport mass back to the gas phase. The rates of mass exchange affect the evolution of droplet spectra and also reflect the molecular-scale processes at the vapor-liquid interface.

Our ability to quantify phenomena such as condensation and evaporation is hampered by our incomplete knowledge of the processes and physical parameters involved. It is difficult, for instance, to quantify the precise conditions at the droplet surface, which are important for calculating mass accommodation coefficients (Kulmala and Wagner 2001). The problem becomes acute when two or more compounds condense or evaporate at the same time (Rudolf et al. 2001).

Experimentation with evaporating droplets offers an opportunity to learn how droplets respond to their environmental ("ambient") conditions. Results from recent experiments (Xue 2002) using binary solutions of water and nitric acid yielded precise evaporation curves from which the mass accommodation coefficient of nitric acid, $\alpha(HNO_3)$, could be estimated. As shown in Fig. 1, repetition of the experiments at different total pressures resulted in analyzed values that tended to increase with decreasing partial pressure of the inert gas (N_2). However, no explicit dependence on the presence of a non-condensing gas is likely. Rather, we suspect that $\alpha(HNO_3)$ may be responding to other parameters, which do depend on pressure. It is our purpose here to examine the theory of droplet growth and evaporation to establish a cause for this apparent pressure dependence.

Corresponding author's address: Dennis Lamb, 503 Walker Bldg., Penn State University, University Park, PA 16802 USA; E-Mail: lno@ems.psu.edu

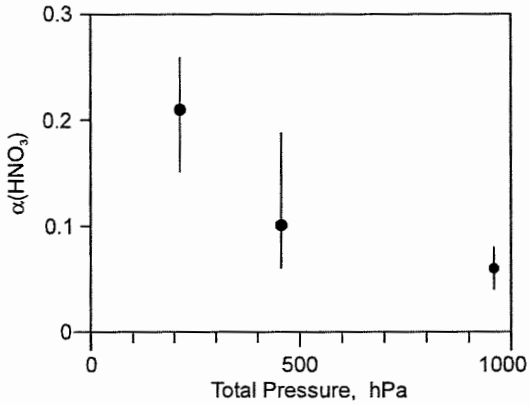

Fig.1. Apparent dependence of the nitric acid accommodation coefficient on system pressure.

2. THEORETICAL CONCEPTS

Several theoretical models have been developed in the past to describe the rates of droplet growth and evaporation. All take into account the transport of mass and heat through the surrounding gas. Maxwell's growth model, however, is inappropriate because it assumes equilibrium at the droplet surface. More complete models, such as those of Fuchs and Sutugin (1970), Fukuta and Walter (1970), and Pruppacher and Klett (1997), account for the molecular processes at the liquid-vapor interface. We have found each of these models to yield equivalent results, so we use Pruppacher and Klett's model because of its conceptual simplicity. For application to our binary system, this kinetic model was coupled to the thermodynamic model of Carslaw et al. (1995) to describe the H_2O-HNO_3 chemical equilibria taking place inside the liquid droplet.

The geometry and variables associated with an evaporating droplet are shown in Fig. 2. For clarity, only a single evaporating species is considered. The droplet, of instantaneous radius *a*, is surrounded by a thin free-molecular region within which molecular collisions are negligible.

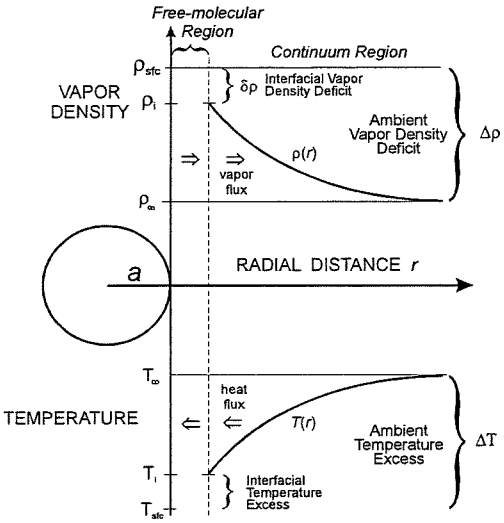

Fig. 2. Schematic depiction of the vapor and temperature fields surrounding an evaporating droplet.

This molecular boundary layer is surrounded by a continuum region, where mass is transported by ordinary diffusion and heat is transported by conduction. By mass continuity arguments, the flow of vapor into the free-molecular zone must equal that leaving the continuum regime.

A characteristic feature of transport in a spherically symmetric field is the non-linear steady-state profile of vapor about the droplet. From an overall deficit Δρ of vapor density far from the droplet surface, the vapor deficit shrinks in magnitude toward the droplet until it becomes δρ at the interface. It is this relatively small deficit of vapor near the surface that drives the net migration of water and nitric acid molecules from the liquid to vapor phases.

Detailed analysis of transport analogous to that for series resistances shows that the ratio of δρ to Δρ, which we here call the "relative interfacial undersaturation" (RIU), varies with both the diffusion coefficient D_v and the mass accommodation coefficient α:

$$\frac{\delta\rho}{\Delta\rho} = \frac{1}{1+\dfrac{\alpha\bar{v}a}{4D_v}}, \qquad (1)$$

where $\bar{v}$ is the mean speed of vapor molecules. Upon noting that the diffusion coefficient varies with pressure p according to $D_v = D_{v0}(p_0/p)$, we see that the interfacial vapor deficit varies with the pressure for any given ambient vapor deficit:

$$\frac{\delta\rho}{\Delta\rho} = \frac{1}{1+\dfrac{\alpha\bar{v}a}{4D_{v0}}\left(\dfrac{p}{p_0}\right)}. \qquad (2)$$

Figure 3 shows how $\delta\rho/\Delta\rho$ varies with the total pressure around the droplet for given α. Note that $\delta\rho/\Delta\rho$ is especially small when the pressure is high and α is large. Under such conditions, the air offers the dominant resistance to mass transfer, and the growth is "diffusion limited". Processes at the liquid-vapor interface are mechanistically important, but theory and experiments based solely on droplet evaporation are relatively insensitive to the details of the surface kinetics in this "high-p" regime. At the other extreme, when the surface processes are inefficient (small α) and the pressure is low, the surface resistance exerts a dominating influence over the total mass transport. In all but the most extreme case of evaporation in pure vapor, $\delta\rho/\Delta\rho$ necessarily varies with total pressure.

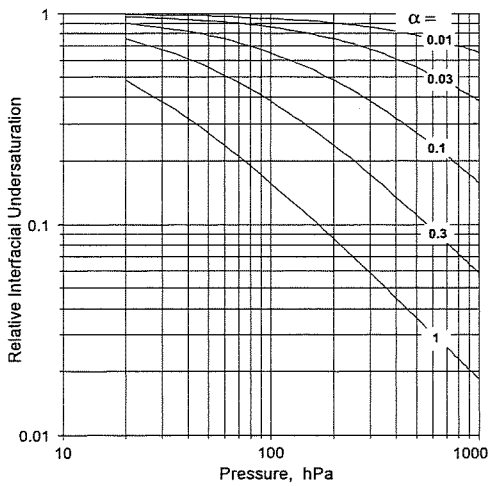

Fig. 3. The relative interfacial undersaturation as a function of total pressure for various values of the mass accommodation coefficient α.

3. APPLICATIONS TO DATA

The point of this analysis is to demonstrate that the relative interfacial undersaturation is a physical variable that depends systematically on the pressure. The exercise is generic, however, and so can show general patterns only. Through Eq. (2), for instance, we note that $\delta\rho/\Delta\rho$ varies not only with the pressure, but

also with the instantaneous radius of the particle. Thus, $\delta\rho/\Delta\rho$ will vary significantly over the course of droplet evaporation even at a given pressure. However, because the impact of the mass accommodation coefficient on growth rate is minimal until the drop radius becomes less than about 10 μm, we need focus attention mainly on the end of droplet evaporation.

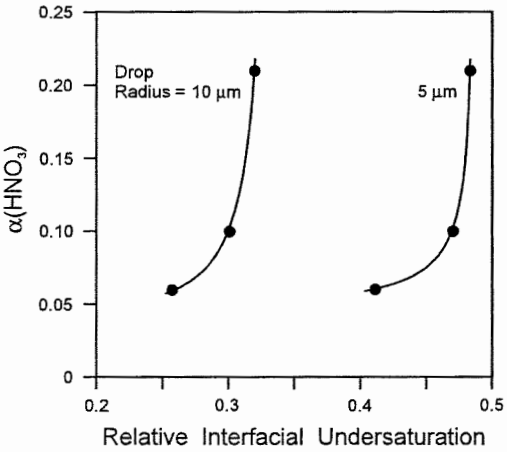

Fig. 4. Dependence of α(HNO₃) on the relative undersaturation.

The numerical model used to analyze the experimental data and extract the values of $\alpha(HNO_3)$ shown in Fig. 1 also allowed $\delta\rho/\Delta\rho$ to be calculated. Out of the complete set of interfacial undersaturations available from each run, those prevailing at two specific drop radii were chosen. Figure 4 shows the result of plotting the analyzed values of $\alpha(HNO_3)$ and the RIU for droplet radii of 10 and 5 μm. As expected from the theoretical analysis of the previous section, the interfacial undersaturations are greater on average for the 5-μm droplets than for the 10-μm droplets.

When a single drop radius is considered, we see that a systematic, in fact a strong dependence of $\alpha(HNO_3)$ on RIU appears. The calculated values of RIU for 5-μm droplets, for instance, increased from low (~ 0.41) to high (~ 0.48) as the experimental pressure was decreased (from 986 to 213 hPa, respectively). The magnitude of the change in the RIU may not seem large, but it must be realized that it is also controlled by $\alpha(HNO_3)$ itself (via Eq. 2) in a self-compensating sense.

Mechanistic interpretation of this result (Fig. 4) is provisionally aided by the work of others. Li et al. (2001), for instance, envision the surface of aqueous drops to be comprised of numerous molecular clusters that serve as gateways between the liquid and gaseous states. The exchange of a trace gas is presumably facilitated by engagement with critical-size water clusters, especially when multiple hydrogen bonds form. As with any nucleation process, the size of the critical cluster should shrink strongly with increasing local supersaturation and lead to trends in mass accommodation as in Fig. 4.

4. CONCLUSIONS

Theory and data may be converging toward a coherent view of molecular exchange at the liquid-gas interface, but detailed scrutiny is needed. A strong dependence of $\alpha(HNO_3)$ on the interfacial undersaturation is one possible reason for its apparent dependence on total pressure, but this conclusion is based on relatively few experiments. We will continue to explore the impacts of uncertainties in model parameters and methods of data collection and analysis on the interpretation of the inferred values of mass accommodation coefficients.

5. ACKNOWLEDGMENTS

This work was sponsored by NSF Grant ATM-9981511. We thank Nathan Magee for discussions.

6. REFERENCES

Carslaw, K. S., et al., 1995: A thermodynamic model of the system $HCl-HNO_3-H_2SO_4-H_2O$, including solubilities of HBr, from <200 to 328 K. J. Phys. Chem. **99**, 11557-11574.

Fuchs, N. A., and A.G. Sutugin, 1970: Highly Dispersed Aerosols. Ann Arbor, Ann Arbor Science Publishers.

Fukuta, N., and L.A. Walter, 1970: Kinetics of hydrometeor growth from a vapor-spherical model. J. Atmos. Sci. **27**, 1160-1172.

Kulmala, M., and P.E. Wagner, 2001: Mass accommodation and uptake coefficients – a quantitative comparison. J. Aerosol Sci. **32**, 833.

Li, Y. Q., et al.. 2001: Mass and thermal accommodation coefficients of $H_2O(g)$ on liquid water as a function of temperature. J. Phys. Chem. **A105**, 10627.

Pruppacher, H. R., and J.D. Klett, 1997: Microphysics of Clouds and Precipitation. Dordrecht, Kluwer.

Xue, H., 2002: Experimental studies of the evaporation and growth of individual aqueous droplets. Ph.D. Dissertation, Penn State Univ.

HOW EFFICIENT IS CLOUD DROPLET FORMATION OF ORGANIC AEROSOLS?

Ulrike Lohmann[1,*], Keith Broekhuizen[2], Richard Leaitch[3], Nicole Shantz[4] and Jonathan Abbatt[2]

[1]Department of Physics and Atmospheric Science, Dalhousie University, Halifax, N.S., B3H 3J5, Canada.
[2]Department of Chemistry, University of Toronto, Toronto, Ontario, M5S 3H6, Canada.
[3]Meteorological Service of Canada, Toronto, Ontario, M3H 5T4, Canada
[4]York University, Toronto, Ontario, M3J 1P3, Canada

1. INTRODUCTION

Atmospheric aerosols consist of a variety of chemical compositions, including both organic and inorganic compounds. Traditionally only soluble inorganic species such as ammonium sulfate or sea salt were thought to act as cloud condensation nuclei (CCN). With the innovation of new measurement techniques, new insights are gained into which organic molecules are common in the atmosphere and which may activate. Facchini et al. (1999) indicated that a lowering of the surface tension of some surface-active organic aerosols as obtained from fog water samples would enhance the cloud droplet number concentration, cloud albedo and, hence, could lead to a negative forcing of up to -1 W m^{-2}. This is of the same magnitude as the indirect aerosol effect of increasing cloud albedo and cloud lifetime, e.g. Lohmann and Lesins (2002). A more systematic evaluation of chemical effects of aerosols (dissolution of soluble gases and slightly soluble substances, surface tension depression by organic substances and accommodation coefficient changes) by Nenes et al. (2002) confirmed that numerous conditions exist in which these chemical effects are as large as the first indirect aerosol effect. On the other hand, analysis of a biomass burning aerosol, that has a large organic fraction, does not unambiguously distinguish between the activation of the organic material or the smaller inorganic fraction (Leaitch et al. 1996).

Some laboratory studies have recently investigated the ability of different organic compounds to act as CCN. For instance, Broekhuizen et al. (2004) studied the ability of adipic acid, a moderately soluble organic, which has been observed in ambient particulate matter (Narukawa et al. 2002, Wang et al. 2002) to become activated. They found that trace levels of either a soluble species or a surface active species dramatically increase the ability of adipic acid to become activated. Similar conclusions were reached by Raymond and Pandis (2003) who investigated an internal mixture of the inactive organic substance leucine with 1% sodium chloride.

Shantz et al. (2003) took these laboratory and field measurement results a step further and compared the activation of ammonium sulfate with a hypothetical ammonium sulfate that is assumed to have the solubility of adipic acid (AA). They found that the delay in dissolution in the case of AA reduced the cloud droplet number concentration considerably despite the higher maximum supersaturation in this case. The supersaturation builds up to higher values because the AA particles require more water to be dissolved. The cloud droplet number concentration is lower for AA because only particles that have had enough water condensing on them to enable sufficient AA to dissolve will be activated. Activation of AA may, however, still be more efficient than that of mineral dust aerosols, whose effectiveness to act as a CCN was studied by Yin et al. (2002). They concluded that after its first encounter with a cloud, the mineral dust particle acquires a sulfate coating upon cloud evaporation which makes it an effective cloud droplet nuclei in subsequent cloud formations.

In this study, we therefore ask the question, how much more efficient an aerosol comprised of AA coated with ammonium sulfate (AS) is as a CCN as compared to a completely insoluble dust particle of the same size coated with AS. We also investigate the difference in cloud droplet nucleation of AA initiated by a surface-active species such as nonanoic acid as compared to AS. With that, this study identifies specific species that represent the different classes of molecules that are now known to be in tropospheric particles: insoluble (dust), water soluble (ammonium sulfate), surface active (nonanoic acid) and partially soluble (adipic acid). By identifying these species and calculating the full Köhler equation as compared to

*Corresponding author's address: Ulrike Lohmann, Dept. of Physics and Atmospheric Science, Dalhousie Univ., Halifax, N.S. B3H 3J5, Canada; e-mail: Ulrike.Lohmann@Dal.Ca, URL: http://www.atm.dal.ca/~lohmann

the kinetic water vapor uptake in a Lagrangian parcel, we can identify what drives their ability to act as a CCN.

2. MODEL DESCRIPTION

A Lagrangian parcel model, described by Shantz et al. (2003), that solves the kinetic formulation for condensation of water on aerosol particles based on the diffusional growth equation following Pruppacher and Klett (1997) is used in this study to simulate the cloud nucleation process. In the reference simulation (simulation CTL) we assume a unimodal lognormal aerosol size distribution with a mode radius of 75 nm and a standard deviation of 1.5 discretized into 80 size bins in order to compare with the equilibrium Köhler curve results discussed below. The mode radius and the chemical properties of the investigated species are taken from the study by Broekhuizen et al. (2004). Surface tension increases with solute amount in case of ammonium sulfate following Pruppacher and Klett (1997) and decreases for the organics as described by Broekhuizen et al. (2004). For the case with nonanoic acid, only its surface tension is used because nonanoic acid is a surface active species. Cloud droplets are defined as particles with a wet radius larger than 1 μm that have a positive growth rate. The simulations were carried out at 20°C at 1000 hPa in accordance with the laboratory measurements. We start the simulations at 99.9% relative humidity assuming a constant updraft velocity of 1 m s^{-1}. We terminate the simulations when the liquid water content reaches a specific value (here 0.1 g m^{-3}), which is well above the height in cloud where the maximum supersaturation is reached.

3. RESULTS

The equilibrium saturation ratio of a solution droplet s as a function of the particle radius r is given according to the modified Köhler curve that considers an insoluble core in a multi-component particle as follows (Laaksonen et al. 1998, Broekhuizen et al. 2004):

$$s = \frac{2\sigma_{sol} M_w}{r \rho_{sol} R_v T} - \frac{3 M_w \Sigma_i \nu_i x_i m_i}{4\pi (r^3 - r_{ins}^3) \rho_{sol} \Sigma_i x_i M_i} \quad (1)$$

where σ_{sol} is the surface tension of the solution, R_v is the gas constant of water vapor, r_{ins} is the radius of the insoluble core, M_w and M_i are the molecular weights of water and species i, respectively, m_i is its mass, ν_i the number of dissociated ions, and x_i the mole fraction of each. Figure 1 shows the Köhler curves for a pure AS particle as compared to various aerosol mixtures. For clarity, the dust-like particle is assumed to have the same chemical properties as adipic acid but with zero solubility and no surface tension effects. Neither a dust particle with only trace amounts of AS (0.1%) nor an adipic acid aerosol particle with 0.1%AS would easily be activated in the atmosphere because the supersaturation increases with decreasing particle size to more than 1% and 0.6%, respectively, to the left of the cusp. The trace amount of 0.1relative humidities below saturation in the subsequent parcel model simulations (see also Shantz et al. (2003)). On the other hand, if the particle contains 10% AS, then the maximum supersaturation required for activation of this mixed dust/AS or AA/AS particle is reduced considerably. The cusp in the curves containing AA is the point at which all solute has dissolved. A reduction in the critical supersaturation can also be obtained by adding a surface active species, such as nonanoic acid (NA) to adipic acid. If 10% NA is added, then the saturation ratio is still rather large at the smallest size but is considerably reduced as compared to the almost pure AA aerosol.

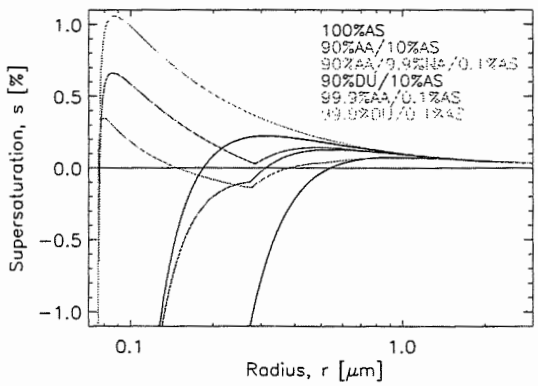

Figure 1: Different Köhler curves for dry particles of 75 nm radius.

The temporal evolution of the cloud droplet number concentration formed on these different aerosols is shown in Figure 2. It ranges from 110 cm^{-3} in the case of the 99.9%DU/0.1%AS aerosol to 921 cm^{-3} in the case of the 100%AS aerosol. By reducing the surface tension, aerosols are activated earlier in the 90%AA/9.9%NA/0.1%AS aerosol (for simplicity, hereafter referred to as 90%AA/10%NA) than in the 90%AA/10%AS aerosol. Thus, water vapor is consumed more readily in the 90%AA/10%NA aerosol decreasing the maximum supersaturation as compared to the 90%AA/10%AS aerosol. This is inconsistent with the equilibrium behavior of the Köhler equation, because the critical supersaturation is higher for the 90% AA/10% NA aerosol in the equilibrium assumption, which illustrates the importance of kinetic effects for surface active species (Figure 1). However, because

of the smaller AS component in the 90%AA/10%NA aerosol, less adipic acid is dissolved, which is a prerequisite for the particles to become activated (see also Shantz et al. (2003)). Hence, the cloud droplet number concentration is smaller in this case and more aerosols with an undissolved core remain interstitially as seen in the larger effective undissolved core radius (Figure 2). Due to the smaller number of cloud droplets in the 90%AA/10%NA aerosol, the supersaturation is more slowly depleted at altitudes above the maximum supersaturation as compared to the 90%AA/10%AS aerosol.

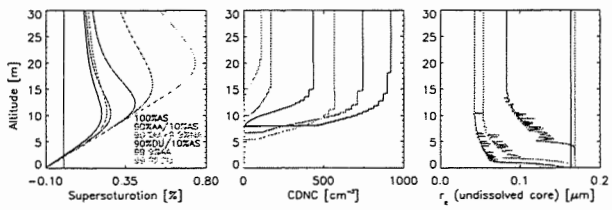

Figure 2: Evolution of supersaturation, cloud droplet number concentration (CDNC) and the effective radius (r_e) of the undissolved core with height for various aerosol particles from simulation CTL.

Note that despite the higher critical supersaturation of the 90%AA/10%NA aerosol as compared to the 90%DU/10%AS aerosol (Figure 1), more aerosols are activated in the former aerosol (Figure 2) because of its smaller critical radius. This is an example where Köhler theory would have led to the opposite conclusions because it neglects kinetic effects (Nenes et al. 2001).

The activated fraction for an aerosol of a given chemical composition mainly depends on the total aerosol number concentration, vertical velocity and aerosol size distribution. In order to investigate the parameter space, we performed sensitivity studies with vertical velocities of 30 cm s^{-1} and 3 m s^{-1}, total aerosol number concentrations of 100 cm^{-3} and 10,000 cm^{-3} and with two bimodal aerosol size distributions. In the first bimodal aerosol a smaller mode with a three times smaller mode radius of 25 nm with 900 particles cm^{-3} and a standard deviation of 1.5 is added. The mode radius and the standard deviation of the larger mode remain the same as in the unimodal case with 100 particles cm^{-3}. We apply the same chemical composition in both modes and discretize the size distribution in 40 size bins each. In the second bimodal aerosol distribution, the smaller mode remains the same as the unimodal simulations with 900 cm^{-3} but here a larger mode having a three times larger mode radius of 2.25 μm with 100 particles cm^{-3} and a standard deviation of 1.5 is added.

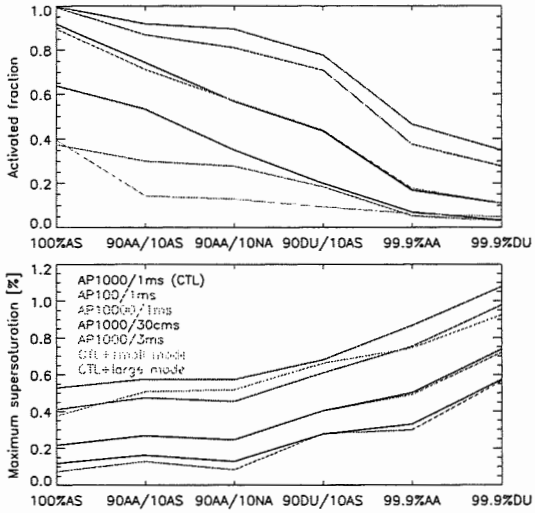

Figure 3: Activated fraction and maximum supersaturation for the different chemical compositions at different updraft velocities (30 cm s^{-1}, 1 m s^{-1} and 3 m s^{-1}), total number of aerosols (100, 1000 and 10,000 aerosol particles cm^{-3}) and size distributions (unimodal and bimodal).

As shown in Figure 3, a higher fraction of aerosols is activated when the vertical velocity is higher or the total number concentration is smaller increasing the maximum supersaturation. In all simulations, the mixed aerosol activates less efficient than a pure AS aerosol and more efficient than an almost pure AA or dust aerosol. Also, the activated fraction is always higher in the 90%AA/10%AS case than in the 90%AA/10%NA case, which in turn has a higher activated fraction than the 90%DU/10%AS case. The biggest differences occur when going from a unimodal to the bimodal distribution with the smaller mode. Here the activated fraction is much lower than in simulation CTL, especially for the mixed aerosol, because the activation is dominated by aerosols from the larger mode. However, because these aerosols are not sufficient to deplete the supersaturation effectively, the maximum supersaturations is much higher. It is comparable to the cases with either a higher updraft velocity or a smaller total number of aerosols.

The activated fraction of the internally mixed 90is always higher than the activated fraction of an externally mixed aerosol estimated by taking 90concentration of the 99.9the number of cloud droplets in this external

mixture is only 2468from all scenarios shown in Figure 3. Likewise only 35externally mixed aerosol consisting of 90pure AS are activated as compared to the internally mixed 90AS aerosol. This illustrates the importance of knowing the mixing state of the aerosol for the cloud droplet nucleation process, which is of paramount importance for estimations of the indirect aerosol effect as outlined by, e.g., Lohmann et al. (2000).

Facchini et al. (1999) estimated that a 20% increase in cloud droplet number concentration due to the surface tension reduction by some organic aerosols could result in a global mean forcing of up to -1 W m^{-2}. Based on our results, one could argue that the opposite effect needs also to be considered, and may be more significant in some cases. A mixture of organics with limited solubility but slightly surface active, here taken to be adipic acid, as commonly observed in the atmosphere (Matta et al. 2003), with 10% AS decreases the number of cloud droplets as compared to a pure AS aerosol by 8% to 64% estimated from all scenarios in Figure 2. On the other hand, consistent with results by Mircea et al. (2002), if adipic acid were to replace mineral dust as the particulate onto which AS condenses, then the number of cloud droplets increases between 18% and 265% for the scenarios in Figure 3.

4. ACKNOWLEDGMENTS

This work was supported by a Canadian Foundation for Climate and Atmospheric Science (CFCAS) collaborative research grant.

5. REFERENCES

Broekhuizen, K., P. P. Kumar, and J. P. D. Abbatt, 2004: Partially soluble organics as cloud condensation nuclei: Role of trace soluble and surface active species, *Geophys. Res. Lett.*, *31*, doi: 10.1029/2003GL018203.

Facchini, M. C., M. Mircea, S. Fuzzi, and R. J. Charlson, 1999: Cloud albedo enhancement by surface-active organic solutes in growing droplets, *Nature*, *401*, 257–259.

Laaksonen, A., P. Korhonen, M. Kulmala, and R. J. Charlson, 1998: Modification of the Köhler equation to include soluble gases and slightly soluble substances, *J. Atmos. Sci.*, *55*, 853–862.

Leaitch, W. R., S.-M. Li, P. S. K. Liu, C. M. Banic, A. M. Macdonald, G. A. Isaac, M. D. Couture, and J. W. Strapp, 1996: Relationships among CCN, aerosol size distribution and ion chemistry from airborne measurements over the Bay of Fundy in August-September, 1995, in *Nucleation and Atmospheric Aerosols*, edited by M. Kulmala, and P. Wagner, pp. 840–843, Elsevier Sci., New York.

Lohmann, U., J. Feichter, J. E. Penner and W. R. Leaitch, 2000: Indirect effect of sulfate and carbonaceous aerosols: A mechanistic treatment, *J. Geophys. Res.* *105*, 12,193–12,206.

Lohmann, U., and G. Lesins, 2002: Stronger constraints on the anthropogenic indirect aerosol effect, *Science*, *298*, 1012–1016.

Matta, E., M. C. Facchini, S. Decessari, M. Mircea, F. Cavalli, S. Fuzzi, J.-P. Putaud, and A. Dell'Acqua, 2003: Mass closure on the chemical species in size-segregated atmospheric aerosol collected in an urban area of the Po Valley, Italy, *Atmos. Chem. Phys.*, *3*, 623–637.

Mircea, M., M. C. Facchini, S. Decesari, S. Fuzzi, and R. J. Charlson, 2002: The influence of the organic aerosol component on CCN supersaturation spectra for different aerosol types, *Tellus*, *54B*, 74–81.

Narukawa, M., K. Kawamura, S.-M. Li, and J. W. Bottenheim, 2002: Dicarboxylic acids in the Arctic aerosols and snowpacks collected during ALERT 2000, *Atmos. Env.*, *36*, 2491–2499.

Nenes, A., S. Ghan, H. Abdul-Razzak, P. Y. Chuang, and J. H. Seinfeld, 2001: Kinetic limitations on cloud droplet formation and impact on cloud albedo, *Tellus*, *53B*, 133–149.

Nenes, A., R. J. Charlson, M. C. Facchini, M. Kulmala, A. Laaksonen, and J. H. Seinfeld, 2002: Can chemical effects on cloud droplet number rival the first indirect effect?, *Geophys. Res. Lett.*, *29*, doi: 10.1029/2002GL015295.

Pruppacher, H. R., and J. D. Klett, 1997: *Microphysics of Clouds and Precipitation*, Kluwer Acad., Norwell, Mass..

Raymond, T. M., and S. N. Pandis, 2003: Formation of cloud droplets by multicomponent organic particles, *J. Geophys. Res.*, *108*, doi: 10.1029/2003JD003503.

Shantz, N. C., W. R. Leaitch, and P. Caffrey, 2003: Effect of organics of low solubility on the growth rate of cloud droplets, *J. Geophys. Res.*, *108*, doi: 10.1029/2002JD002540, 2003.

Wang, G., S. Niu, C. Liu, and L. Wang, 2002: Identification of dicarboxylic acids and aldehyde of PM10 and PM2.5 aerosols in Nanjing, China, *Atmos. Env.*, *36*, 1941–1950.

Yin, Y., S. Wurzler, A. Levin, and T. G. Reisin, 2002: Interactions of mineral dust particles and clouds: Effects on precipitation and cloud optical properties, *J. Geophys. Res.*, *107*, doi: 10.1029/2001JD001544.

AEROSOL RELATED EXTENDED KESSLER-TYPE PARAMETERIZATION FOR USE IN LARGER SCALE MODELS

Frank Müller*, Frank Schimmel, Andreas Chlond

Max Planck Institute for Meteorology, D-20146 Hamburg, Bundesstr. 55, Germany

1. INTRODUCTION

The processes of cloud and precipitation development are strongly linked to the dynamics of clouds. At the same time, the dynamics of clouds is closely associated with energy conversions related to microphysical processes within the cloud. This is an intense mutual interaction between two distinct scales, whereas the scales related to cloud microphysical processes are not resolved by larger scale dynamical models. Therefore, to take into account the effect of these sub-grid scale processes requires their parameterization.

The emphasis of this work is on the investigation of the effect of taking into account both the physicochemical history of cloud drops and the time dependent change of cloud and rain water composition due to chemical processes on cloud microphysics, cloud dynamics, the precipitation development, and the change of gaseous precursor concentrations in contrast to most frequently applied standard Kessler-type parameterizations of cloud microphysics.

2. MODEL DESCRIPTION

2.1 Cloud Dynamics and Budget Equations

Since the focus of this study is to investigate the general effect of different degrees of complexity of parameterized microphysics on the interaction between cloud dynamics and microphysics a relatively simple dynamical model was chosen to predict only the most essential cloud dynamical properties. The applied one-dimensional dynamical cloud model is based on the formulation of Ogura and Takahashi (1971) modified by Park and Droegemeier (1997). The detailed description of the dynamic model equations can be seen in the references. In the following the local changes due to dynamical processes are indicated by the subscript 'dyn' to demonstrate the implementation of the presented scheme into any type of dynamical cloud model.

The following partial differential equations show the local changes for the predicted in-cloud variables and the considered processes. For cloud temperature, T, this gives:

$$\frac{\partial T}{\partial t} = \frac{\partial T}{\partial t}_{dyn} + \frac{L_v}{c_p}\left(\frac{\partial q_c}{\partial t}_{\frac{cond}{evap}} + \frac{\partial q_r}{\partial t}_{evap}\right) . \qquad (1)$$

L_v, c_p, and G_d represent the latent heat of water evaporization, specific heat of water vapor at constant pressure, and the dry adiabatic laps rate. Eq. (1) shows contributions to the local cloud temperature change due to dynamical tendencies and due to phase changes of water. The following Equations (2)-(4) represent the budget equations of water in its considered fractions taking into account sources/sinks due to microphysical processes:

$$\frac{\partial q_v}{\partial t} = \frac{\partial q_v}{\partial t}_{dyn} - \frac{\partial q_c}{\partial t}_{\frac{cond}{evap}} + \frac{\partial q_r}{\partial t}_{evap} , \qquad (2)$$

$$\frac{\partial q_c}{\partial t} = \frac{\partial q_c}{\partial t}_{dyn} + \frac{\partial q_c}{\partial t}_{act} - \frac{\partial q_c}{\partial t}_{deact} - \frac{\partial q_c}{\partial t}_{\frac{cond}{evap}} - \frac{\partial q_r}{\partial t}_{auto} - \frac{\partial q_r}{\partial t}_{accr} , \qquad (3)$$

$$\frac{\partial q_r}{\partial t} = \frac{\partial q_r}{\partial t}_{dyn} - \frac{\partial q_r}{\partial t}_{evap} + \frac{\partial q_r}{\partial t}_{auto} + \frac{\partial q_r}{\partial t}_{accr} - \frac{\partial q_r}{\partial t}_{deact} , \qquad (4)$$

where 'cond/evap', 'act/deact', 'auto/accr' stand for condensation/evaporation, activation of aerosols/deactivation of cloud and rain drops, and auto-conversion of cloud to rain water/accretion of cloud drops by rain drops.

The average cloud drop number concentration is calculated from the change of aerosol number density integrated over the activated particle size range (activation). Deactivation of cloud drops leads to an increase of aerosol number concentration by redistributing the cloud water according to a redistribution number density function. This procedure is applied for any transition of a size resolved aerosol related variable to the corresponding bulk quantities. This can be formally expressed as:

$$\frac{\partial N_c}{\partial t} = \frac{\partial N_c}{\partial t}_{dyn} + \frac{\partial N_{ap}}{\partial t}_{act} - \frac{\partial N_c}{\partial t}_{deact} . \qquad (5)$$

The corresponding changes of the mixing ratio of chemical species in the aerosol particles, $q_{ap,k}$ (m_{ap}) $=G_{ap,k}(m_{ap})/r$, and in the cloud and rain water content, respectively, are given by:

$$\frac{\partial q_{ap,k}(m_{ap})}{\partial t} = \frac{\partial q_{ap,k}(m_{ap})}{\partial t}_{dyn} - \frac{\partial q_{ap,k}(m_{ap})}{\partial t}_{act} + \frac{\partial q_{ap,k}(m_{ap})}{\partial t}_{deact} \qquad (6)$$

*Corresponding author's address: e-mail: frank.mueller@dkrz.de

$$\frac{\partial q_{c,k}}{\partial t} = \frac{\partial q_{c,k}}{\partial t}_{dyn} + \frac{\partial q_{c,k}}{\partial t}_{act} + \frac{\partial q_{c,k}}{\partial t}_{deact} - \frac{\partial q_{c,k}}{\partial t}_{auto} - \frac{\partial q_{c,k}}{\partial t}_{accr} - \frac{\partial q_{c,k}}{\partial t}_{\frac{cond}{evap}} - \frac{\partial q_{c,k}}{\partial t}_{chem} \quad (7)$$

$$\frac{\partial q_{r,k}}{\partial t} = \frac{\partial q_{r,k}}{\partial t}_{dyn} + \frac{\partial q_{c,k}}{\partial t}_{evap} + \frac{\partial q_{c,k}}{\partial t}_{deact} + \frac{\partial q_{c,k}}{\partial t}_{auto} + \frac{\partial q_{c,k}}{\partial t}_{accr} + \frac{\partial q_{r,k}}{\partial t}_{chem} \quad (8)$$

The set of Eqs. (1)-(8) is used to describe the the time-height evolution of the prognostic variables T, q_v, q_c, q_r, N_c, $q_{c,k}$, $q_{r,k}$, and $q_{ap,k}(m_{ap})$. Making use of the fact that m_{ap} is an independent variable the spectral aerosol number density can also be derived from the mixing ratio of chemical species in the aerosols $q_{ap,k}$ (m_{ap}) using the relationship:

$$N_{ap}(m_{ap}) = \rho \frac{\sum_{k=1}^{k_{max}} q_{ap,k}(m_{ap})}{m_{ap}} = \frac{\sum_{k=1}^{k_{max}} G_{ap,k}(m_{ap})}{m_{ap}} \quad (9)$$

where $G_{ap,k}$ is the mass density of the k-th chemical component in the aerosol of mass m_{ap}. The rain drop number concentration is diagnosed assuming a Marshall-Palmer (1948) steady state distribution.

2.2 Microphysical Processes

2.2.1 Aerosol distribution

Cloud properties in terms of cloud and rain water content, cloud drop number concentration, and dissolved chemical species in the cloud and rain water are initialized by activation of size distributed aerosols. The size dependent physico-chemical aerosol properties are chosen to represent marine conditions. They are assumed to be time independent. The consideration of an aerosol spectrum is one of the major extensions of the standard Kessler-type parameterization. It allows the determination of the initial cloud drop number concentration as well as their composition in terms of bulk quantities due to integration of the corresponding aerosol properties over the activated aerosol spectrum. The aerosol number concentration distribution is given by superposition of three log-normal distributions (Jaenicke, 1987).

To account for size dependent changes of the aerosol composition the total aerosol mass distribution is sub-divided into mass distributions of chemical species assuming an internal mixture of chemical aerosol composition. Macroscopic quantities such as mean molar weight, M_{ap}, mean number of ions in solution, n_{ap}, and mass fraction of soluble material, e_{ap}, are mol-weighted sums of the corresponding quantities.

2.2.2 Aerosol activation

Especially small aerosols are able to instantaneously follow changes in environmental temperature or humidity. The corresponding phase flux, and therefore the corresponding heat release, is very small compared to the phase flux, Φ_{act}, resulting from condensation of a droplet population. Hence, equilibrium growth of non-activated particles is not considered throughout this study.

To correctly describe the water budget during activation the corresponding phase flux (difference between critical aerosol water content and current aerosol water content) has to be taken into account. The status of the aerosol at the activation point is deduced from Köhler equilibrium equation, aerosol composition, and the current state of the atmosphere. This can be expressed as:

$$G_{ap,w,eq}(m_{ap}) = N_{ap}(m_{ap})\ m_{w,eq}(m_{ap}, S_{eq}=0.999) \quad (10)$$

$$\frac{\partial G_{ap,w}(S_{eq})}{\partial t}_{act} = \frac{1}{\Delta t}\int_{m_{w,c}}^{\infty} G_{ap,w,eq}(m_{ap})\,dm_{ap} \quad . \quad (11)$$

Eq. (11) states that the local change of the aerosol equilibrium water content is just the integral of size dependent equilibrium water content at RH=99.9% of aerosol particles with sizes larger than the critical activation radius with respect to unit time.

The phase flux, Φ_{act}, together with the equilibrium water content of the aerosols is used to determine the sources/sinks of the budget equations for water due to the activation process:

$$\frac{\partial q_v}{\partial t}_{act} = -\frac{1}{\rho}\Phi_{act} \quad (12)$$

$$\frac{\partial q_c}{\partial t}_{act} = \frac{1}{\rho}\Phi_{act} + \frac{1}{\rho}\frac{\partial G_{ap,w}(S_{eq})}{\partial t}_{act} \quad (13)$$

with ρ being the air density. The corresponding change in aerosol and cloud droplet number concentration, respectively, is given by:

$$\frac{\partial N_{ap}}{\partial t}_{act} = \frac{1}{\Delta t}\int_{m_{w,c}}^{\infty} N_{ap}(m_{ap})\,dm_{ap} \quad (14)$$

$$\frac{\partial N_c}{\partial t}_{act} = -\frac{\partial N_{ap}}{\partial t}_{act} \quad . \quad (15)$$

2.2.2 Rain water production

The production of rain water is ultimately related to the formation of droplets exceeding a certain threshold value r_t due to coagulation processes between cloud droplets (auto-conversion) and cloud and rain drops (accretion). The formulation of the auto-conversion rate applied in this study follows Berry (1968).

$$\frac{\partial q_r}{\partial t}_{auto} = \frac{1.67\ 10^4 q_c^2}{2+\frac{0.0266}{10^6}\frac{N_c}{\gamma_c q_c}} \quad (16)$$

where γ_c is the radius dispersion coefficient of the cloud drop spectrum.

Collection of cloud droplets by larger rain drops with $r>r_t$ (accretion) is parameterized according to Doms and Herbert (1985):

$$\frac{\partial q_r}{\partial t}_{accr} = 0.9346\, q_c\, q_r^{7/8} \quad . \tag{17}$$

The corresponding change of cloud droplet number concentration N_c results from:

$$\frac{\partial N_c}{\partial t}_{\substack{auto\\accr}} = \frac{\left(\frac{\partial q_c}{\partial t}_{auto} + \frac{\partial q_c}{\partial t}_{accr}\right)}{\frac{G_c}{N_c}} \tag{18}$$

where $\overline{m_c}$ G_c/N_c represents the mean cloud drop mass. The transfer of chemical species k from cloud water to rain water due to rain water formation processes is calculated from the relative change of cloud water mass.

$$\frac{\partial q_{r,k}}{\partial t}_{\substack{auto\\accr}} = \frac{q_{c,k}}{q_c}\frac{\partial q_c}{\partial t}_{\substack{auto\\accr}} \tag{19}$$

2.2.3 Deactivation of Cloud and Rain Drops – Aerosol Processing

In the case of deactivation the aerosol number concentration is increased by the average cloud drop number concentration, as well as the aerosol mass density by the mass density of chemical matter inside the cloud and rain water, respectively. Liquid water is partially transferred to water vapor. This is expressed as:

$$\begin{aligned} \frac{\partial G_{ap,k}(m_{ap})}{\partial t} &= f_{deact}(m_{ap})\left(G_{c,k} + G_{r,k}\right) \\ \frac{\partial G_{ap}(m_{ap})}{\partial t} &= \sum_{k=1}^{k_{max}} \frac{\partial G_{ap,k}(m_{ap})}{\partial t} \end{aligned} \tag{20}$$

In Eq. (20) the re-distribution function f_{deact} describes the spectral partitioning of the bulk cloud and rain water related chemical species onto the aerosol distribution. A priori this function is unknown since all spectral information got lost during the transition from the aerosol phase to the bulk liquid water phase. As a first guess the aerosol distribution function is set to $f_{deact}=f_{ap}$. The new aerosol number concentration N_{ap} (m_{ap}) is then determined according to:

$$\frac{\partial N_{ap}(m_{ap})}{\partial t} = \frac{1}{m_{ap}}\frac{\partial G_{ap}(m_{ap})}{\partial t} \quad . \tag{21}$$

The changes of the other cloud and rain water related quantities follow from:

$$\begin{aligned} \frac{\partial q_c}{\partial t}_{deact} &= \frac{1}{\Delta t} q_{c,deact} & \frac{\partial q_r}{\partial t}_{deact} &= \frac{1}{\Delta t} q_{r,deact} \\ \frac{\partial N_c}{\partial t}_{deact} &= \frac{1}{\Delta t} N_{c,deact} & \frac{\partial N_r}{\partial t}_{deact} &= \frac{1}{\Delta t} N_{r,deact} \\ \frac{\partial q_{c,k}}{\partial t}_{deact} &= \frac{1}{\Delta t} q_{c,k,deact} & \frac{\partial q_{r,k}}{\partial t}_{deact} &= \frac{1}{\Delta t} q_{r,k,deact} \end{aligned} \quad . \tag{22}$$

Due to deactivation of cloud and rain drops also water vapor is liberated and balanced in the water vapor equation by setting:

$$\frac{\partial q_v}{\partial t}_{deact} = \frac{1}{\rho \Delta t}\left(G_c + G_r - \left(N_c + N_r\right) m_{w,eq}(S_{eq})\right) \quad . \tag{23}$$

Eq. (23) states that in accord with the activation process only the liquid water mass down to the equilibrium water mass, $m_{w,eq}$, is considered for the water vapor budget in order to avoid detailed treatment of equilibrium growth of aerosols.

2.2.3 Condensation/Evaporation

An important improvement of standard Kessler-type parameterization is the treatment of condensation/ evaporation based on the new available variables cloud drop number density N_c, and mass of chemical matter inside cloud and rain drops $m_{c,ap}$ and $m_{r,ap}$, respectively. The drop mass growth velocity can be written as:

$$\frac{dm_i}{dt} = \frac{4\pi r_i S_{vw} - 1 - \frac{A}{r_i} - B\frac{m_{i,ap}}{m_i - m_{i,ap}}}{\left[\frac{R_v T}{D_v e_{sat}(T)} + \frac{L_v}{k_a T \bar{f}_h}\left(\frac{L_v}{R_v T} - 1\right)\right]} \tag{24}$$

$$A = \frac{2\sigma_i}{R_v T \rho_w} \qquad B = \frac{\nu_i \Phi_i \epsilon_i M_w}{M_{i,ap}} \quad . \tag{25}$$

In Eqs. (24) and (25) the index 'i' denotes cloud 'c' and rain 'r' water related quantities, respectively. The other variables have their standard meaning according i.e. Pruppacher and Klett (1997).

2.3 Chemical Processes

In this study a compact chemical reaction mechanism (50 species and about 130 reactions) was selected according to Lurmann et al., 1987). The aqueous phase chemical reaction system follows essentially the work of Lin and Chameides (1991). Flux formulation according to Schwartz (1986) is employed to calculate the exchange of volatile species.

3. RESULTS

Figures 1-4 exemplary document the results of the application of the new parameterization scheme in a 1D-simulation using maritime aerosol properties. The prediction of the supersaturation instead of applying the saturation adjustment method results in reduced cloud and rain water contents, respectively. Hence, the temperature deviations are smaller for the new parameterization scheme (not shown here).

The evolution of cloud drops from aerosol particles can be followed by the activation of aerosols to build sulfate containing cloud droplets (Figure 1) and the

corresponding loss in sulfate aerosol mass in the cloud interstitial aerosol (Figure 2). Figure 3 shows the resulting cloud drop number concentration as time-height cross section. The smallest cloud drops and cloud droplet sizes can be found at the edges of the cloud due to lateral entrainment of dry air and due to subsequent evaporation processes. The overall cloud drop size varies between 2µm and 20µm (not shown here). A considerable amount of aerosol particles is scavenged by nucleation and redistributed within the cloud. After cloud evaporation the residual particles are liberated and re-suspended.

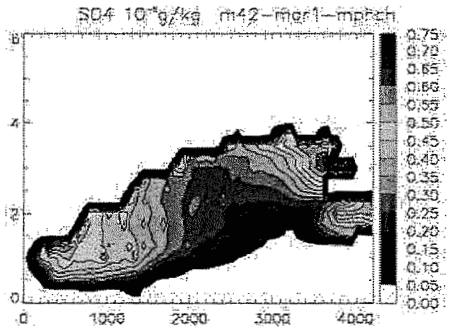

Figure 1:Time-height evolution of the sulfate aerosol content in the cloud water.

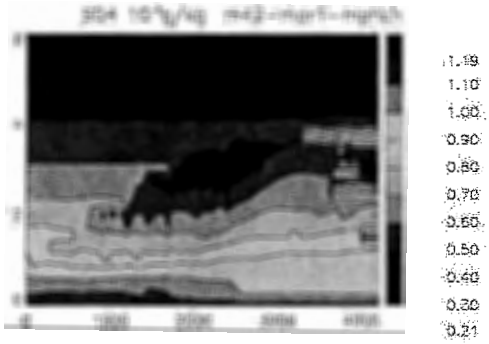

Figure 2:Time-height evolution of the sulfate aerosol content in the air.

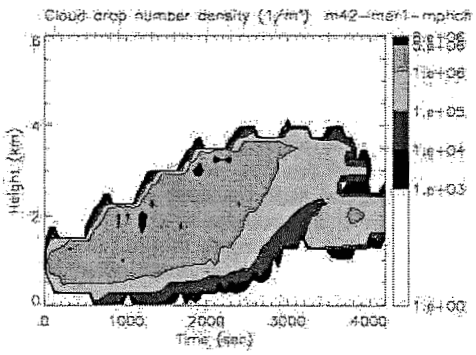

Figure 3:Time-height evolution of the cloud drop number concentration.

Additionally, oxidation processes in the cloud and rain water demand gaseous precursors such as H_2O_2. Consequently, a reduction of the corresponding gas phase species can be seen in Figure 4. The rain-out of gaseous species (in this case H2O2) can also be observed in Figure 4.

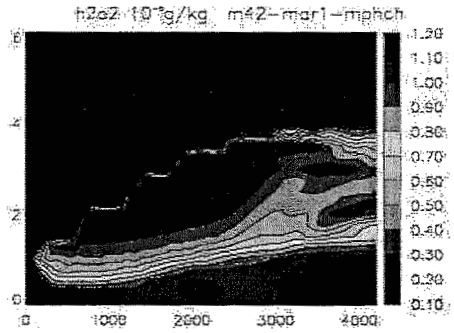

Figure 4:Time-height evolution of the gas phase H_2O_2 concentration.

4. REFERENCES

Berry, E.X.,1968: Modification of the warm rain process, Proc. First Natl. Conf. On Weather Modification, Albany, N.Y., 81-88

Doms, G., Herbert, F., 1985: Fluid und Mikrodynamik in numerischen Modellen konvektiver Wolken, Berichte des Inst. f. Meteorologie und Geophysik der Univ. Frankfurt/Main, Nr. 62

Lin, X, Chameides, W.L., 1991: Model studies of the impact of chemical inhomogeneity on SO_2 oxidation, J. Atmos. Chem. 13, 109-129

Lurmann, F.W., Carter, W.P., Coyner, L.A., 1987: A surrogate species chemical reaction mechanism for urban-scale air quality simulation models I: Adaption of the mechanism, Techn. Rep., 600/3-87/014A, EPA

Ogura, Y., Takahashi, T., 1971: Numerical simulation of the life cycle of a thunderstorm cell, Monthly Weather Rev., 99, 895-911

Park, S.K., Droegemeier, K.K., 1997: Validity of the tangent linear approximation in a moist convective cloud model, Monthly Weather Rev., 125, 3302-3340

Pruppacher, H.R., Klett, F., 1997: Microphysics of Clouds and Precipitation, Kluwer Academic Publishers, Dordrecht, 954pp.

Schwartz, S.E.,1986: Mass-transport considerations pertinent to aqueous phase reactions of gases in liquid water clouds, in W. Jaeschke (ed.), Chemistry of Multiphase Atmospheric Systems, NATO ASI Series, Series G: Ecological Science, Vol. 6, 415-472

COMPARATIVE STUDY OF THE UPTAKE OF NITRIC ACID TO AEROSOL AND CLOUD PARTICLES IN THE MID AND UPPER TROPOSPHERE

Jason Shepherd, Hugh Coe, Gordon McFiggans

Department of Physics, University of Manchester Institute of Science and Technology (UMIST), PO Box 88, Manchester, M60 1QD, United Kingdom.

1. INTRODUCTION

In the upper troposphere nitric acid constitutes the major component of NO_Y and its main sink from the region is thought to be provided by its uptake to cirrus cloud particles. Although the loss of nitric acid to pre-cloud aerosol particles is believed to be inefficient, the ubiquitous nature of aerosol and their long atmospheric residency times may mean that overall they provide a comparable sink to that of cloud particles. A water-ice cloud model and pre-cloud aerosol model have been developed in order to assess the relative and combined nitric acid uptake potential of cirrus clouds and particles.

2. METHODS

A semi-explicit mixed phase microphysical and chemical box model of cirrus cloud has been developed to model the repartitioning of gaseous nitric acid in the mid and upper troposphere at temperatures down to 230K. The uptake of gaseous nitric acid to the liquid and ice phases of cirrus cloud is in found to be low due to the efficient uptake but short freezing times of liquid drops and the longer exposure but lower uptake rate to ice particles. Although individually aerosol particles provide a much smaller surface area than cirrus cloud particles, they are ubiquitous and have longer lifetimes and therefore the relative losses of nitric acid may be comparable. In light of this, an out of cloud aerosol model has also been developed to allow a comparison of the nitric acid repartitioning in and out of cloud. It is hoped that this will lead to a greater understanding of the relative significance of each process and so focus future investigation. An explicit single particle aqueous aerosol model is used with a mono-dispersed aerosol distribution to provide an approximate prediction of the repartitioning of nitric acid to a pre-cloud aerosol distribution. The ZSR relationship is used in order to find the composition of an initial particle as a function of its diameter and mass ratio of aqueous phase components (H^+, NH_4^+, SO_4^{2-}, HSO_4^-, and NO_3^-). The Fuchs-Sutugin gas-to-particle flux relationship detailed by Kerminen and Wexler (1997) is employed to model the transport of nitric acid, ammonia and sulphuric acid from the gas phase to the aerosol surface where it is assumed to instantly diffuse into the bulk solution. An analytical iteration method is used to solve chemical equilibrium equations (activity coefficient equations, mass and charge balance equations) to give a unique solution to the gas-particle system, which provides an estimate of the gas phase partial pressures over the surface of the aerosol solution. The flux of each species, described by the Fuchs-Sutugin relationship, is proportional to the gradient between its ambient partial pressure and this surface partial pressure. A modified forward difference method allows the repartitioning and the growth of the aerosol to be modelled with time. The cloud model employs an explicit ice nucleation routine based on the empirical relationships of Meyers, Demott et al 1992) for deposition/condensation and contact/immersion nucleation. Liquid drops are nucleated implicitly on to a mono-dispersed CCN distribution during supersaturated conditions, which can then be homogeneously nucleated, controlled by a temperature dependent parameterisation. Depositional ice particle growth is explicitly considered (Miller and Young 1979) as are riming and aggregation to create a particle size distribution. Repartitioning of gaseous nitric acid to the aqueous phase is modelled using the flux equation as that of the aerosol model where it may become locked into the ice phase during ice nucleation. The adsorption of gaseous nitric acid to the surface of the ice particles is modelled in one of two ways. The first employs Langmuir's isotherm relationships (Tabazadeh and Turco 1993) to calculate the nitric acid saturation pressure over the surfaces. A diffusion limited scheme not dissimilar to that of the depositional ice growth
routine uses this information to model the kinetic uptake of nitric acid to the ice surface. The second method assumes a liquid layer covering the surface of each ice particle into which the Fuchs-Sutugin gas-to particle transport relationship, as used in the aerosol model, controls the flux of nitric acid, ammonia and sulphuric acid

3. CONCLUSIONS

The amount of gaseous nitric acid repartitioned to the out of cloud aerosol is found to be strongly dependent on the ammonia available to neutralise the sulphuric acid, which tends to drive out the nitric acid. However, the uptake of sulphuric acid tends to drive the growth of the aerosol increasing the water associated with and so diluting the aerosol. This can favour the uptake of nitric acid. Therefore, reducing the sulphuric acid gaseous concentration in an attempt to allow more nitric acid to be repartitioned can have the opposite effect. Nevertheless the presence of ammonia is essential to promote nitric acid uptake to aerosol stressing the importance of good ammonia measurements in this region of the atmosphere if accurate predictions of nitric acid take up are to be made. In general it would appear that over periods of several days the uptake of nitric acid to aerosol at best provides a weak sink under normal upper-tropospheric conditions.
The uptake of nitric acid to the liquid drops that activate initially during the cirrus cloud formation is necessarily short lived at low temperatures common to the upper troposphere. The onset of homogeneous and heterogeneous ice nucleation is followed by depositional growth, which reduces the saturation vapour pressure over liquid. As the ice continues to grow the droplets evaporate releasing nitric acid, which means that although relatively efficient, uptake to the aqueous phase does not provide substantial repartitioning of nitric acid during the formation of cirrus cloud. The longer exposure provided by the subsequent ice-phase particles means that although less efficient, the uptake to the ice phase can be the primary route of repartitioning of nitric acid to cirrus cloud if deposited nitric acid is permitted to become buried in the bulk ice during depositional ice growth. Defining a characteristic timescale of the loss of nitric acid as the inverse of its loss rate, for given conditions, the minimum frequency of cirrus formation is derived for which the nitric acid loss during incloud conditions is comparable to that out-of-cloud. Further, by modelling particle precipitation a prediction of the vertical redistribution of repartitioned nitric acid is given.

4. REFERENCES

Kerminen, V. M., Wexler, A.S. et al. (1997). Growth of freshly nucleated particles in the troposphere: Roles of NH3, H2SO4, HNO3, and HCl. *J. Geophys. Res*, 102(D3): 3715-3724.

Meyers, M. P., Demott, P. J. et al. (1992). New Primary Ice-Nucleation Parameterisations in an Explicit
Cloud Model. *J. Appl. Meteorol.*, 31(7): 708-721.

Miller, T. L. and Young, K. C. (1979). A numerical simulation of ice crystal growth from the vapour phase. *J. Atmos. Sci.* 36: 458-469.

Tabazadeh, A. and Turco, R. P. (1993). A Model for Heterogeneous Chemical Processes on the Surfaces of Ice and Nitric-Acid Trihydrate Particles. *J. Geophys. Res.*, 98(D7): 12727-12740.

DROP-SCALE NUMERICAL MODELING OF CHEMICAL PARTITIONING DURING CLOUD HYDROMETEOR FREEZING

A.L. Stuart[1] and M.Z. Jacobsonr[2]

[1]Department of Atmospheric Sciences, Texas A&M University, College Station, TX, 77843, USA
[2]Department of Civil and Environmental Engineering, Stanford University, Stanford, CA, 94305, USA

1. INTRODUCTION

Thunderstorms can significantly impact chemical distributions in the troposphere by 1) redistribution of air and hydrometeors containing trace chemicals and 2) providing a multi-phase environment for chemical phase changes and reactions. Interactions between ice-containing hydrometeors and chemicals are not well understood. Laboratory and field measurements of chemical partitioning during drop freezing provide greatly varying estimates of the retention efficiency of volatile solutes (e.g., Lamb and Blumenstein, 1987; Iribarne and Pyshnov, 1990, Snider and Huang, 1998; Voisin and Legrand, 2000). Our recent work using a theory based time scales analysis to calculate the retention efficiency provided a basic understanding of the dependence of partitioning on chemical properties and freezing conditions (Stuart and Jacobson, 2003, 2004). In this work, we develop a drop-scale time-dependent numerical model of drop freezing and chemical transfer to investigate the effects on chemical partitioning of dynamical interactions between involved processes.

2. MODEL DESCRIPTION

Our one-dimensional (radial) model represents the freezing of a spherical solute-containing liquid hydrometeor with a riming substrate or ice nuclei at its center. Processes represented by the model include radial inter- and intra-phase heat and mass transfer, freezing kinetics, latent heat release during freezing, and solute segregation and trapping at the freezing interface.

2.1 Process Representation

The model is initiated at freezing nucleation. As time progresses, the drop freezes and solute is expelled at rates governed by both the grid-resolved partial differential equations for radial heat and mass transfer as well as the sub-grid scale differential equations for processes occurring near the ice water interface. We represent the multi-phase (dendritic) character of freezing in the super-cooled drop using average water and ice amounts (fractions) in each radial shell volume. Properties and prognostic variables (temperatures and solute concentrations) are also volume average values for each phase. This 'mushy zone' representation (after Tien and Geiger, 1967) of the non-planar ice-water interface assumes phase changes (freezing) provide a volume source of latent heat. The density of water and ice is assumed to be constant and equivalent in both phases.

Processes resolved on the model grid include radial intra- and inter-phase heat and mass transfer. Equations for diffusive transfer for each phase were derived using energy and mass balances over a shell. Inter-phase transfer coefficients were based on two-film theory (e.g. Sherwood et al., 1975) and account for mass transfer resistances in both phases. Boundary conditions at the grid's outer boundary (the hydrometeor surface) account for flux due to conduction, evaporation, sublimation, and condensation. Flux enhancement due to fluid flow around the hydrometeor is represented with a flow-dependent ventilation coefficient.

Processes represented at the sub-grid scale include phase change, latent heat transfer, inter-phase heat transfer, and solute mass segregation during phase change. Rates of freezing (and melting) are represented by a kinetic equation for the interfacial growth velocity, which is based on theory and experimental data on growth rates of ice in super-cooled water (Bolling and Tiller, 1961; Pruppacher and Klett, 1997). We estimate the interfacial surface area as the ratio of the shell surface area to its volume. To simulate dendrite-like growth, ice initiation in any cell can only occur if an adjacent shell contains ice. To represent latent heat transfer, we perform an enthalpy balance over the grid shell. Energy distribution to each phase is weighted by the volume fraction of each phase in a shell. For phase initiation in a given shell, we assume the temperature in both phases remains equal. Inter-phase heat flux is represented as conductive transfer for which the bulk heat transfer coefficient is a function of the two-film inter-phase transfer coefficient and the dendrite tip radius. We assume free dendritic crystal growth and calculate the dendrite tip radius as a function of the dendrite Peclet number and the interfacial growth velocity (after Caroli and Muller-Krumbhaar, 1995, and Libbrecht and Tanusheva, 1999). Solute mass segregation during freezing is calculated to maintain a mass balance, assuming equilibrium partitioning at the ice-water

Corresponding author's address: Dr. Amy L. Stuart, Dept. of Atmospheric Sciences, Texas A&M University, 3150 TAMU, College Station, TX 77843-3150; E-Mail: amystuart@tamu.edu.

interface. During melting, all mass in the melted ice is assumed to be transferred to the water phase. Trapping of concentrated solute between dendrite branches, leading to bulk non-equilibrium partitioning to ice, is represented by allowing grid shells that freeze completely in a given time step to retain all solute originally in that shell.

2.2 Flow of calculations and numerics

The flow diagram for model calculations is provided in Figure 1. The model is initiated by specifying ambient conditions (constant temperature and pressure), hydrometeor conditions (initial drop and ice substrate sizes, temperatures, and speed in air), initial solute concentrations in all phases, the outer-model time-step (used for grid-resolved processes), and the number of radial grid shells. The grid is determined and initialized with these inputs, assuming the drop water is spread evenly around the ice substrate. Following initialization, the model time cycle of processes begins. For each outer-model time-step, sub-grid processes of phase change with latent heat transfer, inter-phase heat transfer, and solute segregation and trapping are first calculated. Each process is calculated separately in a serial manner (i.e. processes are time-split). Phase change with latent heat transfer and inter-phase heat transfer calculations use an adaptive time-step to ensure physically-consistent results (e.g., temperatures at the interface that do no significantly overshoot the equilibrium freezing temperature). The grid-resolved processes of radial heat and mass transfer are then calculated for the outer-model time-step. A finite volume 2nd-order central difference discretization is used for calculation of radial fluxes. Progression in time is discretized with a Forward Euler formulation. After each outer-model time-step, values of system enthalpy and mass (of water and solute) are calculated to track conservation properties of the simulation. The model is terminated when the hydrometeor is completely frozen.

3. MODEL DEMONSTRATION

To test and demonstrate the model, we have applied it to simulate several cases of freezing of drops of varied sizes and ambient conditions. We will detail results for one demonstration case here and then briefly discuss model performance for all cases.

3.1 Case Description

Our demonstration case simulated the freezing of a hydrometeor falling at its terminal fall speed, formed due to the impaction of a supercooled drop (1000 μm in radius) with a ice substrate (100 μm in radius). The air and initial supercooled drop temperatures were −10 C. The initial ice substrate temperature was −5 C. The ambient pressure was 300 mbar. For demonstration, we used a hypothetical chemical

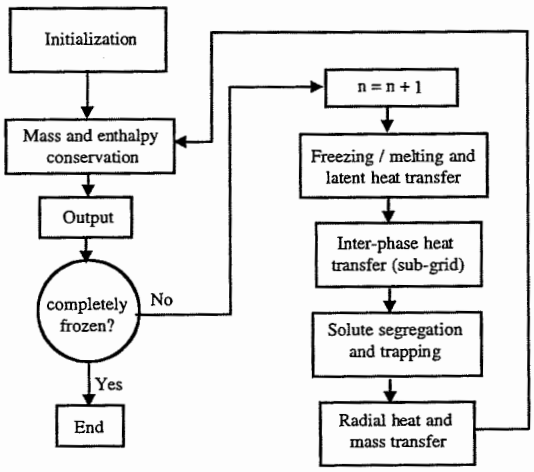

Figure 1. Flow diagram of model calculations, where n is the outer-model time-step.

solute with the following properties: dimensionless (concentration) Henry's constant of approximately 30, ice-water partition coefficient of 0, and diffusivities in air, water, and ice of 0.1 cm^2/s, $1x10^{-5}$ cm^2/s, and $1x10^{-10}$ cm^2/s, respectively. Solute concentrations in the gas phase and supercooled drop where initially at equilibrium, with values of $7x10^{-7}$ g/cm^3 and $2x10^{-5}$ g/cm^3, respectively. Initial solute concentration in the ice substrate was 0. The number of radial grid shells was specified as 10 and the outer-model time-step was $1x10^{-4}$ s.

3.2 Case Results

We will first describe the freezing progression and temperature changes in the hydrometeor. The hydrometeor is initially liquid throughout most of its radius, with a solid core (the original ice substrate). Ice quickly propagates out from the ice core, reaching the hydrometeor surface by $9x10^{-4}$ s. Ice fraction values throughout the mixed-phase region remain below 0.1 during this time. Water and ice temperatures in the mixed-phase region also increase from the inside of the hydrometeor outward (due to release of latent heat of freezing). Temperatures reach an approximately uniform value slightly below 273 K by $2x10^{-3}$ s. Once the mixed-phase region temperatures are approximately equivalent, the temperatures and ice fractions increase more slowly and uniformly. By approximately $4x10^{-3}$ s, we see the ice fraction near the air boundary surpass that in the hydrometeor interior. The temperature in the solid core (the original ice substrate) increases slowly (due to radial heat transfer from the mixed-phase zone), but does not reach the temperature of that zone until about $3x10^{-2}$ s. Far from the air boundary, the temperatures reach the equilibrium freezing temperature of water at approximately 0.1 s.

Temperatures near the air boundary are depressed (due to heat loss to air that is 263 K). By 7 seconds, an ice-shell (ice fraction of 1.0) has formed at the hydrometeor surface. Freezing propagates inward until the entire hydrometeor is frozen by 24.6 s. Temperatures (of ice) also decrease from the outside inward after the freezing front.

This progression of freezing and temperature change can be compared with experimental and theoretical studies of drop freezing (e.g. see Macklin and Payne, 1967, 1968; Griggs and Choularton, 1983; Pruppacher and Klett, 1997). These studies suggest that nucleated drops freeze in approximately two stages. The first stage is termed the adiabatic stage. During this stage, ice propagates out from the nucleation site and the drop heats up to the equilibrium freezing temperature of water, with relatively little heat loss to the drop environment. (This is termed the adiabatic stage.) This stage is very quick, orders of magnitude faster than the complete freezing of the drop. The second stage is termed the diabatic stage. During this stage the freezing occurs more slowly, limited by the rate of heat loss to the ice substrate and the surrounding air. This picture of freezing progression is qualitatively consistent with our results.

For quantitative comparison, we estimate the adiabatic freezing stage during our simulation to be within an order of magnitude of 0.01 s. (Bounded by the time it takes for ice to reach the drop surface, approximately 0.001 s, and the time it takes the mixed-phase zone to heat to approximately the equilibrium freezing temperature, 0.1 s). During this time, approximately 13% of the drop mass froze in our simulation. This is in excellent agreement to the value, $c_w \Delta T/L_m$ (or 13%), derived from drop freezing theory (Pruppacher and Klett, 1997). The complete drop freezing time from our simulation, 24.6 s, can also be compared to the bulk theoretical expression developed for drops falling freely in air (Pruppacher and Klett, 1997). This expression yields a value of 19.4 s for our simulated conditions, which is about 21% lower than our simulated value.

The progression of solute redistribution during freezing was also simulated. Solute concentrations in liquid water were initially 2.0×10^{-5} g/cm^3 throughout the hydrometeor and 0 in the ice core. As ice propagates outward, solute concentrations in water away from the air boundary increase slightly to 2.3×10^{-5} g/cm^3 at 1 s, due to the exclusion of solute from the ice phase during freezing. Concentrations near the air boundary decrease to 1.9×10^{-5} g/cm^3 at 1 s, due to mass transfer to air. After the outer shell of the hydrometeor freezes, and freezing propagates inward, concentrations in water near the inner boundary of the shell increase more dramatically to about 1×10^{-4} g/cm^3 due to exclusion from the ice phase and lack of a sink to air. In ice, average concentrations within and near the original ice core jump to 7.0×10^{-9} g/cm^3 directly after freezing initiation, due to freeze trapping. As ice propagates through the hydrometeor, solute concentrations in ice increase to non-zero values, due to radial mass transfer. When the outer shell of the hydrometeor freezes, the concentration in ice near the air boundary jumps to 9.4×10^{-8} g/cm^3, also due to freeze trapping. As freezing progresses inward, higher concentrations are trapped in ice due to higher concentrations in the liquid. The final solute concentration profile indicates increasing solute concentrations inward, with the area near the hydrometeor surface (air boundary) having very low concentrations (approximately 1×10^{-7} g/cm^3) and the area frozen last (near the original ice core) having a concentration slightly higher that that originally in water (2.3×10^{-5} g/cm^3). The total retention efficiency in the hydrometeor (the ratio of the mass of solute in the hydrometeor to that originally in the drop) decreases precipitously from 1.0 to 0.96 in the first 0.1 s of freezing. It continues to decrease more slowly until an ice shell forms at the surface (at about 7 s). After ice shell formation, there is negligible loss and the retention fraction remains constant at 0.72. These results are qualitatively physical and consistent with the body of literature on crystallization separation (e.g. Zief and Wilcox, 1967). However, they cannot be quantitatively compared to experimental results due to our use of a hypothetical solute for demonstration.

3.3 Model Performance

For all cases simulated, freezing and solute redistribution occurred in a similar manner. Quantitative comparison of simulated freezing times to theoretical bulk estimates of freezing times yielded values in reasonable agreement (differences within approximately 20%). Mass and heat conservation was excellent for all case simulations, with exact solute and water mass balance and a very small (insignificant) heat balance error.

4. CONCLUSIONS

We have developed and demonstrated a one-dimensional radial model of chemical partitioning during hydrometeor freezing. Model results are physically consistent with freezing, heat, and mass transfer theory. The model is exactly mass conserving and also shows good energy conservation. Insights provided by results from model demonstration cases include that the location of nucleation within the drop may not be very important to overall drop freezing. Due to fast dendritic growth, the freezing front quickly moves to the drop surface and overall freezing progresses inward from the surface. Trapping due to ice shell formation at the hydrometeor surface may also play a large role in non-equilibrium bulk solute partitioning to the ice phase hydrometeor. Further development of the model will include 1) improvement of the dendrite initiation representation to account for the distance of tip travel, 2) improvement of the solute trapping representation through use of an effective ice-

liquid distribution coefficient dependent on the freezing rate and/or dendrite characteristics, 3) detailed testing of the freezing and chemical mass transfer modules, and 4) addition of a chemical reaction solver. We plan to apply the model to investigate the dynamics of chemical partitioning and reaction during freezing and riming in clouds. Results from these investigations will inform modeling and understanding of chemical scavenging and redistribution by clouds.

5. REFERENCES

Bolling, G. F. and W. A. Tiller, 1961: Growth from the Melt. III. Dendritic Growth. *Journal of Applied Physics*, **32,** 2587-2605.

Caroli, B. and H. Muller-Krumbhaar, 1995: Recent advances in the theory of free dendritic growth. *ISIJ International*, **35,** 1541-1550.

Griggs, D. J. and T. W. Choularton, 1983: Freezing modes of riming droplets with application to ice splinter production. *Quarterly Journal of the Royal Meteorological Society*, **109,** 243-253.

Iribarne, J. V. and T. Pyshnov, 1990: The effect of freezing on the composition of supercooled droplets - I. Retention of HCl, HNO_3, NH_3, and H_2O_2. *Atmospheric Environment*, **24A,** 383-387.

Lamb, D. and R. Blumenstein, 1987: Measurement of the entrapment of sulfur dioxide by rime ice. *Atmospheric Environment*, **21,** 1765-1772.

Libbrecht, K. G. and V. M. Tanusheva, 1999: Cloud chambers and crystal growth: effects of electrically enhanced diffusion on dendrite formation from neutral molecules. *Physical Review E*, **59,** 3253-3261.

Macklin, W. C. and G. S. Payne, 1967: A theoretical study of the ice accretion process. *Quarterly Journal of the Royal Meteorological Society*, **93,** 195-213.

Macklin, W. C. and G. S. Payne, 1968: Some aspects of the accretion process. *Quarterly Journal of the Royal Meteorological Society*, **94,** 167-175.

Pruppacher, H. R. and J. D. Klett, 1997: *Microphysics of Clouds and Precipitation*. 2nd ed. Vol. 18, Kluwer Academic Publishers, 954 pp.

Sherwood, T. K., R. L. Pigford, and C. R. Wilke, 1975: *Mass Transfer*. McGraw-Hill Book Company.

Snider, J. R. and J. Huang, 1998: Factors influencing the retention of hydrogen peroxide and molecular oxygen in rime ice. *Journal of Geophysical Research*, **103,** 1405-1415.

Stuart, A. L. and M. Z. Jacobson, 2003: A timescale investigation of volatile chemical retention during hydrometeor freezing: Nonrime freezing and dry growth riming without spreading. *Journal of Geophysical Research*, **108,** 4178, doi:10.1029/2001JD001408.

Stuart, A. L. and M. Z. Jacobson, 2004: Chemical retention during dry growth riming. Accepted for publication in *Journal of Geophysical Research*.

Tien, R. H. and G. E. Geiger, 1967: A heat-transfer analysis of the solidification of a binary eutectic system. *Journal of Heat Transfer*, **89,** 230-234.

Voisin, D. and M. Legrand, 2000: Scavenging of acidic gases (HCOOH, CH_3COOH, HNO_3, HCl, and SO_2) and ammonia in mixed liquid-solid water clouds at the Puy de Dome mountain (France). *Journal of Geophysical Research*, **105,** 6817-6835.

Zief, M. and W. R. Wilcox, 1967: *Fractional Solidification*. Vol. 1, Marcel Dekker, Inc, 714 pp.

CHEMICAL EFFECTS ON DROP SPECTRAL BROADENING

Huiwen Xue and Graham Feingold

NOAA/ETL, 325 Broadway, Boulder, CO 80305, USA

1. INTRODUCTION

For decades the cloud physics community has grappled with the disparity between observed droplet spectra, that tend to be fairly broad, and modeled droplet spectra that are significantly narrower. Much effort has been made to understand the broadening effect because spectral broadening plays an important role in the initiation of precipitation in warm clouds. Several mechanisms have been proposed in the past to explain spectral broadening, including the existence of giant or ultragiant cloud condensation nuclei (CCN) (Johnson 1982), turbulent effects (Shaw et al. 1998), entrainment and mixing of air parcels (Baker et al. 1980), chemical processing of droplets in preexisting clouds (Zhang et al. 1999), longwave cooling of cloud drops (Harrington et al. 2000), and the growth retardation of some droplets due to film-forming organic compounds (Feingold and Chuang 2002).

It has been shown that broader droplet spectra are associated with increases in cloud droplet number (N_d) (e.g., Gerber 1996) because for equivalent conditions, growth rates of drops are smaller under higher N_d so that spectral narrowing due to condensation growth is minimized. Investigations of the climate cooling effect due to increased N_d as a result of increases in aerosol number concentration (N_a) (the first aerosol indirect effect or Twomey effect, Twomey 1974) have shown that broader spectra may change the indirect climate forcing by aerosol. Analysis by Liu and Daum (2002) indicates that the broader spectra tend to moderate the cooling effect caused by increased N_d.

This study explores the effects of both HNO_3 and aqueous sulfate production on the evolution of cloud droplet spectra and optical properties in boundary layer clouds. Water-soluble trace gases such as HNO_3 can provide solute to water droplets and lower the equilibrium water vapor pressure at the droplet surface, leading to enhanced growth of the droplet (Charlson et al. 2001, Laaksonen et al. 1998, Kulmala et al. 1997). Previous studies using adiabatic parcel models have shown that at low updrafts, N_d can be increased when HNO_3 is present in the atmosphere (Kulmala et al. 1993, Nenes et al. 2002, Xue and Feingold 2004). This effect tends to increase cloud albedo and enhance the indirect climate forcing by aerosol. Aqueous sulfate chemistry produces sulfate in solution, which modifies droplet growth and cloud spectra in the next cloud cycle (Feingold et al. 1998, Zhang et al. 1999).

Corresponding author's address: Huiwen Xue, NOAA \Environmental Technology Laboratory, Boulder, CO 80305 USA; Email: huiwen.xue@noaa.gov

The changes in droplet growth resulting from these chemical effects have potential implications for cloud microphysics and the aerosol indirect effect. These are discussed in this paper.

2. MODEL

An adiabatic parcel model with coupled microphysics and aqueous sulfate chemistry is used to simulate cloud formation at constant updrafts. The aerosol particles used as model input are assumed to be ammonium sulfate with log-normal size distributions over the radius range 0.1 ~ 1.1 μm. The aerosol/droplet population is divided into 20 Lagrangian mass classes. Water activity is calculated from a thermodynamic model developed by Clegg et al. (1998) for the H^+-NH^+-SO_4^{2-}-NO_3^--H_2O system at tropospheric temperatures. Droplet condensation growth is calculated explicitly using a kinetic droplet growth model (Pruppacher and Klett, 1997, p. 511). No collision-coalescence is simulated. In the aqueous chemistry module, the oxidation of SO_2 by O_3 and H_2O_2 is simulated. Mass transfer of the species (including NH_3 and HNO_3) between phases is simulated and the pH is calculated (Seinfeld and Pandis, 1998, p. 634).

Two categories of simulations involving chemical effects have been performed and compared to the base cases (no chemical effects). In the first set of simulations, only the uptake of HNO_3 on the droplets is simulated; aqueous sulfate chemistry is neglected. In total, 180 initial aerosol size distributions are used. For this set of simulations, aerosol parameters N_a, median radius (r_g), and the geometric standard deviation (σ_g) vary over the ranges N_a = 50 ~ 1000 cm^{-3}, r_g = 0.05 ~ 0.12 μm, σ_g = 1.4 ~ 1.8. The initial gas phase HNO_3 concentrations are assumed to be 1 ppb and 5 ppb. Droplet spectra and the optical properties of the clouds under the effect of HNO_3 are compared to those when HNO_3 is absent.

In the second set of simulations, aqueous sulfate chemistry is simulated but the effects of nitric acid are neglected. The gas phase initial conditions are 2 ppb SO_2, 30 ppb O_3, 2.5 ppb H_2O_2, 1 ppb NH_3, and no HNO_3. Only one aerosol size distribution is used in this set of simulations (N_a = 200 cm^{-3}, r_g = 0.06 μm, and σ_g = 1.8). After the cloud evaporates following the first cycle, the processed aerosols are used as input for the next cloud cycle. The droplet spectra and the optical properties in the second cloud are then compared to the base case (no processing).

3. RESULTS

3.1 EFFECTS OF HNO_3

As mentioned in Section 1, droplet spectra can broaden when N_d increases due to the presence of HNO_3. Figure 1 shows the droplet spectra at cloud top (~ 250 m above cloud base, or liquid water content LWC=0.5 gm^{-3}) from two simulations with and without HNO_3 for an updraft w = 0.1 ms^{-1}. The fraction of activated CCN (*xnf*) at cloud top and the relative dispersion (D = standard deviation/mean radius) of the size distributions are indicated on the figure. It can be seen that the droplet spectrum is broadened at both the small- and large-size ends. D increases from 0.052 to 0.135 as *xnf* increases from 0.57 to 0.84 due to 5 ppb HNO_3. Detailed discussions on the mechanisms causing the spectral broadening under the effect of HNO_3 can be found in Xue and Feingold (2004). Generally it is due to the fact that the partitioning of HNO_3 and water among the gas and liquid phases depends on the characteristics of the polydisperse droplet population.

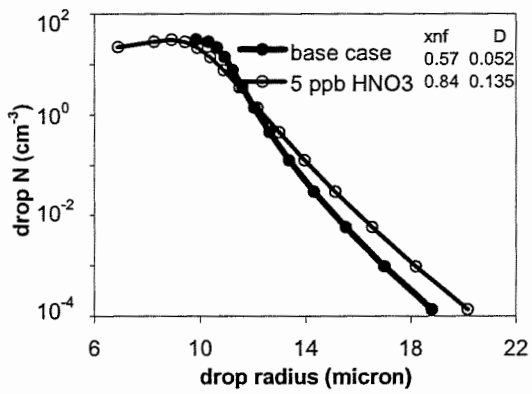

Figure 1. Droplet spectra at cloud top for 2 simulations under different HNO_3 levels. w = 0.1 ms^{-1}. Aerosol parameters are N_a = 200 cm^{-3}, r_g = 0.06 μm, σ_g = 1.8. Increasing the HNO_3 concentration not only results in a higher N_d, but also a broader droplet spectrum.

It should be noted that N_d may not be constant after the maximum supersaturation is achieved; even in an adiabatic cloud deactivation of small droplets can occur. These droplets are activated in the earlier stages of cloud formation but may evaporate later due to the outgasing of HNO_3 (Xue and Feingold 2004). Here, cloud droplets are referred to as droplets with radii larger than 1 μm. Although the deactivated droplets may evaporate to sizes smaller than 1 μm at cloud top, they can be large enough, and for long enough, in the earlier stages of the cloud to have a radiative effect. Because N_d may not be constant due to the effects of HNO_3, N_d or *xnf* discussed in this study are evaluated at cloud top.

Cloud microphysical and radiative properties from 4 simulations at w = 0.1 ms^{-1} are summarized in Table 1. Numbers shown in parentheses are the percentage differences compared to the base case. It is seen that when *xnf* is increased by 26% in the presence of 1 ppb HNO_3, the cloud-top effective radius (r_e) is decreased by 7% and the cloud optical depth (τ) is increased by 7%. However, the commonly-used theory for clouds that relates r_e and τ with N_d to the one-third power predicts that an increase of 26% in *xnf* (or N_d) will result in a decrease of 9% in r_e and an increase of 9% in τ, assuming all else remains unchanged. One can see that the changes in cloud optical properties under the effect of HNO_3 as calculated from the parcel model are moderated when the droplet spectra experience broadening.

	base case	1 ppb HNO_3	5 ppb HNO_3	Proc. aerosol
xnf	0.57	0.72 (+26%)	0.84 (+48%)	0.57
D	0.052	0.086 (+65%)	0.135 (+160%)	0.032
r_e (μm)	10.5	9.8 (-7%)	9.4 (-10%)	10.5
τ	11.4	12.2 (+7%)	12.8 (+12%)	11.5
A	0.477	0.495 (+4%)	0.505 (+6%)	0.478

Table 1. Model results of activated fraction *xnf*, dispersion d, effective radius r_e, optical depth τ, and cloud albedo A for 4 simulations. N_a = 200 cm^{-3}, r_g = 0.06 μm, σ_g = 1.8. w = 0.1 ms^{-1}. Numbers shown in parentheses are the percentage differences compared to the base case. Changes for the case with processed aerosol are not shown because the changes are small.

Figure 2 examines this result in a broader parameter space and shows the change in τ calculated from the parcel model for the 180 aerosol size distributions at w = 0.1 ms^{-1}. The relative change $\Delta\tau/\tau$ is defined as $(\tau_{HNO3} - \tau_{base})/\tau_{base}$, where τ_{base} is the cloud optical depth in the base case and τ_{HNO3} is the optical depth under 5 ppb HNO_3. It is seen that an increase of 0 ~ 110% in N_d and an increase of 0 ~ 20% in τ can occur when 5 ppb HNO_3 is present. However, the theory (black line, $\Delta\tau/\tau = 1/3\Delta N_d/N_d$) that ignores the spectral broadening effect predicts that an increase of 0 ~ 110% in N_d will results in an increase of 0 ~ 37% in τ. The results frequently diverge from the theory. The largest deviations from theory are associated with the largest changes in spectral dispersion. Figure 3 shows the changes in cloud-top r_e

calculated from the parcel model. Again, there are significant deviations from the theory (black line, $\Delta r_e / r_e = -1/3 \Delta N_d / N_d$). Both Figure 2 and Figure 3 show that the cloud optical properties are moderated by the spectral broadening. In the study by Xue and Feingold (2004), comparison between the cloud optical properties with the theory that includes the spectral broadening effect has been performed, and the results show that cloud optical properties are in better agreement with theory.

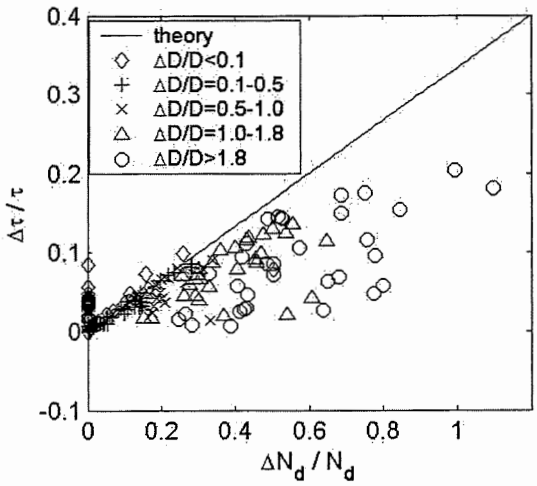

Figure 2. Model results of $\Delta\tau/\tau$ vs. $\Delta N_d / N_d$ for all 180 aerosol size distributions under 5 ppb HNO_3 at w = 0.1 ms^{-1}. The solid line represents the theory for an adiabatic cloud that does not include the spectral broadening effect.

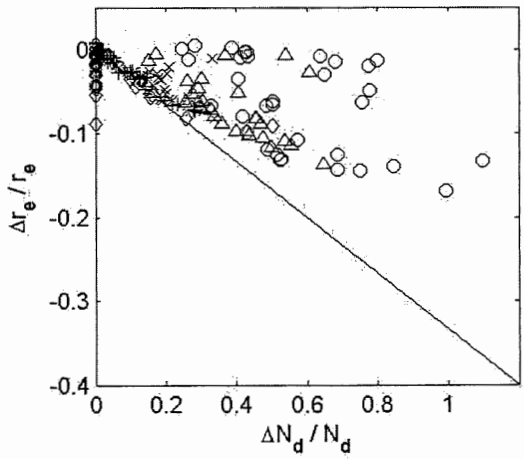

Figure 3. Model results of $\Delta r_e / r_e$ vs. $\Delta N_d / N_d$ for all 180 aerosol size distribution under 5 ppb HNO_3 at w = 0.1 ms^{-1}.

3.2 EFFECTS OF AQUEOUS-PHASE SULFATE CHEMISTRY

Figure 4 shows the size distribution of the processed aerosol after the cloud evaporates. The cloud updraft is w = 0.1 ms^{-1}. Although aqueous-phase sulfate chemistry does not affect N_d and the drop size distribution in the first cloud cycle, the addition of sulfate to the particles leads to a bimodal aerosol distribution after the cloud evaporates. This aerosol distribution is then used as input for the next cloud cycle where no aqueous chemistry or HNO_3 uptake is simulated but other conditions remain unchanged. The resultant droplet spectrum at cloud top is shown in Figure 5. The distribution is noticeably narrower in the second cloud cycle but cloud radiative properties show almost no change for the simulated case when compared to the base case (see Table 1). This result is contrary to the study of Zhang et al. (1999) which showed that broader droplet spectra can be generated under some circumstances. Further investigation of this difference is underway.

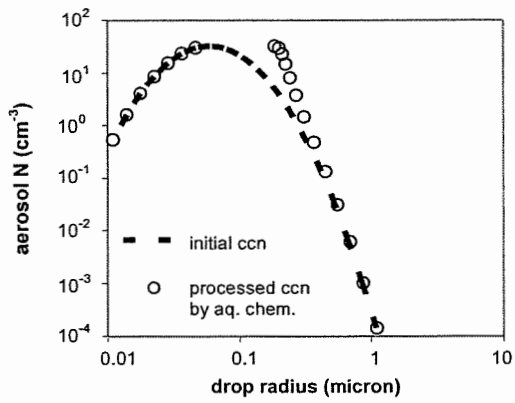

Figure 4. Aerosol size distribution after cloud processing by aqueous-phase chemistry. Gas phase initial conditions are SO_2 = 2 ppb, O_3 = 30 ppb, H_2O_2 = 2.5 ppb, NH_3 = 1 ppb, HNO_3 = 0 ppb. The unprocessed initial aerosol size distribution is shown for reference.

4. CONCLUSIONS

Results show that HNO_3 not only helps activate more CCN into cloud droplets, but that it can also lead to broader droplet spectra. Changes in droplet spectral breadth due to chemical effects may modify the cloud optical properties significantly. The results show that cloud spectral broadening moderates the changes in τ and r_e caused by increases in N_d under the effect of HNO_3. For the case with aqueous phase sulfate chemistry, the cloud optical properties are show to be unaffected by the narrowing effect for the simulated case but calculations need to be performed over broader parameter space.

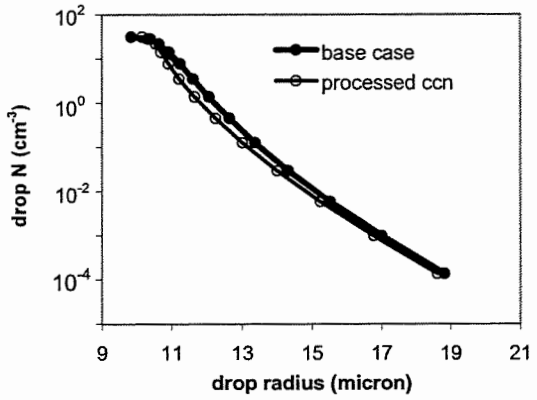

Figure 5. Drop size distributions for a second cloud cycle where the processed aerosol size distribution is used as input. The base case spectrum is shown for reference. Note the reduction in size distribution breadth resulting from aqueous chemistry processing.

ACKNOWLEDGEMENTS

We thank Simon Clegg for providing the code of the thermodynamic model for water activity calculation. We also thank Barbara Ervens and Dennis Lamb for helpful discussions. Huiwen Xue acknowledges support from the NRC Postdoctoral Program.

REFERENCES

Baker, M. B., R. G. Corbin, and J. Latham, 1980: The influence of entrainment on the evolution of cloud droplet spectra: I. A model of inhomogeneous mixing. *Quart. J. Roy. Metor. Soc., 106*, 581-598.

Charlson, R. J., J. H. Seinfeld, A. Nenes, M. Kulmala, A. Laaksonen, and M. C. Facchini, 2001: Reshaping the theory of cloud formation. *Science, 292*, 2025-2026.

Clegg, S. L., P. Brimblecombe, and A. S. Wexler, 1998: Thermodynamic model of the system H^+-NH^+-SO_4^{2-}-NO_3^--H_2O at tropospheric temperatures. *J. Phys. Chem., A102*, 2137-2154.

Feingold, G., S. M. Kreidenweis, and Y. Zhang, 1998: Stratocumulus processing of gases and cloud condensation nuclei. 1. Trajectory ensemble model. *J. Geophys. Res., 103*, 19527-19542.

Feingold, G. and P. Y. Chuang, 2002: Analysis of the influence of film-forming compounds on droplet growth: Implications for cloud microphysical processes and climate. *J. Atmos. Sci., 59*, 2006-2018.

Gerber, H., 1996: Microphysics of marine stratocumulus clouds with two drizzle modes, *J. Atmos. Sci., 53*, 1649-1662.

Harrington, J. Y., G. Feingold, and W. R. Cotton, 2000: Radiative impacts on the growth of a population of grops within simulated summertime Arctic stratus. *J Atmos. Sci., 57*, 766-785.

Johnson, D. B., 1982: the role of giant and ultragiant aerosol particles in warm rain initiation, *J. Atmos. Sci., 39*, 448-460.

Kulmala, M., A. Laaksonen, P. Korhonen, T. Vesala, T. Ahonen, and J. C. Barret, 1993: The effect of atmospheric nitric acid vapor on cloud condensation nucleus activation, *J. Geophys. Res., 98*, 22949-22958.

Kulmala, M., A. Laaksonen, R. J. Charlson, and P. Korhonen, 1997: Clouds without supersaturation. *Nature, 388*, 336-337.

Laaksonen, A., P. Korhonen, M. Kulmala, and R. J. Charlson, 1998: Modification of the Köhler equation to include soluble trace gases and slightly soluble substances. *J. Atmos. Sci. , 55*, 853-862.

Liu, Y., and P. H. Daum, 2002: Indirect warming effect from dispersion warming. *Nature, 419*, 580-581.

Nenes, A., R. J. Charlson, M. C. Facchini, M. Kulmala, A. Laaksonen, and J. H. Seinfeld, 2002: Can chemical effects on cloud droplet number rival the first indirect effect? *Geophys. Res., Lett., 29*, No. 17, 1848, doi:10.1029/2002GL015295.

Pruppacher, H. R., and J. D. Klett, 1997: *Microphysics of Clouds and Precipitation*, Kluwer Academic Publishers, 954 pp..

Seinfeld, J. H., and S. N. Pandis, 1998: *Atmospheric Chemistry and Physics*, John Wiley and Sons, Inc., 1326 pp..

Shaw, R. A., W. C. Reade, L. R. Collins, and J. Verlinde, 1998: Preferential concentration of cloud droplets by turbulence: Effects on the early evolution of cumulus cloud droplet spectra, *J. Atmos. Sci., 55*, 1965-1976.

Twomey, S., 1974: Pollution and the planetary albedo. *Atmos. Environ., 8*, 1251-1256.

Zhang, Y., S. M. Kreidenweis, and G. Feingold, 1999: Stratocumulus processing of gases and cloud condensation nuclei. 2. Chemistry sensitivity analysis, *J Geophys. Res., 104*, D13, 16061-16080.

Xue, H., and G. Feingold, 2004: A modeling study of the effect of nitric acid on cloud properties, submitted to *J. Geophys. Res.*.

EQUILIBRIUM WET GROWTH/EVAPORATION OF PARTICLES CONTAINING SOLUBLE AND INSOLUBLE KERNELS

V. Arkhipov, M. Pinsky and A. Khain

Department of Atmospheric Science, Institute of Earth Science,
The Hebrew University of Jerusalem, Israel

1. INTRODUCTION

Atmospheric aerosol particles (APs) and cloud droplets are the two-coupled components of the complex system affecting radiation budget, chemical properties of the atmosphere, as well as precipitation. The equilibrium APs size for different values of relative humidity is traditionally described by the Köhler equation under assumption that a soluble fraction of APs completely dissolved at the beginning of particle growth. Since the humidity of deliquescence of some important species is of about 70% (i.e, at lower humidity these Aps are dry), a significant fraction APs at 70-80% relative humidities should be either strong solutions or they may contain a non-dissolved kernel. As concerns to giant natural APs, they remain to be strong solutions during a significant time of their growth within a wide humidity range. The Köhler theory APs growth is extended to the cases of watering of initially dry APs, when the liquid envelope of APs is the strong solution and the APs contain dissolving solid kernel.

The second goal of the paper is to investigate the effects of soluble/insoluble fractions in the initially dry APs on the size of nucleated water droplets.

2. DEPENDENCE OF HUMIDITY OF DELIQUESCENCE ON DRY AP SIZE

Using equilibrium conditions a) between particle aqueous solution and the soluble kernel and b) between an aqueous solution drop with non-dissolved soluble kernel and ambient humid air (Arkhipov et al 2004) one can obtain an explicit relationship between the humidity of deliquescence and the particle size describing the curve separating the dry particle and the wet one. The dependence of saturation of deliquescence $S_{del}(r_0)$ on the initial dry particle radius r_0 is

$$S_{del}(r_0) = a_{w,sat} \exp\left[\frac{2M_w\sigma_s(r_0)}{\Re T r_0} + \frac{M_w C_{sat} i}{1000}\left(1-\exp\left(\frac{2\beta}{i r_0}\right)\right)\right],$$

$$\beta = F_s M_s / \rho_s \Re T \qquad (1)$$

where $a_{w,sat}$ is the water activity of the saturated solution over a flat surface; M_w and M_s are the molecular weight of water and soluble material correspondingly; $\sigma_s(r_0)$ is the surface tension of the aqueous solution-humid air interface; C_{sat} is the molality of the saturated solution over a flat surface; F_s is the surface free energy of solute; ρ_s is the mass density soluble material; i is the VantHoff factor; $\Re$ is the gas constant; T is the absolute temperature.

The humidity of deliquescence dependence on dry AP radius calculated using (1) for *NaCl* at 25^0 C is shown in Fig.1. If humidity is less than that of deliquescence an aerosol particle remains dry. This stage is illustrated in Fig.1 by the dash line for the 0.01-μm radius *NaCl* particle. If the radius of dry a AP tends to infinity $S_{del}(\infty) = a_{w,sat}$. Experimental data for selected compounds confirm this equality (Brasseur et al. 1999, Robinson and Stokes, 1959).

F

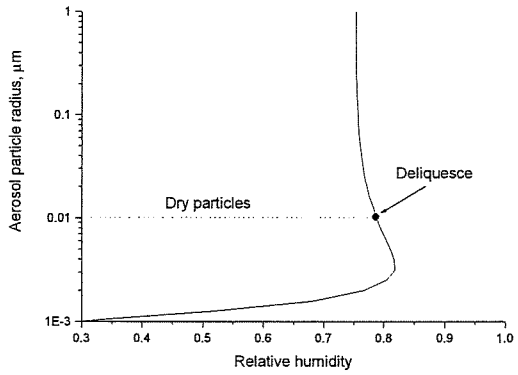

IG.1 Dependence humidity of deliquescence on dry AP radius (the deliquescence curve) calculated using (1) for NaCl at 25^0 C

3. DISSOLUTION OF SOLUBLE KERNELS

The next stage of AP evolution is the process of kernel dissolution. The question is: how does the AP radius change with saturation in the course of kernel dissolution? Dissolution of a soluble kernel takes place according to the equilibrium of an aqueous solution drop with a non-dissolved soluble kernel and the ambient humid air. Using the equilibrium condition we calculated the dependence of the equilibrium particle radius on the saturation *a(S)* in the course of kernel dissolution. This dependence is

Corresponding author's address: Vladimir Arkhipov, Department of Atmospheric Sciences, The Institute of Atmospheric Sciences, The Hebrew University, 91904, Jerusalem, Israel; E-mail: arkh@vms.huji.ac.il

plotted in **Fig. 2** (dashed curve) for the case of a *NaCl* soluble kernel at 25^0 C.

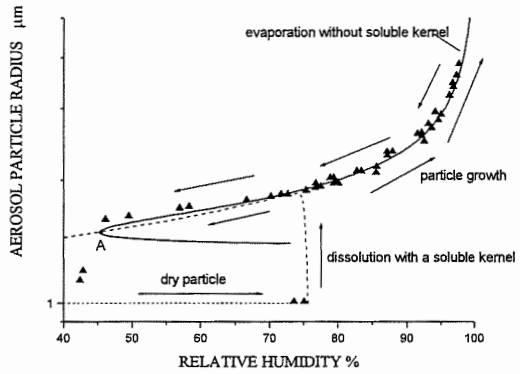

FIG.2

Fig. 2 shows that at the humidity lower than that of deliquescence APs have two equilibrium states: they can exist either as dry APs or as APs covered by a film of oversaturated liquid solution.

If relative humidity remains constant and equal to that of deliquescence, the APs continue growing until complete dissolution. There appear two branches in APs evolution after humidity of deliquescence has been attained. The first branch one is the equilibrium evolution, which requires decreasing the air humidity. This branch can be reproduced in laboratory conditions only.

The second possibility that can be realized in practice is a non-equilibrium growth under increasing or fixed air humidity until a complete dissolution of the soluble part of the kernel is attained. One can show that during the dissolution process equilibrium saturation obeys expression

$$S = \exp\left[\frac{2M_w\sigma_s}{\Re T\rho_w a} - \frac{\nu\Phi_s(C)\varepsilon M_w\rho_s(r_0^3 - r_k^3)}{M_s\rho_w(a^3 - r_0^3)}\right], \quad (2)$$

which is an extension of a widely used Köhler expression for the case when AP contains a non-dissolvable kernel of radius r_k . Radius of particle a after total kernel dissolution can be obtained from (2) by substituting r_k =0.

The next stage of AP evolution under increasing environmental air humidity is its growth without a soluble kernel according to the Köhler equation as shown in Fig 2. Thus, the evolution of AP under growing humidity can be divided into three stages: dry AP, growth during dissolution process and growth after complete dissolution.

4. EVAPORATION AND FORMATION OF A SOLID KERNEL

Evaporation under decreasing humidity can be described by eq.(2) in which r_k =0 and C=1000$\rho_s r_0^3/M_s\ \rho_w(a^3 - r_0^3)$. To take into account the case of a strong solution, we use the expression for the osmotic coefficient that is presented by Tang and Munkelwitz, (1986). The calculated dependence of the AP radius on relative humidity is plotted in Fig. 2 by the solid line. One can see that the curve of equilibrium corresponding to particle containing a solid kernel and the curve corresponding to particle with no kernel intersect at certain air humidity. We believe that this point is the point of the phase transition, where a soluble kernel arises. Actually, Fig.2 shows that when solution becomes oversaturated both curves with and without kernel are quite close to each other. This situation is unstable. A fluctuation, which can arise due to impurity, would cause transition leading to kernel formation. But, in case of an extra pure solution the formation of a solid kernel takes place in point A (the point of a spontaneous kernel formation).

Kernel growth leads to a decrease in the equilibrium concentration of the solution. Thus, no further decrease in air humidity is necessary to continue water evaporation and kernel growth. At this point water in AP evaporates completely and the particle becomes dry. The humidity corresponding to this point is known as the humidity of efflorescence (Martin, 2000). The results of laboratory experiments for *NaCl* (Tang et al., 1977) are presented in **Fig. 2** for comparison (triangles). One can see a good agreement between the theoretical and laboratory results. Figure 2 indicates the hysteresis of AP equilibrium states during dissolution-growth and evaporation-crystallization processes.

5. DROPLET NUCLEATION

If a solid kernel contains both soluble and insoluble fractions the process of dilution continues until the kernel radius r_k decreases to radius r_{ins} of its insoluble fraction. The process of dilution is described in the way similar to the pure soluble kernel. As the process of dilution is finished, further AP growth continues according to the Köhler equation. We calculated equilibrium radii of APs as the function of air saturation (%) for different ratios of soluble and insoluble parts in the kernels and different initial (dry) radii of the APs Analysis of the results shows that.

1) The magnitude of critical super saturation for small APs (dry radius of about 0.01 μm) exceeds 1% even for completely soluble particles and reaches 10% for insoluble particles. The magnitude of super saturation at the cloud base of cumulus clouds is usually under 1%. Thus, APs with dry the radius ≤ 0.01 μm can hardly transform into cloud droplets. These APs do not participate in cloud droplet

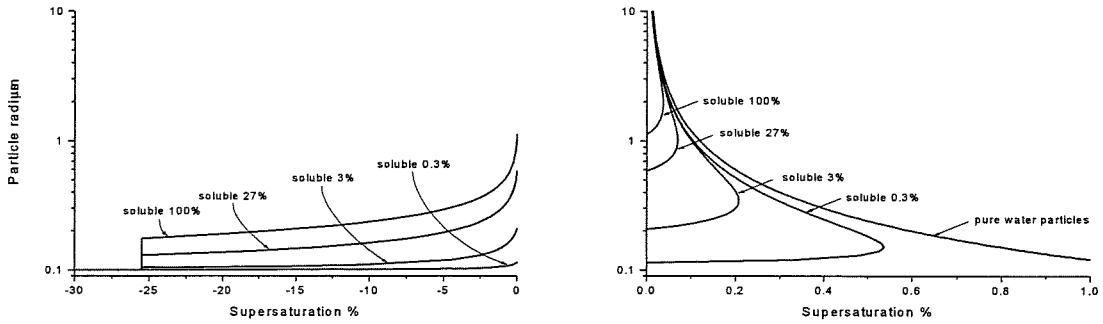

FIG.3a. Particle radius as a function of supersaturation for the different soluble fraction of NaCl at 25° C.

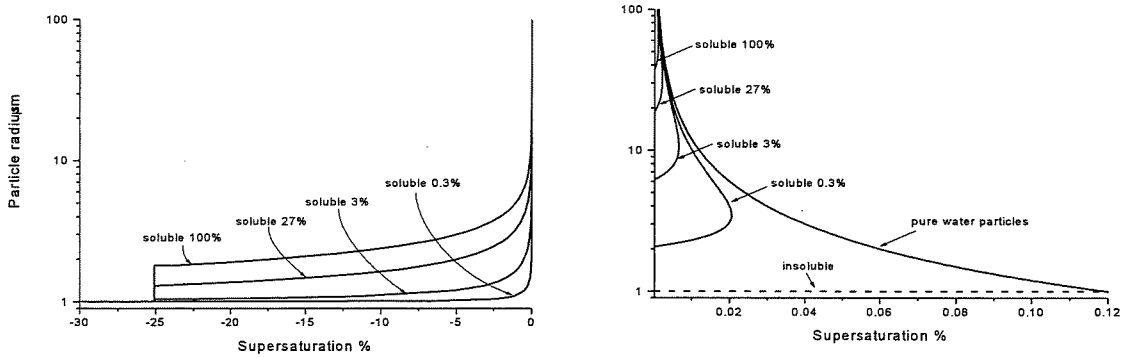

FIG.3b Particle radius as a function of supersaturation for the different soluble fraction of NaCl at 25° C.

and precipitation formation independent of the values of soluble and insoluble fractions.

2) An increase in the soluble fraction of the kernel in case of APs with a dry radius of about 0.1 μm (**Fig. 3a**) leads to a significant decrease in critical supersaturation from 1% to about 0.036%. APs with a larger soluble fraction turn out to be larger nucleated cloud droplets. For example, for APs with a dry of 0.1 μm radius kernel the size of the nucleated droplet with a soluble kernel is about 2 μm, while if the kernel is insoluble the initial droplet size is about 0.2 μm. Thus, even the existence of a small soluble fraction in these APs is of crucial importance for their activation and transformation into cloud droplets.

3) Critical supersaturation of large APs (dry radius of about 1 μm) (**Fig. 3b**) ranges from 0.0011% for a fully soluble kernel up to 0.02% for a fully insoluble one. These large APs transform into droplets independent of their chemical composition. When the dry radius is about 1 μm, the equilibrium radius of a nucleated droplet is about 60 μm in case of a soluble kernel and 1 μm in case of an insoluble kernel. Note, that because of the low rate of diffusion growth in clouds large APs do not usually attain their equilibrium radius, if the latter increases about 20 μm. We see that large APs are able to transform into droplets at very low super saturations, even if they have no soluble fraction.

6. CONCLUSIONS

The Köhler theory is extended for the case of strong solutions and the existent of non-soluble kernel in aerosol particles. **Fig. 4** shows the deliquescence curve (plotted for *NaCl*), as well as the "Kelvin curve" corresponding to the phase equilibrium between the pure water droplet and the humid air. These two curves divide the plane the particle size – air humidity into three zones: zone 1 to the left of the deliquescence curve, zone 2 between these curves, and zone 3 to the right of the Kelvin curve. Zone 1 corresponds to dry aerosol particles and oversaturated solution particles with non-dissolved kernels. There is some limiting humidity (the asymptote), at which the allowable droplet radius tends to the infinity (the humidity corresponding to the plane surface); this humidity is the humidity of deliquescence of given chemical species. Zone 2 corresponds to the water solution of the APs with a completely dissolved of soluble fraction of a kernel. Zone 3 corresponds to pure water droplets.

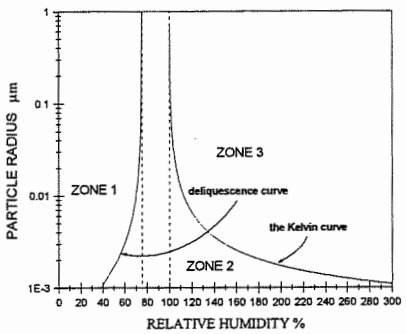

FIG.4

Many aerosols in the atmosphere remain dry and start growing within a comparatively narrow layer below cloud base, where relative humidity exceeds ~ 75%. Having been formed by evaporation of droplets, aerosols of this type become dry in cloud surrounding as well. Some possible scenarios of APs evolution in the sub-cloud layer are shown in **Fig. 5**.

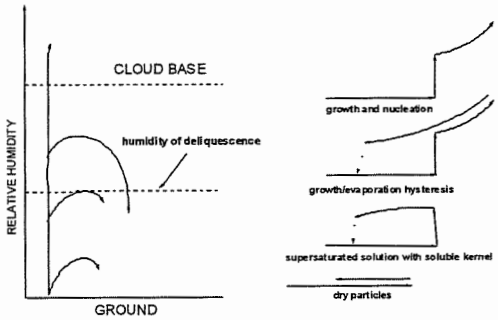

FIG.5

In case relative humidity near the surface is below that corresponding to the deliquescence curve, APs are dry and do not change their size moving up and down within this layer (curves 1) that corresponds to zone 1 in Fig. 4. It is possible that dry aerosols cross the level corresponding to the deliquescence curve, transferring from zone 1 to zone 2 in Fig.4. The curves 2 and 3 are related to the case when kernels first dissolve within updrafts, and then arise again during evaporation in downdrafts. In case APs penetrate cloud base level within the updraft (curve 4), the particles continue growing as solutions with no soluble kernel.

It is possible that relative humidity near the surface exceeds that corresponding to the deliquescence curve. In this case, APs do not contain soluble kernel near the surface, which, however can arise aloft, where relative humidity is lower. These scenarios indicate that APs in the sub-cloud layer and in cloud surroundings may exhibit different transformations accompanied by dissolving and arising solid kernels, by the formation and fading away of the film of solution. The solution can be of different concentration, including saturated and even oversaturated ones. The size of large APs will depend on time during which these APs are located in regions of high humidity. This complex APs structure determines, possibly, the structure of stratiform and convective clouds, affects radiative properties of the atmosphere, etc.

It is shown that the presence of soluble fraction in APs with dry kernels ranged from 0.1 µm to 1 µm determines whether corresponding AP will be activated with formation of a new cloud droplet or not. APs with radii exceeding 1 µm can grow in clouds even under zero soluble fractions. In this case the value of soluble fraction determines the size of nucleated droplet. These results should be taken into account by cloud physicists and modellers, who usually ignore non-soluble APs, while considering the cloud droplet spectrum formation in smoky and polluted air.

Acknowledgements

This study was supported by the Israel Science Foundation (grant 173/03) and the Israel Ministry of Science, (the German-Israeli cooperation in Water Technology, grant WT 0403) as well as by European Project SMOCC.

References

Arkhipov V.I., M. Pinsky and A. Khain Equilibrium wet growth/evaporation of particles containing soluble and insoluble kernels 2004. Atmos. Res. (submitted)

Brasseur, Guy P. *Atmospheric chemistry and global change*. N. Y.: Oxford University Press, Ed. by Guy P. Brasseur, John J. Orlando, Geoffrey S.,1999, 654 pp.

Eichel C., M. Kramer, L. Schultz and S. Wurzler, 1996: The water-soluble fraction of atmospheric aerosol particles and its influence on cloud microphysics. J. Geophys. Res., v. 101, D23, 29,499-29,510.

Martin S.T., 2000: Phase Transitions of aqueous atmospheric particles. Chem. Rev., **100,** 3403-3453

Orr C., Hurd Jr.F.K. and Corbett W.J., 1958: Aerosol size and relative humidity. J.Colloid Sci., **13** 472-482.

Robinson R.A. and Stokes R.H., 1959: *Electrolyte Solutions*. Butterworths, London, 559 pp.

Sedunov, Yu.S., 1974: Physics of Drop *Formation in the Atmosphere*. Ch.2, Wiley&Sons, New York.

Tang I.N., Munkelwitz H.R. and Davis J.G., 1977: Aerosol growth studies –II. Preparation and growth measurements of monodisperse salt aerosols. J. Aerosol. Sci., **8**, 149-159.

Tang I.N., Munkelwitz H.R. and Ning Wang, 1986: Water activity measurements with single suspended droplets: The $NaCl-H_2O$ and $KCl-H_2O$ systems. J.Colloid and Interface Sci., **114**, 409-415.

AIRCRAFT MEASUREMENTS OF HIGH AVERAGE CHARGES ON CLOUD DROPS

Kenneth V. Beard,[1,2] Harry T. Ochs[1,2] and Cynthia H. Twohy[3]

[1]Department of Atmospheric Sciences, University of Illinois, Urbana-Champaign, Illinois
[2]Illinois State Water Survey, Champaign, Illinois
[3]College of Oceanic and Atmospheric Sciences, Oregon State University, Corvallis, Oregon

1. INTRODUCTION

The charge on cloud and precipitation drops can affect coalescence between colliding drops (*Pruppacher and Klett*, 1997) and the capture of ice nuclei (*Beard*, 1992; *Tinsley et al.*, 2000) that result from evaporated cloud drops (*Rosinski and Morgan*, 1991; *Rosinski*, 1995). Previous measurements of cloud drop charges indicate only a few electronic charges per drop with averages near zero [*Webb and Gunn*, 1955; *Phillips and Kinzer*, 1958], but these data were obtained at the surface in mountain top clouds where the electrical environment differs from clouds with bases well above ground. In all other measurements, average cloud drop charges could not be accurately determined because of limited instrument sensitivity [*Twomey*, 1956; *Imyanitov et al*, 1972; *Takahashi*, 1972; *Takahashi*, 1975] and probable contact charging during aircraft sampling [*Gunn*, 1952; *Moore et al.*, 1961]. Here we report the first reliable aircraft measurements of average cloud drop charge.

2. MEASUREMENTS

We obtained measurements of average cloud drop charges aboard a Lockheed Electra operated by the National Center for Atmospheric Research (NCAR) in layer clouds over Lake Michigan. Instrumentation included wing-mounted laser probes for measuring cloud drop and ice particle sizes and concentrations. The NCAR Counterflow Virtual Impactor (CVI) was used to sample the cloud drops. The CVI probe (Fig. 1) and its coaxial flow-straightening shroud were oriented into the air stream 0.6 m from the side of the aircraft fuselage. The probe has a porous inner wall [*Noone et al.*, 1988] so that heated nitrogen gas supplied under pressure enters the inlet radially and divides axially into a counterflow out the probe tip and a carrier flow into the aircraft. During our flights in wintertime layer clouds over Lake Michigan, the probe was heated to prevent icing.

The counterflow out the CVI tip prevents drops smaller than a threshold size of 4 to 5 μm radius, as well as aerosol and outside air, from entering the carrier flow into the aircraft [*Olgren et al.*, 1985]. Cloud drops less than 25 μm radius were completely evaporated so that only drop residue particles with their charge are carried from the CVI probe to the instruments inside the aircraft. For the measurements reported here the cloud drops were less than 15 μm radius.

Corresponding address: Kenneth Beard, Atmospheric Sciences, UIUC, 105 S Gregory St, Urbana, IL 61801.

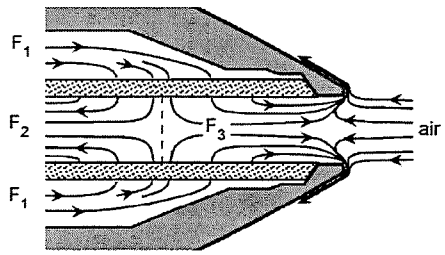

Figure 1. *Cross section of the conical CVI probe tip showing streamlines of internal and external flows [Lauks and Twohy, 1998]. Heated nitrogen under pressure (F1) flows radially through a porous tube where it splits into a sample flow (F2) and a counterflow out the tip (F3).*

An important feature of the CVI probe is the strong exit and external flow adjacent to the surface of the CVI tip that rejects any water that would otherwise accumulate from impacting cloud drops. In contrast to previous aircraft sampling methods [*Gunn* 1952, *Moore et al.*, 1961], spurious contact charges associated with splatter droplets and grazing cloud drops were prevented from contaminating our measurements of average cloud drop charges.

The electrical current carried by the residue particles from evaporated cloud drops was measured using an absolute filter electrometer (TSI Model 3068) having a sensitivity of 1 femtoamp (1fA = 10^{-15} C s^{-1}). The current was recorded using a custom analog to digital interface and software on a laptop computer. The average charge on cloud drops was calculated for each second of data from $q = I/(FN)$, where I is the electrometer current (fC s^{-1}), F is the electrometer flow rate (cm^3 s^{-1}), and N is the residue particle concentration (cm^{-3}) measured by a condensation nucleus counter (TSI Model 3760). For a series of multiple current peaks, the drop charges were obtained using several-second averages over the electrometer and CN peaks: $\langle q \rangle = \langle I \rangle / (f \langle N \rangle)$. The average cloud drop radius in the CVI size range was obtained from cloud drop spectra measured by a wing-mounted laser probe (PMS Model FSSP-100).

Cloud drops carrying an average charge of a single electron could be measured reliably because of a typical 25-fold increase in concentration induced by

drop deceleration in the CVI inlet counterflow. For a typical cloud drop concentration of 100 cm^{-3} and a CVI residue particle concentration of 2500 cm^{-3}, an average charge of one electron produces a current of 7 fA -- seven times the electrometer sensitivity. The CVI substantially increases the sensitivity of our charge measurements while eliminating spurious contact charging that contaminated previous measurements.

3. RESULTS

The drop charge measurements shown in Fig. 2 were obtained on January 20, 1998 during an ascent through a 600-meter stratocumulus (Sc) layer over the lake near Shelby, Michigan. Upon entering the cloud, the cloud drop concentration (N) rose to over 150 cm^{-3} within 5 seconds, but initially most cloud drops were too small to enter the CVI. Better estimates of mean drop charge were obtained above the center of the cloud layer (after 70 sec) where most of the cloud drops were large enough to enter the CVI.

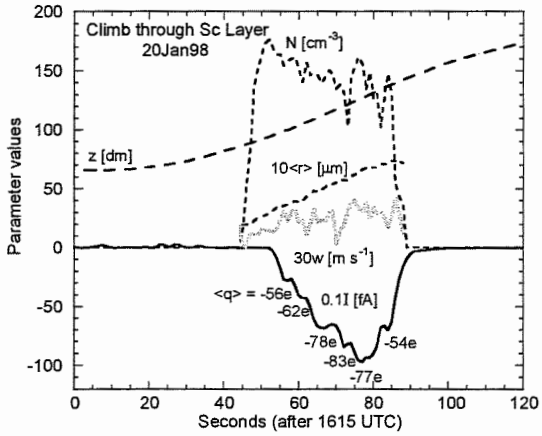

Figure 2. *CVI and aircraft measurements for the climb from 0.6 to 1.5 km elevation through a stratocumulus layer beginning at 1615 UTC. Data are plotted for the cloud drop concentration (N) and mean radius (<r>) from the forward scattering spectrometer probe, the CVI electrometer current (I), the average cloud drop charge (<q>), and the updraft velocity, where w(m s^{-1}) is obtained from the ordinate value divided by 30. The temperature range was −8°C to −12°C from layer base to top.*

The electrometer current was negative throughout the Sc layer with a maximum of -975 fA. The initial peak of <q> = -58 e (elementary charges), occurred about 100 m above cloud base within a local updraft maximum of about 1 m s^{-1}. The mean cloud drop radius of <r> ~ 3.5 µm was below the CVI threshold radius of 4.6 µm so most of the cloud drops were rejected by the CVI. Another 200 m higher in the Sc layer, in a somewhat stronger updraft region, the average cloud drop charge reached its maximum value of -83 e, where about 85% of the cloud drops were large enough to enter the CVI. The average charge decreased higher in Sc layer even though essentially all of the cloud drops were larger than the CVI threshold. Ice particles of 100 - 270 µm diameter at concentrations of 0.4 - 1.3 L^{-1} were measured by diode array probes during just six isolated one-second periods. There was no indication that these small ice particles affected the charge measurements.

Cloud drop charges were also measured in a 250 m thick altostratus (As) layer on January 18, 1998 between 1034 and 1036 UTC (Fig. 3) just after the Electra reached level flight at 3.0 km elevation near Manistee, Michigan. The Electra elevation varied by less than ±10 m in response to vertical air motions between -1.8 and +1.2 m s^{-1}. Downdrafts predominated near the top of this nocturnal layer cloud and the cloud drops apparently formed in radiatively cooled parcels. The temperature before entering the cloud elements was -16°C and typical minimums of -18°C were measured in the cloud elements. Small ice crystals were detected during just four isolated one-second periods and there was no indication that the ice particles affected the measurements of drop charge.

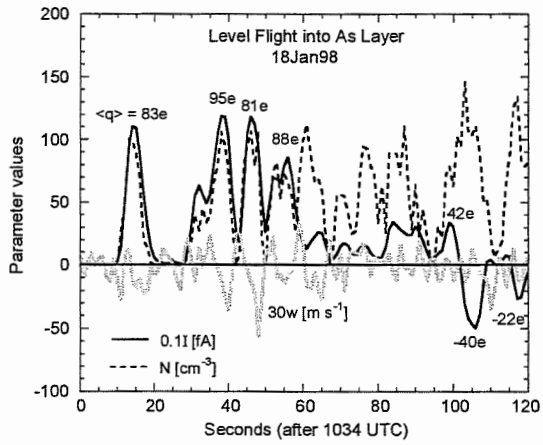

Figure 3. *CVI and aircraft measurements for level flight at 3 km elevation into the top of a rising altostratus layer beginning at 1034 UTC. Shown are the cloud drop concentration (N), the CVI electrometer current (I), the average cloud drop charge (<q>), and the updraft velocity (w). The temperature varied between −16°C and −18°C.*

A series of four strong positive current peaks was observed in the first minute of cloud penetrations at the top of the As layer. The corresponding average drop charges of 83, 95, 88 and 90 e were associated with downdrafts. Since the average cloud drop radius of 7 to 8 µm was significantly larger than the CVI minimum size of 4.1 µm, the measured drop charges were close to average drop charges.

With further penetration into the cloud layer, the downdrafts and positive currents weakened, giving way to negative current peaks with average drop charges of -40 and -22 e. These charge were associated with average cloud drop radii of about 6 μm. Our observed average cloud drop charges in the altostratus layer were similar in magnitude to our measurements in the stratocumulus cloud layer (Fig. 2) and more than a factor of ten larger than previous measurements of average drop charges obtained in similar clouds from mountain top locations [*Webb and Gunn*, 1955; *Phillips and Kinzer*, 1958].

4. DISCUSSION

Cloud drops at the boundaries of a layer cloud acquire a net charge from vertical ion currents driven by the fair weather electric field outside the cloud. In this conceptual model of layer cloud electrification [*Pruppacher and Klett*, 1997; *MacGorman and Rust*, 1998], the opposing ion currents inside the cloud layer are much weaker because ion concentrations are greatly reduced by diffusion to cloud drops. The vertical ion currents become more balanced as the electric field inside the cloud layer intensifies in response to the charges at the layer cloud boundaries. These boundary charges are perturbed when updrafts or downdrafts carry charged drops into the cloud layer.

The time constant for a cloud drop to become charged at boundary of a cloud layer is of the same order as the time constant for depletion of ions by diffusion to cloud drops. It is inversely proportional to drop radius and concentration [*Chiu and Klett*, 1976] and is about 30 seconds for drops of 6 μm radius at a concentration of 100 cm^{-3}. Cloud drops acquire most of their equilibrium charge in 30 seconds, or 30 meters for cloud parcels moving at an average vertically speed of 1 m s^{-1}. Because the vertical ion drift velocities in the weak electric fields inside these cloud layers are significantly less than 0.1 m s^{-1}, cloud parcels in updrafts at cloud base will generally outrun the external source of negative ions at cloud base. Cloud drops in downdrafts originating near cloud top will become separated from the source of positive ion at cloud top.

Inside the cloud layer, the ion concentrations become more neutral as ion pairs, produced by cosmic rays, recombine or are captured by cloud drops. When ion concentrations of each polarity are nearly balanced inside the cloud layer, the discharging time constant for cloud drops is inversely proportional to the ion concentration and is about 3000 seconds for an ion concentration of 100 cm^{-3} in the cloud layer [*Gunn*, 1954]. Therefore, the charge on cloud drops acquired at the cloud boundary cannot decay to an equilibrium charge in the more neutral ion environment inside the cloud layer because the relaxation time is too long -- possibly longer than the lifetime of a typical cloud parcel based on the estimated mean vertical velocity and cloud depth [*Braham and Kristovich*, 1996].

Our measurements of cloud drop charges in layer clouds are consistent with charging at cloud boundaries. The polarity of the cloud drop charge in Fig. 2 is the same as expected from an excess flow of negative ions into cloud base. The upward velocities of 1.0 to 1.3 m s^{-1} carry the charged drops into the cloud layer.

Similarly, the polarity of charges on drops in the top of the nocturnal layer cloud in Fig. 3 is consistent with an excess flow of positive ions into cloud top and with the downward velocities of 1.0 to 1.7 m s^{-1} that carry the charged drops into the cloud layer. The negative drop charges found deeper in the 250 m thick altostratus layer probably resulted from upward transport of negatively charged cloud drops at cloud base.

The significant finding of our study is the unexpectedly large magnitude of average charge on cloud drops, and implications for cloud processes such as the initiation of ice and precipitation. When cloud drops evaporate at cloud top, or in regions of entrainment and mixing, the residue particles can act as evaporation ice nuclei [*Beard*, 1992] because the ice nucleating ability of particles can be greatly enhanced by a condensation-evaporation cycle [*Rosinski and Morgan*, 1991; *Rosinski*, 1995]. If a large cloud drop falls through an entrained filament of dry air containing evaporated cloud drops, contact with evaporation ice nuclei, carrying charges of 10-100 e, will be enhanced by one or two orders of magnitude [*Tinsley et al.*, 2000; *Tinsley et al.*, 2001]. Since ice initiation is often a precursor to precipitation, the charge on cloud drops may play a significant role in triggering precipitation in clouds.

Although our aircraft measurements have demonstrated that cloud drops within cloud layers have much higher charges than expected, the cloud drop sizes in the wintertime layer clouds were generally below the threshold necessary for initiation of significant ice particle concentrations [*Hobbs and Rangno*, 1985]. We plan to extend our charge measurements to stratiform and cumuliform clouds where ice more readily forms and where evaporated cloud drops are likely to make effective ice nuclei [*Rosinski and Morgan*, 2001; *Beard*, 1992]. Further measurements are also needed in other cloud types and seasons to evaluate whether most of the charge on cloud drops acquired near cloud boundaries is carried into the cloud by vertical motion without substantial losses. We plan to improve the response time of our electrometer to better resolve the charges on drops and aerosol particles in the charge generating regions at cloud boundaries.

Acknowledgements

We thank Mark Belding and Dave Rogers for help with instrumentation and field measurements during the Lake-ICE program, and Jasbir Naul for help with data analysis. This project was supported, in part, by the National Science Foundation. Opinions expressed

is there problem with some sort of splashing giving the signal that Ken is getting

are those of the authors and not necessarily those of the Foundation.

References

Beard, K. V., 1992: Ice initiation in warm-base convective clouds: An assessment of microphysical mechanisms, *Atmos. Res.*, **28**, 125-152.

Braham, R. R., and D.A.R. Kristovich, 1996: On calculating the buoyancy of cores in a convective boundary layer, *J. Atmos. Sci.*, **53**, 654-658.

Chiu, C. S., and J. D. Klett, 1976: Convective electrification of clouds. *J. Geophys. Res.*, **81**, 1111-1123.

Gunn, R., 1954: Diffusion charging of atmospheric droplets by ions, and the resulting combination coefficients, *J. Meteor.*, **11**, 339-347.

Gunn, R., 1952: The electrification of cloud droplets in non-precipitating cumuli, *J. Meteor.*, **9**, 283-288.

Hobbs, P. V., and A. L. Rangno, 1985: Ice particle concentrations in clouds, *J. Atmos. Sci.*, **42**, 2523-2449.

Lauks, M. L., and C. H. Twohy, 1998: Size-dependent collection efficiency of an airborne counterflow virtual impactor, *Aerosol Sci. Technol.*, **28**, 40-61.

Imyanitov, I. M., Ye. B. Chubarina, and Ya. M. Shvarts, 1972: *Electricity in clouds*, NASA Tech. Tranl. F-718, Wash. D.C.

MacGorman, D.R., and W. D. Rust, 1998: *The Electrical Nature of Storms*, Oxford Univ. Press, New York.

Noone, K. J., J. A. Ogren, J. Heintzenberg, Charlson, R. J. and D.V. Covert, 1988: Design and calibration of a counterflow virtual impactor for sampling of atmospheric fog and cloud droplets. *Aerosol. Sci. Tech.*, **8**, 235-244.

Moore, C. B., Vonnegut, B. and F. J. Mallahan, 1961: Airborne filters for the measurement of atmospheric space charge. *J. Geophys. Res.*, **66**, 3219-3226.

Ogren, J.A., Heintzenberg, J. and R. J. Charlson, 1985: In-situ sampling of clouds with a droplet to aerosol converter. *Geophys. Res. Lett.*, **12**, 121-124 (1985).

Phillips, B. B., and G. D. Kinzer, 1958: Measurement of the size and electrification of droplets in cumuliform clouds. *J. Meteor* **15**, 369-374.

Pruppacher, H.R. and J. D. Klett, 1997: *The Microphysics of Clouds and Precipitation* Kluwer Acad. Press, Boston.

Rosinski, J., 1995: Cloud condensation nuclei as a real source of ice forming nuclei in continental and marine air masses. *Atmos. Res.* **38**, 351-359.

Rosinski, J. and G. Morgan, 1991: Cloud condensation nuclei as a source of ice-forming nuclei in clouds. *J. Aerosol Sci.* **22**, 123-133.

Tinsley, B. A., Rohrbaugh R. P, M. Hei, 2001: Electroscavenging in clouds with broad droplets size distributions and weak electrification. *Amos. Res.*, **59-60**, 115-135.

Tinsley, B. A., Rohrbaugh R. P, Hei, M and K. V. Beard, 2000: Effects of image charges on the scavenging of aerosol particles by cloud droplets and possible consequences for droplet charging and ice nucleation. *J . Amos. Sci.*, **57**, 2118-2134.

Twohy, C.H., Schanot, A.J. and W. A. Cooper, 1997: Measurement of condensed water content in liquid and ice clouds using an airborne counterflow virtual impactor. *J. Atmos. Oceanic Technol.*, **14,** 197-202.

Twomey, S., 1956: The electrification of individual cloud droplets. *Tellus*, **8**, 445-452.

Takahashi, T., 1975: Electric charge life cycle in warm clouds. *J. Atmos. Sci.*, **34**, 123-142.

Takahashi, T., 1972: Electric charge of cloud droplets and drizzle drops in the warm clouds along the Mauna Loa-Mauna Kea saddle road of Hawaii Island. *J. Geophys. Res.*, **77**, 3869-3878.

Vali, G., 1985: Atmospheric ice nucleation — a review. J. Rech. Atmos. **19**, 105-115.

Webb, W. L. and R. Gunn, 1955: The net electrification of natural cloud droplets at the earth's surface. *J Meteor.* **12**, 211-214.

OBSERVATIONS OF REDUCED LIQUID WATER CONTENT IN THE CENTRE OF CUMULUS CLOUD UPDRAFTS

Alan M. Blyth*, Sonia G. Lasher-Trapp‡, and William A. Cooper§

* University of Leeds, UK,
‡ Purdue University, USA
§ NSF and National Center for Atmospheric Research† Boulder, CO 80307

1 INTRODUCTION

It is well known that cumulus clouds are made up of one or more thermals. Recently, Blyth et al. (2004) showed that the circulation in these cloudy thermals is similar to that found in the laboratory thermals by Woodward (1959), for example. There is downward motion at the edges of the thermal and upward motion elsewhere, with a maximum velocity near the centre. It is common to observe significantly diluted fluid, or even complete holes in the centre of laboratory thermals as a result of entrainment and circulation in towards the centre (e.g. Scorer 1957 and Sanchéz et al. 1987). Simulations of cumulus clouds also often indicate a region of reduced liquid water content, L, in the region of maximum updraft. Blyth et al. (2004) showed examples of reduced L in a few observed clouds where the updraft and horizontal 1D divergence was strongest and complete holes were observed on two occasions. In this paper, we present more details of the phenomenon and illustrate the effect on the droplet size distribution (DSD) in the vicinity of the reduced-L regions.

2 DETAILS OF THE OBSERVATIONS

The observations were made with the National Center for Atmospheric Research (NCAR) C-130 aircraft during the Small Cumulus Microphysics Study which was conducted near Cape Canaveral, Florida from 7 July - 13 August, 1995. Our analysis is limited to shallow cumulus clouds of size up to about 4 km deep and 2 km wide.

Values of liquid water content were calculated by integrating the size distribution measured by the FSSP (e.g. Dye and Baumgardner 1984) and measured with the high-rate (1 kHz) Particulate Volume Monitor (PVM-100A; Gerber et al. 1994). The true air speed of the aircraft was about 110 m s^{-1}. Further details of the experiment are given by Lasher-Trapp et al. (2001).

3 RESULTS

The liquid water content measured by both the FSSP and PVM instruments decreased completely to zero in the region of maximum updraft in a cloud observed on 28 July (Figure 1). The maximum value of the updraft speed was about 12 m s^{-1}, although the maximum value of L was only about 2.3 g m^{-3} (ratio of liquid water content to the theoretical value in an undilute parcel, $L/L_{ad} \approx 0.5$). The cloud was about 800 m wide and downdrafts were observed on either side of the updraft. There is evidence in the PVM liquid water content time series that mixing was actively occurring on both sides of the hole.

Another complete hole was measured by the high-rate PVM in the region of maximum updraft in a cloud observed on 11 August (Fig. 2). There were in fact two major regions of reduced-L measured by the PVM instrument in the updraft, where there was divergence of the horizontal wind (labelled 'A' and 'B' in the figure). The cloud was about 700 m wide and the maximum updraft speed was about 10 m s^{-1}. The maximum value of the liquid water content was between 3 and 3.5 g m^{-3} ($L/L_{ad} \approx 0.8$). The decrease in liquid water content almost to zero towards the far edge of the updraft indicates the turbulent and asymmetric nature of the cloud. This feature may in fact be a hole in the centre of a bifurcated thermal in which a separate circulation pattern had formed. Notice that there was only a slight decrease in the

* *Corresponding author address*: Alan M. Blyth, Institute for Atmospheric Sciences, School of Environment, University of Leeds, Leeds, LS2 9JT, UK; e-mail: blyth@env.leeds.ac.uk

†NCAR is partially supported by the National Science Foundation

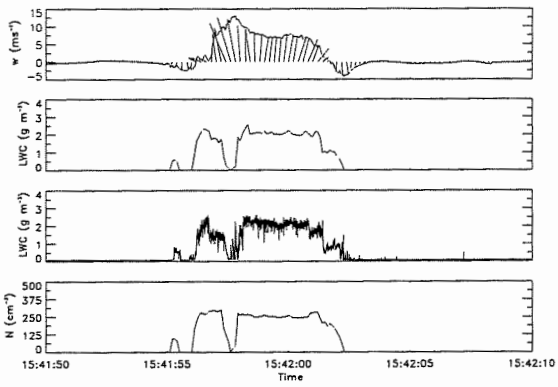

Figure 1: Vertical and horizontal wind along the aircraft track, FSSP-derived liquid water content, PVM liquid water content and total concentration of cloud droplets measured by the FSSP, respectively from top to bottom, for a cloud penetrated on 28 July at 1541:50. The penetration was made at an altitude, $z \approx 2.5$ km MSL.

total concentration of cloud droplets, N, across the first hole ('A'), but there was a substantial decrease across the second ('B').

Additional cases observed on 24 July are shown in Figs. 3 and 4. In the first of these (Fig. 3), the updraft speed, $w < 10$ m s^{-1} and $L < 2$ g m^{-3}. There is an anti-correlation between L and w and between L and N leading up to the centre of the updraft where there was a maximum reduction in L. The high-rate PVM liquid water content to the right of this region in particular is highly variable suggesting that mixing was actively occurring. The width of the reduced-L region is greater than 100

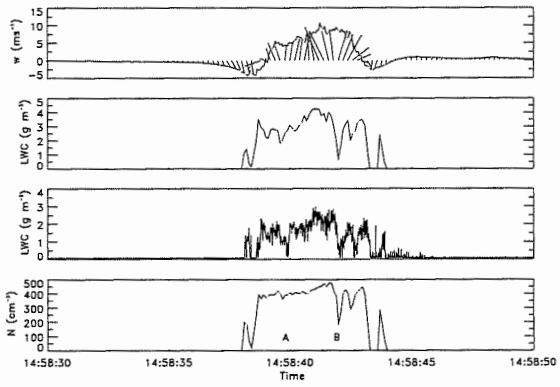

Figure 2: Similar to Fig. 1, but for 11 August, 1458:30; $z \approx 2.4$ km.

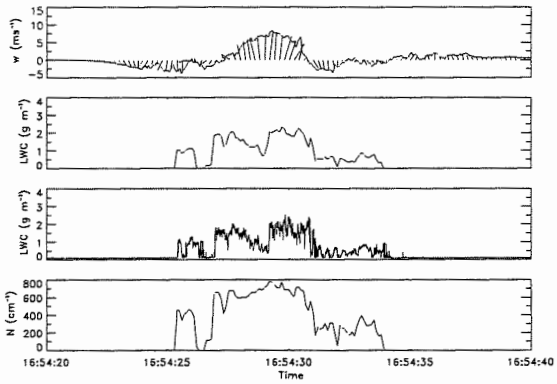

Figure 3: Similar to Fig. 1, but for 24 July, 1654:20; $z \approx 2.7$ km.

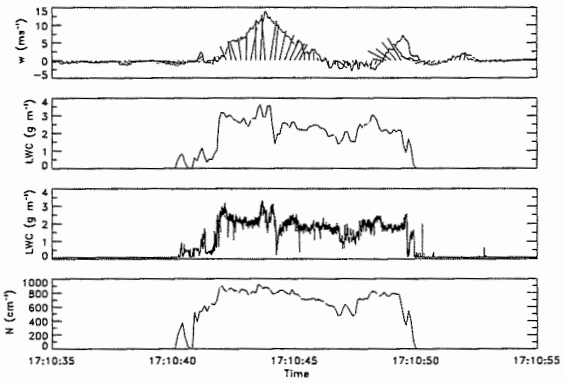

Figure 4: Similar to Fig. 1, but for 24 July, 1710:35; $z \approx 2.7$ km.

m. In contrast, the region of reduced L in the location of the maximum updraft is very narrow in the second July 24 case (Fig. 4). In this case, the maximum updraft speed was about 15 m s^{-1}, and the maximum value of liquid water content was about 3.5 g m^{-3} ($L/L_{ad} \approx 0.8$). The total concentration of cloud drops increased over the region. There was a larger reduction in L in the cloud adjacent to the central reduced-L region, again likely indicating the turbulent nature of the circulation pattern. There was only a slight decrease in N as a consequence of the activation of new drops.

The 10 Hz DSDs measured by the FSSP near the reduced-L regions observed on 28 July, 11 August and 24 July are shown in Figures 5, 6, 7 and 8, respectively. The DSD in the 28 July cloud (Fig. 5) was bimodal on both sides of the hole, with the peak at the smaller size becoming the dominant peak 0.2 s before the hole. This is presumably a consequence of the activation of new drops due

to the high supersaturation in rapidly ascending cloud with low values of L. The total concentration of drops decreased almost to zero. This did not occur in the August 11 case ('B' in Fig. 6) presumably because the hole detected by the fast response PVM probe was too narrow. In this case, the DSD was bimodal for about 0.5 s in the vicinity of the hole, although the peak at the smaller diameter was the dominant one only for 0.2 s. A similar pattern is evident for the smaller reduced-L region ('A').

Most of the DSDs in the first 4 s of the 24 July, 1654:27 case (Fig. 7) were bimodal except, interestingly enough, in the centre of the region of reduced-L, where there was only a peak at the smaller size. Fig. 7 shows that the peak at the large size decreased as the reduced-L region ('A') was approached. There was no apparent change in the DSDs in the vary narrow region of reduced-L at the centre of the updraft in the 24 July, 1710:42 case ('A' in Fig. 8). However, there is evidence in the DSD that new activation occurred in the adjacent, more significant hole at 1710:44.1 - 44.4. Many of the DSDs in the subsequent 1.5 s were bimodal.

4 CONCLUSIONS

Several regions of reduced liquid water content were observed in the "centre" of the updraft close to where the updraft speed and 1D horizontal divergence were maxima. Indeed, the liquid water content was reduced completely to zero in two penetrations. This observation was predicted by Scorer (1957), is observed in laboratory thermals, and is predicted by cloud model results. It is a result of the thermal circulation, with entrained air brought in towards the centre of the thermal and caught in the updraft. It is quite likely that the phenomenon is common in cumulus clouds, although it has not been highlighted previously.

It is likely that the peak at smaller sizes is due to activation on cloud condensation nuclei (CCN) that are either entrained or that result from evaporation of cloud drops. The liquid water content is low and the updraft speed is high, resulting in a high supersaturation. In many cases the number concentration is constant across the reduced-L region. Possibly the greatest significance of these high-supersaturation regions of cloud, however, is the potential for the rapid growth of cloud drops as suggested by Baker et al. (1980) and Cooper (1989).

5 Acknowledgements

We wish to thank the many people involved in SCMS, particularly Dr. Charles Knight and the personnel in ATD at NCAR. This work was supported by the National Science Foundation under grant ATM-9981937. The first author acknowledges the assistance received from the Institute of Atmospheric and Environmental Science, School of GeoSciences, University of Edinburgh.

6 REFERENCES

Baker, M.B., R.G. Corbin, and J. Latham, 1980: The influence of entrainment on the evolution of cloud droplet spectra: I. A model of inhomogeneous mixing. *Quart. J. Roy. Meteor. Soc.*, **106**, 581 - 598.

Blyth, A. M., S. G. Lasher-Trapp, and W. A. Cooper, 2004: A Study of Thermals in Cumulus Clouds. *Quart. J. Roy. Meteorol. Soc.*. In review.

Cooper, W. A., 1989: Effects of variable growth histories on droplet size distributions. Part I: Theory. *J. Atmos. Sci.*, **46**, 1301 - 1311.

Dye, J. E., and Baumgardner, D., 1984: Evaluation of the forward scattering spectrometer probe. Part I: Electronic and optical studies. *J. Atmos. Oceanic Tech.*, **1**, 329–344

Gerber, H., Arends, B. G. and Ackerman, A. S., 1994: New microphysics sensor for aircraft use. *Atmos. Res*, **31**, 235–252

Sánchez, O., Raymond, D. J. Libersky, L. Petschek, A. G., 1989: The development of thermals from rest. *J. Atmos. Sci.*, **46**, 2280–2292

Scorer, R. S., 1957: Experiments on convection of isolated masses of buoyant fluid. *J. Fluid Mech.*, **2**, 583–594

Woodward, B., 1959: The motion in and around isolated thermals. *Q. J. R. Meteorol. Soc.*, **85**, 144–151

explains why reduced LWC when there was most vigorous updrafts, might explain rapid growth of cloud droplets

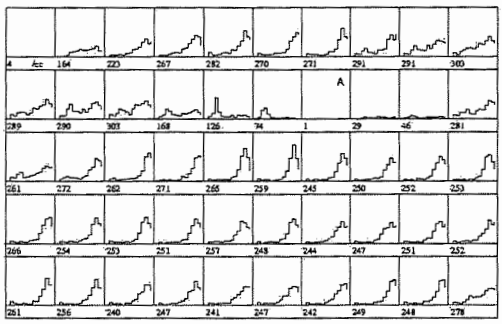

Figure 5: Cloud drop size distributions ($N(d)$ vs d) measured by the FSSP for 28 July, starting at 1541:56. The time period covered is 5 secs. Each distribution is 0.1 s; time increases to the right along the rows. The vertical and horizontal scales are 100 cm^{-3} and 32 μm, respectively. The centre of the hole is marked by the letter 'A'.

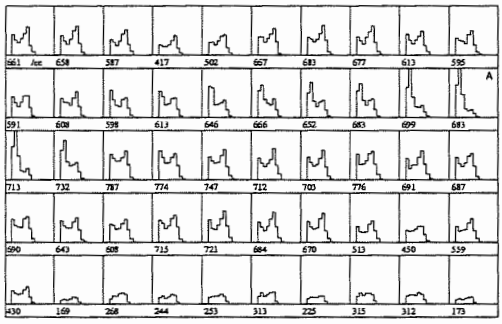

Figure 7: Same as Fig. 5, but for 24 July, 1654:27. The vertical and horizontal scales are 250 cm^{-3} and 51 μm, respectively. The region of maximum reduction in L is indicated by the letter 'A'. Note there is a problem with channel 1.

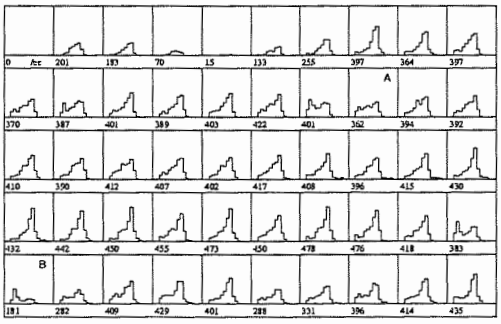

Figure 6: Same as Fig. 5, but for 11 August, 1458:38. The vertical and horizontal scales are 200 cm^{-3} and 51 μm, respectively. The centres of the two indicated reduced-L regions in Fig. 2 are marked by the same letters 'A' and 'B'.

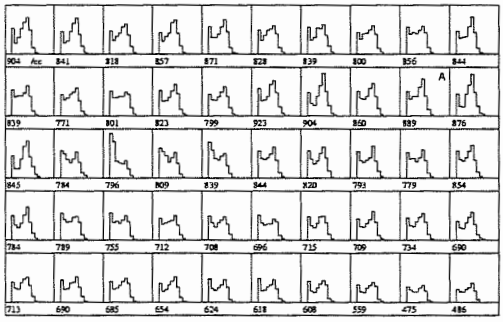

Figure 8: Same as Fig. 5, but for 24 July, 1710:42. The vertical and horizontal scales are 250 cm^{-3} and 51 μm, respectively. The region of reduced-L in the centre of the updraft is indicated by the letter 'A'. Note there is a problem with channel 1.

RELATIONSHIPS BETWEEN WATER VAPOR PATH AND PRECIPITATION OVER THE TROPICAL OCEANS

C.S. Bretherton, M. E. Peters, and L. E. Back

Department of Atmospheric Sciences, University of Washington, Seattle, Washington 98195 USA

1. INTRODUCTION

As known to scientists and nonscientists alike, it tends to be humid when and where there is sustained deep convective rainfall. Raymond (2000) even investigated the large-scale dynamical consequences of a bulk parameterization of tropical rainfall rate *P* in terms of a vertically-integrated moisture deficit from saturation.

Analyses of radiosonde data from various tropical locations (e.g. the TOGA COARE IFA) have shown that episodes of deep convection are followed by increases in mid- to upper-tropospheric relative humidity, while a relatively moist low to mid-troposphere helps initiate tropical deep convection (e. g. Numaguti et al 1995; Brown and Zhang 1997; Sherwood and Wahrlich 1999). Raymond et al. (2003) also found that in the east Pacific warm pool, enhanced surface evaporation driven by stronger winds also is associated with more rainfall.

In this study, we examine the relation of *P* to humidity over the global tropical oceans using four years of daily satellite microwave retrievals of *P*, water vapor path *W* and wind speed *U*. We find a strong quasi-exponential relationship between *P* and column moisture, and a weaker but still highly statistically significant and quite intriguing relation between *P* and wind speed in times and places where the tropospheric column is moist enough to permit substantial deep convective rainfall. We validate our findings using independent radar and satellite datasets. For more details on the P-moisture analysis, see Bretherton et al. (2004).

2. DATA DESCRIPTION

From Remote Sensing Systems Inc., we obtained version 5 retrievals of *P*, *W*, and *U* using the method of Wentz and Spencer (1998) for all available SSM/I and TMI overpasses in the years 1998-2001 over the global tropical ocean (20°S-20°N). Swath data from the 0.25°x 0.25° grid provided was binned into days then averaged to a coarser 2.5°x 2.5° grid. Typically 2-6 swaths intersect each grid box on each day. The retrieval is designed to minimize cross-talk between the retrieved quantities, an important consideration of us and one that requires independent checking.

We also estimated a daily-averaged saturation water vapor path W^* on this grid using ECMWF operational global temperature analyses. Free-tropospheric temperature varies by only 1-2 K over the Tropics, but this still induces 10% changes in saturation mixing ratio and hence W^* which prove important for our analysis. This variation mainly occurs on broad space and time scales adequately sampled by the global atmospheric observation system.

Corresponding author's address: Christopher S. Bretherton, Dept. of Atmospheric Sciences, Box 351640, University of Washington, Seattle, WA 98195, USA; E-Mail: breth@atmos.washington.edu.

3. RELATIONSHIPS BETWEEN SSM/I P AND W

The top panel of Fig. 1 shows the relation between daily-averaged *P* and *W* for all gridbox-days in the four year tropical ocean dataset, partitioned into four regions, the Indian Ocean, the Pacific west and east of the date line, and the Atlantic. For each region, all days in 1998-2001 at all locations were stratified into 1 mm water vapor path bins. In all four regions, *P* increases rapidly with *W*. However, the West Pacific and Indian Ocean regions tend to have a smaller *P* for a given *W*.

The West Pacific/Indian Ocean region has a slightly higher mean tropospheric temperature than other parts of the tropical oceans. Following Raymond (2000), one might conjecture that a given intensity of convection will produce a universal relative humidity profile. This would naturally lead to higher *W* for a given precipitation rate in the West Pacific and Indian Ocean compared to other ocean basins. With this conjecture in mind, we computed daily values of column-averaged relative humidity $r = W/W^*$, and sorted the data into *r*-bins of width 0.01. The bottom panel of Fig. 1 shows bin-averaged *P* vs. *r*. All four tropical ocean basins now more closely follow the same roughly exponential curve $P(r) = \exp[15.6\,(r-0.603)]$.

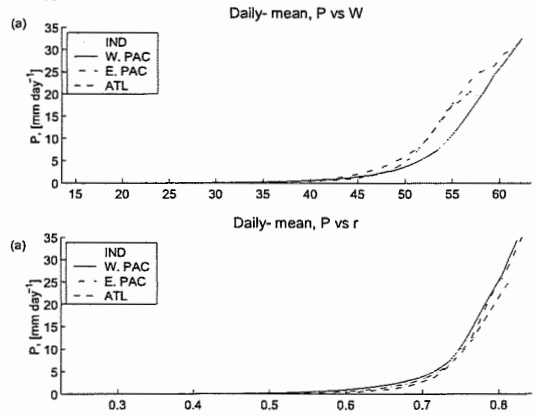

Fig. 1: Daily SSM/I precipitation *P* binned by water vapor path *W* (top) and column relative humidity *r* (middle) for gridpoints in four tropical ocean regions.

There is considerable variability about the mean *r-P* relationship. The 25th, 50th, and 75th percentiles of the daily *P* data for each *r* bin are plotted in Fig. 1c as dotted lines. The daily *P* has a skewed distribution in each bin (hence the mean substantially exceeds the median, lying roughly on the 65th percentile). The interquartile variability of *P* is roughly a factor of four for the moist, heavily precipitating bins, and an even larger factor for the lightly precipitating bins. Some of this variability is real, but some may also reflect SSM/I sampling uncertainty.

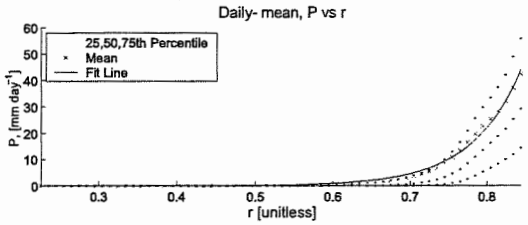

Fig. 2: All-tropics percentiles of *P* in *r* bins.

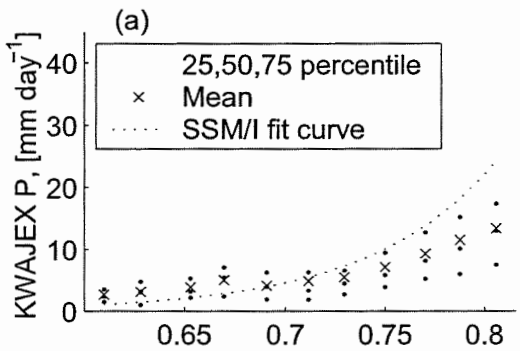

Fig. 3: Kwajalein radar-derived *P* vs. SSM/I *r*.

To check for mean biases and possible crosstalk between SSM/I *P* and *W*, we used radar and radiosonde datasets from Kwajalein Island in the tropical west Pacific Ocean. Soundings from the TRMM KWAJEX experiment during July-September 1999 (Sobel et al. 2004) suggest that SSM/I accurately estimates the mean and daily variability of *W*. Most of this variability comes from humidity variations between 900-600 mb; at this location, humidity in the subcloud layer is surprisingly constant and uncorrelated with daily rain rate. A six month time series of daily rainfall averaged over a 150 km radius circle around the TRMM Kwajalein ground validation radar was obtained by averaging rain maps derived from volume scans every 15 minutes using carefully calibrated rainfall-reflectivity relationships (Houze et al. 2003). Based on this comparison, SSM/I tends to overestimate strong precipitation events while underestimating weak daily area-averaged precipitation rates around Kwajalein. This produces the *r-P* percentile plot shown in Fig. 3, which has a lesser slope but also a tighter fit than Fig. 2. Thus, SSM/I gives a qualitatively correct but quantitatively more uncertain view of the relation of precipitation to column relative humidity.

At monthly averaging scales, the relation between SSM/I *P* and column relative humidity is much tighter, with correlation coefficients of 0.5-0.8 for most grid boxes, and a best-fit relationship *P* [mm d-1] = exp[11.4(*r*-0.522)]. There is slight regional variability that we attribute to varying levels of day-to-day humidity variation in different locations, but the above fit provides (modulo its possible biases) a useful constraint on the monthly climatology of global numerical weather and climate models.

3. RELATIONSHIPS BETWEEN SSM/I P AND U

We examined the relationship between daily averaged windspeed and precipitation (from the SSM/I and TMI) at 10N at several gridboxes which are in the Pacific ITCZ for much of the year. For each gridbox, all four years of windspeed and precipitation data were sorted by windspeed and subdivided into bins containing 60 gridpoint-days. Within each such bin, the mean, 25th, 50th and 75th percentiles of the 60 precipitation estimates are calculated. Fig. 4 illustrates this analysis in the Eastern Pacific ITCZ (at 95W, 10N) and at 160E, 10N in the western Pacific warm pool. In the western warm pool (Fig. 4a) no relationship is visible. In the Eastern Pacific however (Fig. 4b), there tends to be more rainfall on days with stronger winds, as found by Raymond et al. (2003) from limited in situ data from EPIC2001.

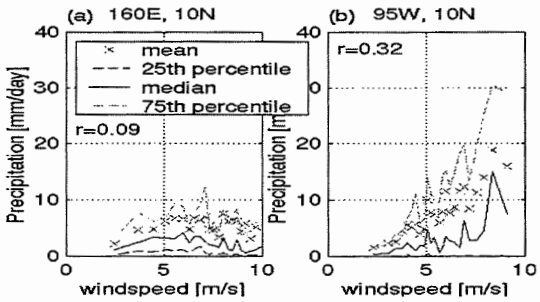

Fig. 4: Distribution of daily precipitation binned against wind speed. X's show bin-mean precipitation, and lines show 25th, 50th and 75th percentiles of 60 2.5° gridpoint-day bins.

A complicating factor in this analysis is that the precipitation belts vary with the seasonal cycle. Only when convection is easily and frequently initiated do we expect to see a correlation between windspeed and precipitation. Outside deep convective regions, high windspeeds still enhance surface moisture fluxes, but this moisture is stored and advected downstream rather than being rained out locally.

To isolate those times and locations where the atmosphere is susceptible to deep convection, we

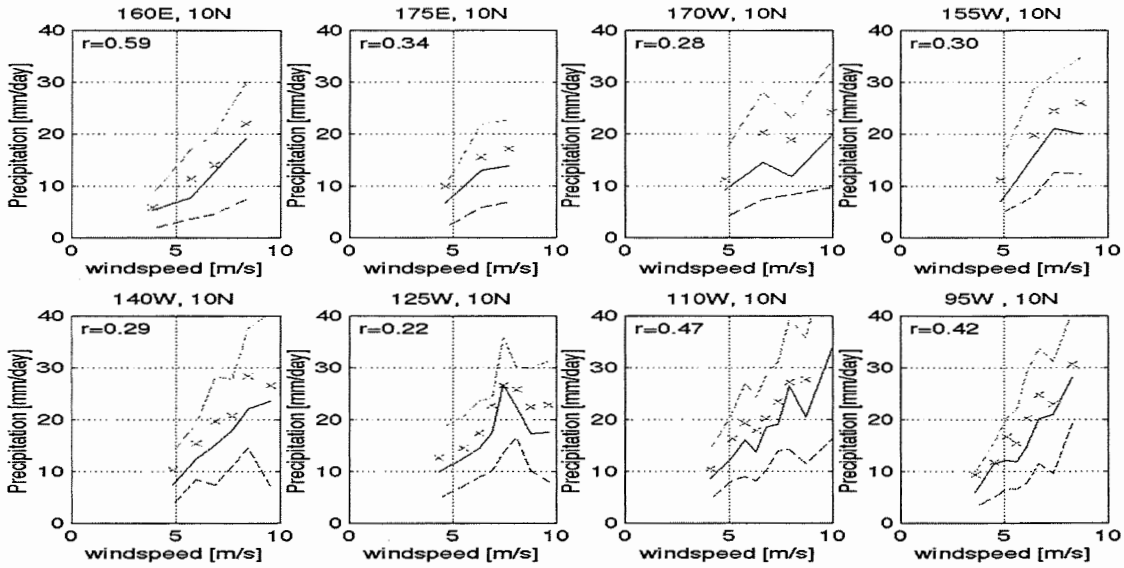

Fig. 5: Daily precipitation distribution binned against wind speed for points throughout the Pacific ITCZ, when column relative humidity is greater than 0.75.

repeated the analysis of Fig. 4, but retaining only those days in the four-year record with column integrated relative humidity greater than 0.. Fig. 5 shows that with this r threshold, at all ITCZ locations examined, there is a remarkable linear correlation between wind speed and precipitation. On days with stronger winds there tends to be more rainfall.

Wind speed explains only a moderate, but highly statistically significant amount of the variability in precipitation, as is visible in the quartiles plotted in Fig. 5. The correlation coefficient is highest in the east and west Pacific warm pools, where it can exceed 0.5. The regression slope also varies somewhat with location.

The estimated increase in evaporation that occurs as SSM/I wind speed rises from 4 to 8 m/s is less than 3 mm/day, small compared with the observed increases in precipitation (Fig. 5). This is consistent with a "convergence feedback" (Zebiak 1986, Sobel and Bretherton 2000), in which enhanced evaporation destabilizes the tropospheric column, producing more convection. The associated low-level moisture convergence adds to the increased evaporation to produce a much larger increase in precipitation. However, both NCEP and ECMWF reanalyses also suggest that stronger winds also tend to enhance horizontal dry advection into the ITCZ, countering the effect of evaporation. We currently do not have a fully satisfactory explanation of the result in Fig. 5.

We tested whether wind speed affects precipitation primarily by increasing column relative humidity. To do this, we binned all daily grid columns in the east Pacific ITCZ (where the *P-U* correlations are particularly pronounced) into *r*-bins of width 0.02, and calculated the *P-U* regression in each *r*-bin separately. We found that a clear linear relationship in each *r*-bin, and the slope increased rapidly with *r*.

4. KWAJALEIN RADAR P-U TEST

There are a number of uncertainties involved in the retrieval of precipitation estimates from the SSM/I on a daily timescale. To address these uncertainties, we used the radar data to calculate the distribution of the Kwajalein radar-derived rainfall, binned by wind speed, for days when column relative humidity is above 0.75 (shown in Fig. 6a). The results of this analysis are similar to those using the microwave-derived precipitation (Fig. 6b).

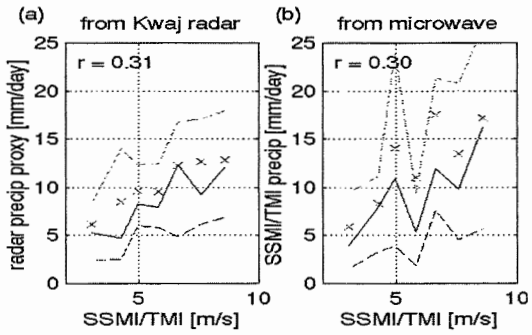

Figure 6: (a) Distribution of daily Kwajalein radar-derived precipitation binned by SSM/I windspeeds (bin size: 30 gridpoint-days). (b) same, using SSM/I precipitation averaged over the two gridpoints closest to Kwajalein.

We also used Quikscat winds vector-averaged onto the same grid in place of the SSM/I winds. Again, a similar linear relationship between P and wind speed

is seen. This suggests that storm-scale gustiness from precipitating convective systems is probably not responsible for the correlation, as this would have a minimal effect on the vector-average wind on 250 km scales.

4. CONCLUSIONS

SSM/I retrievals over the tropical oceans imply robust relationships between daily precipitation and both column relative humidity and wind speed. These relationships help us understand the 'quasi-equilibrium' character of tropical convection. Similar relationships are also seen in limited comparisons with other global datasets, though this comparison also points out quantitative uncertainty and possible biases in the SSM/I retrievals of both precipitation and wind speed. Similar relationships are now being seen in cloud-resolving model simulations and are useful tests of the physical parameterizations of global numerical weather and climate models.

The precipitation-humidity relationship should not be regarded as causal, but correlative. It probably stems from lower tropospheric humidity anomalies that lead convection by a few hours, superposed on upper tropospheric humidity anomalies that lag the convection, to produce the observed simultaneous correlation.

The slope of the SSM/I precipitation-wind speed relationship depends on location and column relative humidity. Although some simple arguments rationalize such a correlation, a quantitative theory that explains this slope and accounts for other effects such as horizontal moisture advection has so far eluded us.

Other datasets such as the TRMM Precipitation Radar combined with TMI water vapor path and Quikscat winds would obviously be useful for corroborating and further understanding our findings.

5. ACKNOWLEDGMENTS

This work was sponsored by NASA grants NAGS5-10624 and NAG5-9657, and NSF grant DMS-0139794. We thank Chelle Gentemann for helping us get started with the RSS microwave datasets.

6. REFERENCES

Bretherton, C. S., M. E. Peters, and L. E. Back, 2004: Relationships between water vapor path and precipitation over the tropical oceans. *J. Climate*, **17**, 1517-1528.

Brown, R. G., and C. Zhang, 1997: Variability of midtropospheric moisture and its effect on cloud-top height distribution during TOGA COARE. *J. Atmos. Sci.*, **54**, 2760-2774.

Numaguti, A., R. Oki, K. Nakamura, K. Tsuboki, N. Misawa, T. Aisai, and Y.-M. Kodama, 1995: 4-5 day-period variation and low-level dry air observed in the equatorial western Pacific during the TOGA-COARE IOP. *J. Meteor. Soc. Japan*, 73, 267-290

Raymond, D. J., 2000: The thermodynamic control of tropical rainfall. *Quart. J. Roy. Meteor. Soc.*, **129**, 889-898.

Raymond, D. J., G. B. Raga, C. S. Bretherton, J. Molinari, C. Lopez-Carillo and Z. Fuchs, 2003: Convective forcing in the intertropical convergence zone of the east Pacific. *J. Atmos. Sci.*, **60**, 2064-2082.

Sherwood, S. C., and R. Wahrlich, 1999: Observed evolution of tropical deep convective events and their environment. *Mon. Wea. Rev.*, **127**, 1777-1795.

Sobel, A. H. and C. S. Bretherton, 2000: Modeling tropical precipitation in a single column. *J. Climate*, **13**, 4378-4392

Sobel, A. H., S. E. Yuter, C. S. Bretherton, and G.N. Kiladis, 2004: Large-scale meteorology and deep convection during TRMM KWAJEX. *Mon. Wea. Rev.*, 132, 422-444.

Wentz, F. J. and R. W. Spencer, 1998: SSM/I rain retrievals within a unified all-weather ocean algorithm. *J. Atmos. Sci.*, **55**, 1613--1627,

Zebiak, S. E., 1986: Atmospheric convergence feedback in a simple model for El Nino, *Mon. Wea. Rev.*, **114**, 1263-1271.

difference between causal and correlative relationships
- need to explore these relationships in the cloud data sets

RELATIONSHIP BETWEEN THE HYDROMETEOR SIZE DISTRIBUTION AND CLOUD MICROPHYSICAL PROPERTIES USING DISDROMETRIC DATA

Clelia Caracciolo[1], Franco Prodi[1,2], Alessandro Battaglia[1]

[1]University of Ferrara, Dept. of Physics, Ferrara, I-44100, Italy
[2]ISAC-CNR, Bologna, I-40129, Italy

1. INTRODUCTION

One of the most complete descriptions of rain is given by its drop size distribution (DSD). Several studies on the DSD, over different climatic regions and in different parts of the world, have been encouraged in the past, since the early work of Marshall and Palmer (1948) (hereinafter MP), by the different applications of the DSD and variety of instruments related to the DSD applications. The problem of accurately describing the DSD temporal evolution and finding analytical functions which fit the observed DSD remains, however, a major obstacle in cloud physics.

Only a few works focus the attention on mid-latitude continental rain (e.g. Waldvogel, 1974; Ulbrich, 1983). Most of them concern the study of tropical rains, (e.g. Willis, 1984; Tokay and Short 1996, hereinafter TS; Testud et al., 2001). Moreover there is an almost total lack of studies performed in Italy.

This work aims at testing the significance of the existent DSD models and parameterizations in the different meteorological conditions in Ferrara (northern Italy), by using a Joss and Waldvogel (1967) (hereinafter JW) disdrometer and, after a critical review of previous works and approaches, to propose modifications and improvements. In particular, two recent normalization approaches (one and two-parameter) to the DSD are tested. Recently some authors (Uijlenhoet, 1999) have investigated the potential of an extension of the Sempere Torres et al. (1994) scaling-law, by formulating a scaling-law for the Doppler velocity spectrum, using the radar reflectivity factor Z as a reference variable. This might provide interesting possibilities for the analyses of data collected with vertically pointing Doppler radars. Motivated by such argumentations, the use of the radar-reflectivity factor Z as a reference variable is applied to the Ferrara database and tested, after the development of a detailed theoretical formulation. Also, the Testud et al. (2001) two-parameter normalization approach is tested. Case studies of the DSDs and rainfall integral parameters time variability are also analysed in order to characterize microphysically the Ferrara events, given the total lack of studies in this area. This aspect also allows a comparison of the results with the ones that have recently appeared in the literature.

The identification between convective (C) and stratiform (S) precipitation involves a variety of subtleties. In the past considerable effort has gone into the development of methods for separating these two types of rainfall, especially ones based on radar images and wind-profilers data (e.g. Williams et al., 1995). A disdrometer approach involves the distinction between the properties of the DSDs (Waldvogel, 1974). In particular, TS and Testud et al., 2001 proposed classification methods based on the DSD analysis applying them to tropical oceanic case studies. In this work, to face the specific characteristics of continental mid-latitude rain, a new C/S discrimination algorithm is developed.

Much of this work is based on the first author's PhD thesis (Caracciolo, 2004).

2. DATA AND METHODOLOGY

The DSD measurements in this work are collected by a standard JW disdrometer. The disdrometer is located on the roof of the Department of Physics of the University of Ferrara, Italy, (about 25 meters from surface level) since November 2001. Ferrara is located in a mid-latitude continental region in the Po Valley, northern Italy, about 60 Km inland from the Adriatic Sea. The latitude and longitude coordinates are: 44.83 N and 11.62 E. The rainfall-rate measurements are validated by a tipping-bucket rain gauge (TB-RG). The gauge data are collected with 1-min resolution (like the JW disdrometer). The JW data consist of number of raindrops n_i of diameter D_i in 20 categories, ranging in size from 0.35 to 5.25 mm. No correction is applied to the DSD to account for the dead time associated with the recovery time of the JW disdrometer transducer.

The analysed database consists of seven months of data, from November 2001 to May 2002. It includes about 30 different precipitation events, for a total of about 800 minutes of rain. According to TS, rainfall-rate intensity can be categorized into six classes: very light ($R<1$ mm/h), light ($1\leq R<2$ mm/h), moderate ($2\leq R<5$ mm/h), heavy ($5\leq R<10$ mm/h), very heavy ($10\leq R<20$ mm/h), extreme ($R\geq 20$ mm/h). To discriminate the C and S precipitation the R and Z 1-minute time series are analysed. The C (S) rainfall is characterized by R> (<)

Corresponding author's address: Clelia Caracciolo, University of Ferrara, Dept. of Physics, Ferrara, I-44100, Italy; E-Mail: caracciolo@fe.infn.it.

looks at various disdrometer relationships

10 mm/h and Z> (<) 38 dBZ; moreover the C rain is highly fluctuating and short in duration, while the S rain can persist per hours.

3. RESULTS

3.1 Characterization of the DSD in Ferrara using a JW disdrometer with classical analysis methods

The chosen events are characterized micro-physically by analysing the time series of raindrop concentrations, DSDs, rainfall integral parameters and median diameters. The C events are characterized by large raindrop concentrations, large median diameters, large reflectivities and wider DSDs than the S events. Empirical Z-R analyses of the data are also performed. A good agreement with theory and past works in mid-latitude continental rainfall is found. The C 1-minute spectra have $Z=703.7R^{1.29}$ while the S 1-minute spectra have $Z=280.74R^{1.35}$ (near to the MP values of $Z=200R^{1.6}$). Considering all the database, it is also found that: $D_0=1.1R^{0.21}$, which compares well with the MP one $D_0=0.9R^{0.21}$ while differing somewhat from the tropical $D_0=0.97R^{0.158}$ and $D_0=1.26R^{0.10}$ of Willis (1984) and TS respectively.

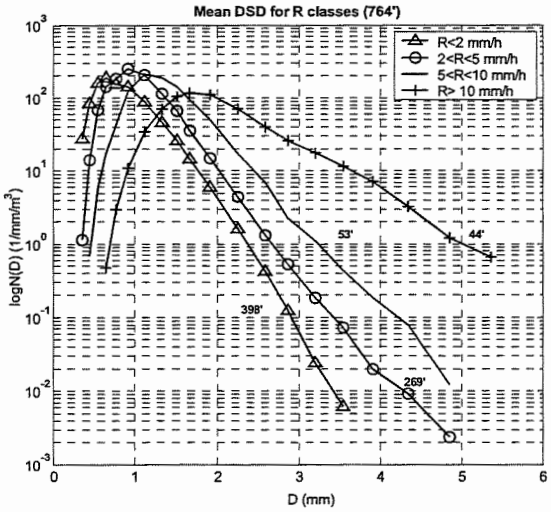

Fig. 1: Average gamma DSDs for the Ferrara database for four rainfall-rate categories

The equivalent exponential and gamma DSDs, according to Waldvogel (1974) and TS methods, are tested. The C events are characterized by wider (large size) spectra with respect to the S events, which are characterized by narrow (small size) spectra. The MP is not a good parameterization, especially in strong C rainfall events. Therefore, with sufficient averaging, the distribution for the Ferrara rainfall can be described approximately well by a gamma DSD and to a lesser extent by an exponential DSD with a value of N_0 less than the one found by MP. The three mean gamma DSD parameters over the entire database are: $\langle\Lambda\rangle=5.66$ [mm^{-1}], $\langle m\rangle=5.18$ and $\langle N_0\rangle=5.52\cdot10^5$ [$mm^{-1-m}m^{-3}$]. The C rainfall is also characterized by less N_0 and Λ parameters with respect to the S rainfall, and a high m. Moreover, the slope and intercept parameters of the gamma fit the DSD decrease, as the rainfall rate threshold increases from 2 to 10 mm/h, while m increases, indicating a more marked presence of large drops (see fig. 1). In addition, the TS and Testud et al., 2001 C/S discrimination algorithms do not work well for the mid-latitude events studied here.

3.2 A new C/S discrimination algorithm based on the three gamma DSD parameters computed with a new method of moments

The attention is therefore focused only on the gamma DSD. A new method of moments that is a modification of the one employed by TS is developed to deduce the values of the three gamma DSD parameters from the higher spectral moments (fourth, fifth and sixth), as shown in the equations below:

$$\Lambda[1/mm]=\frac{M_4M_5}{M_4M_6-M_5^2}=\frac{1}{D_6-D_5}$$

$$m=\Lambda\frac{M_6}{M_5}-6=\Lambda D_6-6$$

$$N_0[1/mm/m^3]=\frac{M_5\Lambda^{m+6}}{\Gamma(m+6)}$$

The advantages of this method are that: the higher order moments are not sensitive to the underestimation of small drops in the JW disdrometer, and is also analytically very simple allowing an immediate physical interpretation of the three gamma DSD parameters. To test the new method, the mean square error between the observed and fitted DSD is computed. It is found that, compared to the TS method of moments, the new method is effective, especially at high R, when the underestimation of small drops due to the JW disdrometer dead time problem is more significant. The new method is also tested by comparing R computed from these values with the observed R. The results indicate a good agreement between the two estimates.

A new C/S discrimination algorithm is subsequently implemented, based on the knowledge of m and Λ. The knowledge of the three gamma DSD parameters is firstly exploited to identify a characteristic parameter, named the peak diameter D_p defined as m/ Λ, which allows the C/S discrimination. Analysing the 1-minute time series of this parameter, it is found that if $D_p\geq1.5$ mm, R can range from very heavy to extreme values; if $D_p\leq1.5$ mm, R<10 mm/h; if $D_p\leq1.0$ mm, R<5 mm/h. In

the case of light or very-light precipitation, $D_p \leq 1$ mm is always obtained. A direct correlation is also found between this parameter and the equation: $1.635\Lambda - m = 1$. In particular, it is found that: if $(1.635\Lambda - m) < 1$, $D_p > 1.5$ mm; if $(1.635\Lambda - m) > 1$, $D_p < 1.5$ mm. Therefore, the line $1.635\Lambda - m = 1$ can be successfully used as a valid alternative to the classical C/S discrimination algorithms (e.g. TS and Testud et al., 2001). All the events above this line are S, the ones below are C (see fig. 2).

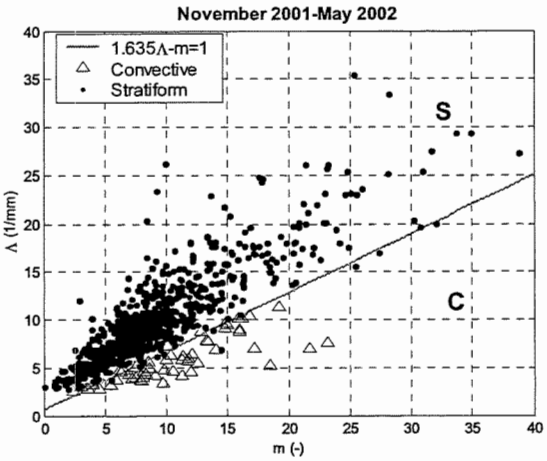

Fig. 2: Relationship between Λ and m for the Ferrara database

3.3 Application of the one and two-parameter DSD normalizations to the Ferrara database

Two recent normalization approaches (one and two-parameter) to the DSD are tested on the Ferrara database, to reveal the typical DSD shapes and attain a further microphysical characterization of the events.

The use of the radar-reflectivity factor Z as a reference variable in the scaling law theory (Sempere Torres et al., 1994) is tested (never appearing in literature), after the development of a detailed theoretical formulation. If Z is used as a reference variable the scaling law becomes: $N(D,Z)=Z^{\alpha}g(D/Z^{\beta})=Z^{\alpha}g(x)$. The advantages of using Z as a reference variable can be synthesized as follows: less dispersion among the data; a better discrimination between C and S events; no dependence on the terminal hydrometeor fall speed; a possible application to wind profiler data to infer vertical profiles of the scaling exponents and of g(x).

For the Ferrara database, it is found that all the events are far from the equilibrium ($\alpha=1$; $\beta=0$) and therefore the DSD must have been varied mainly by a significant variation in the diameter, pointing toward a situation of size-controlled variability. Two different analytical parameterizations are fitted to the empirical g(x): an exponential, $g(x)=ke^{-\lambda x}$, and a gamma, $g(x)=kx^{m}e^{-\lambda x}$, parameterization. The most representative values for each category are: $\beta=0.15$ and $\lambda(\exp)=8.04$ for C events and $\beta=0.17$ and $\lambda=9.43$ for S events (closer to the MP value of $\lambda=9.6$). The statistics over all the database are: $0.1<\beta<0.25$, $8<\lambda<18$, $10^3<k<10^5$ for the exponential fit and $17<\lambda<40$, $10^6<k<10^{14}$, $4<m<11$ for the gamma fit. Moreover, the C events have k and λ values of a gamma DSD, and k and λ values of an exponential DSD less than the S events, but a high m. The gamma parameterization provides a good fit to the data. The shapes of the scaled spectra are narrow and bent downward in the S events, wide and strongly bent downward in the C events. Applying a growth threshold (R>1 mm/h, see fig. 3, R>5 mm/h and R>10 mm/h) on the data, the difference between employing the first two thresholds in the scaling analysis is not very pronounced, either in the scaling exponents or in the shape of the generalized distribution g(x). Moreover, $\lambda(\exp)$ is very low for R>10 mm/h (the median volume diameter is large), m increases to 10.5 for the third category (the spread of the DSD with respect to the mean drop size changes markedly), A of the Z-R relationship is very large (indicative of very large D_0 values), and b is very small for the third category.

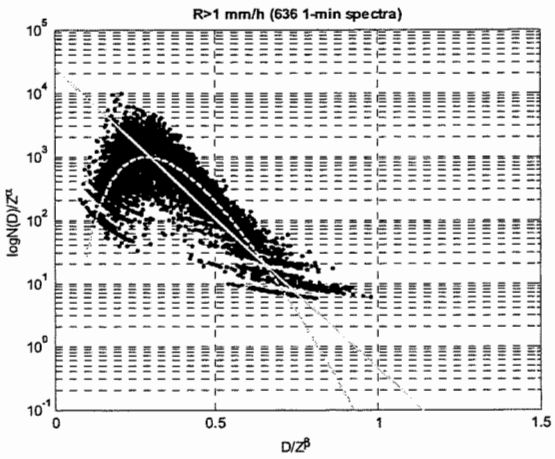

Fig. 3: Scaling analysis of DSDs using Z as a reference variable for the Ferrara database for R>1 mm/h (solid line: exponential; dashed curve: gamma fit).

Applying the Testud et al., 2001 two-parameter normalization to the Ferrara database, it is found that there is no a clear distinction between the C and S categories: S events have $N_0^*=2.99\cdot10^3$ $mm^{-1}m^{-3}$, C events have $N_0^*=3.35\cdot10^3$ $mm^{-1}m^{-3}$ (both very far from the MP value of 8000). Applying a growth threshold (R>1 mm/h, R>5 mm/h and R>10 mm/h) on the data, it is found that whatever the rain category, the physical variability in N_0^* is quite large, while D_m increases steadily.

The average normalized spectra are close to the exponential [F(X)=exp(-4X)], but exhibit a tendency to a bow shape with a marked convexity beyond X=0.5, especially in the C events. The m values do not show very distinct values between each event; most spectra fall in the interval 6<m<10. In conclusion, as in the Testud et al. (2001) work, two features mark the overall statistics (even if with different values): a large variability of N_0^* and D_m and a remarkable stability of the shape of the normalized DSD.

4. CONCLUSIONS AND FURTHER WORK

The principal aim of this work was to test the significance of existent DSD models and parameterizations in Ferrara (northern Italy), using a JW disdrometer and, after a critical review of the previous works and approaches, to propose modifications and improvements. Another aim was to characterize the DSD in Ferrara, given the total lack of studies in this area.

The exponential and gamma DSDs were tested. With sufficient averaging, the distribution for the Ferrara rainfall can be described approximately by a gamma DSD and to a lesser extent (especially the light/moderate events) by an exponential DSD, with a value of N_0 less than the one found by MP. Moreover, the classical C/S discrimination algorithms (e.g. TS) do not work well for the mid-latitude events studied here.

The attention was therefore focused only on the gamma DSD. A new method of moments has been developed for deducing the DSD parameters values using only the higher order moments (fourth, fifth and sixth). This method is effective, especially at high R, when the underestimation of small drops due to the JW disdrometer dead time problem is more significant. Although the new method is applied to experimental data for continental mid-latitude rain, it is general, and it is supposed it could be used also with data acquired in any type of rainfall and in different climatic regions, especially where electromechanical impact disdrometers (in view of their poor sampling of small drops) are used. Based on the knowledge of the three gamma DSD parameters, a new C/S discrimination algorithm was implemented. This new C/S algorithm seems more suitable for mid-latitude continental areas than the classical ones (e.g. TS and Testud et al., 2001). To seek confirmation of this, in future work the algorithm will be tested on other mid-latitude databases.

Finally, two recent normalization approaches (one and two-parameter) to the DSD were tested. For the first time, the use of the radar-reflectivity factor Z as a reference variable in the scaling-law theory (Sempere Torres et al., 1994) was tested, by applying it to the Ferrara database, after the development of a detailed theoretical formulation. The main advantages of using radar reflectivity Z as a reference variable, instead of R, are that any dependence on the terminal fall velocity is removed and a possible application to wind profiler data is allowed. The testing of this scaling law on profiler data is under analysis. Also, the two-parameter normalization approach was tested, showing discrepancies with the values found in Testud et al. (2001).

During this work, radar data were not available. A cooperation with the SMR (Meteorological Regional Service), which manages the C-band radar at S. Pietro Capofiume (about 20 Km from Ferrara) has recently started; this will allow more accurate DSD analysis.

5. REFERENCES

Caracciolo C., 2004: Reconsideration of the analysis methods and measuring instruments for the raindrops size distributions investigation. PhD thesis. Ferrara University, Italy, 265 pp. (available from the author).

Joss J. and A. Waldvogel, 1967: Ein spectrograph für niederschlagstropfen mit automatischer auswertung. Pure and Appl. Geophys., 68, 240-246.

Marshall J.S. and W.M. Palmer, 1948: The distribution of raindrops with size. J. Meteor., 5, 165-166.

Sempere-Torres D., J. Porrá J. and J.D. Creutin, 1994: A general formulation for rain drop size distribution. J. Appl. Met., 33, 1494-1502.

Testud J., S. Oury, R.A. Blank, P. Amayenc, X. Dou, 2001: The concept of "Normalized" distribution to describe raindrop spectra: a tool for cloud physics and cloud remote sensing. J. Appl. Met., Vol. 40, 1118-1140.

Tokay A. and D. Short, 1996: Evidence from tropical raindrop spectra of the origin of rain from stratiform versus convective. J. Appl. Meteor., 35, 355-371.

Uijlenhoet R., 1999: Parameterization of rainfall microstructure for radar meteorology and hydrology. PhD thesis. Wageningen University, the Netherlands, 279 pp.

Ulbrich C., 1983: Natural Variations in the analytical form of the raindrop size distribution. J. Clim and Appl. Met., 22, 1764-1775.

Waldvogel A., 1974: The N_0 jump of raindrop spectra. J. Atmos. Sci., 31, 1067-1078.

Williams C.R., W.L Ecklund and K.S. Gage, 1995: An algorithm for classifying rain in the tropics using 915 MHz wind profiler. J. Atm. Oc. Tech., 12, 996-1012.

Willis P.T., 1984: Functional fits to some observed drop size distributions and parameterization of rain. J. Atmos. Sci., 41, 1649-1661.

CONDENSATIONAL GROWTH OF DROPLETS IN WARM CUMULUS CLOUDS

A. Coals*, A.M. Blyth*, J.-L. Brenguier†, A.M. Gadian, and W.W. Grabowski§

* School of the Environment, University of Leeds, UK
† Météo-France, Toulouse, France
§ National Center for Atmospheric Research, Boulder, CO 80307, USA

1 INTRODUCTION

Despite a great deal of research into the understanding of microphysical properties of warm clouds over the past 40 years, an important issue remains unresolved; that of cloud droplet size distributions predicted by adiabatic parcel models being much narrower than those observed in warm cumulus clouds. In addition, simple calculations of cloud droplet growth tend to produce single-mode distributions, while bi- or multi modal drop size distributions are commonly observed. Adiabatic parcel calculations only seem to replicate this bi- or multi-modality in special cases (Warner 1969; Feingold and Chuang 2002). In this paper we show that the complex nature of these observed size distributions can be explained by the mixing between the cloudy (saturated) and clear (dry) air in the diluted regions of cumulus clouds.

Inaccurate representations of cloud droplet size distributions have a number of consequences, but most important to cloud microphysics is that coalescence rates are very sensitive to the sizes of the cloud droplets. If the size distributions cannot be predicted accurately, the calculations of precipitation development in warm clouds is affected. In this paper, only the condensational growth of cloud droplets – the pre-cursor to coalescence – is considered.

2 NUMERICAL MODEL

The three-dimensional non-hydrostatic anelastic fluid model of Smolarkiewicz and Margolin (1997) is used to simulate observed clouds. The model incorporates the droplet microphysical scheme of Brenguier (1991), where the CCN activation process is parameterized, total droplet condensation in non-diluted cloud volume is assumed constant and equal to initial concentration N_0. Following Brenguier and Grabowski (1993), a simplified form of the droplet condensational growth equation is used,

$$\frac{dr}{dt} = \frac{A\,S(t)}{r+a}\Bigg|,$$

where a is the accommodation coefficient, A is a constant, and S is the supersaturation. When this is integrated along a path in a cloud gives

$$(r+a)^2 = (r_0+a)^2 + b^2(t),$$

where r_0 is the initial radius at initial time t_0 and

$$b^2(t) = (r+a)^2 - (r_0+a)^2 = 2A\int_{t_0}^{t} S(t)dt\Bigg|.$$

This parameter, b^2, represents the summation of the supersaturation history of the parcels, which determines the growth of the spectrum.

3 DETAILS OF THE OBSERVATIONS

The observations were made with the National Center for Atmospheric Research (NCAR) C-130 aircraft during the Small Cumulus Microphysics Study which was conducted near Cape Canaveral, Florida during July–August 1995. Further details of the experiment are given by Blyth et al. (2003).

In this work, we model clouds on two days, the 24th July and 10th August, with maximum observed concentration of cloud drops of about 800 and 500 cm^{-3} respectively. The project days were chosen because the size distribution observed in clouds on the 10th August was rarely bimodal, which is unusual for the SCMS clouds.

4 RESULTS

Results of both cases are discussed in the poster, but only the continental case (24th July 1995) will be presented here.

*Corresponding author address: Alison Coals, Institute for Atmospheric Sciences, School of Environment, University of Leeds, Leeds, LS2 9JT, UK; e-mail: alison@env.leeds.ac.uk

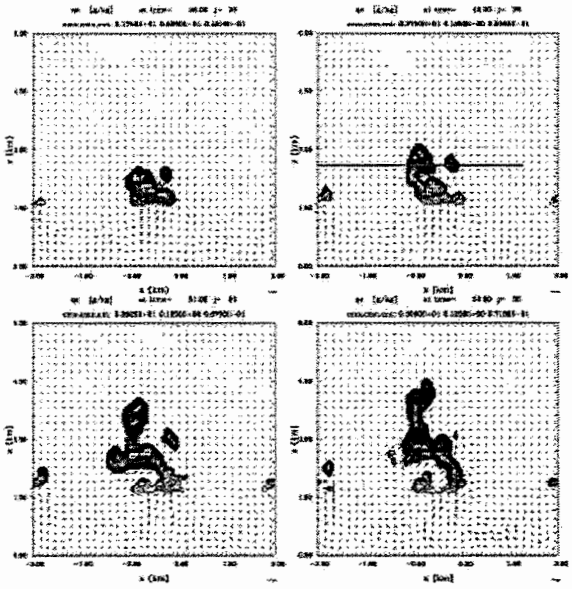

Figure 1: Vertical cross-sections of simulated cloud water mixing ratio with wind vectors overlaid at (a: top left) 46, (b: top right) 48, (c: bottom left) 51, and (d: bottom right) 53 minutes.

The size and dynamics of the modelled cloud compares reasonably well with observations of small cumulus clouds on this day. The ascent rate of one cloud observed by the radar was 8.1 m s^{-1} (Blyth et al 2003) and the maximum updraught speed observed during penetrations of the clouds was about 16 m s^{-1}. The maximum liquid water content measured during the day was 3.8 g m^{-3}, which corresponds to $L/L_{ad} = 0.8$.

Early in the development of the modelled cloud (Fig. 1a), there is a strong updraught across most of the cloud, with downdraughts at the cloud edge and divergence in the upper part of the leading interface. There is an organized flow of air into the thermal below the cloud base. Two minutes later (Fig. 1b), there is a large indentation of clear air at the rear of the thermal on the left side indicating that there is significant entrainment. The updraught remains strong and there are downdraughts at both edges. There is the suggestion of a second thermal below the region of entrainment. Three minutes later (Fig. 1c) the turret has almost become detached from the lower broader region of cloud. There is entrainment on the left side, in the lower half of the turret which results in a clear-air indentation by the time of the next time period (Fig 1d).

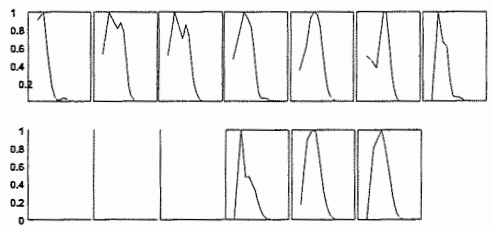

Figure 2: Simulated drop size distributions through cloud along flight path (altitude 2.7 km), for 24th July 1995 (N_0=1000 cm^{-3}). Each plot represents a grid point in the model (95 m), and corresponds to approximately 1 second of flight time, from top left to bottom right. The x-axis is diameter ranging from 0–40 μm and the y-axis is the normalized distribution.

Figure 2 shows the simulated cloud droplet size distributions at every grid point for t = 48 minutes (Fig. 1b) and z = 2.7 km, the same altitude as the aircraft penetration. Updraught velocities corresponding to this height can be see in Table 1. These model results have similarities to the observed DSDs (Fig. 3), which indicate that activation of cloud drops in upward moving mixtures dominated by recently entrained air. In the case of the model, it is likely that the updraught contains a mixture of cloud base air and environmental air which was entrained either at cloud top and descended in the edge downdraughts or at the rear of the thermal at the cloud edge. In Table 1, which shows the vertical velocities and cloud water mixing ratios for the upper region of the cloud at 48 minutes (corresponding to Fig. 1b), it can be seen that the values of $L/L_{ad} \approx 0.6$ while the updraught speed was about 9 m s^{-1}; ideal conditions for enhanced growth due to entrainment and mixing (Baker et al. 1980). The observations suggest that although the number concentration is likely constant in the updraught due to re-activation of CCN, the larger drops compete more effectively for the water vapour and growth of these drops is favoured (Baker et al. 1980). It can also be seen in Table 1 (and Fig. 1b) that a complete 'hole' has developed in the cloud as a result of entrainment.

5 CONCLUSIONS

This approach has been shown to be very useful in examining the drop size distributions in specific regions of the cloud, enabling us to gain a better understanding of the microphysics in relation to the dynamics. In particular, this method has

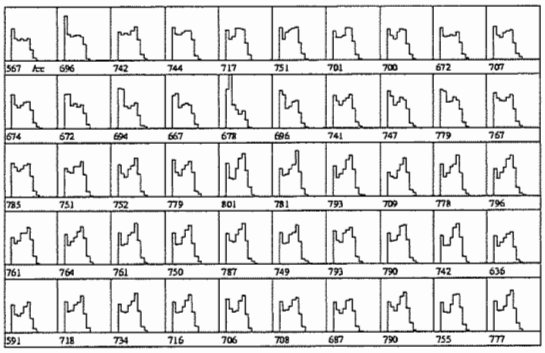

Figure 3: 10 Hz drop size distributions measured by the FSSP on 24 July, commencing at 1732:15 (top left) and ending at 1732:20 (bottom right). The x-axis is diameter ranging from 0–50 μm and the y-axis is $N(d)$, ranging from 0 - 200 cm^{-3}. Each plot represents a distance of approximately 10 m.

great potential for investigating broadening of the droplet spectra in regions of reduced liquid water.

ACKNOWLEDGEMENTS

This work was supported by the Natural Science and Environmental Council under the Cloud, Water Vapour and Climate thematic program (project GST/02/2314). We would also like to thank Piotr Smolarkiewicz for his assistance.

REFERENCES

Baker, M., Corbin, R. and Latham, J., 1980: The influence of entrainment on the evolution of the cloud droplet spectra. *Q. J. R. Meteorol. Soc.*, **106**. 581-98.

Blyth, A. M., Lasher-Trapp, S. G. Cooper, W. A. Knight, C. A. and Latham, J., 2003: The Role of Giant and Ultra-Giant Nuclei in the Formation of Early Radar Echoes in Warm Cumulus Clouds. *J. Atmos. Sci.*, **60(21)**, 26557–72.

Brenguier, J-L., 1991: Parameterization of the condensation process: theoretical approach. *J. Atmos. Sci.*, **48(2)**, 264–82.

Brenguier, J-L. and Grabowski, W W., 1993: Cumulus entrainment and cloud droplet spectra: a numerical model within a two-dimensional dynamical framework. *J. Atmos. Sci.*, **50(1)**, 120–136.

Feingold, G. and Chuang, P. Y., 2002: Analysis of influence of film-forming compounds on droplet growth: Implications for cloud microphysical processes and climate. *J. Atmos. Sci.*, **59**, 2006–18.

Smolarkiewicz, P. K. and Margolin, L. G., 1997: On forward-in-time differencing for fluids: a Eulerian/semi-Lagrangian nonhydrostatic model for stratified flows. *Atmos-Ocean.*,**35**, 127–52.

Warner, J., 1969: The microstructure of cumulus cloud: Part II. The effect of droplet size distribution of the cloud nucleus spectrum and updraft velocity. *J. Atmos. Sci.*, **26** , 1272–1282.

Table 1: Simulated vertical velocities and cloud water mixing ratios for the upper region of the cloud (24th July 1995) at 48 minutes.

Height	Distance from edge of cloud (m)								
(m)	0	95	190	285	380	475	570	665	760
3144			5.14	5.11					
			0.0014	*0.0016*					
3049		1.67	8.50	8.30	2.61				
		0.0008	*0.0028*	*0.0028*	*0.0015*				
2953		3.87	9.10	9.29	5.29	-0.10			
		0.0018	*0.0025*	*0.0025*	*0.0025*	*0.0007*			
2858	-0.76	5.73	8.41	7.72	7.99	1.77			
	0.0003	*0.0020*	*0.0020*	*0.0022*	*0.0024*	*0.0014*			
2763	-0.02	7.21	8.31	5.97	7.58	4.23	-2.03		
	0.0004	*0.0017*	*0.0015*	*0.0017*	*0.0019*	*0.0018*	*0.0002*		
2668	1.36	7.93	7.56	4.87	5.43	5.20	-0.80		
	0.0005	*0.0012*	*0.0012*	*0.0011*	*0.0015*	*0.0016*	*0.0006*		
2572	3.19	7.28	6.72	4.26	3.67	4.37	-0.003		
	0.0008	*0.0010*	*0.0009*	*0.0006*	*0.0010*	*0.0011*	*0.0007*		
2477	3.63	6.50	6.49		2.83	2.76	0.76		
	0.0010	*0.0009*	*0.0005*		*0.0003*	*0.0004*	*0.0003*		
2382	2.41	5.47	6.11				2.68		
	0.0010	*0.0011*	*0.0007*				*0.0003*		
2287	1.13	4.37	6.17	2.80		4.98	6.40	3.03	1.23
	0.0008	*0.0011*	*0.0012*	*0.0002*		*0.0008*	*0.0011*	*0.0006*	*0.0002*
2192	-1.27	1.66	4.59	4.43	2.60	5.94	7.77	6.91	5.43
	0.0003	*0.0004*	*0.0010*	*0.0011*	*0.0004*	*0.0013*	*0.0011*	*0.0012*	*0.0012*
2096			2.18	4.42	5.42	7.31	7.25	6.94	6.13
			0.0007	*0.0010*	*0.0010*	*0.0009*	*0.0011*	*0.0010*	*0.0010*

Vertical velocity in m s^{-1}; cloud water mixing ratio in kg kg^{-1} (in italics, below).

STUDY OF THE PRECIPITATION IN ATHENS (GREECE) WITH A 2D VIDEO DISTROMETER AND RAINGAUGES

E. Defer, K. Lagouvardos, V. Kotroni, and J. Kalogiros

National Observatory of Athens, Institute for Environmental Research, Athens, Greece

1. INTRODUCTION

The National Observatory of Athens is operating a 2D video distrometer since November 2002 in the suburbs of Athens (Greece). We present here some observations recorded during the winter 2002.

2. INSTRUMENTS

The 2D video distrometer, designed by Joanneum Research, consists in two camera orthogonally aligned (Schönhuber, 1998). Each camera is composed of a single 512-pixel line with a resolution of 0.2 mm. Four 0.2 mm tipping bucket raingauges are situated about 2 meters around the distrometer and provide additional rain measurements.

Each particle measured by the distrometer is defined by several parameters such as it equivalent diameter, its volume, and others. Rain accumulation and rain rate can be then computed.

3. CONCURRENT MEASUREMENTS OF THE DAILY RAIN ACCUMULATION

Figure 1 shows the daily rain accumulation recorded by the distrometer and the raingauge #2 between the 21st of November 2002 and 3rd February 2003 in Athens region. Rain accumulation was measured ranging from less than 0.2 (0.4) to 23.5 (25.6) mm from the distrometer (raingauge #2). Figure 1 shows some good consistent rain measurements between the two instruments.

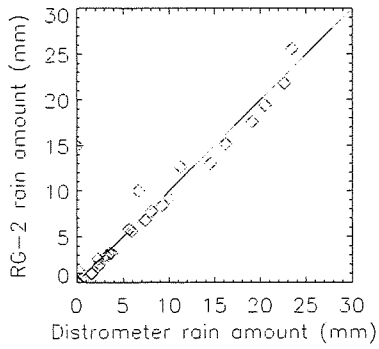

Figure 1. Daily rain accumulations recorded by the distrometer and the raingauge #2.

Corresponding author's address: Eric Defer, National Observatory of Athens, Institute for Environment Research, Lofos Koufou, 15236 Penteli, Greece; E-mail: defer@meteo.noa.gr.

Figure 2 shows the relative difference (in %) as computed by the difference of the rain accumulation between the two instruments divided by the rain accumulation measured by the distrometer. In most cases, the raingauge underestimated the daily rain accumulation (less than 10%) for the entire range of accumulation recorded during the studied period. For low daily rain accumulation (less than 5 mm), the relative difference was greater then 30%. Note also that for few cases, the rain accumulation derived from the distrometer observations was less than the one measured from the raingauge. It was also observed with the measurements of the other raingauges, suggesting some technical problems with the distrometer. Investigations are underway in order to identify the origins of the technical problems.

Detailed investigations of raingauge and distrometer data during significant raining periods showed consistent rain accumulation (not shown in the present paper). It suggests that the differences of rain accumulation can come from precipitation at low rate, precipitation well recorded by the optical sensor, but poorly recorded by the tipping raingauges.

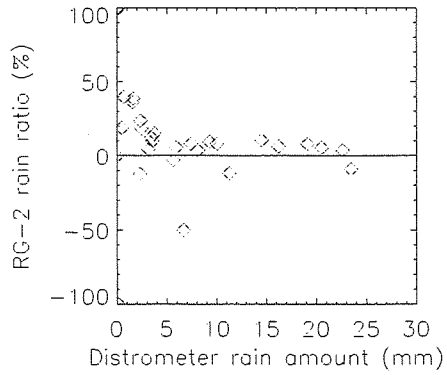

Figure 2. Relative difference of the daily rain accumulation recorded by the distrometer and the raingauge #2.

4. DROP SIZE DISTRIBUTIONS

For 10 significant rainy events recorded during December 2002, we computed the drop size distribution (DSD) per minute based on the distrometer data. According to the records of the National Observatory of Athens (NOA), December 2002 was one of the rainiest months ever recorded in Athens. For the studied period the drop size was found to range from 0.2 to 7.6 mm, with a peak at 0.6-0.8 mm (Figure 3).

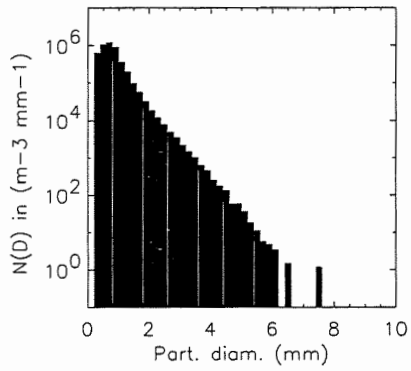

Figure 3. Drop size distribution per 0.2 mm size bins computed for 10 significant rainy events in the Athens region during December 2002.

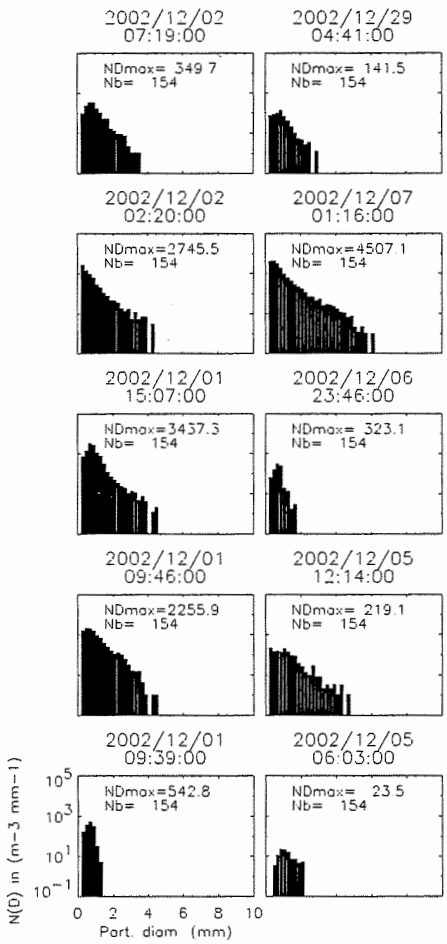

Figure 4. Drop size distribution (per 0.2 mm size bins) computed on 1-min basis for different times and days in the Athens region during December 2002.

Figure 4 show typical DSDs computed per 1-min period for different days and times in December 2002. As expected the size of the raindrops can vary according to the type of rain recorded by the distrometer during the 1-min time period (Figure 4). In the December 2002 dataset, the magnitude of DSD peaks ranged over two orders of magnitude suggesting more or less intense precipitation events. Figure 4 shows typical results recorded during December 2002. For some short periods (a couple of minutes), it was possible to observe DSDs with a large size range such as for the plot at 04:41 on the 7th December 2002. Investigation is currently underway in order to relate the DSD characteristics to the type of rain (convective or stratiform).

4. TIME SERIES OF DROP SIZE DISTRUBUTIONS AND RAIN RATE

Figure 5 shows the time series of the drop size distribution, concentrations of particles for specific diameters, number of particles as well as the rain rate derived from the distrometer dataset for the period 15:20-17:40 UT on the 2nd of December 2002. Cloud-to-ground lightning activity was reported during that period in Athens.

The distrometer recorded precipitation almost during the entire studied period. The number of drops did not exceed 3000 drops per minute during the studied period while the rain rate computed from the characteristics of droplets exceeded 50 mm/h on 1-min time integration.

Droplets with 0.6 mm diameter were recorded during the entire study period at different rates. While 1-mm diameter particles were recorded almost during the entire period, 2-mm diameter droplets were always recorded few minutes after 0.6 and 1-mm droplets were measured. Almost no droplets with diameter more than 4 mm were recorded. Finally the contour plot suggests shows a smoother DSD temporal evolution after 16:40 UT suggesting that a new precipitation regime was recorded by the distrometer.

5. PROSPECTS

We will continue documenting the precipitation events, which occurred in Athens during the past years. We will also compare the characteristics of the raindrops recorded in Athens to the ones recorded elsewhere in the world as well in South of Greece where we are currently performing a field project where the NOA XPOL radar, the distrometer and raingauges are deployed.

6. ACKNOWLEDGMENTS

The Greek General Secretariat for Research and Technology (Excellence in Research Centers – MIS64563) supported this work.

7. REFERENCES

Schönhuber, M., 1998: About interaction of precipitation and electromagnetic waves, Ph. D. Thesis, pp 183, Institute of Communications and Wave Propagation Technical University Graz.

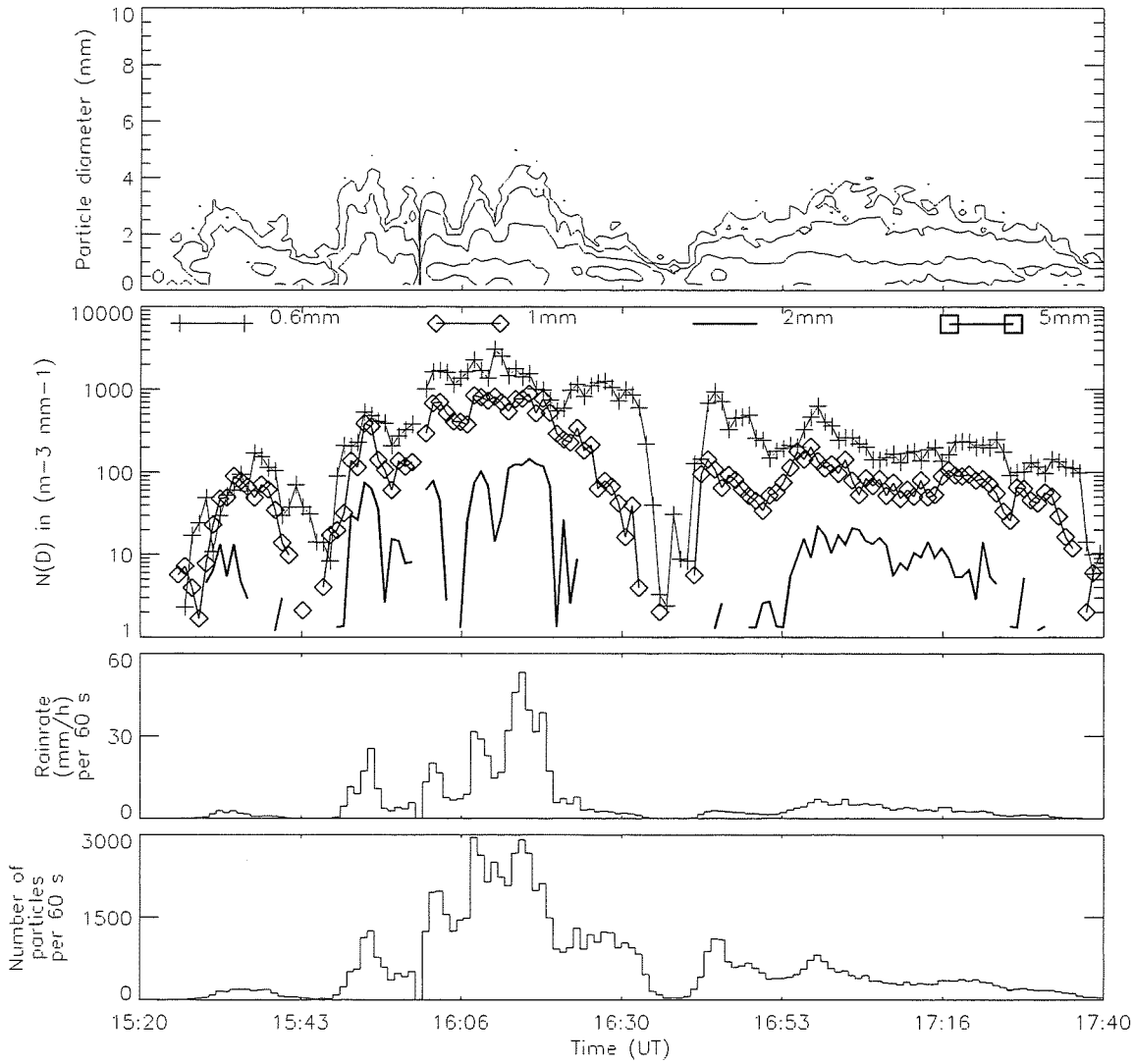

Figure 5. Rain characteristics for the period 15:20-17:40 UT on the 2nd of December 2002. From the lower panel to the upper panel are plotted respectively the number of particles recorded by the distrometer per minute, the rain rate derived from the distrometer data, the drop concentration for specific bin sizes derived from the distrometer data, and finally a contour plot of the DSD time evolution as recorded by the distrometer.

PRECIPITATION AND LIGHTNING ACTIVITY IN ATHENS (GREECE)

E. Defer, K. Lagouvardos, and V. Kotroni

National Observatory of Athens, Institute for Environmental Research, Athens, Greece

1. INTRODUCTION

In the frame of this study the cloud-to-ground (CG) lightning activity and precipitation of different thunderstorms that occurred in the region of Athens (Greece) during the winter 2002-2003 have been studied. Precipitation was determined from raingauges while CG lightning activity was investigated based on the reports of the UK Met Office VLF long range Sferics Arrival Time Difference (ATD) system.

2. INSTRUMENTS AND METHOD

Precipitation was measured from raingauges (tipping buckets) that are operated daily by the National Observatory of Athens at two different sites (Thissio and Pendeli) in Athens. Additional raingauge observations also located in Athens region were studied in order to check the rain accumulation. In the present paper we present only the observations recorded at the National Observatory of Athens (NOA) Pendeli station (38.05N, 23.86E, 509 m msl), where our laboratory is located in the Northern suburbs of Athens.

CG activity was investigated based on the observations of the UK Met Office VLF long range Sferic system (Lee, 1986; Holt et al., 2001). Each of the 8 stations of the ATD system senses the VLF signal radiated during the connection to the ground of the flashes. Each station records accurately the time of the lightning events. After identifying the same events from their waveforms, the location of the strike, called ATD fix, is computed from equations dependent on the difference of time arrival of the VLF signal at the ATD stations. The ATD system covers all the Mediterranean Sea.

Because a CG flash can be composed of many connections to the ground, and consequently many ATD fixes, a simple algorithm was developed in order to combine the ATD fixes in flashes based on time and space criteria. This algorithm applies the same criteria as the ones for the National Lightning Detection Network (NLDN) observations (Cummins et al., 1998). Two ATD fixes are part of the same flash when the time interval between the two fixes is less than 500 ms and the distance between the two fixes is less than 10 km. A flash can be composed by not more than 15 strokes and the flash duration cannot exceed 1 s. We then define the multiplicity as the number of ATD fixes being part of the same flash.

The method in the present study consists in considering only the CG lightning activity located in a range of 10 km around the location where the rain measurement was performed. Investigations are underway in order to study the sensitivity of the range parameter. From the selection of CG flashes, the CG lightning flash rate was computed per 5 min period and compared to the rain amount also computed per 5 min period. Finally total rain amount and number of CG flashes were compared on the daily basis and also on the storm level. We present here the results of this investigation.

3. OBSERVATIONS

3.1 Case of the 7th November 2002

Defer et al. (2004, this conference) describe the CG lightning activity recorded on the 7th November 2002 by the UK Met Office ATD system. Three major events occurred in the region of Pendeli station during 24-h period and according to the 10 km range. The CG flash rate as deduced peaked at 38 flashes per 5 min during the third major event (Figure 1). The third major event exhibited lightning activity for mostly 6 hours, while the two other major events lasted in terms of CG activity for about 1 or 3 hours.

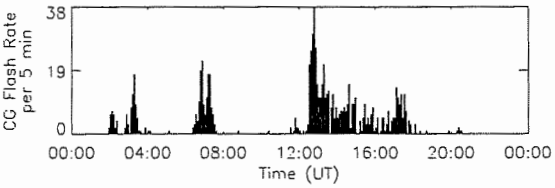

Figure 1. CG flash rate per 5 min recorded 10 km around the NOA Pendeli weather station on the 7th November 2002.

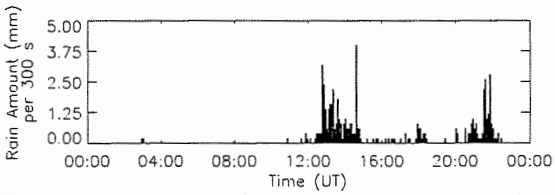

Figure 2. Rain accumulation per 5 min recorded at Pendeli weather station on the 7th November 2002.

Figure 2 gives the rain amount recorded at Pendeli per 5 min period. Continuous rain was recorded during

Corresponding author's address: Eric Defer, National Observatory of Athens, Institute for Environment Research, Lofos Koufou, 15236 Penteli, Greece; E-mail: defer@meteo.noa.gr.

the third event with a first peak exceeding 3.2 mm (in 5 min) and a second peak 105 min later (4 mm). While after 20:00 UTC the lightning activity has stopped in the vicinity of the Pendeli station, rain was still measured probably associated with the stratiform regime associated to the storm system.

Almost no precipitation was recorded during the two first events. CG flashes recorded during the two first thunderstorms were located north-west of the Pendeli suggesting that the storms were enough distant to the weather station that no rain reached the ground at the location of the rain measurement.

3.2 Case of the 7th December 2002

Figures 3 and 4 show respectively the time series of CG flash rate and rain amount recorded on the 7th December 2002. Lightning activity recorded in the early hours of the day was associated with a storm already electrically active during the last hour of the previous day. In Figure 3 CG flash rate peaked at 8

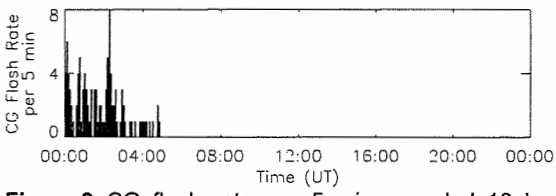

Figure 3. CG flash rate per 5 min recorded 10 km around the NOA Pendeli weather station on the 7th December 2002.

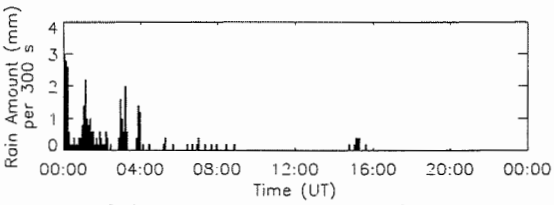

Figure 4. Rain accumulation per 5 min recorded at Pendeli weather station on the the 7th December 2002.

CG flashes per 5 min. Figure 4 shows not only that the rain recorded at the Pendeli station had different rate but also that the rain was more intermittent than during the case of the 7th November 2002 (Figure 2).

4. OVERVIEW

Table 1 gives the results of the analysis of the CG lightning activity recorded during five different days with lightning activity nearby the Pendeli station. The daily number of CG flashes ranged from 1 to more than 800 CG flashes within 10 km range of the weather station. On the storm level, the CG activity was recorded with different peaks of flash rate and number of flashes per storm.

Table 2 gives the daily rain accumulation recorded for the days with CG lightning activity. Significant daily rain accumulations were recorded during the studied cases. For instance more than 59 mm of rain was recorded on the 7th November 2002. Six of the eight

Date	Daily number of Flashes	Period of storms UTC	Main peak of CG flash rate (Flashes per 5 min)	Number of flashes
07-11-2002	817	01:55-04:05	18	96
		06:20-07:35	22	144
		12:30-18:40	38	548
05-12-2002	1	10:15:26	1	1
06-12-2002	40	05:25-06:05	1	4
		23:00-24:00	6	34
07-12-2002	109	00:00-04:50	8	109
29-12-2002	24	09:35-13:10	4	24
01-02-2003	3	15:00-16:00	1	3

Table 1. Period, peak flash rate, and number of flashes for the different time periods for five different days. Because only major thunderstorms were summarized in this table, the number of flashes for a given day is not necessary the sum of numbers of flashes per stroms.

Date	Daily rain accumulation (mm)	Period of storrs UTC	Rain amount (mm)	Maximum rain rate (mm/h per 5 min)
07-11-2002	59.2	01:55-04:05	4.8	2.4
		06:20-07:35	0	0
		12:30-18:40	37.8	48
05-12-2002	19.2	10:15:26	0	0
06-12-2002	16	05:25-06:05	0	0
		23:00-24:00	15.8	55.2
07-12-2002	37	00:00-04:50	32.4	36
29-12-2002	22	09:35-13:10	19.8	16.8
01-02-2003	8.8	15:00-16:00	0.6	2.4

Table 2. Precipitation measured at Pendeli for the days with lightning activity located near Pendeli weather station. Rain amount and maximum rain rate are those measured during the periods of CG activity.

thunderstorms exhibited precipitation at the Pendeli station.

Figure 5 shows the daily rain accumulation as function of the total number of CG flashes recorded during the day. For the studied cases, the highest numbers of CG flashes correspond to the highest daily rain accumulations.

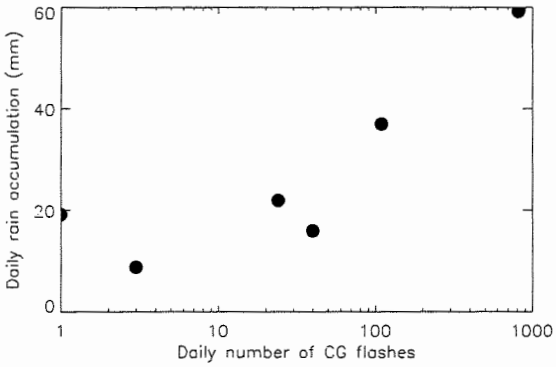

Figure 5. Daily rain accumulation versus daily number of CG flashes for the 6 days of the study in the vicinity of Pendeli weather station.

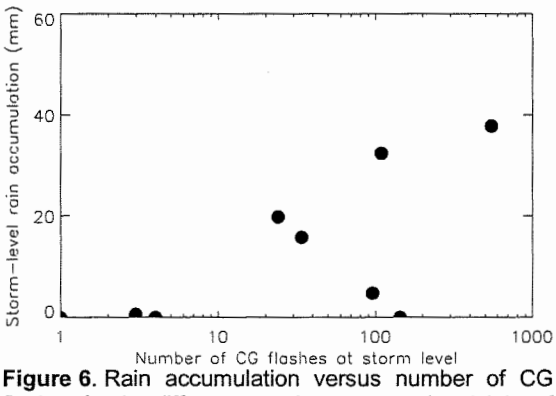

Figure 6. Rain accumulation versus number of CG flashes for the different thunderstorms in the vicinity of Pendeli weather station.

Figure 6 shows now the relationship between the rain accumulation and the number of CG flashes on the storm level. For some storms, a high number of CG flashes was recorded while almost no rain was recorded at the weather station. The rain measurements are performed at a specific location while we are considering lightning activity 10 km around the raingauge station. Precipitation may have occurred but not over the raingauge station. We are facing the problem of comparing observations at a single location to areal observations around a reference location. This fact supports the idea that radar observations are the most suitable observations to relate lightning and precipitation because of its appropriate temporal and spatial sampling.

5. PROSPRECTS

We plan to perform further comparisons of rain measurements from raingauges for other storms in the Athens area as well as in Crete where NOA has deployed new raingauges. We will also investigate the characteristics of the CG flashes such as multiplicity and flash duration as determined from the algorithms developed here and relate them to the rain rate. Finally we will extend our analysis by using the observations from NOA X-pol radar and by comparing rain fields to lightning activity in the region of Athens.

6. ACKNOWLEDGMENTS

The Greek General Secretariat for Research and Technology (Excellence in Research Centers – MIS64563) supported this work. We would like to thank also Dr A. Koussis from the National Observatory of Athens for providing additional rain data over Athens area.

7. REFERENCES

Cummins, K. L., M. J. Murphy, E. A. Bardo, W. L. Hiscox, R. B. Pyle, and A. E. Pifer, 1998: A combined TOA/MDF technology upgarde of the U.S. National Lightning Detection Network, *J. Geophys. Res.*, 103, 9035-9044.

Defer, E., , K. Lagouvardos, D. Katsanos, and V. Kotroni, 2004: Precipitation and lightning activity over the Mediterranean sea, this conference.

Holt, M. A., P. J. Hardaker, and G. P. McLelland, 2001: A lightning climatology for Europe and the UK, 1990-99, Weather, 56, 290-296.

Lee, A. C. L., 1986: An experimental study of the remote location of lightning flashes using VLF arrival time difference technique, Q. J. R. Meteorol. Soc., 112, 203-229.

THE EFFECT OF TURBULENT VELOCITY FLUCTUATIONS ON DROP SPECTRUM BROADENING IN STRATOCUMULUS CLOUDS

C. Erlick, A. Khain, M. Pinsky, and Y. Segal

Department of Atmospheric Sciences, The Hebrew University of Jerusalem, Jerusalem, 91904, Israel

1. INTRODUCTION

Simulating the shape of cloud drop spectra in both cumulus and stratiform clouds has historically been a challenge. Drop spectra measured by aircraft are often broader than what is predicted by the equation of diffusional growth. The broadness of the spectrum reflects not only the existence of drops with radii exceeding the adiabatic value, but also drops with radii smaller than the adiabatic value (1–8 μm), which are regularly observed several hundred meters above cloud base in both cumulus (e.g., Warner 1969; Brenguier 1998) and stratiform clouds (e.g., Noonkester 1984; Nichols 1984; Korolev 1995; Gerber 1996). It is still problematic to reproduce wide drop spectra containing both large drops responsible for drizzle formation and the smallest cloud drops, even using sophisticated models such as large eddy simulations (LES).

A number of mechanisms for broadening of spectra within cloud parcels have been suggested. One of the mechanisms that we investigate further in this study is in-cloud drop nucleation, whereby acceleration of the updraft velocity leads to an increase in supersaturation beyond the typical cloud base peak and activation of new CCN (Ludlam 1980; Korolev 1994; Khain et al. 2000; Pinsky and Khain 2002; Segal et al. 2004). A second mechanism that we investigate is associated with the asymmetry between the rates of condensation and evaporation, where some drops do not fully evaporate during the downdraft segment of a loop and serve to reduce the initial supersaturation peak in a subsequent updraft (Korolev 1995). In the present paper, we use the trajectory ensemble method (TEM) to explore the contribution of in-cloud nucleation and condensation/evaporation asymmetry to drop spectrum formation in a stratocumulus cloud.

2. TRAJECTORY ENSEMBLE METHOD

In the trajectory ensemble method, a stratiform cloud is simulated as an ensemble of a large number of parcels (in this case 680) whose thermodynamic development is dictated by a Lagrangian parcel model (see, e.g., Stevens et al. 1996; Feingold et al. 1998). Each parcel in our simulation follows a trajectory within the velocity field generated by the 3-D LES microphysical model of Kogan et al. (1995), which has a resolution of 75 m in the horizontal and 25 m in the vertical. (See Khairoutdinov and Kogan (1999) for further details.) The initial thermodynamic sounding used to generate the velocity field is from the Third GEWEX Cloud Systems Studies LES Model Intercomparison Workshop, held in Clermont-Ferrand in August 1996, and is based on the Atlantic Stratocumulus Transition Experiment (ASTEX) (Albrecht 1995) flight A209.

The Lagrangian parcel model component describes cloud drop growth by diffusion in an adiabatic ascent as formulated by Pinsky and Khain (2002). To isolate the effect of diffusional growth, no entrainment or mixing processes are included. The model uses a drop mass grid containing 1000 bins with exponentially increasing grid spacing. The large number of size bins allows us to simulate drop nucleation smoothly without sharp jumps in the drop concentration. Time steps of 0.001 s are taken for proper accuracy in the description of the diffusional growth and evaporation of aerosol particles and small drops. To eliminate artificial spectrum broadening, a variable mass grid is used, which avoids the necessity of re-mapping the mass grid onto the regular one.

The size distribution of CCN chosen for the TEM simulations represents marine conditions and is modeled as a bimodal lognormal distribution of sodium chloride particles, with default concentrations, mode radii, and logarithms of the standard deviation: $N_1 = 80\,\mathrm{cm}^{-3}$, $r_{\mathrm{mode}_1} = 0.006\,\mu\mathrm{m}$, $\log\sigma_1 = 0.3$; $N_2 = 240\,\mathrm{cm}^{-3}$, $r_{\mathrm{mode}_2} = 0.03\,\mu\mathrm{m}$, $\log\sigma_2 = 0.3$, respectively.

3. RESULTS

3.1 Simulations with the LES velocity field

The ensemble mean drop size distribution for the 680 parcels is shown in Figure 1a at different altitudes within the cloud layer. All of the distributions below 700 m altitude exhibit more than a single narrow peak, with nonzero drop concentrations out to sizes as small as 1 μm radius, evidence of broadening towards smaller drops as a result of in-cloud nucleation and condensation/evaporation asymmetry during parcel evolution.

Corresponding author's address: Carynelisa Erlick, Department of Atmospheric Sciences, The Hebrew University of Jerusalem, Jerusalem, 91904, Israel; E-Mail: caryn@vms.huji.ac.il.

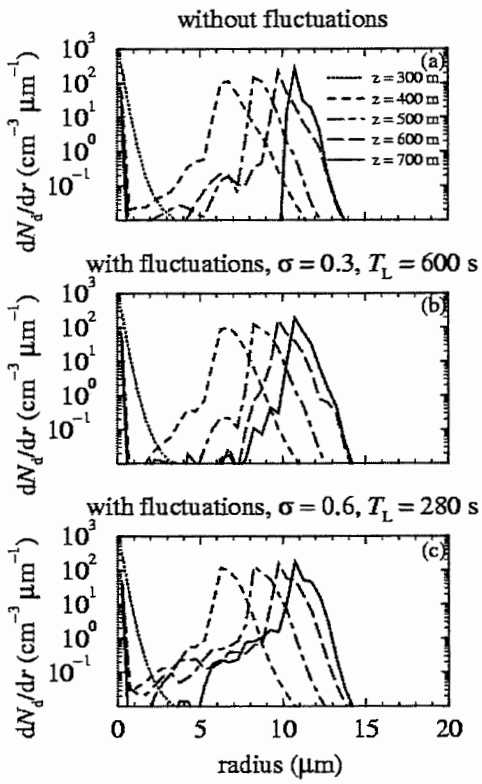

Figure 1. Ensemble mean drop size distributions for the 680 trajectories of the TEM as a function of altitude: (a) without turbulent velocity fluctuations, (b) with weaker turbulent velocity fluctuations, (c) with stronger turbulent velocity fluctuations.

3.2 Simulations with subgrid turbulent velocity fluctuations

While the mean velocities in cumulus clouds are significantly larger than small scale turbulent fluctuations, small scale turbulent fluctuations in stratocumulus clouds may be on the order of or even greater in magnitude than the mean velocities and as such can have a significant influence on parcel motion and microphysics.

As mentioned in section 2, the LES model used to generate the velocity field has a horizontal resolution of 75 m and therefore only explicitly describes large eddies in the boundary layer with scales greater than 150 m. To investigate the possible effects of subgrid velocity fluctuations on the drop spectra, we represent such velocity fluctuations explicitly and superimpose them on the resolvable scale velocity field.

The random velocity fluctuations are generated using the Langevin equation (Pope 1994), where turbulent diffusion is represented as an autoregression process of the 1st order (Yaglom 1987). As a finite difference scheme, each velocity component has the form:

$$\begin{aligned} u'_{t+1} &= au'_t + (1-a^2)^{1/2}\sigma_{u'}\xi_{u'} \\ v'_{t+1} &= av'_t + (1-a^2)^{1/2}\sigma_{v'}\xi_{v'} \\ w'_{t+1} &= aw'_t + (1-a^2)^{1/2}\sigma_{w'}\xi_{w'} \end{aligned} \qquad (1)$$

In these equations, $\sigma_{u'}$, $\sigma_{v'}$, and $\sigma_{w'}$ are the standard deviations of the corresponding velocity fluctuations, $\xi_{u'}$, $\xi_{v'}$, and $\xi_{w'}$ are random numbers with zero mean and unit dispersion, and $t, t+1...$ is the discrete time, where $t+1 = t+\Delta t$. The position of the fluid parcel at time $t+1$ is given by:

$$\begin{aligned} x_{t+1} &= x_t + (\bar{u} + u')\Delta t \\ y_{t+1} &= y_t + (\bar{v} + v')\Delta t \\ z_{t+1} &= z_t + (\bar{w} + w')\Delta t, \end{aligned} \qquad (2)$$

where $\bar{u}$, $\bar{v}$, and $\bar{w}$ are components of the LES velocity field at the current parcel location. In Equation (1), $a = \exp(-\Delta t / T_L) \approx 1 - \Delta t / T_L$, where T_L is the Lagrangian correlation time scale.

Under the assumption of isotropic, homogeneous turbulence, we parameterize the root mean square (rms) magnitude of the turbulent velocity fluctuations as:

$$\sigma_{u'} = \sigma_{u'} = \sigma_{u'} = \sigma(\bar{u}^2 + \bar{v}^2 + \bar{w}^2)^{1/2}, \qquad (3)$$

where σ is the scaling factor.

The range of realistic values for the parameters σ and T_L can be estimated from dimensional analysis using the length scale of the largest turbulent eddy (the smallest LES resolved scale eddy), $L_{\text{eddy}} \sim 150\,\text{m}$, and the dissipation rate, which in stratocumulus clouds can vary in order of magnitude from $\varepsilon \sim 0.001\,\text{m}^2\text{s}^{-3}$ to $\varepsilon \sim 0.01\,\text{m}^2\text{s}^{-3}$ (Kollias and Albrecht 2000; Pinsky and Khain 2003). For $\varepsilon \sim 0.001\,\text{m}^2\text{s}^{-3}$, the maximum velocity $w'_{\max} \sim (\varepsilon L_{eddy})^{1/3} \approx 0.5\,\text{m}\,\text{s}^{-1}$, while for $\varepsilon \sim 0.01\,\text{m}^2\text{s}^{-3}$, $w'_{\max} \approx 1.1\,\text{m}\,\text{s}^{-1}$. Similarly, for $\varepsilon \sim 0.001\,\text{m}^2\text{s}^{-3}$, the eddy lifetime $\tau_{\text{eddy}} \sim L_{\text{eddy}} / w'_{\max} \approx 280\,\text{s}$, while for $\varepsilon \sim 0.01\,\text{m}^2\text{s}^{-3}$, $\tau_{\text{eddy}} \approx 130\,\text{s}$. From Equation (3), assuming a maximum rms fluctuation between $0.5\,\text{m}\,\text{s}^{-1}$ and $1.1\,\text{m}\,\text{s}^{-1}$ and for maximum convective scale velocity components of $1\,\text{m}\,\text{s}^{-1}$, the scaling factor σ ranges from 0.3 to 0.6. Based on the results of Monin and Yaglom (1975), we assume that for an unstable atmosphere, $T_L \sim 2\tau_{\text{eddy}}$, and estimate T_L to be around 600 s for $\sigma = 0.3$ and around 280 s for $\sigma = 0.6$.

The ensemble mean drop size distribution for the 680 parcels with subgrid velocity fluctuations is shown in Figures 1b and c for $\sigma = 0.3$ and $\sigma = 0.6$, respectively. With $\sigma = 0.3$, the concentration of the smallest drops increases, but only in the upper cloud levels, e.g., at 700 m (solid line). With the turbulent

velocity fluctuations, some parcels diffuse into eddies with higher vertical velocity and reach the upper cloud levels while experiencing in-cloud nucleation due to the updraft acceleration. Such parcels spend a shorter time in the lower cloud levels, and thus reduce the occurrences of broadening in the lower levels while increasing the occurrences of broadening in the upper levels. In all, 266 out of the 680 parcels undergo new nucleation during either the first updraft or subsequent updraft/downdraft loops with $\sigma = 0.3$.

The time evolution of a single parcel (out of the 680) with $\sigma = 0.3$ is shown in Figures 2 and 3. Without fluctuations (Figure 2), the supersaturation (S) and drop concentration (N_d) each reach an initial peak and never increase beyond their respective peaks. With fluctuations (Figure 3), there is a strong increase in vertical velocity (w_{tot}) in the vicinity of $t = 500\,s$, accompanied by a peak in supersaturation that supercedes the initial peak and by a jump in the drop concentration (new drop nucleation). Note that the peak in $w_{tot} = \overline{w} + w'$ (the total velocity) corresponds to a peak in $w_{LES} = \overline{w}$ (the LES velocity), indicating that the increase in vertical velocity is caused by the diffusion of the parcel into an area of higher mean updraft plus a positive turbulent scale fluctuation.

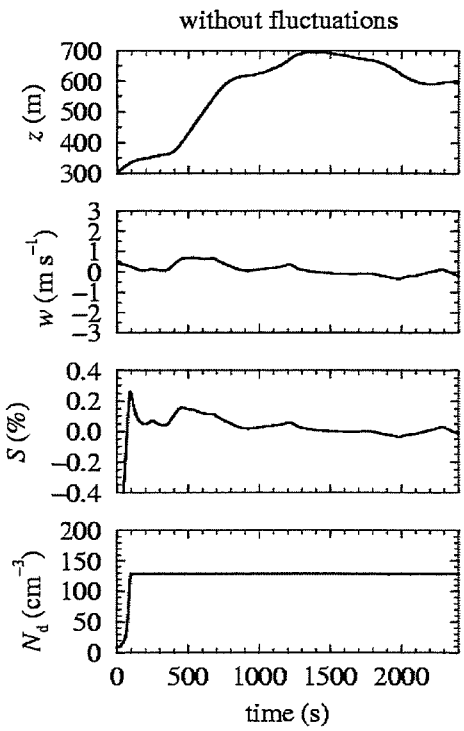

Figure 2. Parcel altitude, vertical velocity, supersaturation, and drop concentration as a function of time for the trajectory with starting point $i = 28, j = 24, k = 13$ without turbulent velocity fluctuations.

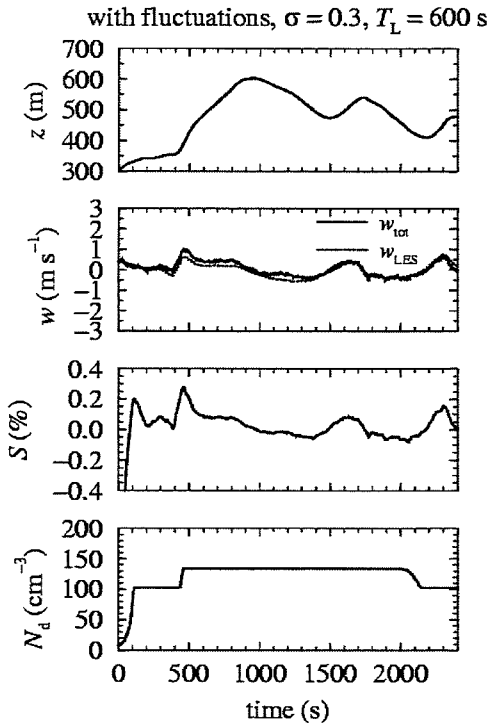

Figure 3. Same as in Figure 2, but with turbulent velocity fluctuations.

With $\sigma = 0.6$ (Figure 1c), the concentration of the smallest drops increases at all altitudes, although again most strikingly near the cloud top. In this case, 346 out of 680, or more than half of the parcels, undergo new nucleation during either the first updraft or subsequent updraft/downdraft loops. This is a clear indication that new nucleation as a result of updraft acceleration and parcel recirculation is an important mechanism in drop spectrum formation, and that subgrid scale turbulent velocity fluctuations should be taken into account in order to properly evaluate the occurrence of in-cloud nucleation in stratiform clouds.

The sensitivity of the results to changes in the CCN spectrum and the Lagrangian correlation time scale will also be presented.

4. ACKNOWLEDGEMENTS

We thank Y. Kogan for providing us with the LES data and H. Z. Krugliak for his assistance with reading the data files. This work was conducted with support of the Israel Science Foundation (Grant 173-03), by the Israel Ministry of Sciences (Grant WT 0403), and by an Intramural Research Fund career development award from The Hebrew University of Jerusalem.

5. REFERENCES

Albrecht, B. A., C. S. Bretherton, D. Johnson, W. H. Schubert, and A. S. Frisch, 1995: The Atlantic

Stratocumulus Transition Experiment – ASTEX, Bull. Amer. Meteorol. Soc., 76, 889-904.
Brenguier, J.-L., 1998: Drop spectra broadening in cumulus clouds: Review of advances in observations and numerical simulations. Proceedings of the AMS Conference on Cloud Physics, Everett, WA, Aug.17-22.
Feingold, G., S. M. Kreidenweis, and Y. Zhang, 1998: Stratocumulus processing of gases and cloud condensation nuclei, 1, Trajectory ensemble model, J. Geophys. Res., 102(D16), 19,527-19,542.
Gerber, H., 1996: Microphysics of marine stratocumulus clouds with two drizzle modes, J. Atmos. Sci., 53(12), 1649-1662.
Khain, A., M. Ovtchinnikov, M. Pinsky, A. Pokrovsky, and H. Krugliak, 2000: Notes on the state-of-the-art numerical modeling of cloud microphysics, Atmos. Res., 55, 159-224.
Khairoutdinov, M. F., and Y. L. Kogan, 1999: A large eddy simulation model with explicit microphysics: Validation against aircraft observations of a stratocumulus-topped boundary layer, J. Atmos. Sci., 56, 2115-2131.
Kogan, Y. L., M. P. Khairoutdinov, D. K. Lilly, Z. N. Kogan, and Q. Liu, 1995: Modeling of stratocumulus cloud layers in a large eddy simulation model with explicit microphysics, J. Atmos. Sci., 52, 2923-2940.
Kollias, P., and B. Albrecht 2000: The turbulent structure in a continental stratocumulus cloud from millimeter-wavelength radar observations, J. Atmos. Sci., 57, 2417-2434.
Korolev, A. V., 1994: A study of bimodal drop size distributions in stratiform clouds, Atmos. Res., 32, 143-170.
Korolev, A. V., 1995: The influence of supersaturation fluctuations on drop size spectra formation, J. Atmos. Sci., 52, 3620-3634.
Ludlam, F. H., 1980: Clouds and Storms, The Pennsylvania State University Press.
Monin, A. S., and A. M. Yaglom, 1975: Statistical Fluid Mechanics: Mechanics of Turbulence (English updated ed.), Volume 1-2, MIT Press, Cambridge, MA.
Nichols, S., 1984: The dynamics of stratocumulus: Aircraft observations and comparisons with a mixed layer model, Q. J. R. Meteorol. Soc., 110, 783-820.
Noonkester, V. R., 1984: Drop spectra observed in marine stratus cloud layers, J. Atmos., Sci., 41(5), 829-845.
Pinsky, M., and A. Khain, 2002: Effects of in-cloud nucleation and turbulence on drop spectrum formation in cumulus clouds, Q. J. R. Meteorol. Soc., 128, 501-533.
Pinsky, M. B., and A. P. Khain, 2003: Fine structure of cloud drop concentration as seen from the Fast-FSSP measurements, 2, Results of in-situ observations, J. Appl. Meteorol., 42, 65-73.
Pope, S. B., 1994: Lagrangian pdf methods for turbulent flows, Ann. Rev. Fluid Mech., 26, 23-63.
Segal, Y., A. Khain, M. Pinsky, A. Sterkin, 2004: Sensitivity of raindrop formation in ascending cloud parcels to cloud condensation nuclei and thermodynamic conditions, Q. J. R. Meteorol. Soc., 130(597), 561-581.
Stevens, B., G. Feingold, W. R. Cotton, and R. L. Walko, 1996: Elements of the microphysical structure of numerically simulated nonprecipitating stratocumulus, J. Atmos. Sci., 53, 980-1006.
Warner, J., 1969: The microstructure of cumulus cloud, II, The effect of drop size distribution of the cloud nucleus spectrum and updraft velocity, J. Atmos. Sci., 26, 1272-1282.
Yaglom, A. M., 1987: Correlation theory of stationary and related random fluctuations, Volume 1-2, Springer, New York, NY.

The study on convective cloud in Qinghai and seeding experiment with 3D model

FANG Wen ZHENG Guo Guang HE Guan Fang.

[1]Chinese Academy of Meteorological Science, Beijing, 100081, P.R.China

1. INTRODUCTION

The research project "the demonstration of precipitation enhancement techniques", which is one of the national key research programs, has been carrying out since 2001. On the basis of the sound data obtained from this project autumn field experiment in Henan country of Qinhai province in Sept. of 2003, we know that the average height of -20 ° C lies in about 8000 meters and the height of 0° C level lies in 4700 meters. This experiment area is at 3500 meters above sea level with the average surface atmospheric pressure 667 hpa. The west-wind speed can arrive at 20-30 m/s at the 8000-10000 meter height with strong wind shear. There are mainly grassland, lakes, marsh and mountains in experiment area and almost no industrial activities. The natural ice nucleus are not enough.

2. Simulating experiment of nature cloud

We simulated the cases during Sept.3 to 21of 2003,in which the disturb center humidity is 90%, disturb temperature is 1.0°C, the disturb range is 5 grid at X-Y and 1-2 at Z. The simulated height of cloud bottom and the maximum height of cloud-top are shown in table2. the result show that our model can forecast the development of convective-cloud and the simulated height of radar echo is similar to actual.

Table 2

Data	Cloud bottom		Cloud top		W (m/s)	Initial radar echo			Amount of precipitation	
	H (km)	T (℃)	H (km)	T (℃)		Time (min)	Height (km)	Temperature (℃)	Rain (kt)	Hail (kt)
9.3	1.5	3.2	14	-66	41	30	7.7	-42	436	7
9.8	1.4	0	8.4	-32	16	33	7.7	-42	3	0.3
9.12	1.0	2.7	10.5	-52	8					
9.14	2.8	-3.8	11.2	-59	21	30	9.1	-45	60	10.4
9.16	1.4	1.1	11.9	-63	13	33	9.1	-45	76	0
9.17	1.4	1.0	11.2	-62	12	36	9.1	-45	37	1
9.18	0.7	3.3	14	-66	15	42	8.2	-43	133	9.3
9.19	1.6	-0.2	15	-65	14					
9.20	1.8	-1.0	14	-63	12	36	7.3	-32	26.5	1.25
9.21	1.6	2	13	-64	32	33	8.4	-45	404	58

We studied the microphysical process of Sept 3 case in detail. The result show that ice crystal are the main sources of graupel, which is generated by conversion from ice and grow by collecting ice crystal.

Corresponding author's address: FANG Wen, Chinese Academy of Meteorological sciences,Beijing, 100081,China; E-Mail: Fangwen@cams.cma.gov.cn.

Ice crystal, cloud water and vapor largely effects the growth of graupel, which is main factor to depleting super-cool water. Before 40 minutes, there are plenty of super cool cloud water and no super cool rainwater. Graupel converted from Ice crystal grows by collecting cloud water. When graupel particles fall into warm level , graupel's melting causes precipitation. Rain's evaporation is the main mechanism of rain's decreasing. Ice crystals are formed by natural nucleus' nucleation. So the concentration of natural nucleus has important effect on the whole precipitation process. In local area, the concentration of natural nucleus is less than that of plain area, but there have relatively more super cool cloud water, this provide possibility for seeding artificial ice crystal or ice-forming nucleus to improve the efficiency of precipitation.

3 Seeding experiment

We will introduce ice crystal into super-cooled cloud in followed tests. Seeding time and position in cloud largely depend on wind field, the height of 0° C level and the area super-cooled cloud water located. If wind speed is stronger when seeding, graupel particles can be blown away before they grow fully. So we must conduct seeding at position where ice crystal have to experience longer distance and do not melt in a short time so that they have a more longer seeding effects. For example, at nearby 0° C level and under the level of maximum super-cooled cloud water. If seeding at the convergence area of updraft, it will be profitable for catalyst's transforming and spreading upward. So the seeding position and occasion is very important , seeding too early or too late can not get rain fall enhancement

The result are shown in following figures and table.

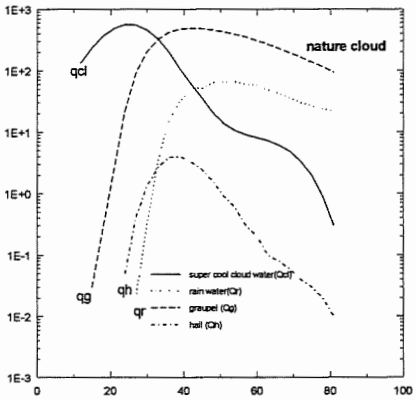

Figure15(A) natural cloud

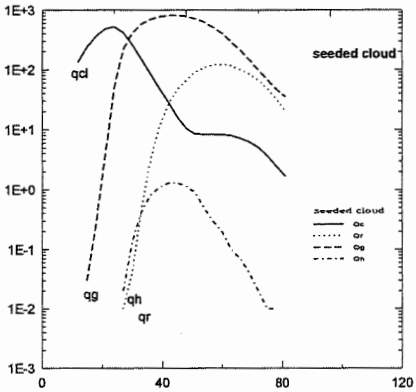

Figure15(B) seeded cloud

Figure15 The distribution of cloud-water, rain-water graupel and hail with time(x-g/kg; y-min).

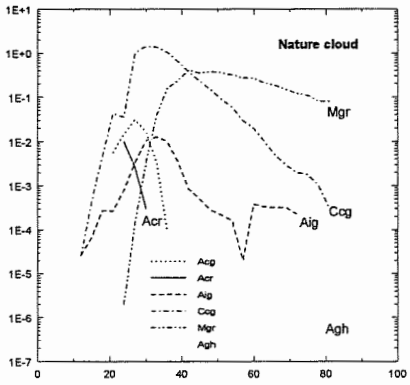

Figure16(A) natural cloud

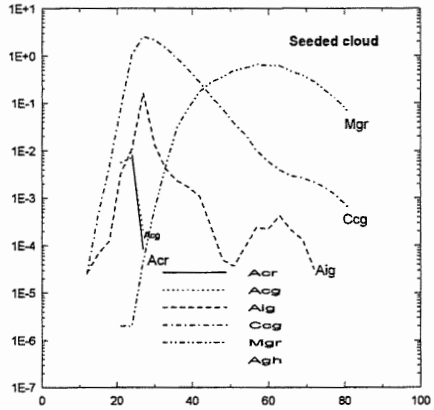

Figure16(B) seeded cloud

Figure16 The distribution of several microphysical process with time (x-g/kg; y-min).

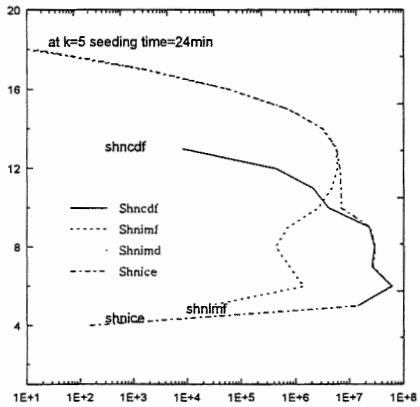

Figure17(A) natural cloud

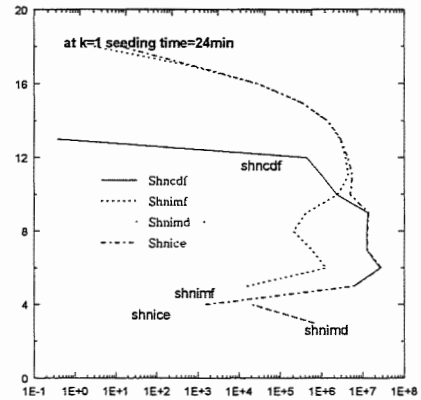

Figure17(B) seeded cloud

Figure17 The distribution of four nucleation process with height(x-km; y-g/kg).

Table3

Serial number	AgI seeding parameters						w (m/s)	The amount of precipitation		Grid precipitation	
	Seeding Time (min)	Dose (/kg)	T (℃)	X-axis (Grid)	Y-axis (grid)	Time(s)		rain (kt)	graupel (kt)	rain (mm)	graupel (mm)
1	Natural cloud						24	508.5	18.3	8.9	1.28
2	12	8×10^6	Ground	30~32	32~34	2	24	673.4	20.8	11.1	0.66
3	15	8×10^6	Ground	30~32	32~34	2	24	579.6	16.7	9.9	0.52
4	18	8×10^6	Ground	30~32	32~34	2	24	506.8	14.2	9.1	0.53
5	18	8×10^6	K=5	30~32	32~34	2	24	701.3	16.8	8.8	0.42
7	21	8×10^6	K=5	30~32	32~34	2	24	536.9	12.8	8.5	0.37
8	18	8×10^6	K=4	30~32	32~34	2	24	661.6	15.8	8.8	0.4

4 Some conclusion

The study show that the precipitation in experiment area was controlled by cold rain process and ice crystal is main source of graupel, which is produced by auto-conversion from ice crystal to graupel and then grow by collection with ice. Seeding AgI should be done before ice nucleus largely activated, so we can enhance rain fall by improving ice content, deleting super-cool water. If not, there will be large amount ice crystal growed in nature cloud, artificial nucleus would be no useful.

Acknowledgements

This work is supported by the National Key Research Program of Science and Technology, China (2001BA610A – 06).

References

1 Hu Z. J. and He G. F, 1988: Numerical simulation of microphysical processes in cumulonimbus, part I: microphysical model, Acta Meteorol. Sinica, 2(4), 471-489.

2 Hu Z. J. and He G. F, 1988, Numerical simulation of microphysical processes in cumulonimbus, part II: microphysical model, Acta Meteorol. Sinica, 46(1), 28-40.

3 <The collected papers of rain enhancement in upper reaches of yellow river> Oct. 1999. edited by The weather modification office of Qinhai province.

4 Zhou M. Y., Xu X. D. and Bian L. G., 2000:the analysis on atmospheric boundary observation and dynamics of Qinghai-Xizang Plateau(QXPMEX,1998). Beijing, 北京，气象出版社，2000。

5 Wang M.K., et al, 1991:cloud and precipitation physics, Beijing, Sciences Publishing House。

6 Yu D.W., et al, 2001: 3D convective cloud seeding model and applying in field experiment. J.Appl.Meteor of CAMS, Vol.12：122-132。

CLOUD DROPLET COLLISION RATES IN EVOLVING TURBULENT FLOWS

C.N. Franklin[1], P.A. Vaillancourt[2], M.K. Yau[1] and P. Bartello[1,3]

[1]Department of Atmospheric and Oceanic Sciences, McGill University, Montreal, Quebec, H3A 2K6, Canada
[2] Recherche en Prévision Numérique, Meteorological Service of Canada, Dorval, Quebec, H9P 1J3, Canada
[3]Department of Mathematics and Statistics, McGill University, Montreal, Quebec, H3A 2K6, Canada

1. INTRODUCTION

The time of transition from cloud droplet growth by condensation to that of effective collision and coalescence is an outstanding issue in cloud physics. Turbulence has long been postulated to reduce the time it takes to produce rain drops by accelerating the growth of droplets in the size range of 10 to 30 μm in radius. Due to the complexity of the problem, previous studies of turbulence-droplet interaction made use of statistical techniques and numerous assumptions about the flow field and the motion of the droplets and hence there is a lot of discrepancy between the results. With the increase in computational power we are now in a position to be able to use direct numerical simulations (DNS) of the flow field to investigate the effect of turbulence on the collisions of the droplets. DNS have the advantage of explicitly resolving the dissipation range dynamics that have been shown to have the most influence on the local particle accumulation and settling rate of small particles whose diameter is less than that of the small eddies of the flow (Wang and Maxey 1993).

As demonstrated by Sundaram and Collins (1997) the collision kernel can be expressed by two statistical quantities of the particle phase; the radial distribution (or pair correlation) function *g(r)* and the particles relative velocity |***w***|. When an inertial particle interacts with a turbulent structure, because of centrifugal forces, the particle will tend to cluster, or become preferentially concentrated in regions of the fluid with low vorticity and increased pressure in the boundaries between the eddies. Since an increased local particle density means that there is an increased probability of finding two particles closely separated in the flow, consequently there is an increase in the collision rate or kernel. Wang et al. (1998) extended this work and demonstrated that the spherical geometry is the correct form to use in the problem of collision in a turbulent flow field and thus the collision kernel for droplets of radius r_1 and r_2 is given by

$$\Gamma = 2\pi(r_1 + r_2)^2 \langle |w_r| \rangle g(r)$$

with the radial relative velocity, w_r, defined as $\mathbf{w}\cdot\mathbf{R}/|\mathbf{R}|$, where **R** is the separation vector for the droplets positions.

Corresponding author's address: Charmaine N. Franklin, Department of Atmospheric and Oceanic Sciences, McGill University, 805 Sherbrooke Street West, Montreal, Quebec, H3A 2K6, Canada; E-mail: cnf@zephyr.meteo.mcgill.ca

2. NUMERICAL METHODS

The turbulent flow field is generated by solving the Navier Stokes equations using a pseudo-spectral model. For a detailed description of the model see Vaillancourt et al. (2001). Four numerical simulations are performed with the number of grid points N^3 equal to 80^3, 120^3, 180^3 and 240^3. The computational domain is fixed for all experiments at 10 cm^3, thus we increase in spatial resolution from a grid length of 0.125 cm to 0.04166 cm. The flow field that is generated by the model is homogeneous and isotropic and this structure is expected to be representative of the small-scale flow of adiabatic cloud cores. The average eddy dissipation rates, $\bar{\varepsilon}$, for the simulations are 95, 280, 656 and 1535 $cm^2\ s^{-3}$, which span the range of observed values.

The equation of motion for the droplets is

$$\frac{d\mathbf{V}(t)}{dt} = \frac{1}{\tau_p}(\mathbf{U}[\mathbf{X}(t),t] - \mathbf{V}(t)) + \mathbf{g}$$

where **V**(*t*) is the droplet velocity at time *t*, **U** is the flow field, **X**(*t*) is the droplet position and τ_p is the droplet inertial response time based on the Stokes drag force. The collision statistics have been calculated for droplets of size 10 and 20 μm in radius. 25000 droplets of each size are tracked through the simulation. The droplets are introduced into the domain once the turbulent flow field has reached a statistically stationary state. To ensure there is no influence of the initial conditions on the results, the droplet positions and velocities are allowed to evolve in time before the calculation of the collision statistics begins. For a description of the collision detection scheme and a discussion on the accuracy of the results see Franklin et al. (2003).

3. RESULTS

3.1 Angle of Approach

Droplet motion is governed by gravitational and turbulent accelerations. When droplets are falling only under the force of gravity, the angle of approach is always from above with a mean of 0 degrees. However, when the droplets also experience accelerations from the turbulent flow field, this angle can be anything from 0 to 180 degrees. Examining the angle of approach can be useful in determining how important the turbulent accelerations are in comparison to the gravitational acceleration. If the turbulent accelerations are small then we expect the

mean angle to be close to zero, and if the turbulent accelerations are large compared to the gravitational forcing then we expect the angle of approach to be a random variable, so the distribution would have a mean angle of 90 with a large variance.

Table 1. Moments of the distribution of the angle of approach for colliding droplet pairs.

$\bar{\varepsilon}$ (cm^2 s^{-3})	95	280	656	1535
mean	33	45	54	64
variance	331	632	958	1231
skewness	1.5	1.3	1.2	0.6
kurtosis	5.8	2.8	1.4	-0.3

As Table 1 shows the trend is for the mean angle of approach to increase with the mean eddy dissipation rate. For the most energetic flow field the mean angle is 64 and the spread in the distribution is large. Since the mean angle is not close to 90, this suggests that the gravitational accelerations are still an important factor in determining the droplet motion. The trend for the skewness and the kurtosis to converge towards zero with increasing eddy dissipation rate, reflects the increasing impact of the fluid accelerations on the droplet motion compared to the gravitational accelerations.

3.2 Radial Relative Velocities

The collision kernel or swept out volume is partly a function of the relative velocity between droplets. Just as the differential inertia effect due to gravitational acceleration defines the relative velocity in a quiescent flow, this effect also contributes to the relative velocities amongst droplets in a turbulent flow field. The quantity that is input into the collision kernel calculation is the mean radial relative velocities of droplet pairs that are separated by a slightly larger distance than that required for a collision. The reason being that the non-uniform flow field results in a local non-uniform relative velocity distribution (Wang et al. 2000). The gradual increase in the mean radial relative velocity between closely separated droplets across the three least energetic flows is shown in the last column of Table 2. For the flow with an average eddy dissipation rate of approximately 1500 cm^2 s^{-3}, the mean relative velocity increases at a much larger rate than across the other three flow fields. Similarly to the angle of approach distributions, the variance increases with the more energetic flow field. This is a reflection of the increasing intermittency of the turbulence causing a wider range of Lagrangian flow accelerations and consequently a broader distribution.

3.3 Preferential Concentration

In a bidisperse system the clustering is determined by the correlation between particle concentrations of the two size groups. Zhou et al. (2001) demonstrated that particles of different sizes will tend to cluster in different regions of the flow field due to the different inertial responses to the flow accelerations. The results for the calculation of the radial distribution function between the 10 and 20 micron droplets are documented in column 5 of Table 2. For the least energetic flow field the droplet positions experience no deviation from a Poisson distribution and thus $g(r)=1$. The clustering effect increases with increasing eddy dissipation rate up to a value of 1.43 for the 240^3 simulation. This means that in this simulation, the probability of observing a pair of 10 and 20 μm droplets at contact in the suspension is 1.43 times greater than in the purely gravitational case.

Table 2. Collision statistics for the four different flow fields. The columns are the mean eddy dissipation rate of the flow (cm^2 s^{-3}), the Reynolds number, the geometric collision kernel based on the direct counting of collisions, the increase in the kernel compared to the gravitational geometric collision kernel, the radial distribution function (gravitational case=1.0) and the mean radial relative velocities (cm s^{-1}) (gravitational case=1.85) of the droplets that are closely separated in the domain.

$\bar{\varepsilon}$	R_λ	Γ_{DNS} x10^{-4} (cm^3 s^{-1})	increase	$g(R)$	$\lvert\langle w_r\rangle\rvert$
95	33	1.12	1.075	1.0	1.99
280	40	1.32	1.27	1.14	2.06
656	48	1.78	1.71	1.33	2.19
1535	55	3.38	3.25	1.43	4.26

3.4 Turbulent Collision Kernels

The collision kernels based on the direct counting of collisions given by

$$\Gamma = \frac{\langle n_c \rangle \Omega}{N_1 N_2 \Delta t}$$

for the four simulations are presented in Table 2. In this equation n_c is the number of collisions per time step, Ω is the volume, N is the number of droplets and Δt is the time step. The kernels are greater than the equivalent gravitational kernel for every turbulent flow field, showing increases ranging from 1.075 to 3.25 times the gravitational case. In the least energetic flow, the increase is solely due to the increase in the radial relative velocities between droplets that are closely separated. For the case with the mean eddy dissipation rate of 280 cm^2 s^{-3} the contribution to the increase of the kernel is equally divided between the two physical mechanisms of clustering and relative velocity. The effect of preferential concentration accounts for a larger percentage of the increased kernel for the case with a mean dissipation rate of 656 cm^2 s^{-3}. The increase of 3.25 times for the most energetic flow field is predominantly due to the increase in $|\langle w_r \rangle|$. These results show that the increase in the turbulent geometric collision kernel with eddy dissipation rate is almost a linear function.

3.5 Collision Efficiencies

When two droplets approach one another, the fluid they push aside as they move through a medium interacts with the other droplet and tends to prevent the droplets from colliding. This means that when we include hydrodynamic forcing between interacting droplets, the number of collisions will differ from the results obtained when these forces are omitted. The Reynolds number of the droplets used in this study is <<1 and thus we use Stokes flow to represent the hydrodynamic flow field and as a consequence neglect any wake effects. Details on the implementation of the Stokes flow solution to a 3 dimensional framework are given in Franklin et al. (2003).

To test the algorithm developed to calculate the hydrodynamic forces between interacting droplets, we first applied it to the case of 10 and 20 micron droplets falling only under gravity. The collision efficiency is defined to be

$$E = \frac{no.\ of\ collisions\ with\ hydrodynamics}{no.\ of\ collisions\ with\ no\ hydrodynamics}$$

When the separation distance is set to be 10 times the radius of the largest drop, 0.02 cm, E = 0.08. Therefore, when the flow fields of the interacting droplets are included in the forcing, only 8% of the collisions that occurred with no hydrodynamic forcing now occur. This value is well within the range of other theoretical studies, which spans from about 0.03 to 0.11 (Pruppacher and Klett 1997). Such a broad range exists due to the necessary use of approximations and the lack of definitive experimental work for comparison.

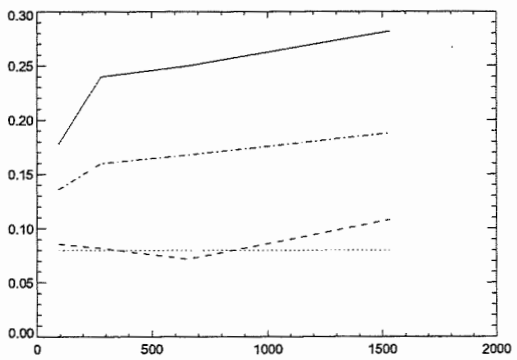

Figure 1. Collision efficiency for the four numerical experiments plotted as a function of eddy dissipation rate ($cm^2\ s^{-3}$). The results are calculated for an initial separation distance of 0.02 cm (solid line), 0.04 cm (dot-dash line) and 0.1 cm (dashed line). The dotted line represents the efficiency for the gravitational case.

The turbulent collision efficiencies have been calculated by taking the background flow field to be fixed over the time of interaction and by assuming that only two drops interact at a time. Figure 1 shows how the collision efficiency changes with respect to the eddy dissipation rates of the four numerical simulations. The collision efficiency for the separation distance of 0.02 cm is greater than the gravitational value of 0.08 for all four flow fields examined. The efficiency increases with increasing eddy dissipation rate from 2.2 times the gravitational value for the least energetic flow field to 3.5 times for the most energetic. This reflects the positive effect that the increased relative velocities have on promoting collisions between interacting droplets.

The total collision-coalescence process is determined by the collection kernel, which is the product of the collision kernel, the collision efficiency and the coalescence efficiency. Figure 2 shows the product of the first two of these processes. For the separation distance of 0.02 cm the increase in the collision kernel including the hydrodynamic effects ranges from 2.4 to 11.4 times the corresponding gravitational case. These increases are significant and are expected to affect the broadening and evolution of the drop size distribution, and as a consequence the onset of precipitation.

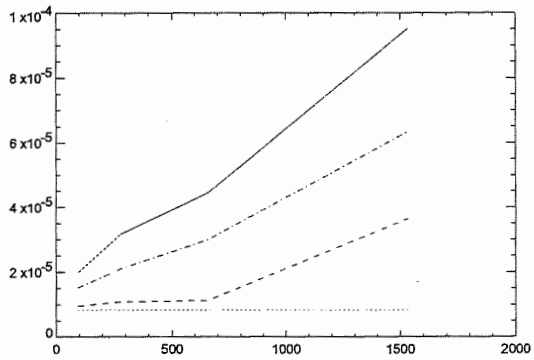

Figure 2. b) Product of the geometric collision kernel ($cm^3\ s^{-1}$) and the collision efficiency as a function of eddy dissipation rate ($cm^2\ s^{-3}$). The results are for a separation distance of 0.02 cm (solid line), 0.04 cm (dot-dash line) and 0.1 cm (dashed line). The dotted line is the corresponding value for the droplets in calm air.

The relative velocities in the turbulent cases are greater than the case with gravitational forcing only and perhaps the characteristic length scale of the interaction between 2 droplets is larger. To test the sensitivity of the collision efficiency to larger separation distances, the efficiencies were calculated with separation distances equal to 0.04 cm and 0.1 cm. For a doubling of the separation distance to 0.04 cm, the efficiencies decrease from the previous results for all flow fields (see Fig. 1). The collision efficiency for the flow field with an average eddy dissipation rate of 95 $cm^3\ s^{-2}$ is 0.136, or 1.7 times the gravitational efficiency. This is 43% less than the increase in efficiency for a separation distance of 0.02 cm. The most energetic case, with an average eddy dissipation rate of about 1500 $cm^3\ s^{-2}$, has a reduction in the

increased efficiency of 53% from the smaller separation distance. The value is 2.4 times greater than the gravitational case and when this is multiplied by the collision kernel the result is 7.95×10^{-4} cm^3 s^{-1}, which is 7.6 times greater than the gravitational kernel including the hydrodynamic forces.

The reason why the efficiencies decrease is due to the longer interaction times associated with a larger separation distance. These results demonstrate that as the relative velocities between droplets increases so do the distance over which the flow fields affect the collision process. This suggests that the parameter that defines the length scale of the interaction distance should be a function of gravity and the turbulence properties that determine the relative velocities. It should be noted that as the separation distance is increased the assumption that the flow field is fixed over this distance becomes less valid. The average interaction times for the largest separation distance for the four cases are 0.025, 0024, 0022 and 0.011 seconds. If we compare these times to the characteristic timescale of the small-scale vortices of the flow, 0.04, 0.02, 0.015 and 0.01 s, it becomes apparent that certainly for the three most energetic flows, the velocity of the flow will have evolved over this length of time. These results however, give a good grounding in understanding the interaction between the droplets and show the necessity to extend these results with an evolving flow field.

4. DISCUSSION

The effect of turbulent flow on the collision rates of cloud droplets has been explored by the use of a direct numerical simulation of the flow field. By implementing an efficient scheme to detect collisions, large numbers of droplets have been explicitly tracked as they move within the turbulent flow and the collision rates and characteristics of the droplets at the time of collision have been investigated. Four numerical simulations with increasing rates of eddy dissipation have been performed. As the intensity of the turbulence increases, the deviation from the gravitational statistics becomes greater. The mean angle of approach diverges from 0 degrees more as the flow becomes increasingly energetic, with a difference in the mean of approximately 30 degrees from the least to the most energetic flow. However, even for the most energetic flow field explored in this study the gravitational acceleration gives the droplets a preferred direction of motion and restrains the angle from being a random variable.

The collision efficiencies were shown to be sensitive to the separation distance over which the calculation is performed. The results presented are for the simplified problem of two interacting droplets, whereby the flow field is stationary over the time of interaction. For a separation distance of 10 times the radius of the largest drop, 0.02 cm, the collision efficiencies increased across the four simulations from 2.2 to 3.5 times the gravitational value. As the distance was increased to 0.04 cm, these values decreased to 1.7 and 2.4 times and to 1.1 and 1.4 times for a distance of 0.1 cm. These increased efficiencies, together with the increases in the geometric collision kernel, translate into increases in the product of these two quantities of a maximum of 2.4 times for the flow with a mean eddy dissipation rate of 95 cm^2 s^{-3} and 11.4 times for the case with an eddy dissipation rate of 1535 cm^2 s^{-3}. These increases are significant and are expected to influence the evolution of the drop size distribution and expedite the growth of rain drops. As demonstrated for the geometric collision kernel, the product of the kernel with the efficiency is also a linear function of eddy dissipation rate. These results illustrate the importance of understanding how the droplets interact to be able to determine a characteristic length scale for calculating the hydrodynamic forces between interacting droplets, and to compute the collision kernels and efficiencies for other sized droplets to verify whether the linear scaling is appropriate for the range of droplet radii involved in the problem of effective coalescence growth.

5. ACKNOWLEDGEMENTS

This work was supported by the Canadian Foundation for Climate and Atmospheric Sciences.

6. REFERENCES

Franklin, C.N., P.A. Vaillancourt, M.K. Yau and P. Bartello, 2003: Collision rates of cloud droplets in turbulent flow. Submitted to *J. Atmos. Sci.*

Pruppacher, H.R. and J.D. Klett, 1997: *Microphysics of Clouds and Precipitation.* Dordrecht, The Netherlands: Kluwer

Sundaram, S. and L.R. Collins, 1997: Collision statistics in an isotropic particle-laden turbulent suspension. Part I: Direct numerical simulations. *J. Fluid Mech.*, **335**, 75-109

Vaillancourt, P.A., M.K. Yau and W.W. Grabowski, 2001: Microscopic approach to cloud droplet growth by condensation. Part I: Model description and results without turbulence. *J. Atmos. Sci.*, **58**, 1945-1964

Wang, L.-P. and M.R. Maxey, 1993: Settling velocity and concentration distribution of heacy particles in homogeneous isotropic turbulence. *J. Fluid Mech.*, **256**, 27-68

Wang, L.-P., A.S. Wexler and Y. Zhou, 1998: Statistical mechanical description of turbulent coagulation. *Phs. Fluids*, **10**, 2647-2651

Wang, L.-P., A.S. Wexler and Y. Zhou, 2000: Statistical mechanical description and modelling of turbulent collision of inertial particles. *J. Fluid Mech.,* **415**, 117-153

Zhou, Y., A.S. Wexler and L.-P. Wang 2001: Modelling turbulent collision of bidisperse inertial particles. *J. Fluid Mech.,* **433**, 7

CLOUD WATER CONTENT AND CLOUD PARTICLE CHARACTERISTICS REVEALED BY DUAL WAVELENGTH CLOUD RADAR OBSERVATIONS

Nicolas Gaussiat, Robin J. Hogan and Anthony Illingworth

Department of Meteorology, University of Reading, Reading, Berkshire, United Kingdom

1 INTRODUCTION

Observations of clouds made with a single frequency radar are difficult to interpret in terms of water content and particles size, shapes and densities, but most of these ambiguities can be removed if two frequencies are used.

In stratocumulus and liquid water clouds, profiles of liquid water content can be derived from the increased attenuation by liquid water at 94GHz. In ice clouds the particle size can be inferred from the reduced reflectivity, Z, due to Mie scattering at 94GHz when compared to the 35GHz reflectivity. The dual-wavelength difference of the Doppler velocities can be combined with the dual wavelength reflectivity ratio to derive the apparent density variation of ice particles with their size. Finally, when size and density informations are combined with the 35GHz reflectivity, more accurate ice water content can be derived, then those inferred from empirical relationships expressing IWC as a function of Z.

In this paper we present results obtained using measurements from the Cloud Profiling Radar System (CPRS) a dual-wavelengh radar at 33- and 95-GHz at the central Atmospheric Radiation Measurement (ARM) site im Oklahoma.

2 STRATOCUMULUS LIQUID WATER CONTENT

The main difficulty in measuring LWC in liquid cloud is that they often contains small concentrations of 'drizzle' drops (those larger than around 50 μm) which can dominate the radar reflectivity but contribute negligibly to LWC (Fox and Illingworth 1997). Dual-wavelength measurements take advantage of the fact that small droplets dominate the attenuation and are small enough to attenuate in the Rayleigh regime.

2.1 Theory

In conventional logarithmic units the reflectivity measured at frequency f and height z may be given by

$$Z_f = Z_0 + 10\log_{10}\left(\frac{|K_f|^2}{0.93}\right) - 2\int_0^z (\alpha_f + \kappa_f \mathrm{LWC})\, dz, \quad (1)$$

where Z_0 is the unattenuated reflectivity factor at centimetre wavelengths in conventional dBZ units, α_f is the one-way specific attenuation coefficient due to atmospheric gases (predominantly molecular oxygen and water vapor) in dB km^{-1}, and κ_f is the one-way specific attenuation coefficient of liquid water and has the units dB km^{-1}(g m^{-3})$^{-1}$. The second term on the right hand side accounts for the fact that at millimeter wavelengths the dielectric parameter of water, $|K|^2$, is less than its centimeter-wavelength value of 0.93, and is a function of temperature. K is related to the complex dielectric constant, ε, by $K = (\varepsilon - 1)/(\varepsilon + 2)$. We have assumed that extinction by absorption dominates extinction by scattering. We define the dual-wavelength ratio in logarithmic units as DWR [dB] $= Z_{35}$ [dBZ] $- Z_{94}$ [dBZ]. From (1), the mean LWC in a layer between heights z_1 and z_2 can then be determined from the DWR measured at the top and bottom of the layer (indicated by the subscripts 2 and 1 respectively):

$$\overline{\mathrm{LWC}} = \frac{1}{\kappa_{94} - \kappa_{35}}\left(\frac{\mathrm{DWR}_2 - \mathrm{DWR}_1 - \beta}{2(z_2 - z_1)} - \alpha_{94} + \alpha_{35}\right), \quad (2)$$

where

$$\beta = 10\log_{10}\left(\frac{|K_{35}(T_1)|^2}{|K_{35}(T_2)|^2}\frac{|K_{94}(T_2)|^2}{|K_{94}(T_1)|^2}\right) \text{ dB}. \quad (3)$$

It has been assumed that the attenuation coefficients α and κ are constant over the depth of the layer. The β parameter accounts for the difference in temperature T at the two heights.

The attenuation coefficients and the β parameter are functions of temperature, and the attenuation of atmospheric gases is also dependent on pressure and humidity, so an independent measure of the vertical profiles of these variables is required in the retrieval. These can be obtained from radiosonde or from the output of a forecast model, although in practice it is always assumed that cloudy air is saturated with respect to liquid water. We calculate ε (and hence β and κ) from temperature using the formulation of Liebe et al. (1989), and the line-by-line model of Liebe (1985) to compute α_f as a function of temperature, pressure and humidity.

2.2 Uncertainties

The accuracy which LWC can be determined depends on the precision of the reflectivity measurements, the accuracy of the temperature profile and the overlap precision of the sample volumes of the radars. It can be shown (Hogan 1998) that the errors in reflectivity are related to

Corresponding author address: Nicolas Gaussiat, Department of Meteorology, University of Reading, Earley Gate, PO Box 243, Reading RG6 6BB, UK; E-mail: N.Gaussiat@reading.ac.uk.

the temporal and vertical averaging and to signal-to-noise ratio. Errors due to Mie scattering effects are smaller than 0.05 g m^{-3} if drizzle drops are smaller than 600 μm. Thus, lidar cloud base is used to screen out data contaminated by large drizzle drops falling below cloud base. Uncertainties due to errors in temperature profile are found to very small. We assume that errors due to cloud inhomogeneity are negligible, since the CPRS is built on a single feed and single lens antenna that reduce pointing errors and since at least a minute averaging is applied to the data.

2.3 Results

In Figure 1, observations are presented from the CPRS on the 23 September 1997. The reflectivity field in Fig.1a shows a complex structure with more than one layer present. Drizzle drops larger than 600 μm will Mie scatter and start to make a contribution to the DWR, but their terminal velocity will be 2.5 m s^{-1}, rather larger than the 2 m s^{-1} measured in Fig. 1b at 21:07. So, we believe that this effect is negligible and after calculating DWR and deriving LWC (Fig.1c and 1d), this assumption is confirmed by the

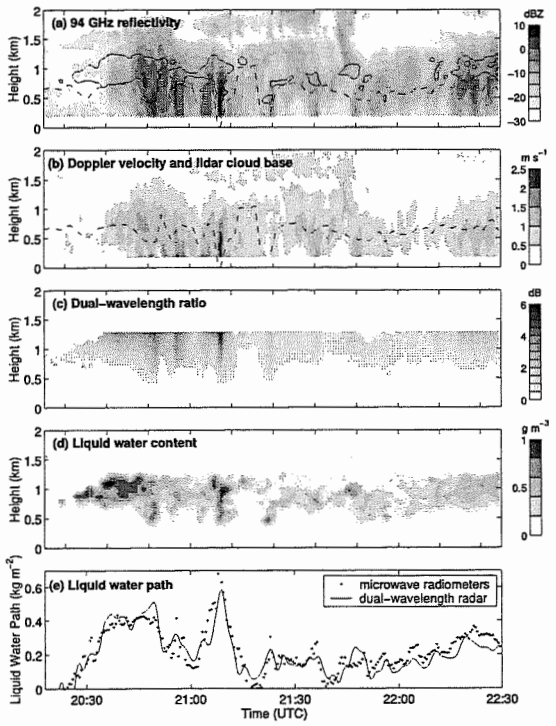

Figure 1: Dual-wavelength measurements by the CPRS on 23 September 1997 : (a) radar reflectivity factor at 95 GHz, ceilometer cloud base (dashed line) and LWC=0.6 g m^{-3} (solid contour) (b) Dopper velocity and ceilometer cloud base, (c) dual wavelength ratio above the ceilometer cloud base, (d) liquid water content (e) comparison of the liquid water paths deduced and from the dual-wavelength technique and microwave radiometers. The data were averaged to 1 minute and 60 m (2 gates) in vertical before liquid water content was derived.

excellent agreement of values of the vertically-integrated LWC presented in Fig.1e with the LWP estimated from microwave radiometer. Note that the values of LWC bear little relationship to Z, confirming the dangers of applying a simple Z-LWC law.

3 ICE PARTICLE DENSITY AND SIZE

Brown et al. (1995) have used aircraft measurements to get values of the mass and the maximum dimension of the ice particles and they found that $\rho(D) = 0.07D^{-1.1}$ where D is the diameter of the equivalent spherical particle in millimeter. Using the same dataset, Francis et al. (1998) derived an alternative formula by expressing the diameter of a circle of area equal to the observed cross-section area and suggested that $\rho(D) = 0.175D^{-0.66}$, but, the choice between these two density functions remains unclear and raise uncertainties in the estimation of size and IWC (Liu and Illingworth 2000).

3.1 Background

In ice clouds, the particle size-distribution is usually well represented by a simple exponential distribution $N(D) = N_0 \exp(-\Lambda D)$ where Λ is related to the median volume diameter by $D_0 = 3.67/\Lambda$. The unattenuated reflectivity factor Z_0, defined in Sec. 2, in the Mie scattering theory depends on the frequency of the radar and is given by:

$$Z_{0,f} = \int D^6 f(D,\lambda) N(D) dD, \qquad (4)$$

where $f(D,\lambda)$ is the ratio of the Mie scattering to an assumed Rayleigh scattering for a given value of λ. If large ice particles are present Mie scattering will occur for mm wave radar and $f(D,\lambda)$ fall below unity. As a result, in the liquid absence of attenuation, DWR defined in section 2 is a function of D_0 and can be used (Sekelsky et al. 1999, Hogan et al. 2000) to infer particles size. However Fig. 2a shows that the results also depend significantly on the density relations used.

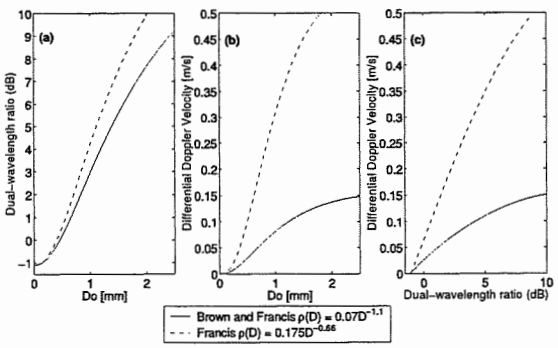

Figure 2: Theoretical results for Brown and Francis (1995) (plain lines) and Francis et al. (1998) (dotted lines) density relations, (a) DWR against Do, (b) ΔV_D against Do, (c) ΔV_D against DWR.

The Doppler velocity measured by a vertically pointing radar is $V_D = V_a + V_Z$ where V_a is the vertical air velocity

and V_Z the reflectivity-weighted particle terminal velocity given by :

$$V_Z = \frac{\int v_t(D) D^6 f(D,\lambda) N(D) dD}{\int D^6 f(D,\lambda) N(D) dD}, \quad (5)$$

where v_t is the terminal velocity of an individual particle. D is usually given as the maximum particle dimension. Since in the following developments we assume that particles are spherical then D is the diameter. A basic equation to estimate the terminal velocity of ice particles is (Mitchell 1996):

$$v_t = a \left(\frac{2g}{\rho_a}\right)^b \nu^{1-2b} D^{2b-1} \left(\frac{m}{A}\right)^b, \quad (6)$$

where g is the gravitational acceleration; ρ_a is the air density; ν is the kinematic viscosity; m is the particle mass; A is the particle cross-section area; and a and b coefficients are derived from the drag law. Considering the spherical assumption and a density relationship $\rho(D)$ for the ice particles, $A = \frac{\pi}{4}D^2$ and $m = \frac{\pi}{6}\rho(D)D^3$ then using (5) and (6):

$$V_Z = \frac{\int_0^\infty a \left(\frac{4g}{3\rho_a}\right)^b \nu^{1-2b} \rho(D)^b D^{5+3b} f(D,\lambda) e^{\frac{-3.67}{D_0}} dD}{\int_0^\infty D^6 f(D,\lambda) e^{\frac{-3.67}{D_0}} dD}. \quad (7)$$

The difference, ΔV_D, in values of V_D at 95 and 33GHz is independent of the vertical air velocity and depends only on D_0 only and $\rho(D)$. Figure 2b shows the variations of ΔV_D with D_0 for the two density relationships. The information in Fig. 2a and 2b is combined in figure 2c where ΔV_D is plotted against the DWR. The two density functions lead to two distinct curves.

3.2 Observations

In March 2000, a long serie of cirrus cloud observations was performed by the CPRS. Figure 3 displays in the two first panels the reflectivity factor distribution and mean Doppler velocity distribution observed by the 33 GHz channel on the 12 March 2000 in 4 km deep ice cloud. The reflectivity field structure is dominated by fall streaks slanted by the wind shear whereas the Doppler velocity field structure is dominated by convective motions at the top and the bottom of the cloud. It is difficult to find any kind of correlation between these two fields. In contrast the differential parameters DWR and ΔV_D shown in the two panels underneath are very well correlated, the similar increases in both DWR and ΔV_D are corresponding to growing values of D_O related to aggregation processes. ΔV_D as a function of DWR from the co-located measurements is plotted Fig.4. On top of the scatter plot, are the theoretical curves from Fig. 2c, for the two density functions. It can be seen without ambiguity that the scatter plot of data matches the theoretical calculations only if the Brown and Francis density relationship is used.

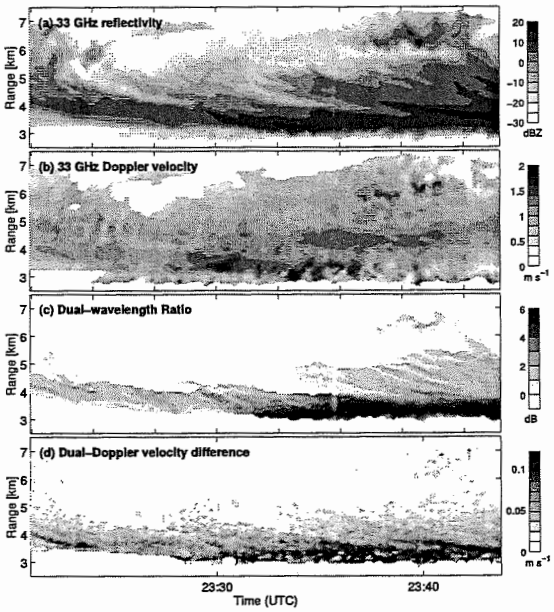

Figure 3: Observations of cirrus by the CPRS on the 12 March 2000: (a) Reflectivity factor at 33 GHz, (b) Doppler velocity measured by the CPRS at 33 GHz (c) Dual-wavelength ratio, (d) Dual-wavelength Doppler velocity difference.

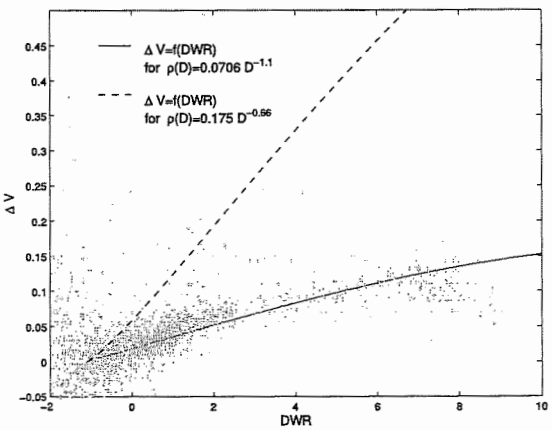

Figure 4: ΔV_D as function of DWR for both theoretical calculations and measurements

3.3 Ice water content calculations

Since the density relationship ambiguity has been resolved, a better estimation of D_0 is obtained from dual-wavelength measurements, and using measurements of the reflectivity at 35 GHz, a more accurate calculation of IWC can be produced (Hogan et al. 2000). Figure 5a and 5b shows values D_0 and IWC retrieved from the observations in Fig. 3. Figure 5c shows the IWC derived with IWC derived from IWC=$0.137Z^{0.643}$ empirical relation based on Brown and Francis density relationship assumption (Liu and Illingworth 2000). In Fig. 6 are plotted profiles of IWC at 23:42 obtained using both dual-wavelength and empirical methods and for the two density relationships.

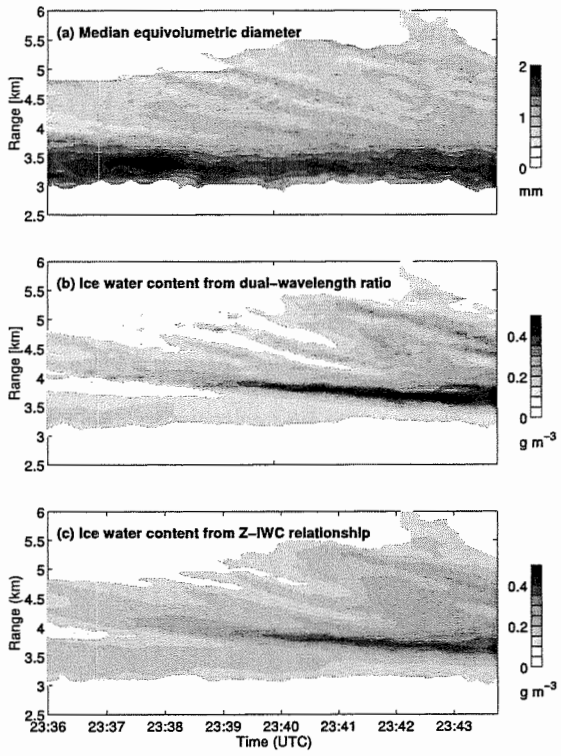

Figure 5: Dual-wavelength retrieved parameters between 23:33 and 23:44 : (a) Median equivolumetric diameter D_0, (b) Ice water content using DWR technique and Brown and Francis (1995) density relation, (c) Ice water content using IWC=0.137Z$^{0.643}$ empirical relation.

It can be seen that empirical and dual-wavelength derived IWC profiles based on Brown and Francis (1995) assumption are matching whereas those based on Francis et al. (1998) assumption disagree and also underestimate IWC by 30% to 60%.

4 CONCLUSION

In this paper, we have shown that from dual-wavelength radars measurements in liquid clouds, detailed vertically resolved measurements of LWC can be derived. Because drizzle is very often present in such clouds, the differential technique is successful when other technique fail. Mie scattering bias when drizzle is present does not appear to be a problem. Dual-wavelength measurements of Doppler velocities are also used to derive the density of ice particles as a function of size. A theoretical relation between the dual-wavelength reflectivity ratio and the dual-wavelength Doppler velocity difference is presented for two density functions. Comparison between observation and theoretical differential Doppler calculations agreed only when Brown and Francis density function is used. In addition, the IWC calculated from dual-wavelength was found to be in very good agreement with the empirical Z-IWC relation only when Brown and Francis density function is used.

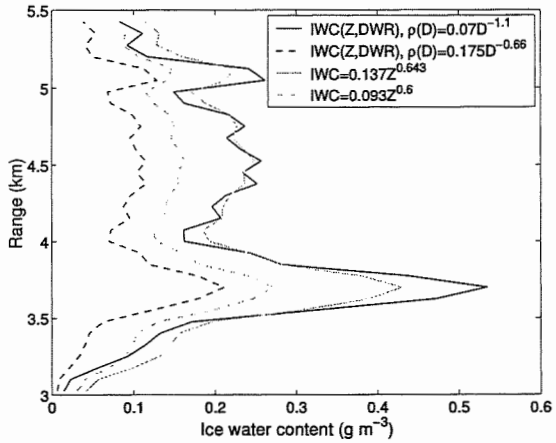

Figure 6: Profiles of ice water content at 23:42 derived from DWR technique (in black) and Z-IWC empirical technique (in gray) for Brown and Francis (1995) (plain lines) and Francis et al. (1998) (dotted lines) density relations.

Acknowledgements

We thank U.S. Department of Energy as part of the Atmospheric Radiation Measurement Program for CPRS radar data and support from NERC grant NER/T/S/1999/00105 and the EU CloudNET contract EVK2-CT-2000-00065.

REFERENCES

Brown, P. R. A., and P. N. Francis, 1995: Improved measurements of the ice water content in cirrus using a total-water probe. *J. Atmos. Oceanic Technol.*, **12**(2), 410–414.

Brown, P. R. A., A. J. Illingworth, A. J. Heymsfield, G. M. McFarquhar, K. A. Browning and M. Gosset, 1995: The role of spaceborne millimeter-wave radar in the global monitoring of ice-cloud. *J. Appl. Meteor.*, **34**(11), 2346–2366.

Fox, N. I., and A. J. Illingworth, 1997: The potential of a spaceborne radar for the detection of stratocumulus clouds. *J. Appl. Meteor.*, **36**(6), 676–687.

Francis, P. N., P. Hignett and A. Macke, 1998: The retrieval of cirrus cloud properties from aircraft multi-spectral reflectance measurements during EUCREX'93. *Quart. J. Roy. Meteor. Soc.*, **124**, 1273–1291.

Hogan, R. J., 1998: *Dual-wavelength radar studies of clouds.* PhD Thesis, University of Reading, UK.

Hogan, R. J., A. J. Illingworth and H. Sauvageot, 2000: Measuring crystal size in cirrus using 35- and 94-GHz radars. *J. Atmos. Oceanic Technol.*, **17**(1), 27–37.

Liebe, H. J., 1985: An updated model for millimeter-wave propagation in moist air. *Radio Science*, **20**(5), 1069–1089.

Liebe, H. J., T. Manabe and G. A. Hufford, 1989: Millimeter-wave attenuation and delay rates due to fog/cloud conditions. *IEEE AP*, **37**, 1617–1623.

Liu, C.-L. and A. J. Illingworth, 2000: Towards more accurate retrievals of ice water content from radar measurement of clouds. *J. Appl. Meteor.*, **39**, 1130–1146.

Mitchell, D. L., 1996: Use of mass- and area-dimensional power laws for determining particle terminal velocities. *J. Atmos. Sci.*, **54**, 1710–1723.

Sekelsky, S. M., W. L. Ecklund, J. M. Firda, K. S. Gage and R. E. McIntosh, 1999: Particle size estimation in ice-phase clouds using multifrequency radar reflectivity measurements at 95, 33 and 2.8 GHz. *J. Appl. Meteor.*, **38**(1), 5–28.

SUPERSATURATION MEASUREMENTS IN A STRATOCUMULUS

H. Gerber

Gerber Scientific Inc., Reston, VA 20190

1. INTRODUCTION

We revisit a method developed years ago (Gerber, 1980) to measure water vapor supersaturation, S, directly in a cloud using a supersaturation hygrometer, SH. The first instrument version of the SH was used for measurements in radiation fog (Gerber, 1991), where it showed significant promise by demonstrating the relationship between isobaric mixing of saturated air parcels and S transients. An opportunity arose to build a second version of SH (Gerber, 1994), where the goals were to slim down the 30-lb weight of the original SH, and to take advantage of newer developments in electronics and optics. We briefly describe unpublished information dealing with the latest version of the SH, and show measurements made with this probe in one traverse with a motorized blimp through a stratocumulus during the MAST study off the coast of Washington and California.

2. SATURATION HYGROMETER

The principle of operation of the newer SH is the same as described in Gerber (1991). Basically, controlled condensation sites on a hydrophobic and thermally-thin mirror respond to ambient relative humidity, RH, which is sensed optically. The response of the probe is referenced to RH=100% generated in a "wet box". When ambient RH exceeds 100% a heater warms the mirror to keep the optical signal at the 100%-RH reference level. The increased temperature of the mirror can be shown to be directly proportional to the ambient value of S. Figure 1 shows a photo of the new SH.

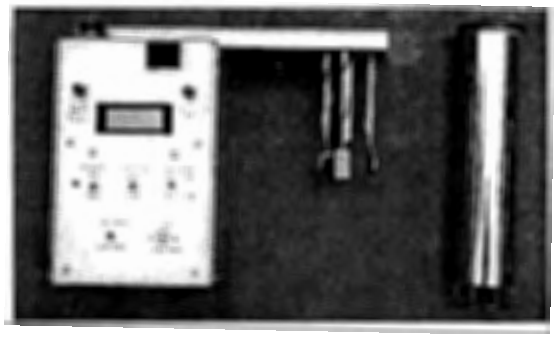

Fig. 1 - Supersaturation hygrometer; height 25cm

Corresponding author's address. H. Gerber, Gerber Scientific Inc., 1643 Bentana Way, Reston, VA 20190, USA, E-Mail: hgerber6@comcast.net

The box on the left side of Fig. 1 contains the electronics, the hollow bar on the top of the box supports the hygrometer mirror, light source, heater, and light sensor. On the far right is the radiation shield which slides over the sensing components and mounts to the bar. A fan in the box aspirates ambient air past the components when the radiation shield is in place.

The means for referencing the SH are shown in Fig. 2, where the sensing components (minus the radiation shield) are projected into the "wet box" which is thermally insulated, has interior walls wetted with distilled water, and has a fan stirring the humidified air. The RH in the wet box reaches saturation after about 5 min at which time the ~100% RH reference has been established for the SH, and the probe can be used for ambient measurements. Ambient deviations in RH about RH-100% are scaled according to prior temperature measurements of the mirror as a function of the heater output; for details see Gerber (1991).

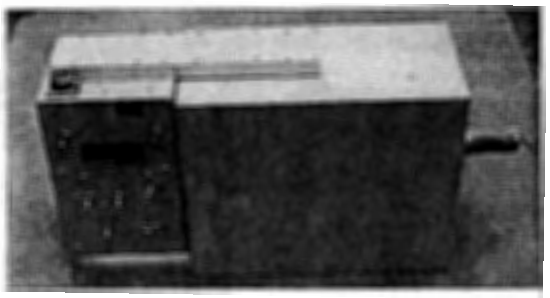

Fig. 2 - The supersaturation hygrometer mated with the wet box used to establish the RH=100% reference.

3. MEASUREMENT

The SH shown in Fig. 1 was deployed on the USA-LTA motorized blimp used during the MAST study of stratocumulus off the West Coast in June of 1994. It was suspended below the forward part of the blimp hull close to a PVM-100A which measured liquid water content, LWC. Unfortunately, for the couple of weeks that this SH deployment lasted, there was a near total lack of stratocumulus, Sc. During this period a vertical profile was made with the blimp through only one thin Sc. The rate of descent of the blimp was slow, and the thickness of the Sc was about 200m. The measured values of S and LWC for this profile are shown in Fig. 3.

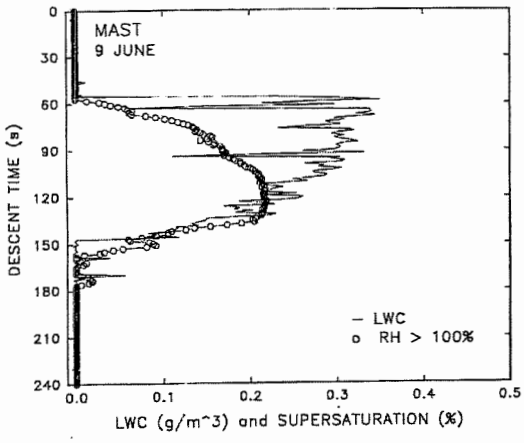

Fig. 3 - Supersaturation (%) and liquid water content profiles measured in a stratocumulus during the descent of the USA-LTA motorized blimp.

The S values appear reasonable, given the sharp increase of S near Sc base and then a gradual decrease of S with height. These trends are similar to what might be expected for a water cloud with an adiabatic profile and a modest updraft (e.g., see Korolev and Mazin, 2003).

The overall performance of the SH during the MAST deployment was judged to be fair; even though the weight of the new unit had been reduced by a factor of about 10 from the earlier unit. Electronic drift, background noise, and time response were the main deficits. It would be desirable to go through another iteration in the development of this measurement approach to produce a practical sensor.

Such a sensor would meet a significant gap in cloud physics, where cloud supersaturations are often calculated and modeled, but never measured.
The sensor would permit comparisons to be made between calculations and measurements under many circumstances. For example, the hypothesized isobaric mixing effect on the activation of new droplets discussed by Gerber (1991) for ground fog and Korolev and Isaac (2000) for Sc could be further tested. The crucial requirement in the measurement of S with the SH is the precise control of the probe's temperature. For example, a measure of S=.1% requires a temperature control of about 0.01 C. This requirement potentially limits the use of the SH for ground-based, balloon, blimp, and perhaps slow-flying aircraft measurements.

4. ACKNOWLEDGMENTS

William Hoppel and Glendon Frick from Naval Research Laboratory are thanked for deploying the saturation hygrometer on the USA-LTA motorized blimp during the MAST study. H.G. was funded by the National Science Foundation.

5.REFERENCES

Gerber, H., 1980: A saturation hygrometer for the measurement of relative humidity between 95% and 105%. *J. Appl. Meteor.*, **19**, 1196-1208.

_____ , 1991: Supersaturation and droplet spectral evolution in fog. *J. Atmos. Sci.*, **48**, 2569-2588.

_____ , 1994: Hygrometer for measurement of relative humidiy in clouds. *Final Report*, NSF Grant 9261243, pp. 19.

Korolev, A.V., and G.A. Isaac, 2000: Drop growth due to high supersaturations caused by isobaric mixing. *J. Atmos. Sci.*, **57**, 1675-1685.

_____ , and I.P. Mazin, 2003: Supersaturation of water vapor in clouds. *J. Atmos. Sci.*, **60**, 2957-2974.

PRECIPITATION DEVELOPMENT IN CLOUDS WITH MARITIME VERSUS CONTINENTAL CHARACTERISTICS

Sabine Göke, Harry T. Ochs, Robert M. Rauber, and Neil F. Laird
Department of Atmospheric Sciences, University of Illinois at Urbana-Champaign, IL, USA

1. INTRODUCTION

A long-standing problem in cloud physics is to determine the physics governing the formation of precipitation in warm clouds. The formation of rain in and below clouds is determined to a large extent by the initial cloud condensation nuclei spectra, condensation or evaporation, the relative fall velocity of drops, collision between drops resulting in coalescence or breakup, and air motions. One of the major unresolved scientific issues in cloud physics is the explanation of the observed short time between initial cloud formation and the onset of precipitation in warm clouds. The growth process must account for growth from condensation nuclei to raindrops in about 15 to 20 minutes. Although diffusional growth theory can adequately explain the early stages of cloud droplet development with narrow size spectra, it cannot account for the observed broadening with time of the drop size distribution.

Recent evidence from field and modelling studies support the hypothesis that the onset of precipitation in warm cumulus clouds results from the early accretion of cloud water by deliquesced giant and ultragiant nuclei ingested into clouds through cloud base. Although giant and ultra-giant nuclei have the potential to produce large raindrops in observed times of 15 to 20 minutes, it is uncertain to date whether the concentration of these particles is sufficient to account for the onset of rain in warm maritime and continental clouds and the observed radar signatures of these clouds.

The purpose of this study is to determine whether significant differences exist in radar reflectivity evolution between two different populations of clouds: clouds with maritime characteristics and clouds with continental characteristics. If precipitation development is dominated by accretional growth on giant and ultragiant aerosol then there is likely to be little difference in the early evolution of the radar signatures. On the other hand, if growth of precipitation is dependent on the spectral broadening associated with other processes, then the evolution of the radar reflectivity in these two cloud populations should be distinct since the continental clouds, with their narrow initial droplet spectra, require greater time for spectral broadening.

Corresponding author address: S. Göke, Dept. of Atmospheric Sciences, Univ. of Illinois at Urbana-Champaign, 105 S. Gregory St., Urbana, IL 61801, USA; e-mail: sabine@uiuc.edu.

2. THE SCMS FIELD PROJECT

The Small Cumulus Microphysics Study (SCMS) took place in July/August 1995 near Cape Canaveral, Florida. The objective of this field project was to study warm cumuli in their earliest stages with the goal to understand 1) the onset of precipitation, 2) the evolution of droplet and raindrop size distributions, and 3) the process of entrainment and mixing. The small cumuli measured during SCMS grew in similar thermodynamic environments. The thermodynamic structure of the ambient environment in the vicinity of the clouds was well documented and cloud base temperature and altitude could be determined.

The CP2 radar of the National Center for Atmospheric Research (NCAR) provided information on the evolution of radar reflectivity of small cumuli at two wavelengths (3 and 10 cm). The antennas of the X- and S-band radars were collocated on the same pedestal and adjusted to the same pointing angle. Clouds were scanned in the elevation angle direction (RHIs) at a series of azimuth angles spaced about 1° - 1.5° apart. The series of azimuths were usually repeated every 2 - 3 minutes. Measurements were taken every 100 m in range and about every 0.3° - 0.7° in elevation. Each measurement came from a pulse volume with both azimuth and elevation beamwidths of 1°.

3. DATA ANALYSIS

The SCMS data set span 44 consecutive days of radar operations. These days were partitioned into days where the clouds had either continental or maritime characteristics. The partitioning was based on 1) observed on-shore or off-shore winds, and 2) cloud condensation nuclei (CCN) and cloud droplet concentrations published by Hudson and Yum (2001). For the former criterion we analyzed the composite mean 1000 mbar winds from the NCEP/NCAR Reanalysis, and the winds between 700 and 1000 mbar from the NCAR mobile CLASS soundings, which were launched one to four times per day in the vicinity of the radar. Generally westerly winds (off-shore winds) indicated continental air masses and generally easterly winds (on-shore winds) maritime air masses. A transitions between the two regimes was indicated by northerly or southerly winds. Regarding the latter criterion, Hudson

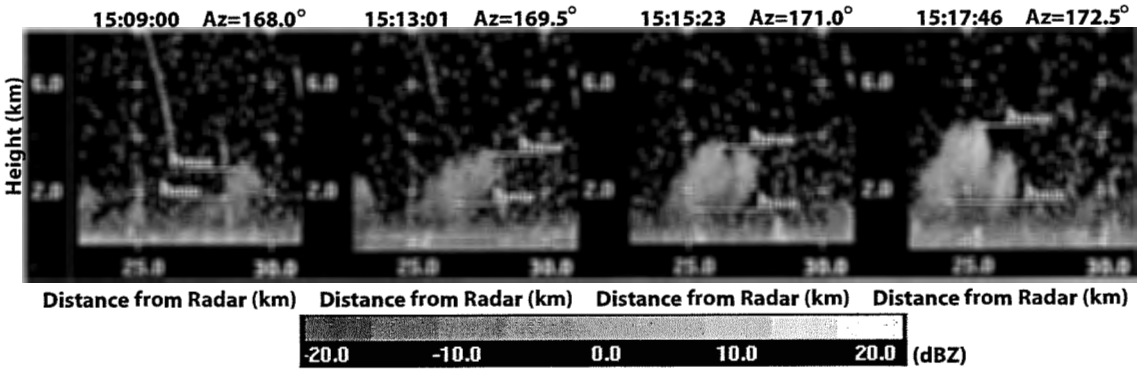

Figure 1: *Example of subsequent RHI scans representing the time evolution in X-band radar reflectivity of a cloud on 4 August 1995. Maximum and minimum heights of the -5 dBZ contour are indicated.*

and Yum's study suggested that differences in CCN and cloud droplet concentrations between clouds with maritime and clouds with continental characteristics are not large. Continental CCN and cloud droplet concentrations were in the order of 1500 cm^{-1} and 300 cm^{-1}, respectively. Maritime CCN concentrations were less than 500 cm^{-1} and maritime cloud droplet concentrations less than 200 cm^{-1}.

To determine the characteristic time for precipitation development, we analyzed the time evolution of radar reflectivity for all clouds that feature sufficient radar history. Figure 1 shows an example of subsequent RHI scans representing a typical temporal evolution of a cloud in X-band radar reflectivity. Maximum and minimum heights of each 2.5 dB contour were taken from these RHI scans, starting at -15 dBZ. Using these data a time-height cross-section of radar reflectivity was created similar to Knight and Miller (1998). From this cross-section, we defined a characteristic time for the precipitation process as the length of time between the first occurrences of X-band radar echoes ranging from -5 dBZ to 5 dBZ. Figure 2 shows the time-height cross-section of the cloud depicted in Fig. 1. The characteristic time for this particular cloud is 531 seconds.

The cloud liquid water content (LWC) is fundamental in controlling the rate a which the warm rain process proceeds, since the cloud environment must support the rapid particle growth to explain the formation of rain in the observed 15 to 20 minutes. Lawson and Blyth (1998) showed that several of the small Florida cumulus clouds observed during SCMS contained regions where the observed LWC was very close to adiabatic. Thus we defined the LWC that characterizes the precipitation formation process as the adiabatic LWC determined at the altitude of the first occurrence of the 5 dBZ contour. The adiabatic LWC is only a function of height above cloud base, and it was calculated using aircraft measurements of cloud base altitude, pressure and temperature (Laird *et al.*, 2000).

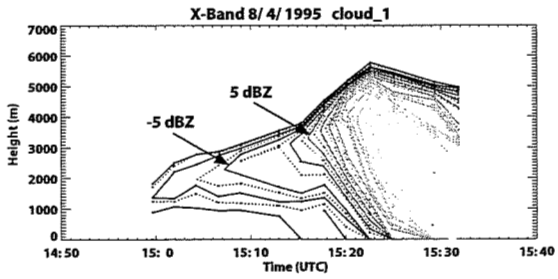

Figure 2: *Time-height cross-section of X-band radar reflectivity of the cloud depicted in Fig. 1. Lines in different grayscales represent the temporal evolution of maximum and minimum heights of each 2.5 dB contour, which are taken from RHI scans, starting at -15 dBZ (black solid line). The -5 dBZ and 5dBZ contour lines are indicated.*

4. RESULTS

A total of 63 clouds that feature radar histories suitable for this analysis were found in the entire SCMS data set. Twenty-two clouds were found during days where clouds had maritime characteristics, 23 clouds during days where clouds had continental characteristics, and 18 clouds during transitional days. For each analyzed cloud a characteristic time and LWC were determined. Figure 3 shows a scatter plot of the characteristic time for precipitation development versus the characteristic LWC. Each point represents the analysis of one growing cumulus cloud. Clouds with maritime characteristics are depicted as gray dots, clouds with continental characteristics as black dots and clouds observed during transitional days as white dots. The population of clouds with continental characteristics show a fair amount of overlap with the population of clouds with maritime characteristics, though over all the pop-

ulation of continental clouds have slightly higher LWC than the population of maritime clouds. This might suggests that continental clouds rise to higher altitude during the precipitation formation process than maritime clouds.

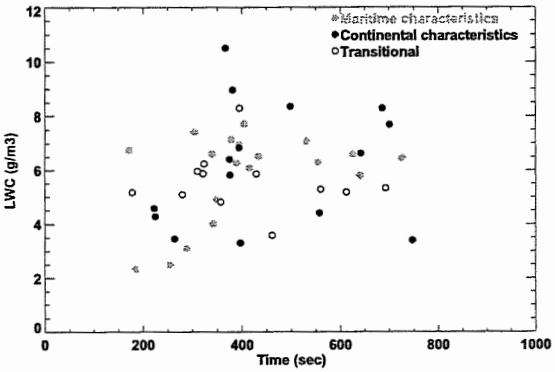

Figure 3: *Scatter plot of characteristic time for precipitation formation versus characteristic LWC. Gray dots indicate clouds with maritime characteristics, black dots clouds with continental characteristics and white dots clouds observed during transitional days.*

We partitioned the data set further and analyzed subsets. During SCMS the radar was located on the barrier island north of Cape Canaveral and obtained data on small cumuli developing on the Florida sea breeze either over the ocean (when scanning to the east) or over land (when scanning to the west). Figure 4 shows the same scatter plot as Fig. 3 depicting clouds developed over land as dots and clouds developed over the ocean as 'x'. Maritime clouds developed over the ocean feature short characteristic times for precipitation development and low characteristic LWCs. Maritime clouds developed over land show a wider variety of characteristic times, but consistently higher LWCs compared to maritime clouds developed over the ocean. Continental clouds developed over the ocean overlap entirely with both cloud populations mentioned above. Continental clouds developed over land feature higher LWCs than all other populations of clouds.

5. DISCUSSION AND OUTLOOK

In this study, we are testing a new method of analyzing radar data with the objective to determine if there is a statistical difference between the rates of precipitation development in different populations of clouds. Each point in a scatter plot of the characteristic time for precipitation development versus the characteristic LWC represents the analysis of one growing cumulus cloud. The technique has the advantage that the updraft speed, which is difficult to measure, is not necessary to characterize the evolution of precipitation. The adiabatic LWC is only a function of height above cloud base, given knowledge of cloud base pressure and temperature, and the analysis can be viewed as considering a characteristic height in time and thus a characteristic velocity.

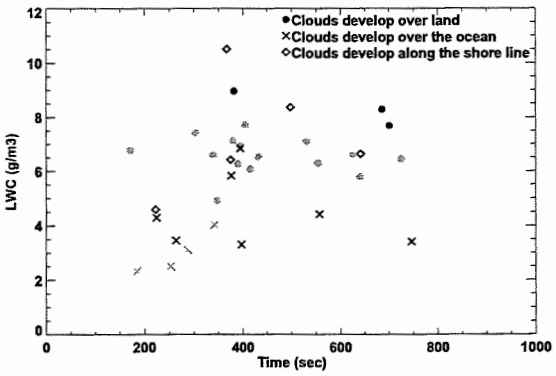

Figure 4: *Scatter plot of characteristic time for precipitation formation versus characteristic LWC. Gray symbols indicate clouds with maritime characteristics and black symbols clouds with continental characteristics.*

We are now performing statistical tests on subsets of the data set to determine the statistical significance of these findings.

ACKNOWLEDGMENT

This work was supported by the National Science Foundation under the research grant ATM-0121517. Opinions expressed are those of the authors and not necessary those of the Foundation.

REFERENCES

Hudson, J. G., and S. S. Yum, 2001: Maritime - continental drizzle contrasts in small cumuli. *J. Atmos. Sci.*, **58**, 915-926.

Knight, C. A., and L. J. Miller, 1998: Early radar echoes from small, warm cumulus: Bragg and Hydrometeor scattering. *J. Atmos. Sci.*, **55**, 2974-2992.

Laird, N. F., H. T. Ochs III, R. M. Rauber and L. J. Miller, 2000: Initial precipitation formation in warm Florida cumulus. *J. Atmos. Sci.*, **57**, 3740-3751.

Lawson, R. P., and A. M. Blyth, 1998: A comparison of optical measurements of liquid water content and drop size distribution in adiabatic regions of Florida cumuli. *Atmos. Res.*, **47**, 671-690.

RAINDROP SHAPE AND SIZE DISTRIBUTION: IMPACT ON RADAR PRECIPITATION RETRIEVALS

E. Gorgucci[1], V. Chandrasekar[2], V.N.Bringi[2] and L. Baldini[1]

[1] Istituto di Scienze dell'Atmosfera e del Clima, Via Fosso del Cavaliere, 100 – 00133 Roma, Italy
[2]Colorado State University, Fort Collins CO 80523-1373, USA

1. INTRODUCTION

The shape of raindrops plays a fundamental role in defining the characteristics of dual-polarization radar observation of rainfall. Raindrop shape and oscillations have been studied extensively over the past two decades and several models describing the shape-size relation are available in the literature. The shape-size relationship of raindrops leads to a self consistency condition in the covariance matrix of dual-polarization radar observation. This principle has been used recently to derive radar-based retrievals of mean raindrop shapes (Gorgucci et al., 2000).

The actual shapes of raindrops in unsteady flow are expected to be different from equilibrium shapes. Transverse oscillations of raindrops tend to decrease the mean axis ratio for a given size. This uncertainty in raindrop shape if uncorrected could bias the retrievals based on radar observations. However the self consistency based retrievals of mean raindrop shapes can be used to correct for this. This paper presents an analysis of the mean raindrop shape retrievals from radar measurements. Specifically the application of radar derived "bulk mean shape" in precipitation retrieval algorithms is evaluated.

The simplest radar model assumes a linear shape-size relation over the entire drop size spectrum. However in reality there may be non-linearities in the shape-size model. These non-linearities will be manifested as varying slope with drop size distribution parameters, because of the varied weighting from different diameters. This paper presents studies of the variations in the raindrop shape-size relation in conjunction with raindrop size distribution parameters.

2. BACKGROUND

The equilibrium shape of a raindrop is determined by a balance of forces on the interface involving hydrostatic, surface tension, and aerodynamic forces. A simple model for the shape of raindrop is oblate spheroidal, and the axis ratio defined here as b/a, with b being the semi-minor axis length and a the semi-major axis length, changes as function of the volume equivalent spherical diameter D (Green, 1975). A more accurate description of equilibrium shape was derived by Beard and Chuang (1987), using a numerical model, which included aerodynamic effects. While the larger drops have slightly flatted bases, it is sufficient for radar applications to calculate an effective axis ratio between the maximum vertical and horizontal chords.

In absence of the wind shear and turbulence, raindrops are expected to fall with their symmetry axes vertical. The rotating linear polarization data in heavy rain clearly shows that the mean canting angle is close to 0° (Hendry et al., 1976). The actual shapes of raindrops in unsteady flow are expected to differ from the equilibrium shapes. Based on field studies of Tokay and Beard (1996) there is clear evidence that raindrops from 1 to 4 mm oscillate, but the cause of oscillation and the resultant distribution of oscillation amplitudes, especially for the larger drops, is still uncertain. Laboratory studies of the axis ratios of artificially generated water drops (Kubesh and Beard, 1993) show that raindrops tend to oscillate in the steady state in two preferred modes of the fundamental harmonics: *i*) the axisymmetric mode oscillations between oblate-prolate shapes, which produce two-sided scatter in the axis ratio about the equilibrium value; and *ii*) asymmetric transverse mode oscillations, which produce mostly one-sided scatter about the equilibrium value. Raindrops oscillate with a range of amplitudes with most drops experiencing only small amplitudes oscillations, while a relatively low fraction of drops were oscillating with amplitudes near the maximum. The axis ratio distribution of natural raindrops supports this viewpoint as shown by Bringi et al. (1998) and Chandrasekar et al. (1988). Andsager et al. (1999) have combined the laboratory axis ratio results with the natural raindrop shape results of Chandrasekar et al. (1988) for D<4 mm. There is a systematic upward shift in the mean axis ratio relative to equilibrium shape in the interval 1<D<4 mm based on this composite results and this shift can be explained by transverse mode oscillations. Andsager et al. (1999) have provided a fit to all the laboratory data as well as to the Chandrasekar et al. (1988) data to arrive at a mean axis ratio versus D relation. Thus the last decade has seen extensive research into raindrop shape and oscillations essentially motivated by the advances in dual polarization observation of rainfall. Accompanying this research, has been radar based study of drop oscillations in the context of retrievals.

The simplest approximation for raindrop shape is the commonly used approximation of Pruppacher and Beard (1970)

Corresponding author's address: Eugenio Gorgucci, Institute of Atmospheric Sciences and Climate-CNR, Rome, Italy; E-Mail: gorgucci@radar.ifa.rm.cnr.it

$$r = \frac{b}{a} = 1.03 - 0.062D \quad \text{for } 1 \le D \le 9\text{mm} \qquad (1)$$

Equation (1) is a linear form with a negative slope of 0.062 mm^{-1}. Gorgucci et al. (2000) recognized that drop canting and oscillations could be incorporated into an "effective" slope parameter (β_{eff}) and proceeded to develop an algorithm to estimate β_{eff} from the radar measurements. It is important to recognize that even if drop axis ratio is in fact a nonlinear function of D, it is possible to define an equivalent linear model with a slope of β_{eff} such that it results in the same radar observations.

The concept of an "effective" slope of the mean axis ratio versus D relation is important since drop oscillations or canting are likely to be different in, for example, tropical rain versus rain in the mid latitudes. Oscillations/canting may be suppressed when rain is formed via melting of graupel or tiny hail as compared with warm rain formation. Gorgucci et al. (2001) applied the β_{eff} concept to an unusual tropical-like flash flood–producing storm in Colorado and showed that rainrate estimators based on β_{eff}, resulted in better agreement with gauge data as compared with the standard algorithms. May et al. (1999) also found that use of the Pruppacher and Beard equilibrium shape model (β fixed at 0.062 mm^{-1}) resulted in a systematic underestimate in rainfall when using $R(K_{dp})$, as compared with a dense gauge network in the Tropics, and attributed this bias to drop oscillations causing an upward shift in mean axis ratio (toward sphericity). More recently, Fulton et al. (1999) have suggested an empirical adjustment to the $R(K_{dp})$ algorithm using a multiplicative bias correction factor which they found reduced the temporal bias in rain accumulation. This correction factor, though empirical, tends to account for the tendency of drop oscillations/canting to cause an upward shift in mean axis ratio. Thus, there appears to be sufficient evidence to warrant investigation of the physics of raindrop oscillation in the context of radar observations and the corresponding implication for retrievals. This paper investigates the implication of raindrop oscillation and accompanying size distribution on radar retrievals.

The paper is organized as follows. Section 3 presents the impact of raindrop shape on dual polarization radar measurements, and the retrieval techniques. Section 4.1 discusses the impact on rainfall rate retrieves whereas section 4.2 studies the retrieval of DSD parameters. The important results are summarized in section 5.

3. RAINDROP SHAPE, OSCILLATION AND RADAR OBSERVATION

The radar measurement set of reflectivity at horizontal polarization (Z_h), differential reflectivity (Z_{dr}), and specific differential phase (K_{dp}) can, in the Rayleigh scattering limit, be related to the microphysics of raindrops. Specifically, the Z_h is related to the sixth moment of the DSD, Z_{dr} is related to the reflectivity-weighted mean axis ratio, and K_{dp} is related to the product of the water content and the deviation of the mass-weighted mean axis ratio from unity (Jameson, 1985). If a model relating the axis ratio (r) of oriented oblate raindrops versus the equivolumic spherical diameter (D) is selected, then Z_{dr} can be related to the reflectivity-weighted mean diameter of the DSD, while K_{dp} can be related to the product of water content W and D_m (the mass-weighted mean diameter of the DSD). Generally, the linear fit to the windtunnel data of Pruppacher and Beard (1970), (eq. 1), or the equilibrium shape model of Beard and Chuang (1987) has been used. If the DSD is modeled as a normalized gamma form (Willis 1984; Testud et al. 2001),

$$N(D) = N_w f(\mu)\left(\frac{D}{D_0}\right)e^{-(3.67+\mu)\left(\frac{D}{D_0}\right)} \qquad (2a)$$

with

$$f(\mu) = \frac{6}{(3.67)^4}\frac{(3.67+\mu)^{(\mu+4)}}{\Gamma(\mu+4)} \qquad (2b)$$

where N_w is the normalized intercept parameter of an equivalent exponential DSD that has the same water content and median volume diameter (D_0) as the gamma DSD, then it follows that $Z_h = N_w F_1(\mu)$, $Z_{dr} = F_2(\mu, D_o)$, while $K_{dp} = N_w F_3(\mu, D_o)$ where F represents a functional form. Thus, in principle, estimates of D_0, N_w, and μ (and W or rain rate R) can be obtained from the radar measurement set of Z_h, Z_{dr}, and K_{dp}.

The effects of raindrop shape oscillations (either due to resonance maintained by vortex shedding or due to collisions) and raindrop canting (due to turbulence) will bias the retrieval of the gamma DSD parameters under the above model assumptions (e.g., see Bringi and Chandrasekar 2001, chapter 7 and references therein). Both drop oscillations and canting angle distributions tend on average to drive the effective axis ratio toward sphericity relative to equilibrium axis ratios and perfect orientation. The rain microphysics model can be improved by accounting for drop oscillations using the axis ratio versus D fit proposed by Andsager et al. (1999) and by using a Gaussian canting angle distribution with a mean of zero and a standard deviation σ (Bringi and Chandrasekar 2001). For example, if the axis ratio versus D relation is assumed to be linear with a slope of β, $r = 1.03 - \beta D$, then K_{dp} is modified as (see Bringi and Chandrasekar 2001)

$$K_{dp} = \beta N_w F_3(\mu, D_0)\exp(-2\sigma^2) \qquad (3a)$$

$$= \beta_{eff} N_w F_3(\mu, D_0) \qquad (3b)$$

A simpler form of the above equation is

$$K_{dp} = \left(\frac{180}{\lambda}\right)10^{-3} C W \beta_{eff} D_m \quad (\text{deg}.km^{-1}) \qquad (3c)$$

where D_m is the mass weighted mean diameter, W the water content, λ is the wavelength in meters and C is a dimensionless constant. Thus it can be seen that K_{dp} is directly dependent on β_{eff} and water content.

4. RAINFALL AND DSD RETRIEVAL

4.1 Rainfall retrieval

A simple example is chosen here to illustrate the impact of drop oscillation. The rainfall estimate using K_{dp} say at X-band is written as:

$$R(K_{dp}) = c(\beta)K_{dp} \tag{4}$$

where the multiplicative constant c is a function of the effective slope β. It was discussed in the background that for a given DSD, K_{dp} is proportional to β, W and D_m. Therefore, if the rain rate is the same the multiplicative coefficient c should be inversely proportional to β. Fig. 1 shows a plot of $c(\beta)$ versus β for widely varying DSD parameters.

It is argued by Bringi et al. (2001) that Andsager et al. (1999) shape model yields an equivalent β of 0.0475, producing a multiplicative constant of approximately 17, whereas the standard Pruppacher and Beard (1970) model yield a constant of 12. If one assumed the wrong model this gives a bias error of about 30% as reported by May et al. (2001).

4.2 DSD retrieval

The DSD retrieval problem is more subtle. It was shown by Scarchilli et al. (1996) using the principle of self consistency that the triplet of measurements Z_h, Z_{dr} and K_{dp} lie on a surface for a given shape model (β). When β changes this surface moves. The equation describing the surface in the 3D space of Z_h, Z_{dr} and K_{dp} at X-band is given by

$$Z_h^{-0.290}\xi_{dr}^{1.126}K_{dp}^{0.286} = 1.792\beta \tag{5a}$$

where $Z_{dr} = 10\log_{10}\xi_{dr}$; or

$$\left(\frac{\xi_{dr}^{3.9}\cdot K_{dp}^{0.99}}{Z_h}\right) = 7.47\ \beta^{3.45} \tag{5b}$$

Fig 2a shows the surface (5b) when β=0.062.

One needs to be careful with the interpretation of the retrieval process. If one estimates β first, then only N_w, D_0 and μ can be retrieved. It is a two step process. The three measurement variables Z_h, Z_{dr} and K_{dp} do not have enough sensitivity to the third parameter μ. The two step process may be interpreted as estimating four quantities from three measurements. This can happen if the surfaces of two β values intersect, and we have an imposed inversion process. It may well happen that choosing the wrong β will yield different estimates of N_w, D_0 that may be physically meaningful.

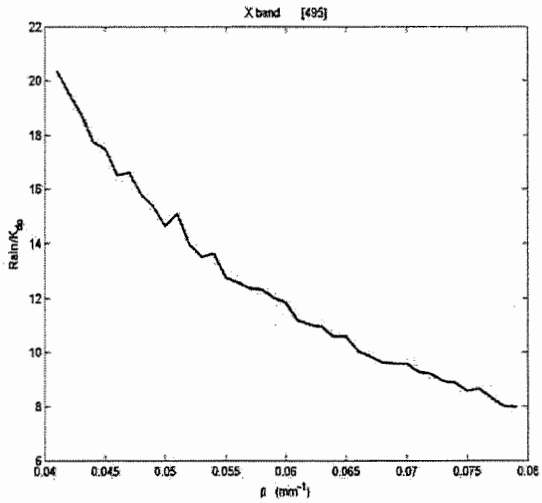

Figure 1: *Multiplicative constant c of the equation (4) as a function of the slope β for a widely varying of DSD parameters*

In order to understand the impact of the surface described by (5b), the difference in the surface between two values of β, namely β=0.04 (close to Andsager at al. model) and β=0.062 (corresponding to Pruppacher and Beard model) is shown in the Fig 2b. It can be seen that a difference of about 6 to 8 dB in Z_h, for a given pair (Z_{dr}, K_{dp}) in the surface is significant, thereby indicating the principle of self-consistency imposed by raindrop shape and size relationships.

5. SUMMARY

The advent of polarimetric radar measurements gives us the opportunity to study the shape/size microphysics of rainfall at the scale of radar resolution volume. Dual polarization radar data also provide a mechanism to retrieve DSD parameters. The "effective shape" concept provides a methodology to extract the underlying shape model which can be used to estimate the correct rainfall rate and prevailing drop size distribution. The shape parameter will be weighted by the actual drop size distribution, if there is a size dependent non linear shape.

Acknowledgements

This research was supported partially by the National Group for Defense from Hydrological Hazard (CNR, Italy), by the Italian Space Agency (ASI) and by the National Science Foundation (ATM-0313881).

REFERENCES

Andsager, K., K. V. Beard, and N. F. Laird, 1999: Laboratory measurements of axis ratios for large raindrops. *J. Atmos. Sci.,* **56,** 2673–2683.

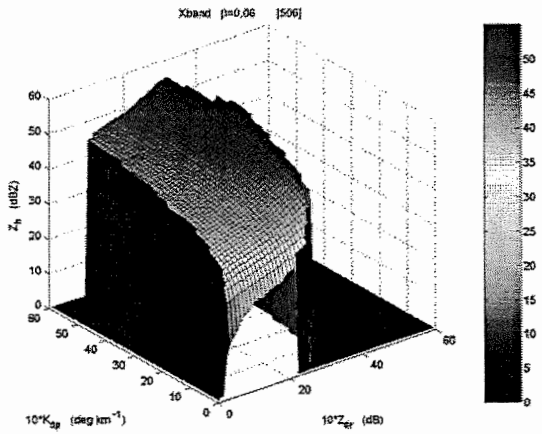

Figure 2a: *Surface obtained from eq. 5b with β=0.062*

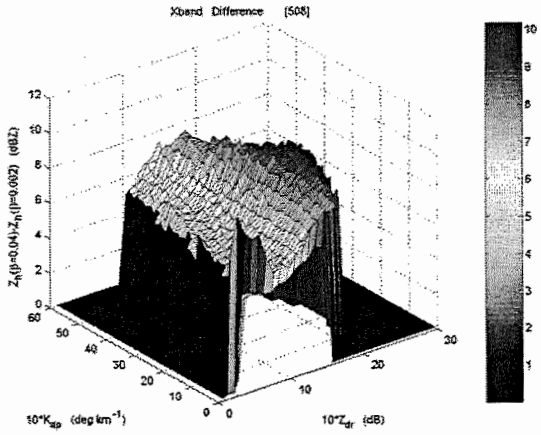

Figure 2b: *Difference between two surfaces obtained from eq. 5b. with β=0.04 and β=0.062*

Beard, K. V., and C. Chuang, 1987: A new model for the equilibrium shape of raindrops. *J. Atmos. Sci.,* **44,** 1509–1524.

Bringi, V. N., V. Chandrasekar, and R. Xiao, 1998: Raindrop axis ratios and size distributions in Florida rainshafts: An assessment of multiparameter radar algorithms. *IEEE Trans. Geosci. Remote Sens.,* **36,** 703–715.

Bringi, V. N., and V. Chandrasekar, 2001: *Polarimetric Doppler Weather Radar: Principles and Applications.* Cambridge University Press, 648 pp.

Bringi, V.N., Keenan, T.D., and V. Chandrasekar, 2001: Correcting C-band radar reflectivity and differential reflectivity data for rain attenuation: a self-consistent method with constraints. *IEEE Trans. Geosci. Remote Sens.*, , **39,** 1906 –1915.

Chandrasekar, V., W. A. Cooper, and V. N. Bringi, 1988: Axis ratios and oscillations of raindrops. *J. Atmos. Sci.,* **45,** 1323–1333.

Fulton, R. A., A. V. Ryzhkov, and D. S. Zrnic′, 1999: Areal rainfall estimation using conventional and polarimetric radar methods. Preprints, *29th Conf. on Radar Meteorlogy,* Montreal, QC, Canada, Amer. Meteor. Soc., 293–296.

Gorgucci, E., G. Scarchilli, V. Chandrasekar, and V. N. Bringi, 2000: Measurement of mean raindrop shape from polarimetric radar observations. *J. Atmos. Sci.,* **57,** 3406–3413.

Gorgucci, E., G. Scarchilli, V. Chandrasekar, and V. N. Bringi, 2001: Rainfall estimation from polarimetric radar measurements: Composite algorithms immune to variability in raindrop shape–size relation. *J. Atmos. Oceanic Technol.,* **18,** 1773–1786.

Green, A. W., 1975: An approximation for the shapes of large raindrops. *J. Appl. Meteor.,* **14,** 1578–1583.

Hendry, A., McCormick, G. C., and B.L. Barge, 1976: The Degree of Common Orientation of Hydrometeors Observed by Polarization Diversity Radars. *J. Appl. Meteor.*, **15,** 633–640.

Kubesh, R. J., and K.V. Beard, 1993: Laboratory Measurements of Spontaneous Oscillations for Moderate-Size Raindrops. *J. Atmos. Sci.*, **50**, 1089–1098

Jameson, A. R., 1985: Microphysical interpretation of multi-parameter radar measurements in rain. Part III: Interpretation and measurement of propagation differential phase shift between orthogonal linear polarizations. *J. Atmos. Sci.,* **42,** 607–614.

May, P. T., T. D. Keenan, D. S. Zrnic′, L. D. Carey, and S. A. Rutledge, 1999: Polarimetric radar measurements of tropical rain at a 5-cm wavelength. *J. Appl. Meteor.,* **38,** 750–765.

May, P. T., Jameson, A. R., Keenan, T. D., and P. E. Johnston, 2001: A Comparison between Polarimetric Radar and Wind Profiler Observations of Precipitation in Tropical Showers. *J. Appl. Meteor.,* **40,** 1702–1717.

Pruppacher, H. R., and K. V. Beard, 1970: A wind tunnel investigation of the internal circulation and shape of water drops falling at terminal velocity in air. *Quart. J. Roy. Meteor. Soc.,* **96,** 247–256.

Scarchilli, G., Gorgucci, V., Chandrasekar, V., and A. Dobaie, 1996: Self-consistency of polarization diversity measurement of rainfall. *IEEE Trans. Geosci. Remote Sens.*, **34**, 22 –26.

Testud, S. Oury, P. Amayenc, and R. A. Black, 2001: The concept of "normalized" distributions to describe raindrop spectra: A tool for cloud physics and cloud remote sensing. *J. Appl. Meteor.,* **40,** 1118–1140.

Ulbrich, C. W., and D. Atlas, 1998: Rainfall microphysics and radar properties: Analysis methods for drop size spectra. *J. Appl. Meteor.,***37,** 912–923.

Willis, P. T., 1984: Functional fits to some observed drop size distributions and parameterization of rain. *J. Atmos. Sci.,* **41,** 1648–1661.

NORMALIZED DROP SIZE DISTRIBUTIONS

Jan Handwerker*, Winfried Straub and Klaus D. Beheng

Institut für Meteorologie und Klimaforschung, Forschungszentrum Karlsruhe, Germany

1 Introduction

Raindrop size distributions are in so far of signi?cant importance as they act as an interface between cloud physics and radar meteorology. From a cloud physicist's point of view they represent the result of the rain forming process whereas radar meteorologists are interested in the derivation of rain intensity from measured radar re-?ectivity. In both cases it is desirable to ?nd a description of raindrop size distributions that (i) ?ts well to measurements, (ii) uses only very few parameters which are (iii) mutually independent and (iv) allow a physical interpretation of the parameters.

The Marshall-Palmer distribution (Marshall and Palmer, 1948) $N(D) = N_0 \exp(-\lambda D)$ is usually favored because it uses only two parameters, the slope λ and the intercept parameter N_0, and full?ls all four demands as long as the measured spectra represent averages over suf?cient long times. For short term measurements, down to 1 minute averages, it is observed that there are fewer very small and very large drops in the measurements compared to the Marshall-Palmer distribution (e.g., Joss and Gori, 1978).

The shape of the distribution in these cases is met better by a gamma distribution $N(D) = N_\gamma D^\mu \exp(-\lambda D)$, introducing the additional shape parameter μ. But this distribution violates the demands (iii) and (iv) through a strong coupling of N_γ and μ and the loss of any physical interpretation of the intercept parameter N_γ, whose dimension depends on the shape parameter μ. As a further disadvantage N_γ varies over more than 15 orders of magnitude.

2 Normalized Drop Size Distributions

Willis (1984) proposed to normalize the gamma distribution by the liquid water content (LWC), i.e. the LWC becomes independent of the shape parameter μ. Illingworth and Johnson (1999) and Illingworth and Blackman (1999) obtain[1]

$$N(D) = \frac{6}{3.67^4} \frac{N_L D_0^4 \lambda_L^{\mu_L+4} D^{\mu_L}}{\Gamma(\mu_L+4)} \exp(-\lambda_L D) \qquad (1)$$

introducing the equivolumetric median drop diameter D_0 which is given by $D_0 = (3.67 + \mu_L)/\lambda_L$. The numerical factor is introduced to ensure, that Eq. (1) reduces to the Marshall-Palmer distribution for $\mu_L = 0$.

To gain the parameters N_L, λ_L and μ_L from measured drop size spectra, three different, (in principle) arbitrary moments (M_i) may be used. Speci?cally using the third, fourth and sixth moment of the distribution we have to solve

$$M_3^2 M_4^{-3} M_6 = (\mu_L+6)(\mu_L+5)(\mu_L+4)^{-2} \qquad (2)$$

$$\lambda_L = \left[\frac{M_3 \Gamma(\mu_L+7)}{M_6 \Gamma(\mu_L+4)}\right]^{1/3} \qquad (3)$$

$$N_L = M_4 \frac{\lambda_L^{\mu_L+5}}{\Gamma(\mu_L+5)}. \qquad (4)$$

Eq. (2) reduces to a quadratic equation for μ_L.

In contrast, Testud et al. (2001) introduce the volume-weighted mean diameter $D_m = M_4/M_3 = (4+\mu^*)/\lambda^*$ leading to a slightly different drop size representation

$$N(D) = \frac{6}{4^4} \frac{(\mu^*+4)^{\mu^*+4}}{\Gamma(\mu^*+4)} N_0^* \left(\frac{D}{D_m}\right)^{\mu^*} \exp\left(-(\mu^*+4)\frac{D}{D_m}\right) \qquad (5)$$

The two normalized raindrop size distributions Eq. (1) and Eq. (5) are nearly equivalent except with respect to the de?nition of the reference diameter D_0 or D_m. Both of them reduce to the Marshall-Palmer distribution if μ becomes 0. Nevertheless, Eq. 5 allows the calculation of D_m and N_0^* directly, independent from the shape of the distribution (Testud et al., 2001)

$$N_0^* = \frac{4^4}{6} \frac{M_3^5}{M_4^4}. \qquad (6)$$

The shape parameter μ^* is found by a least square ?t of $\log(N(D)/N_0^*)$ (from Eq. (5)) to the corresponding values from the measurements.

3 Data Base

Previous investigations relied on (a) 1260 spectra recorded for every 30 second period of rainfall during July 1988 in UK (Illingworth and Johnson, 1999) and on (b) 7112 spectra recorded with a 2D-P probe ?ying with the Electra aircraft of NCAR during the TOGA COARE experiment (Testud et al., 2001).

We tested the representations Eq. (1) and Eq. (5) on nearly 500 000 data sets collected with 5 different Joss-Waldvogel distrometers. All distrometers worked

*Corresponding author address: Jan Handwerker, Institut für Meteorologie und Klimaforschung, Forschungszentrum Karlsruhe, Postfach 3640, D-76021 Karlsruhe; E-Mail: jan.handwerker@imk.fzk.de

[1]The unit of N is m^{-4} in this study.

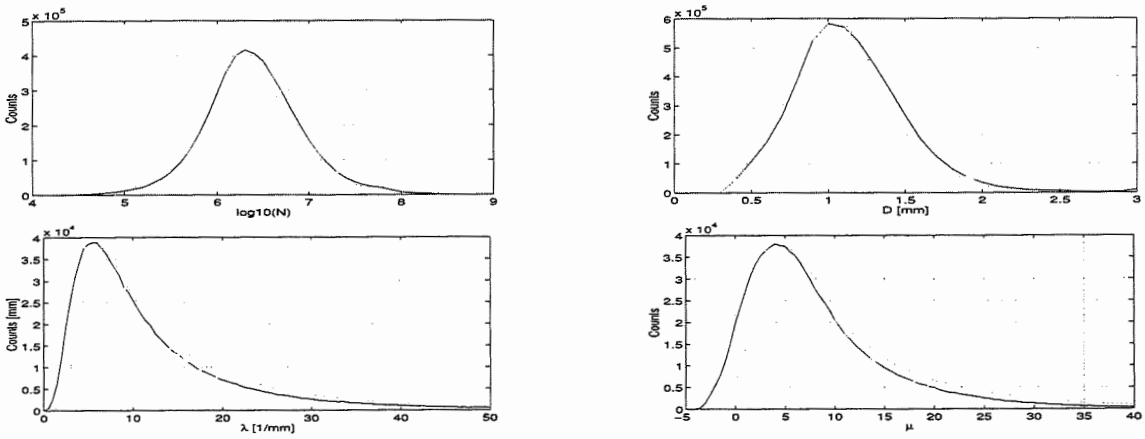

Figure 1: Histograms of the intercept parameter, reference diameter, slope parameter and shape parameter of the measured drop size distributions. The dotted lines correspond to the approach after Illingworth and Johnson (1999), the solid lines to Testud et al. (2001).

Table 1: Statistical characteristics of the parameters after eqn. (1).

	Total	$\log(N_L)$			D_0 [mm]			μ_L		
	amount	median	mean	std.dev.	median	mean	std.dev.	median	mean	std.dev
JW1	66 638	6.39	6.40	0.54	1.00	1.06	0.37	7.05	9.06	7.63
JW2	172 306	6.49	6.50	0.50	0.95	0.98	0.33	6.47	9.18	8.87
JW3	15 456	6.58	6.58	0.53	0.96	1.03	0.38	5.17	6.82	6.46
JW4	3 951	6.46	6.55	0.64	0.97	1.02	0.41	5.79	7.93	7.55
JW5	223 159	6.10	6.09	0.45	1.18	1.22	0.32	10.54	13.39	9.86
all	481 510	6.28	6.30	0.52	1.07	1.11	0.35	8.23	11.03	9.39

Table 2: Statistical characteristics of the parameters after eqn. (5).

	Total	$\log(N_0^*)$			D_m [mm]			μ^*		
	amount	median	mean	std.dev.	median	mean	std.dev.	median	mean	std.dev
JW1	66 638	6.47	6.48	0.54	1.04	1.10	0.39	4.90	6.27	6.32
JW2	173 306	6.57	6.59	0.50	0.98	1.02	0.35	4.30	6.12	7.00
JW3	15 456	6.66	6.65	0.53	1.00	1.08	0.40	2.70	3.90	4.99
JW4	3 951	6.53	6.63	0.65	1.00	1.06	0.43	2.20	3.78	5.42
JW5	223 159	6.20	6.19	0.45	1.21	1.26	0.34	8.90	10.76	7.63
all	481 510	6.37	6.39	0.52	1.10	1.14	0.37	6.40	8.20	7.55

with a temporal resolution of 60 seconds. The distrometers were located at the at the German Weather Service in Stuttgart (JW1), at the Forschungszentrum Karlsruhe (JW2), at Swiss Meteorological Institute in Zurich (JW3), during the REKLIP – SOP in Bad Bergzabern (JW4) and at the University of Karlsruhe (JW5). We took the results only from measured spectra with an appropriate rainfall rate of $R \geq 0.1$ mmh^{-1}.

4 Results

Fig. 1 shows the frequency distributions of the parameters $\log(N)$, λ, D_0 or D_m and μ for both normalized drop size distributions. The dotted lines are derived from Eq. (1) whereas the solid lines correspond to Eq. (5). The averages and standard deviations of these frequency distributions are given in Tab. 1 and Tab. 2.

For both normalized drop size distributions the mean of parameter $\log(N)$ is slightly smaller (6.3, 6.4, respectively) than the traditional value from Marshall-Palmer (6.9). This ?nding corresponds to the results of Testud et al. (2001) ?nding the mean of $\log(N)$ to be roughly 6.5 in stratiform events. Illingworth and Johnson (1999) report an average of $\log(N)$ to be nearly identically to the Marshall-Palmer value.

The average volume-weighted mean Diameter D_m is 1.14 mm and thus slightly smaller than the values given by Testud et al. (2001), which vary between 1.19 mm and 1.78 mm. The average equivolumetric diameter D_0 is 1.11 mm, indicating that both parameters are nearly identically.

The mean value of the shape parameter is strongly

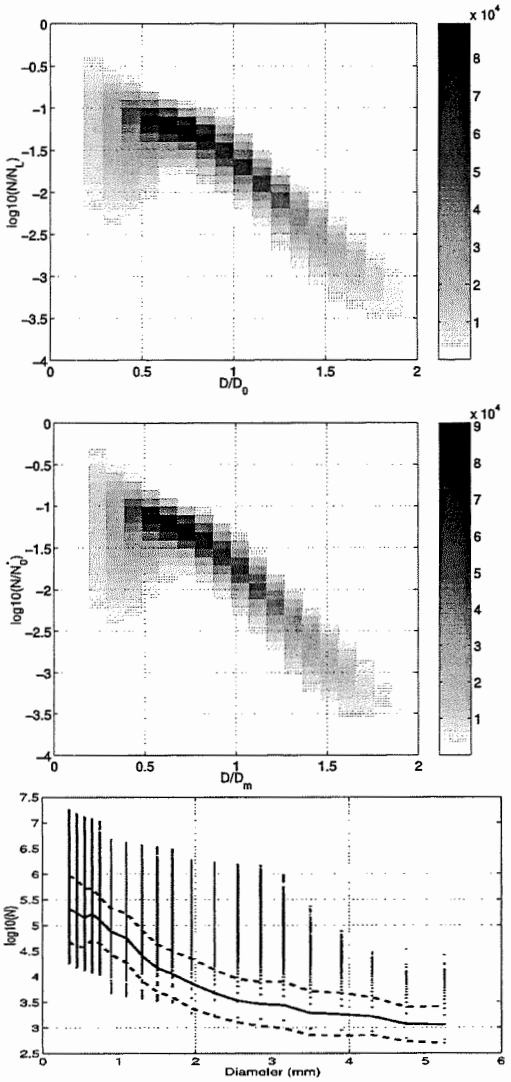

Figure 2: All normalized drop size spectra shown as 2D-distributions after Illingworth and Johnson (1999) (top) and after Testud et al. (2001) (mid). The median un-normalized spectrum and the standard deviations within in drop size class are shown in the lower image.

in?uenced by a few very large values (up to 80 and larger). Thus we use the median values. The median of μ_L is 8.23 and that of μ^* is 6.40. If we remove the data from JW5 (which is located on the roof of a 50 m high university building and may thus strongly be effected from drop sorting) the median values are 6.52 and 4.30, respectively. This corresponds well with the results from Illingworth and Johnson (1999) reporting $\langle\mu_L\rangle$ to be 6.43, but differs signi?cantly from the results of Testud et al. (2001) ?nding $\langle\mu^*\rangle = 0.86$ for stratiform events. Even in convective events this value is always smaller than 1.8 in their study.

The only plausible reason for this difference in the shape parameter is the fact, that our drop size distributions as well as those from Illingworth and Johnson (1999) are measured at ground level, whereas the data from Testud et al. (2001) are recorded at 3000 m ?ight level. The difference of the shape parameter might indicate an evolution of the drop size distribution during sedimentation or it might indicate a severe drop sorting problem of ground based distrometer measurements. Using optical distrometers we found μ-values even larger than those reported here.

There is still a signi?cant difference between the μ_L values from Eq. (2) and the μ^* values from the ?t of the $\log(N(D))$ values: μ_L is on the average signi?cantly larger than μ^*. A visual comparison between the measured spectra and the two normalized gamma functions indicates clearly that the μ_L values are too large, whereas the μ^* values seem to be very reasonable.

A probable reason for this difference might be the cut-off of the measured spectra at small diameters. The Joss-Waldvogel distrometer measures drop sizes not smaller than roughly 0.3 mm. Smaller drops are neglected. The integrals that lead to Eqs. (2) – (4) and (6) do not suffer from this problem. The moments of the distributions are affected differently from this neglection. The higher the moment, the less important are the small drops. Whereas the technique of Testud et al. (2001) uses only the third and fourth moment, Illingworth and Johnson (1999) also include the sixth moment.

Fig. 2 shows the normalized distributions $N(D/D_0)/N_0$ (Eq. (1)) and $N(D/D_m)/N_0^*$ (Eq. (5)), respectively, as 2D-distributions. Compared to the un-normalized distributions they show a signi?cant reduced scatter.

The most important advantage of the normalized gamma distributions is the physical interpretation of the three parameters and the mutual independence. These properties may be seen in Fig. 3, which gives the 2D-distributions of two parameters, each. On the left hand side the parameters are calculated as in Testud et al. (2001), on the right hand side we followed Illingworth and Johnson (1999). As can be seen, the distributions are very similar in shape, indicating that both approaches are nearly equivalent.

The intercept parameter N and the shape parameter μ are in both cases mutually independent. This is a important advantage compared with the un-normalized gamma distribution. Nevertheless, there is still a dependency between the reference drop sizes and N. The lower boundary of the N/D-shape is due to the preset minimum rain intensity of 0.1 mm/h, required in our evaluation. Nevertheless, the upper limit corresponds to a physical limitation of real rain: there is no rain event with very much very large drops. Thus median drop size and the intercept parameter are not totally independent.

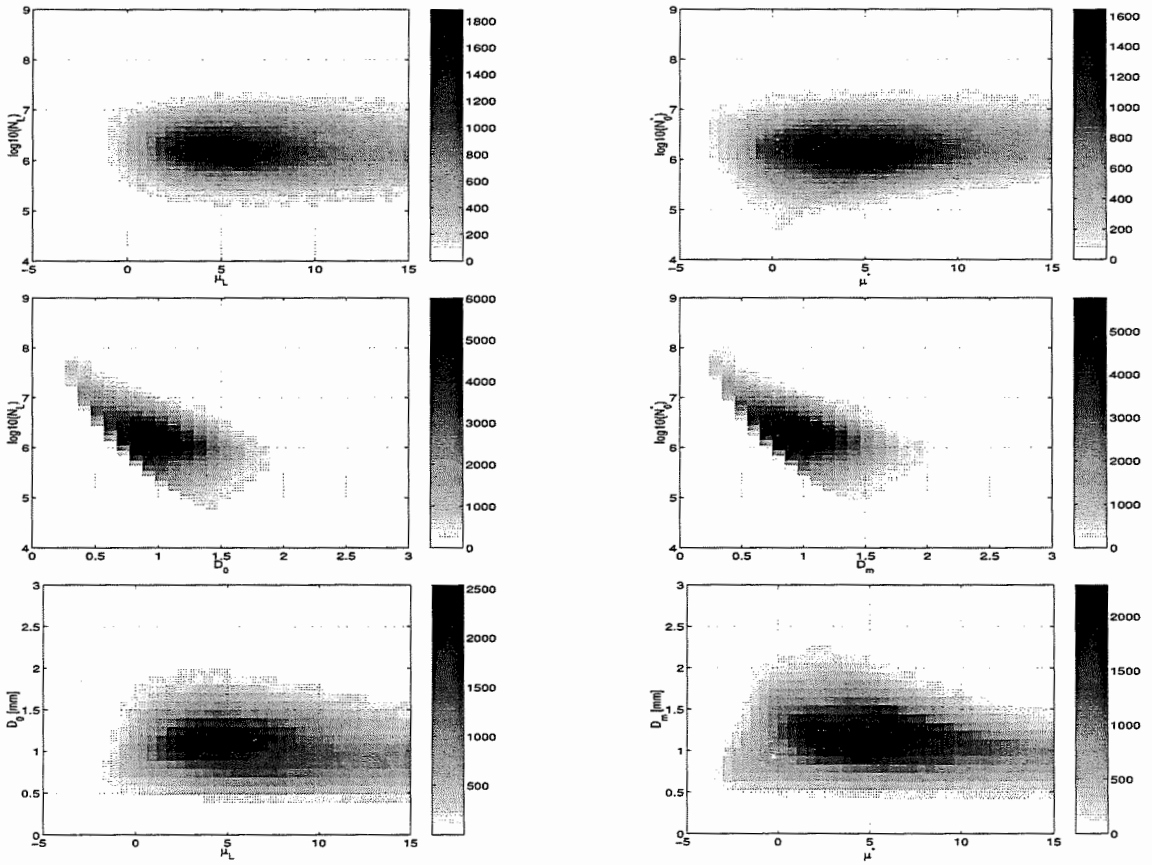

Figure 3: Mutual dependencies between the three parameters of the distributions. On the left corresponding to Illingworth and Johnson (1999), on the right after Testud et al. (2001).

5 Conclusions

The two approaches to normalize drop size distributions are nearly equivalent in their de?nition and thus produce nearly equal results. Nevertheless, determining the shape parameter from a ?t of the logarithm of the drop size distribution performs better than the calculation from the third, fourth and sixth moment.

Ground level measurements produce a much larger shape parameter μ than reported from the aircraft measurements at 3 km altitude. The reason might be a further evolution of the drop size spectrum during sedimentation or a principle measurement problem with ground based distrometers.

An interdependence of the mean drop size and the intercept parameter remains with both approaches, leaving a chance for further improvement.

References

Illingworth, A. J. and T. M. Blackman, 1999: The need to normalize RSDs based on the gamma RSD formulations and implications for interpreting polarimetric radar data. *29th Conf. on Radar Meteorology*, Amer. Meteor. Soc., Montreal, Canada, 629–631.

Illingworth, A. J. and M. P. Johnson, 1999: The role of raindrop shape and size spectra in deriving rainfall rates using polarization radar. *29th Conf. on Radar Meteorology*, Amer. Meteor. Soc., Montreal, Canada, 301–304.

Joss, J. and E. G. Gori, 1978: Shapes of raindrop size distributions. *J. Appl. Meteor.*, **17**, 1054–1061.

Marshall, J. S. and W. McK. Palmer, 1948: The distribution of raindrops with size. *J. Meteor.*, **5**, 165–166.

Testud, J., S. Oury, R. A. Black, P. Amayenc, and X. Dou, 2001: The concept of "normalized" distribution to describe raindrop spectra: A tool for cloud physics and cloud remote sensing. *J. Appl. Meteor.*, **40**, 1118–1140.

Willis, P. T., 1984: Functional ?ts to some observed drop size distributions and parameterization of rain. *J. Atmos. Sci.*, **41**, 1648–1661.

Evaluation of Quantitative Precipitation Estimation (QPE) Algorithms from Weather Radar and Rain-Gauge Data

Yuxiang HE, Hui XIAO, and Shuyan LIU

Institute of Atmospheric Physics, Chinese Academy of Sciences, Beijing 100029, China

1. INTRODUCTION

Radar observational results were influenced by many disturbing factors leading to the data existing rather significant error. So only the calibrated observational precipitation data can be accepted. Measures do not use rain gauge to calibrate such as tuning Z-I relationship method (Brands, 1985), probability partnership method (Marks, 1991; Rosemfeld, 1991), area-time integral method (Rogers, 1989), the virtue of theses methods is convenient to use, but they do not concern the specific features of certain precipitation process. The paper evaluated Z-I relationship method utilizing rain gauge to implement composite calibrating method, and through combining rain gauge and radar on point and area to make up deficiency of no rain gauge participating calibration. Among various methods of radar and rain gauge practicing composite calibration, the paper dealt with average calibrating method (AVG)(Barnston,1991), Kalman filtering calibration method (KALMAN) (Ahnert,1986), optimal interpolating calibration method (OPTI)(Seaman,1988), variational method (VAR), composite of Kalman filtering and optimal interpolating method (KALOPTI), Kalman variational calibrating method (KALMANVAR).

2. PARTENERSHIP OF RADAR AND RAIN GAUGE

Using observational data Z on different altitude as ground value to retrieve ground precipitation will result in certain errors. So radar composite plane and radar-rain gauge partnership (figure omitted) were adopted. First calculate average wind velocity and direction as well as raindrop falling velocities at the adjacent 9 points in the composite plane right above rain gauges, then figure out the 9 points in which direction takes part in average calculation and finally obtain radar position that suits with ground rain gauge.

3. DATA SOURCE

Radar Data: Original format Doppler radar data file of 21:00 (Beijing time) June 1~14:00 June 2, 2000 with an interval of approximate 5 minutes from the WSR-88D Doppler radar station of Hefei, Anhui Province.

Corresponding author's address: Yuxiang HE, Institute of Atmospheric Physics, Chinese Academy of Sciences, Beijing 10029, China; E-Mail: heyuxiang@mail.iap.ac.cn.

Rain gauge data: 10 minute interval rain gauge data corresponding with radar data in time. Rain gauge data were provided by Huanghe and Huaihe Rivers water Conservancy Committee in total of 453 stations among which there are 254 stations situated in the scope that centered with 230km radius. During evaluation, select 127 stations to participate in radar-rain gauge composite calibration and the other 127 stations for evaluation..

4. EVALUATION METHODS

When conducting evaluation, convert longitude-latitude coordinate of the rain gauge to rectangular. Utilize radar-rain gauge composite calibrating 1h accumulative precipitation and corresponding time level 1h accumulative precipitation to evaluate radar estimated precipitation.

7 types of 1h precipitation threshold are adopted in the paper: 0.5mm, 1.0mm, 2.5mm, 5.0mm, 7.5mm, 10.0mm, 12.5mm. For 0.5mm threshold, evaluation was conducted if precipitation takes place at 30 stations or more; for 1.0mm, 20 stations or more; and for others, 10 stations or more.

Three grading methods were used, namely threat scores (T_s) which indicates proportion of points that radar and observational data reach or surpass some threshold simultaneously among the total points that at least one of the radar and observational values reach or surpass some threshold during a specific time level and it reflects whether or not the position of radar value is coincident with observational value for some threshold; percentage bias (B_p) shows percentage of the bias between radar and observational data; and root mean squared error (RMSE) gives the difference of radar and observational data and it was influenced by the few points of radar value with a big error.

4. RESULTS ANALYSES

In the paper, only the case of strong rain intensity was discussed.

Fig. 1 depicts T scores. Fig. 1 shows that KALOPTI and OPTI have the highest T scores while ZI the lowest. And the others in turn are: KALMANVAR, VAR, KALMAN and AVG, but T scores of KALMAN are lower than that of AVG between 2.5mm and 10.0mm. The facts indicate that the precipitation position by KALOPTI and OPTI coincide better with the position of the factual precipitation and better than KALMAN and AVG while the later two are better than the ZI during the precipitation process with a strong

intensity. But the precipitation position of all the methods coincide worse and worse with the factual with threshold increasing, indicating that the stronger the precipitation, the greater departure of evaluation for strong precipitation center. The results in Fig.1 are interpreted as follows: because of the absence of composite calibrating and fixed coefficient, ZI cannot but lower than the other methods that have rain gauge taking part in composite calibrating as to position coincidence; since OPTI use ground rain gauge field as factual value and optimal linear interpolation of square error in its minimum sense, so it has avoided randomicity of general weighted scheme; VAR obtained much better precipitation distribution field from curve fitting of radar and ground rain gauge field, seeing that individual deficiency of radar and rain gauge as well as suited fault of them plus the choice of contrasting parameter of the two, the evaluation error thus generated; while AVG and KALMAN both only concerned average bias, so OPTI is better than them.

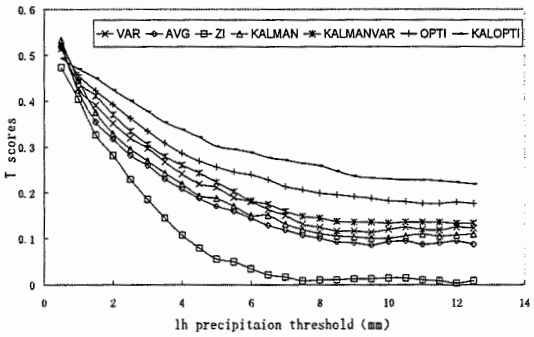

Fig.1 T scores (for the follow figures, legend same)

Fig.2 shows Bp scores. Among the stations of both radar and observational data reached a specific threshold, the former are higher than the latter for all the other methods except VAR for 0.5mm threshold and all of the method results are lower as to 1.0mm threshold. These show that by comparing radar and

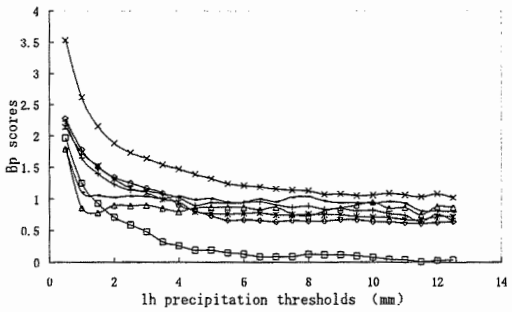

Fig.2 Bp scores

observational value among the stations of radar and prediction value that both reached a specific threshold, all the other methods are higher with exception of ZI lower sometimes. These are also due to the fact that radar observed echoes are at high altitude while rain gauge on the ground and rain drop not always fall onto ground owing to evaporation effect during falling process.

Fig.3 is RMSE scores. RMSE scores all increase with thresholds for all methods but the scores of KALOPTI and OPTI are smaller than KALMANVAR, VAR, KALMAN and AVG with ZI the highest. The results indicate that comparing the precipitation obtained from KALOPTI and OPTI with rain gauge value, the two methods have the smallest error and extreme low/high also small so they have the highest calculation precision. The precision of KALMAN and AVG are lower than KALOPTI and OPTI method with ZI the lowest.

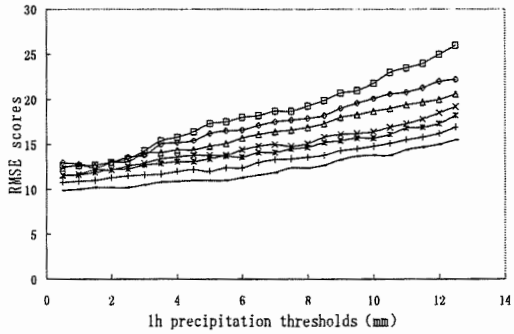

Fig.3 RMSE scores

6. CONCLUSIONS

(1) All the methods are higher when calculating precipitation scope of 0.5mm or above, the other methods are all a little lower than factual except Z-I relationship method when calculating strong precipitation scope (7.5mm or above), Z-I relationship method has seriously lower value than the factual for strong precipitation.

(2) Comparing observational precipitation with that calculated from the calibration methods, Kalman optimal interpolating and optimal interpolating methods are better than the other five with Z-I relationship the worst. Comparing the precipitation position that obtained from all the methods and observational, we find that the coincidence of them are worse and worse with thresholds increasing, that is the stronger the rainfall, the greater the evaluation bias.

(3) Among the stations of both radar and prediction value reached a specific threshold, radar data are a little higher at large with the exception of Z-I relationship method sometimes.

(4) Rainfall calculated from Kalman optimal calibrating method and optimal interpolating calibration method have the highest precision compared with rain gauge data and the precision of Kalman filtering calibration method and average calibration method are lower than composite calibrating method and optimal interpolating method with Z-I relationship method the lowest.

The parameters that were used in the methods mentioned in the paper are all empirical parameters summed up by other people and it is necessary to make the methods working under optimal states on the base of adjusting parameters and further comparing the methods.

Acknowledgements

This work was supported by Chinese National Science Foundation under Program Grants 40333033 and 40175001, the Key Foundation of Chinese Academy of Sciences under Grant Y2003002, Chinese National Scientific Key Program under Grants 2001BA610A-06-05 and 2001BA904B09, and the Key Foundation of IAP/CAS under Grant 8-4605 .

References

Ahnert,P.A.et al., 1986: Kalman filter estimation of radar-rainfall field bias, 23th Conference on Radar Met., JP33-37.

Barnston,A.G.,1991:An empirical method of estimating aingage and radar rainfall measurement bias and resolution ,J. Appl. Met. 30(3), 282-296.

Brands.F.A., 1985: Rainfall measurements with radar in "Next generation weather radar", Edited by Meteorological Institute of China (in Chinese) ,61-70.

Marks, F.D., 1991: Probability matched Z-R relations for hurricanes from aircraft observations.25th Conference on Radar Met., 63,778-781.

Rogers,R.R., 1989: Average rain rate in a model rainstorm. 24th Conference on Radar Met., 652-653.

Rosemfeld,D., 1991: Method to relate observed radar reflectivity to surface rainfall based on intensity distributions. 25th Conference on Radar Met. ,836-839

Seaman,R.S.,1988: Some read data tests of the Interpolation accuracy of Bratseth's successive correction method . Tellus, 40A,173-176.

THE COMPARISON OF MICROWAVE STATISTICAL ALGORITHMS FOR PRECIPITATION RETRIEVAL OVER LAND

Wenying HE[1], Hongbin CHEN[1], Jinli LIU

LAGEO, Institute of Atmospheric Physics, Chinese Academy of Sciences, Beijing, 100029, China

1 INTRODUCTION

In this paper, we present some results of comparison and validation of several retrieval algorithms for microwave remote sensing of rainfall rates over land. The combined data from the precipitation radar(PR), TMI on the Tropical Rainfall Measuring Mission satellite and the hourly rainfall measurement from surface stations in Henan province of China were used to analyze several statistical algorithms for precipitation retrieval over land. It is shown that it is hard to establish better retrieval algorithm if we only use the relation between the hourly rainfall from rain gauges and the microwave brightness temperatures. However, the TRMM satellite data has better correlation between rainfall and TMI brightness temperatures. Hence, by using the temporal and spatial matching satellite data, several statistical algorithms have been obtained and then validated.

2. ALGORITHMS TO BE COMPARED

Three statistical algorithms developed by foreign and Chinese researchers for precipitation retrieval over land are taken for comparison.

2.1 Algorithm 1

A scatter index algorithm was established by Grody (1991) and also developed by Ferraro (1995)

$$I_{s1} = 451.9 - 0.44 \bullet Tb_{19v} - 1.775 \bullet Tb_{22v} + 0.00575 \bullet Tb_{22v}^{2} - Tb_{85v}$$

$$R_{S1} = 0.00513 I_{s1}^{1.9468} \qquad I_{s1} > 10 \qquad (1)$$

2.2 Algorithm 2

Combined the scatter index and the polarization corrected temperature algorithm developed by Li and Zhu(2001) is given as

$$I_{s2} = -65.487 - 0.1836 \bullet Tb_{10v} - 0.4546 \bullet Tb_{19v} + 1.8605 \bullet Tb_{22v} - Tb_{85v}$$

$$R_{S2} = 124.236 - 0.42906 \cdot T_{pc} - 0.34318 \cdot I_{s2} \qquad (2)$$

Where $T_{pc}=1.818T_{b85v}-0.818T_{b85h}$, having good relation to rainfall, is called polarization corrected temperature.

2.3 Algorithm 3

The composite microwave index algorithm developed by Li and Chen(1998) is given as

$$I_{cm} = (D / D_0 - 1) + 30 \bullet (1 - T_{pc} / T_{pc0})$$

$$R_{FF} = 1 + a \bullet I_{cm}^{b} \qquad (3)$$

Where $D=Tb_{37v}-Tb_{37h}$, the subscript "0" denotes D or T_{pc} at the threshold of rain onset.

2.4 New statistical algorithms

By using the database of the TMI brightness temperatures and averaged rainfall at 2km from TRMM products of 2A25, we develop four algorithms for precipitation retrieval over land by means of

Corresponding author's address: Wenying HE, LAGEO, Institute of Atmospheric Physics, Chinese Academy of Sciences, Beijing, 100029, China; E-mail: flybirdhwy@yahoo.com.cn

step-regression method. They are:

$$R_1 = 41.9 + D_{VH} - 0.17 \bullet Tb_{37V} - 0.25 \bullet Tb_{85V} + 0.27 \bullet Tb_{85H} \quad (4)$$

$$R_2 = 34.8 + D_{VH} + 0.14 \bullet I_F - 0.13 \bullet T_{PC} \quad (5)$$

$$R_3 = 41.9 + D_{VH} + 0.16 \bullet I_F - 0.22 \bullet T_{PC} - 0.67 \bullet I_{CM} \quad (6)$$

$$R_4 = 38.4 + D_{VH} + 0.11 \bullet I_F - 0.14 \bullet T_{PC} - 0.05 \bullet I_{S1} \quad (7)$$

Where $I_F = Tb_{37h} - Tb_{85h}$, which is another cited index having strong negative correlation with rainfall; $D_{VH} = 0.35 \cdot D_{V1937} + 0.09 \cdot D_{H1910}$, and $D_{V1937} = Tb_{19v} - Tb_{37v}$, $D_{H1910} = Tb_{19h} - Tb_{10h}$. So D_{VH} reflects the rainfall signal in 3 low frequency channels of the TMT.

3 VALIDATION OF ALGORITHMS

7 algorithms mentioned above have been compared and validated with rainfall data acquired from several precipitation events in Henan province of China.

3.1 A typical precipitation event during Agu. 28-30, 2003 (samples N=13037)

The correlation coefficients between retrieval estimate and "real" rainfall for 7algorithms were calculated . Meanwhile , we use three basic parameters to analyze the errors of 7algorithms: first is mean error (BIAS), second is Root Mean Square Error (RMSE) , and third is standard error (RMSE'). The results are shown in Fig.1 and Fig.2.

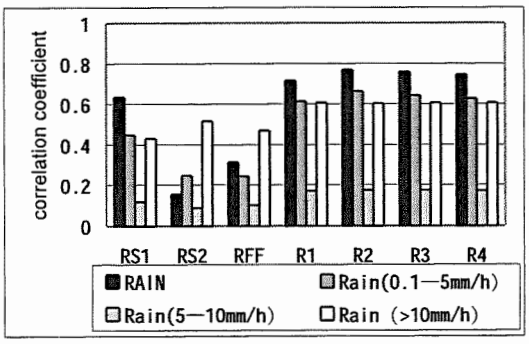

Fig.1 Correlation coefficients of 7 algorithms for different ranges of rainfall

It's seen that the new algorithms can obviously improve the results than the old ones about 20%,

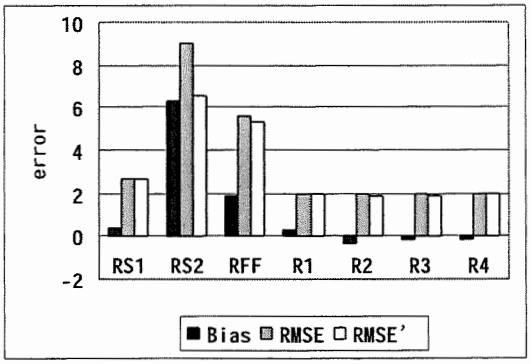

Fig.2 Errors of 7 algorithms

especially, for the weak (<5mm/h) or heavy (>10mm/h) rainfall, moreover, the errors reduce at least 25% than old ones. It also shows the first algorithm is best among the cited three algorithms, and the other two have lower ability to estimate rainfall, especially, the second one has larger error and bias.

3.2 Validation with station rainfall data

The ground hourly rainfall data obtained from rain gauges were used to validate those algorithms, and all samples were divided into spring and summer station rainfall. Fig.3 and Fig.4 show the similar trend: the new algorithms are better than old ones both correlation and error results, and the improvement in summer is more obvious than that in spring, while the comparisons in spring are better than those in summer. It is also show that the errors in summer are more larger than those in spring.

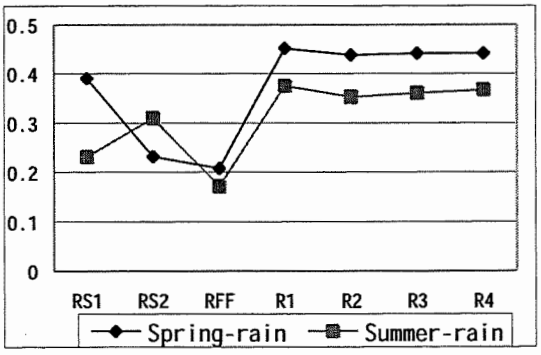

Fig.3 Correlation coefficients for spring and summer

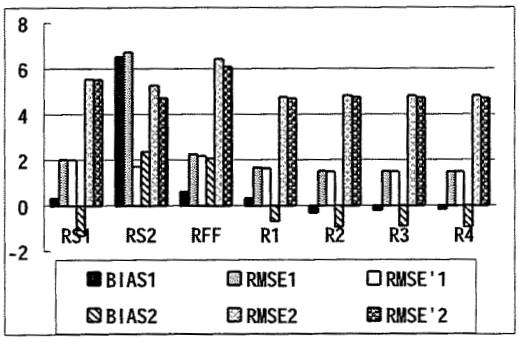

Fig.4 Errors comparison for spring and summer (1、2 stand for spring and summer respectively)

Furthermore, we compare the estimated rainfall from formula 4 (R1) with the nearest hourly rainfall (12:00, local time) on Apr.28, 2002(Fig.5). It is shown that the distribution of estimated rainfall is closer to that of observed data, especially, the positions of heavy rainfall center.

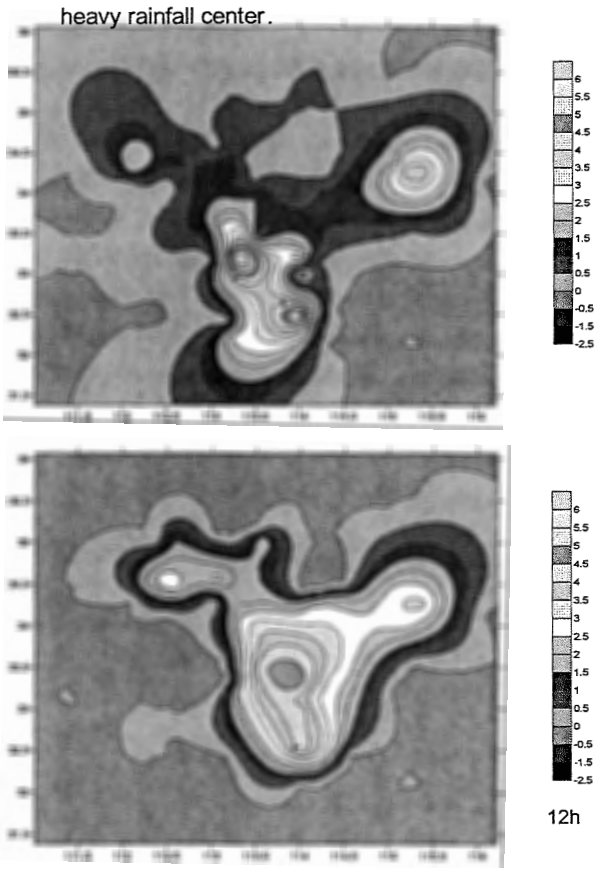

Fig.5 Retrieval rainfall by R1 (top) and the nearest Hourly rainfall on Apr. 28 ,2002 (bottom)

4 CONCLUSIONS

By comparing three typical algorithms and new developed formulas, we obtain the following results

1) Among the cited algorithms, the first one is better than the other two, the later have lower ability to retrieve weak and medium rainfall, but with better results to heavy rainfall(>10mm/h), meanwhile, the second one has larger error and bias.

2) Among the 7 algorithms, the new formulas can obviously improve the retrieval rainfall about 10-20% and reduce the error at least 25% for light(<5mm/h)and heavy (<10mm/h) rainfall, and yield same lower retrieval precision for medium rainfall (5 -10mm/h) as the statistical algorithms in the literature.

3) It can be improved the precision of precipitation retrieval over land by combining the low and high frequency of microwave which can provide more information of precipitation.

Acknowledgments: TRMM satellite data were provided by NASA Goddard Distributed Active Archive Center. This research was supported by National 973 project grant 2001CB309402.

References

Ferraro, R. R. , 1995: The development of SSM/I rain rate retrieval algorithms using ground based radar measurements. *J. Atmos. Oceanic Technol.*, 12, 755-770.

Grody, N. C., 1991: Classification of snow cover and precipitation using the Special Sensor microwave/Imager(SSM/I). *J. of Geophys. Res.*, 96, 7423-7435.

Lili and Zhuyuanjing, 1998: Microwave remote sensing of rainfall rates over land. Chinese Science Bulletin, 43(17), 1877-1880.

Li wanbiao and Chenyong, 2001: Retrieval of rain over land by using TRMM/TMI measurements. Acta, Meteor. Sinica, 59(5), 591-601.

Observations of Florida Convective Storms Using Dual Wavelength Airborne Radar

G. M. Heymsfield[1], A. J. Heymsfield[2], L. Belcher[3]
[1]NASA/ Goddard Space Flight Center, Greenbelt, MD
[2]National Center for Atmospheric Research, Boulder, CO
[3]Science Systems and Applications, Inc., Lanham, MD

1. INTRODUCTION

NASA conducted the Cirrus Regional Study of Tropical Anvils and Cirrus Layers (CRYSTAL) Florida Area Cirrus Experiment (FACE) during July 2002 for improved understanding of tropical cirrus. One of the goals was to improve the understanding of cirrus generation by convective updrafts. The reasons why some convective storms produce extensive cirrus anvils is only partially related to convective instability and the vertical transport ice mass by updrafts. Convective microphysics must also have an important role on cirrus generation, for example, there are hypotheses that homogeneous nucleation in convective updrafts is a major source of anvil ice particles. In this paper, we report on one intense CRYSTAL- FACE convective case on 16 July 2002 that produced extensive anvil.

During CRYSTAL-FACE, up to 5 aircraft flying from low- to high-altitudes, were coordinated for the study of thunderstorm-generated cirrus. The NASA high-altitude (20 km) ER-2 aircraft with remote sensing objectives flew above the convection, and other aircraft such as the WB-57 performing in situ measurements flew below the ER-2. The ER-2 remote sensing instruments included two nadir viewing airborne radars. The CRS 94 GHz radar (Li et al 2004) and the EDOP 9.6 GHz radar (Heymsfield et al. 1996) were flown together for the first time during CRYSTAL-FACE and they provided a unique opportunity to examine the structure of 16 July case from a dual-wavelength perspective. EDOP and CRS are complementary for studying convection and cirrus since CRS is more sensitive than EDOP for cirrus, and EDOP is considerably less attenuating in convective regions. In addition to the aircraft, coordinated ground-based radar measurements were taken with the NPOL S-Band (3 GHz) multiparameter radar. One of the initial goals was to determine whether dual-wavelength airborne measurements could identify supercooled water regions.

Corresponding author address: Gerald M. Heymsfield, Goddard Space Flight Center, Lab. For Atmospheres, Code 912, Greenbelt, MD 20771; e-mail: gerald.heymsfield@nasa.gov

2. CONVECTIVE EVENT ON 16 JULY 2002

The forecast for 16 July 2002 called for mid-afternoon convection along a synoptic-scale band of low-level moisture convergence extending from an off-shore (Florida east coast) disturbance across the Florida peninsula. The KAMX (Miami) 1200 UTC sounding indicated a moist lower layer (up to 1.5 km) and a strong instability (CAPE of 2598 J kg^{-1}), while the 0000 UTC sounding showed a CAPE of 2119 J kg^{-1} with moderate directional wind shear (300° shear vector). Sea-breeze convection began shortly after 1600 UTC on the east coast of Florida producing a strong thunderstorm north of the KAMX radar. A region of inland convection began at 1845 UTC along an outflow boundary generated by the above mentioned storm. The convective system had many embedded cells, with some strong cells typical of those observed during the CRYSTAL-FACE flights on other days. Figure 1 shows the 3 km and 8 km CAPPIs from NPOL during one of the ER-2 passes. A particularly intense cell (Cell 2) is noted with reflectivities exceeding 60 dBZ at 3 km altitude, and 55 dBZ at 8 km altitude.

Figure 2 shows a height-time history of Cell 2's maximum reflectivity constructed from NPOL CAPPI data. The cell underwent rapid development prior to 1940 UTC and maximum radar-derived storm top height was at 1950 UTC. The peak reflectivity for this cell also occurred at 1950 UTC with 62 dBZ at 4 km altitude; this was about 5 min after the ER-2 pass over the cell. The cell evolution presented in Fig. 2 is typical of convection evolution where an intense growth period is followed by a weakening of the updraft followed by descent of precipitation from higher altitudes.

Figure 3 provides an NPOL-derived vertical reflectivity cross-section through the high reflectivity core of Cell 2 at 1950 UTC. The

differential reflectivity (Z_{DR}) contours up to about 3 dB below the freezing level (5 km) are typical for rain drops, and the near-zero (Z_{DR}) values combined with >55 dBZ reflectivities above the freezing level are commonly observed in hail storms (e.g., Bringi et al. 1996). The NPOL volume scan 10 min earlier at 1940 UTC was very different in that the enhanced Z_{DR} region indicating the presence of liquid or mixed phase region, extended up to about 6-6.5 km altitude and the maximum refelctivities were ~55 dBZ (not shown). If hail were present, strong updrafts would be required to loft particles to high altitudes.

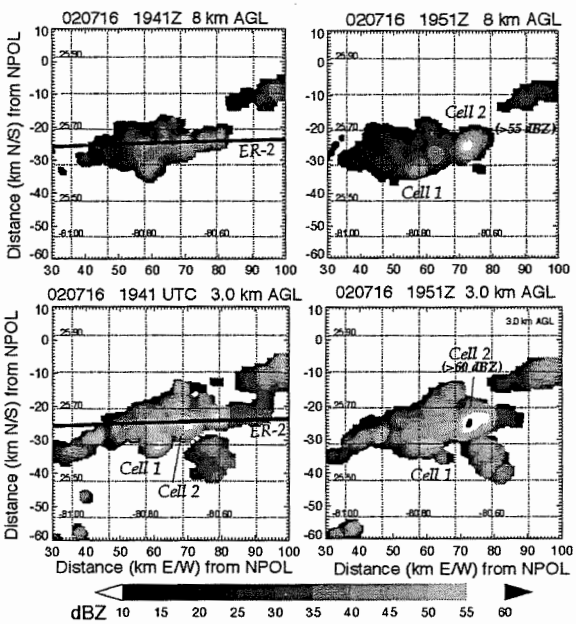

Figure 1. NPOL CAPPIs at 3 km and 8 km altitudes at 1941 UTC and 1951 UTC. Two larger cells are indicated. The ER-2 flight track on 1941 UTC CAPPI passes over Cell 2 at 1946 UTC.

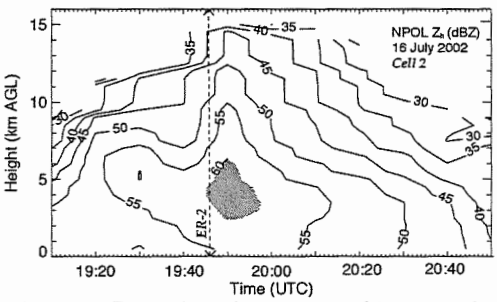

Figure 2. Reflectivity time history of Cell 2 derived from NPOL data

3. DUAL WAVELENGTH OBSERVATIONS

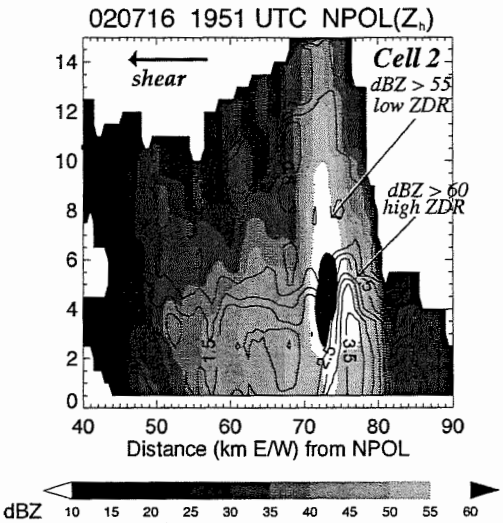

Figure 3. Vertical reflectivity cross section at 1951 UTC. Contours of Z_{DR} are superimposed.

EDOP and CRS images covering Cell 2 at about 1946 UTC is shown in Fig. 4. The EDOP reflectivity (middle panel) has a downshear tilted (toward west) reflectivity core that extends up to ~12 km altitude. Because of strong attenuation and Mie scattering at 94 GHz, CRS reflectivity (top panel) is completely attenuated within 2-3 km penetration of the high reflectivity core. The Doppler velocities bottom panel) show a strongly downshear tilted updraft with Doppler velocities exceeding 15 ms^{-1}. The westward tilted updraft embedded in moderate environmental shear is ~2 km in width. Because of Nyquist considerations and unfolding issues, CRS velocities (not shown) exceeded the acceptable range of +/-15 ms^{-1}.

4. Discussion: Observations of Large Graupel/Hail

The ground-based NPOL measurements clearly point to the presence of hail or large ice in Cell 2. What is of particular interest is the extent of supercooled water and ice in the updrafts and what can be inferred from the dual-wavelength measurements. Individual radar profiles are examined in this preliminary study but will involve further analysis and modeling in future work.

Figure 5 shows vertical profiles of EDOP/CRS dual wavelength measurements and derived properties at three locations in Cell 2's updraft region (Fig. 4). In addition, we have superimposed the 3 GHz reflectivity measurements from the NPOL radar even though the sampling volume is considerably different than

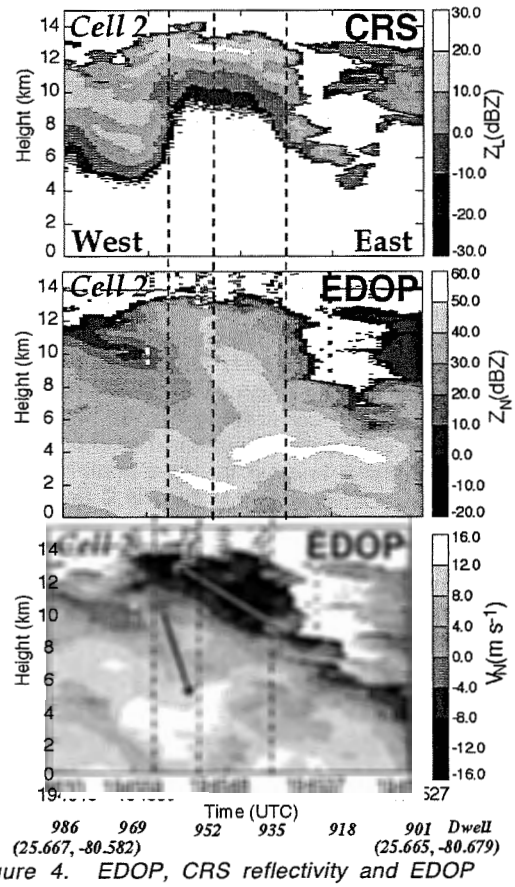

Figure 4. EDOP, CRS reflectivity and EDOP Doppler velocity for Cell 2 at ~1946 UTC on 16 July 2002. Doppler convection: positive (downward) and negative (upward). Vertical dashed lines show locations of profiles in Fig. 5; arrows depict hydrometeor motions. The shear vector is oriented from right to left in the figure. Total cross section width is 8.5 km.

the downlooking measurements from EDOP and CRS. The westernmost profile (left side) in Fig. 5 is on the downshear side of Cell 2's updraft. In constructing the profiles, we have used Florida *in situ* microphysical measurements in graupel regions to derive relations to convert between EDOP 9.6 GHz reflectivity and reflectivity-weighted fallspeed, 94 GHz attenuation, and 94 GHz Mie effects (Fig. 6). These relations have used full Mie calculations.

Cell 2's updraft is indicated by the shaded regions in Fig. 5 (middle row). The vertical air velocities were calculated by adding graupel reflectivity-weighted fall velocity (Fig. 6) to the EDOP Doppler velocities above 6 km altitude, and a rain fall velocity below 4 km altitude; air

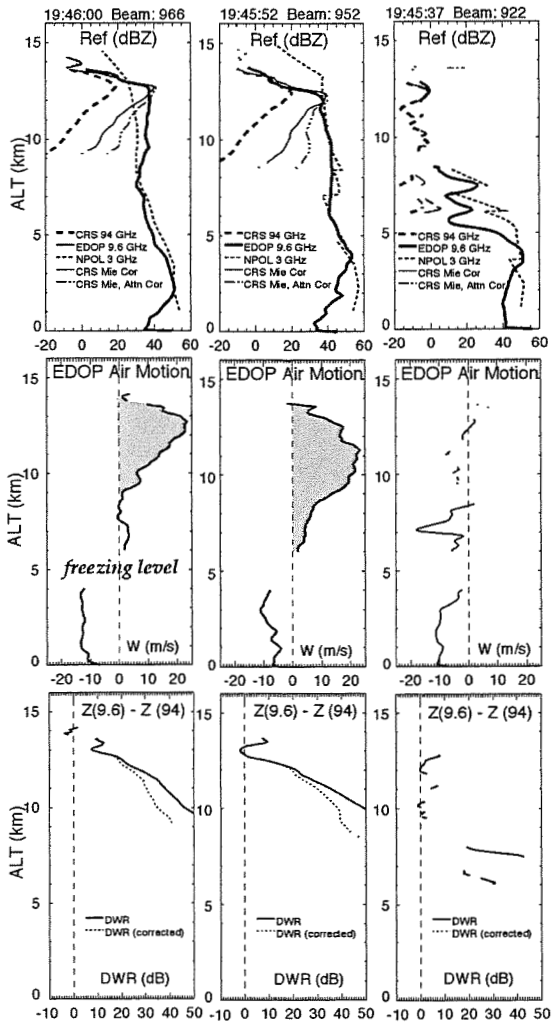

Figure 5. Vertical profiles derived from EDOP and CRS data on 16 July 2002. Top row: EDOP, CRS, NPOL reflectivity, CRS corrected for Mie scattering, CRS corrected for Mie scattering and graupel attenuation. Middle row: Vertical air motion derived from EDOP with assumed rain and graupel fallspeeds. Bottom row: DWR from raw reflectivity data and with CRS corrected for attenuation.

velocities were not calculated near the freezing level. The tilted updraft in Cell 2 exceeds 20 ms^{-1}, as shown by peak values at 11 km and 12.5 km altitudes in the left two profiles. The EDOP and NPOL reflectivity profiles indicate ~40 dBZ extending up to 12.5 km altitude, which is rather high and further suggestive of hail. The CRS profiles show an extremely large decrease with altitude near the level of the updraft maximum, at

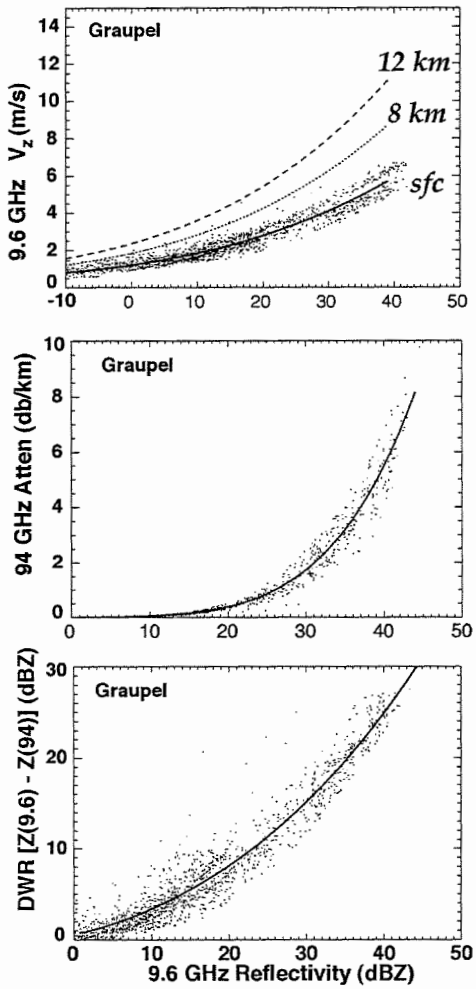

Figure 6. Relations derived for 9.6 and 94 GHz based on Florida in situ measurements of graupel size distributions. Curves are fitted to the in situ observations. The fitted graupel fallspeed curves (top panel) are shown for the altitudes ranging from the surface to 12 km.

the top of the EDOP high reflectivity column. To examine the implications of the 94 GHz reflectivity measurements, we have used the Mie-derived results in Fig. 6 to correct CRS reflectivity for Mie scattering and attenuation by graupel. What is evident from this exercise is that the Mie correction is much larger than the attenuation correction, but the both of these corrections are significant. In addition, it is clear that the graupel relations do not completely correct for Mie scattering and attenuation below the 12 km level.

The lack of agreement between the corrected 94 GHz reflectivity and the EDOP reflectivity that is near Rayleigh, may be due to two factors: a) the presence of cloud water, or, b) the presence of hail that will have larger Mie scattering and attenuation depending on its size distribution and characteristics (density, etc.). The presence of supercooled water would be highly attenuating at 94 GHz if the amounts were greater than 0.5 gm^{-3} for example. In support of the presence of hail, the reflectivity and vertical motion observations suggest that ice hydrometeors are falling from approximately the 12 km level where the updraft magnitude is ~20 ms^{-1}. At the 12 km altitude, fall velocities of 20 ms^{-1} would imply hail dimensions of about 1-1.5 cm depending on the type of hail (Knight and Heymsfield 1983). This would clearly be out the the range of the graupel calculations assumed in constructing Fig. 6. On the other hand, supercooled cloud water must be present in the updraft in order for large graupel or hail to grow. Considering that the –35 C level is in the range of 10-11 km altitude in a rising updraft parcel, this is fully within reason. Future work will focus on providing a consistent picture of the relation between the updrafts, particle growth, and the remote measurements.

Acknowledgements

This effort was supported by NASA's Radiation Sciences Program at NASA HQ. EDOP was supported under the NASA's Atmospheric Dynamics Program. Special appreciation goes to Drs. Lihua Li and Lin Tian for their careful efforts on EDOP and CRS instrumentation, data set, and analysis.

References

Bringi and co-authors, 1996: Dual multiparameter radar observations of intense convective storms: The 24 June 1992 case study. *Meteor. Atmos. Phys.*, 3-31.

Heymsfield, G. M., S. Bidwell, I. J. Caylor, S. Ameen, S. Nicholson, W. Boncyk, L. Miller, D. Vandemark, P. E. Racette, and L. R. Dod, 1996: The EDOP radar system on the high altitude NASA ER-2 Aircraft, *J. Atmos. Oceanic Tech.*, **13**, 795-809.

Knight, C. A., and A. J. Heymsfield, 1983: *J. Atmos. Sci.*, **40**, 1510.

Li, Lihua, G. Heymsfield, P. Racette, L. Tian, E. Zenker, 2004: The 94 GHz cloud radar system on the NASA ER-2 aircraft, in press, *J. Atmos. Ocean. Tech.*

THE EFFECTS OF PARTICLE CLUSTERING ON IN-SITU AND REMOTE SENSING MEASUREMENTS OF MEANS AND VARIANCES

A.R. Jameson

RJH Scientific, Inc., El Cajon, CA, 92020 , USA

1. INTRODUCTION

In astronomy, observations play a crucial role in the evolution of theory. Conversely, theory suggests critical observations. The same constructive symbiotic relation exists in the atmospheric sciences, although perhaps more grudgingly. Nevertheless, it is important that measurements reflect reality with a specifiable degree of certainty so as not to mislead theoreticians and modelers inadvertently.

In cloud physics and precipitation meteorology, particle counts obviously play a crucial role since clouds and precipitation are aggregations of discrete entities. Yet, throughout the history of cloud and precipitation physics, instruments, often out of necessity, and investigators, often arbitrarily, impose restrictions upon observations without realizing the statistical consequences or assumptions. It was not until Cornford (1967) offered Poisson statistics to answer questions such as "How many drops are needed before we can estimate the mean concentration to a specified certainty?" Since then, Poisson statistics have been used with universal abandon.

Poisson statistics, however, is based upon three assumptions including that the appearance of one particle is completely statistically independent of the appearance of another for all particle separations. This means that the particles are distributed in space as randomly as possible. Yet, observations, available in the literature and far too numerous to list here, show that this is generally not the case because of particle 'clustering', i.e. because the presence of one particle statistically alters the likelihood that there is another particle nearby.

This has some significant implications with regard to in-situ and remote sensing observations not generally recognized in the field. The purpose of this work is to provide explicit expressions showing the effects of clustering on measurements of means and variances of some parameters and to provide guidance for avoiding or at least minimizing such effects. We do this by considering the simplest case of a statistically homogeneous field of particles, the implicit assumption behind almost all past analyses of counting statistics. Unlike past studies, however, we include clustering. We show that where there is particle clustering, the observed means can and the variances do depend upon the size of the sampling volume when the characteristic sample volume dimension is less than several times the correlation length of the field.

These findings affect comparisons among different instruments having different sample volumes as well as the observed variances for solo instruments. Partial solutions include (1) increasing the sampling volume or interval, (2) spacing samples to be several times the likely correlation length of the field and (3) post-processing raw times series data to assure either that the sampling is consistent with the correlation length of the data field or that the data are appropriately randomized so that any correlation between measurements is destroyed. This latter approach will only work when the data are statistically homogeneous over a sufficiently large domain, of course. An adequate treatment of statistical inhomogeneity remains the major obstacle to further advances in quantifying measurement accuracy in cloud and precipitation physics.

Corresponding author address: A.R. Jameson, RJH Scientific, Inc., 5625 N. 32nd St., Arlington, VA 22207-1560 USA; email: arjatrjhsci@earthlink.net

2, THEORY AND DISCUSSION

We begin by repeating the argument of Shaw et al. (2002, 1049-1050), namely, consider a space of size $\mathcal{V}$ containing N particles. For an elemental volume, dv, the probability that it contains either 1 or zero particles is then given by $N dv/\mathcal{V} = \bar{n}\, dv$. Next consider a finite volume $\mathcal{V}$ and, in addition, suppose volume $\mathcal{V}$ is *centered* on a particle. Then the likelihood that a particle lies in a neighboring elemental volume is given by

$$P = \bar{n}(1+\eta)dv \tag{1}$$

That is, the probability of finding a particle in the second elemental volume is enhanced (or decreased) by $(1+\eta)$ where h is the so-called pair-correlation function. Now since the elemental volume either contains a particle or does not, integrating (1) over many such V yields the average number of particles in V. That is,

$$\bar{N}_V = \bar{n}V + \bar{n}\int_0^V \eta dv \tag{2}$$

which can also be written as

$$\bar{N}_V = \bar{n}V(1+\bar{\eta}) \tag{3}$$

where $\bar{\eta} = \frac{1}{V}\int_0^V \eta dv$. Dividing (3) by V we also have, then, for the concentration that

$$\overline{n}_V = \overline{n}(1+\overline{\eta}) \tag{4}$$

as pointed out already by Shaw et al. (2002).

First, we note that if the particles obey a Poisson process, then $\overline{\eta} = 0$ and $\overline{N}_V = \overline{n}V$ on all scales as one would expect. More generally, however, particles exhibit 'clustering' so that $\overline{\eta} \neq 0$. Practically speaking, this means that when the counting begins centered on a particle, the average number of particles found in a sample volume of size *V* at a fixed location *depends upon the size of the sample volume, i.e., the resolution of the instrument* unless *V* is so large that $\overline{\eta} \to 0$. Expressed differently, if we center observations on a particle but allow *V* to increase, the measured mean concentration will be a function of *V*.

Most real sample volumes, however, are not elemental nor centered on a particle. Consequently, in statistically homogeneous conditions, $\overline{N} = \overline{n}V$ on average, regardless of *V*. (Note that in statistically inhomogeneous conditions this will *not* be true.)Yet in a clustered environment, correlation, on average, still appears among the neighboring sample volumes so that convergence to the true mean is slowed by the scarcity of independent samples. What this means is that the observed mean value is still affected by *V*, but not in the manner expressed in (2)-(4) unless the sampling volume just happens to be centered on a particle.

The effect of clustering on variances is more complicated. Moreover, since the variance is usually of interest only with regard to uncertainties in measuring the mean, we will instead consider the relative error or relative dispersion from which the variance can be easily determined. For the rainfall rate, it has been shown (Jameson and Kostinski 2002a) that the expected relative square error is given by

$$\frac{\sigma_R^2}{E^2(R)} = \frac{1}{E(N)} + \overline{\eta} + \frac{F_R}{E(N)}\left[\frac{\sigma^2(D^3V_t)}{E(D^3V_t)}\right] \tag{5a}$$

where

$$F_R = \frac{E_N\left[\sigma^2(R|N)\right]}{E(N)\sigma^2(D^3V_t)} \tag{5b}$$

E denotes the expectation, *D* is the drop diameter, V_t is the terminal fall speed of drop having diameter *D*, s^2 is the variance, and *N* is the total number of drops in the sample volume. The vertical bar denotes conditioning, while F_R is a factor equal to unity when the drops occur statistically independently but increases when the occurrences of drops in the volume are positively correlated. The numerator of F_R is the expected value of the variance of *R* given that we know *N* over the distribution of all *N*. That is, it is the variance of *R* weighted by the frequency of occurrence of *N*. [Note that his relation is based upon the statistical independence between *N* and the size distribution. In the past there are many claims that these two quantities are correlated. However, closer inspection reveals that those conclusions are based entirely upon measurements having insufficient sample sizes so that much of the reported 'correlation' can, in fact, be attributed to sampling size effects (Jameson and Kostinski 2002b). While a weak statistical correlation between *N* and the size distribution may exist, it remains to be demonstrated. Moreover, it is often claimed that such a correlation has a physical origin although a convincing explanation has never been given. If one exists, a detailed physical description needs to be provided.]

The first term in (6a) has to do only with the number of drops so that the more there are in the sample volume, the smaller its contribution to the relative dispersion. The third term in (6a) contains all the variability of the drop sizes. As important as such variability may be at times, it too is weighted by the 1/*E(N)* so that its influence wanes with increasing sample volume, *V*. The second term, however, does not depend inversely upon *E(N)*. Furthermore, positive clustering tends to enhance the relative importance of the correlation term with respect to the other two. To see this and the role of *V* more explicitly, (6a) may be rewritten as

$$\frac{\sigma_R^2}{E^2(R)} = \frac{1}{\overline{n}V} + \overline{\eta} + \frac{F_R}{\overline{n}V}\left[\frac{\sigma^2(D^3V_t)}{E^2(D^3V_t)}\right] \tag{6}$$

Similar expressions apply to both *W* and to *Z*, namely

$$\frac{\sigma_W^2}{E^2(W)} = \frac{1}{\overline{n}V} + \overline{\eta} + \frac{F_W}{\overline{n}V}\left[\frac{\sigma^2(D^3)}{E^2(D^3)}\right] \tag{7a}$$

and

$$\frac{\sigma_Z^2}{E^2(Z)} = \frac{1}{\overline{n}V} + \overline{\eta} + \frac{F_Z}{\overline{n}V}\left[\frac{\sigma^2(D^6)}{E^2(D^6)}\right] \tag{7b}$$

To be sure $\overline{\eta} = \frac{1}{V}\int_0^V \eta dv$ depends inversely on *V* as well, but because the integral is a sum over smaller scales, it generally decreases much more slowly than 1/*V*. In fact, in some quite general cases, $\overline{\eta}$ is constant *regardless of V* (Jameson and Kostinski 2002a) and the variance does not decrease with increasing *V* even for statistically homogeneous data!

As problematic as this appears, in statistically *inhomogeneous* fields the situation is even more serious because there are 'trends' or systematic, deterministic variations in the mean values. In such cases, the mean

value will depend on V as well, but for reasons different from those discussed above. Moreover, these systematically changing mean values add an apparent but artificial contribution to the variance, which, remember, is only a characteristic of purely stochastic, random variables. The identification and proper treatment of systematic variations as opposed to random fluctuations in the mean values particularly in a clustered environment containing large scale fluctuations is not a trivial task. It has yet to be addressed effectively if, indeed, it is even possible to do so in any general sense. What this brief note shows, however, is that even in the most statisticallyoptimistic case, clustering and sampling volume (interval) can affect measurements and distort comparisons among different instruments. Care must be taken to acknowledge the importance of intrinsic correlations within clouds and rain by not imposing any arbitrary, a priori sampling resolution upon the natural field.

Acknowledgments: This work was supported under grants from the U. S. National Science Foundation NSF ATM02-42418.

3. REFERENCES

Cornford, G.S., 1967: Sampling errors in measurements of raindrop and cloud droplet concentration. *Meteor. Mag.*, **96**, 271-282.

Jameson, A.R. and A.B. Kostinski, 2002a: When is rain steady? *J. Appl. Meteor.,* **41**, 83-90.

_____ and _____, 2002b: Spurious power-law relations among rainfall and radar parameters., *Quart. J. Roy. Met. Soc.*, **128**, 2045-2058.

Shaw, R.A., A.B. Kostinski and M.L. Larsen, 2002: Towards quantifying droplet clustering in clouds., *Quart. J. Roy. Met. Soc.*, **128**, 1043-1057.

Relationship between the low-level cloud fields from satellites and precipitation from ground over China

K. Kawamoto and T. Hayasaka

Research Institute for Humanity and Nature, Kyoto 602-0878 Japan

1. INTRODUCTION

Aerosols, that is, particles suspended in the atmosphere, are being paid attention in view of climate change. They scatter solar radiation, and serve as cloud condensation nuclei (CCN) to control cloud optical properties. The former is called the direct effect, and the latter is called the indirect effect. The indirect effect is further divided mainly two effects, such as the first and second kinds. The first effect is to change the cloud droplet size and optical depth due to cloud droplet number change, and the second effect is to influence the cloud lifetime and precipitation owing to alter precipitation efficiency. In particular, a comprehensive knowledge of the aerosol indirect effect of the second kind is currently lacking.

More and more pollutants have been emitted recently in China due to rapid economical growth caused from the political changeover, so this influence on the atmosphere is of quite concern from social and scientific points of view. In this paper, we try to investigate the relationship between the low-level cloud fields derived from satellite data and precipitation amount obtained from ground-based rain gauges over China. We focus on low-level clouds here because of more interaction with aerosols compared to middle and higher clouds.

2. DATA AND RESULTS

We use three channels of visible (0.6micron), near-infrared (3.7micron) and infrared (10.8micron) wavelengths of Advanced Very High Resolution Radiometer (AVHRR) Global Area Coverage (GAC) data for cloud retrievals. With these satellite data, we infer the optical depth (τ), effective particle radius (r_e) and integrated droplet number (N_c) of low-level water clouds. The retrieving principle is based on the fact that that solar reflection at a non-absorbing visible wavelength is essentially determined by τ, while solar reflection at a water-absorbing near-infrared wavelength is largely determined by r_e. Cloud thermal emission included in near-infrared wavelength, which is not desired for r_e determination, is corrected by cloud top temperature obtained by the infrared wavelength. Water vapor absorption by above and below the cloud is also taken into account in the processing (Kawamoto et al. 2001). N_c is calculated from τ and r_e, assuming vertically homogeneous cloud layer. N_c is calculated τ and r_e, assuming vertically homogeneous cloud layer. Cloud parameters thus obtained are monthly-averaged in the 0.5-degree resolution for January and July in 1990 over China (E90-E135, N15-N50). General characteristics of these parameters are consistent with previous studies for r_e (Han et al. 1994), τ (Rossow et al. 1996) and N_c (Han et al.1998).

As for precipitation, the data are collected from the surface rain gauges and are originally compiled in the 0.1-degree resolution grid with daily temporal resolution, but are averaged in the 0.5-degree resolution in order to make appropriate comparison with cloud data.

In order to examine the relation between precipitation and cloud properties, we make comparisons using a following procedure for July case. Precipitation amount is divided into several buns, and cloud properties are collected for each precipitation amount bin. Then the average and standard deviation are calculated. Figure 1 and 2 show relationships between precipitation amount and r_e, and N_c, respectively. Error bars denote standard deviation. We find that r_e gets larger as precipitation becomes stronger. On the other hand, N_c, however, gets less as precipitation becomes stronger. These phenomena can be understood as follows. The number of cloud droplets is reduced due to scavenging by precipitation, and each cloud droplet can grow larger in less CCN, that is, clean environment. Furthermore, water vapor supply is enough.

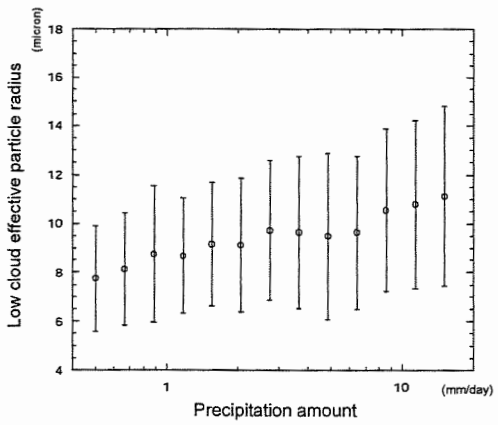

Fig.1 Relationship between precipitation amount and

Corresponding author's address: Kazuaki Kawamoto, Research Institute for Humanity and Nature, Kyoto 602-0878 Japan; E-Mail: kawamoto@chikyu.ac.jp.

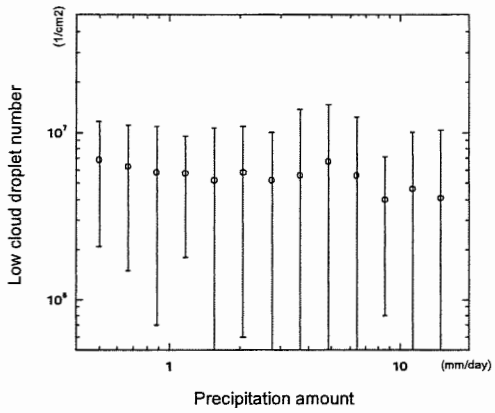

Fig.2 Relationship between precipitation amount and N_c

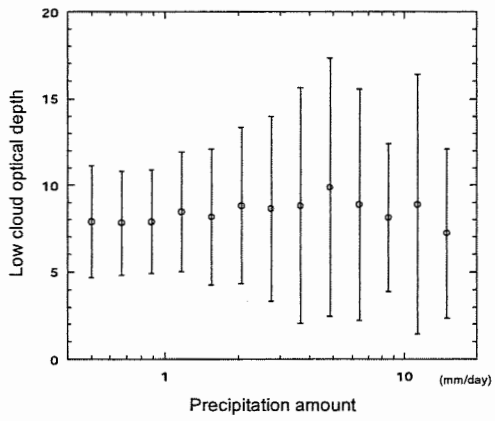

Fig.3 Relationship between precipitation amount and τ

Next, we try to investigate the relationship between precipitation amount and τ. Fig. 3 illustrates the result. Variation of τ with precipitation amount is almost constant. To the first approximation, optical depth is proportional to a product of the particle size and particle number, and a decrease in the droplet number and an increase in the particle size would maintain low cloud optical depth.

3. CONCLUDING REMARKS

Cold rain process (precipitation from high ice clouds) in conjunction with Asian monsoon is predominant in this region. Thus we need to be careful to make direct comparisons as performed here. This sort of preliminary investigation would be, however, valuable as a primary step to get further understanding of the aerosol effect on precipitation. We should continue more detailed analyses on this issue for not only low clouds but also high clouds.

Acknowledgements

The authors are grateful to Dr. P. P. Xie of NOAA for providing precipitation data over China.

References

Han, Q., Rossow, W. B. and Lacis, A.A. (1994). Near-global survey of effective droplet radii in liquid water clouds using ISCCP data. *J. Climate*, **7**, 465-497.

Han, Q., Rossow, W. B., Chou, J. and Welch, R. M. (1998). Global Variation of Cloud Effective Droplet Concentration of Low-level Clouds. *J. Geophys. Lett.* **25**, 1419-1422.

Kawamoto, K., Nakajima, T. and Nakajima, T. Y. (2001). A Global Determination of Cloud Microphysics with AVHRR Remote Sensing, *J. Climate*, **14**, 2054-2068.

Rossow, W. B., Walker, A. W., Beuschel, D. E. and Roiter, M. D. (1996). International Satellite Cloud Climatology Project (ISCCP) documentation of new cloud datasets. WMO/TD737, World Climate Research Programme (ICSU and WMO), 115 pp.

LARGE WATER DROPS IN CONTINENTAL CUMULUS IN THEIR "FIRST-ECHO" STAGE

C.A. Knight

National Center for Atmospheric Research*, Boulder, CO, USA

1. INTRODUCTION

Caylor and Illingworth (1987) and Illingworth (1988) found several-millimeter-sized raindrops early in convective clouds in England and in Alabama (USA), using Z_{DR}, and interpreted their presence in terms of ultra-giant CCN. Knight et al. (2002) obtained more detailed data on early echo formation in Florida, finding large raindrops both very early and very low in convective clouds. Again ultra-giant CCN are a possible explanation, but the first appearance of these drops very low in the clouds was puzzling. Observations are reported here from the STEPS project, along the Northern part of the Colorado/Kansas (USA) border, June-July, 2000. The clouds there are continental, the South Dakota School of Mines and Technology T-28 consistently finding maximum droplet concentrations in the 800-1000 cm^{-3} range in cloud penetrations during that project (A. Detweiler, personal communication). Radar data from the S-Pol and CHILL radars are used to examine early echo formation, with particular reference to Z_{DR} and to the earliest radar echo histories of the clouds. Since these clouds are not only continental but also have cloud bases generally colder than those in the previous studies, there was no strong expectation of seeing large drops in connection with the earliest radar echoes from precipitation.

Another objective was to obtain radar data on the clouds with the sensitive, 10-cm-wavelength radars, using the Bragg scattering signal from cloud top to determine how long their tops had been above the freezing level before the first precipitation echo. Such data are fundamental and have been lacking, though relatively easy to obtain with modern research radars.

Corresponding author's address: Charles A. Knight, NCAR, P.O. Box 3000, Boulder, CO, 80307, USA; E-mail: knightc@ucar.edu

NCAR is sponsored by the National Science Foundation

2. RESULTS

The data discussed here concern the early echoes from energetic clouds that quickly become cumulonimbus. Time-height diagrams of Z_e and Z_{DR} for three of the four rather complete cases that were obtained are shown in Figs. 1-3. In all these cases there was appreciable potential instability and wind shear. The case shown in Fig. 1 was covered by alternate PPI and RHI volume scans (times indicated by Ps and Rs along the bottom) and the other two were covered by PPIs only, at 6- or 7-minute intervals. PPI scans in the clouds studied are indicated by the dashed lines.

All of these cases showed a conventional first precipitation echo that formed first above the freezing level and spread downwards and upwards as the clouds grew. The significantly positive Z_{DR} signal (0.5dB and greater) is shown in the Figures by a line delineating its upper boundary and, very early, a short stretch of lower boundary. (The X's in Figs. 1 and 2 show the early, positive Z_{DR} data points that are ascribed to hydrometeors.) The positive Z_{DR} values commence in Figs. 1 and 2 slightly before or at about the same time as the "conventional precipitation echo" (generally identified at $Z_e > 0$ to 10dBZ) but in Fig. 3 they appear 5 - 10 minutes later than the conventional, first precipitation echo aloft. (The Bragg echo is commonly as strong as 0dBZ, and > 10dBZ appears almost always to be scattering from the hydrometeors, while interpretation of values between about 0 and 10 dBZ may be ambiguous.)

Three distinct areas in the convective cells are often identifiable in the PPIs: areas of Z_e maximum, areas of significantly positive Z_{DR} (>0.5dB), and areas of radial velocity different from that of the surroundings in the PPI, but characteristic of air from beneath the level being scanned. One instance of the spatial association of these three areas is shown in Fig. 4, from the case in Fig. 1. The middle panel

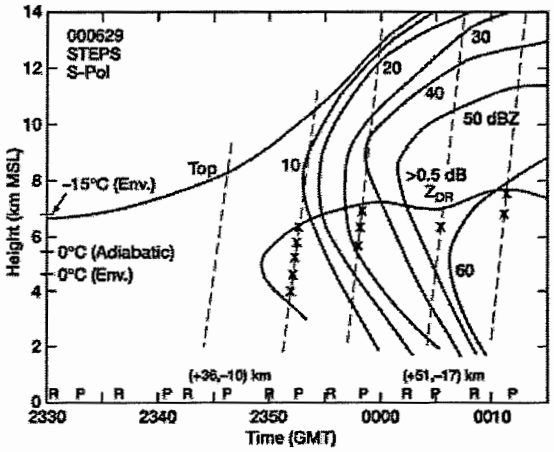

Fig. 1. Time-height diagram of Z_e for the June 29 case that formed some 10 km West of a severe storm. The 0°C (Adiabatic) temperature was calculated for the severe storm. The Z_{DR} contour encloses the positive values ascribed to water drops. Radar coordinates at two times are on the Figure. The earliest tops (about 2330-2340) are from precursor cells. High values of Z_{DR} in the clear-air boundary layer are not included in Figs. 1-3.

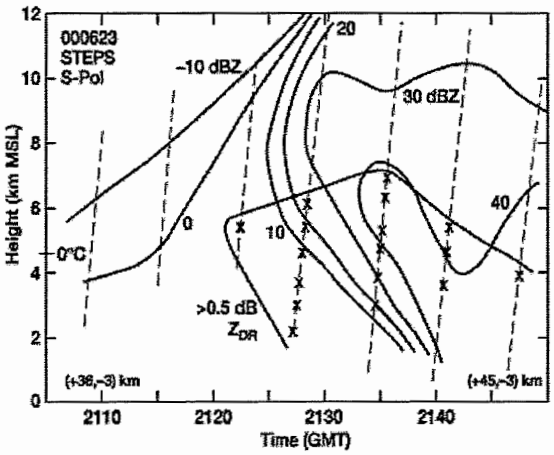

Fig. 2. The June 23 case, similar to Fig 1. The X's represent the Z_{DR} values >0.5dB considered to be due to water drops (omitted in heavy precipitation below the freezing level, where this signal is always present).

shows the area of lower level velocity centered in the panel; the upper panel shows the maximum Z_e area to the SE; and the lower panel, the area of positive Z_{DR} to the NW. The NW is (very roughly) up-wind, the SE down-wind. This kind of pattern is repeated many times in all the cases, though there are a number of instances, especially very early in a

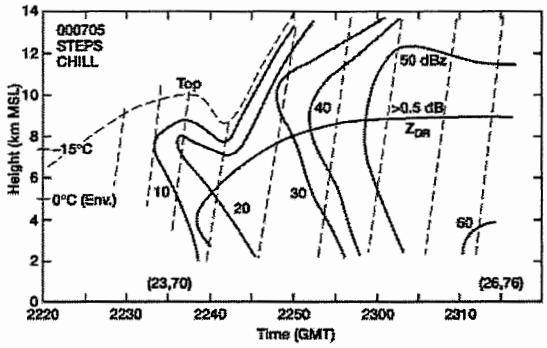

Fig. 3. The July 5 case, similar to Fig 2. As of June 29, this cell also formed to the West of a severe storm.

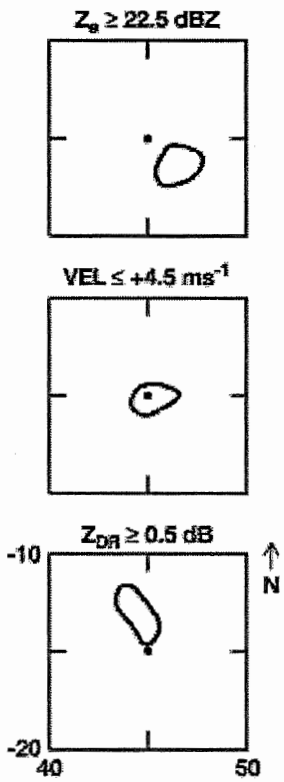

Fig. 4. Contours of Z_e, radial velocity, and Z_{DR} from the 5.4° elevation angle PPI, at 2358, from the case of Fig. 1, showing the opposite displacements of Z_e and Z_{DR} from the presumed updraft, indicated by the radial velocity contour. Elevation at the center of the panels is about 5.6 km MSL, environmental temperature about –7°C.

cell's lifetime, of the positive Z_{DR} corresponding very closely with the presumptive updraft, the area where the radial velocity matches that from a lower level.

Note that presenting the Z_{DR} and maximum Z_e data on a single time-height diagram can be deceptive if taken to imply that the two coincide within the cloud. Except for below the freezing level this is never the case. The Z_{DR} coincides with lower (often much lower) Z_e than that at which it appears in the diagram. Note also that the maximum height of positive Z_{DR} in Figs. 1-3 represents the lower limit of the height to which the water drops responsible for it may extend. Especially at the time of the first echo, Z_e from Bragg scattering increases upward and could mask the Z_{DR} at higher levels.

The most noteworthy feature of the data is that the first significant, positive Z_{DR} appears to precede the first conventional precipitation echoes by a few minutes in Figs. 1 and 2. ("Conventional" is added to distinguish this from the positive Z_{DR} column itself, which also is a precipitation echo).

3. DISCUSSION

In all of these cases the convection formed initially in association with a radar "thin line", a surface convergence causing an unusual concentration of insects near the surface that is highly visible on radar (Wilson et al., 1994), with Z_e values commonly up to 15dBZ, high values of LDR, and Z_{DR} values > 4.5dB. These are common features on the High Plains, often not associated with clouds at all, but also often indicating favored places for convective initiation (Wilson and Schreiber, 1986). No indication of the above radar signature of insects (very high LDR and Z_{DR}) being advected upward into the clouds is seen in the early echo stage, though the radar data allow for more possibility of this later on, when the clouds (storms) are mature.

The two main issues here for cloud physics are the microphysical origin of the very early raindrops, and their significance, if any, for the cloud's behavior *vis a vis* glaciation or precipitation production. The answer to neither of these questions is known, but each is worth consideration.

3.1 Origin of the big drops

The possible origins are (1) primary coalescence, perhaps on ultra-giant nuclei and (2) growth of recycled drizzle, either melted ice or formed directly through coalescence. During most of the lifetimes of these clouds (all of the lifetime for the case in Fig. 3) the radar data fit well the recycling mechanism suggested in a similar case (though without data in the early echo stages) by Tuttle (1993) in which the sheared cloud precipitates downwind, but the updraft then overrides the precipitation and ingests some of it. In Figs. 1 and 2, and also in one case not shown here, the fact that the positive Z_{DR} slightly precedes the early, conventional precipitation echo adds some doubt to this interpretation, though it does not rule it out.

Kinematic evolution of the clouds is key to understanding the origin of the drops, and thanks to the insects and the Bragg scattering, there is quite good coverage of the radial velocity field well before precipitation is visible to the radar. Knight et al. (2002), speculating about the presence of large drops very early and very low in Florida cumulus, suggested that cloud models may not initiate the convection properly. The present data also raise this difficulty, since it takes a fairly long time for millimeter-sized drops to grow, by any origin. It seems that an early history that allows for a relatively long time in cloud with relatively weak updraft is probably needed.

In the cases here, each mature cell can be traced back into an area of weak convective cells with very little variation in radial velocity, but still with their tops above the freezing level. (There are no data before the start of the time-height diagrams because in each case the radar was scanning elsewhere.) Judging convective vigor simply by noting the magnitude of local variations of radial velocity within the cloud, it is particularly striking in these cases that the energetic convection initiates high above the ground: well above the echo tops of the radar thin lines, the insect accumulations. This is not surprising, since the level of free convection, where buoyancy first appears in a parcel forced upward by horizontal convergence, is also quite high: for the three cases of Figs. 1-3, the values of the LFC are, from selected nearby soundings, respectively about 4.1, 4.3, and 5.0 km MSL (4, 2.5, and –1.5°C), as compared to LCL values of 2.5, 3.6, and 4.5 km (15.5, 8, and 3°C). (There is a lot of uncertainty here in attaching these values to these storms, because of considerable local variability in surface conditions.) The convection within cloud can therefore have considerably weaker updrafts well before first echo than during the first-echo stage, and

according to Figs. 1-3, the times for hydrometeor growth above the freezing level are more than 20, 10, and 10 minutes; perhaps quite a lot more. One can conclude that there may well by ample time for these drops to originate by any of the origins suggested above. It would be desirable in further field studies to place a high priority on both earlier data and better time resolution, though these are contradictory desires in terms of the limitations of radar scanning.

3.2 Significance of the big drops

Do these big drops make a difference? In many cases, they very well might. In assisting glaciation of the clouds, they might act through drop shattering, which could be an important source of ice from the freezing of drops this large; or, frozen and growing by riming, they may initiate the Hallett-Mossop process. Their presence in the radar data may be an indicator of the presence of larger populations of drizzle-sized drops that themselves would not produce a Z_{DR} signature, but could be important in precipitation formation in the above ways. In three of the four cases observed in STEPS, the positive Z_{DR} column above the freezing level coincides with or precedes the otherwise conventional-looking first echo from ice, and this suggests the distinct possibility that these drops may be important in the early formation of precipitation. The exceptional case (Fig. 3) is also notable for probably having much the coldest cloud base temperature, therefore the lowest cloud liquid water content. (And note its much slower intensification rate of Z_e than the others. It was visually an LP storm {M. Weisman, personal communication}).

ACKNOWLEDGMENTS

Thanks to the S-Pol and CHILL radar crews and the operations people of STEPS, and thanks particularly to Bob Rilling and Jay Miller for help with the radar data.

REFERENCES

Caylor, I. J., and A. J. Illingworth, 1987: Radar observations and modeling of warm rain initiation. *Quart. J. Roy. Meteor. Soc.*, **113**, 1171-1191.

Illingworth, A. J., 1988: The formation of rain in convective clouds. *Nature*, **336**, 754-756.

Knight, C. A., J. Vivekanandan, and S. G. Lasher-Trapp, 2002: First radar echoes and the early ZDR history of Florida cumulus. *J. Atmos. Sci.*, **59**, 1454-1472.

Tuttle, J. D., 1993: Multiparameter radar observations of developing turrets in a High Plains storm. 26th Int. Conf. On Radar Meteor., Norman, OK. Am. Meteor. Soc., Boston, 516-518.

Wilson, J. W., and W. E. Schreiber, 1986: Initiation of convective storms at radar-observed boundary-layer convergence lines. *Mon. Wea. Rev.*, 114, 2516-2536.

Wilson, J. W., T. M. Weckwerth, J. Vivekanandan, R. M. Wakimoto, and R. W. Russell, 1994: Boundary layer clear-air radar echoes: Origin of echoes and accuracy of derived winds. *J. Atmos. Oceanic Tech.*, 11, 1184-1206.

On the role of large-scale turbulence in cloud microstructure formation

Yefim L. Kogan

Cooperative Institute for Mesoscale Meteorological Studies
University of Oklahoma, Norman, Oklahoma

1. INTRODUCTION[1]

Since the late 1940s, the ascending air parcel model has served as a basic, although quite idealized, dynamical representation of cloud microstructure formation. In this model the cloud drop spectra depend on local parameters, such as supersaturation, updraft, CCN spectra, collision efficiencies, etc. It was, however, well recognized that the latter may be significantly affected by turbulence. Numerous studies explored the effects of fine-scale turbulence fluctuations on variations in local parameters. These included the effects of inhomogeneous mixing of saturated and dry volumes on supersaturation and drop concentration leading to drop spectral broadening (Baker et al 1980, Telford and Chai 1980, Korolev and Isaac 2000, among others). Turbulence can also lead to drop concentration fluctuations resulting in drop condensation and collision rates fluctuations (Shaw et al 1998 and Sundaram and Collins 1997). Pinsky et al (1999) showed that increases in relative velocity between droplets caused by fluid accelerations lead to increased collision rates due to enhanced collision efficiencies.

The large-scale turbulent eddies[2] in addition to their effect on the local parameters in an air parcel, may also alter the history of the air parcel itself. Kogan (1993) showed high sensitivity of the air parcel trajectory to small variations in parcel's position. It was also shown that different air parcel constituents may have different trajectories (e.g. drops of different sizes due to differences in their fall velocities). As a result the notion of an air parcel as an entity containing various constituents (water vapor, CCN particles, cloud drops, etc) - all evolving under the same dynamical conditions - may be rather limited. In general, not only air, water vapor, and particles' trajectories will diverge, but also in a turbulent medium the shape of an air parcel may be significantly distorted by inhomogeneous fluid accelerations. No less significant is the turbulent mixing between adjacent parcels. As this paper demonstrates, their time and spatial histories differ quite dramatically.

2. MODEL

The study is based on the CIMMS LES explicit (size-resolving) microphysical model. The detailed description and verification against observations can be found in Khairoutdinov and Kogan (1999). The current experiment was initialized with data obtained ASTEX flight A209 on 12-13 June 1992. The integration domain extends 3.0 km in the two horizontal directions and 1.25 in the vertical direction, with 40×40×51 grid points uniformly spaced 75 m in the horizontal and 25 m in the vertical. Under the specified conditions, the simulated cloud layer was about 300-350 m thick with cloud base at about 400 m. Horizontally averaged drizzle rates during the 3 hours simulation varied in the 0.2-0.6 mm/day range.

To explore the effect of an air parcel (AP) history and mixing between parcels on cloud microstructure, we analyze the trajectory ensemble of 40×40×28=44800 APs that were initialized at one hour into simulation at each grid point in the region below the cloud top height and tracked forward every 5 time steps (20 sec) for two hours.

All APs which at hour 3 into simulation were inside the cloud were binned into 6 vertical 50-m thick layers. Each vertical layer was further divided into 13×13=169 "air volumes" (AV). An individual AV (225×225×50 m^3) was comprised of 3×3 grid points in horizontal and 2 grid points in the vertical. The number of trajectories that end up in a particular AV depends on flow characteristics and may vary quite significantly. For each analyzed parameter in an AV we consider its *mean* and *standard deviation* (*std*) value *averaged over all parcels that at the destination time (3 hours into simulation) end up in this AV.*

---

[1] Corresponding author address: Yefim Kogan, CIMMS, University of Oklahoma, 100 E. Boyd, Room 1110, Norman, OK 73019. Email: ykogan@ou.edu

[2] Large-scale refers here to resolvable turbulent eddies, i.e., larger than 2Δx (~100m).

3. RESULTS

3.1. Cloud residence time

We start with the analysis of air parcels' cloud residence time (RT)[3]. Fig. 1 shows box-chart of the *mean* residence time for all AVs at six cloud layers[4]. The *mean* RT in an AV varies significantly at each vertical level and continuously increases with height except for the layer near cloud top where RT decreases due to entrainment of fresh air or detrainment of old parcels. In the latter case, according to our definition of RT, the RT will be reset to zero.

The solid and dashed lines in Fig. 1 display residence time of a lagrangian air parcel (LAP) ascending from cloud base with velocity at cloud base equal to 0.5 m/s and 1 m/s, respectively[5]. Fig.1 shows that at all levels the mean RT is several times larger than the time of the LAP's direct ascent. Clearly all these APs have already been recycled in the cloud.

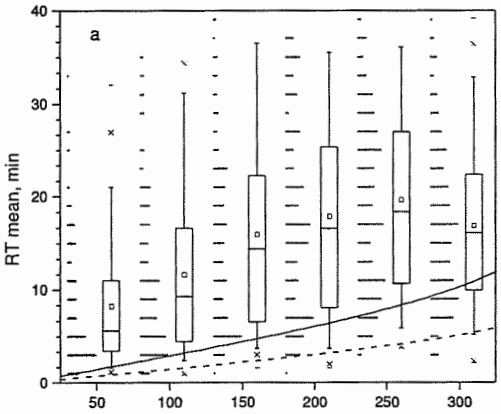

Fig. 1. Residence times of air parcels at six cloud levels.

The *std* of RT in each AVs (not shown) is of the same magnitude as the *mean* RT, indicating that the RT of individual air parcels varies in even wider range. The results for all air parcels are shown in Fig. 2 in the form of a scatter plot between the air parcel's RT and W: a) for the whole 300-m thick cloud layer and b) for the 100-m layer at cloud base. Throughout the cloud the APs with strong updrafts have small residence times, e.g. updrafts larger than 0.5 m/s have residence times less than 10 min, while updrafts larger than 1 m/s have residence times less than 5 min. In the 100-m layer near cloud base (Fig. 2b) the strong updrafts have even smaller RT. On the other hand, APs with velocities smaller than 0.5 m/s have a much wider range of RT, indicating that all these APs have been *repeatedly recycled in the cloud.* As Fig. 3 shows these APs dominate in cloud: recycled parcels account for about 85% of all APs in the whole cloud and 80% in the 100-m lower layer near cloud base.

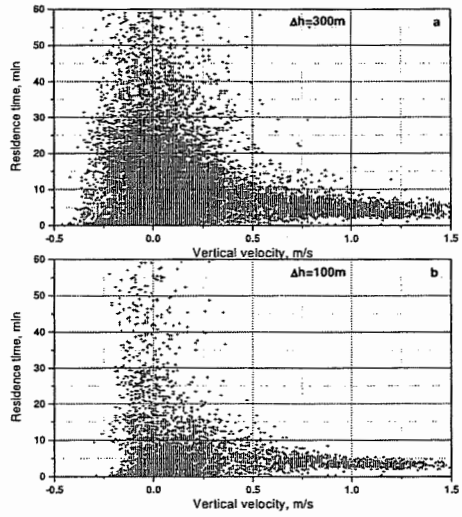

Fig. 2. Scattergram of air parcels' residence time vs vertical velocity at destination point.

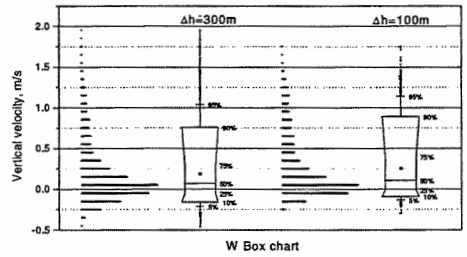

Fig. 3. Box chart of vertical velocity in the whole cloud layer and the 100-m layer near cloud base.

3.2. Spatial intermittency of residence time

[3] We considered an AP to be inside the cloud starting from the *last* time its supersaturation crossed and remained larger than the -0.1% threshold.
[4] Box range is 25-75%, whisker range is 5-95%.
[5] Our crude estimation assumes the harmonic oscillator solution for the lagrangian air parcel equation of motion.

Fig. 4 shows an example of spatial distribution of the *mean* RT and its *std* at four 50-m thick vertical layers. Remember that the *mean* RT values are calculated by averaging of up to several dozens APs that end up in a specific AV and that a 50-m thick vertical layer consists of 13×13=169 AVs each comprised of 3×3 grid points in horizontal and 2 grid points in the vertical (volume of 225×225×50 m^3). In Fig. 4 we line up all 169 AVs in a one-dimensional array and depict RT as a function of the AV number. In a sense, the plot mimics the 2 Hz (200m) data collected by an airplane flying through the cloud at a speed of 100 m/s. One can see that the scatter of RTs inside each individual AV is quite significant; in most cases the *std* is comparable to the *mean* value of RT. One can also note the substantial spatial variability of RT and evidence of clustering.

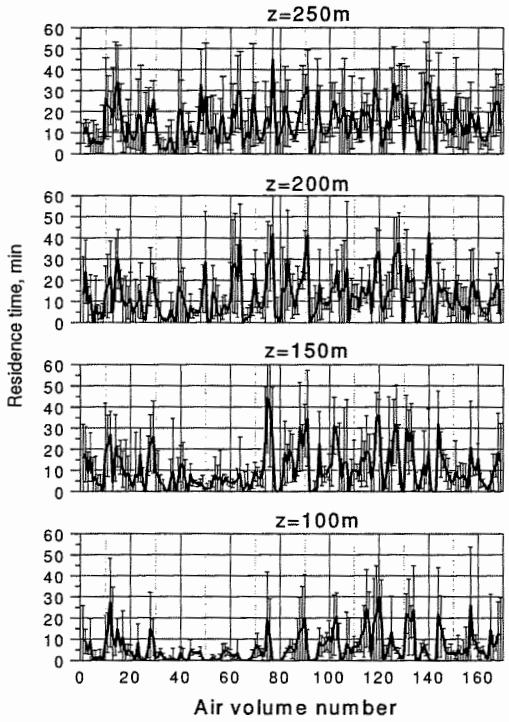

Fig. 4. Mean and *std* RT as a function of AV number.

3.3. Mixing of air parcels in a fixed air volume

Fig. 4 demonstrated significant variability of *mean* RTs on scales larger than the AV size (225m). Large values of RT's *std* point to a significant variability of AP's RT inside each individual AV. The nature of this variability is revealed in Fig. 5 that shows examples of trajectories that end up in four selected AVs at z=200m above cloud base.

The bottom panel shows an AV where majority of APs came directly from the surface layer in updrafts of different intensities. These APs have small (3-12 min) cloud RT (the cloud base is approximately at z~0.4 km). On the other hand, five APs in this AV have been repeatedly moving up and down in the cloud and have RTs exceeding 60-80 min.

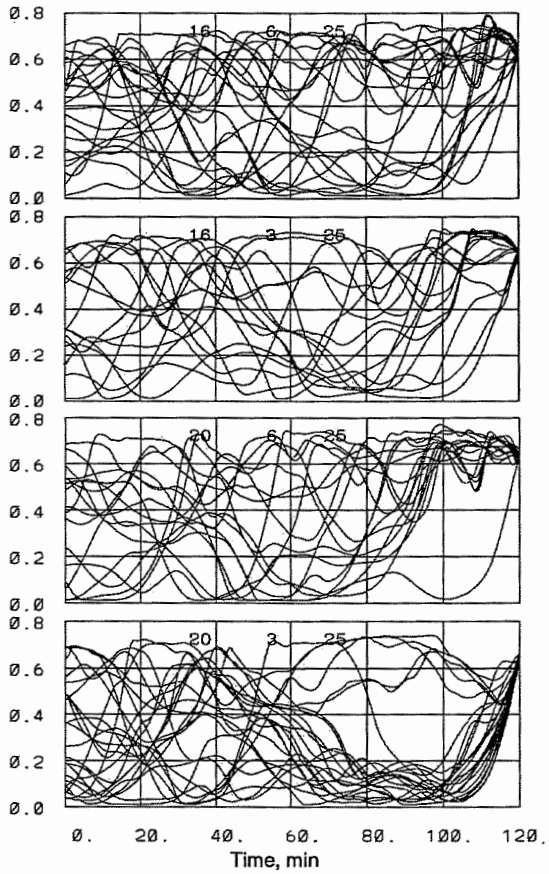

Fig. 5. Time evolution of air parcels' vertical coordinate (z, km) in four selected air volumes. The numbers in each panel are grid coordinates of the lower left corner of the AV's 3x3x2 grid box.

The second from the bottom panel shows an example of an AV where majority of APs resided in the cloud for a long time and only one AP direct ascended from the surface. The middle and top panels show examples of various degree of mixture of AP with RTs varying in a wide range.

4. DISCUSSION AND CONCLUSIONS.

1. The paper presents statistics of cloud residence times from LES simulation of an ASTEX case. The results show that residence times are significantly larger than the cloud eddy turnover time, t_c, defined as L/w^* (L cloud depth, w*- convective scaling velocity). In our case t_c is about 9 min. For all cloud levels about 70% of air parcels reside in clouds for more than one cloud eddy turnover time, about 50% have been cycling in the cloud for 2-5 times. The residence time will obviously depend on parameters of boundary layer which affect the size and distribution of turbulent eddies. Among them is the presence of drizzle which is one of the key factors in transition from a well mixed to a decoupled BL (Stevens et al 1998).

2. The results demonstrate significant inhomogeneity of AP's residence time; as a result old and new air parcels frequently coexist in close proximity on a variety of scales, both larger and smaller than the size of an AV defined in this study (~200m). Such inhomogeneity in cloud and rain parameters is a consistent feature of observations.

3. The implications of recycling for cloud microstructure formation are obvious and quite significant. The older parcels contain larger droplets and previously processed CCNs. Non-adiabatic mixing between old and new parcels will provide new embryos for coagulation and accelerate drizzle formation. In the framework of parcel mixing, the drop spectral broadening may be the result of mixing of parcels with different histories, i.e., representing drop size distributions at different stages of their evolution. In this sense we distinguish between fine-scale turbulence that affects local parameters in an air parcel and large-scale turbulence that affects air parcel history.

4. Given the large diversity of air parcels histories, one may ask how AP's history affects its microphysical parameters, such as, e.g., droplet and drizzle concentration, mean radius, etc. In other words, which of the parameters are essentially, non-local and which are defined mostly by the local conditions. Our analysis shows that the drizzle concentration and drizzle liquid water content are much more sensitive to AP's history, while the concentration, mean radius and liquid water content of cloud droplets ($r<25\mu$) are mostly local parameters. The non-local nature of drizzle parameters may be due to a larger phase relaxation time ($\tau_r \sim 1/NR$) of drizzle drops compared to smaller cloud drops[6].

5. Our LES results suggest that recycling is prevalent in stratocumulus-topped boundary layer clouds. We may expect that recycling may also be important in cumulus clouds where cloud scale turbulent eddies are essential part of cloud dynamics and microphysics. Clearly more studies of well-mixed and decoupled BL stratocumulus clouds, as well as cumulus type convective clouds are necessary to fully understand the role of recycling.

Acknowledgement. This research was supported by the ONR Grants N00014-96-1-0687 and N00014-03-1-0304 and the Environmental Sciences Division of the U. S. Department of Energy (through Battelle PNR Contract 144880-A-Q1 to the Cooperative Institute for Mesoscale Meteorological Studies) as part of the Atmospheric Radiation Measurement Program.

REFERENCES

Baker, M. B., R. G. Corbin, and J. Latham, 1980: The influence of entrainment on the evolution of cloud droplet spectra: I. A model of inhomogeneuous mixing. *Quart. J. Roy. Meteor. Soc.*, **106**, 581-598.

Telford, J. W., T. S. Keck and S. K. Chai, 1984: Entrainment at cloud tops and the droplet spectra. *J. Atmos. Sci.*, **41**, 3170-3179.

Kogan, Y. L., 1993: Drop size separation in numerically simulated convective clouds and its effect on warm rain microphysics. J. Atmos. Sci., **50**, 1160-1189.

Korolev, A. V., and I. P. Mazin, 2003: Supersaturation of Water Vapor in Clouds, JAS, 60, 2957–2974.

Korolev, A. V., and G. A. Isaac, 2000: Drop growth due to high supersaturation caused by isobaric mixing. *J. Atmos. Sci.*, **57**, 1238-1252.

Pinsky, M. B., and A. P. Khain, 1997: Turbulence effects on the collision kernel. I: Formation of velocity deviations of drops falling within a turbulent three-dimensional flow. *Quar. J. Roy. Meteor. Soc.*, **123**, 1517-1542.

Shaw, R. A., W. C. Reade, L. R. Collins, and J. Verlinde, 1998: Preferential concentration of cloud droplets by turbulence: Effects on the early evolution of cumulus cloud droplet spectra. *J. Atmos. Sci.*, **55**, 1965-1976.

Stevens, Bjorn, W. R. Cotton, G. Feingold and C.-H. Moeng, 1998: Large-Eddy Simulations of Strongly Precipitating, Shallow Stratocumulus-Topped Boundary Layers *J. Atmos. Sci.*, **55**, 3616-3638.

Sundaram, S., and L. R. Collins, 1997: Collision statistics in an istoropic particle-laden turbulent suspension. Part 1. Direct numerical simulation. *J. Fluid Mech.*, **335**, 75-109.

[6] See Korolev and Mazin (2003) for a comprehensive description of the phase relaxation issue.

MODEL SIMULATIONS ON THE FORMATION OF UNACTIVATED FOGS

H. Kokkola S. Romakkaniemi and A. Laaksonen

Department of Applied Physics, University of Kuopio, P.O.Box 1627, FIN-70211 Finland

1. INTRODUCTION

In Po Valley, Italy, the fog frequency is 30% during the fall-winter season. Po Valley is surrounded by three high mountain ranges, so the geography of the area is favourable for temperature inversion which enhances fog formation.

Po Valley is also a highly polluted area and high concentrations of gaseous nitric acid and ammonia have been measured during out-of-fog periods. During in-fog periods, ammonia and especially nitric acid is depleted from the gas phase.

A study by Frank et al. (1998) indicated that Po Valley fogs are mostly unactivated. In the study, it was shown that low cooling rate and high mass load of particles can lead to formation of unactivated fogs.

Below, we point out indicates that the condensation of nitric acid increases the hygroscopic mass of particles and in some conditions can lead to formation of unactivated fogs.

2. SIMULATIONS

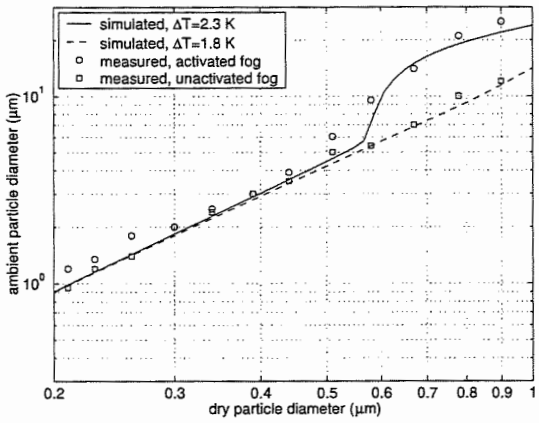

Figure 1. Wet diameter against dry diameter for two simulations (solid and dashed line) and two measurements (squares and circles).

Simulations were made using a moving sectional model that describes condensational growth of an aerosol population (Kokkola 2003).

Corresponding author's address: Harri Kokkola, Department of Applied Physics, University of Kuopio, P.O.Box 1627, FIN-70211 Kuopio, Finland; EMail: harri.kokkola@uku.fi.

TABLE 1. Calculated maximum and final supersaturations, for two simulated activated and unactivated fogs

Fog type	S_{max}(%)	S_{min}(%)
activated fog	0.047	0.0079
unactivated fog	0.019	0.0059

Aerosol composition used in the simulations was taken from measurements by Matta et al (2003).

The squares in Fig. 1 represent a typical fog droplet size distribution for Po Valley fogs. The size distribution is continuous and shows no sign of activation. The circles represent a more rarely observed size distribution in fog. In this case, the increased growth of the largest droplets indicates that the droplets larger than 0.5 μm are activated.

Table 1 shows the maximum and final supersaturation for two simulations which reproduce formation of an activated and unactivated fog.

In both cases, the air remains supersaturated. But in the second case, the supersaturation is so low that the particles that are activated are so large that diffusion is not sufficiently fast to enhance their growth.

3. RESULTS

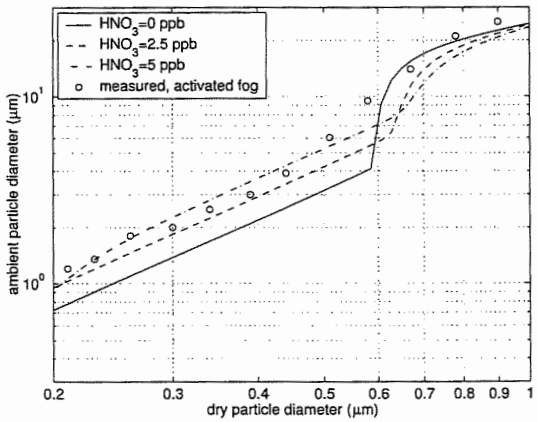

Figure 2. Wet diameter against dry diameter for three different simulations with different initial concentration of nitric acid.

To test the effect of semi-volatile species on the activation of fog droplets, simulations were made for 0—5 ppb initial volume mixing ratio of nitric acid.

TABLE 2. Initial volume mixing ratio (VMR) of nitric acid, the dry mass load of the particle population at 90 % relative humidity and the maximum supersaturation reached during the simulation

VMR_{HNO3}	mass load	S_{max}
0.0 ppb	52.0 μg m^{-3}	0.059 %
2.5 ppb	60.7 μg m^{-3}	0.044 %
5.0 ppb	69.8 μg m^{-3}	0.035 %

The initial volume mixing ratio of ammonia was 5 ppb in all the simulations. Fig. 2 shows the final size distribution for three different simulations.

From Fig. 2 it can be seen that increase of gaseous nitric acid decreases the growth of the largest droplets compared to the smallest droplets. Table 2 illustrates how the condensed nitric acid increases the hygroscopic mass of the droplets and thus decreases the maximum supersaturation.

3. CONCLUSIONS

In polluted conditions, the condensation of semi-volatile species under fog formation can increase the hygroscopic mass of fog droplets significantly. The high concentration of ammonia neutralizes the droplets and concurrently enhances the partitioning of gaseous nitric acid into the particle phase. Furthermore, the increased hygroscopic mass can lead to the formation of an unactivated fog.

4. REFERENCES

Kokkola, H., 2003: Model studies on the evolution of fogs and clouds in the presence of semi-volatile gases, Report Series in Aerosol Science, no 61. PhD thesis

Matta, E., 2003: Mass closure on the chemical species in size-segregated atmospheric aerosol collected in an urban area of the Po Valley, Italy. Atmos. Chem. Phys., **3**, 623-637.

Frank G., 1998: Droplet formation and growth in polluted fogs. Contr. Atmos. Phys., **71**, 65-85.

DRIZZLE VARIABILITY IN MARINE STRATUS DURING EPIC 2001

Pavlos Kollias[1], C. W. Fairall[2] and B. A. Albrecht[3]

(1) NOAA/CIRES, University of Colorado

(2) NOAA, Environmental Technology Laboratory

(3) RSMAS/MPO, University of Miami

1. INTRODUCTION

The SE Pacific stratocumulus region extends from near the Equator to central Chile (25-30 S) to about 1500 km off the South American continent nearly year-round (Klein and Hartmann, 1993). Stratocumulus clouds form over oceans with relatively cold sea surface temperatures (SSTs) and beneath a strong temperature and moisture inversion that caps the MBL (e.g., Albrecht et al., 1988). They strongly influence global climate because their high albedo (compared with the ocean background) gives rise to large deficits in absorbed solar radiative flux at the top of the atmosphere, while their low altitude prevents significant compensation in thermal emission (Randall *et al.* 1984). Coupled model studies show that the radiative effects of MBL clouds are essential in producing the observed equatorial cold tongue sea surface temperature structure (e.g., Philander et al. 1996). The SE Pacific stratocumulus regime deserves focused attention, due to not only its size, but to its strong, documented feedbacks with ENSO, its large north-south extent encompassing gradients in both microphysical and dynamical conditions, and a variety of interesting and potentially important feedbacks with the S. American continent on many time scales.

2. EPIC 2001

Here, observations of marine stratocumulus in the SE Pacific during the East Pacific Investigation of Climate (EPIC) research cruise (Bretherton et al., 2004) supported by NSF and NOAA are presented. The observations were conducted on October 2001, during the climatological peak of stratus cloud amount (Klein and Hartmann, 1993). The sea-going NOAA/ETL remote sensing suite included 8.6 mm cloud radar (MMCR), a ceilometer, and a two-channel (20.6 and 31.6 GHz) microwave radiometer (MWR). The ceilometer determines the height of cloud bases with a temporal resolution of 30 sec and vertical resolution of 30 m. The MMCR measures the moments of the Doppler spectrum, the cloud reflectivity, the mean Doppler velocity and the Doppler spectrum width. The MWR measures the atmospheric column integrated liquid and vapor. Soundings launched every six hours, surface meteorology, turbulence and radiative flux measurements, and Particle Measurement System (PMS) aerosol spectrometer measurements provided a near surface complemented the NOAA/ETL remote sensing suite.

Corresponding author address: Pavlos Kollias, University of Miami, Meteorology and Physical Oceanography, 4600 Rickenbacker Cswy, Miami FL,33149,email:pkollias@rsmas.miami.edu

The stratocumulus cruise took place during the second phase of the EPIC 2001 field experiment. The NOAA research vessel Ronald Brown (hereafter Brown) departed from the Galapagos Islands on October 9. After a short westerly route, the Brown cruised south following the 95 W and followed by southeasterly route to the WHOI buoy at 20 S 85 W(Fig. 1) where it remained for 6 days (16-22 October).

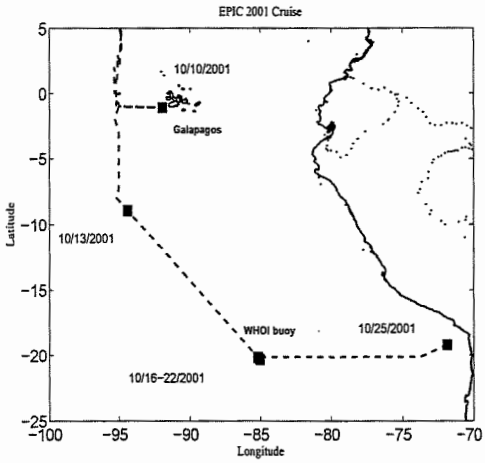

Fig. 1 The Brown cruise track during the EPIC stratus leg. The position of the Brown every three days is shown. The Brown stationed at the WHOI buoy location for six days (16-22 October).

Throughout the cruise, the MBL is capped by a strong inversion (inversion thickness 60-150 m, $\Delta\Theta$ ~ 8-15 K, Δr ~ 4-7 gkg^{-1}). The vertical gradients of the potential temperature and mixing ratio within the MBL were very small (well mixed MBL) and no cumulus clouds were observed.

The stratocumulus deck was persistent throughout the cruise (typical cloud thickness ~300 m, LWP ~ 0.1-.2 mm), with evidence of mesoscale organization of drizzle clusters. Fig. 2

shows the stratus cloud boundaries as observed by the vertically pointing active sensors. The ceilometer is immune (in most occasions) to the presence of drizzle below the cloud base and thus detects the "true" cloud base, while the MMCR often observed drizzle below the cloud base throughout the cruise.

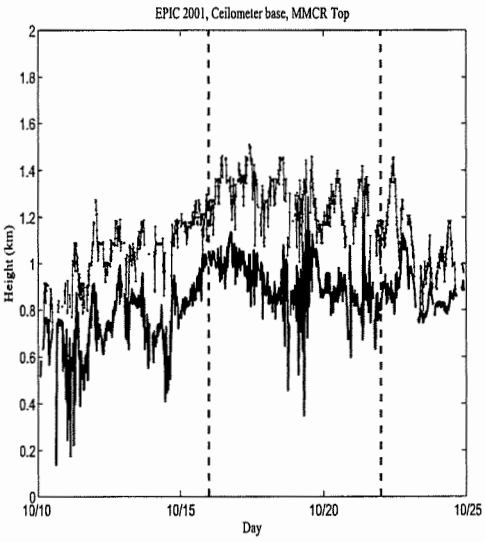

Fig. 2 Stratocumulus cloud boundaries during the EPIC cruise. The cloud top is retrieved by the MMCR cloud reflectivity and the cloud base by the ceilometer. The dashed lines indicate the time the Brown was stationed at the WHOI buoy.

The cloud top at the WHOI buoy location had a strong diurnal cycle, while the cloud base variability was small. The cloud layer was thin during the local afternoon and thick and often drizzling during the nighttime period. Gravity waves forced by the diurnal cycle of heating over S. America may be responsible for a strong diurnal cycle of subsidence. Near the coast of Chile, the clouds were thinner and no drizzle was observed. Along the north-south track, the drizzle frequency increases and reaches a maximum at the buoy location.

3. DIURNAL VARIABILITY

The mean diurnal cycle of stratocumulus bulk properties at the buoy location is shown in Fig. 3; the clouds are physically thinner, with much less liquid water, and some clearing in the early afternoon. Retrievals of solar cloud optical thickness (Fig. 5) show a similar rapid decrease associated with decreasing cloud water. These are unexpectedly strong diurnal variations for the open ocean.

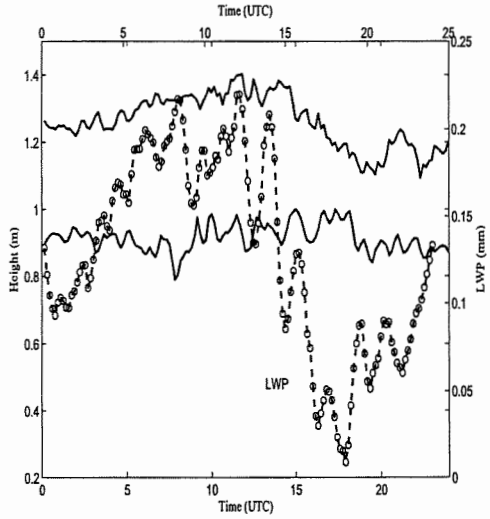

Fig. 3 Diurnal cycle of cloud boundaries and LWP at the WHOI buoy location. Local noon is at 18 UTC.

Using the MMCR cloud reflectivity (30 m vertical and 10 sec temporal resolution) the radar observations were classified into drizzling and non-drizzling periods using a radar reflectivity threshold of -14 dBZ. The mean diurnal cycle of the stratocumulus fractional coverage along with the fractional coverage of drizzling periods is shown in Fig. 4.

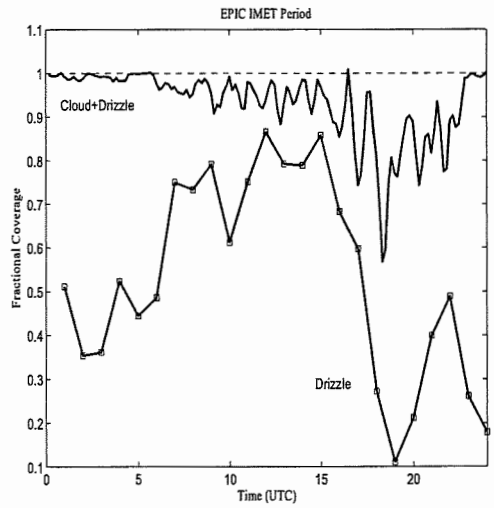

Fig. 4 Diurnal cycle of stratocumulus fractional coverage and drizzle fractional coverage

A maximum in the occurrence of drizzle was observed in the early morning and the minimum was observed at local noon. The radar detected drizzle at different levels below the cloud base and often to the sea surface. The MMCR Doppler

velocity measurements were contaminated by the ship motion and close to the radar (below 500 m altitude) the radar receiver often saturated (dBZ>15) from the strong drizzle returns. Thus, a quantitative retrieval of drizzle microphysical parameters is difficult. However, the measured reflectivities (typical drizzle reflectivity values between 0 and10 dBZ), and averaged Doppler velocities around 1-2 ms^{-1} indicate the presence of strong drizzle rates below a stratus deck with typical cloud thickness of 300 m. Using hourly records of mean Doppler velocity at different levels with the cloud we attempted to investigate the relationship between drizzle and turbulence levels especially near the cloud top. The upper part of the cloud was characterized by low reflectivity values (dBZ<-20) during both drizzling and non-drizzling periods. The analysis revealed no significant change of the turbulence levels as measured by the variance of the MMCR Doppler velocity during drizzle and non-drizzle and nighttime and daytime period in contrast to ground-based observations (e.g. Kollias and Albrecht, 1999).. However, the under sampling of the low frequency ship motions and their strong magnitude could have inhibited the detection of changes in the in-cloud turbulence.

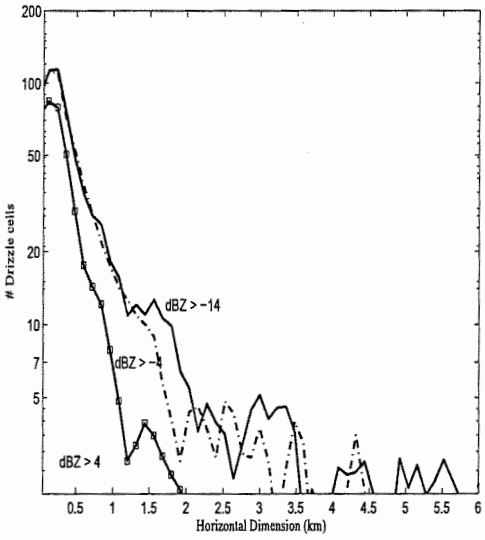

Fig. 5 Distribution of drizzle cell horizontal extent for three reflectivity threshold values [-14, -4, 4] dBZ.

A noticeable feature of drizzling stratus is the patchiness and clustering of drizzle cells. While mesoscale organization (15-40 km) was observed by the scanning C-band radar on board the Brown; smaller scale variability within these mesoscale structures was observed. Using the 6-day long records of maximum observed reflectivity from the MMCR (10 sec temporal resolution) and the horizontal wind measurements at cloud level from the soundings (8 per day), we investigate the horizontal extent of drizzle cells defined as contiguous records of max observed reflectivity above a certain threshold value. Fig. 5 shows the distribution of the horizontal scales of drizzle cells and Fig. 6 shows the distribution of horizontal spacing between such contiguous drizzle clusters of drizzle

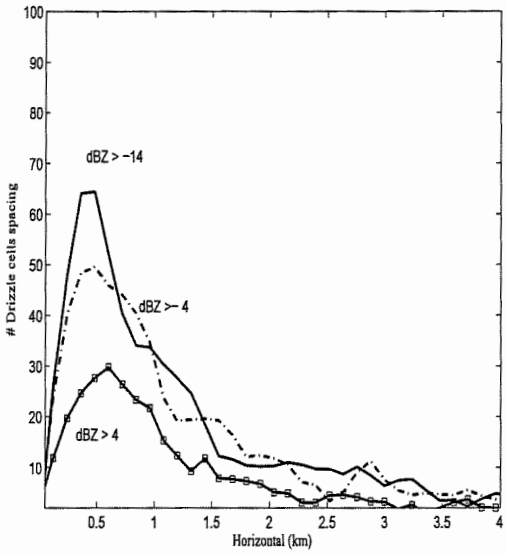

Fig. 6 Distribution of drizzle cell horizontal extent for three reflectivity threshold values [-14, -4, 4] dBZ.

As expected, the lower the reflectivity threshold used for the definition of a drizzle area, the larger the horizontal extent of these areas reaching up to 4 km. For higher reflectivity values the distribution becomes narrow with no contiguous drizzle cell with reflectivity higher than 4 dBZ exceeding 2 km in horizontal extend. Similarly the spacing of such cells increases for higher reflectivity values.

4. DISCUSSION

The EPIC cruise provided an unprecedented data set of marine stratocumulus clouds. The MBL is well mixed, resulting in small LCL variability, and the MBL is capped by a strong capping inversion. Episodes of higher relative humidity subsiding from aloft to the top of the boundary layer and associated with periods of higher humidity during drizzling periods. Stratus clouds with cloud thickness greater than 250 m had drizzle below the cloud base. A strong diurnal cycle in cloud thickness, cloud top height and LWP of marine stratocumulus was documented at the WHOI buoy location. During the night, strong drizzling conditions were observed.

Recently (November 2003), a similar dataset was collected in the SE Pacific during a research cruise part of the NOAA CLIVAR Pan American Climate Studies (PACS) program. During the PACS 2003 cruise, moderate vertical gradients of potential temperature and mixing ratio that overlap with periods of small cloud fractional coverage, decoupled layers and shallow cumuli clouds were observed. Furthermore, during PACS 2003 the LCL varies substantially with time in conjunction with MBL variability. Large periods of clear skies were observed at the WHOI buoy location, especially during the solar flux maximum. The stratus observed at the buoy location during PACS revealed a different picture from the one captured during EPIC. This reflects the complexity of the coupled atmospheric-ocean system and highlights the need for future systematic observations of stratus clouds in the region.

5. ACKNOWLEDGMENTS

The EPIC 2001 stratocumulus cruise was a great success. We would like to acknowledge the efforts of the scientists, staff and students involved in the project and especially the Cloud, Radiation and Surface Processes Division of the NOAA Environmental Technology Laboratory.

6. REFERENCES

Albrecht B. A., D. A. Randall and S. Nicholls, 1988. Observations of marine stratocumulus during FIRE. *Bull. Amer. Meteor. Soc.*, **69**, 618-626

Albrecht B. A., C.S. Bretherton, D. Johnson, W.H. Schubert and A.S. Frisch, 1995: The Atlantic stratocumulus transition experiment – ASTEX. *Bull. Amer. Soc.*, **76,** 889-903.

Bretherton C. S., et al., 2004: The EPIC 2001 Stratocumulus Study. Accepted in *Bull. Amer. Meteor. Soc.*

Klein, S. A., and D. L. Hartmann, 1993: The seasonal cycle of low stratiform clouds. *J. Climate*, **6**, 1587-1606.

Kollias, P. and B.A, Albrecht, 2000: The turbulence structure in a continental stratocumulus cloud from millimeter wavelength radar observations. *J. Atmos. Sci.* **57**, 2417-2434

Philander, S. G. H., D. Gu, D. Halpern, G. Lambert, N.- C. Lau, T. Li, and R. C. Pacanowski 1996: Why the ITCZ is mostly north of the equator. *J. Clim.*, **9**, 2958-2972.

Randall, D. A., J. A. Coakley, C. W. Fairall, R. A. Kropfli, and D. H. Lenschow, 1984: Outlook for research on subtropical marine stratiform clouds. *Bull. Amer. Meteor. Soc.*, **64**, 1290-1301.

Tiedke, M., W. A. Hackky, and J. Slingo, 1989. Tropical forcasting at ECMWF: The influence of physical parameterizations on the mean structure of the forecasts and analyses. *Quart. J. Roy. Meteor. Soc.*, **115**, 639-664.

PARTICLE IMAGE VELOCIMETRY OF CLOUD DROPLETS IN THE PROCESS OF TURBULENT MIXING

Piotr M. Korczyk[1], Szymon P. Malinowski[2], Tomasz A. Kowalewski[1]

[1]Institute of Fundamental Technological Research, Polish Academy of Sciences, Warszawa, Poland
[2]Warsaw University, Institute of Geophysics, Warszawa, Poland

1. INTRODUCTION

Interaction between small-scale turbulence and cloud particles is a key issue in warm rain formation mechanism, which is an important meteorological and climatological challenge (Vailliancourt and Yau 2000, Shaw 2003). We investigate this interaction observing motion of cloud droplets in a glass walled chamber 1m deep, 1m wide and 1.8m high described in Malinowski et al, 1998. The second smaller chamber, placed above the main one is filled with water droplets of diameters in range from 7 to 25 micrometers. Cloudy air containing water droplets enters the main chamber forming the negatively buoyant, turbulent plume, mixing with

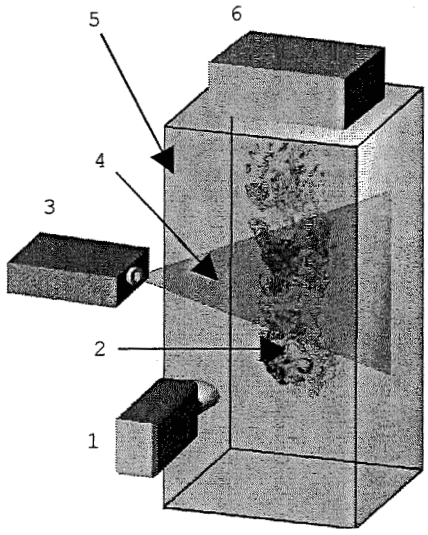

Fig 1. The experimental setup: 1) CCD camera 2) cloud during mixing, 3) impulse laser, 4) laser sheet, 5) cloud chamber, 6) small chamber with the droplet generator inside.

unsaturated air in the main chamber and producing additional turbulence by evaporative cooling of droplets. The plume is illuminated with a 1.2mm wide sheet of laser light (Nd:YAG, λ=532nm), forming the vertical cross-section through the central part of the chamber.

Corresponding author address:
Piotr Korczyk, IPPT PAN, Department of Mechanics & Physics of Fluids, PL 00-049 Warszawa, Poland;
e-mail: piotr.korczyk@ippt.gov.pl

Images, formed due to Mie scattering of laser light on cloud droplets are recorded with a high-resolution (1280x1024) CCD camera placed in front of the chamber, with the optical axis perpendicular to the light sheet. Images are recorded in pairs. From the shift of patterns recorded in consecutive images, knowing the time interval between exposures, it is possible to retrieve information on droplets' velocities. This technique is known as Particle Image Velocimetry (PIV) and is widely used in laboratory fluid dynamics. Typical PIV applications obey stationary or slowly changing flows (e.g. flow around the wing), where turbulence is relatively weak compared to the mean velocity. In the investigated case the flow is highly turbulent and application of standard PIV algorithms results in a large amount of errors and artefacts in the retrieved velocity field. Therefore a special multi-scale algorithm, which can handle chaotic flow field was developed for the purpose of this sudy. In the following section details of this algorithm are described. A short summary of experimental results and planned future development of the technique form the final part of this extended abstract. More details about observed properties of small-scele turbulence in clouds can be found in Malinowski et al. (2004).

2. MULTI-SCALE PIV PROCESSING

In order to evaluate displacement of a droplet pattern at position (x,y) a square sample from the first

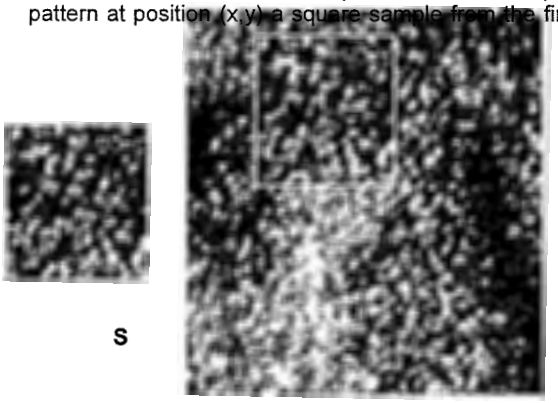

Fig 2. An example sample S (40×40 pixels) from the first exposure and the interrogation area A (100×100 pixels) from the second exposure from the pair of the images. The most similar part is highlighted.

exposure centered at this position is taken. Then we search the most similar sample in the second exposure within the interrogation area, also a square centered at (x,y). The size of the interrogation area depends on the expected greatest displacement and on the size of the sample. Images are matrices and each pixel is treated as an element of matrix: an integer corresponding to the grey level (brightness) of this pixel. For a sample **S** of size MxM and for an interrogation area **A** of size LxL the evaluation function used to process recordings is defined by the following formula:

$$\phi(m,n)=\sum_{i=1}^{M}\sum_{j=1}^{M}[\mathbf{S}(i,j)-\langle\mathbf{S}\rangle][\mathbf{A}(i+m,j+n)-\langle\mathbf{A}\rangle]$$

Here:

$$\langle\mathbf{S}\rangle=\frac{1}{M^2}\sum_{i=1}^{M}\sum_{j=1}^{M}\mathbf{S}(i,j)\ ,$$

$$\langle\mathbf{A}\rangle=\frac{1}{M^2}\sum_{i=1}^{M}\sum_{j=1}^{M}\mathbf{A}(i+m,j+n)\ .$$

For

$m\in[0,L-M]\quad n\in[0,L-M]$.

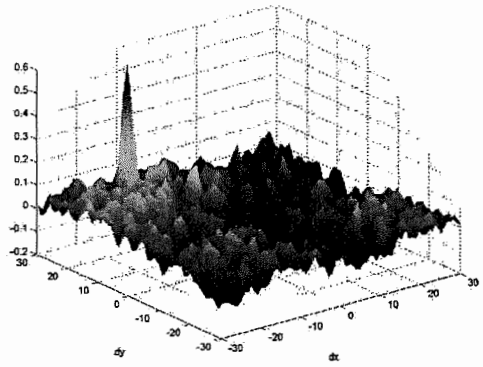

Fig 3. The evaluation function $\phi(m,n)$ for real data (see Fig 2).

the evaluation function can be written as:

$$\phi(m,n)=\sum_{i=1}^{M}\sum_{j=1}^{M}\mathbf{S}(i,j)\mathbf{A}(i+m,j+n)-M^2\langle\mathbf{S}\rangle\langle\mathbf{A}\rangle$$

which can be efficiently calculated with use of FFT algorithm. Maximum of $\phi(m,n)$ corresponds to best similarity between samples from both exposures, from which displacement of the ensemble of droplets contained in **S** is evaluated. In standard PIV

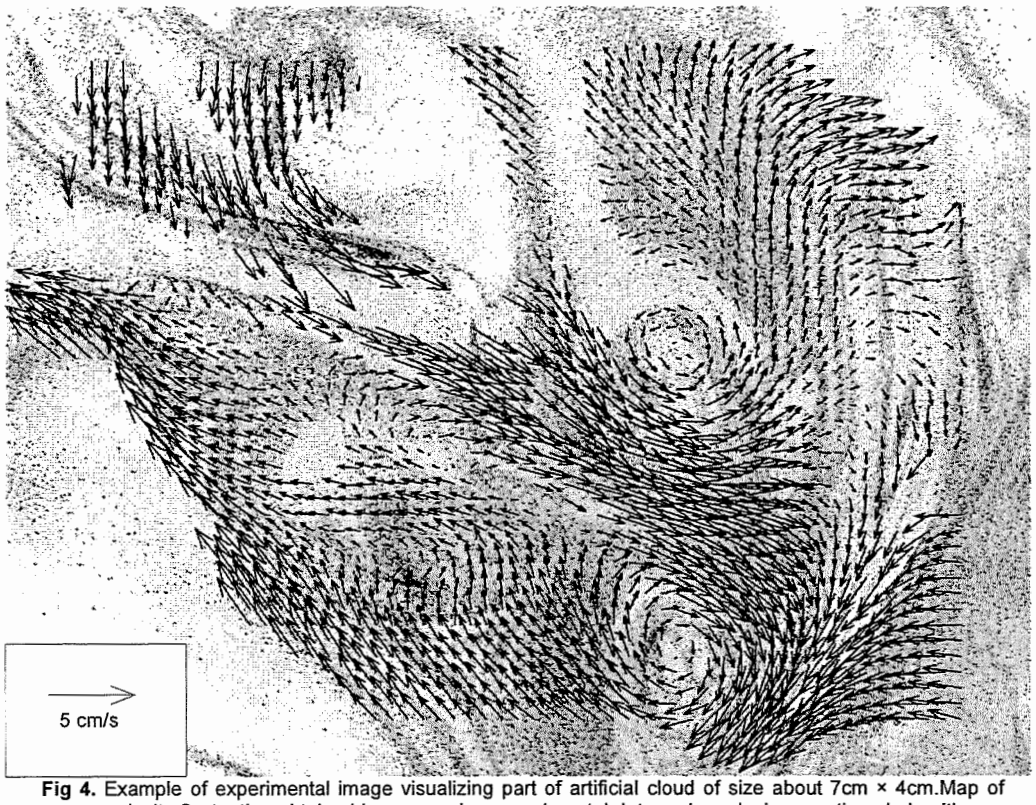

Fig 4. Example of experimental image visualizing part of artificial cloud of size about 7cm × 4cm.Map of velocity fluctuation obtained by processing experimental data and employing mentioned algorithm

algorithms the choice of the size of a sample is a significant technical problem (Gui and Merzkirch, 1998). In the following we propose successive, multi-scale selection of smaller and smaller samples.

In a first step we look for the displacement in the whole image in order to remove the bulk motion of the plume. At the next step the size of the sample is reduced and the position of the interrogation area is determined by the displacement vector evaluated earlier. In this way the displacement is corrected. This algorithm can be repeated few times decreasing the size of the sample. After the sequence of operations two components of turbulent velocity are evaluated for small patterns containing small number of droplets. The spatial resolution of retrieved velocity field corresponds to 1.2mm which is close to the Kolmogorov microscale.

In the test/development procedure the algorithm was applied to artificial (benchmark) images for which correct displacements were known. Then the accuracy of displacement (velocity) retrieval was calculated by averaging difference between correct field of displacements and the field obtained from the multiscale algorithm. The resulting displacement accuracy reaches 0.5 pixel. It corresponds to 0.06 mm in the experimental images, which for the time interval between exposures of 0.02s gives accuracy of the velocity retrieval equal to 0.3 cm/s. In the case of data from the experiment the accuracy can be slightly worse because of low quality of images and other technical problems. Maximum velocities observed during the experiment were around 15cm/s, thus the best relative accuracy obtained was 0,2%.

It must be underlined, that application of the PIV technique to the cloud droplets, which, due to inertia and gravity may move with respect to the airflow, causes some problem in the interpretation. However, sedimentation velocity of small droplets is of order of few mm/s and regions with large accelerations are relatively rare. Thus, most of the errors caused by these effects are of order of the accuracy of the method and should not affects results significantly.

3. CONCLUSIONS AND FUTURE WORK

The new PIV algorithm is employed to investigate properties of a cloud in a laboratory chamber. Its application provides insight into the structure of small-scale in-cloud turbulence down to the Kolmogorov microscale. In principle this laboratory setup may help us to investigate processes important for initiation of the warm precipitation.

Observation of the cloud structures falling down through the chamber gives an opportunity to study the mixing process of the cloud with an unsaturated environmental air. Application of the multi-scale algorithm provides information on turbulent velocities of the cloud droplets and perform statistical analysis of the properties of in-cloud turbulence as well as individual case studies of patterns created during mixing. Comparison of histograms of vertical and horizontal velocity fluctuations show (Malinowski et. al. 2004) that flow in regions of mixing is anisotropic with preferred vertical direction.

The experimental technique presented here will be developed in order to increase its accuracy and resolution. We also plan it as well as expanded to use in other application like stereo PIV Raffel et al., 1998, allowing to retrieval of all three components of velocity vector.

Acknowledgments.
This research was supported by a research grant No 5 T07A 052 24 of the Polish Committee for Scientific Research.

References:

Andrejczuk M, W.W. Grabowski, S.P. Malinowski and P.K. Smolarkiewicz 2004. *J. Atmos. Sci.*, accepted for publication.

Banat P. and Malinowski S.P. 1999. Properties of the turbulent cloud-clear air interface observed in the laboratory experiment. *Phys. Chem. Earth (B)*, 24, 741-745

Gui L., Merzkirch W. 1998. Generating arbitrarily sized interrogation windows for correlation-based analysis of particle image velocimetry recordings. *Experiments in Fluids* 24, 66-69

Malinowski S. P., Zawadzki I., and Banat P. 1998. Laboratory observations of cloud-clear air mixing in small scales. *J. Atmos. Oceanic Technol.* 15, 1060

Malinowski S.P., Piotr M. Korczyk and Tomasz A. Kowalewski, 2004: Mixing of cloud and clear air in centimeter scales observed in laboratory by means of particle image velocimetry. *In this volume.*

Raffel M., Willert Ch. E., Kompenhans J. 1998. Particle image velocimetry: a practical guide. *Springer*

Shaw R. A. 2003. Particle-turbulence interactions in atmospheric clouds. *Annu. Rev. Fluid Mech.* 35, 183-227, 2003.

Vailancourt P. A. and Yau M. K. 2000. Review of Particle-Turbulence interactions and Consequences for Cloud Physics. *Bull. Am. Meteorol. Soc.* 81, 285-98

RECONSIDERATION OF CERTAIN ASPECTS OF THE $Z - R$ PROBLEM

Michael L. Larsen* and Alexander B. Kostinski
Department of Physics, Michigan Technological University. Houghton, MI 49931.

1. INTRODUCTION

The problem of relating the rainfall reflectivity factor Z to rainfall rate R is of great interest in radar meteorology. Both of these variables are inextricably related to the droplet size distribution (DSD); Z being the sixth moment, and R usually approximated as the DSD's 11/3 moment.

Historically, relations of the form $Z = aR^b$ have been utilized, where a and b are fitting parameters, adjusted to minimize the square of the error in predicting R given an observation of Z. Studies far too numerous to mention have searched for the optimal values of a and b using a host of different methods. Empirical studies have often been employed the use of both radars (to measure Z) and disdrometers/rain gauges (to measure R). (Alternatively, it is becoming more common to use disdrometer DSD measurements to infer both quantities). Additionally, many numerical and theoretical studies have assumed a plausible form of the DSD and solved for the "correct" value of the fitting parameters.

It has been found that the fitting parameters can depend on the "type" of rain (e.g. stratiform, convective, or transition), geographical region of the rainfall, instrumental effects (which kind of radar and/or disdrometer is employed and instrument drift/bias), the functional form and properties of the underlying droplet size distribution, and the relative sample volumes of radars and disdrometers used.

The above list is not exhaustive, nor are the factors listed necessarily independent. Even if a $Z - R$ relation specifically tuned to a specific scenario, however, the rainfall rate inferred from a given value of the reflectivity can have very large errors. The utility of using this method to infer rainfall rate may be questionable, especially with the advent of other tools (e.g. polarimetric radar) that give sufficient independent measurements to more accurately characterize the quantities of interest. Nevertheless, efforts are still made to find a way to unambiguously and accurately estimate R from easily obtained meteorological information and a measurement of Z.

Similar work and conclusions have been drawn from investigations that relate other quantities related to moments of the DSD of meteorological interest (e.g. liquid water content, attenuation, median droplet diameter, total drop number, etc.)

This study uses simple numerical methods to investigate new aspects of two lines of inquiry – the differences of the best fitting parameters based on (i) rain type and (ii) as a function of disdrometer sample size. For simplicity, this study examines $Z - W$ (radar reflectivity factor - liquid water content relations) instead of $Z - R$ relations so that we need not make any assumptions regarding a power-law parameterizations of raindrop terminal velocity; analogous results should carry-over to relationships between any other pair of DSD moments. Further, we will be limiting our analysis to the behavior of the exponent b in the relation $Z = aW^b$.

2. THE FITTING EXPONENT IN STRATIFORM VS. CONVECTIVE RAIN

Several investigations have studied the differences observed in the exponent "b" found in different rain types. In particular, we reference the study of Atlas *et al.* (1999). Therein, most of the attention is focused on how the different DSDs in stratiform and convective rain bring about systematic differences in the underlying $Z - R$ relations.

Crudely, if we assume the Marhsall-Palmer relationship (Marshall and Palmer, 1948) is true for all rain, we would expect the DSD for stratiform rain to, in general, behave differently than that for convective rain; the rain-rate in convective rain tends to be much higher than in stratiform rain, and since the rain-rate is related to the mean diameter in the Marshall-Palmer distribution, this infers a different underlying DSD. Using more realistic assumptions about the functional form of the DSD results in a similar conclusion; stratiform and convective rain tend to have significantly different droplet size distributions. The conclusions by Atlas *et al.* are accurate; we should have different $Z - R$ or $Z - W$ relations because of the

*Corresponding author's address : Michael L. Larsen, Department of Physics, Michigan Technological University. Houghton, MI 49931; E-Mail: mllarsen@mtu.edu

different DSD.

However, we argue that this is not the only pertinent difference between the two types of rain. In addition to raining "harder" than stratiform rain, convective rain tends to be much more variable (e.g. fluctuations about the mean rain-rate and reflectivity are more pronounced). This point, although widely known, has not been discussed in regards to the different fitting parameters in the $Z - R$ relations for stratiform and convective rain.

3. THE FITTING EXPONENT AS A FUNCTION OF SAMPLE SIZE

A study by Smith *et al.* (1993) showed using numerical methods that moments of a droplet size distribution are underestimated for modest sample sizes. This effect is more pronounced for very small sample sizes and higher moments of the DSD. A typical duration for a DSD measurement used in a $Z - R$ study to determine the fitting parameters is 1 minute. Therefore, a typical sample can potentially contain from a few to a few thousand drops, depending on the rain rate and the cross-sectional area of the disdrometer used. Certainly, the under-estimation of higher moments of the DSD noticed by Smith *et al.* (1993) can be important unless at least several hundred drops are observed in each measurement.

Jameson and Kostinski (2002) demonstrated that, since this under-estimation is more pronounced for radar reflectivity factor than the rainfall rate, a spurious non-unity b could potentially be introduced from the use of small sample sizes. Their numerical experiments showed that, for a population with an inherent linear relationship between Z and R, the estimated value of b monotonically decreased with increasing sample size. The value of "b" asymptotically approached the true value of 1; for "realistic" disdrometer sample sizes, exponents were obtained that are comparable to values of b in the literature.

Here, we argue that *part* of the observed difference in b between stratiform and convective rain may be due to the *difference in variability of 1 minute drop-counts* for these types of rain.

4. THE SIMULATION

For simplicity, we used an exponential DSD with $0.5mm < D < 5.5mm$, and $\bar{D} = 1.1mm$ throughout (for both rain types). We then randomly selected droplets from the collection, and used the selection to estimate Z and W (liquid water content). The random variable was the number of droplets chosen in each measurement. In "steady" rain, this number is Poisson distributed. However, as has been noted frequently in the literature, raindrop arrivals tend to be more clustered than this. (See, for example, Hosking and Stow, 1987). To simulate this, we also tried drawing from a uniform distribution (as used in Jameson and Kostinski (2002)) and the even more variable (and perhaps more physically feasible) geometric distribution. Figure 1 displays the result of this numerical experiment.

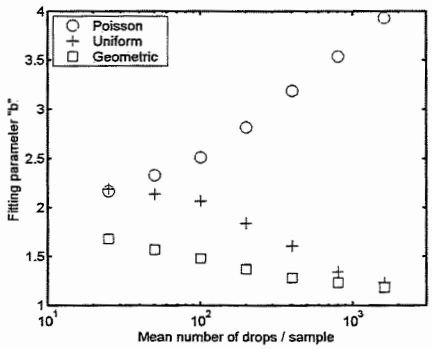

FIG. 1: The value of "b" for three sampling methods. For all of these simulations, the same truncated exponential DSD was used. The true value of b here should be 1, if the DSD was adequately sampled. For the uniform sampling, we chose the number of drops in the interval $0.1\bar{n} < x < 1.9\bar{n}$. One sees that convergence improves proportionally to the sample-to-sample drop number variability. The unbounded growth of the Poisson b is explained in the text.

Note that, for the range of values chosen for the mean number of drops per sample, $\sigma_P^2 < \sigma_U^2 < \sigma_G^2$, where the subscripts denote Poisson, Uniform, and Geometric distributions, respectively.

5. DISCUSSION

Referencing the curve for the uniform pdf, we rediscover the conclusion of Jameson and Kostinski (2002) that, for uniform sampling, the estimated exponent b decreases monotonically with sample size and asymptotically approaches the true value of 1.

We see that the more variable the sampled drop-number distribution, the more rapidly we obtain convergence to the true value (or, interpreting the result differently, there is less bias in a measurement for a given mean number of raindrops if there is larger sample-to-sample variability).

The lack of convergence for Poisson sampling is likely due to the very narrow range of log-log space the measurements take up in the scatter-plot used

to calculate the regression. With a relatively narrow "blob" of measurements, many different linear fits are reasonable. Running several trials at large mean sample sizes show a large simulation-to-simulation variability in the inferred value of b for the Poisson distribution function. Luckily, even very regular stratiform rain is rarely so uniform as Poisson statistics requires (Larsen *et al.*).

Finally, to relate this to the notion of finding the exponent in convective vs. stratiform rain, we can argue that although part of the shift to different $Z - R$ relations is assuredly due to the different DSD present, there is likely a bias resulting from undersampling in both types of rain, and the bias potentially alters stratiform rain significantly more than convective rain.

6. CONCLUSIONS

Power-law relationships among moments of raindrop size distributions are frequently utilized in meteorology. When sampling the droplet size distribution to estimate these relationships, the moment estimators are biased due to the skewness of the underlying distribution. This can result in measured relationships that are different than those theory predicts. Because different types of rain exhibit varying properties, we do observe different relationships among parameters. Previously, these varied relationships were attributed solely to physical differences in the underlying distribution. A complete treatment needs to also take into account the different sampling properties of this rain and how it influences the estimates for the moments.

ACKNOWLEDGEMENTS

This work was supported in part by NSF grant ATM01-0106271, the Michigan Space Grant Consortium, and the National Defense Science and Engineering Grant Fellowship Program.

REFERENCES

Atlas, D., Ulbrich, C.W., Marks, F.D., Amitai, E. and Williams, C.R., 1999: Systematic variation of drop size and radar-rainfall relations. *Journal of Geophysical Research*, **104** (D6), 6155-6169.

Hosking, J.G. and Stow, C.D., 1987: The arrival rate of raindrops at the ground. *Journal of Climate and Applied Meteorology*, **26** (4), 433-442.

Jameson, A.R. and Kostinski, A.B., 2002: Spurious power-law relations among rainfall and radar parameters. *Quarterly Journal of the Royal Meteorological Society*, **128**, 2045-2058.

Larsen, M.L., Kostinski, A.B., and Tokay, A. Observations and analysis of steady rain events. In preparation for *Journal of the Atmospheric Sciences*

Marshall, J.S. and Palmer, W. McK., 1948: The distribution of raindrops with size. *Journal of Meteorology*, **5**, 165-166.

Smith, P.L., Liu, Z., and Joss, J., 1993: A study of sampling-variability effects in raindrop size observations. *Journal of Applied Meteorology*, **32**, 1259-1269.

THE SCALING OF DROP SIZE DISTRIBUTIONS AND THEIR NORMALIZATION

GyuWon Lee and Isztar Zawadzki

J.S. Marshall Radar Observatory, McGill University, Montreal, Quebec, H9X 3V9, Canada

1. INTRODUCTION

Recently, normalization of drop size distributions (DSD) became a tool to study the variability of DSDs in a systematic manner. Sempere-Torres et al. (1994, 1998: refer to as ST) described a normalization procedure based on the basic notion of scaling functions, power law relationships between moments of DSDs. In essence, this procedure states that if drop size is scaled by a factor, its number concentration is also scaled in a predetermined manner. Their proposed formula for the scaling DSD is

$$N(D) = M_i^{\alpha} g(x_1) \qquad (1)$$

where $M_i (= \int N(D) D^i dD)$ is the ith moment of DSDs and x_1 $(= DM_i^{-\beta})$ is the scaled diameter. The normalized function $g(x_1)$ is called the general distribution function.

Testud et al. (2001; refer to as TT) have proposed a double-moment normalization:

$$N(D) = N_0^* F(D / D_m) \qquad (2)$$

where D_m is the volume-weighted mean diameter, a particular characteristic diameter that is derived by $D_m = M_4 / M_3$, and N_0^* is defined as $N_0^* = C_T M_3^5 M_4^{-4}$, where C_T is an arbitrary constant that is chosen as $4^4/\Gamma(4)$. Testud *et al.* point out that the remaining scatter around the normalized function is below the noise level of the disdrometric data, suggesting that their two parameters, the third and fourth moments of the DSDs, are sufficient to capture all the discernable variability.

The purpose of this paper is to extend the ST single-moment scaling normalization to a double-moment scaling normalization and establish an explicit relationship between the TT and ST approaches. Furthermore, we will show the advantage and disadvantage of each normalization method and that the scaling normalization of DSDs is a general way of describing DSDs.

2. A GENERAL DOUBLE-MOMENT SCALING DSD

A general form of ST normalization with two moments of DSDs can be derived by re-normalizing $g(x_1)$ with the jth moment of $g(x_1)$:

$$N(D) = M_i^{\frac{j+1}{j-i}} M_j^{\frac{i+1}{i-j}} h(x_2) \text{ with } x_2 = DM_i^{\frac{1}{j-i}} M_j^{\frac{-1}{j-i}} \qquad (3)$$

where x_2 is the scaled diameter and $h(x_2)$ the "second normalized" DSD. In addition, we obtain the general multiple power law relationship among moments of DSDs:

$$M_n = C_{2,n} M_j^{\frac{n-i}{j-i}} M_i^{\frac{j-n}{j-i}}. \qquad (4)$$

Although we use j[th] moment of $g(x_1)$, the ith and j[th] moment of DSDs are necessary in the final form. For a detailed derivation and overall contents of this paper, see Lee et al. (2003). Interestingly, all scaling exponents disappear and only the orders (*i* and *j*) of the two DSD moments used in the normalization remain in this final form. In addition, we have not assumed any functional form of the shape of normalized DSDs that remains free and to be determined from observations.

In the single-moment normalization, a simple power law between any two moments is assumed. The exponent of this power law is the function of scaling exponent β $[M_n = C_{1,n} M_i^{1+(n-i)\beta}]$ and the coefficient is the nth moment of $g(x_1)$ $[C_{1,n} = \int g(x_1) x_1^n dx_1]$. Similarly, in the double-moment normalization, the coefficient of the multiple power law in (4) is now the nth moment of $h(x_2)$ instead of $g(x_1)$. However, the exponent is purely determined by the orders of moments. Therefore, in this approach the role of β and the normalized general function *g* is now played by the two moments of the original DSD used in the normalization. Thus the two moments should jointly contain all the information for the stratification of DSDs.

In addition, the normalization of TT is a particular case of the double-moment scaling normalization (3) in which the moments of order 3 and 4 have been selected as the reference variables. The normalization of TT can also be generalized using the generalized characteristic number density $N_0^{'}$ and the generalized characteristic diameter $D_m^{'}$, leading to (3):

$$N(D) = N_0^{'} F(D / D_m^{'}) \text{ with } \begin{array}{l} N_0^{'} = M_i^{(j+1)/(j-i)} M_j^{(i+1)/(i-j)} \\ D_m^{'} = (M_j / M_i)^{1/(j-i)} \end{array} \qquad (5)$$

Thus, normalization by ST and TT are a particular case of (3) and are based on the same concept, the *scaling law* of DSDs.

3. *R-Z* RELATIONSHIPS

When we choose $M_i = C_u R$ (~3.67[th] moment of the DSD) and $M_n = Z$ (6th moment of the DSD) in (4), the following relationship $Z(M_j, R)$ is obtained:

$$Z = \left[C_{2,6} C_u^{\frac{j-6}{j-3.67}} M_j^{\frac{2.33}{j-3.67}} \right] R^{\frac{j-6}{j-3.67}} \qquad (6)$$

Corresponding author address: GyuWon Lee, J. S. Marshall Radar Observatory, P.O.Box 198, Macdonald Campus, Ste-Anne-de-Bellevue, QC, Canada, H9X 3V9.
E-mail:gwlee@zephyr.meteo.mcgill.ca

where C_u is a constant that adjusts the units. In the single-moment scaling normalization, the coefficient *a* of $Z=aR^b$ is the 6th moment of $g(x_1)$ and the exponent *b* is related to the scaling exponent β by $b=1+2.33\beta$. In (6), the exponent of *R-Z* relationship depends on the choice of *j*. We can also obtain $Z(N_0^{'},R)$ and $Z(D_m^{'},R)$:

$$Z = C_{2,6}C_{2,3.67}^{-1.5}C_u^{1.5}\left(N_0^{'}\right)^{-0.5}R^{1.5} \quad (7)$$

$$Z = C_{2,6}C_{2,3.67}^{-1}C_u\left(D_m^{'}\right)^{2.33}R \quad (8)$$

The explicit exponent in (7) and (8) does not imply any universal value. It depends on the correlation between $N_0^{'}$ and *R* or between $D_m^{'}$ and *R*. The explicit exponent on *R*, *b*=1.5, in (7) is close to the climatological value ($Z=210R^{1.47}$ in Montreal, for example). This implies that the correlation between $N_0^{'}$ and *R* is low when a set of data is taken from a climatological variety of situations. For Marshall-Palmer DSDs, we expect $Z=aR^{1.5}$ since $N_0^{'}$ is a constant and $D_m^{'} \propto R^{0.21}$. For the equilibrium process, the evolution of DSDs is controlled by the number of drops with increasing *R* and the characteristic diameter remains as a constant. Thus, a proportionality between *R* and *Z* is expected. With a strong aggregation between snow particles, $N_0^{'}$ decreases with increasing *R* and the dependence of $D_m^{'}$ on *R* is stronger than that expected in M-P DSDs, that is, the exponent *f* of $D_m^{'}=eR^f$ is larger than 0.21. Thus, the exponent of *R-Z* relationship should be larger than 1.5.

4. DATA ANALYSIS

The data used consist of 1208 one-minute DSDs (over 20 hours) measured by the optical spectro-pluviometer (OSP: Salles et al. 1998). DSDs are divided into convective and stratiform rain using the presence of the bright band (BB) and the horizontal gradient of reflectivity obtained from a nearby scanning radar.

4.1 Compact representation of DSDs

The normalization of the set of these data is shown in Fig. 1 for the single moment (*R*) and in Fig. 2 for the double moment (M_i and M_j).

The scaling exponent β is slightly smaller than the value of M-P DSDs, indicating that the exponent of $Z=aR^b$ is less than 1.5. The scatter of normalized DSDs in Fig. 1a and the standard deviation in Fig. 1b (vertical bars) are quite large. This shows the limitation of a single-moment scaling normalization in terms of compact representation of DSDs. When all DSDs from different physical processes are normalized together, they do not collapse onto one normalized curve. In other words, all the DSD variability cannot be explained by a single parameter.

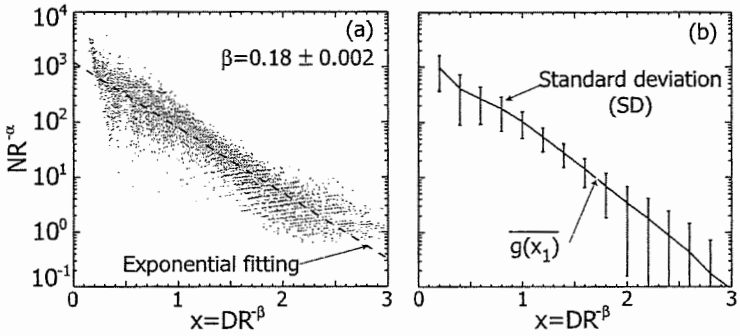

Fig.1: Single-moment normal -ization on observed DSD data. (a): Scattergram of all normalized DSDs with Mi=R. An exponential adjustment is shown as a dashed line. (b): The average $\overline{g(x_1)}$ of the data points in (a) with bars (dark solid line) indicating the standard deviation.

In the double-moment normalization in Fig. 2a and b, $\overline{h(x_2)}$ is very similar to those reported by TT. In general, the scatter drastically decreases compared with the single-moment normalization, illustrating an advantage of double-moment normalization in terms of a compact representation of DSDs. The standard deviation (*SD*: thick vertical bars in Fig.2b) is still larger than that from the statistical noise (lighter vertical bars next to *SD*) derived by assuming Poisson fluctuations due to undersampling. This can be explained by two facts: 1) the possible physical variability that cannot be described by this normalization and 2) underestimation of the statistical noise by the Poisson process.

The degree of the scatter in normalized DSDs is quantified in terms of the standard deviation of fractional error in the estimation of various moments with average normalized DSD $\overline{h(x_2)}$. Fig. 3 shows results from various combinations of two moments used for the normalization. Not surprisingly, when two consecutive moments are used, the error is almost zero for moments close to the ones used for the normalization due to the self-consistency constraints. When the order of the two moments used for the normalization is lower (higher), the error is smaller at lower (higher) moments. The minimum is broader when the order is higher. This simply indicates that the slope of the DSDs has less variability at the larger drop sizes.

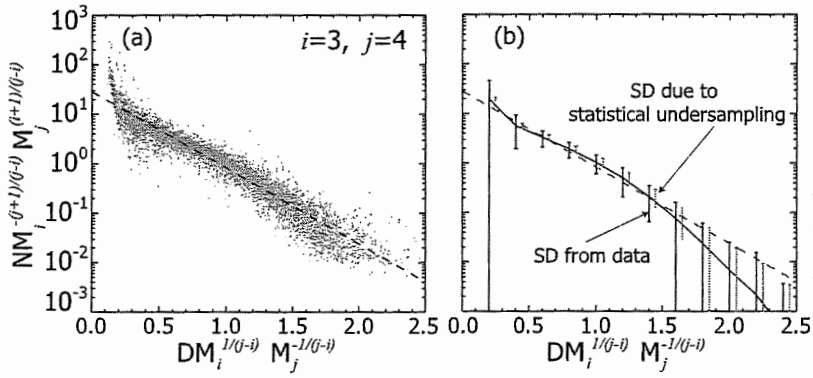

Fig. 2: Two moment normalization on the observed DSD data. (a): Scattergram of all normalized DSDs with M_i=M_3 and M_j=M_4. An exponential adjustment is shown as a dashed line. (b): The average $\overline{h(x_2)}$ of the data points in (a) with dark vertical bars indicating the standard deviation. The standard deviation due to the statistical fluctuation is shown as the grey vertical bars.

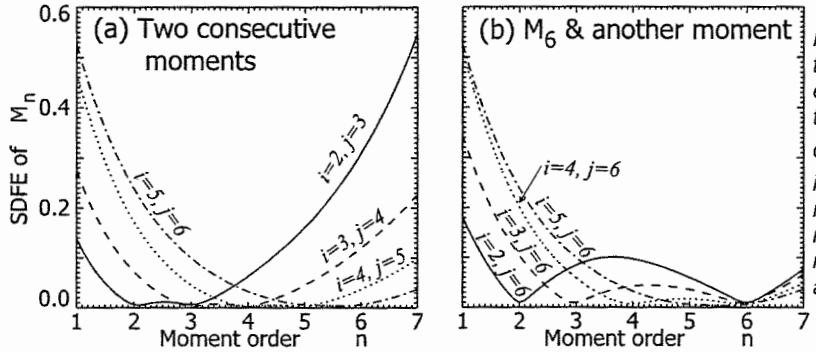

Fig. 3: (a) Standard devia-tion of the fractional error (SDFE) in the estimate of the nth moment from the average normalized drop size distribution $\overline{h(x_2)}$ when the indicated two consecutive moments are used for the normali-zation. (b) Same when reflectivity and any other moment are used for the normalization

When reflectivity factor $(M_j = M_6)$ and another moment (M_i) are used for the normalization the standard deviation of the fractional error of Fig. 3b is obtained. Again not surprisingly, there are two minima (zero) in the error. As the order *i* is lower, the error at lower (higher) moments decreases (increases). When the order of two moments is far from each other, the overall error is much lower and the error between two moments slightly increases. However, *R* (*n*=3.67) is estimated always with a precision better than 10%. Since the reflectivity factor is directly measured from radar, in the application to radar remote sensing we prefer to fix the one moment as reflectivity factor.

4.2 Connection between scaling normalizations and physical processes.

We now compare the single moment normalization with the double-moment normalization on the data stratified according to precipitation types (stratiform and convective rain). This comparison illustrates the capability of each normalization to identify different precipitation types.

Fig. 4a shows the weighted-total-least-square regression (WTLS: Amemiya 1997) of *R* and *Z* for the two types of precipitation. Although the points are weakly separated, the difference in the two regressions is statistically significant. Note the significantly different exponent. Fig. 4b shows the exponent $\gamma(n)$ of the power-law relationship [$M_n = C_{1,n} R^{\gamma(n)}$] between *R* and all other moments of the indicated order. Again, the two regression lines are clearly distinctive for the convective and stratiform rain. The slope of these two regression lines defines the scaling exponent β of single-moment normalization for the two populations.

The average normalized DSDs $\overline{h(x_2)}$ in Fig. 5a are remarkably stable, indicating that in this case stratiform and convective rain do not generate distinctive shapes of DSDs. $\overline{h(x_2)}$ is slightly different from the normalized exponential DSDs. These DSD shapes are quite consistent with those of TT. The next question is how well two moments or N_0^* and D_m^* jointly contain information on the scaling exponent β that nicely separates the two rain regimes in the single-moment normalization. TT showed that N_0^* and D_m^* from the two regimes of tropical rain are well separated so that they are good indicators for the classification. In Fig 5b, we see the correlation between N_0^* and D_m^*. The separation of the two types of precipitation in the (N_0^* , D_m^*) space is poor. Convective rain shows no correlation (determination coefficient r^2 =0.01) and a wide distribution with an upper limit of N_0^* at $N_0^* = 3x10^2$ $m^{-3}mm^{-1}$. Some points from convective precipitation are mixed with those from stratiform rain.

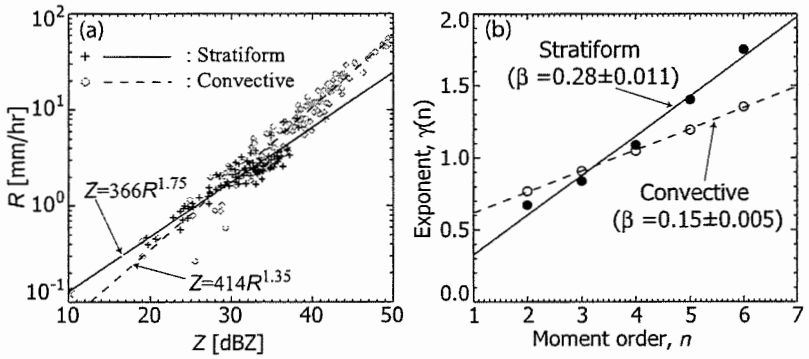

Fig. 4: (a) R-Z WTLS regressions for stratiform and convective rain. (b) Exponent $\gamma(n)$ of $M_n = C_{1,n}R^{\gamma(n)}$ as a function of n. The scaling exponent β is determined by the slope in $\gamma(n)$ vs n $[\gamma(n) = \alpha + (n+1)\beta]$.

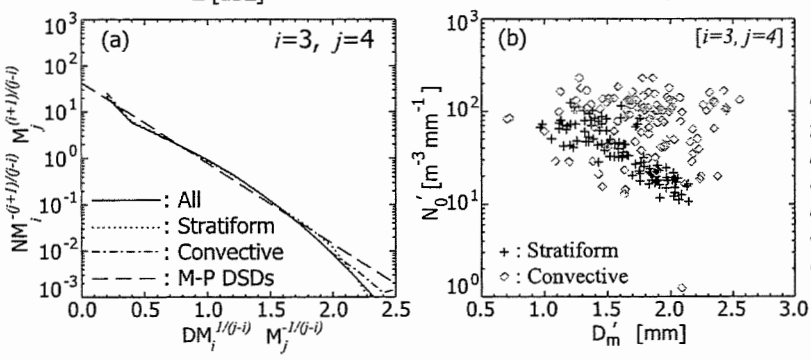

Fig. 5 (a) Comparison of $\overline{h(x_2)}$ from different rain regimes. The normalized exponential DSD is also shown as the long dashed line. Note the remarkably stable shape. (b): Distribution of data in (N_0', D_m') space.

5. THE FUNCTIONS $g(x_1)$, $h(x_2)$ AND A SCALING MODEL DISTRIBUTION.

From the original generalized gamma DSD suggested by Auf der Maur (2001), we obtain the following inherent scaling property and the normalized form of generalized gamma DSDs.

$$M_n = C_{GG,2,n} M_i^{\frac{n-j}{i-j}} M_j^{\frac{i-n}{i-j}} \tag{9}$$

$$N(D) = N_0' h_{GG,(i,j,\mu,c)}(D/D_m')$$

$$h_{GG,(i,j,\mu,c)}(x_2) = c\Gamma_i^{\frac{j+c\mu}{i-j}} \Gamma_j^{\frac{-i-c\mu}{i-j}} x_2^{c\mu-1} \exp\left[-\left\{\frac{\Gamma_i}{\Gamma_j}\right\}^{c/(i-j)} x_2^c\right] \tag{10}$$

$$\Gamma_i = \Gamma(\mu + i/c);\ \Gamma_j = \Gamma(\mu + j/c)$$

where $C_{GG,2,n} = [\Gamma(\mu+i/c)]^{\frac{j-n}{i-j}} [\Gamma(\mu+j/c)]^{\frac{n-i}{i-j}} \Gamma(\mu+n/c)$ and $x_2 = D/D_m'$. Thus, the generalized gamma DSDs also satisfy scaling properties. Since all naturally occurring DSDs can be reasonably well described by the generalized gamma DSD, this suggests a very general description of all types of DSDs within the scaling framework.

6. CONCLUSIONS

We have shown here that the ST's and TT's formulations of normalized DSDs are particular cases of the general scaling normalization presented here in some detail. No functional form of DSDs is imposed in the normalization. Therefore, the general scaling normalization can reveal any stable shape of normalized DSDs. The single-moment scaling normalization applied after a stratification of DSDs according to a likely dominance of a given microphysical process shows that the scaling exponent β is a clear indicator of the processes. However, in the double-moment normalization, the separation of N_0' and D_m' that was a good indication of two rain regimes in TT is poor in our data set. The generalized gamma DSDs also have scaling properties, indicating that the derived double-moment scaling DSD formulation is a general way of describing observed DSDs.

7. REFERENCES

Amemiya, 1997:Van Huffel,ed.,Philadelphia,SIAM,77-86.

Auf der Maur, 2001:*J. Atmos. Sci.*, **58**, 407-418.

Lee et al., 2004: *J. Appl. Meteor.* **43**, 246-281

Salles et al., 1998:*J. Atmos. Oceanic Technol.*, **15**, 1215-1222.

Sempere-Torres et al., 1994:*J. Appl. Meteor.*, **33**, 1494-1502.

Sempere-Torres et al., 1998:*J. Geophys. Res.*, **103**, 1785-1797.

Testud et al., 2001: *J. Appl. Meteor.*, **40**, 1118-1140.

peaks mainly appear in this work

TETHERED-BALLOON BORNE MEASUREMENTS IN BOUNDARY LAYER CLOUDS. PART II: MICROPHYSICAL PROPERTIES

Katrin Lehmann, Sebastian Schmidt, Holger Siebert, and Manfred Wendisch

Institute for Tropospheric Research, Leipzig, Germany

1. INTRODUCTION

Micro-scale dynamical processes such as entrainment and turbulence are of great importance for the microphysical properties of boundary layer clouds. Condensational growth of cloud drops might be enforced by small-scale fluctuations of the water vapor supersaturation field. Clustering of drops due to inertial coupling with turbulent motion can enhance collision and coalescence rates. All of these processes lead to modifications of the drop size distribution. An overview of this topic is given in Shaw (2003).

In order to identify and quantify the effects of these processes, measurements of turbulent and microphysical parameters with high spatial resolution are needed. However, such data are rare. This was one of the motivations to compile the tethered balloon borne instrument payload ACTOS (Airship-borne Cloud Turbulence Observation System) (Siebert et al. (2003)). Originally ACTOS was designed to study turbulent processes in the atmospheric boundary layer. Recently, the setup of ACTOS was extended to allow cloud microphysical measurements in warm boundary layer clouds. The so-called Modified Fast Forward Scattering Spectrometer Probe (M-Fast-FSSP) (Schmidt et al. (2004)) was implemented in the ACTOS payload. In May 2003 first measurements with the revised ACTOS instrument package were performed in Cabauw, The Netherlands, within the scope of the Baltex Bridge Cloud (BBC2) campaign.

In this abstract drop size distribution measurements with the M-Fast-FSSP within fair weather cumuli at two different altitudes are presented. An analysis of turbulent parameters during this flight is reported in Part I of this paper (Siebert et al. (2004)).

Corresponding author's address: Katrin Lehmann, Institute for Tropospheric Research, Germany
Permoser Straße 15, 04318 Leipzig
lehmann@tropos.de

2. INSTRUMENTATION

Originally the FSSP measures the number concentration and size of cloud drops. From these data the number size distribution in units of $cm^{-3}nm^{-1}$ and respective integrated properties like Liquid Water Content (LWC) or total drop number concentration are derived. For this purpose the sample volume of the probe has to be determined. Usually, the FSSP is mounted on aircraft and the sampling volume is calculated using the air velocity which is approximated by the True Air Speed (TAS) of the aircraft. For ground based operation, the FSSP is aspirated with a defined air speed. A third method to determine the sample volume of the FSSP is to measure the velocity of each single drop by dividing the geometric distance of the laser beam maximum to half of its amplitude by the time the drop needs to pass that distance. The M-Fast-FSSP was designed such that this quantity can be recorded. Thus, the M-Fast-FSSP offers the unique possibility to calculate the sample volume directly using the drop velocity.

Figure 1 shows a time series of the wind velocity measured with the sonic anemometer and the averaged drop speed derived from the M-Fast-FSSP. Both instruments were mounted at the tip of ACTOS. The data were taken on May 22, 2003. The correlation coefficient between the two speeds is 0.92, whereas the drop velocity is systematically lower than the wind speed by a factor of 0.2 - 0.3. This offset is most probably due to the different positions of the sonic and the M-Fast-FSSP, which is much closer to the stagnation point of the platform body. For the determination of the FSSP-sampling volume and hence the drop number concentration

and drop size distribution shown in the following text the drop speed is used.

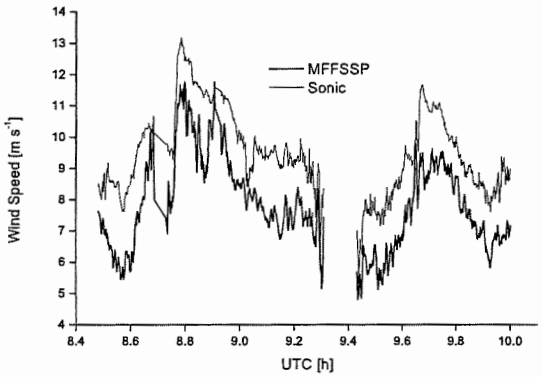

Figure 1: Time series of wind velocity measured with a sonic anemometer (grey line) and the averaged drop speed derived with the M-Fast-FSSP (black line). For cloud free regions no drop velocity could be calculated.

3. DATA ANALYSIS

Figure 2 displays measurements taken at a constant altitude of about 700 m on May 19, 2003.

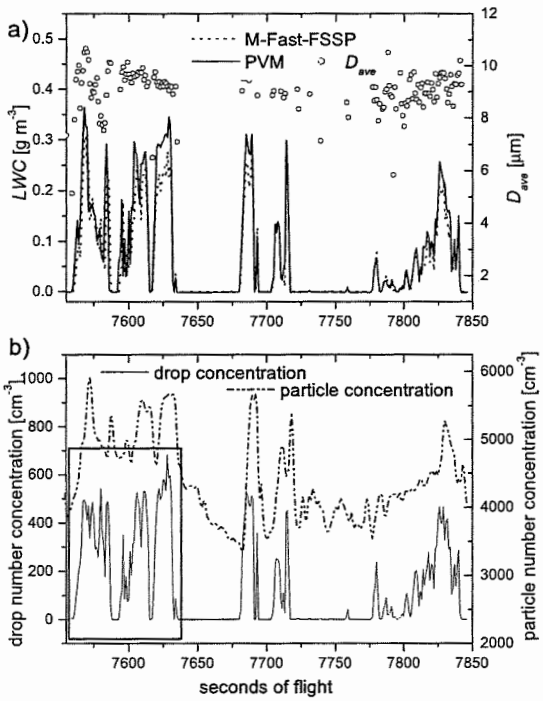

Figure 2: Time series (1 Hz) of (a) *LWC* measured with the PVM-100A (solid line) and M-Fast-FSSP (dashed line) and the geometric mean diameter (circles), and (b) drop (solid) and particle (dash-dotted line) number concentration.

Peak *LWC* values of about 0.3 $g\,m^{-3}$ with drop number concentrations in the order of 500 cm^{-3} and a mean drop diameter between 9 and 10 μm were observed. The particle number concentration measured with a Condensation Particle Counter (CPC) was found to be almost twice as high in cloudy air compared to cloud free air, suggesting the air parcel to origin in lower levels with much higher particle loads. A rough estimate from ceilometer data yields the cloud base at an altitude of about 500 - 550 m. Calculation of the *LWC* in 700 m using the adiabatic assumption gives values between 0.3 and 0.4 $g\,m^{-3}$. The marked region in Fig. 2b reveals small scale variations in *LWC* and drop number concentration (Fig. 3).

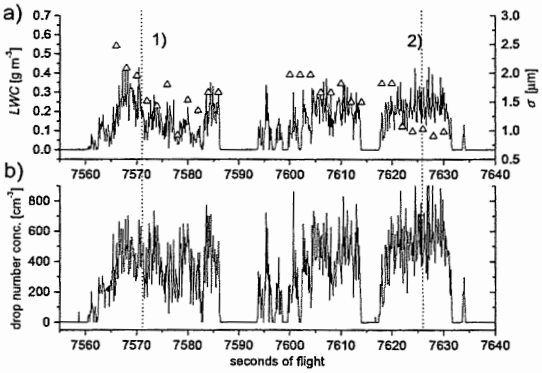

Figure 3: Time series (10 Hz) of *LWC* (a) and drop number concentration (b) for the region marked in Fig. 2. In a), the width of the drop size distribution is displayed as triangles.

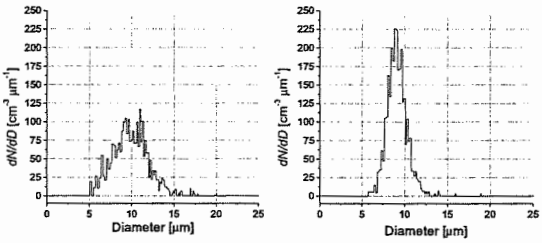

Figure 4: Drop size distributions for cloud 1 and 2 in Fig. 3 (5 sec averages for the times indicated by the dashed lines).

For cloud 1 and 2 in Fig. 3, drop size distributions were calculated (5 sec averages)(Fig. 4). For cloud 2, that looks more homogenous and possesses the highest drop number concentrations, the drop distribution is very narrow with a mode at 8 μm. Cloud models predict narrow drop size distributions for adiabatically raising cloud parcels. For cloud 1, the distribution is broader and contains some larger drops. The width of the distribution,

which is obtained by applying a Gaussian to the measured distribution, is marked by triangles in Fig. 3. It is quite variable for cloud 1, but reaches its smallest values of about 1 μm in the second part of cloud 2, where it remains almost constant.

Figure 5 shows the same parameters as displayed in Fig. 2, measured 20 min earlier at an altitude of about 1050 m.

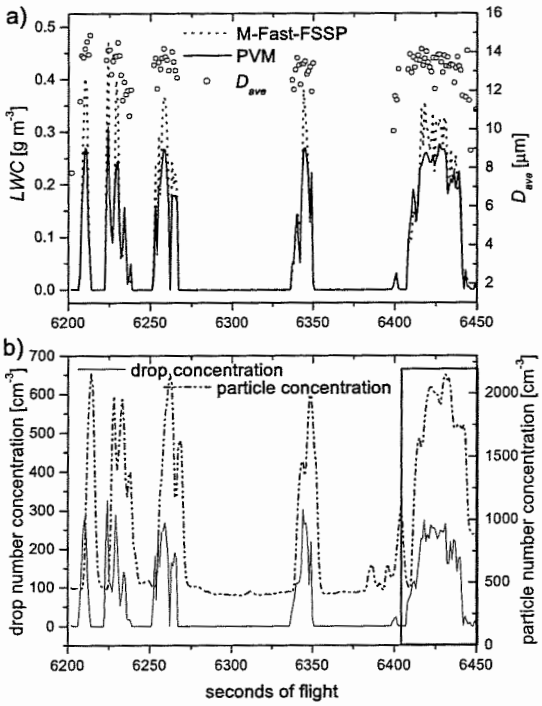

Figure 5: Same as Fig. 2 for a leg flown 22 min earlier at an altitude of about 1050 m.

For the clouds at this height, *LWC* values of about 0.25 g m^{-3} were measured by the PVM-100A, whereas the M-Fast-FSSP yields slightly higher values. The mean drop diameter ranges between 8 and 15 μm. The cloud drop number concentration was smaller compared to the clouds in the lower leg. The particle number concentration inside the clouds reached values of about 2200 cm^{-3}, which is more than four times higher than the particle number concentration in the cloud free air. A sharp decrease of the particle number concentration with height (in this case 3500 cm^{-3} in 700 m to 500 cm^{-3} in 1050 m) in cloud free air can often be observed (Stratmann et al. (2003))

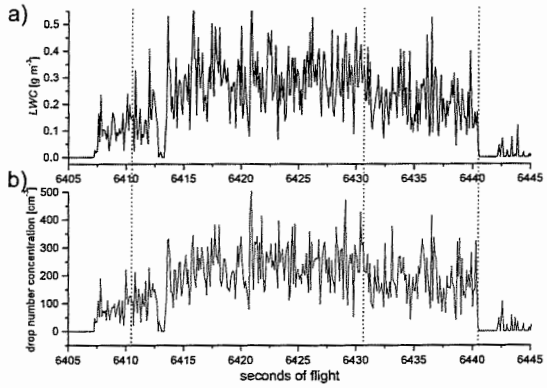

Figure 6: Time series (10 Hz) of drop number concentration and *LWC* for the marked region in Fig. 4.

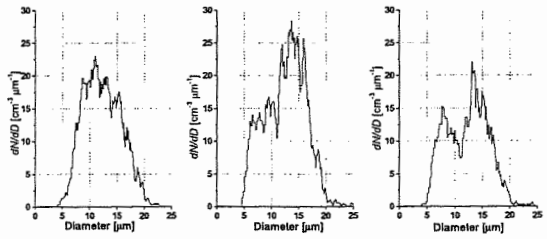

Figure 7: Drop size distributions for the cloud in Fig. 6 (smoothed 10 sec averages for the times indicated by the dashed lines)

The drop size distributions (Fig. 7) for the cloud marked in Fig. 5b are significantly different from the ones observed 350 m below. The distributions contain much larger drops and reveal a trend to be bimodal, with one peak at about 8 μm and another one at 14 μm. Similar drop size distributions were found throughout the whole leg and are not an artefact caused by sampling in two clouds with different drop size distributions. The existence of larger drops together with a relative low drop number concentration indicates that the clouds in the higher leg are in a more mature stage than the lower ones. The existence of a bimodal drop size distribution could be explained by homogenous mixing with subsaturated environmental air, that leads to a dilution of the drop concentration as well as to an evaporation of drops (e.g., Brenguier (1993)). The bimodal size distribution could be the overlap of a grown drop mode and a partly evaporated drop mode. Such a spread of the drop size distribution over a large diameter range could also lead to differences in the sedimentation velocities which are necessary to onset collision and coalescence.

4. SUMMARY

First measurements show that the balloon-borne application of the M-Fast-FSSP was successful. Due to the low true air speed of the balloon, drop size distributions and related microphysical parameters could be measured with high spatial resolution. Cumulus penetrations at different altitudes are presented with narrow drop size distributions at 700 m and bimodal drop size distributions at 1050 m. The existence of two modes in the drop size distribution is most likely caused by homogenous mixing with subsaturated environmental air.

5. ACKNOWLEDGEMENTS

The authors acknowledge the Bundeswehr Technical Center for Ships and Naval Weapons for their kind provision of the tethered balloon MAPSY and the KMNI who hosted the BBC2 campaign. Part of this work is financed by the Deutsche Forschungsgesellschaft (DFG).

6. REFERENCES

Brenguier, J.-L.: 1993, 'Observations of cloud microstructure at the centimeter scale'. *J. Appl. Meteor.* **32**, 783–793.

Schmidt, S., K. Lehmann, and M. Wendisch: 2004, 'Minimizing instrumental broadening of the drop size distribution with the M-Fast-FSSP'. *J. Atmos. Oceanic Technol.* **(submitted)**.

Shaw, R. A.: 2003, 'Particle-turbulence interactions in atmospheric clouds'. *Annu. Rev. Fluid Mech.* **35**, 183–227.

Siebert, H., K. Lehmann, S. Malinowski, and M. Wendisch: 2004, 'Tethered-balloon borne measurements in boundary layer clouds. Part1: Turbulence and dynamics'. In: *Preprints 14th International Conference on Clouds and Precipitation.* Bologna, Italy, (18-23 July 2004).

Siebert, H., M. Wendisch, T. Conrath, U. Teichmann, and J. Heintzenberg: 2003, 'A new tethered balloon-borne payload for fine-scale observations in the cloudy boundary layer'. *Boundary-Layer Meteorol.* **106**, 461–482.

Stratmann, F., H. Siebert, G. Spindler, B. Wehner, D. Althausen, J. Heintzenberg, O. Hellmuth, R. Rinke, U. Schmieder, C. Seidel, T. Tuch, U. Uhrner, A. Wiedensohler, U. Wandinger, M. Wendisch, D. Schell, and A. Stohl: 2003, 'New-particle formation events in a continental boundary layer: first results from the SATURN experiment'. *Atmos. Chem. Phys.* **3**, 1445 – 1459.

SIMULATIONS OF STRATOCUMULI CLOUDS WITH A 3D CLOUD MODEL WITH WARM DETAILED MICROPHYSICS

M. Leporini, W. Wobrock, A.I. Flossmann

Laboratoire de Météorologie Physique, Université Blaise Pascal, OPGC, CNRS, Aubière, France

1. INTRODUCTION

Stratocumulus clouds are frequently present over large areas and especially over the sea. These clouds are known to play a crucial role in the global radiation balance and thus, on the climate of the Earth. Most current models for global, synoptic or even meso and cloud scales are not able to represent these cloud fields in a way that contains sufficient information on their microphysical properties. However, the accurate determination of the microphysical (e.g., cloud droplet size and concentration) and macrophysical (e.g., cloud cover) properties of the boundary layer cloud is essential for the correct treatment of these clouds in radiative transfer modelling. In addition, the interactions between aerosol particles and clouds are not yet completely understood and the current parameterisations considering clouds and aerosol particles only by simple bulk quantities, which are prescribed and which do not evolve as a function of time and space, are not adequate.

In order to improve our understanding in the complex interaction between aerosol particles and clouds, and in order to be able to simulate such a complex system, we developed a three-dimensional warm cloud model with spectral microphysics, called DESCAM-3D, on the basis of the detailed microphysical concept of Flossmann and Pruppacher (1988). There exists in the literature a number of cloud models with varying complexity and some, e.g. the 3D cloud model of Kogan (1991) and the cloud model of Khain (2001), even consider an explicit microphysics. In DESCAM-3D, however, the detailed formulation of the microphysical processes allows the prediction of variation in time and space of the complete cloud microstructure (i.e. drop size distribution, interstital and residual aerosol particle size distribution) at each grid point of the model.

The objectives of the current study are to present the microphysical scheme of the three-dimensional warm cloud model and its application to the simulation of a stratocumulus cloud case of 19 July 1997 from the ACE-2 (Second Aerosol Characterisation Experiment) campaign. Moreover, in the current paper, we present the results of a sensitivity study on the effects of different dry initial aerosol particles spectra on the microphysics of the cloud field.

Corresponding author's address: Andrea I. Flossmann, Laboratoire de Météorologie Physique/UBP, 24, avenue des Landais, F - 63177 Aubière CEDEX, France ; email: A.Flossmann @opgc.univ-bpclermont.fr

2. MODEL DESCRIPTION

The cloud model DESCAM-3D is a modified version of the model DESCAM (DEtailed Scavenging Model) of Flossmann et al. (1987). This model has been simpified to enable its use in a 3D dynamic frame. The model describes the time evolution of a drop size distribution, f_d, originating on aerosol particles of a given size distribution of a given uniform composition and its subsequent growth by warm microphysical processes. Furthermore, it describes the simultaneous time evolution of the aerosol particle mass distribution, g_{APd}, captured and redistributed among the various cloud drop size categories and finally predicts the distribution of the aerosol particles left unactivated in the air, f_{APa}, as drop interstitial aerosol. It includes the processes of nucleation, condensation/ evaporation, collision/coalescence, break-up, sedimenttation and scavenging of aerosol particles by cloud droplets.

In contrast to the more explicit 2D version of Flossmann and Pruppacher (1988) we refrained from the use of an independent mass distribution function for the non activated aerosol. Consequently, the interstital aerosol particles were assumed to be always in a thermodynamic equilibrium with the ambient air (eq.4).

The time rate of change of the cloud drop number density function f_d is given by the relation:

$$\frac{\partial f_d(m)}{\partial t} = -\nabla\cdot\left[v f_d(m)\right] + \nabla\cdot\left[K_m \nabla f_d(m)\right] + \frac{\partial}{\partial z}\left[V_\infty(m) f_d(m)\right] + \left.\frac{\partial f_d(m)}{\partial t}\right|_{act} + \left.\frac{\partial f_d(m)}{\partial t}\right|_{con/eva} + \left.\frac{\partial f_d(m)}{\partial t}\right|_{AP,coll} + \left.\frac{\partial f_d(m)}{\partial t}\right|_{d,coal} + \left.\frac{\partial f_d(m)}{\partial t}\right|_{d,break} \quad (1)$$

The time rate of change of the number density distribution function for aerosol particles remaining in the air, f_{APa}, is given by

$$\frac{\partial f_{APa}(m_{AP})}{\partial t} = -\nabla\cdot\left[v f_{APa}(m_{AP})\right] + \nabla\cdot\left[K_m \nabla f_{APa}(m_{AP})\right] + \left.\frac{\partial f_{APa}(m_{AP})}{\partial t}\right|_{act} + \left.\frac{\partial f_{APa}(m_{AP})}{\partial t}\right|_{con/eva} + \left.\frac{\partial f_{APa}(m_{AP})}{\partial t}\right|_{AP,coll} \quad (2)$$

And for the mass density distribution function of aerosol particles in the drops, g_{APd}

$$\frac{\partial g_{APd}(m)}{\partial t} = -\nabla\cdot[v g_{APd}(m)] + \nabla\cdot[K_m \nabla g_{APd}(m)] + \frac{\partial}{\partial z}[V_\infty(m) g_{APd}(m)] + \left.\frac{\partial g_{APd}(m)}{\partial t}\right|_{act} + \left.\frac{\partial g_{APd}(m)}{\partial t}\right|_{con/eva} + \left.\frac{\partial g_{APd}(m)}{\partial t}\right|_{AP,coll} + \left.\frac{\partial g_{APd}(m)}{\partial t}\right|_{d,coal} + \left.\frac{\partial g_{APd}(m)}{\partial t}\right|_{d,break} \quad (3)$$

Finally, the mass density distribution function for the aerosol particles remaining in the air, g_{APa}, is found from the computation of the dry aerosol particle radius r_N by means of the Köhler equation and from f_{APa} following:

$$g_{APa}(m_{AP}) = r_N^{\,3}\,\frac{4}{3}\pi\rho_{AP} f_{APa}(m_{AP}) \quad (4)$$

where m is drop mass, m_{AP} the aerosol particle mass, v the velocity field of air, ρ_{AP} the aerosol particle density; $|_{act}$ is the change due to the activation of aerosol particles to drops, $|_{con/eva}$ the change due to condensation and/or evaporation of drops, $|_{AP,coll}$ the change due to aerosol particle collection by drops, $|_{d,coal}$ the change due to collision and coalescence of drops and $|_{d,break}$ the change due to drop break up. The first terms concerning the dynamical processes are evaluated from the three-dimensional non-hydrostatic mesoscale model of Clark et al. (1996) which has been linked to our cloud module. The remaining microphysical terms are evaluated following essentially Flossmann et al. (1987).

3. INITIAL CONDITIONS

The present model was initialised with a sounding taken during the ACE2 campaign the 19 July 1997. In order to initiate the formation of the cloud layer in the model simulations, a surface latent heat was imposed at the lower boundary. As the vertical depth of the cloud layer was quite thin (around 200 m) special care was given to the model's vertical grid. In order to highly resolve the thin cloud layer, a stretched vertical coordinate was calculated by 4th order polynoms. Around 15 points covered the cloud layer wherein $(dz)_{\min} \approx 12\ m$. The numerical characteristics of the simulations are summarized in Table 1.

Δt	Δx	Δy	Nx	Ny	NZ
3 s	150m	150m	100 pts	100 pts	50 pts

Table 1: *Numerical characteristics of the simulations.*

For the initial aerosol particles spectrum we use three lognormal distributions:

$$\frac{dN}{d\ln r} = f_{APa}(\ln r) = \sum_{i=1}^{3} \frac{n_i}{(2\pi)^{1/2}\log\sigma_i \ln 10} * \exp\left(-\frac{[\log(r/R_i)]^2}{2(\log\sigma_i)^2}\right) \quad (5)$$

The parameters of these distributions are fitted to the measurements of the aerosol particle spectrum observed during the campaign. Figure 1 shows the measured and fitted spectra for three different "golden days" of the ACE-2 experiment: 26 June 1997 (maritime case), 09 July 1997 (case of strong pollution) and 19 July (case of mean pollution).

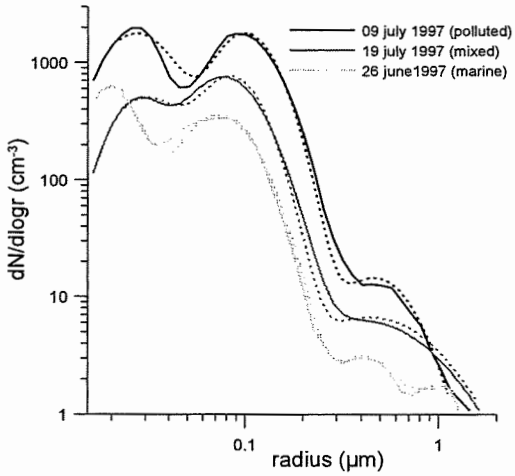

Figure 1: *Dry aerosol particles spectra measured (full line) and fitted (dotted line) for the polluted case-09 July (black), the mixed case-19 July (grey) and the maritime case-26 June (bright grey)*

We decide to divide each of the microphysical distributions (aerosol particles and droplets) in 39 bins, reaching from r = 0.0219 μm to 1.76 μm for the aerosol particle distributions and from r = 1.25 μm to 100.3 μm for the droplet distributions.

In the first part of our study, we simulate the formation and evolution of a stratocumulus cloud observed the 19 July 1997 and we compare our results with some observations made during this day. Then, sensitivity studies are made with respect to the initial dry aerosol particle spectrum. In these studies, simulations are performed with the aerosol particle spectrum measured the 26 June 1997 (less aerosol particles) and measured the 09 July 1997 (significantly more aerosol particles) in order to study the effects on the microphysics of the cloud layer. The results are presented in the next section.

4. RESULTS AND DISCUSSIONS

4.1 The stratocumulus cloud of the 19 July 1997

We first compared our results with the measurements studies of Pawlowska and Brenguier (2003). After one hour of model time a cloud has formed and during the following two hours the stratocumulus developed a persistent dynamical

and microphysical structure. We define a cloud once the mixing ratio of cloud water exceeds 0.025 g/kg. The cloud develops at an altitude between 1050 and 1250 m which corresponds quite well to the observations. The cloud cover simulated is around 65% and the horizontal and vertical cross sections show the existence of "holes" which were confirmed by the aircraft measurements. This shows the ability of our cloud model to reproduce the horizontal and vertical heterogeneity of stratocumulus clouds.

Looking at the cloud water mixing ratio, q_c, after 90 min of integration, we find a maximum of 0.37 g/kg and the maximum simulated cloud droplets concentration, N_{drops}, at 1150 m altitude around 180 cm^{-3}. These results are compared with the analysis of Pawlowska and Brenguier (2003) in Table 2.

	Cloud cover	q_c	N_{drops}
Pawlowska and Brenguier (2003)	87%	0.2 g/kg (average)	134 cm^{-3} (average)
Simulations	65%	0.37 g/kg (maximum)	180 cm^{-3} (maximum)

Table 2: *Comparisons between observed and simulated fields.*

We note that the macroscopic and microscopic characteristics of the simulated stratocumulus are in reasonable agreement with the observations made during the campaign except for the cloud cover where the measurements depend on the selected flight tracks of the aircraft.

One of the advantages of our bin model is that it allows comparing the microphysical properties of the simulated cloud, i.e. especially droplet distribution fields, with the measurements made by the aircraft in the cloud during the campaign.

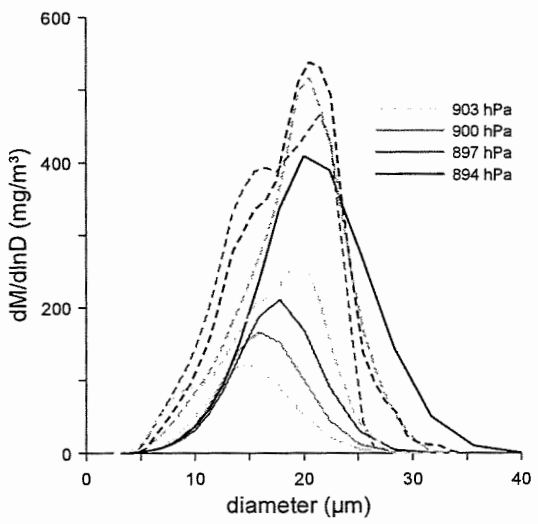

Figure 2: *Droplets spectra observed (dashed line) and simulated (full line) in the cloud top for different altitudes.*

Figure 2 shows the observed and simulated droplet size distribution for different altitudes near the top of the cloud.

We notice that the vertical heterogeneity is well reproduced and that the simulated spectra are in a quite good agreement with the measured ones.

Thus, DESCAM-3D, linked with the dynamical model of Clark, seems to reproduce the stratocumulus field in a quite good way as well as the microphysics of this cloud field.

Below, we present a sensitivity study of the initial dry aerosol particles spectrum and the impact on the previous results.

4.1 Sensitivity study of the initial aerosol

We performed two other simulations by replacing the initial dry aerosol particles spectrum by those measured during 26 June 1997 (maritime case - less aerosol particles) and 09 July 1997 (polluted case - more aerosol particles). The results show that an increase of the aerosol particles number causes also an increase in the cloud droplets concentration. The modelled droplets are smaller and the water cloud mixing ratio decreases slightly. These results are summarised in the Table 3, where we present, after 90 min of integration, the maximum cloud droplet concentration, N_{drops}, at 1150 m for every case as well as the maximum cloud water mixing ratio.

	Cloud cover	q_c	N_{drops}
Aerosol of the 26 June 1997	68%	0.39 g/kg	110 cm^{-3}
Aerosol of the 19 July 1997	65%	0.37 g/kg	180 cm^{-3}
Aerosol of the 09 July 1997	60%	0.35 g/kg	460 cm^{-3}

Table 3: *Results of the simulated fields by changing the initial dry aerosol particles spectrum.*

Figure 3 presents the simulated spectra for the three different initialisations after 85 min of model time.

We can note here again that an increase in the initial aerosol particle number produces droplet distributions centred on smaller diameters. This is a well known effect of the increase of the aerosol particles concentration in the atmosphere and shows the good response of our cloud model to such modifications.

5. CONCLUSIONS

A three dimensional cloud model with warm spectral microphysics has been presented in order to understand the interactions between aerosol particles and drops in stratocumulus clouds. This cloud model, called DESCAM-3D, contains a detailed representation of aerosol particle spectra in the interstitial air and in the drops as well as droplet spectra, includes the processes of nucleation, condensation/evaporation, collision/coalescence,

break up, sedimentation and scavenging of the aerosol particles by cloud droplets. This cloud model is linked to the 3D non-hydrostatic mesoscale dynamical model of Clark.

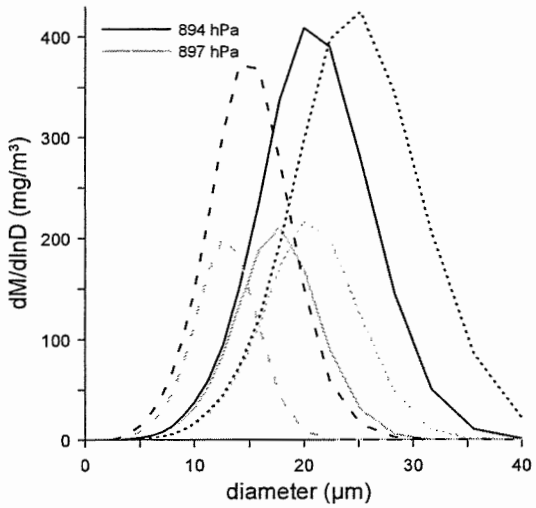

Figure 3: *Simulated droplets spectra for different altitudes for the maritime case (dotted line), the mixed case solid line) and the polluted case dashed line).*

First, we presented a simulation concerning the formation and the evolution of a stratocumulus cloud over the sea observed during the ACE2 campaign the 19 July 1997. Our results have been compared with observations and show a reasonable agreement. Then, a sensitivity study has been performed by changing the initial dry aerosol particles spectrum in the air. These spectra were measured during the campaign for two other different air masses (maritime and polluted).
Results show a good ability of our model to reproduce the response of such modifications.

Our model will be now very useful to test and improve the parameterisations of warm microphysics in bulk models and to show the role of the nucleation of cloud droplets on an aerosol spectrum for the formation of clouds.

Acknowledgments. The authors acknowledge with gratitude the Institut du Développement et des Ressources en Informatique Scientifique (IDRIS, CNRS) in Orsay (France) for the hours of computer time and the support provided. Furthermore, the authors acknowledge the support provided by the French national program PATOM.

6. REFERENCES

Clark, T.L., Hall, W.D., Coen, J., 1996: Source code documentation for the Clark-Hall cloud scale model, code version G3CH01; NCAR/TN-426+STNRCAR Technical Note, 1996, NCAR, Boulder, CO, USA.
Clark, T.L., 1979: Numerical simulations with a three-dimensional cloud model. *J. Atmos. Sci.*, **36**, 2191-2215.
Flossmann, A.I and H.R. Pruppacher, 1988: A theoretical study of the wet removal of atmospheric pollutants. Part II: The uptake, redistribution, and deposition of (NH4)2SO4 particles by a convective cloud using a two-dimensional cloud dynamics model. *J. Atmos. Sci.*, **45**, 1857-1871.
Khain A. P., D. Rosenfeld and A. Pokrovsky, 2001: Simulation of deep convective clouds with sustained supercooled liquid water down to -37.5 C using a spectral microphysics model. *Geophysical Research Letters*, 3887-3890.
Kogan Y.L., 1991: The simulation of a convective cloud in a 3D model with explicit microphysics. Part I: Model description and sensitivity experiments. *J. Atmos. Sci.*, **48**, 1160-1189.
Pawlowska, H. and J.L. Brenguier, 2003: An observational study of drizzle formation in stratocumulus clouds for general circulation model (GCM) parameterizations. *J. Geoph. Res.*, **108 (D15)**, 8630, doi:10.1029/2002JD002679.

CLOUD CONDENSATION NUCLEI IN CLEAR AND POLLUTED ATMOSPHERIC CONDITIONS IN THE AMAZONIAN REGION

Martins, J.A.[1,2], Gonçalves, F.L.T.[2], Oliveira, J.C.P.[3], Costa, A.A.[4,6], Leal Júnior, J.B.V.[5], Silva Dias, M.A.[2]

[1] Centro Federal de Educação Tecnológica do Paraná, C. Procópio, PR, Brazil

[2] Departamento de Ciências Atmosféricas, IAG/USP, São Paulo, SP, Brazil

[3] Universidade Federal do Ceará, Fortaleza ,CE, Brazil

[4] Fundação Cearense de Meteorologia e Recursos Hídricos, Fortaleza ,CE, Brazil

[5] Universidade Estadual do Ceará, Fortaleza, CE, Brazil

[6] Yale University, New Haven, CT, USA

1. INTRODUCTION

The cloud condensation nuclei (CCN) characteristics are quite relevant in the rainfall structure development as well as in the atmospheric radiation balance. There are several investigations dealing with CCN vertical distributions in order to understand the precipitation development (Squires and Twomey, 1966; Twomey and Wojciechowski, 1969; Hoppel et al., 1973), and with air pollution from industrial sources (Hobbs et al., 1970; Fitzgerald and Spyers-Duran, 1973; Eagan et al., 1974; Hindman et al., 1977) or from biomass burning (Warner and Twomey, 1967; Hobbs and Radke, 1969; Eagan et al., 1974; Rosenfeld, 1999; Sherwood, 2002). However, there are only few studies about tropical regions.

Amazonian region has a large inter-seasonal variability related to the large emission of aerosols due to the biomass burning activity during the dry season. Consequently, CCN should also present a similar behavior, with local measurements providing this high variability from polluted to clean conditions during this period.

The local measurements were obtained, during the Large Scale Biosphere-Atmosphere Experiment in Amazonia (LBA), which has been developed since 1999 as reported in Silva Dias et al. (2002). The data were collected during September and October 2002, including the end of dry season as well as the beginning of wet season.

Corresponding author's address: Jorge A. Martins
Rua do Matão, 1226 – Cidade Universitária USP
05508-900 São Paulo, SP Brazil
e-mail: jmartins@model.iag.usp.br

2. METHODOLOGY

The air sampling measurements were obtained from aircraft flights conducted from September 21 to October 15, 2002. The flights were carried out at the Southwest part of the Amazonian Basin including the Brazilian States of Acre, Amazonas, Mato Grosso and Rondônia (Figure 1). In the States of Acre and Amazonas there were clean atmospheric conditions while the others presented biomass burning activities.

Fig. 1. The map shows the States and main cities: Cruzeiro do Sul (CS), Rio Branco (RB), Porto Velho (PV), Ji-Paraná (JP), Vilhena (VL) and Alta Floresta (AF).

The flight measurements were conducted by the aircraft Embraer-Bandeirante as described in

Almeida et al. (1992). A static thermal-gradient chamber at the following supersaturations sampled CCN concentrations: 0.2%, 0.3%, 0.5% and 0.7%. Although these results are still preliminary, they compare CCN concentrations with clean and polluted atmospheric conditions.

Table 1 shows a summary of the flights conducted during this LBA Campaign period. The first line indicates the day with flight measurements from September 21 to October 13. The second line shows the flight initial and final times (in UTC). When two or more flights were conducted at the same day, different letters were used in order to identify each one. At the end, more than forty flight hours were performed during the Campaign.

TABLE 1 FLIGHT SUMMARY FROM 2002/09/21 TO 2002/10/13

DAY	21	23	24	26	27	28	30a	30b	01a	01b	04a	04b
TIME	17:24	18:07	18:43	18:02	18:27	17:37	15:14	17:49	14:16	18:47	15:06	17:54
(UTC)	19:30	20:16	21:04	20:18	20:03	19:38	16:17	20:40	16:25	21:20	16:25	19:49

DAY	04c	05a	05b	06a	06b	08	09	11a	11b	12	13	
TIME	20:48	16:13	19:24	15:12	18:19	18:53	17:32	14:43	17:21	15:45	17:20	
(UTC)	22:36	18:18	21:01	17:15	20:45	20:30	19:27	16:10	18:46	17:38	19:50	

3. RESULTS

The average CCN concentration was obtained in two layers, the first one from surface to 1000 m high and the second one from 1000 m to 1800 m high (see Figure 2). From this Figure, the average CCN concentration is shown with 0.5% supersaturation and the explanations for the differences will be discussed here. It is important to note that Figure 2 does not include fire spots in the calculations because it is taking in account only the atmosphere average conditions. The main results show a strong variability during the Campaign, which can be related to the large scale circulation, precipitation systems and horizontal variability of sampling. September 21 was the driest day of the Campaign with a high number of fire spots (the relative humidity was only about 40% during the afternoon period). September 24 night presented a nocturnal low level jet (supported by sounding data) which probably could explain a steeply CCN concentration decrease as well as the concentration difference between the two layers (around 55% for the first layer until 1000 m high). On the other hand, during September 28 a rainfall event started before the flight, which could explain the low CCN concentration (CCN concentration decreased by about 45%). During October 4 and 5, the flights occurred in the west of the region, where there was little biomass burning and the lower atmosphere was clean. During October 8 and 9, an intense precipitation system was present in the Rondônia State area, which could also clean the atmosphere, explaining the lowest CCN concentrations. It is possible to verify a general CCN concentration decrease from the beginning to the final period of the Campaign, from the dry to wet season, as expected (about 50% decrease).

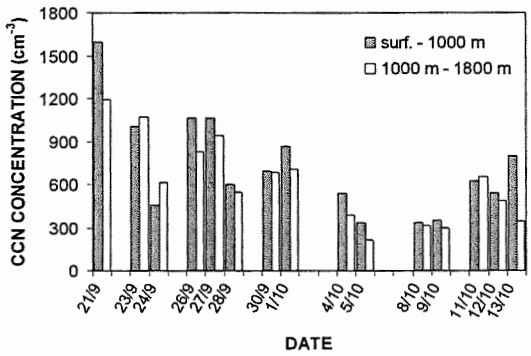

Fig. 2. Daily variability of CCN concentration obtained from aircraft measurements at 0.5% supersaturation for two layers near surface. Fire spots were not included in this analysis.

During some flights, the aircraft kept a steady altitude for hundreds of kilometers. Therefore, these flights provide a horizontal average of CCN concentration as altitude function. Figure 3 shows the average CCN spectra obtained from aircraft measurements at 0.5% supersaturation. The two letter groups are associated with flight location (AF - Alta Floresta, JP - Ji-Paraná, VL - Vilhena, RB - Rio Branco, CS - Cruzeiro do Sul, c.f. Figure 1). The samplings are related to the time they were performed in (a flight during the morning and the other in the afternoon) which shows interesting results about the CCN daily cycle. For example, the CCN average concentration obtained during the flight JP-AF (3100m high) is around half of the concentration during the flight AF-JP (3400m high), in spite of the fact that this later flight was performed in a higher level. On the other hand, both flights had similar trajectories, the first one

occurred at local time 11:00 AM (when biomass burning activity was starting) and the later occurred at 4:00 PM, after a long time of strong aerosol emission into the atmosphere. Another example, the flight JP-VL (1600 m high at 12:00 AM) was conducted when the emission was starting, within the boundary layer (BL) while the flight VL-JP (2600 m at 16:00 PM) was conducted after a long emission time, above the BL. Despite of similar profiles in both flights, it may be masking the results due to the level differences.

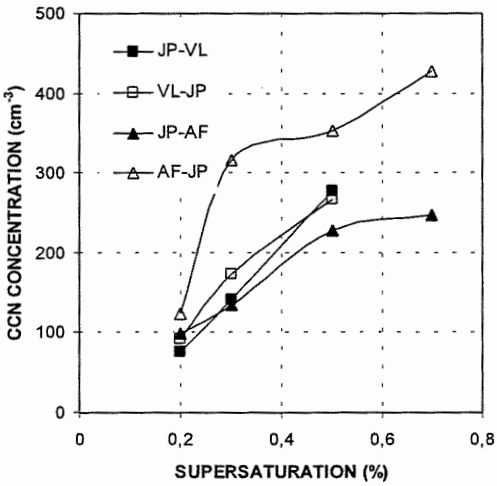

Fig. 3. CCN concentration as function of supersaturation measured during horizontal flights. The four letters indicate the cities where the flights had left and arrived (see map in the Fig. 1).

The CCN vertical profile is shown in Figure 4. This Figure presents the high amount of CCN concentration in low levels as expected due to the surface source of biomass burning. There were very polluted conditions observed during September 21 and 23, with high concentrations (more than 1000 cm^{-3}) within the boundary layer. It is interesting to note the differences between polluted (21/09, near JP) and clean (05/10, near CS) areas indicating the presence of a horizontal gradient of aerosol concentration. Within the boundary layer (from surface to 1800m high) JP shows a CCN concentration four times higher than CS, with 1395 cm^{-3} and 274 cm^{-3}, respectively. Considering the distance between the two sites as a reference, it is possible to conclude that the CCN concentration horizontal gradient is about 1 $cm^{-3}km^{-1}$ in Southeast-northwest direction. The gradient is quite strong due to the fire spot number of both areas. During dry season JP region presents a high fire spot density with extensive deforested areas while the region near CS presents intact rainforest and without biomass burning activity. According to the forest fire monitoring, provided by National Institute of Space Research (http://www.inpe.br), using data from NOAA 12, NOAA 16, TERRA 01, AQUA 01 and GOES 12 satellites, the number of fire spots detected, during September 21, was about 500 per 10^6 km^2 for Mato Grosso and Rondônia States and only about 30 for Acre and Amazonas States.

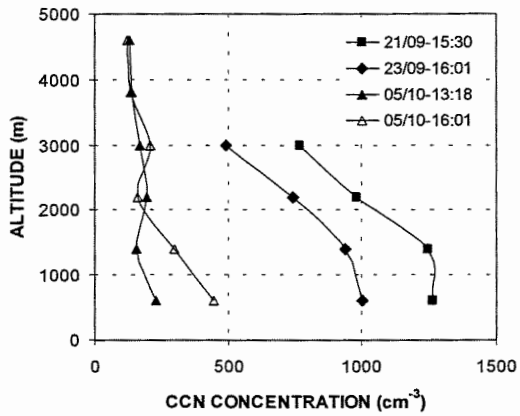

Fig. 4. CCN vertical profiles at 0.5% supersaturation. Dates and local times are indicating each sampling flight.

4. CONCLUSIONS

Aircraft CCN measurements were obtained in Amazonia during the LBA. The measurement flights were performed in the Southwest area of the Amazon Basin during the months of September and October 2002. The Campaign emphasized the dry to wet season transition which is linked to the biomass burning emissions. It is possible to verify that there is a general decrease of CCN concentrations from the dry season to the wet season. The main results indicate that the biomass burning contributes significantly to increase the CCN concentration in the atmosphere. The comparison between clean and polluted areas shows four times larger CCN concentrations over polluted areas. During the transition period, the results also show a daily cycle in the CCN concentrations, following the biomass burning activity, which accumulates high concentration levels inside of the boundary layer.

5. ACKNOWLEDGEMENTS

This study was supported by the Programa Institutos do Milênio/Conselho Nacional de Desenvolvimento Científico e Tecnológico (CNPq), Financiadora de Estudos e Projetos (FINEP) and Fundação de Amparo a Pesquisa do Estado de São Paulo (FAPESP).

6. REFERENCES

Almeida, F.C., Munroe, G.W., Morales, C.A.R., Pereira, M.C., Barros, F.A., Sampaio, A.J.C., Oliveira, J.C.P., 1992. An instrumented aircraft for tropical precipitation physics research: description and opportunity. *WMP report*, 19, 145-150.

Eagan, R. C., Hobbs, P. V., Hadke, L. F., 1974. Particle emissions from a large kraft paper mill and their effects on the microstructure of warm clouds. J. Appl. Meteorol., 13, 535-552.

Eagan, R. C., Hobbs, P. V., Hadke, L. F., 1974. Measurements of cloud condensation nuclei and cloud droplet size distributions in the vicinity of forest fires. J. Appl. Meteorol., 13, 553-557.

Fitzgerald, J.W., Spyers-Duran, P. A.,1973. Changes in cloud concentration and cloud droplet size distribution associated with pollution from St. Louis. J. Appl. Meteor., 12, 511-516.

Hindman, E. E., Hobbs, P. V., Radke, L. F., 1977. Cloud condensation nuclei from a paper mill. Part I: Measured effects on clouds. J. Appl. Meteor., 16, 745-752.

Hobbs, P. V., Radke, L. F., Shumway, S. E., 1970. Cloud condensation nuclei from industrial sources and their apparent influence on precipitation in Washington State. J. Atmos. Sci., 27, 81-89.

Hobbs, P.V., Radke, L.F., 1969. Cloud condensation nuclei from a simulated forest fire. Science, 163, 279-280.

Hoppel, W.A., Dinger, J.E., Ruskin, R.E., 1973. Vertical profiles of CCN at various geografical locations. J. Atmos. Sci., 30, 1410-1420.

Rosenfeld, D., 1999. TRMM observed first direct evidence of smoke from forest fires inhibiting rainfall. Geophysical Research Letters, 26, 3105-3108.

Sherwood, S., 2002. A microphysical connection among biomass burning, cumulus clouds, and stratospheric moisture. Science, 295, 1272-1275.

Silva Dias, M. A. F., Rutledge, S., Kabat, P., Silva Dias, P.L., Nobre, C., Fisch, G., Dolman, A.J., Zipser, E., Garstang, M., Manzi, A., Fuentes, J. D., Rocha, H., Marengo J., Plana-Fattori A., Sá, L., Alvalá R., Andreae, M. O., Artaxo, P., Gielow, R., Gatti, L., Clouds and rain processes in a biosphere atmosphere interaction context, J. Geophys. Res. 107, D20, LBA, pp. 39.1-39.20, 2002 doi: 10.1029/2001JD000335.

Squires, P., Twomey, S., 1966. A comparison of cloud nucleus measurements over central North America and the Caribbean Sea. J. Atmos. Sci., 23, 401-404.

Twomey, S., Wojciechowski, T.A., 1969. Observations of the geographical variation of the cloud nuclei. J. Atmos. Sci., 26, 684-688.

Warner, J., Twomey, S., 1967. The production of cloud nuclei by cane fires and the effect on cloud drops concentrations. J. Atmos. Sci., 24, 704-706.

OBSERVATIONS OF VERTICAL VARIABILITY OF CLOUD HYDROMETEORS IN STRATIFORM REGIONS BEHIND BOW ECHOES: IMPLICATIONS FOR DOWNDRAFT FORMATION

Greg M. McFarquhar, Michael S. Timlin, Robert Rauber, and Brian Jewett

University of Illinois at Urbana-Champaign, Urbana, IL

1. INTRODUCTION

Prior studies have shown that microphysical processes, such as sublimation, melting and evaporation, substantially influence the structure and dynamics of mesoscale convective systems (MCSs). For example, Biggerstaff and Houze (1991) and Braun and Houze (1994) showed that cooling associated with sublimation and melting forces the downdrafts that are observed near the melting level in the MCS transition zone. Braun and Houze (1996) also showed that the development of a rear inflow jet in the 10-11 June PRE-STORM squall line followed the onset of strong sublimative cooling at the back edge of the storm, with its magnitude strongly influenced by microphysical processes.

Modeling studies (e.g., Yang and Houze 1995) have also demonstrated the importance of microphysical processes to the development and intensity of the rear inflow jet in squall lines and have shown that microphysical processes within the stratiform region can generate strong subsidence and a wake low (Gallus 1996; Haertel and Johnson 2000). Despite these and other significant advances in the understanding of MCSs, processes leading to extreme surface winds that accompany some MCSs are still poorly understood. A quantitative understanding of the roles of evaporation, melting, and other processes in the evolution of MCSs and the accompanying severe surface winds have not yet been attained.

The Bow Echo and Mesoscale Vortex Experiment (BAMEX) was held over the central United States from May 20, 2003 to July 6, 2003 to investigate processes leading to the formation of bow echoes, severe windstorms, tornadoes and mesoscale convective vortices (MCVs) that are often part of a MCS. As part of BAMEX, the NOAA P-3 aircraft made extensive observations of the vertical variability of cloud microphysical properties in stratiform areas behind bow echoes. In this paper, the vertical profile of hydrometeor shapes, sizes, phases, and concentrations above, within, and below the melting layer are presented.

2. FLIGHT STRATEGY

During BAMEX, the NOAA P-3 and NRL P-3 flew in tandem, the NRL P-3 sampling the area in front of the convective line and the NOAA P-3 the stratiform regions behind the line. In addition to mapping the convective line with radars mounted on the P-3s, special microphysical modules were flown by the NOAA P-3 to document the vertical variability of the stratiform region and to examine interactions of the rear inflow jet with hydrometeor microphysics to evaluate hypotheses related to the role of latent cooling processes in driving high mid-level winds down to the surface.

To map the vertical profile of hydrometeor shapes, sizes and phases above, within and below the melting layer, 17 Lagrangian spiral descents were performed through horizontally extensive stratiform areas. During these descents, the NOAA P-3 flew circles of about 5 km radius in storm relative coordinates so that a constant distance from the leading convective line was maintained. For the first spirals, the P-3 descended at approximately 1 m s^{-1} above the melting layer and approximately 5 m s^{-1} below the melting layer to match the expected fall speeds of hydrometeors, in order to trace the evolution of the same population of particles. To increase the number of spirals and to reduce problems associated with aircraft charging, the descent rate above the melting layer was increased to 5 m s^{-1} for spirals flown during the second half of the project.

The NOAA P-3 was equipped with a two-dimensional cloud probe (2DC), nominally sizing particles between 50 and 1600 μm, and a two-dimensional precipitation probe (2DP), sizing between 200 and 6400 μm. Other than the June 22, 2003 flight, when the 2DP did not work, both probes worked on all days. The data were processed using software designed at NCAR (W. Hall, personal communication 2001) that was modified to accommodate the P-3 data structures. Although clear-air updating and stuck bits were occasionally observed on some flights, the probes functioned well and the 2DC and 2DP size distributions agreed remarkably well in the overlap region of approximately 1200 μm. To the best of our knowledge, these observations represent the first data of cloud microphysical properties acquired behind bow echoes.

3. BAMEX OBSERVATIONS

On June 29, 2003, the complete life cycle of a bowing segment of a MCS was sampled over north central Kansas. The cells in the system were tracking eastward during the time of the spiral descents and the NOAA P-3 penetrated into a notch behind the bowing segment of the line. Observations acquired by the NOAA tail radar immediately before the first spiral descent indicated a significant tilt or slope in the radar bright band, with the melting layer extending to progressively lower heights closer to the line. The spiral

Corresponding Author: Prof. McFarquhar, University of Illinois, Dept. of Atmospheric Science, 105 S. Gregory Street, Urbana, IL, 61801, email: mcfarq@atmos.uiuc.edu.

descent was conducted right in the rear inflow jet at an early stage in the lifetime of the bow echo, when there was not yet an extensive stratiform region present. This particular spiral is unique because most other spirals were conducted during mature or dissipating stages of the bow when a more extensive stratiform region existed.

Figure 1 shows hydrometeors imaged by the 2DC during this spiral. Significant amounts of graupel are likely present given the quasi-spherical shapes of the crystals. Larger aggregate snowflakes are also observed in the 2DP images (not shown). One unique aspect of this spiral is the presence of ice to temperatures as great as 7°C, most likely due to its position in the rear inflow jet. Most other cases did not show solid particles at temperatures above approximately 2°C.

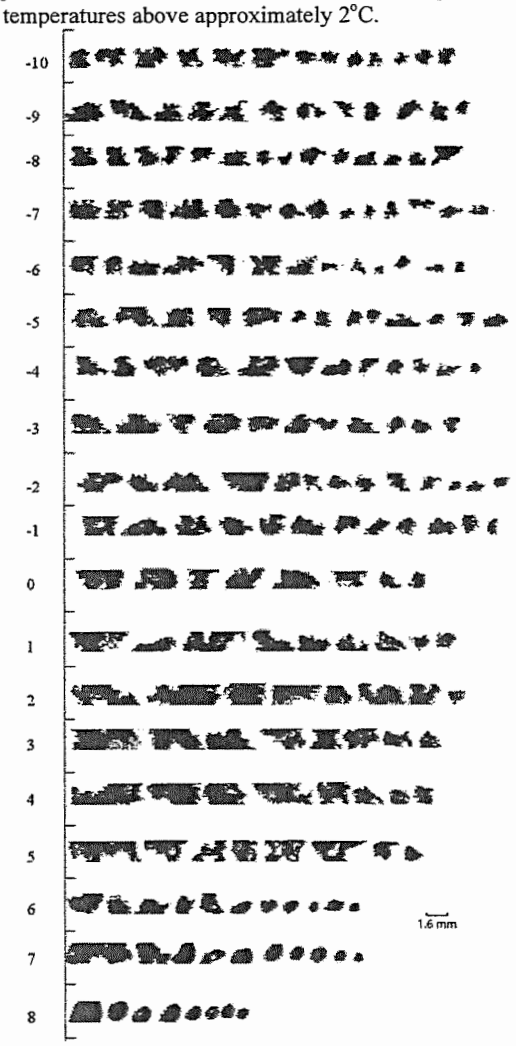

Figure 1: Examples of particles imaged at different times during spiral descent behind bow echo on June 29, 2003, 0525 to 0539 UTC.

Figure 2 shows particles imaged two hours later in a more extensive bright band at a time when there was no longer a strong tilt in the bright band. This spiral was made at a time when the bow echo was no longer in the developing or mature stage, and although the quasi-spherical particles (i.e., graupel) still occur, the solid particles are melted for temperatures above about 2°C. This suggests that the strong downdrafts are no longer transporting the graupel to low levels. Another major difference between the first and second spiral is the measured humidity, especially for temperatures above 0°C. For the first spiral, dew point depressions were up to 8.5°C, whereas for the second spiral they were only up to 1.2°C. The rapid descent of the rear inflow jet at the time of the first spiral likely caused compressional warming, leading to drier air.

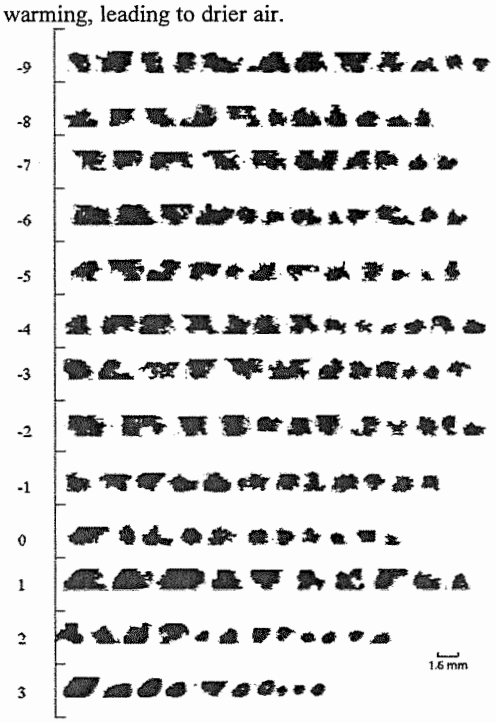

Figure 2: As in Fig. 1, except at the time of the second spiral between 0729 to 0741 UTC.

To quantitatively examine vertical profiles of cloud properties in these stratiform regions, the total number concentration and size distributions are plotted for all spirals as a function of temperature. Figure 3 shows the evolution of the size distributions with temperature during the first spiral descent on June 29. Although a small decrease in small particle concentration occurs between –4 and –6°C, strong evidence for aggregation is not seen as the sizes of particles or concentrations of larger crystals does not increase. The decrease in small crystal concentration between –4 and –6°C may be associated with horizontal variations in the stratiform region given the 5 km turning radius of the P-3.

The horizontal inhomogeneities are more clearly seen in early spirals when the P-3 descended at 1 m s^{-1} above 0°C because the same population of particles were sampled in sequential turns and because the longer spiral meant more samples were obtained at the same

horizontal location. Figure 4 shows the temperature dependence of the size distribution during a slow spiral on June 2, 2003, obtained behind a small bowing segment of a MCS over southeast Arkansas. Cyclical pulsations in the concentrations of small and medium sized particles are noted at time periods of about 3 minutes, corresponding to the time period of the spirals.

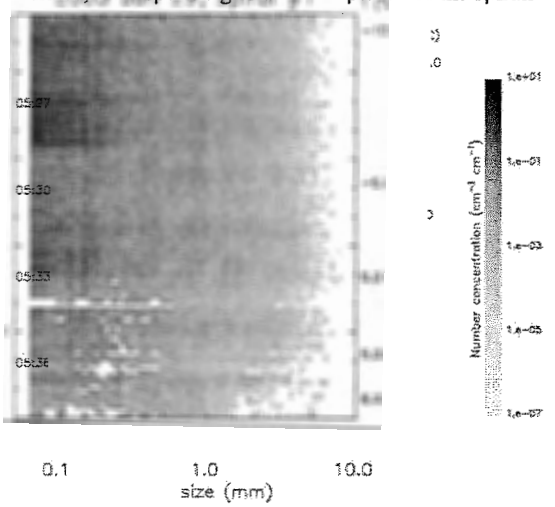

Figure 3: Number concentration, from 2DC and 2DP, as function of time and temperature for first spiral on June 29, 2003 (0525-0539 UTC). The 2DC gives the size distribution for sizes larger than 1.2 mm, and the 2DP for sizes above.

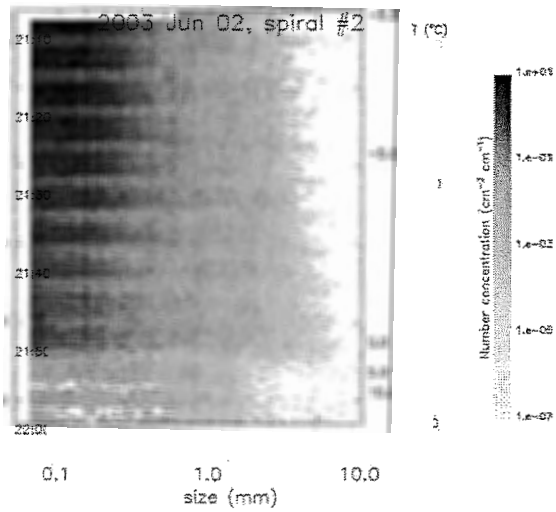

Figure 4: As in Fig. 2, except for second spiral conducted on June 2, 2003 (2110 to 2203 UTC).

Trends noted in Fig. 4 are different than in Fig. 3. Despite the horizontal variability in Fig. 4, aggregation is clearly seen above the melting layer at 2°C with a gradual decrease in small crystal number for each penetration, and a gradual increase in both the sizes and concentrations of larger crystals. A strong increase in the number and sizes of large particles is seen between 0 and 2°C, likely caused by aggregation that becomes increasingly important once melting starts. This was also seen in many other spirals, and by Willis and Heymsfield (1989) behind MCSs and by Heymsfield et al. (2002) in deep tropical cirrus and stratiform precipitating clouds. However, there is no evidence of this aggregation between 0 and 7°C for the first spiral sampled in the rear inflow jet in a dry and less extensive region of stratiform cloud sampled on June 29, 2003; instead, given the large dew-point depressions and rapid decrease of mass and number, it is suggested that significant sublimation was present between 0 and 7°C, where melting abruptly occurs.

4. FITS TO OBSERVED DISTRIBUTIONS

To quantify the dependence of size distributions on temperature, to intercompare spirals, and to place observations in a form conducive for use by numerical models, distributions were fit to analytic functions. Because small crystals made substantial contributions to measured distributions, exponential functions did not adequately describe them. Therefore, the size distributions were characterized by gamma functions,

$$N(D) = N_0 D^{\mu} e^{-\lambda D} \qquad (1)$$

where the parameters of the fit are obtained by a non-linear Levenberg-Marquardt fitting algorithm which minimizes χ^2 describing differences between observed and fitted distributions.

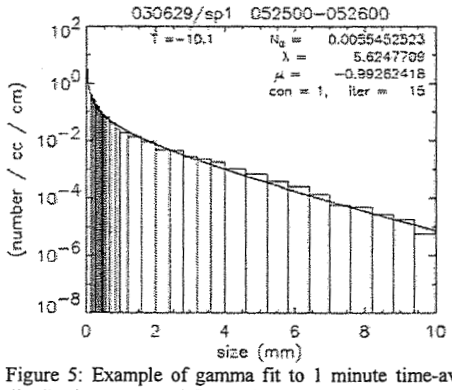

Figure 5: Example of gamma fit to 1 minute time-averaged size distribution measured June 29, 2003, 0525-0526 UTC. Particles smaller than 1200 μm measured by 2DC, larger by 2DP.

Figure 5 shows a typical fit to a one-minute averaged size distribution observed at –4°C on June 29. The μ of approximately –1 gives a good fit to the data. Figure 6 illustrates the variation of the slope parameter λ with temperature for the June 29 spiral, where the downdrafts pushed the ice down to temperatures of 7°C. λ has an almost constant value about 5 cm^{-1} during the spiral, then increases to about 30 cm^{-1} when melting occurs. The solid line, representing observations of deep tropical cirrus and precipitating stratiform clouds, shows λ larger than those observed behind the bow echoes, suggesting more large particles occur behind the bow than in observations not directly behind bow echoes (Willis and Heymsfield 1989; Heymsfield et al. 2002).

Figure 7, illustrating the temperature-dependence of λ for the spiral on June 2, shows different behavior than in Fig. 6. A gradual decrease of λ with temperature, most likely due to aggregation, occurs up to approximately 2°C, after which a sharp jump in λ corresponding to melting is observed. This behavior is more commonly seen in the spiral observations than that in Fig. 6, perhaps because few stratiform areas were sampled in the rear inflow jet and at early stages in the development of the MCS.

The parameters N_0, λ, and μ are not independent, and relationships between them for all 17 spirals will be shown at the meeting. There are essentially 2 clusters of points observed when plotting relationships between N_0, λ, and μ, with one family corresponding to situations where melting has and has not yet occurred. These types of relationships are not only useful for numerical model parameterizations, but also for determining the role of evaporation, melting, and sublimation in the development and maintenance of rear inflow jets and severe surface winds.

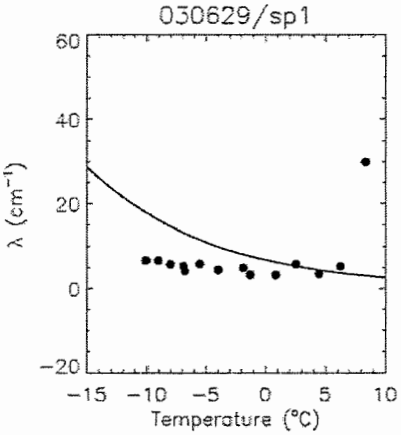

Figure 6: λ as function of temperature based on fits to 1-minute averaged size distributions observed during first spiral, June 29, 2003. Heymsfield et al. (2002) λ values, observed in deep tropical anvils and precipitating stratiform clouds, given by solid line.

5. CONCLUSIONS

Observations obtained during BAMEX characterize the vertical and horizontal variability of stratiform areas behind bow echoes. Substantial differences in the characteristics are noted depending on the location of the observations behind the bow, the life cycle stage, the strength and location of the rear inflow jet, and other storm characteristics. These observations are currently being used to further our understanding on the role of microphysical processes in MCSs and bow echo evolution, and to determine whether microphysical or dynamical processes are most responsible for severe surface winds that are frequently associated with such systems.

6. ACKNOWLEDGMENTS

This research was sponsored by the National Science Foundation (NSF) Dynamics Program. The findings reported here do not necessarily represent the views of NSF. The efforts of Sean McMillan, Bobby Peek, and the NOAA flight crew in the acquisition of high quality data are acknowledged. W. Hall and R. Black provided preliminary versions of some processing programs.

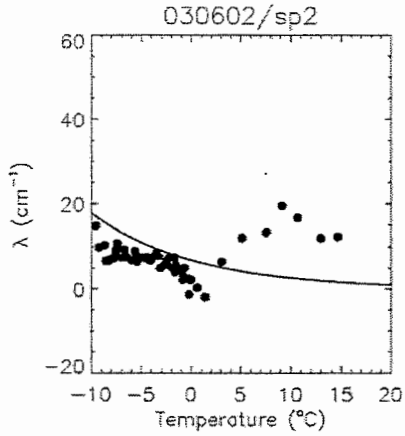

Figure 7: As in Fig. 6, except for second spiral on June 2, 2003, between 2110 and 2203.

7. REFERENCES

Biggerstaff, M.I., and R.A. Houze, Jr., 1991: Kinematic and precipitation structure of the 10-11 June 1985 squall line. *Mon. Wea. Rev.*, **119**, 3034-3065.

Braun, S.A., and R.A. Houze, Jr., 1994: The transition zone and secondary maximum of radar reflectivity behind a midlatitude squall line: results retrieved from Doppler radar data. *J. Atmos. Sci.*, **51**, 2733-2755.

Braun, S.A., and R.A. Houze, Jr., 1996: The heat budget of a midlatitude squall line and implications for potential vorticity production. *J. Atmos. Sci.*, **53**, 1217-1240.

Gallus, W.A., 1996: The influence of microphysics in the formation of intense wake lows: a numerical modeling study. *Mon. Wea. Rev.*, **124**, 2267-2281.

Haertel, P.T., and R.H. Johnson, 2000: The linear dynamics of squall line mesohighs and wake lows. *J. Atmos. Sci.*, **57**, 93-107.

Heymsfield, A.J., and 7 Co-authors, 2002: Observations and parameterizations of particle size distributions in deep tropical cirrus and stratiform precipitating clouds: results from in situ observations in TRMM field campaigns. *J. Atmos. Sci.*, **59**, 3457-3491.

Willis, P.T., and A.J. Heymsfield, 1989: Structure of the melting layer in mesoscale convective system stratiform precipitation. *J. Atmos. Sci.*, **46**, 2008-2025.

Yang, M.J., and R.A. Houze Jr., 1995: Sensitivity of squall line rear inflow to ice microphysics and relative humidity. *Mon. Wea. Rev.*, **123**, 3175-1393.

ANALYSIS OF DIFFERENT CLOUD MODELS' OUTPUT OF THE SAME STORM FOR CLOUD RADIATION DATABASE GENERATION

Medaglia C.M.[1], Dietrich S.[1], Kotroni V.[2], Di Michele S.[1], Adamo C.[1], .Bechini R.[4], Tripoli G. J.[3],and K. Lagouvardos[2]

(1) Institute of Atmospheric Sciences and Climate, CNR, Roma, Italy (c.medaglia@isac.cnr.it / fax +39 6 2066 0291)
(2) Institute for Environmental Research, NOA, Athens, Greece
(3) Department of Atmospheric and Oceanic Sciences, UW, Madison, Wisconsin, USA,
(4) ARPA Piemonte, Settore Meteoidrografico e Reti di Monitoraggio, Turin, Italy

1 INTRODUCTION

The generation of physically-based Cloud Radiation Databases (CRDs) to be used for inverting microwave satellite observations of radiometers– like the Tropical Rainfall Measuring Mission Microwave Imager (TMI), the Special Sensor Microwave Imager (SSM/I) and the Advanced Microwave Scanning Radiometer (AMSR) – is a difficult task. Nowaday, sophisticated physically-based retrieval algorithms make use of CRDs composed of thousands of detailed microphysical cloud profiles, obtained from the output of cloud-resolving models, coupled with the corresponding brightness temperatures, calculated by applying Radiative Transfer (RT) schemes. The complete verification of simulated microphysics is still not possible due to the incredible amount of different sensors and measurements techniques necessary [illegible] the consistency of model outputs,

Italian peninsula, raising surface temperatures up to 25° C in northwest Sardinia (Alghero).
On 25th November, the storm system moved towards the eastern area of the Alps, spawning intense thunderstorms, and in some cases hail, over Lombardia and Friuli. Heavy rains continued into 26th November when the precipitation terminated in response to subsidence from a high pressure system centered over eastern Europe.

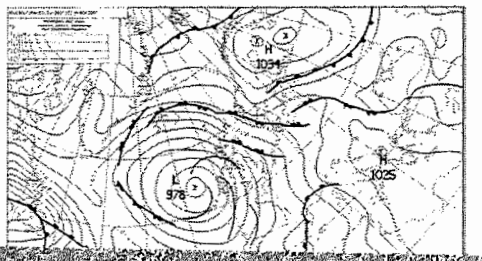

AN EXAMINATION OF THE IMPACT OF DRIZZLE DROPS ON SATELLITE-RETRIEVED EFFECTIVE PARTICLE SIZES

Patrick Minnis[1], Robert F. Arduini[2], David F. Young[1], J. Kirk Ayers,[3], Bruce A. Albrecht[4]
Tarah Sharon[4], Bjorn Stevens[5]

[1]Atmospheric Sciences, NASA Langley Research Center, Hampton, VA, 23681 USA
[2]SAIC, Hampton, VA 23666 USA
[3]AS&M, Inc., Hampton, VA 23666 USA
[4]University of Miami, Miami, FL 33149 USA
[5]University of California at Los Angeles, Los Angeles, CA 90095 USA

1. INTRODUCTION

conditions were monitored and recorded with a weather station located besides the OAP's. Rainfall rates were derived from the precipitation

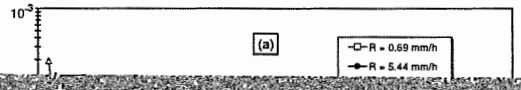

STATISTICAL ANALYSIS OF MICRO RAIN RADAR SPECTRA

I.V. Petenko[1] and Gerhard Peters[2]

[1]Oboukhov Institute of Atmospheric Physics RAS, Pyzhevsky 3, 109017 Moscow, Russia,
[2]Meteorologisches Institut, Universität Hamburg, Bundesstrasse 55, D-20146 Hamburg, Germany

1. INTRODUCTION

New insights into the behavior of spatial and temporal structure of precipitation can be obtained using short time (□ 1 min) average data on Doppler spectra measured with high vertical resolution (□ 100 m) by a micro rain radar, as well as a cloud radar. Some recent studies (Peters et al., 2003) show that Doppler spectra obtained by rain and cloud radars normally have rather complicated shapes which seem to reflect the complicated microphysical structure of precipitation. The form of observed spectra is quite variable both in time and with height. Visual inspection of the measured Doppler spectra shows that often they have a non-uniform complicated form indicating the presence of more than one mode. From a statistical point of view, the indication of the presence of multi-modal structures can come from the estimation of the third and forth moments, or, that is more suitable in practice, from the estimation of skewness and kurtosis values. The detection of multi-modal structures in some cases may not be so trivial. Sometimes, the presence of real bimodality is masked when one of the modes is substantially larger than others and they are close enough in frequency. Petenko and Shurygin (2000) considered the possibility of presentation of functions having an asymmetric form as a combination of two gaussians earlier for different atmospheric applications. In this study, a Doppler spectra data set obtained with a vertically pointing 24 GHz Micro Rain Radar (MRR) by Metek [Peters et al., 2002] with 1 min time resolution and 100 m height resolution deployed on the German Baltic coast (Zingst peninsula) in 2002 was analyzed. The purpose of this study was () to develop the statistical processing algorithms for the measured Doppler spectra, taking into account their multi-modal structure observed during rain events, (ii) to develop the clear forms of presentation of temporal and spatial variability of the statistics.

2. SPECTRAL MOMENTS ANALYSIS

From a visual inspection of measured micro rain radar spectra, it is possible to distinguish several typical forms of spectra. Examples of them are presented in Figure 1. The simplest form (Figure 1a), close to gaussian, is always observed above the melting layer. The spectra with negative asymmetry presented in Figure 1b and c are normally observed essentially below the melting layer. Spectra with positive asymmetry (Figure 1d and e) are normally observed just near the bottom of the melting layer and inside it. Three-modal spectra with distinguishable peaks (Figure 1f) occur preferrably at the lowest range gates or just below the melting layer.

A set of programs was developed to read, view, and process numerically the available spectral data set and to store the results. The Matlab computational language is used to process the data.

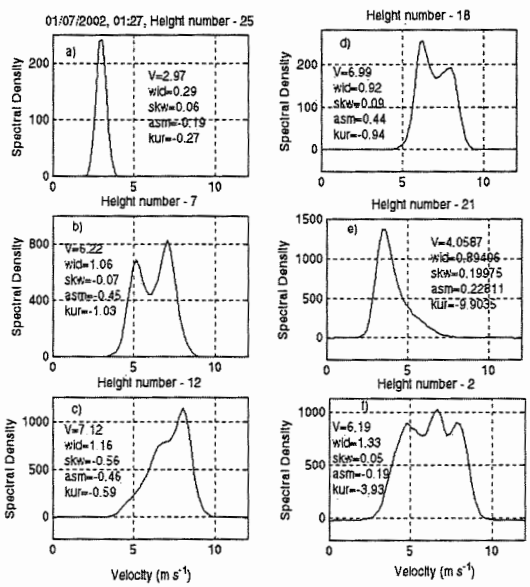

Figure 1. Examples of different types of spectra.

2.1 Profiles of Spectral Moments

The conventionally used first three moments, namely, the power (attributed to the reflectivity), the mean (velocity) and the variance (width of spectrum) are not sufficient to characterize properly the presented forms of observed spectra. To provide more statistical information on the form of spectra it we suggest considering the next two moments: the 3rd and 4th central moments, or, some combination with the 2nd moment, namely, skewness and kurtosis. The presented estimates of the moments are calculated from a periodogram using the conventional formulas.

Corresponding author's address: Igor V. Petenko, ISAC/CNR, Tor Vergata, Via Fosso del Cavaliere 100, Rome, 00133, Italy; E-mail: i.petenko@isac.cnr.it

The developed program shows plots of the height distribution of spectra (as waterfall presentation) sequentially for every 1-min profile. Simultaneously it shows every 1-min profile of all considered spectral moments (from 0th to 4th). Finally, it shows the plots of time variations of the spectral moments at some chosen heights averaged over some layer depth.

In Figure 2 an example of the height behavior of Doppler spectra (top panels; waterfall presentation) and vertical profiles of their moments (bottom panels) are given.

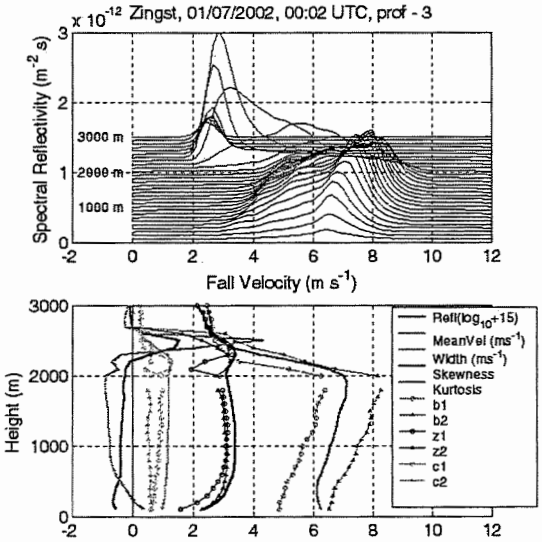

Figure 2. Example of 1-min Doppler spectra with the multi-modal structure (top panel) and profiles of their spectral moments and coefficients of gaussian modes (bottom panel).

One unusual feature should be noted. Sometimes a decrease of the mean velocity to the surface along the profile under the melting layer occurs. This behavior is not always observed, but during some rain events this tendency is prevailing.

2.1 Histograms of Spectral Moments

The average histograms for a given time interval and a layer depth are calculated. As an example of the results obtained with the suggested approach, we present histograms of the statistics calculated for one rain event. The height distributions of the occurrence percentage of the statistics estimated over two hours on 01 July 2002 are shown in Figures 3 separately for the mean and the width. The upper panels provide the waterfall presentation form of the height behavior. The bottom panels provide the same height distribution in the form of contour color plots. We give both the forms of presentation in order to provide more details of the behavior of the obtained height distribution of histograms of the statistics.

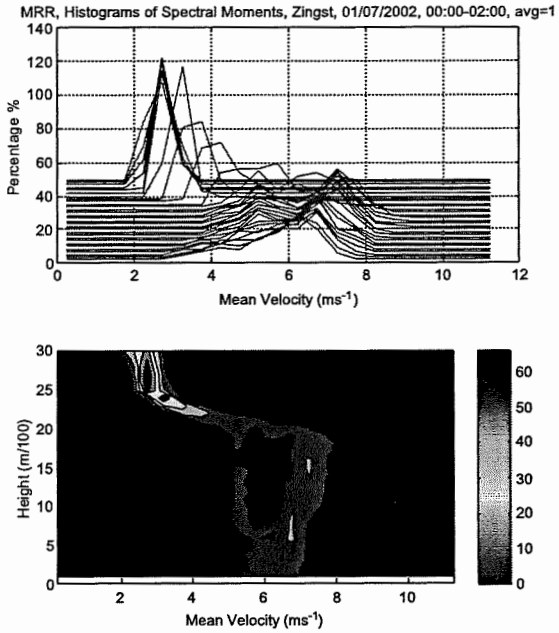

Figure 3. Example of the height behavior of the 1-hour histogram of the mean velocity. Top panel – waterfall presentation; bottom panel – contour plot.

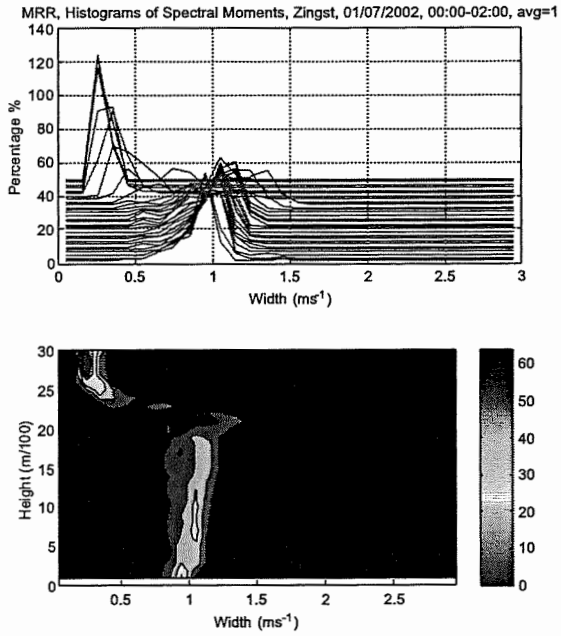

Figure 4. Example of the height behavior of the 1-hour histogram of the spectrum width. Top panel – waterfall presentation; bottom panel – contour plot.

The time variations of the estimated spectral moments at some heights during analyzed time intervals are given in Figure 5.

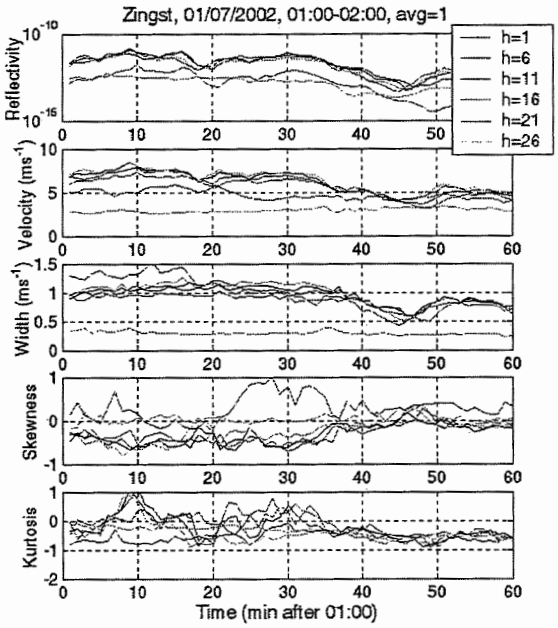

Figure 5. Example of the time behavior of the spectral moments at different heights.

The presented results allow us to make some conclusions about the features of the probability distribution of the spectral moment values. The first is that quite different properties of Doppler spectra are observed at the melting layer (above about 2000 m) and within the rain layer. All spectral moments are substantially different in these regions. In the melting layer they are close enough to the gaussian form, meanwhile within the layer of rain a large variety of spectral forms with essential asymmetry and flatness is observed.

3. DECOMPOSITION OF SPECTRA INTO GAUSSIAN MODES

Visual inspection of the form of a spectrum allows, in many cases, to reveal enough easy the presence of several modes, even if they do not show separated peaks. Meanwhile, the computational algorithms of automatic detection the multi-modal structure are not so trivial. A more often observed form of spectra is shown in Figures 1ñ to demonstrate the only maximum, but providing a clear idea about the presence of two modes.

The decomposition of spectra into two individual modes can be viewed as an advanced Doppler spectrum analysis. This idea was motivated by the visual inspection of the measured rain radar Doppler spectra. In this approach we assumed that a total spectrum $S(V)$ is the sum of two spectra $S_1(V)$ and $S_2(V)$. At this point, we restrict the algorithm to two modes. As a first rough approximation, each spectral mode can be described by the normal law:

$$S_i(V) = S_{0i}\frac{1}{c_i\sqrt{2\pi}}\cdot\exp\left[-\frac{(V-b_i)^2}{2c_i^2}\right],$$

where i = 1 or 2 is the number of the mode; b_i is the mean velocity , and c_i is the spectral width, $S_i(V)$ is the spectrum of the mode i , S_{0i} is the amplitude of the i-th mode. We number the modes according to the criteria $b_1<b_2$.

To realize computational algorithms of this approach, the Parametric Fitting procedure from MatLab Software was taken as a base. The method of least squares is used when fitting data. We use the Trust-region algorithm, because we specify coefficient constraints. To optimise calculation and to accelerate it we can constrain the coefficient starting values, based on some *a priori* information about the behavior of spectra characteristics. This information about the statistical distribution of spectral moments was obtained from the preliminary statistical processing of MMR Doppler spectra described above. Moreover, lower and upper bounds to constraint coefficients are estimated automatically for every individual spectrum from estimates of its spectral moments. The choice of the model (one or two gaussians) is also done automatically, based on preliminary spectral moment estimates. The main difficulty of this procedure is to determine a criteria to choose the proper number of gaussian modes, which is necessary to be taken for the fitting model. The final step of the procedure is evaluating the goodness of the fit. Two types of measures of goodness are used: graphical and numerical. The first is a visual examination of the displayed fitted curve. Moreover, the numerical values of the goodness of fit measures are provided.

Application of the developed procedure to real spectra showed a high goodness of fitting the spectra by the two-gaussian model in many observed cases. An example of decomposition of a spectrum into two gaussian modes is shown in Figure 6. The vertical profiles of the calculated parameters $z_i = \int S_i(V)dV$, b_i, and c_i corresponding to the reflectivity, mean velocity and width of spectral modes are given in Figure 2 together with vertical profiles of spectral moments of received spectra.

At the same time, there is a large number of cases when spectra indicate more complicated forms and the bi-gaussian model does not provide sufficient fitting. A special study to develop reliable algorithms to detect the number of modes > 2 is necessary.

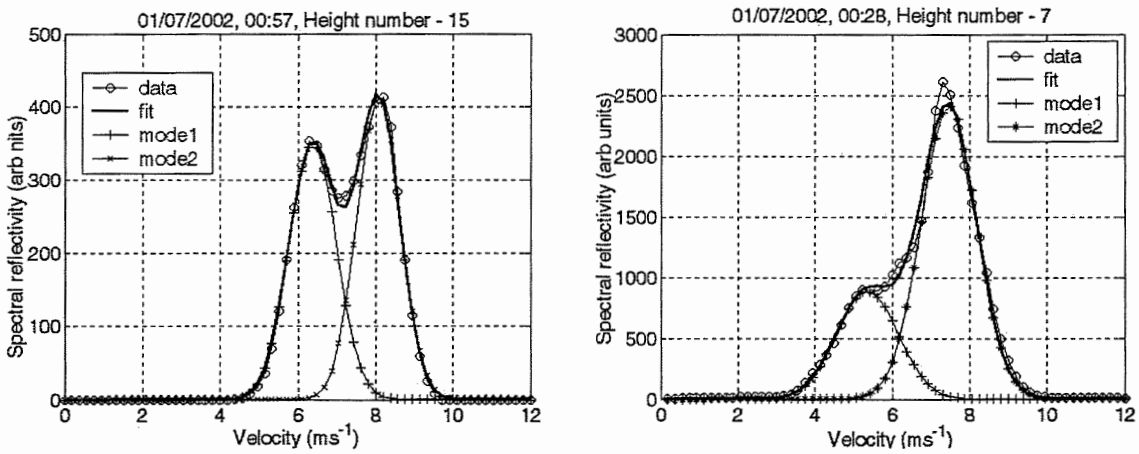

Figure 6. Examples of decomposition of 1-min Doppler spectra into two gaussian modes.

4. SUMMARY

The present work is a preliminary study of multi-modal structure of Doppler spectra observed with a 24 GHz micro rain radar with 1-min time and 100 m height resolution.

It was shown that the form of spectra in many cases indicate the presence of multiple modes. From visual inspection, several typical forms of spectra are revealed for different height ranges. Algorithms for statistical processing of the measured Doppler spectra, taking into account their multi-modal structure, were developed. It was suggested to use the higher order spectral moments (up to the fourth one) to have a more complete information about the form of spectra.

The performed analysis showed the substantial difference in the probability distribution of all spectral moments within and below the melting layer. The prevailing skewness and kurtosis values within the melting layer are close to zero evidencing that the form of Doppler spectra in this region is close to gaussian. Meanwhile, below the melting layer, mainly negative kurtosis values are observed being accompanied with non-zero skewness values having the probability tendency to be negative.

The behavior of histograms of the spectral moments can be considered as a possible criterion, which can be used for the classification of rain events.

One revealed feature that should be noted is the decrease up to the surface of the mean fall velocity, which was observed to be dominating during some rain events. This behavior is not always observed, but during some rain events is prevailing.

The decomposition of spectra into two individual modes was suggested as an advanced way of the analysis of Doppler spectra. In such approach it is assumed that a total spectrum can be considered as the combination of two gaussian spectra. The developed procedure applied to real spectra showed a high goodness of fitting the spectra by the two-gaussian model in many observed cases.

At the same time, there is a large number of cases when spectra indicate more complicated form, and the two-gaussian model does not provide sufficient fitting. Development of the retrieval algorithms for the decomposition procedure of spectra into three modes can be considered as a further desirable step in statistical analysis of the modal structure of Doppler spectra observed by rain and cloud radars.

But before this, the proper physical interpretation of the origin of these modes is necessary. This question is addressed to the experts in microphysical properties of precipitation. For the moment there are no clear ideas on the interpretation of modal structure of Doppler spectra, that should be paid attention in the further studies. As one of the possible reasons of multi-modal structure of 1-min average Doppler spectra we can assume the horizontal non-homogeneity of precipitation, so the alteration of areas with different rain rates can result in such spectral forms.

Acknowledgements

The authors are thankful to B. Fischer for his help in obtaining the experimental data. The study was carried out when Dr. I. Petenko was as a visiting scientist at the Meteorological Institute of the University of Hamburg.

References

Petenko, I.V., and E.A. Shurygin, 2000: A two-regime model of the probability density function of the temperature structure parameter in the convective boundary layer. Boundary-Layer Meteor., **93**, 381-394.

Peters, G., B. Fischer, and T. Andersson, 2002: Rain observations with a vertically looking Micro Rain Radar (MRR). Boreal Env. Res., **7**, 10 pp.

Peters, G., B. Fischer, M. Schrader, H. Münster, 2003: Fine structure of rain observed by Micro Radar. Proceedings of the 6th Intern. Symp. on Tropospheric Profiling, Leipzig, 14-20 September, 2003.

PROFILES OF MICROPHYSICAL RAIN PARAMETERS AS OBSERVED WITH MICRO RAIN RADARS

Gerhard Peters[1], Bernd Fischer[1], Hans Münster[2]

[1]Meteorologisches Institut, Universität Hamburg, Germany
[2]Max-Planck-Institut für Meteorologie, Hamburg, Germany

1. INTRODUCTION

The accuracy of quantitative radar-based precipitation estimation is not yet satisfying although much effort was devoted to reduce the typical "factor-2-uncertainty" during the past decades. Here we focus on two basic uncertainties of the measuring principle, namely the variability of drop size distributions and the fact that radar measurements aloft do not necessarily represent surface conditions. The last circumstance is often referred to as vertical reflectivity profile problem. Attempts to mitigate these uncertainties range from generalized formulations of drop size distributions [Sempere Torres *et al.*, 1994], [Testud *et al.*, 2001] and adapted R-Z -relations [Sempere Torres *et al.*, 2000] to the use of more sophisticated radars in order to obtain additional microphysical information e.g on the basis of polarimetric data [Bringi and Chandrasekar, 2001].

At present the validation of weather radar measurements is nearly solely based on surface data obtained with in-situ rain gauges or distrometers. As pointed out by Jameson and Kostinski [2001, 2002], even more sources of uncertainty and systematic errors can take effect in such comparisons due to the different spatial and temporal sampling characteristics of in-situ sensors and radars, respectively. In the best case, the combined effect of the above mentioned uncertainties can be captured in this way but the contributions can hardly be separated. The task, to pin down the various sources of uncertainty and bias, is difficult, as long as no simultaneous reference data are available in the radar scattering volume.

Here we return to the suggestion of Atlas *et al.* [1973] to use Doppler radar at vertical incidence for deriving the drop size distribution via the relation between terminal fall velocity and drop size. Special low power micro rain radars (MRR) operating at 24.1 GHz are used for this purpose. The characteristics and performance of these radars are described in more detail in Peters *et al.* [2002]. While no areal coverage is possible in this mode of radar operation, it allows the observation of the vertical structure of precipitation and of its microphysical parameters. This method is particular promising for supporting weather radar measurements, if the MRR profiles intersect with the weather radar beam. Simultaneous measurements in common volumes may eventually allow the use of continuously updated Z-R-relations. In addition, the on-going MRR observations form a data base to establish a better founded link between radar measurements aloft and precipitation at the surface. We show that significant transformations of drop size distributions can occur on the fall path between melting layer and ground with the consequence that the application of surface based R-Z-relations to radar reflectivity would yield erroneous rain fall.

Corresponding author's address: Gerhard Peters, Meteorologisches Institut, Universität Hamburg, Bundestraße 55, D 20146 Hamburg, Germany, E-Mail: peters@miraculix.dkrz.de

2. MRR MEASUREMENTS

A data set comprising 3 years, obtained with a vertically pointing Micro-Rain-Radar (MRR-2, Metek) at 54°26' N, 12°42' E on the peninsula Zingst at the German south coast of the Baltic Sea is analyzed. The radar resolves a height range from 100 to 3100 m into 31 range gates of 100 m depth with a sampling period of one minute. So far the analysis is restricted to measurements in the lower 1500 m during summer seasons, in order to remain safely below the melting layer.

The Doppler spectra, obtained at vertical incidence, reflect the fall velocity distribution of hydro-meteors and can be converted into drop size distributions (DSD) using the known relation between drop size D (in mm) and terminal fall velocity v (in m/s). We used the analytic fit of Atlas *et al.* [1973] to the data of Gunn and Kinzer [1949]:

$$D(v,z)=\frac{1}{0.6}\ln\frac{10.3}{9.65-v/\delta(z)} \qquad \textbf{Eq. 1}$$

The factor $\delta(z)$ describes the height dependence of this relation due to the air density profile $\rho(z)$. We assumed US-standard atmosphere conditions and the relation $v \propto \rho^{-04}$ [Foot and du Toit, 1969], yielding for $\delta(z)$ the polynomial approximation (z in m):

$$\delta(z)=1+3.68\cdot10^{-5}z+1.71\cdot10^{-9}z^2 \qquad \textbf{Eq. 2}$$

Eq. 1 is valid only under the assumption of zero vertical wind, which is certainly not generally justified, and vertical wind is probably the most severe source of error of retrieved DSDs and corresponding rain parameters. Nevertheless, the discussion below supports our surmise that the most prominent vertical structures (obtained by averaging over many thousand

rain events) are dominated by the micro physics rather than by the vertical wind.

For the analysis, the actually observed DSDs – resolved into more than 45 size classes between 0.25 and 6 mm diameter - were used rather than some parameterized form of DSDs. As individual (1 min average) DSDs show significant deviations from usual parameterized forms (some 10 % of the DSDs are even bi-modal) we believe to avoid unrecoverable errors by this approach. Due to the non-linear relation in eq. 1 the drop size resolution is not constant. Figure 1 shows the relative size resolution.

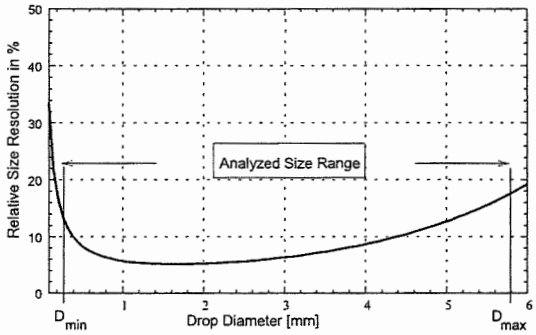

Figure 1: Relative drop size resolution versus *D* and limits of analyzed range.

A waterfall-presentation of 1-min Doppler spectra between 100 and 3000 m is shown in Figure 2.

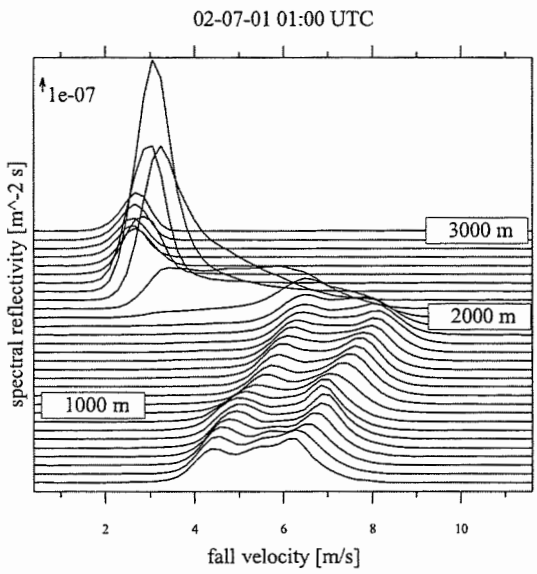

Figure 2: 1-min MRR Doppler spectra in waterfall presentation between 100 and 3000 m.

The jump of spectral peak position at about 2000 m height marks the melting layer. In this example, all spectra below the melting layer show a bi-modal structure, and the fall velocity shifts towards smaller values on the fall path below the melting layer. We refrain from further interpretation of such individual profiles, because the distinction between

a) temporal changes at the melting layer during the fall time, (The fall time between the melting layer and ground is about 5 min.)
b) advective effects (Typically tilted fall streaks drift through the MRR-beam.) and
c) DSD-transformations on the fall path

remains speculative without adequate temporal and/or spatial horizontal coverage. The following conclusions are rather based on averages over many rain events, where effects according a) and b) on the profile structure should cancel out.

3. DATA ANALYSIS

The data were stratified into rain rate classes according to the mean rain rate observed during the corresponding rain event. "Mean" refers to the spatial average within the analyzed height range (100 – 1500 m). A "rain event" is one min averaging period were a rain rate of more than 0.02 mmh^{-1} was detected by the MRR. Each rain rate class comprises one decade with the limits 0.02, 0.2, 2, 20, 200 mmh^{-1}. The number of observations falling into each class is given in table 1.

Year	2000		2001		2002	
Rainrate mm/h	Events	%	Events	%	Events	%
0.02-0.2	6478	38,5	7068	34,8	4383	35,9
0.2-2	7841	46,6	9262	45,6	5246	43,0
2-20	2422	14,4	3742	18,4	2354	19,3
20-200	96	0,6	249	1,2	213	1,7

Table 1: Number of events in each rain rate class in each year.

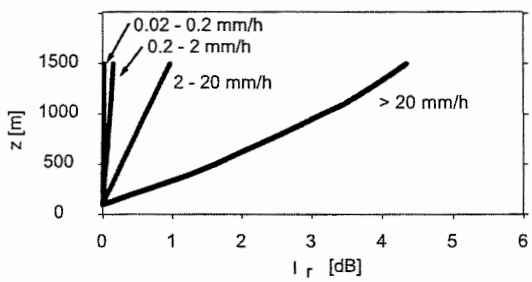

Figure 3: 2-way rain attenuation profiles for all 4 rain rate classes measured in 2000.

Despite of the short ranges, rain attenuation must not be neglected at this wavelength. It was estimated by integrating the single particle extinction coefficient over the drop size distributions in range gate 1 (the lowest range gate) assuming that no attenuation correction is necessary here. The calculated attenuation of range gate 1 was used to correct the drop size distribution in range gate 2. The general procedure was then to use the corrected drop size distribution in range gate *i* to

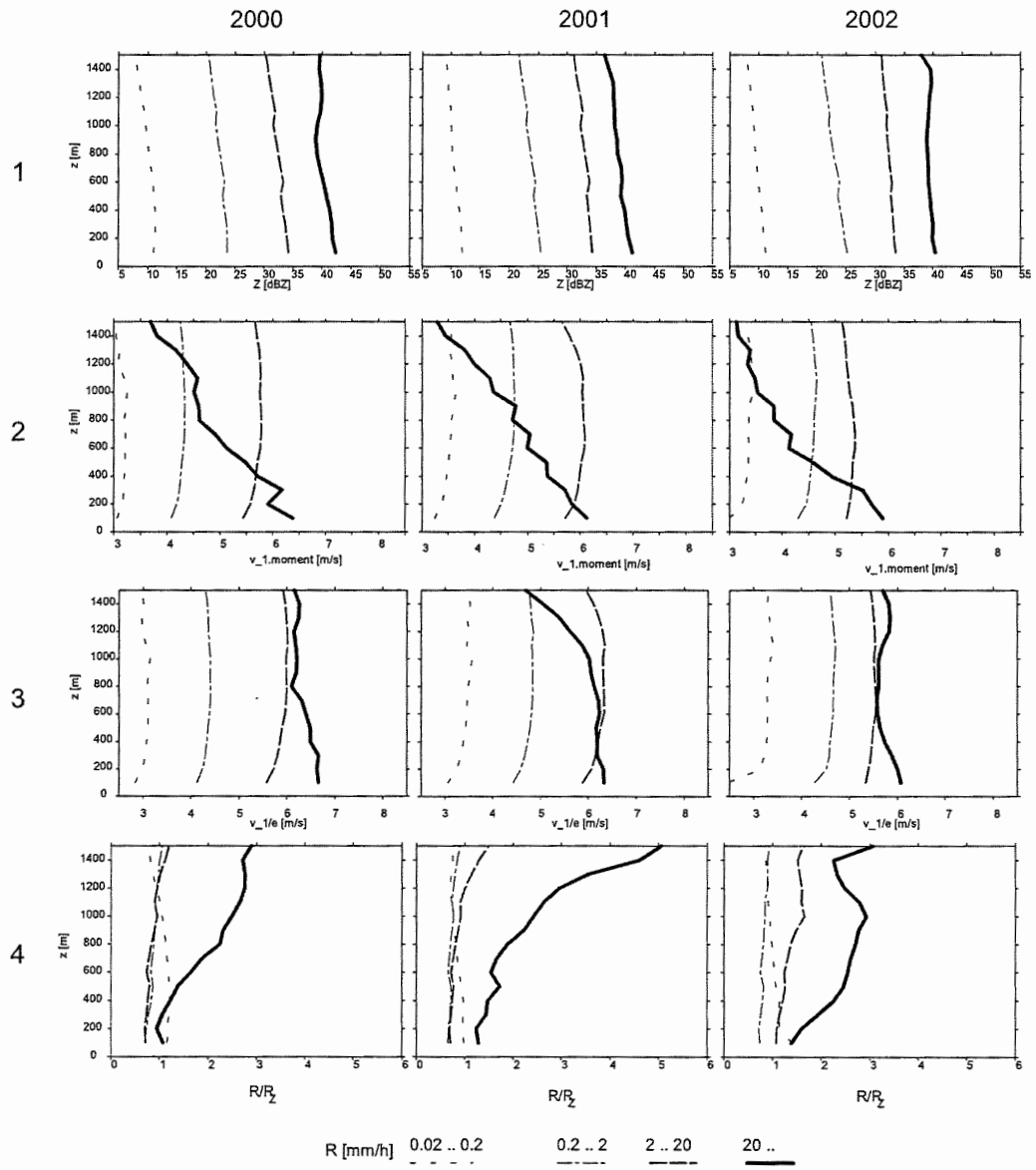

Figure 4: Mean profiles of rain parameters, stratified in 4 rain rate classes for 3 years. Row 1: Radar reflectivity. Row 2: Fall velocity $v_{1,moment}$. Row 3: Fall velocity $v_{1/e}$. Row 4: Quotient of rain rate, derived from $N(D)$, and rain rate, derived from fixed Z-R-relation.

calculate the attenuation correction for range gate $i+1$ for i from 2 to 14. The mean attenuation profiles, obtained in this way, are shown in figure 3 for data of year 2000.

Various moments and rain parameters were calculated from the attenuation corrected Doppler spectra of each rain event. The corresponding parameter-profiles were averaged separately for each rain fall class. Results for selected parameters are shown in figure 4. In order to assess the representativeness of the results the profiles were averaged separately for each year.

4. DISCUSSION

Row 1 of figure 4 shows the radar reflectivity

$$Z = \sum_i N(D_i)\Delta(D_i)D_i^6 , \qquad \text{Eq. 3}$$

where $N(D_i)\Delta(D_i)$ is the number of drops corresponding to the ith line of the Doppler spectrum. Due to the short wave length of the MRR (λ = 1.24 cm) the Rayleigh approximation is not applicable for all drop diameters. Therefore, Z is not proportional to the received power but must be calculated using eq. 3. Z decreases slightly with increasing height in all rain rate classes. The negative air density

gradient causes a positive fall velocity gradient and therefore, negative LWC gradients for a given constant rain flux. Nevertheless, only a small fraction of the observed gradients can be explained in this way. The prevailing reasons are probably different in the different rain rate classes: Drizzle typically originates from shallow clouds with tops often below 1500 m in this area. At higher rain rates – at least in the highest rain rate class – the cloud tops are certainly above 1500 m. Here another process must be responsible for the gradient of Z. We believe that the primary reason is here the transformation of the drop size distribution on the fall path. This is supported by the mean fall velocities $v_{1,moment}$ and $v_{1/e}$ in row 2 and 3 of figure 4. Both velocities are defined as truncated first moments of the Doppler spectrum $s(v)$

$$v = \left(\int_{v1}^{v2} s(v) v dv \right) / \left(\int_{v1}^{v2} s(v) dv \right) \qquad \text{Eq. 4}$$

For $v_{1,moment}$ the integration limits v_1, v_2 embrace the whole valid range of the spectrum corresponding to $D_{\max}$ and $D_{\min}$ (see figure 1). For $v_{1/e}$ the integration interval is centered at the spectral peak, and the integration limits are at the 1/e-peak values of the spectrum. Thus, in comparison with $v_{1,moment}$, $v_{1/e}$ is more sensitive to the spectral peak position and less sensitive to the spectral tails.

The shape of the v-profiles does not change much in the lower three rain rate classes except of the expected shift towards higher velocities with increasing rain rates. This reflects the well-known trend that the contribution of drop sizes shifts to larger drops with increasing rain rates. The v-profiles of the highest rain rate class differ strikingly from the lower rain rates: The v-profiles show a very strong negative gradient although the air density gradient would implicate the opposite sign. While v shows normal behavior at the ground (highest values for the highest rain rate), the negative gradient is so strong that $v_{1,moment}$ falls even below the corresponding values of lower rain rates. While the $v_{1/e}$-profiles show also some overall negative gradient, it is much less pronounced. In case of a pure v-translation of the spectra, which could be caused by vertical wind, the gradients of the $v_{1,moment}$- and $v_{1/e}$-profiles would agree. The remarkable difference between the $v_{1,moment}$- and $v_{1/e}$-profiles on the other hand, can hardly be explained by vertical wind. It rather indicates that the DSDs transform towards larger drops on the fall path. Probably the great number of small drops existing aloft is wiped out on their fall path by coalescence with large drops, and this process is not in balance with the break up of large drops. Hu and Srivastava [1994] pointed out that the transformation speed is proportional to the rain rate, which may explain that the transformation process is only visible at high rain rates. The DSD-transformation implicates of course a corresponding height dependence of the *Z-R*-relation. In order to demonstrate the effect on radar rain fall estimation, row 4 of figure 4 shows the ratio of rain rates *R*, using the actual DSD, divided by the rain rate R_Z, using a fixed *Z-R*-relation, here, $Z = 350 \cdot R^{1.42}$. (To be exact: The annual mean values of *R* and R_Z were divided.) One recognizes that a fixed *Z-R*- relation performs reasonably for $R < 20$ mmh^{-1} but leads to significant height dependent deviations between *R* and R_Z for $R > 20$ mmh^{-1}. According to these findings, weather radar would significantly underestimate high rain rates, if surface based *Z-R*-relations are employed.

5 REFERENCES

Atlas, D., Srivastava R. and Sekhon R., 1973: Doppler radar characteristics of precipitation at vertical incidence, Rev. Geophys. Space Phys. 11, 1-35.

Bringi, V.N. and V. Chandrasekar, 2001: Polarimetric Doppler Weather Radar: Principles and Application, Cambridge University Press, Cambridge, 636 pp.

Foot, G.B. and P.S. duToit, 1969: Terminal velocity of rain drops aloft, J. of Appl.Meteor. 8, 249-253.

Gunn, R. and G.D. Kinzer, 1949: The terminal velocity of fall for water droplets in stagnant air, J. Meteorol., 6, 243-248.

Hu, Z., and R.C. Srivastava, 1994: Evolution of rain drop size distribution by coalescence, breakup, and evaporation, theory and observations, *J. Atmos. Sci.*, 52, 1761-1783.

Jameson and Kostinski, 2001: Reconsideration of the physical and empirical origins of Z-R-Relations in radar meteorology, Q.J.R. Meteor. Soc., 127, 517-538.

Jameson, A.R. and Kostinski, A.B., 2002: Spurious power law relations among rainfall and radar parameters. Q.J.R. Meteorol. Soc., 128, 2045-2058.

Peters, G., Fischer, B., and Andersson, T., 2002: Rain observation with a vertically looking Micro Rain Radar (MRR), *Boreal Env. Res.* **7**, 353-362.

Sempere Torres, D., J.M. Porra`, and J.D. Creutin, 1994: A general formulation for raindrop size distribution, J. Appl. Meteor., 33, 1494-1502.

Sempere Torres, D., Sa´nchez-Diezma, I. Zawadzki, and J.D. Creutin, 2000: Identification of stratiform and convective areas using radar data with application to the improvement of DSD analysis and Z-R relations, Phys. Chem. Earth, 25, 985-990.

Testud, J., S. Oury, R.A. Black, P. Amayenc, and X. Dou, 2001: The concept of ``normalized" distribution to describe rain drop spectra: a tool for cloud microphysics and remote sensing, J. Appl. Meteor., 40, 1118-1140

THE MICROPHYSICAL AND THERMODYNAMIC CHARACTERISTICS OF TROPICAL CONVECTIVE CLOUDS BY RESULTS OF MEASUREMENTS ON CUBA

Victor V. Petrov[1], Daniel Martinez[2] and Carlos A. Perez[3]

[1] Agency of Atmospheric Technologies, Moscow, Russia
[2] Centro de Fisica de la Atmosfera, Instituto de Meteorologia, Havana, Cuba
[3] Centro Meteorologico de Camaguey, Camaguey, Cuba

1. INTRODUCTION

Convective clouds above islands in low latitudes, in comparison with clouds of moderate latitudes have a number of distinctive features, which are connected to the conditions of their formation. During realization of the Cuban Weather Modification Project (Koloskov et al., 1996), experiments were made to assess the opportunities of precipitation enhancement from convective clouds in the eastern part of Cuba in the period from 1982 to 1990, including complex investigations of the microphysical and thermodynamic characteristics of tropical convective clouds.

2. INSTRUMENTATION AND EXPERIMENTAL TECHNIQUES

Airborne measurements were made using two instrumented aircrafts: IL - 14 which carried out measurements in the lower and middle part of clouds up to 3,5 km level and AN-26, which made measurements inside the cloud tops up to the height 6 km. IL-14 aircraft was equipped with a large particle photoelectric spectrometer (LPPS), Nevzorov LWC/TWC probe, aircraft extinction probe (Nevzorov, 1996), acceleration complex for measuring of vertical velocities of air motions and a temperature fluctuation meter (Dmitriev and Strunin, 1983). AN-26 was equipped with a similar instrument set, excluding the LPPS, but including a photoelectric ice crystal counter Mee-120.

All measurements were carried out on horizontal parts of flight - so-called regimes, on which the pilot kept constant altitude, speed and direction of flight.

For radar cloud tracking, a dual-frequency meteorological radar MRL-5, established on Camaguey meteorological site was used.

The use of radar measurements made it possible to determine the stage of cloud development (from the first echo appearance) at the time of aircraft penetrations through the clouds and to follow the evolution of their microphysical and thermodynamic parameters.

3. RESULTS OF MEASUREMENTS

The amount of measuring regimes executed during the penetrations of convective clouds of various thicknesses is presented in the Table 1. The top heights of the sampled clouds reached up to 11,5 km (average value 6-7 km), and their diameters reached 10 km (average value 2 - 4 km).

Table 1.

Cloud top height	Aircraft	Measuring parameter						
		W	T	U	N	lwc	γ	N*
< 4 km	IL-14	65	47	40	42	58	49	-
4 – 6 km	IL-14	67	66	41	98	62	58	-
	An-26	43	41	43	-	36	30	8
6 – 8 km	Il-14	51	49	48	59	56	56	-
	An-26	139	141	139	-	122	92	49
> 8 km	IL-14	43	35	40	51	49	41	-
	An-26	15	15	15	-	4	6	6
All clouds		423	394	366	250	387	332	63

Here: W - speed of vertical movements, T – temperature fluctuation, U - fluctuation of horizontal speed of a wind, N - concentration of a large particles in clouds (0,2 < D < 6 mm), lwc – liquid water content, γ - extinction factor, N* - concentration of large ice crystals.

Most clouds were crossed once. In 23 % of cases clouds were crossed twice and in 9 % of cases 3-5 times.

In the Table 2 are presented the thermodynamic characteristics of investigated clouds, averaged on cloud diameters, their absolute maxima and minima, and root-mean-square deviations.

Table 2.

Parameter	Cloud top height						
	<4 km	4 ÷ 6 km		6 ÷ 8 km		> 8 km	
	Measurement level [km]						
	2÷3	2÷3	5÷6	2÷3	5÷6	2÷3	5÷6
<W'>	1,3	1,1	1,1	1,6	1,53	1,8	1,3
W'_{max}	10.2	15,5	19,5	28	25	15,5	13,8
W'_{min}	-4,5	-9,3	-11,1	-12	-14,1	-11,3	-4,6
σ_w	1,37	2,75	3,1	3,02	3,5	2,98	2,7
W'>0 (%)	54,3	54,2	52	58	52,8	54,5	53
<U>'	0,8	1,0	0,9	1,8	1,3	0,7	1,03
U'_{max}	9,9	10,1	11,8	13,9	15,5	12,0	9,2
U'_{min}	-5,3	-7,8	-8,2	-8,1	-9,6	-11,0	-5,0
σ_U	2,0	2,2	2,4	2,3	3,2	2,7	2,2
<T'>	-0,11	-0,12	0,08	-0,01	0,03	0,05	0,4
T'_{max}	2,23	3,02	2,2	2,1	3,2	4,26	3,4
T'_{min}	-2,23	-4,2	-1,7	-4,1	-4,4	-3,15	-2,5
σ_T	0,37	0,51	0,56	0,51	0,52	0,46	0,48

Corresponding author's address: Victor Petrov, Agency of Atmospheric Technologies, Novovagankovsky 8, Moscow, Russia; E-mail: attech@attech.ru

Here: W (m/s) is the vertical velocity, W>0% relative length of parts (in relation to a cloud diameter) with updraft, U (m/s) -fluctuations of horizontal speed of a wind and T (^{0}C) –fluctuations of temperature.

With the growth of thickness of clouds an increase of amplitudes of all measured parameters was detected. Inside growing clouds the updraft occupied 40 - 60 % of the a cloud cross section. The maximal values of updraft speed were observed a little bit above the middle of a cloud.

In the warm layer the amount of updrafts was greater, than downdrafts. In the top parts of the clouds the number of drafts of both signs is approximately equal, which is caused by the formation of downdrafts in cloud tops.

In the investigated clouds, the anisotropy of a wind speed fluctuation components is observed - in 90 % of cases $\sigma_W / \sigma_U > 1$. The value of σ_W / W on the average is decreasing with clouds thickness.

In the table 3 the averaged and maximal values of specific speed of kinetic energy dissipation ε_W and a factor of turbulence K in a tropical convective clouds of various thickness are submitted.

Table 3.

Parameter	Thickness of a cloud (km)			
	1 -4	4 -7		
	Measurement level (km)			
	2 – 3,5	1-1,5	2-3,5	5,5-6,5
<K> m^2s^{-1}	44	27	54	46
K_{max} m^2s^{-1}	179	44	184	67
<ε> cm^2s^{-3}	148	5	145	82
ε_{max} cm^2s^{-3}	254	16	577	237

The intensity vertical turbulent mixing in the investigated clouds is less, than in continental clouds of similar thickness, in which the average of K = 150 - 220 m^2/s and the of kinetic energy dissipation rate reaches several hundreds cm^2/s^3 (Shmeter, 1987). At the same time, in purely maritime convective clouds, investigated during GATE experiments, less intensive vertical movements were observed, than in clouds developing over the island of Cuba.

The clouds developing above Cuba, according to their cloud drops size spectra of, are close to continental ones (r=6mkm, N=400 cm-3), while in 30 - 70 km from the coast above water surface of the Caribbean sea are observed purely maritime convective clouds (r=17mkm, N = 70 cm-3) (Fig. 1). Thus, it has been experimentally found that despite the fact that the maritime tropical air is a predominant air mass in the Cuba island environment, convective clouds developing over the Camaguey experimental area are closer to continental clouds by their microstructure and can be considered as of an intermediate type. This may be attributed to a process in which aerosols from the surface layer are entrained upward, as purely maritime clouds are observed only at a distance of 30 - 70 km from the seashore.

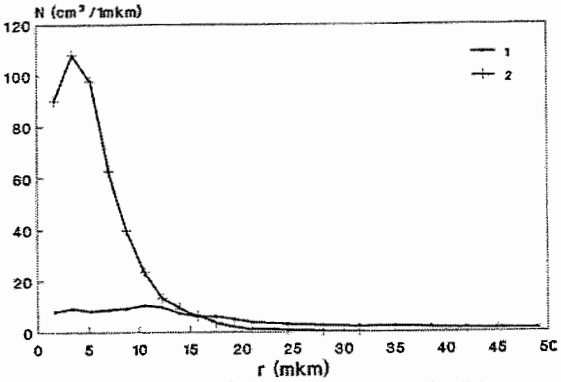

Fig. 1. Size spectra of cloudy drops over Caribbean Sea (1) and Cuba island (2).

In the Table 4 the repeatability's (%) of the maximal concentration N (m^{-3}) of large cloudy particles (with diameter > 200 microns) measured in convective clouds of various thickness with the help of large particle photoelectric spectrometer are presented.

Table 4.

N (m^{-3})	Cloud thickness (km)				
	Cuba				Ukraine
	2-3	3-5	5-7	>7	2-3
10					100
20					95
50	100				87
100	98	100			75
200	95	99	100		57
500	91	96	99	100	33
1000	83	89	95	98	17
2000	67	77	89	93	6
5000	35	64	77	87	
10000	15	21	56	79	
>10000	4	10	28	41	

For the comparison in the table are presented dates on repeatability of large particles concentration in convective clouds of Ukraine (Kosarev at al., 1978). In clouds developing above an island Cuba higher concentration of large particles are observed, than in continental clouds of similar thickness, but lower than in maritime clouds of the eastern zone of the tropical Atlantic. The slopes of the averaged large particles size spectra of in convective clouds of various thicknesses above Cuba for particles of less than 600 microns are close to an the slope of those measured in continental clouds. In a range of the drop sizes of 600-6000 microns the slope of the spectra is smaller, specially for the thicker clouds, being closer to the size spectra for maritime clouds of the eastern tropical Atlantic (Kosarev et al., 1978).

Fig. 2. shows the averaged vertical distributions of liquid water content (LWC) and extinction factor (γ) in the investigated clouds of different thickness.

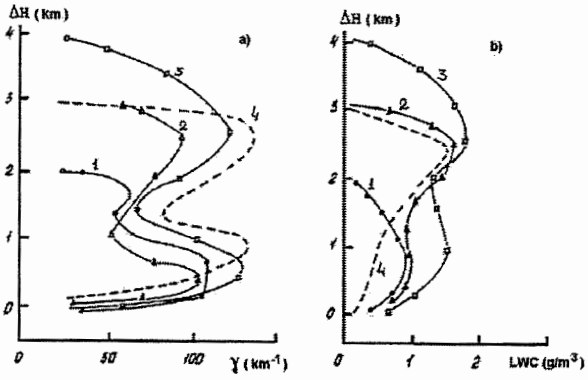

Fig. 2. Vertical distribution of extinction factor (a) and liquid water content (b) in the investigated clouds of various thickness: < 2km (1), 2-3 km (2), 3-5 km (3) and in clouds of Ukraine with thickness of 2-3 km (4).

The two-modality of the vertical distributions of LWC and extinction factor is connected with two-layer convection, which formation is caused by presence of inversion layers at heights of 2-2,5 km. Convective clouds, developing above an island Cuba, are optically less dense as a rule, than cloud of Ukraine, but more dense, than maritime clouds of eastern zone of tropical Atlantic, for which the values of extinction factor changed in limits from 8 up to 40 km^{-1} (Kosarev et al., 1978). The values of LWC of the Cuban clouds are higher, than LWC values of Ukrainian clouds. With increasing cloud thickness (ΔH), LWC grows in average as LWC=0,43ΔH, i.e. is faster, than in clouds of Ukraine, where LWC=0,34ΔH. In 50 % of the investigated clouds, averaged on cloud diameter, LWC values are exceeded 0,6 g/m^3, in 20 % of clouds the values of LWC were greater than 1,5 g/m^3. The maximal values of LWC were reached 5.2 g/m^3 in the warm part of investigated clouds and 3.4 g/m^3 at the level of the -10^0C isotherm. On the average, the values of LWC in the warm part of clouds were more than those measured in the cold part of the clouds.

The values of liquid water content of precipitation particles with d > 200 microns (RWC), measured inside the clouds, are also increasing with an cloud thickness. In clouds with thickness < 5 km, the average value of RWC was 0,46 g/m^3, average maximal - 1,45 g/m^3. In Cb clouds these values are 3,2 and 9,3 g/m^3. Observable super-adiabatic values of RWC can be explained by existence of accumulation zones in the investigated clouds.

In the Table 5, the average and maximal values of liquid water content (LWC), ice water content (IWC), the relation of IWC to the total water content – K_{ice}=IWC/(IWC+LWC), and the concentration of a large (a>150 microns) crystals (N^* L^{-1}) in the investigated clouds are presented.

All investigated clouds above the level of zero degrees had mixed phase structure. The characteristics of phase composition of this clouds was dependent on the structure of updraft flows, the stage of development of the cloud and can vary in a wide range within the limits of one cloud.

Table 5.

Parameter	Mean value	Max. value	St. deviation
<LWC>	0.51	1.59	0.37
LWC_{max}	1.04	2.3	0.6
<IWC>	0.2	0.6	0.14
IWC_{max}	0.35	0.96	0.2
$<K_{ice}>$	0.32	0.8	0.22
$K_{ice\ max}$	0.8	1.0	0.21
<N*>	7.2	18.6	4.3
N^*_{max}	16.7	52.0	11.2

In parts with intensive updraft, persistent (more than 17 min), zones with high values of liquid water content, free from large ice crystals were detected.

It is shown, that according to their microphysical and thermodynamic characteristics the investigated clouds may be classified as intermediate between purely maritime and continental.

Investigations of the entrainment process, and of the interrelation and spatial - temporary variability of microphysical and thermodynamic parameters in tropical convective clouds were also carried out as a part of the research program.

In the Table 6, the values of the rate of the measured LWC quantities to adiabatic water content (LWC/LWCa), for levels 3 and 6 km for clouds of different thickness and types (A – isolated clouds, C-clusters) are presented.

Table 6.

Parameter	3 km			6 km		
	5<ΔH<7km		>7km	5<ΔH<7km		>7km
	A	C	C	A	C	C
$(lwc/lwc_a)_{max}$	1.03	0.91	0.91	0.35	0.49	0.25
$<lwc_{max}/lwc_a>$	0.34	0.52	0.48	0.16	0.22	0.14
$<lwc_{med}/lwc_a>$	0.12	0.24	0.21	0.08	0.1	0.07
$<lwc_{W>0}/lwc_a>$	0.16	0.28	0.27	0.09	0.13	0.08

Values of LWC and the relation LWC/LWCa depend on the structure of vertical movements. In updraft zones (W>0) the values LWC/LWCa are greater, than cloud average. In the investigated clouds, it was found no dependence between values LWC/LWCa and cloud diameter (the correlation factors is - 0.1 for a level of 3 km and -0.09 for a level of 6 km), which points to a low influence of the mechanism of lateral entrainment. At the same time, the dependence between LWC/LWCa and vertical speed (correlation factors are: 0.5 for a level of 3 km and 0.65 for a level of 6 km) is observed, that testifies to influence of entrainment through cloud top and vertical mixing on evolution of clouds.

The analysis of the entrainment mechanisms with the help of the Paluch diagram (Perez et al., 1992) has shown, that in all cases air in a cloud at a level of penetration consists of a mix of air come from the top and bottom levels, that testified the essential

influence of entrainment through the top level on the evolution of investigated clouds.

From the results of joint radar-tracking and airborne measurements the averaged evolution of the thermodynamic and microphysical characteristics of convective clouds is constructed. On a Fig. 3 the time evolution of mean velocities of vertical airflows at the level 3 km is shown.

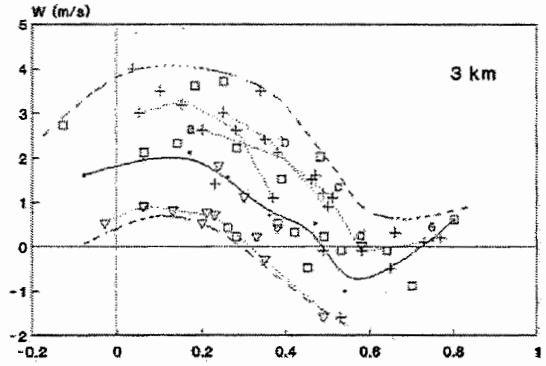

Fig. 3. Evolution of vertical airflows velocities.

It's possible to distinguish three stages of evolution of a cloud: a stage of growth, stage of maturity and dissipation stage. The average duration of life cycle for the investigated clouds was about 1 hour.

Fig. 4 gives an averaged evolution of the concentration of crystals N*, mean velocities of vertical airflows W, the LWC values, volumetric - modal radius of cloud droplets r_{mv} and a relationship between the ice and the total water content K_{ICE} measured at the level of 5 – 6 km, at temperatures between -6 and -11°C in convective clouds developing over Cuba Island.

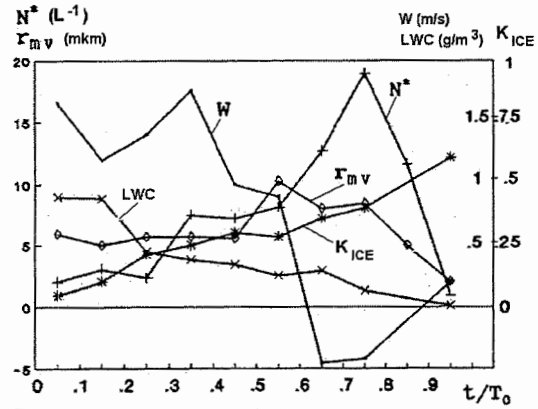

Fig. 4. An averaged evolution of cloudy parameters.

In a picture of evolution of cloudy parameters pay attention on itself two facts: presence in clouds of the supercooled liquid phase up to their complete dissipation and growth of volumetric - modal radius of drops r_{mv} during increase of concentration of large crystals.

The presence of a powerful warm layer in tropical convective clouds has essential influence on formation of precipitation processes in these clouds. In a fig. 5 the evolution of size spectra of precipitation particles, constructed on the joint data of radar-tracking and 139 aircraft penetrations of clouds is presented.

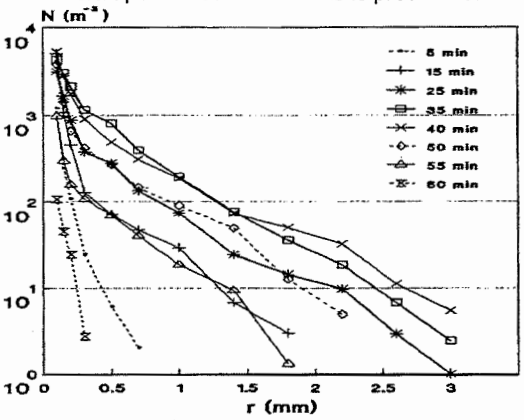

Fig. 5. Precipitation particles size spectra evolution.

At the initial stage of cloud evolution, during the first 10 or 15 min, when the cloud top is still below the 0°C isotherm, the power drop size spectrum is observed. In the subsequent period the top of a cloud reaches a zone of negative temperatures, where there is a formation of ice crystals. The particles size distribution in this period (20-25 mines after occurrence of a radioecho) has a mixed shape: - power left part and exponential right.

The data obtained suggest that in convective clouds developing in the Camaguey experimental area, two mechanisms operate simultaneously, the drop coalescence being further intensified by the diffusion growth of ice particles.

The duration of process of precipitation formation in the investigated clouds has made about 60 minutes.

4. References

Dmitriev V.K., Strunin M.A., 1983: Aircraft measurements of the vertical components of wind speed fluctuations. Trudy CAO, issue **147**, 39-51.

Koloskov B., Zimin B., Beliaev V., Seregin Yu., Chernikov A., Petrov V., Martinez D., Perez C., Puente G., 1996: Results of experiments on convective precipitation enhancement in the Camaguey experimental area. Cuba. Jour. Appl. Meteorol, 45, 9, pp. 1524-1534

Kosarev A.L., Mazin I.P., Nevzorov A.N., Shygaev V.Ph., 1978: Intercomparison of some microphysical parameters of clouds in different geographical areas. Some problems of cloud physics. Coll. papers. Gidrometeoisdat. Leningrad. pp.113-134.

Nevzorov A.N., 1996: CAO aircraft instrumentation for cloud physics. 12th international Conf. on Cloud Phys. and Precipitation. Aug. 19-23, V.1, Zurich, Switzerland, pp. 371-374.

Perez C., Martinez D. and Petrov V.V., 1992: Microstructure, mixing and turbulence in cumulus clouds over Cuba and Caribbean Sea. WMO Rep. No.19, pp. 245-256.

Shmeter S.M., 1987: Thermodynamics and physics of convective clouds. Gidrometeoisdat. 288 p.

RAIN ENHANCEMENT BY SEEDING WITH CHARGED DROPLETS

M. Pinsky, A. Khain, V. Arkhipov, Y. Feldman and Ya. Ryabov

The Hebrew University of Jerusalem, Jerusalem, 91904, Israel

1. INTRODUCTION

Rain enhancement and fog elimination are two main fields of weather modification activities that have attracted researchers' attention for many years. Enhancement of rain is of special importance in countries suffering from water shortage for agriculture and other human activities. Fog elimination is highly necessary, for example, to increase visibility, on roads and runways of airports. A shortage of the fresh water in some of the mountainous, desert, semi-desert and coastal regions sets human thinking about the methods of the utilization of fog as an alternative source of the fresh water in these regions.

Cloud (and especially fog) droplets are usually small, so that collisions between them are inefficient. Therefore, if a cloud does not have a sufficient number of large drop-collectors, it cannot realize fully its precipitation potential. Thus, the increase the precipitation efficiency and acceleration of fog elimination require acceleration in the collision rate. A method of acceleration of droplet collisions with the purposes of rain enhancement and fog elimination is proposed. According to the method some fraction of cloud and fog droplets or droplets produced by droplet generators should be charged and injected back into clouds or fogs. This method is described by Khain et al (2004) in more detail.

2. ELECTROSTATIC INTERACTION BETWEEN DROPS

Cloud droplets are formed on aerosol particles containing a certain soluble fraction and contain a sufficient number of ions to be regarded as conductive particles. The approximated solution for the electrostatic forces of droplet interaction can be represented as (Khain et al 2004):

$$F_{el} \approx \frac{Q_1 Q_2}{4\pi\varepsilon_0 R^2} + \frac{1}{4\pi\varepsilon_0}\left(Q_1^2 r_2\left(\frac{1}{R^3} - \frac{R}{(R^2 - r_2^2)^2}\right) + Q_2^2 r_1\left(\frac{1}{R^3} - \frac{R}{(R^2 - r_1^2)^2}\right) + \right.$$
$$\left. + Q_1 Q_2 r_1 r_2\left(\frac{1}{R^4} + \frac{1}{(R^2 - r_1^2 - r_2^2)^2} - \frac{1}{(R^2 - r_1^2)^2} - \frac{1}{(R^2 - r_2^2)^2}\right)\right), \quad (1)$$

where Q_1 and Q_2 are charges of two conductive insulated spheres, r_1 and r_2 are the radii of these spheres; R is the distance between the centers of the spheres, ε_0 is the dielectric permittivity of free space. The first term on the right hand of (1) represents Coulomb force (it decreases with distance as R^2); the next two terms represent interaction between point charges and the dipole (force decreases as R^3). The last term describes interaction between induced imaginary charges (this force decreases as R^4).

As follows from (1), at small distances two droplets can attract each other even in the case when they are loaded with charges of the same polarity. In these cases the attraction force arising between the charge of a droplet and the imaginary charges induced in the counterpart droplet dominates over Coulomb's repulsion between the droplets. At the same time, for separation distances much bigger than the sum of droplet radii the Coulomb force always dominates.

Cloud droplet situated in the air cannot be charged more than a certain maximum value Q_{max} which is determined by the air breakdown voltage (Meek and Craggs, 1953) and is the quadratic function of the droplet radius: for r=1 μm $Q_{\max} = 3.3 \cdot 10^{-16}$ C, while for r=10 μm $q_{\max} = 3.3 \cdot 10^{-14}$ C. Due to the conductivity of air, a charged droplet loses its charge according to the exponential law $Q = Q_0 Exp\{-t/\tau\}$, where $\tau = \varepsilon_0 / \sigma$ is the relaxation time, σ is the conductivity of air and Q_0 is the initial charge of a droplet. Since the free ions concentration inside a cloud (or fog) is significantly lower than that in the cloud-free air, the conductivity of cloudy and foggy air is significantly lower than the fair weather conductivity, so that the relaxation time τ is from 20 min up to 4 hours (Tinsley et al.2000). Thus, the time period of droplet discharge is much longer than the time scale of coagulation processes leading to raindrop formation.

3. CALCULATION OF COLLISION EFFICIENCIES

Collision efficiencies were calculated using the superposition method (Pruppacher and Klett 1997; Pinsky and Khain 2001). The droplet motion equations

Corresponding author's address: Alexander Khain, Department of Atmospheric Sciences, The Institute of Atmospheric Sciences, The Hebrew University, 91904, Jerusalem, Israel; E-mail: khain@vms.huji.ac.il

were written taking into account the electrostatic forces:

$$\frac{d\vec{V}_1}{dt} = -\frac{1}{\tau_1}\left(\vec{V}_1 - V_{1t}\vec{e}_z - \vec{u}_2\right) + \frac{\vec{F}_{el}}{m_1}$$

$$\frac{d\vec{V}_2}{dt} = -\frac{1}{\tau_2}\left(\vec{V}_2 - V_{2t}\vec{e}_z - \vec{u}_1\right) - \frac{\vec{F}_{el}}{m_2}, \quad (2)$$

where $\vec{V}_i$, $\vec{V}_{it}$ and $\tau_i = \vec{V}_{it}/g$ are the velocity, terminal velocity and a characteristic relaxation time of drop i (=1,2), respectively. We limit our analysis by small Stokesian droplets with radii $r_i \le 20\mu m$. In eq. (2) $\vec{u}_2$ (or $\vec{u}_1$) is the perturbed velocity induced by drop 2 (or drop 1) in the location of drop-1 (or drop 2) center; $\vec{F}_{el}$ is the electrical force between two droplets given by relation (1), m_1 and m_2 masses of droplets.

Using the method described in detail in Pinsky and Khain (2001) a four-dimensional (with respect to droplet size and charge) table of the collision efficiency has been calculated.

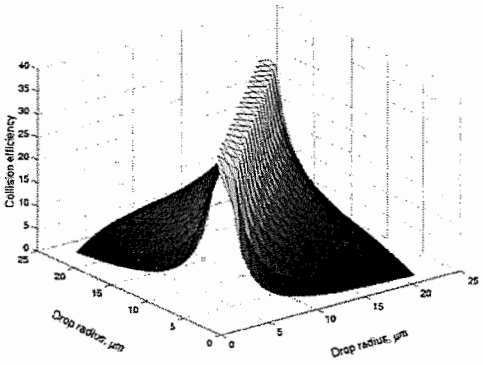

Fig. 1 Collision efficiencies between drops of different radii charged with their maximum possible charge and neutral droplets.

Fig. 1 shows the collision efficiencies between drops of different radii charged with their maximum possible charge and neutral droplets. One can see that In case of charged- neutral droplet collisions the collision efficiencies can reach 20-30, i.e., the values, which are several hundred times higher than the gravity-induced values. In case droplets are charged by opposite polarities, the collision efficiencies can reach a few thousand, i.e. $\sim 10^4$ times higher than the gravity-induced values (not shown). This means that charged drop collectors can collect droplets within the volume, which cross section significantly exceeds the geometrical cross section. In parallel to the collision efficiencies, the charge and mass dependent collision kernels were also calculated.

4. MODELING OF STOCHSTIC COLLISIONS

Process of droplet collisions is described by a stochastic collision (or collection) equation

$$\frac{\partial f(m,Q,t)}{\partial t} = \int_0^{m/2} f(m_c,Q_c,t)K(m_c,m',Q_c,Q')f(m',Q',t)dm' - \int_0^{\infty} f(m,Q,t)K(m,m',Q,Q')f(m',Q',t)dm', \quad (3)$$

in which the collection kernels $K(m_c,m',Q_c,Q')$ depend on droplet masses and charges. Size-distribution function for water droplets $f(m,Q,t)$ becomes to be two-dimensional: in each mass category there are droplets with different charges. As a result, we introduce logarithmically equidistant two-dimensional mass-charge grid, which contains 1000 mass bins describing the droplet size distribution with droplet radii ranged from 1 μm up to 1000 μm and 35 charge bins with charges ranged from $2\cdot 10^{-13}$ up to $2\cdot 10^{+13}$ Coulombs. Collision kernels are calculated as described in the previous section. When calculating the collisions, we take into account that there is a maximum charge that each droplet can be charged. Within the mass grid two ranges of droplet sizes is considered: droplets with radii below 21 μm and droplets with radii above 21 μm. Within the first range the fully two-dimensional (size–charge) droplet distribution is considered. It is assumed that the effect of droplet charge on collisions is negligible for drops with radii above 21 μm. Respectively, droplets with radii larger 21 μm are described using a one dimensional mass grid. Collisions between droplets within pairs containing droplet with radius below 21 μm are calculated taken into account the effect of droplet charge. The collisions of droplets with radii exceeding 21 μm are calculated using gravity-induced collision efficiencies. The charges in exceed the maximum charge of corresponding droplets are assumed to lose in the surrounding air. The charge transported to droplets with radii exceeding 21 μm are also considered to be lost. Thus approach leads, to some underestimation of the collision rate.

5. RESULTS OF SEEDING SIMULATIONS

5.1 Cloud seeding modeling

To illustrate the efficiency of the collisions caused by charging of a small fraction of cloud droplets, a

simulation of droplet spectrum evolution was conducted using the equation of the stochastic equation of collisions (3). An initially narrow droplet size distribution (DSD) centered at $r=9\ \mu m$ and total cloud water content (CWC) of 3 gm^{-3} was chosen for simulations. Droplet concentration was 1100 cm^{-3}. This spectrum is similar to that observed in deep Texas summertime continental clouds by Rosenfeld and Woodley (2000). According to these observations and numerical simulations (Khain et al, 2001) these clouds produce no warm rain.

Several simulations of droplet spectrum evolution have been conducted using different fractions of charged droplets in the drop population (see Fig.2). We assumed that all charged droplets are distributed homogeneously within a certain cloud volume, where collisions are simulated.

Time dependencies of rainwater content (normalized to the total liquid water content) in cases of neutral (natural) cloud and different combination of charged droplet concentrations of both polarities are presented in **Fig. 2.**

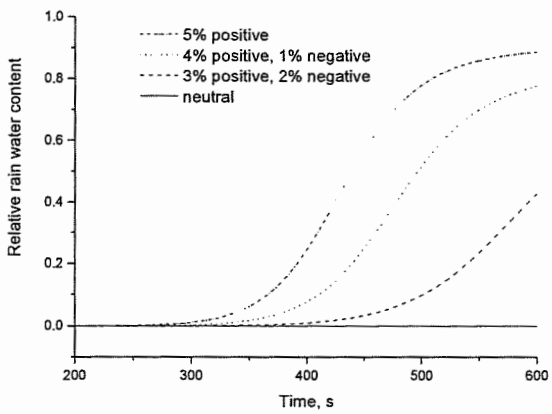

Fig. 2. Time dependence of relative rain water content in numerical experiments, in which different fractions of droplets were initially charged.

The results depicted in Fig.2 show that unipolar charged cloud develops more effectively then bipolar. Indeed, in case of collision of droplets of opposite polarity theirs total charge decreases, which leads to a decrease of charge in droplets as well as its effect on collisions. One-polarity charges do not disappear by collisions and their effect continues during longer period of time.

Simulations indicate a significant acceleration of raindrop formation in maritime clouds as well, when a small fraction of the droplets is charged.

5.2 Simulations of fog seeding

The problem of fog elimination is the problem of increase in the visibility. The visibility (*VIS*) was calculated as $VIS = \ln \varepsilon / \beta$, where ε is the contrast threshold equal to ~0.02 (Kunkel, 1984), $\beta = N \int_0^\infty \pi r^2 K(\rho) f(r) dr$ is the extinction coefficient,

$$K(\rho) = 2 - \frac{8n^2 \sin[2\rho(n-1)]}{\rho(n+1)^2(n-1)},\ \rho = 2\pi r/\lambda .$$

Here N is the droplet concentration, r is radius of a droplet, $f(r)$ is the droplet size distribution function, n =1.33 is the refractive index of water, λ is the wavelength of the scattered radiation. **Fig. 3** shows time dependencies of visibility in a quite dense fog (Roach et al. 1976) with the liquid water content of 0.4 $g \cdot m^{-3}$ for different fractions of charged droplets of different polarity introduced into the size spectra at t=0.

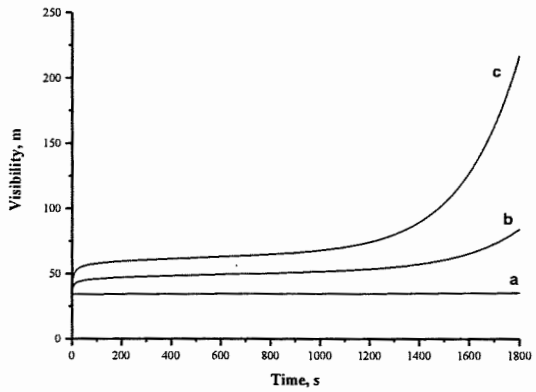

Figure 3. Time dependencies of visibility in a fog for different fractions of charged droplets of different polarity: a) all droplets were neutral, b) 30% positively and 30% negatively charged droplets, c) 50% positively and 50% negatively charged droplets).

One can see that the visibility does not actually change under the natural (neutral droplets) conditions. In case of injection of charged droplets the visibility significantly increases with time. In case the fog is seeded with droplets charged by charges of opposite polarity, the time variation in the visibility consists of several stages: a) short-time increase in the visibility, b) some latent period when visibility slowly increases with time and c) the third period characterized by a rapid increase in the visibility. During the first short time period the visibility increases due to a decrease in droplet concentration caused by collisions of droplets charged with charges of the opposite polarity. It should be noted that optimum concentrations and sizes of seeding droplets should be chosen to provide most efficient fog elimination.

6. CONCLUSIONS

A new method of acceleration of collisions with the purposes of rain enhancement and fog elimination is proposed. According to the method some fraction of droplets taken from clouds or fogs (or produced by droplet generators) is charged and injected back into clouds or fogs. The simulations conducted indicate a high efficiency of the proposed method aimed at acceleration of droplet collisions in clouds and fogs. The advantages of the method proposed are the following: a) The collision efficiencies between charged and neutral droplets, as well as between droplets containing charges of opposite polarity are many orders higher than the corresponding gravity-induced collision efficiencies. Thus, droplets of radii well below 25 μm can contribute to the collision process, significantly increasing the rate of raindrop formation and decreasing the concentration of small droplets (responsible for the low visibility in fogs). b) There is no necessity in a special reagent material; c) This method allows consideration of fogs as a source of fresh water.

Acknowledgments

This study has been conducted under support of YISSUM (The Hebrew University of Jerusalem), the Yeshua Horowitz Association and the Israel Ministry of Science (the German-Israel collaboration in Water Technology, grant WT 0403).

References

Khain A. P., Rosenfeld D. and Pokrovsky, A., 2001: Simulation of deep convective clouds with sustained supercooled liquid water down to –37.5 C using a spectral microphysics model. Geophys. Res. Lett., 3887-3890

Khain, A., V. Arkhipov, M. Pinsky, Y. Feldman and Ya. Ryabov, 2004: Rain enhancement and fog elimination by seeding with charged droplets Pt.1: Theory and numerical simulations. J. Appl. Meteorol. (in press).

Kunkel B.A., 1984: Parameterization of droplet terminal velocity and extinction coefficient in fog models. Journal of Climate and Applied Meteorology. **23**, 34-41.

Meek J. M., Craggs J. D., 1953: Electrical Breakdown of Gases. Clarendon Press, Oxford, 507 pp.

Pinsky M., Khain A. and Shapiro M., 1999: Collisions of small drops in a turbulent flow. Part I: Collision efficiency. Problem formulation and preliminary results. J. Atmos. Sci., **56**, 2585–2600.

Pinsky, M., A. P. Khain, and M. Shapiro 2001: Collision efficiency of drops in a wide range of Reynolds numbers: Effects of pressure on spectrum evolution. J. Atmos. Sci., **58**, 742-764.

Pruppacher H. R., Klett J. D., 1997: Microphysics of Clouds and Precipitation. Kluwer Academic Publishers, Dordrecht/Boston/London, 954 pp.

Roach W.T., Brown R., Caughey S.J., Garland J.A. and Readings C.J., 1976: The physics of radiation fog: I – a field study. Quart. J. R. Met. Soc., **102**, 313-333.

Rosenfeld D. and W. L. Woodley, 2000: Convective Clouds with Sustained Highly Supercooled Liquid Water Down to –37.5°C. Nature, 405, 440-442.

Tinsley B.A., Rohrbauch R.P., Hei M., Beard K.V., 2000: Effects of image charges on the scavenging of aerosol particles by cloud droplets and on droplet charging and possible ice nucleation processes. J. Atmos. Sci., **57**, 2118-2134.

Tinsley B.A., Rohrbauch R.P., Hei M., 2001: Electroscavenging in clouds with broad droplet size distributions and weak electrification. Atmos. Res., 59-60, 115-135.

TOWARD THE PARAMETERIZATION OF TURBULENT EFFECTS ON PARTICLE COLLISIONS IN TURBULENT CLOUDS

M. Pinsky[1], A. Khain[1], B. Grits[1], and M. Shapiro[2]
[1] Department of Atmospheric Sciences, Institute of the Earth Science, The Hebrew University of Jerusalem, Israel
[2] Faculty of Mechanical Engineering, Technion-Israel Institute of Technology, Haifa, Israel

1. INTRODUCTION

Turbulence is known to have a significant effect on the motion and collisions of droplets. Still quantitative evaluation of its effect remains an unsolved problem. Simulation of turbulent flows under Taylor microscale Reynolds numbers Re_λ $((1\div5)\times10^4)$ typical of atmospheric turbulence is a difficult problem. Some results were obtained by Pinsky *et al* (1999) and Pinsky and Khain (2004) under simplified assumptions.

We propose a new approach to solve the problem of collisions of cloud droplets in a turbulent flow. Briefly, it can be formulated as follows. Analytical considerations indicate that droplet motion at small scales in a turbulent flow is fully determined by turbulent shears and the Largangian accelerations having characteristic spatial scales of about one cm and time scales of ~ 0.2 s. Spatial and temporal scales of droplet hydrodynamic interactions (DHI) are much less than the respective turbulent flow scales. This means that turbulent shears and accelerations can be considered "frozen" during the process of DHI. Thus, at scales of DHI the total homogeneous and isotropic turbulent flow can be represented as a set of "elementary" volumes with liner size of about 1 cm. Each volume is characterized by a random flow velocity field, which is independent of the fields in other volumes. The droplet concentration can be considered constant within each volume (Pinsky and Khain 2003). The collision efficiency, swept volume and collision kernel in this flow are random values that do not change within an elementary volume but randomly change from volume to volume.

Two statistical models were developed, which generated series of turbulent shears and accelerations reproducing their probability distribution functions (PDF) at high Re_λ, as which were measured in recent laboratory studies and predicted theoretically. We calculated collision efficiencies and kernels for each realization of acceleration-shear pair. Their mean values and distributions are calculated by an adequate averaging over a set of realizations, which is equivalent to the spatial averaging over the whole flow field, or to the time averaging in any point of turbulent field. The dependencies of the collision efficiencies and collision kernels on droplet radii and on the turbulent dissipation rate ε and Re_λ are also calculated.

2. MOTION AND FLUXES OF DROPLETS

The droplet motion can be described by the following equations:

$$\frac{dV_i}{dt} = -\frac{1}{\tau}\left(V_i - W_i(x_i,t)\right) + g\delta_{3i}\ ;\ \frac{dx_i}{dt} = V_i \qquad (1)$$

Corresponding author: Mark Pinsky, The Institute of Earth Sciences, The Hebrew University of Jerusalem, Jerusalem 91904, Israel. Email: mark@dina.es.huji.ac.il

where $i=1,2,3$, V_i and W_i are the droplet and flow velocities, respectively; $\tau = V_t / g$ is the droplet's characteristic relaxation time; $g\delta_{3i}$ is the gravity acceleration, V_t is the droplet terminal fall velocity in calm air. We limit our consideration to Stokesian droplets of radii $r \le 20\mu m$ with the maximal Stokes number $St \approx 0.1 << 1$.

An approximate solution of motion Eq. (1) in a homogeneous turbulent flow was obtained by Maxey (1987) for small particles as

$$V_i = \frac{dx_i}{dt} = S_{ij}x_j + V_t\delta_{3i} + \tau\left(A_i + V_t S_{i3}\right) \qquad (2)$$

where A_i is the Lagrangian acceleration of turbulent flow along drop trajectory and S_{ij} is the shear tensor. Eq. (2) was obtained as asymptotic equation for small St by integrating by parts of a non-linear solution of (1). Eq. (2) can be interpreted both as an equation of motion of a single drops and as an equation of motion of a droplets' continuum. One can see that droplet motion is fully determined by the Largangian acceleration and shear components. The droplet velocity relative to the air does not change within the elementary volume ($V_i' = const$) and does not depend on the droplet location.

Equations (2) are linear and have constant coefficients. Using these equations, one can obtain an equation for relative motion of two different droplets. Let us denote $\tilde{x}_i = x_{2i} - x_{1i}$ is the position vector between the centers of two droplets and their relative velocity is $\tilde{V}_i = V_{2i} - V_{1i}$. The equation for relative velocity can be written as

$$\tilde{V}_i = \frac{d\tilde{x}_i}{dt} = S_{ij}\tilde{x}_j + \tilde{V}_i' \qquad (3)$$

where $\tilde{V}_i' = V_{2i}' - V_{1i}' = const$.

The relative location of two droplets $\tilde{x}_i(t)$ depends only on their distance vector and does not depend on the location of droplets in the elementary volume.

The relative droplet trajectory depends on the Lagrangian acceleration and shear tensor components. In all cases there is a stagnation point that determines the character of the relative trajectories. When the distance between droplets is

~100 times greater than the distance from the stagnation point to the origin, the trajectory is a quite smooth curve. In case these two distances are of the same order, the character of trajectory depends on engenvalues of the shear tensor. The stagnation point can be either saddle-node (diverge or converge trajectories) or saddle-focus (spiral trajectories).

Collision rate between droplets of radii r_1 and r_2 is determined by the flux of droplets of radius r_1 on droplets of radius r_2, or in other words, by the droplet flux through a spherical surface of $r_1 + r_2$ radius. In the absence of hydrodynamic interaction between the droplets, the flux can be calculated, using Eq. (3) as

$$\Phi = \frac{1}{r_1 + r_2} \int_{\Omega_+} N\left(S_{ij}\tilde{x}_j\tilde{x}_i + \tilde{V}_i'\tilde{x}_i\right) d\Omega_+ , \qquad (4)$$

where N is the droplet concentration and Ω_+ is the part of the spherical surface with radius of $r_1 + r_2$, where $\tilde{V}_i\tilde{x}_i < 0$. Since the droplet concentration in the elementary volume is uniform, instead of the droplet flux one can use the rate of change of the swept volume, which is the flux of relative velocity $\tilde{V}_i$ through the surface Ω_+. The swept volume of any drop pair does not change within the elementary volume. The turbulent swept volume normalized by that quantity in the pure gravitational coalescence is:

$$G = \frac{1}{\pi(r_1 + r_2)^3 |V_{t2} - V_{t1}|} \int_{\Omega_+} \left(S_{ij}\tilde{x}_j\tilde{x}_i + \tilde{V}_i'\tilde{x}_i\right) d\Omega_+ \qquad (5)$$

3. MODELING OF TURBULENT FLOW PROPERTIES

The fine turbulent properties especially shear rate and Lagrangian acceleration components in clouds have not been measured. It is possible however to estimate ε and Re_λ and to use them for parameterization of droplet collision rate. We assume that small-scale turbulence in clouds is homogeneous, isotropic and stationary in statistical sense.

As it follows from theory of homogeneous and isotropic turbulence (Monin and Yaglom, 1975) (see also Pinsky et al, 2000b) the Lagrangian acceleration field is approximately potential. At the same time the turbulent velocity W_j is a solenoidal vector field because of turbulent flow non-compressibility. Solenoidal and potential isotropic fields are uncorrelated (Monin and Yaglom, 1975). Therefore, the Lagrangian acceleration and shear components are uncorrelated: $\langle A_i S_{jk} \rangle \approx 0$. It means that models of shears and accelerations can be based on uncorrelated (actually independent) random number series.

The parameterization of turbulent shears is based on the following statistical properties (Pinsky et al, 2004):

- Variance and tensor of correlations between shears components are given by formula

$$B^s_{jk} = \frac{\varepsilon}{30\nu}\left(4\delta_{mn}\delta_{jk} - \delta_{nj}\delta_{mk} - \delta_{nk}\delta_{mj}\right) \qquad (6)$$

where $j, k, m, n = 1,2,3$. This tensor does not depend on Re_λ.

- The PDF of shears component describes by 4-parametric Pearson distribution.
- Skewness *Sk* and flatness *F* was evaluated as a function of Re_λ using parameterization formula (Antonia, 1981)

$$Sk = -0.27\,\mathrm{Re}_\lambda^{0.11};\; F = 1.33\,\mathrm{Re}_\lambda^{0.32} \qquad (7)$$

The algorithm and design of turbulent shears' generator were introduced by Pinsky et al (2004). For given dissipation rate, skewness and flatness the model allows an efficient generation of all components of turbulent strains in each elementary volume.

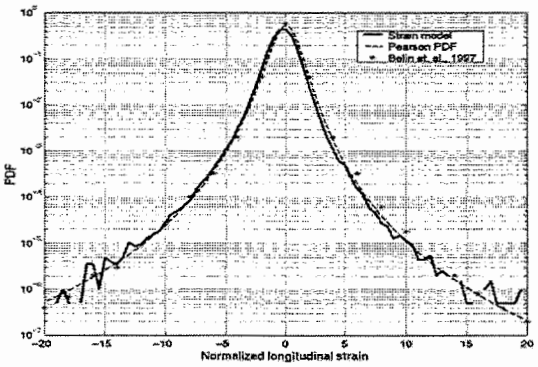

Figure 1. *PDF of normalized longitudinal strain component s_{xx} calculated using the statistical model by Pinsky et al (2004) (solid line); the Pearson approximating distribution (dashed line) and the distribution measured in a turbulent flow with $\mathrm{Re}_\lambda = 1500$ (Belin et al, 1997) (asterisks).*

Figure 1 shows a very good agreement between simulated and measured PDFs down to values as small as 10^{-6} (tails of distributions).

Parameterization of the Lagrangian acceleration in a very high Re_λ turbulent flow is based on the following theoretical and laboratory results:

- In isotropic and homogeneous turbulent flow the components of acceleration are of the same variation and should be uncorrelated. We assumed that they are independent.
- According to LaPorta *et al* (2001) the components of Lagrangian acceleration have a limiting PDF in case large Re_λ that is shown in **Fig. 2**.
- According to (Hill, 2002) the variance of acceleration always increases with Re_λ as

$$\langle A^2 \rangle = \frac{1}{3}\varepsilon^{3/2}\nu^{-1/2}\left(2.5\,\mathrm{Re}_\lambda^{0.25} + 0.08\,\mathrm{Re}_\lambda^{0.11}\right) \qquad (8)$$

Series of the Lagrangian accelerations were calculated using a simple random number generator. In calculations we used the PDF approximation of the acceleration obtained by LaPorta et al (2001), but with the Re_λ dependent variation (8).

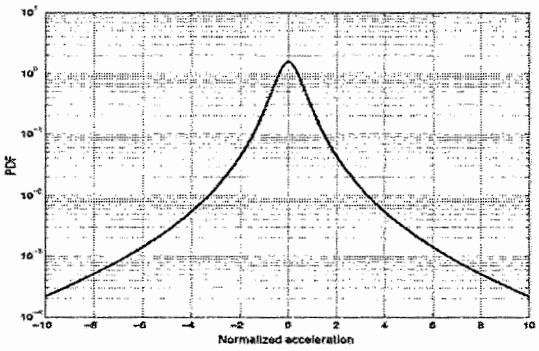

Figure 2. PDF of Lagrangian acceleration (LaPorta et al, 2001)

4. STATISTICAL PROPERTIES OF NON-DISTURBED DROPLET FLUXES

We calculated statistical properties of relative droplet fluxes (swept volumes), using the model described above and Eq.5. **Fig. 3** shows PDFs of normalized swept volume for drop pair 15-10 μm calculated for real (Non-Gaussian) and Gaussian PDFs of shears and accelerations. One can see an elongated tail of the PDF in the case of intermittent turbulence. The intermittency increases the asymmetry of the PDF toward large values of swept volumes.

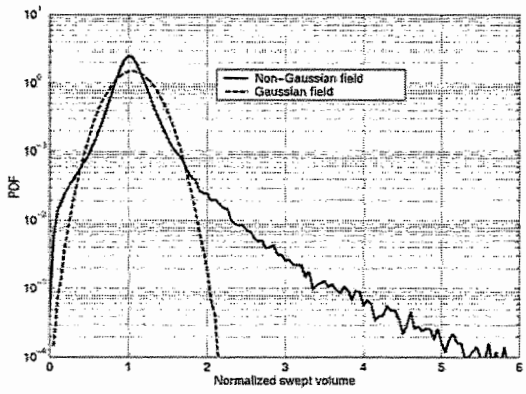

Figure 3. PDF of normalized (by the pure gravity value) swept volume for drop pair 15-10 μm in Non-Gaussian and Gaussian PDF of shears and accelerations, $\mathrm{Re}_\lambda = 2\cdot 10^4$, $\varepsilon = 0.02 m^2 s^{-3}$

Fig. 4 shows that the mean normalized (by the pure gravity value) swept volume increases both with ε and Re_λ. This stresses the importance of the utilization of realistic Re_λ to describe relative droplet motion even, when the hydrodynamic interaction is not taken into account. Note that the increase in swept volume (relative to the pure gravity value) is moderate for this drop pair.

Analysis shows that the main factor governing increase in the swept volume is the Lagrangian acceleration.

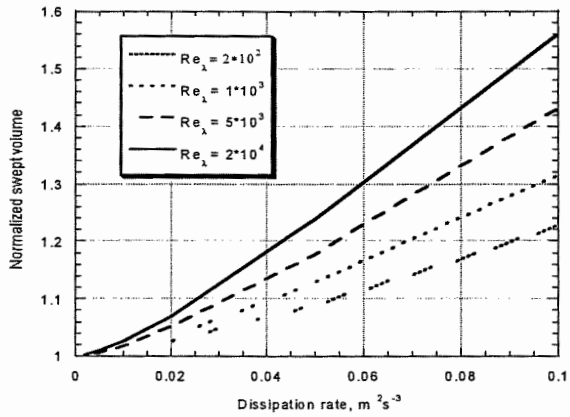

Figure 4. Dependence of mean normalized swept volume on turbulent dissipation rate ε. for drop pair 15-10 μm at different Re_λ.

5. CALCULATION OF COLLISION EFFICIENCY

Calculation of collision efficiency in a turbulent flow represents a difficult problem. Below we present a method for calculation of the collision efficiency, which has a clear geometrical interpretation. Eq. (3) allows one to calculate un-disturbed (no hydrodynamic interaction) trajectories of droplets that cross the spherical surface $|\tilde{x}_{0i}| = r_1 + r_2$. To this aim one should solve Eq. (3), using initial positions, located on the surface (target), in inverse direction (using negative time step). This backward integration was performed for a certain time period corresponding to the distances of about 20 radii of larger droplet, at which hydrodynamic interaction can be neglected. The end points of backward trajectories form a 2nd order surface that can be either an ellipsoid or pair of paraboloids or a hyperboloid depending on values of shear components. Each point on the surface can be interpreted as an elementary square producing droplet flux (**fig. 5**)

$$d\Phi = \frac{N\left(S_{ij}\tilde{x}_{0j}\tilde{x}_{0i} + \tilde{V}_i'\tilde{x}_{0i}\right)d\Omega_+}{r_1 + r_2} \qquad (9)$$

Starting with the points at this surface, we calculated forward time trajectories calculations when DHI were taken into account. These calculations were performed using a version of the superposition method (Pinsky et al. 1999). A certain fraction of

these trajectories reveals drop collisions. The geometry of the problem is illustrated in **Fig. 5**. The black sphere of radius $r_1 + r_2$ is the target. Droplets starting from the gray surface penetrate the target in case of no DHI (total droplet flux). The black spot located on the gray surface represents droplets, which penetrate the target in case where DHI are included. **The collision efficiency is determined, therefore, as the ratio of the flux of droplets experienced collisions when the hydrodynamic interaction is included, to the flux of droplets experienced collisions when no hydrodynamic interaction is taken into account**. In the pure gravity case this ratio coincides with the collision/geometrical cross-sections' ratio.

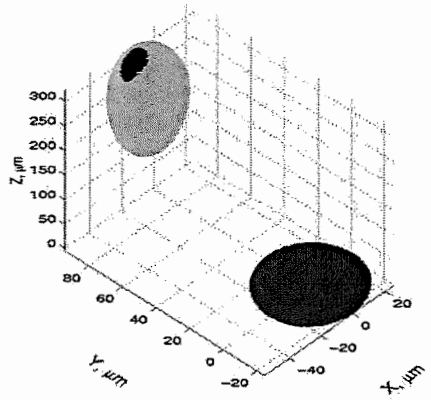

Figure 5. *An example clarifying the definition and calculation of the collision efficiency.*

The PDF of the collision efficiency between 10 and 15 μm radii droplets calculated using the approach described above is presented in **Fig. 6**. Fig. 6 corresponds to the PDF of swept volume plotted in Fig. 3. The PDF of collision efficiency is quite wide with the mean value that is 4.7 times exceeds the pure gravity value. Analysis shows that when the turbulent stresses are taken into account, the correlation between the swept volume and the collision efficiency is quite weak. It means that the tail in the PDF of the swept volume seen in Fig.3 does not result in the corresponding tail in the PDF of the collision efficiency. As a result, the PDF of collision efficiency in non-Gaussian case turns out to be close to that obtained under assumption of the Gaussian distributions of accelerations and shears.

6. CONCLUSION

An efficient method of calculation for droplet collisions in high Reynolds number turbulent flows is described. Recent laboratory and theoretical results obtained at high Re_λ have been used for generation of a set of turbulent flow velocity realizations with required PDF of the Lagrangian accelerations and shears. A significant increase in the collision rate in a turbulent flow is found. While both the collision efficiency and the swept volume increase with Re_λ, the increase in the collision efficiency turns out to be factor dominating collision rate. Calculations of detailed tables of collision efficiencies and collision kernels are under way.

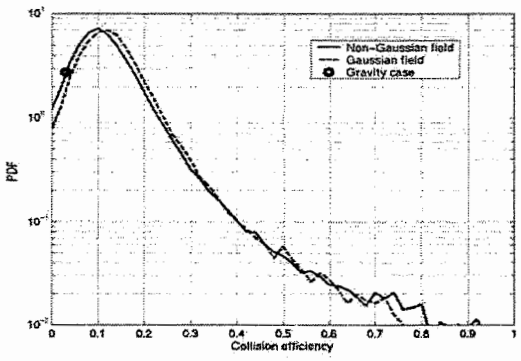

Figure 6. *PDF of collision efficiency for 15-10 μm radii droplets in Non-Gaussian and Gaussian PDF of shear and acceleration components,* $\mathrm{Re}_\lambda = 2 \cdot 10^4$, $\varepsilon = 0.02 m^2 s^{-3}$

Acknowledgments

The study was performed under support of the Israel Science Foundation (grant 173/03) and the Israel Ministry of Science (grant WT 0403).

References

Antonia, R.A., Chambers, A.J. & Satyaprakash, B.R.,1981: Reynolds number dependence of high-order moments of the streamwise turbulent velocity derivative. *Boundary-layer Met.*, **21**, 159-171.

Belin F, Maurer J, Tabeling P. and Willaime H., 1997: Velocity gradient distributions in fully developed turbulence: An experimental study. *Phys. Fluids,* **9**, 3843-3850.

Hill, R. J. 2002: Scaling of acceleration in locally isotropic turbulence. *J. Fluid Mech.*, **452**, 361-370.

LaPorta A., G.A. Voth, A. M. Crawford, J. Alexander and E. Bodenschatz, 2001: Fluid particle accelerations in fully developed turbulence. *Nature*, **409**, 1017-1019.

Maxey, M. R. 1987: The gravitational settling of aerosol particles in homogeneous turbulence and random flow fields. *J. Fluid Mech.*, **174**, 441-465.

Monin, A. S. and A. M. Yaglom, 1975: Statistical fluid mechanics: Mechanics of turbulence, v.2, p.874. MIT Press.

Pinsky, M., A. P. Khain, and M. Shapiro, 1999: Collisions of small drops in a turbulent flow. Pt.1: Collision efficiency: problem formulation and preliminary results. *J. Atmos. Sci.* , **56**, 2585-2600.

Pinsky, M.B., A. P. Khain, and A. Tsinober, 2000: Accelerations in isotropic and homogeneous turbulence and Taylor's hypothesis. *Phys. Fluids,* **12**, 3195-3204.

Pinsky M.B. and A.P. Khain, 2004: Collisions of small drops in a turbulent flow. Part 2. Effects of flow accelerations. *J. Atmos. Sci.,* (in press).

Pinsky, M. B., and A. P. Khain 2003: Fine structure of cloud droplet concentration as seen from the Fast-FSSP measurements. Part 2: Results of in-situ observations" *J. Appl. Meteor.*, **42**, 65-73.

Pinsky M., Shapiro M., Khain A. and Wirzberger H., 2004: A statistical model of strains in homogeneous and isotropic turbulence. *Physica D*, (in press).

MEASUREMENTS OF PHORETIC VELOCITIES OF AEROSOL PARTICLES IN MICROGRAVITY CONDITIONS

[1,2] F.Prodi, [1]G.Santachiara, [1]S.Travaini,
[3]A.Vedernikov, [3]F.Dubois, [3]J.C.Legros

[1] Institute ISAC-CNR, Clouds and Precipitations Group, Bologna, Italy
[2] Department of Physics, University of Ferrara, Ferrara, Italy
[3] Microgravity Research Center, Chimie-Physique EP-MRC, Université Libre de Bruxelles , Belgium

1. INTRODUCTION

Small particles suspended in non-isothermal gas and/or in an isothermal gas mixture with concentrations gradients of chemical species, experience a force, that is induced by thermal or concentration gradients. The particle motion is commonly termed thermophoresis and diffusiophoresis, respectively. Such phenomena are of considerable importance in a variety of engineering fields (coating of surfaces, gas cleaning, optical fiber production, advanced ceramics, nanophase materials, combustion processes, microcontamination control in the electronics industry, etc.). They certainly play a crucial role in the scavenging of aerosol particles in clouds, when droplets and/or ice crystals grow or evaporate, and below clouds, during the fall of hydrometeors.

Experiments to measure the thermophoretic force or velocity have mainly been performed in normal gravity employing several different experimental methods: the modified Millikan cell with heated upper and cooled lower electrodes, the deflection of a particle suspended from a small wire, the penetration method, the electrodynamic levitation and the deflection of particles moving in a jet formed by a slit.

While in the free-molecule regime (Knudsen >>1), Waldmann's theory (Waldmann, 1959) seems to be in good agreement with the experimental results, in the slip-flow regime (Kn < 0.1) and in the transition region ($0.1 \leq Kn < 10$) previously published measurements are contradictory.

Talbot et al.(1980) observed that Brock's thermal force (Brock, 1962), when $Kn \rightarrow \infty$, is identical to Waldmann's equation, except for the multiplicative factor c_s/c_m, where c_s is the thermal-slip coefficient and c_m is the velocity-slip coefficient. As this ratio should be about unity, Talbot proposes an equation that should be valid throughout the entire interval $0<Kn<\infty$, and suggests for c_s, c_t, c_m the values 1.17, 2.18 and 1.14, respectively.

The transition regime is difficult to analyse. Numerical solutions of the integral transport equation for the BGK model have been attempted.

Corresponding author address: F. Prodi ISAC-CNR Bologna, Italy.
E-mail: f.prodi@isac.cnr.it

The solutions of Yamamoto and Ishihara (1988), Loyalka (1992), and Ohwada and Sone (1992), all predict negative thermophoresis for sufficiently large values of the ratio between thermal conductivities of the particle and gas and for Kn<0.2.

In normal gravity the thermophoretic effect cannot be studied alone, as particles move due to gravity force and eventually owing to natural convection. These difficulties can be avoided by utilizing a microgravity environment.

Up to now only Toda et al. (1996, 1998) and Oostra (1998) have performed experiments in microgravity, in the drop tower facilities of JAMIC (10^{-5} g_0 , t=10s) and Zarm, in Bremen (10^{-6} g_0, t=4.7s), respectively.

Concerning diffusiophoresis, a case of great interest occurs when vapour molecules are diffusing through resting air, i.e. when a Stephan flow exists. This phenomenon was studied theoretically and experimentally by Waldmann (1959), Schmitt and Waldmann (1960), Derjaguin et al. (1966), Kousaka and Endo (1993).

As in the case of thermophoresis, the microgravity environment simplifies the problem, as it eliminates the continuous renewal of the vapour concentration field. So far there are no published data concerning diffusiophoretic velocities in microgravity.

2. EXPERIMENTAL ARRANGEMENT

The microgravity environment was obtained in Parabolic Flights (PF, Bordeaux, 2000 - 2001 campaigns) and the Bremen Drop Tower facility (DT1 and DT2, April and December 2003, respectively).

2.1 Parabolic flights

The reduced gravity environment is achieved by flying through a series of parabolic manoeuvres, which results in approximately twenty-two second periods of 0-g (actually around 10^{-2} g_0). A normal mission lasts two to three hours and consists of thirty parabolic manoeuvres. All the operations involved in the experiments are performed manually. The experimental apparatus is assembled on a rack, which is fixed to the floor of the Airbus A300.

The cell used for the experiments consists of two plane plates (surface about 100 cm^2) at a fixed

distance (0.8 cm). In the case of thermophoresis experiments, the upper plate was heated by an electric heater and its temperature was electrically controlled. The lower one was maintained at environmental temperature. In the case of diffusiophoresis, the water vapour gradient is obtained with sintered plates imbued with a water solution of $MgCl_2$ and distilled water, at the top and at the bottom of the cell, respectively. The plates are separated with three glass side walls, while the fourth plate was in an insulating material, with holes for the inlet and outlet of aerosol.

Carnauba wax aerosol (CW, $k_p \cong 0.10$ W m^{-1} K^{-1}) was produced by the condensation monodisperse aerosol generator (MAGE, Prodi et al., 1972). The mean diameter of the aerosol was 0.57 μm. The carrier gas was nitrogen.

Sodium chloride particles (k_p= 6.4 W m^{-1} K^{-1}) were obtained by the homogeneous condensation of vapours, obtained by heating a ceramic tube coated with a salt layer.

Test were performed to ensure that the aerosol was not charged. The aerosol concentration inside the cell was sufficient to obtain a good statistics for the velocity calculations. Aerosol particles were observed through a digital holographic velocimeter (Dubois et al., 1999), a device allowing the determination of 3-D coordinates of particles (30 frames/s; space resolution of about 0.2 microns) from the observation volume of 0.5x0.5x0.5 mm. Based on digital image processing, the experimental volume is reconstructed slice by slice in order to achieve a fully focused volume. Particle trajectories, and consequently particle velocities, were reconstructed through the analysis of the sequence of particle positions.

In order to compare experimental data obtained in different experimental conditions (e.g. temperature gradient) we introduce the reduced thermophoretic velocity, defined as :

$$V_{thr} = -\frac{V_{th} \cdot T_0}{\nu \cdot \nabla T}$$

where V_{th} is the thermophoretic velocity, ν the kinematic viscosity, T_0 the mean gas temperature and ∇T is the temperature gradient in the gas, and the reduced diffusiophoretic velocity

$$V_{dr} = -\frac{V_d \cdot p_2}{D_v \cdot \frac{dp_1}{dx}}$$

where V_d is the diffusiophoretic velocity, p_2 the partial pressure of the carrier gas, p_1 the water vapour partial pressure and D_V is the diffusion coefficient of water vapour against nitrogen.

2.2 Bremen Drop Tower

This is a ground-based and short-term microgravity laboratory. The Drop Tower system consists of a 110 m high drop tube with an internal diameter of 3.5 m, and a 10 m high shaft deceleration chamber at its foot. The drop tube and the deceleration chamber form a vacuum system with a volume of 1700 m^3, which can be evacuated, with the help of a system of pumps, down to a residual pressure of 1 Pa in about 2.5 hours. The drop tube is built into a tower of 146 m height. The experimental apparatus is inserted in a special pressurized capsule. Before the free fall, the capsule is held by an electropneumatical tensioning element fixed at the release platform. A specially constructed tank filled with fine-graded polystyrene is used to decelerate the capsule. The deceleration tank has a cylindrical shape (1.6m diameter, 8.5m height). A complete installed electronic system of Bremen Drop Tower allows the automatic control of the experiment.

The cells used by us in the Bremen Drop Tower for thermo- and diffusiophoretic experiments were improved with respect to the ones used in the parabolic flights. The temperature gradient was obtained through two metal plane plates (18.5 x18.5 mm), one at the top and the other at the bottom of the square mono-block vessel of Pyrex optically polished. The distance between the plates was 7 mm.

The inlet and outlet of the aerosol occurs through two small holes located on the bottom plate, which are closed immediately after the introduction of the aerosol, assuring good sealing. The variation of the Knudsen number was obtained by varying both the diameter of the aerosol, and the mean free path of the gas, by changing the pressure inside the cell.

Concerning the diffusiophoretic experiments, the water vapour gradient was obtained with a sintered plate imbued with distilled water at the top and silica gel located at the bottom of the cell.

Paraffin particles were produced through a new generator (Minimage), while sodium chloride particles were obtained by nebulizing a water solution of salt (5g/l and 10 g/l) by the Omron U1 device. The droplets evaporate, flowing through a tube with silica gel. The mean diameter of the sodium chloride aerosol particles was 0.9 and 1.2 μm, respectively.

Using the electronic system of the Bremen Drop Tower, the aerosol was automatically injected into cell 4 s before the free fall (i.e. beginning of microgravity). The aerosol inside the cell was observed through the digital holographic velocimeter (Dubois et al., 1999), as in the parabolic flight.

3. RESULTS AND DISCUSSION

Fig.1 and 2 show the experimental data concerning thermophoresis and diffusiophoresis obtained during Parabolic Flights and Bremen Drop Tower experiments.

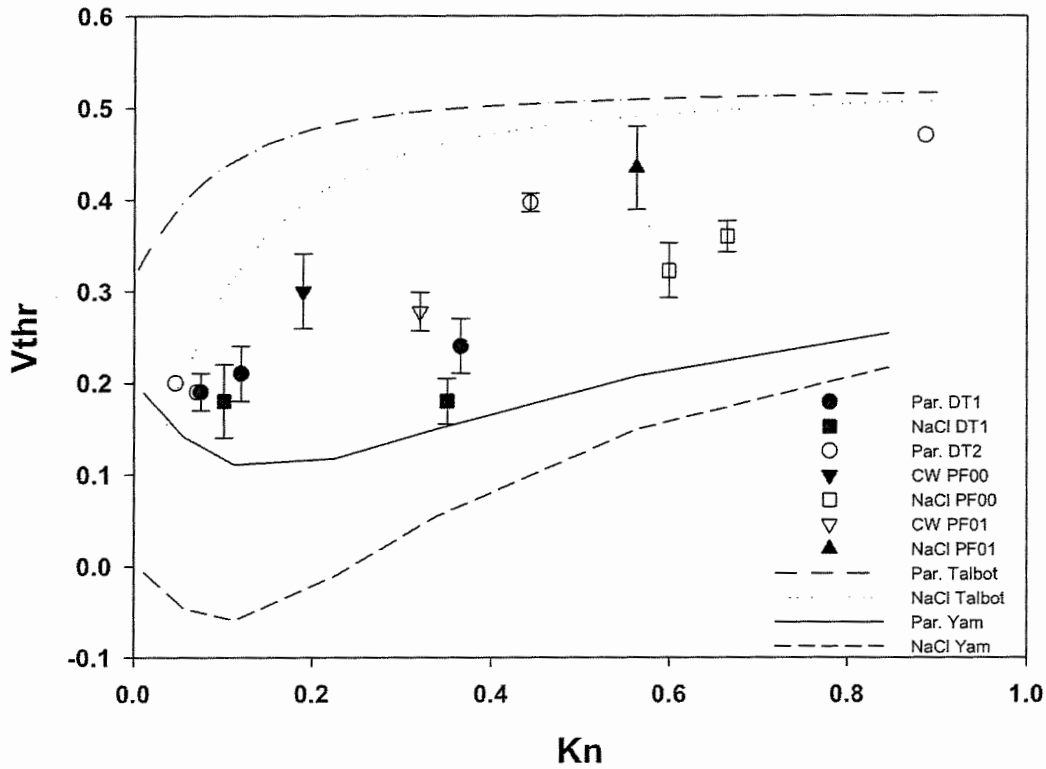

Fig.1. Reduced thermophoretic velocity vs Knudsen number

Concerning thermophoretic experiments, our experimental data do not show a clear dependence of V_{thr} on thermal conductivity of the aerosol. This outcome disagrees with Talbot and Yamamoto's theories, but agrees with data obtained at 1-g experiments (Schadt and Cadle, 1961; Keng and Orr,1966; Derjaguin et al., 1966; Tong, 1975; Li and Davies, 1995b; Santachiara et al., 2002; and theoretically by Loyalka, 1992).

The experimental values of V_{thr} are between the Talbot and Yamamoto curves. The existence of negative thermophoresis is not confirmed in our experiments with NaCl particles at ambient pressure and temperature.

The microgravity experiments of Toda gave values two or three times larger than those predicted by Talbot's equation, in experiments performed with SiO_2, and about seven times higher for MgO (k=1.4 and 42 W m^{-1} K^{-1}, respectively). Concerning experiments with PMMA (k=0.15 W $m^{-1}K^{-1}$), the values were a little lower than Talbot's theoretical ones. Oostra's results obtained with TiO_2 , M1200, and glass (k= 11.7, 1.01 and 0.93 W m^{-1} K^{-1}, respectively), even if scattered, are generally lower than values predicted by Talbot's equation. During the experimental campaign performed in the Bremen Drop Tower, we carried out an additional preliminary test, confirming the existence, even in the absence of gravity, of a thermal creep velocity, due to wall temperature gradient. The influence on the measured thermophoretic velocity, which we suppose to be small, will be evaluated later.

As regards diffusiophoresis, previous experimental and theoretical results are contradictory. Following Waldmann (1959), Schmitt and Waldmann (1960), Chernyak et al. (2001), the theoretical velocity should be independent of particle radius, for both large (Kn <1) and small aerosol particles (Kn >1). While Schmitt's (1961) experimental results are in accordance with the above statement, Deryaguin et al. (1966) obtained a decrease in reduced diffusiophoretic velocity with the Knudsen number.

Experimental results obtained in experiments performed in microgravity conditions show an independence of reduced thermophoretic velocity on the Knudsen number, and agree with the above cited theories.

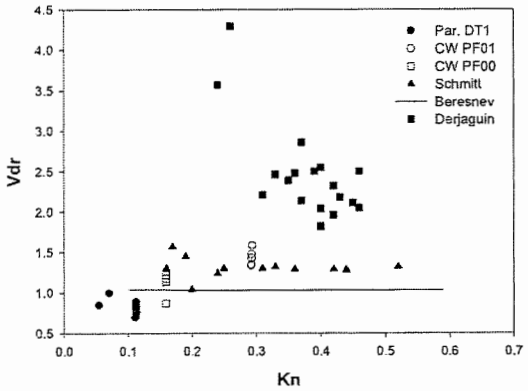

Fig.2. Reduced diffusiophoretic velocity vs Knudsen number

4. ACKNOWLEDGEMENTS

This work was supported by the European Space Agency and the Belgian Federal Science Policy Office.

The Bremen Drop Tower Operation and Service Company ZARM FABmbH (Germany) is gratefully acknowledged.

5. REFERENCES

Beresnev, S., Chernyak, V., Starikov, S., 1999: Diffusiophoresis of aerosol particles in a binary gas mixture. *Journal of Aerosol Science*, 30 (Suppl. 1), S761-S762).

Brock, J.R. , 1962: On the theory of thermal forces acting on aerosol particles. *J. Colloid Sci.,* **17**, 768-780.

Chernyak, V.G., Starikov, S.A. and Beresnev , S.A., 2001: Diffusiophoresis of an aerosol particle in a binary mixture. *J.Appl. Mechanics and Technical,* **42**, 445–454.

Derjaguin, B.V., Storozhilova, A.I. and Rabinovich, Ya.I.,1966: Experimental verification of the theory of thermophoresis of aerosol particles. *J. Colloid Interface Sci.,* **21**, 35-58.

Dubois, F., Joannes,L. and Legros, J.C., 1999: Improved three-dimensional imaging with digital holography microscope using a partial spatial coherent source. *Appl.Opt.*, **38**, 7085-7094.

Keng, E.Y.H. and Orr Jr, C., 1966: Thermal precipitation and particle conductivity. *J.Colloid Interface Sci.*, **22**, 107-116.

Kousaka,Y., and Endo,Y., 1993: Experiments on diffusiophoresis of aerosol particles at low Knudsen number. *J.Aerosol Sci.*, **24**, 611-617.Li, W. and Davis, E.J. 1995b: The effects of gas and particle properties on thermophoresis. *J.Aerosol Sci.,* **26**, 1085-1099.

Loyalka, S.K. 1992: Thermophoretic force on a single particle-I. Numerical solution of the linearized Boltzmann equation. *J.Aerosol Sci.,* **23,** 291-300.

Ohwada, T. and Sone, Y. 1992: Analysis of thermal stress slip flow and negative thermophoresis using the Boltzmann equation for hard-sphere molecules. Eu. *J. Mecch. B/Fluids,* **11**, 389-414.

Oostra, W. 1998: An experimental approach into the phenomenon of thermophoresis. Ph.D. Thesis, Delft University of Technology, The Netherlands.

Prodi, V. 1972: A condensation aerosol generator for solid monodisperse particles. In: *Assessment of airborne particles.* Edited by T.T.Mercer, P.E.Morrow and W.Stober, 169-181.

Santachiara, G., Prodi, F., and Cornetti, C., 2002: Experimental measurements on thermophoresis in the transition region. *J.Aerosol Sci.*, **33**, 769-780.

Schadt, C.F. and Cadle, R.D. 1961: Thermal force on aerosol particles. *J.Phys.Chem.*, **65**, 1689-1694.

Schmitt, K.H. and Waldmann, L., 1960: Untersuchungen an Schwebstoffteilchen in diffundierenden Gasen.*Z.Naturforsch,* ***15a,*** *843-851.*

Schmitt, K.H., 1961: Untersuchungen an Schwebstoffteilchen in diffundierendem Wasserdampf . *Z.Naturforsch.*, **16a**, 144-149.

Talbot, L., Cheng, R.K., Schefer, R.W. and Willis, D.R., 1980: Thermophoresis of particles in a heated boundary layer. *J.Fluid Mech.*, **101**, 737-758.

Toda, A., Ohi,Y., Dobashi,R., Hirano, T., and Sakuraya, T., 1996: Accurate measurement of thermophoretic effect in microgravity. *J.Chem.Phys.*, **106**, 7083- 7087.

Toda, A., Ohnishi, H., Dobashi, R., and Hirano,T., 1998: Experimental study on the relation between thermophoresis and size of aerosol particles. *Int. J. Heat Mass Transfer*, **41**, 2710-2713.

Tong, N.T. 1975: Experiments on photophoresis and thermophoresis. *J.Colloid Interface Sci.,* **51**, 143-151.

Waldmann, L., 1959: Über die Kraft eines inhomogenen Gases auf kleine suspendierte Kugeln. *Z. Naturforsch,* **14a**, 589-599.

Yamamoto, K. and Ishihara, Y., 1988: Thermophoresis of a spherical particle in a rarefied gas of a transition regime. *Phys. Fluids,* **31** , 3618-3624.

EXPERIMENTAL STUDY OF DRIZZLE FORMATION - RESULTS FROM DYCOMS-II

Piotr Rasinski * and Hanna Pawlowska
Institute of Geophysics, Warsaw University, Poland

1. INTRODUCTION

Stratocumulus clouds persist over the large ocean's and land's areas re?ecting sunlight back to space. Aerosol indirect effect refers to the in?uence of anthropogenic aerosols on cloud microphysics and therefore on their radiative properties and thus on climate. An increase of cloud condensation nuclei (CCN) of anthropogenic origin added to the natural CCN modi?es clouds properties. At constant liquid water content (LWC) an increase of cloud droplet number concentration (CDNC) will be followed by a decrease of the droplet size. This process implies the growth of cloud re?ectivity (Twomey, 1977) known as a ?rst aerosol indirect effect. A decrease of the droplet size is also likely to impact warm cloud precipitation formation. It refers to as second indirect aerosol effect (Albrecht, 1989). This latter effect is still very poorly understood and even less quanti?ed. Parameterization of an impact of aerosols on precipitation and therefore cloud lifetime and extent is of great importance.
Our interest is to ?nd some essential microphysical conditions of the formation of drizzle in marine stratocumulus clouds using experimental data. The ultime objective is to allow better parameterization of these processes in large scale models. This study continues research on precipitation formation started during ACE-2 experiment (Pawlowska and Brenguier, 2003).

2. DATA SET AND PROCESSING

All data presented in this paper are in-situ, airborne measurements performed on NCAR/NSF130 aircraft during Dynamics and Chemistry of Marine Stratocumulus Experiment (DYCOMS-II). One of the goals of DYCOMS-II was to better understand the processes in marine stratocumulus-topped boundary layer that control formation and evolution of drizzle (Stevens et al., 2003).
The cloud droplet spectra have been measured with the Fast Forward Scattering Spectrometer Probe (FFSSP, Brenguier et al., 1998) and One-dimensional Array Probe Particle Measuring Systems 260X (OAP). Data obtained from the FFSSP - called cloud droplets - are in the diameter range 5 - 44 μm, (256 classes with varying bin sizes), and for the OAP - called drizzle drops - in the diameter range 15 - 645 μm (64 classes, bin size equals 10 μm). First three classes of the OAP measurements were omitted due to low accuracy (Korolev et al., 1998) and to avoid class overlapping with the FFSSP.
The data have been processed with 1 Hz frequency resolution that corresponds to the 100 m spatial averages.

* *Corresponding author address*: Piotr Rasinski, Institute of Geophysics, Warsaw University, ul. Pasteura 7, 02-093 Warszawa, Poland; e-mail: rasinski@igf.fuw.edu.pl

3. MICROPHYSICAL CLOUD STRUCTURE

From a large data set (7 ?ights, each about 8.5 hour long) the ?ight hc0106 (20 July 2001) was selected for the present case study. The reason for this choice is a presence of very different microphysical structures that is very expedient for the investigation of precipitation formation. Figure 1 shows time series of measurements performed during the ?ight through the cloud layer - one descent and one ascent (from 07:36:30 to 07:41:18 local time). This part of the ?ight is very interesting because they represent two different microphysical structures in adjacent cloud parts. The upper panel of the ?gure (Fig.1a) represents the aircraft track through the cloud layer. The cloud base is estimated at 220 m and the cloud top at 685 m. The position of the cloud base and cloud top are marked by dashed lines on the ?gure. Each descent and ascent lasted about 140 s. With the aircraft speed of about 100 m/s the horizontal distance ?own by the aircraft during each vertical traverses was about 14 km. Impossibility of obtaining a real vertical pro?le through the cloud layer is an inherent problem of airborne research. Assuming quasi homogeneity of boundary layer conditions (night ?ight over ocean) one can study difference in microphysical structure due to a difference in the stage of development of a cloud cell. CDNC is shown on the panel (b). On the ?rst part of the track the mean CDNC is equal to 103 cm^{-3} and on the second one 32 cm^{-3}. The very low values of CDNC close to the cloud base are due to the instrument's limitation, that misses very small droplets which are quite common at the cloud base. Difference in CDNC is striking. If it is not due to the difference in the aerosol boundary conditions, another explanation should involve droplet spectrum evolution, namely precipitation formation. The graph (c) informs us that drizzle is present in the second leg with the drizzle concentration up to 1.15 cm^{-3}. The ?rst part of the track (descent) is nearly void of drizzle. The lowest panel (Fig.1d) shows a time serie of droplet spectrum represented by 5 and 95 percentiles (dotted line), 25 and

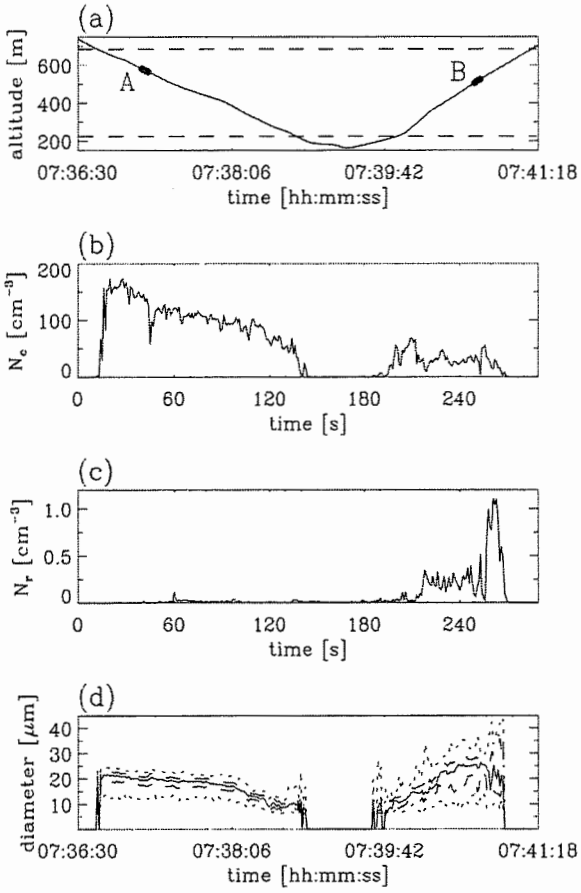

Fig. 1: Airborne measurements performed on the 20 July 2001. Data on 1 Hz resolution. (a) panel: aircraft track; (b) panel: droplets concentration measured by the FFSSP; (c) panel: raining drops measured by OAP 260X; (d) panel: percentiles of droplets spectrum.

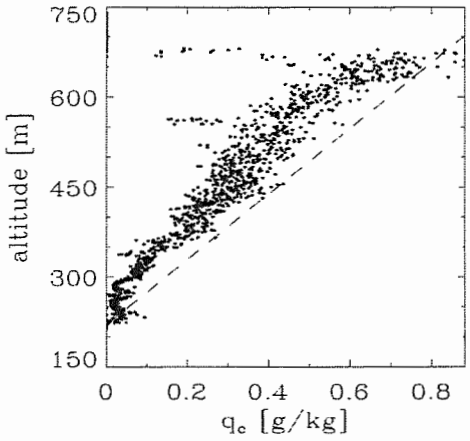

Fig. 2: Cloud droplets liquid water mixing ratio (q_c) vertical pro?le from descent through the cloud layer (Fig.1a).

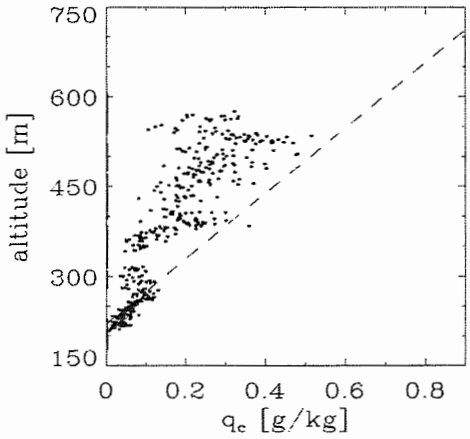

Fig. 3: Cloud droplets liquid water mixing ratio (q_c) vertical pro?le from ascent through the cloud layer (Fig.1a).

75 percentiles (dashed line) and 50 percentile (solid line). As could be expected that presence of drizzle involves smaller droplets concentration, bigger droplets sizes and wider spectrum.

Figure 2 presents liquid water mixing ratio vertical pro?le in non-precipitating part of the cloud (descent). Each dot represents a 10 Hz sampled value. Dashed line is following the adiabatic value of liquid water mixing ratio, which in shallow clouds is linearly dependent upon hight above the cloud base. The measured values are very close to the adiabatic approximation, reaching $q_c = 0.8 g/kg$ at the cloud top. This behavior corresponds well to what has been already observed in stratocumulus clouds (Pawlowska and Brenguier, 2000). In presence of drizzle one can not expect an adiabatic vertical pro?le in a cloud layer - this pro?le is shown on Figure 3.

To understand the difference in microphysical structure we shall study in details cloud droplets and drizzle spectra. Theory of precipitation formation in warm convective clouds de?nes three stages. First, condensation nuclei are activated, mainly at cloud base. Second, droplets formed on activated nuclei grow by vapor diffusion in convective cell. The droplet growth rate is inversly proportional to the droplet size. Small droplets are growing faster than big ones. The droplet spectrum becomes narrower with altitude. The third and last stage involves collision between cloud particles and their coagulation, referred to as collection. Droplets with diameter smaller than 12 μm have a negligible probability of coagulation. Above this size, this probability increases sharply. The combinantion of the three stages generally results on the following scenario for the particle spectrum. On a diameter scale, the particle growth rate starts with a maximum during activation and decreases with increasing diameter. A minimum is reached at about 40 μm that corresponds to the transition between

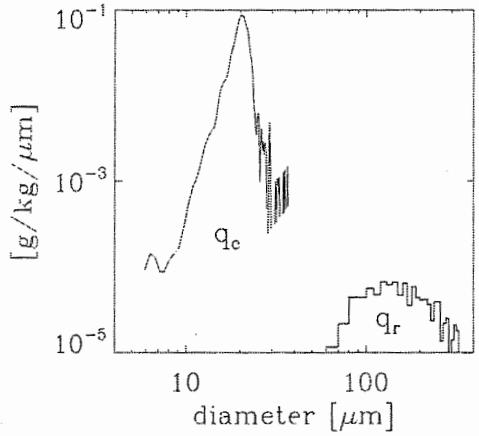

Fig. 4: Cloud droplets liquid water mixing ratio density (q_c) and drops liquid water mixing ratio density (q_r). The mean values are: $q_c = 0.40 g/kg$ and $q_r = 0.01 g/kg$.

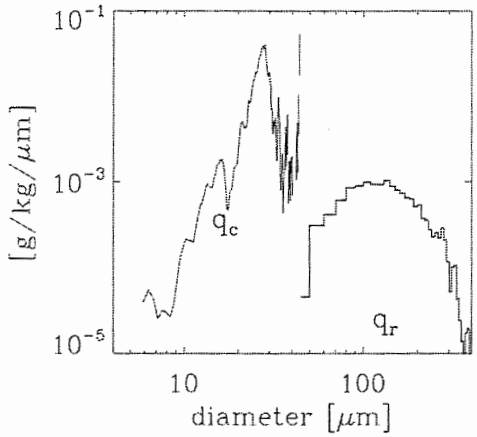

Fig. 5: Cloud droplets liquid water mixing ratio density (q_c) and drops liquid water mixing ratio density (q_r).The mean values are: $q_c = 0.22 g/kg$ and $q_r = 0.13 g/kg$.

condensation and collection processes.

Two examples of combined cloud droplets and drops liquid water mixing ratio density spectra are presented on Figures 4 and 5. Cloud evolution is usually vertically depended, therefore one can compare cloud droplets spectrum on a given level above the cloud base. The FFSSP data illustrated on Fig.4 and Fig.5 represent two 5 s intervals measured at about 570 m altitude, 350 m above the cloud base. Position of these sections are shown on Fig.1a and marked by letter A and by B.

Spectrum of drizzle drops does not depend on the altitude, therefore to get a better statistical representation of the OAP spectrum we decided to treat the data from a longer intervals corresponding to the whole pro?le in the cloud layer. Cloud droplets spectrum shown on Figure 4 is unimodal and quite narrow. Drizzle presence in this spectrum is very limited. Broad, bimodal cloud droplet spectrum is shown on Figure 5. Large amount of drizzle was observed. Bimodality of the cloud droplet spectrum is an evidence that collection process is developped in this part of the cloud.

4. CONCLUSIONS AND PERSPECTIVES

A case study of microphysical structure of a stratocumulus cloud in different stage of development was shown. Some interesting questions appears. Is bimodality of the droplets spectrum the cause or the effect of drizzle? How are related condensation and collision-coalescence processes with? What is the rate of drizzle production? To satisfy these questions we are planning to use in our further investigation two-dimensional kinematic model described in Grabowski (1998) with bulk parametrization Khairoutdinov et al., (2000) and explicit representation of microphysics with a stochastic scheme of drop collection (Tzivion et al., 1987).

5. ACKNOWLEDGMENTS

This work is sponsored by the European Union under grant EVK2-CT2002-80010-CESSAR and by the Polish State Committee for Scienti?c Research (KBN) under grant SPUB-M.

6. REFERENCES

Albrecht, B.A., 1989: Aerosols, cloud microphysics, and fractional cloudiness, *Science*, **245**, 1227-1230.

Brenguier, J.L., T. Bourrianne, A. Coelho, J. Isbert, R. Peytavi, D. Trevarin, and P. Wechsler, 1998: Improvements of the droplet size distribution measurements with the Fast FSSP, *J. Atmos. Oceanic Technol.*, **15**, 1077-1090.

Grabowski, W.W., 1998: Toward cloud resolving of large-scale tropical circulations: A simple cloud micropysics parametrization. *J. Atmos. Sci.*, **55**, 3283-3298.

Khairoutdinov, M., and Y. Kogan, 2000: A new cloud physics parametrization in a large-eddy simulation model of marine stratocumulus. *Mon. Weather Rev.*, **128**, 229-243.

Korolev, A.V., J.W. Strapp, and G.A Isaac, 1998: On the accuracy of PMS. Evaluation of optical array probes. *J. Atmos. Oceanic Technol.*, **15**, 708-720.

Pawlowska, H., and J. L. Brenguier, 2000: Microphysical properties of stratocymulus clouds during ACE-2. *Tellus, Ser. B*, **52**, 867-886.

Pawlowska, H., and J.-L. Brenguier, 2003: An observational study of drizzle formation in stratocumulus clouds for general circulation model (GCM) parameterizations. *J. Geophys. Res.*, **108**, 8630-8643.

Stevens, B., et al., 2003: Dynamics and Chemistry of Marine Stratocumulus Experiment - DYCOMS-II. *BAMS*, **84**, 579-593.

Twomey, S., 1977: The in?uence of pollution on the structure of clouds. *J. Atmos. Sci.*, **34**, 1149-1152.

Tzivion Shalva, Feingold G., and Zev Levin, 1987: An ef?cient numerical solution to the stochastic collection equation. *J. Atmos. Sci.*, **44**, 3139-3149.

Vanzanten, M.C., Stevens, B., Vali, G., and D.H. Lenschow, 2003: Observations of drizzle in nocturnal marine stratocumulus. *submitted to the J. Atmos. Sci.*

Droplet Growth by Turbulent Coagulation

N. Riemer[1] and A.S. Wexler[1,2,3]

[1]Department for Mechanical and Aeronautical Engineering, University of California Davis, Davis, CA, 95616, USA
[2]Department for Civil Engineering, University of California Davis, Davis, CA, 95616, USA
[3]Department of Land, Air and Water Resources, University of California Davis, Davis, CA, 95616, USA

1. INTRODUCTION

Clouds are an important environment for multiphase chemical transformations. These processes are crucially dependent on the cloud microphysical properties and have far reaching consequences concerning the direct and indirect climate effect of aerosols (Kreidenweis et al., 2003).

Droplet composition is observed to depend on droplet size, so an adequate description of the heterogeneous reactions in clouds therefore relies on a detailed knowledge of the factors controlling the droplet size distribution. In this context, droplet - turbulence interactions may play a major role (Pinsky and Khain, 1997; Shaw, 2003).

As laboratory and numerical work have shown the velocity and spatial distributions of particles may be modified significantly in a turbulent flow field. The key mechanisms of particle-turbulence interactions are that: (1) particle inertia leads to relative velocities and less correlated velocity directions and hence to higher collision rates, (2) wind field shear produces collisions between particles even with the same inertia (Saffman and Turner, 1956), and (3) coagulation rates should be enhanced due to local concentration increases for particles with response times on the order of the Kolmorgorov scale (Maxey, 1987). Although there is a general agreement in current literature that turbulence enhances the collision frequency of cloud droplets, this process is not yet well understood and therefore ignored in most current cloud models.

Corresponding author's address:
Nicole Riemer, Department for Mechanical and Aeronautical Engineering, University of California Davis, Davis, CA, 95616, USA. E-Mail: nsriemer@ucdavis.edu.

In our study we investigate by numerical simulation the impact of turbulence on the coagulation of cloud droplets using a kernel derived from direct numerical simulations (DNS) (Zhou et al., 2001). The developed model will be the basis for further evaluation of in-cloud chemistry, in particular addressing the question of sulfate production.

2. METHOD

Since experimental data of the droplet-turbulence interactions is difficult to obtain, modeling studies are an important tool for investigation. Zhou et al. (2001) recently developed a model for the turbulent coagulation kernel on the basis of the solution of the Navier-Stokes equations using direct numerical simulations (DNS). Their parameterization covers all three mechanisms mentioned above.

Employing this kernel, we consider a Lagrangian box model of a cloud parcel simulating the evolution of the cloud droplet size distribution, thereby addressing two questions:

- Can turbulence enhance the coagulation process in a way that large droplets are formed fast enough to explain the observed rapid production of warm rain?
- Do our predictions reproduce the observed broadening of the size distribution?

2.1 The turbulent coagulation kernel

The ensemble average of the collision kernel $K_t(r,r')$ for two particles with the radii r and r' in a turbulent fluid can be expressed in a generalized form by (Sundaram and Collins, 1997):

$$K_t(r,r') = 2\pi(r+r')^2 \langle |w_r| \rangle g(r+r'), \qquad (1)$$

$\langle |w_r| \rangle$: Ensemble average of the relative velocity of the particles.

$g(r+r')$: Radial distribution function at contact.

The functions $g(r+r')$ and $\langle |w_r| \rangle$ are parameterized on the basis of the DNS simulations

depending on the Stokes number of the droplets, the dissipation rate ε of the fluid and the r.m.s. velocity fluctuation u' of the fluid

2.2 Calculation of the size distribution

The stochastic collection equation describes the evolution of a colliding and coalescing cloud droplet size distribution (Pruppacher and Klett, 1997). In a first set of simulations, we solve this equation using the flux method by Bott (1998) and the turbulent coagulation kernel K_t according to equation (1). We use a Gamma function of the form $n(m,t) = L_w / m_g^2 \, exp(-m/m_g)$ as initial distribution, where L_w is the total cloud water content and m_g is the mean droplet mass which is related to the mean droplet radius by $m_g(r) = 4/3\pi\rho r_g^3$. For our simulations, L_w is set to 1 g m^{-3} and r_g to 10 μm.

In a second set of simulations we consider an air parcel with a prescribed aerosol distribution that undergoes a cooling process. The aerosol particles are activated and the processes of condensation/evaporation and coagulation shape the size distribution and feed back on the supersaturation of the system. The growth rate of the particles is calculated according to Majeed and Wexler (2001).

The dry aerosol mass is treated on a fixed grid, for the water mass we use a moving grid. The advantage of this hybrid approach for the treatment of condensation/evaporation of water is that it avoids unwanted numerical diffusion. It also ensures that the aerosol mass is regenerated after evaporation, which is important for the investigation of aerosol processing.

We use a log-normal distribution with a mean dry diameter of 0.3 μm, a total number of 1000 cm^{-3}, and a standard deviation of 1.65 as initial dry aerosol distribution. The temperature is 283 K at the start of the simulation and decreases over the course of the simulation with $\partial T / \partial t =$ 0.006 K s^{-1}.

3. RESULTS

Figure 1 shows the turbulent coagulation kernel K_t according to equation (1) for the base case (ε = 300 cm^2 s^{-3} and u' = 3.5 m s^{-1}). The turbulent coagulation kernel K_t exhibits a distinct local maximum for the combination of droplet radii near 65 μm and 250 μm using the base case values for ε and u'. The exact position as well as the magnitude of this maximum depend on ε and u'. For droplets smaller than 100 μm and/or equally sized droplets the turbulent kernel is two magnitudes larger that the sedimentation kernel in calm air. We can therefore expect that the impact of turbulent coagulation is especially significant in the initial stage of the development of the cloud whereas the impact decreases for large cloud droplets or rain drops.

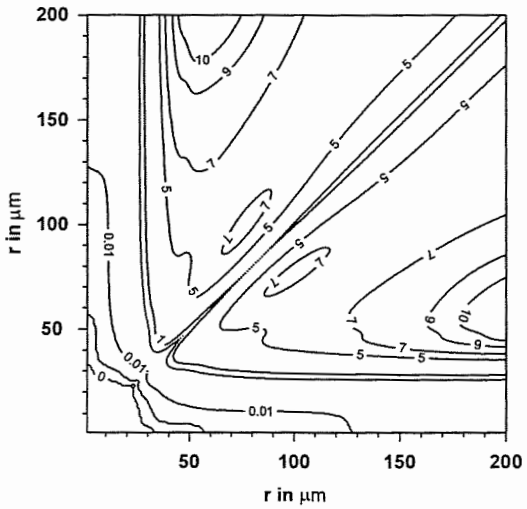

Fig. 1: K_t in cm^3 s^{-1} for ε = 300 cm^2 s^{-3} and u' = 3.5 m s^{-1} (base case).

Figure 2 shows results of the first set of simulations where only coagulation is considered and condensation is not included. Figure 2(a) and Figure 2(b) display the development of the mass distribution $g(\ln r)$ with time for the sedimentation kernel and for the turbulent kernel for the base case. For the sedimentation kernel a second mode appears only after about 30 minutes. At t = 30 min., most of the mass (97%) is still distributed over the droplet size range smaller than 100 μm, confirming the well known fact that sedimentation alone cannot explain the fast formation of large droplets.

For the turbulent kernel, the second mode forms already after 10 minutes indicating that the turbulent coagulation kernel of Zhou et al. (2001) accelerates the formation of large drops. Figure 2(c) shows the effect of the combined sedimentation and turbulent kernel. For this case, the second mode becomes visible after only 5 minutes, and after 30 minutes 96% of the mass is transferred to sizes larger than 100 μm.

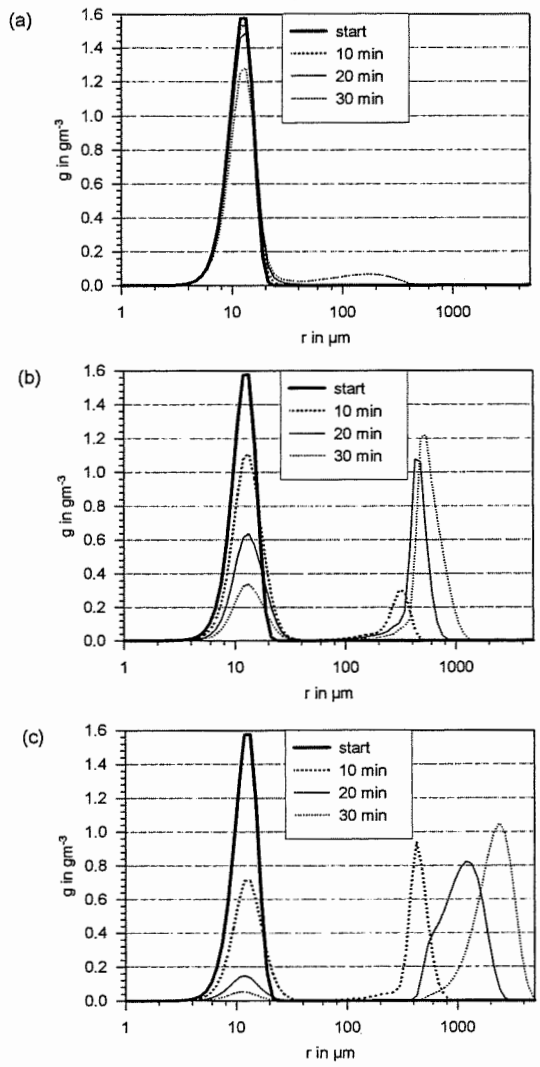

Fig. 2: (a) Temporal evolution of the mass size distribution with sedimentation kernel according to Hall (1980). (b) Same as Fig. 2(a), but for the turbulent kernel, base case. (c) Same as Fig. 2(a), but for the combined turbulent and sedimentation kernel.

The results so far show that turbulent coagulation significantly enhances the droplet growth, primarily due to the accumulation effect. To improve our approximation of real atmospheric conditions, we now also include the processes of condensation and evaporation as outlined in Section 2.

Figure 3 shows results of this second set of simulations where an aerosol distribution in an air parcel is considered that undergoes cooling. In Figure 3(a) the growth of the particles is shown when coagulation is not included. The well known narrowing of the distribution is obvious. Figure 3(b), on the other hand, includes turbulent coagulation and clearly shows a fast growth accompagnied by a broadening of the size distribution.

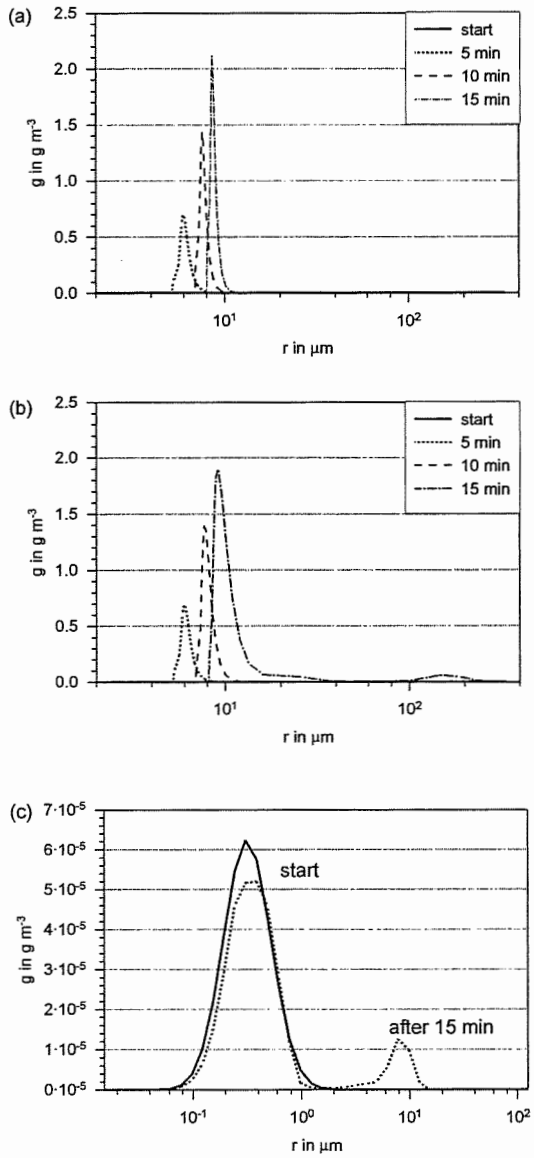

Fig. 3: (a) Temporal evolution of the mass size distribution of water, condensation only. (b) same as Fig, 3(a) but for condensation and turbulent coagulation. (c) same as Fig. 3(b) but for dry aerosol mass.

With the formation of larger droplets also aerosol mass is transferred to larger sizes. This is demonstrated by Figure 3(c) and illustrates that turbulent coagulation of cloud droplets plays a role in aerosol processing.

4. CONCLUSIONS

In this paper we investigate the impact of turbulence on the development of cloud droplet spectra. In a two-step approach we show first that – compared to the effect of sedimentation in calm air only – even moderate turbulence can enhance the formation of large droplets significantly. The largest impact of turbulence is expected for similar sized particles and/or for particles in the size range smaller than 100 μm. Here, the collision kernel is enhanced by several orders of magnitude if turbulence is included, which accelerates the growth of droplets dramatically.

By treating both coagulation and condensation we show that turbulent coagulation is also consistent with the observed broadening on the right side of the size distribution.

The presented model framework will be further extended to investigate in-cloud chemical processes and aerosol processing.

References

Bott, A., 1998: A flux method for the numerical solution of the stochastic collection equation, J. Atmos. Sci., 55, 2284 – 2293.

Hall, W.D., 1980: A detailed microphysical model within a two-dimensional dynamic framework: Model description and preliminary results. J. Atmos. Sci., 37, 2486 – 2507.

Kreidenweis, S.M., C.J. Walcek, G. Feingold, W. Gong, M.Z. Jacobson, C.-H. Kim, X. Liu, J.E. Penner, A. Nenes, J.H. Seinfeld, 2003: Modification of aerosol mass and size distribution due to aqueous-phase SO_2 oxidation in clouds: Comparisons of several models. J. Geophys. Res., 108, doi:10.1029/2002JD002697.

Majeed, M.A. and A.S. Wexler, 2001: Microphysics of aqueous droplets in clouds and fogs as applied to PM-fine modeling. Atmos. Environ., 35, 1639 – 1653.

Pinsky, M.B. and A.P. Khain, 1997: Turbulence effects on droplet growth and size distribution in clouds – A review. J. Aerosol Sci., 28, 1177 – 1214.

Maxey, M.R., 1987: The gravitational settling of particles in homogeneous turbulence and random flow fields. J. Fluid Mech., 174, 441 – 465.

Sundaram, S. and L.R. Collins, 1997: Collision statistics in an isotropic, particle-laden turbulent suspension. I. Direct numerical simulations, J. Fluid. Mech., 335, 75 – 110.

Pruppacher, H.R., and J.D. Klett, 1997: Microphysics of cloud and precipitation, Kluwer.

Shaw, R.A., 2003: Particle-turbulence interaction in atmospheric clouds. Annu. Rev. Fluid Mech., 35, 183 – 227.

Zhou, Y., A.S. Wexler, L.-P. Wang, 2001: Modelling turbulent collision of bidisperse inertial particles. J. Fluid Mech., 433, 77 – 104.

THEORETICAL STUDY OF COLLISION INDUCED DROPLET BREAKUP PHENOMENA

N. Roth, M. Hase, B. Weigand

Institute of Aerospace Thermodynamics, University of Stuttgart

1. INTRODUCTION

The size distribution of liquid droplets in clouds and during rain fall changes due to various processes as for instance evaporation, condensation, or breakup processes. For more reliable predictions of precipitation the size distribution of the droplets has to be known. Here, the collision induced breakup processes are studied in more detail with an inhouse DNS (*direct numerical simulation*) code. In the code the VOF (*Volume-of-Fluid*) method of Hirt and Nichols (1981) is used to obtain the additional information about the two-phase flow. With this code free surface flows like oscillating, colliding or free falling droplets can be simulated. Recently the equations for heat and mass transport with phase change has been implemented into the program in order to simulate evaporation processes (Hase and Weigand, 2004).

The initial conditions of the collision processes simulated here are shown in Fig. 1 schematically. The outcome of droplet collisions depends on the Weber number $\mathrm{We}_l = \varrho_l v_r^2 d_1/\sigma$ and the Reynolds number $\mathrm{Re}_l = \varrho_l d_1 v_r/\mu_l$ of the collision process as well as on the ratio $D = d_1/d_2$ of the droplet diameters of the collision partners and the excentricity $B = 2b/(d_1 + d_2)$ of the collision. For the Weber number and the Reynolds number the relative velocity between the droplets before the collision v_r, the droplet sizes d_i, and the properties of the droplet liquid, which is here certainly water, have to be taken into account here. It was assumed, that the droplets are falling at constant velocity driven by gravity forces, which are in equilibrium with the aerodynamic drag forces. Therefore the relative velocity is a function of the diameter ratio. As initial conditions for a droplet collision each collision partner started with the fallspeed according to its size. During the collision process the droplets are falling. Therefore, the flow around the droplets influences the collision and breakup processes in addition. For the flow field and for the interaction of the droplet liquid with the surrounding gas the Weber number We_g and the Reynold number Re_g defined by means of the material data of the gaseous atmosphere (subscript g), the drop diameter d_i, and the droplet fallspeed v_i are the essential dimensionless parameters (Prandtl et al., 1984).

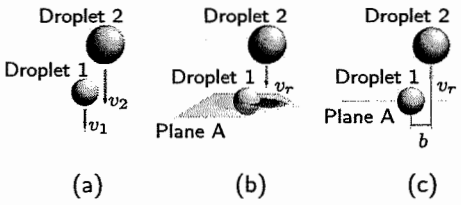

Fig. 1: Schematic view of the collision of two droplets in different coordinate systems. In the laboratory system the initial velocities of the droplets are $\vec{v}_1$ and $\vec{v}_2$ (a). In the coordinate system, which is located on the smaller droplet (b) the larger droplet approaches with the velocity $\vec{v}_r = \vec{v}_2 - \vec{v}_1$, where $\vec{v}_r$ is perpendicular to plane A, which contains the center of the smaller droplet. In (c) the distance b between the centers of the droplets can be seen clearly.

The initial values for the droplet velocity have been taken from a paper of Schönhuber et al. (1995). In this work velocity measurements of falling raindrops with a 2D-Video-Distrometer are compared with relationships of Atlas et al. (1973) and Gunn and Kinzer (1949). In order to obtain a collision between two falling droplets a second smaller droplet, which therefore has a lower initial velocity, has been placed close to the larger one, but below it, with an excentricity $B < 1$.

Corresponding author's address: Norbert Roth,Institute of Aerospace Thermodynamics, University of Stuttgart, Pfaffenwaldring 31, 70550 Stuttgart, Germany

2. NUMERICAL METHOD

The inhouse 3D CFD program FS3D (Free Surface 3D) has been developed to compute the Navier-Stokes equations for incompressible flows with free surfaces. The equations are solved without using a turbulence model or any other model by DNS. The governing conservation equations for momentum and mass are

$$\begin{aligned} \frac{\partial(\rho\mathbf{u})}{\partial t} &+ \nabla\cdot[(\rho\mathbf{u})\otimes\mathbf{u}] = -\nabla p \\ &+ \nabla\cdot\mu\,[\nabla\mathbf{u}+(\nabla\mathbf{u})^T]+\nabla\cdot\mathbf{T} \quad (1) \\ \nabla\cdot\mathbf{u} &= 0 \quad , \quad (2) \end{aligned}$$

where $\mathbf{T}$ is the capillary stress tensor which adds the surface tensor force to the momentum equation. Furthermore $\mathbf{u}$, ρ, μ and p are the velocity vector, the density, the dynamic viscosity and the pressure, respectively.

In two-phase flows additional information about the interface position between the disperse and the continuous phase are needed. In FS3D a Volume-Tracking method, well known as the VOF-method, is used (Hirt and Nichols, 1981). In the VOF-method an additional transport equation

$$\frac{\partial f}{\partial t}+\nabla\cdot(\mathbf{u}f) = 0 \quad (3)$$

for the volume fraction of the disperse phase is solved.

The variable f is called the VOF-variable. The VOF-variable is

$$f(\mathbf{x},t)=\begin{cases} 0 & \text{in the gas} \\ 0<f<1 & \text{at the interface} \\ 1 & \text{in the liquid}. \end{cases} \quad (4)$$

With the VOF-variable the change of the fluid properties across the interface can be computed by using the equations

$$\begin{aligned} \rho(\mathbf{x},t) &= \rho_l+(\rho_g-\rho_l)\,f(\mathbf{x},t) \quad (5) \\ \mu(\mathbf{x},t) &= \mu_l+(\mu_g-\mu_l)\,f(\mathbf{x},t) \quad . \quad (6) \end{aligned}$$

To ensure a sharp interface and to suppress numerical dissipation of the disperse phase in each time step the interface is reconstructed by the PLIC-method (*Piecewise linear interface reconstruction computation*) (Rider and Kothe, 1998). After the reconstruction, the liquid phase is transported on the basis of the reconstructed interface.

The code has been tested in different simulations and validated with experiments. Drag coefficient calculated with FS3D were in good agreement with an empirical calculation of Mulholland et al. (1988) which is derived from experimental data. The comparison of the drag coefficents are given in Rieber et al. (2000). More details of the numerical method can be found in Hase and Weigand (2004) and Rieber (2004).

3. RESULTS

Here the collision of a rain droplet of diameter $d_1 = 2.2\,\mathrm{mm}$ with a smaller droplet has been simulated. Without any collision the large rain droplet with a fallspeed of $v_1 = 6.9\,\mathrm{m/s}$ does not breakup as simulations showed (not displayed here).

The simulation of a collision with a cloud droplet of $d_2 = 0.2\,\mathrm{mm}$ with a fallspeed of $v_2 = 0.72\,\mathrm{m/s}$ did not result in a breakup for the tested excentricities $B = 0$ and $B = 0.5$, despite the high relative velocity $v_r = 6.18\,\mathrm{m/s}$. Only a grazing collision with $B \to 1$ is expected to result in one large and one or more very small droplets.

The collision with a drizzle droplet of diameter $d_2 = 0.9\,\mathrm{mm}$ with a fallspeed of $v_2 = 3.7\,\mathrm{m/s}$ and therefore, the relative velocity $v_r = 3.2\,\mathrm{m/s}$ results in a breakup. The sizes of the droplets in the outcome of the collision are quiet different. The size distribution depends on the excentricity B, as can be seen from Fig. 2.

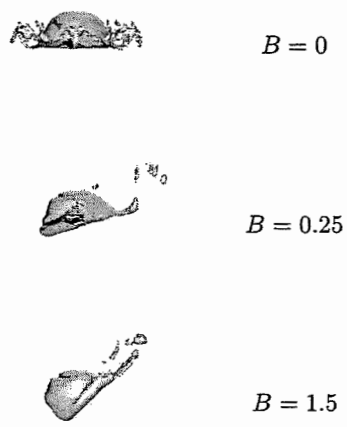

Fig. 2: Outcome at the collision time $t = 1.25\,\mathrm{ms}$ of the collision of a rain droplet with diameter $d_1 = 2.2\,\mathrm{mm}$ and fallspeed $v_1 = 6.9\,\mathrm{m/s}$ and a drizzle droplet with diameter $d_2 = 0.9\,\mathrm{mm}$ and fallspeed $v_2 = 3.7\,\mathrm{m/s}$. Shown is the result for different excentricities B.

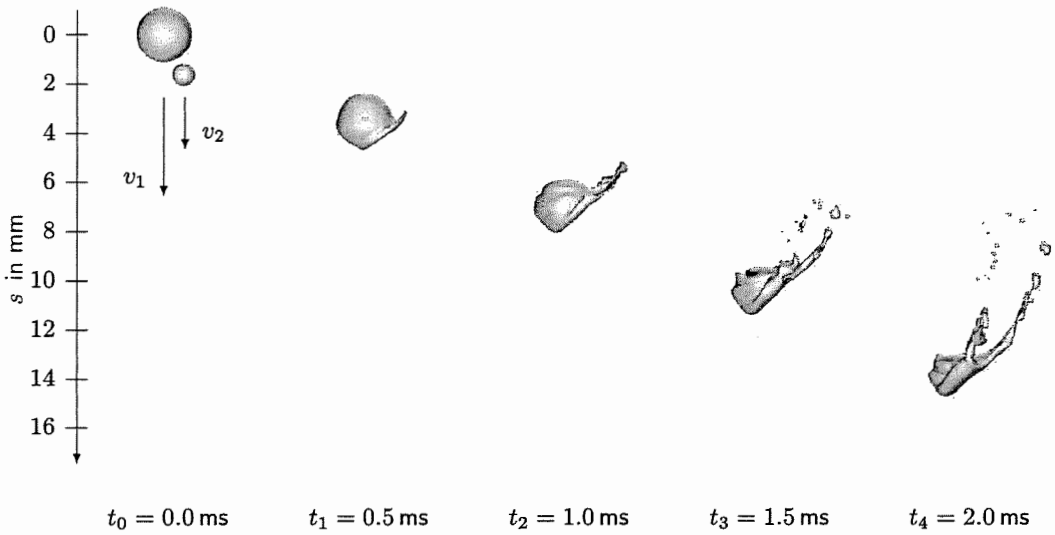

Fig. 3: Results of a collision process at different times t_i. Shown is the simulation of a collision between a droplet with diameter $d_1 = 2.2$ mm and fallspeed $v_1 = 6.9$ m/s and a drizzle droplet with diameter $d_2 = 0.9$ mm and fallspeed $v_2 = 3.7$ m/s. The excentricity was $B = 0.5$. On the left hand side the axis indicates the distance s the droplets fall during the collision process. The distance s is in the same scale as the images of the droplets. The droplets are moving in vertical direction

It can be seen, that for the excentricity $B = 0$ the final result contains many small droplets besides a larger one, whereas for increasing excentricity B the collision seems to result in a size distribution containing more larger droplets.

In order to make the collision processes clear different stages of a collision process are shown in Fig. 3 as example. In the figure rendered images of the colliding droplets are shown at different times during the collision process. The vertical positions of these images indicates the distance s the droplets have fallen during the collision process. As the distance s is plotted in the same scale as the droplets, this figure gives a better feeling about the collision process. Due to the impact of the larger droplet onto the smaller one ligaments are formed, which disintegrate into droplets caused by aerodynamic forces and Rayleigh instabilities. The smaller droplets are decelerated as their fallspeed is lower. As can be seen this process seperates the smaller droplets from the larger ones.

4. CONCLUSIONS

Collision processes between freely falling droplets have been simulated. It has been shown, that the breakup processes are influenced strongly by the excentricity B. The cases studied make clear, that much more simulations have to be performed in order to detect the limits between breakup and nonbreakup and to take account for the influence of the excentricity. In future works the initial conditions have to be modified to take the initial deformation of the droplet due to the flow into account. Evaluation methods have to be developed in order to obtain distributions of the droplet sizes from the outcomes of the collisions. These results are needed as input for the modelling of clouds and precipitation.

5. REFERENCES

Atlas D., Shrivastava R.C., and Sekhon R.S. Doppler radar characteristics of precipitation at vertical incidence. *Rev. Geophys. Space Phys.*, 2, 1973.

Gunn R. and Kinzer G.D. The terminal velocity of fall for water droplets in stagnant air. *J. Meteorol.*, 6:243–248, 1949.

Hase M. and Weigand B. A numerical model for 3d transient evaporation processes based on the Volume-of-Fluid method. In *Proceedings CHT-04*, Norway, 2004. accepted for publication.

Hirt C.W. and Nichols B.D. Volume of fluid (VOF) method for the dynamics of free boundaries. *Journal of Computational Physics*, 39:201–225, 1981.

Mulholland J.A., Srivastava R.K., and Wendt J.O.L. Influence of droplet spacing on drag coefficient in nonevaporating, monodisperse streams. *AIAA Journal*, 26:335–354, 1988.

Prandtl L., Oswatitsch K., and Wieghardt K. *Führer durch die Strömungslehre*. Vieweg, Braunschweig, Wiesbaden, 8th edition, 1984.

Rider W.J. and Kothe D.B. Reconstructing volume tracking. *Journal of Computational Physics*, 141: 112–152, 1998.

Rieber M. *Numerische Modellierung der Dynamik freier Grenzflächen in Zweiphasenströmungen*. Ph.D. thesis , Universität Stuttgart, 2004.

Rieber M., Graf F., Hase M., Roth N., and Weigand B. Numerical simulation of moving spherical and strongly deformed droplets. In *Proceedings ILASS-Europe 2000*, 2000.

Schönhuber M., Urban H.E., Poiares Baptista J.P.V., Randeu W.L., and Riedler W. Measurements of precipitation characteristics by a new distrometer. Technical report, Applied Systems Technology report, Joanneum Research, 1995.

PARTICLE–TURBULENCE INTERACTIONS IN CLOUDS: A MEASUREMENT PERSPECTIVE

R. A. Shaw*
Department of Physics, Michigan Tech, Houghton, Michigan 49931, USA

1. INTRODUCTION

Our current understanding of fundamental processes in clouds such as the collision and coalescence of droplets and the propagation of electromagnetic radiation, is based on the assumption, often implicit, that droplets are distributed in space in a perfectly random manner at small (sub-meter) scales. In fact, droplets in a cloud often do not follow what we might call the Poisson assumption, but instead are 'clustered' on various scales (Kostinski and Shaw 2001). Correlations in droplet positions can be caused by turbulent mixing of cloudy and clear air, by the inertial response of cloud droplets to fluid accelerations, or even by gravitational sedimentation in still air. The degree of spatial correlation is quantified by the pair correlation function, and its scale dependence is expected to vary with such variables as droplet size, energy dissipation rate, and turbulence Reynolds number (e.g., Shaw 2003). The very few sub-meter-scale spatial correlations measured in turbulent clouds are observed to be strongest at centimeter scales and below (Gerber et al. 2001, Kostinski and Shaw 2001, Pinsky and Khain 2001), and the pronounced clustering on these scales is consistent with the inertial clustering hypothesis. It should be noted, however, that all data from convective atmospheric clouds have been collected using one-dimensional instrument geometries (FSSP measurements, etc.) and this leaves a fundamental ambiguity in the magnitude and scale dependence of the pair correlation function at small scales (Holtzer and Collins 2002). Furthermore, most instruments are plagued by coincidence effects, which can become severe when droplets are clustered. The preliminary experimental evidence motivates further study of the physical mechanisms and possible atmospheric effects from cloud droplet clustering and turbulence interactions, but it is argued here that such studies will have to be carried out with great care.

Two new measurement approaches for detecting droplet clustering in clouds are under development. First, an airborne digital holographic system (HOLODEC, see description by Fugal et al. elsewhere in these proceedings) has been designed and tested in the field. This instrument will provide three-dimensional spatial distributions of cloud droplets. Second, a phase-Doppler interferometer (PICT, in collaboration with P. Chuang, UC Santa Cruz) is currently being constructed, and will be capable of measuring droplet spacing and droplet speed in one dimension. The purpose of this abstract is to develop a simple, analytical model for estimating the required instrument resolution, the resulting coincidence effects, and the subsequent effects on the estimated pair correlation function.

2. DISTRIBUTION OF FREE PATHS

Consider the detection of cloud particles with an fast-moving instrument with measurement cross section σ, given that the number density of particles is n. We wish to know know the probability of finding a subsequent (nearest neighbor) particle at distance z from the *most recently detected* particle. (Note that we are taking z to be the direction normal to the detection cross section of the instrument.) Let $p(z)dz$ be defined as the probability of finding a *nearest neighbor* particle between z and $z+dz$. Assuming there are no spatial correlations, this is equal to the product of the probability of *not* finding a particle in a distance less than z, and the probability of finding a particle between z and $z+dz$. The latter is simply $n\sigma dz$ as long as we choose dz to be sufficiently small such that $n\sigma dz \ll 1$. The probability of encountering no particles in distances less than z is simply 1 *minus* the probability of finding a particle in the same distance. Therefore we obtain the following expression (see Pruppacher and Klett 1997, Appendix A-2.1.5 for a similar treatment):

$$p(z)dz = (n\sigma dz)\left(1 - \int_0^z p(z')dz'\right).$$

The only solution satisfying this equation is

$$p(z) = n\sigma \exp\left(-n\sigma z\right),$$

which can be confirmed by noting that the integral has the simple solution $1 - \exp(-n\sigma z)$. This, of course, is the commonly known result that free

*Corresponding author's address : Raymond A. Shaw, Department of Physics, Michigan Technological University. Houghton, MI 49931, USA; E-Mail: rashaw@mtu.edu.

paths are exponentially distributed in a perfectly random medium, with mean free path $\bar{z} = (n\sigma)^{-1}$. Analogous expressions appear in the basic theory of optical propagation (the Beer-Lambert law) and the kinetic theory of droplet collision rates.

3. PAIR CORRELATION FUNCTION FROM FREE PATH PDF

Now, what is the procedure to follow when particles are spatially correlated? We use the pair correlation function $\eta(z)$, which is defined from the conditional probability of finding a particle distance z from another:

$$P_{1,2}(z) = ndV\left[1 + \eta(z)\right].$$

It follows that in our geometry the probability of finding a particle between distances z and $z + dz$ is $n\sigma dz[1+\eta(z)]$, and the probability density for nearest neighbors becomes

$$p(z)dz = n\sigma dz\left[1 + \eta(z)\right]\left(1 - \int_0^z p(z')dz'\right).$$

It should be possible, therefore, to determine the pair correlation function if the pdf $p(z)$ for nearest neighbor distances is known. Alternatively, if we know a functional form for $\eta(z)$ it is plausible that this equation could be used to find an expression for $p(z)$.

4. PARETO-DISTRIBUTED FREE PATHS

The pair correlation function for Pareto-distributed nearest neighbor distances serves as an example of droplet clustering. When the mean of the Pareto is constrained to be equal to the mean of the exponential distribution ($\bar{z}$) there is one remaining parameter, a, which determines the peak probability density at zero inter-particle distance. When this 'shape parameter' is appropriately chosen, the Pareto gives enhanced probability of finding particles closely spaced and far apart, and decreased probability of finding particles separated by the mean distance, relative to the exponential distribution (see Fig. 1). The distribution is

$$p(z) = \frac{a\left(\bar{z}(a-1)\right)^a}{z + \bar{z}(a-1)},$$

and the corresponding pair correlation function, obtained by the method outlined in Sec. 3, is

$$\eta(z) = \frac{\bar{z}a}{z + \bar{z}(a-1)} - 1.$$

As a model for droplet clustering we may choose $a = 2$ as a reasonable shape parameter, resulting in

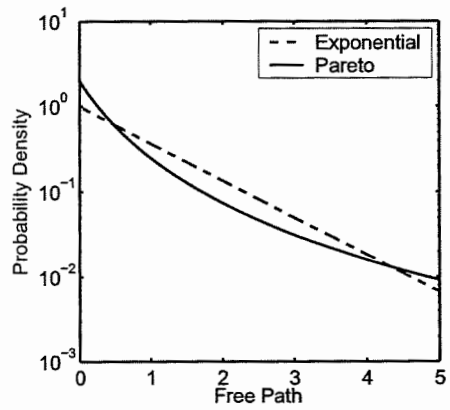

FIG. 1: Pareto and exponential free path distributions.

a peak value of $\eta(z = 0) = 1$ for the pair correlation function. Note that the collision kernel would be increased by a factor of approximately $\eta(z \approx 0) + 1$ if we were to treat that aspect of the problem here (Shaw 2003).

5. APPLICATION TO MEASUREMENTS

Here we estimate the influence of clustering on our ability to measure the very same clustering, or even more fundamentally, our ability to quantify droplet concentration. Instruments measuring droplet spacing have a finite detection volume and therefore are vulnerable to under-counting droplets due to the coincidence of two or more droplets in the measurement volume. A very simple estimate of this may be made by considering the cumulative distribution of free paths, evaluated at the instrument scale (along the flight direction), which we will call δz. For a perfectly random distribution of droplets, uncorrelated on all spatial scales, we have cumulative distribution

$$P_e(z) = 1 - \exp\left(-z/\bar{z}\right),$$

and for Pareto-distributed free path we have

$$P_p(z) = 1 - \left(\frac{\bar{z}(a-1)}{z + \bar{z}(a-1)}\right)^a.$$

Assuming that $\delta z \ll \bar{z}$ we may approximate the uncorrelated distribution as $P_e(z \ll \bar{z}) \approx z/\bar{z}$ and the correlated distribution as $P_p(z \ll \bar{z}) \approx (1 - 1/a)^{-1}z/\bar{z}$. Alternatively, we see that in this limit we may write $P_p \approx (\eta(0)+1)P_e$. The number of coincidence counts can be approximated as $P(z = \delta z)$. Therefore, the fraction of uncounted drops due to coincidence is strongly increased when droplet clustering occurs. It should be noted that this clustering can arise not only from droplet inertia but such

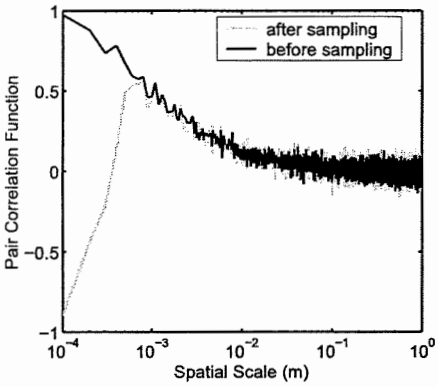

FIG. 2: Scale dependence of the pair correlation function before and after instrument sampling. The calculations are based on a population of 2×10^4 drops with realistic probe geometry and instrument-drop mean free path.

simple processes as turbulent mixing. Even modest clustering such as that used above with $a = 1$ results in a significant increase (doubling) of the fraction of uncounted drops. Furthermore, the uncounted drops are *the very drops* that are closely spaced and therefore contribute most to an estimate of $\eta(z)$ at small scales. Indeed, a Monte Carlo model based on Pareto-distributed free paths with $a = 2$ and accounting for realistic instrumental coincidence, shows that the peak of the estimated pair correlation function is reduced by a factor of 2 (for realistic cloud droplet sizes and concentrations). The pair correlation function $\eta(z)$ for this Monte Carlo simulation, both for the original distribution of 2×10^4 drops and after instrument effects are accounted for, are shown in Fig. 2.

So what can be done? First, instruments can be designed with much smaller measurement volumes, or with some other detection mechanism allowing closely-spaced particles to be counted as such. Indeed, the PICT instrument previously mentioned includes a signal processing feature for identifying the presence of more two particles in the detection volume at a given time such that coincidence effects are greatly reduced. Second, recognizing that most instruments will have a finite detection volume and therefore will miss closely-spaced drops, one can properly adjust for the under-counting during data post-processing. However, this adjustment requires that the pair correlation function or the free path distribution is known: it should be clear from this analysis that a correction based on Poisson-distributed particles may greatly underestimate the number of coincidence counts. The free path pdf or pair correlation function, necessary for a proper adjustment, could be obtained with a theory of droplet clustering or by making laboratory measurements with extremely high resolution and essentially no coincidence effects. No matter what approach one chooses, the detection of particle clustering at small scales is likely to remain a challenge experimentally.

ACKNOWLEDGEMENTS

I thank P. Chuang, M. Ftaclas, and A. Kostinski for helpful discussions. This research was supported by the U.S. National Science Foundation (ATM-9984294 and ATM-0320953).

REFERENCES

Gerber, H., J. B. Jensen, A. B. Davis, A. Marshak, and W. J. Wiscombe, 2001: Spectral density of cloud liquid water content at high frequencies. *J. Atmos. Sci.*, **58**, 497-503.

Holtzer, G. L., and L. R. Collins, 2002: Relationship between the intrinsic radial distribution function for an isotropic field of particles and lower-dimensional measurements, *J. Fluid Mech.*, **459**, 93-102.

Kostinski, A. B., and R. A. Shaw, 2001: Scale-dependent droplet clustering in turbulent clouds. *J. Fluid Mech.*, **434**, 389-398.

Pinsky, M., and A. P. Khain, 2001: Fine structure of cloud droplet concentration as seen from the Fast-FSSP measurements. Part 1. Method of analysis and preliminary results. *J. Appl. Meteor.*, **40**, 1515-1537.

Shaw, R. A., 2003: Particle-turbulence interactions in atmospheric clouds. *Ann. Rev. Fluid Mech.*, **35**, 183-227.

Observational Study on the Microphysical Structures of Rainfall-Producing Strati-form Clouds

Niu Shengjie, Sun Zhaobo and Fan Shuxian
Nanjing Institute of Meteorology, Nanjing 210044, P.R.China

I. INTRODUCTION

Rainfall is the result from the interactions among such factors as large-scale weather systems, in-cloud microphysical and dynamic processes, and those related to the formation and development of precipitation. In investigating the physical mechanisms and characteristics of rainfall it is necessary to combine macro- with microscopic processes. And the macroscopic aspects are explored by means of weather conditions, radar and satellite soundings while the microscopic features are gained by dint of cloud-droplet sizes, in-cloud water content, snow and ice crystals and raindrop spectrum.

In view of the importance of mid-level clouds to flight and rainfall, especially artificial rain increasing, many writers have undertaken research of the problem[1-7]. Based on flight measurements we carry out study of meso- and small-scale microphysical features of stratiform clouds and the precipitation therefrom.

II. DATA SOURCES

Microscopic measurements came from artificial rain increasing flights during June of 1994 and May of 1996, with samplers consisting of a PMS (Particles Measuring System), JH-90 temperature, pressure and humidity probing system developed by the Chinese Academy of Meteorological Sciences, of which the PMS had 3 probes of FSSP-100, OAP-2D-C and OAP-2D-P, the first measuring one-dimensional data of particles having diameters ranging over 2 to 47 um, the second and third over 25-800 and 200-6400 um, respectively, with 2D images recorded. All PMS soundings were processed by related software provided by the makers.

III. DATA ANALYSIS

3.1 Microphysical Characteristics and Persistent Precipitation with Their Evolution

Under the effects of an upper-air cold trough, Qaidam vortex, shear line and surface occluded front, light to moderate rain happened all over the region of Ningxia in NW China in 13-15, May, 1996, with total rainfall of 19.2 mm. At 2000 BT (Beijing Time), May 13, occasional drizzles occurred in Xiji county, followed by an 11-hr break; from 1000 BT, May 14, rain started in the county of Haiyuan, intensifying gradually and moving eastward, covering regions Xiji, Guyuan, Tongxin, Wuzhong, Yinchuan and Yanchi, step by step, with precipitation lasting 15 hrs and weakening in its easterly course. At 0800 BT, May 15 Haiyuan had rainfall and half an hour later rainfall began in Yinchuan. The event had its main zone in the two areas, peaking in intensity around 1130 and 1030 BT of the day, respectively, with a secondary maximum of 4.8 mm/h reached about 1600 BT observed at Yinchuan.

Four sorties are flown during precipitation, with the highest levels of 4.9 to 5.9 km, where the lowest temperatures were -7.7 ~ 12.3°C. The first flight corresponds to rainfall formation and development phases (2010 to 2200 BT, May 13) during which only Xiji station receives a small quantity of rain, FSSP-measured maximum content of water is 0.017 g/m^3, cloud droplets have mean diameter of 3.1 um and their maximum number concentration arrives at 1.29×10^8/m^3, indicating that in these phases the concentration is high, the spectrum narrow and water content small.

With rate of conversion into rainfall defined as $PE = LWC_{2DP} / \Sigma (LWC_{FSSP} + LWC_{2DC} + LWC_{2DP})$, we get mean PE of 63% for the duration. It is noted that the value given here represents only that for the given space and time intervals rather than that for rainfall from any part of the cloud at any time but nevertheless it can be utilized as a reference index for artificial rain increasing operations. The second flight (0920 - 1105 BT, May 14) is in the jump growth phase of precipitation and in the horizontal detection between 5.0 to 5.2 km levels the maximum FSSP-measured water content is 0.036 g/m^3, with mean droplet diameter of 5.4 um and maximum number concentration of cloud droplets of 9.5×10^7/m^3, during which larger-size ice particles emerge and 2DP-probed number concentration reaches 19/L, meaning that rainfall particles grow at the expense of cloud droplets. The time-dependent conversion rates at 5.0 to 5.2 km levels are shown in Fig.2. The third flight (1446 to 1700 BT, May 14) is performed in the peak rainfall stage, maximizing at 1.5 mm/h and maximal FSSP content of water is 0.0318 g/m^3 at 5.1 to 5.5 km heights, with the biggest number concentration of cloud droplets reaching 9.2×10^7/m^3. The fourth flight (2000-2342 BT, May 14) obtains maximum FSSP water content of 0.021 g/m^3, with particle diameters averaging 3.9 um. Fig.1 (omitted) shows that at the jump growth stage the conversion rates are quite big on the whole, despite their noticeable fluctuation.

By defining the zone between neighboring valleys on the time curve of the microphysical quantities as a cloud mass,

which is scaled from 35 to 80 km, we notice that the water content is roughly one order of magnitude bigger inside the mass than outside and the number concentration of cloud droplets differs by 1-2 orders of magnitude in and out of it. In their study on microphysical structures for rain happening on June 28, 1994, Fan and An[10] showed multiple small-scale cloud masses inside the research nephsystem, with <10 km scale clouds accounting for as high as 91%.

Fig.2 presents the distribution of mean size of particles in the different phases of the persisting rain-producing cloud, indicating that at the different stages of precipitation, the number concentrations of larger cloud droplets with mean sizes covering >20 to 30 um are 10^6 - 10^7/ m^3 (differing by one order of magnitude) and genesis of larger cloud droplets represents a key link for converting cloud into rain water for precipitation. Huang[8] et al. made observation of larger cloud droplets in a cumulus in Shanghai, showing that their number concentration is closely associated with macroscopic conditions, e.g., cloud thickness, whether rainfall is to occur or not, etc.[12] As a result, further studies are required of the distribution of larger cloud droplets in a warm portion of stratiform clouds.

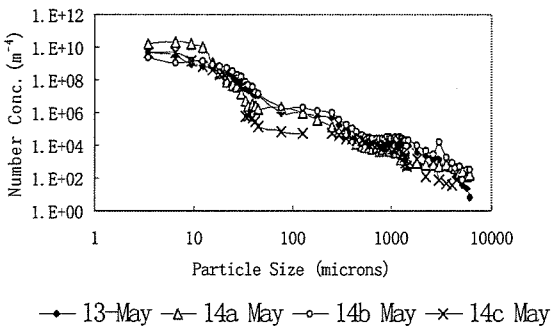

Fig.2. Distribution of mean sizes at different phases of the persistent rain-generating cloud.

3.2 Features of Vertical Microphysical Structures of the Clouds

Dominant systems affecting the rainfall on June 28, 1994 include a Hexi (westward of the Yellow River) cold trough, Qaidam vortex, inter-high shear line and surface cold front. The rainfall lasts approximately 13 hrs, producing a primary peak and a secondary one at all the stations but Yinchuan area, with the major interval giving 8.5 mm/h.

Fig.3 gives a temperature-dependent number concentration of cloud droplets and water content during rainfall. It is seen from Figs.3a and b that below 0°C level

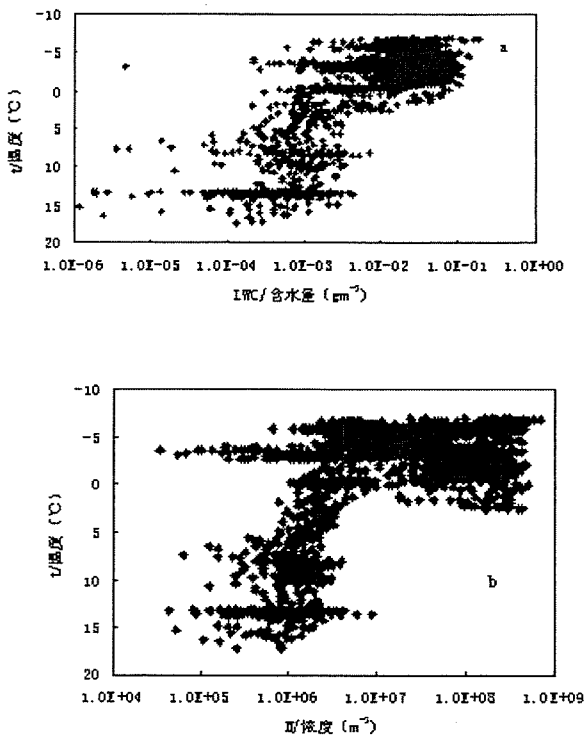

Fig.3. Distribution of temperature-varying microphysical structures of water content (a) and number concentration of cloud droplets (b) for rainfall on 28. June 1994.

both increase versus temperature drop and above the level the content of ice water is augmented with altitude, suggesting greater quantities of super-cooled water in the cloud for high potentials of precipitation. Hence, catalysis should be done in a more strongly negative temperature zone as far as possible. Fig.3c (not shown) presents that the size of cloud droplets is comparable under the melting level but greater amounts of larger droplets are present above, a condition making it easy to start rainfall, which is likely to be a cause of stronger happening observed.

IV. CONCLUDING REMARKS

A rain-producing stratiform cloud system contains 35-80 km cloud masses of which the microphysical structures differ greatly inside and outside. The full spectrum consisting of 2 to 6400 um differs, to some extent, from phase to phase for rainfall occurrence, differing dominantly in number concentration and spectral width.

For the rain generating stratiform cloud the water content and concentration of cloud droplets increase as a function of temperature drop and height rise, reaching maximum above

the melting level. Cloud droplets change little in diameter below the level but considerably above, suggesting some bigger particles present there that contributes to rainfall intensity.

This gives us a hint that rain-increasing operation should be performed in stratiform cloud mass as much as possible and the target level ought to be high enough to reach a zone with maximum amount of super-cooled water.

The problem concerning cloud-into-rain-water conversion rates and microphysical structures remains to be studied in depth.

ACKNOWLEDGEMENT This work is sponsored jointly by the Natural Sciences Foundation of China under Contract 40175003 and Ministry of Sciences and Technologies of China 2001BA901A.

REFERENCES

[1] Fleishauer, R. P., V. E. Larson and T. H. Vonder Haar, 2002, Observed microphysical structure of middlelevel mixed-phase clouds, *J. Atmos. Sci.*, 59(1):1779-1804.

[2]You Laiguang and Ma Fumin, 1989, Advances in research on resources for artificial rain-making in the north of China, in Symposium of the 9th National Meeting on Cloud Physics and Weather Modification, *China Meteorological Press*, Beijing,1-9.

[3] Niu Shengjie, Ma Tiehah, Lu Yulian, etc, 1993, Observational study on microphysical structure of summertime rainfall-providing stratiform clouds in Ningxia, *Plateau Meteor.*, 11(3): 241-248.

[4] Niu shengjie, An Xialan and Sang Jianren, 2002, Observational research into the parameters of distribution of raindrop sizes from summer different synoptic systems in Ningxia, *Plateau Meteo.*, 2002, 21(1), 37-44.

[5] Niu Shengjie, Ma Lei and Zhe Tao, 1999, Preliminary study on spectral distribution of hailstones and Ze-E relation, *Acta Meteorological Sinica*, 57(2):217-225.

[6] Niu Shengjie, An Xialan, Chen Yue et al., 2000, Measurement and initial analysis of the number concentration of atmospheric ice nuclei in the Helanshan mountain district of Ningxia, *J. Nanjing Institute of Meteorology*, 23(2):294-298.

[7] Fan Shuxian and An Xialan, 2000, Measurement and analysis of the concentration of cloud condensation nuclei over the Hrlanshan Mountains, *China deserts*, 20(3):338-340.

[8] Huang Meiyuan, Chen Yanjuan, He Zhenzhen et al. 1986, Study on the distribution of large cloud droplets in cumulus over the region of Shanghai, in Collection on Cloud Physics and Artificial Rain making in the South of China, *China Meteorological Press*, Beijing, pp.74-84.

CHARACTERISTICS OF RAINDROP SPECTRA OF STRATIFORM-CLOUD PRECIPITATION IN AUTUMN 2002 IN HENAN

SHI Aili[1] ZHENG Guoguang[1] HUANG Gen[1] ZHOU Yuquan[2]

[1]Chinese Academy of Meteorological Sciences, Beijing, 100081, CHINA
[2]Henan Office of Weather Modification, Zhengzhou, 450003, CHINA

1 Introduction

Raindrop spectra is important for us to deeply understand microphysics process; research the mechanism of precipitation; access the cloud water conditions for rainfall enhancement; check the effect of rainfall enhancement; give the scientific basic for numerical simulation. Based on the observations of raindrop spectra collected from the precipitation processes of stratiform cloud during October 17-20, 2002 in the Henan province, the characteristics of raindrop spectra in different observing sites have been analyzed.

2 Raindrop spectra distribution and its characteristics of fluctuation and Z-I relation

Table 1 Distribution of Microphysical Characteristics Parameters of Stratiform-cloud Precipitation Raindrop Spectra in 6 Sites of Henan from October 17 to 20, 2002

Station	N(m^{-3})	I(mm/h)	Q(g/m^3)	$\overline{D_1}$ (mm)	$\overline{D_2}$ (mm)	$\overline{D_3}$ (mm)	$\overline{D_{max}}$ (mm)
Tanghe	398.6	0.52	0.04	0.44	0.476	0.52	1.51
Taikang	1020.3	2.62	0.19	0.58	0.618	0.70	1.60
Kaifeng	468.7	0.50	0.04	0.46	0.498	0.54	1.50
Xiping	691.2	0.62	0.06	0.46	0.481	0.56	2.03
Xinmi	278.2	0.67	0.04	0.52	0.567	0.63	1.90
Xinzheng	346.8	0.28	0.02	0.44	0.458	0.49	1.26
Meanvalue	534.0	0.87	0.07	0.48	0.516	0.57	1.63

In table1, $\overline{D_1}$、$\overline{D_2}$、$\overline{D_3}$、$\overline{D_{max}}$ are mean diameter, mean square diameter, mean cube root diameter and maximum diameter of raindrop. N, I are raindrop number concentration and rainfall intensity, Q is mean water content. The average diameter, mean maximum diameter, and number concentration of raindrops, rainfall intensity and liquid water content of the precipitation were as follows: 0.48mm, 1.63mm, less than 1000/m^3 , 0.87mm/h and 0.07g/m^3, respectively. Table2 was the ratio and contribution of each range of raindrop. The number concentration of raindrops less than 1mm, between 1mm and 2mm, between 2mm and 3mm and larger than 3mm were n, N_{12}, N_{23} and N_3, and rainfall intensity of which less than 1mm, between 1mm and 3mm and larger than 3mm were I_{01}, I_{13} and I_3, respectively. According to the formula $Z=\Sigma N_i D_i^6$, we calculated the echo of radar Z and the echo intensity by the formula 10*LgZ. Table2 showed that the most contribution to rainfall intensity was the raindrops less than 3mm and the mean value of contribution was amount to 97.47%. Among of which, raindrops between 1mm and 3mm played an important role, the value was 59.35%. The contribution of raindrops less than 1mm was 38.12%. For the contribution to number concentration of raindrops, contribution of raindrops less than 1mm, larger than 1mm and larger than 3mm were 95.75%, 3.52% and 0, respectively. The mean value of calculated echo intensity of radar was 23.2 dBz, which was in lined with the actual value 20-30dBz and was in the range of usual echo intensity of stratiform cloud precipitation. According to formula of $Z=aI^b$, the relation of Z-I retrieved in this precipitation process was $Z=298.4I^{0.8}$.

Shi Aili, Chinese Academy of Meteorological Sciences, No.46, Nandajie, Zhongguancun, Haidian District, Beijing, China;E-Mail: shial@cams.cma.gov.cn

Table 2 Contribution to number concentration and rainfall intensity of each range raindrop

Station	n/N (%)	N_{12}/N (%)	N_{23}/N (%)	N_3/N (%)	I_{01}/I (%)	I_{13}/I (%)	I_3/I (%)	Echo intensity(dBz)
Tanghe	97.6	2.3	0.10	0.005	28.6	61.2	2.4	23.9
Taikang	92.6	7.4	0.03	0.000	39.9	61.1	0.0	27.6
Kaifeng	97.7	2.3	0.12	0.000	38.9	59.7	0.0	21.5
Xiping	94.4	5.6	0.09	0.006	30.9	67.5	1.5	23.9
Xinmi	94.6	1.5	0.02	0.000	52.7	47.4	0.0	18.9
Xinzheng	97.6	1.7	0.04	0.005	37.7	59.2	3.1	23.5
Mean value	95.8	95.8	0.05	0.003	38.1	59.4	1.2	23.2

Table 3 Fluctuation of microphysical parameters

site	Tanghe	Taikang	Kaifeng	Xinmi	Xinzheng	Xiping	Mean value
δ N	0.123	0.043	0.104	0.071	0.093	0.097	0.089
δ D	0.010	0.013	0.176	0.021	0.011	0.020	0.042
δ I	0.168	0.080	0.145	0.138	0.126	0.147	0.134

In order to quantitively analyze the characteristics of fluctuation of precipitation, we calculated the quantity of fluctuation δ (x): δ (x)= σ (x)/ μ (x), in the formula, σ (x) stands for the of variation x, μ (x) stands for the of variation x. We can see from table 3 that the fluctuation of stratiform cloud was comparatively small. The fluctuation quantity was as follows: rainfall intensity was the biggest, which was 0.134; mean diameter was 0.042; number concentration was between the above mentioned, which was 0.089. The precipitation fluctuation of Taikang was the smallest in all the observing sites, each fluctuation of which was less than the mean value.

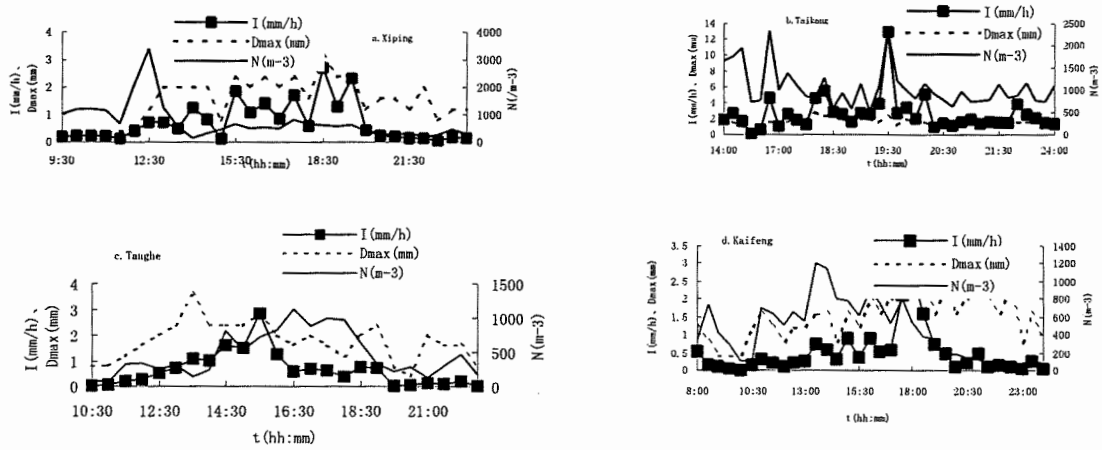

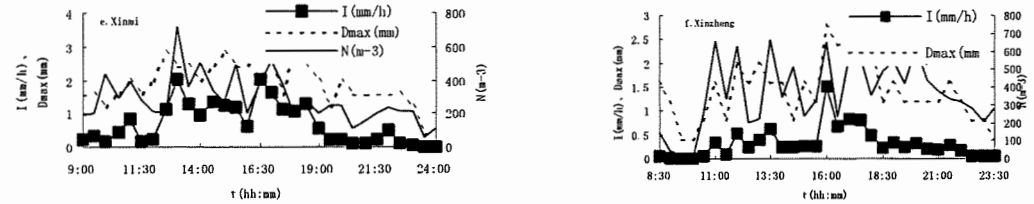

Fig.1Distribution of microphysical characteristics parameters in 6 sites in Henan from October 17 to 20, 2002

Fig. 1 was the evolvement of the microphysical parameters rainfall intensity, number concentration and maximum diameter with time on October 19 in different sites. There was an obvious specialty that in most sites, the variation of N and I was the same phase and the position of peak value was the same while the variation of Dmax and I was same sometimes. It was also shown that Dmax had the tendency of emergency ahead of time, such as at the time of 15:30, 21:50 of Fig. 1(a), 13:30, 16:30 and 20:30 of Fig. 1(c), 19:00 of Fig. 1(d), 12:30, 20:30 of Fig. 1(e), 12:30 of Fig. 1(f), Dmax added up to peak value, followed with peak value of N and I, then Dmax was low value. That is, there was big raindrop dropping before N and I increased, which was the same as the results that Gu Zhenchao (1962) found.

3 Space and Temporal distribution characteristics of raindrop spectra

We adopted the M-P distribution (1948) and the Γ distribution (1978) to analyze raindrop spectra in different sites. Fig. 2 showed the raindrop spectra and retrieved spectra of different sites. From Fig. 2 we can see that the raindrop of Taikang station with the M-P distribution was best, on the larger and smaller sides the retrieve error was comparatively small. While at other sites, the error was big, the possible reasons of which were the limited samples and natural changes and reading error. From Fig.3, we can see that the variation of n_0、 λ was consistent.

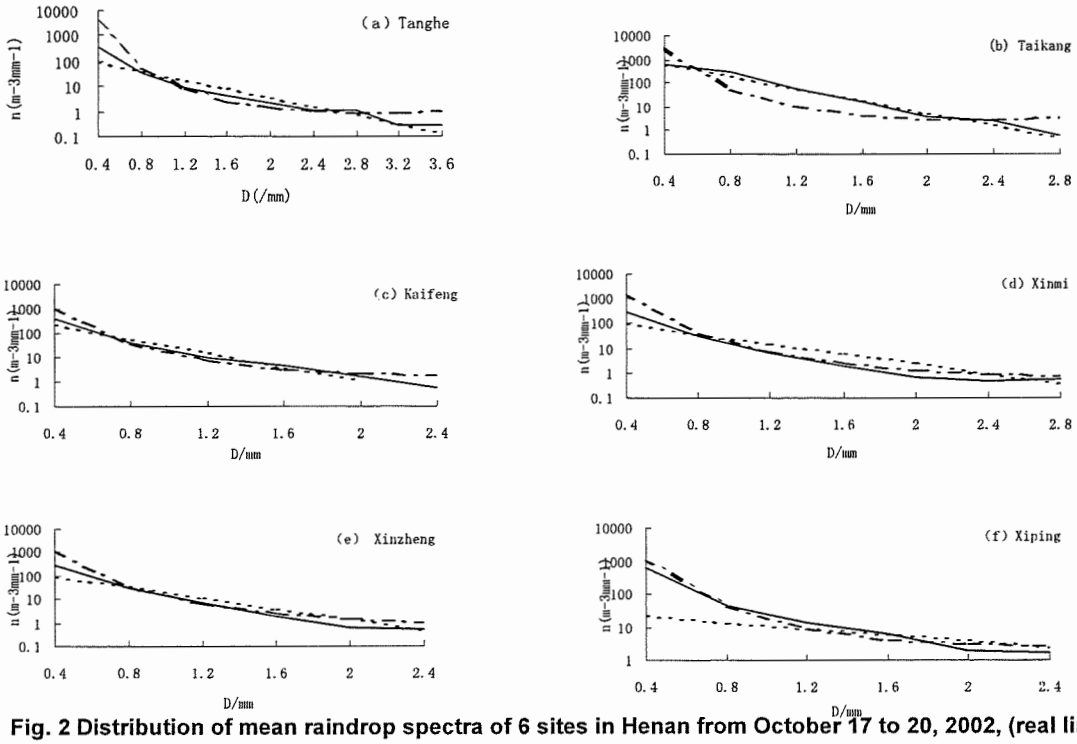

Fig. 2 Distribution of mean raindrop spectra of 6 sites in Henan from October 17 to 20, 2002, (real line was actual distribution, dash line was retrieved M-P, dot and line was retrieved Γ distribution)

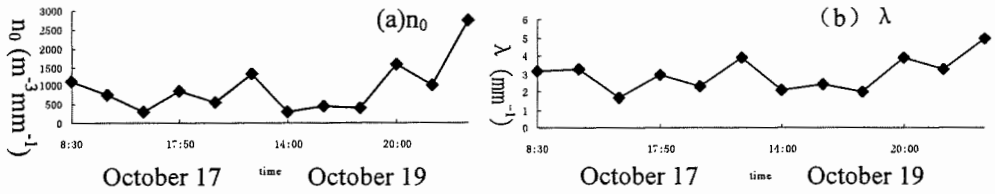

Fig. 3 Distribution of parameters n_0、λ with time. (a) distribution of n_0 (b) distribution of λ

4 conclusions

(1)The microphysical characteristics of this stratiform cloud precipitation process were that the average diameter, average maximum diameter, and number concentration of raindrops, rainfall intensity and liquid water content of the precipitation were as follows: 0.48mm, 1.63mm, less than 1000/m^3 , 0.87mm/h and 0.07g/m^3, respectively. The fluctuation quantity of precipitation was small.

(2)The calculated intensity of radar echo was close to the observed one. The relation of Z and I was $Z=298.4I^{0.8}$.

(3)The observed raindrop spectra can be expressed by a M-P distribution, except the bigger and smaller sides of raindrop spectra. The Γ distribution was better to express the raindrop spectra. The actual raindrop spectra and retrieved raindrop spectra was closest in Taikang station.

(4)The variation tendencies of n_0、λ with time in the M-P distribution were in good correlation.

Acknowledgements

This paper was supported by the "the tenth five years" project "the Research and model of Rainfall enhancement Technology " (2001BA610A-06) of Ministry of Science and Technology. We sincerely thank the weather modification office of Henan for giving us the data.

References

[1] Gu Zhenchao. Microphysical Characteristics of Cloud and Fog Precipitation in China, Science Press, 1962.

[2]Marshall J S and Palmer W M. The distribution of raindrops with size.J Meteor.1948(5):165-166.

[3]Takeuchi D M. Characterization of raindrop size distribution. Preprints of Conference on Cloud Physics and Atmospheric Electricity, Issaquah, Amer Meteor Soc, 1978. 154-161.

[4]Ulbrich C W. Effect of size distribution variations on precipitation parameters determined by dual-measurement techniques. Preprint of 20th Conference on Radar Meteor, Boston, Amer Meteor Soc,1981.276-281.

[5] Wang Pengfei, Li Zihua. Microphysical cloud physics. Meteorological Press, 1989.

[6] Zhang Peichang, Dai Tiepie, Du Binyu, Tang Dazhang. Radar Meteorology, Meteorological Press, 1988.

Characteristics of Water Vapor Conditions in Autumn Stratiform Clouds And It's Potential for Rainfall Enhancement in Henan Province in 2002

[1]Shi Aili and [1]Zheng Guoguang

([1]Chinese Academy of Meteorological Sciences, Beijing, 100081, CHINA)

1. Introduction

The abundant moisture in clouds is one of the necessary conditions for rainfall enhancement. The characteristics of water vapor conditions of stratiform clouds and their potential for rainfall enhancement in autumn 2002 in the Henan Province of the central part of China have been investigated by means of data from meteorological observation, from upper-air soundings with 3-hr interval, and from Ground-Based Dual-Wavelength Microwave Radiometer (GBDWMR) System and meteorological satellites. The characteristics of water vapor conditions of statiform cloud and it's rainfall enhancement from October 16 to 19 2002 in Henan province was analyzed in the paper.

2. Water vapor and potential precipitation

The content of integral water vapor (V) and integral cloud liquid water (L) can be retrieved from data of Ground-Based Dual-Wavelength Microwave Radiometer System. We can see from the results that during the whole process, the variation range of V was smaller that that of the L. V and L amounted to the maximum before the precipitation. With the development of precipitation, the value of V and L were gradually decreased, which decreased one order respectively. The fluctuation of L was larger and had a momentous add up near the precipitation. The moment of maximum rain intensity happened at 15, 16 and 21 October 19, the value of V and L were added at that time, The maximum and minimum of V amounted to 50mm and 6mm respectively. The value of V was 10.7mm, 9,19mm and 12.74 mm at time 07, 10 and 13 respectively. Yang Jinmei(1996) showed the relation between potential precipitation and surface pressure.

$$W=0.321+0.193e \qquad (1)$$

W is the potential precipitation (cm), e is surface pressure (hPa). According to formula (1), the value of W and e can be calculated (see Table 1). We can see from the table1 that the relation of W and e is linear. During the whole process, e was accumulated to maximum of 19.3hPa and gradually decreased. W increased at first and was expensed gradually. Compared with the results of the GBDWMR of Xinxiang station, the value of W in formula (1) was larger, but the trend was same.

Table1 Surface pressure and potential precipitation in Zhengzhou from October 16 to 19, 2002

Month	October										
Day	16		17		18		19				
Time	07	19	07	19	07	19	04	07	10	13	16
e(hPa)	12.1	14.8	17.1	19.3	14.8	10.0	9.8	9.7	9.2	9.3	9.2
W(cm)	2.65	3.18	3.62	4.05	3.18	2.26	2.21	2.19	2.09	2.12	2.09

3. Water vapor transportation

We computed the maximum of water vapor transportation and water vapor content between different levels. (see Fig.1). Fig.2 shows that in the development of this process, the fluctuation of θse and q was comparatively big. At 04, 13 October 17 and 04 October 19, below the level of 500hPa, the contour of θse above Zhengzhou station obviously concaved and the contour of q protruding, which showed that there was evident updraft in cloud and good condition for water vapor transportation.

Shi Aili, Chinese Academy of Meteorological Sciences, No.46, Nandajie, Zhongguancun, Haidian District, Beijing, China;E-Mail: shial@cams.cma.gov.cn

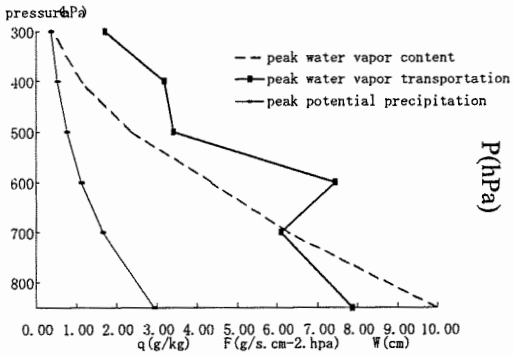

Fig. 1 Distribution of water vapor with the height from 850hPa to300hPa level in Zhengzhou station from October 16 to 19.

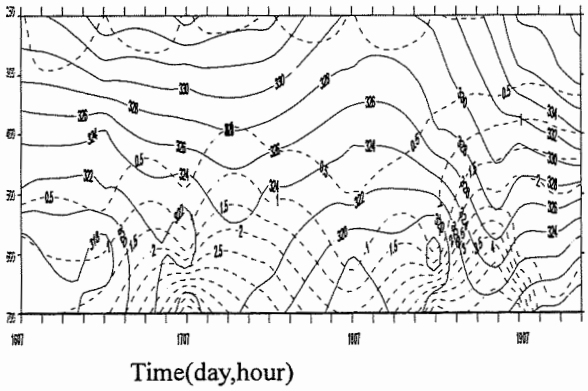

Fig. 2 Vertical cross-section of θ_{se}(real line, K),q (dashed line, g/kg) of Zhengzhou station from October 16 to 19

4. Regions with saturation and ice-water transition

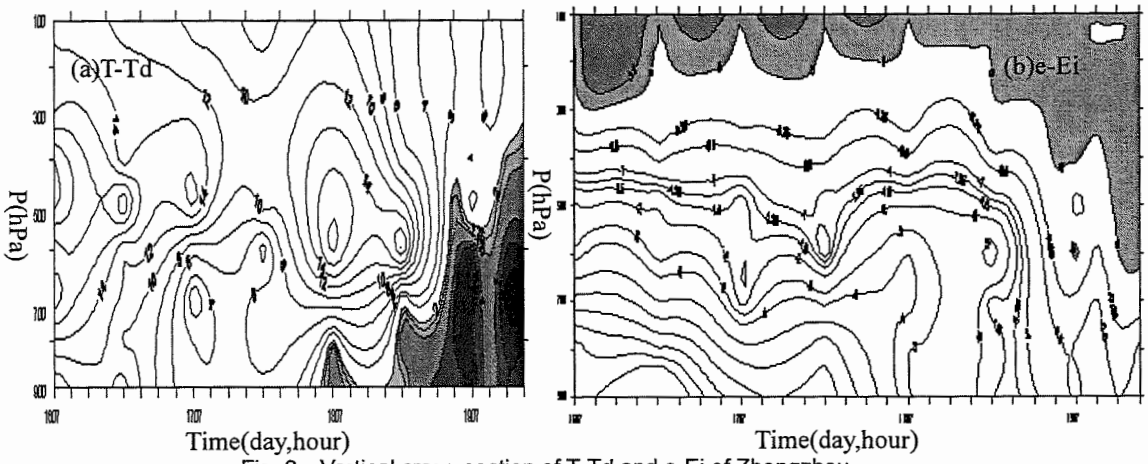

Fig. 3 Vertical cross-section of T-Td and e-Ei of Zhengzhou Station from October 16 to 19. a. T-Td . b. e-Ei

From Fig. 3(b) we can see that at 04 October 19 the region of e-Ei>0 was located at the level above 400hPa; at 07 October 19 the region was located at the level of 600hPa-500hPa and above the level of 400hPa; at 10, 13 and 16 the region were located at the level above 300hPa and 600hPa respectively. The above showed that the region of ice-water transition was generated originally at the high level, that is, with the time went by, the region of ice-water transition evolved towards the low level. From the shape of the contour, we can see the distribution of

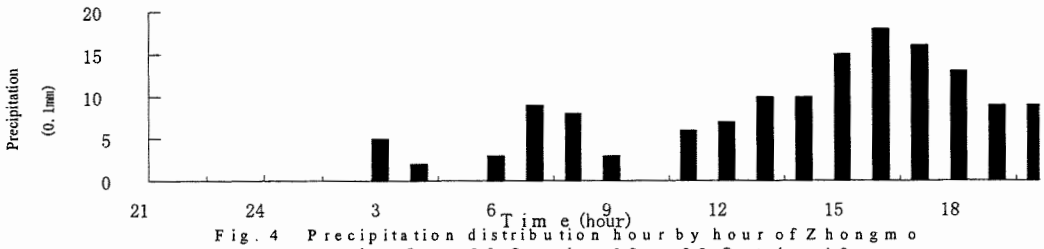

Fig. 4 Precipitation distribution hour by hour of Zhongmo station from 20 October 18 to 20 October 19

contour was horizontal before precipitation while it became vertical with the forthcoming ofprecipitation. The horizontal grads of contour below the level of 400hPa obviously increased, that is, the vice value of e-Ei had a quick increase before precipitation. For example, at 07 October 18, the value of e-Ei at the level of 925hPa was -3.0hPa, it added up to -1.43hPa at 19 and to -0.69hPa at 04 October 19. The increment was the result of the increment of water vapor pressure. Before precipitation, the accumulation and transportation of water vapor above the level of 0^0C resulted in the increment of water vapor pressure, which was helpful for rainfall enhancement. With the development of precipitation, the consumption of water vapor was large than the complement of water vapor, which made the water vapor pressure in the cloud and the value of e-Ei decrease. So the region of ice-water transition disappeared quickly. Fig.4 was the precipitation distribution of Zhongmu County from 20 October18 to 20 October 19. We can see from it that the precipitation was in good harmony with the region of ice-water transition and the peak value of ice-water transition and precipitation was originated at the same time. Compared with the Fig.3(a), the time was corresponding with the period of most high and most deep saturation, which was benefit for the increment of precipitation particles.

5. Analysis of potential for rainfall enhancement

The index of potential for rainfall enhancement can be assured by the following formula that was brought forward by Wang Yilin et al. (2002):

$$p = \int_{h1}^{h2} F(h)dh \begin{cases} F(h) = e - E_i (e > E_i) \\ F(h) = 0 (e < E_i) \end{cases} \quad (2)$$

In the formula, h1 and h2 were the height of the region that the peak value of e-Ei>0 at every time.

Table 2 Index of potential for rainfall enhancement in Zhengzhou withtime on October 19

Time	04	07	10	13	16
Thickness (m)	2052	1421	1242	1416	1409
Height (m)	7427-9479	4326-5747	9483-10725	4312-5728	4311-5720
P(hpa • m)	45.86	112.16	8.42	87.86	95.43

We calculated the index by the sounding data of Zhengzhou station from 04 to 16 October 19 (see Table2).

6. Conclusions

(1) The main sources of water vapor in the concerned stratiform cloud precipitation system were south-west current of cold front in the head of 500hPa trough, water vapor transportation from Tibet and from south-east direction (Yellow Sea) at the lower level.

(2) The variation of water vapor amount retrieved from GBDWMR was similar to that computed from the empirical formula.

(3) The cloud regions with saturation and ice-water transition were located in the level of 500-400hPa. The regions with the high potential for rain enhancement were located at 4300-5800m. The time of seeding was at 07, 13 and 16 October 19.

Acknowledgements

This paper was supported by the "the tenth five-year" key project "the Research and Demonstration of Rainfall Enhancement Technology " (2001BA610A-06) of Ministry of Science and Technology. We sincerely thank the weather modification office of Henan for giving us the data and Dr. Liu Qijun for his valuable comments.

References

[1] Hu Zhijin. Numerical Simulation of Cold Stratiform Cloud. Acta of Meteorologica Sinica, 1983, 194-203.

[2] Li Tielin, Zheng Hongwei. Remote of Water Vapor and Liquid Water Content by Ground-Based Dual-Wavelength Microwave Radiometer System. The Research of Technology for Weather Modification. Meteorological Press, 2000, 110-113.

[3] Lei Hengchi, Wei Zhong. Sounding the Water Vapor and Cloud Liquid Water before Precipitation by the Ground-Based Dual-Wavelength Microwave Radiometer System. Quarterly Journal of Applied Meteorology. 2001, 12 (Suppl): 73-78.

[4] Wang Yilin, Liu Wen, Wang Guanghe. Sounding of the Seeding Area of Cold Cloud. Acta of Meteorologica Sinica, 2002, 60(1), 117-121.

[5] Xu Xiangde. Project and Technology System of Angricultural Meteorology. Meteorological Press, 2002, 322.

[6] Yang Jinmei, Qiu Jinhuan. The empirical Formula of the Relation of Potential Precipitation and Surface Water Vapor Pressure. Atmospheric Sciences, Vol. 20, No. 5, 1996.

THE BIAS IN MOMENT ESTIMATORS FOR PARAMETERS OF DROP-SIZE DISTRIBUTION FUNCTIONS: SAMPLING FROM EXPONENTIAL DISTRIBUTIONS

Paul L. Smith* and Donna V. Kliche
IAS, South Dakota School of Mines and Technology, Rapid City, SD, USA

1. INTRODUCTION

Investigators frequently acquire observations of raindrop sizes and seek to describe the drop-size distributions (DSDs) by analytical expressions, the exponential or gamma function being most common. While moment methods to estimate parameters for the DSD functions have become more or less traditional, Haddad et al. (1996, 1997) pointed out that the methods are biased and Smith and Kliche (2003) provided examples of this bias. The methods are indeed biased – in the statistical sense that the expected values of the "fitted" parameters differ from the parameters of the underlying raindrop populations – and so lead to erroneous inferences about the characteristics of the DSDs being sampled.

The bias in the moment methods can be demonstrated by testing their ability to recover parameters of known DSDs from which samples are taken. This must be done by computer simulation, as the DSDs in nature are inherently unknown. The simulations herein use a Monte Carlo simulation procedure similar to that described in Smith et al. (1993); the Appendix below summarizes the procedure. This paper gives preliminary results for samples taken from a hypothetical exponential DSD.

2. CHARACTERISTICS OF SAMPLING DISTRIBUTIONS

Sampling from long-tailed DSDs like the exponential exhibits certain general features. Sample values of the DSD moments $M_i = \Sigma D^i$ ($i = 3$ gives LWC; $i = 6$ gives Z) are unbiased: the expected, or mean, sample value of M_i corresponds to that of the drop population being sampled. However, the sampling distributions are skewed, as indicated by the fractional standard deviations calculated by Gertzman and Atlas (1977) and as shown in Smith et al. (1993). The skewness is greater for higher-order moments and for smaller sample sizes.

Sampling the small drops can be a major instrumental problem for exponential DSDs, and adequately sampling the relatively rare large drops is also a concern. Fewer than one drop in 400 in an exponential DSD is larger than $D = 1.5\ D_m$, where D_m is the mass-weighted mean diameter, and about one in 3000 is larger than $D = 2\ D_m$. However, the drops larger than $1.5\ D_m$ contribute more than 15% of the LWC and more than 60% of the reflectivity factor. Consequently, the relatively large but relatively rare drops tend to be important in determining the moments of physical significance. The sample values of the moments are therefore correlated with the size of the largest drop in each sample (Fig. 1). This correlation is stronger for higher-order moments (Fig. 2) and remains appreciable even for fairly large sample sizes (Fig. 3).

Figure 5 of Smith et al. (1993) showed that the maximum drop size in an exponential DSD is rarely approached in samples of even hundreds of drops. The distribution of values along the abscissa in Fig. 3 here demonstrates the same thing. There is clearly no basis for assuming truncation of the underlying DSD at the maximum observed drop diameter, with samples of such sizes.

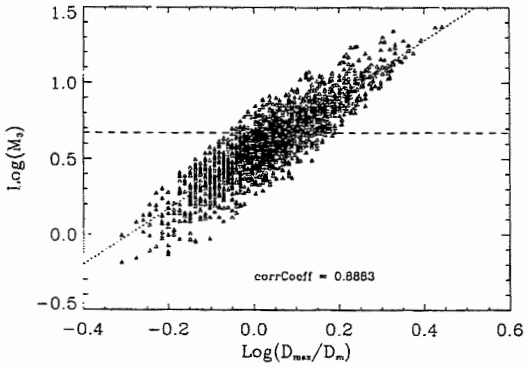

Fig. 1: Sampling distribution of third moment (M_3, proportional to LWC) plotted against maximum drop size in the sample. Population DSD: exponential. Mean sample size: 100 drops. Dashed line indicates population value of M_3.

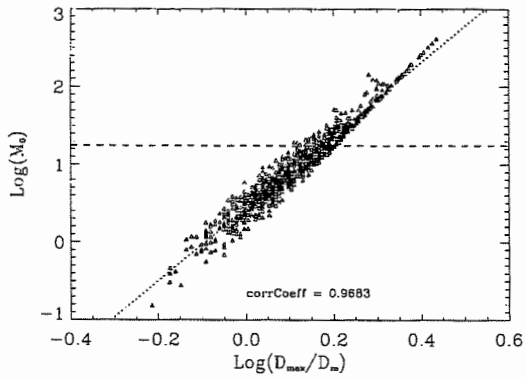

Fig. 2: Sampling distribution of sixth moment (M_6, proportional to reflectivity factor) plotted against maximum drop size in the sample. Population DSD: exponential. Mean sample size: 100 drops. Dashed line indicates population value of M_6.

Corresponding author address: P.L. Smith, 501 East Saint Joseph Street, Rapid City, SD 57701-3995; e-mail: paul.smith@sdsmt.edu

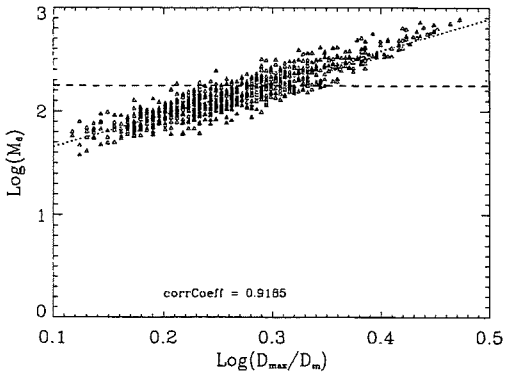

Fig. 3: Sampling distribution of sixth moment (M_6, proportional to reflectivity factor) plotted against maximum drop size in the sample. Population DSD: exponential. Mean sample size: 1000 drops. Dashed line indicates population value of M_6.

3. MOMENT ESTIMATORS

The use of moment methods to estimate parameters for DSD functions evidently began with Waldvogel's (1974) paper on the "N_0 jump" of DSDs. He used moments M_3 and M_6 (i.e. LWC and Z) to determine pairs of parameters for exponential functions that purportedly represented the observed DSDs. However, most distributions "fitted" in this way do not look at all like the samples upon which they are based. Figure 4 shows an example from raindrop camera data illustrating the large discrepancies involved.

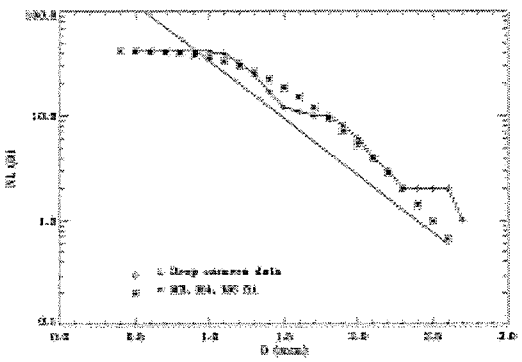

Fig. 4: Example of drop-size data from Illinois State Water Survey raindrop camera (Majuro, Marshall I., 0930 16 May 1959). Ordinate shows "inverse cumulative" number concentration $N_L(D)$ of drops of diameter D or larger. Unlabelled straight line shows "Waldvogel fit" based on M_3 and M_6. Asterisks indicate "moment-method gamma fit" based on M_3, M_4, and M_6.

More recently, estimators involving three moments have been used in attempts to fit gamma distributions to DSD observations. Examples include Ulbrich (1983); Kozu and Nakamura (1991); Smith (1993); Tokay and Short (1996); and Ulbrich and Atlas (1998). These procedures can produce closer fits to the observations, at least for part of the size spectrum (e.g. Fig. 4). The gamma parameters for that figure were estimated using the moments M_3, M_4, and M_6, as employed by Ulbrich (1983), Kozu and Nakamura (1991), and Tokay and Short (1996). However, the apparent closeness of fit is misleading, because these "fitted" distributions also typically do not resemble the original drop populations from which the samples are taken – as illustrated in the next section.

4. THE BIAS IN MOMENT ESTIMATORS

As noted, Haddad et al. (1996, 1997) pointed out that moment estimators are biased, and worthy statisticians are appalled at the idea of using this approach. That estimates of DSD parameters obtained in this way are biased was actually indicated in Smith et al. (1993) and further illustrated in Smith and Kliche (2003). Figure 5, reproduced from the former paper, compares sample estimates of D_m to the value of D_m for the exponentially-distributed population from which the (simulated) samples were drawn. In this example, more than 80% of the values are underestimates, and the mean (the expected value) is about 78% of the population value. In terms of the more familiar exponential slope parameter Λ (= $4/D_m$), this means that Λ is generally overestimated and the "fitted" DSDs will contain too many small drops and too few large ones.

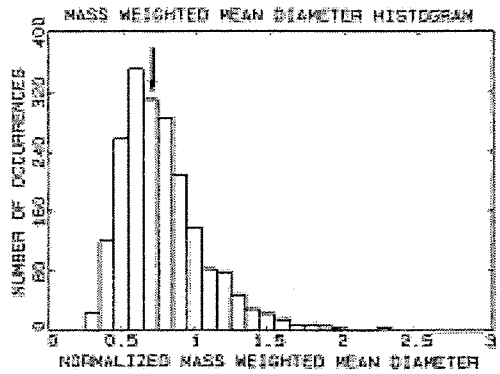

Fig. 5: Example of sampling distribution for mass-weighted mean diameter D_m. Population DSD: exponential. Mean sample size: 20 drops. (From Smith et al., 1993).

Of even greater concern is the bias that arises when moment methods are used with an assumed gamma form for the DSD. Figure 6 shows an example where a sample of 50 drops was drawn from an exponential DSD. While the gamma M_3, M_4, M_6 fit matches part of the sample distribution reasonably well, it in no way corresponds to the population from which the sample was drawn. The "fitted" value of the gamma shape parameter μ is 7.66; the expected value of μ for samples of this size, drawn from an exponential DSD (μ = 0), is about μ = 7.7. Thus, sampling the DSD with samples of this size will not reveal that the underlying DSD is exponential. The bias is quite misleading. Here one has sampled from what is actually an exponential

DSD; used moment methods in an attempt to "fit" parameters of a gamma distribution to the observations; found a (biased) high value of μ; and concluded, quite erroneously, that the population DSD was gamma after all. The hybrid approach used by Testud et al. (2001) does not employ a moment-based calculation to determine μ, but the estimators for their other gamma parameters (D_m and N_o*) are biased.

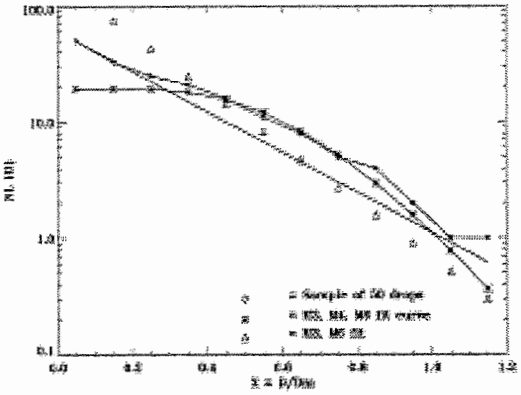

Fig. 6: A sample of 50 drops drawn from an exponential population (population DSD indicated by unlabelled straight line). Gamma curve with asterisks indicates "moment-method fit" based on M_3, M_4, and M_6. Triangles indicate "Waldvogel fit" based on M_3 and M_6. Ordinate as in Fig. 4.

As the sample size increases, the sampling variability decreases and the correlations between the various sample moments weaken. Consequently, the bias diminishes, so that with very large samples the moment methods may give approximations of the population parameters that become sufficiently accurate for practical purposes. Further simulations are exploring the sample sizes required for this to occur, but thus far it appears that the samples required are in the hundreds, if not thousands, of drops.

5. RELATED FINDINGS

The correlations of the various sample moments with the maximum drop size in the sample, and the resulting correlations between moments, lead to correlation of the "fitted" parameters with the maximum drop size (e.g. Fig. 7). The parameters are in turn correlated with each other (Fig. 8), and such correlations can be mistaken for physical relationships. The correlations between estimated parameters are stronger when higher-order moments are used in the "fitting" process (Fig. 9). The latter two figures also illustrate the general tendency for the moment methods to overestimate both the slope and intercept parameters of an exponential function, and comparing the two illustrates the stronger bias that results when higher-order moments are employed.

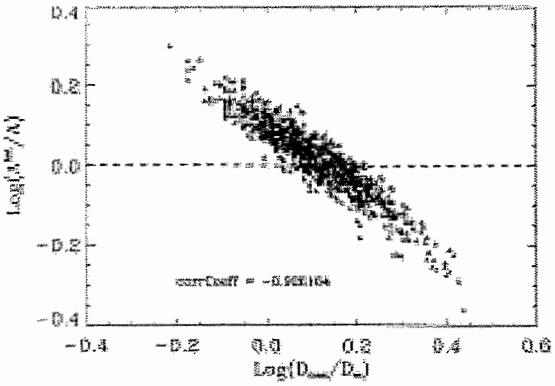

Fig. 7: Scatter plot of DSD slope parameter for an exponential function, estimated from moments M_2 and M_3, versus maximum drop size in the sample. Population DSD: exponential. Mean sample size: 100 drops. Dashed line indicates population value of Λ.

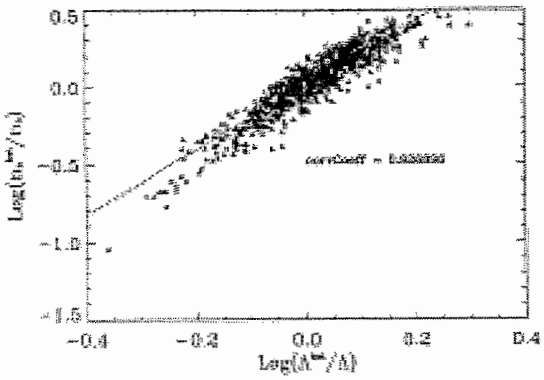

Fig. 8: Scatter plot of DSD intercept parameter n_o and slope parameter Λ for an exponential function, as estimated from moments M_2 and M_3. Population DSD: exponential. Mean sample size: 100 drops.

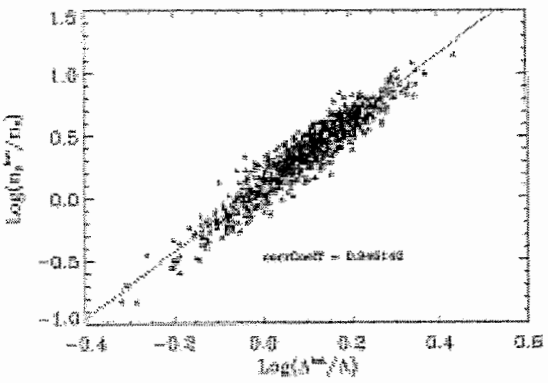

Fig. 9: As Fig. 8, but for DSD parameters estimated by using moments M_3 and M_6.

6. CONCLUSIONS

Moment estimators for parameters of DSD functions are inherently biased. They tend to give erroneous values of the DSD parameters unless the drop samples are much larger than those commonly available. In particular, estimates of the gamma shape parameter μ tend to be far larger than the shape parameter of the underlying DSD from which the samples are taken. The bias is greatest for small sample sizes, and also greater when higher-order moments of the observed DSDs are used in the fitting process.

Moment methods may provide estimates of DSD parameters of sufficient accuracy if very large samples (hundreds, perhaps thousands) of drops are available. Failing that, some alternative approach to fitting the observed DSDs must be used. Haddad et al. (1996, 1997) suggested a maximum likelihood approach, which may be satisfactory if the sampling errors are not too great.

Acknowledgment: This material is based upon work supported by the National Science Foundation under Grant No. ATM-9907812.

Appendix: Summary of Simulation Procedure for Raindrop Sampling

First write the drop-size distribution n(D) as the product of the (average) total drop concentration N_T (m^{-3}) and the probability density function (PDF) of drop diameter D:

$$n(D) = N_T\,(\mathrm{PDF})$$

According to Mielke (1976), the gamma PDF is

$$\mathrm{PDF} = (\lambda^{\mu+1} / \mu!)\, D^{\mu} \exp(-\lambda D)$$

In terms of the mass-weighted mean diameter D_m, this becomes

$$\mathrm{PDF} = \frac{(\mu+4)^{\mu+1}}{\mu!}\,\frac{D^{\mu}}{D_m^{\mu+1}}\, e^{-(\mu+4)D/D_m}$$

Define $x = D/D_m$; then

$$n(x) = N_T \frac{(\mu+4)^{\mu+1}}{\mu!}\, x^{\mu}\, e^{-(\mu+4)x}$$

To simulate sampling from a DSD with a specified value of μ ($\mu = 0$ gives an exponential DSD), specify the value of N_T and assume a 1 m^3 sampling volume. (This is equivalent to a combination of any arbitrary N_T and a sample volume that will lead to the same average number of drops in a sample.) Use a Poisson random number generator with mean value N_T to generate values of the drop count C in individual samples, followed by a second random number generator for each sample to generate C values of the normalized drop diameter x from the PDF. The latter is readily represented (for integer values of μ) in a look-up table. For the simulation here, we truncated the PDF at $x = 3.0$.

---

7. REFERENCES

Gertzman, H.S., and D. Atlas, 1977: Sampling errors in the measurement of rain and hail parameters. J. Geophys. Res., 82, 4955-4966.

Haddad, Z.S., S.L. Durden and E. Im, 1996: Parameterizing the raindrop size distribution. J. Appl. Meteor., 35, 3-13.

Haddad, Z.S., D.A. Short, S.L. Durden, E. Im, S. Hensley, M.B. Grable and R.A. Black, 1997: A new parameterization of the rain drop size distribution. IEEE Trans. Geosci. Remote Sensing, 35, 532-539.

Kozu, T. and K. Nakamura, 1991: Rainfall parameter estimation from dual-radar measurements combining reflectivity profile and path-integrated attenuation. J. Atmos. Oceanic Tech., 8, 259-270.

Smith, J.A., 1993: Marked point process model of raindrop-size distributions. J. Appl. Meteor., 32, 284-296.

Smith, P.L. and D.V. Kliche, 2003: The bias in moment estimators for parameters of drop size distribution functions. Preprints, 31st Conference on Radar Meteorology, Seattle, WA, Amer. Meteor. Soc., 47-50.

Smith, P. L., Z. Liu and J. Joss, 1993: A study of sampling-variability effects in raindrop-size observations. J. Appl. Meteor., 32, 1259-1269.

Testud, J., S. Oury, R.A. Black, P. Amayenc and X. Dou, 2001: The concept of "normalized" distribution to describe raindrop spectra: A tool for cloud physics and remote sensing. J. Appl. Meteor., 40, 1118-1140.

Tokay, A. and D.A. Short, 1996: Evidence from tropical raindrop spectra of the origin of rain from stratiform versus convective clouds. J. Appl. Meteor., 35, 355-371.

Ulbrich, C.W., 1983: Natural variation in the analytical form of the raindrop size distribution. J. Climate Appl. Meteor., 22, 1764-1775.

Ulbrich, C.W. and D. Atlas, 1998: Rainfall microphysics and radar properties: Analysis methods for drop size spectra. J. Appl. Meteorol., 37, 912-923.

Waldvogel, A., 1974. The N_0 jump of raindrop spectra. J. Atmos. Sci., 31, 1067-1078.

THE EFFECT OF SURFACTANTS ON KÖHLER CURVES RECONSIDERED

R. Sorjamaa, T. Raatikainen and A. Laaksonen

Department of Applied Physics, University of Kuopio, Kuopio, Finland

1. INTRODUCTION

Several variables, such as condensing gases, particle chemical composition and particle size, are known to affect cloud droplet formation and thereby the cloud albedo. The largest uncertainty in predicting the effect of aerosols on climate change is the aerosol indirect effect, i.e. clouds. One of the factors controlling the vapour pressure of small droplets is their surface tension. Decrease in surface tension has been found in cloud water sample measurements. The decrease has been found out to be caused by surface active compounds, surfactants, which are organic compounds present in atmospheric particles (Facchini et al., 1999). This effect is especially important when atmospheric aerosol particles containing such compounds act as cloud condensation nuclei (CCN). The lowering of surface tension causes a decrease in critical supersaturation, which may lead to an increased number of CCN (Shulman et al., 1996, Facchini et al., 1999).

Surface active compounds have a tendency to concentrate on droplet surface, which leads to difficulties in defining the droplet surface. This is because the surfactant concentration varies as a function of distance from droplet interior and therefore also surface tension depends on how the droplet surface has been defined. A correct evaluation of droplet surface and surfactant bulk concentration (concentration in droplet interior) has been studied by Li et al. (1998). They found out that when the surfactant partitioning is correctly evaluated, surface tension is not as low as earlier studies suggest. The correct evaluation leads to higher critical supersaturation and hence the droplet activation may become overestimated if the partitioning is neglected. What they did not consider is that besides surface tension, the partitioning alters also the solute effect (Raoult effect). This is because the number of solute moles in droplet bulk becomes smaller as some of the surfactant is partitioned to the surface, leading to an increased water vapor pressure. When the partitioning is accounted for in evaluation of both the surface tension and the solute effect, the critical supersaturation becomes even higher than calculated by Li et al., and thus the cloud droplet activation is further decreased. We have studied the surfactant partitioning in two and three component cases with different particle sizes and considered both the decrease of surface tension and the alteration of the solute effect.

Corresponding author's address: Riikka Sorjamaa, Department of Applied Physics, University of Kuopio, P.O. Box 1627, 70211, Kuopio, Finland; E-Mail: Riikka.Sorjamaa@uku.fi

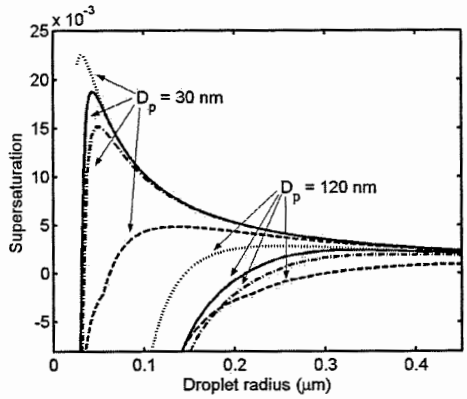

Figure 1. Köhler curves for initially dry SDS particles with dry diameters of 30 nm and 120 nm. Different approaches to partitioning are marked with different lines and are explained in the text.

2. METHODS

Gibbs adsorption equation was used to determine the excess surface concentrations in two and three component cases. Surface tension as well as solute effect were evaluated using solute concentrations in the bulk of the droplet, i.e. surfactant partitioning was included in both the Kelvin and the Raoult effects.

Four different approaches were taken to show how the partitioning alters the shape of the Köhler curve:

1. Surfactant partitioning affecting both, surface tension and solute effect (solid line)
2. Surfactant partitioning affecting only surface tension (dash-dotted line)
3. no partitioning, lowered surface tension (dashed line)
4. no partitioning, surface tension of water (dotted line)

Sodium dodecyl sulfate (SDS) and pinonic acid were used as surfactants. SDS is a model compound that was included in the study because of the available reference study (Li et al. 1998). SDS was then replaced with pinonic acid (and sodium chloride with ammonium sulphate) in order to show the effect of partitioning with a relevant atmospheric surfactant.

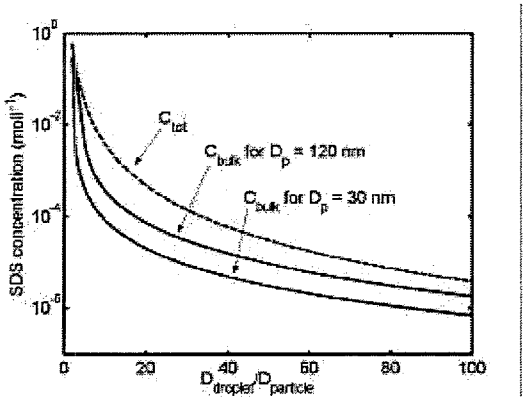

Figure 2. SDS bulk concentrations (C_{bulk}) for two droplets with different dry particle radii but with equal total concentrations (C_{tot}).

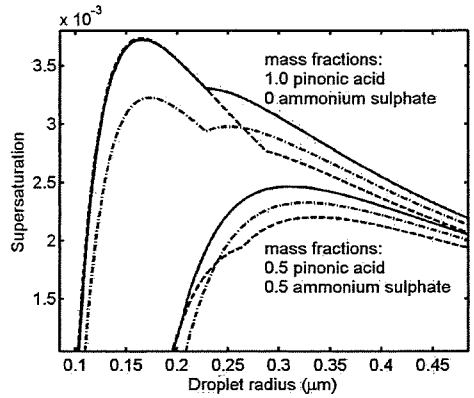

Figure 3. Köhler curves for a particle with dry diameter of 100 nm and with two different pinonic acid mass fractions (1 and 0.5).

3. RESULTS

Figure 1 shows Köhler curves for aqueous SDS droplets with dry particle diameters of 30 nm and 120 nm. The dotted line is calculated assuming constant (water) surface tension and uniform partitioning of the solute between the bulk and the surface. When the surface tension lowering caused by SDS is accounted for, but the non-uniform distribution of SDS between the bulk and the surface is ignored, the resulting (dashed) Köhler curve has greatly reduced critical supersaturation. With the dash-dotted curve (Li et al., 1998), the non-uniform SDS distribution has been accounted for in the Kelvin term but not in the Raoult term. Finally, the solid line is the Köhler curve in which both the Kelvin and the Raoult terms have been evaluated correctly. The difference between the maxima of the dashed and solid lines is expected to be large enough to matter when cloud model calculations are carried out.

Figure 2 shows the effect of particle size on bulk concentration. Two droplets with equal total concentration (C_{tot}), that is the concentration without partitioning consideration, show a clear difference in bulk concentrations with lower bulk concentration (C_{bulk}) in smaller droplets. This is simply because smaller droplets have larger ratio between the surface area and bulk volume. Thus, in small droplets a relatively larger fraction of the surfactant is moved from the bulk to the surface, and the surface tension decrease is not as efficient as in larger droplets.

It is true that SDS is not a relevant surfactant as far as atmospheric studies are concerned, and we have used it as a model compound to be able to compare our results with those of Li et al. (1998), and to show the difference between the different partitioning considerations. To find out if the partitioning is worth considering with real atmospheric compounds, pinonic acid was used. As pinonic acid is a slightly soluble compound, and the solubility measurement gives the droplet bulk concentrations, the Köhler curves calculated with correct partitioning consideration (solid line) and without partitioning (dotted line) are identical until the complete dissolution occurs (Figure 3). In order to find out how this may alter cloud droplet formation, we are going to continue this study by developing a cloud model that includes the effect of surfactants in order to find out the effect that surfactant particle size and partitioning have on cloud formation as well as making comparisons between calculated and measured critical supersaturations.

ACKNOWLEDGEMENTS

This work was supported by the Academy of Finland.

REFERENCES

Facchini, M.C., Mircea, M., Fuzzi, S. and R.J. Charlson, 1999: Cloud albedo enhancement by surface active organic solutes in growing droplets, Nature, 401, 257-259.

Li, Z., Williams, A.L. and M.J. Rood, 1998: Influence of soluble surfactant properties on the activation of aerosol particles containing inorganic solute, J. Atm. Sci., 55, 1859-1866.

Shulman, M.L., Jacobson, M.C., Charlson, R.J., Synovec, R.E. and Young, T.E., 1996: Dissolution behaviour and surface tension effects of organic compounds in nucleating cloud droplets. Geophys. Res. Lett., 23, 277-280.

WHEN IS BETTER TO DETERMINE THE SUPER-SATURATION INTEGRAL FOR A TIME STEP OF THE SIMULATION ?

Cristina Stefanof[1], Alexandru Stefanof[1], Wanda Szyrmer[2], Jean-Pierre Blanchet[1]

1. University of Quebec at Montreal,Department of Earth and Atmospheric Science, Montreal, 201 Avenue President Kennedy, Quebec, H3C 3P8, Canada
2. McGill University, Department of Atmospheric and Oceanic Sciences, Montreal, Quebec, Canada

1.INTRODUCTION

Air super-saturation controls nucleation and growth of cloud particles and therefore determines the formation of rain. Models, which calculate cloud microphysics, have to correctly determine super-saturation.

This study analyzes the methods used to calculate the mean super-saturation and the time dependent super-saturation. The analytical method is the first method that has been studied and is hereby presented. The present work was motivated by the following questions: Is it correct to keep the super-saturation constant in simulations for an entire time step? How to find the equilibrium super-saturation? What is the temporal variability of super-saturation in the clouds? How to determine the super-saturation integral for a time step of the simulation?

2.THE TIME EVOLUTION OF THE SATURATION WITH RESPECT TO WATER

In this study the saturation ratio is defined as the ratio between the vapor mixing ratio and the the saturation vapor mixing ratio.

In the absence of the ice, the time evolution of the saturation with respect to water is given by:

$dS/dt = A_1 W - A_2(dy_L/dt)$;

$dy_L/dt = aS-b$

where W is vertical speed and y_l is the liquid water mixing ratio with respect to air,

$$a = F\sum_j r_j N_j \quad \text{and} \quad b = F\sum_j r_j S_j N_j$$

and A_1, A_2, F are thermodynamic functions. (Squires 1952; Pruppachet et Klett 1997).

The solution to the above equation with initial saturation ratio S_0 at time t is given by:

$S_1=(S_0-S_{eq})\exp(-t/\tau)+S_{eq}$ where τ the saturation relaxation time as $\tau = 1/(A_2 a)$.

3. THE ERROR IN THE CONDENSATION CALCULATIONS INTRODUCED BY THE BULK MODEL

Kogan and Martin (1994) studied the differences between the condensation treated with the bulk model and with the explicit microphysics model. The error in the condensation calculations introduced by the bulk model, based on the fact that there cannot be super-saturation at the end of a time step, can be explained using figure1.

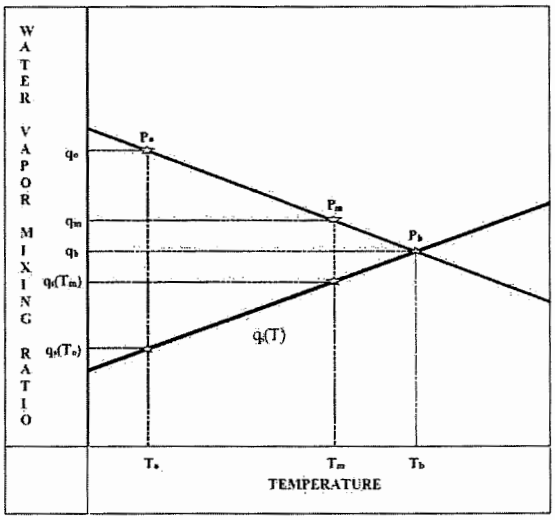

Figure 1. Conceptual model of the moist saturation adjustment process (after McDonald 1963). Kogan and Martin 1993

Corresponding author's address: C.Stefanof, UQAM, 201 Av.President Kennedy, Mtl, H3C 3P8, Quebec, Canada; E-mail: cristina@sca.uqam.ca

This error is proportional to the ratio S_m/S_0,

where

$S_m=(q_m-q_s(T_m))/q_s(T_m)$

and

$S_0=(q_0-q_s(T_0))/q_s(T_0)$

The error is small in the case of intense convection or high vertical speeds when the difference $q_0-q_s(T_0)$ is large.

4. THE INTEGRAL OF SATURATION RATIO

If we are using a new variable $f = t/\Delta t$ (the number of time steps existing in the time interval t) the time dependence of the saturation becomes:

$$S(f) = (S_0-S_{eq})e^{-f\,\Delta t/\tau} + S_{eq}$$

where the time step interval Δt is known.

The geometrical interpretation of the integral of S = F(f) is represented on the graphs below. The graphs in figure 2 and figure 3 are of S versus f. The y-axis crosses the x-axis at x=0.0 and the separation between vertical grid line represents one time step.

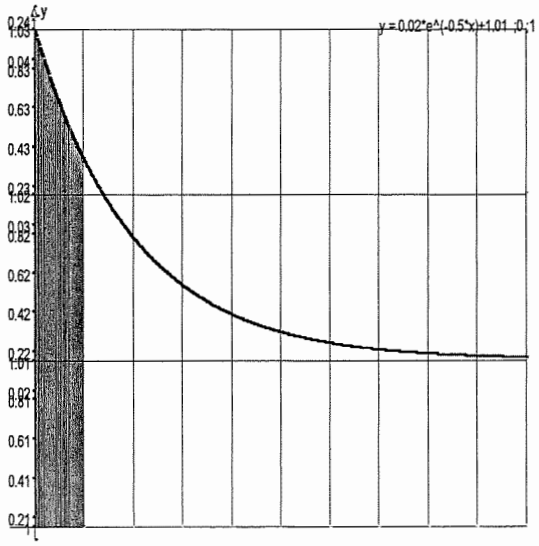

Figure 2 : Saturation ratio S versus number of time steps f for time step < relaxation time

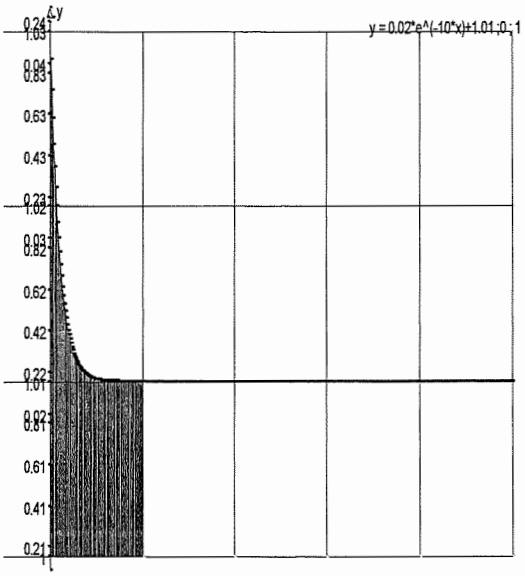

Figure 3 : Saturation ratio S versus number of time steps f for time step > relaxation time

Removal of excess water vapor so that there is no super-saturation at the end of each time step of the model usually gives an over-estimation of the latent heat exchanged with the system during phase changes. The energy balance is not the only one affected by saturation. The activation of condensation nuclei and ice nuclei is very sensitive to the value of super-saturation in clouds.

To introduce the temporal variation of saturation into the models is, therefore, necessary. In the work presented two different cases arise: the time step is smaller than the saturation relaxation time and the time step is larger than the saturation relaxation time.

The solution of the differential equations of saturation for warm and cold clouds should be calculated from the integral of saturation in the case where the time step is smaller than the saturation relaxation time. In the case where the time step is longer than the relaxation time, the model should calculate the equilibrium saturation. In order to confirm our assumption, we present in our poster some results obtained with the Cloud Resolving Model using the integral of the saturation ratio versus the results given by the same model which cuts the saturation at 100% at the end of each time step.

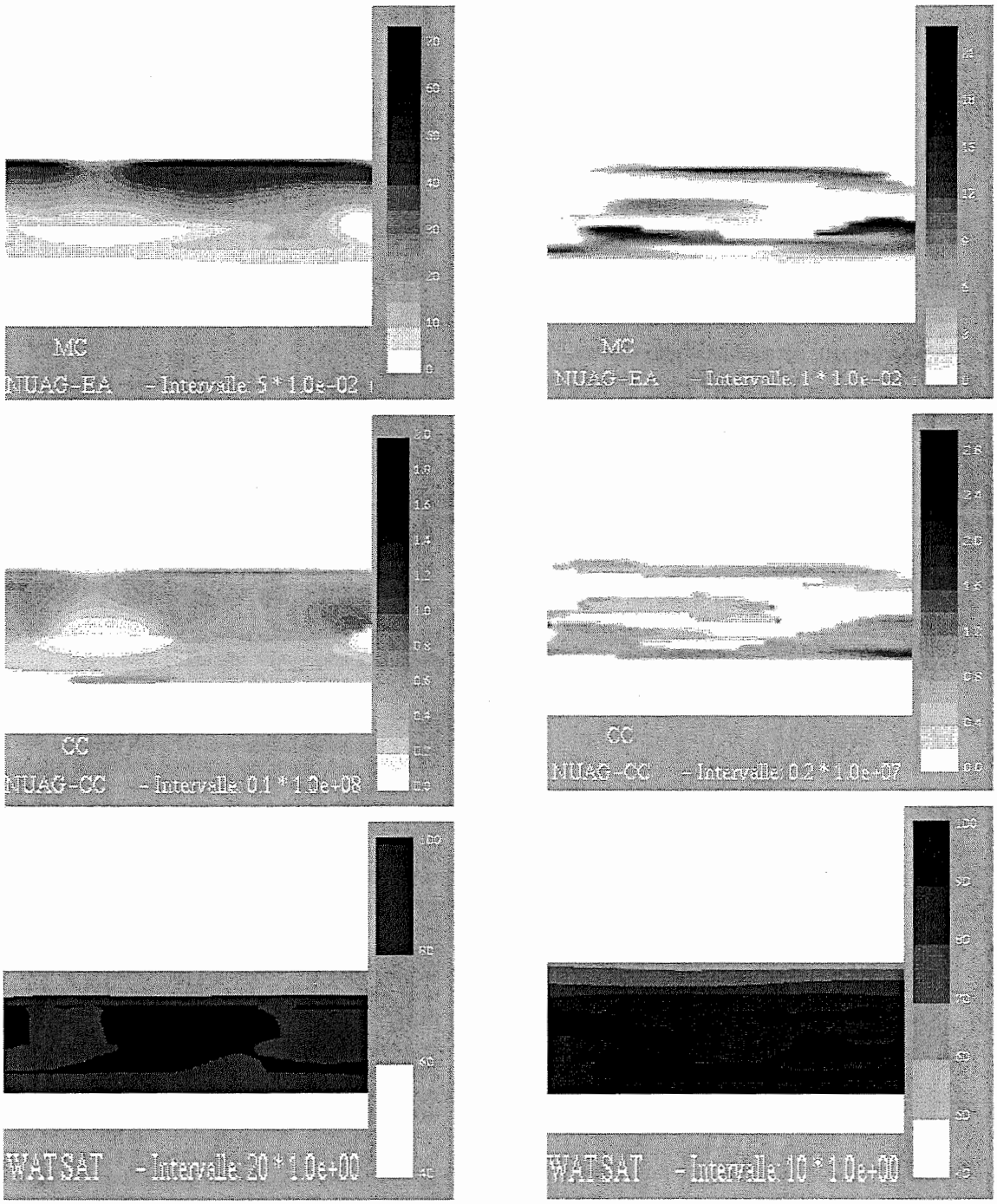

Figure 4: Liquid water contents (g/kg), drops concentration (m^{-3}), water vapor saturation (%) for time step 2 s, resolution 25 m, initial no.aerosol 200 cm^{-3} with integral of saturation (left) and cut of saturation (right).

another possible way of day adjusted slip

5. BRIEF DESCRIPTION OF THE CLOUD RESOLVING MODEL

The 2D/3D cloud resolving model includes the following, fully coupled, parts:

a) The dynamic module, a version of the Cooperative Center for Research (CCRM) mesoscale nonhydrostatic community model dynamics (Laprise et al. 1997; Caya and Laprise 1999) as well as of the Northern Aerosol Regional Climate Model (NARCM) adapted to utilization at fine scale.

b) The Smagorinsky-type subgrid turbulence scheme modified to include stability effects and calculations of turbulent mixing across cloud top (MacVean and Mason 1990).

c) The atmospheric radiation model for short-wave and long-wave radiative transfer through clear, cloudy or partly cloudy air parcels the same as in NARCM but adaped to fine-scale experiments and with cloud characteristics obtained from detailed microphysics scheme.

d) Different microphysical schemes: two-moments microphysics with three hydrometeor categories –cloud liquid water, pristine ice crystals and larger precipitation crystals.

- The conventional one-moment bulk microphysical package with five hydrometeor categories (cloud droplets and cloud ice crystals, raindrops, snowflakes and graupel particles).
- The new bulk parameterization scheme for melting layer (Szyrmer & Zawadzki 1999)
- The detailed microphysics module predicting the evolution of the cloud droplet spectra (Brenguier & Grabowski 1993) in link with the CCN concentration.
- The bulk scheme describing the drizzle category with prediction of two prognostic variables: concentration per unit mass (number mixing ratio) and mass mixing ratio (Khairoutdinov and Kogan 2000).

The model has been successfully tested with spatial resolutions of a few microns (study of air flow and cloud droplet trajectories around the airborne temperature sensor: Szyrmer 1998), of tens of meters (atmospheric melting layer: Papagheorghe 1996, Szyrmer and Zawadzki 1999; summertime Arctic stratus: Szyrmer et al. 1999), and hundred(s) meters (warm rain formation: Szyrmer 1998, supercooled clouds in the presence of snow: Zawadzki et al. 2000).

6. REFERENCE

Àrnason, G., and P.S. Brown, Jr., 1971: Growth of cloud droplets by condensation : A problem in computational stability. *J. Atmos. Sci.*, 28, 72-77.

Chen, J.-P., 1994 : Predictions of Saturation Ratio for Claud Microphysical Models. *J. Atmos. Sci.*, 51, 1332-1338

Clark, T.L., 1973 : Numerical Modeling of the Dynamics and Microphysics of Warm Cumulus Convection. *J. Atmos. Sci.*, 30, 857-878.

Girard, E., Blanchet J.P., 2001: Microphysical Parameterization of Arctic Diamond Dust, Ice Fog, and Thin Stratus for Climate Models. *J. Atmos. Sci.*, 58 ,1181-1198.

Girard, E., Blanchet J.P., 2001: Simulation of Arctic Diamond Dust, Ice Fog, and Thin Stratus Using an Explicit Aerosol-Cloud-Radiation Model. *J. Atmos. Sci.*, 58 , 1199-1221.

Hall,W.D., 1980 : A Detailed Microphysical Model Within a Two-Dimensional Dynamic Framework : Model Description and Preliminary Results. *J. Atmos. Sci.*, 37, 2486-2507.

Khvorostyanov, V.I., J.A. Curry, 1999 : Toward the Theory of Stochastique Condensation in Clouds. Part I : A General Kinetic Equation. *J. Atmos. Sci.*, 56, 3985-3996

Kogan, Y.L., W.J. Martin, 1994 : Parameterization of Bulk Condensation in Numerical Cloud Models, *J. Atmos. Sci.*, 51, 1728-1739.

Pruppacher, H.R. and J.D.Klett, 1997 : Microphysics of Clouds and Precipitation Rasmussen, R.M. & all, 2002 : Freezing Drizzle Formation in Stably Stratified Layer Clouds : The role of Radiative Cooling of Cloud Droplets, Cloud Condensation Nuclei, and Ice Initiation, *J. Atmos. Sci.*, 59, 837-860.

Rogers, R.R.and M.K.Yau, 1989 : A Short Course in Cloud Phyics

Srivastava R.C., 1989 : Growth of Cloud Drops By Condensation: A Criticism of Currently Accepted Theory and a New Approach, *J. Atmos. Sci.*, 46, 869-887.

revisit way of looking at updraft dynamics of INDEX clouds

A COMPARISON OF THE MICROPHYSICAL AND KINEMATIC CHARACTERISTICS OF MID-LATITUDE AND TROPICAL CONVECTIVE UPDRAFTS

J. L. Stith[1], J. Haggerty[1], C. Grainger[2], and A. Detwiler[3]

[1]National Center for Atmospheric Research, Boulder CO, USA
[2]University of North Dakota, Grand Forks, ND, USA
[3]South Dakota School of Mines and Technology, Rapid City, SD, USA

1. INTRODUCTION

Updrafts in convective storms play a major role in determining the characteristics of the storms. The lifting of air in these updrafts, acting with available nuclei for condensation or ice formation, determines the rate of formation of precipitation and its form in a manner that is only partially predicted by present day skills. Although updrafts and downdrafts in these storms have been studied for many years, there have been relatively few studies comparing the kinematic and microphysical structures of updrafts from different parts of the world where differences in stability and cloud active nuclei are likely to substantially influence both the formation of precipitation and the nature of the vertical wind.

In this study we compare in situ airborne data from four convective field campaigns. Two of the campaigns were from summer thunderstorms in the upper Midwestern United States (North Dakota), during the summers of 1989 and 1993, the North Dakota Thunderstorm Experiment (NDTE, Boe et al., 1992) and the North Dakota Tracer Experiment (NDTE), respectively. The tropical data were collected during two Tropical Rainfall Measuring Mission (TRMM) field campaigns, one in Rondonia, Brazil [TRMM Large-Scale Biosphere-Atmosphere Experiment in Amazonia (LBA)] in January and February of 1999, and the other near Kwajalein, Marshall Islands [Kwajalein Experiment (KWAJEX)], in August and September 1999. The North Dakota data represent summertime continental conditions The KWAJEX data represent clean oceanic tropical conditions. The LBA data were collected during the wet, nonburning, season which exhibited CCN concentrations more like tropical. maritime conditions than continental conditions (Roberts et al., 2001). The microphysical and kinematic properties of the KWAJEX clouds and the LBA clouds were found to be similar (Stith et al. 2002; Stith et al. 2004, Anderson et al. 2004).

Corresponding author's address: Jeffrey L. Stith, Research Aviation Facility, NCAR, Box 3000, Boulder CO, 80307, USA. E-mail: stith@ucar.edu.

2. DESCRIPTION OF EXPERIMENTAL DATA

Data were collected by the University of North Dakota Citation research aircraft (NDTE, NDTP, LBA, KWAJEX) and the South Dakota School of Mines and Technology T-28 research aircraft (NDTP and NDTE). They carried similar instrumentation for microphysical measurements, including Particle Measuring Systems, Inc. (PMS) probes (2DC, FSSP, and others), liquid water measuring instruments (Johnson Williams for the T-28; CSIRO for the Citation for all projects except the NDTP, where a Johnson Williams was used on the Citation). Standard instruments were used for temperature and pressure measurements. Citation wind measurements were obtained from an Inertial Navigation/gust probe system (a flow angle sensor on a nose boom was used for attack and sideslip measurements in the North Dakota experiments, while a five hole radome method was used for the tropical measurements). The T-28 utilized the techniques described in Kopp (1985) for vertical wind measurements. Due to the substantial changes in altitudes and attitudes during these projects, the accuracy of the vertical wind measurements reported here is expected to be only about 1 m s^{-1}. The Citation instrumentation and the TRMM field campaigns are further described in Stith et al. (2002).

Clouds sampled during these projects included a wide range of sizes from small convective turrets, to feeder cells associated

with vigorous thunderstorms. However, severe regions of the clouds were excluded, so the results are somewhat biased toward smaller, but still vigorous convection. Tropical sampling included sampling of stratiform regions, but most of the main stratiform regions have been excluded from this data set. For all the cases, areas of weak updrafts near the stronger convective elements are included (e.g. detrained regions near the active updrafts).

Data were averaged to produce 5 second averages or approximately 0.5 km of flight path at typical sampling speeds of the Citation and T-28. Data with FSSP concentrations above 10 cm^{-3} or concentrations from the 2DC of above 0.5 $liter^{-1}$ were selected for inclusion in the data set. (The FSSP was not available for all the KWAJEX cases, so the 2DC criterion alone was used for these clouds.) This selection process produced 6120, 12130, 2281, and 6069 0.5 s data points for each of NDTP, NDTE, LBA, and KWAJEX (over 10,000 km of in cloud data).

As with most aircraft sampling there is no reliable way to assure that the in situ data are representative of clouds in a region. However, these data do allow us to examine features from a wide variety of moderately sized clouds, that, by virtue of the number of clouds sampled, exhibit properties that are likely to be reflected in many other clouds from the region. Indeed, Anderson et al. (2004) has compared the in situ KWAJEX and LBA updraft data with previously published tropical updraft results and found good agreement among the vertical profiles of updrafts from tropical convection in most parts of the world that have been studied. This is a reflection of the similarities in the vertical structure of the atmosphere in these regions (e.g. height of cloud base, Convective Available Potential Energy, lapse rates, etc.)

3. RESULTS

3.1 The Distribution of Updrafts.

Figure 1 displays a plot of all the data from the projects, using temperature as a vertical coordinate.

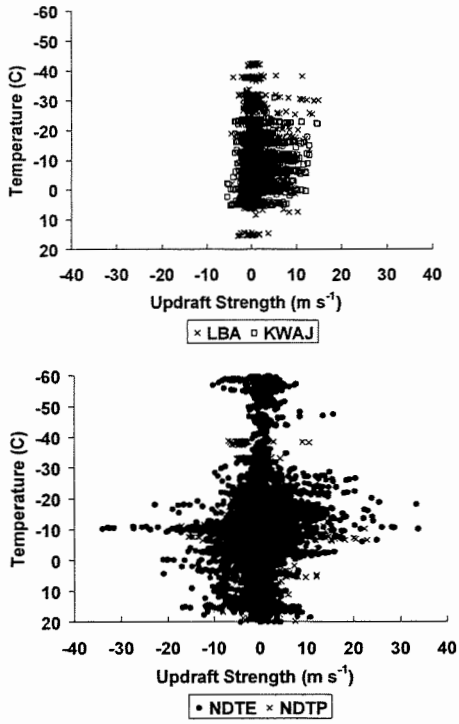

Figure 1. The vertical distribution of updrafts for the North Dakota (NDTE, NDTP) and tropical (LBA, KWAJ) regions.

As expected, the North Dakota data exhibited much stronger updrafts and downdrafts than those found in the tropical clouds. The North Dakota storms exhibited similar numbers of updrafts and downdrafts of a given magnitude. In contrast, the peak tropical updrafts increased gradually with altitude. Downdrafts were much weaker (peak values of only about 5 m s-1) and varied little with altitude. These results are also shown in the frequency distributions of vertical wind which are shown in Figure 2.

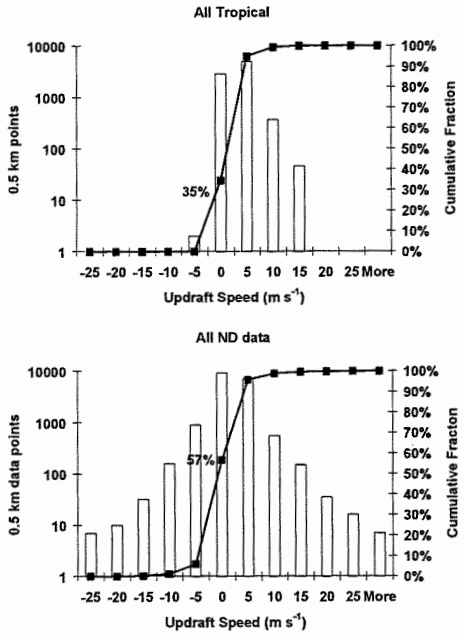

Figure 2. The frequency distribution of updraft speeds in the tropical and North Dakota data corresponding to the data shown in Fig. 1. Updrafts speeds listed indicate the upper bound of the bar immediately above the number.

Just over half (57%, Fig. 2) of the North Dakota data were downdrafts, while only 35% of the tropical data were downdrafts. The greater tendency for downdrafts in the mid-latitude data is likely a reflection of the dryer conditions present in the midlevels of these clouds, which enhances the likelihood of downdraft through evaporation of precipitation. Examination of the data in Figs. 1 and 2, but excluding regions with precipitation, suggests than nearly all of the mid-latitude downdraft regions were associated with precipitation (not shown). The lower regions of the tropical clouds are not included in this analysis; however, and more significant numbers of stronger downdraft may be found there.

3.2 Distribution of Liquid Water in Updrafts

The frequency distribution of liquid water in updrafts for two different temperature regions is given in Figures 3 and 4.

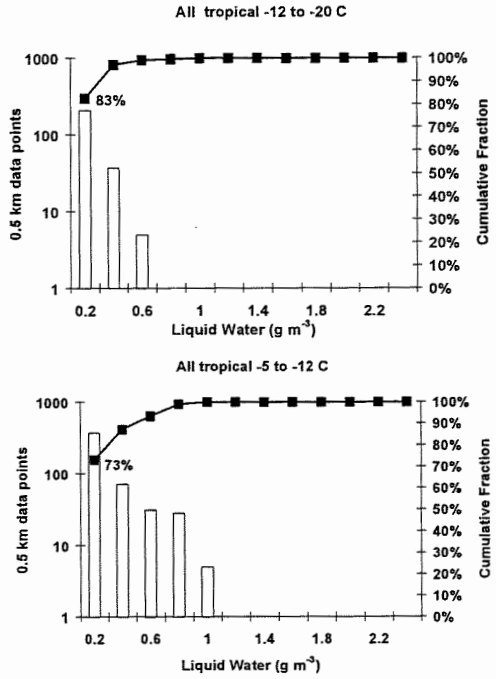

Figure 3. The frequency distribution of liquid water in updrafts greater than 2 m s^{-1} for all of the tropical clouds. Liquid water values listed indicate the upper bound of the bar immediately above the number.

Freezing of liquid droplets and their subsequent accretional growth is likely to be an important process in precipitation formation in tropical updrafts. The rapid glaciation that occurs in these updrafts is likely to rapidly remove much of the liquid water in cold cloud regions (e.g. Stith et al. 2004 and references therein). Thus, even at relatively warm temperatures, 73% of the updrafts had liquid water less than 0.2 g m^{-3} (a value which is hard to distinguish from the effects of ice particles on the CSIRO instrument).

Similar data for the North Dakota clouds is given in Figure 4. A little over half (54% and 62%) of the updrafts in the North Dakota cases exhibited low (less than 0.2 g m^{-3}) liquid water. The likelihood of finding liquid water was similar in the two temperatures ranges in Fig. 4. Liquid water in the mid-latitude clouds in these temperature intervals was about 80% or less of adiabatic values, while the tropical clouds had only about 15% or less of adiabatic values at these temperatures.

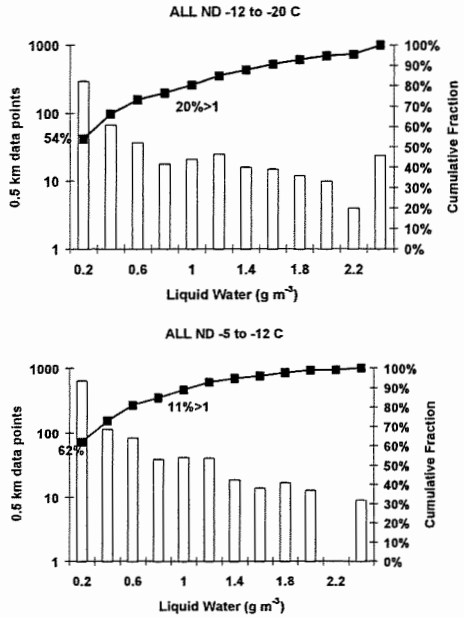

Figure 4, As in Fig. 3, except for the North Dakota clouds.

Maximum FSSP drop concentrations of over 1000 cm^{-3} were found 200 to 300 hPa above the cloud bases in the mid-latitude clouds (Fig. 5). This suggests that droplets may be activating well above the cloud base in mid-latitude updrafts.

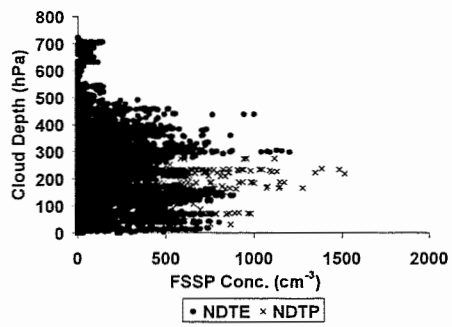

Figure 5. The concentration of particles measured by the FSSP vs the depth of the cloud above its base.

Acknowledgements

The National Center for Atmospheric Research is supported by the National Science Foundation. Additional support was provided by NSF grants ATM-9104474 (SD), ATM-940117 (SD), ATM-9221528 (SD), cooperative agreement NA47RA0184 (UND) with the National Oceanic and Atmospheric Administration through the North Dakota Atmospheric Resource Board, NASA grants NAG5-9715 (NCAR) and NAG5-9656 (UND), through the TRMM program. The views expressed herein are those of the authors, and to not necessarily reflect the view of NOAA or any of it sub-agencies.

References

Anderson, N. F., C. A. Grainger, and J. L. Stith, 2004: Updraft characteristics of tropical oceanic and tropical continental convective storms. Submitted to J. Appl. Meteor.

Boe, et al., 1992: The North Dakota thunderstorm project: A cooperative study of high plains thunderstorms, Bull. Amer. Meteor. Soc., **73**, 145-160

Kopp, F. J. 1985: Deductions of vertical motion in the atmosphere from aircraft measurements. J. Atmos. Ocean. Technol., **2**, 684-688.

Roberts, G. C., M. O. Andreae, J. Zhou, and P. Artaxo, 2001: Cloud condensation nuclei in the Amazon Basin: "Marine" conditions over a continent? Geophys. Res. Lett., **28**, 2807-2810.

Stith, J. L., J. E. Dye, A. Bansemer, A. J. Heymsfield, C. A. Grainger, 2002: Microphysical observations of tropical clouds. J. Appl. Meteor., **41**, 97-117.

Stith, J. L., J. A. Haggerty, A. Heymsfield, and C. A. Grainger, 2004: Microphysical characteristics of tropical updrafts in clean conditions. In Press. J. Appl. Meteor.

ANALYSES OF MICROPHYSICAL AND DYNAMICAL CHARACTERISTICS OF SUMMER CLOUDS IN THE UPPER REACHES OF THE YELLOW RIVER

An-Ping **Sun**[1], Lunge **Li**[1], Guoguang **Zheng**[2], Hengchi **Lei**[3], Guanghe **Wang**[4]

[1]Qinghai Provincial Weather Modification Office, Xining, Qinghai 810001, P. R. China

[2]China Meteorological Administration, Beijing 100081, P. R. China

[3]Institute of Atmospheric Physics, Chinese Academy of Sciences, Beijing 100029, P. R. China

[4]Chinese Academy of Meteorological Sciences, Beijing 100081, P. R. China

1. INTRODUCTION

During the past several decades, much effort has been made in field experiments to comprehensively investigate dynamical and microphysical characteristics of cloud, precipitation mechanisms, as well as the way how to scientifically assess and evaluate cloud seeding efficiency in operational rain enhancement programs (e.g., Smith, P. et al. 1984; David, S, 1987; Klimowski, B. A. et al. 1998; Long, A. B., and A. W., Huggins 1992; Daniel, R., 1993; Rlangno, A. L., and P. V. Hobbs 1993; Gayet, J. F., et al. 1993; Korolev, A. V., and I. P., Mazin 1993). Through these field experiments, scientists get much detailed information about interested clouds which can be hardly obtained in both laboratories and numerical modeling, even in normally operational observation networks. The field experiments, therefore, is considered to be the primary approach in atmospheric physics, especially in weather modification aspect.

Qinghai Province, located in the eastern fringe of Qinghai-Tibet plateau, is one of northwestern provinces frequently suffered from natural disasters, particularly drought and hail. The shortage of fresh water resource has been impacting the sustainable developments of economy and community in local area and the whole region along the Yellow River. Additionally, as a result of persistent drought occurred in this area, the ecosystem in the origin area of the Yangtze River, the Yellow River, and the Mekong River has become much worse gradually in most recent years. Along with improper human activities, the ecosystem in this area which usually play an important role in climate change in China and even globally would be seriously destroyed if without any measures taken to solve this problem. Recently, [1]Chinese central and local governments have already realized the importance for alleviating this influence and made many efforts to protect environment there. As one of the most important and cheapest method to augment fresh water resource, precipitation enhancement activity has been treated a primary approach and implemented over the Upper Reaches of the Yellow River in the past seven years to increase natural precipitation, augment runoff of the Yellow River, and eventually improve the ecosystem, financially supported by Chinese central government.

Up to now, there are few research works and papers focused on the investigation of cloud microphysics and dynamics in this area. In order to scientifically implement cloud seeding operational works, fully realizing the general characteristics of rain enhancement-targeted clouds, the cloud water resources, and the potential for conducting cloud seeding, a comprehensive field experiment which is one of two demonstration experimental regions selected in the Chinese national key research project was conducted in the Upper Reaches of the Yellow River in July – October 2002 and 2003, respectively. This *situ* experiment is the one subproject of this Chinese national key research project: Demonstration of Precipitation Enhancement Techniques that is supervised by Dr. Guoguang Zheng. The main goal for this project is to produce the new techniques of precipitation enhancement suitable to the typical regions in China.

2. OVERVIEW OF THE FIELD EXPERIMENT

. The Upper Reaches of the Yellow River Field Experiment for Rain Enhancement (hereafter referred to as URYRFERE), led and organized by Qinghai Provincial Weather Modification Office (QPWMO), is a comprehensive program for both research and cloud seeding operational works. Other institutions involved in this experiment include the Division of Meso-Micro scale weather in Institute of Atmospheric Physics (IAP), Chinese Academy of Sciences (CAS),

Corresponding author's address: An-Ping Sun, Qinghai Provincial Weather Modification Office, Xining, Qinghai 810001, P. R. China; Email: sapyzn@yahoo.com

Research Center for Weather Modification (RCWM), Chinese Academy of Meteorological Sciences (CAMS). The primary objective of URYRFERE was to better understand the general features about cloud microphysics and dynamics in the Upper Reaches of Yellow River, then establish an appropriate cloud seeding approach and assessment & evaluation design for normally operational works. More specifically, seven main purposes were defined as follows:

(i) Obtain and collect experimental data to supply other subprojects for deeper analyses.

(ii) Realize general features for stratocumulus and cumulus on the Qinghai-Tibet plateau.

(iii) Design an relatively scientific ground and airborne cooperative observation scheme.

(iv) Understand the distribution of cloud water resource over the Upper Reach of Yellow River, and get the potential for rain enhancement at this area.

(v) Characterize relationships between cloud properties inferred from satellite and radar observations, as well as numerical outputs.

(vi) Observe the effects of hygroscopic or glaciogenic seeding on hydrometeor concentrations, growth, and precipitation formation.

(vii) Test the proposed cloud seeding hypothesis, physically and statistically, in a future field experiment.

3. EXPERIMENTAL FACILITIES

In order to obtain improved knowledge of the microphysical and dynamical properties of targeted cloud in the Upper Reaches of Yellow River, several kinds of facilities, both airborne and ground-based instrument, were involved in this intensive field experiment simultaneously. *Chyenne*-III aircrafts, equipped with FSSP-100 (Forward Scattering Spectrometer Probe), FSSP-ER (Forward Scattering Spectrometer Probe, Extended Range), OAP-2D-GA2 (two-dimensional Optical Array Probe with image resolution 25 μ m, OAP-2D-GB2 (two-dimensional Optical Array Probe with image resolution 100 μ m) manufactured by Particle Measuring Systems, Inc. (PMS), and *Yun*-12 aircraft (made-in-China), equipped with FSSP-100 (Forward Scattering Spectrometer Probe), FSSP-2D-C (two-dimensional Optical Array Probe), FSSP-2D-P (two-dimensional Optical Array Probe) manufactured by Particle Measuring Systems, Inc. (PMS) were used to collect data simultaneously. Further, Airborne GPS & thermometer and hygrometer were installed in these two aircrafts and Model KLWC-5 and microwave radiometer were also equipped in *Chyenne*-III and *Yun*-12 aircraft, respectively. The data from the probes equipped in *Chyenne*-III aircraft were recorded via Model 300 Data Acquisition System (hereafter referred to as M300 DAS) designed by CAM. Ground-based facilities included a C-band Doppler radar, high-resolution raingage network, and ground-based microwave radiometer, etc.

4. EXPERIMENTAL DESIGN

This experiment site was focused to be placed in Henan county, the southern part of Qinghai province, China, where is approximately 350 km away from Xining, the capital of Qinghai province. The targeted area was inside the Yellow River basin and average elevation is generally above 3500 m (ASL) (Fig. 1). Southwestern moist air flowing from Indian Ocean provides continuing uplift of approaching water vapor and promotes development of orographic clouds containing significant supercooled liquid water. Therefore, This area is most appropriate for implementing rain enhancement activity for increasing runoff of the Yellow River.

The experimental unit was primarily stratocumulus with a horizontal scale more than 200 km, which qualified the unit for treatment regarding aircraft flight safety policies. In accordance with experimental design, *Chyenne*-III aircraft took off form Xining airport directly to experimental area (in Fig. 1, from point A to B), firstly flied down form cloud top to 3800 m (ASL, aircraft safety height) to make a vertical observation at location approximately 40 km west to the mobile C-band radar for precisely cooperative observation between aircraft and radar to get the knowledge of vertical characteristics of microphysical features inside targeted cloud (in Fig.1 from point B to C), then started to release seeding material-silver iodide (AgI) along the direction from northwest to southeast at the level with temperature approximately –12 $^{\circ}C$ After carrying out cloud seeding work, this aircraft was guided to fly through the area inside targeted cloud where cloud seeding was implemented with the height at 300 m lower than cloud seeding height (in Fig.1 from point C to D), then finished observation and return to Xining airport (form D to A). One hour later after taking off of *Chyenne*-III aircraft, *Yun-12* aircraft took off form the same airport directly flying from A to B', and started to fly through the target cloud that was seeded by *Chyenne*-III aircraft to observe microphysical characteristics and seeding responses (from B' to C'). Then, *Yun-12* aircraft made a vertical flying observation at location C'. Finally, after finishing vertical observation, *Yun-12* aircraft fly back to Xining airport.

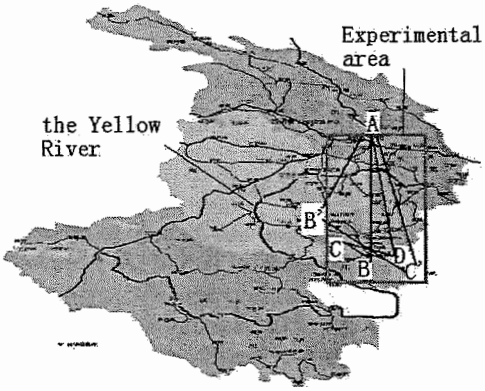

Fig. 1. Map of Experimental area in the Upper Reaches of the Yellow River

5. PRELIMINARY RESULTS AND DISCUSSIONS

In this paper, data observed during vertical observation in case Oct. 11, 2003 are firstly analyzed to explore the vertical structure of stratum cloud. Others will be investigated in more detailed latter in other papers.

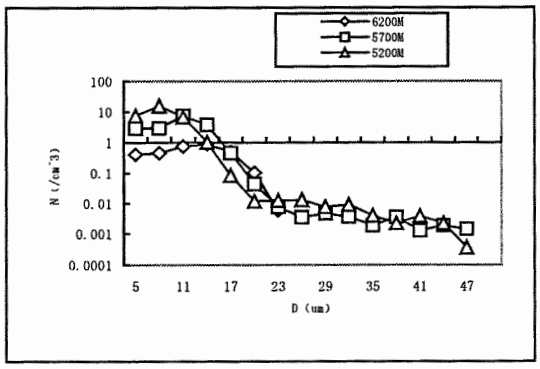

Fig. 2. Distribution of droplet spectrum observed by FSSP-100 probe at different height

Fig. 2 illustrates the distribution of droplet spectrum detected by FSSP-100 probes. It is clearly shown that distribution of concentrations of droplet at the 5700m and 5200m (ASL) are basically same. The concentration of droplet with diameter smaller than 14 μ m around is remarkably more than that with diameter larger than 14 μ m. The maximum concentration of drop reaches 12 Cm^{-3} at 5200 m. Specifically, the concentration decreases with respect to increased height for the cloud drop with diameter 5-11 μ m and 22-45 μ m and there are no relatively larger drops at 6200 m. For cloud drop with diameter from 17-21 μ m, however, the concentration of cloud drop increases with the increased height. Thus, general feature of cloud distribution is that, the concentration of smaller drop (<14 μ m) is much more than that of larger drop (22-45 μ m) and cloud drop primarily exists in the lower atmosphere (around 5200m). Additionally, larger cloud drop only exists at the height below 5700 m.

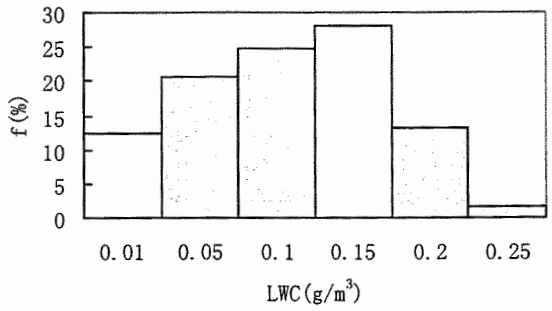

Fig. 3. Distribution of LWC during vertical observation

Distribution of LWC (liquid Water Content), calculated with data observed by FSSP-100 and FSSP-ER probes, in the whole vertical observation, is given in Fig. 3. It can be easily obtained that, in the targeted cloud, the content of liquid water is mainly around 0.1-0.15 g m^{-3}, with the maximum existence frequency arriving 28%.

4. SUMMARY AND CONCLUSION

Some general feature regarding targeted cloud in the Upper Reaches of the Yellow River is basically analyzed. The results show that the decreases with respect to increased height for the cloud drop with diameter 5-11 μ m and 22-45 μ m and there are no relatively larger drops at 6200 m. The content of liquid water is mainly around 0.1-0.15 g m^{-3}.

It should be noted that all results presented in this paper is only preliminary investigation. Much work remains and will be done in future. More detailed analysis of observational data should be carried out to further exploit some characteristics of microphysics and dynamics particularly occurred in this area.

ACKNOWLEDGMENT: This research was supported by the Ministry of Science and Technology of China through National Key Research Program (2001BA610A-06).

REFERENCES

Daniel, R., W. L. Woodley, 1993: Effects of cloud seeding in West Texas: Additional results and new insights. *J. Appl. Meteor.*, 32, 1848-1864.

David, S., 1987: A cirrus-cloud experiment: Intensive field observation field observations planned for FIRE. *Bull. Aim. Meteorol. Soc.*, **68**, 119-124.

Gayet, J. F., P. R. A., Brown, and F. Albers, 1993: A comparison of in-cloud measurement obtained with six PMS 2D-C probes. *J. Atmos. Oceanic Technol.*, **10**, 180-194.

Long, A. B., and A. W., Huggins, 1992: Australian winter storms experiment (AWSE) I: Supercooled liquid water and precipitation-enhancement opportunities. *J. Appl. Meteor.*, **31**, 1041-1055.

Klimowski, B. A., R. Becker, *et al.*, 1998: The 1995 Arizona Program: Toward a better understanding of winter storm precipitation development in mountainous terrain. *Bull. Aim. Meteorol. Soc.*, **79**, 799-813.

Korolev, A. V., and I. P. Mazin, 1993: Zones of increased and decreased droplet concentration in stratiform clouds. *J. Appl. Meteor.*, 32, 760-773.

Rlangno, A. L. and P. V. Hobbs, 1993: Further analyses of the climax cloud-seeding experiments. *J. Appl. Meteor.*, **32**, 1837-1846.

Smith, P., A. S., Dennis, and B. A., Silverman, et al., 1984: HIPLEX-1: Experimental design and response variables. *J. Climate Appl. Meteor.*, **23**, 497-512.

Zheng, G., 2003: Weather Modification, 8th WMO Scientific Conference on Weather Modification, Casablanca, Morocco, 7-12 April, WMP, No. 39, p 31-33.

Storm Systems and Precipitation Processes in East Asian Monsoon Rain

Tsutomu Takahashi

Obirin University, Machida-shi, Tokyo, 194-0294, Japan

1. INTRODUCTION

The monsoon rains of East Asia are vitally important to the region, each year bringing heavy rainfall across many countries. The dynamic and thermodynamic structures of monsoon systems have been extensively investigated in international projects such as MONEX. Despite such programs, there have been only a few attempts to understand the systems and precipitation mechanisms in clouds producing heavy rain, among them Churchill and Houze in 1984 and Houze and Churchill in 1987. Yanai et al. (1973) reported differences in latent heat profiles in different monsoon areas, suggesting that precipitation mechanisms may differ in each region.

As reported by Christian et al. (2003), results from TRMM showed almost two orders of magnitude difference in lightning frequency between maritime continent and the open ocean although the total annual rainfall amounts were quite similar. Inasmuch as the major charge separation mechanism should be riming electrification (Takahashi, 1978), there should also be differences in the ice content in clouds in the different areas. The aims of the work presented here are to identify the storm systems and major precipitation mechanisms in each area as well as the rain accumulation processes, and to investigate the reported differences in lightning activity.

2. INSTRUMENTS

The primary instrument in these investigations is the videosonde (Fig. 1, Takahashi, 1990). The videosonde features an induction ring that measures the electric charge on falling precipitation particles and a videocamera that records particle images larger than 0.5 mm in diameter. The images are converted to frequencies between 10 H and 1 Mh and sent to a ground station by a 1680 Mh carrier wave where they are projected onto a TV screen at 10x magnification and recorded on video tape. The particle electric charge and the atmospheric pressure, temperature, and humidity are also displayed and recorded.

Other instruments are portable radar and electric field mill used to determine the best times for releasing the videosondes. In many of the investigations C-band radars from host meteorological agencies have also been available. Satellite pictures and weather charts help to characterize synoptic patterns.

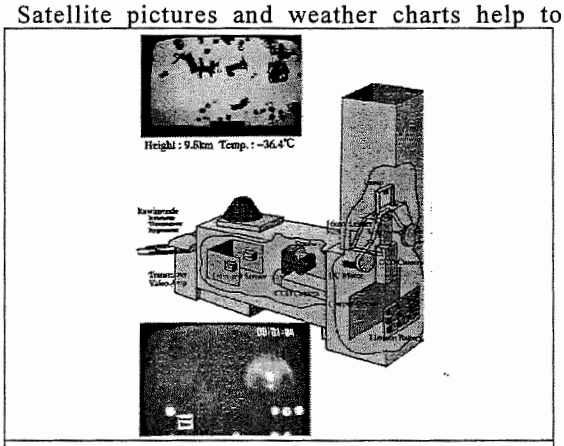

Fig. 1. Videosonde.

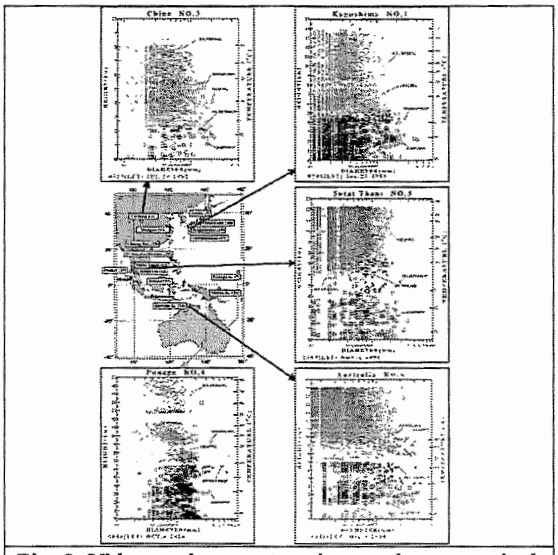

Fig. 2. Videosonde ascent stations and some typical examples.

During the past 12 years, observations have been conducted in 13 different locations, using 208 videosondes launched in periods chosen by determining the optimum monthly rainfall in each location. From the videosonde data, the number

Corresponding author's address : T. Takahashi
Obirin University , 3758 Tokiwa-Cho, Machida-Shi, Tokyo, 194-0294, Japan ; E-Mail : t2@obirin.ac.jp.

concentration and masses have been calculated for every 500 m of height, assuming the particles to be spherical and of densities of 0.9 (frozen drops), 0.3 (graupel) and 0.1 for ice crystals and snowflakes.

3. RESULTS

3.1 Precipitation particle distributions and features of primary rain systems

At every location in East Asia during the monsoon season, unique cloud systems and precipitation particle distributions have been observed. In Ponape, MCSs in the ITCZ consisted of rainbands and thick, upper-layer clouds. In the rainbands, the particle distribution was characterized by large frozen drops close to the freezing level with relatively low concentrations of graupel and ice crystals(Fig. 2). Similar features were also observed at Manus Island. Intense rainbands developed in the low-level convergence zone formed by the influence of easterlies and typhoons.

During the winter monsoons, cloud systems approaching from the Indochina peninsula were intensified by a small vortex off Brunei. The particle distributions observed were characterized by frozen drops near the freezing level and graupel growth in the upper levels.

A pre-monsoon squall line (HECTOR) developed over Melville Island, Australia in which particle distributions were found to be different in different areas of the storm. Frozen drop growth in the low-level forward edge of the storm was followed by abundant graupel and ice crystals in the upper-level convective area with concentrations reaching as high as 10/cm^3.

During the winter monsoon in Songkhla and Surat Thani, longitudinal rainbands moved from the eastern ocean producing heavy rain. Northeasterlies blowing from a continental high are accelerated by the depression and meet easterlies, causing low-level convergence. In this situation, extensive frozen drops and graupel grow near the freezing level. In contrast, during the summer monsoon in Phuket, southwesterlies are intensified by a vortex over the ocean east of the Indochina Penninsula. Here, close to the freezing level, freezing drop growth was highly accelerated, with graupel growth occurring in a wide range above it. Particle distributions in some cases were dominated by frozen drops.

At Ubon, when an upper vortex was located above a monsoon trough, heavy rain fell from an intense squall line. Frozen drops dominated particle distribution near the freezing level and graupel grew on small drops. When a depression, formed off Vietnam, entered the monsoon trough, an unique cloud system developed, consisting of a thick, upper-layer cloud and low-level stratocumuli.

Fig. 3. Peak rainwater contents with respect to peak frozen drop and graupel water contents.

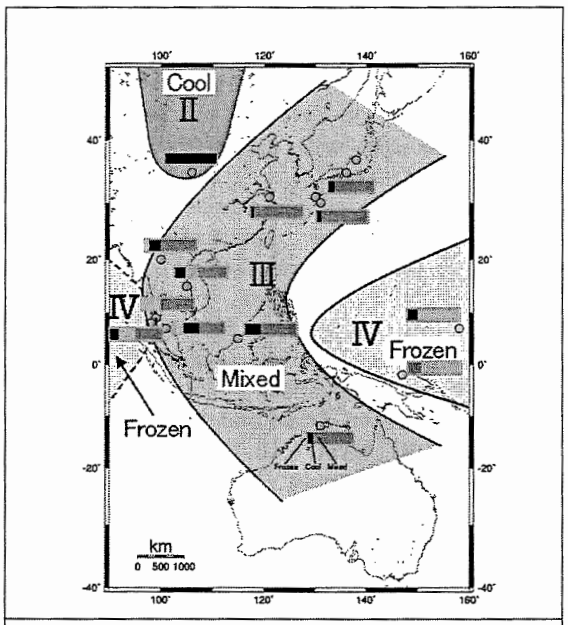

Fig. 4. Areal dominance characterized by precipitation mechanisms.

As the stratocumuli reached the thick, upper-layer, active convection began. Large graupel formed near the freezing layer fell and small graupel and ice crystals were transported to the surroundings. The system persisted for several hours, producing heavy rainfall.

In Pingliang, intense thunderstorms developed over the mountainous terrain when cold, upper level air approached from the north. During the night, the storms migrated to the plain with graupel being the major precipitation particle. Substantial rain also fell from rainbands developed in association with Baiu and Meiyu fronts.

In Shanghai, heavy rain also developed in a rainband associated with a mesoscale convective system where both graupel and frozen drops grew extensively, close to the freezing level. Flooding occurred in Kagoshima and Tanegashima when a convective cell in a MCS ceased moving and small cells forward of the cell merged with it, producing extremely high concentrations of frozen drops and graupel, close to the freezing level.

3.2 Precipitation mechanisms and rain accumulation processes

Frozen drops may represent lower-level, liquid phase activities and graupel, ice phase activities. Rainwater contents show peak values in four different regions (Fig. 3). This may correspond to different precipitation mechanisms: (1) warm rain, in areas with low numbers of frozen drops and graupel(I); (2) cool rain where there are high numbers of graupel and low numbers of frozen drops(II); (3) frozen, with high numbers of frozen drops and low numbers of graupel(IV); and (4) mixed regions with high numbers of both(III). Videosonde records were examined with reference to these precipitation domains.

The salient feature of these examinations was that monsoon rain does differ with respect to these precipitation mechanisms (Fig. 4). Ponape and Manus are designated as frozen. Pingliang is "cool". "Mixed" mechanisms occur over maritime continent and in Phuket, "frozen" also frequently appears.

The most outstanding features are the extremely large rainwater contents in some of the mixed region. The continuous supply of supercooled drops from merging cell plays a vital role in such rapid particle growth. Both frozen drops and graupel grow large near the freezing level (Fig. 3). A three-dimensional cloud model with detailed microphysics (Takahashi and Shimura, 2004) simulates the rapid growth of graupel and frozen drops near the freezing level during cell merging (Fig. 5). Continuous supply of these large frozen drops and graupel, in addition to increased warm rain activity, may enhance collection growth at lower levels, leading to larger raindrops and higher rainwater content.

3.3 Lightning activity and ice crystals

The peak number concentrations of graupel and ice crystals were multiplied and related to the peak rainwater contents. The multiplied upper values of rainwater contents at $1 g/m^3$ were then interpolated and compared with lightning frequencies from Christian et al. (2003). The most notable results of these computations were that, over the maritime continent with high lightning frequencies, there were high number concentrations of graupel and ice crystals (Fig. 6). On the other hand, over the open ocean with weaker lightning activity, the graupel and ice crystal numbers were low. Since graupel and ice crystals separate gravitationally in clouds, the square root of the multiple is meaningful. It was found that as lightning frequencies differ by two orders of

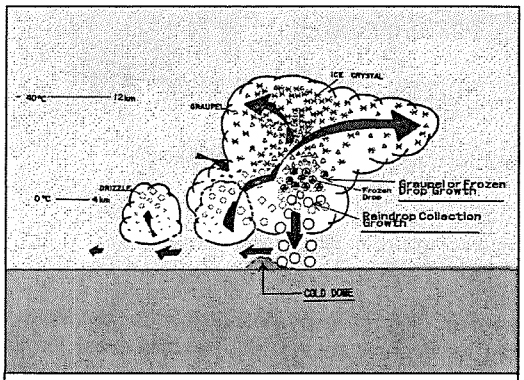

Fig.5. Heavy rain model based on numerical. model.

magnitude between the maritime continent and the open ocean, so do the ice particle concentrations differ by the same order of magnitude.

4. CONCLUSIONS

During the past twelve years, more than 200 videosondes have been launched into monsoon rain from 13 different locations in East Asia. Precipitation processes in the storms have been investigated from videosonde data giving hydrometer shapes and charges in clouds monitored by radar.

Monsoon rain has been subdivided into three different precipitation mechanisms: "frozen " over an open ocean; "mixed" over a maritime continent; and "cool" over an inland desert area. The accumulation process leading to heavy rainfall occurs through the rapid growth of frozen drops and graupel near the freezing level in clouds.

Analysis also shows that lighting activity is closely correlated with ice crystal and graupel concentrations. The results match closely with areal lightning frequencies from satellite data.

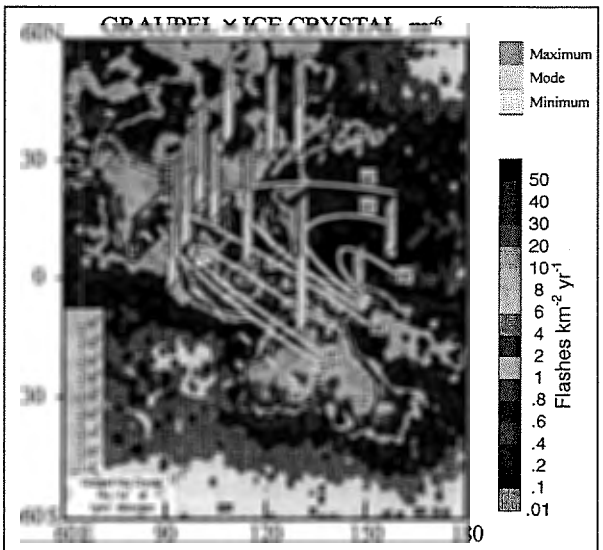

Fig. 6. Lightning frequencies and multiplied number of peak graupel and ice crystal concentrations at 1 g m^{-3} rainwater content.

Acknowledgements

This research was supported by funding from the Japan Ministry of Education, Culture, Sports, Science and Technology, the Japan Aerospace Exploration Agency (JAXA) and the Climate Center of Tokyo University.

References

Christian, H. J., R. J. Blakeslee, D. J. Boccippio, W. L. Boeck, D. E. Buechler, K. T. Driscoll, S. . Goodman, J. M. Hall, W. J. Koshak, D. M. Mach, and M. F. Stewart, 2003: Global frequency and distribution of lightning as observed from space by the optical transient detector, J. Geophys. Res., 108, DO 10. 1029/2002JD002347.

Churchill, D.D. and R.A. Houze, Jr., 1984: Development and structure of winter monsoon cloud clusters on 10 December 1978. J. Atmos. Sci., 41, 933-960.

Houze, R. A. Jr. and D. D. Churchill, 1987: Mesoscale organization and cloud microphysics in a bay of Bengal Depression. J. Atmos. Sci., 44, 1845-1867.

Krishnamulti, T. N., 1985: Summer monsoon experiment-A review. *Mon. Wea. Rev.*, **1123**, 1590-1626.

Takahashi, T., 1978: Riming electrification as a charge generation mechanism in thunderstorms. *J. Atmos. Sci.*, *35*, 1536-1548.

_____, 1990: Near absence of lightning in torrential rainfall producing Micronesian thunderstorms. Geophys. *Res. Lett.*, **17**, 2381-2384.

_____, and K. Shimura, 2004: Tropical rain characteristics and microphysics in a three dimensional cloud model. Submitted to J. Atmos. Sci.

Yanai, M., S. Esbensen and J. H. Chu, 1973: Determination of bulk properties of tropical cloud clusters from large scale heat and moisture budgets. *J. Atmos. Sci.*, **30**, 611-627.

EFFECT OF TURBULENCE ON COLLISION EFFICIENCY OF CLOUD DROPLETS

Lian-Ping Wang[1]*, Orlando Ayala[1], Scott E. Kasprzak[1], and Wojciech W. Grabowski[2]

[1] Department of Mechanical Engineering, University of Delaware, Newark, Delaware 19716-3140, USA
[2] Mesoscale and Microscale Meteorology Division, National Center for Atmospheric Research
PO Box 3000, Boulder, Colorado 80307-3000, USA

1. INTRODUCTION

Although the importance of turbulence on rain formation was noted more than 60 years ago (Arenberg 1939), progress has been very slow in identifying and understanding the nature and quantitative importance of turbulence effects. Adequate treatment of the turbulence effects on droplet growth represents a major gap in our understanding of cloud microphysical processes.

Air turbulence in atmospheric clouds can modify the collision-coalescence process in at least three ways. First, the relative velocity between two colliding droplets is affected by the turbulent ?uid motion and is usually larger than the differential terminal velocity in still air (Saffman and Turner 1956; Wang *et al.* 1998b; Dodin and Elperin 2002). Second, in local regions of the ?ow where the air streamlines are severely curved (e.g., regions of high vorticity or high strain rate), droplets, as a result of their ?nite inertia, can be nonuniformly distributed (Wang and Maxey 1993), leading to potentially much higher rates of collisions on average (Sundaram and Collins 1997; Wang *et al.* 2000). Third, turbulence may also alter the local droplet-droplet hydrodynamic interactions (HI) and collision ef?ciencies as both the magnitude and orientation of droplet-droplet relative motion and local droplet distribution can be altered by local turbulent characteristics. In this talk, we focus on the effect of air turbulence on collision ef?ciency.

For the hydrodynamical-gravitational problem, the collision ef?ciency is often de?ned simply as (Pruppacher and Klett 1997)

$$E_{12}^{g} = \frac{y_c^2}{R^2}, \tag{1}$$

where the geometric collision radius R is the sum of the radii of two colliding droplets, $R = a_1 + a_2$; y_c is the far-?eld, off-center horizontal separation of the grazing trajectory of the smaller droplet relative to the larger droplet. The undisturbed or *background* air turbulence makes the concept of relative grazing trajectory not so useful for hydrodynamical interactions in a turbulent ?ow. Speci?cally, for the case of nearly equal-size droplets, the relative motion due to turbulent air can be larger than that due to differential terminal velocity, therefore, the smaller droplet could approach and collide with the larger droplet from almost any directions relative to the larger droplet. The quantity y_c in equation (1) can no longer be properly de?ned.

In this work, we shall develop a general kinematic formulation that can describe the collision rates of hydrodynamically-interacting droplets in turbulent air by extending a formulation used for geometrical collision rates (Sundaram and Collins 1997; Wang *et al.* 1998b, 2000). We note that only a very few studies exist in the literature regarding collision ef?ciencies of cloud droplets in turbulent air (Almeida 1979; Grover and Pruppacher 1985; Koziol and Leighton 1996; Pinsky *et al.* 1999). In these studies, *different* kinematic formulations were used to de?ne the collision ef?ciency, almost all of which are some extensions to equation (1). These de?nitions of collision ef?ciency were used without *direct* validation against dynamic collision statistics. This problem along with different, inaccurate representations of the air turbulence and different droplet-size combinations generated somewhat controversial conclusions regarding the in?uence of turbulence on collision ef?ciencies.

We shall introduce a more general and accurate kinematic de?nition of collision ef?ciency that separates out the effect of turbulence on geometric collision rates. We then present some preliminary results comparing collision ef?ciencies in a turbulent ?ow with pure gravitational collision ef?ciencies.

2. THEORETICAL CONSIDERATIONS

The collision kernel Γ_{12} is an *average* rate coef?cient de?ned as

$$\Gamma_{12}^{D} = \frac{< \dot{\mathcal{N}}_{12} >}{n_1 n_2}, \tag{2}$$

where $< \dot{\mathcal{N}}_{12} >$ is the average number of collisions per unit time per unit volume between two size groups of *average* number concentrations n_1 and n_2. In DNS, all dynamical collision events can be detected and so $< \dot{\mathcal{N}}_{12} >$ can be directly obtained. We shall refer to the collision kernel computed by equation (2) as the *dynamic* collision kernel.

When hydrodynamic interactions are not considered, the average geometrical collision kernel between two arbitrary particle size groups can be described

*Corresponding author's address: Lian-Ping Wang, Department of Mechanical Engineering, 126 Spencer Laboratory, University of Delaware, Newark, Delaware 19716-3140, USA. E-mail: lwang@me.udel.edu

kinematically as (Saffman and Turner 1956; Sundaram and Collins 1997; Wang *et al.* 1998b, 2000)

$$\Gamma_{12}^{K} = 2\pi R^2 < |w_r(r=R)| > g_{12}(r=R). \quad (3)$$

where w_r is the radial relative velocity, g_{12} is the radial distribution function measuring the effect of preferential concentration on the pair number density at separation r. The above kinematic formulation has been validated using DNS (Wang *et al.* 2000) and recovers the well-known gravitational collision kernel

$$\Gamma_{12}^{g} = \pi R^2 |W_1 - W_2|, \quad (4)$$

since for the pure gravitational case, $g_{12} = 1$ and $< |w_r|(r=R) >= 0.5|W_1 - W_2|$. Here W_1 and W_2 are the terminal velocities of the droplets.

When hydrodynamic interactions are taken into account, particles can no longer overlap in space. It can be shown that the kinematical formulation, equation (3), could still be used if appropriate correction factors due to non-overlap are incorporated into the kinematic properties (Wang *et al.* 2004b).

A general collision ef?ciency in a turbulent ?ow can be de?ned as the ratio of collision kernel with hydrodynamic interactions (HI) to the geometric collision kernel (No HI):

$$E_{12}^{D} = \frac{\Gamma_{12}^{D}(\mathrm{HI})}{\Gamma_{12}^{D}(\mathrm{No\ HI})}. \quad (5)$$

Alternatively, if the kinematic formulation applies to both cases with and without hydrodynamic interactions, we would have

$$E_{12}^{K} = \frac{< |w_r| > (\mathrm{HI})}{< |w_r| > (\mathrm{No\ HI})} \times \frac{g_{12}(\mathrm{HI})}{g_{12}(\mathrm{No\ HI})}. \quad (6)$$

In the atmospheric sciences community, the collision kernel is often written relative to the hydrodynamical-gravitational case. As long as the collisions of droplets of unequal sizes are considered, we can write

$$\Gamma_{12} = \eta_G \eta_E \Gamma_{12}^{g}(\mathrm{No\ HI}) E_{12}^{g}, \quad (7)$$

where $\Gamma_{12}^{g}(\mathrm{No\ HI})$ is the geometrical gravitational collision kernel given by equation (4), E_{12}^{g} is the collision ef?ciency for the hydrodynamical-gravitational problem given by equation (1). η_G represents an enhancement factor due to turbulence on the geometric collision kernel and η_E represents an enhancement factor due to turbulence on the *true* collision ef?ciency:

$$\eta_G = \frac{\Gamma_{12}(\mathrm{No\ HI})}{\Gamma_{12}^{g}(\mathrm{No\ HI})}, \quad \eta_E = \frac{E_{12}}{E_{12}^{g}}. \quad (8)$$

For the hydrodynamical-gravitational problem, both enhancement factors reduce to one, so our formulation is consistent with the established formulation for this simple situation.

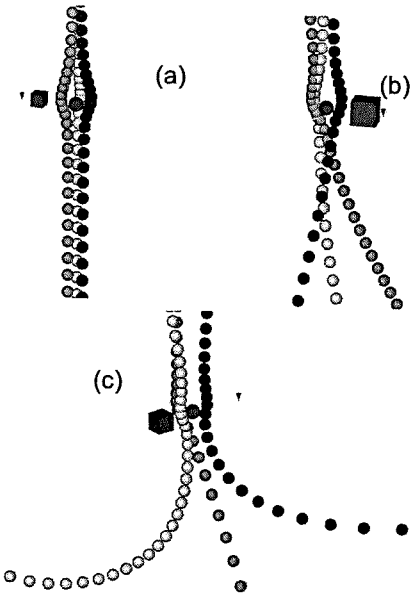

Figure 1: Three grazing trajectories of $20-\mu m$ droplets relative to $30-\mu m$ droplets: (a) suspension without turbulence; (b) turbulent suspension at $\epsilon = 100\ cm^2/s^3$; (c) turbulent suspension at $\epsilon = 400\ cm^2/s^3$.

3. DIRECT NUMERICAL SIMULATIONS

There are ?ve components to the development of DNS codes (Wang *et al.* 2000, 2004b): (a) direct numerical simulation of *background* turbulent air ?ow, (b) a representation of disturbance ?ows due to the presence of droplets, (c) tracking the motion of cloud droplets, (d) dynamic detection of collision events, and (e) computation of relative velocity and radial distribution function.

We model the air ?ow in the core region of adiabatic cumulus clouds as a homogeneous and isotropic turbulence. The small-scale features of the ?ow are characterized by the Kolmogorov scales de?ned based on the viscous dissipation rate and kinematic viscosity. The large-scale features may be characterized by the r.m.s. ?uctuation velocity u' or ?ow Taylor-microscale Reynolds number $R_\lambda = \sqrt{15}\,(u'/v_k)^2$. The disturbance ?ows are represented analytically as a superposition of Stokes ?ows, with observations of boundary conditions on the surface of the droplets (Wang *et al.* 2004a,b). The simulation typically involved tracking 200,000 droplets moving under the in?uence of both undisturbed air turbulence and the disturbance ?ows, with half of the droplets of size 1, and second half of size 2. The simulation considered all hydrodynamic interactions among and between size-1 and size-2 droplets.

4. RESULTS AND DISCUSSIONS

In ?gure 1, we display a few grazing trajectories of $20-\mu m$ droplets relative to $30-\mu m$ droplets for three different levels of air turbulence. While the rela-

Table 1: A case study for geometrical-gravitational or hydrodynamical-gravitational collisions.

	No HI	HI
$\frac{\Gamma^D_{12}}{\Gamma^g_{12}}$	1.000 ± 0.026	0.257 ± 0.012
$\frac{\Gamma_{12}}{\Gamma^g_{12}}$ †	1.026 ± 0.046	0.286 ± 0.023
$\frac{<\lvert w_r \rvert>}{\Delta W}$ †	0.516 ± 0.013	0.132 ± 0.005
g^K_{12} †	0.99 ± 0.04	1.08 ± 0.04

† The kinematic value was computed based on the shell $R \leq r < 1.05R$. Droplets were not allowed to overlap.

tive motion is vertical when there is no turbulence, the trajectories are strongly curved for the turbulence ?ow cases. In turbulent ?ows, pairs may approach from any relative directions in the far ?eld, making the use of y_c inapplicable.

To quantify the effects of air turbulence on hydrodynamic interactions, we report results from three case studies in Tables 1, 2, and 3. In these studies, we consider a system containing 50,000 droplets of radius $a_1 = 25\ \mu m$ and 50,000 droplets of radius $a_2 = 20\ \mu m$ in 64^3 DNS with $R_\lambda = 40$. For the runs in Tables 1 and 2, the simulation domain size was set to 8.329 cm in each direction. For the runs in Table 3, the simulation domain size was set to 11.80 cm. The terminal velocity is 8.0147 cm/s for 25 μm droplets and 5.1294 cm/s for 20 μm droplets.

In Table 1, the air turbulence was turned off and two simulations are considered: the ?rst is geometrical collisions with non-overlap droplets, and the second is the hydrodynamical-gravitational collisions. The ?rst line shows that hydrodynamic interactions reduce the collision kernel to 25.7% of the geometrical kernel, or a collision ef?ciency of 0.257. This collision ef?ciency is the same as the collision ef?ciency obtained by ?nding the relative grazing trajectory based on two isolated droplets, i.e., the result based on equation (1). This serves as a validation of our box-based simulations with many droplets. The second line gives the kinematical collision kernels which agree with dynamic collision kernels to within numerical uncertainties. The kinematical properties also reveal that the main effect of hydrodynamic interactions is to reduce the relative radial velocities. There is also some evidence that the hydrodynamic interactions result in a slight accumulation of pairs even without ?uid turbulence due to the changing relative motion caused by HI.

The cases shown in Table 2 are similar to the cases in Table 1, but now the background air turbulence is switched on with an average dissipation rate of 400 cm^2/s^3. The Stokes numbers for the two droplet sizes are 0.396 and 0.254, while the non-dimensional terminal velocities W/v_k are 2.791 and 1.786. Turbulence enhances the geometrical collision kernel by 42%. The true collision ef?ciency for turbulent ?ow

Table 2: A case study for geometrical-turbulent or hydrodynamical-turbulent collisions with $\epsilon = 400\ cm^2/s^3$.

	No HI	HI
$\frac{\Gamma^D_{12}}{\Gamma^g_{12}}$	1.420 ± 0.032	0.584 ± 0.021
$\frac{\Gamma_{12}}{\Gamma^g_{12}}$	1.544 ± 0.109	0.656 ± 0.052
$\frac{<\lvert w_r \rvert>}{\Delta W}$	0.561 ± 0.015	0.218 ± 0.007
g^K_{12}	1.38 ± 0.06	1.50 ± 0.07

Table 3: A case study for geometrical-turbulent or hydrodynamical-turbulent collisions with $\epsilon = 100\ cm^2/s^3$.

	No HI	HI
$\frac{\Gamma^D_{12}}{\Gamma^g_{12}}$	1.117 ± 0.032	0.315 ± 0.016
$\frac{\Gamma^K_{12}}{\Gamma^g_{12}}$	1.180 ± 0.130	0.302 ± 0.048
$\frac{<\lvert w_r \rvert>^K}{\Delta W}$	0.533 ± 0.020	0.129 ± 0.011
g^K_{12}	1.11 ± 0.08	1.17 ± 0.09

is $E_{12} \approx 0.584/1.420 = 0.411$, therefore, turbulence also increases the collision ef?ciency by a factor of $0.411/0.257 = 1.60$. The net increase in collision kernel due to turbulence is by a factor of 2.27. This level of overall increase is comparable with previous results of Koziol and Leighton (1996); Pinsky *et al.* (1999). Once again, within the numerical uncertainties, the kinematical collision kernels are the same as the dynamical collision kernels. The hydrodynamic interactions reduce the radial relative velocity by a factor of 0.387 but increases the radial distribution function by a factor of 1.11. While in the absence of turbulence, the hydrodynamic interactions reduce the radial relative velocity by a factor of 0.260 but increases the radial distribution function by a factor of 1.09. Therefore, hydrodynamic interactions become less effective in changing the radial relative motion when droplets are suspended in a turbulent ?ow – this is the main reason for the increase in collision ef?ciency by turbulence.

The relative importance of the turbulence effects changes with the ?ow dissipation rate. In Table 3 results are shown for the same droplet sizes as in Table 2 but with a ?ow dissipation rate at 100 cm^2/s^3. The Stokes numbers for the two droplet sizes are 0.198 and 0.127, while the non-dimensional terminal velocities W/v_k are 3.947 and 2.526. The true collision ef?ciency for the turbulent ?ow is $E_{12} = 0.315/1.117 = 0.282$, so at this level of ?ow dissipation, turbulence increases the collision ef?ciency by a factor of $0.282/0.257 \approx 1.10$ only. The enhancement

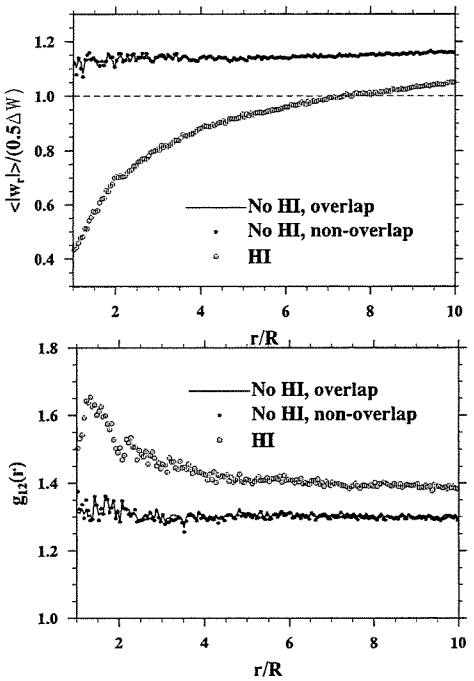

Figure 2: Radial relative velocity and radial distribution function for $1-2$ turbulent coagulation.

factor on the geometrical collision rate is about 1.12. The overall enhancement by turbulence is about a factor of 1.23, which is much smaller than 2.28 for the case of $\epsilon = 400\ cm^2/s^3$.

In ?gure 2 we show the radial relative velocity and radial distribution function for $1-2$ pairs for the same cases discussed in Table 2. Turbulence reduces relative velocity and increases pair concentration level for all r.

5. CONCLUSION AND FUTURE WORK

In this work, we have developed and validated a kinematic formulation capable of quantitatively addressing the collision rate in a turbulent ?ow. A general kinematic representation of the collision ef?ciency has also been introduced. We observe that hydrodynamic interactions become less effective in changing the relative radial velocity in a turbulent ?ow, when compared to the pure hydrodynamical-gravitational problem. This is the main reason that turbulence enhances the collision ef?ciency, in addition to augment the geometric collision rate. Hydrodynamic interactions also increase the nonuniformity of near-?eld pair density distribution. The level of increase in collision ef?ciency by turbulence appears to be comparable with the results of Koziol and Leighton (1996). There is also evidence that the collision ef?ciency for collisions among equal-size droplets is much higher than that for collisions between unequal droplets.

We are in the process of conducting a parametric study of collision ef?ciency for different droplet-pair sizes, different ?ow dissipation rates, and Reynolds numbers.

Acknowledgments This study has been supported by the National Science Foundation through grant ATM-0114100 and by the National Center for Atmospheric Research (NCAR). NCAR is sponsored by the National Science Foundation. OA is grateful to the additional computing resources provided by the Scientifi c Computing Division at NCAR.

References

Almeida, F.C. de, 1979: The collisional problem of cloud droplets moving in a turbulent environment - Part II: turbulent collision effi ciencies. *J. Atmos. Sci.*, **36**, 1564-1576.

Arenberg, D., 1939: Turbulence as a major factor in the growth of cloud droplets. *Bull. Amer. Met. Soc.* **20**, 444-445.

Dodin, Z. and T. Elperin, 2002: On the collision rate of particles in turbulent fbw with gravity. *Phys. Fluids*, **14**, 2921-2924.

Grover, S.N. and H.R. Pruppacher, 1985: The effect of vertical turbulent fluctuations in the atmosphere on the collection of aerosol-particles by cloud drops. *J. Atmos. Sci.*, **42**, 2305-2318.

Koziol, A.S. and H.G. Leighton, 1996: The effect of turbulence on the collision rates of small cloud drops. *J. Atmos. Sci.*, **53**, 1910-1920.

Pinsky, M. B., A. P. Khain, and M. Shapiro, 1999: Collision of small drops in a turbulent fbw. Part I. Collision effi ciency, Problem formulation and preliminary results. *J. Atmos. Sci.*, **56**, 2585-2600.

Pruppacher, H.R., and J.D. Klett, 1997: *Microphysics of Clouds and Precipitation* (2nd edition). Kluwer Academic Publishers, Boston, 954 pp.

Saffman, P.G. and Turner, J.S. 1956 On the Collision of Drops in Turbulent Clouds. *J. Fluid Mech.*, **1**, 16-30.

Sundaram, S. and L.R. Collins, 1997: Collision Statistics in an Isotropic, Particle-Laden Turbulent Suspension. *J. Fluid Mech.*, **335**, 75-109.

Wang, L.-P. and M.R. Maxey 1993: Settling velocity and concentration distribution of heavy particles in homogeneous isotropic turbulence. *J. Fluid Mech.*, **256**, 27-68.

Wang, L.-P., A.S. Wexler, and Y. Zhou, 1998b: Statistical Mechanical Descriptions of Turbulent Coagulation. *Physics of Fluids*, **10**, 2647-2651.

Wang, L.-P., A. S. Wexler, and Y. Zhou, 2000: Statistical Mechanical Descriptions of Turbulent Coagulation of Inertial Particles. *J. Fluid Mech.*, **415**, 117-153.

Wang, L.-P., O. Ayala, and W. W. Grabowski, 2004a, On improved formulation of the superposition method. Submitted to *J. Atmos. Sci.*

Wang, L.-P., O. Ayala, S. Kasprzak, and W.W. Grabowski, 2004b, Theoretical formulation of collision rate and collision effi ciency of hydrodynamically-interacting cloud droplets in turbulent atmosphere. Submitted to *J. Atmos. Sci.*

EFFECTS OF STOCHASTIC COALESCENCE AND AIR TURBULENCE ON THE SIZE DISTRIBUTION OF CLOUD DROPLETS

Lian-Ping Wang[1]*, Yan Xue[1], Orlando Ayala[1], and Wojciech W. Grabowski[2]

[1] Department of Mechanical Engineering, University of Delaware, Newark, Delaware 19716-3140, USA
[2] Mesoscale and Microscale Meteorology Division, National Center for Atmospheric Research
PO Box 3000, Boulder, Colorado 80307-3000, USA

1. PRELUDE

Cloud droplets of size less than 10 to 30 microns in radius are produced mainly by nucleation and condensation, while gravitational collision and coalescence among cloud droplets is known to be an effective growth mechanism for droplets larger than 50 to 60 microns in radius. An open question in warm (i.e., liquid-phase) rain process and precipitation formation is how the cloud droplets grow as quickly as often observed, particularly in the size range of 30 to 50 microns in radius (i.e., the so-called size gap) for which neither the condensation nor the collision-coalescence mechanism is very effective. Based on recent studies of droplet-laden turbulent ?ows, we speculate that turbulent air?ow may play a key role in promoting the growth and size evolution of cloud droplets. Here we shall brie?y explore several aspects of the collision-coalescence process where the air turbulence can certainly play a role, although the exact nature and quantitative measures of the effects of turbulence on promoting the growth of cloud droplets through the size gap will unlikely to be fully resolved in near future.

2. GEOMETRIC COLLISION RATES

Recent studies of particle-laden turbulent ?ows (Sundaram and Collins 1997; Wang *et al.* 2000; Zhou *et al.* 2001) show that air turbulence may signi?cantly enhance the average collision rates. The average geometrical collision kernel between two arbitrary droplet size groups can be described *kinematically* as (Saffman and Turner 1956; Sundaram and Collins 1997; Wang *et al.* 1998b, 2000)

$$\Gamma_{12}^{K} = 2\pi R^2 < |w_r(r=R)| > g_{12}(r=R). \quad (1)$$

where the geometric collision radius R is the sum of the radii of two colliding droplets, $R = a_1 + a_2$, w_r is the radial relative velocity, g_{12} is the radial distribution function measuring the effect of preferential concentration on the pair number density at separation r. When the inertial response time of droplets is on the order of the ?ow Kolmogorov time scale, droplets could interact effectively with small-scale ?ow structures and become nonuniformly distributed, a phenomenon known as the preferential concentration (Maxey 1987). Since the average collision rates are related to the second moment of the droplet concentration, the preferential concentration can cause g_{12} to be much greater than one (Sundaram and Collins 1997; Wang *et al.* 2000) and thus signi?cantly increases the collision rates.

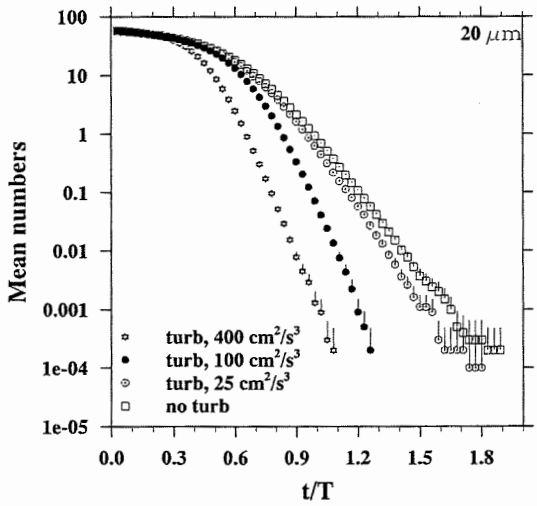

Figure 1: The time evolution of average number in bin 3 (20 μm in diameter).

To gain a quantitative understanding of how the enhanced geometric collision rates by turbulence may promote to growth of cloud droplets, the following idealized calculation was performed. Consider a system initially containing 60 droplets of 20 μm in diameter and another 60 droplets of 22 μm in diameter. These two droplet sizes were placed in bin 3 and bin 4 as two discrete sizes since their mass ratio is very close to 4/3, as such bin 1 and bin 2 were unoccupied in the full discrete mass representation.

*Corresponding author's address: Lian-Ping Wang, Department of Mechanical Engineering, 126 Spencer Laboratory, University of Delaware, Newark, Delaware 19716-3140. E-mail: lwang@me.udel.edu

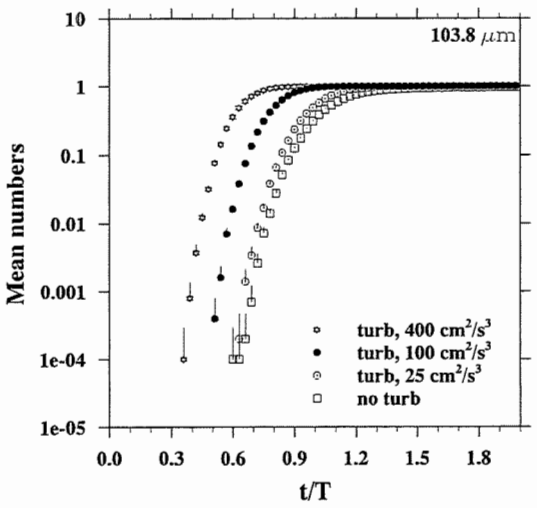

Figure 2: The time evolution of average number in bin 420 (103.8 μm in diameter).

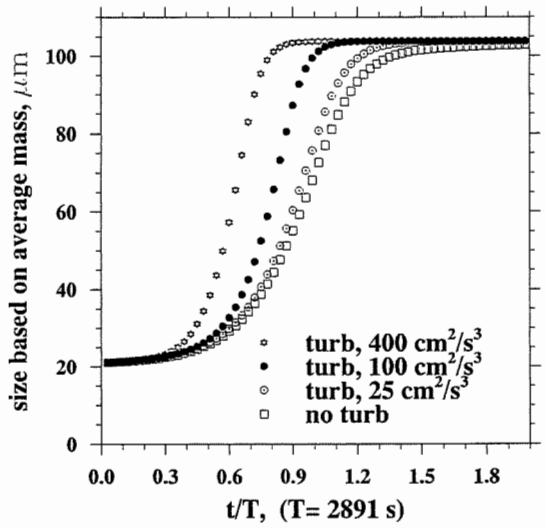

Figure 3: Diameter in μm based on the average droplet mass as a function of time.

If all these droplets were to coalesce to form a single droplet, the ?nal droplet size would be 103.8 μm in diameter and would belong to the mass bin 420. An *exact* collision-coalescence calculation was carried out using the Monte-Carlo method of Gillespie (1975b) with geometric collision kernel parameterization of Zhou *et al.* (2001). The parameterization was developed based on direct numerical simulations at low ?ow Reynolds numbers but was extrapolated to any ?ow Reynolds numbers. Stokes drag was assumed and the collision ef?ciency was set to unity. 10,000 Monte-Carlo realizations were used to obtain the average droplet size distribution and related statistics. The r.m.s. ?uctuation velocity of the air turbulence was assumed to be 1 m/s.

In ?gure 1 we show time evolution of the average number in bin 3 or for droplets of 20 μm in diameter. Three levels of ?ow dissipation were considered and the results was compared to the base case of no air turbulence. Statistical uncertainties, an inherent feature of Monte-Carlo simulations, were also shown. The time was normalized by the characteristic time scale T of the gravitational coagulation process. The average number for each case decreases monotonically due to collision-coalescence events, however, the rate of depletion depends on the ?ow dissipation rate. The higher the ?ow dissipation, the faster the depletion rate.

The time evolution of the average number for the last bin or the ?nal size is shown in ?gure 2. One can see that turbulence can shorten the time for the largest droplet to form. For the case of $\epsilon = 400 cm^2/s^3$, the time for the coalescence process to complete is roughly half of that for the pure gravitational case.

Table 1: Time in seconds for the droplet diameter based on mean mass to reach a certain size.

$\epsilon(cm^2/s^3)$	40 μm	60 μm	90 μm
0	2208	2703	3354
25	2148, 97%	2594, 96%	3131, 93%
100	1938, 88%	2270, 84%	2646, 79%
400	1500, 68%	1763, 65%	2081, 62%

To better quantify how turbulence promote the growth of droplets, we computed the droplet diameter based on the mean droplet mass and show its time evolution in ?gure 3. Clearly, the droplets grow faster as the ?ow dissipation rate is increased. We show in Table 1 the time in seconds for the droplet diameter based on mean mass to reach a certain size. At high ?ow dissipation rate, turbulence may shorten the growth time by as much as 30 to 40%. This clearly shows that turbulence can promote the growth of cloud droplets.

The main open issue here is the modeling of the radial distribution function g_{12} at high ?ow Reynolds numbers, since the relative velocity, w_r, can be more easily modeled. Theoretical advances in this direction are currently being made (Zaichik and Alipchenkov 2003; Sigurgeirsson and Stuart 2002; Jeffery 2001). DNS and experimental data at higher ?ow Reynolds are certainly desired as well.

3. COLLISION EFFICIENCIES

In another paper at this meeting, we study the effect of turbulence on the collision ef?ciency of cloud

droplets. Our main ?ndings to date are summerized here. We have developed and validated a kinematic formulation that can separate the effect of turbulence on collision ef?ciency from the enhanced geometric collision rate. Preliminary results show that air turbulence can increase the collision ef?ciency by as much as 60% for $\epsilon = 400cm^2/s^3$. We observe that hydrodynamic interactions become less effective in changing the relative radial velocity in a turbulent ?ow, when compared to the pure hydrodynamical-gravitational problem. This is the main reason that turbulence enhances the collision ef?ciency, in addition to augment the geometric collision rate. We also ?nd that hydrodynamic interactions increases the near-?eld pair density, resulting in higher radial distribution function at contact when compared to the geometric collision case. Furthermore, collision ef?ciency for collisions among equal-size droplets is much higher than that for collisions between unequal droplets.

We are in the process of conducting a parametric study of collision ef?ciency for different droplet-pair sizes, different ?ow dissipation rates, and Reynolds numbers. The goal will be to develop a model to quantify the enhanced collision ef?ciency by air turbulence which can later be used to study its effect on the size evolution of cloud droplets.

4. STOCHASTIC COALESCENCE

Typically, the modeling of size distribution in a collision-coalescence or coagulation system is performed by a mean-?eld equation such as the classical Smoluchowski coagulation equation (Smoluchowski 1917), which describes how the number density of a certain mass evolves in time due to coagulation of this mass group with all other mass groups in the system, assuming the average collision rate constants or collision kernels are known. As pointed out in the literature, coalescence events occur randomly and its local rates vary in space, time, and with realizations, the size distribution modeling must consider the stochastic nature of the coagulation process. Historically, there have been a few discussions on the effects of stochastic coalescence on the droplet growth modeling (Warshaw 1967; Gillespie 1972, 1975a,b; Bayewitz *et al.* 1974). The common wisdom is that when the system volume or number of droplets is very large, the stochastic ?uctuations tend to be small compared to the mean values. However, we may argue that, when a particular droplet size is considered, the number or volume may not always to large simply due to the system initial condition. Spatial inhomogeneity and ?uctuations can also be augmented by air turbulence, which adds another dimension to the stochastic nature of the coalescence process.

We have recently revisited the question of stochastic completeness of coalescence modeling and have derived the following true stochastic coalescence equation (TSCE) for arbitrary collision kernels:

$$\begin{aligned}\frac{d<x_m>}{dt} = & \underbrace{\frac{1}{2}\sum_{k=1}^{m-1} C_{k,m-k} < x_k x_{m-k} >}_{\text{Term A}} \\ & \underbrace{-\sum_{k=1}^{N_0-m} C_{m,k} < x_m x_k >}_{\text{Term B}} \\ & \underbrace{+\omega(m) C_{m,m} < x_m >}_{\text{Term C}} \\ & \underbrace{-\frac{\epsilon(m)}{2} C_{m/2,m/2} < x_{m/2} >}_{\text{Term D}} \qquad (2)\end{aligned}$$

where

$$\epsilon(m) \equiv \begin{cases} 1, & \text{if } m \text{ is even} \\ 0, & \text{if } m \text{ is odd} \end{cases} \qquad (3)$$

$$\omega(m) \equiv \begin{cases} 1, & \text{if } m \leq \text{int}(\frac{N_0}{2}) \\ 0, & \text{if } m > \text{int}(\frac{N_0}{2}) \end{cases} \qquad (4)$$

This TSCE contains correlations among instantaneous droplets of different sizes. In ?gure 4, we display all terms in TSCE for the case of constant collision kernel using the analytical solution of Bayewitz *et al.* (1974). This ?gure demonstrates that the left hand side of TSCE and the right hand side of TSCE are exactly the same. We can also conclude that the additional term C and term D in TSCE can be important for large particle sizes or for long time. Using the analytical solution of Bayewitz *et al.* (1974), we can obtain correlation coef?cients of droplet number ?uctuations for different mass pairs for the case of constant collision kernel. Figure 5 shows results for 1-2 and 2-3 pairs for two different system sizes N_0. When plotted against $N_0 t$, the results overlap for two system sizes. The magnitude of correlation coef?cients can be quite large.

TSCE can be used to identify the conditions under which the usual deterministic collision-coalescence mean-?eld equation such as DSCE can be applied, or else how the mean ?eld equation could be improved to account for the stochastic nature of the coalescence process.

5. SUMMARY

We have demonstrated that the enhanced geometric collision rates by air turbulence may reduce the time for drizzle formation due to coalescence by 40% at $\epsilon = 400\ cm^2/s^3$. Uncertainties remain on the level of droplet accumulation due to turbulence at high ?ow Reynolds numbers. Preliminary results also show that air turbulence increases collision ef?ciency by as mush as 43%. Combining these two enhancements by turbulence could shorten the time for drizzle formation by a factor of 2. A true stochastic coalescence equation

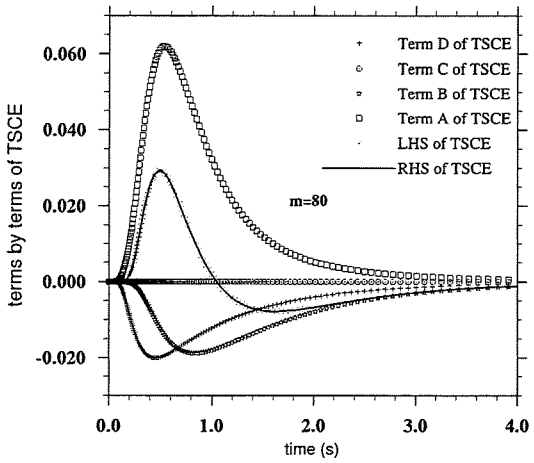

Figure 4: Validation of the TSCE for the case of constant collision kernel for bin 80, with the initial system size equal to 100.

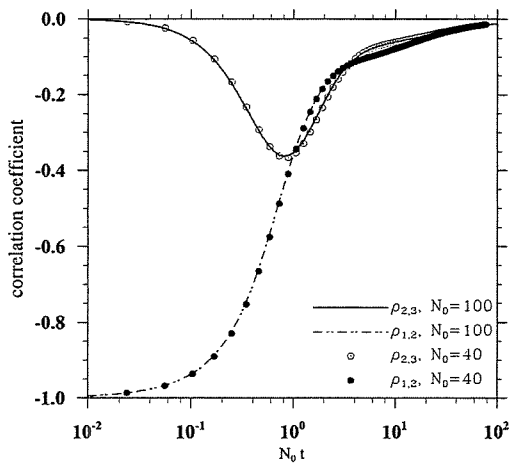

Figure 5: Analytical correlation coef?cients for the case of constant collision kernel.

has been derived and validated. Stochastic correlations and numerical integration errors could be other sources of uncertainty in modeling rain formation.

Acknowledgments This study has been supported by the National Science Foundation through grant ATM-0114100 and by the National Center for Atmospheric Research (NCAR). NCAR is sponsored by the National Science Foundation. OA is grateful to the additional computing resources provided by the Scientifi c Computing Division at NCAR.

References

Bayewitz, M.H., J. Yerushalmi, S. Katz, and R. Shinnar, 1974: The extent of correlations in a stochastic coalescence process. *J. Atmos. Sci.*, **31**, 1604-1614.

Gillespie, D, 1972: he stochastic coalescence model for cloud droplet growth. *J. Atmos. Sci.*, **29**, 1496-1510.

Gillespie, D.T., 1975a: Three models for the coalescence growth of cloud drops. *J. Atmos. Sci.*, **32**, 600-607.

Gillespie, D.T., 1975b: An exact method for numerically simulating the stochastic coalescence process in a cloud, Journal of the Atmospheric Sciences, Vol.32, 1977-1989.

Jeffery CA, 2001: Investigating the small-scale structure of clouds using the delta-correlated closure: effect of particle inertia, condensation/evaporation and intermittency, *Atmos Res* **59**: pp. 199-215 Sp. Iss.

Maxey, M.R., 1987: The gravitational settling of aerosol-particles in homogeneous turbulence and random fbw fi elds. *J. Fluid Mech.*, **174**, 441-465.

Saffman, P.G. and Turner, J.S. 1956 On the Collision of Drops in Turbulent Clouds. *J. Fluid Mech.*, **1**, 16-30.

Sigurgeirsson, H and Stuart, A.M., 2002: A model for preferential concentration. *Phys. Fluids*, **14**, pp. 4352-4361.

Smoluchowski, M. von, 1917: *Z. Physik. Chem.* **92**, 129.

Sundaram, S. and L.R. Collins, 1997: Collision Statistics in an Isotropic, Particle-Laden Turbulent Suspension. *J. Fluid Mech.*, **335**, 75-109.

Wang, L.-P. and M.R. Maxey 1993: Settling velocity and concentration distribution of heavy particles in homogeneous isotropic turbulence. *J. Fluid Mech.*, **256**, 27-68.

Wang, L.-P., A.S. Wexler, and Y. Zhou, 1998b: Statistical Mechanical Descriptions of Turbulent Coagulation. *Physics of Fluids*, **10**, 2647-2651.

Wang, L.-P., A. S. Wexler, and Y. Zhou, 2000: Statistical Mechanical Descriptions of Turbulent Coagulation of Inertial Particles. *J. Fluid Mech.*, **415**, 117-153.

Wang, L.-P., O. Ayala, S. Kasprzak, and W.W. Grabowski, 2004b, Theoretical formulation of collision rate and collision effi ciency of hydrodynamically-interacting cloud droplets in turbulent atmosphere. Submitted to *J. Atmos. Sci.*

Warshaw, M., 1967: Cloud Droplet Coalescence: Statistical Foundations and a One-Dimensional Sedimentation Model, J. Atmos. Sci., **24**, 278-286.

Zhou, Y., A. S. Wexler, and L.-P. Wang, 2001: Modelling turbulent collision of bidisperse inertial particles. *J. Fluid Mech.*, **433**, 77-104.

Zaichik, L.I. and V.M. Alipchenkov, 2003: Two statistical models for predicting collision rates of inertial particles in homogeneous isotropic turbulence, *Phys. Fluids*.

CLOUD DROPLET SIZE SPECTRAL BROADNESS OF ADIABATIC CLOUDS

Seong Soo Yum[1] and James G. Hudson[2]
[1]Department of the Atmospheric Sciences, Yonsei University, Seoul 120-749, Korea
[2]Division of Atmospheric Sciences, Desert Research Institute, Reno, NV 89512, USA

1. INTRODUCTION

Cloud droplet spectral broadening is an important issue that is directly related to the warm rain initiation problem. Theoretical condensational growth equation predicts narrowing of droplet spectrum when droplets are growing under adiabatic conditions (Rogers and Yau, 1989) as opposed to broadening that is prevalently observed in real clouds(e.g., Hudson and Yum, 1997). The discrepancy between the theory and observations has been a major dilemma in cloud physics for the last several decades and remains so even today although there has been some significant progress in recent years in understanding the problem (e.g., Beard and Ochs, 1993). Nevertheless, the observed fact of droplet spectral broadening is a key to explain how coalescence can occur efficiently enough in warm clouds and eventually lead to precipitation in a realistic time scale of about 30 min.

At least in the earlier stage of cloud development, cloud droplet growth may be considered adiabatic, meaning that the cloud is not yet affected by entrainment and mixing. Therefore for these young cloud parcels, droplet spectrum may be almost exclusively determined by adiabatic condensational growth. Important questions raised here is then how much the droplet spectra can differ between clouds when subjected only to adiabatic condensational growth, whether the differences are negligibly small, or if not, what causes these differences. The evolution of cloud droplet spectrum in the later stage of cloud development will be dependent on the spectrum of the earlier stage. Whatever the real spectral broadening mechanisms are, they would work more efficiently when clouds have less narrow droplet spectra before they are involved in the broadening processes.

This study examines what determines droplet spectral broadness of adiabatic clouds, using a condensational growth model (Robinson, 1984). Various different CCN spectra that may be representative of various different geographic locations are used as input and the model is run for variety of updraft conditions. Several factors are identified to be important in determining the droplet spectral broadness of adiabatic clouds. Results are also compared with observed cloud microphysics during the same field experiments that provided the CCN data.

2. THE MODEL

The adiabatic condensational growth model used in this study (Robinson, 1984) employs the full Kohler curve equation that includes both the solute and curvature effects. The model calculates growth of individual cloud droplets in a cloud parcel moving in a predetermined updraft condition. Therefore this model is Lagrangian in droplet size space. CCN spectrum from 0.02% to 1.0% S ranges is divided into 52 S classes and the evolution of the particles in each of the size classes is calculated. All CCN are assumed to be composed of NaCl. The condensation coefficient, β, which is the fraction of molecules retained by the water surface to the total impinging molecules, is not universally accepted. The effect of changing the value of β was examined in detail by Yum (1998). Higher β leads to increase in activated droplet concentrations but the fundamental aspects of spectral broadening of adiabatic clouds remain the same regardless of what β values are used. Therefore, only one β of 0.036, one of the commonly accepted values, is used in this study.

Corresponding author's address: Seong Soo Yum, Dept of Atmospheric Sciences, Yonsei University, Seoul 120-749, Korea; E-Mail:ssyum@atmos.yonsei.ac.kr

3. RESULTS

3. 1 Different CCN spectra

The eight input CCN spectra used in this study are boundary layer average values that were measured by the DRI CCN spectrometers (Hudson, 1989) during six different field projects. All of the measurements were made mostly over the marine environment but in two projects distinct air mass changes occurred and thus they are treated separately here. Therefore, each of the CCN spectra may be representative of the particular area or the air mass that passed the area. Table 1 lists the names of the projects along with the average CCN concentrations at 1% S (N_{CCN}) for the eight CCN spectra. Also shown in Table 1 are the condensation model (Robinson, 1984) run results of the maximum S (S_{max}), the activated droplet concentration(N_c) in the cloud parcel when the updraft (w) is fixed at 50 cm s^{-1}, and the mean diameter (MD) and standard

Table 1. Average CCN concentrations at 1% supersaturation from various field projects and cloud microphysical parameter values after 150 m ascent under 50 cm s^{-1} updraft condition. Reference to all project names are in Yum and Hudson (2004).

Project name	N_{CCN} (cm^{-3})	S_{max} (%)	N_{ac} (cm^{-3})	MD (μm)	σ_c (μm)
Sc	1411	0.215	445	11.2	2.1
Xc	1061	0.236	542	10.5	1.8
Sm	359	0.313	220	14.4	1.3
A	202	0.489	127	17.3	1.1
Xm	195	0.477	158	16.1	1.0
S2	191	0.493	130	17.2	1.0
F	122	0.517	98	18.9	1.0
S1	32	0.905	29	28.3	0.9

The meaning of each parameter is described in the text.

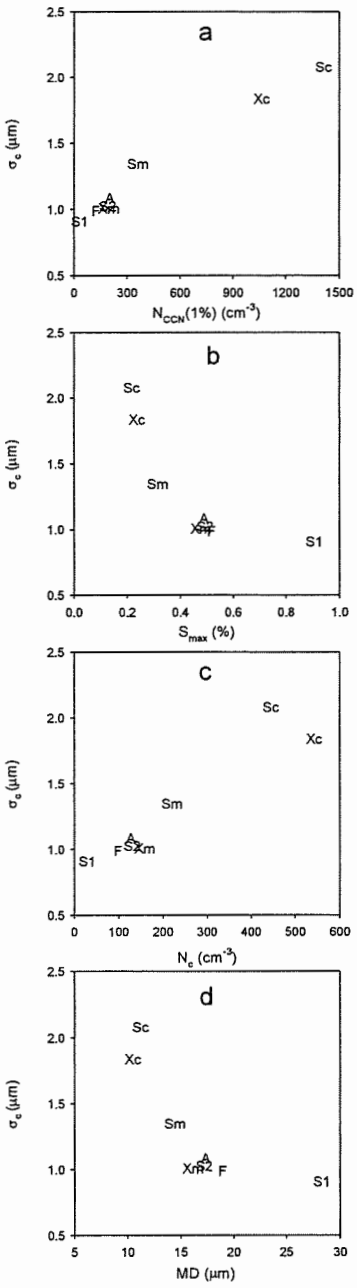

Fig. 1. Relationships between model calculated values of σ_c and other parameters in Table 1. Symbols are identical to project names in Table 1.

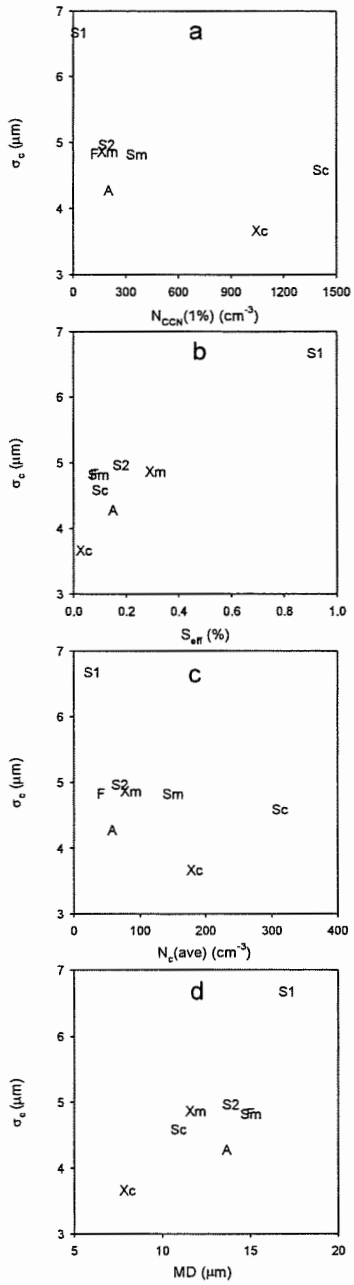

Fig. 2 Same as Fig. 1 except project or air mass averages.

deviation of diameter (σ_c) after 150 m ascent under the same updraft condition. In Table 1, the N_c is generally higher for more continental (i.e., higher N_{CCN}) clouds although the S_{max} is in reverse order, indicating that CCN are more readily activated in more continental clouds because of relative abundance of lower critical supersaturation (S_c) (i.e., larger in size) CCN. The reason for low S_{max} for more continental clouds is because of more intense competition for available water vapor among the more numerous activated droplets. For the same reason, MD is smaller for clouds with higher N_c.

Relationships between σ_c and other parameters in Table 1 are shown in Fig. 1. An

interesting feature is that σ_c is larger for lower S_{max} (Fig. 1b); that is, for more continental clouds (Fig. 1a). Although droplets are smaller in sizes, droplet spectra are broader in these clouds (Fig. 1d). Yum(1998) demonstrated that the differences in growth rates between different size droplets are smaller for lower S. Cloud droplets in more continental clouds experience lower S during growth and therefore less narrow droplet spectra (Fig. 1a).

Fig. 2 shows corresponding relationships for observed data from the same field projects or air masses listed in Table 1. Here all parameters are averages for a project or an air mass. In Fig. 2, S_{eff} is the effective supersaturation (Hudson, 1984) based on the average cloud droplet concentration, N_c(ave). All corresponding panels in Figs. 1 and 2 show exactly the opposite trends. These contrasting results are possible because all cloud microphysical parameters except σ_c show the same trends between observations and model calculations. The discrepancies in magnitude are also notable but the most conspicuous difference is for σ_c. From model calculations σ_c is barely over 2 μm for the largest but in observations all exceed 3.5 μm and the largest is close to 7 μm.

3. 2 Different updraft conditions

For the same CCN spectra, w determines supersaturation in a cloud parcel, and thus the activated droplet concentration. Fig. 3 (see "calculated") shows some of the important cloud microphysical relationships at the cloud altitude of 150 m for the 29 cloud parcels ascent under 29 different updrafts that ranged from 10 to 200 cm s^{-1}. The input CCN spectrum for these runs is taken from "A" project (Table 1). In Fig. 3, cloud parcels with stronger w appear in higher N_c, smaller MD, and smaller σ_c regions. Stronger w produces higher S_{max} and therefore activates more CCN, and thus higher N_c. Droplets in cloud parcels with stronger updrafts are smaller since more activated droplets are competing for the available water vapor. Moreover, droplet spectra are narrower in these cloud parcels because higher S makes the spectra narrower faster (Yum, 1998). This means that there should be a positive relationship between MD and σ_c when the droplet spectra of the adiabatic cloud parcels that ascend under different w are compared at a constant cloud altitude (Fig. 3c). Broader spectra and larger MD for lower w parcels suggest that lower w is more favorable for initiating gravitational collection process.

Also shown in Fig. 3 is the observed cloud microphysical relationships (see "observed") for near adiabatic cloud parcels taken from a horizontal penetration through an extensive clouds at about 200 m cloud altitude. There are 35 data points for observation and each represents individual 1 s averages. However, these data are not taken from one continuous segment of the cloud but from four different segments that are separated by considerable distance. In Fig. 3a, MD for the observed near adiabatic cloud parcels shows the

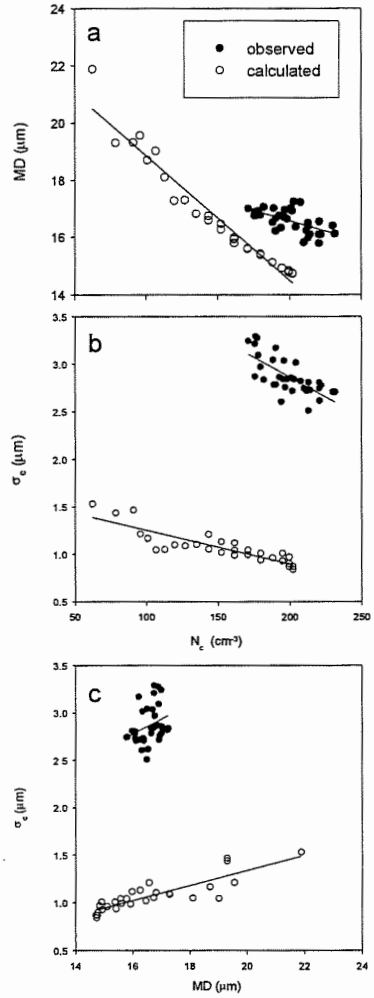

Fig. 3. Comparisons of the three cloud microphysical relationships between observed near adiabatic parcels and the model calculation at a similar altitude.

tendency to decrease as N_c increases. Clearly observed droplet spectra are broader (larger σ_c) for parcels with lower N_c (Fig. 3b). The observed σ_c tends to become larger as MD increases (Fig. 3c). All three observed relationships are similar in trends to those for the model calculations. Unlike the model calculations, however, the w in the observed parcels had no correlations (not shown) with each of the three parameters displayed in Fig. 3. This may not be fully expected since the w that is the most relevant should be the w at the near cloud base altitudes, especially for N_c. In Fig. 3, direct comparisons of magnitudes between observations and model calculations are fundamentally difficult. The MD and σ_c are functions of cloud altitude for adiabatic clouds (i.e., MD increases and σ_c decreases with altitude) but the cloud altitudes for the observed parcels were

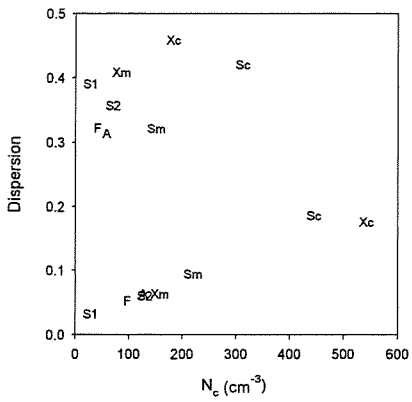

Fig. 4. Observed (data in the upper region) and model calculated dispersions (σ_c/MD) as a function of cloud droplet concentrations.

not exactly known. However, notable is the large difference in magnitude of σ_c that may not be explained only by the difference in cloud altitudes between the two. The model calculated N_c spanning much wider ranges may also indicates that the w at the near cloud base altitudes for the observed parcels might not have varied as widely as 10-200 cm s^{-1}, especially to the lower end.

4. DISCUSSION

The observed cloud microphysical parameters in Fig. 2 reflect various other processes than just condensational growth of droplets that may have occurred in the clouds, such as entrainment of outside clear air and evaporation, mixing between in-cloud parcels, and gravitational collection between large drops and droplets. All these processes add up to determine cloud droplet size spectrum. It has been suggested that these processes are associated with droplet spectral broadening (e.g., Beard and Ochs, 1993), and may indeed explain most of the discrepancies in magnitude of σ_c between Figs. 1 and 2). Perhaps the bigger discrepancy is in the trend of σ_c: observations showed larger σ_c for more maritime (i.e., lower CCN) clouds, contrary to model calculations. It is notable here that MD exceeded or were close to 15 μm, the drizzle threshold (e.g., Hudson and Yum, 2001), for most of maritime clouds (Fig. 2d). This implies that gravitational collection process should have played a crucial role to broaden cloud droplet spectrum for more maritime clouds. The model also calculated that MD were larger than 15 μm for most of the maritime clouds (Fig. 1d) but σ_c were smaller than those of continental clouds because gravitational collection process was never considered.

Dispersion (σ_c/MD) is sometimes used as a measure of broadness of droplet spectrum. Fig. 4 shows that the model calculated dispersions increase with continentality. This is expected since more continental clouds have smaller MD and larger σ_c. Observed dispersions in Fig. 4 generally follow the same trend. However, this trend is basically caused by the smaller MD of more continental clouds but not by larger σ_c (broadness in an absolute sense) for these clouds. Moreover, the more than a factor of two differences in magnitude between observed and model calculated dispersions are difficult to compromise. Liu and Daum (2002) found similar results from a composite plot of various observational studies that included some of the observational results shown here. Liu and Daum (2002) suggested that larger dispersions for more continental clouds act to diminish the cooling effect that is exerted by more reflective continental clouds, adding yet another thought to the indirect aerosol effects (e.g., Twomey, 1977). However, this effect in real clouds does not seem to be as pronounced as the condensation theory predicts.

Acknowledgments.
This work is supported by KOSEF Grant R14-2002-031-01000-0.

References

Beard, K. V., and H. T. Ochs III, 1993: Warm rain initiation: An overview of microphysical mechanisms. *J. Appl. Meteor.*, **32**, 608-625.

Hudson, J.G., 1984: CCN measurements within clouds, *J.Climat. Appl. Meteorol..*, **23**, 42-51.

Hudson, J.G., 1989: An instantaneous CCN spectrometer, *J. Atmos. Oceanic Technol.*, **6**, 1055-1065.

Hudson, J. G., and S. S. Yum, 1997: Droplet spectral broadening in marine stratus. *J. Atmos. Sci.*, **54**, 2642-2642.

Hudson, J. G., and S. S. Yum, 2001: Maritime/continental drizzle contrasts in small cumuli, *J. Atmos. Sci.*, **58**, 915-926.

Liu, Y., and P. H. Daum, 2002: Indirect warming effect from dispersion forcing. *Nature*, **419**, 580-581.

Robinson, N. F., 1984: The efficient numerical calculation of condensational cloud droplet growth, *J. Atmos. Sci.*, **41**, 697-700.

Rogers, R. R., and M. K. Yau, 1989: *A Short Course in Cloud Physics.* Pergamon Press, 293pp.

Twomey, S., 1977: The influence of pollution on the shortwave albedo of clouds. *J. Atmos. Sci.*, **34**, 1149-1152.

Yum, S. S., 1998: Cloud droplet spectral broadening in warm clouds-an observational and model study. Ph. D dissertation, University of Nevada, Reno, 191pp.

Yum, S. S., and J. G. Hudson, 2004: Wintertime/summertime contrasts of cloud condensation nuclei and cloud microphysics over the Southern Ocean. *J. Geophys. Res.*, in press.

THE PHYSICAL CAUSES OF THE VARIABILITY OF DROP SIZE DISTRIBUTIONS

I. Zawadzki and Gyu Won Lee
Department of Atmospheric and Oceanic Sciences, McGill University, Montreal, QC, CANADA

1. INTRODUCTION

Drop size distributions (DSDs) are a subject of interest as old as cloud physics. In this work we will interpret disdrometer observations collocated with a vertically pointing radar in terms of a conceptual model of particle growth. Our main interest here is stratiform precipitation as defined by the presence of a well defined radar bright band.

We distinguish here:

i) The stochastic DSD variability, which we will strive to filter out.

ii) The DSD variability associated with space-time fluctuations of rain rate in which all moments of the DSD may change while maintaining their relationship e.g. one R-Z relationship holds. We will disregard this variability.

iii) Our interest is the DSD variability caused by well identified physical processes that lead to the variability in relationships between two moments of the DSDs (i.e: *R-Z*) around a climatological one.

In order to concentrate on the last, we filter out instrumental noise and "observational noise". By the latter we mean the changes in DSDs due to the fact that small and large drops arriving at ground at any given instant originate at cloud base at positions several kilometers away. This creates a spurious variability that depends on the horizontal gradients of liquid water content and on storm speed of motion.

The filter we use is applied as follows: all DSDs in a time window of one hour are ordered by increasing value of reflectivity and a running mean over 10 consecutive DSDs is performed. We call this Sequential Intensity Filtering Technique (SIFT).

A one-moment scaling normalization is applied to the DSD observations.

$$N(D) = R^{\alpha} g(DR^{-\beta}) \quad \text{with} \quad \alpha = 1 - 4.67\beta \qquad (1)$$

where α and β are two scaling or normalization exponents and $g(x)$ is the normalized DSD defining a generic shape of DSDs. The normalized diameter is defined by $x = DR^{-\beta}$ where *D* [mm] is the diameter of drops. The relationship between α and β is determined by self-consistency of the formulation, that is, by the requirement that the rainfall intensity *R* should be the 3.67th moment of DSD. The exponent in the *R-Z* relationship is $b = 1 + 2.327\beta$ and is independent of the form of $g(x)$. The coefficient in *R-Z* is the 6th moment of $g(x)$. In fact, β determines all exponents in power-laws relating pairs of moments while the moments of $g(x)$ determine the coefficients of these relationships. Of course, the parameter β is not a universal constant and neither is $g(x)$ the same in all situations. Both may change with the processes governing particle growth. A few examples of the relationship between the behavior of DSDs with increasing rain rate and β follow:

a) For the Marshall-Palmer (MP) distribution, N_0 is constant and hence $\alpha = 0, \beta = 0.214$. The DSDs pivot around *D*=0 mm. In this case $b = 1.5$.

b) At equilibrium between coalescence and break-up, all DSDs become multiples of a generic form. Thus, in one-moment scaling normalization, equilibrium DSDs correspond to $\beta = 0, \alpha = 1$. The number concentration increases independently of *D* and *Z* is proportional to *R* (*b*=1).

c) If β becomes negative the number concentration of small drops increases with rain rate faster than the concentration of large drops and *b*<1.

d) α becomes negative for β larger than the M-P value and the DSDs pivot around a diameter *D*>0 mm. For $\alpha < -1$, $\beta > 0.43$ and *b*>2 as it is the case for the Sekhon and Srivastava (1970) distribution for snow particles.

The parameter α describes the change in number concentration while the parameter β describes the growth of particle sizes. In the one-moment scaling normalization, the two are linearly related and the scaling of size and the scaling of number concentration are tied together.

2. THE CONCEPTUAL MODEL

A conceptual model of the physical causes of DSD variability can be best discussed with reference to the conservation equation of the number of precipitating particles, *N* of a given size. In one dimension, for an anelastic atmosphere at rest, and in its simpler form for the source terms, the conservation equation of the number of particles can be written as:

$$\frac{\partial N}{\partial t} = \frac{\partial [N\{w - v(D)\}]}{\partial z} + AC + CC + C[A] + B[F] + \ldots, \quad (2)$$

where w indicates the vertical air velocity. The first term on the right hand side is the vertical differential advection, that is, the effect of drop sorting due to the difference in fall speed with size (sedimentation effect). AC, CC, $C[A]$, $B[F]$ denote conversion of cloud to precipitation through coalescence of cloud droplets, cloud collection by precipitating particles (coalescence or riming), coalescence [aggregation] between raindrops [of snowflakes], and breakup of raindrops [fragmentation of snowflakes], respectively. Other processes, such as evaporation and processes

Corresponding author's address: Isztar Zawadzki, Department of Atmospheric and Oceanic Sciences, 805 Sherbrooke St. O., Montreal, P.Q., H3A 2K6 Canada; E-Mail: isztar.zawadzki@mcgill.ca.

involving hail and graupel could be also included by adding terms representing liquid water collection and water shedding in wet growth. In complex situations, rain falling at ground may have been influenced by a variety of processes and the DSDs behavior may retain an imprint of this complexity.

Most of past simulations with (2) retained coalescence and break-up only. A balance between these two leads to the "equilibrium DSDs" ($\beta = 0$). We can see in (2) that in principle balance between several left side terms is possible, hence leading to other "near-equilibrium", $\beta = 0$ states.

Let us first reduce the concepts of particle growth to their simplest form: the size attained by a particle is determined by its average rate of growth $\overline{\partial D/\partial t}$ and the time it resides in a growth situation (residence time, T). If, say $T \propto 1/D$ and $\overline{\partial D/\partial t} \propto D$, then all sizes grow uniformly and the size distribution moves to the right (as in a balance between sedimentation and cloud collection, resulting in $\beta \approx 0$).

If T is independent of size (that is, the sedimentation term in (2) is neglected) and $\overline{\partial D/\partial t}$ is proportional to diameter, the size distribution pivots around $D = 0$ ($\beta = 0.214$). This is the situation in the so-called "box-model" of (2). Whether this represents growth in a convective situation is debatable, but any process, or a combination of processes, in which $\overline{\partial D/\partial t} \cdot T \propto D$ will lead to pivoting around $N(D = 0)$. For results on modeling these processes see Rogers et al (1991).

At temperatures above –6°C the growth of snow in a cloud-free environment is mainly by aggregation, leading to a size distribution that pivots around the moment proportional to mass-flux. These cases are depicted in Figure 1.

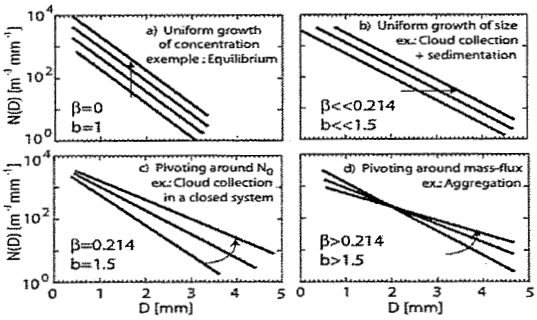

Fig. 1: *Illustration of processes leading to basic changes in size distribution.*

The exact shape of $g(x)$ is determined by the kernel of the right hand side terms in (2) but the main changes in size distributions can be described by these simple concepts. Scaling normalization of all the cases depicted in Fig. 1 leads to a single line but with a different β in each case. Given our emphasis on stratiform rain, processes occurring in snow are the most relevant. In these situation we often have a wet-adiabatic lapse rate over most of the depth of precipitation, growth manly by deposition at temperatures below –6°C and rapid aggregation starting at approximately –6°C (one km above the BB). The changes in DSDs below the melting layer are minimal for low to moderate rates associated with most stratiform rain.

3. CASE EXAMPLES

We start with a reference case (Fig.2a) of a stratiform precipitation in which the sounding indicated a wet-adiabatic profile in the layer above 1km.

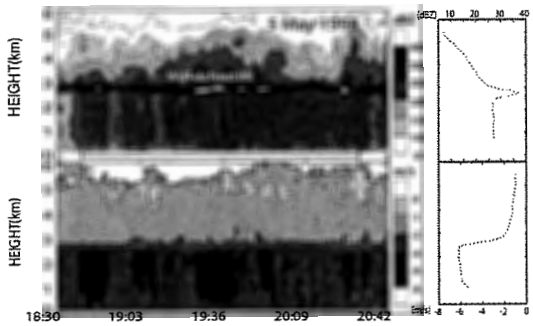

Fig.2a: *time-height section of reflectivity and Doppler velocity in an uneventful stratiform precipitation. Average profiles are also shown.*

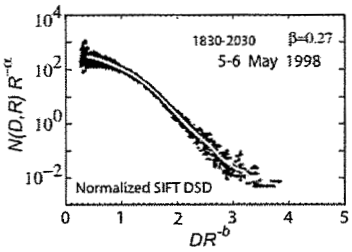

Fig. 2b: *DSDs at ground after applying SIFT filtering and normalization. Dots: individual observations.*

The profile of reflectivity is typical, with the intensity of the BB corresponding to low-density snow; the velocity profile indicates some evaporation below the BB. The small scatter around the normalized DSD in Figure 2b indicates a very uniform situation with little changes in the physical process shaping the DSDs. The behavior is very close to M-P. There is no difference between the first and the second hour of precipitation, both with the same β and the same shape of $g(x)$. This situation will be used as a reference.

A very different situation is depicted in Figure 3a. Here we have a clear case of heavy riming. The average BB intensity is consistent with graupel-like particles for which aggregation is negligible. Growth over the 2 km before melting is dominated by cloud collection (riming). For more detailed interpretation of these profiles see Zawadzki et al (2001). The increased differential fall speed for the heavy rimed particles makes the sedimentation term in (2) more important, that is, the residence time is shorter the larger is the particle.

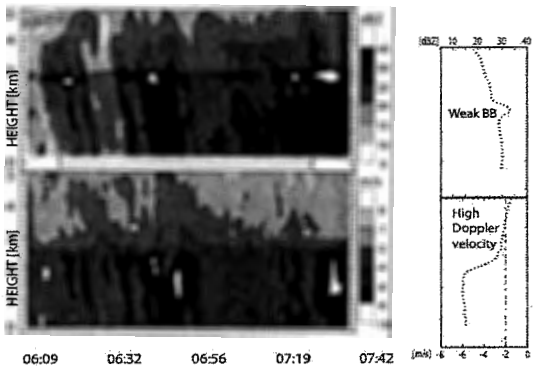

Fig. 3a: *Same as Fig. 2a for a heavy rimed snow.*

As seen in Fig. 3b the DSDs at ground indicate a balance between cloud collection and sedimentation leading to parallel curves with increasing intensity (as in Fig 1b) with small scatter around the average $g(x)$.

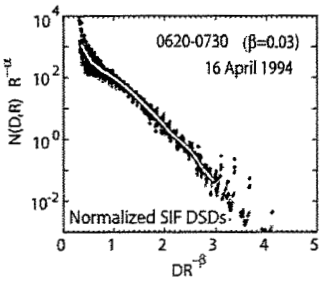

Fig. 3b: *This set of normalized DSDs show "equilibrium" between cloud collection and sedimentation in a graupel precipitation above the BB.*

An opposite situation is depicted in Fig. 4a: A deep layer of aggregation is indicated by a rapid growth of reflectivity at 5 km (2 km above the melting level), fall velocity below 2 m/s down to the melting layer, and by the very intense bright band below, indicative of low-density snow.

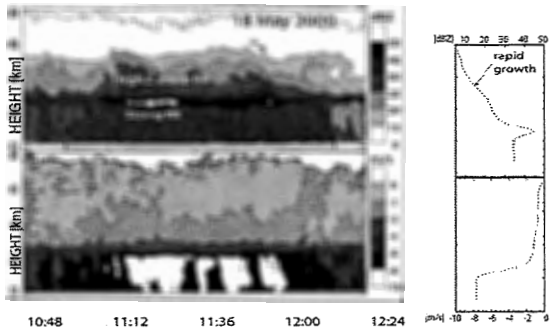

Fig 4a: *Time-height profiles of reflectivity and Doppler velocity for a situation with a deep layer of aggregation. The average profiles are on the right.*

The rapid growth of reflectivity cannot be attributed to riming: this would lead to high-density snow, increased fall velocity and a weak bright band, neither of which is observed here.

Note in Fig.4b the depleted number of small particles consistent with aggregation.

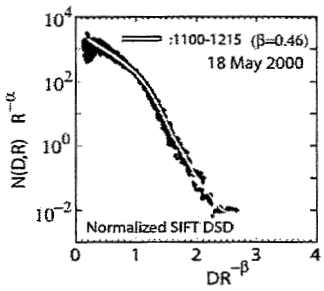

Fig. 4b: *The normalized DSDs for the case of Fig. 4a.*

The next case is more complex (Fig. 5a). It contains periods when the dominant processes of DSDs formation changed in time. During the first period an inversion over the layer 1.5-2.5 km was present. Thus, temperatures between 0 and –6°C extended over 2 km depth. During this period we should expect enhanced aggregation. A general air descent at ~06:50 produced a sudden jump in the BB (with occasional double BB) level restoring the normal depth (on the wet-adiabat) of the 0 to –6°C layer to 1km. In the DSD analysis we eliminated the transition period.

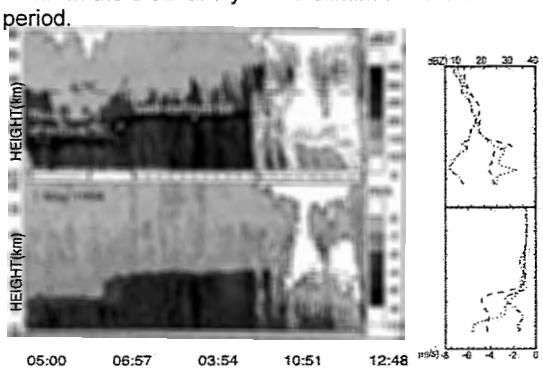

Fig. 5a: *A precipitation event with distinct periods of microphysics. A double BB is present around 07:00.*

The period from 07:30 to 10:20 is similar to Figure 2a. During the period 10:21 to 12:45 a low-level drizzle cell is seeded from above.

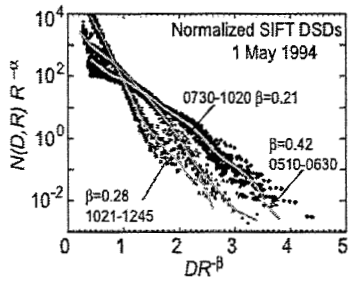

Fig. 5b: *The DSD for the 3 periods in Fig. 5a after applying SIFT and normalization.*

Figure 5b shows the normalized DSDs for the three periods. The first period exhibits a DSDs much like in Fig. 4a with a high value of β. The second period, in spite of the deeper layer of snow growth, and consequent higher precipitation rates, exhibits a

behavior close to the most common conditions (close to M-P value of β). In the drizzle the pivoting seems to occur around a diameter larger than zero.

Finally we will show a convective case for which data were taken in Iowa. No vertically pointing radar was available for this case. Nevertheless, the observed DSDs are not mistakable. They show a very clear case consistent with equilibrium between coalescence and break-up. In Figure 6a, for clarity we show a few of the DSDs in the sequence of intensities together with the function modeled by a "box-model" of the quasi-stochastic growth equation (QSGE). The resemblance in shape is remarkable, even with peaks predicted by the QSGE. The position of these peaks is not at the exact expected diameters and with some variability in position. This is not surprising: some stochasticity in the process is expected.

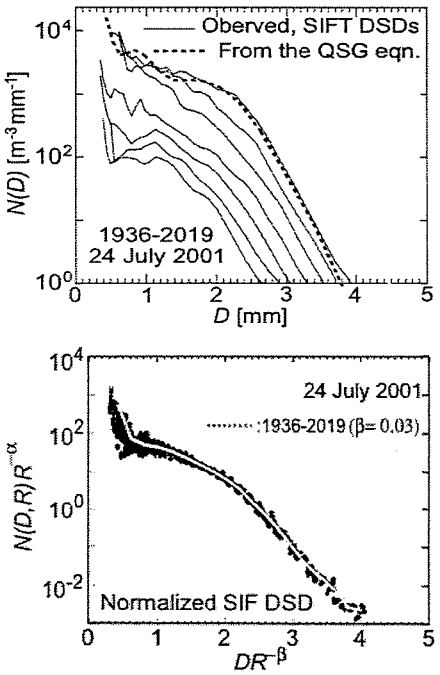

Fig. 6: *DSDs observed in a deep and intense convective system. Above are some of the one-minute observations and below the entire set of data after applying SIFT and normalization.*

It is argued sometimes that the time to establish the balance between coalescence and break-up is insufficient in real situations. Another argument sometimes advanced is that break-up produces local concentration of daughter drops that cannot interact with the rest of the population. The presence of DSDs with characteristics so close to the expected equilibrium DSD indicates that differential fall speed, turbulence, recycling of drops by the updraft (thus approximating the close system of a "box model") makes the balance between cloud collection and break-up possible, even at relatively moderate rates.

4. Discussion

After 50 years of having been introduced, the Marshall-Palmer distribution is still awaiting a solid explanation. The near-exponential DSDs at the large sizes, pivoting around the $N(D=0)$ with changing intensity, is a common occurrence in stratiform rain. It can be observed just below the melting layer. Thus, its origin must be found in snow processes.

If we restrict our attention to weak-to-moderate rates and air vertical motion, w weak enough so that all excess of water vapor with respect to saturation is consumed by snow (i.e. no riming) then growth of precipitation originating in snow can be schematically described as the result of four distinct stages: rapid growth of ice crystals near the top of the system, growth by deposition down to the level of –6°C, aggregation between –6°C and 2°C, and melting. Although not strictly bound to these layers these processes are dominant in each of the layer.

Rate of growth by deposition of precipitating size snow is weakly dependent of size. Thus, the change in size distribution with intensity will closely follow Fig. 1b. The subsequent aggregation will follow Fig. 1d. During melting no additional changes occur in weak to moderate rates. Thus, M-P is the result of these two stages. It is logical that the greater the growth by deposition the greater the subsequent aggregation. Exactly how is it that the perfect balance between growths illustrated in Figs. 1b and 1d leads to Fig. 1c begs a theoretical explanation.

The most extreme variations in DSDs occur around this basic balance. Stronger air vertical motions, leading to cloud formation and snow riming, enhance the stage represented in Fig. 1b and deeper layers of warmer air enhance the aggregation stage. We have seen the extreme examples of the two.

Note that the $g(x)$ in these observation are not perfect straight lines, but all of them, and all of our 5 years of observations are better approximated by an exponential than a gamma shape. A generalized gamma is needed to adjust all the observed $g(x)$ [see Szyrmer et al. elsewhere in these Proceedings].

Convective systems imbedded in stratiform rain and other physical processes affecting DSDs are not discussed here due to the limited space.

5. Acknowledgements

The authors are grateful to Prof. W. Krajewski for taking care of the disdrometer with it was displayed in Iowa.

6. References

Rogers, R., I. Zawadzki and E. Gossard, 1991: Development of drop-size distribution in steady light rain. Quart. J. Royal Met. Soc.**117,**1341-1369.

Zawadzki, I., F. Fabry and W. Szyrmer, 2001: Observations of supercooled water and of secondary ice generation by a vertically pointing X-band Doppler radar. Atmospheric Research, **59-60**, 343-359.

Pyro-cloud over the Amazon as seen from the aircraft. The environment was very turbulent and the aircraft penetrated the cloud falling in complete darkness due to the presence of highly absorbing aerosol and ashes so that instrumental flight had to be engaged. The cloud was a water cloud with no precipitation at all. Courtesy of D. Rosenfeld.

International Conferences on Clouds and Precipitation

1954	I	4-6 October	Zürich, ETH
1960	II	9-13 August	Verona
1961	III	September	Canberra, Sydney
1965	IV	24 May- 1 June	Tokyo, Sapporo
1968	V	26-30 August	Toronto, University of Toronto
1972	VI	August	London, Royal Society
1976	VII	26-30 June	Boulder
1980	VIII	15-19 July	Clermont-Ferrand
1984	IX	21-28 August	Tallinn
1988	X	15-20 August	Bad Homburg
1992	XI	17-21 August	Montreal, McGill
1996	XII	19-23 August	Zürich, ETH
2000	XIII	14-18 August	Reno, DRI
2004	XIV	19-23 July	Bologna, CNR